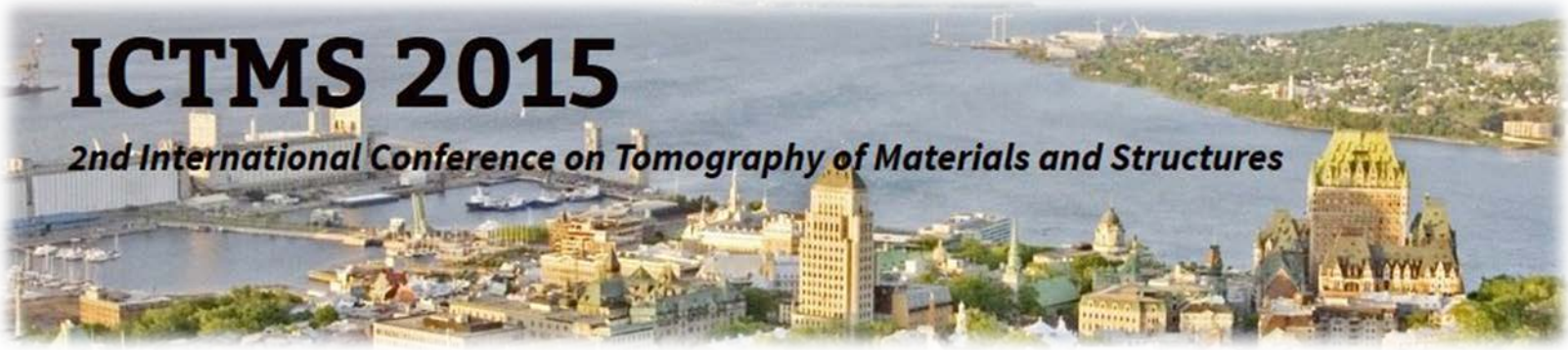

Proceedings

2nd International Conference on Tomography of Materials and Structures

June 29th – July 3rd, 2015

Québec, Canada

INRS
UNIVERSITÉ DE RECHERCHE
A RESEARCH UNIVERSITY

Lab CT Scan
Laboratoire multidisciplinaire de tomodensitométrie
pour les ressources naturelles et le génie civil

Edited by INRS-ETE, August 2015
2nd Edition, January 2017

Bernard Long Editor
ISBN : 978-2-89146-876-3

Contents

Welcome

The conference Organizing Committee welcomes you to the second International Conference on Tomography of Material and Structure. This conference is held every two years. The first one was hosted by the Ghent University in Gent, Belgium, in 2013.

The International Conference on Tomography of Materials and Structures is dedicated to CT-Scanning for non-medical applications. This four full-day congress will bring together an international group of scientists to discuss a broad range of issues related to the use of computed tomography in materials and structures and all its related topics.

The main focus of this conference will be:

- X-ray and neutron tomography acquisition hardware, software and set-ups:
- Advances in reconstruction algorithms:
- 3D image analysis
- Applications of recent advances in CT imaging.
- New equipment (Medical CT, Micro-Scan, Nano-Scan)
- 10 specifics themes including Hydraulics and sediment transport, Geomaterial,
- Materials, Structures and Mineralogy, Wood, Sediments structures, ancient and Modern, Innovative geotechnical Applications, Concrete & building rocks, Porous Material, Hydrogeology, water infiltration and Pollution, Archaeology, Petroleum core analysis

New studies and contributions from universities, governmental agencies and industry are presented.

92 oral presentations and 70 poster presentations will be done. The allocated time for each presentation will be 20 minutes (15 minutes for the presentation itself and 5 minutes for questions).

The abstracts are included inside this program and all the extended abstracts will be provided on a USB stick.

We expect that a special issue of some international journal will be produced to include the 15 more promising papers.

Enjoy the conference, and have a great time in Quebec City, the Oldest city of North America!

ICTMS2015 Organizing Committee

Committees

Chairs:

Prof Dr. Bernard Long – INRS, Québec, Canada (Chair)
Prof Dr. Pierre Francus – INRS, Québec, Canada (Co-chair)

Local organising committee:

Regis Xhardé – INRS
Stéphane Montreuil – INRS
Louis-Frédéric Daigle – INRS
Mathieu Des Roches – INRS
Sally J. Selvadurai – McGill
Geneviève Treyvaud – INRS
Michel Malo – lNRS
Mathieu Duchesne – NRCan, Québec
Richard Martel – lNRS
Corinne B.-Brunelle – INRS

Scientific committee:

Prof Dr. Robert Aller – Stony Brook University, USA
Prof Dr. Khalid Alshibli – University of Tennessee, USA
Prof Dr. Richard W.C. Arnott – University of Ottawa, Canada
Prof Dr. Reginald Auger – Université Laval, Québec, Canada
Dr. Frederic De Beer – NECSA, South Africa
Dr. Dominique Bernard – CNRS, Bordeaux France
Dr. Mattieu Boone – Ghent University, Belgium
Prof Dr. Jean-Yves Buffiere – INSA, Lyon, France
Prof Dr. Leslie Butler – LSU, Baton Rouge, USA
Prof Dr. Jan Carmeliet – ETH Zurich, Switzerland
Prof Dr. Veerle Cnudde – Ghent University, Belgium
Dr. Francesco De Carlo – Argonne National Laboratory, USA
Dr. Dominique Derome – Empa, Zurich, Switzerland
Prof Dr. Philippe Després – Université Laval, Canada
Prof Dr. Jacques Desrues – CNRS, laboratoire 3SR, Grenoble, France
Prof Dr. Subhasis Ghoshal – McGill University, Montréal, Canada
Prof Dr. Giovanni Grasselli – University of Toronto, Canada
Dr. Stephen Hall – Lund University, Sweden
Dr. Ross Harder – Argonne National Laboratory, USA
Prof Dr. Yohsuke Higo – Kyoto University, Japan

Edited by:
INRS-ETE
ISBN- 978-2-89146-847-3

Thanks to our sponsors

Keynote Speakers

Dr. KARL STIERSTORFER (Siemens Healthcare, Forchheim, Germany)

Born in 1963, Karl Stierstorfer studied Physics, finishing with a PhD thesis in the field of many-particle physics in Erlangen. In 1991 he joined Siemens Medical. His first project was the design of a Monte Carlo simulation program for X-ray scatter simulation. The results of this project were the programs MOCASSIM and DRASIM which are still being used in Siemens Medical and by cooperation partners. After joining the business unit CT, Karl Stierstorfer worked mainly in the fields of data preprocessing, CT reconstruction and iterative reconstruction. Since 2007, he is head of the CT physics team which is responsible for concepts of new medical CT scanners. Karl has a list of over 30 publications and holds more than 50 patents.

In this keynote talk, Dr. Stierstorfer will give an overview of the technologies and capabilities of medical CT. Since its invention in the early 1970s, medical Computed Tomography (CT) has gone through a dramatic evolution from a device that could image a patient's head in a scan time of several minutes to a tool that can scan whole patients within a few seconds and is fast enough to image a moving heart. The purpose of this talk is to review the current state of the art in medical CT, to give some examples for advanced medical applications and finally, to present a few examples of scans of non-medical objects.

Dr. GREG BANIAK (BP CANADA, CALGARY CANADA)

Originally from Saskatoon, Saskatchewan, Canada, Greg Baniak completed his B.Sc. Honors degree in Geology from the University of Saskatchewan in 2008. Following this, he moved west to Edmonton, Alberta, Canada where he worked on his PhD under the supervision of Drs. George Pemberton and Murray Gingras. His thesis focused on characterizing permeability and porosity distributions within bioturbated intervals using both carbonates and siliciclastics as case studies. All of his thesis work has been published in peer-reviewed journals such as Sedimentology, Marine and Petroleum Geology, Journal of Sedimentary Research, and Ichnos. Following the completion of his PhD in 2013, Greg moved south to Calgary, Alberta, Canada to begin working full-time as a Petroleum Geologist with BP Canada. Since March 2015, Greg has been seconded from BP Canada to Devon Energy where he is working as a Project Geologist on the joint venture Pike Oil Sands asset.

In this keynote talk, Dr. Baniak will present the application of X-ray micro-CT to bulk reservoir permeability. In the Pine Creek gas field, the primary reservoir intervals occur in the Upper Devonian Wabamun Group. A prominent feature within the Wabamun Group is the presence of the dolomitized burrow fabrics that have permeabilities ranging between 1 and 350 millidarcies (mD), while the adjacent lime mudstone-wackestone have permeabilities of less than 1 mD. To better understand the influence of bioturbation on bulk reservoir permeability, high-resolution X-ray microtomography (micro-CT) and helical computed tomography (helical-CT) imaging techniques were used.

Prof. David Cooper (UNIVERSITY OF SASKATCHEWAN, SASKATOON, CANADA)

Dr. Cooper is an Associate Professor and Canada Research Chair in Synchrotron Bone Imaging within the Department of Anatomy and Cell Biology at the University of Saskatchewan. During his training, he completed two degrees at the University of Saskatchewan, Paleobiology (1998) and Anatomy and Cell Biology (2000), before earning his PhD in Archaeology and Medical Science at the University of Calgary (2005) and then pursuing post-doctorate training at the University of British Columbia within the Centre for Hip Health. Dr. Cooper's interdisciplinary research focuses on high resolution imaging of cortical bone microarchitecture and related applications in the study of bone adaptation, aging and disease. In recent years, these pursuits have increasingly focused on the unique capabilities of synchrotron-based imaging.

In this keynote talk, Dr. Cooper will present the BioMedical Imaging and Therapy (BMIT) facility. This facility provides synchrotron-specific imaging and radiation therapy capabilities. There are two separate endstations used for experiments: the Bending Magnet (BM) 05B1-1 beamline and the Insertion Device (ID) 05ID-2 beamline. Examples of imaging techniques devloped at BMIT include: K-edge subtraction imaging (KES), phase contrast imaging (PCI) and Diffraction Enhanced Imaging (DEI, also known as Analyzer-Based Imaging, or ABI) both in projection and CT modes. The BM endstation provide monochromatic (15-40 keV) or a pink beam (~50 keV peak) for samples up to 50 kg, and the ID endstation extend the program to higher energies (up to 120 keV) and a higher capacity positioning system (up to 450 kg). The beam in both endstations is up to 200 mm wide and 10 mm high. Core research programs include human and animal reproduction, cancer imaging and therapy, spinal cord injury and repair, cardiovascular and lung imaging and disease, bone and cartilage growth and deterioration, mammography, developmental biology, gene expression research as well as the introduction of new imaging methods.

Prof. Oleg Shpyrko (UNIVERSITY OF CALIFORNIA AT SAN DIEGO)

Dr. Shpyrko is associate professor at the department of physics, UC San Diego. He have a PhD in Physics, Harvard University, Department of Physics. PhD Advisor: Prof. Peter S. Pershan in 2004, he was after that Posdoctoral Fellow at Havard University, between 2004 and 2005, and CNM Distinguished Post doctor Argonne National Laboratory, Center for Nanoscale Materials. Advisor: Prof. Eric D. Isaacs, 2005-2007, and Professor at University of California San Diego, Department of Physics, 2007-present.

The center of interest are: Experimental condensed matter physics using scattering probes ; X-ray synchrotron scattering and nanoscale imaging ; Strongly Correlated Systems: Metal-Insulator Transition, Magnetism in Correlated Oxides, Charge and Spin Density Wave systems, Search for Novel High-Temperature Superconducting materials ; Magnetic Thin Films and Nanostructures, Magnetoelectric heterostructures, Magnesium-Ion Battery materials ; Surface and interfacial properties of liquids, soft and biologically relevant materials ; Dynamics and structure of materials in nanoscale

confinement ; Light scattering and microscopy studies of capillary phenomena and self-assembly. Attempts to produce focusing x-ray optics date back to the days of Roentgen, however, it was not until the past decade that X-ray Microscopy has finally been able to achieve sub-100 nm resolution.

In this keynote talk, Dr. Shpyrko will introduce a novel X-ray microscopy technique, which relies on coherent properties of X-ray beams, and eliminates the need for focusing optics altogether, replacing it with a computational algorithm. He has applied this technique to image magnetic domains, as well as to image the distribution of lattice strain in nanostructures. I will also discuss recent results of in-operando imaging of lithium ion diffusion and dislocation dynamics in lithium ion energy storage devices. He will discuss applications of these novel X-ray imaging methods in context of new generation of fully coherent X-ray sources.

Prof Gioacchino (Cino) Viggiani (UNIVERSITÉ JOSEPH FOURIER, GRENOBLE, FRANCE)

Cino Viggiani was born in Napoli (Italy), where he obtained a B.S. in Civil Engineering (1988), a Ph.D. in Geotechnical Engineering at the University of Roma “La Sapienza” (1994), and a H.D.R. (Habilitation) in Mechanics at Université Joseph Fourier, Grenoble, France (2004), where he is full Professor since 2004. In 2012 he was advanced to the rank of Professeur de Classe Exceptionnelle by the French National Council of Universities (CNU). He served in the capacity of Vice-President for Research in Physics and Engineering, and he is the Head of Laboratoire 3SR since 2013. He is Editor of the International Journal Acta Geotechnica (Springer) since 2006. He is the author of about 120 scientific papers and delivered numerous keynotes and invited lectures worldwide. His research involves experimental investigations as well as theoretical and numerical modeling of the behavior of geomaterials, including localized failure and hydro-mechanical coupling. Applications are principally in geoenvironmental, petroleum, and civil engineering. On the experimental side, he has been using quite a range of soils and rock testing apparatus, including plane strain compression devices for soils and rocks equipped with ultrasonic tomography / acoustic emission systems, and a generalized shear apparatus with principal stress rotation. Advanced methods such as Digital Image Correlation and X-ray tomography have been developed, and they are applied to experimentally detect the onset of localized deformation.

In this keynote talk, Dr. Viggiani will discuss about X-ray tomography for granular materials: current trends and perspectives. Combining X-ray tomography and three-dimensional (3D) image analysis has finally opened the way for experimental micro-(geo)mechanics, allowing access to different scales of interest. When these correspond to a scale that has been imaged at high spatial resolution, high-quality measurements can be obtained (*e.g.*, 3D displacements and rotations of individual grains of sand sample under load). However, there are issues when the scale of interest is smaller, for example the characterization of grain-to-grain contacts (their orientations and evolution) or production of fines by grain breakage. This paper presents a short selection of new grain-scale measurements obtained using existing techniques. The challenges associated with smaller scale measurements on the same images are also discussed through a few examples from ongoing work.

Keynote Speakers

Session 101 - Synchrotron

Session 102 – Micro CT

Session 103 – Interferometry

State University, [6]Center for Advanced Microstructures & Devices, Louisiana State University, Baton Rouge, LA, and [7]Department of Chemistry, College of Science, Louisiana State University, USA.

Session 201 - Advance in reconstruction algorithms

Session 202 - Geotechnic

Session 203 - Multi-tissue quantitative imaging technique

Session 204 - 3D imaging

[2]MINES ParisTech, PSL Research University, MAT - Centre des matériaux, CNRS UMR 7633, France [3]ANKA/Institute for Photon Science and Synchrotron Radiation, Karlsruhe Institute of Technology (KIT), Germany, [4]European Synchrotron Radiation Facility (ESRF), BP 220, Grenoble Cedex, France.

Session 205 - Developing image analysis tools for synchrotron

IIS/EZRT/AMS/RBV, Fuerth, Germany.

Page 369 **(210): In-situ 3D nano-imaging at the advanced photon source** *by V. De Andrade, M. Wojcik, D. Gursoy, A. Deriy, F. De Carlo from Advanced Photon Source, Argonne National Laboratory, Lemont, Il, USA.*

Session 301 - Hydraulics and sediment transport

Pages 370-374 **(194): X-ray measurement of sand ripples bedload transport** *by S. Montreui, B.Long from INRS-ETE, Québec, QC. Canada.*

Pages 375-378 **(199): The internal density structure of sediment-propelled turbidity currents as revealed by CT imagery** *by R. W. C. Arnott[1], M. Tilston[1], C. Rennie[1], B. Long[2] from [1]Ottawa University, Ottawa, ON., Canada, [2]INRS-ETE, Québec, QC. Canada.*

Pages 379-382 **(203): The influence of grain size on the velocity and sediment concentration profiles and depositional record of turbidity currents** *by M. Tilston[1], R.W.C. Arnott[1], C. D. Rennie[2], B. Long[3] from [1]Department of Earth Sciences, University of Ottawa, Ottawa ON, Canada, [2]Department of Civil Engineering, University of Ottawa, Ottawa, ON, Canada, and [3]Centre Eau Terre Environnement, INRS, Québec City QC Canada.*

Pages 383-387 **(118): Wave-sediment interaction imaging with X-ray tomography: A small-scale experiment to characterize the artefacts** *by C. B. Brunelle[1], B. Long[1], Pi. Francus[1], L. F. Daigle[1], M. Des Roches[1], H. Takayama[2] from INRS-ETE, Québec, Canada and [2]Kumamoto University, Japan.*

Session 302 - Geomaterial, materials, structures and mineralogy

Page 388 **(006): Through-porosity induced corrosion under a Fe-based amorphous coating revealed by in-situ X-ray tomography** *by *S. G.Wang[1], S. D. Zhang[1], J. Q.Wang[1], S. C.Wang[1], L. Zhang[1] from [1]Shenyang National Laboratory for Materials Science, Institute of Metal Research, China and Academy of Sciences, Shenyang, PR China.*

Pages 389-393 **(007): Characterization of three-dimensional fatigue pre-crack propagation for 316L stainless steel with lab-based X-ray tomography** *by *S. G.Wang[1], L. Xiong[1], S. C.Wang[1], L. Zhang[1] from [1]Shenyang National Laboratory for Materials Science, Institute of Metal Research, Chinese and Academy of Sciences, Shenyang, PR China.*

Pages 394-398 **(020): Microstructural characterization of SiC foams used as solar absorber devices** *by J. Mollicone[1], *B. Duployer[1], P. Lenormand[1], C. Tenailleau[1], J. Vicente[2], F. Ansart[1] from [1]CIRIMAT, UMR - CNRS 5085, Université de Toulouse, Toulouse, France and [2]Laboratoire IUSTI, Marseille, France.*

Session 303 - Wood

Session 304 - Sedimentary structures: modern and ancients

Session 306 - Innovative geotechnical applications

Session 308 - Concrete & building rocks

Session 309 - Porous material

Session 310 - Hydrogeology, water infiltration and pollution

Session 311 - Archaeology

Session 313 - Petroleum core analysis

I.A. VARFOLOMEEV[1,2], B.D. SHARCHILEV[1], D.A. LISICIN[1,2], * I.V. YAKIMCHUK[1]
[1] Schlumberger, Moscow, Russia
[2] Moscow Institute of Physics and Technology, Dolgoprudny, Russia

What medical CT can do for material science (and what not)

K. STIERSTORFER

Siemens Healthcare, Siemensstr. 1, D 91301 Forchheim, Germany – karl.stierstorfer@siemens.com

Keywords: Computed Tomography, spatial resolution, temporal resolution

Abstract

Since its invention in the early 1970s, medical Computed Tomography (CT) has gone through a dramatic evolution from a device that could image a patient's head in a scan time of several minutes to a tool that can scan whole patients within a few seconds and is fast enough to image a moving heart. The purpose of this talk is to give an overview of the technologies and capabilities of medical CT. The current state of the art in medical CT is reviewed and some examples for advanced medical applications are given. Finally, a few examples of scans of non-medical objects are presented.

Introduction: What is that that makes CT so successful in medical diagnosis?

In over 40 years of development, medical CT has evolved into one of the most important workhorses in medical imaging.

The reasons for this success are manifold:

- CT has excellent capabilities to resolve small contrast differences,
- the imaging technique is fast and robust,
- injection of contrast agent enables the imaging of blood vessels,
- the so-called Hounsfield scale which fixes the displayed pixel values at air (-1000 HU) and water (0 HU) enables quantitative assessment of CT images,
- the spatial resolution is well adapted to the needs of clinical imaging,
- the temporal resolution can be high enough to image even moving organs, including the heart,
- there is virtually no geometric distortion in CT,
- patient radiation doses have been dramatically reduced over the years. For most examinations, they are now significantly below the annual dose received from the natural background radiation.

The state of the art in medical CT

System

All medical CT systems built today are 3rd generation CT systems. This means that an x-ray tube/fan beam detector system rotates around the patient. Rotation times are between 2 s and 0.25 s. Rotation time determines the achievable temporal resolution and thus is a major differentiator between systems. The patient is moved through a funnel with an opening diameter between 70 and 80 cm. The most frequently used scan mode is a spiral or helical scan where the patient table is moved continuously while the

tube/detector system is rotating. Scan ranges are up to 200 cm, limited by the patient table. The diameter of the scannable field of view is typically 50 cm. Due to the high tube power and the low efficiency of the x-ray tubes, the systems need substantial cooling which can be accomplished either by air-only cooling or by using the hospital water supply. The data are continuously transferred from the rotating part to the stationary reconstructing units. Typically, between 1000 and 2000 full detector readouts per rotation have to be transmitted, leading to data rates up to several Gbit/s.

X-ray Tube

Due to the high tube powers necessary, all tubes used in clinical CT scanners are rotating anode tubes. Tube powers may vary between 40 and 120 kW. Tube power is another major differentiator between CT systems. Tube voltages are between 70 and 150 kV. Only a number of fixed voltages is usable, e.g. 80, 100, 120 and 140 kV. The focus size, which is an important ingredient for achieving good resolution, is of the order of 0.6 – 1.5 mm. Many tubes offer a number of different focal spot sizes, thus allowing the navigation of the trade-off between tube power and resolution. Medical CT tubes are optimized for scan times between 2 and 15 s. Some systems make use of a so-called *flying focal spot,* synchronized with the detector readout, in order to improve the data sampling.

Detector array

CT detectors are 2D arrays located on an arc, concentric to the focal spot, covering a certain distance along the patient length direction and containing several rows. The number of detector rows or the coverage, respectively, are major differentiators between CT systems. Mid-range systems now use 64 rows, covering 4 cm. The number of detector channels along the arc is an important factor for the achievable resolution. Most systems use between 650 and 950 channels per row. CT detectors are satisfying very tight specifications concerning dynamic range, linearity and stability. Modern detectors all follow the scintillator-photodiode principle: the x-ray quanta are converted into visible light in a scintillator which absorbs most of the quanta; the optical photons are converted to electrical charge in a scintillator array. The electric charge is eventually converted into a digital signal. Detectors with direct conversion from x-ray quanta to electrons in an x-ray absorbing semiconductor (e.g. CdTe) which are also capable of counting individual photons are currently being investigated. Antiscatter collimators in front of the detector reject scattered radiation which would otherwise significantly deteriorate the image quality.

Image reconstruction

For the reconstruction of images out of the measured data, most clinical CT systems use variants of the filtered backprojection algorithm. The main steps of this approximate algorithm are filtering the data with a ramp-like filter, followed by a projection of the data back into the volume.

Prior to reconstruction, the data have to be cleaned from detector and system imperfections, e.g. by division by data from an air scan. One of the preprocessing steps also takes care of the beam hardening effect, albeit only for water – patients can be considered as water as a first approximation.

Many vendors now offer so-called iterative reconstruction algorithms: The image volume from a first reconstruction is used to create virtual raw data by forward projection. These can be compared with the original data and used in a feedback loop to improve the first reconstruction. This technique has been shown to be capable of removing artifacts due to the fact that the initial reconstruction algorithm is non-exact. A regularization term in the feedback loop can also reduce the image noise.

The user can influence the reconstruction in a number of ways, e.g.

- by choosing the reconstruction kernel (algorithm), thus navigating the noise vs. sharpness trade-off,
- by choosing the position and thickness of the reconstructed image slices,
- by choosing the reconstructed field of view which also affects the achievable resolution.

Reconstruction speed is typically several images per second. There is a number of special reconstruction features, available on many systems, including

- iterative correction of beam hardening artifacts originating from bony structures,
- metal artifact correction algorithms venturing to avoid artifacts from metal structures like dental fillings or hip implants,
- time gated reconstructions, controlled by an external trigger.

Some typical medical applications

To illustrate the clinical versatility of CT, a number of advanced applications is briefly described here:

- Contrast-enhanced CT angiography: In order to display blood vessels in a CT scan, a well-defined solution of contrast agent (typically iodine loaded solutions) is injected in a vein. After a certain delay, the scan is started. In the CT image, blood vessels show up as hyperdense structures. Stenoses can be seen as a thinning or interruption of the imaged vessel.
- Cardiac CT: There are two main techniques to image the beating heart: i) Cardiac sequence: no continuous table movement; the scan is triggered by the ECG (electrocardiogramm) signal. One stack of images is produced from the scan. After a successful scan, the table moves to the next position. ii) Cardiac spiral: continuous table movement; only the data taken during the cardiac rest phases are used. The table moves slow enough so that the image stacks overlap. Cardiac scanning is either done with contrast agent as angiography of the coronary vessels, in order to detect stenoses, or without contrast agent as calcium scoring, in order to detect calcifications in the coronary vessels which are indicators of coronary heart disease.
- Volume perfusion CT: In the case of a stroke it is necessary to assess the provisioning of blood for critical tissues. To accomplish this, a contrast agent is administered and the temporal change of the contrast agent concentration in the volume is monitored by repeated CT scanning. This can be done either with a detector covering the whole volume in question or with a repeated back and forth movement of the table.
- Dual Energy CT: Except for air and water, the reconstructed attenuation (HU) values of materials depend on the x-ray energy spectrum used for imaging. Hence a combination of various spectra can provide information beyond morphological density. Examples for this are i) the differentiation between bone and contrast agent, ii) the differentiation between various types of kidnes stones, iii) the detection of uric acid in gout cases. Various techniques are being used to achieve spectral variations including rapid switching of the tube voltage, using different filtrations in the beam, dual layer detectors, or dual source CT with different tube voltages.

Limitations of medical CT for non-medical applications

Certainly limitations of medical CT have to be considered when it comes to using it for non-medical applications:

- The system geometry is fixed,
- the beam hardening correction is optimized for water,
- the tube voltage is limited to 140 or 150 kV,
- the user interface is made for medical users,
- the image format is DICOM, a standard for medical images, jpeg exporting is possible,
- systems will typically be sold to non-medical customers on a take-it-or-leave-it basis
- regulatory system release is for medical usage. Issues may arise for other usages.

Sample images from some non-medical objects

In order to demonstrate the non-medical usage of CT, a few objects were scanned which might be of interest for material scientists. Figure 1 shows a photo of a pebble sample showing white quartz veins. Scanning this pebble in a CT scanner reveals the internal structure nicely. The white quartz veins appear as hyperdense structures (figure 2).

Pebble sample

Figure 1: Photo of the pebble sample

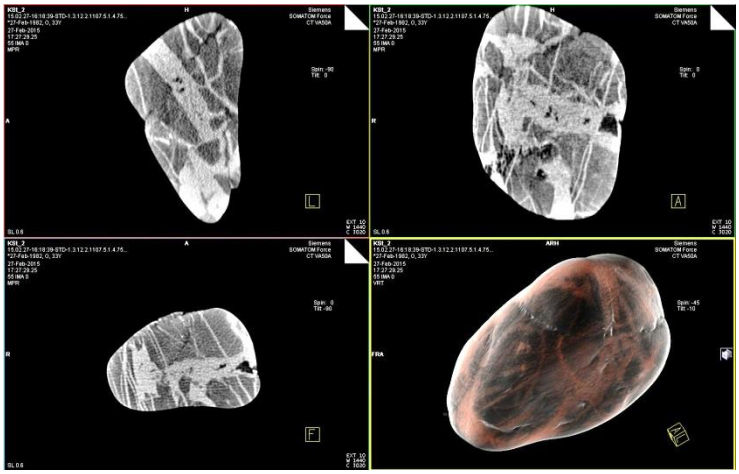

Figure 2: Three orthogonal cross sections and a volume rendering of the reconstructed pebble.

Oyster shell sample

Another object, an oyster shell sample, is depicted in figure 3. Scanned on a Siemens Somatom Force in the so-called ultrahigh resolution mode, its layered structure is nicely resolved (figure 4). The ultra-high resolution mode uses the smallest achievable focal spot sizes in combination with a reduced aperture of the detector array. This allows the resolution of structures as small as 0.16 mm with a medical CT system.

Figure 3: Photo of the oyster sample

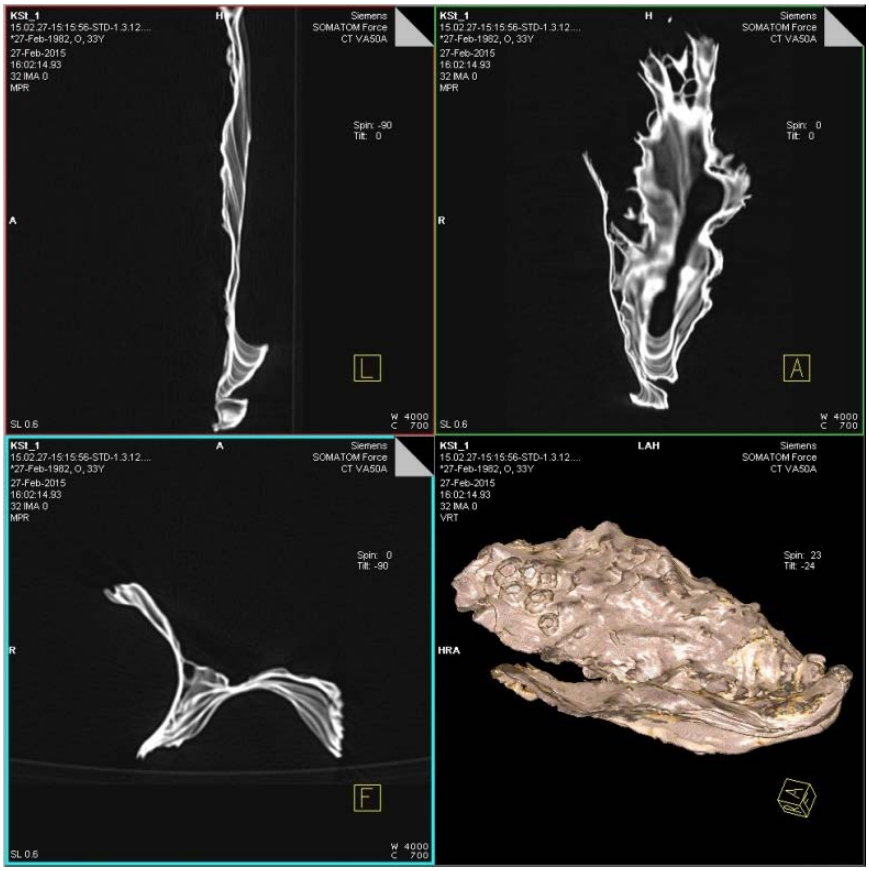

Figure 4: Three orthogonal cross sections and a volume rendering of the reconstructed oyster sample.

Characterization of Reservoir Quality in the Upper Devonian Wabamun Group using Micro-CT and Helical-CT Imaging Techniques

G.M. Baniak[1]

[1] BP Canada Energy Group, 240-4th Avenue SW, Calgary, AB, Canada – Greg.Baniak@bp.com

Keywords: Ichnology, Carbonates, Dolomitized Burrows, Micro-CT, Helical-CT

Abstract

In the Pine Creek gas field, the primary reservoir intervals occur in the Upper Devonian Wabamun Group. A prominent feature within the Wabamun Group is the presence of the dolomitized burrow fabrics that have permeabilities ranging between 1 and 350 millidarcies (mD), while the adjacent lime mudstone-wackestone have permeabilities of less than 1 mD. To better understand the influence of bioturbation on bulk reservoir permeability, high-resolution X-ray microtomography (micro-CT) and helical computed tomography (helical-CT) imaging techniques were used.

Introduction

The Pine Creek gas field (Townships 56-58 and Ranges 19-20 west of the fourth meridian) is located in central Alberta, Canada, roughly 110 km east of the Rocky Mountains (Fig. 1). Within the study area, bioturbated mudstones-wackestones and peloidal grainstones-packstones have been identified by Fong et al. (2001) and Green and Mountjoy (2005) as the primary reservoir facies. Further to this point, the bioturbated mudstones-wackestone form the primary reservoir intervals (Baniak et al., 2013) and therefore represents the primary focus for this study.

Methods

For micro-CT scanning, a SkyScan 1172 Desktop X-ray microtomograph was used (Fig. 2A-B). The core sample size used was approximately 2.5 cm in height and 1.0 cm in width. The X-ray point source was operated at 110 kV and 250 mA. Aluminum-copper and aluminum filters were applied, when necessary, to reduce beam hardening and allow for clearer images. The transmission X-ray images were acquired as the core sample on the stage rotated through 180° at 0.5° increments. Upon generation, the 2D cross-sectional projections were opened and reconstructed using NRecon and CT-Analyser software (SkyScan, 2005).

For helical CT scanning, an Aquilion 64-Slice Helical Scanner was used (Fig. 2C-D). The core sample size used was approximately 12 cm in height and 8 cm in width and the helical CT was operated at a point source of 110 kV and 250 mA. Unlike the micro-CT, which acquires individual 2-D slices of the sample as it rotates through 180° on the rotary stage, the helical CT acquires a volume of data with the core sample in one position. Upon completion of scanning, the volume data was reconstructed using OsiriX software.

Permeability measurements of the burrows and matrix were obtained using a Core Laboratories PDPK 400 Pressure-Decay Profile Permeameter (Fig. 2E-F). Using this imaging and permeability data, numerical flow simulations were then completed to better understand single-phase fluid in bioturbated media.

Results

The micro-CT and helical-CT images show that the dolomitized burrows are spatially heterogeneous and their dimensions and orientations are highly variable at the

centimeter to millimeter scale (Fig's. 3 and 4). As such, the Wabamun Group is composed of an interconnected network of burrows, with the burrow density and burrow interconnectivity varying considerably throughout the sample. Notably however, horizontal burrow connectivity was found to be more common than vertical burrow connectivity, except in the most pervasively bioturbated sections (i.e., 90 to 100% bioturbation). It was from these high-resolution images that a more detailed and accurate depiction of the bulk reservoir permeability could be constructed using numerical modeling.

Within dual-porosity numerical models (i.e., contrast in permeability between the matrix and burrows is less than two orders of magnitude), bulk permeability was best projected using the geometric mean at low to moderate volumes of burrow dolomite (25-65%) and arithmetic mean at high volumes of burrow dolomite (65-80%). Within dual-permeability numerical models (i.e., contrast in permeability between the matrix and burrows is greater than three orders of magnitude), bulk reservoir permeability is best estimated using the geometric mean at low to moderate volumes of burrow dolomite (10-50%) and arithmetic mean at moderate to high volumes of burrow dolomite (50-80%).

Figures

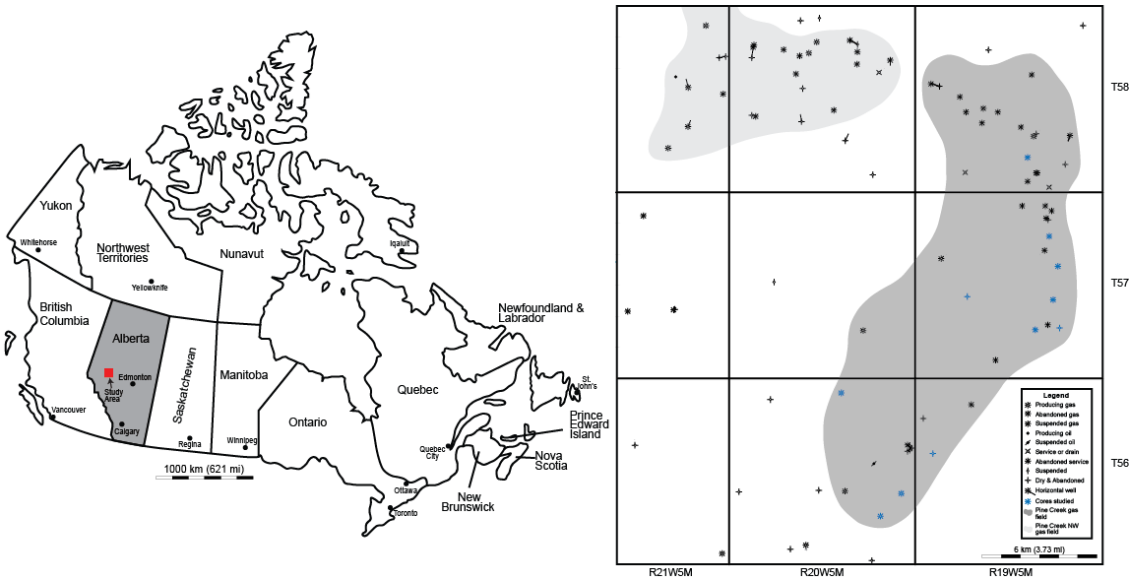

Fig. 1. Location map of Canada (left) demarcating the Pine Creek gas field study area in west-central Alberta (denoted by the red box). The map on the right outlines the 11 cores (in blue) used in this study.

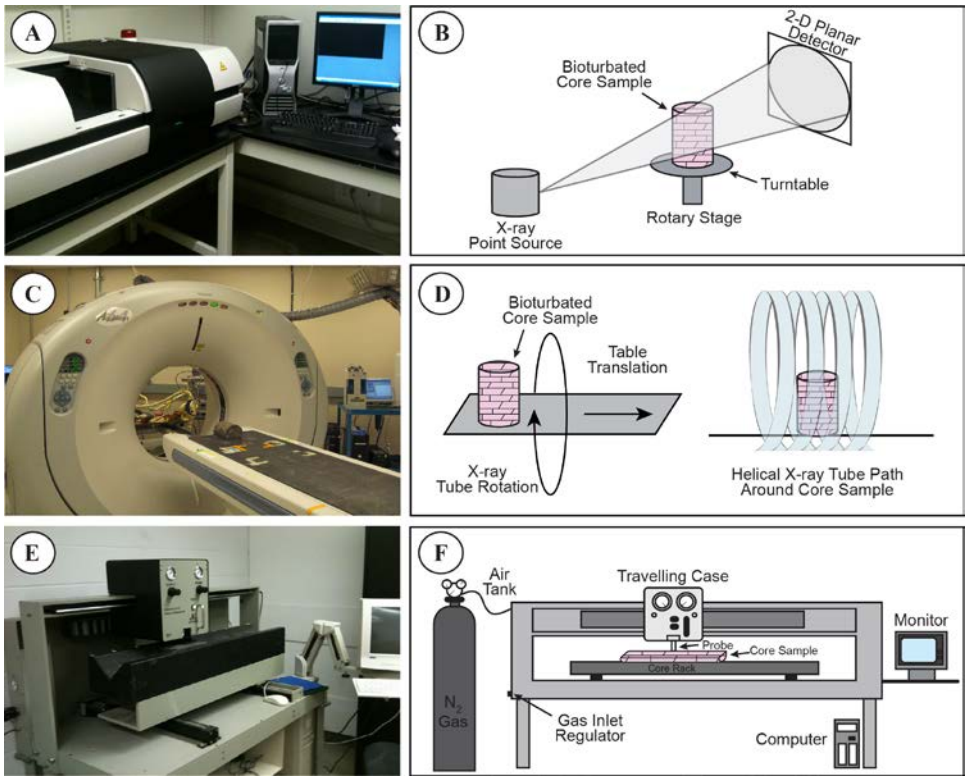

Fig. 2. Devices used to capture scanned images and measure permeability. **A)** SkyScan 1172 Desktop X-ray microtomograph. **B)** The core sample rotates on a stage between a static X-ray source and a detector. **C)** An Aquilion 64-Slice Helical Scanner. **D)** The X-ray tube rotates around the core sample as the core sample and table are moved through the gantry. Modified from Bushberg et al. (2002). **E)** A Core Laboratories PDPK 400 Pressure-Decay Profile Permeameter. **F)** A core sample is placed onto the sliding core rack and a probe injects nitrogen gas into the core sample. Modified from Lemiski (2011). Figure taken from Baniak et al. (2013).

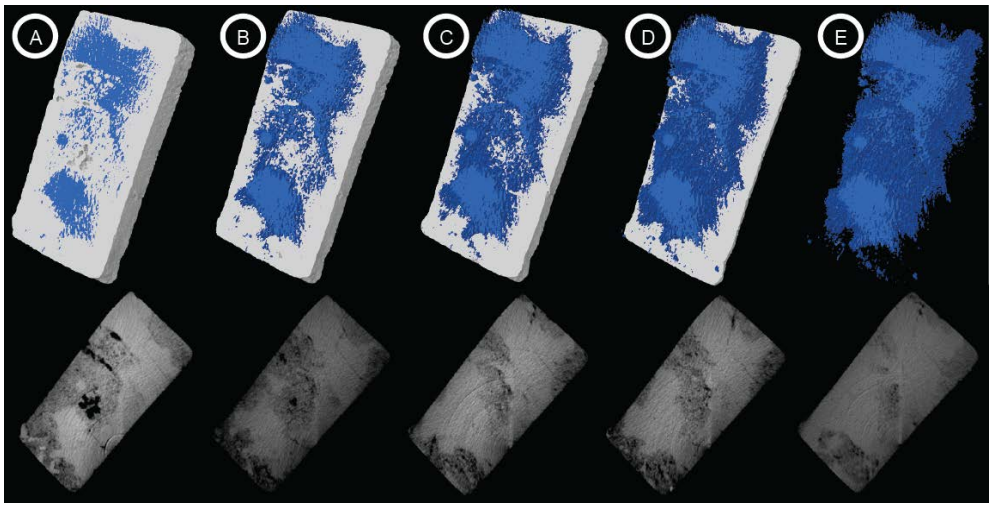

Fig. 3. Micro-CT scans at 34 µm resolution from well 10-10-57-19W5M (3180.32m depth). The images at the top represent 3-D visualization of mineral phases through different cross-sections of the samples (A through E). The burrows are dark blue, matrix is grey, and porosity is the unfilled holes. The images at the bottom are the two-dimensional (2-D) cross-sections (burrows are light grey, matrix is dark grey, and porosity is the black space).

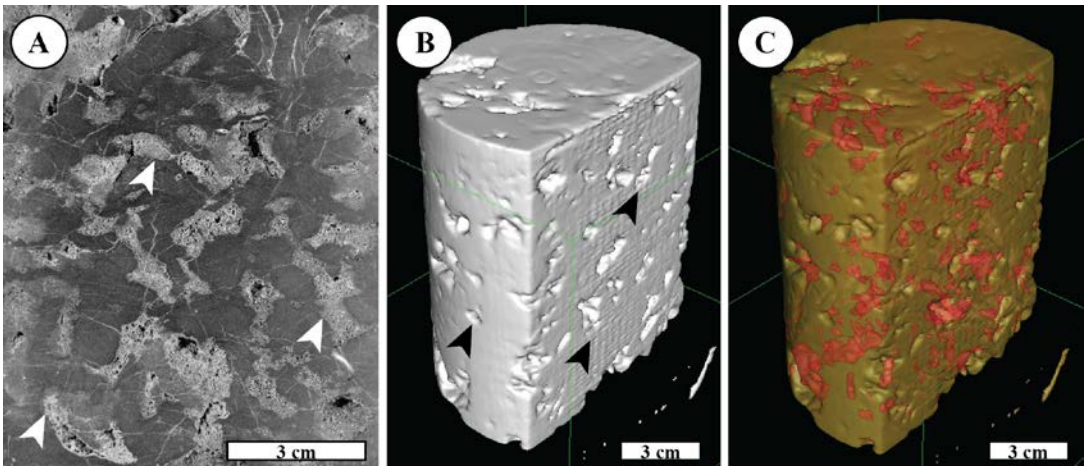

Fig. 4. Wabamun core sample (Facies 1) and associated helical-CT analysis. (A) Core sample scanned with helical-CT. Well 11-26-57-19W5M, depth 3012.80 m. The dolomitized burrows (white arrows; lighter colored rock) are present within a non-dolomitized lime mud matrix (darker, non-mottled rock). (B) 3D visualization of the core sample in Figure 7A. The black arrows highlight macropores associated with burrow dolomitization. (C) 3D visualization of macropores associated with burrow dolomitization within the core sample. The burrow-associated dolomite is highlighted in red color and the lime mud matrix in lime green color.

References

Baniak, G.M., Gingras, M.K. & Pemberton, S.G. (2013). Reservoir characterization of burrow-associated dolomites in the Upper Devonian Wabamun Group, Pine Creek gas field, central Alberta, Canada. **Marine and Petroleum Geology** 48, 275-292.

Bushberg, J.T., Seibert, J.A., Leidholdt Jr., E.M. & Boone, J.M. (2002). The Essential Physics of Medical Scanning, second ed. **Lippincott, Williams and Wilkins**, Baltimore, Maryland, 933 p.

Fong, G., Hunter, I.G. & Bloy, G.R. (2001). Burrow-Mottled Carbonates in the Devonian Wabamun Formation, Pine Creek Gas Field, Alberta, Canada. **Canadian Society of Petroleum Geologists (CSPG) Conference Abstracts**, Calgary, Alberta, 6 p.

Green, D.G. & Mountjoy, E.W. (2005). Fault and conduit controlled burial dolomitization of the Devonian west-central Alberta Deep Basin. **Bulletin of Canadian Petroleum Geology** 53, 101-129.

Lemiski, R.T. (2010). Sedimentology, ichnology, and resource characteristics of the low-permeability Alderson Member, Hatton Gas Pool, Southwest Saskatchewan, Canada (M.Sc. thesis). **University of Alberta**, Edmonton, 131 p.

SkyScan. (2005). SkyScan 1172 Desktop X-Ray Microtomograph. **Instruction Manual**. 53 p.

CT imaging Capabilities at BMIT at the Canadian Light Source

*D.M.L Cooper[1], M. A. Webb[2], G. Belev[3], D. Miller[4], T.W. Wysokinski[5], N. Zhu[6] and D. Chapman[7]

[1]Anatomy and Cell Biology, U. of Saskatchewan, Saskatoon, SK S7N 5E5, Canada - dml.cooper@usask.ca
[2]Canadian Light Source Inc. 44 Innovation Blvd, Saskatoon SK S7N 2V3, Canada- adam.webb@lightsource.ca
[3]Canadian Light Source Inc., - george.belev@lightsource.ca
[4]Canadian Light Source Inc., - denise.miller@lightsource.ca
[5]Canadian Light Source Inc., - tomasz.wysokinski@lightsource.ca
[6]Canadian Light Source Inc., - ning.Zhu@lightsource.ca
[7]Anatomy and Cell Biology, U. of Saskatchewan - dean.chapman@usask.ca
* presenting author

Keywords: Synchrotron, Phase Contrast, K-edge Subtraction, Monochromatic

Introduction

The Canadian Light Source (CLS), located in Saskatoon, Saskatchewan is Canada's national synchrotron facility. The CLS now consits of 14 operating beam lines, each specialized in specific areas of research. Academic scientific access is open to regional, national and international users and is primarily granted via a peer-review process. The facility also conducts industrial research on a fee-for-use basis. Computed Tomography (CT) capabilities have primarily been developed at the BioMedical Imaging and Therapy (BMIT) facility (Fig. 1) of the CLS which focuses on hard X-ray imaging ranging from 15-140 keV [1-5]. This presentation provides an overview of the CT-related infrastructure and capabilities of the BMIT facility, focusing on synchrotron specific approaches.

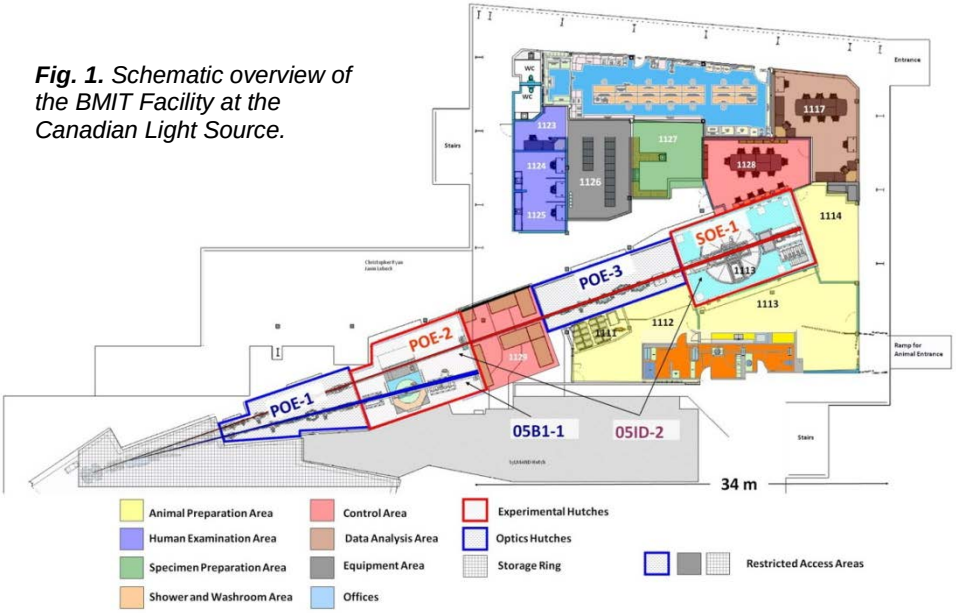

Fig. 1. *Schematic overview of the BMIT Facility at the Canadian Light Source.*

While the core mandate of the BMIT facility lies in the area of biomedical and biological science, its capabilites (including CT) have the potential to advance research in other areas including material science. Thus, while this presentation will utilize largely biological examples to illustrate key opportunities, its overarching objective is to communicate these opportunities to a broader audience. This includes potential users from non-biological fields.

The BMIT facility is comprised of two complementary beam lines based upon a bending magnet (BM) [3] and an insertion device (ID) [4-5] source, respectively:

Bending Magnet (BM) 05B1-1: The BM endstation (Fig. 2) provides monochromatic (15-40 keV) or a pink (polychromatic) beam (~50 keV peak with 1 mm of Cu filtering) for samples up to 50 kg. Maximum resolution is on the order of 2-3 microns with most imaging occuring with voxel sizes ranging from 4 to 100 microns. The maximum size of the beam is 200 mm wide and 7 mm high. Intial experiments on this beamline were conducted in late 2008 and there has been an active user program on 05B1-1 since 2011.

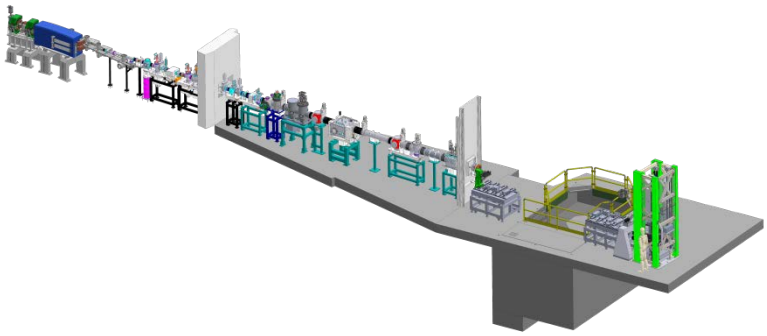

Fig. 2. BMIT Bending Magnet (05B1-1) beamline model

Insertion Device (ID) 05ID-2: The ID SOE-1 endstation (Fig. 3) extends BMIT's capabilities to higher energies (20-140 keV) and a higher capacity positioning system (up to 450 kg) for larger targets. Maximal resolution is similar but somewhat coarser than the BM beamline due to the size of the source. Similar to 05B1-1, the maximal beam size is 220 mm wide and 10 mm high. The ID endstation regular user program started in January 2015 for some imaging modalities (see below).

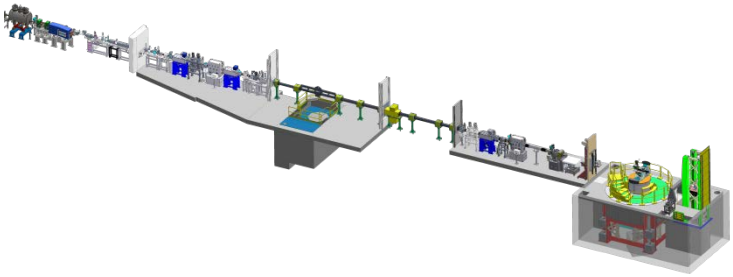

Fig. 3. BMIT Insertion Device (O5ID-2) beamline model

The two BMIT beamlines provide a wide range of possible energies and target sizes and have seen increasing use for CT imaging. A particular focus has been on capitalizing on the strengths of the synchrotron to enhance CT capabilities including phase contrast, analyzer-based imaging, and K-edge subtraction.

Methods

Phase Contrast Imaging (PCI): The primary phase contrast method employed thus far at BMIT has been 'propagation' or 'in-line' phase contrast. The monochromatic and coherent properties of the synchrotron-generated beam allow the simple implementation of this approach by increasing the target-to-dector distance. Large distances (up to 6 m) are possible thanks to the large imaging hutches. PCI has been combined with CT to study a number of different samples at BMIT ranging from soft-tissue targets, to bones,

to materials such as dough and metals. This modality is currently available on both the BM and ID lines.

Analyzer-Based Imaging (ABI): This modality (and related methods such as Diffraction Enhance Imaging or 'DEI') employs an 'analyzer' crystal placed between the target and the detector. In addition to excellent scatter rejection, this crystal provides a means of developing diffraction-based contrast through small alterations in its angular alignment across what is know as the 'rocking curve'. This aproach has been implemented in CT mode at BMIT through the development of a beam monitoring system which enables the position on the rocking curve to be locked [6]. ABI is currently available on the BM line and is in development for the ID line.

K-edge Subtraction (KES): The narrow energy bandwidth and tunability of the monochromatic synchrotron beams provide a powerful means of interrogating samples for differential absorption across attenuation discontinuities associated with the K-edge. In it simplest form, imaging above and below these edges and subtracting the difference provides a means of identifying the location of an individual element within a sample. When implemented in CT mode, this localization is possible in 3D. The method can be highly quantiative through the use of algorithms to compensate for differential absorption created by the background sample and target element of interest. Elements explored by KES at BMIT have included Iodine, xenon, barium and strontium. The wide range of energies possible (15-140 keV) create the possibility of exploring a host of other elements. This dual energy KES approach generally requies two consecutive scans but simultaneous capture is currently being develped at the facility [7]. Again, this method is currently available on the BM line and is in development for the ID line.

Discussion & Conclusions

The BMIT facility provides unique opportunities within Canada for CT utilizing specialized synchrotron modalities. The user community continues to grown and includes researchers from both within and outside the biomedical sciences. The large imaging hutches provide a means for the development of in-line phase contrast but also create the possibility for experiments involving complex and large equipment. The flexibility and dynamic nature of the equipment are simultaneously a great strength and a great challenge. Looking forward, BMIT is adding new capabilities such as a larger vertical beam, faster detectors and access to all the modalities noted on the ID line.

References

1. Chapman LD, (2007) CLSI Doc. No. 26.2.1.1 Rev. 0.A
2. Chapman LD, (2006) CLSI Doc. No. 26.2.1.2 Rev. 0
3. Wysokinski T.W., Chapman D., Adams G., Renier M., Suortti P., and Thomlinson W. (2007) *Beamlines of the biomedical imaging and therapy facility at the Canadian light source—Part 1.* ***Nuclear Instruments and Methods in Physics Research Section A: Accelerators, Spectrometers, Detectors and Associated Equipment***, 582, 1: 73 – 76.
4. *Wysokinski T.W., Chapman D., Adams G., Renier M., Suortti P., and Thomlinson W. Beamlines of the Biomedical Imaging and Therapy Facility at the Canadian Light Source - Part 2.* ***Journal of Physics: Conference Series*** (2013) 425, 7:072013.
5. Wysokinski T.W., Chapman D., Adams G., Renier M., Suortti P., and Thomlinson W., *Beamlines of the biomedical imaging and therapy facility at the Canadian light source – part 3.* ***Nuclear Instruments and Methods in Physics Research Section A: Accelerators, Spectrometers, Detectors and Associated Equipment*****,** (2015) 775, 0:1 – 4.
6. Rhoades G., Belev G., Rosenberg A. and Chapman D. A Novel Analyzer Control System for Diffraction Enhanced Imaging. Journal of Physics: Conference Series. 425 Part 2: 425.
7. Zhu Y., Samadi N., Martinson M., Bassey B., Wei Z., Belev G. and Chapman D. (2014) *Spectral K-edge subtraction imaging.* ***Physics in Medicine and Biology****.* 45, 3:300-311.

Title: Coherent X-ray Nanovision
Speaker: Oleg Shpyrko, Department of Physics, University of California San Diego

Lithium ion batteries are the dominant power source for mobile devices, are increasingly used in hybrid and fully electric cars, and are promising candidates for both stationary and mobile storage in the smart electrical grid that incorporates intermittent renewable energy sources. To fulfill their powerful promise, electrodes with increased capacity, faster charge rates, and minimal capacity fade must be developed. Understanding the nanomechanics due to lithium ion movement and the resulting strain distribution at the individual particle level is a crucial step and key to achieving these ambitious goals.

Among major scientific challenges related to energy storage materials is detailed understanding of nanoscale processes involved in ionic diffusion, as well as deterioration of battery electrodes that happens over many cycles. Repeated charge and discharge cycles involving intercalation and extraction of ions a can lead to inhomogeneous distribution of strain, nucleation of topological defects and structural phase transformations in the electrode, leading to degradation of battery performance. These effects are especially important near surfaces and interfaces, since structural degradation of near-surface region can prevent ions from diffusing deeper into the bulk of the electrode material.

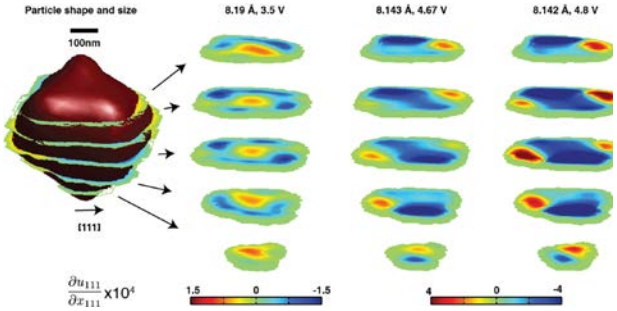

Figure 1. 3D distribution of Li ions within a single cathode particle evaluated at selected cross sections at positions shown by the leftmost figure. Single-particle strain cross sections show the onset of coherency strain and resulting stripe patterns at different voltages corresponding to different lithium concentrations. From Ref. [2]

Morphology of electrode materials can be commonly described as a powder-like distribution of single-crystalline grains, with typical dimensions on the order of hundreds of nanometers. While such materials can maximize the surface-to-volume ratio, they also make it particularly challenging to characterize the nanoscale crystalline strain, distortions, defects or phase transformations during charge-discharge cycling in a working cell electrode, deeply buried in liquid or gel electrolyte. High penetrating ability of hard x-rays makes x-ray diffraction ideally suited for these types of measurements, however, until recently x-ray diffraction lacked spatial resolution needed for these measurements. In the past few years our group has developed advanced Coherent X-ray Diffractive Imaging and Scanning X-ray Nanodiffraction techniques that will allow detailed characterization of nanoscale distribution of crystalline strain, defects, and phase transitions in a single grain of electrode material.

We have used coherent x-ray scattering and in particular Coherent X-ray Diffractive Imaging (CXDI) experiments on operando lithium battery devices during charge/discharge. The approach of CXDI is a lens less alternative to lens-based techniques – the diffraction pattern formed by scattering a coherent x-ray beam from a sample is inverted numerically to form an image of the object. By removing the need for the optics, the spatial resolution achievable is no longer limited by the quality of the optical elements, but by the highest spatial frequencies measured in the x-ray diffraction pattern.

The basic principle of these studies is to apply CXDI in Bragg reflection geometry. The technique is extremely sensitive to the periodic arrangement of atoms and slight variations thereof. Applying in-situ CXDI we reveal three-dimensional (3D) displacement field evolution of a single $LiNi_{0.5}Mn_{1.5}O_4$ nanoparticle in a coin cell battery under operando conditions during charge/discharge cycles. The distribution of the displacement field of these Lithium-ion materials is dominated primarily by the diffusion of the Li ions and by corresponding changes in local value of the lattice parameter. Therefore, 3D distribution of displacement field can be used as indirect, yet highly reliable measure of ionic density distribution at any given time during the charge/discharge process. By repeating these measurements over various parts of the charge cycle we are able to track, in-situ, the diffusion of Li ions within a single grain of electrode material. Our CXDI measurements provide direct observation of both ionic stripe morphologies, which confirm the predictions of coherency strain model at the nanoscale, and phase separation.

The coherency strain argument and phase separation of Lithium-ion-rich and Lithium-ion-poor regions resulting in formation of stripes can be thought of as a balance between entropy, energy associated with strain mismatch, and enthalpy of mixing. We applied the Cahn and Hilliard theory [3,4], which treats the free energy of a non-uniform binary solution as

$$F = N_V \int (f_0(c) + \kappa(\nabla c)^2 + \frac{1}{2}\sigma_{ij}\epsilon_{ij})\, dV, \qquad (1)$$

where the local lithium ion concentration, c, is the order parameter of the phase field model, N_V is the number of molecules per unit volume, $f_0(c) = \Omega c(1-c) + kT[c\log c + (1-c)]\log(1-c))$, where the first term represents enthalpy contribution and the second term represents entropy contribution, κ represents the "gradient energy" that is a function of local composition gradient, and the final term is the elastic energy. The enthalpy term favors phase separation while entropy promotes phase mixing. Spatial concentration modulation is penalized by the gradient and the elastic energy. Simulation of the functional (2) leads to phase separation, despite coherency strain, and the appearance of stripes due to elastic relaxation on the particle boundaries. In maps shown in **Fig. 1**, blue and red represent the Li-rich and Li-poor phases, respectively.

The width of the stripes (see **Fig. 1**) is related to the interfacial energy by a scaling relation, derived from minimization of the free energy functional: $\lambda = 2w = \sqrt{\frac{2\gamma L_c}{\Delta f}}, \gamma \sim 106\, mJ/m^2$. This interfacial energy is similar to $LiFePO_4$. The diffuse width of the stripe boundary, estimated from the images as 50 nm, provides an estimate for the minimum size for two-phase coexistence. Particles below this size should not phase separate, but exist entirely as one phase or the other. Our results suggest the critical size for stripe formation is 50 nm, which provide us with a direct measurement of elastic properties of the electrode materials.

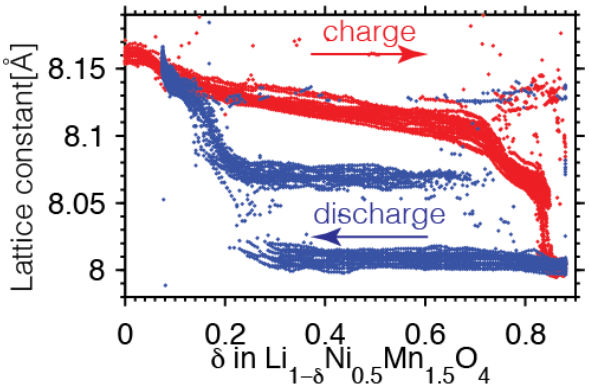

Figure 2. Positions of the Bragg peaks representing different structural phases as a function of lithium concentration. Each point corresponds roughly to a single nanoparticle undergoing charge-discharge cycle. [1]

Since CXDI measurements provide us with full 3D distribution of Li ions (order parameter *c* in Cahn-Hilliard Eq. 1 above), this allows us to determine the overall elastic energy of the particle, and track it's evolution during charge/discharge cycle – therefore mapping out the elastic energy landscape over the entire cycle. Surprisingly, the single nanoparticle elastic energy landscape, which we are able to "map", with femtojoule precision, depends on charge versus discharge, indicating strong degree of hysteresis at the single particle level. This approach opens a powerful new avenue for studying battery nanomechanics, phase transformations, and capacity fade under operando conditions at the single particle level that will enable profound insight into the nanoscale mechanisms that govern electrochemical energy storage systems.

We have also recently studied nonequilibrium structural dynamics in $LiNi_{1/2}Mn_{3/2}O_4$ spinel cathode material during fast charge/discharge under operando conditions using coherent x-ray diffraction. Our in situ measurements reveal a hysteretic behavior of the structure upon cycling and we directly observe the interplay between different transformation mechanisms: solid solution and two-phase reactions at the single nanoparticle level.
For high lithium concentrations solid solution is observed upon both charge and discharge. For low lithium concentration, we find concurrent solid solution and two-phase reactions upon charge, while a pure two-phase reaction is found upon discharge. A delithiation model based on an ionic blockade layer on the particle surface was proposed to explain the distinct structural transformation mechanisms in nonequilibrium conditions. This study addressed the controversy of why two-phase materials show exemplary kinetics and opened new avenues to understand fundamental processes underlying charge transfer, which will be invaluable for developing the next generation battery materials.

Imaging of topological defects in battery nanoparticles

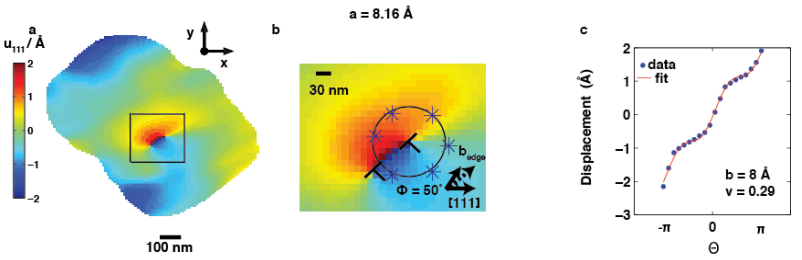

Figure 4: Edge dislocation pairs induced by repeated cycling in a single nanoparticle. Scale bar (color) is displacement field in Å and applies to all color images. (a) shows a cross-section through the particle of the u_{111} displacement field in Å. 2b is magnified region in (a) with Burgers vector orientation relative to [111] sketched. Edge dislocations are indicated by ⊤. Blue stars in (b) correspond to blue points in (c). (c) shows the displacement field plotted as a function of azimuthal angle $\boldsymbol{\theta}$ around dislocation cores defined using standard polar coordinates. The red line is theoretical predictions of the displacement field expected for an edge dislocation, blue points are the data from b). From Ulvestad et al., to appear in Science (2015).

Topological defects are ubiquitous in physics and manifest themselves as magnetic monopoles in quantum field theories and crystallographic imperfections in condensed matter systems. In the latter, the defect properties determine many of the material's properties and as such represent substantial novel opportunities for design and optimization of desired functionalities through deliberate defect engineering and manipulation.

However, this approach of "defect engineering" currently suffers from the lack of suitable nanoscale probes to track buried single defects in-situ and in-operando. The observation of dislocations has been previously achieved with low resolution using techniques such as X-ray topography and reciprocal space mapping. The coherence of third generation synchrotron X-ray beams enabled several new defect imaging technique, including detection of dislocations based

on coherent speckle symmetry analysis, phase contrast tomography, and Bragg X-ray ptychography [5], which was recently used to visualize the displacement field of a dislocation in silicon. For a recent review of defect imaging using coherent methods, see [6]. Bragg CDI [7,8] used by us to image dislocations, relies on interference produced by coherent x-rays coupled and phase retrieval algorithms to reconstruct the 3D electron density and atomic displacement fields in nanocrystals. The displacement field information Bragg CDI provides is complementary to the aforementioned techniques and crucial in identifying the character of single dislocations. Bragg CDI can also track, with nanoscale resolution, buried single defects under operando conditions thereby accelerating defect engineering in materials for energy storage, conversion, and catalysis.

The role of defects, such as dislocations in Lithium-ion battery performance remains largely underexplored, and one of the few areas where materials can be further optimized. On the one hand, the appearance of dislocations correlates with capacity loss as dislocations induce stress and strain. On the other hand, dislocations can relieve strain during phase transformations by allowing the interface between the phases to "decohere", and thus prevent cracking and the associated active material loss and undesirable surface reactions with the electrolyte. In order to understand these nuances, we must first track single defects in operating devices under working conditions. Recently we used Bragg CDI to study single defects in the nanostructured disordered spinel material $LiNi_{0.5}Mn_{1.5}O_4$ (LNMO), see **Figs. 3 and 4**. LNMO is a promising high voltage cathode material in which the lithium diffusion pathway is three-dimensional. In addition, the material exhibits both two-phase coexistence and phase transformations at certain lithium concentrations during charge and discharge as evidenced by both electrochemical and diffraction data. The phases are different in their lattice constant but have the same symmetry group.

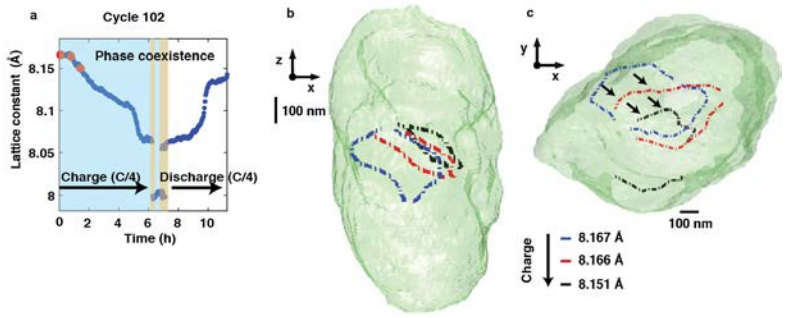

Figure 5. Dislocation dynamics due to ionic currents: (a) data points indicate the lattice constant at which imaging was done, blue shading indicates states with a dislocation. Gold shading highlights two-phase coexistence regions. Red points correspond to the measurement times of the three dislocations shown in (b) and (c). In (b), different dislocation colors correspond to images taken at three different charge states, indicated by their lattice constant, while the green surface represents the overall shape of the particle. The arrow indicates temporal evolution. (c) is the projection of (b) along the z direction. From Ulvestad et al., to appear in Science (2015).

Using Bragg CXDI, we were able to capture dislocation dynamics in 3D during charging and discharging (**Fig. 5**) and find that the movement of the dislocations is associated with charge transport. We further observe the dislocation act as a nucleation point during the structural phase transformation. Using the dislocation field as a local nanoprobe of elastic properties, we find that the surrounding region enters a regime of negative Poisson's ratio, so-called auxetic, regime at high voltage.

Dislocation imaging is thus a powerful nanotechnology in the form of a highly localized probe of a material's elastic properties that are otherwise difficult to measure, and it opens a new, powerful avenue for facilitating improvement and rational design of nanostructured materials.

References:

[1] A. Singer, A. P. Ulvestad, H.-M. Cho, J. W. Kim, J. Maser, R. Harder, Y. S. Meng, and O. G. Shpyrko, "Non-equilibrium structural dynamics of nanoparticles in LiNi1/2Mn3/2O4 cathode under operando conditions," *Nano letters* **14**, 5295 (2014).
[2] A. Ulvestad, A. Singer, H.-M. Cho, J. N. Clark, R. Harder, J. Maser, Y. S. Meng, and O. G. Shpyrko, "Single Particle Nanomechanics in Operando Batteries via Lensless Strain Mapping," *Nano letters* **14**, 5123 (2014).
[3] J. W. Cahn and J. E. Hilliard, "Free Energy of a Nonuniform System. I. Interfacial Free Energy," *The Journal of Chemical Physics* **28**, 258 (1958).
[4] J. W. Cahn and J. E. Hilliard, "Free Energy of a Nonuniform System. III. Nucleation in a Two-Component Incompressible Fluid," *The Journal of Chemical Physics* **31**, 688 (1959).
[5] Y. Takahashi, A. Suzuki, S. Furutaku, K. Yamauchi, Y. Kohmura, and T. Ishikawa, "Bragg x-ray ptychography of a silicon crystal: Visualization of the dislocation strain field and the production of a vortex beam," *Phys. Rev. B* **87**, 121201 (2013).
[6] B. Abbey, "From Grain Boundaries to Single Defects: A Review of Coherent Methods for Materials Imaging in the X-ray Sciences," *JOM* **65**, 1183 (2013).
[7] M. Holt, R. Harder, R. Winarski, and V. Rose, "Nanoscale Hard X-Ray Microscopy Methods for Materials Studies*," *Annual Review of Materials Research* **43**, 183 (2013).
[8] I. Robinson and R. Harder, "Coherent X-ray diffraction imaging of strain at the nanoscale," *Nature materials* **8**, 291 (2009).

X-ray tomography for granular materials: current trends and perspectives

G. Viggiani[1,2] and E. Andò*[1,2]

[1] Univ. Grenoble Alpes, 3SR, F-38000 Grenoble, France – cino.viggiani@3sr-grenoble.fr
[2] CNRS, 3SR, F-38000 Grenoble, France

Keywords: x-ray tomography, granular materials

Abstract

Combining x-ray tomography and three-dimensional (3D) image analysis has finally opened the way for experimental micro-(geo)mechanics, allowing access to different scales of interest. When these correspond to a scale that has been imaged at high spatial resolution, high-quality measurements can be obtained (*e.g.*, 3D displacements and rotations of individual grains of sand sample under load). However, there are issues when the scale of interest is smaller, for example the characterization of grain-to-grain contacts (their orientations and evolution) or production of fines by grain breakage. This paper presents a short selection of new grain-scale measurements obtained using existing techniques. The challenges associated with smaller scale measurements on the same images are also discussed through a few examples from ongoing work.

Introduction

When modelling grain-scale phenomena such as shear banding, standard continuum approaches are well known to have difficulties. Discrete element models are a valid alternative and have allowed insights to be gained into grain-scale behavior of particulate matter, through simulations with simple interaction laws between the particles. However, fundamentally, these remain simulations and consequently require experimental observations at the grain scale for validation. The ability to perform experiments *in-situ* inside an x-ray scanner is allowing a true revolution in the data that can be obtained from experiments – x-ray tomography allowing not only the measurement of grain-scale quantities in 3D on real materials, but also their evolution under loading. Moreover, laboratory x-ray scanners are rapidly becoming a widespread tool, increasingly available for experimental geomechanics (see Viggiani *et al.* 2015).

Previous work on the measurement of granular kinematics (Hasan & Alshibli 2012 and Andò *et al.* 2012a, 2012b) shows that grain displacements and rotations can be measured individually and accurately in small specimens of sand, subjected to triaxial compression. However, when imaging a given assembly of particles with a fixed-resolution detector, a trade-off must be made between the detail with which the particles are imaged and the number of particles imaged. In fact, mechanical representativity demands a sufficiently large number of particles, whereas a precise three-dimensional (3D) description of each grain requires a small specimen.

The specimens in this work were composed of around 50 000 grains (with a D_{50} of around 400 μm), which allows individual grains to be imaged (with around 5000 voxels per grain) and therefore successfully tracked throughout a test. However, there are related issues where imaging is ideally desired at a smaller scale – such as the characterization of grain-to-grain contacts (orientations and evolution) or the production of fines by grain breakage. In this paper, recent observations of grain-scale kinematics are briefly presented and the considerable challenges associated with smaller scale measurements (mentioned above) on the same images are discussed using a few

examples from very recent work. The philosophy adopted in this paper is that of making mechanically representative measurements rather than a high-detail characterization of single occurrences of small-scale mechanisms; the long-term objectives are not to characterize breakage or contact orientations on a few grains, but rather to make quantitative measurements of breakage on a meaningful number of grains in order to statistically relate this quantity to macro-behavior. The objective of this paper is therefore not to present major findings, but to discuss a general point. In doing so, some challenges and possible solutions are discussed that might make a significant impact on current understanding of the behavior of granular materials.

Existing techniques and results

Triaxial compression tests on dense specimens of dry sand performed inside the x-ray scanner in Laboratoire 3SR (Fig. 1) allow specimens to be scanned at key points during the test. Since the objective of this work is to image each individual grain, the specimen size is considerably less than standard (22 mm height, 11 mm diameter). Further details on the experimental apparatus and procedures are reported by Andò (2013) and Viggiani *et al.* (2015). A 3D image of x-ray attenuation in the scanned domain is obtained each time the specimen is scanned.

A variety of image analysis techniques have been developed to identify and measure individual grains in these 3D images. Very simply, these methods require the reliable identification of the inside of each grain by a marker, and the markers are then expanded to occupy all the grain volume by the watershed algorithm implemented in Noesis' Visilog 6.910, based on the work of Beucher (1991). When these procedures are applied to several different images from a test, ID-Track (see Andò *et al.* 2012a) is used to follow the grains. This paves the way for measurements of the 3D displacement (by following each grain's center of mass). The measurement of each grain's 3D rotation presents more of a challenge, which has been met by developing a hybrid ID-Track and digital image correlation (Andò *et al.* 2012b).

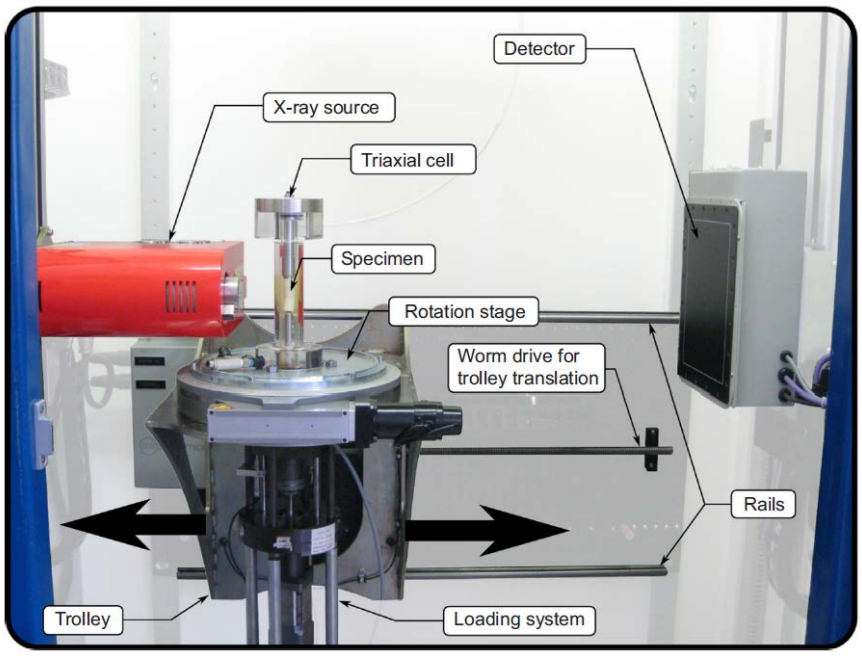

Fig. 1. *Laboratoire 3SR x-ray scanner. The background is faded out for clarity; blue edges visible left and right are the cabin door frame.*

These grain-based measurement tools are extremely powerful in that they allow micro-scale explanations of macro-scale responses. As an example, Fig. 2 shows the micro-mechanisms at play in the macroscopic residual stress state for three different sands – angular Hostun HN31 sand, rounded Ottawa 50–70 and the very rounded Caicos ooid – all tested at 100 kPa confinement. The measured grain displacements described above were triangulated (in the style of Bagi 1996) using YADE (see Šmilauer *et al.* 2010), providing access to a grain kinematics-derived strain tensor. The second invariant of the strain tensor thus derived (maximum shear strain) is plotted (Fig. 2a) in the triangulated domain of the specimen. In all three cases, this deviatoric strain can be seen to be strongly localized into a thin band. For Hostun sand, discrete blocks of very intense shear in the direction of the band can be clearly seen. These blocks are situated inside a wider shear band than that in Caicos ooid and one which has a less abrupt change in shear strain in the direction normal to the band. The change in the shear strains in Ottawa sand in the direction normal to the band presents an intermediate case.

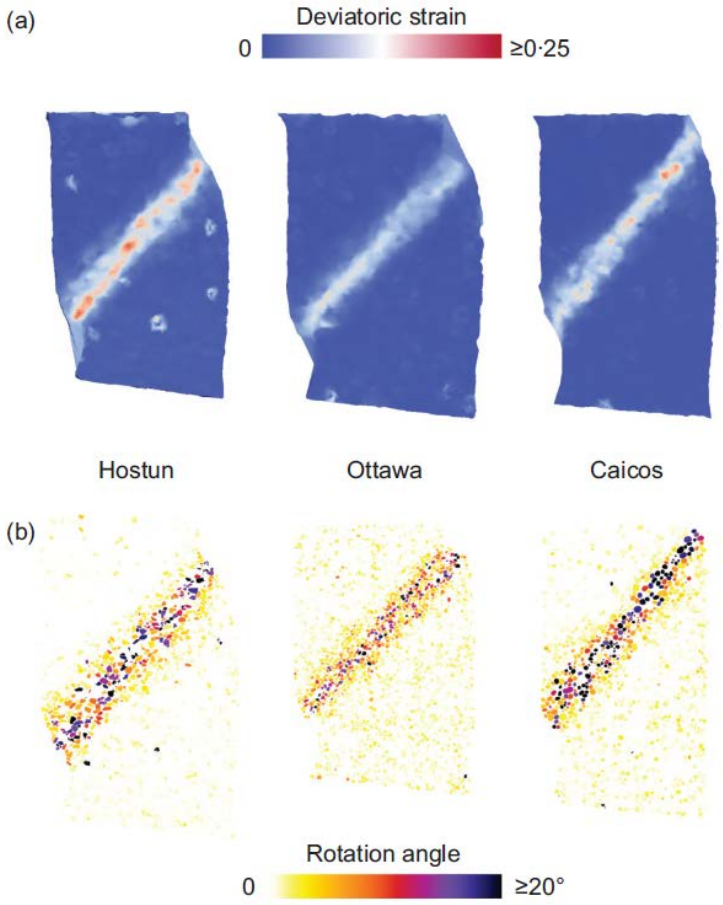

Fig. 2. *Measurements made on increments in the residual stress state of three sands tested in triaxial compression at 100 kPa confinement. The fields plotted are deviatoric shear strain (a) and the intensity of 3D grain rotation (b). Note that the strain increments are not all the same: the one for Hostun sand is particularly larger than the rest.*

The mechanism behind the increasing sharpness of shear strains with increasing grain roundness may find its origin in the grain-based rotation fields (Fig. 2b), which also show a concentrated band of grains with intense rotations coincident with the band of

high shear strain in all three cases (the scalar shown is the angle in the 'axis and angle' representation of a 3D rotation). The intensity of grain rotations appears to be correlated to grain roundness in the residual stress state – in the rounded material, grains rotate in a thin band whereas, in the angular material, grains rotate in a wider band with smaller rotations. In the Caicos and Ottawa specimens, when the shear band is fully developed, grain shapes offer little resistance to rotation (and therefore to shear), so the band is very concentrated. In the angular material however, grains are not able to rotate as freely due to interlocking; this causes 'secondary rotations' and therefore a wider band. Shearing this localized but interlocked system is likely to require more energy than shearing a localized material with less interlocking; this may explain why larger resistance to shear is obtained in the residual state.

Challenge 1: Contact characterization

A full micro-mechanical description of the kinematics occurring at the grain scale needs to go beyond grain kinematics (*i.e.*, the rotations and displacements of grains shown in the previous section). In particular, it requires the characterization of contact kinematics (the gain or loss of contacts and the orientation of those contacts) during deformation. In the work described thus far, the material was imaged at a resolution sufficient to resolve individual grains but not the details of the surface of each grain – these are visible in Fig. 3b, which shows a voxelated image of a single Caicos ooid. When contacts between such voxelated objects are characterized using relatively standard image processing tools, the lack of detail at each contact surface will inevitably result in extremely biased measurements (see Andò *et al.* 2012)). Figures 3a and 3c illustrate this challenge for 3D images of glass ballotini and Hostun sand, respectively.

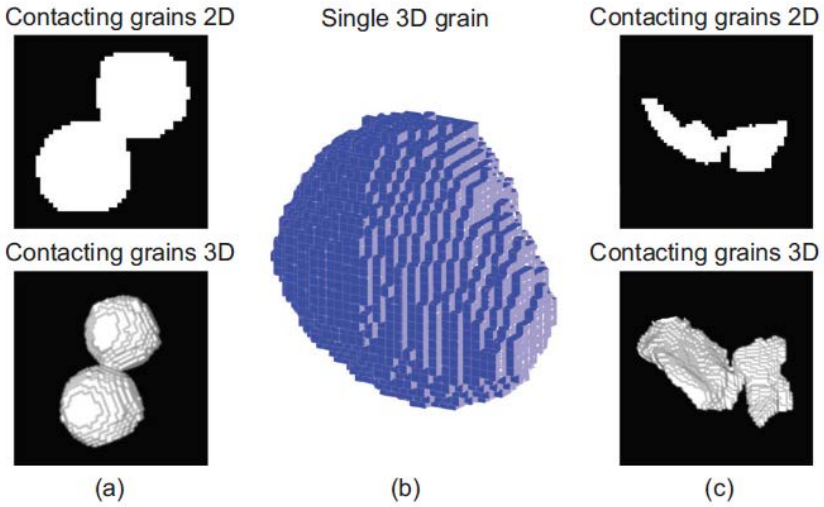

Fig. 3. *(a) Two-dimensional (2D) and 3D views of two glass ballotini in contact (these particles are close to spheres). (b) 3D view of a single Caicos ooid, with its jagged, voxelized nature underlined (courtesy of J. Andrade). (c) 2D and 3D views of two Hostun sand grains in contact.*

When the solid phase of a 3D image is to be split into individual grains, a separation surface between each grain must be defined in some way in order to isolate individual grains – this is currently obtained using a classical watershed algorithm (using a Euclidean distance map). It is tempting to consider the voxels defining the separation surfaces directly as a volumetric representation (of unit thickness) of a contact. However, Fig. 3a and Fig. 3c underline how small the contact areas can be in these images (*i.e.*,

how few voxels are used in the definition of the separation surface). The orientations of these separation surfaces are highly dependent on the particular watershed implementation used (and, furthermore, are highly biased) and therefore cannot be considered accurate. This is clearly visible in Fig. 4, where the contacts between a series of automatically generated touching spheres are analyzed. Figure 4a shows the orientation of the contacts as obtained from the branch vectors (*i.e.*, the vectors connecting the centers of the two spheres in contact – this is the 'exact' distribution since, in the special case of spheres, contact orientation and branch vector coincide). It is clear that the 'measured' orientation distributions coming from classical watershed approaches (Fig. 4b and Fig. 4c) are both highly biased and substantially different from each other (reproducing an error already noted by Andò *et al.* 2012b). More importantly, they are both a long way from the known distribution of orientations (Fig. 4a).

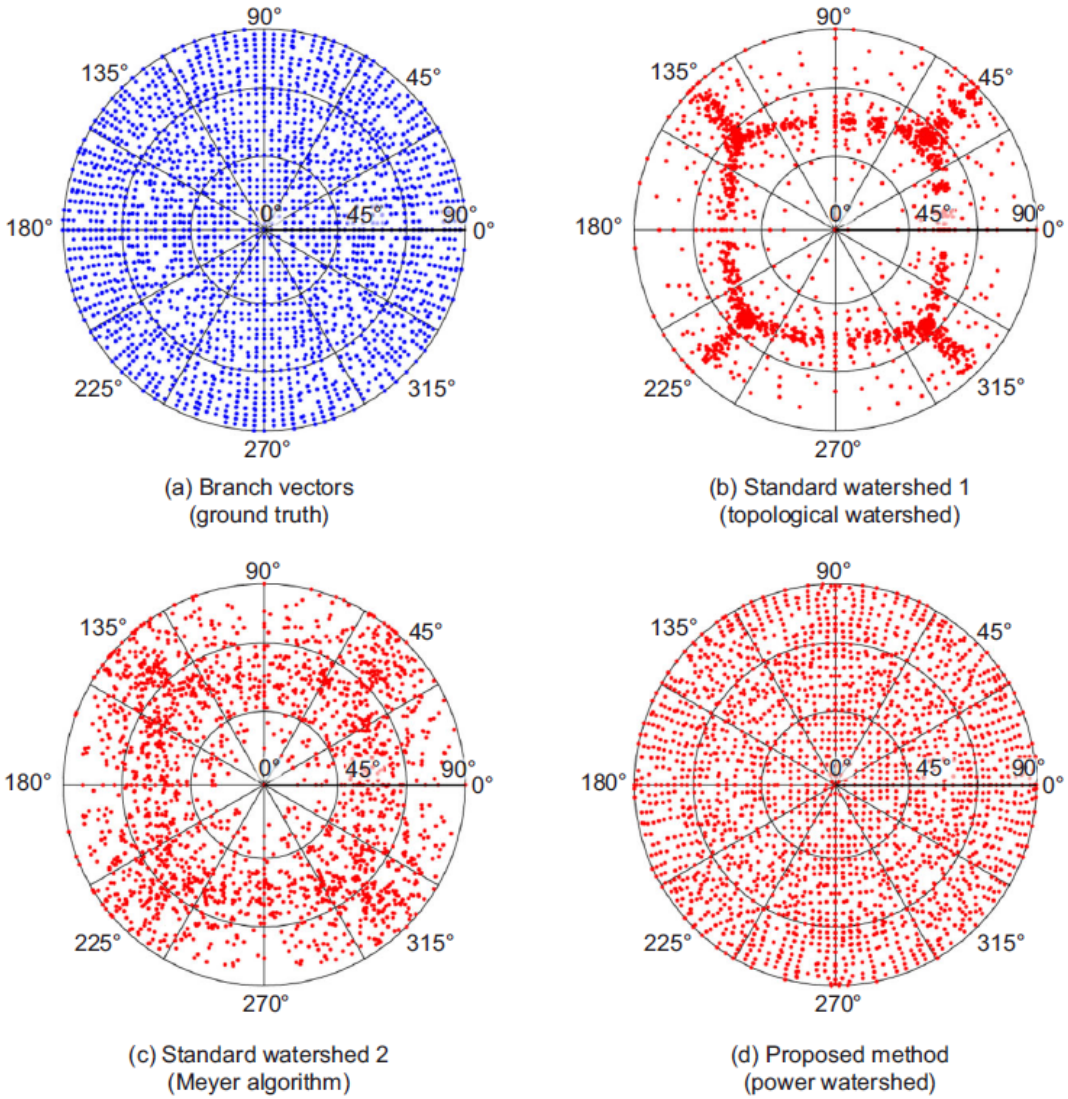

Fig. 4. *Equal-area projection of contact orientations from simulated spheres (after Jaquet et al. 2013).*

When a mechanically representative set of grains is imaged at a given resolution, this appears to cause serious problems with measurements of features at a smaller scale – in this case the local surface of the grains, which should yield the critically important information of contact orientation. Given the importance of this measurement, considerable efforts have been made in this direction. Recent work has involved the deployment of much more advanced techniques, whose results are shown in Fig. 4d for the case studied above. The technique is currently implemented on a 'per contact' basis (i.e. treating one pair of grains at a time). Starting from markers well inside the grains, it assigns – for each voxel of the solid phase – the probability of belonging to either marker using a power watershed. The contact plane is then estimated with subvoxel precision by estimating the equal-probability isosurface between the two grains. Despite the considerable computational cost of this approach, it gives high-quality results that are extremely encouraging; Jaquet *et al.* (2013) present further details of the implementation. Another, even more recent study is presented by Andò *et al.* (2015). It makes use of the so-called "Kalisphera" tool (Tengattini & Andò 2015), a piece of software that is able to analytically (and therefore rapidly) create 3D spheres, with correct "Partial Volume" values at the border of the shape. Improvements have been made to the tool to allow it to correctly simulate the point-spread function of a real imaging system (which can be therefore measured). Very interesting results have been recently obtained on the analysis of the detection of contacts between grains, by using Kalisphera-generated spheres (see Andò *et al.* 2015 for details).

Challenge 2: Grain breakage

Grain breakage is another grain-scale phenomenon, and is responsible for the difference between the low- and high-pressure behavior of sands. Several triaxial compression tests (up to the maximum cell pressure of 7000 kPa) were performed on different sands with in situ x-ray scanning. See Alikarami *et al*. (2015) for further details o the tests and the entire set of results obtained.

Figure 5 shows the micro-mechanisms occurring at high pressure in the case of Hostun sand, which go a long way to explaining the difference in the behavior of this material at a higher mean stress: grain breakage can be seen to occur on a very large scale as the specimen is sheared. Figure 5d follows a grain and its neighbors through five different states in the high pressure test. These pictures show the grain in the center of the image first cracking in two (with a vertical crack, images 2 and 3) and then being progressively broken into smaller pieces (images 4 and 5). These images suggest the progressive evolution of the specimen's grain size distribution (the production of fines during shearing): the clearly binary (*i.e*., grain and pore) image of state 1 develops into an image where pores are filled with an intermediate color greyscale value representing a porous material – a new material whose grains are smaller than the voxel size. Tools such as ID-Track are clearly no longer relevant in this case since the grains are no longer persistent objects in the images and, furthermore, rapidly become so small that they cannot be individuated.

In order to quantify the amount of grain breakage occurring during a test, an ideal quantity to be able to evaluate locally would be grain size distribution. However, this presents an image processing challenge similar to the measurement of contact orientations: the scale of the object to be measured is now smaller than the grain scale and, therefore, less well-resolved. Work is underway to permit this measurement, see Karatza *et al.* (2015).

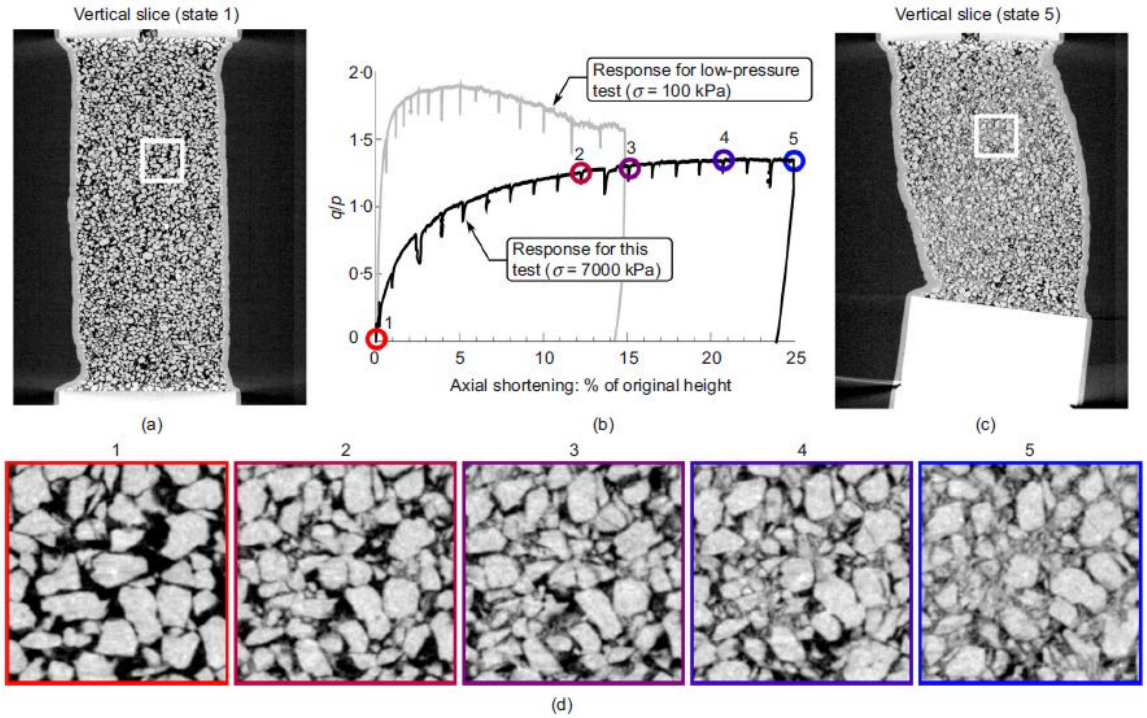

Fig. 5. *Production of fines during a triaxial compression test on Hostun sand at a relatively elevated confining pressure of 7000 kPa: (a) and (c) vertical slices through the 3D image of the specimen after isotropic compression and at the end of deviatoric loading, respectively; (b) q/p versus axial shortening for a test on Hostun sand at cell pressure of 7000 kPa (black) and 100 kPa (grey); (d) zoomed images of the region shown in the full slices ((a) and (c)) for states 1–5 indicated in (b).*

Conclusions

This paper has attempted to highlight some of the challenges that arise when smaller-than-grain-scale measurements are required in the characterization of the deformation of a granular material. This is quite a natural requirement: in situ x-ray tomography combined with advanced image processing now allows experimental micro-geomechanics. The application of this tool can reveal different scales of interest.

When imaging the samples discussed in this paper, a trade-off had to be made between sample size and the precision of the description of each grain. Objects at a smaller scale are therefore described less precisely than would ideally be the case, but sample size cannot be safely reduced in order to benefit from a larger zoom. Consequently, the simplest approach is to accept the images as they are and try to meet the challenges of paucity of information with advanced techniques.

In the case of the natural progression from grain kinematics to the measurement of contact orientations and their evolution, the ‘ordinary’ approach to the orientation of a contact plane between two grains imaged at this scale has been shown to introduce extreme bias into the measurements to the extent that they are no longer usable. Close collaboration with experts in image processing has allowed this measurement to be made successfully using very advanced techniques.

At higher mean stresses, imaging of the production of fines during shearing is exciting. Although local porosity can be calculated from these images, measurement of a grain size distribution from these images remains a challenge that requires the development of new tools.

References

Alikarami R., Andò E., Gkiousas-Kapnisis M., Torabi A., Viggiani G. (2015) - Strain localisation and grain breakage in sand under shearing at high mean stress: insights from in-situ x-ray tomography. **Acta Geotechnica**, 10(1), 15-30.

Andò E. (2013) – *Experimental investigation of micro-structural changes in deforming granular media using x-ray tomography*. PhD thesis, Université de Grenoble, France.

Andò E., Hall S.A., Viggiani G., Desrues J., & Bésuelle P. (2012a) – Grain(scale experimental investigation of localised deformation in sand: a discrete particle tracking approach. **Acta Geotechnica**, 7(1), 1-13.

Andò E., Hall S.A., Viggiani G., Desrues J. & Bésuelle P. (2012b) – Experimental micromechanics: grain-scale observation of sand deformation. **Géotechnique Letters**, 2(3), 107-112.

Andò E., Tengattini A., Wiebicke M., Viggiani G., Salager S. & Desrues J. (2015) – Multi-resolution characterisation of grain-based measurements from x-ray tomography. *This conference*.

Bagi K. (1996) – Stress and strain in granular assemblies. **Mechanics of Materials**, 20(3), 165-177.

Beucher S. (1991) – The watershed transform applied to image segmentation. *Proc. Pfefferkorn Conf. on Signal and Image Processing in Microscopy and Microanal*., Cambridge, UK, September 1991, 299-314.

Hasan A. & Alshibli K.A. (2012) – Three Dimensional Fabric Evolution of Sheared Sand. **Granular Matter**, 14(4), 469-482.

Jaquet C., Andó E., Viggiani G., & Talbot H. (2013) – Estimation of Separating Planes between Touching 3D Objects Using Power Watershed. In Mathematical Morphology and Its Applications to Signal and Image Processing (452-463). Springer Berlin Heidelberg.

Karatza Z., Andò E., Papanicolopulos S.A., Ooi J. & Viggiani G. (2015) – Observing breakage in sand under triaxial and oedometric loading in 3D. *Submitted to IS-Buenos Aires*, 2015.

Šmilauer V., Catalano E., Chareyre B. *et al.* (2010) – *The Yade project*, 1st edn. See http://yade-dem.org/doc/

Tengattini A & Andò E. (2015) – Kalisphera: an analytical tool to reproduce the partial volume effect of spheres imaged in 3D. **IOP Measurement Science and Technology**, in print.

Viggiani G., Andò E., Takano D., Santamarina, J.C. (2015) – X-ray tomography: a valuable experimental tool for revealing processes in soils. **Geotechnical Testing Journal**, ASTM, 38(1), 61-71.

Session 101

Taming the flood: Distributed image processing made easy on large tomographic datasets

Kevin Mader[1,2,3],Alessandra Patera[1,2] Rajmund Mokso[1] , Marco Stampanoni[1,2]

Overview

The combination of improving detector technologies, more efficient measurements, and parallel acquisition have increased both the amount and the rate of data being produced in tomographic measurements. By contrast, the tools available for analyzing these ever growing datasets have remained relatively static. Additionally, with the latest acquisitions having sustained rates of 8GB/s[1], the memory of even most powerful workstations is fully saturated after 1 minute of collection. Furthermore, while transistor count has continued to grow at an exponential rate, the speed of processors has been relatively stagnant since the early 2000s. The accumulation of these effects demand a radical change in the approach to handling large datasets.

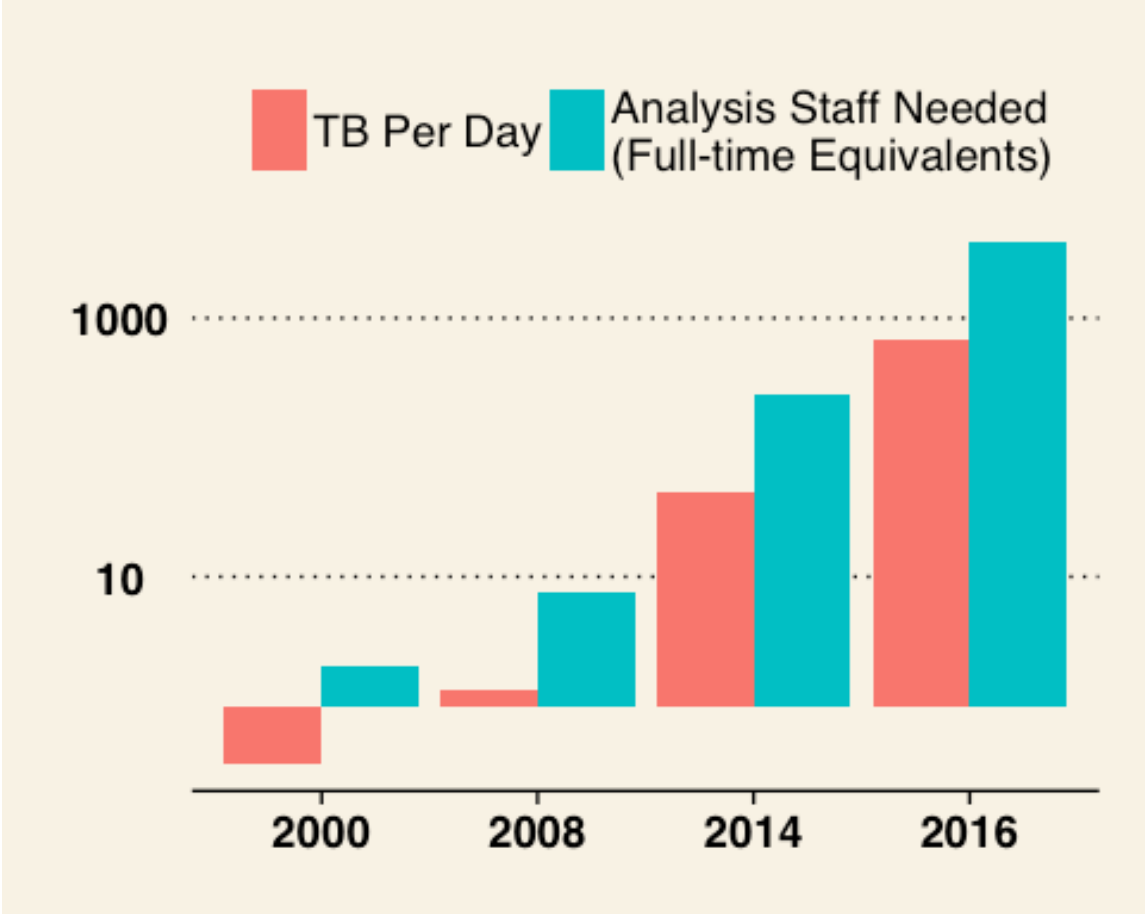

The figure highlights the exponential growth in both: the amount of data and analysis time. The results are based on statistics over the last 16 years at the TOMCAT Beamline with a constant analysis rate of 1Mpx/second

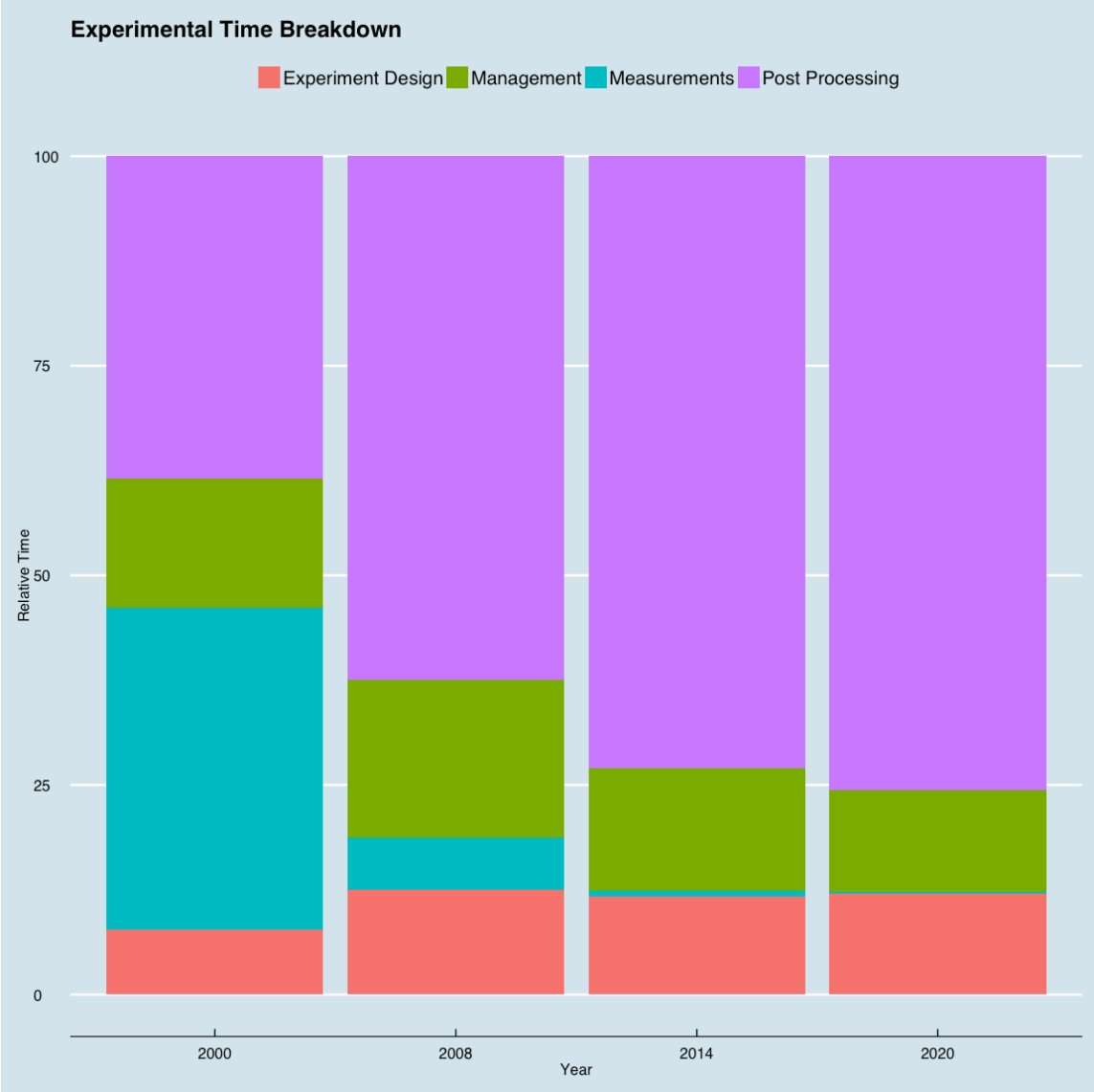

A graph illustrating the rapid change in the distribution of experiment time compared with post-processing and other steps.

Small vs Big Data

For the purposes of this abstract we will define small, medium, and big data by the scalability and degree of automation rather than actual size of the datasets. *Small Data* represents the least degree of both scalability and automation and consists of interactively, manually analyzing each dataset in ways that require minutes to hours of human time to complete. *Medium Data* is an increased degree of automation, but

involving the interaction of many (3+) different tools to complete an analysis. The human time per sample is low, but per analysis is high since configuration is a major challenge. Finally *Big Data* is complete or nearly complete automation and scalability to at least 10-100X the current problems size given enough computational resources.

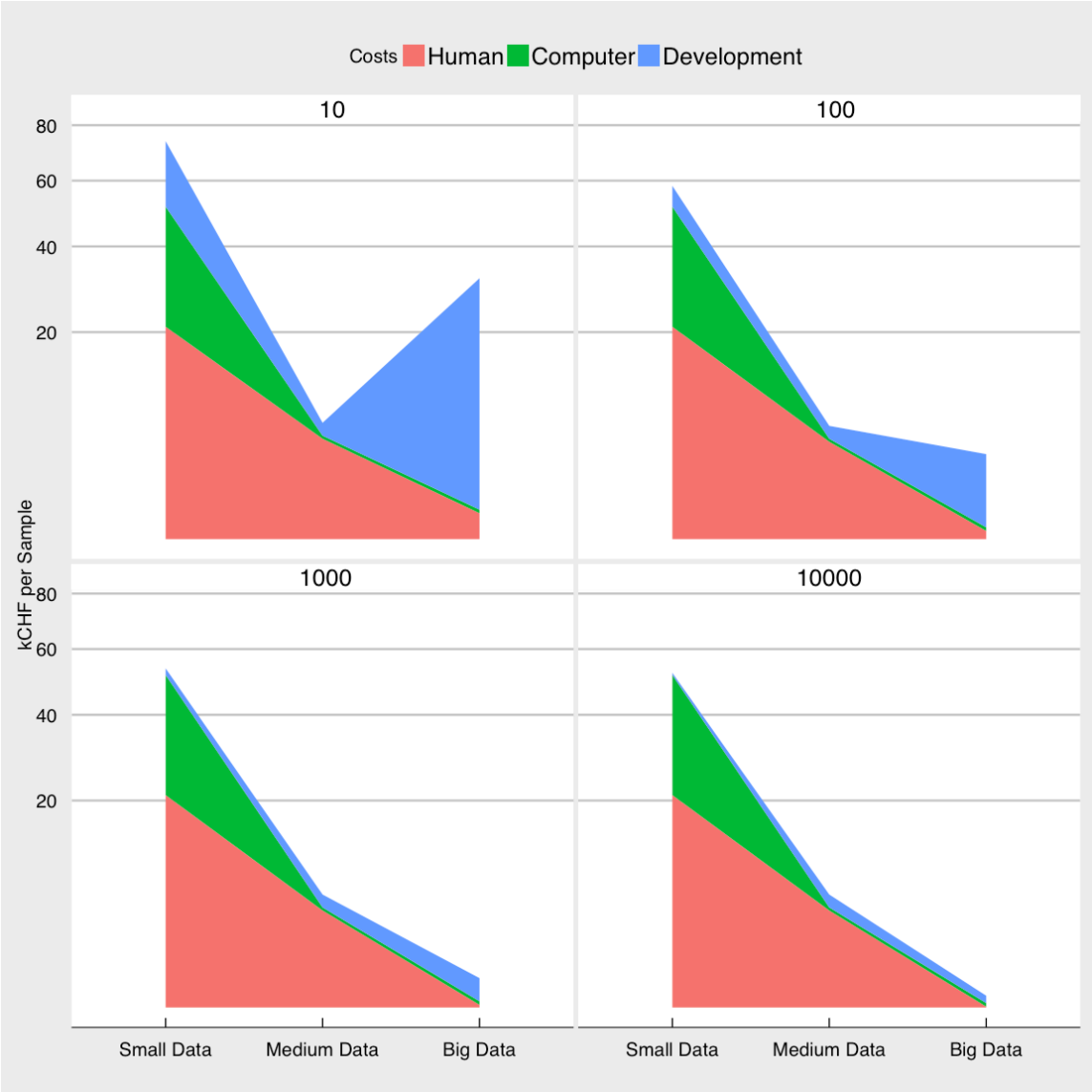

Time required per sample for each approach with a different (10,100,1000,10000) number of samples. The development time is divided by the number of samples. For the small/typical use case of 10 samples, the Medium Data approach is the best balance of development time and automation and the Big Data approach requires far too much development for it to be beneficial for such few samples.

Tomography

While the growth in tomography has been unique in the sheer magnitude of data produced, the fields of bioinformatics[2], and web analytics[3] have experienced similar growth spurts and made significant progress on developing flexible, scalable frameworks for processing massive datasets in a distributed, fault-tolerant manner. Using the Apache Spark framework developed in[4], we have implemented a series of image processing tools for common image processing tasks. Building on top of Spark and Hadoop means cloud-support, distribution, and fault-tolerance is automatic.

The layer currently includes a range of basic image processing operations including filtering / noise reduction, segmentation, contouring, distance / thickness map generation, shape, distribution, and texture analysis as described in[5]. The various components can then be pipelined into a workflow using scripts written in Java, Python, or Scala. Alternatively the tools can be run from a web-based interface. The status of the analysis and the results can be queried interactively from the web interface which provides both image, rendered, and plotted visualizations based on the type of analysis being performed. Given access to enough computational resources, the analysis can even be run in a streaming mode to process the images in real-time rather than single static analyses after the data are measured and saved.

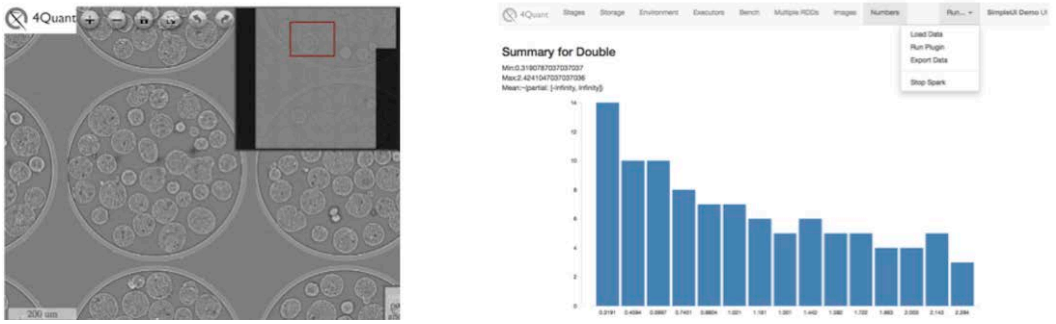

The GUI interface for the Spark Image Layer tools. The left panel shows the DeepZoom-based tool to explore a multi-gigabyte dataset using a web-browser. The right panel shows the D3.js-based visualizations showing histograms.

The framework can be applied to a wide variety of datasets with successful results, but where the tools really excel is the area where no existing approach provides a viable solution. Specifically we have focused on two major projects. The first is imaging of full adult Zebra fish at cellular resolution having a final volume of 11500 x 2800 x 628 → 20-40GVx / sample. The second is a full measurement of the mouses brain vasculature with capillary resolution ≈ 10,000 x 10,000 x 10,000 → 1000 GVx / sample. While the information content of the images is very different, the same sorts of analyses will need to be performed on both. In order to convert an overwhelming mass of image data into a deeper understanding, many different segmentation and analysis techniques will need to be tested and validated quickly. We demonstrate how these data can be segmented and how machine learning

algorithms can be leveraged to further improve the reliability and automation of such analyses.

1.Mokso, R., Marone, F. & Stampanoni, M. Real-Time Tomography at the Swiss Light Source. in *AIP conf. proc.* (SRI2009, 2009).

2.Altintas, I. Workflow-driven programming paradigms for distributed analysis of biological big data. in *2013 iEEE 3rd international conference on computational advances in bio and medical sciences (iCCABS)* 1–1 (IEEE, 2013). doi:10.1109/ICCABS.2013.6629243

3.Dean, J. & Ghemawat, S. MapReduce: simplified data processing on large clusters. *Communications of the ACM* **51,** 107 (2008).

4.Matei Zaharia, M. J. F., Mosharaf Chowdhury. Spark: Cluster computing with working sets. at <http://citeseerx.ist.psu.edu/viewdoc/summary?doi=10.1.1.180.9662>

5.Mader, K., Mokso, R. & Raufaste, C. Quantitative 3D Characterization of Cellular Materials: Segmentation and Morphology of Foam. *Colloids and Surfaces A: ...* **415,** 230–238 (2012).

PSICHE: A SYNCHROTRON TOMOGRAPHY BEAMLINE AT SOLEIL DESIGNED FOR MATERIALS SCIENCE

*A. King[1], N. Guignot[1], P. Zerbino[1], K. Desjardins[1], J.-P Perrillat[2], Y. Le Godec[3], S. Delzon[4], L. Gelebart[5], N. Lenoir[6], M. Bornert[7], J.-P. Itié[1]

1 Synchrotron SOLEIL, St Aubin, Gif-sur-Yvette, 91192, France. mailto:king@synchrotron-soleil.fr

2 Observatoire des Sciences de l'Univers de Lyon, UMR5276-CNRS-ENSLyon-UCBLyon1, Villeurbanne, 69622, France.

3 IMPMC, University P and M Curie, Paris Cedex 5, France.

4 UMR BIOGECO, INRA, University of Bordeaux, Pessac 333615, France

5 CEA SACLAY DEN/DMN/SRMA, Gif-sur-Yvette, 91191, France

6 PLACAMAT, UMS3626-CNRS/Université de Bordeaux, Pessac, 33608, France.

7 Laboratoire NAVIER, UMR8205-CNRS/ENPC/IFSTTAR/Université Paris-Est, Champs-sur-Marne, 77455, Marne-la-Vallée, France.

* presenting author

Keywords:

Synchrotron SOLEIL, tomography, materials science, instrumentation, beamline

Abstract

PSICHE is the high-energy beam line for imaging and diffraction at the French national synchrotron SOLEIL. The tomography instrument has just entered service, with the first experiments successfully performed in September 2014. The tomograph has been optimized for in-situ materials science experiments, with a high speed, high load capacity rotation stage and white beam compatible optics. The instrument uses parallel beam geometry for imaging with pixel sizes from 0.325 to 8 microns. Beam energies from 20 to >80 keV are available, and a full dataset can be acquired in ~15 seconds in pink beam mode. It has already proven equally useful for life science and cultural heritage applications. The beam line also hosts diffraction experiments from samples at extreme pressures in both energy dispersive and angular dispersive modes. Consequently, many possibilities exist for combining diffraction and imaging in order to obtain more complete knowledge of a given sample or process. Future perspectives and plans include extending the scope of tomography measurements, but also for combining imaging and reciprocal space information with grain mapping or correlative tomography approaches in unique and innovative experiments.

Introduction

Synchrotron tomography is well established as an important research tool in a range of fields of research, including materials science and engineering, life sciences, cultural heritage and paleontology. As in laboratory x-ray tomography, a series of radiographs are recorded during a rotation of the sample about an axis perpendicular to the beam. The 3D structure of the sample is then reconstructed from these projections, typically using a filtered backprojection algorithm. Compared to a laboratory instrument, the synchrotron source offers much greater beam intensities, permitting a scan to be completed much more quickly, in minutes or even seconds, or allowing the use of monochromatic radiation to provide quantitative imaging. The greater coherence of the beam permits phase contrast imaging techniques to be used, improving resolution of weaky contrasting features, or permitting the quantitative measurement of electron density.

PSICHE Tomograph

The PSICHE beam line of the SOLEIL synchrotron offers a tomograph optimised for materials science experiments. The instrument is built around an large, high precision air bearing rotation stage. The stage features a 250 mm diameter central aperture, as does the granite experimental table below and the sample translation stages above. This space is available for the installation of large or heavy in-situ sample environments, or to allow very tall samples to be studied. This concept is inspired by the laboratory instrument at the NAVIER laboratory, ENPC, and allows the easy migration of

experimental setups from this laboratory device to the synchrotron for fast development of new devices and procedures [Bruchon 2013]. The mecanical precision of the instrument is compatible with sub-micron spatial resolution.

The detector system has been developed at SOLEIL. It is a flexible, modular, white beam compatible design, equipped with a Hamamatsu Flash 4.0 sCMOS camera. By selecting different scintillators and visible light optics, the pixel size can be varied from 0.325 to 8 microns, with a corresponding field of view of 0.65 to 15 millimetres. A mirror immediately behind the scintillator means that the optics are not exposed to the direct beam, reducing degradation. By using an x-ray transparent mirror, x-rays scattered from the sample can be detected simultaneously with the radiographic image, allowing experiments combining imaging and diffraction to be performed.

The tomograph can be installed at two different locations on the beam in order to use either monochromatic or polychromatic (filtered white beam) radiation. In either case, simultaneous imaging and diffraction is possible. Filtered white beam radiation provides much greater flux at the sample position (typically 20-100 times greater), allowing measurements to be made faster. With the current camera, a full resolution scan can be recorded in as little as 15-30 seconds.

Application examples

The first user experiments were been performed in September 2014. Since then a number of external user and in-house test experiments have been performed. Some examples are given here.

In-situ loading of SiC/SiC composites.

In-situ loading experiments are a typical materials science application of synchrotron tomography. The speed of acquisition and the high signal to noise ratio allows damage processes to be investigated in-situ. In this example, SiC/SiC composite tubes have been loaded in compression, with several tomograms recorded. Digital volume correlation has been used to study deformation and failure mechanisms, giving particular attention to subsurface cracking which is not visible in surface observations. This measurement was performed in monochromatic beam mode (~5µm pixel size, 33keV). A recent in-house test experiment was dedicated to a trial of similar samples under tensile loading, using higher resolution with pink beam illumination to increase imaging speed. The testing and imaging procedures were previously validated using the Navier laboratory instrument.


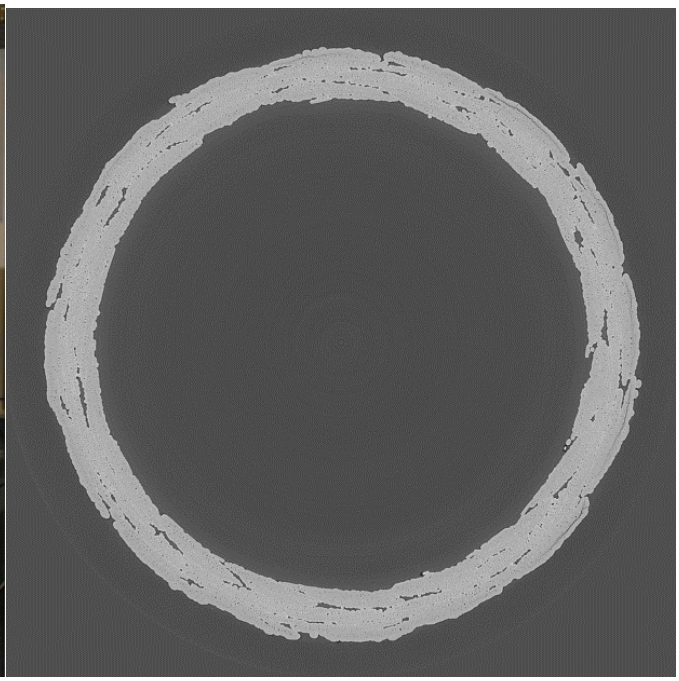

RoToPEC. Pink beam diffraction and imaging at extreme pressure.

The RoToPEC (Rotational Tomography Paris-Edinburgh Cell) is a Paris-Edinbugh high pressure cell in which the two anvils are independently motorised, allowing the sample to be rotated, or for torsional loads to be applied, while under isostatic pressure [Philippe 2013]. By rotating the sample through 180° and recording a series of radiographs, the sample volume can be reconstructed. This allows the study of the high pressure behaviour of amorphous materials which do not give rise to easily exploitable diffraction signals. Tomography was performed in pink beam mode (2.45µm pixel size, ~44keV mean energy), combined with energy dispersive diffraction in order to measure the pressure using a calibrant material. Reconstructions were performed using the Paganin phase retrival approach, exploiting the partial coherence of the beam.

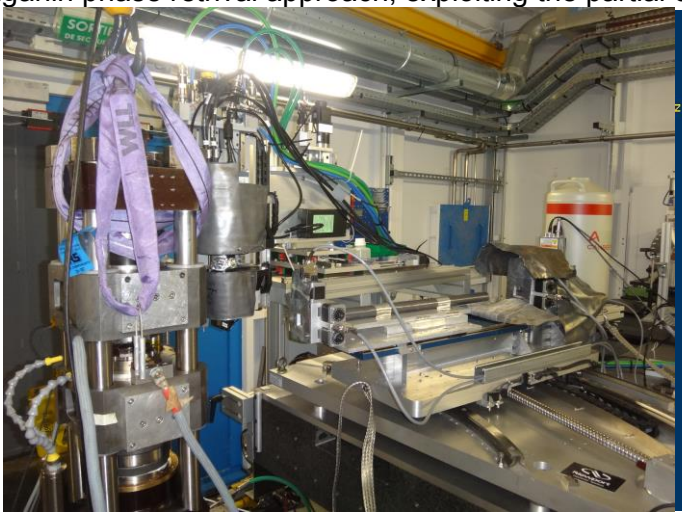
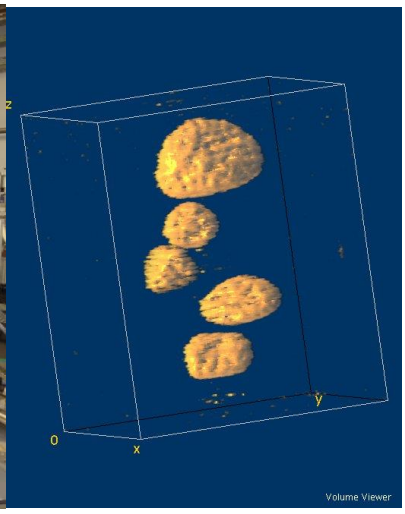

Plants in-vivo.

A final example is from a recent user experiment investigating the effects of drought stress on living plants. The presence of caviation in the water transported in the xylem was determined using phase contrast tomography in monochromatic beam mode (~3µm

pixel size, 25keV). These conditions gave the best imaging quality combined with relatively low radiation dose to avoid beam damage effects. The experiment was made possible by the clear aperture of the rotation stage, which allowed tall plants (up to 1m) to be installed inside the stage so that imaging could be carried out near the top of the stems.

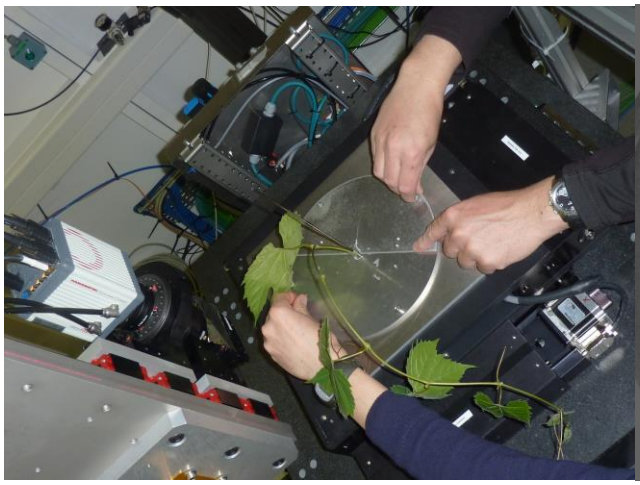

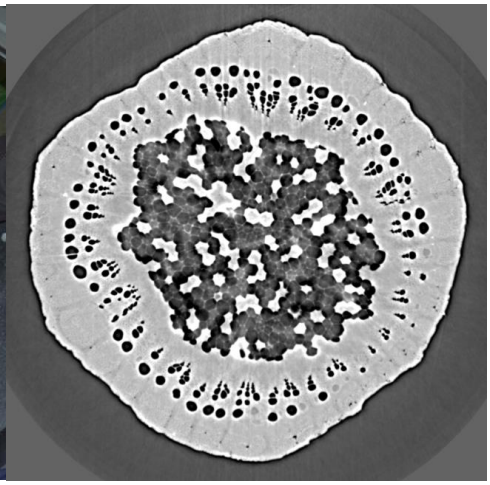

Acknowledgements

Part of the tomograph was funded by ANR project MicroNaSel, ANR-10-BLAN-935. The examples are drawn from measurements made at PSICHE by, M. Bornert and L. Gelebart, J.-P. Perrilat, and L. Delzon. The SiC/SiC composite study was supported by the “NEEDS-Matériaux” program (project TRISIC).

References

J.-F. Bruchon, J.-M. Pereira, M. Vandamme, N. Lenoir, P.Delage, M.Bornert, Granular Matter DOI 10.1007/s10035-013-0452-6 (2013)

J. Philippe, Y. Le Godec, F. Bergame, M. Morand, European Patent 2984798, 2013.

Studying water/porous materials interactions with X-ray tomography

*D. DEROME[1], A. PATERA[2, 3], M.DASH[4,1], M. PARADA[4,1], S. LAL[1], J. CARMELIET[4,1]

[1] Laboratory for Multiscale studies for the built environment, Swiss Federal Laboratories for Materials Science and Technology, EMPA, Dübendorf, Switzerland, dominique.derome@empa.ch
[2] Swiss Light Source, Paul Scherrer Institute, Villigen, Switzerland
[3] Centre d'Imagerie BioMedicale, Ecole Polytechnique Federale de Lausanne, 1015 Lausanne, Switzerland
[4] Chair of Building Physics, ETH Zurich, Switzerland
* presenting author

Keywords: fluids, porous media, transport, swelling

Abstract

Water, a common fluid, displays a wide range of interactions with porous materials. We use X-ray tomography to capture the configuration of the porous material and of the liquid, in a variety of experiments. We often couple these investigations with neutron imaging, most often in projection, for moisture quantification. The datasets acquired are designed to validate advanced computational models. We investigate here porous materials of the following classes: cellular (with vapor), fibrilar and aggregate agglomerate (both with liquid water), at scales ranging from a few hundreds of nanometers to millimeters. We present the role of imaging in our multiscale experimental and modeling programs on wood, textiles and porous asphalt.

Introduction

We have developed a combined experimental and modeling mutiscale approach to capture and understand the transport and storage of fluids, mostly water, in porous media. We have devised several experimental set-ups at different scales of investigation in order to validate models and their upscaling.

Wood cellular structure

Many biological and engineering materials are essentially cellular, a feature which provides them with a low density, ~~a~~ high strength and ~~a~~ high toughness. The deformation of cellular materials in response to environmental stimuli such as changes in relative humidity, is of practical interest to evaluate, amongst others, their durability. We have used wood, more specifically xylem, as a "model" material for such hygroscopic cellular materials (Derome et al 2013, 2012, 2011, Rafsanjani 2014, Sedighi Gilani 2014).

Using phase-contrast synchroton-radiation X-ray tomographic microscopy, we isolated different tissues, i.e. pure earlywood or latewood of different porosity, to look at the configuration of the cellular structure at different moisture contents, due to exposure to different relative humidities. Such investigation allowed to quantify a swelling anisotropy dependent on porosity and to identify the total absence of hysteresis of swelling for homogeneous tissues [Patera et al. 2013, 2014]. Using nanotomography, we could isolate components of the cell wall and study their swelling behavior.This multiscale investigation of the complex hierarchical structure of wood shows that its configuration reduces the swelling/shrinkage strains and increases its dimensional stability in a humid environment. Similar work is being carried out on the living tissue of the tree, phloem.

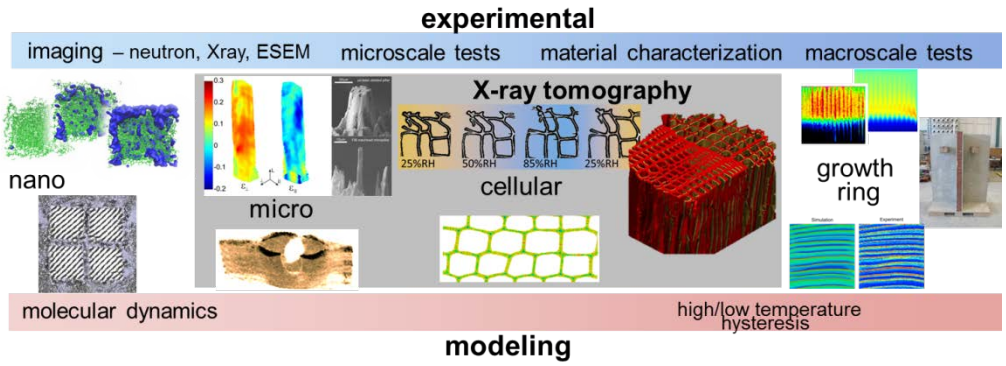

Fig. 1. *Schematic representation of the place of X-ray (mainly synchroton) tomography in our mutiscale experimental and modeling research program on wood.*

Yarns and textiles

Yarns and textile are porous, highly deformable materials which configuration induces a strong directionality on liquid water flow. Within hydrophilic yarns, the rapid water uptake is captured using phase contrast synchrotron-radiation X-ray fast tomographic microscopy, where three full scans are acquired per second. This technique provides the actual configuration of water amongst the fibers, and leads to the novel capacity of tracking several capillaries. Parallel paths and mergers of paths can be identified, providing a sub-yarn-scale understanding of capillary flow in fibrilar materials.

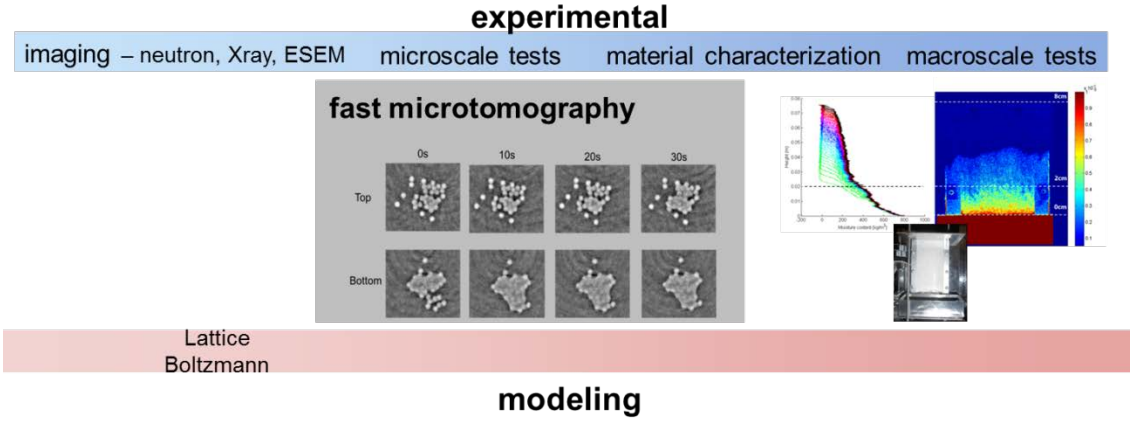

Fig.2. *Schematic representation of the place of fast synchroton X-ray tomography and neutron radiography in our mutiscale experimental and modeling research program on textiles and yarns.*

Porous asphalt

Porous asphalt, made of bonded aggregates and with a porosity of up to 20%, has the particular behavior to allow gravity-driven drainage. We use neutron imaging to acquire the spatial distribution of liquid water in porous asphalt during drainage and controlled drying. Neutron imaging provides ~~a~~ quantitative information of very high resolution in terms of moisture content in porous materials with high resolution. Nevertheless, a full understanding of the water flow could only be performed by combining the saturation degree distribution obtained by neutron radiography with the exact 3D geometry of the sample obtained with lab-based X-ray tomography [Lal et al. 2014, Poulikakos et al 2013a,b]. Thus, the actual path of water during drainage and drying could be identified.

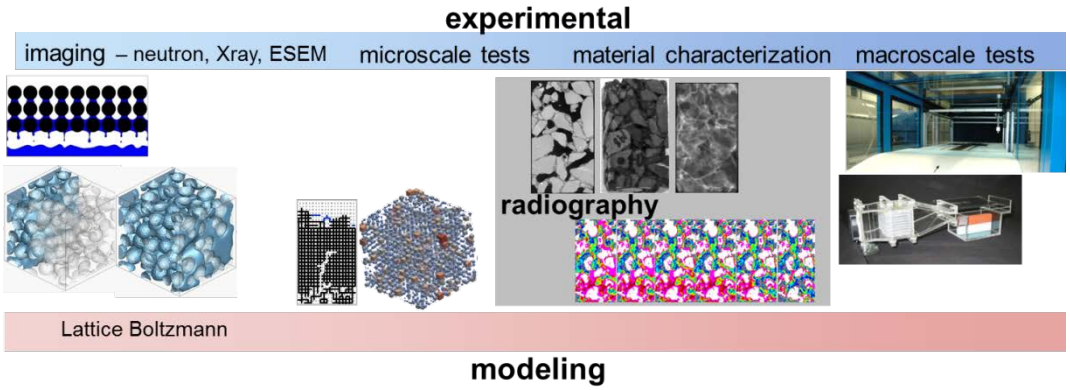

Fig. 3. *Schematic representation of the place of X-ray and neutron radiography in our mutiscale experimental and modeling research program on porous asphalt.*

The measurements were performed at the TOMCAT beamline of the Swiss Light Source, headed by Prof Marco Stampanoni, and at the NEUTRA and ICON beamlines of SINQ, headed by Dr. Eberhard Lehmann, at Paul Scherrer Institute, Villigen, Switzerland. We acknowledge the invaluable help of their scientific teams.

References

Derome D, Rafsanjani A, Hering S, Dressler M, Patera A, Lanvermann C, Sedighi Gilani M, Wittel F, Niemz P, Carmeliet J. (2013). The role of water in the behavior of wood, J. Building Physics, 36(4): 398-421.

Derome D, Rafsanjani A, Patera A, Guyer R, Carmeliet J. (2012). Hygromorphic behaviour of cellular material: hysteretic swelling and shrinkage of wood probed by phase contrast X-ray tomography, Philosophical Magazine, 92: 3680-3698

Derome, D., Griffa, M., Koebel, M., Carmeliet, J. (2011) “Hysteretic swelling of wood at cellular scale probed by phase contrast X-ray tomography”, J. Structural Biology, 173:180-190.

Lal S, Poulikakos L, Sedighi Gilani M, Jerjen I, Vontobel P, Partl M, Carmeliet J, Derome D.(2014) Investigation of Water Uptake in Porous Asphalt Concrete Using Neutron Radiography, Transport in Porous Media, 105 (2), 431-450.

Patera A, Jefimovs C, Rafsanjani A, Voisard F, Derome D, Carmeliet J. (2014) Micro-scale restraint methodology for humidity induced swelling investigated by phase contrast X-ray tomography, Experimental Mechanics, 54:1215-1226

Patera, A., Derome, D., Griffa, M., & Carmeliet, J. (2013). Hysteresis in swelling and in sorption of wood tissue. Journal of Structural Biology,182(3), 226–234.¨

Poulikakos L, Sedighi Gilani M, Derome D, Jerjen I, Vontobel P. (2013a). Time resolved analysis of water drainage in porous asphalt concrete using neutron radiography, Applied Radiation and Isotopes, 77:5-13.

Poulikakos L, Saneinejad S, Sedighi Gilani M, Jerjen I, Lehmann E, Derome D. (2013b). Forced convective drying of wet porous asphalt imaged with neutron radiography, Advanced Engineering Materials 15:1136-1145

Rafsanjani A, Stiefel M, Jefimovs K, Mokso R, Derome D, Carmeliet J. (2014) Hygroscopic swelling and shrinkage of latewood cell wall micropillars reveal untrastructural anisotropy, J. Royal Society Interface, 11:20140126.

Sedighi Gilani M, Vontobel P, Lehmann E, Carmeliet J, Derome D. (2014). Liquid uptake in Scots pine sapwood and heartwood visualized and quantified by neutron radiography, Materials and Structure, 47: 1083-1096.

Oral presentation

Time-resolved (4D) in situ x-ray tomographic microscopy at TOMCAT: Understanding the dynamics of materials

*J.L.FIFE[1], F. MARONE[1], R. MOKSO[1], M. STAMPANONI[1,2]

[1] Swiss Light Source, Paul Scherrer Institut, Villigen PSI, Switzerland
[2] Institute for Biomedical Engineering, Swiss Federal Institute of Technology and University of Zurich, Zurich, Switzerland
* presenting author

Non-destructive synchrotron-based x-ray tomographic microscopy is ideal for studying various materials systems in three and four dimensions (3D and 4D, respectively), and the TOMCAT beamline[1] at the Swiss Light Source is one of the premier beamlines in the world for such experiments. Spatial resolution ranges from 1-20μm with fields-of-view from 1-15mm, and temporal resolution is as fast as 0.1s for a full 3D data acquisition[2]. Contrast varies from standard absorption, typically used in metal and composite systems, to propagation- and grating-based phase contrast, predominantly used for biological and other traditionally low-contrast materials. The efficient image processing pipeline provides a full 3D reconstruction within a few seconds[3], making visualization of selected slices close to real time. To exploit these state-of-the-art capabilities and to explore the dynamics of materials at elevated temperatures, a dedicated laser-based heating system has been developed[4] and a mechanical testing device is being commissioned.

This talk will summarize the novel capabilities available at TOMCAT, as well as focus on recent achievements in dynamic, time-resolved experimentation. Particularly, it will highlight the results that have been achieved when using the gigaFROST detector[5]; a worldwide unique system that provides true dynamic experimentation with continuous image acquisition up to 7.7GB/s and decouples the temporal resolution from the total imaging time. Other results like the vesiculation of bubbles in geological materials at high temperatures under simple dead-weight compression, 4D self-healing of ceramics and 4D solidification of metals will be discussed. Since dynamic experimentation generates large amounts of data, typically on the order of terabytes, *automated* tools for visualizing and characterizing the resulting phenomena are necessary. This talk will also underscore these developments and summarize the future of time-resolved, 4D imaging at TOMCAT.

References:
[1] Stampanoni, M, Groso, A, Isenegger, A, et. al. (2006): Trends in synchrotron-based tomographic imaging: the SLS experience.—Proceedings of the SPIE, 6318: 63180M-1—63180M-14.
[2] Mokso, R, Marone, F, Stampanoni, M, et. al. (2010): Real time tomography at the Swiss Light Source.—AIP Conference Proceedings, 1234: 87-90.
[3] Marone, F, Stampanoni, M. (2012): Regridding reconstruction algorithm for real-time tomographic imaging.—Journal of Synchrotron Radiation, 19: 1029-1037.
[4] Fife, JL, Rappaz, M, Pistone, M, et. al. (2012): Development of a laser-based heating system for in situ synchrotron-based x-ray tomographic microscopy.—Journal of Synchrotron Radiation, 19: 352-358.
[5] Mokso, R, et. al. (2015): SRI Proceedings, in preparation.

High speed and time resolved tomography of fluid flow in porous media at Diamond Light Source Beamline I12

R. C. ATWOOD*[1], S. B. COBAN[4], K. J. DOBSON[2], D. KAZANTSEV[3,5], S. A. MCDONALD[3], N.T. VO[1], M. DRAKOPOULOS[1] P.J. WITHERS[3]

1 Diamond Light Source, Didcot, UK

2 Ludwig-Maximilians-Universität, Department of Earth and Environmental Sciences„ Germany

3 School of Materials, University of Manchester, Manchester UK

4 School of Mathematics, University of Manchester, Manchester UK

5 The Manchester X-Ray Imaging Facility, Research Complex at Harwell, Didcot, UK

* presenting author

Keywords: Flow, High-speed, Time-resolved

Abstract

X-ray tomography has the ability to provide a detailed sample assessment in 3D, and quantification of porosity, grain orientations, fracture alignments, some information about the material compositoin, and many other features. Monochromatic synctrotron X-rays can provide imaging conditions allowing the discrimination of water, air and solid particles even at relatively high energy required to penetrate macroscopic samples of minerals. The images can be obtained quickly enough to provide tomography of a column of mineral particles while fluids are percolating through the intergranular spaces, with sub-second resolution.

This allows better understanding of the development and maintenance of flow pathways, which is of interest in diverse fields of geophysics, chemical engineering, mining and mineral processing, as well as life sciences. To capture such processes, recent work at I12 has focused on developing experimental capability for sample manipulation, data acqusition and processing, and at University of Manchester, on novel mathematical approaches for obtaining information about the process from the X-ray image data. In recent experiments, high speed synchrotron x-ray tomography has been used to acquire each 3D image in under 1 second, over a period of 5-20 seconds. Plain water and contrast-enhanced brine flowing in columns of natural aggregate and in well characterized glass spheres are imaged, and improvments in reconstructing the time-series by use of 4D reconstruction methods are illustrated.

Introduction

Ongoing improvments in tomography instrumentation and mathematics promise to enable the capture of the three-dimensional structure during rapidly evolving processes. But the challenge of acquiring the data, and producing usable time-resolved information is not trivial, and new approaches including the use of time series information in the mathematical reconstruction; and data acquisition strategies for high-speed processes and large data management are required. One system that is of great interest that requires high speed image acuqision, yet avoids complex experimental environments, is the process itself is the study of fluid flow through a porous medium

Improving resource management (hydrocarbons, water, CO2) relies on making significant advances in our knowledge of saturated and unstarurated fluid flow within rock pore spaces and fractures. The ability to directly follow and observe two and three phase fluid flow through complex porous rock structures, in 3D and in real-time is critical for improving our understanding of how the interconnected pore/channel structure modifies the flow characteristics, and for validating widely used CFD models that have little empirical basis, especially at the pore and intra-granual scale.

Developments at Diamond and collaborating institutes, in tight hardware integration[1] and time-resolved tomography reconstruction[2] combine with commercial high-speed

detector technology to enable acquisition and reconstruction of 3D datasets of this process at up to 14 3D images per second.

Methods

The experiment aims to reveal the preferred flow pathways during initiation of flow through the porous medium. In the experiment, a 4M aqueous solution of KI has been introduced drip-wise to a porous sandstone gravel bed, and the wetting and establishing of flow under gravity has been observed in-situ using high-speed high-energy tomography. The experiment has also been repeated with well-characterized spherical bead packs to study the behaviour in a simpler geometry and with different particle roughness.

A sequence of several hundred tomographic acquisitions has been recorded at a speed of 14 3D-volumes per second (vps). This is equivalent with a frame rate of 14 frames per second (fps) for any virtual 2D-slice inside the volume. 3D imaging acquisition rate was limited by stage rotation speed and not exposure times, even for 13 mm dimater samples. The synchronization of successive frames, ensuring each 3D dataset is well aligned with the others, is enabled by the high-speed Zebra signal device[1], which has capability of reading the sample manipulator position and recieivng or transmitting signals to other devices.

The flow cell was mounted on a rotation stage nominally capable of 14Hz rotation, and the Zebra was programmed to respond when the stage reached any multiple of 360 degrees. Upon reaching the trigger position, the Zebra would transmit a series of equally spaced pulses to the detector, to capture a tomographic series. The total number of images to be captured without interruption was fixed by the acquisition system, and the time for each image short enough to avoid significant motion blur during acquisiton. The series could either be sequential, or programmed with a gap of one or more full rotations between 3D dataset, keeping the data spatially registerd at all times.

The time series tomographs could then be reconstructed by the method of Kazantsev et al[2]; using a higher resolution prior of the unchanging subtsrate; collected either before flow was initiated, or by using an average of an initial independent reconstruction of all frames to extract the unchanging substrate geometry. Using this method it was possible to obtain good quality datasets with as little as 90 projection per 3D dataset.

Results

The results obtained for flow through sandstone are illustrated in Figure 1. The fluid may be clearly distinguished from both the air and the solid substrate, and has well defined edges. Liquid-Air-Rock contatcs can easly be defined for calculating interface curvatures, and rock, pore and liquid volumes can be quantiatively assessed. The sequence illustrates the initial establishment of the flow pathways, from (nearly) dry state (top left) to a spreading network of fluid (bottom right) and the liquid volume in the sample was increased. In Figure 2, a sub volume of the same data is rendered in 3D. Further study of the changing geometry of the fluid interfaces and local fluid volumes, based upon these reconstructions, is ongoing, but the suitablitliy of this method for imaginy highly dynamic processes is clear.

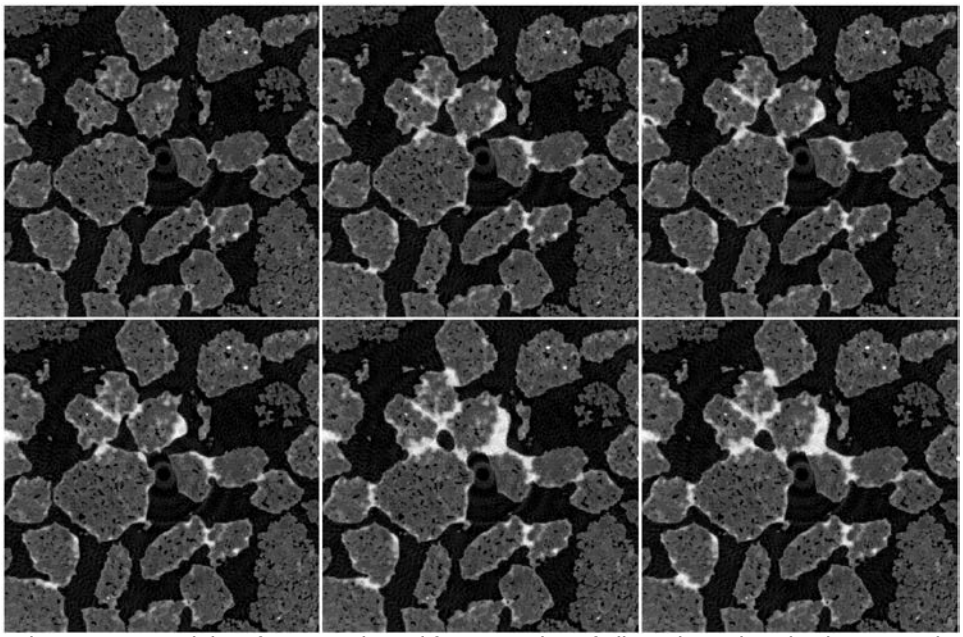

Figure 1. Several time frames selected from a series of slices through 3-d volumes each obtained in 73 ms . These are spaced 7 time frames apart (0.5 seconds)

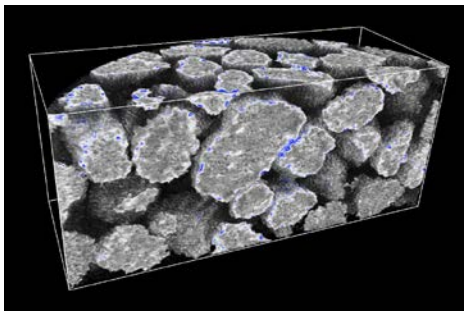

Fig 2: Sandstone wetted with KI-solution, X-ray tomography. Grains rendered grey, solution blue, porous network transparent.

References

[1] T. Cobb, Y. Chernousko, I.Uzun (2013), "*ZEBRA: -- A Flexible Solution For Controlling Scanning Experiments*" Proceedings of **ICALEPCS-2013**, Oct 6-11, San Francisco, CA, USA

[2] D. Kazantsev, G Van Eyndhoven, WRB Lionheart, PJ Withers, KJ Dobson, SA MacDonald, R.C.Atwood and P.D.Lee, "Employing Self-Similarity Across The Entire Time Domain In Computed Tomography Reconstruction", (2015) *Philisophical Transactions A* 373:3043 article 20140389

MAGNETIC CONTRAST NANOTOMOGRAPHY

*R. WINARSKI[1]

[1]Center for Nanoscale Materials, Argonne National Laboratory, 9700 S. Cass Avenue, Argonne, Illinois, USA
* presenting author

We are using the X-ray polarization selectivity (linear, right and left circularly polarized) available at the Hard X-ray Nanoprobe Beamline to examine magnetic materials in three dimensions using magnetism as a contrast mechanism [1,2,3]. X-ray magnetic circular dichroism (XMCD) refers to the differential absorption of left and right circularly polarized (LCP and RCP) X-rays, induced in a sample by an applied magnetic field. By closely analyzing the difference in the XMCD absorption spectra, information can be obtained on the magnetic properties of the elements in the system, such as spin and orbital magnetic moments. Differences in the near-edge X-ray absorption spectra are proportional to the differences in spin densities of the unoccupied electron bands in the sample. We are measuring these differences in absorption contrast while controlling the polarization during nanotomography acquisition.

References:
[1] Winarski, R. P., Holt, M. V., Rose, V., Fuesz, P., Carbaugh, D., Benson, C., Shu, D., Kline, D., Stephenson, G. B., McNulty, I. and Maser, J. (2012), A hard X-ray nanoprobe beamline for nanoscale microscopy. Jnl of Synchrotron Radiation, 19: 1056–1060. doi: 10.1107/S0909049512036783
[2] J. C. Lang and G. Srajer, Rev. Sci. Instrum. 66, 1540 (1995).
[3] G. Schütz, W. Wagner, W. Wilhelm, P. Kienle, R. Zeller, R. Frahm, and G. Materlik, Phys. Rev. Lett. 58, 737

Poster presentation

Ultrafast Data Post Processing Pipeline for Real-Time Tomographic Imaging at TOMCAT

F. MARONE[1], A. STUDER[2], H. BILLICH[2], L. SALA[2], T. ZAMOFING[3], R. MOKSO[1], *M. STAMPANONI[1,4]

[1] Swiss Light Source, Paul Scherrer Institute, Villigen, Switzerland
[2] Information Technology Division AIT, Paul Scherrer Institute, Villigen, Switzerland
[3] Controls Group, Paul Scherrer Institute, Villigen, Switzerland
[4] Institute for Biomedical Engineering, University and ETH Zurich, Zurich, Switzerland
* presenting author

At the TOMCAT beamline at the Swiss Light Source, the endstation, devoted to tomographic microscopy with sub-second temporal resolution, has been delivering new scientific results for few years. Dynamic processes (e.g. evolution of liquid foams and physiology in small living animals (Simon et al., 2014)) could for the first time be captured in 3D through time. Until recently, a major limitation for in-situ and in-vivo experiments has lain in the finite RAM (36 GB) of the used CMOS detector permitting only short continuous acquisition, typically only few seconds. To overcome the limited data transfer rates of commercially available detectors, we developed a new GIGAbit Fast Read-Out SysTem (Gigafrost). This new system has no on-board RAM: the sensor can be read out continuously in an unlimited manner providing rates as high as 8 GB/s.

To fully exploit the potential of the TOMCAT experimental endstation equipped with this innovative system, tools to look almost in real time at least at a slice selection of the tomographic volumes are mandatory. We report here on our recent scientific activities focussed namely on the development of new strategies for efficient handling and fast post processing of large amount of data to optimally complement the hardware implementation. We are active on several fronts. Large efforts were spent on tomographic reconstruction algorithms, validating Fourier methods (in particular gridrec) as alternatives to the standard Filtered Back-Projection approach (Marone and Stampanoni, 2012). Furthermore, the entire post processing pipeline concept as originally implemented at the TOMCAT beamline has been completely revised to match the new challenging data rates. In this context, the data format has been optimized permitting fast I/O and compatibility with data from other synchrotron sources: we adopted the Scientific Data Exchange data format, based on the HDF5 technology (De Carlo et al, 2014). The original implementation of the algorithm computing corrected sinograms has been completely substituted by a more transparent and modular version, ensuring higher flexibility and scalability. For highest speed, I/O to disk is minimized and the reconstruction routine, gridrec in our case, can read computed sinograms directly from memory and the correct center of rotation is automatically estimated to ensure high-quality tomographic reconstructions.

The raw data are typically first written to disk. The reconstruction parameters can be fully controlled and optimized via a user-friendly Graphical User Interface (GUI) implemented as a Fiji plugin and the reconstruction of the entire tomographic volume can be submitted to the reconstruction cluster per simple mouse click. The raw data can however also be streamed directly to the ultrafast post-processing pipeline with the aim of obtaining preliminary tomographic reconstruction of few selected slices almost in real time to better follow the acquisition process in 3D. This new pipeline can deliver about 20 tomographic slices in less than 3 s.

Python has been the language of choice, in combination with Message Passing Interface (MPI) for the implementation of this post-processing pipeline. Cython has been used to improve the computational performance of few selected parts. We use the Sun Grid Engine (SGE) batch queuing system for optimal use of all available distributed computational resources. With this approach, efficient management of the priorities for online-user and offline work is facilitated.

Current work is also focussed on complementing the pipeline with tools aimed at offline post-processing at a later stage. On one hand, more sophisticated algorithms for the mitigation of artifacts typical to ultrafast tomographic volumes (e.g. sample instabilities, flat-field modulations, low signal-to-noise ratio) are needed. On the other hand, for highest quality results, the reconstruction of strongly undersampled tomographic datasets necessitates routines based on iterative algorithms and a priori information.

Number of words: 597

Session 102

3D CHEMICAL IMAGING IN THE LABORATORY BY X-RAY ABSORPTION EDGE MICROTOMOGRAPHY

C. K. Egan[1],* S. D. M. Jacques[1,2], M. D. Wilson[3], M. C. Veale[3], P. Seller[3], A. M. Beale[2,4], R. A. D. Pattrick[5], P. J. Withers[1], R. J. Cernik[1]

[1] School of Materials, University of Manchester, Manchester, UK

[2] UK Catalysis Hub, Rutherford Appleton Laboratory, Research Complex at Harwell, Didcot, UK

[3] Science and Technology Facilities Council, Rutherford Appleton Laboratory, Harwell Science and Innovation Campus, Didcot, Oxfordshire OX11 0QX, UK

[4] University College London, Department of Chemistry, 21 Gordon Street, London, UK

[5] School of Earth, Atmospheric and Environmental Sciences, University of Manchester, Manchester, UK

* presenting author - christopher.egan@manchester.ac.uk

Keywords: Spectroscopic X-ray detectors, computed tomography, geosciences, analytical chemistry

Abstract

A spectroscopic X-ray imaging detector was installed in a laboratory microtomography scanner enabling the X-ray absorption spectrum of a material to be measured. With a high energy resolution, the detector can distinguish individual absorption edges, the position of which identifies the atomic elemental composition in the sample. Using computed tomography, the internal elemental chemistry of a sample can be reconstructed and visualised in three dimensions (3D). Segmentation of elemental phases can be performed by K-edge subtraction, or alternatively, semi-quantitative analysis can be employed by voxel-wise spectral fitting, giving a measure of relative atomic concentrations in the sample. We demonstrate the application of 3D chemical imaging in the laboratory by mapping of minerals and inclusion phases inside a mineralised ore sample.

Introduction

The majority of laboratory-based X-ray computed tomography (XCT) systems operate in the hard X-ray range (approximately 10 - 100 keV) primarily using the bremsstrahlung and characteristic radiation resultant from high energy electrons impacting onto metal target. In this energy range, the main component to a material's X-ray attenuation is the photoelectric effect, the magnitude of which is approximately proportional to the 4th power of the atomic number (Z) and inversely proportional to the 3rd power of the X-ray energy (E). Additionally, the atomic photoelectric absorption cross-section shows rapid changes at energies corresponding to core-electron states, the K, L, M-edges. Because these characteristic step-changes in absorption occur at well defined X-ray energies, it is feasible to use these edges to identify individual chemical elements inside the object, as well as reconstruct the sample's absorption contrast. All that is required to achieve this additional chemical sensitivity is the ability to precisely tune the X-ray photon energy to an absorption edge. Using extremely bright X-rays generated at synchrotron radiation facilities, it is possible to use highly-selective optics (e.g. monochromators and focusing mirrors) that can produce radiation with a very narrow bandwidth (down to the 0.01% level) which can be tuned to specific absorption edges. By applying computed tomography, 3D chemical imaging can then be performed by twice repeating the same tomographic scan at two different X-ray energies, one slightly above and one slightly below the desired absorption edge. A basic subtraction of these datasets reveals the 3D

distribution of the chemical element corresponding to the absorption edge. An alternative method for 3D chemical imaging is to use the X-ray fluorescence (XRF) signal emitted after sample absorption. In this case a small, intense beam of X-rays from a synchrotron source is focussed down to a point and scanned across the object recording weak XRF signals at each point. This is then repeated at distinct small rotation steps of the object, and a reconstruction algorithm is used to build a 3D map of the atomic elements in the sample. This approach has additional sensitivity but is much slower due the beam scanning process. Both of these methods require the use of a synchrotron radiation facility, which unfortunately has a major limitation from a throughput and access point of view inhibiting wide-scale adoption. Laboratory-based XCT instruments do not have the same limitations in terms of access, but they lack chemical sensitivity, largely due to low intensity radiation emitted from a laboratory X-ray tube. Over recent years, however, a range of pixelated spectroscopic X-ray detectors have been actively researched and developed which have the ability to measure X-ray energy in specific energy bands with positional sensitivity. If these new types of spectroscopic detectors have sufficient energy resolution, it could be possible to measure the position of an absorption edge using the broadband radiation emitted from a laboratory X-ray tube. Here, we describe the installation of a spectroscopic pixelated detector (with a high energy-resolution) inside a commercially available laboratory-based XCT system for performing 3D, micron scale, chemical imaging via absorption-edge tomography.

Methods

The principle of the method is the same to that of a regular laboratory-based XCT system, as shown in Figure 1. X-rays generated from a microfocus X-ray tube illuminate a sample object and the projected radiograph is recorded on an area detector. In this case however, we replace the conventional area detector with a HEXITEC spectroscopic detector which can record the absorption spectrum in each pixel with an energy resolution of about 1 keV. By taking the natural logarithm of the normalised intensity in every spectral band we get a linear measurement of the absorption cross-section as a function of X-ray energy. A step-change in the absorption spectrum indicates the position of an absorption-edge, which can be used to identify and map chemical elements in the sample. Tomographic reconstruction creates a 4D dataset (3 spatial dimensions, 1 spectral dimension) with each voxel containing an absorption spectrum. The position of an absorption edge in each reconstructed voxel spectrum is used as a characteristic marker, enabling chemical elements to be mapped in 3D.

The HEXITEC spectroscopic detector was installed in a NIkon XTH 225 system. The detector consists of a 1 mm thick CdTe single crystal detector (20 × 20 mm^2) bump-bonded to a large area ASIC packaged with a high performance data acquisition system. The detector has 80 × 80 pixels on a 250 µm pitch with an energy resolution (FWHM) of ~800 eV @ 59.5 keV and ~1.5 keV @ 141 keV. During operation each photon event has its charge and pixel position and the frame in which it occurs recorded. Events are processed and histogrammed according to measured charge, typically using between 400 - 800 bins, depending on the energy range studied.

The Nikon XTH 225 system uses a microfocus reflection Cu target X-ray tube which was operated at a beam current of 15 µA and tube voltage of 160kV. We scanned the detector along 5 separate positions in the horizontal direction to increase the field of view. Each sub-projection was recorded for an exposure time of 45 seconds (225 seconds for a full projection) and we performed 120 projections covering 360° (total scan time 7.5 hrs). Tomographic reconstructions were performed using a GPU based SIRT algorithm operating in series on each energy channel, producing a 4D dataset (3 spatial dimensions, 1 spectral dimension).

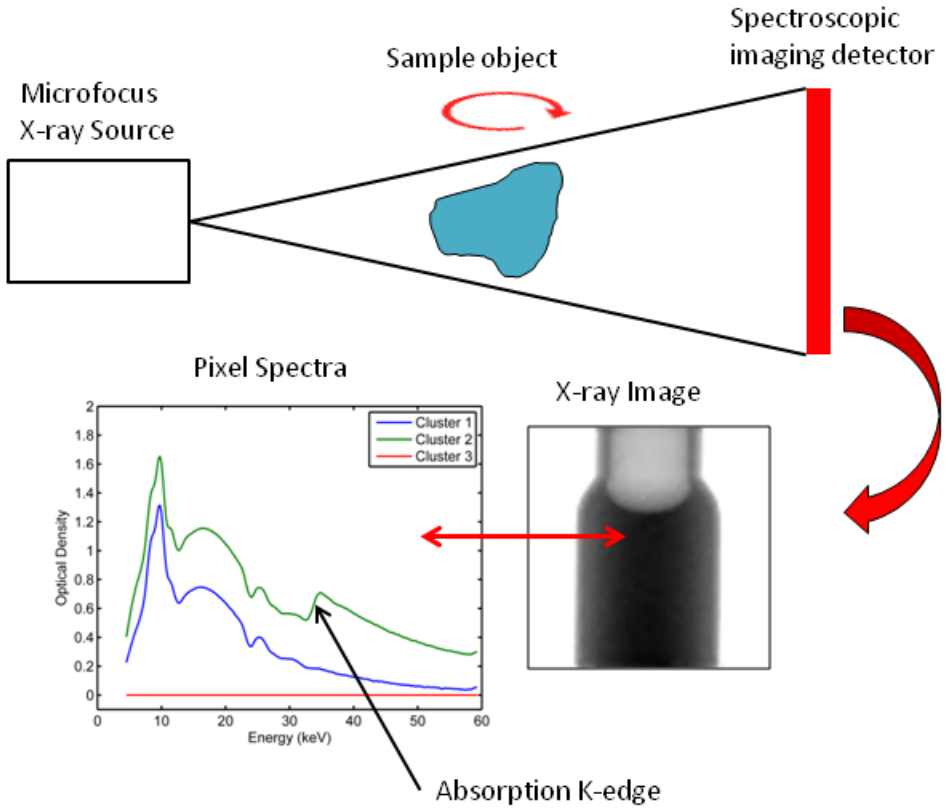

Fig. 1. *Spectroscopic XCT: The regular area detector in a commercially available microtomography scanner is replaced with a spectroscopic imaging detector such that the absorbed spectrum in every pixel can be measured. Each reconstructed voxel now contains an absorption spectrum as opposed to a grayscale value. Step-changes in the absorption spectrum signify the position of an absorption edge, which can be used to map chemical elements inside the object with micron scale resolution.*

Results

To demonstrate the method, we investigate the 3D distribution of mineral phases and inclusions in a mineralised ore sample. The sample is taken from a hydrothermal vein comprising pyrite (FeS_2), quartz (SiO_2), gold (Au) and minor amounts of galena (PbS), chalcopyrite ($CuFeS_2$) and bornite (Cu_5FeS_4). Optical 2D examination of polished sections of this sample reveals quartz and euhedral pyrite (mm to cm sized) to have precipitated first in the vein and been subsequently brecciated with the angular pyrite fragments re-cemented by quartz derived from later fluids. Gold precipitation was coeval with this second quartz episode and occurs as irregular masses (mostly <100µm) and in fractures replacing the pyrite. Gold also occurs as small masses in the quartz and at quartz-pyrite interfaces.

Understanding the distribution of gold in pyritic and other mineralogically complex ores is important in the development of processing pathways. Economic gold deposits often involve Au in very low concentrations (<10gm/t) and the gold is as discrete grains. 3D spectroscopic imaging has the potential to provide definitive information on the size, distribution and mineralogical association that will control liberation during processing. As gold mining has increasingly used heap leaching to extract gold, spectroscopic XCT imaging during processing has an important role in explaining extraction rates and allowing pathway tuning. Furthermore, the search and exploitation of new mineral

resources to replace exhausted deposits and satisfy increasing demand will employ chemical or bio-leaching of large volumes of low grade ore and 3D spectroscopic imaging has the potential to play a significant role in ensuring efficient exploitation.

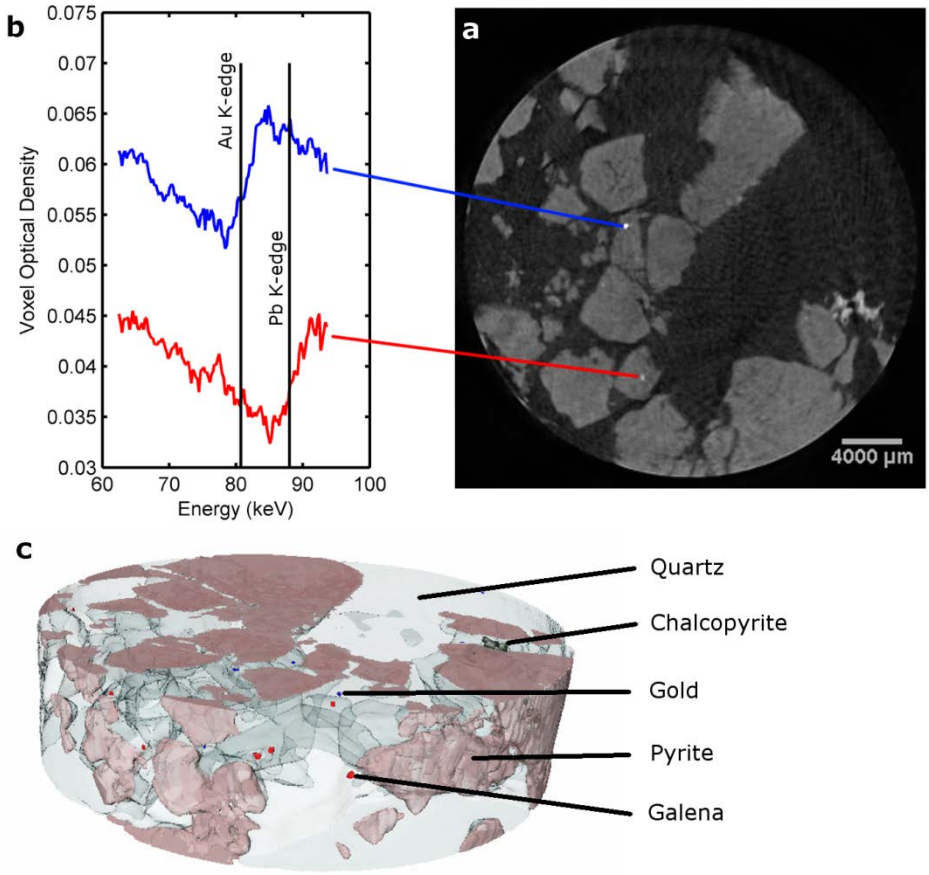

Fig. 2. *3D distribution of mineral phases in a mineralised ore sample from a gold-rich hydrothermal vein. (a) Grayscale tomographic slice through the sample created by integrating over the full spectral range. (b) Voxel spectra showing Au and Pb K-edges. (e) 3D visualisation of the distribution of mineral phases in the ore sample.*

A 20mm diameter ore sample was scanned in the spectroscopic XCT system - the data was reconstructed with a 95 µm voxel size. Figure 2a shows a grayscale tomographic slice through the sample produced by integrating over the full spectral range. Different mineral phases are observed by their variation in gray level contrast. Figure 2b shows two voxel spectra from two separate inclusions. The first spectrum shows a step change in attenuation corresponding to the Au K-edge at 80.7 keV and the second inclusion spectrum shows a Pb K-edge at 88.0 keV. The measured position of these edges positively differentiates the gold and galena (PbS) mineral phases. In order to segment and separate these two phases we used a K-edge subtraction method. By extracting images at energies above and below the desired absorption edge and subtracted them, we produced Au only and Pb only 3D datasets. An important feature of this data is that due to inter-particulate variations in the attenuation of these particles, it was impossible to accurately segment the Au and PbS phases using just gray level contrast. Some of the gold inclusions show a much higher density which can be easily segmented using a threshold, but many particles show either similar gray level contrast, or a much lower contrast to that of PbS. As such, when looking at data produced by scanning this sample in a non-spectroscopic (standard) XCT system, it was impossible

to reliably differentiate and segment PbS from Au. Only the K-edge sensitivity of the spectroscopic XCT system can produce a positive identification and therefore successful segmentation. Other mineral phases in the sample (quartz, pyrite and chalcopyrite) show no observable absorption edges since they contain only low Z-atomic elements with edges below the sensitivity of the system. They can be easily segmented based upon their relative attenuation contrast. In this case however, we exploited the spectroscopic nature of the data and segmented based upon a least square fit of a linear function to the absorption spectra in the range 60-90 keV. The gradient of the linear function is used as a segmentation tool by thresholding. This approach gives better inter-phase distinguishability since it is less sensitive to image noise and was particularly useful in the quartz mineral due its low attenuation and high level of reconstruction artefacts. 3D visualisations of the distributions of each segmented mineral phase, including Au and Pb containing particles, are shown in Figure 2c. From this data we found that the Au inclusions are almost always embedded in pyrite, whereas Galena inclusions can be either embedded in pyrite or quartz. Many inclusions may exist below the resolution of the system, either spatially - i.e. smaller than the voxel size of the scan (95 µm), or spectrally - i.e. with concentrations below the sensitivity limit of the system. With regards spatial resolution, spectroscopic XCT can ultimately produce voxel sizes on a par with current microtomography scanners (< 5 µm) and is only really limited by the pixel size of the detector. For this sample with a 20 mm diameter, it could be possible to achieve resolutions of around 10-15 µm, given a large enough field-of-view. With a smaller sized sample it could be possible to achieve < 5 µm resolution. With regards chemical sensitivity, we have yet to perform a systematic study, however previous experience suggests a lower limit of around 1-2 %wt per voxel.

Conclusions

In summary, we have developed a laboratory-based XCT system that has the ability to produce 3D images with chemical sensitivity and micrometer scale resolution. By exchanging the regular area detector on an XCT scanner with a pixelated spectroscopic X-ray detector we can produce 3D datasets with voxels containing absorption spectra. Step-changes in the absorption spectra signify the position of absorption-edges which are used as a fingerprinting tool to identify chemical elements inside each voxel. A particular attribute of this method is that it can be very simply retrofitted to most XCT systems, simply by adding in a spectroscopic detector, in turn enabling wide scale adoption and expanding the available range of materials characterisation techniques. This can be exploited further by utilising the non-destructive nature of X-ray tomography to study 3D chemical processes occuring inside materials and structures which are functioning under real-world conditions (e.g. temperature, pressure, corrosive environments etc...). We expect this method will find applications to a wide range of scientific disciplines covering materials science, planetary, earth and environmental sciences, chemistry and catalysis, and archaeology.

References

Bleuet P. *et al.* (2010) 3D chemical imaging based on a third-generation synchrotron source. ***Trac-Trends in Analytical Chemistry*** 29, 518-527, doi:10.1016/j.trac.2010.02.011.

De Samber B. *et al.* (2008) Three-dimensional elemental imaging by means of synchrotron radiation micro-XRF: developments and applications in environmental chemistry. ***Analytical and bioanalytical chemistry*** 390, 267-271.

Egan, C. K., Jacques, S. D. & Cernik, R. J. (2013) Multivariate analysis of hyperspectral hard X-ray images. ***X-Ray Spectrometry*** 42, 151-157.

Egan C. K. *et al.* (2014) Material specific X-ray imaging using an energy-dispersive pixel detector. ***Nuclear Instruments and Methods in Physics Research Section B: Beam Interactions with Materials and Atoms*** 324, 25-28.

Ghorbani Y *et al.* (2011) Large particle effects in chemical/biochemical heap leach processes–a review. ***Minerals Engineering*** 24, 1172-1184.

Ordavo, I. *et al.* (2011) A new pnCCD-based color X-ray camera for fast spatial and energy-resolved measurements. ***Nuclear Instruments and Methods in Physics Research Section A: Accelerators, Spectrometers, Detectors and Associated Equipment*** 654, 250-257.

Seller P. *et al.* (2011) Pixellated Cd(Zn)Te high-energy X-ray instrument. ***Journal of Instrumentation*** 6, C12009.

Mapping grains in 3D by laboratory X-ray diffraction contrast tomography

S.A. MCDONALD*[1], C. HOLZNER[2], P. REISCHIG[3], E.M. LAURIDSEN[3], P.J. WITHERS[1], A. MERKLE[2], M. FESER[2]

[1] School of Materials, University of Manchester, Manchester, M13 9PL, UK
[2] Carl Zeiss X-ray Microscopy Inc., 4385 Hopyard Road, Suite 100, Pleasanton, CA 94588, USA
[3] Xnovo Technology ApS, Galoche Alle 15, 4600 Køge, Denmark
* presenting author

Keywords: diffraction contrast tomography, microstructure evolution, powder sintering

Abstract

Here we describe a new commercial laboratory X-ray diffraction contrast tomography (DCT) modality which has been enabled and present some early experimental results. One of the advantages of the technique over destructive methods of mapping grains in 3D is the ability to track changes, in grain size and orientation, over time, e.g. '4D' time lapse studies. An example of this capability is provided by following the sintering of 100μm diameter copper particles at a temperature of 1050°C, through a series of time lapse lab-DCT measurements. Local diffusion and deformation-related shape changes of the sintering particles are captured using conventional absorption tomography. At the same time, lab-DCT enables particle rearrangements (rotations and translations) as well as competitive grain growth from particle to particle through the sintering cycle to be tracked. This new laboratory based method could have a wide range of applications as well as supporting 3D polycrystalline modeling of materials performance.

Introduction

The majority of metallic and ceramic engineering materials of interest are polycrystalline. The properties of these materials can be significantly affected by behaviour at the length scale of the crystalline grain structure. The ability to characterise this crystallographic microstructure, non-destructively and in three-dimensions, is thus a powerful tool for understanding many facets of materials performance. The technique of X-ray diffraction contrast tomography (DCT) using monochromatic X-ray beams of very high flux found at 3rd generation synchrotron sources has been shown to be capable of mapping crystal grains and their orientations in 3D non-destructively [Johnson *et al*., 2008; Ludwig *et al*., 2009; Ludwig *et al*., 2010]. Clearly given the much wider availability and accessibility of laboratory X-ray microtomography systems the development of a laboratory DCT technique is an attractive prospect.

Sintering of loose or compacted granular bodies has a strong influence on the final microstructure and properties of engineering components produced via the powder metallurgical route [Cocks 2001]. In applying the lab-DCT technique to follow changes occurring over time at the level of the individual crystal grains within copper particles during sintering, information regards the rearrangement of particles and the competitive growth of grains both within and between particles can be extracted. This will give an improved understanding of the extent to which the different mechanisms contribute towards densification during sintering and their influence on the final microstructure, which should be controlled for optimal component performance. Here we introduce the technique and present some initial experimental results obtained from a time lapse particle sintering study.

Methods

The experiment was performed using a ZEISS Xradia 520 Versa system from Carl Zeiss X-ray Microscopy. In order to collect diffraction spot images due to diffraction from crystal grains within a sample, two additional elements are introduced to the setup of the standard instrument used for conventional absorption and phase contrast X-ray tomography measurements. Firstly, an aperture is placed between the source and sample, which restricts the size of the direct X-ray beam, illuminating the sample only in the central region of the detector and leaving the outer part dark as shown in Fig. 1(a). Secondly, a beam stop is used to attenuate the direct X-ray beam. The direct beam has a much stronger signal than a diffracted beam and thus blocking it improves the signal of the diffraction spots obtained on the detector. For the lab-DCT measurements two consecutive scans are performed. The first scan collects the absorption contrast projections in the direct beam (see Fig. 1(a)). These images are used to produce an absorption contrast reconstruction of the sample (absorption mask). The second scan collects the diffraction spot images with the beam stop in position, an example image of which is shown in Fig. 1(b). Grains diffract the beam on to the outer part of the detector. These images are used to calculate the positions of grains in relation to the sample reconstruction obtained from the first scan and their size and orientation.

The source–sample and sample–detector distances were both set to 14 mm. This 1:1 distance ratio of the source and detector benefits from a Laue focusing effect resulting in the appearance of the diffracted signals as line-shaped spots (see Fig. 1(b)) that reduces the chance of overlapping diffraction spots and increases their signal intensity. Based on this source and detector distance geometry, and using the full pixel readout of the detector, an effective pixel size of 1.7 µm was achieved. An accelerating voltage of 120 kV and current 75 µA gave a transmission of the direct beam through the loose particle structure of ~ 25 %. For the DCT scan 360 diffraction spot images were acquired around a 360° rotation of the sample with an exposure time per image of 60 s. 720 projection images each of 2 s exposure were acquired for the absorption contrast scan. Reconstruction of grain maps from the diffraction spot images is performed using GrainMapper3D™ software from Xnovo Technology.

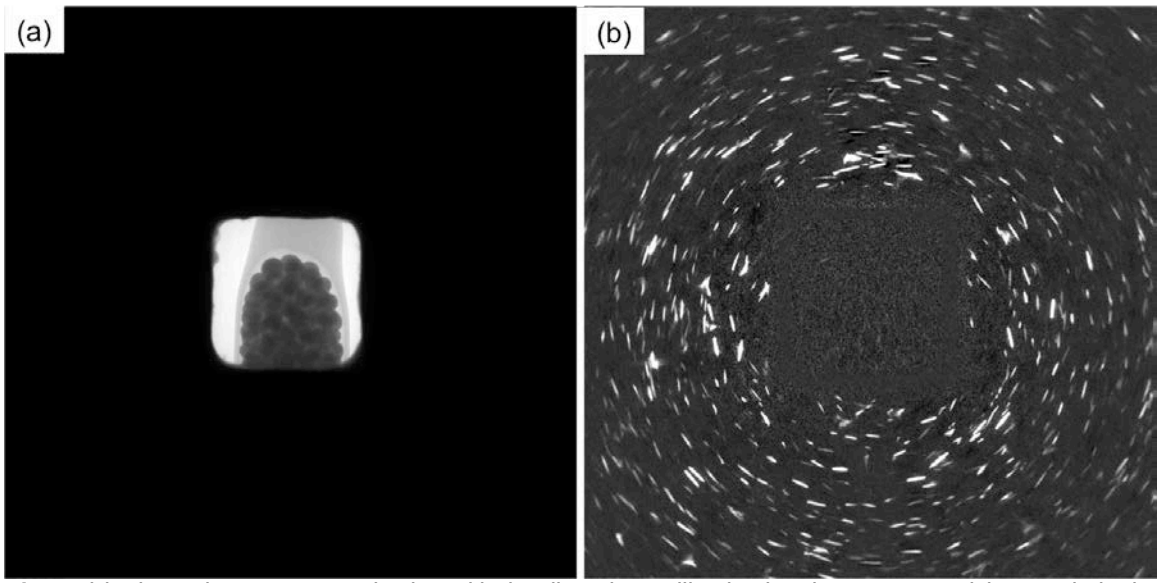

Fig. 1. *(a) Absorption contrast projection with the direct beam illuminating the copper particle sample in the central region of the detector. (b) Image showing diffraction spots from grains within the sample at a single rotational position. Note the direct beam is blocked by the beam stop.*

The sample comprised spherical polycrystalline copper powder particles, supplied by Makin Metal Powders (UK) Ltd., with a mean particle size of 100 µm. The initially loose copper particles were contained within a quartz capillary of 0.7 mm diameter. Sintering was performed *ex situ* at a temperature of 1050 ºC in a tube furnace within reducing atmosphere of Ar / 5 % H. A series of sintering steps were applied to the powder body in order to follow its evolution and to measure the progression of particle rearrangement and grain growth.

Results

Fig. 2 shows the copper powder body at two different stages of the sintering cycle, at the initial state and after a combined sintering time of 64 min at 1050°C, acquired from absorption contrast tomography scans. Indicated by circles in the images are examples of the local diffusion and deformation-related shape changes occurring during sintering, the development of interparticle bonds or necks between neighbouring particles.

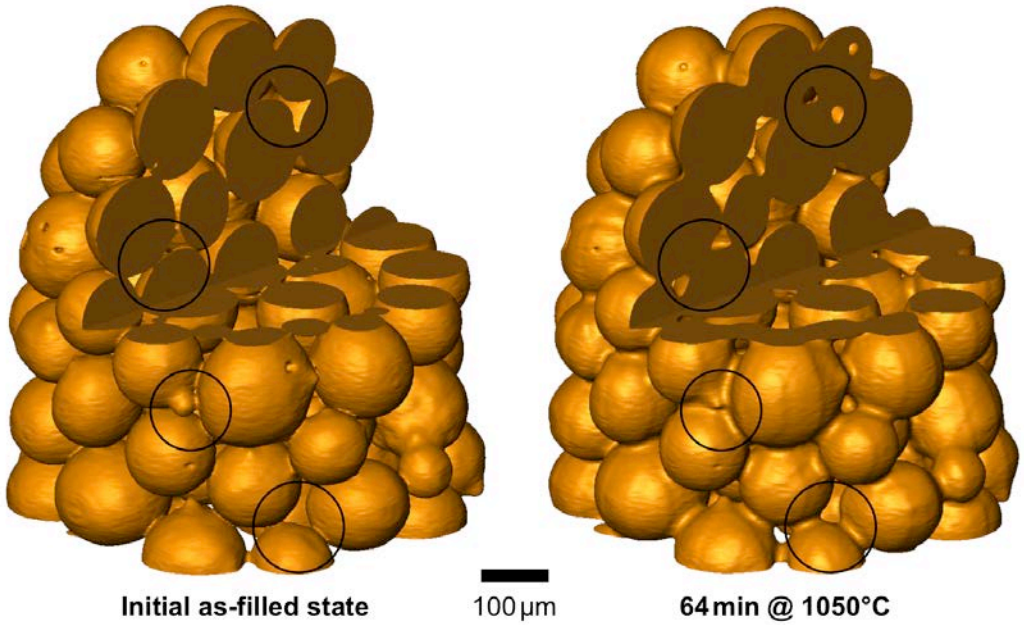

Fig. 2. *3D isosurface reconstructions of the scanned region of the copper particles within the capillary showing the initial state and after a sintering heat treatment.*

Fig. 3 shows grain maps reconstructed from the lab-DCT scans of the sample at the two different time steps (and two different views for each). The grains are represented by cubes showing their positions in relation to the sample absorption mask. Revealed are the crystallographic orientation of the grains and their relative size. Individual cubes representing the grains can be followed between time steps and are observed in general to increase in size on applying a sintering heat treatment, indicating the degree of grain growth that has occurred. The mean grain size increases from a value of 68.6 µm at the initial step to a value of 82.4 µm. Also, the number of grains is observed to decrease significantly as competitive grain growth occurs within and between particles, from 226 grains to 132 grains for 90 particles within the scanned region of the powder body. The occurrence of any particle rotations will be investigated through analysis of changes in crystallographic orientation of grains.

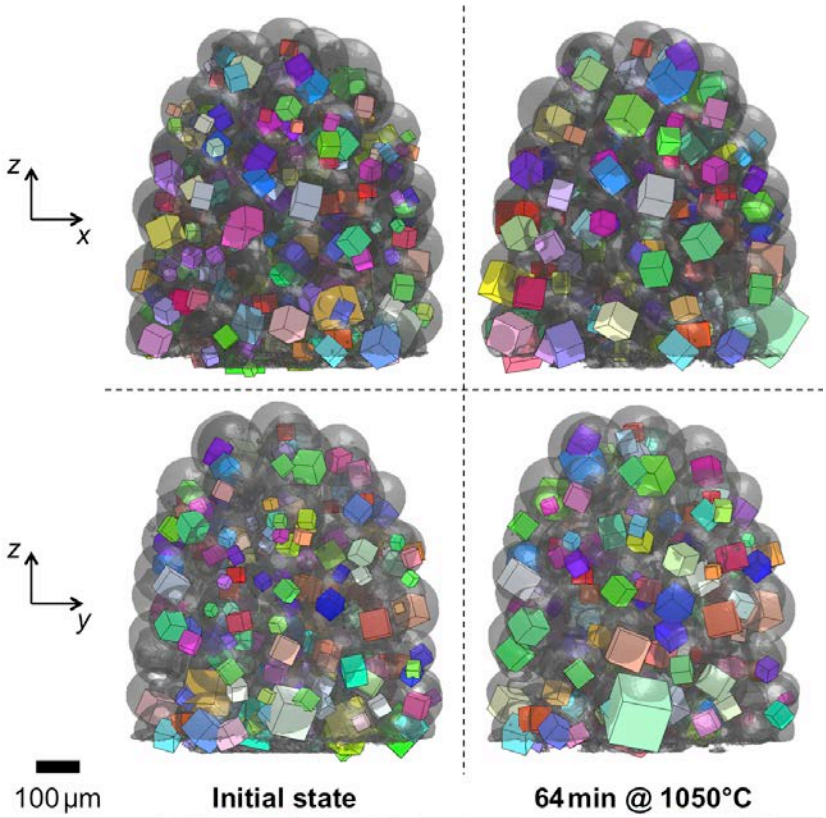

Fig. 3. *Reconstructed grain maps from two different time steps. The grains are plotted as cubes at their measured positions within the absorption mask of the sample, which is shown transparent, revealing their (relative) size and crystallographic orientation (by colour).*

Summary

A new laboratory based X-ray diffraction contrast tomography technique has been combined with conventional absorption contrast tomography to follow the processes that occur during sintering of copper particles, non-destructively and in three-dimensions. Absorption CT has identified changes in the local morphology, such as the development of interparticle contacts between neighbouring particles. At the same time, DCT has enabled the quantification of the individual crystallite grains contained within the polycrystalline copper particles in terms of their size and crystallographic orientation. Such experiments will allow the development of an improved theoretical description of the sintering process with the aim, in the future, of developing fully dense metal powder processed products that retain finer grain structures.

References

Cocks, A.C.F. (2001). Consitutive modeling of powder compaction and sintering. ***Progress in Materials Science*** 46, 201–229.

Johnson, G., King, A., Goncalves Honnicke, M., Marrow, J. & Ludwig, W. (2008). X-ray diffraction contrast tomography: a novel technique for three-dimensional grain mapping of polycrystals. II. The combined case. ***J. Appl. Crystallogr.*** 41, 310–318.

Ludwig, W., Reischig, P., King, A., Herbig, M., Lauridsen, E.M., Johnson, G., Marrow, J. & Buffière, J.-Y. (2009). Three-dimensional grain mapping by X-ray diffraction contrast tomography and the use of Friedel pairs in diffraction data analysis. ***Rev. Sci. Instrum.*** 80, 033905.

Ludwig, W., King, A., Herbig, M., Reischig, P., Marrow, J., Babout, L., Lauridsen, E.M., Proudhon, H. & Buffière, J.-Y. (2010). Characterisation of polycrystalline materials using synchrotron X-ray imaging and diffraction techniques. ***JOM*** 62, 22–28.

Liquid-Metal-Jet X-Ray Tube Technology and Tomography Applications

EMIL ESPES * [1], FREDRIK BJÖRNSSON[1], CHRISTINA GRATORP[1], BJÖRN A. M. HANSSON[1], OSCAR HEMBERG[1], GÖRAN JOHANSSON[1], JOHAN KRONSTEDT[1], MIKAEL OTENDAL[1], PER TAKMAN[1], RICKARD TERFELT[1] AND TOMI TUOHIMAA[1]

[1] Excillum AB, Torshamnsgatan 35, 164 40 Kista, Sweden – info@excillum.com
* presenting author

Keywords: Maximum of 5 keywords

Abstract

The power and brightness of electron-impact micro-focus X-ray sources have long been limited by thermal damage in the anode. Here we describe a novel X-ray microfocus source based on a new anode concept, the liquid-metal-jet anode (MetalJet). The regenerative nature of this anode allows for significantly higher e-beam power density than on conventional anodes, resulting in this source generating significantly higher brightness than other X-ray tubes in the microfocus regime (~5-50 µm). We describe the fundamental properties of the technology and will review the current status specifically in terms of spot size, stability, lifetime, flux, acceleration voltage and brightness.

1. Introduction and System Description

As illustrated in Fig 1a, a conventional X-ray tube generates X-rays when highly energetic electrons are stopped in a solid metal anode. The fundamental limit for the X-ray power generated from a given spot size is when the electron beam power is so high that it locally melts the anode. The liquid-metal-jet anode (MetalJet) technology solves this thermal limit by replacing the traditional anode by a thin high-speed jet of liquid metal (see Figure 1b). Melting of the anode is thereby no longer a problem as it is already molten, and significantly (currently about 10x) higher e-beam power densities can therefore by used.

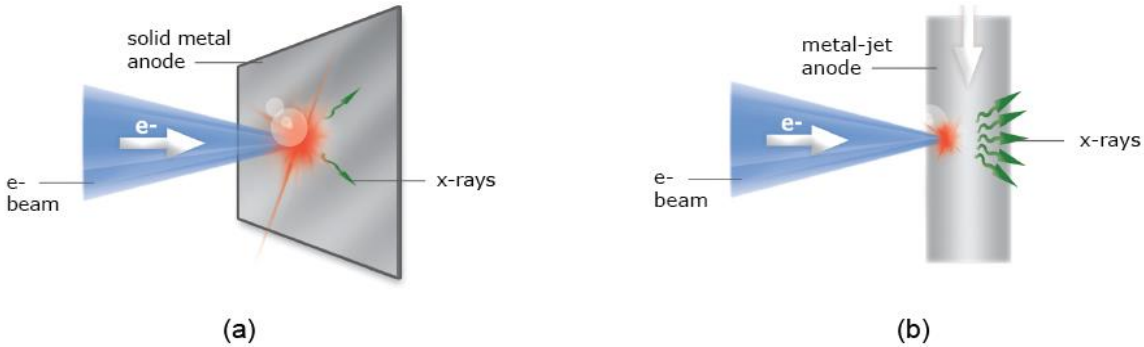

Fig. 1. *The principle of a solid anode X-ray tube (a) and a liquid-metal-jet X-ray tube (b).*

Figure 2 illustrates a complete MetalJet X-ray source. The upper part is the source head with the electron gun and the vacuum pump. This part is similar to any open-type X-ray tube apart from the metal-jet anode that is formed by ejecting a ~200 µm diameter metal jet through what is essentially a standard water cutting nozzle. One key requirement to achieve 24/7 operation is that the liquid-metal-alloy can be 100% recirculated. This is achieved by a reliable standard industrial pump which is located in the pumping unit typically situated right below the source as seen in Fig. 2. This pump pressurizes the metal alloy to approximately 200 bar to allow the jet to reach a speed of ~75 m/s.

***Fig. 2**: A complete MetalJet X-ray source with source head, pump box and support electronics.*

A pump like this can run uninterruptedly and reliably for at least a year without any service or maintenance. The path of the circulating liquid alloy is illustrated by the arrows in Fig. 2. The lower pump-box also contains the fore-vacuum pump and in addition the two smaller rack-mounted boxes seen in the background in Fig. 2 are needed for the high-voltage and low-voltage electronics and power supply. The shape and size of the source is such that it should easily fit into cabinets for X-ray computed tomography with the pump box situated below the main table.

The engineering aspects of closed-loop recirculation are significantly relaxed if anode alloys molten at room temperature can be used. This limits the corrosiveness of the alloys, that tend to increase rapidly with temperature,and also simplifies the draining of the system at times of service. The first available sources use either a mainly gallium (95% Ga and 5% In) based alloy or an alloy which also contain significant amounts of indium (68.5% Ga, ~21.5% In, and ~10% Sn). The gallium Kα line is at 9.3 keV, which makes it an attractive high-brightness replacement of copper Kα at 8.0 keV. The indium Kα is at 24.2 keV making it an attractive high-brightness replacement of silver Kα at 22.2 keV. Figure 3 shows the emitted Ga and In spectra as well as the Cu and Ag spectra, for comparisons.

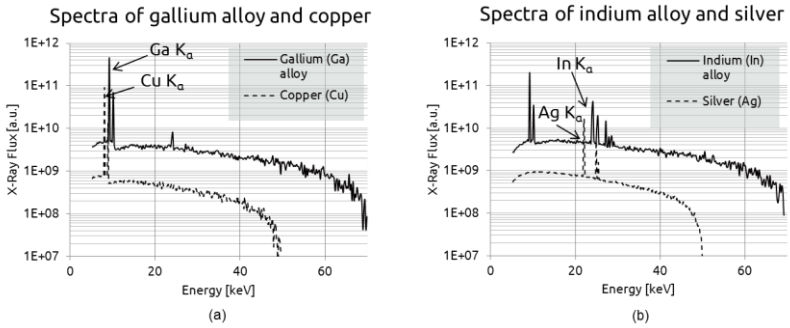

***Fig. 3:** Typical spectra at 70 kV acceleration voltage for gallium alloy (a) and indium alloy (b).*

Recently, the development of a heated system was finished, which allows for an alloy with a melting point slightly above room temperature to be used. The new alloy contains more indium (~40% Ga, ~40% In and ~10% Sn) which will result in a higher intensity from the indium Kα at 24.2 keV as well as a higher yield of the Brehmstrahlung spectrum, due to a higher effective atomic number.

2. Typical source performance

The main specifications of current MetalJet sources are listed in Table 1. Table 2 summarizes typical source parameters for operation in four different configurations. Normally we employ 1:4 e-beam line focus which results in a round spot with angled viewing. For example, for X-ray diffraction the source is typically operated at 200 W with an approx. 20×80 μm2 spot viewed at an angle to generate an effective ~20-μm-diameter spot. However, the spot shape may be freely tuned from larger sizes, limited only by the size of the liquid jet, down to 5-6 μm diameters, limited by the e-beam focus and electron scattering. The aspect ratio is also freely tuneable. The brightness is given as the Kα (double) line brightness. Here quantitative spectrometer measurements and pin-hole source size measurements have been combined with e-beam power scaling to obtain typical data.

***Table 1**: Typical source specification*

Voltage	Power	Max. current	Min. focal spot size	Min. spot-object distance	Available beam angle
10-160 kV	0-300 W	4.3 mA	~5 μm	18 mm	18°

Table 2: Typical source performance

Alloy	Acceleration voltage [kV]	Apparent Spot Size[a]	E-beam power	Line	Kα peak brightness [photons/(s·mm2·mrad2·line)]
Gallium alloy	70	20	200	Ga K-alpha	2.6×10^{10}
Gallium alloy	70	10	100	Ga K-alpha	5.2×10^{10}
Indium alloy	70	20	200	In K-alpha	1.3×10^{9}
Indium alloy	70	10	100	In K-alpha	2.6×10^{9}

[a] *Actual e-beam spot has a 1:4 aspect-ratio line focus, but the projected diameter is essentially circular.*

The spot size as well as the energy distribution in the spot is important for many applications. These parameters are measured with a pinhole/CCD hole-camera arrangement. The pinhole had a diameter of 4.3 µm, the magnification was 6.44× and the CCD pixel size was 6.45 µm. Figure 4a shows typical 2D intensity distributions in both the horizontal and vertical direction of a 10-µm-diameter source. We note that the shape is smooth and with very little energy in the wings. The X-ray spot intensity distribution is also verified by acquiring images of a JIMA target.

Figure 4b shows such an image with the source operating at 10 µm diam spot, clearly resolving the 3 µm vertical lines and 4 µm horizontal lines, thereby supporting the high quality of the X-ray spot.

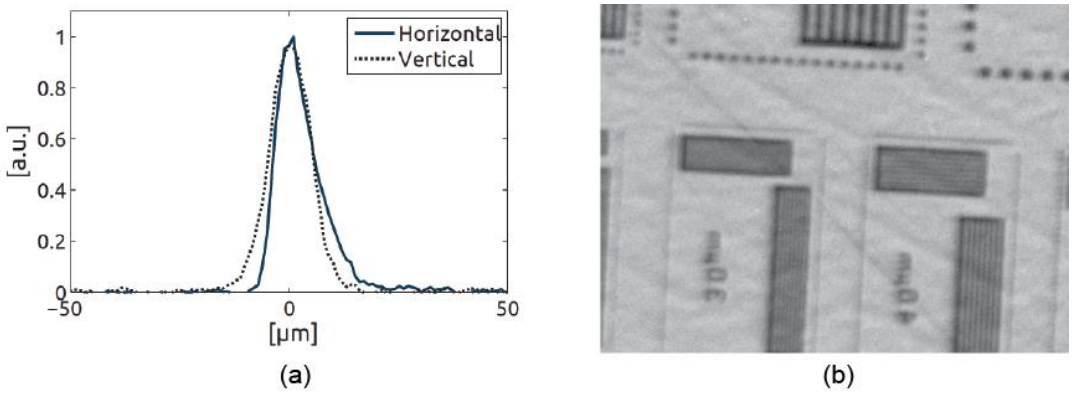

***Fig 4**: X-ray spot intenstity distribution (a) of a 10 µm X-ray spot and a corresponding JIMA target image (b).*

3. Imaging Applications

During the last few years, several articles has been published were the authors has used MetalJet x-ray tubes, below a short summary of some of the papers will follow.

3.1 X-ray phase contrast for CO2 microangiography [Lundström]

U. Lundström et. al. demonstrates the use of carbon dioxide as an efficient contrast agent for phase-contrast imaging of microvasculature, providing high contrast with Excillum MetalJet sources. The method is demonstrated on rat kidney, showing 3D tomographic imaging down to 60 µm vessels at acceptebale dose, which are illustrated in figure 6.

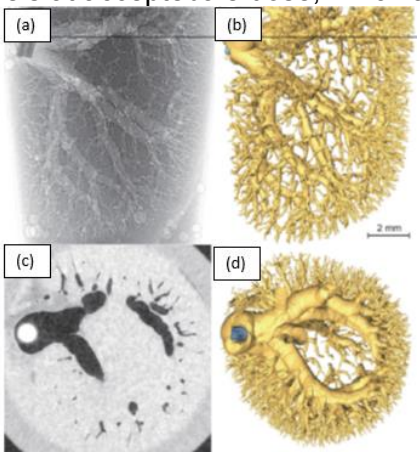

***Fig 6**: (a) unprocessed projection, (b) tomographic reconstruction, (c) tomographic slice throught the line in (a) and (b), (d) tomographic reconstruction. Vessels down to 60µm has been gas filled, and are clearly visible in projections and tomographic reconstruction. The scale bar is applicable to all parts of the image.*

3.2 Phase contrast tomography of the mouse cochlea at microfocus x-ray sources [Bartels]

M. Bartels et. al. present phase-contrast x-ray tomography of functional soft tissue within the bony cochlear capsule of mice, carried out with laboratory microfocus sources from Excillum. With well-matched source, detector, geometry, and reconstruction algorithms they achieve spatial resolutions down to 2 µm.

3.3 X-ray grating interferometry with a liquid-metal-jet source [Thüring]

T. Thüring et. al. combines Excillum MetalJet sources with grating phase-contrast imaging and compares it with the use of a conventional microfocus source. They conclude that exposure times can be significantly reduced and visibility significantly improved with the metal-jet sources, as illustrated by the comparison in figure 7.

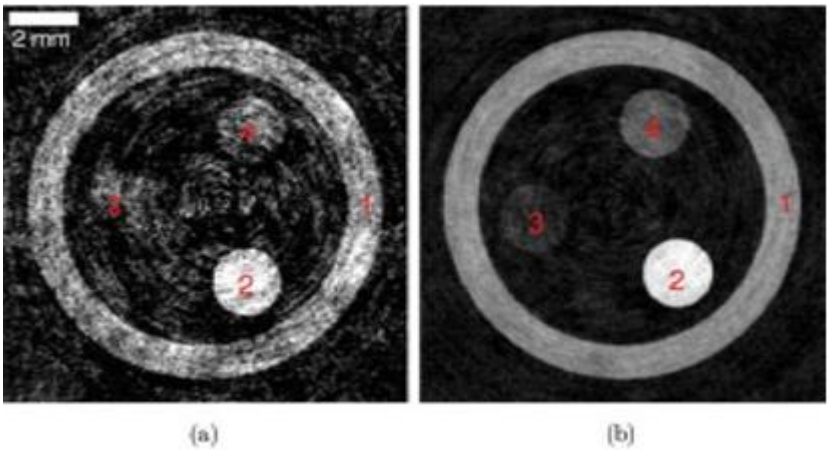

***Fig 7**: A tomographic slice from a phantom, produced with a standard microfocus tube in (a) and with a MetalJet x-ray source in (b). The improved image quality and SNR are both clearly visible.*

References

Lundstrom, U., Larsson, D.H., Burvall, A., Takman, P. A. C., Scott, L., Brismar, H. and Hertz, H. M., "X-ray phase contrast for CO2 microangiography", Phys. Med. Biol. 57 (2012) 2603–2617

Bartels, M., Hernandez, V. H., Krenkel, M., Moser, T. and Salditt, T., "Phase contrast tomography of the mouse cochlea at microfocus x-ray sources", Applied Physics Letters 103, 083703 (2013)

Thüring, T., Zhou, T., Lundström, U., Burvall, A., Rutishauser, S., David, C., Hertz, H. M. and Stampanoni, M., "X-ray grating interferometry with a liquid-metal-jet source", Applied Physics Letters 103, 091105 (2013)

Arion: a realistic projection simulator for optimizing laboratory and industrial micro-CT

J. DHAENE*[1], E. PAUWELS[1], T. DE SCHRYVER[1], A. DE MUYNCK[1], M. DIERICK[1], L. VAN HOOREBEKE[1]

[1] UGCT – Dept. Physics and Astronomy, Ghent University, Proeftuinstraat 86/N12, B-9000 Gent, Belgium – Jelle.Dhaene@UGent.be
* presenting author

Keywords: Computed tomography; Simulation; Polychromatic; X-rays

Abstract

Optimal scanning conditions in a X-ray Computed Tomography scan are determined by the source and detector of the CT-scanner and composition, size and density of the sample. Because all these components have an energy-dependent behaviour, optimizing a CT scan is not straightforward. In order to ease this process a GPU-accelerated realistic projection simulator, Arion, is developed.

Arion allows the user to simulate realistic radiographic projections for a certain geometry while taking into account the polychromatic behaviour of X-ray tube, detector and sample. This allows the user to produce realistic CT datasets that can be used to optimize the scanning conditions for a certain sample.

Introduction

The 'Ghent University Centre for X-ray Tomography' (UGCT; www.ugct.ugent.be) is a research facility that develops both hardware and software for high resolution computed tomography (CT). The available hardware consists of 4 state-of-the-art micro-CT scanners (Masschaele et al., 2007; Dierick et al., 2014) and is used for a wide range of research applications. In order to increase the quality of the scans and simultaneously reduce scan time and thus cost of X-ray CT, the scanner parameters need to be optimized.

A CT scan results in a reconstructed, voxelized 3D volume. Each voxel in this volume contains a calculated grey value which represents the linear attenuation coefficient for the materials present in that voxel. This linear attenuation coefficient is the product of a local density and the measured mass attenuation coefficient in that voxel with the latter being dependent on both sample composition and the detected X-ray spectrum. This reconstructed attenuation coefficient will thus be dependent on initial spectrum, sample shape and composition and detector sensitivity. To optimize a CT scan, the polychromatic behaviour of all these components must be known in order to simulate the radiographic images as accurately as possible.

At UGCT a method to determine this polychromatic behaviour of source and detector as well as a programme, called Arion, to simulate these realistic images for a CT-scanner were developed (Dhaene et al., 2015). Arion can be used to determine the optimal scanning conditions for a specific setup, geometry and sample. The method section describes the functionalities of Arion and the parameters used to determine an optimal scanning setup. The results section shows a validation done at the HECTOR scanner (Masschaele et al., 2013) present at UGCT and an example to optimize the scanning condition for visualizing water inside a butter sample.

Methods

Arion is a realistic projection simulator that takes the polychromatic behaviour of the source, sample and detector into account. This behaviour is modelled as described by

Dhaene et al. (2015) by performing Monte Carlo (MC) simulations using BEAMnrc (www.nrc-cnrc.gc.ca/eng/solutions/advisory/beamindex.html). Both source and detector are simulated separately by using a model for their geometric design, which is given as input parameter in the MC simulations. This results in a simulated spectrum emitted by the modelled X-ray tube at a given voltage and simulated energy-dependent behaviour and efficiency of the detector. Both source and detector simulations produce datafiles that are used by Arion. This simulated data is preferred over semi-empirical data as they are significantly more accurate, since they take into account the secondary effects due to the actual construction of the X-ray tubes and detectors present at the UGCT. Further, Arion uses a ray-tracing technique to calculate the projection images.

The polychromaticity of the setup is simulated in Arion by dividing the spectrum in energy bins and in each of these energy bins, the contribution to the radiographic projection is calculated. During this calculation, each bin is treated as it was monochromatic. Further, the noise in each energy bin is calculated assuming Poisson statistics where $\sigma_{N_i} = \sqrt{N_i}$. i represents the energy bin, N_i is the number of detected photons in that energy bin and σ_{N_i} is the error on the number of photons in that energy bin. These detected photons can be converted into a detected energy based on the data from the Monte Carlo simulations. Also the error on the total deposited energy can be calculated by assuming gaussian error propagation. This can be assumed when the number of photons is larger than 20, which is certainly the case in X-ray CT.

Another feature of Arion is the flexibility in defining a scan geometry. Three types of scan geometry are implemented in the GUI of the programme. These are circular, helical and conveyer belt geometry. Circular and helical geometry are usually used in a research environment because they provide information about the whole angular range, from 0° to 360°. A conveyer belt setup is included to investigate more industrial setups were there is often a restriction on the scan time and thus on the number of projections and angular range of the scan. Further, Arion uses a GPU-implemented code which reduces the simulation time for a complete realistic CT scan to the order of a few minutes

A validation of Arion for HECTOR is presented. This is done by scanning two samples: a cylindrical phantom of polyoxymethylene (POM) and an aluminum (Al) sphere. Both samples were scanned at HECTOR over a whole range of energies ranging from 30kV up to 210kV (in intervals of 30kV). In addition, a virtual representation of these samples was made and Arion was used to simulate radiographic projections of these phantoms. These projections were generated emulating the the same conditions as the real scans. This implies the same number of projections and flatfields, the same tube voltage and power and the same integration time of the detector. This was done in order to verify the predicted noise levels in the simulated versus the real datasets.

Finally, as an example, optimal settings to discriminate water nodules inside a butter sample were obtained. Water and fat have a composition that behaves very similar under X-ray CT conditions. This makes it a challenging problem in X-ray CT. A virtual butter sample containing water fractions was generated and simulations were performed over a range of tube voltages. This way, an optimal setting in terms of geometry, voltage and filtration can be derived. Arion can thus be used to predict signal to noise ratios of materials in the sample, which are defined as

$$SNR = \frac{\mu}{\sigma_\mu},$$

in which μ is the reconstructed attenuation coefficient in the 3D volume and σ_μ is the error on this value. Similarly, a contrast-to-noise ratio

$$CNR = \frac{|\mu_1 - \mu_2|}{\sqrt{\sigma_{\mu_1}^2 + \sigma_{\mu_2}^2}}$$

can be defined. This is an indication in how well two materials can be distinguished in a reconstructed volume.

Reconstructions of the datasets presented below were performed using Octopus (www.octopusreconstruction.com) (Vlassenbroeck et al., 2007), a softwarepackage developed at UGCT, using the algorithm of Feldkamp, Davis and Kress (FDK) (Feldkamp et al., 1984).

Results and discussion

As mentioned before, real scans of an Al sphere and POM cylinder were acquired on HECTOR at a tube voltage from 30kV up to 210kV. Simulations were performed for these scans by using virtual phantoms for both samples. Both real and simulated scans were reconstructed and a line profile at similar places in the real and simulated reconstructed 3D volumes are given in figure 1 (POM) and figure 2 (Al) for the datasets acquired at a tube voltage of 60kV and 120kV. At the other voltages (not shown here) a similar behaviour was found. Both the reconstructed attenuation coefficients and noise for the Al and POM samples are well predicted by Arion over the whole range of energies. The noise level in the simulations is a little higher than the noise in the real scans. This probably originates in the fact that there is a slight smoothening of the real projection images due to the Modular Transfer Function (MTF) of the detector which is supposed to be ideal in Arion.

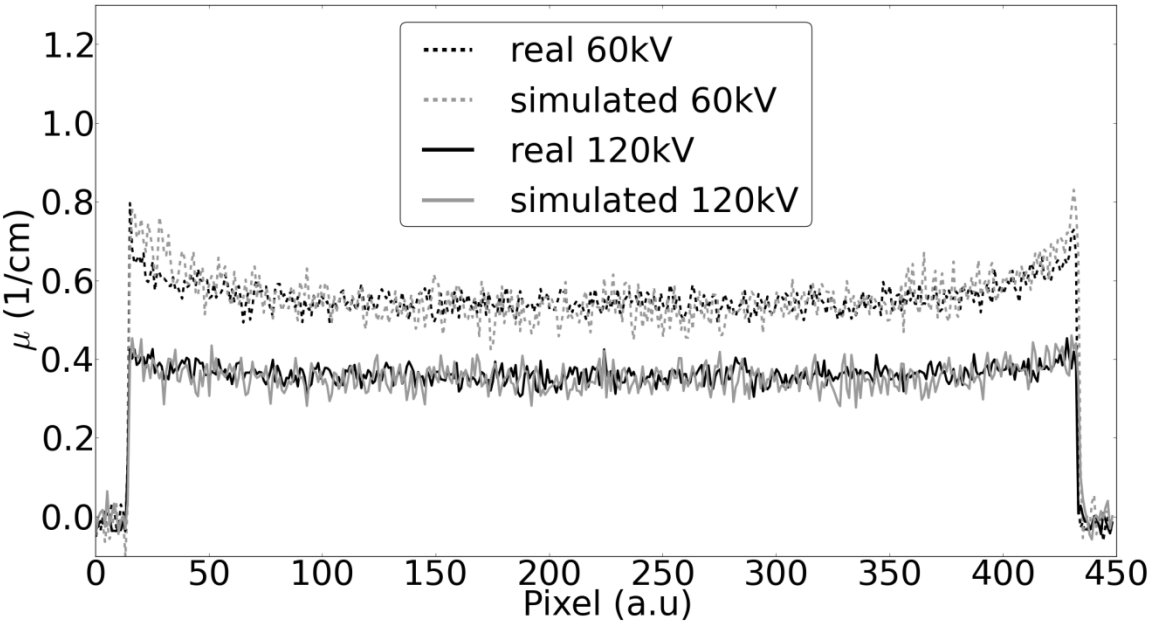

Fig. 1. *Line profile of a reconstructed slice of the POM cylinder. Line profiles of the real and simulated data are compared at a tube voltage of 60kV and 120kV.*

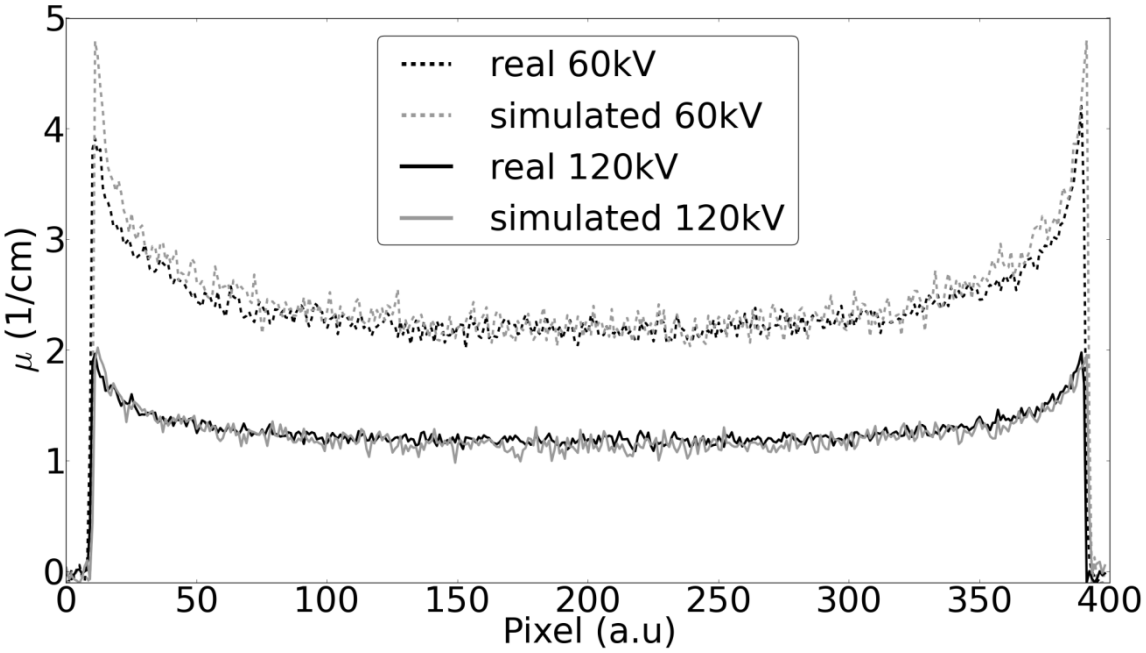

Fig. 2. *Line profile of a reconstructed slice of the Aluminum sphere. Line profiles of the real and simulated data are compared at a tube voltage of 60kV and 120kV.*

Further, Arion was used to scan a virtual butter phantom which contains air and water bubbles (figure 3a). Figure 3b and 3c show reconstructed slices of a simulated dataset at 30kV and 120kV for HECTOR. Figure 4 shows a real scan of a butter sample at HECTOR at the same tube voltages. In both simulated and real reconstructed slices the CNR of water and butter is higher in the 30kV slice than in the 120kV slice. Consequently, the segmentation of water is easier in the 30kV slice than in the 120kV slice. This confirms the usability of Arion to predict the optimal scanning conditions for a certain sample.

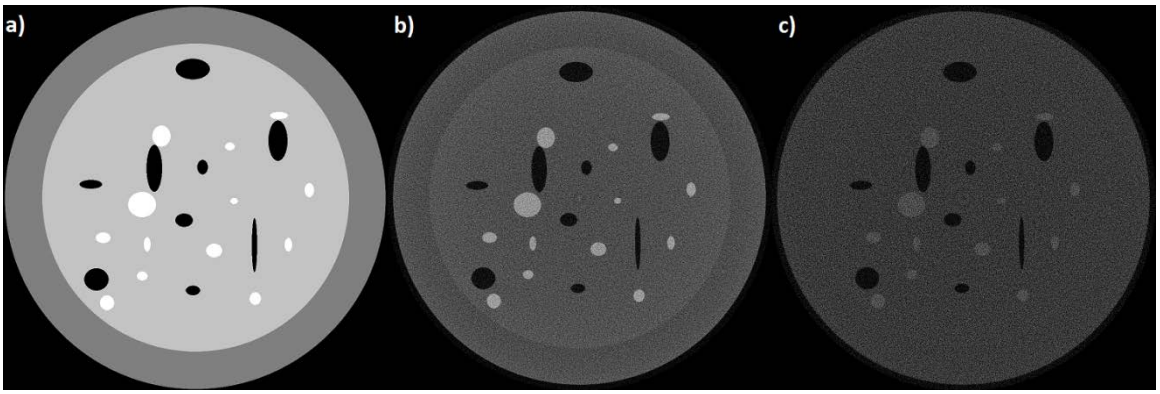

Fig. 3. *A virtual phantom of a plastic cylinder containing butter (left). Inside the phantom there is air (black) and water (white). A reconstructed slice of a simulated dataset, using the phantom, is shown at 30kV (center) and 120kV (right).*

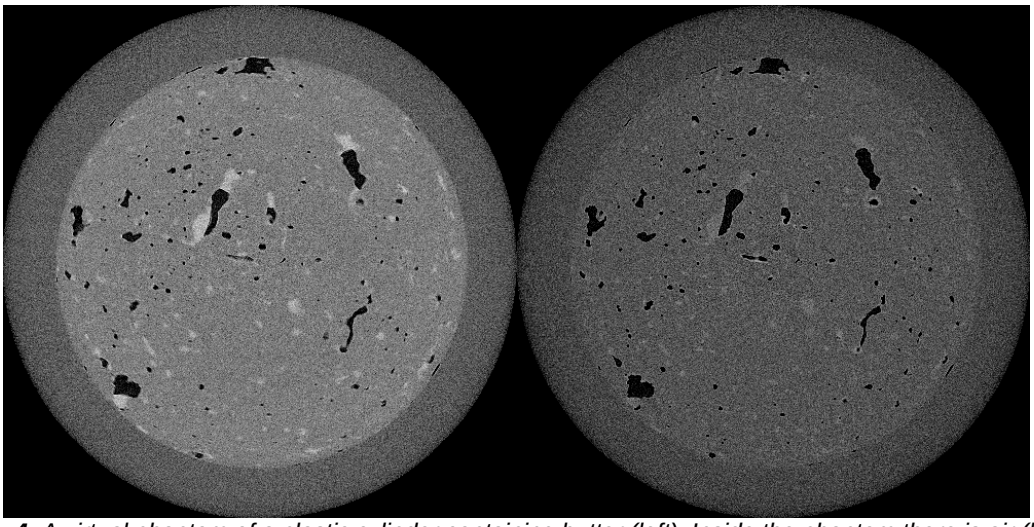

Fig. 4. *A virtual phantom of a plastic cylinder containing butter (left). Inside the phantom there is air (black) and water (white). A reconstructed slice of a simulated dataset, using the phantom, is shown at 30kV (left) and 120kV (right).*

Conclusion

Simulated and real scans performed at HECTOR for the Al and POM samples are in good agreement with each other over the whole voltage range of HECTOR. From this it can be concluded that simulations performed with Arion reliably predict both reconstructed attenuation coefficients and noise levels in real datasets. The example of optimizing water and fat contrast in a butter sample also confirms this statement. Nevertheless, secondary contributions such as the MTF of the detector can be implemented in Arion in the future to reduce the difference between real and simulated datasets even more.

Acknowledgments

We acknowledge the Agency for Innovation by Science and Technology in Flanders (IWT, SBO project 120033 ‘‘TomFood’’) and Sofie Deman of The Institute for Agricultural and Fisheries Research (ILVO) for providing the butter sample.

References

J. Dhaene, E. Pauwels, T. De Schryver, A. De Muynck, M. Dierick, L. Van Hoorebeke, A Realistic Projection Simulator for Laboratory Based X-ray micro-CT, ***Nucl. Instr. Meth. Phys. Res. B*** 342 (2015) 170-178.

M. Dierick, D. Van Loo, B. Masschaele, J. Van den Bulcke, J. Van Acker, V. Cnudde, L. Van Hoorebeke, Recent micro-CT scanner developments at UGCT, ***Nucl. Instr. Meth. Phys. Res. B*** 324 (2014) 35–40.

L.A. Feldkamp, L.C. Davis, J.W. Kress, Practical cone-beam algorithm, ***J. Opt. Soc. Am. A Opt. Image Sci. Vis.*** 1 (6) (1984) 612–619.

B. Masschaele, V. Cnudde, M. Dierick, P. Jacobs, L. Van Hoorebeke, J. Vlassenbroeck, UGCT: new X-ray radiography and tomography facility, ***Nucl. Instr. Meth. Phys. Res. A*** 580 (1) (2007) 266–269.

B. Masschaele, M. Dierick, D. Van Loo, M.N. Boone, L. Brabant, E. Pauwels, V. Cnudde, L. Van Hoorebeke, Hector: A 240 kv micro-CT setup optimized for research, ***J. Phys. Conf. Ser.*** 463 (2013).

J. Vlassenbroeck, M. Dierick, B. Masschaele, V. Cnudde, L. Van Hoorebeke, P. Jacobs, Software tools for quantification of X-ray microtomography at the UGCT, ***Nucl. Instr. Meth. Phys. Res. A*** 580 (1) (2007) 442–445.

NanoCT imaging with a prototype nanofocus source and a single-photon counting detector

M.MÜLLER*[1], S. FERSTL[1], S. ALLNER[1], M. DIEROLF[1], , P. TAKMAN[2], T. TUOHIMAA[2], B. HANSSON[2], F.PFEIFFER[1]

[1] Department of Physics and Institute of Medical Engineering, Technische Universität München, James-Franck-Straße 1, 85748 Garching, Germany – mark_mueller@ph.tum.de
[2] Excillum AB, Torshamnsgatan 35, 16440 Kista,
* presenting author

Keywords: nanoCT, transmission X-ray tube, single-photon counting detector

Abstract

We present a novel laboratory-based nanoCT setup featuring a prototype nanofocus X-ray source and a single-photon counting detector. The system relies on mere geometrical magnification and can reach a resolution of 500 nm at its current state.

The nanofocus X-ray tube (Excillum AB, Sweden) consists of a tungsten transmission target on a diamond layer and can produce focal spot sizes down to about 300 nm.

The X-ray camera is a PILATUS 300K-W 20Hz detector with a 1000 µm silicon sensor, 1475 x 195 pixels, and a pixel size of 172 x 172 µm^2.

First results demonstrate that the focal spot of the tube is stable enough to permit CT imaging with submicron resolution. The small focal spot size also results in sufficient spatial coherence to exploit edge enhancement effects. As a first application, we show attenuation contrast CT slices of a piece of human tooth.

Introduction

Ever since the discovery of X-rays [1], their ability to penetrate matter that is opaque for visible light has been used to investigate the inner structure of various specimens. Radiographic X-ray imaging was used in clinical diagnostics since the beginning of the 20th century, but had the drawback that depth information along the direction of the X-rays was lost. A new technique that overcame this limitation was developed in the 70s [2]. X-ray computed tomography (X-ray CT) allows for the reconstruction of the three-dimensional distribution of the attenuation coefficient of an object and has become an invaluable tool in many fields, such as medical diagnostics, industrial testing, and scientific research [3].

Over the years the demand for higher resolution in X-ray CT created a new research field, commonly known as X-ray microCT imaging (µCT). While at synchrotron facilities, µCT imaging with submicron resolution has been performed for years [4, 5], the first laboratory-based setups with resolution in the nanometer range were developed rather recently. Nowadays scientific setups and commercially available microCT scanners, can achieve resolutions below 1 micron by using X-ray optics [6] or transmission X-ray tubes with very small focal spot sizes [7, 8, 9].

We present an advanced laboratory-based setup with a novel prototype transmission tube and a commercially available single-photon counting detector. The setup is based on geometrical magnification and can so far reach a maximal resolution of approximately 500 nm.

As a first application, we show attenuation contrast CT slices of a sample consisting of coronal dentin from a human tooth. The coronal dentin is directly underlying the enamel, and is penetrated by a system of tubules, each of which is surrounded by a hypermineralized tissue called peritubular dentin (PTD). The dentin tubules extend from the dentin-enamel junction to the pulp chamber of the tooth and typically have diameters of 1-2 µm [10, 11].

Methods

NanoCT setup:

The setup consists of a nanofocus X-ray source, an overhead rotation stage and a single-photon counting detector. The system does not contain any X-ray optics and is based on geometrical magnification only. The geometry of the setup is designed for magnification factors up to 1500.

The prototype X-ray tube (Excillum AB, Sweden) comprises a thin tungsten transmission target on a diamond layer with integrated water cooling. The design of the head of the source allows for positioning of the object very close to the focal spot and consequently for high magnification factors. The spot size can be fully controlled through software and goes down to about 300 nm at its current state.

The X-ray camera is a PILATUS 300K-W 20 Hz detector system with a 1000 µm thick silicon sensor. The image area of this detector consists of 1475 x 195 pixels with a pixel size of 172 x 172 μm^2. In contrast to conventional CCD and flatpanel detectors, this camera is operated in single-photon counting mode and only counts X-ray photons above a certain threshold energy. Moreover, the detector has no readout or dark current noise and its point spread function is the pixel size. The camera is motorized and can be moved with micron precision into x-, y-, and z-direction.

The sample is rotated on a high precision air bearing rotary stage that can be moved precisely into x-, y-, and z-direction. Additionally, it is possible to correct the sample position relative to the rotation axis. The entire sample motorization is mounted upside down to facilitate measurements of samples in solutions.

Sample preparation:

A piece of tooth comprising coronal dentin was manually polished into an approximately 50 µm thick plate, from which a splinter was cut parallel to the tubules orientation and mounted on a sample holder. The cross section of the tooth piece was roughly 50 x 20 µm².

Data acquisition and reconstruction:

The CT scan of the tooth sample was performed at a peak voltage of 60 kVp. 801 projection angles distributed over 360° were acquired with 100 seconds exposure time per projection image. The source-to-detector distance for this measurement was 1100 mm and the source-to-sample distance 1.78 mm. This results in a magnification factor of 618 and an effective voxel size of 278 nm.

For the tomographic reconstruction a state-of-the-art Filtered Backprojection (FBP) algorithm was utilized.

Results

In Figure 1, a transversal CT slice of the tooth sample is depicted. The dentin tubules, can be clearly identified as the darks spots within the sample. The diameter of the tubules varies between 0.9 µm and 1.8 µm. Edge enhancement is clearly visible at the borders of the sample and at the boundaries between the tubules and the surrounding highly mineralized tissue. The fact that the tubules have even lower absorption values than the background of the sample can be explained by the overlap of edge enhancement and beam hardening effects.

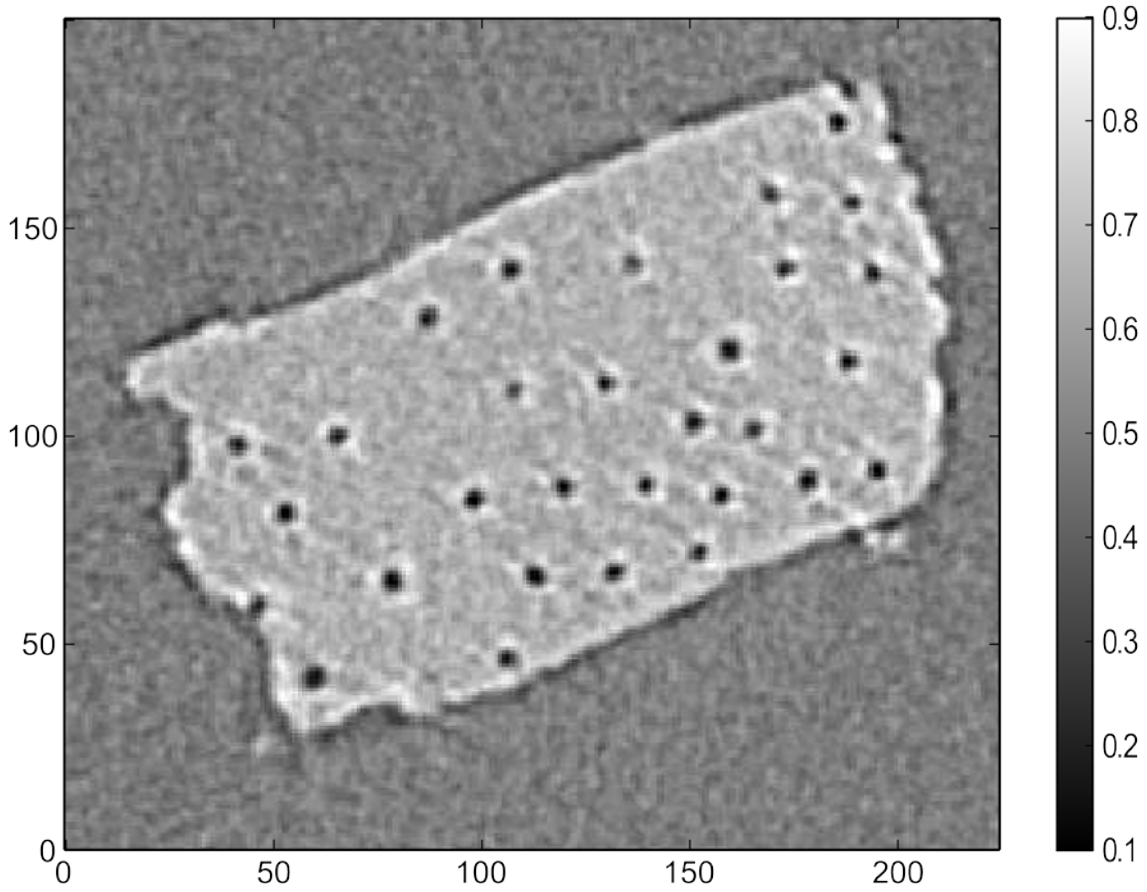

Figure 1. *Transversal CT slice of a human tooth sample comprising coronal dentin. The dark spots are the dentin tubules penetrating the coronal dentin. Reconstructed voxel size: 278 nm*

Conclusion

The first results demonstrate that focal spot size and flux of the tube are stable enough over the time of a high resolution scan (up to 25 hours) to acquire CT images with submicron resolution. Due to the very small focal spot size of the tube, the resulting contrast in the reconstructed CT data is a superposition of conventional attenuation-based contrast and edge enhancement caused by Fresnel Diffraction.

References

[1] Roentgen, W. C. (1896). On a new kind of rays. ***Nature*** 53, 274-277.

[2] Hounsfield, G.N. (1973): Computerized transverse axial scanning (tomography): Part 1. Description of system. ***British Journal of Radiology***, 46, 1016-1022 .

[3] Slaney M. and Kak, A. C. (2001). *Principles of computerized tomographic imaging*. Society for Industrial and Applied Mathematics, USA

[4] Baruchel, J.-Y et al. (2006). Advances in synchrotron radiation microtomography. ***Scripta Materialia*** 55, 41-46

[5] Rack, A. et al. (2008). High resolution synchrotron- based radiography and tomography using hard X-rays at the BAMline (BESSY II). ***Nuclear Instruments and Methods in Physics Research Section A: Accelerators, Spectrometers, Detectors and Associated Equipment*** 586 (2), 327-344

[6] *http://www.xradia.com/?page_id=798?Product=810*

[7] *http://www.skyscan.be/products/2011.htm*

[8] Salamon, M. et al. (2008). Realization of a computed tomography setup to achieve resolutions below 1 µm. ***Nuclear Instruments and Methods in Physics Research, Section A: Accelerators, Spectrometers, Detectors and Associated Equipment*** 591, 50-53

[9] Dierick, M. et al. (2014). Recent micro-CT scanner developments at UGCT. ***Nuclear Instruments and Methods in Physics Research Section B: Beam Interactions with Materials and Atoms*** 324, 25-40

[10] Weber, D. F. (1968). The distribution of peritubular matrix in human coronal dentin. ***Journal of Morphology*** 126, 435-445

[11] Weiner, S. et al (1999). Peritubular Dentin Formation: Crystal Organization and the Macromolecular Constituents in Human Teeth ***Journal of Structural Biology*** 126, 27-41.

Rock deformation and micro-CT analyses

N. TISATO*[1], Q. ZHAO[2], G. GRASSELLI[3]

[1] University of Toronto, Dept. of Civil Eng., 35 St George st., Toronto (CA) – nicola.tisato@utoronto.ca
[2] University of Toronto, Dept. of Civil Eng., 35 St George st., Toronto (CA) – q.zhao@mail.utoronto.ca
[3] University of Toronto, Dept. of Civil Eng., 35 St George st., Toronto (CA) – giovanni.grasselli@utoronto.ca
* presenting author

Keywords: Rock-deformation, CT-scan, seismic-wave-attenuation, fluid-flow.

Abstract

Experimental rock–mechanics and –physics have been greatly improved in the last century, enhancing our understanding of deformation processes in geo-materials. Nevertheless, many questions have not yet been addressed and new challenges such as hydrocarbon extraction from unconventional reservoirs, pose new ones.

As many mechanical and physical properties of rocks are intimately related to microscopic features, such as grain orientation and pore distribution, one of the next frontiers is to perform deformation experiments while imaging the internal structure of the specimen. Such a technology will be extremely beneficial to understand, for instance, how granular materials fail or how fluids and dissolution and precipitation of new mineral phases influence the apparent (i.e. macroscopic) rock properties.

The present contribution presents the design and the preliminary calibrations of a couple of new X-ray-transparent vessels which can be paired with the micro-CT system installed at the University of Toronto. The vessels will be used to measure dynamic elastic moduli, seismic wave attenuation and friction in rocks. Finally, we discuss the expedients which will be utilized to improve the methodology.

Introduction

Exploration geophysics rely on effective properties of geo-materials, which are strongly influences by microscopic features. For instance, in porous media, distribution and orientation of mineral grains, pores and cracks, and pore-fluid distribution affect elasticity. During laboratory tests, at high confining pressures (P) and temperatures (T), none of these aspects can be easily observed, and often, this is possible only after that the experiment has been performed and by destructive analyses.

Hitherto, studies demonstrating that the non-uniform distribution of fluids in sandstones causes viscoelasticity (i.e., attenuation) laid bare limitations: the fluid distribution was estimated as a function of the injection method and the total saturation (e.g. Tisato and Quintal, 2013). Similarly, Tisato et al. (2015) demonstrated that microscopic bubbles dispersed in saturated porous media cause seismic velocity dispersion and attenuation. However, it was impossible to directly observe the behavior, distribution and shape of such bubbles in the rock.

On the other hand, friction in rocks is an important parameter for natural and induced seismicity, and its study is rather limited to the measurement of apparent physical and mechanical quantities. One of the key to understand tribological processes might come from the observation of powders, and gouge formation between the sliding surfaces (e.g. Tisato et al., 2012). To date, it was only possible to study the fracturing process and gouge formation by perturbing the gouge layer, thus introducing uncertainties on the final state of the deformed sample (Tatone and Grasselli, 2014).

Many natural and anthropogenic activities cause thermodynamic disequilibria, which in turn causes the variation of subsurface physical property and possibly the variation of

the signals recorded by a contingent geophysical monitoring. For instance, the injection of carbon dioxide, to pursuit carbon sequestration, is believed to cause the dissolution and/or precipitation of mineral phases in crustal rocks. However, how these reactions, which occur at high P-T conditions, affect the rock physical properties is still unclear. The limitation is again entrenched in the inability to perform laboratory experiments and concurrently "see" the evolution of the sample interior.

Lately, X-Ray tomography became a versatile, accessible and effective technique to image materials and their saturating phases. Here we report the design of two new high-pressure X-Ray transparent vessels which can perform measurements inside the X-Ray computed tomography apparatus installed at the University of Toronto (μCT). The first apparatus (ERDμ-Q) will allow measuring dynamic elastic moduli and seismic wave attenuation changes in the sample and, simultaneously, link them to saturation variations, or precipitation-dissolution of minerals. The second apparatus (ERDμ-μ) will allow measuring friction in rocks and, concurrently link it to the formation and evolution of gouge. We focus on the ERDμ-Q to discuss the design, the methodology and the machine calibrations.

Methods

The ERDμ apparatus are X-ray transparent pressure vessels which can confine a 12x36 mm cylindrical sample up to 30 MPa. The machines are equipped with a saturation circuit composed of 2 syringe pumps and some valves allowing saturating the samples (e.g. water and CO_2) (Tisato et al., 2014).

The ERDμ-Q is equipped with a linear actuator which can increase the differential stress (σ_d) along the vertical direction up to 8 MPa and a piezoelectric motor which modulates σ_d (Fig. 1). Thus, the vertical stress oscillates around σ_d with amplitude σ generating a sinusoidal vertical strain (ε) across the sample with amplitude $\varepsilon<10^{-5}$. Vertical stress and strain across the sample are measured by means of a load cell and strain gauges applied on the specimen, respectively.

The dynamic Young's modulus (E) and the attenuation ($1/Q$) of seismic waves is calculated as $1/Q = \tan\varphi, \quad E = \sigma/\varepsilon\cos\varphi$, where φ is the phase shift between σ and ε. Calibration is performed testing standard materials: Plexiglas (PMMA) and Aluminum alloy (Aluminum), which exhibit a pronounced and well characterized visco-elastic and elastic behavior, respectively (Lakes, 2009).

X-Ray microtomography was performed on a Trigonodus-Dolomite (dolostone) sample hosted in the ERDμ-Q. The pressure vessel was mounted on the 4-axis rotation stage of the μCT. X-rays were irradiated on the ERDμ-Q external surface while rotating by 360° in 1080 equally spaced increments. The emission energy was 180 keV, and at each angle step we acquired 5 projections, which averaged, provided a 2D 16-bit gray scale projection. The chosen magnification of the specimen within the field of view corresponded to a voxel resolution of ~50 μm. A 0.5 mm thick copper filter was used to reduce beam hardening artifacts in the reconstructed three-dimensional (3D) volume.

Image reconstruction was performed using the Pheonix X-ray datos—x-reconstruction software, including: a beam hardening correction of 3/10, automatic ring artefact reduction, and a 'scan optimization' which compensates for small translations of the specimen during scanning and correctly locates the centre of reconstruction.

Segmentation of the reconstructed data and production of 3D models in figure 3 were performed using the free version of the commercial software MeVisLab. However, as the voxel was too big to reconstruct micrometric and sub-micrometric features we checked the possibility of performing analyses on the effective properties of the voxels. We

employed a strategy similar to that utilized by Dunsmuir (2006) to obtain the density (ρ_L) and the porosity (Φ_L) of single voxels.

Results

ERDμ-Q calibration was performed measuring five times *E* and 1/*Q* of the PMMA and Aluminum sample. We collected data at 45 frequencies logaritmically distributed between 0.1 and 100 Hz. Repeatibility– was calculated considering the standard deviation between the five repetitions, and was ~0.003 for 1/*Q* and ~0.1 GPa for *E*. The results show that the ERDμ-Q can measure extensional attenuation between 0.01 and 0.1 rad with a total error ~0.003, and dynamic Young's modulus between 3 and 70 GPa with an error ~0.1 GPa (Fig. 1B).

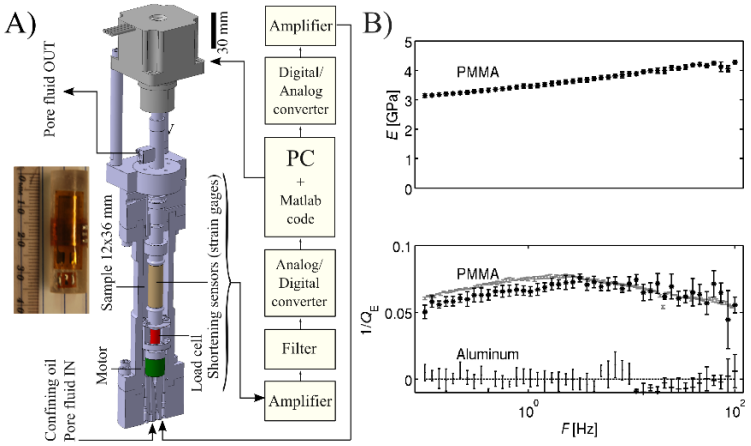

Fig. 1. *A) Scheme of the ERDμ-Q. The inset shows the PMMA sample used for calibration. B) Young's modulus and related attenuation of PMMA and Aluminum as a function of frequency. The gray curve for PMMA was collected with an independent apparatus (Tisato and Madonna, 2012).*

The rock tested in our experiment has density and porosity ranging between 2200 and 2560 kg m^{-3}, and between 5 and 22%, respectively. It presents large pores as result of karstification processes and micro-porosity in the micritic phase (Shih, 2013) (Fig. 2).

The collected μCT dataset has a good quality with no ring artefacts and high signal-to-noise ratio (Fig. 2). However, the sample holder, which is made of stainless steel, shows a rather significant beam hardening effect (i.e. edges are brighter than the center), and it also emanates bright streaks into adjacent objects, therefore the sample bottom part (i.e. close to the sample holder) presents some artefacts.

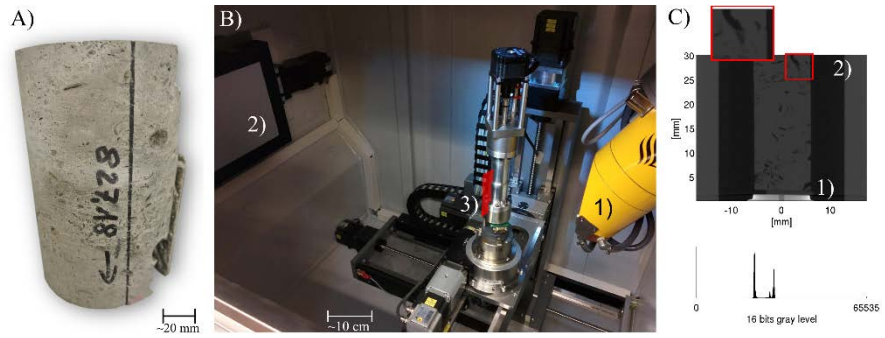

Fig. 2. *A) Dolostone sample from which we cored the scanned sample. B) The ERDμ-Q pressure vessel (3) is mounted between the X-ray tube (1) and the CCD sensor (2). C) Example of vertical slice from the reconstructed μCT dataset. The sample is mounted on the sample holder (material AISI 304) and surrounded by the pressure vessel (material Aluminum alloy 7075-T6).*

Segmentation of the μCT dataset was performed using a "3D region growing" method with 2% gray threshold parameter (Rittel et al., 2011) (Fig. 3A-C). With such analysis we calculated the sample porosity, which was 11.3%, in agreement with the literature range. However, segmentation does not allow calculating the effective density and porosity of single voxels (i.e. micro-porosity identification).

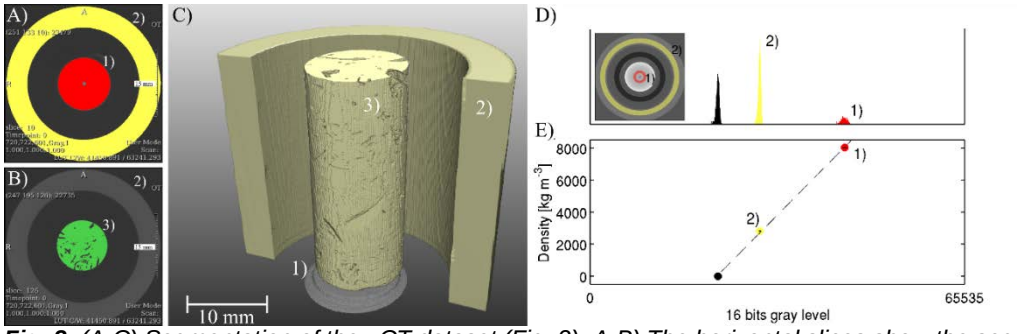

Fig. 3. *(A-C) Segmentation of the μCT dataset (Fig. 2). A-B) The horizontal slices show the segmentation of the sample holder (1), the pressure vessel (2) and the dolostone sample (3). C) 3D volume reconstruction. The sample (3) is mounted on the sample holder (1) and is surrounded by the pressure vessel (2). (D-E) Calibration of the gray-to density algorithm. A) Slice and voxel gray level histograms of some portions of the μCT dataset. The sample holder (1) is made of stainless steel (AISI304, $\rho_{AISI304}$=8020 kg m^{-3}) and represented by voxels with gray level ~43000 (red). The pressure vessel (2) is made of aluminum alloy (7075-T6, ρ_{7075}=2720 kg m^{-3}) and is represented by voxels with gray level ~30000 (yellow). Between 1 and 2 there is air (ρ_{air} ~ 0 kg m^{-3}) which is represented by voxels with gray level ~22000 (black). B) Linear relation between the gray levels representing AISI304, 7075-T6 and air, and their densities. Such a linear relation was used to calculate the local density (ρ_L) of the sample voxels (i.e. gray-to-density calibration).*

The pressure vessel and the sample holder are made of stainless steel and aluminum alloy whose densities are known. According to the Beer's law, we utilized the gray level distributions of the dataset portions showing these two parts to obtain a gray-to-density calibration $\rho_L(kg\ m^{-3}) = 0.36\ GrayLevel\ -\ 7972$, where ρ_L is the voxel density and *GrayLevel* is the 16-bits-gray value of the reconstructed voxel. Thanks to this calibration we obtained the ρ_L of each voxel with an error ~10%. The error was due to the *GrayLevel* distribution and the fitting regression uncertainty.

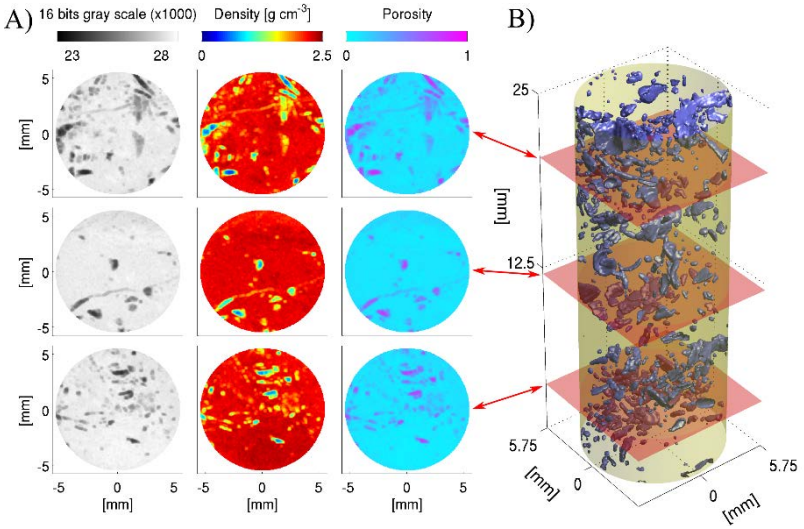

Fig. 4. *A) Gray level, density and porosity for 3 slices extracted from the μCT dataset. Density was calculated upon to the gray-to-density calibration (Fig. 3E). Porosity of single voxels was calculated according to the bulk-density and -porosity, which can be experimentally measured. B) Sample 3D representation, the blue-rendered surface shows voxels with local porosity~0.5.*

Moreover, the calculated sample bulk density was 2150 kg m^{-3}. The accuracy of the gray-to-density calibration can be checked comparing the calculated and the experimentally measured bulk density, and eventually adjusted processing the dataset with morphological image processes (e.g. erosion-dilation).

Finally, we estimated the voxel porosities ($0<\Phi_L<1$) assuming: i) monomineralic rock composition, ii) $\Phi_L=1$ for $\rho_L=0$, iii) that Φ_L is inversely proportional to ρ_L for $\rho_L \leq \rho_M$, and iv) $\Phi_L=0$ for $\rho_L>\rho_M$, where ρ_M is the threshold density above which the voxel is considered to have no porosity. With this procedure we obtained a density-to-porosity calibration. The calculated bulk porosity Φ_C was 18.6% much higher than that calculated through segmentation and more plausible as the analyzed sample was particularly porous. However, density-to-porosity calibration can be adjusted varying ρ_M and imposing Φ_C equal to the measured porosity, which can be estimated with a helium pycnometer.

Discussion and Conclusions

The ERDμ-Q can measure the dynamic Young's modulus and the seismic wave attenuation of PMMA and Aluminum alloy in the bandwidth (0.1 – 100 Hz) (Fig. 1B). However, the results, especially for Aluminum, are rather scattered, this is probably due to a non-perfect parallelisms between the sample end-faces and can be solved with an enhanced surface polishing. We also show that PMMA results agree with the literature (Tisato and Madonna, 2012).

Both ERDμ pressure vessels are X-ray transparent and they do not introduce significant artefacts. As the drawback between resolution and investigated volume cannot be easily solved information about fluid-flow and mineral phase dissolution-precipitation can be assessed considering the effective properties of the voxels, rather than binary segmentation. This can be achieved only with an accurate definition of the gray-to-density-to-porosity conversion and accurate measurements of density and porosity of the rock sample. In particular we will locate inside the pressure vessel, close to the sample, some targets with known density that will be used as standard materials.

To conclude, we designed, developed and calibrated the ERDμ pressure vessels, and identified some expedients that will be kept to improve the methodology. The ERDμ-Q will help to uncover the relationships between i) chemical-physical and fluid-solid interactions and ii) variations of effective elastic properties. The ERDμ-μ will help to better understand the formation and the geometrical evolution of a brittle shear zones. These achievements will aid the monitoring and imaging of subsurface domains.

References

Dunsmuir, J. H., S. Bennett, L. Fareria, A. Mingino, and M. Sansone (2006), X-ray microtomographic imaging and analysis for basic research, Powder Diffraction, 21(02), 125–131, doi:10.1154/1.2204956.

Lakes, R. S. (2009), Viscoelastic materials, Cambridge University Press, Cambridge ; New York.

Ritter F, Boskamp T, Homeyer A, Laue H, Schwier M, Link F, Peitgen H-O (2011), Medical Image Analysis: A visual approach, IEEE Pulse, 2(6):60-70.

Shih, R. (2013), Simulating the in Situ Physical properties of the Upper Muschelkalk Aquifer in norhtern Switzerland, Master Thesis ETH Zurich.

Tatone, B. S. A., and G. Grasselli (2014), Characterization of the effect of normal load on the discontinuity morphology in direct shear specimens using X-ray micro-CT, Acta Geotechnica, doi:10.1007/s11440-014-0320-5.

Tisato, N., G. Di Toro, N. De Rossi, M. Quaresimin, and T. Candela (2012), Experimental investigation of flash weakening in limestone, Journal of Structural Geology, 38, 183–199, doi:10.1016/j.jsg.2011.11.017.

Tisato, N., and C. Madonna (2012), Attenuation at low seismic frequencies in partially saturated rocks: Measurements and description of a new apparatus, Journal of Applied Geophysics, 86, 44–53, doi:10.1016/j.jappgeo.2012.07.008.

Tisato, N., and B. Quintal (2013), Measurements of seismic attenuation and transient fluid pressure in partially saturated Berea sandstone: evidence of fluid flow on the mesoscopic scale, Geophysical Journal International, 195(1), 342–351, doi:10.1093/gji/ggt259.

Tisato, N., B. Quintal, S. Chapman, C. Madonna, S. Subramaniyan, M. Frehner, E. H. Saenger, and G. Grasselli (2014), Seismic attenuation in partially saturated rocks: Recent advances and future directions, The Leading Edge, 33(6), 640–646, doi:10.1190/tle33060640.1.

Tisato, N., B. Quintal, S. Chapman, Y. Podladchikov, and J.-P. Burg (2015), Bubbles attenuate elastic waves at seismic frequencies: first experimental evidence: Bubbles Attenuate Seismic Waves, Geophysical Research Letters, n/a–n/a, doi:10.1002/2015GL063538.

A laboratory micro-CT setup for fast continuous scanning: applications for pore scale fluid flow research

M.A. BOONE[1,2], *J. VAN STAPPEN[1], T. BULTREYS[1], M.N. BOONE[3], T. DE SCHRYVER[3], B. MASSCHAELE[2,3], D. VAN LOO[2],L. VAN HOOREBEKE[3], V. CNUDDE[1]

[1] UGCT – PProGRess, Dept. Geology and Soil Science, Ghent University, Krijgslaan 281/S8, B-9000 Gent, Belgium
[2] XRE – X-ray Engineering bvba, De Pintelaan 111, B-9000 Gent, Belgium
[3] UGCT, Dept. Physics and Astronomy, Ghent University, Proeftuinstraat 86/N12, B-9000 Gent, Belgium
* presenting author

The migration of fluids through a porous material and the influence of those fluids migration processes on the porous material itself are crucial in numerous geological and engineering applications. In order to obtain a better understanding of the dynamics of these processes, a fast time-resolved 3D characterization of the pore space is required. In recent years, fast micro-CT imaging with sub-second temporal resolution has become available at synchrotron facilities. In laboratory based micro-CT imaging however the temporal resolution is often bound due to the limited X-ray flux. At the Centre for X-ray Tomography of the Ghent University (UGCT) a gantry-based micro-CT system (environmental micro-CT; EMCT) was developed in cooperation with XRE (www.xre.be) (Dierick et al., 2014). This setup allows a continuous acquisition with a spatial resolutions below 10 µm and a temporal resolution of 12s for a complete 360° scan. The EMCT setup is quite different compared to more common micro-CT setups as the X-ray tube and detector rotate in a horizontal plane around the sample which remain stationary. This setup is ideal to image fast dynamic processes using peripheral equipment such as a cooling stage, fluid flow cell, pressure cell, … in a top-bottom geometry.

Here we present the first results of fast dynamic imaging using the EMCT scanner and a specially designed flow cell to visualize single and multiphase flow in porous rocks. In the single phase flow experiment, advection and diffusion of a tracer salt in a water saturated limestone sample was monitored during fluid injection (animation: http://youtu.be/LfvL2-AUIrE). This illustrates the presence of preferential flow paths in the limestone which were dominated by advection and less connected pore bodies dominated by diffusion. In the multiphase flow experiment oil was injected in a brine saturated sandstone, which allow to visualize the pore scale displacement of water by oil in discrete drainage events (animation: http://youtu.be/H3Zf4xfUSbw). These first results illustrate the potential of this setup for fast dynamic micro-CT imaging in a laboratory environment.

Number of words: 324

References

Dierick, M., Van Loo, D., Masschaele, B., Van den Bulcke, J., Van Acker, J., Cnudde, V., & Van Hoorebeke, L. (2014). Recent micro-CT scanner developments at UGCT. *Nuclear Instruments and Methods in Physics Research Section B: Beam Interactions with Materials and Atoms*, *324*, 35–40.

Oral presentation

Multi-Energy Nano Computed Tomography Phase Retrieval for Material Discrimination

*H. LI[1], A. KINGSTON[1], G. MYERS[1], B. RECUR[1], A. SHEPPARD[1].

[1] Department of Applied Mathematics, RSPE, Australian National University, Canberra, ACT 2601, AUSTRALIA
* presenting author

X-ray nano-CT is a useful tool to study the high-resolution features in a sample of interest. Most samples distort the x-ray phase non-uniformly, altering the intensity distribution during propagation from the object to the detector. This effect is known as phase contrast. Current tomographic reconstruction methods assume the effect of this phase shift on the recorded attenuation can be ignored. This assumption is not valid for the nano-CT system under construction at the ANU. To achieve high X-ray detection accuracy and efficiency, we used a 400mm wide 3k*3k pixel detector. Using such a large detector, and still achieving a voxel size of 300 nanometres for a 1 mm diameter sample, a fine-focus geometry nano-CT requires at least 0.5 metre of X-ray propagation after going through the object. Small voxel resolution coupled with long propagation distance create significant phase-contrast edge artefacts in the reconstructed volume.

Phase contrast can both improve and diminish the quality of certain types of CT reconstruction. On one hand, phase-contrast imaging is more sensitive to low-density and low-atomic-number materials. This enhances the transition edges between different materials in the reconstruction. On the other hand, without phase retrieval, it introduces edge artefacts in the reconstruction [1], making quantitative analysis difficult. There is much research to devise phase retrieval algorithms to both reduce these phase shift artefacts and obtain the phase shift information through the object. Currently used near-field phase retrieval algorithms include the Born's approximation approach [2], and Paganin's single material approach [1]. Generally, Paganin's approach is not appropriate at our ANU facility because samples are not single material, and Born's approximation approach is not applicable since our x-ray wave field is not slowly varying nor small in magnitude.

To obtain a phase retrieval algorithm with valid assumptions for our experimental setup, we started with the Transport of Intensity (TIE) formulation [3], collecting two monochromatic radiographs at the same propagation distance. We first derived a set of coupled intensity-propagation equations, in terms of density (ρ) and atomic number investigated the magnitude of higher-order phase contrast terms and found they were significant for our nano-CT set-up. We found this by comparing the higher-order influence on intensity for different X-ray energies, different X-ray propagation distances, and for different sample feature size.

We have decoupled the two propagation equations to obtain a single-variable second-order propagation equation, relating density (ρ) in the sample
This differs from other phase retrieval algorithms ([2] and [3]) only directly relating attenuation in the sample to measured intensity at the detector.

We derive a phase-retrieval algorithm based on our single-variable propagation model, designed to calculate a 3D density (ρ) and atomic number (Z) radiographs collected at two different energies. We investigate the performance of this algorithm, for multi-material objects which violate the assumptions of Paganin's approach [1].

Number of words: 587

Reference:
[1] D. Paganin and et. al., "Simultaneous phase and amplitude extraction from a single defocused image of a homogeneous object," Journal of Microscopy 206, 33-46 (2002).
[2] T. Gureyev and et. al., "Optical phase retrieval by use of first Born- and Rytov-type approximations," Applied Optics 43, 2418-2430 (2004).
[3] M. Reed Teague, "Deterministic phase retrieval: a Green's function solution," Journal of the Optical Society of America 73, 1434-1441 (1983).

Investigation of Carbon Nanostructure in Copper Covetics by X-ray Nanotomography[§]

B. MA[1*], R.P. WINARSKI[2], J. WEN[2], D.J. MILLER[2], C.U. SEGRE[3], U. BALACHANDRAN[1], D.R. FORREST[4]

[1] Energy Systems Division, Argonne National Laboratory, Argonne, IL 60439, USA
[2] Nanoscience and Technology Division, Argonne National Laboratory, Argonne, IL 60439, USA
[3] Department of Physics, Illinois Institute of Technology, Chicago, IL 60616, USA
[4] U.S. Department of Energy, Advanced Manufacturing Office, Washington, DC 20585, USA
* presenting author, email: bma@anl.gov

Keywords: Carbon nanostructure, covetics, X-ray nanotomography, computed tomography

Abstract

Covetic materials with large amount of nanoscaled carbon infused into metal matrixes exhibit unique physical properties. The enhanced electrical and thermal conduction of covetic copper originate from carbon nanostructures dispersed in the metal. Scanning electron microscopy and transmission electron microscopy revealed nanoscale features of distinct carbon concentration when compared to the matrix. Nondestructive imaging of nanostructures in three-dimension is desirable for understanding the formation of carbon nanostructures and their interaction with surrounding metal matrix. We utilized synchrotron hard X-ray nanotomography to examine the 3D nanoscale features in a covetic copper. For the first time, visualization of nanoscale features in covetic copper was accomplished by computed tomography imaging measured near copper K-edge using hard X-ray nanoprobe.

Introduction

Recent advancements in nanoscience and nanomaterials engineering have made it possible to incorporate carbon nanostructures into metals such as aluminum, copper, and silver. This new class of materials, known as covetics, may be a game-changer for materials scientists and engineers who have long sought to combine high-strength carbon with metal in their pursuit to improve materials performance [1,2]. The resulting covetic materials exhibit many unique and improved properties over the base metal from which they are produced. The carbon is dispersed through the metal matrix in several ways which together contributes to the enhanced properties. The carbon is strongly bound into the material, resisting some standard methods for its detection and characterization, such as LECO analysis [1]. Nanocarbon raises the melting point and significantly alters surface tension, and thus porosity, during solidification. In covetic copper, thermal conductivity was anisotropic: up to 50% higher in the extrusion direction and at least 25% lower in the transverse direction, and was different between transient and steady state test conditions [1]. Carbon nanoparticles of 5-200 nm diameters along with lattice diffused carbon structures were reported in the covetic aluminum [2]. Imaging of nanostructures in three-dimension (3D) is highly desirable for understanding the formation of nanoscaled carbon structures and their interactions with surrounding metal matrix. For this purpose, we utilized synchrotron hard X-ray nanoprobe station at sector 26ID at the Advanced Photon Source (APS) at Argonne National Laboratory to examine the 3D nanoscale features in covetic copper material.

Full-field imaging by soft X-ray microscopes underwent rapid progression due in part to the relative ease of manufacture of diffraction-limited optics for longer wavelengths. Soft X-ray full-field imaging and nanotomography efforts have been successfully applied to examinations of biological systems [3]. Such efforts take advantage of the high contrast of biological matter to X-rays relative to that of water within the so-called water window from 300 to 500 eV. Hard X-ray nanoscale imaging is a more recent technique that is ideally suited for thicker heterogeneous samples, chemical state imaging of transition metals within samples, and observation of bulk samples [4]. Tomography and fluorescence imaging can be combined to provide information about both the internal structure and the internal nanoscale elemental composition of a complex object [5]. The Hard X-ray Nanoprobe Beamline operated by the Center for Nanoscale Materials and the Advanced Photon Source at Sector 26 of the Advanced Photon Source at Argonne National Laboratory is an X-ray microscopy system incorporating diffraction, fluorescence and full-field imaging capabilities. The Nanoprobe utilizes three different techniques for probing the nanoscale structure of samples: X-ray fluorescence, X-ray diffraction and full-field X-ray imaging (which, combined with a precision rotation stage, can also yield nanoscale tomographic images). The precision optics manipulation necessary for imaging at a resolution approaching 30 nm required the development of unique sensing and motion controls to ensure accurate detection of features inside of samples. The Nanoprobe optics and control platforms were designed to achieve a spatial resolution of 10 nm with the contemporary development of higher-resolution zone plates [6]. This unique tool offers great potential for advancing the knowledge about carbon nanostructures in covetic materials such as how they interact with surrounding metal atoms, why the bonding is so strong, and what mechanisms promote the improved physical properties.

Materials and Method

Covetic copper of 0.21 wt.% carbon was prepared by Third Millennium Metals, LLC (Waverly, OH) using a proprietary procedure [7]. The as-received cast ingot was hot compressed in inert atmosphere, followed by multiple repetitions of rolling and annealing for densification. Scanning electron microscopy (SEM) was performed on both tensile fracture and ion polished surfaces. Samples for transmission electron microscopy (TEM) were prepared by mechanically polishing to a thickness of ≈30 μm followed by Ar ion milling. Specimens of ≈5 μm x 5 μm x 20 μm were fabricated using a Zeiss 1540XB Focused Ion Beam FE-SEM for hard X-ray experiments. A photograph of the sample stage used for hard X-ray measurement is shown in Fig. 1a. The actual specimen is mounted onto a tungsten tip as indicated by the red arrow in the photograph. A micrograph of the covetic copper specimen mounted on the tip of a tungsten needle is shown in Fig. 1b. The experiment was conducted under helium (inert environment) gas, inside the closed chamber to eliminate air currents near the sample. The thermal stability of the staging was monitored during data acquisition.

Monochromatic X-rays of 8.9 keV (just below the copper K-edge) were used for the experiment. For full-field imaging and nanotomography, the X-ray beam is directed through a capillary condenser which focuses the X-rays onto the sample. X-rays transmitted through the sample are collected by a zone plate and focused onto the imaging optics and a CCD camera with 1024 x 1024 pixels. Detailed configurations of the experimental setup were reported earlier [6]. Transmission X-ray radiographs collected at 1° interval over a total rotation span of 180° were aligned and reconstructed to produce a three-dimensional representation of the sample's internal structural features. A standard filtered back-projection method (inverse Radon transform of the projections) was used for reconstruction [8,9].

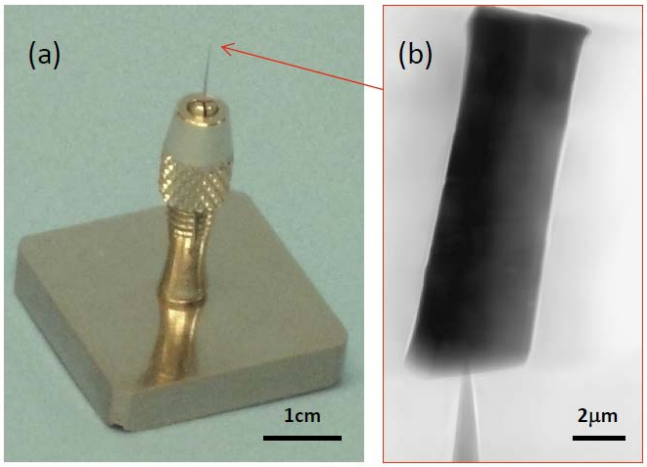

Fig. 1. *(a) Photograph of sample stage used for hard X-ray experiment, and (b) micrograph of the specimen mounted ont the tungsten tip.*

Results and Discussion

Figure 2a shows an SEM image of the tensile fracture surface of covetic copper sample of 0.21wt.% carbon. We observed spherically-shaped inclusions of 0.5 to 3 μm size. Those particles exhibit higher oxygen content. The inclusion particulates are again visible as dark spots from the SEM image of the ion polished surface, as shown in Fig. 2b. The oxygen rich particulates are likely formed during the initial infusion process. They are aligned in bands, as observed from SEM micrographs, due to hot metal work (high temperature annealing and rolling). Regions of different contrast shown for the matrix phase in Fig. 2b are due to differences in sputtering resistance to ion milling for grains of different crystalline orientations. SEM Energy Dispersive Spectroscopy (EDS) analysis revealed no measurable difference in carbon content.

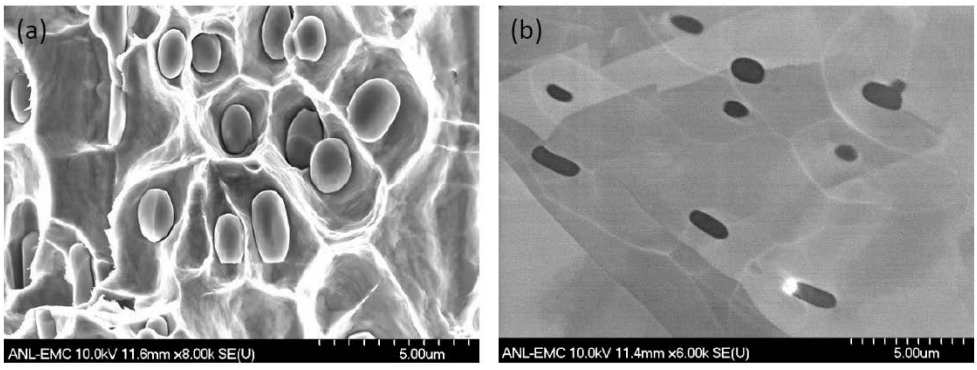

Fig. 2. *(a) Fracture surface and (b) ion polished surface SEM micrographs of covetic copper.*

Figure 3 shows bright field TEM micrograph and dispersive energy spectroscopy (EDS) of a covetic copper of 0.21 wt.% carbon. EDS spectra of two areas, the spherical phase A and the matrix phase B, were measured. It is evident that the spherical phase shown at the center of the TEM image contains higher concentration of oxygen when compared to the matrix phase.

Full-field X-ray transmission radiographs were measured while the specimen was rotating over 180° with step size of 1°. Figure 4 shows three of these images measured at angular positions of 0°, 22°, and 44°. Features resembling the spherical particulates as shown in Fig. 2 are observable from the full field transmission images.

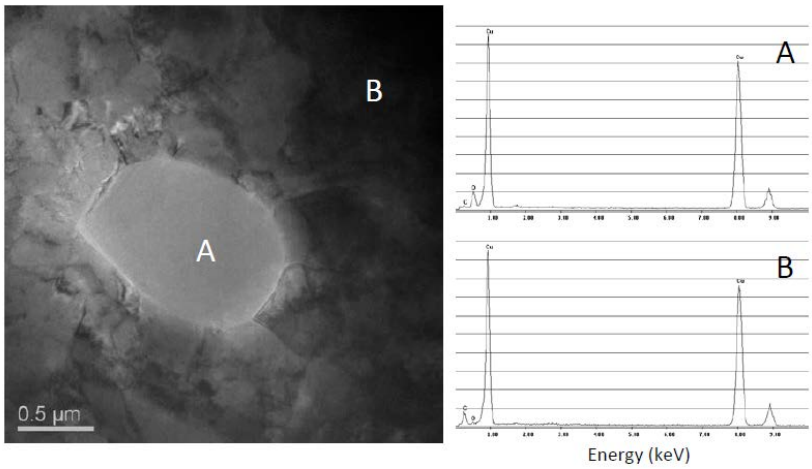

Fig. 3. *Bright field TEM image and energy dispersive spectra of a covetic copper of 0.21 wt.% carbon.*

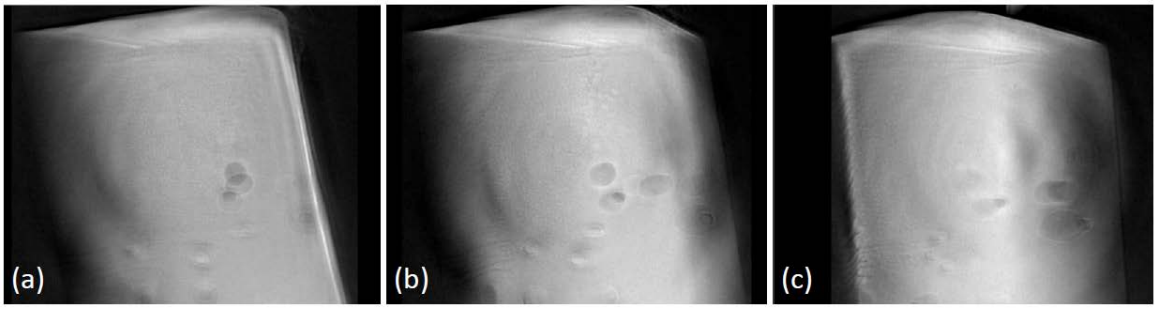

Fig. 4. *X-ray transmission micrographs taken at rotation angle of (a) 0°, (b) 22°, and (c) 44°.*

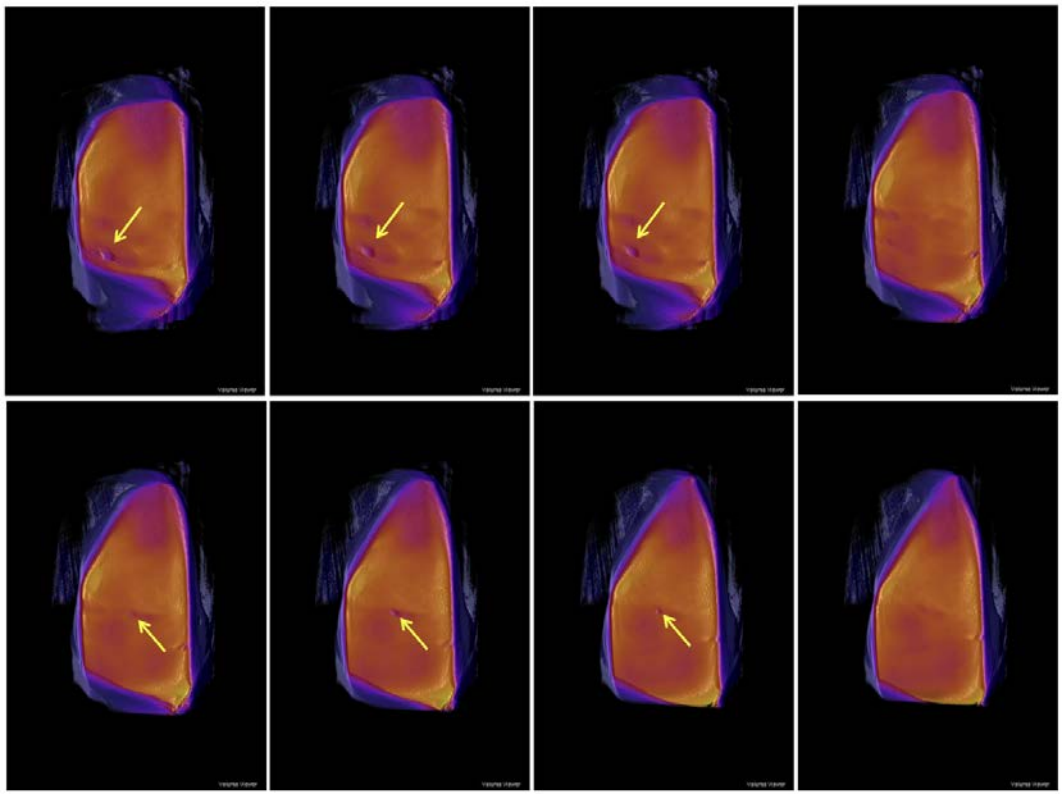

Fig. 5. *CT images of covetic copper sample sliced at different positions.*

These transmission X-ray radiographs were used to determine the two-dimensional projections of the linear attenuation coefficient in the object with flat-field correction. The 3D distribution of the linear attenuation coefficient was reconstructed using standard algorithms (filtered back projection). 2D slices of the volume-view 3D computed tomographic images are shown in Figure 5, where nanoscale spherical features are clearly visible (as highlighted by arrows). Those images are slices at different positions with a constant interval for illustration of the evolution of spherical nanoscale features. In addition, we observed regions of different density. Yellow and purple colors correspond to higher and lower density, respectively.

Conclusions

Full field transmission radiographs of covetic copper specimens were measured using a monochromatic X-ray of 8.9 keV at the hard X-ray nanoprobe beamline at sector 26ID at APS of Argonne National Laboratory. Transmission X-ray radiographs collected at 1° interval over an angular space of 180° were aligned and reconstructed to produce a 3D representation of the sample's internal structural features. A standard filtered back projection method (inverse Radon transform of the projections) was used for reconstruction. Computed nanotomographic images revealed nanoscale features inside the specimen that coincide to that observed from electron microscopy.

Acknowledgments

This work was supported by the U.S. Department of Energy, Energy Efficiency and Renewable Energy, Advanced Manufacturing Office, under Contract DE-AC02-06CH11357. Electron microscopy was carried out at the Electron Microscopy Center (EMC) of the Center for Nanoscale Materials at Argonne National Laboratory. Use of the Hard X-ray Nanoprobe Beamline operated by Center for Nanoscale Materials and the Advanced Photon Source was supported by the U. S. Department of Energy, Office of Science, Office of Basic Energy Sciences, under Contract No. DE-AC02-06CH11357.

References

1. D.R. Forrest, I. Jasiuk, L. Brown, P. Joyce, A. Mansour, L. Salamanca-Riba, "Novel Metal-Matrix Composites with Integrally-Bound Nanoscale Carbon," ***Proc. Nanotech Conference and Expo 2012***, 18–21 June 2012, CRC Press, Santa Clara, CA.
2. L. Salamanca-Riba, I. Isaacs, A. Mansour, A. Hall, D.R. Forrest, M.C. LeMieux, J. Shugart, "A New Type of Carbon Nanostructure Formed Within a Metal-Matrix," ***Proc. Nanotech Conference and Expo 2012***, 18–21 June 2012, CRC Press, Santa Clara, CA.
3. J. Kirz , C. Jacobsen , M. Howells, "Soft X-ray microscopes and their biological applications," ***Q. Rev. Biophys.*** 28, 33–130, 1995.
4. P.J. Withers, "X-ray nanotomography," ***Materials Today*** 10:12, 26-34, 2007.
5. M. Holt, R. Harder, R.P Winarski, V. Rose, "Nanoscale Hard X-Ray Microscopy Methods for Materials Studies," ***Annual Review of Materials Research*** 43(1) 183-211, 2013.
6. R.P. Winarski, M.V. Holt, V. Rose, P.L. Fuesz, D.A. Carbaugh, C. Benson, D. Shu, D. Kline, B. Stephenson, I.L. Mcnulty, J.M. Maser, "A hard X-ray nanoprobe beamline for nanoscale microscopy," ***J. Synchrotron Radiat.*** 19, 1056–1060, 2012.
7. J.V. Shugart, R.C. Scherer, ***US Patent*** 8647534, issued February 11, 2014.
8. S.R. Deans, The Radon transform and some of its applications, John Wiley & Sons, New York, 1983.
9. G.T. Herman, Image reconstruction from projections, Academic Press, New York, 1980.

Modelling of X-ray tube spot size and heel effect in Arion

J. DELEPIERRE[1], J. DHAENE*[1], M. N. BOONE[1], M. DIERICK[1], L. VAN HOOREBEKE[1]

[1] UGCT – Dept. Physics and Astronomy, Ghent University, Proeftuinstraat 86/N12, B-9000 Gent, Belgium – Jelle.Dhaene@UGent.be
* presenting author

Keywords: Computed tomography; Simulation; Polychromatic; X-rays

Abstract

X-rays produced in X-ray tubes originate from a focal spot on the target material. This spot is not infinitely small, but has a finite size. This finite size of the spot will affect the radiographic projections taken during X-ray Compted tomography. In order to simulate correct radiographic projections, this finite spot size needs to be taken into account during the simulations. This can be done by modelling a two dimensional profile of the spot and use this model to convolve the simulated radiographic projections simulated with an infinitely small spot size. A second effect, the heel effect that originates in directional X-ray tubes will also have an influence on the final projections. This effect can also be modelled and this model can be used to correct the simulated projections for this effect.

Introduction

X-ray Computed Tomography (CT) is a non-destructive technique used to produce three-dimensional images of objects, allowing the user to visualize the inside of these objects. This reconstructed object is represented by a discrete three-dimensional volume and each voxel inside this volume contains a grey value that represents a calculated linear attenuation coefficient μ. In laboratory-based X-ray CT, polychromatic sources are typically used in combination with energy-integrating detectors. Changes in the emitted spectrum or use of different detectors will thus result in different reconstructed attenuation coefficients.

To optimize the scanner settings such as high voltage and filtration for a given sample, a fast and realistic projection simulator called Arion (Dhaene *et al.*, 2015) was developed at the 'Centre for X-ray Tomography' of Ghent University (UGCT, www.ugct.ugent.be). This GPU-accelerated polychromatic simulator takes into account the characteristics of the setup such as emitted spectrum, detector energy response, beam filtration and the sample itself. This could also be very useful in iterative reconstruction methods where a simulated projection of a temporary solution is compared to the actually measured projection.

Arion already takes into account the above described effects caused by the polychromatic nature of the imaging process. Although this description of a virtual scanner is sufficient in most cases, sometimes it is useful to take into account other effects such as the finite spot size and the heel effect of the X-ray tube to perform the simulations. The finite spot size can result in a reduction of spatial resolution in the radiographic projection. The heel effect causes a gradient in the spectral distribution over the projection image, which may influence the above mentioned optimization.

Methods

An X-ray tube produces a primary spot, of which the size depends on the tube power, and in some tube geometries also an "unwanted" secundary spot caused by the internal structure of the X-ray tube (Boone et al., 2012). The effect of the former is usually minimized by choosing the tube settings (i.e. focussing mode and tube power)achieving

a spot size that corresponds to or is smaller than the resolution one wants to achieve during the CT scan. Nevertheless, it can be interesting to use a higher tube power resulting in a spot size that gives rise to a worse resolution because at the same time the higher power increases the image statistics and thus reduces the noise in the data. The secondary focal spot on the other hand has a fixed size. Unless a hardware correction is made, as described in Boone et al., the effect of the secondary spot is always present in the radiographic projections.

The effect of a finite spot, both primary and secondary, can be implemented by performing the following convolution:

$$I'(x', y') = \int_{-\infty}^{+\infty} \int_{-\infty}^{+\infty} I(x' - x, y' - y) F(x, y)\, dx\, dy,$$

in which $I(x' - x, y' - y)$ represents the original simulated projection that was performed with the infinite small spot size and $F(x, y)$ is a normalized two-dimensional profile of the finite spot. x and y represent the coordinates in the detector plane. For an infinitely small spot, F is represented by a Dirac delta function and I and I' will be the same.

The primary spot on HECTOR (Masschaele et al., 2013) was modeled by taking radiographs of an Al Sphere of 6mm diameter at a tube voltage of 100kV with different tube powers. A tube power of 10W was used to achieve a spot size that was smaller than the 'resolution' of the radiograph which represents a radiograph with an infinitely small spot. Further, radiographs at the same tube voltage with a power of 100W and 200W were taken that represents radiographs with a finite spot size larger than the resolution of the radiographies.

A correction for the secondary spot present in the transmission tube described by Boone et al. requires information about the profile of the spot. This information is obtained by performing a Monte Carlo (MC) simulation of the tube with BEAMnrc (www.nrc-cnrc.gc.ca/eng/solutions/advisory/beamindex.html). The inner structure of the tube was modeled and given as input to the MC simulations. During the simulations accelerated electrons impinge on the tungsten target and interactions can be traced. Photons are produced by the interactions between the electrons and the target material and detected on a 1cm x 1cm scoring plane at a distance of 5cm away from the target. Some electrons will scatter towards the molybdenum case of the inner tube. These electrons can also interact with this inner tube material and produce photons. Around 17% of the produced photons in the X-ray tube emanate from this molybdenum case, which results in a large secondary spot. The location of the production of these secondary photons can be traced in the MC simulations and thus a model of the secondary spot can be extracted from these data.

A complete scan of an Al sphere was performed at the scanner described in Masschaele et al. (2007). This scanner uses the transmission tube described by Boone et al. in which the above described secondary spot is produced. For the same scan two simulations were performed with Arion, one with and one without the correction for the secondary spot. These real and two simulated datasets were reconstructed by using Octopus (www.octopusreconstruction.com) (Vlassenbroeck et al., 2007), a software package developed at the UGCT.

Monte Carlo simulations with BEAMnrc can also be used to model the heel effect in a directional tube. In these tubes both the intensity and spectrum depend on the direction in which the X-rays escape from the target material as the probability for absorption depends on the distance the photons travel within the anode material. Due to the geometry of the electron beam on the anode, this distance depends on the direction of emission. This behaviour was modeled by using the results of the MC simulations

performed for the X-ray tube present at HECTOR. The model can be used to correct the radiographic images obtained by Arion for a heel effect of a directional tube.

Results

Figure 1 shows a real projection of an Al sphere (diameter 6mm) taken at HECTOR at 100W and 100kV, a projection with the same parameters acquired by a simulation performed with Arion by supposing an infinite small spot and a simulated projection where a correction for the finite spot size is executed.

Fig. 1. *Real projection of an Al sphere taken at HECTOR (right), simulated projection without (left) and with (middle) spot correction.*

The simulated profile of the spot of the transmission tube is shown in figure 2. Figure 3 shows a radial intensity profile for the secundary spot only. The geometry of the spot is assumed to be cylindrically symmetric and the normalized intensity is expressed in function of the distance to the central axis of the tube. This model was used to correct the simulated data from Arion. Figure 4 shows a line profile of a reconstructed slice of the scanned Al sphere. A comparison between the real scan, the simulated scan without secondary spot correction and the simulated scan with secondary spot correction is shown.

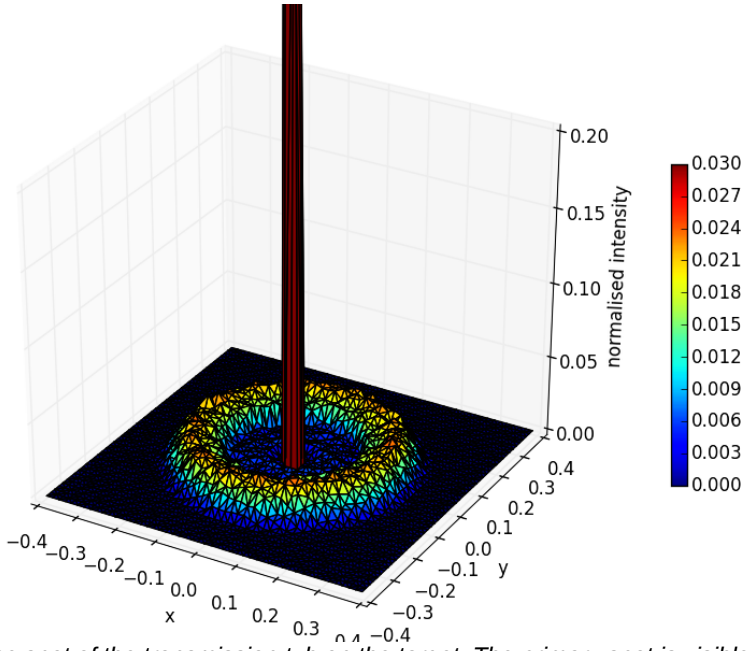

Fig. 2. *3D profile of the spot of the transmission tub on the target. The primary spot is visible on the central axis while the torus around this axis represents the secondary spot.*

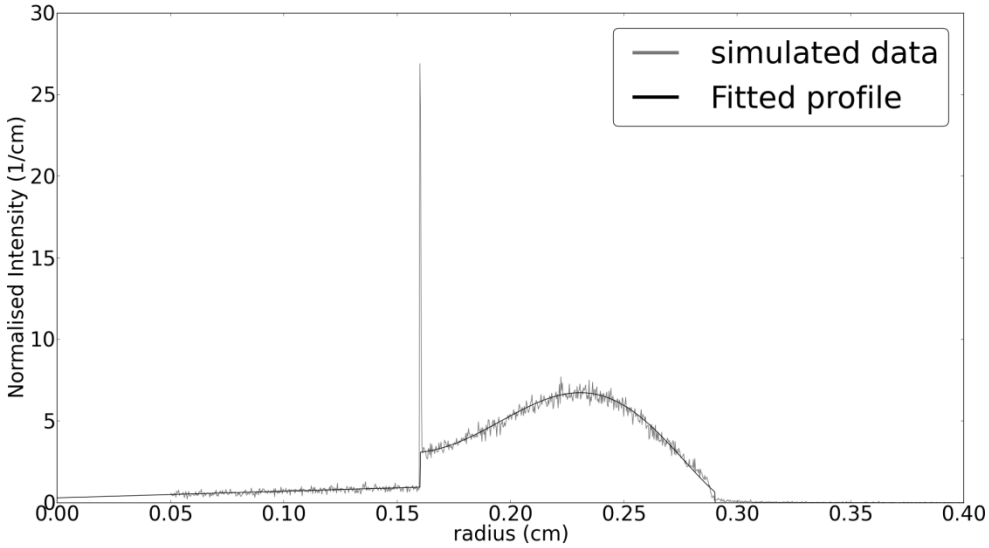

Fig. 3. *Normalised intensity of the secondary spot in function of the distance to the centre of the transmission tube. A profile is fitted to the data.*

Fig. 4. *A line profile of the real and simulated scan in a reconstructed slice of the Al sphere .*

Figure 5 shows a line profile in an open beam image taken at HECTOR and the line profile acquired in a simulation with Arion. The measured open-beam image is corrected for detector inhomogeneity by normalization with an image acquired using a transmission-type tube, where the heeling effect is not present and the X-ray beam is expected to be very homogeneous. The simulated open beam image takes into account the modelled direction of the photons emitted by the source and thus corrects for the heel effect.

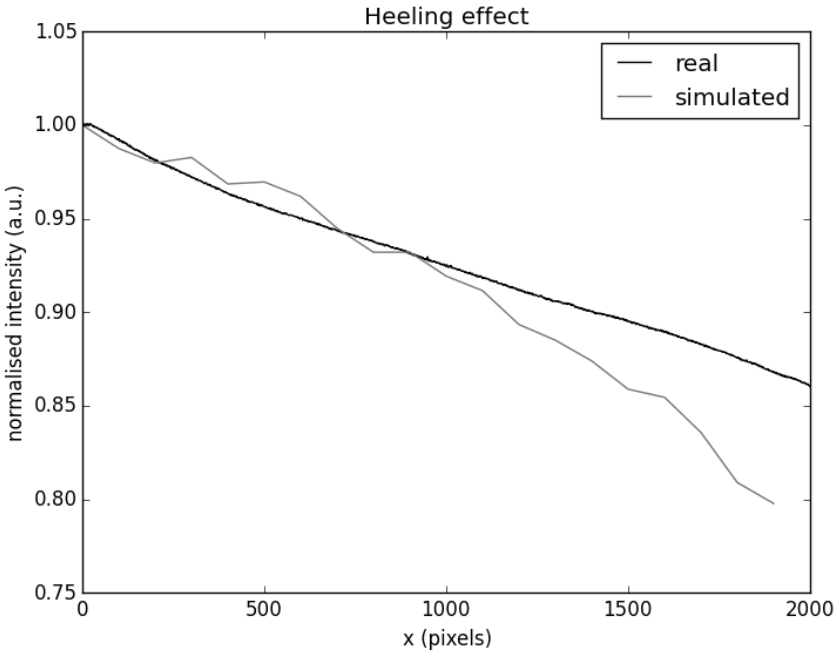

Fig. 5. *Comparison between the real and simulated line profile in an open beam image.*

Conclusion

The finite size of a spot can be modeled and used to improve the simulations performed with Arion. This is done by performing a convolution between the simulated projection with infinite small size and a profile of the finite spot. Further the heel effect in the directional tube mounted on HECTOR was studied and modelled. A maximum deviation of 15% between simulated and real data was found.

These models of the finite spot size and heel effect can help to improve image quality of the simulated scans but future research is needed to model these effects more accurately.

References

M. N. Boone, J. Vlassenbroeck, S. Peetermans, D. Van Loo, M. Dierick, L. Van Hoorebeke, Secondary Radiation in Transmission-type X-ray Tubes: Simulation, Practical Issues and Solution in the Context of X-ray Microtomography, ***Nuclear Instruments & Methods in Physics Research Section A-accelerators Spectrometers Detectors and Associated Equipment*** 661 (1) (2012) 7–12.

J. Dhaene, E. Pauwels, T. De Schryver, A. De Muynck, M. Dierick, L. Van Hoorebeke, A Realistic Projection Simulator for Laboratory Based X-ray micro-CT, ***Nucl. Instr. Meth. Phys. Res. B*** 342 (2015) 170-178.

B. Masschaele, V. Cnudde, M. Dierick, P. Jacobs, L. Van Hoorebeke, J. Vlassenbroeck, UGCT: new X-ray radiography and tomography facility, ***Nucl. Instr. Meth. Phys. Res. A*** 580 (1) (2007) 266–269.

B. Masschaele, M. Dierick, D. Van Loo, M.N. Boone, L. Brabant, E. Pauwels, V. Cnudde, L. Van Hoorebeke, Hector: A 240 kv micro-CT setup optimized for research, ***J. Phys. Conf. Ser.*** 463 (2013).

J. Vlassenbroeck, M. Dierick, B. Masschaele, V. Cnudde, L. Van Hoorebeke, P. Jacobs, Software tools for quantification of X-ray microtomography at the UGCT, ***Nucl. Instr. Meth. Phys. Res. A*** 580 (1) (2007) 442–445.

Optimization of scanner parameters for dual energy micro-CT

E. PAUWELS*[1], J. DHAENE[1], A. DE MUYNCK[1] E., M. DIERICK[1], L. VAN HOOREBEKE[1]

[1] UGCT – Dept. Physics and Astronomy, Ghent University, Proeftuinstraat 86/N12, B-9000 Gent, Belgium – Elin.Pauwels@UGent.be
* presenting author

Keywords: Computed tomography; Simulation; Polychromatic; X-rays; DECT

Abstract

Two materials of different composition can have very similar grey values in an X-ray Computed Tomography (CT). This is because X-ray CT uses polychromatic sources in combination with energy-integrating detectors and the materials have a mass attenuation coefficient that is dependent on composition and photon energy. A distinction between different materials with similar grey values can be made by combining information from scans performed with different spectra, which can be achieved by varying the tube voltage and filtration. However, the polychromatic behaviour of laboratory based X-ray CT complicates the choice of the appropriate scanning conditions for such dual energy methods. Here, the programme Arion, for simulating realistic radiographic projections is used to determine optimal scanning parameters.

Introduction

In X-ray Computed Tomography (CT), the reconstructed sample is represented by a discrete 3D volume. Each voxel in this volume contains a grey value that represents a linear attenuation coefficient μ. This is the product of the local mass attenuation coefficient μ/ρ, which is both energy and material dependent, and the local density ρ of the material, averaged over the detected X-ray energy spectrum. Therefore, the reconstructed linear attenuation coefficients of two materials of different composition can still have similar grey values, making them practically indistinguishable. Since the mass attenuation coefficient of a chemical element solely depends on the photon energy, a distinction between different materials with similar grey values can be made by combining information from scans performed at two or more different X-ray energies. This technique is called Dual Energy CT (DECT).

DECT yields very good results when a (quasi-)monochromatic X-ray source is used which is often the case in synchrotron imaging. However, when using a laboratory-based micro-CT, the polychromatic behaviour of the photon beam and detector sensitivity and efficiency complicates the choice of the appropriate scanning parameters for applications of DECT methods.

A programme for simulating realistic radiographic projection images, Arion (Dhaene et al., 2015), has recently been developed at the 'Ghent University Centre for X-ray Tomography' (UGCT, www.ugct.ugent.be). This programme can also be used to identify optimal scanning parameters for different applications, including DECT.

Methods

A virtual phantom of three aqueous solutions was created and used as a sample. These 3 solutions contained $Pb(NO_3)_2$, PTA and KBr respectively, which are typical staining materials used for the visualization of soft tissue with micro-CT. Simulations were performed for different scanning conditions, which covered a range of voltages (80, 100, 120 and 160kV) and filters (1mm Cu, 1mm Al and 0.1 mm W). Varying these parameters will result in a broad range of different spectra. Covering this range is

necessary to find the best signal-to-noise ratio (SNR) or contrast-to-noise ratio (CNR) for the materials inside the phantom for a specific application.

The datasets acquired by the simulations are reconstructed using Octopus (www.octopusreconstruction.com) (Vlassenbroeck et al., 2007), a software package developed at the UGCT. First, all single energy scans were studied in terms of distinctiveness between the three solutions. In most cases at least two out of three materials are not distinguishable. Then a post-reconstruction method (Granton et al., 2008) was applied for the range of simulations. This method allows to combine the information from scans performed at two different energies and calculate the volume fractions of the three materials present in the phantom. In this way, the best settings to perform DECT can be selected.

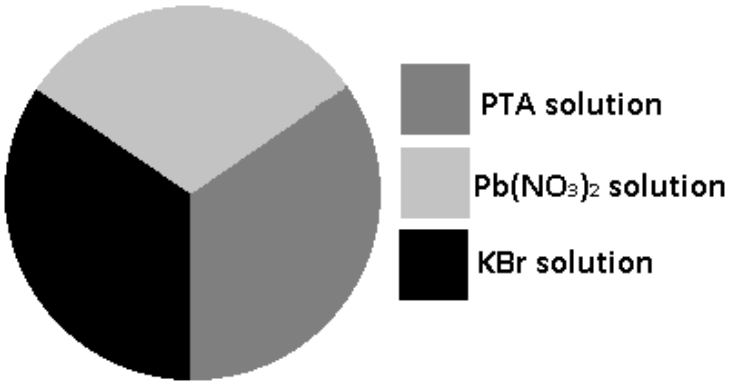

Fig. 1. *Phantom that consists of three aqueous solutions, containing $Pb(NO_3)_2$, PTA and KBr.*

Results

Figure 2 shows the reconstructed attenuation coefficients of the aqueous solutions in terms of tube voltage and filtration and the noise measured on these attenuation coefficients in the slices. It is clear that most settings do not distinguish more than two solutions. Only the scans with 1mm Al at 120kV and 160kV show no significant overlap between the reconstructed attenuation coefficients. Note that the errors shown in the figure represent a one sigma standard error.

Figure 3 shows a reconstructed slice and histogram of the 160kV Al and 80kV Cu scan, which are respectively the best and worst in terms of SNR. At 80kV with 1mm Cu filtration, the three different components cannot be individually identified. As such, they will be visually indistinguishable in a realistic sample where the three materials are mixed. At 160kV with a filter of 1mm Al, the three solutions can be clearly identified in the histogram. However, due to the significant overlap mainly between the peaks of the PTA and KBr solution, segmentation of a real sample where the three materials are mixed, will not be straightforward. The application of DECT could provide a solution for this.

In most cases the $Pb(NO_3)_2$ and KBr solutions can be separated relatively easily. PTA, however, exhibits a different behaviour. It overlaps mainly with $Pb(NO_3)_2$ when using the Cu filter, while it similarly behaves to KBr when using the Al filter. This effect originates in the alterations to the spectrum due to the filtration material. A DECT post-reconstruction method proposed by Granton et al. (2008) was applied for two different cases. This technique allows to combine the information from scans performed at two different energies and calculate the volume fractions of the three materials present (Figure 4). For the first case, the two scanner settings for which PTA differs most from $Pb(NO_3)_2$ (80kV Al) and KBr (120kV Cu) were chosen. For the second case the scanner

setting with the best SNR (160kV Al) was selected to replace the 80kV Al setting in the first case. The three solutions can be easily distinguished by using DECT. Despite the better SNR of the 160kV Al setting, the results are better when the 80kV Al setting is combined with the 120kV Cu setting. This indicates that it can be useful to give up on some image quality in a single scan to increase the quality of the analysis when using DECT.

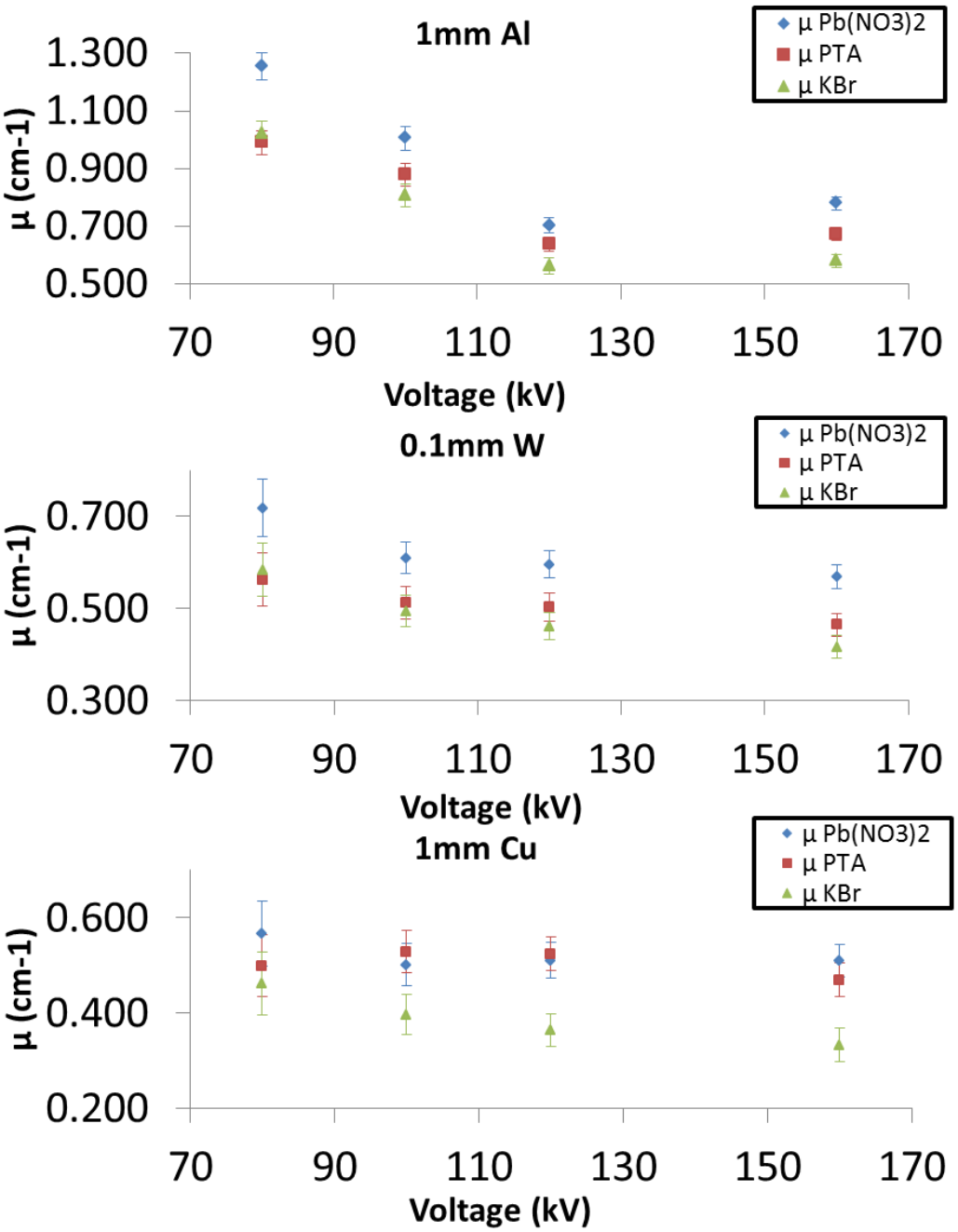

Fig. 2. *The reconstructed attenuation coefficients and their errors(noise) as a function of the tube voltage for the three tested filters.*

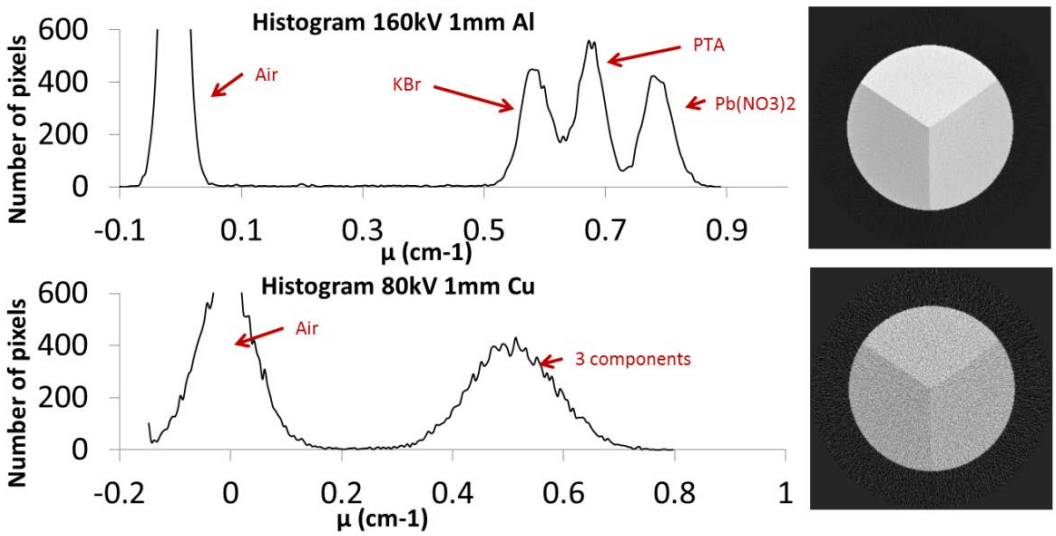

Fig. 3. *The histogram of the reconstructed slices of the scan settings at 160kV with 1mm Al and at 80kV with 1mm Cu.*

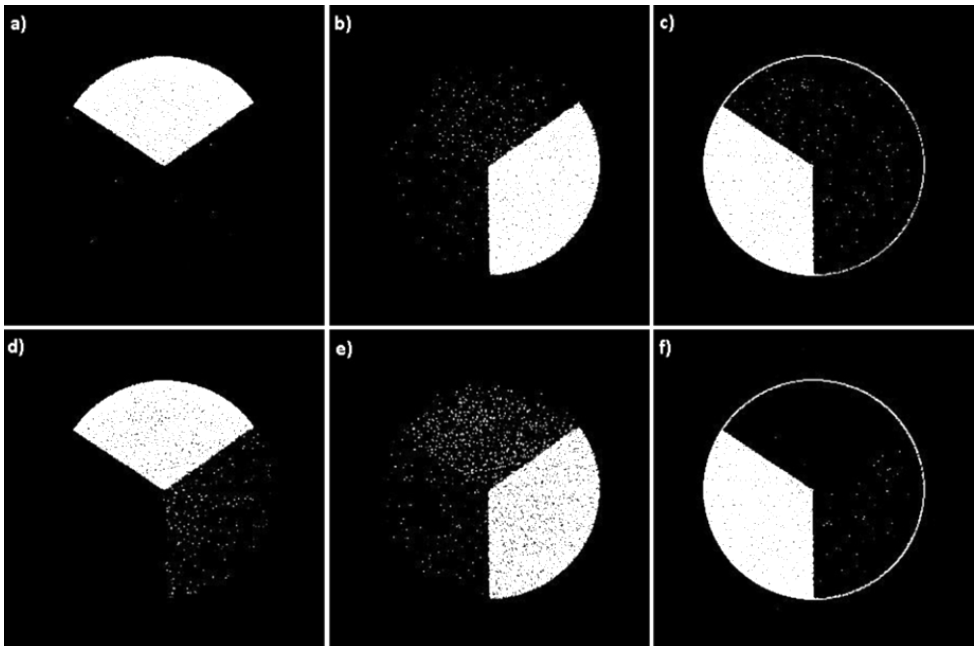

Fig. 4. *DECT applied to the 80kV Al and 120kV Cu slice (a,b & c) and to the 160kV Al and 120kV Cu slice(d,e & f).*

Conclusion

Arion can be used to determine scanning conditions for DECT which optimize the sensitivity for a given element using dual energy techniques. Arion takes into account the energy dependence of the complete imaging chain, including source spectrum, sample size and composition, and detector spectral sensitivity. The applicability was demonstrated on a virtual 3-solution phantom and experimentally validated. It is worth noting that the best settings for discriminating a particular element using a dual energy approach are not necessarily those that offer the best SNR for any particular phase of the sample. It is more important to maximize the difference in reconstructed attenuation coefficient of the material of interest with respect to the other materials present in the sample, taking into account the noise levels for each.

Acknowledgments

We acknowledge the Agency for Innovation by Science and Technology in Flanders (IWT, SBO project 120033 ‘‘TomFood’’) and the Special Research Fund of the Ghent University (BOF, GOA project 01G01008) for financial support.

References

J. Dhaene, E. Pauwels, T. De Schryver, A. De Muynck, M. Dierick, L. Van Hoorebeke, A Realistic Projection Simulator for Laboratory Based X-ray micro-CT, ***Nucl. Instr. Meth. Phys. Res. B*** 342 (2015) 170-178.

Granton P.V., Pollmann S.I., Ford N.L., Drangova M., Holdsworth D.W. *Implementation of dual- and triple-energy cone-beam micro-CT for postreconstruction material decomposition.* ***Med Phys****.* 2008 Nov; 35(11):5030-42

J. Vlassenbroeck, M. Dierick, B. Masschaele, V. Cnudde, L. Van Hoorebeke, P. Jacobs, Software tools for quantification of X-ray microtomography at the UGCT, ***Nucl. Instr. Meth. Phys. Res. A*** 580 (1) (2007) 442–445.

Phase-contrast imaging applied on biological and material samples using a commercial X-ray system

P. BIDOLA*[1], K. ACHTERHOLD[1], M. WILLNER[1], F. PFEIFFER[1]

[1] Department of Physics & Institute of Medical Engineering, Technische Universität München, James-Franck-Str 1, 85748 Garching, Germany – pidassa.bidola@tum.de
* presenting author

Keywords: Phase-contrast, X-ray microscopy, phase retrieval

Abstract

Single-distance propagation-based phase-contrast imaging is one of the fast evolving phase-contrast imaging techniques available nowadays [1, 2]. Because these imaging methods require coherent X-ray beams, they commonly have been used at synchrotrons. However, technical developments have enabled the translation of some of the techniques to laboratories using polychromatic X-ray tubes [3, 4]. The improvement of phase-retrieval algorithms, extended to cone-beam geometry [5, 6] allows for the retrieval of amplitude and phase images, which usually hold complementary information. In fact, the use of phase-contrast and phase-retrieval algorithms in a cone-beam geometry are successfully applicable on materials [7], and biological samples [8]. Here, the application of the single-distance propagation-based phase-contrast imaging in tomography including the phase-retrieval, especially, at an X-ray microscope system (VersaXRM-500 by Carl Zeiss, former Xradia) is presented.

Introduction

VersaXRM-500 is provided with a commercial closed source microfocus X-ray tube operated up to 160 kV and focal spot of around 3 µm. High spatial resolution is achieved down to detector pixel resolution of < 0.7µm by using detector optics. Therefore, high resolution images can be recorded to around 1µm resolution at large working distances.

With its submicron spot size X-ray source the system achieves a partial transversal coherence which is required for propagation-based phase-contrast imaging [4]. The detector optics allow to perform high resolution imaging without having to place the sample very close to the source. Hence, the simultaneous displacement of source and detector away from the sample still enables high resolution imaging but also increases the effective propagation distance Z defined as

$$\boldsymbol{Z} = (\boldsymbol{a}.\boldsymbol{b})/(\boldsymbol{a}+\boldsymbol{b}),$$

where *a* and *b* are source-to-sample and sample-to-detector distances, respectively. This propagation distance is responsible for the increase of gradients at the edge of structures within an object and highlights the phase contrast. The phase retrieval algorithm by Paganin et al. [5] is one of the algorithms developped to retrieve the phases in holographic phase-contrast imaging and has been applied in this work.
Here, results of phase retrieval applied on phase-contrast images of a seed of ~1.5mm in diameter acquired at VersaXRM-500 are shown.

Methods

A tomographic acquisition was performed with 1601 projections taken with 25s exposure time each. A source tube voltage and current of 50kV and 80µA, respectively, were set during the scan. The sample position from the source and detector was a=30mm and b=120mm. With a 4x objective lens, an effective pixel size of 1.36µm was achieved. The phase retrieval has been adapted from the algorithm by Paganin et al. [5] which reads

$$\varphi(x,y) = \frac{1}{2}\frac{\delta}{\beta} ln\left(\mathrm{F}^{-1}\left\{ \frac{\mathrm{F}[I(x,y)/I_o(x,y)]}{1 + \left[\frac{\lambda Z}{4\pi}\right]\frac{\delta}{\beta}(u^2+v^2)} \right\} \right).$$

Here, x and y are the Cartesian coordinates in the object plane. The forward and backward Fourier transform operators are represented by F and F^{-1}, respectively. I(x, y) is the intensity distribution in the phase contrast radiograph, I_0(x, y) the incident intensity without the object at the position of the detector, u and v the Fourier conjugate coordinates of x and y, and Z the propagation distance. In addition to the decrement from unity of the X-ray refractive index δ and a linear attenuation term β of the object, a wavelength λ is required to calculate the phase $\varphi(x,y)$. Therefore, a weighted sum of the energy spectrum at 50kV was considered to calculate λ. $\delta$and β were obtained from the CXRO X-ray database [9]. The phase retrieval was performed on the projections, then reconstructed with the standard filtered backprojection.

Results

In Fig. 1a, a tomographic phase-contrast images shows the features of an endive highlighted through the edge enhancement. A tomogram of the retrieved phases in Fig. 1b shows the density distributions of tissues in the seed. The contrast achieved in this figure shows the evidence of the successful performance of the phase retrieval on this sample.

Moreover, zooms within Fig. 1a and 1b, plotted in 1c and 1d reveal some details, which are only observed in the tomogram of retrieved phases. The arrows in Fig. 1d point to areas with different densities. This contrast is not observed in Fig. 1c, although some phase contrast occurred.

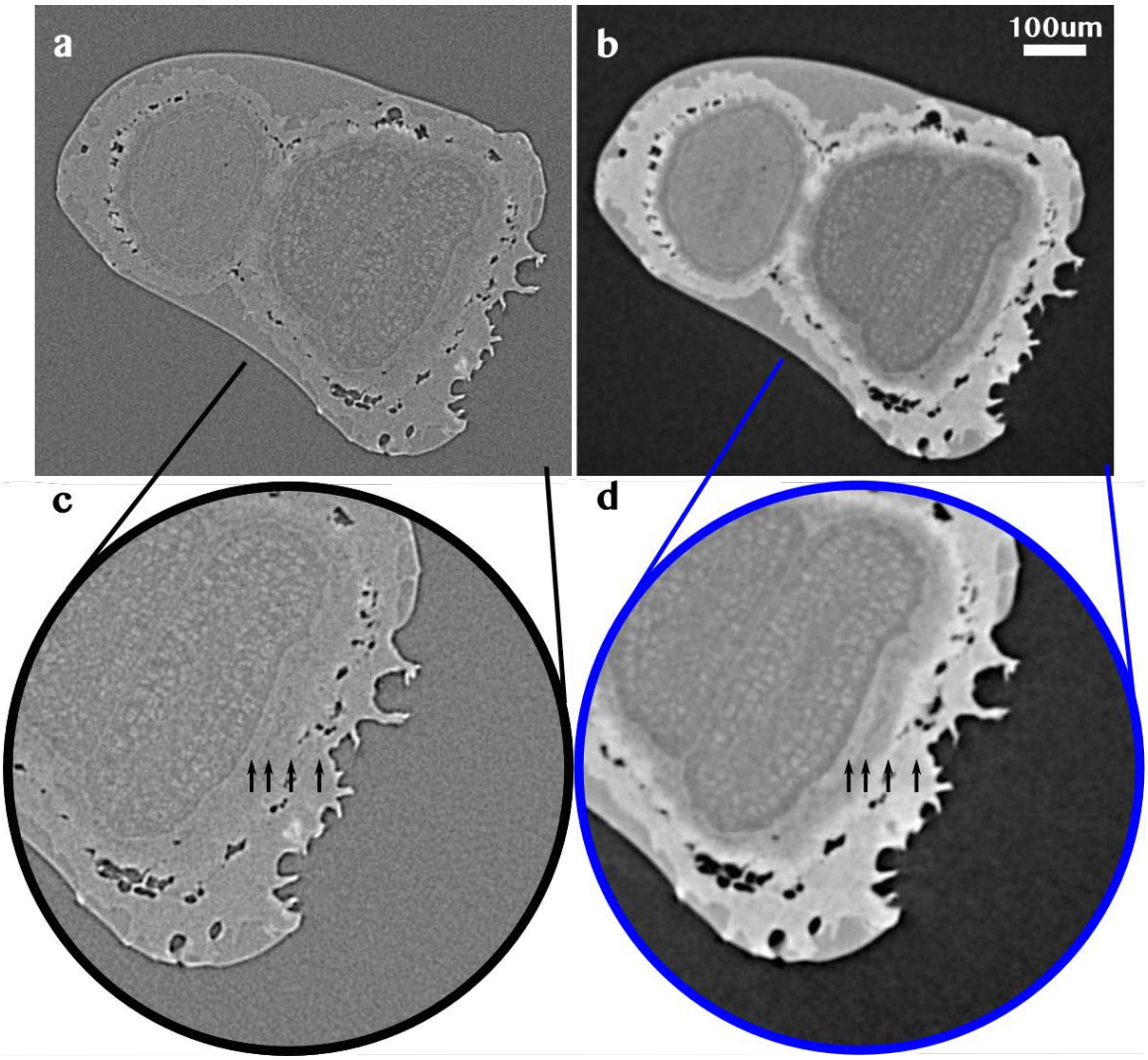

Fig. 1. *Phase-contrast tomogram of an endive seed* ***(a)****. Tomogram of retrieved phases using the algoritm by Paganin* ***(b)****.* ***(c), (d):*** *Zoom within* ***(a)*** *and* ***(b)****, respectively. The arrows in* ***(d)*** *show four different densities which are not seen in attenuation contrast* ***(c).***

Conclusion and outlook

The presented results in this work show the applicability of tomographic phase-contrast imaging as well as phase retrieval at the X-ray microscope VersaXRM-500. In addition to the primarily known advantage of the phase retrieval, which is a reduction of noise, it has been shown that a better contrast is achievable due to the density distribution. Thus, these results represent a step towards in-vivo measurements of biological samples, especially, at VersaXRM-500. Also, the applicability of the technique on low absorbing metal matrix composites such as Al2O3-Alloys or Carbon reinforced matrix composites at this system is to be performed. It might help to detect failures in materials under severe mechanical stresses.

Acknowledgements
We acknowledge financial support through the DFG Cluster of Excellence Munich-Centre for Advanced Photonics (MAP), the DFG Gottfried Wilhelm Leibniz program and the European Research Council (ERC, Starting Grant OptImaX).

References

[1] Bonse, U., & Hart, M. (1965). An X- ray interferometer. *Applied Physics Letters*, *6*(8), 155-156.

[2] Fitzgerald, R. (2007). Phase- sensitive X- ray imaging. *Physics Today*, *53*(7), 23-26.

[3] Pfeiffer, F., Weitkamp, T., Bunk, O., & David, C. (2006). Phase retrieval and differential phase-contrast imaging with low-brilliance X-ray sources. *Nature physics*, *2*(4), 258-261.

[4] Wilkins, S. W., Gureyev, T. E., Gao, D., Pogany, A., & Stevenson, A. W. (1996). Phase-contrast imaging using polychromatic hard X-rays. *Nature*, *384*(6607), 335-338.

[5] Paganin, D., Mayo, S. C., Gureyev, T. E., Miller, P. R., & Wilkins, S. W. (2002). Simultaneous phase and amplitude extraction from a single defocused image of a homogeneous object. *Journal of microscopy*, *206*(1), 33-40.

[6] Burvall, A., Lundström, U., Takman, P. A., Larsson, D. H., & Hertz, H. M. (2011). Phase retrieval in X-ray phase-contrast imaging suitable for tomography. *Optics express*, *19*(11), 10359-10376.

[7] Mayo, S. C., Stevenson, A. W., & Wilkins, S. W. (2012). In-line phase-contrast X-ray imaging and tomography for materials science. *Materials*, *5*(5), 937-965.

[8] Bartels, M., Hernandez, V. H., Krenkel, M., Moser, T., & Salditt, T. (2013). Phase contrast tomography of the mouse cochlea at microfocus x-ray sources. *Applied Physics Letters*, *103*(8), 083703.

[9] Henke, B. L., Gullikson, E. M., & Davis, J. C. (1993). X-ray interactions: photoabsorption, scattering, transmission, and reflection at E= 50-30,000 eV, Z= 1-92. *Atomic data and nuclear data tables*, *54*(2), 181-342.

Automated processing of series of micro-CT scans

A.DE MUYNCK*[1], M.N. BOONE[1], M. DIERICK[1], I. CAMBRÉ[2], E. LOUAGIE[2], D. ELEWAUT[2], L. VAN HOOREBEKE[1]

[1] UGCT - Dept. Physics and Astronomy, Ghent University Proeftuinstraat 86/N12, B-9000 Gent, Belgium – amelie.demuynck@ugent.be
[2] Department of Rheumatology, Faculty of Medicine and Health Sciences, Ghent University, De Pintelaan 185, B-9000 Ghent, Belgium. VIB Inflammation Research Center, Ghent, Belgium
* presenting author

Keywords: micro-CT, batch scanning, automation

Abstract

For some applications of high-resolution X-ray Tomography (micro-CT) scanning, a large set of similar samples is to be analyzed in order to obtain statistically significant results. The complete process, including the micro-CT scan itself, the reconstruction and the analysis is almost identical for every sample. However, in a typical workflow every step is manually performed for every individual sample. This could be optimised by automation of this process, which results in less human intervention and thus a smaller cost and a lower risk to human error. We developed a reliable method to semi-automatically scan several stacked samples and automatically reconstruct the resulting series of data sets. The reconstruction step includes the manual reconstruction of one data set in order to optimize the reconstruction parameters, which can then be used for the rest of the batch. In future work, the automatic handling of the next step in the micro-CT workflow, 3D analysis, will also be improved.

Introduction

At the 'Centre for X-ray Tomography' of Ghent University (UGCT; www.ugct.ugent.be) a wide variety of samples is imaged at different state-of-the-art home built micro-CT systems. For some applications, a large number of similar samples need to be scanned in order to obtain statistical relevant results (Mader *et al.*, 2011). This is quite common in (bio-)medical applications, where for example specific parts of small animals are imaged. Conventionally, these samples must be properly positioned, scanned and reconstructed one by one. Given the desired resolution and the sample size, the sample has to be positioned accurately on the rotational axis, which requires human intervention due to the variation between samples. This causes a large number of delays in the scanning procedure, and makes scanning without human supervision impossible. After acquisition, the raw projection data needs to be reconstructed, yet most software packages do not allow for batch processing. The goal of this research was to limit the amount of human intervention in CT scanning and processing and to even be able to scan and process multiple samples without intervention of the operator and without the presence of an automated sample mounting system (Mader *et al.*, 2011).

Methods and results

A simple method to improve efficiency without complicated automated sample mounting is by vertical stacking. In this method, multiple samples are mounted on top of each other and subsequently scanned one by one. However, precision positioning systems mounted on the rotation stage often have no absolute positioning, hence automatic centering based on this can not be separately performed for each sample. To overcome this issue, we have developed several methods to perform the centering for

stacked objects without absolute positioning. This is easily implemented at the home built scanners at UGCT, because they are controlled by in-house developed software, which gives the opportunity to modify the acquisition schemes.

Before scanning a batch of stacked samples, the vertical position of each sample has to be specified and two reference images for each sample, separated in angle by 90°, are made. During the execution of the scanner script, the sample is moved to the correct heigth and a test image is made at the first rotational position. By comparing the test image with the reference image, the sample is moved to obtain a better agreement. This procedure continues until the test images corresponds sufficiently with the reference image. At that moment the x-position of the sample is optimised. The same methodology is done at the second angular position using the second reference image to optimize the y-positioning. If needed, this procedure can be executed iteratively in order to optimize the result.

For the comparison of the test image and the reference image, two possible techniques are investigated. The first method is based on the calculation of the centre of mass of the images, for example a horizontal strip. The method is designed to be able to adjust the horizontal position of the sample, so only the horizontal component of the centre of mass is relevant. Therefore the grey values of all the pixels within one column are summed, column by column. The centre of mass (COM) is defined as

$$COM = \frac{\sum_{columns} im_i}{\sum_{columns} m_i},$$

with i, the index of each column and m_i the mass of every column, defined as $m_i = -\ln(columnvalue_i)$. By neglecting the vertical component, the computing time is significantly reduced. Figure 1 shows the centre of mass of several normalized projection images. It is important to note that this centre of mass depends on the amount of material which is out of the field-of-view.

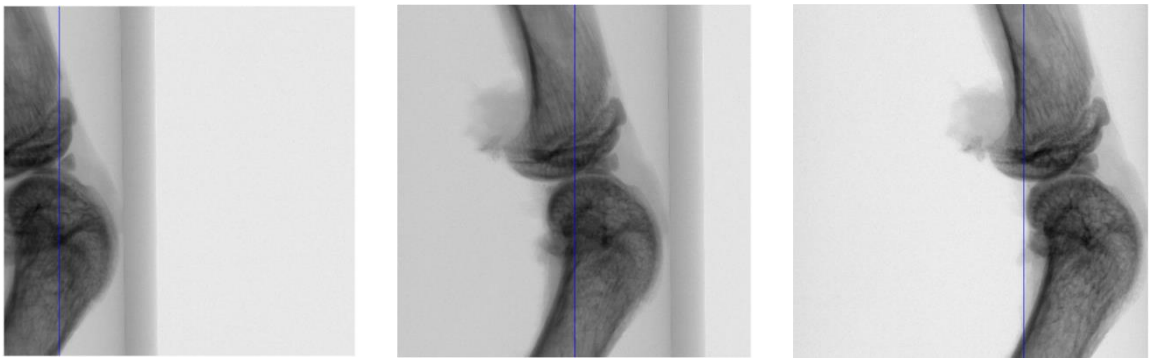

a *b* *c*

Fig. 1. *The blue line indicates the x-component of the centre of mass of normalised projection images.*

The difference between the centre of mass of the two images gives an indication of how far the sample is situated from its ideal position and whether the correction needs to be done in positive or negative direction. To speed up the correction, the distance between the centre of mass of both images is used as input to the relative movement, yet this is not necessary for the proper operation of the method. If the object under

investigation is prone to a mass being outside the field-of-view, the script foresees in an automated reduction of the geometrical magnification.

The second method is to compare the obtained image at a specific location with the reference image by summing the square of the differences (SD) between each pixelvalue. This also gives a good idea of the deviation between the two images but gives no information of the direction in which the sample has to be moved to improve the sample location. This effect is clearly shown in figure 2. Therefore, the first method is the one currently used at UGCT.

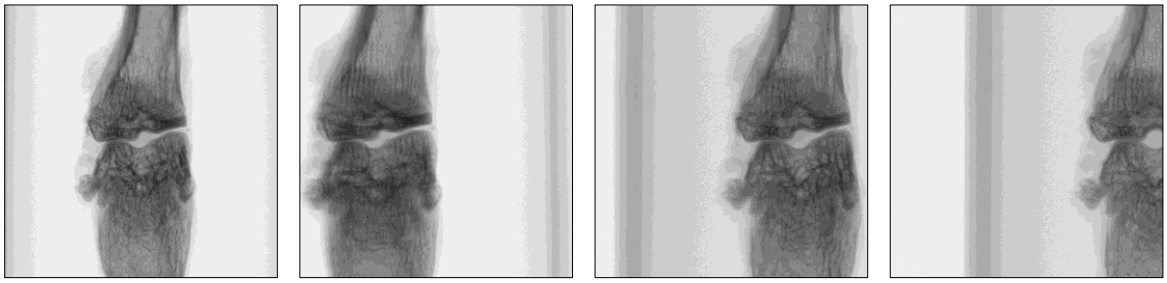

a *b* *c* *d*

Fig. 2. *Figure a is the reference image. Figures b, c & d have similar SD values, (respectively, SD = 60282, SD = 62138 and SD = 61028), but they all are located on different positions, which makes it almost impossible to use this method to adjust the sample position.*

To avoid infinitely repositioning and diverging movements, the number of steps to obtain the ideal position is limited to a user-defined number.

Another issue with a large number of similar scans is the reconstruction and analysis. Previously, ~~the~~ data ~~was~~ reconstructed per scan using Octopus Reconstruction (Inside Matters, www.octopusimaging.eu). This allowed for a high degree of optimization, but is a time-consuming and tedious method. Additionally, this is prone to human error. We used the Software Development Kit (SDK) of Octopus Reconstruction to develop a framework to automate this process. This framework allows for setting the optimization parameters determined using the Octopus Reconstruction Grapical User Interface (GUI), hence the reconstruction quality can remain similar. The GUI of the batch reconstruction tool is shown in figure 3. The reconstruction of the first scan needs to be done manually. The parameters used for the first reconstruction, such as tilt, skew and beam hardening correction, are the input parameters for every following sample.

For future research, the automation of the analysis of the scans will be investigated. This will drastically reduce the human time spent on 3D analysis, and reduce the operator dependency in repeated studies.

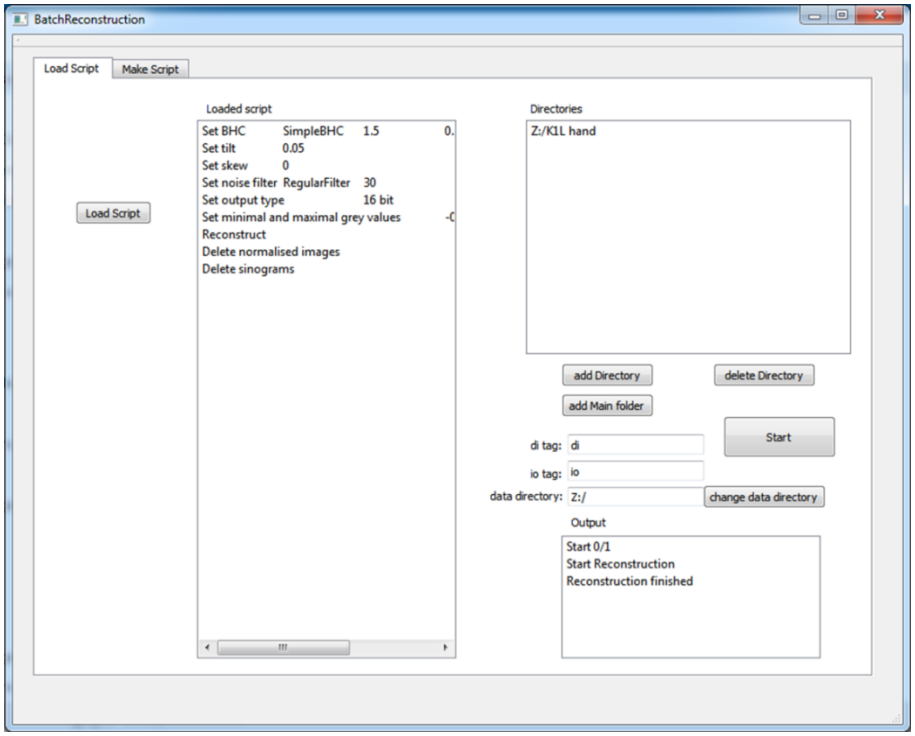

Fig. 3. *Gui of the batch reconstruction tool*

Conclusion

A part of the complete scanning process of a large set of similar samples has been semi-automated. Multiple samples are vertically stacked and sequentially properly positioned and scanned. The amount of samples that can be scanned during one run is limited by the available vertical stacking space. Next to the scanning itself, the reconstruction has also been semi-automated. The first dataset of a batch is manually reconstructed and the obtained parameters are used for the automatic reconstruction of the remaining data sets.

Acknowledgements

The Special Research Fund (BOF) of the Ghent University is acknowledged for the post-doctoral grant of M.N. Boone. I. Cambré is supported by the SBO-programme of the agency for Innovation by Science and Technology in Flanders (IWT). E. Louagie is supported by the Interuniversity Attraction Poles Programme of the Belgian Science Policy Office (IAP project DevRepair). D. Elewaut is a member of a multidisciplinary platform group (MRP-GROUPID) from Ghent University.

References

Mader, K., Marone, F., Hintermüller, C., Mikuljan, G., Isenegger, A., & Stampanoni, M. (2011). High-throughput full-automatic synchrotron-based tomographic microscopy. **Synchrotron Radiation**, 18(2), 117-124.

Evaluation of the absorbed dose in X-ray microtomography

A.DE MUYNCK*[1], S.BONTE[1], J.DHAENE[1], M. DIERICK[1], K. BACHER[2], L. VAN HOOREBEKE[1]

[1] UGCT – Dept. Physics and Astronomy, Ghent University, Proeftuinstraat 86/N12, B-9000 Gent, Belgium – amelie.demuynck@ugent.be
[2] Department of Basic Medical Sciences, Division of Medical Physics-Gent, Ghent University, Ghent, Belgium
* presenting author

Keywords: micro-CT, absorbed dose

Abstract

It is widely known that a sample receives a radiation absorbed dose during a CT-scan. Although this can have unwanted effects on the sample such as discolouration, little can be found in literature about the absorbed dose in micro-CT applications (except for small animal micro-CT). This research aims to validate the accuracy of dose simulations to be able to predict the dose before scanning the sample. Both Monte Carlo simulations with BEAMnrc and simulations with the in-house developed Setup Optimizer are compared with measurements with an ionisation chamber. The simulations nearly always underestimate the experimental values with a maximal deviation of 40%. In contrast the dose reduction after a layer of material obtained with the simulation programmes is relatively accurate.

Introduction

A drawback of X-ray imaging is the deposition of a radiation absorbed dose in the object being imaged. For medical applications, it is important to quantify this dose, because it can be harmful to the patients' health. In comparison to medical scans, micro-CT scans have a much higher resolution, which typically gives rise to a higher dose in the scanned object. Next to a higher resolution, micro-CT scanners have more degrees of freedom than medical CT scanners. In medical CT, the scan geometry is nearly always the same. The patient is placed between an X-ray source and a detector, which rotate simultaneously around the patient. The typical degrees of freedom are the tube voltage, tube power, collimation and filtration. In most micro-CT applications, the sample rotates between the source and detector. In modern systems, both the source to object distance (SOD) and source to detector distance (SDD) can be varied independently and are additional degrees of freedom, as well as the scan time, the type of source and the type of detector. Furthermore, micro-CT can be used in a large number of research domains, and the objects under investigation can vary strongly in size and composition. Both the extra degrees of freedom and the variety of samples make standardized dosimetry tests very difficult to define and perform.

Due to the differences between micro-CT and medical CT, the standardized dosimetry calculations and measurements of medical applications cannot be applied in micro-CT scans. For practically all micro-CT scan applications (except for small animal micro-CT scanners) very little information is available in literature about dose deposition in the samples. Sometimes, for non-living samples such as metal objects, the dose is less important, because the limited dose involved in laboratory-based micro-CT will not affect the sample. However, some samples are radiation sensitive, such as minerals of which the colour can change due to radiation or plants which need to be examined several times during growth. Although the plants do not die, they can stop growing after

a single scan (Dhondt et al, 2010). These two examples prove that it can be important to know the exact dose (or at least an estimate) that the sample under investigation will obtain during the total scan time.

The aim of this study is to examine the absorbed dose in lab-based micro-CT. This research is performed at HECTOR (Masschaele et al., 2013), one of the scanners at the 'Centre for X-ray Tomography' of Ghent University (UGCT; www.ugct.ugent.be), which is a research facility specialised in high resolution X-ray computed tomography, where several home built modular micro- and nano-CT scanners are in use.

Materials & methods

In this research we have evaluated different absorbed dose simulation techniques by comparing them with experimental data. First, measurements in air were performed. Second, a bar of PMMA (a kind of transparant plastic, Fig.1a) was irradiated, while the absorbed dose was measured by placing the ionisation chamber in the drilled holes in the bar. The dose was measured using an ionisation chamber during different scan protocols. The used ionisation chamber (Fig. 1b) is a device of Capintec, with an aluminum central wire and air equivalent plastic wall. These measurements are compared with two different simulations: Monte Carlo simulations with BEAMnrc (www.nrc-cnrc.gc.ca/eng/solutions/advisory/beamindex.html) and simulations with the in-house developed Set-up Optimizer. This programme is based on the law of Lambert-Beer to determine the total attenuation through slabs (Dhaene et al, 2015).

a b

Fig. 1. *Used bar of PMMA (a) and ionisation chamber (b).*

For both measurements, in air and in PMMA, the source object distance was 200 mm. The bar was positioned in such a way that the active volume of the ionisation chamber was fixed at 200 mm of the focal spot of the X-ray source. No beam filter was used and the target current was 700 µA. The tube high voltage was varied between 20 and 240 keV. The Monte Carlo simulations were performed with a phantom representing the ionisation chamber as good as possible. The phantom is shown in Fig.2.

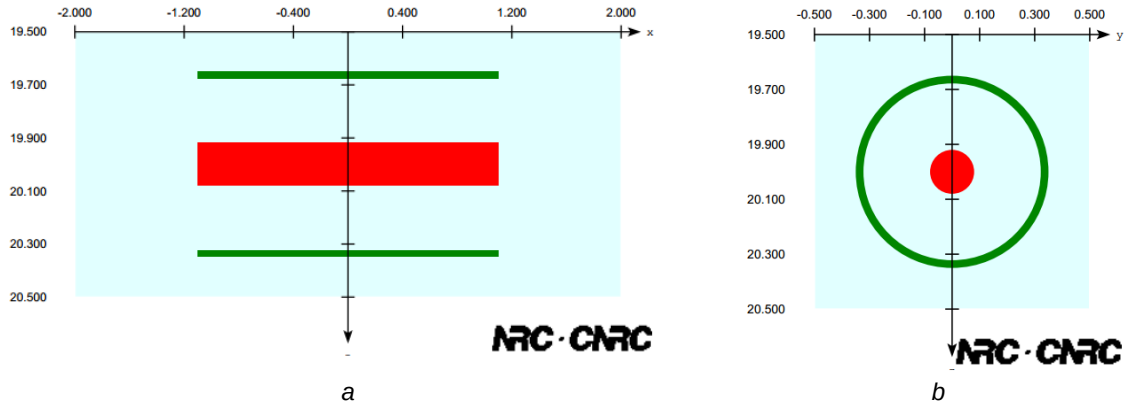

a b

Fig. 2. *The xz-view (a) and the yz-view (b) of the phantom used in BEAMnrc. Colour scheme: red = aluminum, green = air-equivalent plastic, blue = air.*

Results

The resulting absorbed dose in air as a function of tube voltage is shown in Fig.3a. The Monte Carlo simulations yield an underestimation of the actual dose with a maximum deviation of 40%. The second set of measurements is performed at a depth of 10mm in the bar of PMMA. There is a good agreement between the measurements and simulations at low energies. In contrast, for high voltages the deviation rises to 37%.

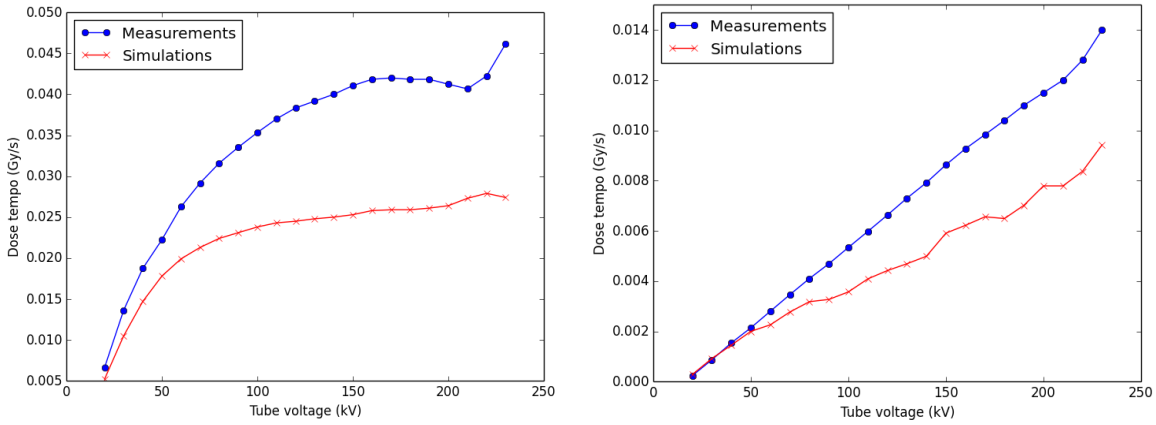

a b

Fig. 3. *The measurements and simulations of the absorbed dose in air (a) and after 10 mm PMMA (b)*

Next to the absorbed dose, also the dose reduction after traversing a slab of material can be calculated. Beside measurements and Monte Carlo simulations with BEAMnrc, two other methods are tested. The two additional methods are based on the Setup Optimizer, which is a programme developed at UGCT to calculate the beam attenuation in multiple layers of different materials. The first method is to compare the transmission of photons with and without a slab of PMMA. If 85% of the photons reaches the air sample if no PMMA is present and 40% reaches the air sample if 10mm PMMA is present, the dose reduction would roughly be 0.40/0.85 = 47% in case of a monochromatic beam. This method seems to be a too rough estimation to calculate dose reductions (Fig. 4) because we are dealing with a polychromatic beam. The other method takes into acount that the energy of the spectrum changes while traversing a sample. From the incoming and outgoing spectrum calculated by the setup optimizer the absorbed part of the spectrum can be calculated, which can be divided in a Compton-scattered part, a Rayleigh-scattered part and a photo-electric absorbed part. The

absorbed dose is then due to all the photo-electrically absorbed photons and a part of the Compton scattered photons, depending on their energy. The fraction by which they contribute is a linear function of the energy. This is 1 for a photon of 0 keV and 0.4 for a photon energy of 240 keV. These values are chosen to match the experimental data and are logical. Low-energy photons are completely absorbed, while most high-energetic photons are able to leave the sample, even after scattering. The Rayleigh-scattered photons do not contribute to the dose, because they are mostly leaving the sample. Although the agreement between measurement and simulation is not sufficiently accurate to predict the absorbed dose, the dose reduction in PMMA in respect to the air is relatively good. This is clearly illustrated in Fig.4.

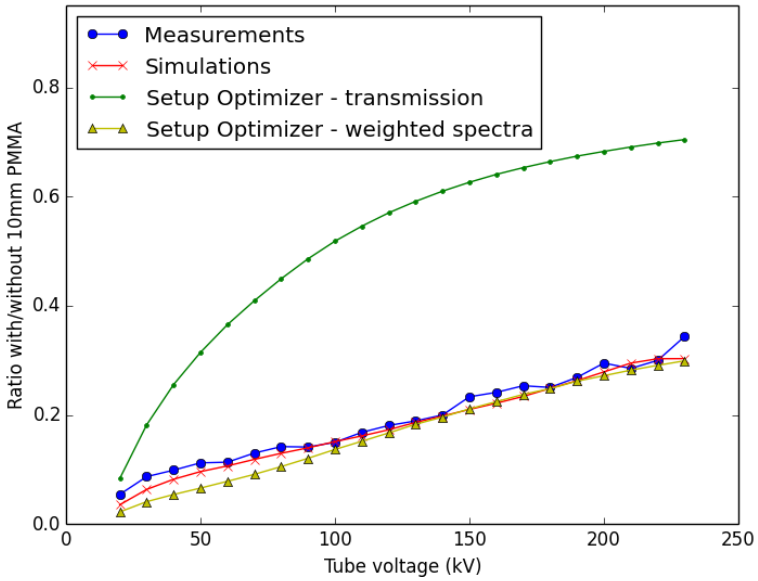

Fig. 4. *Dose rate reduction after 10 mm PMMA: 4 different methods*

Conclusion

At this moment the accuracy for fast absorbed dose estimation prior to scanning is not yet good but sufficient if only absorbed dose estimations are necessary. However, the dose reduction after traversing a slab can be more correctly estimated. Combining the dose reduction with an experimentally obtained standardized table of the absorbed dose in air at different distances with different tube settings, could result in a good dose estimation.

Acknowledgements

We acknowledge the Agency for Innovation by Science and Technology in Flanders (IWT, SBO project 120033 "TomFood") and the Research Foundation-Flanders (FWO-project 3G.0426.13) for financial support.

References

Dhaene, J., Pauwels, E., De Schryver, T., De Muynck, A., Dierick, M., & Van Hoorebeke, L. (2015). A realistic projection simulator for laboratory based X-ray micro-CT. **NUCLEAR INSTRUMENTS & METHODS IN PHYSICS RESEARCH SECTION B-BEAM INTERACTIONS WITH MATERIALS AND ATOMS, 342**, 170–178.

Dhondt, S., Vanhaeren, H., Van Loo, D., Cnudde, V., & Inzé, D. (2010). Plant structure visualization by high-resolution X-ray computed tomography. **TRENDS IN PLANT SCIENCE**, 15(8), 419–422.

Masschaele, B., Dierick, M., Van Loo, D., Boone, M., Brabant, L., Pauwels, E., Cnudde, V., et al. (2013). HECTOR: a 240kV micro-CT setup optimized for research. **Journal of Physics Conference Series (Vol. 463)**. Presented at the 11th International conference on X-ray Microscopy, Bristol, UK: IOP.

Application of Micro-CT to Material Characterization for Industrial R&D using a very versatile tomography system

A. SINGHAL[1]

[1] General Electric Global Research Center, One Research Circle, Niskayuna, NY – singhal@ge.com
* presenting author

Keywords: microfocus, nanofocus, crack, oil sands, pore size distribution

Abstract

This work shows how high-resolution x-ray tomography is being used for materials characterization at GE Global Research, by showing examples of several materials which are of interest to GE. The information obtained from CT images is used both as a qualitative and quantitative method to understand material behavior and fine tune material processing steps. The tomography system used here is the vtomex M300 micro/nano-CT (GE Sensing and Inspection Technologies), which has a 300kVp micro-focus source and a 180kVp nano-focus source. The dual tube configuration makes this is a very verstalie system, and provides spatial resolution ranging from sub-micron level to about 150μm, allowing a wide variety of material systems, and parts of various sizes to be imaged.

Introduction

Micro-computed X-ray tomography has gained increasing importance in the field of 3D materials characterization and inspection because of its non-destructive nature. The CT data is used to generate 3D imagery of the internal structure of the material, which would otherwise be obtained only destructively. State-of-the-art laboratory-based Micro-CT X-ray tube-based systems, although suffering from some limitations, are now at par with synchrotron-based tomography. The measurement speed and quality of the data obtained has resulted in this technique being widely used in the vast area of materials science.

Methods

The tomography system primarily used for the described work is the vtomex M300 micro/nano-CT made by GE Sensing and Inspection Technologies. It has a 300kVp micro-focus source and a 180kVp nano-focus source. The dual dual tube configuration makes this a very versatile system, and provides spatial resolution ranging from sub-micron level to 150µm, allowing a wide variety of material systems, and parts of various sizes to be imaged. The data reconstruction is done using a filtered back-projection method, by GE's proprietary software Datos™. Data visualization and analysis is done by a combination of the softwares Volume Graphics and Avizo Fire.

Results & Discussion

Nickel-base superalloys will be discussed as the first application. Figure 1 shows a fractured cylindrical bar of a single-crystal Ni-base superalloy for gas turbine blade applications. The cylindrical specimen with a gage diameter of 5 mm was subjected to fatigue testing, with loading along the long-axis of the cylinder at elevated temperature until failure. The goal of this CT inspection was to determine the size, shape, and distribution of cracks within the gage section of the sample. The microfocus tube of the X-ray system was used to image the test specimens at a 11 μm spatial resolution. Figure 1c & 1d shows CT slices along the longitudinal and transverse cross-sections of the

sample. The crackd shown in Figure 1c & 1d is one of the largest cracks found in the sample, and spans a large circumferential length. Figure 1b also shows a large number of smaller circumferential surface cracks. The micro-CT images show a bright outer band due to the beam hardening artifact. These artifacts cause problems in determining a universal threshold for segmenting the cracks; therefore only a selected few cracks were segmented manually and shown in the volume rendering of the scanned object showin in Figure 2. The shape of the crack can be clearly seen as a typical thumbnail shape; the crack tipa advances in a direction perpendicular to the applied axial tensile stress. The complete morphology of the crack is difficicult to obtain by traditional metallography techniques because of ambiguity in the location of the cut sections with respect to the deepest part of the cracks.

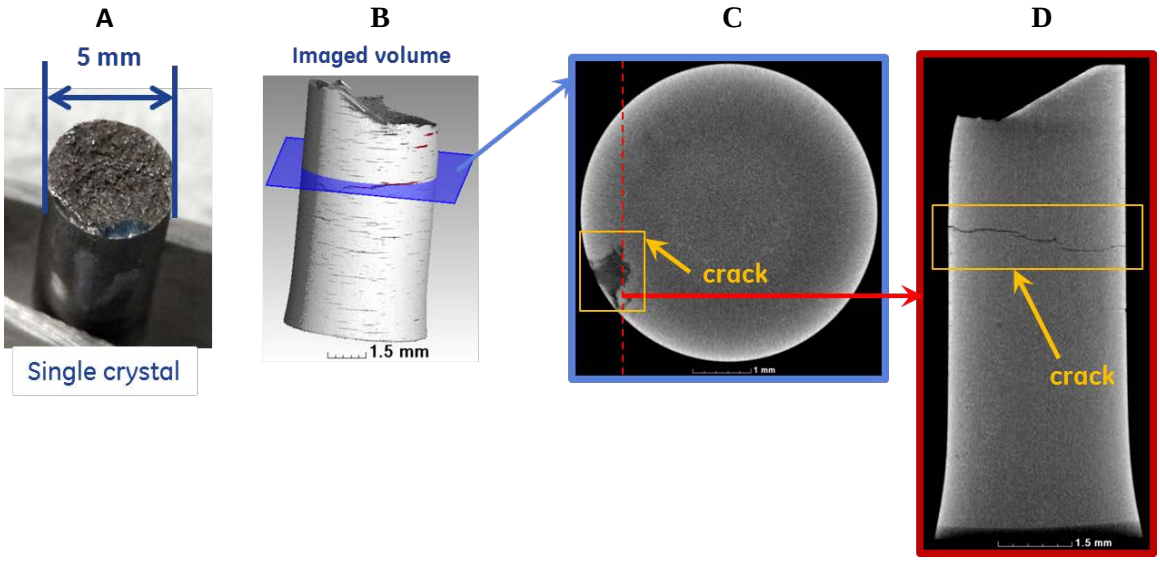

Figure 1 : *Orthogonal micro-CT images of the large crack observed in the specimen.*

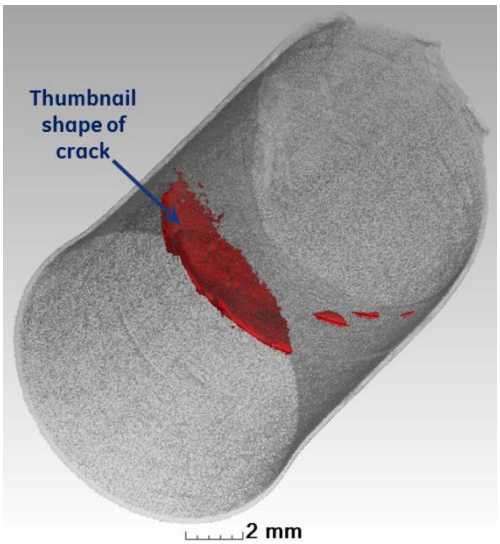

Figure 2 : *3D volume rendering of the large crack in the specimen. The subtrate material has been rendered transparent to allow visualization of the crack.*

The specimens imaged using the lab micro-CT were also imaged at ESRF beamline ID-19 at a spatial reslution of 1.8µm. Figure 3 shows a comparison of the images taken at the same location from the two techniques. There is no beam hardening in the

synchrotron micro-CT images, and the details of the crack morphology are more clearly visible in the higher resolution images. A comparison of crack depths measured from the two sets of images shows that on an average, the synchrotron micro-CT measurements are greater by 11 μm than the lab micro-CT measurements, which is equal to the spatial resolution in the lab images. Although the lab micro-CT does not capture the crack tip very well at this resolution, this is a great easy-to-access tool overall for locating the cracks in the sammples.

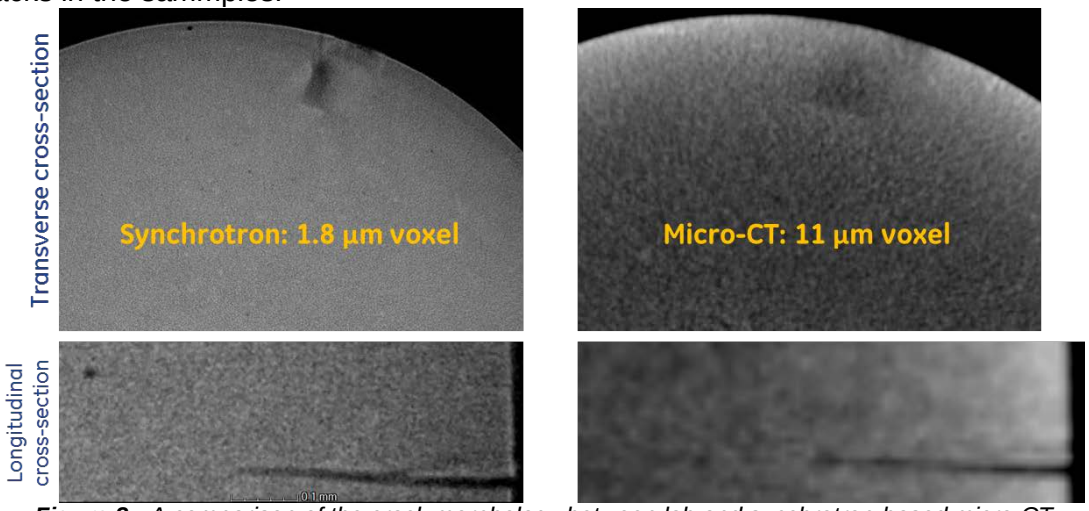

Figure 3 : *A comparison of the crack morphology between lab and synchrotron-based micro-CT*

The next application described below is the imaging of Oil Sands Tailings, specifically Mature Fine Tailings (MFT). Tailings are generated as waste in the oil sands extraction processes used in mining operations. Tailings consist of natural minerals, clay, residual bitumen and water. Tailings reduction operations, currently underway at Suncor Energy Inc., include methods to speed up the transition of large ponds, where tailings are stored, into a reclamable landscape. The nanofocus tube of the vtomex M 300 was used to study the microstructural evolution of tailings for various mixing parameters during the addition of a flocculant. A unique feature of this system is that the X-ray detector of this system translates horizontally on rails, thus doubling its field of view. This enables the imaging of wide objects at high magnification. A novel method of imaging these specimens was developed whereby liquid specimens were imaged in a frozen state using a CT cooling stage, as shown in Figure 4. A high resolution of 5 μm was achieved for these specimens.

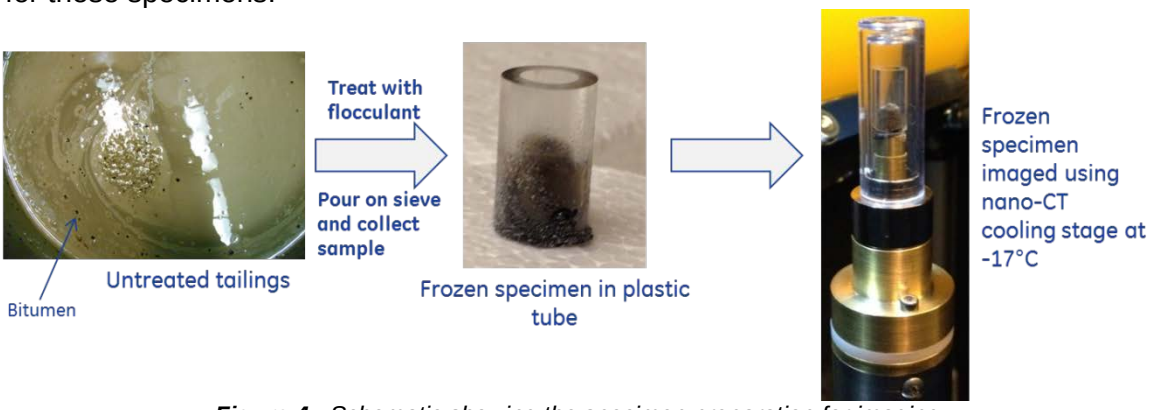

Figure 4 : *Schematic showing the specimen preparation for imaging.*

The flocculation of MFT is very sensitive to the dose of flocculant and the shear time. The micro-CT images were analyzed using Avizo Fire, to calculate the porosity and pore size distribution in the tailings treated at various conditions. At each condition, samples were obtained after various drying times, frozen and imaged. The results of optimal dose with over-shear are shown in Figure 5. The volume fraction analysis showed that the mean pore size decreased with drying of the sample. This is also observed visually in the micro-CT inset images in Figure 5. This was further confirmed by the pore size distribution which showed that the number of small pores increased with drying of samples.

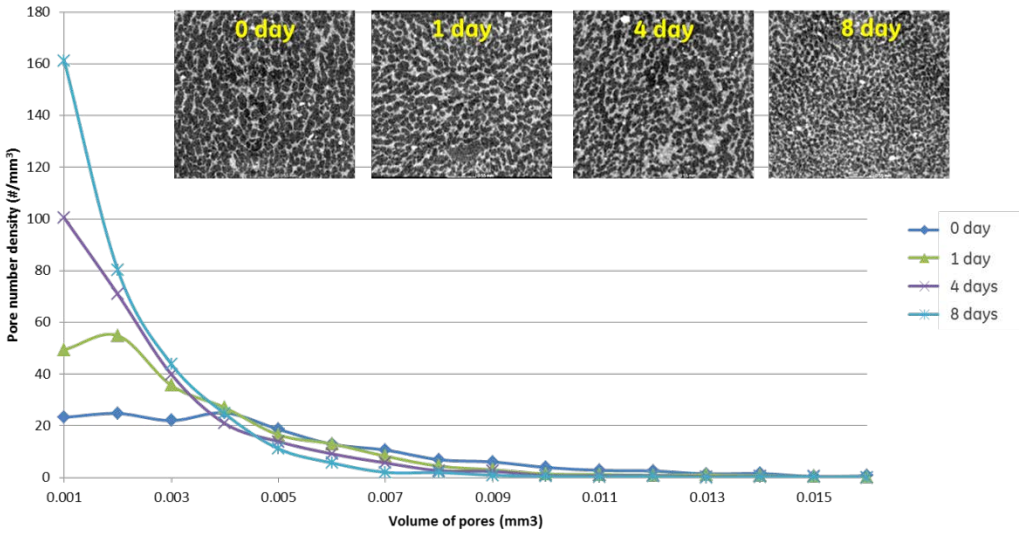

Figure 5: *Plot of pore sizes at optimal flocculant dose and over-shear. The inserts at the top show the micro-CT images at different drying times.*

Such analysis was useful in providing fundamental understanding of the drying processes in these materials and dosing effect of the flocculant, by comparing results from various treatments to MFT. The method developed to image this material can also be applied to imaging of other materials which have similar fluid consistency.

The final example is that of a carbon-epoxy composite test part for an aerospace application. The complex geometry of the part can be seen from the volume rendering of the test piece in Figure 6a. The ability of CT to virtually slice the sample in any direction and at any angle proves very advantageous here because it allows the part to be inspected in a plane tangential to the curved sections. The measured angles between the +45° and -45° plies are shown for sections at locations 1-5 shown in Figure 6b. The variation in measured angles suggests that as the plies are formed to their final shape, the resin allows sliding between and within them. Incomplete consolidation of the plies is evident at location 4 in Figure 6b. This can also be seen in other cross-sections shown in Figures 6e (near the bottom) and 6g (near the top) as gaps between the layers. Such information is valuable for optimizing the temperature and pressure conditions for consolidation of the plies in the composite.

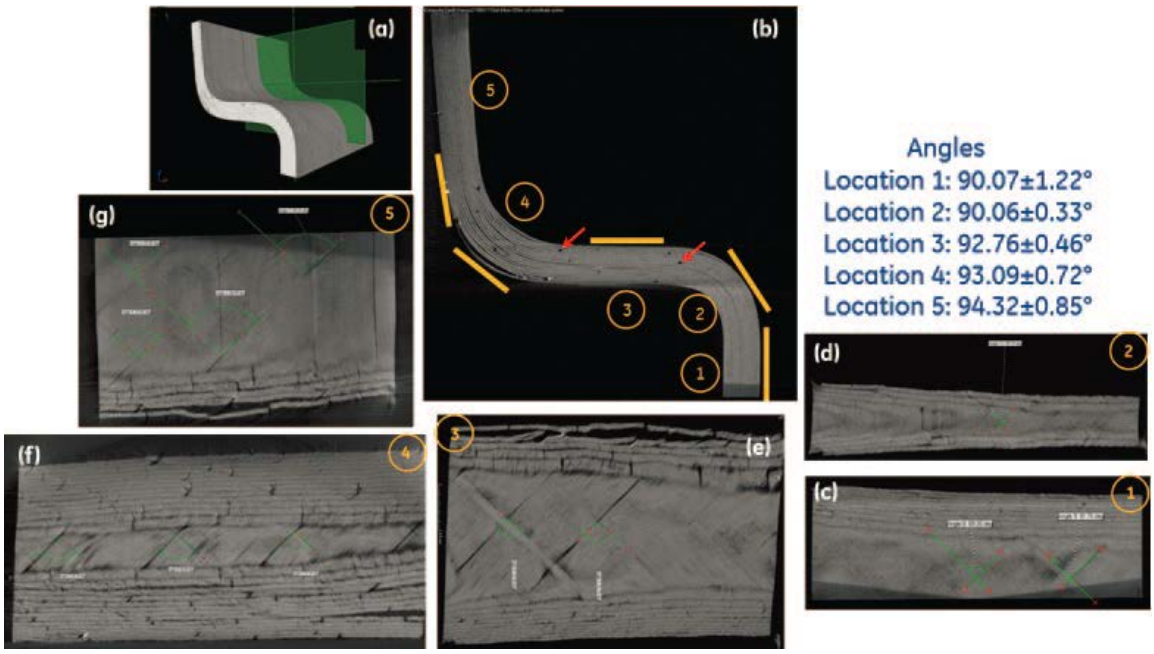

Figure 6 : *(a) Overall 3D view test part. (b) CT slice of the test piece for one orthogonal view indicated by the green plane in (a). The solid yellow lines indicate the orientation of the CT slices going into the plane, with respect to the sample geometry. (c)-(g) show the different locations (1-5 indicated in (b)) where the angle between the 45° plies was measured.*

Session 103

Laser interactive 3D computer graphics

J.-B. BELLET*[1], I. BERECHET[2], S. BERECHET[2], G. BERGINC[3], G. RIGAUD[1]

[1] Université de Lorraine, Institut Elie Cartan de Lorraine, UMR 7502, Ile du Saulcy, 57045 Metz Cedex 1, France, jean-baptiste.bellet@univ-lorraine.fr, rigaud@num.uni-sb.de

[2] Société SISPIA, 18, Allée Henri Dunant, 94300 Vincennes, France, ion.berechet@sispia.fr, stefan.berechet@sispia.fr

[3] Thales Optronique, 2, Avenue Gay Lussac CS 90502, 78995 Élancourt Cedex, France, gerard.berginc@fr.thalesgroup.com

* presenting author

Keywords Reflective tomography, 3D laser imaging, real-time 3D visualization

Introduction

A non-conventional three-dimensional optical imaging technique with laser system or LADAR (LAser Detection And Ranging) has emerged [Berginc and Jouffroy, 2009a, Berginc and Jouffroy, 2009b, Berginc and Jouffroy, 2010, Berginc and Jouffroy, 2011, Berginc, 2014]. A scene is illuminated by a laser source, in the visible or near-infrared band (500-2200 nm). At the same time, a high pixel density detector collects the backscattered radiation. Such a record provides a high-resolution image with a large dynamic range, and can be obtained in various experimental conditions: day, night, sun, fog,... Even better, combining a set of laser images provides a 3D reconstruction of the scene with ability to detect and recognize occluded objects. Such a laser system could be applied in many areas, such as surveillance or robotic vision. New scientific and industrial challenges have arisen from laser imagery, including the need of mathematical algorithms and dedicated visualization tools.

Concerning the algorithm, Computerized Tomography has been extended to 3D laser imaging in [Berginc and Jouffroy, 2009b]: the FDK algorithm maps a set of 2D laser images to a 3D volume which represents the scene. Numerical results show that the highest values in such a computed volume are features from the scene. Let us illustrate this method by the means of real laser images of a complex scene: car under branches (courtesy of Thales). The scanning provides a laser sinogram of the scene over 180 degrees: see Figure 1. It contains 181 laser images of size 342×421. Some images of the sequence are depicted on Figure 2. Orthogonal slices of the resulting FDK volume are represented in Figure 3.

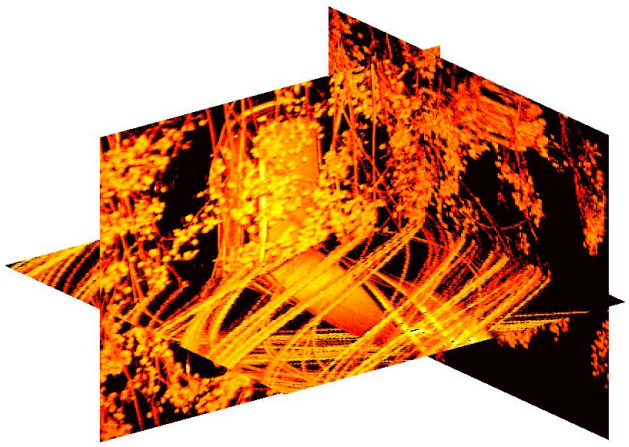

Figure 1: Slices through a real laser sinogram.

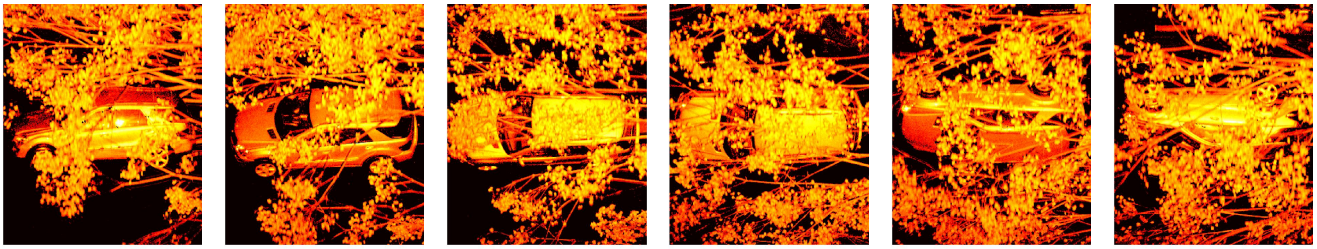

Figure 2: A few laser images of the sequence : 20, 50, 80, 110, 140, 170 degrees.

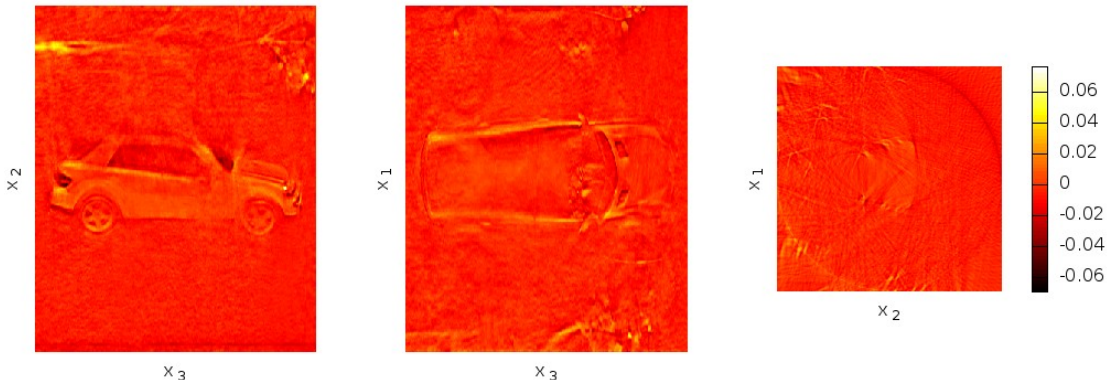

Figure 3: Slices through the computed laser FDK volume.

This paper tackles two issues in laser imaging. The first one concerns an upstream mathematical question. We provide some link between transmission tomography and reflective tomography [Knight et al., 1989] on a canonical case. It reinforces the credibility of transmission algorithms in reflective imaging. The second one concerns a downstream visualization issue. The Maximum Intensity Projection (MIP) [Wallis and Miller, 1991] is shown to be well suited; the FDK algorithm and the MIP are combined in a home-made software whose functionnalities include real-time displacements in the virtualized scene. The relevancy of this approach is shown on the considered laser imagery example.

From transmission to reflection

Laser imaging using the FDK algorithm introduces a mathematical upstream challenge. Filtered BackProjections (FBP), such as the FDK algorithm, are designed to invert Radon-kind transforms from transmission tomography. Since laser measurements result mainly from backscattering by opaque surfaces, laser imaging extends the validity of FBP from transmission to reflection. Is there a mathematical proof? One of the first papers about the use of transmission algorithms for reflective data is [Knight et al., 1989]; in particular the authors notice that the sum of data from opposite angles yields transmission kind data. This idea has been used later in [Jin et al., 2011] to design a method which is based on this sum. In this paper we use Radon inversion without using explicitely this sum. We prove here that without any pre-processing, FBP of reflective data coincides exactly with FBP of the built transmission data, and thus the FBP already contains the building of transmission-kind data.

So we assume that for each angle β, for each $s \in \mathbb{R}$, we know reflective data $R(\beta,s)$ on the line $L(\beta,s)$: $x \cdot \theta(\beta) = s$, with $\theta(\beta) = (\cos\beta, \sin\beta)$. Of course, R is 2π-periodic in β. Reflective data on the opposite side is $R(\beta+\pi,-s)$, on $L(\beta,s) = L(\beta+\pi,-s) : x \cdot \theta(\beta+\pi) = -s$. Then we define the sum $T(\beta,s) = R(\beta,s) + R(\beta+\pi,-s)$. For a convex object, $T(\beta,s)$ looks like transmission data wich are generated by the boundary of the object: see Figure 4.

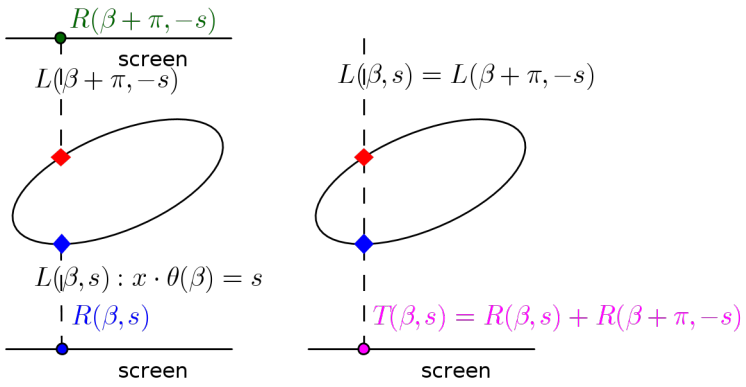

Figure 4: Transmision data $T(\beta,s)$ deduced from reflection data $R(\beta,s)$.

Definition. Let $v(s)$ be an even filter and $f(\beta,s)$ be a 2π-periodic function in β. The FBP (over 360 degrees) of f is:

$$\mathscr{R}^*[v\star f](x)=\int_0^{2\pi}\int_{\mathbb{R}} v(x\cdot\theta-t)f(\beta,t)\mathrm{d}t\mathrm{d}\beta.$$

Theorem. The FBP of the transmission-kind data T is twice the FBP of the reflection data R:

$$\mathscr{R}^*[v\star T(\beta,s)]=2\mathscr{R}^*[v\star R(\beta,s)].$$

Proof. The proof relies on basical properties of the integral. By linearity, FBP of T is $\mathscr{R}^*[v\star T(\beta,s)]=\mathscr{R}^*[v\star R(\beta,s)]+\mathscr{R}^*[v\star R(\beta+\pi,-s)]$. FBP of $R(\beta,s)$ is by definition $\mathscr{R}^*[v\star R](x)=\int_0^{2\pi}\int_{\mathbb{R}} v(x\cdot\theta-t)R(\beta,t)\mathrm{d}t\mathrm{d}\beta$ and FBP of $R(\beta+\pi,-s)$ is $\mathscr{R}^*[v\star R(\beta+\pi,-s)](x)=\int_0^{2\pi}\int_{\mathbb{R}} v(x\cdot\theta-t)R(\beta+\pi,-t)\mathrm{d}t\mathrm{d}\beta$. The change of variable $(\beta,t)\leftarrow(\beta+\pi,-t)$ yields $\mathscr{R}^*[v\star R(\beta+\pi,-s)](x)=\int_\pi^{3\pi}\int_{\mathbb{R}} v(-x\cdot\theta+t)R(\beta,t)\mathrm{d}t\mathrm{d}\beta$. But the integrand is 2π-periodic and v is even so $\mathscr{R}^*[v\star R(\beta+\pi,-s)](x)=\int_0^{2\pi}\int_{\mathbb{R}} v(x\cdot\theta-t)R(\beta,t)\mathrm{d}t\mathrm{d}\beta$. □

Corollary. The FBP (over 360 degrees) of the reflection data is exactly the FBP over 180 degrees of the transmission-kind data:

$$\mathscr{R}^*[v\star R(\beta,s)]=\int_0^{\pi}\int_{\mathbb{R}} v(x\cdot\theta-t)T(\beta,t)\mathrm{d}t\mathrm{d}\beta.$$

Proof. It comes from the fact that T satisfies: $T(\beta,s)=T(\beta+\pi,-s)$, and so its FBP between 0 and π is equal to its FBP between π and 2π. □

This elementary result gives a partial answer to the mathematical question: applying FBP on reflective data generated by an opaque convex object looks like applying FBP on transmission data which are generated by the surface of the object. As a result, reflective FBP tends to reconstruct a function which is supported by this surface. More general extensions such as FBP for several arbitrary occluded objects are still under study.

From 2D laser images to interactive 3D computer graphics

A sequence of 2D laser images is fastly converted into a 3D volume. The FDK algorithm has indeed been implemented in CUDA C to be executed on a GPU. Using one Nvidia Tesla C2075 for the considered example, the current version of the code computes the weighted filtering by cuFFT in 0.4 second and computes the massively parallelized backprojection in 3.6 seconds. The result is a laser FDK volume which is stored on the GPU.

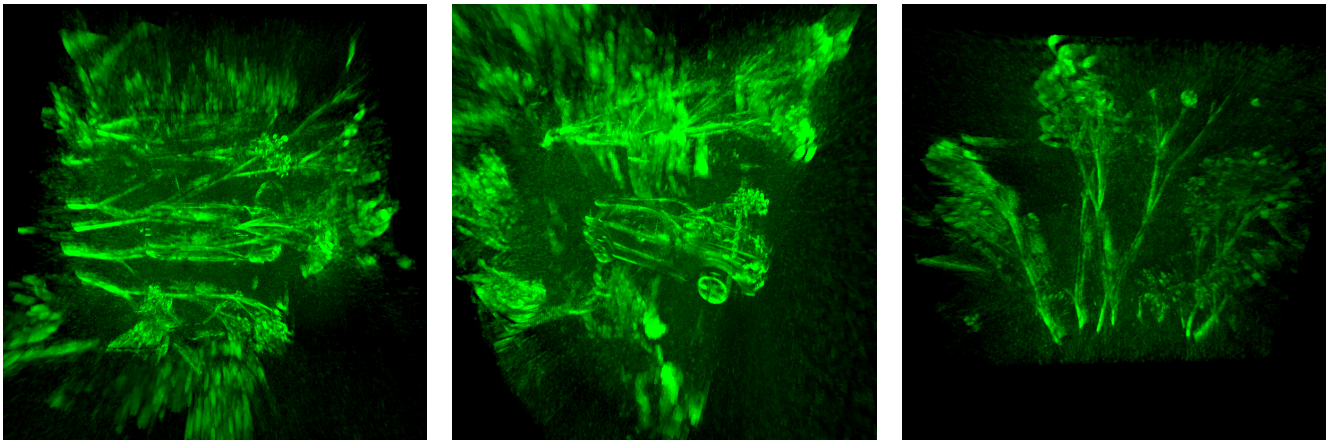

Figure 5: MIP through the laser FDK volume: full scene and interactively extracted branches.

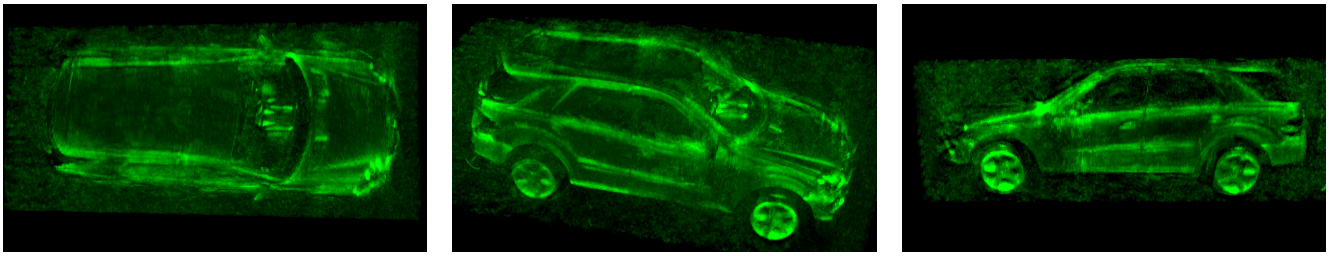

Figure 6: MIP of interactively extracted sub-volumes.

The next step of the process deals with visualization of a laser FDK volume. Several ways will be investigated [Wallis and Miller, 1991]. The easiest one is slicing the volume as above (Figure 3). But it is difficult to appreciate structures in that way. The second way is surface rendering. This has already been done in [Berechet and Berginc, 2011, Berechet et al., 2013], where extraction of incomplete surfaces by thresholding is combined with a completion algorithm. Another way that needs to be investigated is volume rendering, which consists in projecting the volume into a plane, along a set of rays. We have mentionned before that the voxels of interest in a laser FDK volume are the most intense ones. So we choose in this paper to focus on the Maximum Intensity Projection (MIP) which takes advantage of this fact [Wallis and Miller, 1991]: it selects the most intense voxel along each ray of projection. MIP has numerous advantages. It is fast and efficient. It provides high contrasted images. Its easiest version is free of parameters, which is very comfortable to get automatic visualization. Some easy improvements are available: thresholding can delete unexpected voxels, an attenuation coefficient can improve the perception of distance; also the first local maximum above a threshold can be used instead of the maximum to increase spatial localities [Sato et al., 1998].

In this paper we propose to use the MIP as the visual field of a virtual observer (or the field of view of a camera). A MIP view is computed directly on the GPU, in real time. Then it is displayed on the computer screen using OpenGL. Changing the set of rays provides several points of view. Using the GLUT library to manage interactions with mouse/keyboard, we get at the end a software that enables to move as a virtual observer inside the laser FDK scene. Displacements are managed by the mouse, whereas some other parameters such as attenuation coefficient are managed by the keyboard. Last but not least, every thing works in real time.

Two different views of the whole scene using MIP have been represented on Figure 5. Another interesting point is interactive extraction of zones of interest. This is another option of the software; it is useful for object identification [Berechet et al., 2014]. Here it is used to get separate views of the car and the branches: see views of Figure 6 for the car and Figure 5 (on the right) for some branches and foliage. High contrasted images of the objects are observed; they include features and details.

Conclusion

This paper starts with a short mathematical consideration that reinforces the extension of Computerized Tomography to reflective imaging, including 3D laser imaging. The second part combines on a GPU the laser FDK algorithm with an interactive 3D computer graphics approach which is based on the MIP. The quality of the real-time results demonstrates the power of this laser FDK-MIP approach.

Ackowledgements This work has been partially supported by the *DatDriv3D+* project, which is sponsored by the French Ministry of Economy: Directorate General of Competitiveness, Industry and Services; this project is part of program RAPID implemented by French Directorate General of Armament.

References

[Berginc and Jouffroy, 2009a] Berginc, G. and Jouffroy, M. (2009a). Optronic system and method dedicated to identification for formulating three-dimensional images. US patent 20110254924 A1, European patent 2333481 A1, FR 09 05720 B1.

[Berginc and Jouffroy, 2009b] Berginc, G. and Jouffroy, M. (2009b). Simulation of 3D laser systems. In *Geoscience and Remote Sensing Symposium, 2009 IEEE International, IGARSS 2009*, volume 2, pages 440–444. IEEE.

[Berginc and Jouffroy, 2010] Berginc, G. and Jouffroy, M. (2010). Simulation of 3D laser imaging. *PIERS Online*, 6(5):415–419.

[Berginc and Jouffroy, 2011] Berginc, G. and Jouffroy, M. (2011). 3D laser imaging. *PIERS Online*, 7(5):411–415.

[Berginc, 2014] Berginc, G. (2014). Scattering models for range profiling and 2D-3D laser imagery. In Hanssen, L. M., editor, *Reflection, Scattering, and Diffraction from Surfaces IV, 92050K*, volume 9205 of *Proc. of SPIE*.

[Knight et al., 1989] Knight, F., Kulkarni, S., Marino, R., and Parker, J. (1989). Tomographic Techniques Applied to Laser Radar Reflective Measurements. *Lincoln Laboratory Journal*, 2(2).

[Wallis and Miller, 1991] Wallis, J. and Miller, T. (1991). Three-Dimensionnal Display in Nuclear Medicine and Radiology. *The Journal of Nuclear Medicine*.

[Jin et al., 2011] Jin, X., Sun, J., Yan, Y., Zhou, Y., and Liu, L. (2011). Modified Radon-Fourier transform for reflective tomography laser radar imaging. International Symposium on Photoelectronic Detection and Imaging, *Proc. of SPIE*, 8192.

[Berechet and Berginc, 2011] Berechet, I. and Berginc, G. (2011). Advanced algorithms for identifying targets from a three-dimensional reconstruction of sparse 3D Ladar data. In Berginc, G., editor, *Optical Complex Systems: OCS11, 81720Z*, volume 8172 of *Proc. of SPIE*.

[Berechet et al., 2013] Berechet, I., Berginc, G., and Berechet, S. (2013). Method for 3D reconstruction of an object in a scene. United States Patent, No US 2013/0100131 A1.

[Sato et al., 1998] Sato, Y., Shiraga, N., Nakajima, S., Tamura, S., and Kikinis, R. (1998). Local Maximum Intensity Projection (LMIP): A New Rendering Method for Vascular Visualization. *Journal of computer assisted tomography*, 22(6):912–917.

[Berechet et al., 2014] Berechet, S., Berginc, G., Bellet, J.-B., and Berechet, I. (2014). Procédé de discrimination et d'identification par imagerie 3D d'objets d'une scène. Demande de brevet.

A Study on the Hydration Processes in Cementitious Material based on X-ray Dark-Field Imaging

*F. PRADE[1], F. MALM [2], C. GROSSE[2], F. PFEIFFER[1]

[1] Chair of Biomedical Physics, Physics Department & Institute for Medical Engineering, Technische Universität München, 85748 Garching, Germany– friedrich.prade@ph.tum.de
[2] Chair of Non-destructive Testing, Center for Building Materials, Technische Universität München, 81245 München
* presenting author

Keywords: Phase-Contrast Imaging, Cement, Microstructure

Abstract

The hardening of cementitious materials was studied with a X-ray grating interferometer. A strong change of the dark-field signal was observed due to the microstructural developments in the cement. Based on this finding we further studied the influence of temperature and admixtures on the hardening process.

Introduction

In the research on cementitious materials X-ray microscopy techniques have recently been successfully applied at synchrotron facilities in order to obtain information on the micro-structure of cementitious materials and its development during the setting and hardening. Using the attenuation of soft X-rays the growth of the hydration layer around single cement particles was studied [1,2]. However, X-ray microscopy techniques require a small sample size or a special sample preparation in order to resolve the microstructural features in cement. Since the dark-field scattering contrast can provide information on sample features, which are well below the system pixel size, such limitations hold not true for grating-based X-ray imaging [3]. To study the hydration process of this material we measured the evolution of the dark-field signal during the first 48 hours after the samples were prepared. Our results demonstrate that the hardening of the cement leads to a strong decrease in the dark-field signal [4]. Furthermore the time-resolved dark-field signal showed a strong correlation with ultrasound velocity measurements on the same material, thus indicating that the dark-field indeed detects changes within the microstructure of the cement. While other testing methods such as the Vicat-needle test (DIN EN 196-3), the slump test (DIN EN 12350-5) or compaction test (DIN EN 12350-4) and numerous other techniques only provide bulk information on the hardening process, X-ray dark-field imaging allows probing the microstructural development in-situ while also adding the two dimensional information of the images which are obtained. We utilized this advantage in order to test the influence of temperature and certain admixtures on the cement hardening.

Methods

Grating-based X-ray imaging allows probing the phase-shift and small-angle scattering, which X-rays experience in addition to the attenuation when passing through an object. The origin of the two additional signals lies in the wave-optical interaction between the X-rays and the electrons within the sample. The general layout of a grating-based X-ray

imaging system is illustrated in figure 1. Due to the Talbot-effect grating G1 produces a periodic intensity pattern at the site of G2 by imprinting a periodic phase-shift to the X-ray wave-front. In order to observe this interference pattern the absorption grating G0 is placed in front of the tube which results in a sufficient spatial beam coherence when working with laboratory X-ray tubes. Grating G2 acts as an analyzer ensuring that the intensity pattern can be analyzed even with X-ray detectors having a much larger pixel-size than the period of the interference pattern. By stepwise moving one of the gratings along the x-axis the periodic pattern is analyzed. When the sample is placed into the beam the periodic intensity pattern changes due to the attenuation, refraction and scattering of X-rays within the sample. By determining the changes of the mean, the relative phase and the amplitude of the periodic intensity pattern in each pixel, the three different image contrasts are obtained, namely the attenuation-, differential phase- and the dark-field contrasts. As the dark-field originates from small-angle scattering, which is illustrated in figure 1, it is also often referred to as a scattering signal. It was shown that the scattering signal follows a similar exponential decay as the Lambert–Beer law states for the attenuation signal when the X-rays pass through a sample of thickness Δz [5]:

$$D(\Delta z) = \exp\left(\frac{2\pi^2 d_{S,D}^2}{p_2^2} * \varepsilon * \Delta z\right) \qquad (1)$$

with $d_{S,D}^2$ corresponding to the distance between the sample and the detector and p the period of grating G_2. Based on this equation the dark-field signal can be related to a material dependent scattering coefficient ε (formerly introduced as the linear diffusion coefficient) describing the scattering strength per unit length [5].

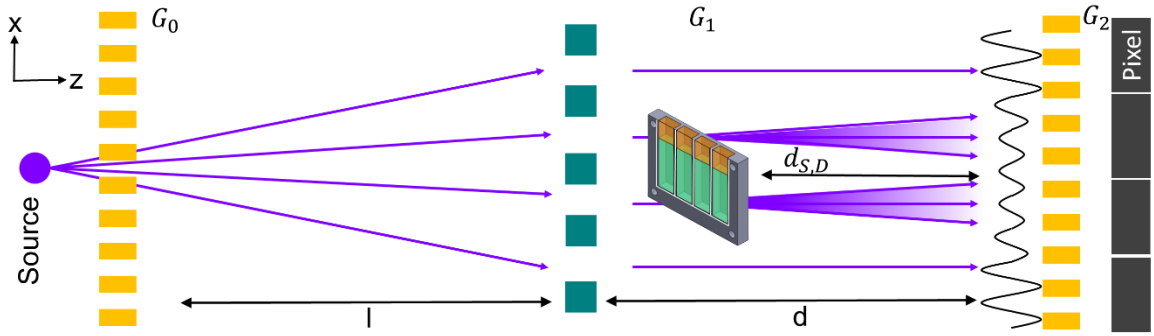

Fig. 1. General layout of a grating-based X-ray imaging setup and origin of the dark-field signal. Note that the dimensions are scaled for a good visualization and the sample is much bigger in real.

Experiment

The measurements for this study were carried out at a laboratory setup at the Institute for Medical Engineering at the Technische Universität München. A COMET XRS-160 (MXR-160HP/11), manufactured by COMET AG in Switzerland, served as the X-ray source, using a tungsten target and a focal spot of 0.4 mm in diameter. The X-ray detector was a Varian PaxScan 2520 D with a pixel-size of 127 µm and a CsI scintillator with a thickness of 600 µm. The distances l and d were both equal with 92.7 cm. The distance between G1 and G2 corresponds to the first fractional Talbot-distance at the design energy of 45 keV. The gold lamella of Gratings G0 and G2 were 150—160 µm in height and had a period of 10 µm while G1 consisted of Nickel lamella with 8 µm height and a 5 µm period. 3.9 g of

distilled and deionized water were mixed manually with 12.5 g of the cement powder for one minute at room temperature. The resulting water to cement ratio therefore was w/c = 0.312. After mixing, the sample was filled into one of the four chambers of the plastic sample holder shown in figure 1. In the first experiment the plain cement was tested. In order to apply heating and cooling during the second experiment we used a Peltier element and Aluminium pieces for the heat transport. In the third experiment lime- or quartz particles with a size of approximately 3-4 mm were added during the mixing process.

Results

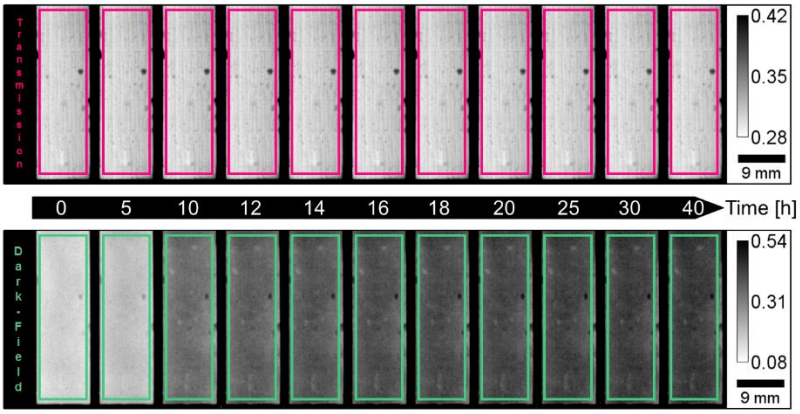

Fig. 2. Top: Transmission images of a cement sample. Bottom: Dark-field images of a cement sample. The coloured rectangles indicate the area from which the average signal was calculated.

The dark-field and transmission images for one cement sample for different points in time after the sample preparation are shown in figure 2. While the transmission images show no change during the experiment the dark-field signal exhibits a significant rise after 10 hours of sample preparation.

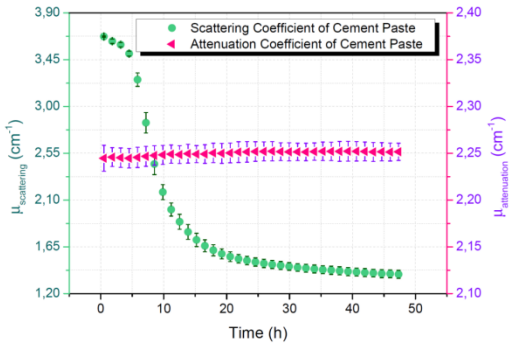

Fig. 3. Mean attenuation (pink) and scattering coefficient (green) over 60 hours after sample preparation. The error bars correspond to the standard deviation of 3 individual measurements.

To further analyse this behaviour the mean signals were calculated according to equation (1) for the regions of interest indicated by the colored rectangles in figure 2. Figure 3 shows

the mean attenuation coefficient and the mean scattering coefficient over the time after sample preparation. The curves emphasize the finding already made based on the images in figure 2 as the scattering signal strongly decreases after 5 hours while the attenuation remains constant. The observed shape of the dark-field curve also corresponds to ultra-sound measurements which were also obtained for the same cement but are not shown here. The agreement of ultra-sound and dark-field measurements shows that the evolution of the dark-field signal is related to the evolution of the microstructure which also determines the mechanical properties of the cement.

Figure 4 illustrates the results of the temperature experiment. The image on the left shows the cement sample which was cooled during the experiment and the corresponding regions of interest from which the mean scattering signal was calculated. The same is shown on the right for a heated cement sample. At the top of the images the Aluminium piece is visible which was used for heat transport from and to the sample.

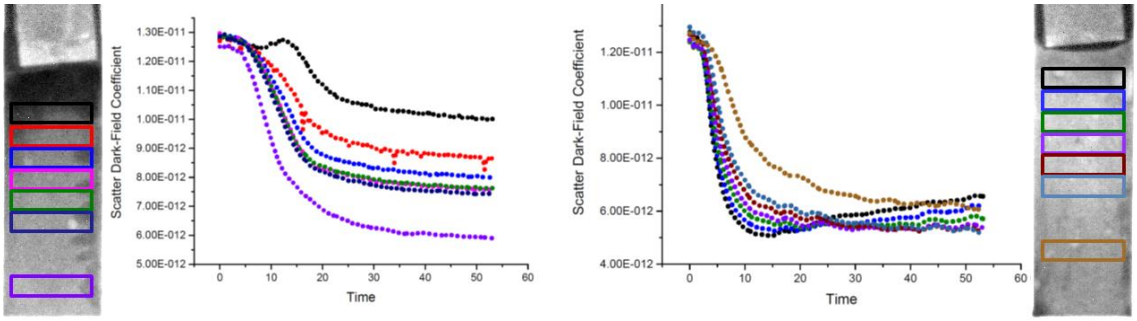

Fig. 4. Image and mean scattering coefficient for the cooled (left) and heated (right) cement sample.

Clearly the heating and cooling influences the signal evolution and the evolution of the microstructure which is as expected since the chemical reactions taking place in the cement strongly depend on the temperature. While heating speeds up the reactions and therefore the scattering coefficient decreases faster, cooling slows down the process and accordingly also the dark-field decreases more slowly.

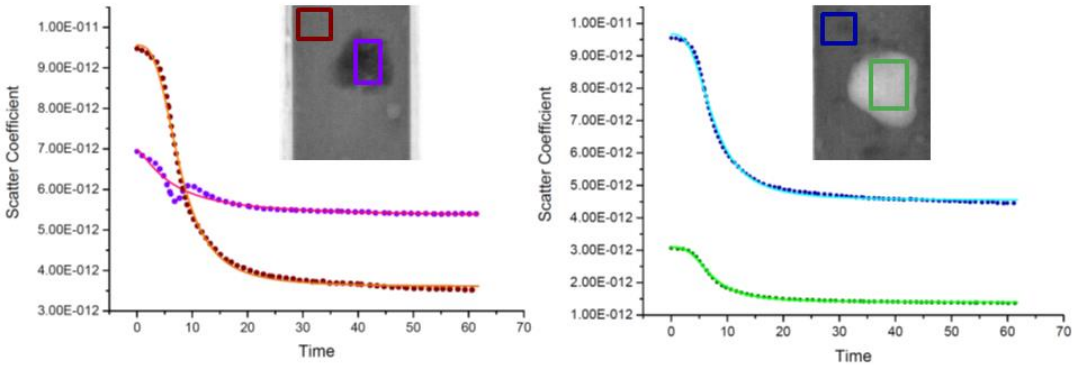

Fig. 5. Images and mean scattering-signal for limestone-particle (left) and a quartz-particle (right).

As a first application we studied the influence of additives such as quartz- and limestone-particles on the hardening process. An exemplary measurement is presented in figure 5. On the left hand side the results for a limestone particle is shown while the right side illustrates the result for the qartz-particle. The two images correspond to the dark-field image taken after 60 hours. As the curves of the mean signal show, the initial scattering signal is lower for both particle types since the particles decrease the distance the X-rays have to propagate through the cement. Therfore also the total amplitude of the signal decrease is smaller as compared to the plain cement. However between 5 to 15 hours the limstone particle shows a deviation in the shape of the curve which is not observed for the quartz particle. Thus our results indicate that limestone influences the dynamics of the hardening process.

Conclusion

We described how the microstructural developments in cementitious materials can be studied with grating-based X-ray dark-field imaging. Our results on the temperature influence show that this technique allows to visualize deviations in the structural processes taking place. The findings for the additives can be explained by different porosity values of the limestone and quartz. This would result in the penetration of the particles with water decreasing the scattering signal from the particle itself as it was recently shown in reference [6]. However further experiments have to be carried out in order to determine wether this change occurs within the particle or in its vicinity in the cement. Therefore a “time resolved” dark-field tomography is the next challenging step.

Acknoledgements

We acknowledge financial support through the DFG Cluster of Excellence Munich-Centre for Advanced Photonics (MAP), the DFG Gottfried Wilhelm Leibniz program and the European Research Council (ERC, FP7, StG 240142). This work was carried out with the support of the Karlsruhe Nano Micro Facility (KNMF, www.kit.edu/knmf), a Helmholtz Research Infrastructure at Karlsruhe Institute of Technology (KIT).

The preparation of the cement samples for the ultrasound experiments was done at the Center for Building Materials of the Technical University of Munich. In several meetings the results were discussed with the experts from the Chair of Mineral Engineering, namely Dr. Urbonas and Dr. Beddoe. Their help is gratefully acknowledged.

References

[1] E.M. Gartner, K.E. Kurtis, P.J.M. Monteiro, Cem. Concr. Res. (2000)
[2] M.C.G. Juenger, P.J.M. Monteiro, E.M. Gartner, G.P. Denbeaux, Cem. Concr. Res. (2005)
[3] F. Pfeiffer,M. Bech, O. Bunk, P. Kraft, E.F. Eikenberry, C. Brönnimann, C. Grünzweig, C. David, Nat. Mater. (2008)
[4] F. Prade, M. Chabio, F. Malm, C. U. Grosse, F. Pfeiffer, Cem. Con. Res. (2015)
[5] M. Bech, O. Bunk, T. Donath, R. Feidenhans'l, C. David, F. Pfeiffer, Phys. Med. Biol. (2010)
[6] F. Yang, F. Prade, M. Griffa, I. Jerjen, C. D. Bella, J. Herzen, A. Sarapata, F. Pfeiffer, P. Lura, Appl. Phys. Lett. (2014)

Biomedical and materials science applications of grating-based phase-contrast imaging with conventional X-ray sources

J. HERZEN*[1], M. WILLNER[1], K. SCHERER[1], F. PRADE[1], A. SARAPATA[1], A. Yaroshenko[1], A. FINGERLE[2], P. NOËL[2], E. RUMMENY[2], S. GRANDL[3], F. MEINEL[3], H. HETTERICH[3], T. SAAM[3], S. Auweter[3] & F. PFEIFFER[1]

[1] Department of Physics & Institute for Medical Engineering, Technische Universität München, Germany – julia.herzen@tum.de
2 Department of Radiology, Klinikum rechts der Isar, Technische Universität München, Munich, Germany
[3] Department of Clinical Radiology, Ludwig-Maximilians-Universität München, Germany
* presenting author

Keywords: Grating interferometer, phase contrast, dark-field imaging, conventional X-ray sources

Abstract

In the last decade, X-ray phase-contrast imaging has been widely used to enhance the contrast for weakly absorbing materials, as for example in biological soft tissue. The extendibility to conventional polychromatic X-ray sources opened this modality to an even broader community. The most interesting aspect is the multimodality of the information provided by phase-contrast methods. It has the potential to improve clinical diagnostic as well as material characterization in non-destructive testing.

In this work we studied the multimodality of the grating-based X-ray phase-contrast method for a variety of applications from biomedical imaging to materials science. Its three signals – the attenuation, the phase-contrast and the dark-field signal – allow extracting complementary information on the objects inner structure from one single measurement. Here, the information gain using this imaging method at different length scales will be demonstrated for various human diseases and for materials analysis. Our results indicate that the combination of the signals can even help visualizing microstructural changes in two-dimensional radiographies avoiding more time-consuming 3D tomography aquisitions.

Introduction

X-ray phase-contrast imaging is an emerging modality that is based on a fundamentally different image formation process compared to conventional attenuation-based imaging and might improve diagnostics in the future by providing additional information and enhanced soft-tissue contrast. Several techniques have been developed to extract this kind of information. Some of these techniques are limited to highly brilliant X-ray radiation, which is only available at large scale synchrotron facilities with a very limited accessibility.

Grating-based phase-contrast imaging is a promising candidate to enter the clinical arena and the field of non-destructive testing, as it can be efficiently operated at standard polychromatic X-ray sources [Pfeiffer 2006]. This imaging method allows extracting three different signals– the attenuation, the phase-contrast and the dark-field signal – from one single measurement containing complementary information on the objects inner structure. Especially this multimodality yields the highest potential for varous fields of applications [Fingerle 2014, Herzen 2014, Sarapata 2015].

Dark-field (small-angle scatter) image contrast is created through differences in the local scattering power within the sample. Small-angle scattering results from microstructures of a much smaller scale than the spatial resolution of the imaging system. It can be gathered experimentally e.g. by a grating interferometer (Fig. 2). For homogeneous objects, which have only negligible small-angle scattering power, the dark-field signal is close to zero, whereas strongly scattering samples yield a significant dark-field signal. The dark-field signal reveals indirectly structural information on the nanometer and micrometer length scale that is inaccessible from the conventional attenuation CT image [Pfeiffer 2008]. Studies on ex-vivo [Schleede 2012] and in-vivo small-animal models [Bech 2013; Meinel 2014] demonstrated the potential of this method for the diagnosis of destructive pulmonary diseases, which change the structure of the lung parenchyma on a micrometer length scale. Similar impact of the dark-field signal has been demonstrated for other human diseases like breast tumours [Grandl 2015] or kidney stones [Scherer 2015] and in materials science applications, where tiny microstructural changes can be visualized being inresolvalbe with the other two signals – the attenuation and the phase contrast [Yang 2014].

Here, we intend to give an overview of the potential biomedical and materials science applications of grating-based X-ray phase-contrast imaging. These results were obtained using imaging setups employing conventional X-ray tube sources.

Methods

When electromagnetic waves like X-rays traverse an object, two phenomena occur: The amplitude of the wave decreases and its phase gets shifted compared to a reference wave (Fig. 1a). The first effect can be observed as a loss in intensity and is exploited in conventional attenuation-based X-ray imaging. The phase information cannot be accessed directly, but local differences in the phase shift cause a slight refraction of the X-rays (Fig. 1b), which can be detected e.g. by using a grating interferometer (Fig. 2). Very small refraction angles induced by fine (unresolvable) microstructures are further denoted by scattering. The grating interferometer provides three completmentary information with one single measurement (Fig. 1c).

The grating interferometer method uses a beam-splitter grating (G1) and an analyser grating (G2) to detect the x-ray refraction in the sample. The refraction angle is related to the first derivative of the x-ray phase shift produced by the sample. Additionally, it provides information, which is related to the small-angle scattering signal. In the case of sufficiently coherent illumination the beam-splitter grating splits the incoming X-ray beam into spatially not separated, overlapping diffraction orders. This overlap leads to interference and causes a periodic intensity pattern in certain distances downstream the beam-splitter grating. A sample refracts the beam producing a transverse shift of the interference pattern perpendicular to the beam direction. This pattern can be detected directly with a high-resolution detector or indirectly using an analyser grating.

In 2006, a method was developed to expand the use of the grating-based phase-contrast method to polychromatic radiation sources like x-ray tubes [Pfeiffer 2006]. By utilising an additional attenuation grating (G0) the incoming beam is divided in many small sources of higher transverse coherence.

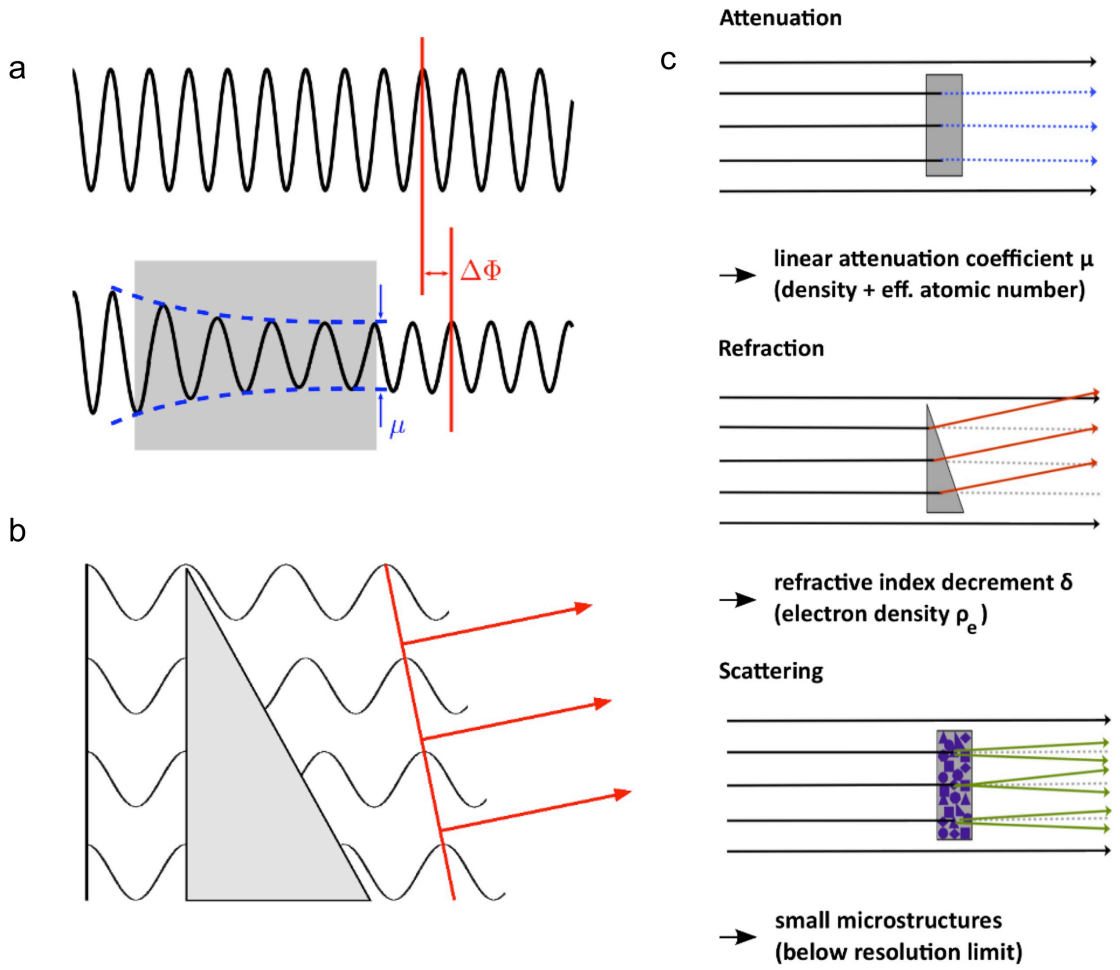

Fig. 1. *X-ray interaction with matter. (a) The change in amplitude and phase of a wave passing through an object. (b) Differences in phase shift cause local X-ray refraction. (c) Three complementary information extractable from one single measurement with a grating interferometer.*

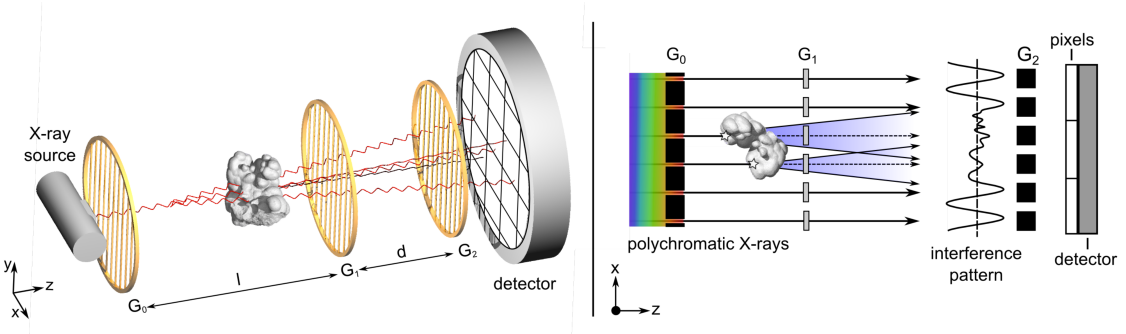

Fig. 2. *Contrast generation in grating-based X-ray phase-contrast and dark-field imaging. (left) Typical setup with a conventional X-ray source, a source grating G0, a phase grating G1, an analyzer grating G2 and a flat panel detector. (right) Diffuse X-ray scatter originating from sub-structures of an inhomogeneous object. By analyzing the dark-field signal, information on the object micro-morphology that is well below the detector resolution limit can be retrieved [Scherer 2015].*

Results

Liver lesions

The use of iodine contrast agents greatly improves detectability of focal hepatic liver lesions in conventional computed tomography, but the characterization of subcentimetric findings remains challenging. The three ex-vivo liver specimen in Figure 3 demonstrate the potential of grating-based phase-contrast imaging for the visualization of soft tissue.

Fibrous septa are visible as high signal bands in the first sample showing a cirrhotic liver with HCC nodules. The subcapsular hematoma in the lower left part of the second example can be clearly differentiated from normal tissue. In the last sample, various gray values depict mucinous carcinoma, liver tissue and necrotic/hemorrhagic areas.

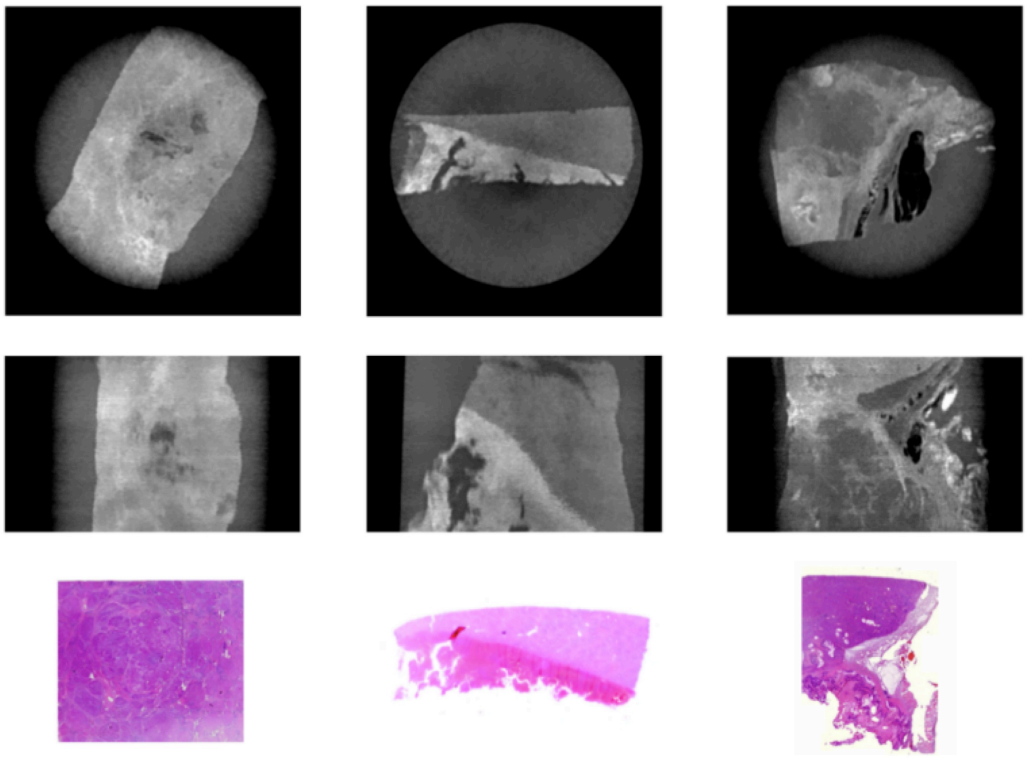

Fig. 3. *Phase-contrast 3D imaging results of three exemplary liver lesions and histological slices (H&E stain). (left) Hepatocellular carcinoma in a cirrhotic liver, (middle) subcapsular hematoma, (right) metastasis of a mucinous adenocarcinom [Herzen 2014].*

Lung imaging

The dark-field signal depends on various parameters of the microstructures within an object including their size and shape, their orientation with respect to the grating lines and the actual magnitude of electron density differences. Assuming other parameters being constant, the dark-field signal allows drawing conclusions on the size of the microstructures. This can be used for example to monitor the changes that the alveoli network undergoes in the progression of a lung disease like pulmonary emphysema as illustrated in Figure 4. In the healthy lung tissue high electron density variations of air and tissue within the dense network of alveoli cause strong X-ray scattering. Lung emphysema leads to irreversible destruction of alveolar walls and enlargement of distal airspaces, which strongly lowers the scattering and thus the dark-field signal.

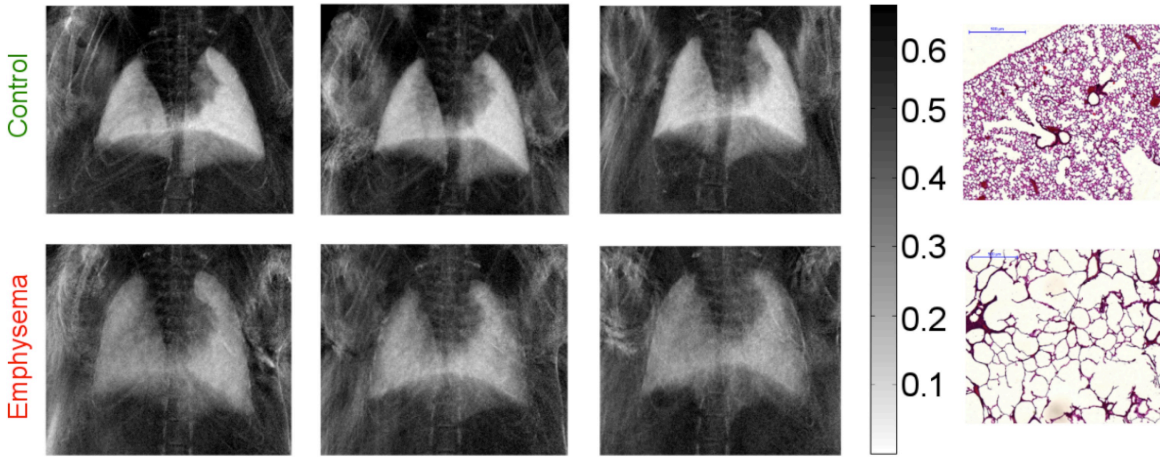

Fig. 4. *In vivo 2D dark-field (scatter) imaging of healthy and emphysemateous mouse lungs and the corresponding exemplary histological slice (H&E stain, right). Emphysema decreases scattering and the associated dark-field signal compared to healthy lungs. The scattering is normalized in all images showing the reduction in visivility of the interferometer [Meinel 2014].*

References

Bech M., Tapfer A., Velroyen A., Yaroshenko A., Pauwels B., Hostens J., Bruyndonckx P., Sasov A. & Pfeiffer F. (2013). *In-vivo dark-field and phase-contrast x-ray imaging*. **Nature Scientific Reports** 3, 3209.

Fingerle A.A., Willner M., Herzen J., Noël P.B. & Pfeiffer F. (2014). *Quantitative x-ray phase-contrast computed tomography of simulated cystic kidney lesions – an in vitro phantom study*. **Radiology** 272(3), p. 739-48.

Grandl S., Scherer K., Sztrókay-Gaul A., Birnbacher L., Willer K., Chabior M., Herzen J., Mayr D., Auweter S., Pfeiffer F., Bamberg F. & Hellerhoff K. (2015). *Improved visualization of breast cancer features in multifocal carcinoma using phase-contrast and dark-field mammography: an ex vivo study*. **European Radiology**, published ahead of print, doi: 10.1007/s00330-015-3773-5.

Herzen J., Willner M.S., Fingerle A.A., Noël P.B., Köhler T., Drecoll E., Rummeny E.J. & Pfeiffer F. (2014). *Imaging liver lesions using grating-based phase-contrast computed tomography with bi-lateral filter post-processing*. **PLOS ONE** 9(1), e83369.

Meinel F.G., Yaroshenko A., Hellbach K., Bech M., Müller M., Velroyen A., Bamberg F., Eickelberg O., Nikolaou K., Reiser M.F., Pfeiffer F. & Yildirim A.Ö. (2014). *Improved diagnosis of pulmonary emphysema using in vivo dark-field radiography*. **Investigative Radiology** 49(10), 653-8.

Pfeiffer F., Weitkamp T., Bunk O. & David Ch. (2006). *Phase retrieval and differential phase-contrast imaging with low-brilliance X-ray sources*. **Nature Physics** 2(4), p. 258-261.

Pfeiffer F., Bech M., Bunk O., Kraft P., Eikenberry E.F., Brönnimann Ch., Grünzweig C. & David C. (2008). *Hard-X-ray dark-field imaging using a grating interferometer*. **Nature Materials** 7, 2096.

Sarapata A., Ruiz-Yaniz M., Zanette I., Rack A., Pfeiffer F. & Herzen J. (2015). *Multi-contrast 3D X-ray imaging of concrete using a grating interferometer*. **Applied Physics Letters** 106, 154102.

Scherer K., Braig E., Willer K., Willner M., Fingerle A.A., Chabior M., Herzen J., Eiber M., Haller B., Straub M., Schneider H., Rummeny E.J., Noël P.B. & Pfeiffer F. (2015). *Non-invasive Differentiation of Kidney Stone Types using X-ray Dark-Field Radiography*. **Nature Scientific Reports** 5, 9527.

Schleede S., Meinel F.G., Bech M., Herzen J., Achterhold K., Potdevin G., Malecki A., Adam-Neumair S., Thieme S.F., Bamberg F., Nikolaou K., Bohla A., Yildirim A.Ö., Loewen R., Gifford M., Ruth R., Eickelberg O., Reiser M. & Pfeiffer F. (2012). *Emphysema diagnosis using X-ray dark-field imaging at a laser-driven compact synchrotron light source*. **Proceedings of the National Academy of Sciences** 109, 17880-17885.

Yang F., Prade F., Griffa M., Jerjen I., Di Bella C., Herzen J., Sarapata A., Pfeiffer F. & Lura P. (2014). *Dark-field X-ray imaging of unsaturated water transport in porous materials*. **Applied Physics Letters** 105, 154105.

Grating Based Differential Phase Contrast Imaging of an Interpenetrating AlSi12/Al_2O_3 Metal Matrix Composite

J. MAISENBACHER[1]*, F.PRADE[2], J.GIBMEIER[1], F.PFEIFFER[2], J.MOHR[3]

[1] Institute for Applied Materials IAM-WK, Karlsruhe Institute for Technology, 76131 Karlsruhe, Germany – Jens.Maisenbacher@kit.edu

[2] Physics Department (E17), Technische Universität München, 85748 Garching, Germany

[3] Institute for Microstructure Technology IMT, Karlsruhe Institute for Technology, 76131 Karlsruhe, Germany

Keywords: computed tomography, phase contrast, metal matrix composite

Abstract

Metal-matrix compounds made from freeze-cast lamellar Al_2O_3 preforms filled with eutectic AlSi12 alloy were investigated regarding the interpenetrating structure of the constituent phases. Using differential phase contrast tomography in a lab setup with a microfocus tube and a Talbot-Lau interferometer the benefit of phase contrast tomography could be demonstrated for similarly absorbing materials in the non-medical field.

Introduction

In lightweight construction metal matrix composites (MMC) play an important role due to their high wear and fatigue resistance, high specific stiffness and enhanced high temperature properties. The MMC researched in this study was fabricated using a freeze cast ceramic preform filled with a metallic phase. The process thereby not only allows to create preforms with porosities varying between 15 Vol.-% to 85 Vol.-%, but also to adjust the properties of the lamellae during the directional freezing. The compound itself poses as a hierarchical structure with interpenetrating ceramic and metall phases. The elastic properties are hence anisotropical and differ from those of the respective monolithical materials. Finite element models describing those properties have so far been based on metallographic cross sections and the assumption of parallel lamellae **[1]** (see also **fig. 1**). Comparisons with experimental results obtained from ultrasonic phase spectroscopy have so far shown good agreement parallel to the lamella direction, however in direction normal to the lamellae the material seems to be stiffer than predicted. The reason for this might be interconnections (i.e. sinter bridges) between the lamellae which do not fit into the assumptions for the FE-models. A tomografic investigation, and FE-models based on the actual 3D structure of the compound, seems indispensable. Due to similar absorption properties of the employed metal and ceramic phase (Al_2O_3 and an AlSi12-alloy), the required segmentation of both materials is problematic. In order to increase the contrast between Al_2O_3 and AlSi12, differential X-ray phase contrast (DPC) tomography is considered a vital alternative **[2]**. From the various available methods, grating based DPC has the benefit of also providing the possibility to analyse the absorption and dark field signal from the same raw data **[3][4][5]**.

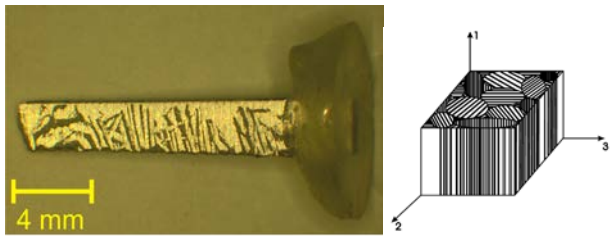

Fig. 1. Images of the investigated samples. *(left):* metal matrix composite consisting of a freeze cast, lamellar Al_2O_3 structure and an AlSi12 matrix. The glue from fixing the sample on the rotation stage can be seen on the right side. *(right):* assumption for FE-based models for elastic constants: ideal, parallel arrangement of the lamellae **[1]**.

Methods

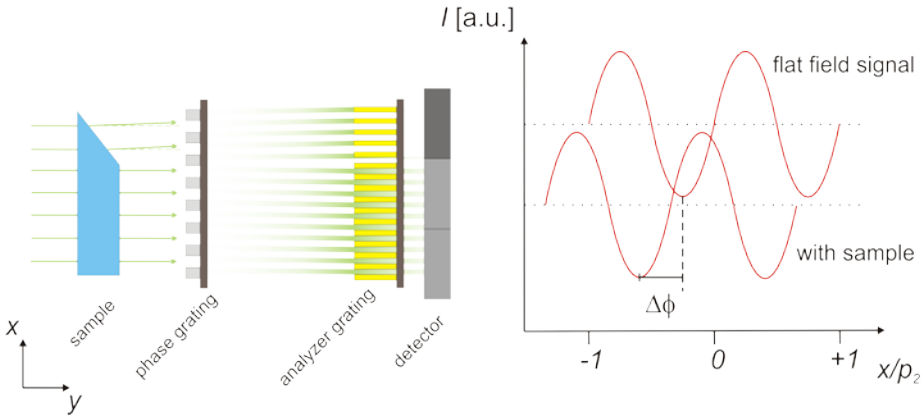

Fig. 2. The sample introduces a phase shift resulting in a local shifting of the interference pattern. An analyzer grating is employed in order to resolve the displacements which are small compared to the pixel size in the given setup.

Grating based DPC is based on the detection of small, angular beam deviations introduced by a sample and caused by diffraction on surfaces between regions with different refractive indices. These are compared to reference measurements without sample (flat field). Due to the magnitude of the angular beam deviations (~10^{-9} rad for X-rays and most materials) a phase grating introducing a diffraction pattern and an analyzer grating are needed in order to resolve the small deviations. In the experiment, one of the gratings is moved one grating period in lateral direction in several steps while taking an image at each step. Hence, looking at one arbitrary detector pixel, a cosine-like intensity course can be observed. With a sample in the field of view (FOV), this curve gets shifted due to the diffraction pattern being angularly deviated (see also **fig. 2**). From the angular shift α, the local gradient of the sample's phase shift $\partial\Phi/\partial x$ and hence the real part of the complex refractive index can be obtained. For a more in detail description of the method see also **[3][4][5].**

$$\alpha = \frac{\lambda}{2\pi}\frac{\partial\Phi(x,y)}{\partial x}$$

Experiment:

The measurements were carried out using a micro focus lab X-ray source by *X-Ray worX* and a source grating in a non-commercial setup at Physics Department E17 at TU Munich. The design energy was 45 keV at grating distances of l = d = 92 cm with an acceleration voltage of 60 kV at 20 W. The gratings were fabricated by IMT at Karlsruhe Institute for Technology (KIT). The source and analyzer grating had a period of 10 µm at 160-170 µm height (material: Au) at a duty cycle of 0,5. The phase grating was made of Ni-lamellae with a period of 5 µm at 8 µm height and a duty cycle of also 0,5. For the measurement, 35 blocks of 21 projections each and 5 single images at 1 frame per second were taken for each projection. Between the blocks there was a flat field measurement with the sample removed from the field of view. For the reconstruction a filtered back-projection algorithm has been employed.

The sample was a 12 × 3 × 2 mm^3 slab of an Al_2O_3-AlSI12 MMC (see **fig. 1.**). The ceramic preform of the sample was produced at IAM-KM at KIT and exhibited a mean porosity of 56 Vol.-%. The water-based suspension for the freeze cast process contained 22% Al_2O_3 powder (CT3000SG by *Almatis*) with an Al_2O_3 content of 99,8% within the powder. The particle size was 2,5 µm / D90 Cilas at a fired density of 3,90 Mg/m^3. The freeze casting temperature was -10°C, the structure was then sintered at 1550°C for one hour. In the next step, the structure was infiltrated with an eutectic AlSi12 alloy using squeeze casting at the Casting Technology Centre at Aalen University of Applied Sciences, Germany.

Results:

An example for the obtained projections can be seen in **fig. 3**. where on the left hand side a projection taken in absorption contrast and on the right hand side taken in differential phase contrast can be seen. In the absorption signal the sample holder at the bottom, the glue holding the sample in place and the sample itself can be identified. Structures within the sample however are not recognizeable. In the differential phase contrast image the sample holder appears as an area with increased noise. Some of the noisy region on the bottom corners of the image represent the border of the FOV, which does not appear in the absorption image. On the brighter left side of the sample some structural details can be perceived.

Exemplary slices of the reconstructed volume can be seen in **fig. 4**, where the data in absorption contrast are now compared to the phase contrast images. In both images sample, glue and rotation stage can be seen. While there are slight structural details visible in absorption contrast the darker AlSi12 areas and the brighter Al_2O_3 regions in the sample can be readily observed in phase contrast.

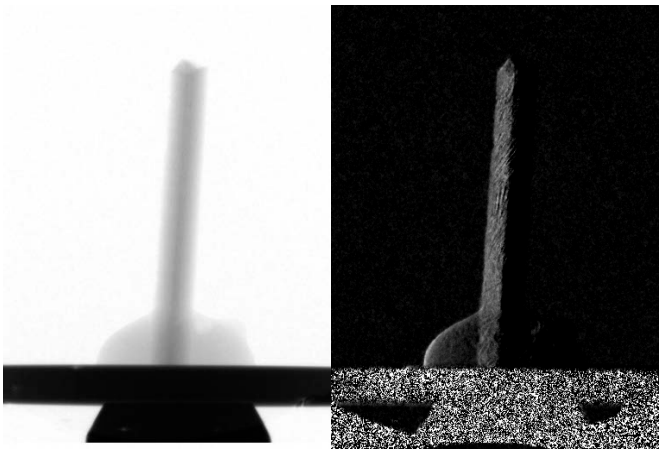

Fig. 3. Projections of an Al_2O_3-AlSi12 metal matrix composite sample obtained at Physics department E17 at TU Munich. Also depicted are the rotation stage and the glue holding the sample in place. *(left):* absorption contrast *(right):* differential phase contrast.

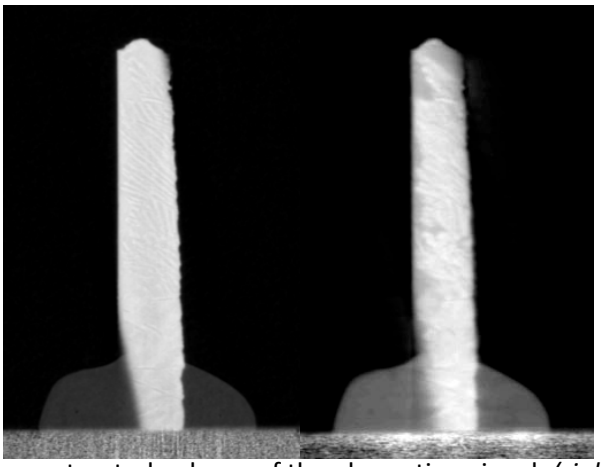

Fig. 4. *(left):* Slice of the reconstructed volume of the absorption signal. *(right):* slice of the reconstructed volume of the phase contrast signal. The respective positions of the slices in the sample are identical. Notice the clearer distinction of the darker AlSi12 regions as compared to the brighter, more absorbing Al_2O_3 regions in the phase contrast images. In the absorption contrast the edges of the reconstructions are sharpest.

Conclusion:

The overall gain in information the phase contrast provides as compared to the absorption signal in this measurement are evident. Thereby no further image processing other than the reconstruction using filtered back-projection has been conducted. However it must be taken into account, that the possibilities using pure absorption setups are not fully comparable to those in this investigation. The benefit in comparison to a metallographic analysis is depicted in detail in **fig. 5**. In the three cross sections examples for interconnections of two Al_2O_3 lamellae and the broadening of the AlSi12 matrix are presented; both of which cannot be reliably characterized using metallographic cross sections. Hence, the results establish a basis to provide a realistic FE model of the interpenetrating metal matrix composite.

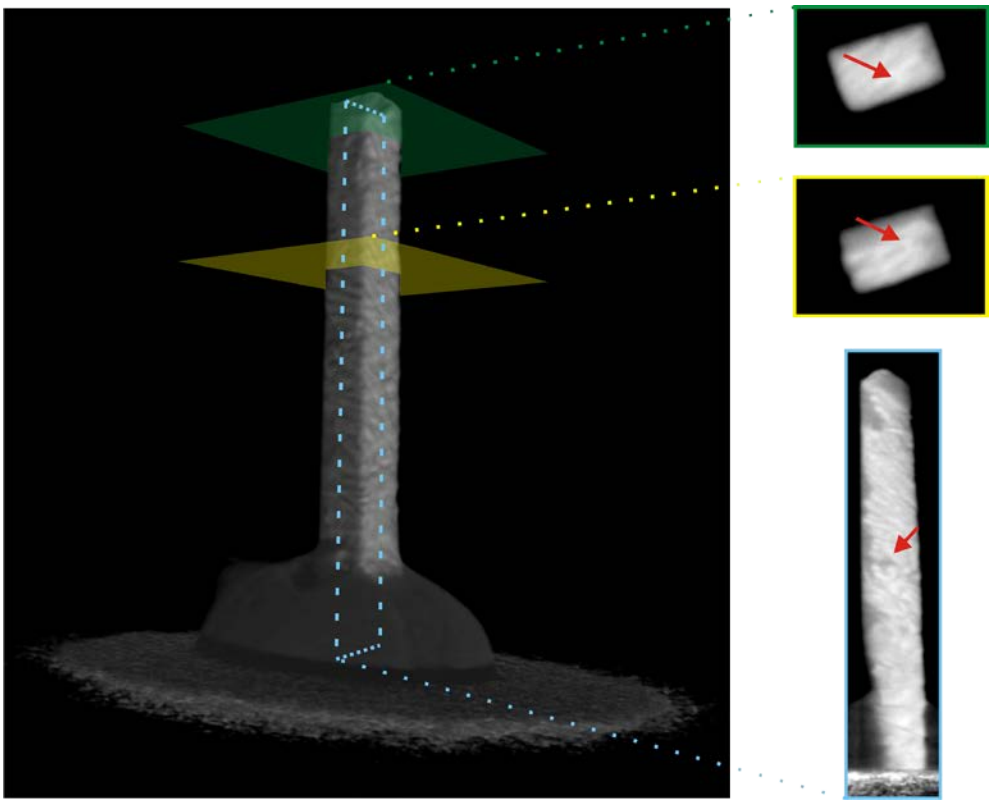

Fig. 5. Rendered 3D-volume of the phase contrast reconstruction of the Al_2O_3-AlSi12 MMC sample. The cross sections on the right demonstrate necessity and benefit of a tomographic analysis. Some of the Al_2O_3 lamellae are interconnected by sinter bridges *(green and yellow cross section),* the interconnection are indicated by red arrows respectively. However the opposite effect has also to be taken into account *(blue cross section),* as broader AlSi12 areas are difficult to be taken into account using metallographic methods.

Acknowledgement

The authors appreciate financial support by the Helmholtz-Society via the Virtual Institute – New X-Ray Analythical Methods in Material Science (VI-NXMM). We also thank M.J. Hoffmann, R. Oberacker and T. Waschkies of IAM-KWT, Karlsruhe Institute for Technology; as well as A. Nagel at Aalen University of Applied Sciences for providing the specimen material. The gratings have been fabricated in the framework of the Karlsruhe Nano Micro Facility (KNMF).

References

[1] Ziegler T., Neubrand A., Roy S., Wanner A. & Piat R. (2008). Elastic constants of metal/ceramic composites with lamellar microstructures: Finite element modelling and ultrasonic experiments. ***Composite Science and Technology 69****:* p.620-626.
[2] Bonse U. & Hart M. (1965): Principle and Design of Laue-Case X-Ray Interferometers. **Zeitschrift für Physik 188:** p.154-164
[3] Pfeiffer F., Weitkamp T., Bunk O. & David C. (2006). Phase retrieval and differential phase-contrast imaging with low brilliance X-ray sources. ***Nature Physics 2****:* p.258-261.
[4] Pfeiffer F., Kottler C., Bunk., & David C. (2007). Hard X-ray Phase Tomography with Low-Brilliance Sources. **Physical Review Letters 98:** 108105
[5] Engelhardt M., Baumann J., Schuster M., Kottler C., Pfeiffer F., Bunk O. & David C. (2007). High-resolution differential phase contrast imaging using a magnifying projection geometry with a microfocus x-ray source. **Applied Physics Letters 90:** 224101

Single-grating interferometer for high-resolution phase-contrast imaging at synchrotron radiation sources

*A. HIPP[1], J. HERZEN[2], I. GREVING[1], J. U. HAMMEL[1], P. LYTAEV[1], A. SCHREYER[1], AND F. BECKMANN[1]

[1] Helmholtz-Zentrum Geesthacht, Max-Planck-Strasse 1, Geesthacht, Germany
[2] Technische Universität München, James-Frank Strasse 1, Garching, Germany
* presenting author (alexander.hipp@hzg.de)

Keywords: grating interferometer, synchrotron

Introduction

Differential phase-contrast imaging (DPC) has proven to be a valuable tool when investigating weak absorbing materials like soft tissue, due to its increased contrast compared to conventional absorption-contrast imaging.
The most common type of grating interferometer consists of two gratings, a phase grating and an analyzer grating. Although a two-grating interferometer comes with a high sensitivity its performance is mainly limited by the feasible aspect ratio of the analyzer-grating structres. The period of these structures (state of the art 2.4 µm) has to be smaller than the used pixel size and have to be highly absorbing which strongly limits the usable energy range.
In contrast to this, a single-grating interferometer comes with several advantages: The absence of an analyzer grating increases the photon flux at the detector plane by almost a factor of two and at the same time allows for using this type of interferometer at any energy. Additionally, the setup itself is more stable and easily adjustable. With a single-grating interferometer it is also possible to use two different modes of phase-retrieval: The so-called stepping approach [1] and the singe-shot or fringe analysis approach [2]. These two modes make the same interferometer usable for high-resolution phase-contrast imaging and for very fast measurements.
Main requirement for this type of setup is a detector system with a high spatial resolution, that allows to resolve the interference pattern directly. The microtomography endstation at the beamline P05 is operated by the Helmholtz-Zentrum Geesthacht at the synchrotron radiation storage ring PETRA 3 at DESY, Hamburg, Germany. The imaging detector consists of a CCD-camera and a magnifying optics, which results in an effective pixel size between 0.3 µm and 2.4 µm. This is an ideal basis for high-resolution phase-contrast imaging using a single-grating interferometer.
Here we will present our investigations of a single-grating interferometer based on simulations. Focus of these calculations is on the reachable sensitivity, depending on the grating period and the effective pixel size, as well as on the spatial resolution of the setup. Additionally, we will prove the usability of the interferometer for high-resolution phase-contrast measurements with first experimental results obtained at the Imaging Beamline P05.

Methods

For simulations in this study all gratings are assumed to be perfectly fabricated and therefore are represented by one-dimensional functions with a duty cycle (ratio of bar width to grating period) of 0.5. The incoming wave is always assumed as perfect plane wave. For a certain phase shift $\Delta\varphi$ and the attenuation coefficient µ, dependent on the grating material and X-ray energy, the resulting wave front behind the phase grating with height d is defined as:

$$A_0(x) = e^{-\mu d(x)} e^{-i\Delta\varphi(x)}$$

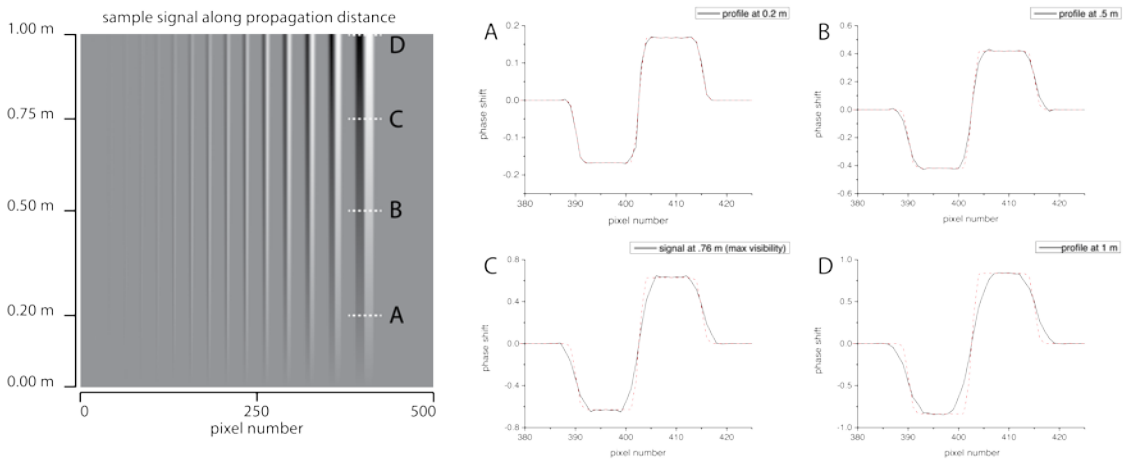

***Fig.** 1: The image shows the simulated projected profile of the test sample along the propagation distance. The test sample consists of several Silicon rods with a squared cross-section sized between 1 µm and 60 µm. The phase-projection was retrieved from a stepping-scan with 5 steps and with a grating period of 10 µm. Structures below 5 µm are detectable. The plotted profiles of the largest rod at different distances (A, B, C, D) show significant blurring of the edges already at the 1st fractional Talbot distance (C). At short distances (A, B) the projected profile is in very good agreement with the expected signal (red dashed curve).*

The dependency on x of the variables is used to distinguish between grating bar and gap. This modified wave front is propagated along the z-axis applying the Fresnel propagator

$$\widetilde{P_z}(k_x) = e^{ikz}e^{-ik_x^2/2k}$$

in Fourier space with $\mathcal{F}$ denoting a Fourier transformation and $\mathcal{F}^{-1}$ denoting an inverse Fourier transformation:

$$A_{z(x)} = \mathcal{F}^{-1}\{\mathcal{F}\{A_0(x)\}\widetilde{P_z}(x)\}.$$

The resulting intensity pattern at the detector plane is then given as

$$I_{z(x)} = |A_z(x)|^2.$$

These equations were used to simulate a single grating interferometer with varying grating period p and adjusted pixels size s (p_1=10 µm / s_1=2.4 µm, p_2=7 µm / s_2=1.2 µm, p_3=5 µm / s_3=1.2 µm and p_4=2.4 µm / s_4=0.6 µm) for different distances. To analyze the performance of each setup the projection of a test pattern, consisting of silicon rods with a square cross-section of different edge-lengths [Fig. 1], was simulated using the stepping approach.

Results

The simulations for every grating interferometer show significant blurring at the edges of the test patter, increasing with the propagation distance [Fig. 1]. This blurring is a result of the beamsplitter characteristic of the phase grating and can be observed due to the small pixel sizes used. From the diffraction equation for small angles

$$\theta_m = \arcsin(m\lambda/p) \approx m\lambda/p$$

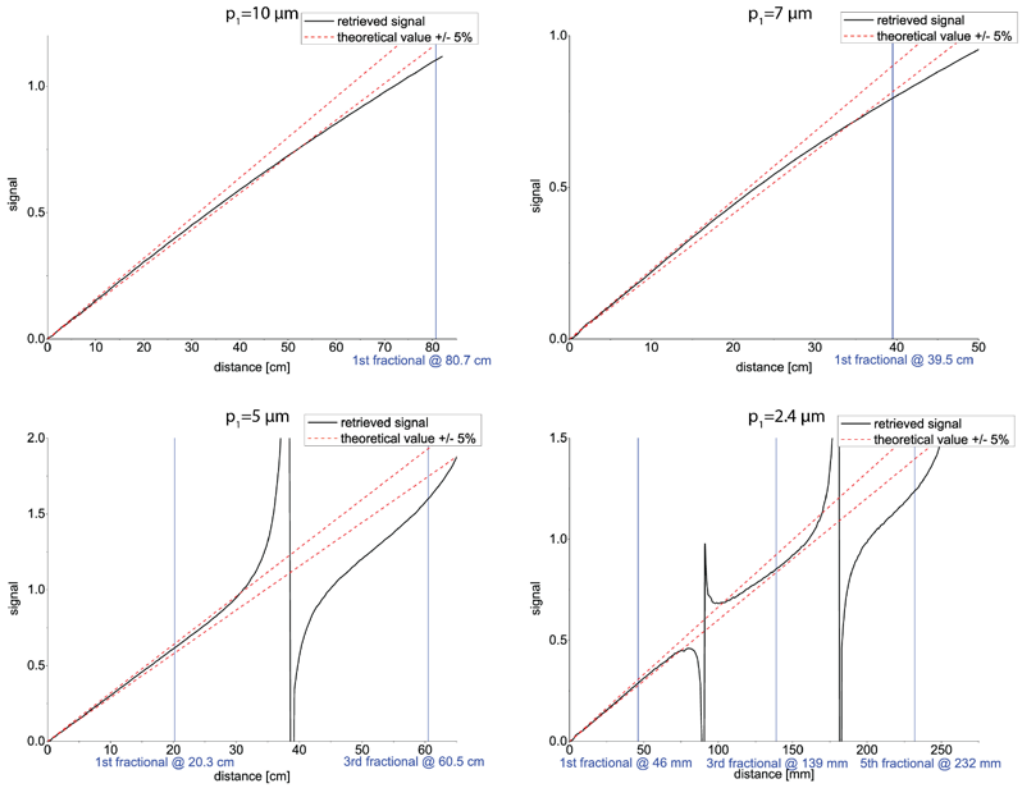

Fig. 2: The image shows the obtained signal of single-grating setups with varying phase-grating periods. The red dashed lines mark the area where the signal varies less than 5% from the theoretical value. For the setups with a 10 µm and 7 µm period the critical distance where the signal varies more than 5% is shorter than the 1st fractional Talbot-distance. For the setups with a 5µm and 2.4 µm periods the exact position of the critical distance is covered by imprecise signal values in the area of the 2nd and 4th fractional Talbot-distance.

we see that the blurring will be inversely proportional to the grating period *p* and is scaled proportional to the propagation distance due to the geometric magnification.
Figure 2 shows how the blurring affects the obtained phase-shift values at the edge of a rod. The red dotted lines mark the area, where the deviation of the signal from the theoretical value is lower than 5%. The blue lines mark the odd fractional Talbot-distances. The distinct distance where the signal rises over 105% or falls below 95% of the theoretical signal will be called critical distance d_c in the following. The Talbot-distance is inversely proportional to p^2, thus a larger relative propagation distance (in terms of the Talbot-distance) is applicable the smaller the grating period is.
To compare the performance of the different setups we calculated the sensitivity of each setup, which depends on the propagation distance *d*, grating period *p*, visibility *V* and the photon counts *N.*

$$S \sim d/p \cdot V\sqrt{N}$$

Figure 3 show the comparison of the sensitivity for the case that the visibility of each setup is almost not affected by the optical components of the whole setup (FWHM of point spread function (PSF) equal to 10 % of the grating period) and more realistic case where a gaussian-shaped PSF (FWHM=1µm) is added to the simulation. The comparison of the sensitivity up to the relative critical distance shows an advantage in reducing the grating period and enlarging the relative propagation distance, if the visibility is comparable to a setup with a larger period. For a camera system with a not negligible PSF the sensitivity drops rapidly with smaller grating periods, because the

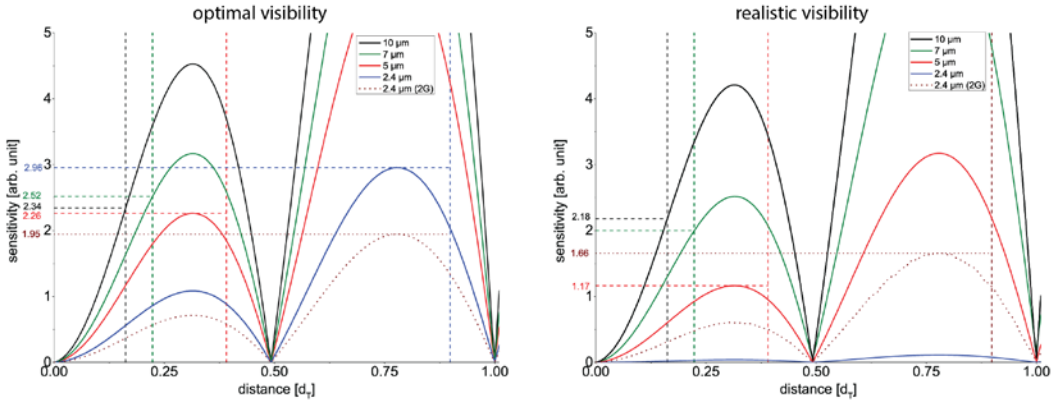

Fig. 3: The comparison of the sensitivity shows an advantage in using smaller grating periods when the achieved visibility is in the same range as for larger grating periods (optimal visibility). By adding a not negligible point spread function to the simulations (realistic visibility), the sensitivity drops dramatically for small grating periods. The plots are compared to a conventional two-grating setup (2G) with 2.4 µm grating periods.

visibility is lowered until the interference pattern is not resolvable anymore. In this case such small grating periods can only be used in a two-grating setup (2G). For this type of setup the second grating preserves the contrast of the interference pattern, but reduces the photon counts to almost 50%.

Figure 4 shows the projection of the test pattern at the distance with maximal sensitivity below the critical distance for a setup with a period of 10 µm and 2.4 µm, respectively. For both setups the smallest structures with 1 µm width are still detectabel. Nevertheless, the achieved signal for the small structures strongly differs from the theoretical value up to a structure size of 12 µm and 9 µm, respectively. By reducing the propagation distance of the 2.4 µm period setup to the first fractional Talbot-distance, correct values are achieved for structures with a size of 3 µm or bigger.

As a first proof of the usability of a single grating interferometer at the PETRA III beamline P05, a grating with a period of 22.4 µm, a pixel-size of 2.4 µm and a propagation distance of 30 cm at an X-ray energy of 15 keV has been used to measure a soft tissue sample (human cerebellum) by users from the *Bimomedical Material Science Center Basel* (Georg Schulz, Simone Hieber, Peter Thalmann and Bert Müller). Figure 5 shows a recunstructed slice from this measurement. The measurement was anlysed using both phase-retrieval methods, the

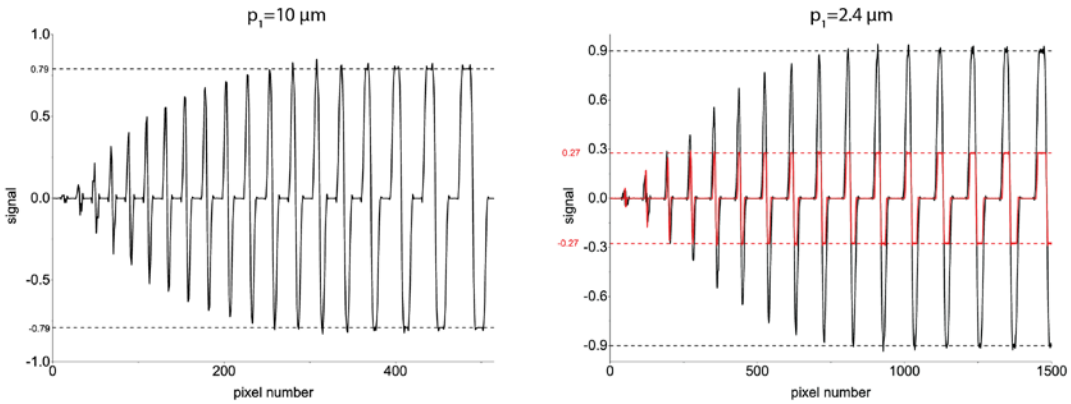

Fig. 1: Projection of a test pattern for a setup with a 10 µm period grating and a 2.4 µm period grating at the distance for maximal sensitivity. In both setups, structures down to a size of 1 µm are visible but lack of a correct signal value. At the 1st fractional Talbot-distance the 2.4 µm period setup is able to give a correct signal for structures to a size down to 3 µm (red lines).

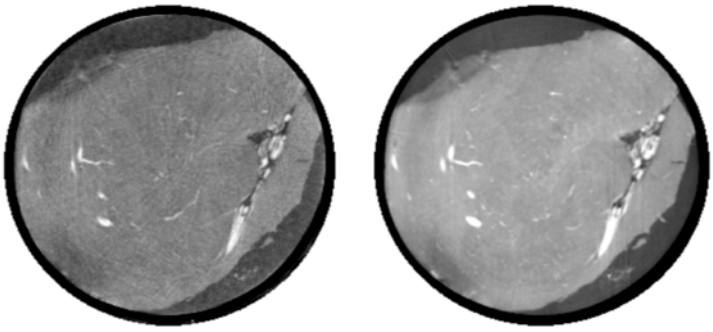

FIg. 5 : First successful measurement with a single grating setup at the beamline P05. The human cerebellum was measured using a phase-grating with a period of 22.4 µm and a propagtion distance of 30 cm. The reconstruction using the fringe analysis approach (left) shows more artefacts and lower resolution then the reconstuction using the stepping approach (right). The sample had a diameter of 6 mm.

single-shot fringe analysis approach and the stepping approach. The reconstructed slices show the functionallity of the setup using both phase-retrieval methods. By comparing the both reconstructions, an advantage of the stepping approach in terms of image quality is recognizable due to less artefacts and better visibility of small image features.

Conclusion

The simulations of a single-grating interferometer predict the possibility to realize a high sensitive setup for differential phase-contrast measurements, but is limited by the available propagation distance. Due to the beam-splitter characteristic of the phase-grating and the small pixel sizes the usable propagation distance is severely limited to avoid strong blurring of the projection.
Smaller grating periods allow to go for higher fractions of the Talbot distance, but are more vulnerable to the point spread function of the optical components of the experimental setup.
The investigation of the reachable resolution of the different single grating setups reveal that even with a period of the phase grating structures of 10 µm sample structures down to 1 µm are detectable. Nevertheless, all setups fail giving reliable signal values for structures in the range of 1 µm and 10 µm at distances for high sensitivity.
Aiming at a high-resolution single-grating interferometer these limitations lead to a setup with a small phase-grating period (state of the art: 2.4 µm). Using such small grating periods require a detector system of the experiment where the FWHM of the PSF does not exceed 10% of the grating period to achieve an adequate visibility. For a experimental setup with a larger PSF, a two-grating setup is required using these periods. Additionally, the propagation distance between grating and detector has to be kept as short as possible to avoid loss of accuracy due to image blurring occuring from the beam-splitter characteristic of the phase grating.
At the Imaging Beamline P05 a single-grating interferometer has been successfully implemented and tested with a biomedical sample in tomography mode. The first results demonstrate the ability of such a system for fast DPC-measurements using the fringe analysis approach and also for high resolution DPC-measurements using the stepping approach.

References

[1] T. Weitkamp, A. Diaz, C. David, F. Pfeiffer, M. Stampanoni, P. Cloetens, and E. Ziegler, "X-ray phase imaging with a grating interferometer," Opt. Express 13, 6296-6304 (2005)

[2] M. Takeda, H. Ina, and S. Kobayashi, “Fourier-transform method of fringe-pattern analysis for computer- based topography and interferometry,” Journal of the Optical Society of America 72, p. 156, Jan. 1982.

[3] A. Hipp, F. Beckmann, P. Lytaev, I. Greving, et al. -based x-ray phase-contrast imaging at PETRA III ", Proc. SPIE 9212, Developments in X-Ray Tomography IX, 921206 (September 12, 2014)

Oral presentation

Grating-based X-ray phase-contrast imaging at PETRA III

*A. HIPP[1], F. BECKMANN[1], I. GREVING[1], J. U. HAMMEL[1], P. LYTAEV[1], A. SCHREYER[1], AND J. HERZEN[2]

[1] Helmholtz-Zentrum Geesthacht, Max-Planck-Strasse 1, Geesthacht, Germany
[2] Technische Universität München, James-Frank Strasse 1, Garching, Germany
* presenting author

Conventional absorption-based imaging often lacks in good contrast at special applications like visualization of soft tissue or weak absorbing material in general.
To overcome this limitation, several new X-ray phase-contrast imaging methods have been developed at synchrotron radiation facilities. Our aim was to establish the possibility of different phase-contrast imaging modalities at the Imaging Beamline (IBL, P05) and the High Energy Material Science beamline (HEMS, P07) at Petra III (DESY, Germany).

We installed a grating interferometer (consisting of two gratings) with a fixed geometry usable at a large variety of without need of mechanical changes energies at the HEMS beamline. This has the strong advantage that measurements at different energies are directly comparable without any need for image registration.

We will present first results of a high-energy phantom sample obtained at different energies in the range from 33 up to 100 keV. Also first results on biomedical samples will be presented. By reference to those we will demonstrate the advantage of using a high-energy setup to avoid artifacts in the tomographic reconstruction usually occurring from phase-wrapping or too high absorbing samples.

Construction and Preliminary Results from a 70 keV X-ray Tomography Beamline with a Stepped-Grating Interferometer

K. HAM[1], W. W. JOHNSON[2], K. L. MATTHEWS II[2], G. KNAPP[3], J. YUAN[3], J. GE[4], A BROOKS[3], D. VAN LOO[5], L. G. BUTLER[3]*,

[1]CAMD, Louisiana State University, Baton Rouge, LA, 70806, USA
[2]Department of Physics & Astronomy, Louisiana State University, Baton Rouge, LA, 70803, USA
[3]Department of Chemistry, Louisiana State University, Baton Rouge, LA, 70803, USA
[4]CCT, Louisiana State University, Baton Rouge, LA, 70803, USA
[5]X-Ray Engineering (XRE) bvba, De Pintelaan 111, 9000 Gent, Belgium
* presenting author

Keywords: X-ray interferometry, data processing, dark-field, 3D printing

Abstract

An interferometer is being constructed at the LSU CAMD synchrotron, a 2nd generation synchrotron with a newly installed 7-Tesla, 11-pole wiggler and double crystal Laue monochromator. With 70 keV interferometry, new opportunities are opened in materials science imaging. The LSU system is instrumented to measure vibrations during data collection. One of the team members has experience with the 4 km long optical interferometers used for the Laser Interferometer Gravitational-Wave Observatory (LIGO) project. The three-grating, stepped-grating interferometer will be operated with the gratings oriented either horizontally or vertically with respect to the tomography sample. High precision rotation stages should enable rapid and reliable grating alignment. The two-directional differential phase contrast data will be used for improved tomography reconstructions. The two-directional dark-field images are expected to show anisotropic structure in materials science samples.

Introduction

We are in the process of building two X-ray tomography/interferometry systems. The first system will be a synchrotron X-ray based system, intended to operate at 40 to 70 keV with an Oxford-made Laue monochromator downstream from a 7-Tesla, 11-pole wiggler. However, the new monochromator is not yet operational—new crystal mounts are being designed—so the system is now operating in a low-power mode with a microfocus X-ray tube.

When both instruments are completed, we should have a synchrotron-based system with monochromatic X-rays from 6 keV to over 70 keV at a flux enabling 50 ms exposure times. A complementary laboratory system will support a stationary sample surrounded by a gantry rotating about the vertical laboratory axis and holding an X-ray tube, detector, and interferometer.

Both interferometers are based on a stepped, three-grating Talbot-Lau geometry. The motor stages for the synchrotron system are installed and are being tested. The grating stages allow rotation of the linear gratings to access two-directional phase and scattering data from the tomography sample. The three gratings are positioned on an X95 rail to allow easy positioning for different X-ray energies and Talbot distances. With the X-ray tube, the detector is a Pilatus 100K. A PCO sCMOS will be used when the Laue monochromator is operational and the flux is an estimated 1000x greater.

Herein, we describe some of the data processing now used with the X-ray tube and to be transferred to the synchrotron-based system. The software features a workflow that enables a wide choice of grating step patterns, including both periodic and aperiodic grating motions. The intent of the aperiodic motions is to explore data acquisition

strategies that most effectively mitigate the image defects resulting from support structures needed for high-aspect ratio gratings.

Methods

The tomography/interferometry experiment generates a large number of sample and reference image files, leading to a formidable bookkeeping problem. First, at each sample rotation angle, a complete interferogram must be collected by stepping the moving grating over, for example, twelve different positions. Then, the sample rotation angle is incremented by either a fixed angle increment or changed based on the Greek golden ratio, as appropriate for slowly changing samples. One bookkeeping strategy is based on a data acquisition software that labels each image file with image type, whether sample or reference, as well as other key parameters: (a) grating step number within the interferogram, (b) sample rotation angle, and (c) image sequence number. We have found the image sequence number to be essential for processing data sets that may have an interruption. Our data acquisition software recovers from an interruption by first re-acquiring a reference interferogram, and then resuming full collection of an interferogram at a the interrupted sample rotation angle.

With the file naming strategy described above, the user can visually ascertain which files are needed to generate an interferogram for a given sample rotation angle, as well as which files are needed for generating the reference interferogram. We feel that user-understanding of the data processing is an important component of reliable experimentation. The list of filenames used to generate a sample projection and the corresponding reference filenames are always available during the data processing. For example, the images giving the interferogram shown in Fig. 1 have sequence numbers 499-510; the corresponding reference images have sequence numbers 451-462. The code processing all interferograms is parallelized; a simple If-test is used to recalculate the reference interferogram on that kernel if the reference filenames have been updated.

Fig.1 shows images corresponding to the transmission, visibility, and phase shift of

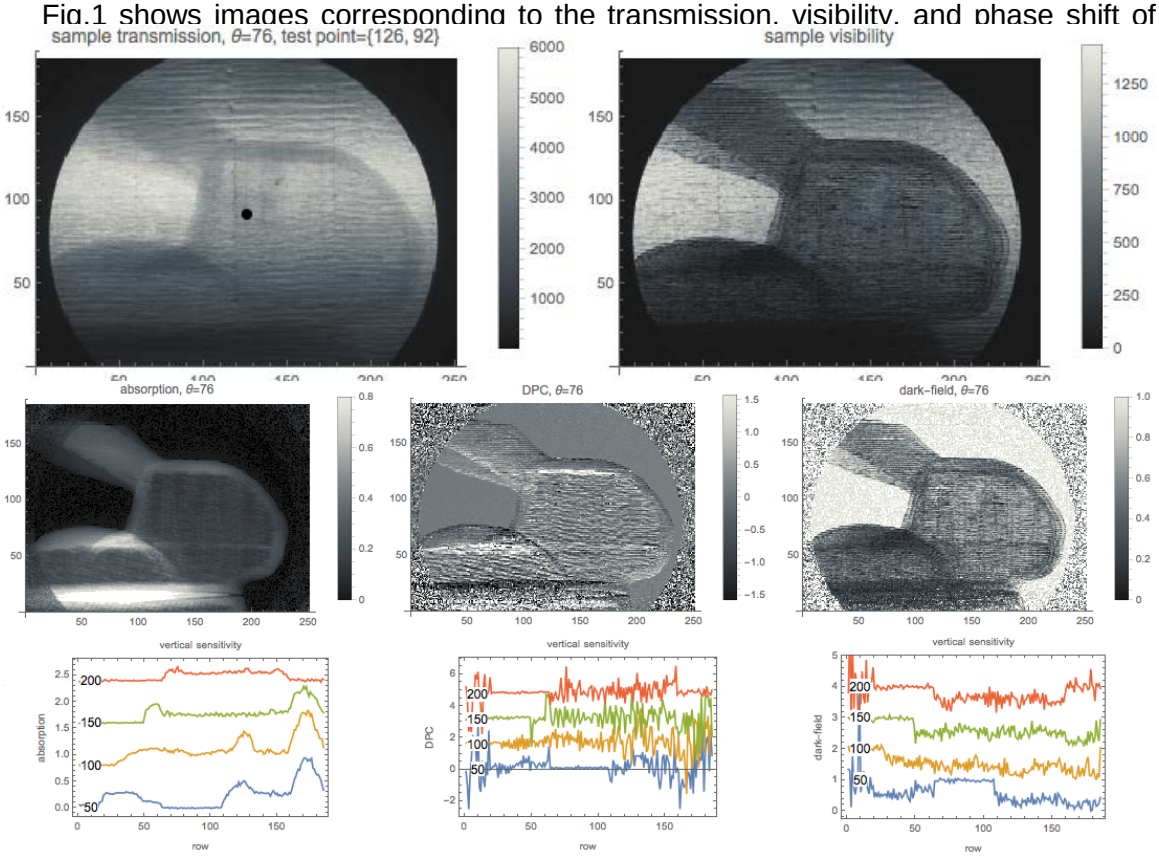

Fig. 2. *Absorption, differential phase contrast (vertical, radians) and dark-field (vertical) projections.*

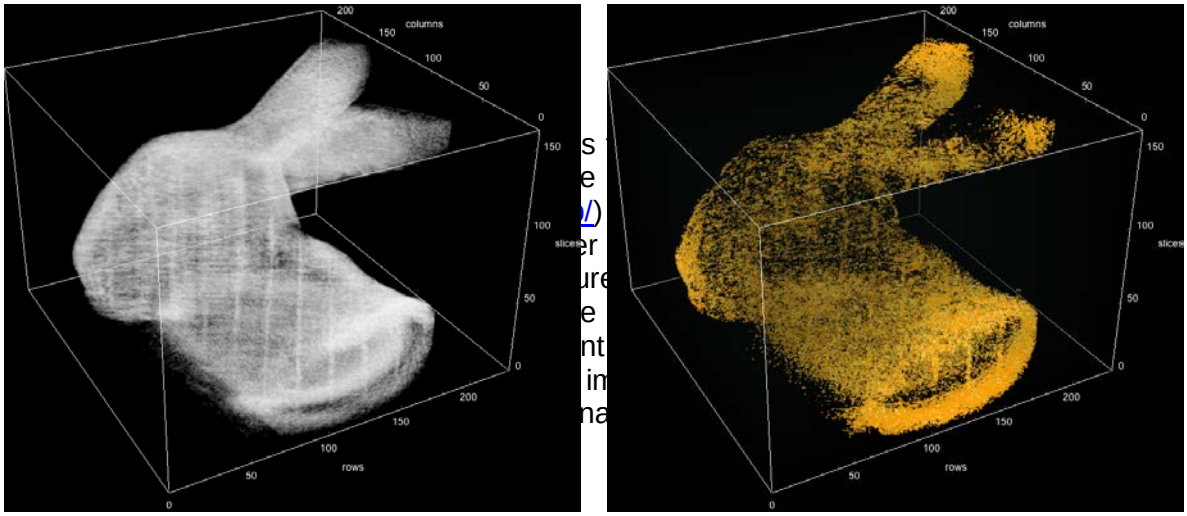

Fig. 3. *Absorption (left) and dark-field (right) volumes of a 3D print of the Stanford Bunny.*

Stepped-grating interferometry imaging offers unique insight into the structures of materials. The data processing is somewhat involved, but can be presented to the user in way that is perhaps more understandable with attention to human-readable filenames and analysis workflows that preserve the filename association.

References

[1] Marathe, S., L. Assoufid, X. Xiao, K. Ham, W. W. Johnson and L. G. Butler (2014). "Improved Algorithm for Processing Grating-Based Phase Contrast Interferometry Image Sets." Rev. Sci. Instrum. 85: art. no. 013704.

Proposed *In situ* analysis of 3D Printing Processes using Grating-Based X-ray Interferometry

*O. KIO[1], P. DAVIS[2], X. LI[3], J. GE[4], M. MATHIS[5], K. HAM[6], L. BUTLER[7]

[1] Department of Chemistry, Louisiana State University, Baton Rouge, Louisiana 70803. - okio1@tigers.lsu.edu
[2] Department of Construction Management, LSU- pdavis3@lsu.edu
[3] School of Electrical Engineering and Computer Science and Center for Computation and Technology, LSU - xinli@lsu.edu
[4] Center for Computation and Technology, LSU– jinghuage@cct.lsu.edu
[5] Department of Comparative Biomedical Sciences, School of Veterinary Medicine, Louisiana State University, Baton Rouge, Louisiana 70803. - jmathis@lsu.edu
[6] Center for Advanced Microstructures & Devices, Louisiana State University, 6980 Jefferson Hwy., Baton Rouge, LA 70806 – kham1@lsu.edu
[7] Department of Chemistry, LSU – lbutler@lsu.edu
* presenting author

Keywords: 3D printing, in situ experiments, interferometry, residual stress

Abstract

The performance of 3D printing will be evaluated through non-destructive analysis with grating-based X-ray interferometers. Two interferometers, one synchrotron–based and the other using a laboratory X-ray source, are currently being built. Application of interferometry will provide high quality images—absorption, differential phase contrast, and dark-field—that should better highlight errors such as dimensional errors, density variations, and sub-pixel defects. 3D images may also show evidence of residual stress. 2D movies acquired with single-shot interferometry will be used to study polymer flow from the printhead onto the structure; adhesion failure may be visible in phase contrast or dark-field images.

Introduction

The application of 3D printing has expanded beyond the production of prototypes to the manufacture of functional parts and end-user products with a growing range of sizes as well as materials. 3D printing, also known as rapid prototyping, involves layer-by-layer fabrication of parts by the controlled addition of material. Based on previous work at the Advanced Photon Source (APS) synchrotron observing polymer sample combustion, there are interesting opportunities for observation of 3D printing**.** The decomposition of a polymer during combustion can be viewed, in a time-reversal sense, as the controlled accumulation of a polymer, in other words, 3D printing. Previous work reported on the study of 3D printed materials have applied X-ray tomography and optical microscopy (Song & Nur, 2004; Gagg *et al.*, 2013). Tensile strength of 3D printed components can be improved by reinforcements. This has been investigated using a CAD model that takes build parameters into consideration (Sugavaneswaran & Arumaikkannu, 2014). This research work will combine X-ray interferometry with high-speed image capturing to provide images with better contrast compared to those obtained with conventional X-ray absorption imaging. Of interest are extrusion-based printers. Preliminary work was done on a few 3D printed objects. This involved X-ray CT scans on 3D printed bunnies (Stanford bunny) and cubes (Figure 1). The print quality metrics were assessed with the

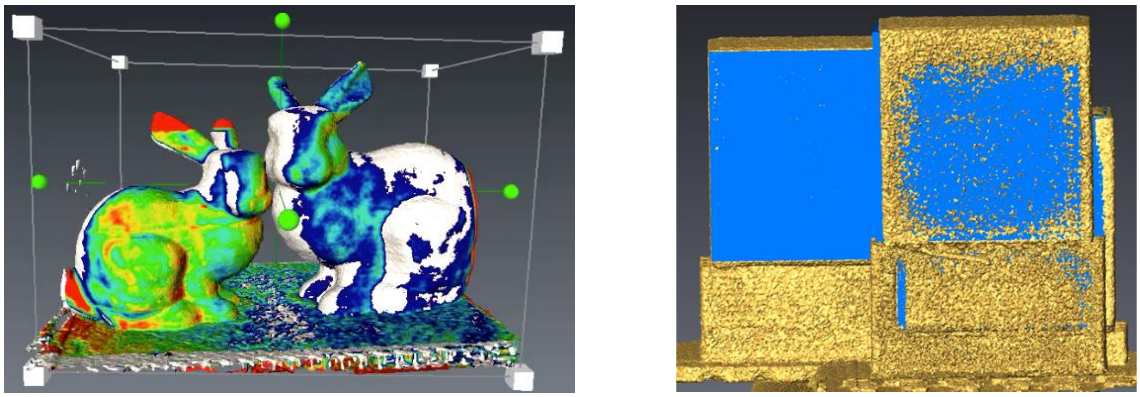

a b

Fig. 1. *(a) X-ray Tomography isosurface image and STL image of 3D printed bunnies (Stanford bunny) aligned. White color indicates surface of printed bunnies. Other colors indicate extent of variation between both surfaces. (b) X-ray Tomography isosurface image (gold color) and STL image (blue) of 3D printed cubes aligned. Evidence of anisotropy in printed cubes.*

iterative closest point algorithm incorporated in Avizo version 9 as well as a new algorithm developed at LSU.

Methods

I. The X-ray Tomography/Interferometry Systems

Two tomography/interferometry systems are currently being built at Louisiana State University (LSU). These systems will have different but complementary capabilities. The design parameters include stepped-gratings at various Talbot orders and orientations (horizontal or vertical) of the linear gratings with respect to the sample. One system will be based on X-ray synchrotron radiation of up to 70 keV while the other can study a stationary sample with its gantry-based microfocus X-ray tube and interferometer.

Synchrotron System: The first system is being built at the LSU CAMD synchrotron beamline. A combination of a 7 Tesla wiggler and Laue monochromator will produce X-rays to over 70 keV and provide a field-of-view 3 mm high and 4 mm wide. In the absorption mode the image digital resolution is 2 microns. In phase-contrast and dark-field modes, it is estimated to be 5 microns. The frame rate will be 10 Hz or higher as one of the detectors can operate at 300 Hz. With operation at 70 keV, this system will enable imaging of polymer-metal systems in addition to polymer systems. Due to the limited field of view, application of this system to 3D printing will involve extracting the printhead from the printer and mounting it above the tomography sample stage. The tomography sample stage can be programmed to generate simple 3D structures, especially straight and curved walls. Due to the high flux, this system is suited for both stepped-grating interferometry (Kottler *et al.*, 2007) and single-shot interferometry (Wen *et al.*, 2008; Wen *et al.*, 2010). We have previously used single-shot interferometry to study the burning of polymer/flame retardant blends, as shown below (Figure 2).

Laboratory System: The second system will utilize a microfocus tungsten target X-ray tube that can be operated at up to 130 kV. The cone-beam geometry facilitates a field of view of 8 cm x 8 cm or more (with image stitching). This system will have an image resolution on the order of 40 microns. Operation will involve a stationary sample and rotating gantry containing the X-ray tube, interferometer and the detector. This system is also suited for both stepped-grating interferometry and single-shot interferometry.

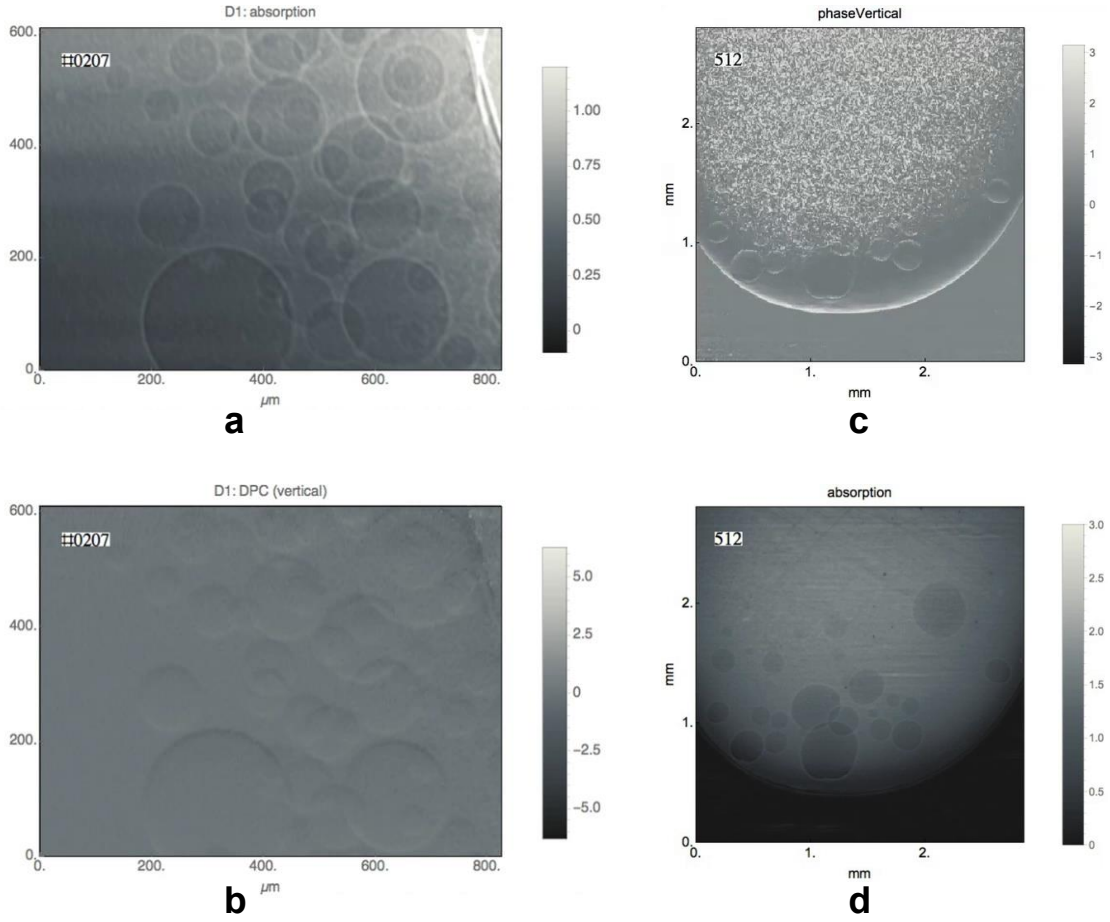

Fig. 2. *Four frames from absorption and differential phase-contrast (DPC) movies obtained for burning polymer using single-shot interferometry. (a) and (b) Images obtained using linear gratings. (c) and (d) Images obtained using checkerboard gratings. The irregular motion of the burning sample is challenging to image with a small field-of-view interferometer; the more predictable motion of a printhead should yield even better imaging results.*

II. Experimental Plan

During the course of printing, the printhead, the currently printed layer and a few older layers will constantly be in view as the print stage is gradually lowered. For this dynamic system single-shot interferometry will be used. The data quality is diminished–roughly to 30% of stepped-grating data–but data rate can be as fast as X-ray flux and detector frame rates permit. Single-shot interferometry was employed in observing the combustion of polymers at APS using single linear phase gratings first and later using checkerboard phase gratings (Wen *et al.*, 2008; Wen *et al.*, 2010). Checkerboard gratings provided good two-dimensional images but their small size limited the field of view. The linear gratings had a better field of view but could yield only one-dimensional images.

The printed objects will also be analyzed with the high-data-quality method of stepped-grating interferometry. Both interferometers will have grating stages to accommodate two-directional interferometry, particularly important for the integration of the differential phase contrast images (Kottler *et al.*, 2007). A new algorithm we developed for data analysis is both fast and can accommodate the imperfections in the X-ray optics currently available (Marathe *et al*., 2014). A CAMD spin-off company, the X-

ray Grating Factory, will explore grating/algorithm options to improve interferometry operation at high X-ray energies.

The internal and external dimensional quality of the 3D printed objects will be evaluated using phase contrast tomography. Phase contrast and dark-field imaging will result in clearly defined edges and better highlight the voids in print layers. Residual stress arising from print order will be investigated with dimensional information obtained using different print orders. A simple example is a cube printed in simple layer-by-layer order versus a square pyramidal structure. The image quality for widely varying materials will be evaluated as a function of X-ray energy up to 70 keV. Typical samples will be composed of discrete polymer and metal components. For image standards, resolution test objects for dimension, phase evolution, and dark-field image intensity will be developed. The printhead operation as a function of print speed, feed, ancillary motions, and feed/substrate temperatures will be observed. With feed/substrate temperatures, the possibility of autophobic dewetting will be taken into account (Reiter & Khanna, 2000a, 2000b).

Conclusion

Two distinct strategies will be explored for assessment of 3D printing performance: (1) fast single-shot X-ray interferometry for 2D movies of printhead operation and (2) high-quality, stepped-grating X-ray interferometry to generate 3D tomographic data sets of the printed object. The movies are expected to reveal the initiation of print defects due to high print rates or adhesion problems; 2D movies of burning polymer/flame retardant samples have been highly informative. The tomography data sets should, based on preliminary results, reveal evidence of residual stress within the printed object.

References

Song J. & Nur H. (2004). *Defects and prevention in ceramic components fabricated by inkjet printing*. ***Journal of materials processing technology*** *155*: 1286-1292.

Gagg G., Ghassemieh E., & Wiria F. E. (2013). *Effects of sintering temperature on morphology and mechanical characteristics of 3D printed porous titanium used as dental implant*. ***Materials Science and Engineering: C*** *33*, 7: 3858-3864.

Sugavaneswaran M. & Arumaikkannu G. (2014). *Modelling for randomly oriented multi material additive manufacturing component and its fabrication*. ***Materials & Design*** *54*: 779-785.

Kottler C., David C., Pfeiffer F., & Bunk O. (2007). *A two-directional approach for grating based differential phase contrast imaging using hard x-rays*. ***Optics Express*** *15*, 3: 1175-1181. doi: 10.1364/oe.15.001175

Wen H., Bennett E. E., Hegedus M. M., & Carroll S. C. (2008). *Spatial harmonic imaging of x-ray scattering—initial results*. ***Medical Imaging, IEEE Transactions on*** *27*, 8: 997-1002.

Wen H. H., Bennett E. E., Kopace R., Stein A. F., & Pai V. (2010). *Single-shot x-ray differential phase-contrast and diffraction imaging using two-dimensional transmission gratings.* ***Optics Letters 35, 12*: 1932-1934.**

Marathe S., Assoufid L., Xiao X., Ham K., Johnson W. W., & Butler L. G. (2014). *Improved algorithm for processing grating-based phase contrast interferometry image sets*. ***Review of Scientific Instruments*** *85*, 1: 013704.

Reiter G. & Khanna R. (2000a). *Real-time determination of the slippage length in autophobic polymer dewetting*. ***Physical review letters*** *85*, 13: 2753.

Reiter G. & Khanna R. (2000b). *Kinetics of autophobic dewetting of polymer films*. ***Langmuir*** *16*, 15: 6351-6357.

Session 201

Computed Tomography from Limited Data Using a Robust Discrete Algebraic Reconstruction Technique (R-DART)

X. ZHUGE*[1], K. J. BATENBURG[123]

[1] Centrum Wiskunde & Informatica (CWI), Science Park 123, 1098 XG Amsterdam, The Netherlands – zhuge@cwi.nl, joost.batenburg@cwi.nl
[2] Mathematical Institute, Leiden University, Niels Bohrweg 1, 2333 CA Leiden, The Netherlands
[3] IMinds-Vision Lab, University of Antwerp (CDE), Universiteitsplein 1, Building N, 2610 Wilrijk, Antwerp, Belgium
* presenting author

Keywords: Computed Tomography, Discrete Tomography, Sparse Reconstruction, Prior Knowledge

Abstract

Obtaining accurate reconstruction from a small number of projection images is of high importance in tomography applications. Discrete tomography incorporates prior knowledge in the reconstruction in terms of limited number of material compositions of the scanned object to achieve accurate reconstructions using significantly less data. In this work, we propose a robust discrete algebraic reconstruction technique (R-DART), which performs more consistently under noisy conditions than the original DART. Both numerical simulations and experimental results show that the proposed algorithm yields accurate reconstructions under practical conditions.

Introduction

In tomographic imaging, three-dimensional morphology and inner structures of the object can be reconstructed from a series of projection images acquired over a range of rotation angles. There are wide applications for tomography ranging from medical imaging (Herman, 2009) to material science (Midgley and Dunin-Borkowski, 2009). Achieving fast and accurate reconstruction from limited data is one of the major problems in current tomographic research. This is due to the fact that many practical considerations limit the number of projection angles and/or the angular range in applications. For example, reducing the applied dose on patients or biological samples is of high importance for medical imaging. Imaging moving objects also requires fast acquisition to reduce blurring cause by motion during acquisition. In electron tomography, there are many beam-sensitive materials which are easily damaged or changed during exposure to the electron beam. All these practical conditions requires the reconstruction algorithm to perform using limited data.

Many advanced reconstruction techniques have been proposed in the past for limited data problems. Most of them achieve such goal by exploiting the prior information we have on the object under imaging. For example, it has been shown that if the object has rather sparse boundaries, significantly improved reconstructions can be obtained by applying the total variation minimization technique (Beck and Teboulle, 2009). In another type of problem, the scanned object consists of only a few different materials, each corresponding to an approximately constant gray value in the reconstructed image. By incorporating this knowledge as prior information, discrete tomography (Batenburg and Sijbers, 2011) can produce superior reconstructions using significantly less data compared to conventional reconstruction methods such as the filtered backprojection (FBP).

Discrete Algebraic Reconstruction Technique (DART) is one of such algorithm that utilizes the discrete nature of the object. Assuming the gray values are known, DART

alternates iteratively between discretization steps of segmentation based on gray values, and continuous steps of reconstruction on the boundary of segmented image (Batenburg and Sijbers, 2011). DART has been successfully applied for reconstructing samples from applications in CT (Van Aarle, et al., 2014) and ET (Batenburg, et al., 2009). Despite its success in many cases, DART encounter problems when the projection data contain noise. The fact that DART imposes strict constrains on the boundary pixels during iterations leads to noise being spread over these boundary pixels. As a result, the reconstruction of the boundary regions becomes less accurate in the results from DART under noisy conditions.

In this paper, we propose a modified version of DART, named R-DART. Instead of segmenting the pixels and updating boundary pixels during iterations, the new algorithm only softly pushes the gray values toward discrete sets and the update is focused on both boundaries and regions where large changes of gray values took place. The results from simulations and micro-CT data of polyurethane foam show that the proposed algorithm performs accurate reconstruction in practical noisy conditions using limited number of projection images.

Methods

DART alternates between a continuous algebraic reconstruction step and a discrete segmentation step, and uses a well-designed procedure to gradually improve the segmented solution (Batenburg and Sijbers, 2011). The algorithm starts with an initial continuous reconstruction using an algebraic reconstruction method (ARM). SIRT or SART are typically used. As the first step, a hard segmentation is applied on the reconstruction, rounding all pixels into the nearest gray value. In the second step, *boundary* pixels that have at least one neighbor pixel with a different gray value, and some randomly chosen pixels from the non-boundary region are selected as *free* pixels. The probability of a *non-boundary* pixel to be classified as *free* pixel is $1-p$, with p known as the *fix probability*. In the third step, the unknowns corresponding to the pixels other than *free* pixels, known as *fixed* pixels, are removed from the system of linear equations. Then the *free* pixels are updated with a continuous reconstruction step with ARM. In the fourth step, the free pixels are smoothed with a Gaussian filter of a small kernel as a way to regulate strong fluctuations. The whole procedure iterates between step 1 and 4 until a termination criteria is met.

The main reason behind DART's problem of dealing with noisy projections is rooted on the strategy of the algorithm which pushes abruptly the pixels toward discrete gray values in each iteration and fix the flat regions of the segmented image assuming these pixels are accurately reconstructed. This leads to spread of errors and noise in the boundary pixels. In this work, we proposed a robust discrete algebraic reconstruction technique (R-DART), where a new procedure is utilized to deal with these problems.

Two main changes are made on the algorithm. First in step 1, the hard segmentation step is replaced with a soft segmentation step where the pixels are gently pushes toward the specified gray values. Specifically, pixels with values that is close to either the specified gray values or thresholds are only slightly altered while the ones far away are rounded further toward the nearest gray values. The reasoning behind such function is based on the probability of errors. When the value of pixel is close to the threshold (in between of two adjacent gray values), it is less certain whether it is the correct move to abruptly round it towards one of the nearest gray values. On the other hand, pixels with values which is already close to the specified gray values are only slightly altered in order to cope with inconsistencies caused by the presence of noise in the projection data. The second change is made on the second step of the algorithm. The pixels that are greatly altered during the soft segmentation step are also selected as free pixels,

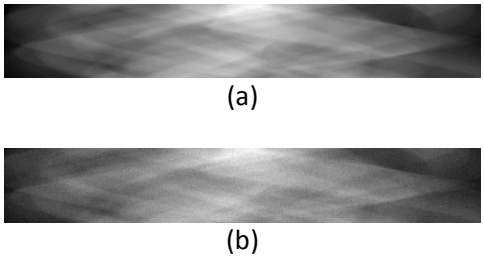

Fig. 1. Simulated projection data at different noise levels. (a) photon count of 50k, (b) photon count of 5k

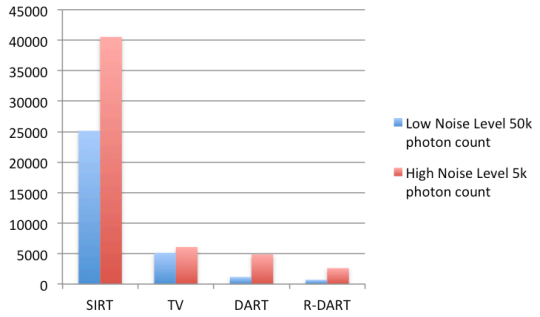

Fig. 2. Comparison of phantom pixel errors from reconstructions of different algorithms, including SIRT, TV, DART and the proposed R-DART.

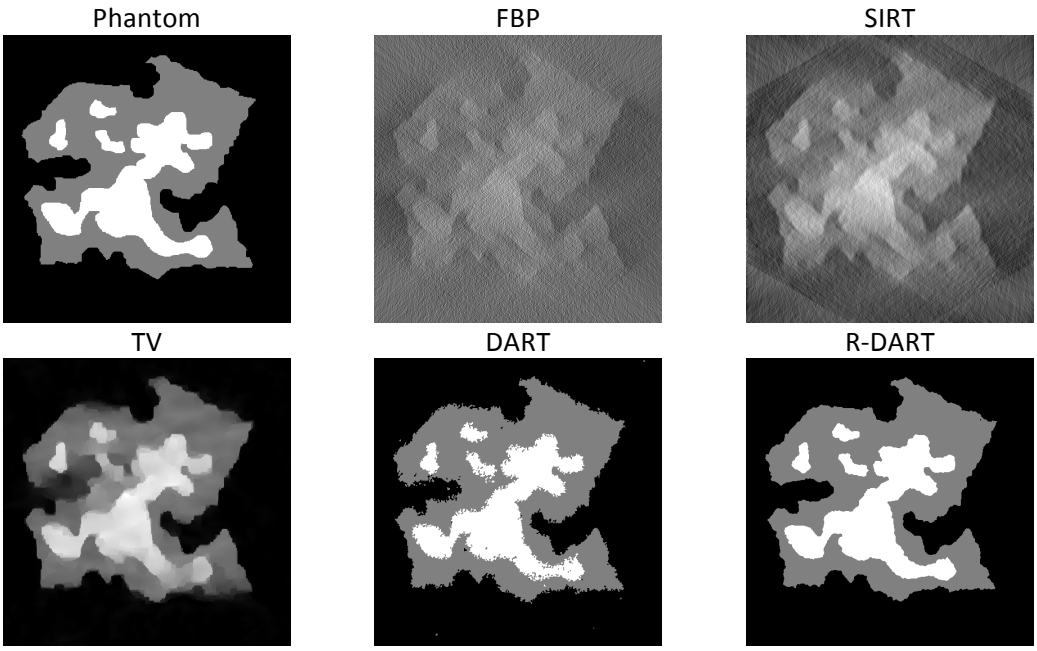

Fig. 3. Reconstructions of simulated projection data under 5K photon counts, 61 projection images within the limited angular range of -60 to 60 degrees

besides the previous choice of boundary pixels. By smoothly steering the solution toward discrete gray values, the R-DART algorithm is less sensitive to noise and mismatches in the data than the original DART implementation.

Experiments and Results

Numerically simulated data are first used to investigate the behavior of the proposed algorithm and evaluate its performances. The complete algorithm is implemented using the ASTRA Tomography Toolbox (Palenstijn, et al., 2013), where basic forward and backward projection operations are efficiently computed in parallel using Graphical Processing Unit (GPU). The used 2D phantom is 512x512 pixels in size and contains 3

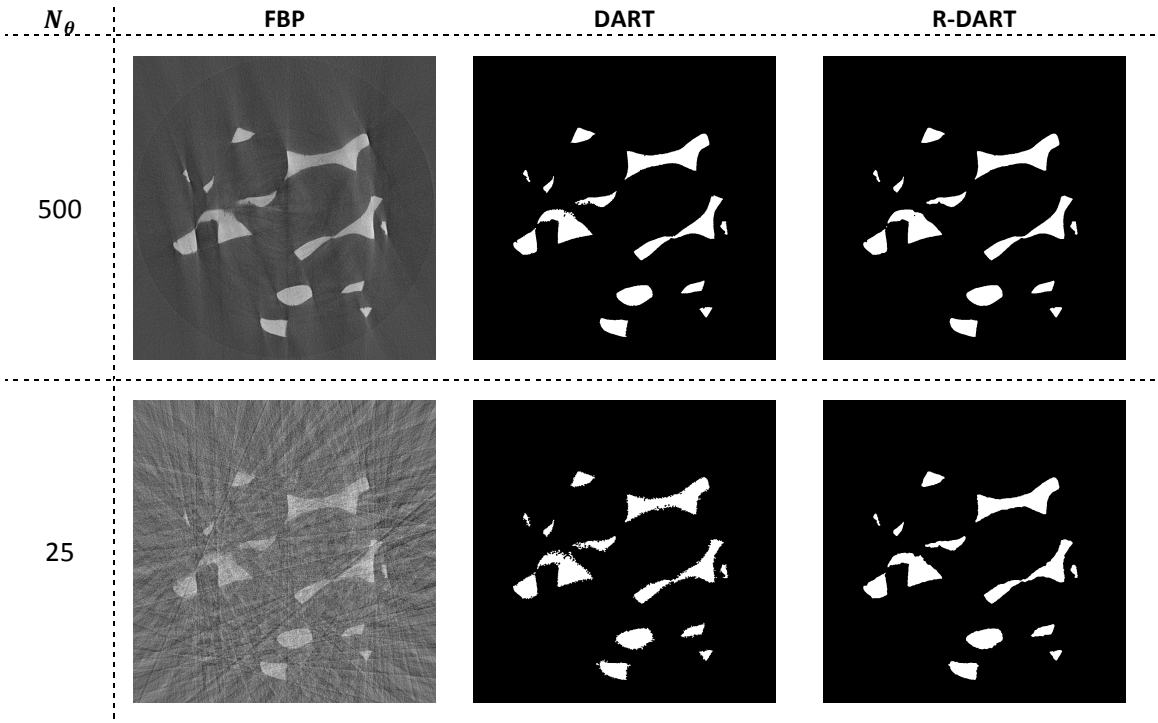

Fig. 4. Experimental results of μ CT scan of polyurethane foam. Reconstructions from different algorithms using all 500 projections and only 25 out of the available angles are compared.

discrete gray values. The projection data (sinogram) is generated assuming parallel beam geometry. The Radon transform of the phantom is first computed and further polluted with Poisson noise assuming different maximum photon counts. The generated projection data under two different noise levels with 61 projection angles from a limited angular range of 120 degrees are illustrated in Figure 1. Four algorithms are used here for comparison with R-DART: Filtered Back Projection (FBP), Simultaneous Iteration Reconstruction Technique (SIRT), Total Variation Minimization (TV) and DART. The comparison of phantom pixel errors (number of pixels different from the phantom) is shown in Figure 2., while Figure 3 shows the reconstructed images under high noise level. It is clear the proposed R-DART algorithm out performs all other techniques even under noisy and limited data conditions.

Figure 4 shows the reconstruction of polyurethane foam taken with a SkyScan 1172 µCT scanner. Here we not only compare the results of a single slice of the full 3D reconstruction from FBP, DART and R-DART, but also evaluate the reconstructions degrade when only a small subset angles out of the complete 500 projections is used. The results indicate that R-DART is able to maintain a high level of accuracy even using only 25 projections, in contrast to the significantly degraded results from FBP and DART.

Conclusions

In this paper, we proposed a robust discrete algebraic reconstruction technique (R-DART), which is oriented for discrete tomography under challenging and noisy conditions. We show that the proposed algorithm is capable of producing accurate

reconstruction under limited number of projection angles, small angular range and high level of noise. This could give rise to advances in many CT applications in material science in practice.

Acknowledgement

This work is supported in part by the Technology Foundation STW (Veni grant No. 13610), the Netherlands Organization for Scientific Research (NWO) (Vidi grant No. 639-072-005) and ExxonMobil Chemical Europe Inc. We would like to thank Dr. Anton-Jan Bons from European Technology Center at ExxonMobil Chemical Europe Inc. for his support within our joint project. We thank Prof. Jan Sijbers from iMinds - Vision Lab at the University of Antwerp for providing the μCT datasets. Networking support was provided by the EXTREMA COST Action MP1207.

References

Beck, A., and Teboulle, M. (2009). A Fast Iterative Shrinkage-Thresholding Algorithm for Linear Inverse Problems. SIAM Journal on Imaging Sciences 2, 183–202.

Batenburg, K.J. (2005). An evolutionary algorithm for discrete tomography, Discrete Appl. Math. 151 36-54.

Batenburg, K.J., Sijbers, J. (2011). DART: a practical reconstruction algorithm for discrete tomography, IEEE Trans. Image Process., vol. 20, no. 9, pp. 2542-2553.

Herman G.T. (2009). Fundamentals of computed tomography: Image reconstruction from projection. 2Nd ed, Springer.

Midgley P.A. and Dunin-Borkowski R.E. (2009). Electron tomography and holography in materials science. Nat. Mater. 8, 271-280.

Palenstijn, W.J., Batenburg, K.J., Sijbers, J. (2013). The ASTRA Tomography Toolbox, 13th International Conference on Computational and Mathematical Methods in Science and Engineering, CMMSE.

Van Aarle, W., Batenburg, K.J., van Gompel, G., van de Casteele, E., Sijbers, J. (2014). Super-Resolution for Computed Tomography Based on Discrete Tomography, IEEE Trans. Image Process., vol. 23, pp. 1181-1193.

Van Aert, S., Batenburg, K.J., Rossell, M. D., Erni, R., and Van Tendeloo, G. (2011). Three-dimensional atomic imaging of crystalline nanoparticles, Nature, 470, 374-377.

A new method for measuring grain displacements in granular materials by X-ray computed tomography

M-H. Khalili*, S. Brisard, M. Bornert, J-M. Pereira, M. Vandamme and J-N. Roux

Université Paris-Est, Laboratoire Navier (UMR 8205), CNRS, ENPC, IFSTTAR, F-77455 Marne-la-Vallée

*presenting author : mohamed-hassan.khalili@enpc.fr

We aim to measure the individual grain displacements in a granular material under constant load (creep). X-ray computed tomography imaging provides images of the granular medium microstructure during the experiment, and discrete volumetric image correlation (DV-DIC) [1] allows the determination of the grain individual rigid body motion from the reconstructed tomography images. However, for short-term creep, and time-resolved experiments in general, the sample evolutions can be very quick and occur before the full tomography scan is complete. This constitutes a serious limitation of standard experimental procedures for the investigation of the micromechanics of the creep of granular media at the grain scale.

We present a new method for measuring grain displacements, that overcomes the above-mentioned limitation. Indeed, in a granular material, assuming no breakage occurs, each grain undergoes a rigid body motion. Therefore, the displacement field reduces to a set of six degrees of freedom per grain. This suggests that the information contained in a full set of projections (necessary to perform an accurate 3D reconstruction) is excessively redundant for the determination of the grain displacements. Our method requires only few projections of the sample at its current state, thus reducing dramatically the acquisition time. Displacements are estimated from the projections directly, without 3D reconstruction.

Our method is formulated as an inverse problem. A forward model based on Beer-Lambert's law is developed to efficiently perform numerical projections. The grain displacements are estimated by fitting the numerical projections to experimental projections of the current state of the sample.

We also study the sensitivity of the estimated displacements to image noise, both numerically and through a theoretical model which highlights the influence of the setup parameters on the measurements.

The method has been validated and its accuracy assessed against 2D and 3D numerical experiments on virtual microstructures.

Keywords: Displacements measurement, X-ray tomography, granular medium

1 Introduction

Investigating micro-scale mechanisms in granular materials is an increasing trend to understand their macro-scale behavior. X-ray imaging tomography is an efficient way to characterize the evolution at the scale of the grain during a mechanical experiment. Once the tomographic projections are acquired and 3D image reconstruction is performed, Digital Image Correlation techniques (DIC) [2, 3, 4] can be used to measure strain fields. While this approach considers the medium as a continuum, more recent works provide a discrete analysis of the medium where grains are individuated, as for the Discrete Volumetric DIC (DV-DIC) [1] or ID-Track [5] techniques. In this work, we present an alternative approach, where displacements of grains are directly measured on the tomographic projections (as opposed to the reconstruction). This new approach allows us to reduce the number of required projections and thus the acquisition time, so that it is better suited to study time-resolved phenomena.

2 General principles

The proposed method consists in resolving an inverse problem that was formulated on the tomographic projections rather than the reconstructed images. From a reconstruction of the initial state, grains are individuated in order to compute numerical projections where a trial rigid body motion is applied to every grain. Then, we estimate the grain displacements in the current state by fitting the numerical projections to the measured experimental projections of the current state. This fitting is performed through minimization of an objective function that we define as follows:

$$\mathrm{F}(\mathbf{q}) = \sum_{\theta} \sum_{\underline{p}} \left(\hat{P}(\theta, \underline{p}; \mathbf{q}) - P(\theta, \underline{p}) \right)^2 \tag{1}$$

where $\mathbf{q}$ is a column-vector that gathers the parameters defining the rigid body motion of each grain. The forward model $\hat{P}(\theta, \underline{p}; \mathbf{q})$ gives a numerical projection of the medium for a trial generalized displacement $\mathbf{q}$; $\underline{p}$ is the pixel of the detector, and θ is the rotation angle of the sample stage. It is detailed in the next section, and more details can be found in [6]. $P(\theta, \underline{p})$ is the measured experimental projection.

3 Forward problem

The forward problem aims to compute numerical projections of the granular medium for any given trial generalized displacement $\mathbf{q}$. For a grain i in some reference position in the sample, the intensity measured at the pixel $\underline{p}$ of the detector is given by the Beer–Lambert's law as follows:

$$I(\underline{p}) = I_0 \exp\left(- \int \mu^{(i)} \left(\underline{p} + s\underline{T}(\underline{p}) \right) \mathrm{d}s \right), \tag{2}$$

where I_0 is the initial X-ray intensity, $\underline{T}(\underline{p})$ denotes the direction of the ray going from the source to the center of pixel $\underline{p}$, and crossing the grain. s denotes the arc-length along the

ray $(\underline{p}, \underline{T}(\underline{p}))$ and $\underline{x} \mapsto \mu^{(i)}(\underline{x})$ is a mapping of the local linear attenuation coefficient of grain i in some reference position. In what follows we define the projection as the integral of the attenuation. Assuming the sample stage to be rotated by an angle θ, let $\hat{P}^{(i)}(\theta, \underline{p}; \mathbf{q}^{(i)})$ denote the projection at pixel $\underline{p}$ of the i-th grain subjected to the rigid body motion defined by $\mathbf{q}^{(i)}$. Then, from Eq. (2)

$$\hat{P}^{(i)}(0, \underline{p}; \mathbf{0}) = \int \mu^{(i)} \left(\underline{p} + s\underline{T}(\underline{p}) \right) \mathrm{d}s, \tag{3}$$

Given a segmented image of the medium, the projection of the medium can be evaluated as the sum of the projections of the individual grains moved according to their respective rigid body motion parameters. With the assumption of null absorption outside the grain,

$$\hat{P}(\theta, \underline{p}; \mathbf{q}) = \sum_i \hat{P}^{(i)}(\theta, \underline{p}; \mathbf{q}^{(i)}), \tag{4}$$

where $\mathbf{q}^{(i)}$ is the part of $\mathbf{q}$ containing the degrees of freedom of the i-th grain. $\mathbf{q}^{(i)}$ can also be expressed as a rotation tensor $\underline{\underline{\Omega}}^{(i)}$ and translation vector $\underline{u}^{(i)}$, by choosing an adequate parameterization [7]. Now, consider that the grain underwent a rigid body motion $(\underline{u}^{(i)}, \underline{\underline{\Omega}}^{(i)})$ with respect to its reference position and that the sample is rotated by an angle θ (the corresponding rotation tensor is $\underline{\underline{R}}_\theta$), then

$$\hat{P}^{(i)}(\theta, \underline{p}; \mathbf{q}^{(i)}) = \int \mu^{(i)} \left({\underline{\underline{\Omega}}^{(i)}}^T \cdot \left[\underline{\underline{R}}_\theta^T \cdot \left(\underline{p} + s\underline{T}(\underline{p}) \right) - \underline{u}^{(i)} \right] \right) \mathrm{d}s. \tag{5}$$

In practice, the attenuation field is voxelized, which leads us to evaluate (5) for every voxel. It reduces to the summation of the intersection lengths of the ray with voxels it crosses weighted by the attenuation coefficient at that voxel. This summation is efficiently evaluated by means of Siddon's algorithm [8]. However, a further numerical gain can be made if we only consider the set of rays that actually intersect a given grain. This was achieved by the introduction of a minimal bounding box that contains the grain.
For the applications of the method, an improved version of Siddon's algorithm proposed by Jacobs [9] was implemented and adapted to our context.

4 Numerical test of the method

In this section, we present a numerical validation of the method. Results of simulations, based on numerically generated "experimental" projections, are given for planar 2D and full 3D situations.

Materials To perform numerical experiments, we need a segmented reference image of the medium. For the 2D case, we obtained this image from 30 grains taken from a cross section of a real tomography image of a Hostun sand. These grains were randomly distributed in an array of size 500x500 pixels to form an aggregate of 300 grains. For the 3D case, two grains extracted from the same sand image were distributed in a volume of 100x100x100 voxels.

Simulations For both cases, we create experimental projections by applying a displacement field to the grains, with translations of the grain centers randomly chosen between -1 and 1 pixel and rotation angles between -0.1 and 0.1 radians. These projections were computed by means of the forward model developed in Sec. 3. Then, we used a Levenberg–Marquart algorithm[1] to carry out the minimization starting from an initial guess $\mathbf{q}_0$ equal to the reference state.

Results In the 2D case, simulations of individual grains and of groups of grains (up to 300 grains) were successful with only two projections for individual grains and six projections for the group simulations.
For the 3D case, we ran simulations with two grains. Two different simulations are presented here, in parallel beam and cone beam projections. The results show that for the cone beam case, the simulation returns the exact applied displacements, while in the parallel case an error on the translation component along the sample rotation axis is observed. This is due to the fact that in parallel beam setup a translation along this direction, with an amplitude below the pixel size, does not induce any change to the simulated projections and hence, cannot be measured.
To deal with this issue improvements of the forward model taking into account a heterogeneous attenuation inside voxels and integration of rays over the width of the pixels will be explored.

5 Accuracy assessment

In this section, we evaluate the influence of noise in the projections on the accuracy of the methods. As expected, introducing noise in the previously presented simulations induces errors on the solution, i.e. a deviation of the minimum of the objective function with respect to its value without noise. This deviation can be characterized by its bias and its standard deviation from a statistical set of randomly chosen image noise. Following the procedures described in [10, 11], this error can also be evaluated by a theoretical perturbation analysis, assuming a white noise with uniform standard deviation σ. To do so, we assume the error on displacement sufficiently small so that the objective function can be linearized about its minimum without noise $\mathbf{q}^\star$, and write:

$$\mathbf{q} = \delta\mathbf{q} + \mathbf{q}^\star. \tag{6}$$

The objective function with noise $N(\theta, \underline{p})$ added to the experimental projections reads:

$$\mathrm{F}^N(\mathbf{q}) = \sum_{\theta,\underline{p}} \left[\hat{P}(\theta, \underline{p}; \mathbf{q}) - \left(\hat{P}(\theta, \underline{p}; \mathbf{q}^\star) + N(\theta, \underline{p})\right)\right]^2 \tag{7}$$

According to the noiseless simulations $P(\theta, \underline{p})$ was taken equal to $\hat{P}(\theta, \underline{p}; \mathbf{q}^\star)$. Then, assuming the perturbation induced by noise is sufficiently small, we can write:

$$\hat{P}(\theta, \underline{p}; \mathbf{q}) = \hat{P}(\theta, \underline{p}; \mathbf{q}^\star) + \delta\mathbf{q}^T \cdot \frac{\partial \hat{P}}{\partial \mathbf{q}}\left(\theta, \underline{p}; \mathbf{q}^\star\right), \tag{8}$$

[1] Provided by Scipy package for Python

and get the expression of the error:

$$\delta\mathbf{q} = \mathbf{M}^{-1} \cdot \mathbf{b}^N \tag{9}$$

with :

$$\mathbf{M} = \sum_{\theta,\underline{p}} \frac{\partial \hat{P}}{\partial \mathbf{q}} \left(\theta, \underline{p}; \mathbf{q}^\star\right) \cdot \frac{\partial \hat{P}}{\partial \mathbf{q}}^T \left(\theta, \underline{p}; \mathbf{q}^\star\right) \qquad \mathbf{b}^N = \sum_{\theta,\underline{p}} N(\theta, \underline{p}) \frac{\partial \hat{P}}{\partial \mathbf{q}} \left(\theta, \underline{p}; \mathbf{q}^\star\right) \tag{10}$$

Assuming uniform white noise over the pixels $(\theta, \underline{p})$, we obtain the statistical expectation $\mathrm{E}[\delta\mathbf{q}]$ and variance $\mathrm{var}(\delta\mathbf{q})$ of this error:

$$\mathrm{E}\left[\delta\mathbf{q}\right] = \mathbf{M}^{-1} \cdot \mathrm{E}[\mathbf{b}^N] = 0 \qquad \mathbf{\Sigma}^2 = \mathrm{var}\left(\delta\mathbf{q}\right) = \mathrm{E}[\delta\mathbf{q} \cdot \delta\mathbf{q}^T] = \sigma^2\mathbf{M}^{-1} \tag{11}$$

Further developments show that the matrix $\mathbf{M}$ is block diagonal with blocks associated to individual grains, which means that the error induced by white image noise on the results of one grain displacements does not depend on the other grains. This property allows us to study individual grain for the evaluations of matrix $\mathbf{M}$.

Figure 1 shows the evolution of the standard deviation $\sqrt{\Sigma_{11}^2}$ of a displacement of one grain in the 2D case. It corresponds to the horizontal translation along the plane of the detector. It was computed in two different ways. The first way is by numerical estimation of the matrix $\mathbf{M}$, where its components were computed by means of the forward model developed in 3. The second method is by running 10 simulations with different noise realizations and directly compute the standard deviation from the results (Monte-Carlo simulations). The signal to noise ratio P_{max}/σ was set to 500. This value gives a noise level that is slightly greater than the maximal noise level observed in our local tomography facility.

The two computations were performed for several numbers of projections. We can see that the results from the model are in good agreement with simulations. We also observe how increasing the number of projections reduces the noise error. Similar behaviors are observed for the other components of the translation and the rotation. At about 30 projections, the standard deviation amplitudes are comparable to theoretical ones estimated for a cubic shape in [10] for standard DV-DIC routines. At 60 projections the values of errors become lower by one order of magnitude and start to stabilize with respect to the increase of the number of projections.

6 Conclusion

In this work, we developed a new technique that bypasses the 3D reconstruction stage, and measures the displacements directly from tomographic projections. The acquisition time is dramatically reduced, which makes this technique well suited to investigate fast evolutions such as short-term creep. We presented in this paper a numerical validation to illustrate the feasibility of this technique. Finally, we probed the effect of image noise and proposed a model to estimate the error induced by noise.

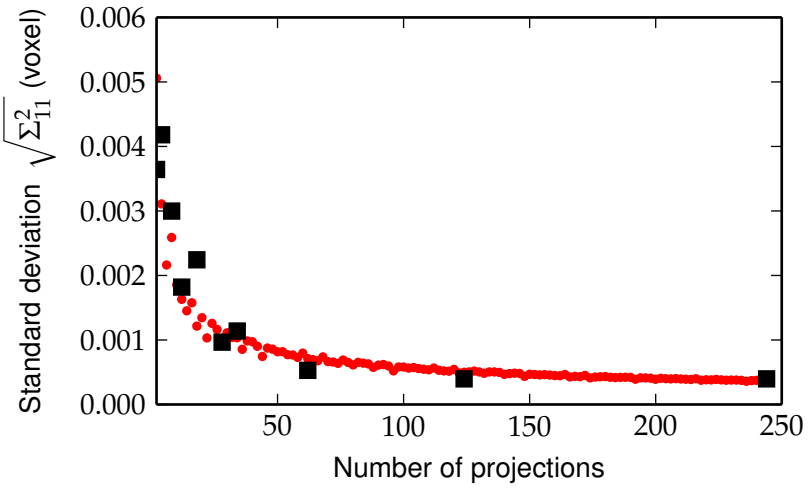

Figure 1 – Standard deviation of the estimated translation of the center of the grains, versus the number of used projections: Black squares indicate results of Monte-Carlo simulations (using 10 realizations for each simulation). The red points are the standard deviation estimated from our model [see Eqs. (9), (10) and (11)].

Acknowledgment: This work has benefited from a French government grant managed by ANR within the frame of the national program Investments for the Future ANR-11-LABX-022-01

References

[1] S-A. Hall, M. Bornert, J. Desrues, , Y. Pannier, N. Lenoir, , G. Viggiani, and P. Bésuelle. Discrete and continuum analysis of localised deformation in sand using X-ray μCT and volumetric digital image correlation. *Géotechnique*, 60(5):315–322, January 2010.

[2] B. K. Bay, T. S. Smith, D. P. Fyhrie, and M. Saad. Digital volume correlation: Three-dimensional strain mapping using X-ray tomography. *Experimental Mechanics*, 39(3):217–226, 1999.

[3] M. Bornert, J-M. Chaix, P. Doumalin, J-C. Dupré, T. Fournel, D. Jeulin, E. Maire, M. Moreaud, and H. Moulinec. Mesure tridimensionnelle de champs cinématiques par imagerie volumique pour l'analyse des matériaux et des structures. *Instrumentation, Mesure, Métrologie*, 4(3-4):43–88, 2004.

[4] N. Lenoir, M. Bornert, J. Desrues, P. Bésuelle, and G. Viggiani. Volumetric digital image correlation applied to x-ray microtomography images from triaxial compression tests on argillaceous rock. *Strain*, 43(3):193–205, 2007.

[5] E. Andò, S-A. Hall, G. Viggiani, J. Desrues, and P. Bésuelle. Grain-scale experimental investigation of localised deformation in sand: a discrete particle tracking approach. *Acta Geotechnica*, 7(1):1–13, November 2011.

[6] M-H. Khalili, S. Brisard, M. Bornert, J-M. Pereira, M. Vandamme, and J-N. Roux. Measuring grain displacements in a granular medium by means of X-ray microtomography: a reconstruction-free approach. In preparation.

[7] O. Rodrigues. Des lois géométriques qui régissent les déplacements d'un système solide dans l'espace, et de la variation des coordonnées provenant de ces déplacements considérés indépendamment des causes qui peuvent les produire. *Journal de Mathématiques Pures et Appliquées*, 5:380–440, 1840.

[8] R-L. Siddon. Fast calculation of the exact radiological path for a three-dimensional CT array. *Medical Physics*, 12(2):252, 1985.

[9] F. Jacobs and E. Sundermann. A fast algorithm to calculate the exact radiological path through a pixel or voxel space. *J. Comput. Inf. . . .*, 1998.

[10] Y. Pannier, N. Lenoir, and M. Bornert. Discrete volumetric digital image correlation for the investigation of granular type media at microscale: accuracy assessment. *EPJ Web of Conferences*, (Dic), 2010.

[11] S. Roux and F. Hild. Stress intensity factor measurements from digital image correlation: post-processing and integrated approaches. *International Journal of Fracture*, pages 1–37, 2006.

Assessment and reduction of the scatter effects in an industrial 300kV micro-focus CT system

M. PLAMONDON*[1], P. SCHUETZ[2], T. LUETHI[1], J. HOFMANN[1], A. FLISCH[1]

[1] Empa, Swiss Federal Laboratories for Materials Science and Technology, Dübendorf, Switzerland – Mathieu.Plamondon@empa.ch, Thomas.Luethi@empa.ch, Juergen.Hofmann@empa.ch, Alexander.Flisch@empa.ch
[2] Lucern University of Applied Sciences and Arts, Horw, Switzerland – philipp.schuetz@hslu.ch
* presenting author

Keywords: Scatter, micro-focus, industrial-CT

Abstract

In this contribution, we investigate the influence of individual CT components on scattered radiation registered on the detector using Monte Carlo (MC) simulations. This assessment is performed on a system with a 300kV micro-focus source. A proposed correction factorizes the various scatter sources. The scattering due to the object is estimated using a simplified MC model. Exploiting parallelism and a variance reduction technique, all scatter contributions can be evaluated in a sufficiently short time suitable for the integration into the workflow of an industrial CT appliance.

Introduction

High energetic X-ray photons are scattered in both the object and components of a computed tomography (CT) system, causing artefacts and a loss in effective dynamic range. The influence of each CT components on scattered radiation can be estimated using Monte Carlo (MC) simulations. This assessment is performed on an upgraded system with a 300kV micro-f5ocus source (Finetec FOMR300.0) and flat-panel detector (Perkin-Elmer XRD 1621 AN14 ES) as shown in Fig. 1.

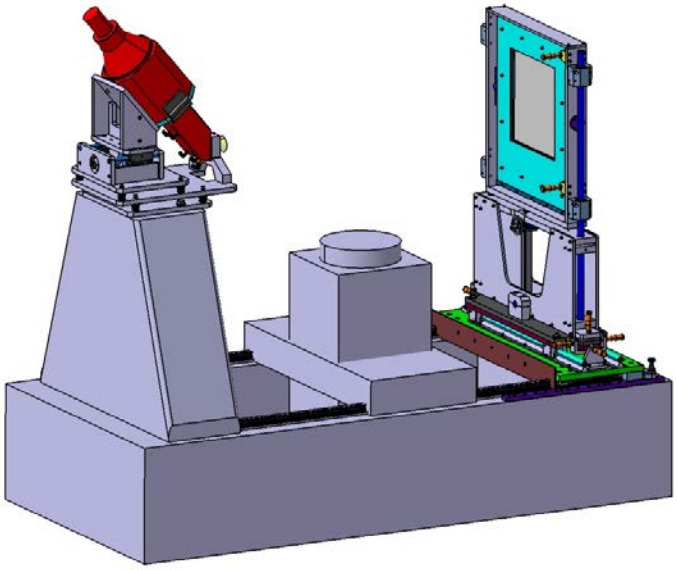

***Fig. 1** Schema of the 300 kV micro-focus setup.*

The energy regime involved requires a careful study of the scatter. Fig. 2 illustrates well this fact in the case of 300kV spectrum filtered by 2mm of copper. The signal attenuation is dominated by Compton processes even in the case of material like stainless-steel.

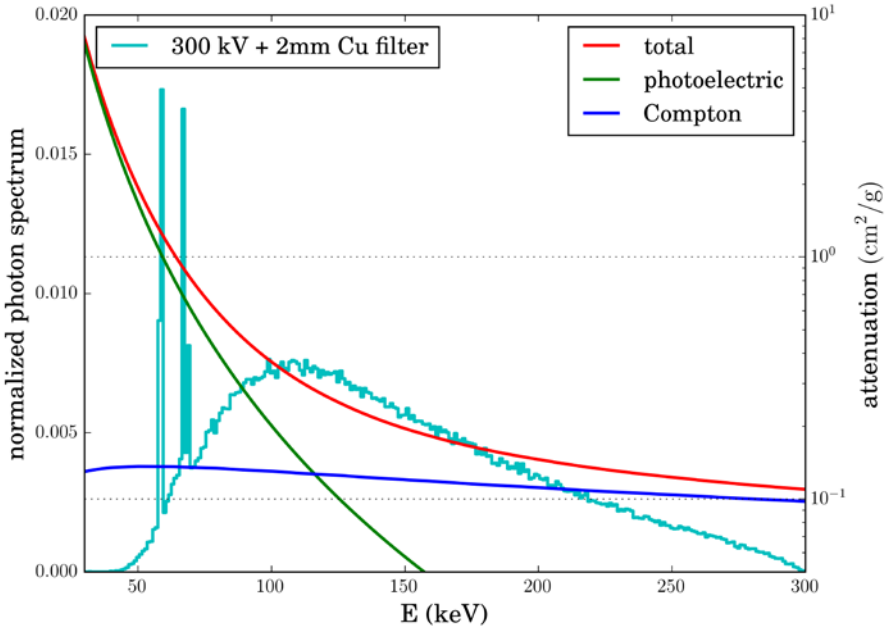

Fig. 2 *Filtered spectrum superimposed with the two main physics processes in the case of stainless-steel.*

Methods

A detailed GEANT4[1)] simulation framework of the source, detector and hall has been developed for this purpose (see Fig. 3). Applying the recipe from a previous study[2)], a 75% reduction of the hall scatter, i.e. the intensity of radiation scattered in the hall and detected on the flat panel, is estimated by the use of specially designed lined walls. Minimized in such a way by hardware modifications, the signal intensity of the hall scatter I_{hall} is kept below 0.5% of the flat-field level I_{flat}.

Simple modifications to the detector housing would also allow reducing the internal detector scatter I_{det} by a factor 3 to less than 3% of I_{flat}. The strengths of these two scatter contributions, respectively $T_{hall}=I_{hall}/I_{flat}$ and $T_{det}=I_{det}/I_{flat}$, are expected to show weak spatial variations and can be characterized experimentally with in-situ measurements.

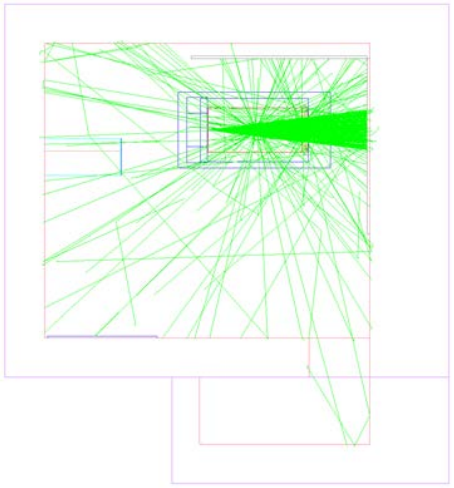

Fig. 3 *Simulation of the environmental scatter (hall and internal to the detector).*

The measured transmission T_{meas} is then decomposed in the following way

$$T_{meas} = \frac{I_{sig} + I_{hall} + I_{obj+det}}{I_{flat} + I_{hall} + I_{det}}$$

which leads to this expression to obtain the actual transmission signal T_{sig}:

$$T_{sig} = \frac{I_{sig}}{I_{flat}} = T_{meas} - (1 - T_{meas}) T_{hall} + T_{meas} T_{det} - T_{obj+det}$$

The last factor $T_{obj+det}$ depending on the complete object will typically dominate the other terms in the context of a 300kV CT setup as illustrated in *Fig. 4*. This example shows the marginal impact of the hall scatter (in blue) for moderately absorbing samples as well as the importance of the internal detector scattering (in green) if left at its current value of T_{det}=9%.

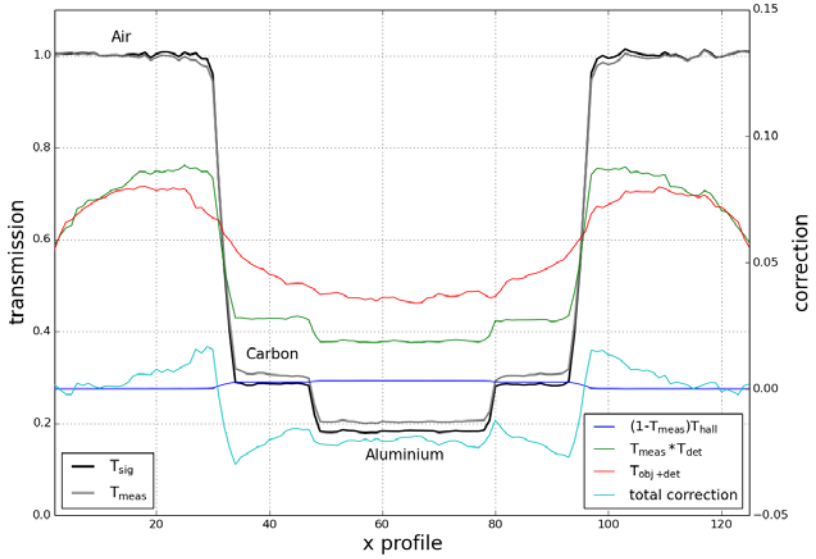

Fig. 4 *Illustrative example of the corrections applied to a given slice in the case of an object made of concentric cubes of carbon and aluminium.*

The factor $T_{obj+det}$ can be rewritten to lead to an expression as follows:

$$T_{sig} = \frac{I_{sig}}{I_{flat}} = T_{meas} - (1 - T_{meas}) T_{hall+det} - T_{obj} + T'_{det}$$

where $T_{hall+det}$ is a global contant that is evaluated once for a given system configuration, T_{obj} is the signal deposited by photons scattered in the object and T'_{det}, the internal detector scatter subtracted due to the attenuation by the object. This last factor can be visualized as primary photons that would have scattered either in the front window and back housing of the flat panel. The full spatial information for this correction is maintained by applying to each projection appropriate kernels determined from MC.

In order to obtain an accurate assessment of T_{obj}, the correction scheme must take into account the scattering in both object and detector as well as the energy dependent detector response. The raw data from a CT measurement are first reconstructed with a conventional Feldkamp-Davis-Kress[3] algorithm. A simplified MC model is then presented, which allows to predict the object scatter from the reconstructed voxel model and subsequently correct this component. In this contribution, we show that the object scatter can be estimated in a sufficiently short time by swift combination of variance reduction techniques[4] and code parallelism. This indicates that the suggested algorithm is suitable for the integration into the workflow of an industrial CT appliance.

References

1) ***IEEE Transactions on Nuclear Science*** 53 No. 1 (2006) 270-278.
2) Schütz, Philipp; Jerjen, I; Hofmann, J; Plamondon, M; Flisch, A & Sennhauser, U (2014). Correction algorithm for environmental scattering in industrial computed tomography. ***NDT & E International***, 2014(64), 59-64.
3) L. A. Feldkamp, L. C. Davis, and J. W. Kress, ***JOSA A***, Vol. 1, Issue 6, pp. 612-619 (1984)
4) ***Z Med Phys***. 2014 Jun 24. pii: S0939-3889(14)00063-4. doi: 10.1016/j.zemedi.2014.04.001

Accurate measurements of features near the resolution limit of tomographic data: extension to heterogeneous matrix, multiple feature types, and shape determination

R.A. KETCHAM*[1], A.S. MOTE[1]

[1] High-Resolution X-ray CT Facility, Jackson School of Geosciences, The University of Texas at Austin, Austin, TX 78712, USA – ketcham@jsg.utexas.edu
* presenting author

Keywords: computed tomography, 3D measurement, partial-volume effect

Abstract

In geological investigations utilizing X-ray computed tomography (XCT), the features of interest, such as trace phases, pores, and vesicles, are in many cases small compared to the data resolution. If at least one dimension of a feature subtends only a small number of voxels – generally, less than the point-spread function (PSF) width – then accurate segmentation and measurement is complicated by partial-volume and blurring effects. Typically, such features will appear relatively large compared to their true size, but their contrast with surrounding material will be diminished compared to larger instances of the same material.

These complications can be addressed if one can make the simplifying assumption that the X-ray attenuation caused by the feature of interest is fully present in the CT data, but distributed over a larger volume. We present a set of methods based on this principle that enable accurate measurement of the size, shape, and orientation of features in CT volumetric data sets that are small compared to the data resolution. We demonstrate these methods using a series of gold particles embedded in a pseudo-sandstone matrix of quartz and epoxy.

Introduction

Regardless of how high the resolution of a CT data set is, there will tend to be features of interest to the geologist at the edge of that resolution limit.

One example is economic phases. For examle, gold can be economic to mine even when present only in gram/tonne (or, equivalently, ppm) concentrations. Studying such phases with tradiational thin-section petrography is difficult; dozens of thin sections can be cut and inspected and few grains found. The high density and atomic number of many economic trace phases results in their having very high attenuation coefficients, making even very small grains distinguishable and potentially measurable.

The main obstacle to accurate measurementof trace phases stems from their small size relative to the resolution of CT system. If at least one dimension of a feature subtends only a small number of voxels (generally, less than the point-spread function (PSF) width, as characterized by Ketcham et al. 2010 and Ketcham and Hildebrandt, 2014), then accurate segmentation and measurement is complicated by partial-volume and blurring effects. Typically, such features will appear relatively large compared to their true size, but their contrast with surrounding material will be diminished compared to larger instances of the same material.

An example is shown in Figure 1. A set of gold grains, embedded in a 10-mm core of quartz and epoxy to make a pseudo-sandstone, were scanned with the same X-ray beam conditions and the same reconstruction scaling. The left scan is of the core alone, and the scan in the center and right imaged the same core placed in a 50-mm tube and surrounded with quartz powder, to simulate grains being embedded within a larger rock.

The grains in the right image are much dimmer than in the left, and also appear diffuse. Two primary mechanisms are at work. The primary one is that the grains are smaller with respect to the coarser scan resolution, and are blurred. This results in their attenuation signal being spread across a broader voxel neighborhood. Another factor is that the X-ray beam is harder, diminishing somewhat the effective attenuation coefficient of gold.

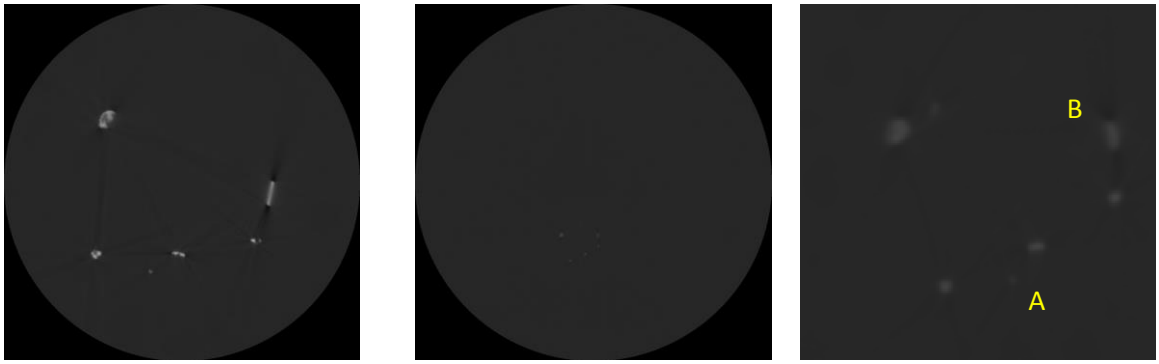

Fig. 1. *Two CT scans of the same set of gold grains embedded in quartz and epoxy, and surrounded by quartz powder. Left image field of view is 10 mm; center is 50 mm, and the right image is a zoom-in of the center image.*

Measuring these particles accurately is not straightforward. The typical method is to select a threshold level, and count the number of voxels associated with a given particle that are above that threshold. The difficulties inherent in obtaining an accurate measurement with this approach are evident. The proper threshold to use is CT number half-way between the feature and the matrix that surrounds it. Particle A in the right image is very dim compared to its counterpart in the left, and would be missed by a threshold selected based on the larger particles; artificially lowering the threshold will make all particles appear much larger than they are. Particle B is long and thin in the scan plane in the left image, and much wider in the right because of blurring, which will complicate accurately determining its shape.

Methods

The general principle underlying the approach presented here is the preservation of X-ray attenuation; we assume that the attenuation associated with any object is fully represented in the CT data, but due to blurring the attenuation is distributed over a larger volume in the data than it really occupies in the scanned object. If the "true" CT number of the material of interest can be ascertained, corresponding to the value it would achieve if unaffected by blurring, then the volume of a small feature can be accurately determined by summing the X-ray attenuation surplus or deficit associated with it relative to the surrounding matrix. The voxels associated with the anomaly for each grain are segmented using a threshold-plus-expand algorithm as described in Figure 2 and implemented in Blob3D (Ketcham 2005).

Once the voxels are selected, the volume of the particle is determined using an equivalent to the method outlined by Ketcham et al. (2010, Eq. 2, 4) for fracture aperture, adapted to feature volume. The volume of the feature of interest v_f is calculated as the sum over each voxel i of the proportion $p_{f,i}$ of voxel volume (v_{vox}) attributable to the feature:

$$v_f = v_{vox} \sum p_{f,i}; \quad p_{f,i} = (CT_i - CT_{mat})/(CT_f - CT_{mat})$$

The value of $p_{f,i}$ is calculated based on its CT number (CT_i) and CT number of the surrounding matrix (CT_{mat}) and the non-blurred CT number of the feature CT_f (or, in other words, the CT number corresponding to the true attenuation coefficient of the feature).

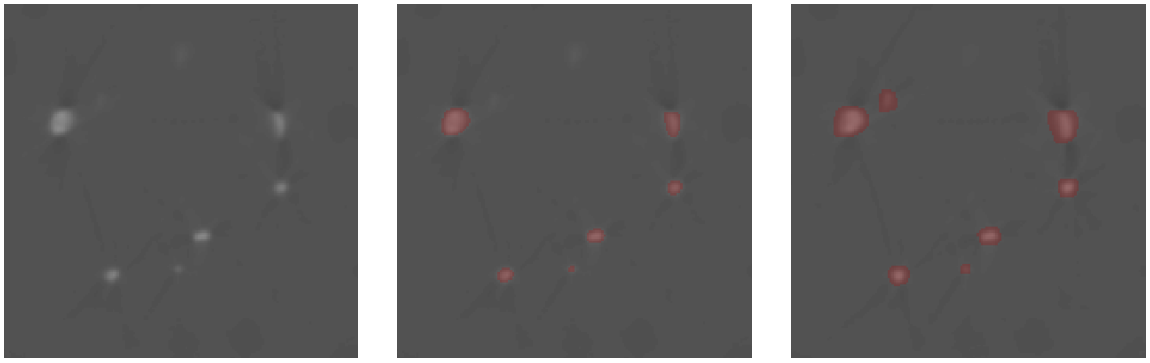

Fig. 2. *Initial part of segmentation using PVE method. All voxels that contain any part of the attenuation signal from the gold particles are selected. This is done by first selecting the range of CT numbers unique to gold particles in this data set. The result (center) still shows light haloes around the selected region, so the selection is expanded by additional voxels in all directions until the entire regions are selected.*

The only calibration required for the method is a value for CT_f, and possibly CT_{mat}. CT_{mat} can be estimated as the mean CT value of the matrix, or it can be estimated locally on a grain-by-grain basis by averaging the voxel values in the annulus surrounding the selected region. The latter method will compensate for inhomogeneity in the surrounding matrix, but additional care may be necessary to ensure that region selection is properly done. CT_f may be obtained directly if there are particles in the data large enough that their interiors are not blurred. Alternatively, it may be back-calculated if the volume of a particle is already known, and thus may be calibrated with an appropriate standard. It is also possible to estimate the value based on the feature's expected effective attenuation coefficient relative to other materials in the sample.

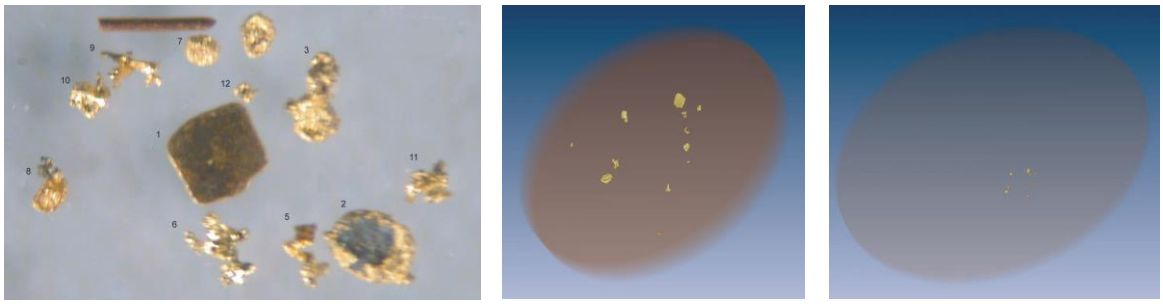

Fig. 3. *Left: Gold grains used for experiment. Center: volume rendering of 13 µm resolution scan, 13 mm field of view. Right: volume rendering of 50 µm resolution scan, 50 mm field of view.*

Experimental Verification

Twelve natural grains of native Au (Fig. 3, left) were weighed, photographed, and embedded in quartz powder and epoxy in a ~12.7 mm tube. Scanning was done at the University of Texas High-resolution X-ray CT Facility (UTCT; Ketcham and Carlson, 2001); the scanner was built by Bio-Imaging Research (Lincolnshire, IL). For all scans, X-ray energy was 180 kV, intensity 88 µA, and focal spot ~20 µm. A series of 1024x1024 scans were taken at varying resolutions by placing the sample in 13-50 mm cylinders filled with quartz powder, to simulate imaging the same grains in progressively larger

cores. Scan resolutions were 10, 13, 20, 30 and 50 μm (Fig. 3, center and right); except for the 10 μm scan, cylinder diameters were 1000x the voxel size.

Grain volumes are not perfectly known, because nature gold is commonly alloyed with silver, and the contents of these grains are unknown and likely variable between grains. The most common range of Au values is 60%-100%, and 80% was assumed here to convert from mass to volume.

Values of CT_f were determined for each scan to best match the measured volumes. These ranged from 108 to 92 times attenuation value for the matrix. This fall is due to the increasing hardness of the X-ray beam. Notably, a single value for a scan fitted the all of the grains in that scan well (Fig. 4). The variation in volume is within the bounds present due to the uncertainty in grain composition.

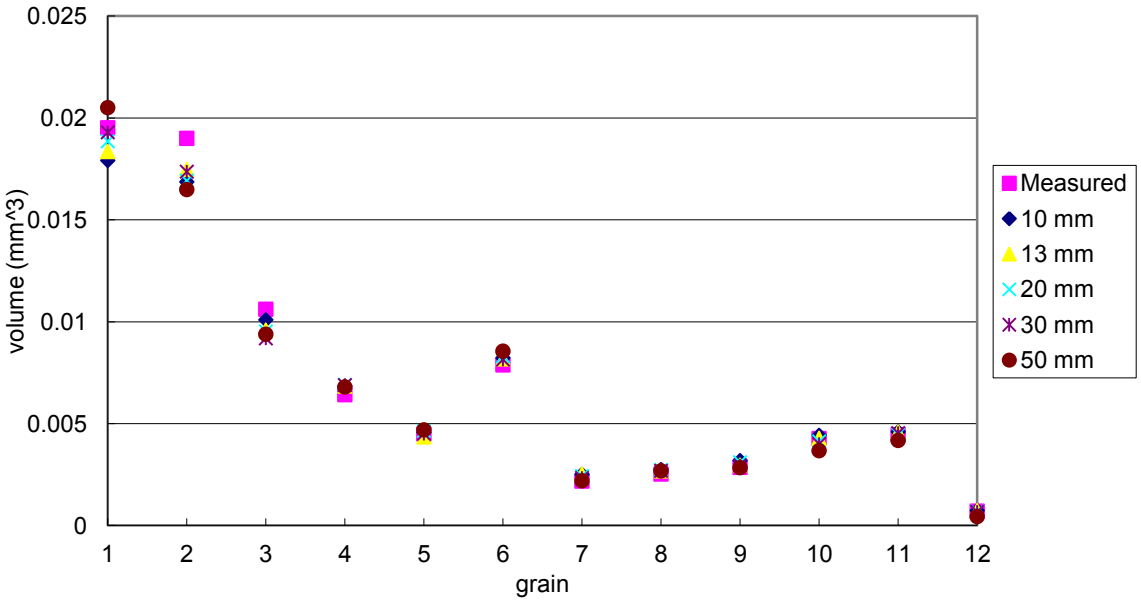

Fig. 4. *Results of CT measurements.*

Grain shapes are simplified to a best-fitting ellipsoid. Analysis of small grains is again complicated by the partial volume effect, which tends to "inflate" their appearance. One method for compensating is to fit an ellipsoid to the extended region associated with the particle (Fig. 2) and reduce each major axis by a constant factor so that the resultant ellipsoid volume equals that derived from partial-volume calculations. Results using this method are shown in Table 1. For large and relatively convex grains this approximation works well, but it becomes less robust for small and/or irregular grains. An alternative method is to calculate the ellipsoid by fitting only the highest-CT-number voxels, using the number that most closely corresponds to the true volume of the particle.

Discussion and extension to other cases

We take the success of this test to indicate that the method outlined here is sound for measuring particles that are small compared to the data volume. In many ases, though, geological samples contain multiple phases that are small relative to data volume, giving rise to the question of how to interpret them quantitatively. The principles underlying this work can also provide guidance for these situations. Specifically, if during an initial segmentation encompassing many particle types, one plots particle size versus maximum or mean CT number, a diagnostic pattern may arise (Fig. 5).

	Measured			13 µm			50 µm		
Grain #	A	B	C	A	B	C	A	B	C
1	0.754	0.687	0.066	0.761	0.690	0.067	0.708	0.566	0.096
2	0.675	0.523	0.094	0.698	0.464	0.103	0.677	0.430	0.108
3	0.685	0.298	0.091	0.627	0.311	0.094	0.633	0.355	0.082
4	0.391	0.352	0.082	0.358	0.318	0.114	0.286	0.231	0.197
5	0.512	0.162	0.094	0.409	0.168	0.119	0.394	0.230	0.100
6	0.538	0.243	0.105	0.454	0.259	0.134	0.455	0.248	0.147
7	0.287	0.267	0.050	0.233	0.183	0.109	0.198	0.167	0.130
8	0.384	0.231	0.050	0.284	0.169	0.105	0.244	0.186	0.115
9	0.505	0.121	0.082	0.368	0.195	0.077	0.339	0.195	0.082
10	0.432	0.275	0.063	0.296	0.244	0.115	0.289	0.247	0.100
11	0.286	0.257	0.106	0.274	0.199	0.164	0.352	0.206	0.110
12	0.230	0.162	0.033	0.137	0.127	0.074	0.124	0.103	0.065

Table 1 : *Measured versus CT-determined grain shapes. A, B, C: best-fit ellipsoid major axes (mm). "Measured" based on best-fit ellipse to cross-section image for A and B and assumption of ellipsoid geometry for C. "13 µm" and "50 µm" based on best-fit ellipsoid to CT data at named resolution, with all axes reduced by uniform factor to match CT-determined volume.*

The sample (left) is a schist with large garnet porphyroblasts, smaller agglomerations of ilmenite, quartz, and feldspar, and tiny zircons, in a quartz-feldspar-biotite matrix. Due to blurring effects and small grain size, zircon grains have lower CT numbers than the other phases, even though its true attenuation coefficient is much higher. By plotting mean CT number against a simplified volume determined by thresholding, a pattern arises in which different materials are grouped together, and can be subsequently distinguished, and the measurements re-done using the method described here.

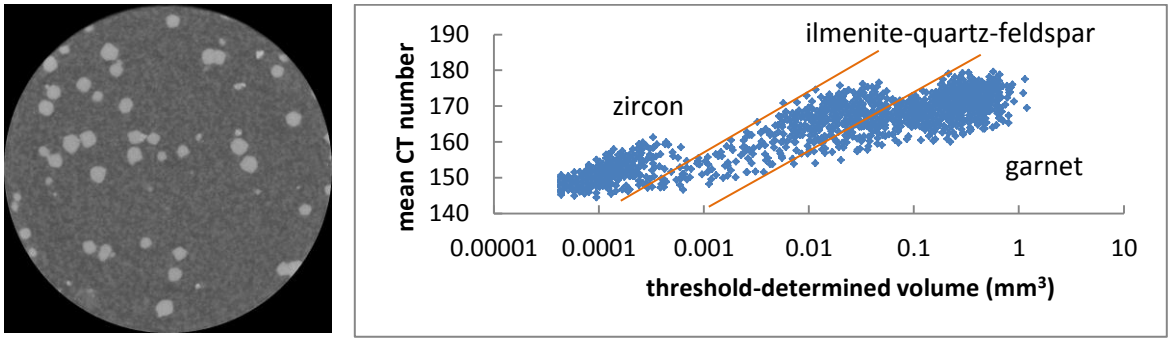

Fig. 5*: CT scan and analysis of schist containing three garnet*

Acknowledgements

We thank L. Minter for the Au grains, and E. Kelly and R. Ruthven for the use of the CT data and analysis of the schist. This work was supported by support from U.S. National Science Foundation grants EAR-0345710 and EAR-1258878.

References

Ketcham, R.A. (2005) Computational methods for quantitative analysis of three-dimensional features in geological specimens. ***Geosphere***, 1, 1: 32-41.

Ketcham, R.A., & Carlson, W.D. (2001) Acquisition, optimization and interpretation of X-ray computed tomographic imagery: Applications to the geosciences. ***Computers and Geosciences***, 27: 381-400.

Ketcham, R.A., & Hildebrandt, J. (2014) Characterizing, measuring, and utilizing the resolution of CT imagery for improved quantification of fine-scale features. ***Nuclear Instruments and Methods in Physics Research B***, 324: 80-87.

Ketcham, R.A., Slottke, D.T., & Sharp, J.M.J. (2010) Three-dimensional measurement of fractures in heterogeneous materials using high-resolution X-ray CT. ***Geosphere***, 6, 5: 499-514.

Material discrimination using dual energy computed tomography

Mahsa Paziresh*[1], Shane Latham[1], Glenn Myers[1], Benoit Recur[1], Andrew Kingston[1]

[1] Dept. of Applied Mathematics, RSPE, ANU 2601, Australia – firstname.lastname@anu.edu.au

Keywords: Dual-Energy Computed Tomography, Material Discrimination, Density and Atomic number mapping

Abstract

In this paper we investigate an attenuation coefficient model that consists of two basis functions: photoelectric absorption and Compton scattering. These are the two main interactions of X-rays with atoms. We apply the model in its un-simplified form for material discrimination in both reference phantoms and rock samples. Dual-energy ρ, Z estimation with this attenuation model requires precise knowledge of X-ray spectra and reference materials. Here we describe how we have chosen and simulated appropriate spectra. We also demonstrate how to determine the optimal parameter values for the model given a particular setup using a set of reference phantoms. Finally, we use the simulated spectra and calibrated model to calculate the properties of unknown rock samples. The model in its full form can account for beam hardening effects.

Introduction

In the context of 3D imaging, the ability to discriminate material composition improves understanding by enabling more accurate modeling of the properties of imaged samples. For example in petrophysics, identifying Quartz from Feldspar or Calcite from Dolomitee provides insight into diagenesis, gives better estimation of geo-mechanical and transport properties.

Micro-CT provides high spatial resolution information. Here we investigate the use of dual-energy CT imaging techniques for material discrimination. For materials with similar attenuation coefficient but different physical properties, a second image acquired with a n altered energy spectrum of X-rays can help distinguish these materials if their attenuation varies differently with X-ray energy.

There are two main X-ray interactions below 120 keV, namely photoelectric absorption (PE) and Compton scattering (CS). One can decompose the linearised attenuation coefficient (Alvarez and Macovski 1976) as follows:

$$\mu(E) = K_1 A_1 f_1(E) + K_2 A_2 f_2(E) = \frac{K_1 A_1}{E^n} + K_2 A_2 f_{KN}(E), \quad (1)$$

where A_1 and A_2 are integrals of $\rho Z^m/a$ and $\rho Z/a$ respectively along the direction of X-ray propagation, ρ is density, Z is the atomic number and a is the atomic weight of materials. $f_{KN}(E)$ is the Klein-Nishina function, K_1 and K_2 are constants, E is X-ray energy and m is in the range of 3 to 3.5 and n is between 3 to 4 (Cho et al 1975). We note that PE,(modeled as $K_1 A_1 f_1(E)$), dominates at lower energies (e.g., < 60 keV) and depends primarily on Z, while CS, (modeled as $K_2 A_2 f_2(E)$), dominates at higher energies and is proportional to ρ . It is this observation that enables material discrimination.

The Alvarez and Macovski model requires intensity measurements over two distinct X-ray spectra. These are analysed to determine the contribution of PE and CS to the projection images captured at lower and higher energies modeled as follows:

$$I_1(A_1, A_2) = \int S_1(E) \exp\left(\frac{-K_1 A_1}{E^n} + K_2 A_2(E) f_{KN}(E)\right) dE,$$
$$I_2(A_1, A_2) = \int S_2(E) \exp\left(\frac{-K_1 A_1}{E^n} + K_2 A_2(E) f_{KN}(E)\right) dE. \quad (2)$$

Here S_1 and S_2 are X-ray source energy spectra which are required to be known *a priori* and I_1 and I_2 are total intensities. The attenuation model (1), combined with dual energy measurements (2), has been used for material discrimination in various simplified forms (e.g., Alvarez and Macovski 1976, Heinsmann 2002, Siddiqui and Khamees 2003,

Derzhi et al 2012). Alvarez and Macovski (1976) simplified the model with polynomials of A_1 and A_2. Siddiqui and Khamees (2003) simplified the model by assuming dual monochromatic energies (e.g., at synchrotron). Derzhi et al (2012) applied a post-correction technique on the Siddiqui and Khamees (SK) method. Heismann et al (2002) assumed density and atomic number of sample materials varied as a linear functions of attenuation coefficient values at two chosen energy levels. They plotted ρZ projection with the ratio of dual energy attenuation coefficients over a range of atomic numbers for different materials. They achieved quantitative estimation of physical properties of materials based on these plots. In this paper, instead, we investigate using the full model in (2). We simulate source spectra *a priori* and calibrate the model in the next section before we perform ρ and Z calculation.

Calibration

The spectra mentioned in (2) are simulated to be as seen by detector accounting for the source radiation as well as the absorbing materials between source and sample. Bremsstrahlung radiation is simulated using Kramer's law (Kramers 1923) and transmission lines were added according to (Child 1911). The spectra is further modulated by the spectral transmission of each absorbing materials between the source and detector including 2 um tungsten, 350 um diamond window, 300 mm air and sensor protection materials (0.25 of Aluminium and 2.5 mm of carbon fiber) and absorbance of the detector through a 700 um Cesium Iodide scintillator to give the plots in Fig. 1.

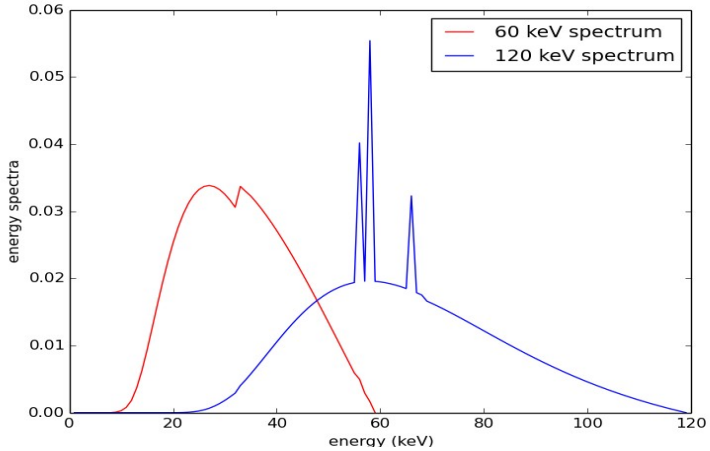

Fig. 1. *A low energy spectra at 60 keV tube volatge with 0.5 mm Aluminium filter and a high energy spectra at 120 keV with 0.35mm Copper filter. Spectra chosen such that PE can be dominant at low and CS be dominant at higher energies in the 0-120 keV range.*

Before the model (1) can be used, it must be calibrated to find the constants K_1, K_2 and the exponents m, n. To achieve this we have selected several reference materials over a range of atomic number and density as follows: (Aluminium (Al), Carbon (C), Acrylic $(C_5O_2H_8)_n$, Marble $(CaCO_3)$, Teflon $(C_2F_2)_n$, Glass (SiO_2), Titanium (Ti)). The attenuation coefficients data obtained from National Institute of Science and Technology (NIST) was used to estimate parameters. We simulated projection through cylinders made of each of the reference materials given the two spectra in Fig. 1. (These simulations are similar to the experimental calibration described later and the projection of the rock cores to be measured). The model was fit in a least square sense for both the 60keV and 120keV spectra to the simulated data in order to estimate parameters: $K_1=11.380$, $K_2=0.300$, $m=3.006$ and $n=3.228$ with relative error calculation minimised, i.e., $(\Delta Z/Z)^2$.

We imaged cylindrical samples of the reference materials using the 60keV and 120keV spectra. Using the above optimised parameters along with the simulated spectra, we matched the full model (1) with the imaged data using the Newton-Raphson method and estimated material property projections A_1 and A_2. These were then reconstructed using standard filtered back-projection and the map of density and atomic numbers of reference materials obtained. Table 1 shows average ρ and Z estimation applying simulated cylinder images of NIST data, the same estimation applying the real data images and also the theoretical values. The average density and atomic number errors are 3% and 5% respectively which is very good results comparing to the SK method which has minimum 10% error. The SK method was calibrated using the same reference material data. As shown

in Table 1, Aluminium and marble have similar density value but different atomic numbers in this case dual energy can discriminate these materials.

Material	Estimated $\rho(gr/cm^3)$ using simulated data	Estimated $\rho(gr/cm^3)$ using real data	Theoretical $\rho(gr/cm^3)$	Estimated Z using simulated data	Estimated Z using real data	Theoretical Z
Al	2.627	2.672	2.700	12.877	13.046	13.000
C	1.508	1.390	1.460	5.221	5.639	6.000
Marb	2.627	2.803	2.714	15.285	15.217	15.140
Acr	1.312	1.221	1.180	5.931	6.274	6.470
Tef	2.198	2.015	2.150	7.926	8.338	8.440
glass	2.222	2.223	2.230	11.459	11.188	10.974
Ti	4.508	5.172	4.540	22.126	20.159	21.500

Table. 1. *Estimation of simulated and real material properties of reference materials*

Geological application

We applied the same method to calculate the density and atomic number of several rock samples: Bentheimer sandstone, Berea sandstone and a carbonate. The rock samples imaged with the 60keV and 120keV spectra shown in Fig. 1. The optimised values of K_1, K_2, m and n from simulations have been used for the full model to compare with the 3D rock images to estimated properties of constituent materials. The reconstructions of the high and low energy attenuation tomograms where used as dual-channel inputs for the segmentation program “iLastik” (Sommer 2011). The main component of sandstone's is Quartz. For the Bentheimer sandstone the mode value of segmented Quatrz is estimated to be 2.4 for $\rho(gr/cm^3)$ and 11.7 for Z which shows relative error of 9.4% and 1.7% while the SK method shows relative error of 10% and 14.43% respectively.

Material	Estimated $\rho(gr/cm^3)$ estimation using full model	Estimated $\rho(gr/cm^3)$ using Siddiqui method	Theoretical $\rho(gr/cm^3)$	Estimated Z using full model	Estimated Z using Siddiqui method	Theoretical Z
Bentheiemer (Quartz)	2.40	2.92	2.65	12.877	10.09	11.78
Berea (Quartz)	2.36	2.97	2.65	11.84	9.78	11.78
SA89 (Dolomite)	2.60	3.06	2.87	13.22	12.22	13.74
SA89 (Calcite)	2.28	2.91	2.71	14.86	13.28	15.71

Table. 2. *Estimation of simulated and real material properties of rocks*

For the Berea sandstone, the mode value of segmented quartz comparing to quartz theoretical ρ and Z values shows relative error of 10% and 5%, while the SK method has 12% and 17.6% error. Bentheimer and Berea sample ρ and Z mapping using full model shows more accurate but more noisy results.

The attenuation model (1) in its full form is a function of energy, it models the beam-hardening effect. In conventional reconstruction algorithms, X-ray radiation is assumed to be monochromatic which results in inconsistent values in the attenuation coefficient when incident radiation is polychromatic. Fig. 2i) shows cupping artifacts around the edges of the a slice through the reconstructed image of Berea sandstone captured at 60 keV. Fig 2ii) and 2iii) shows the beam hardening (BH) effect is removed reasonably well when analysing using the model in (1).

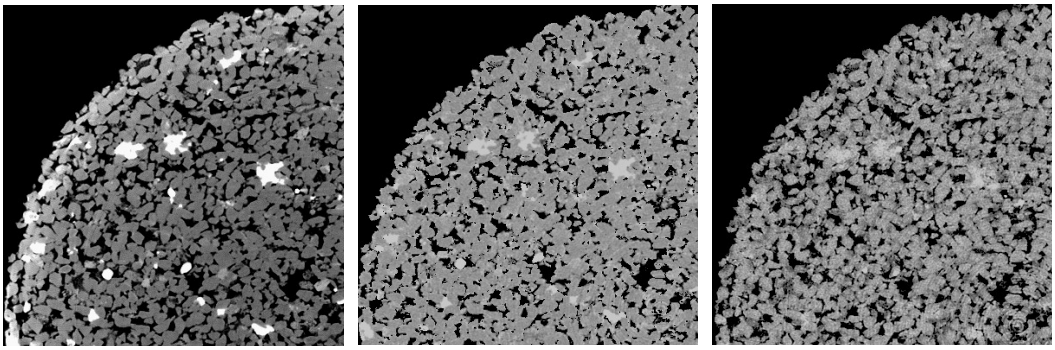

i) ***ii)*** ***iii)***

Fig. 2. *A slice through reconstruction of Berea sandstone image: i) captured with 60 keV spectra showing the BH artifact, ii) estimated atomic number and iii) estimated density using full model (1).*

For the Carbonate, dual-channel segmentation was again performed by "iLastik" using the the attenuation tomograms as inputs (See Fig. 3ii). Here Dolomite and Calcite which is difficult to distinguish in the single-energy tomogram (See Fig. 3i) could be identified. The relative error of Calcite and Dolomite atomic numbers estimation using full model show 3.7% and 5.4% relative error while Z estimations using siddiqui method has 11.1% and 15.5% error. The relative error of Calcite and Dolomite density estimation using the full model show 9.4% and 15% while ρ estimation using the SK method has 6.62% and 7% error. Dolomite and Calcite have similar densities but totally different atomic numbers. The Z results obtained using full model reveal the difference between these materials well.

The density estimations using the full model seem consistently low. This could be contributed to Z/a uncertainty in A_1 and A_2 of (1). For simulations, the materials were known so we were able to set a precise Z/a value for each material. We used the average value Z/a of reference materials which is generally lower than expected Z/a value for Quartz.

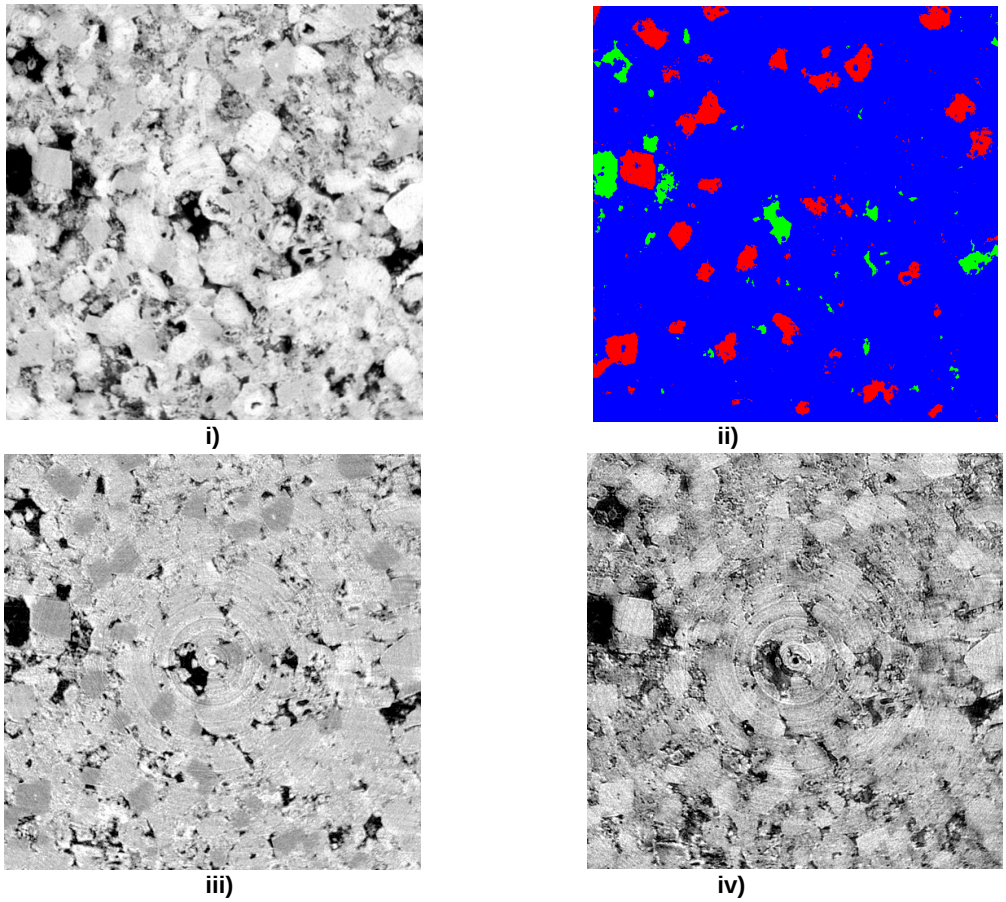

i) ***ii)***

iii) ***iv)***

Fig. 3. *A slice through reconstruction of carbonate image: i) captured with the 120 keV spectra, ii) the dual-channel segmentation using "iLastik" [blue: Calcite, red: Dolomite, green: pore space], iii) estimated atomic number and iv) estimated density using full model (1).*

Atomic number measurements in the Carbonate using the full model is about 10% more accurate than the SK method but our Carbonate density estimation had more error due to higher noise of our projection data captured using the 120keV spectrum. The heavy filtering used means there is a low X-ray flux and therefore a poor signal-to-noise ratio (SNR). As said before, PE is mainly dominant at low energies and dependent to Z while CS is dominant at higher energies and varies with ρ. The higher noise in images captured with the 120keV spectrum degraded the density value estimation. However, the low energy imaging having higher SNR resulted in a more stable estimation of Z and less deviation from expected values.

The results from the SK method are more stable and precise since analysis is performed directly on the tomogram. However, since beam-hardening correction must be performed on the low-energy reconstructions, this hinders any accurate estimation of ρ and Z. The full model by contrast analyses the projection images directly and inherently accounts for beam-hardening. It is therefore more accurate in estimation of material properties but less stable, i.e., more noisy. This can be seen in the results of the Carbonate presented in Fig. 4.

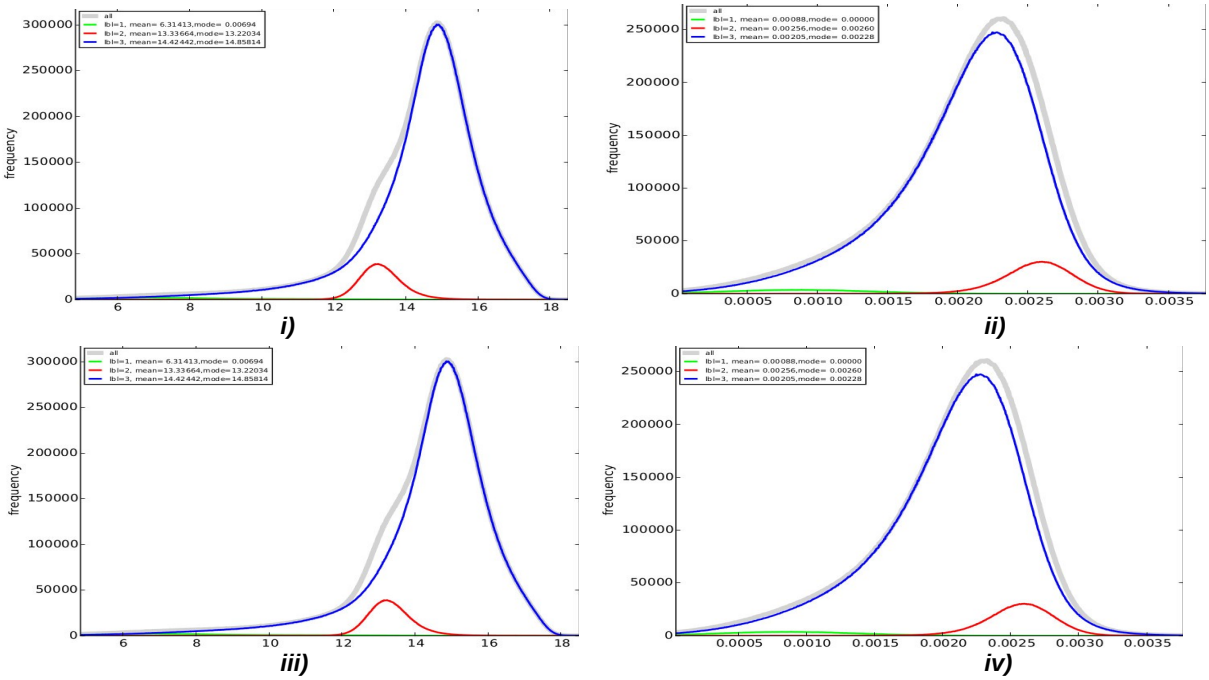

Fig. 4. *Plots of i) mode of estimated atomic number and ii) mode of estimated density using SK method, and iii) mode of estimated atomic number and iv) mode of estimated density using full model (1).*

Conclusion

We calibrated the Alvarez and Marcovski (1976) attenuation coefficient model and applied the model in its full form for material discrimination. The proposed method is able to identify several materials from ρ and Z images even if the constituent materials have similar attenuation coefficients. The model reasonably corrected beam hardening effect in ρ and Z reconstructions (See Fig. 2). The full model calculations requires precise knowledge of spectra and reference materials. Although results are more noisy than simplified methods such as that by Siddiqui and Khamees, it can yield a better average estimated ρ and Z material properties to within 10% of expected values (See Table 1). For further improvement, we plan to apply an iterative modification of the density and atomic number estimations via material library matching and correction.

References

Alvarez, R. E. and Macovski, A. (1976). “Energy-selective reconstructions in x-ray computerised tomography,” Physics in medicine and biology 21(5), 733.

Heismann, B., Leppert, J., and Stierstorfer, K. (2003). “Density and atomic number measurements with spectral x-ray attenuation method,” Journal of Applied Physics 94(3), 2073–2079.

Siddiqui, S., Khamees, A., et al. (2004). “Dual-energy ct-scanning applications in rock characterization,” SPE.

Derzhi, N. (2012). “Method for estimating effective atomic number and bulk density of rock samples using dual energy x-ray computed tomographic imaging,” US Patent App. 13/527,660.

Cho, Z. H., C. M. Tsai, and G. Wilson. (1975). "Study of contrast and modulation mechanisms in x-ray/photon transverse axial transmission tomography." *Physics in medicine and biology* 20.6: 879.

Sommer, C; Straehle C; Koethe U; Hamprecht FA (2011). "ilastik: Interactive Learning and Segmentation Toolkit". *IEEE International Symposium on Biomedical Imaging*: 230–33.

Kramers, H.A. (1923). "On the theory of X-ray absorption and of the continuous X-ray spectrum". *Phil. Mag.* **46**: 836.

Child, C. D. (1 May 1911). "Discharge From Hot CaO". *Physical Review*. Series I **32** (5): 492–511.

Recent advances in X-ray Computed Tomography and potential impact for non-medical applications

Philippe Després,

Laval University, Québec,Qc. Canada

X-ray Computed Tomography (CT) did not change significantly since the advent of multisclice scanners and helical acquisitions. This technology nevertheless kept evolving at a steady pace and now offers features allowing innovative applications in medicine but also in other fields of research. This presentation will focus on three technological advances in CT that might have a significant impact in non-medical applications: advanced tomographic reconstructions, dual-energy CT and 4D applications.

From a computational perspective, CT image reconstruction can nowadays rely on larger processing resources. Massively parallel Graphics Processing Units (GPUs), for instance, can be used to offset the numerical burden of advanced reconstruction algorithms relying on complex physical models of image acquisition. These algorithms and models can potentially yield better images with fewer artifacts, thanks to a priori knowledge injected into the problem. Another promising research avenue is dual-energy CT, either with dual-tube or kV-switching systems. Dual-energy CT, in the context of non-destructive testing, can potentially improve material identification. Finally, sub-second full rotation of the X-ray tube allows time-resolved (4D) applications that are very useful in the study of dynamical systems. The current state and limitations of 4D gating in CT will be presented along with possible applications in non-destructive testing.

Evaluation of phase correction algorithms outside the validity boundaries

*M.N. BOONE[1], L. VAN HOOREBEKE[1]

[1] UGCT – Dept. Physics and Astronomy, Ghent University, Proeftuinstraat 86/N12, B-9000 Gent, Belgium
* presenting author

Keywords: Phase contrast, phase retrieval, phase correction

Abstract

In high-resolution X-ray Computed Tomography, the phase shift and refraction of X-rays can under certain circumstances become visible in the projection images, being superimposed on the attenuation images. As such, it can also become visible in the reconstructed volume. This can be beneficiary for the visualization, yet it is often considered an imaging artefact which hinders proper 3D analysis. Under normal experimental conditions, it is mathematically not possible to retrieve the phase information or the attenuation information correctly without multiple acquisitions. However, several methods exist to perform phase retrieval or phase correction, which use assumptions on the object or the imaging setup. In this presentation, the effect of a violation of these assumptions is discussed.

Introduction

In recent years, high resolution X-ray CT (micro-CT) has gained importance in many research domains, including materials science. For low-density materials such as composites or organic materials, the attenuation of X-rays is relatively low, and the real part of the refractive index of materials can provide more image contrast. Several methods have been developed to measure this refractive index accurately, which however usually require highly coherent sources or X-ray optics such as gratings. However, as for visual light, the phase shift induced by the refractive index difference causes refraction, which can be visualized by beam propagation and is as such inherent to the imaging process.

After propagation (within certain limits), the phase shift results in an edge-enhancement effect which is superimposed over the attenuation signal. In the reconstruction process, this phase contrast effect yields artificial effects when left unprocessed. Although this edge enhancement can be beneficial for visual inspection, it often hinders proper analysis and can lead to false conclusions. To correct for or even exploit the phase contrast, several algorithms have been developed to cope with single-image in-line phase contrast data, each with specific advantages and disadvantages.

Methods

The methods discussed in this presentation are the Modified Bronnikov Algorithm (MBA, Groso *et al.*, 2006), the Simultaneous Phase and Amplitude Retrieval (SPAR, Paganin *et al.*, 2002), the Bronnikov Aided Correction (BAC, De Witte *et al.*, 2009) and the Post-Processing Phase Correction (PPPC, Wernersson *et al.*, 2013). The first three are implemented as pre-processing filters, operating on the projection data, the last one is a post-processing method, operating on the 3D reconstructed volume. They are all derived from an inversion of the Transport of Intensity Equation (TIE), which yields an

upper limit for the propagation distance. Furthermore, it is known that these methods all require homogeneous objects in order to reconstruct both phase and attenuation information from only one propagation distance. The MBA method additionally requires a low-attenuating object (Boone *et al.,* 2012).

Results

In this presentation, the influence of a violation of one or more of these requirements is discussed. It is shown that MBA is very sensitive to remaining attenuation in the sample, resulting in a cupping effect (Fig 1. a,c,e). Despite being very similar, SPAR does not suffer from this cupping artefact and can be used for strongly attenuating samples as well. On the other hand, both are affected similarly by heterogeneity of a sample. In this case, the edge enhancement can not be completely compensated in regions where phase inclusions are present (fig 1. c,d), and alternatively strong smoothing occurs for attenuation inclusions (Fig 1. e,f). Similar effects occur for PPPC and BAC, although the latter is less prone to image smoothing.

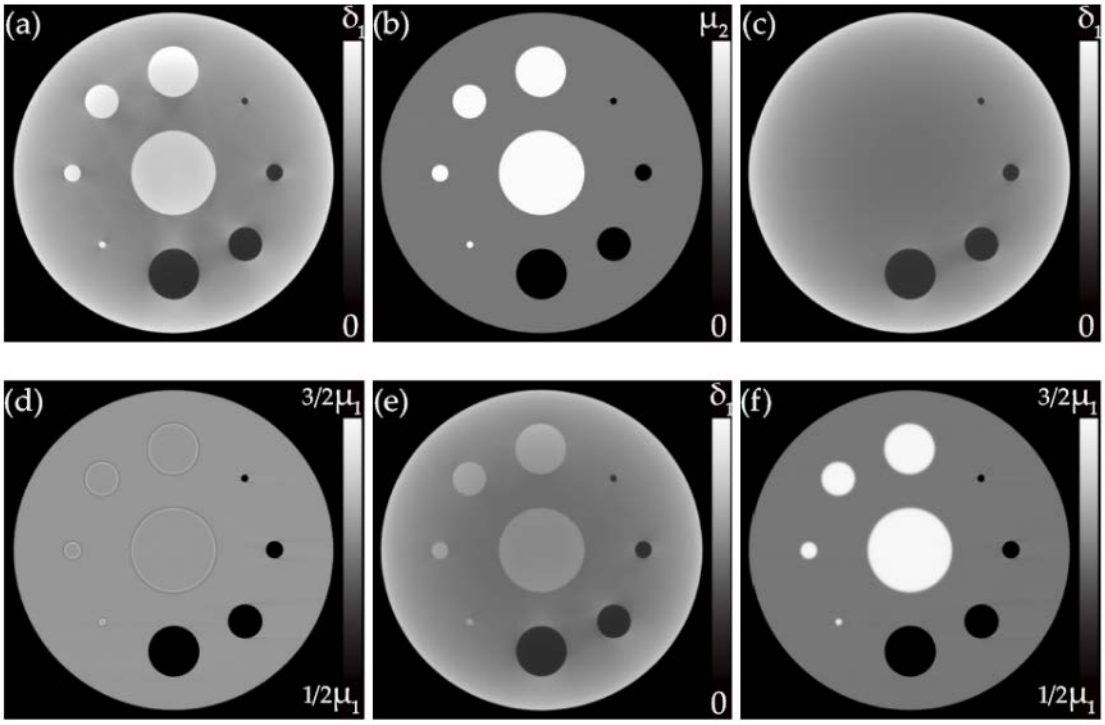

Fig. 1. *Reconstructed slices from a phantom (a) homogeneous object, MBA reconstruction; (b) homogeneous object, SPAR reconstruction; (c) sample with phase inclusion, MBA reconstruction; (d) sample with phase inclusion SPAR reconstruction; (e) sample with attenuation inclusion, MBA reconstruction; (f) sample with attenuation inclusion, SPAR reconstruction.*

Another parameter which has been investigated is the propagation distance. In lab-based CT, the propagation distance is linked to the geometric magnification and X-ray flux, hence it can not be altered drastically. At synchrotron sources however, the distance between source and object is sufficiently large for these effects to become negligible. Therefore, a relatively homogeneous sandstone sample (Bentheimer) is

scanned at ESRF ID19 at a pixel size of 3.5 µm using different propagation distances, ranging from 30 mm to 1001 mm. As such, the propagation distance and consequently the validity of the TIE is investigated as well.

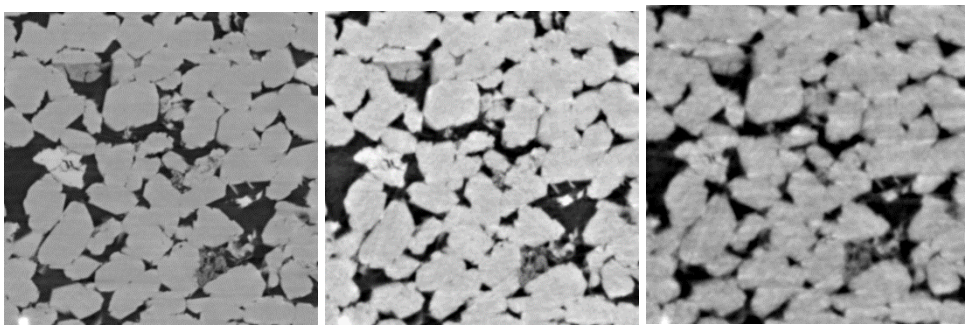

Fig. 2. *Reconstructed slices using SPAR phase processing of the sandstone sample at different propagation distances (30 mm, 400mm and 1001 mm, resp.). Note that the gray scale range is different for the largest distance.*

Fig. 2 shows a part of a reconstructed slice after phase processing using the SPAR algorithm. The main advantage of this algorithm, particularly at monochromatic radiation, is the physical relevance of the parameters, hence the shown images are considered the optimal phase processing. It is clear that phase retrieval fails at large object-to-detector distances due to the violation of the TIE. A similar result is found for the other phase processing algorithms, where it is in some cases even impossible to determine the optimal parameters for the processing.

Conclusion

It is shown that artefacts occur when the boundary conditions of the phase processing algorithms are violated. In a first place, the requirement of a homogeneous object often hinders proper phase processing in real objects. Furthermore, it is shown that a good selection of propagation distance is required, regardless the low visibility of the phase effects in the projection data at low propagation distances.

Acknowledgement

The Special Research Fund of the Ghent University (BOF) is acknowledged for the post-doctoral grant of M.N. Boone. Dr. Irene Zanette is acknowledged for the acquisition of the sandstone scans at ESRF.

References

Boone, M. N., Devulder, W., Dierick, M., Brabant, L., Pauwels, E. & Van Hoorebeke, L. (2012) “Comparison of two single-image phase-retrieval algorithms for in-line x-ray phase-contrast imaging” **J. Opt. Soc. Am. A** 29, 2667-2672

De Witte, Y., Boone, M. N., Vlassenbroeck, J., Dierick, M. & Van Hoorebeke, L. (2009) “Bronnikov-aided correction for x-ray computed tomography” **J. Opt. Soc. Am. A** 26, 890-894

Groso, A., Abela, R. & Stampanoni, M. (2006). “Implementation of a fast method for high resolution phase contrast tomography” **Opt. Express** 14, 8103-8110

Paganin, D. M., Mayo, S. C., Gureyev, T. E., Miller, P. R. & Wilkins, S. W. (2002) “Simultaneous phase and amplitude extraction from a single defocused image of a homogeneous object” **J. Microsc.** 206, 33-40

Wernersson, E. L. G., Boone, M. N., Van den Bulcke, J., Van Hoorebeke, L. & Luengo Hendriks, C. L. (2013) “Postprocessing method for reducing phase effects in reconstructed micro-CT data” **J. Opt. Soc. Am. A** 30, 455-461

Effect of an initial solution in iterative reconstruction of dynamically changing objects

M. HEYNDRICKX[1], T. DE SCHRYVER[1], M. DIERICK[1], M. N. BOONE*[1], T. BULTREYS[2], V. CNUDDE[2], L. VAN HOOREBEKE[1]

[1] UGCT – Dept. Physics and Astronomy, Ghent University, Proeftuinstraat 86/N12, B-9000 Gent, Belgium
[2] UGCT – Dept. Geology and Soil Science, Ghent University, Krijgslaan 281/S8, B-9000 Gent, Belgium
* presenting author

Keywords: Iterative reconstruction, prior knowledge, tomographic reconstion, SART

Abstract

Visualizing and analyzing dynamic processes in 3D is an emerging topic, e.g. in geosciences (Berg *et al.*, 2009; Cnudde and Boone, 2013; Bultreys *et al.*, accepted), which has only recently become possible due to fast, high-resolution CT scanning. However; dynamically changing objects pose a challenge in CT-imaging because the existing reconstruction algorithms, which reconstruct the sample volume from a number of scan images, presume an unchanging sample during the acquisition of the projection images. Movements or changes during the scan cause artefacts in the resulting volume. Furthermore, when fast processes are visualized, the acquisition time needs to be reduced, thus drastically decreasing the signal-to-noise ratio (SNR).

To address these issues, an iterative reconstruction technique is applied, where an initial solution is provided to the algorithm. In this work, we present an evaluation of this method based on both simulations and real experimental data.

Introduction

The simultaneous Algebraic Reconstruction Technique (SART) is an iterative algorithm to reconstruct volumes from CT-scans (Beister *et al*. 2012). A (typically empty) volume is initiated and improved by back-projecting the difference between a simulated projection of this (empty) initial solution and the measured projection at the same viewing angle. This is done for every measured projection. The resulting volume is then used in the next iteration step, where the projection/back projection process is repeated using the intermediate solution. After a number of iterations, the solution converges to a final reconstructed volume.

Instead of an empty volume, an initial solution can be used in the first step. This can be the reconstruction of an earlier scan of the same object or another volume resembling the one that's being reconstructed. An initial solution may improve the convergence speed and the quality of the resulting reconstruction (Brabant 2013).

An initial solution can reduce the number of projections needed to get the same quality of reconstruction. In this way a scan for one reconstruction needs less time. To a lesser extend, an initial solution can also cope with more noise than the conventional SART-reconstruction, starting from an empty volume. Therefore, less time is needed per projection and the total scanning time decreases.

A reconstruction algorithm can be further improved if it is known which regions in the initial solution are most likely to undergo changes. These regions recieve a higher weight during the back projection process. The number of projections needed can thus be further reduced. Using only a small number of projections, even partial CT-scans can be reconstructed at an improved quality.

Methods

The SART-reconstruction using an initial solution is compared with the conventional SART-reconstruction using an empty volume as initial solution for a number of

parameter values. Specifically, the projection angle, the relaxation factor, the number of projections, the number of iterations and the amount of simulated noise are varied. Most work is performed using phantom data, where a slightly modified version of the ideal solution one is used as the initial solution (Fig. 1). Because these are phantoms, the reconstruction can be compared with a ground truth to quantitatively evaluate the reconstruction. Two effects are investigated: when the initial phantom has a part that has a different attenuation coefficient and when it has a part that has moved. Both effects give rise to artefacts when not addressed properly.

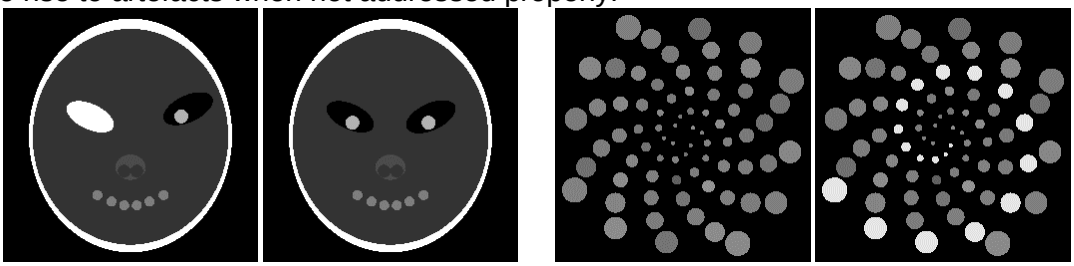

Fig. 1. *Two phantoms. (a) and (c) are the initial solutions, (b) and (d) the ideal solutions*

An example of a dynamic process is fluid flow through porous media such as geomaterials. This dynamic process will be used to test the reconstruction with an initial solution on a real-life example. Images of this are shown in figure 2.

A high-quality scan of the dry sample is acquired before the dynamic process is initiated. This scan is reconstructed with conventional SART. The result is used as an initial solution for the scans acquired during the process. The fluid presumably follows the pores in this rock, further limiting the regions where the reconstruction can differ from the initial solution. Again, the result is compared with conventional SART to evaluate whether the initial solution is an improvement.

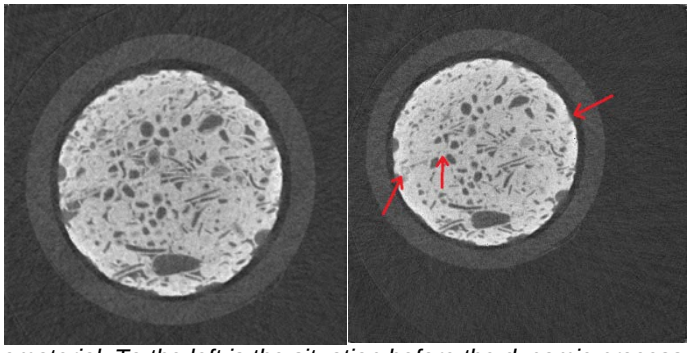

Fig. 2. *The scanned geomaterial. To the left is the situation before the dynamic process was initiated; this is used as the initial solution. To the right is the situation after fluid flow, which is being reconstructed. The major differences are indicated with arrows.*

Both methods, a phantom and the scanning of fluid flow through porous media, are used to test the extented algorithm, in which an initial solution is backed up with different weighting in the back projection process for different regions of the volume. The weightings are based on the grey values of the initial solution: for the geomaterial heigher weightings are assigned to the attenuation coefficient of air. These are the pores where the fluid will most likely flow. These reconstructions are compared with conventional SART and with the naive implementation of an initial solution. The effect of the number of projections and of the signal to noise ratio is investigated by variing them.

Results

Movement artefacts occur when the relaxation factor, the projection angle, the number of projections or the number of iterations is too low. Noise can obscure the artefacts if it is strong enough, as can be seen in figure 3.

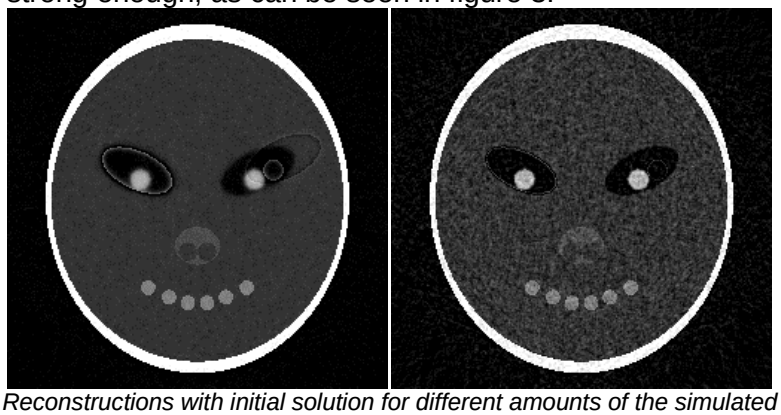

Fig. 3. *Reconstructions with initial solution for different amounts of the simulated noise.*

The initial solution yields an improvement when compared with conventional SART. The same reconstruction quality can be achieved for a lower number of projections, both in phantom and in real data. Therefore an initial solution can help reconstruct a dynamically changing sample.

This effect becomes even larger when combining an initial solution with variable weighting. A good reconstruction can be obtained with a very low number of projections, as demonstrated in figure 4.

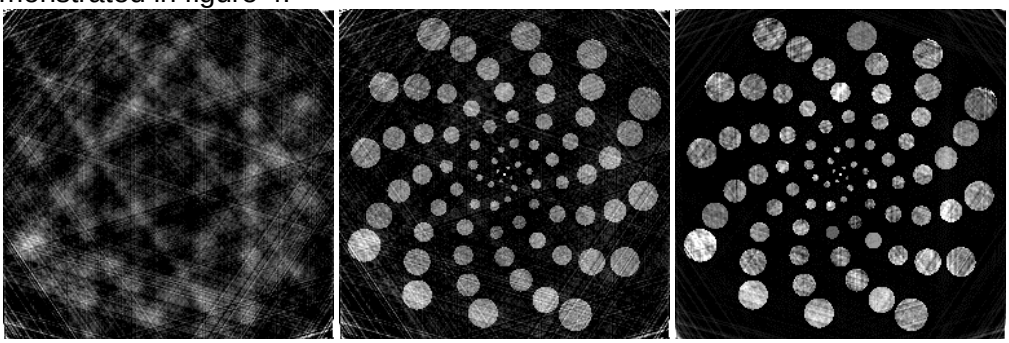

Fig. 4. *At the left a conventional SART-reconstruction. In the middle a reconstruction with an initial solution and at the right one with the use of weightings. 6 projections were used.*

A necessary condition to get good results with weighted reconstruction is a correct choice of the weighting volume. Giving a low weight to regions were change is present results in reconstructions worse than the ones with a naive implementation of the initial solution and in some cases even worse than the conventional SART-reconstruction.

A disadvantage of using a weighted reconstruction is the relative contribution of noise. The noise is now primarily backprojected in the relatively small volume with large weightings, augmenting its importance. This is especially important because these regions with high weights are where the initial solution differs from the reconstructed volume and where the dynamic process takes place. The negative effect of noise on the quality of the reconstruction increases fast with the number of iterations and projections.

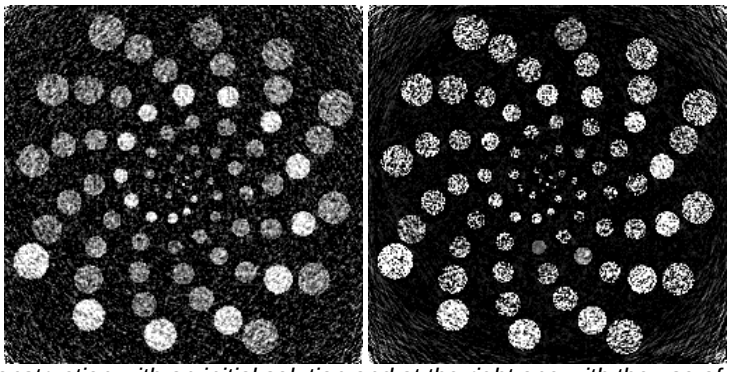

Fig. 5. *Left is a reconstruction with an initial solution and at the right one with the use of weightings. 300 projections were used.*

An example of the effect of noise on the reconstruction with both an initial solution and a weighted algorithm is shown in figure 5. Especially the smaller regions in the center suffer from noise in the weighted algorithm.

The reconstructions of the geomaterial need less projections when using an initial solution, compared to the conventional SART. A reconstruction with correct weights pushes this number down even more. This can be seen in figure 6.

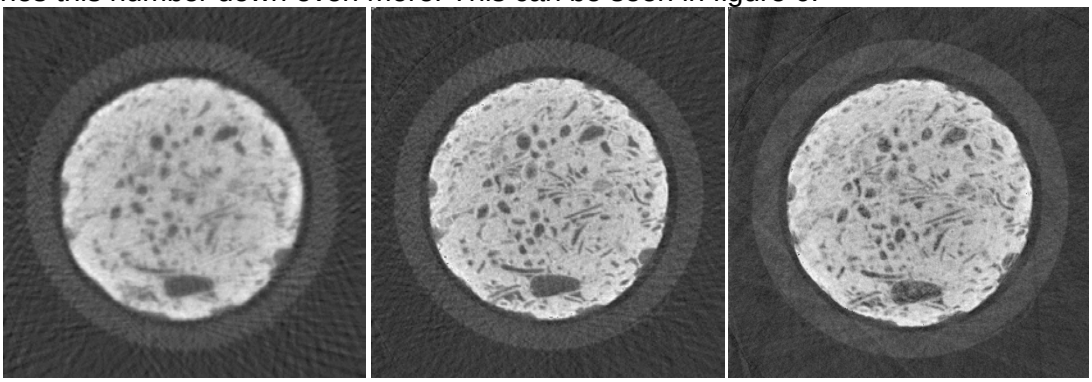

Fig. 6. *At the left a conventional SART-reconstruction. In the middle a reconstruction with an initial solution. Both used 100 projections. At the right a reconstruction with weights, using 15 projections.*

Conclusion

An initial solution, potentially with a weighting volume, can greatly improve the quality of a reconstruction with a low number of projections.

This can be benificial in reconstructing dynamic processes, provided a detailed scan before or after the process is taken to serve as the initial solution. The weights, if used, should correctly represent the changing volume. A wrong weighting volume reduces the reconstruction quality instead of improving it.

While a naive implementation of an initial volume can reduce the scanning time both by reducing the number of projections and reducing the time per projection (increasing the noise), the adding of a weighting volume only reduces the number of projections needed, since noise has an increased effect on this reconstruction. The number of projections may, however, be lowered to a great extend. In this way the scanning time gets reduced further than with an initial solution alone.

Acknowledgement

The Special Research Fund of the Ghent University (BOF) is acknowledged for the post-doctoral grant of M.N. Boone. The Agency for Innovation by Science and Technology in Flanders, Belgium (IWT) is acknowledged for the PhD grant of T. Bultreys.

References

Beister M., Kolditz D. and Kalender W. A. (2012). Iterative reconstruction methods in X-ray CT ***Physica Medica 28***, 94-108.

Berg S., Ott H., Klapp S.A., Schwing A., Neiteler R., Brussee N., Makurat A., Leu L., Enzmann F., Schwarz J.-O. (2013). Real-time 3D imaging of Haines jumps in porous media flow. **Proceedings of the National Academy of Sciences 110(10),** 3755-3759.

Brabant L. (2013). *Latest developments in the improvement and quantification of high resolution X-ray tomography data*. UGent, Belgium, http://hdl.handle.net/1854/LU-4193900

Bultreys T., Boone M.A., Boone M.N., De Schryver T., Masschaele B., Van Hoorebeke L. and Cnudde V. (accepted for publication). Fast laboratory-based micro-computed tomography for pore-scale research: illustrative experiments and perspectives on the future. **Advances in Water Resources**

Cnudde V. and Boone M.N. (2013). High-resolution X-ray computed tomography in geosciences: A review of the current technology and applications. **Earth-Science Reviews 123**, 1-17

SEMI-EMPIRICAL BEAM-HARDENING CORRECTION OF DENSE MATERIALS USING A BIO-MEDICAL SCANNER

D.R. EDEY*[1], S.I. POLLMANN[2], D.LORUSSO[2,4], M. DRANGOVA[2,5,6], R.L. FLEMMING[3], D.W. HOLDSWORTH[2,5,6]

[1]Department of Geological Sciences, University of Texas at Austin, Austin, TX, 78712-9000
[2]Imaging Research Laboratories, Robarts Research Institute, Schulich School Of Medicine & Dentistry, Western University, 1151 Richmond Street North, London, ON, N6A 5B7
[3]Department of Earth Sciences, Western University, 1151 Richmond St., London, ON, N6A 5B7
[4]Department of Physiology and Pharmacology, Schulich School Of Medicine & Dentistry, Western University, 1151 Richmond St., London, ON, N6A 5C1
[5]Department of Surgery; Schulich School of Medicine & Dentistry, Western University 1151 Richmond Street, London, ON, N6A 3K7
[6]Department of Medical Biophysics; Schulich School of Medicine & Dentistry, Western University, 1151 Richmond Street, London, ON, N6A 3K7
*presenting author: dave.edey@utexas.edu

Keywords: *micro computed tomography; beam hardening; geomaterials; empirical correction*

Abstract

X-ray computed tomography is able to non-destructively interrogate scanned objects to produce high-resolution three-dimensional images of their internal structure. The ubiquitous availability of bio-medical micro-computed tomography scanners (micro-CT) offers increased access to scanners, but micro-CT images of dense objects are susceptible to artifacts, particularly due to beam hardening and scatter. This study proposes and evaluates a simple semi-empirical correction method for beam hardening and scatter that can be applied to available biomedical scanners. Novel calibration phantoms – consisting of plates of varying diameters – were designed and built from both aluminum (Al) and poly[methylmethacrylate] (PMMA). The phantoms were used to derive linearization functions, based on non-linear fitting of a second order polynomial and inverse exponential to absorbance measurements made through different sections of the phantoms. Corrections based on the linearization functions were implemented and applied to x-ray projection data prior to reconstruction. The correction method was evaluated on two different biomedical micro-CT scanners using sets of aluminum and PMMA test rods. Effective correction for beam hardening was achieved on both scanners using all correction methods (different functions and calibration phantoms) and test objects; the best improvement was achieved when using the polynomial correction based on the aluminum calibration phantom. Semi-empirical linearization of x-ray projection data with a custom calibration phantom enables the use of biomedical micro-CT scanners for dense material applications.

Introduction

With recent hardware advances in micro-computed tomography (micro-CT), non-destructive CT analysis can be implemented on previously incompatible dense materials such as meteorites, core samples, minerals, and soil samples. Acquisition of micro-CT images of dense materials enables rapid compositional analysis and provides archival advantages over destructive methods. However, micro-CT can suffer from dynamic range-limiting artifacts that can obscure detail and limit quantitative and qualitative analysis. Micro-CT imaging provides resolution comparable to traditional qualitative analysis methods and also enables additional qualitative and quantitative analysis. The non-destructive nature of micro-CT is especially advantageous for use with specimens that cannot be sectioned (Fry et al., 2013). Examples of such specimens that are of particular interest include rare samples in both private and museum collections, samples

where destruction would inhibit future research (soil peculation, pycnometry), or for initial scout work (Hyde et al., 2014), where micro-CT can be used to determine the best locations for sectioning (Ketcham and Carlson, 2001), or where 3D information is required for analysis (McCoy et al., 2006).

While high-energy industrial CT scanners can be used, micro-CT scanners built for biomedical applications are advantageous for use in geomaterial analysis because they: 1) are more commonly available, 2) are installed at an increasing number of university research centers; 3) have higher spatial resolution, appropriate for small specimens; and 4) allow the specimen to remain stationary (in comparison to industrial scanners, which typically rotate the specimen, potentially disrupting samples). Unfortunately, most biomedical micro-CT scanners do not have an adequate dynamic range to study dense objects and often are only available with a lower peak voltage (90 – 120 kVp) when compared with industrial units (> 200 kVp).

Although x-ray photons at the lower energies can penetrate most dense samples, artifacts are common when imaging these materials. These artifacts arise due to three sources of error: 1) beam hardening – an artifact due to the preferential removal of low-energy photons in a poly-energetic spectrum, 2) photon scatter, and 3) under-ranging – the low dynamic range condition that occurs when very few photons are detected (dark signal) making differentiation of different densities and thicknesses difficult. Typical artifacts resulting from these sources of error are incorrect reconstructed values in the interior of specimens, which confounds quantitative analysis, and streak artifacts from the denser objects that obscure details both on the interior and exterior of specimens.

We present a simple correction for x-ray beam hardening and scatter that can be readily applied to available biomedical scanners. The correction takes the form of a semi-empirical calibration method that can be applied to the raw x-ray absorbance data, prior to CT reconstruction. The correction relies on the acquisition of calibration data acquired on materials of known composition and thickness using the x-ray protocols to be utilized for specimen scanning. Numerical fits to the empirical calibration data are generated to produce a correction function that is able to linearize the absorbance projection data, thereby removing (or at least reducing) the cupping artifacts and streaks caused by beam hardening and scatter. The proposed correction method is described, implemented, and tested on two different biomedical micro-CT scanners. Two numerical functions are explored for two separate calibration materials and evaluated for their ability to reduce the aforementioned artifacts.

Methods

From the Beer-Lambert law, which relates the absorbance of photons and a material's attenuation properties, absorbance and material thickness is linear for mono-energetic x-ray beams in the absence of scatter. Deviations from this relationship arise with poly-energetic x-ray beams (as are typically used in micro-CT scanners). When poly-energetic beams are used, the low-energy photons are absorbed preferentially, resulting in a "harder beam" (*i.e.* the mean energy of the transmitted x-ray spectrum is higher than that of the incident x-ray spectrum). As a result, more photons will be detected than if a mono-energetic x-ray beam (of an effective mean energy) was used. In addition, scattering of x-rays within the material also results in an increase of detected photons. By "mimicking" increased absorbance, both beam hardening and scatter result in an underestimation of the material's attenuation coefficient, particularly for longer path lengths through the material. The artifacts following the CT reconstruction process appear as "cupping" in the CT image (*i.e.* decrease of measured attenuation coefficient in the centre of the image, compared to the edges of the object).

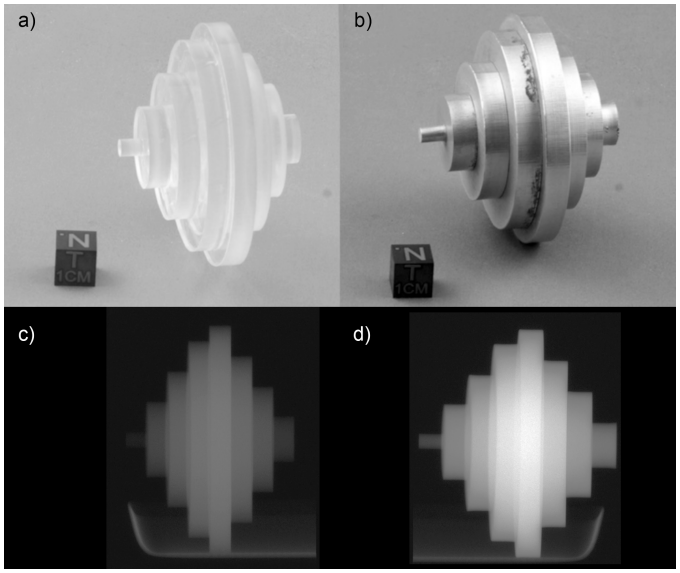

***Fig. 2**. Calibration phantoms for beam hardening correction in CT. Phantoms were fabricated from a) PMMA and b) aluminum. Note the flattened areas on each plate, machined to provide a larger measurement area. The scale cube (1 cm) provides a size reference. Representative absorbance images of the PMMA (c) and aluminum (d) phantoms are also shown.*

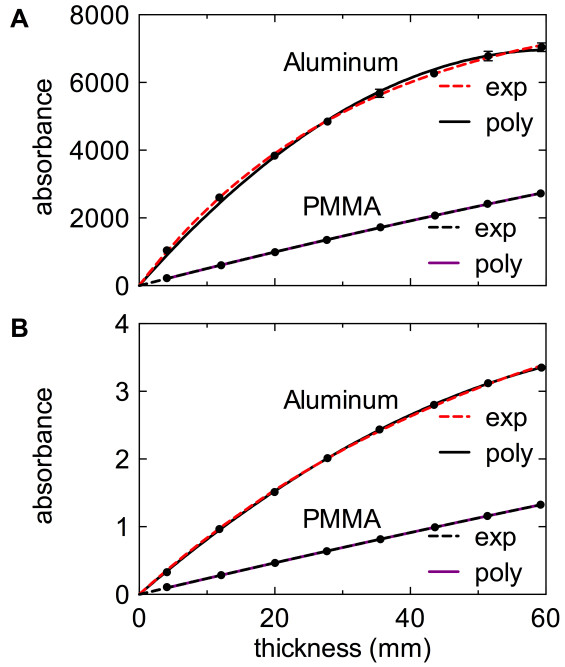

***Fig. 1**. Plots of absorbance vs. thickness for the aluminum and PMMA calibration phantoms scanned in the Ultra (a) and specCZT (b) scanners. The symbols represent the measured data (error bars are plotted, but in most cases are smaller than the symbol size). The lines represent the polynomial (poly) and inverse exponential (exp) fits as indicated in the legend.*

For the empirical determination of absorbance *vs.* material thickness curves, two calibration phantoms (*i.e.* calibration objects) were designed and built. Each phantom was fabricated of a single material and covered a range of thicknesses appropriate for the range of anticipated applications. The phantoms comprised eight coaxial cylindrical plates with known diameters ranging from 4.5 mm to 60 mm arranged in an alternating pattern to mimic the general shape of geomaterial specimens, as shown in Fig. 1. One calibration phantom (Fig. 1a) was manufactured using poly[methylmethacrylate] (PMMA, Lucite), which mimics soft, water-like materials typically used in biomedical applications (Chen et al., 2001). The second calibration phantom (Fig. 1b) was manufactured using aluminum (6061-T6) to mimic dense objects like bone, silicate minerals, and other geomaterials with similar electron densities; the Al plate thickness was 6.4 mm. To ensure larger areas of uniform thickness on each plate, two opposing sides were flattened prior to imaging. Using these calibration phantoms, a single x-ray projection image yields the eight absorbance measurements (Fig. 1 c, d) required to determine characterize the relationship between absorbance and material thickness.

For each scanner, calibration was performed using both the aluminum and PMMA phantoms. Each phantom was placed on the scanner bed and the source-detector system was oriented perpendicular to the flat edges of the calibration phantom. A single x-ray image of each phantom was acquired and was sufficient to generate measurements of absorbance for all thicknesses. The images were corrected for detector-element non-uniformity, then converted to absorbance images (Fig. 1 c, d) prior to analysis. ImageJ software (National Institutes of Health, Bethesda,

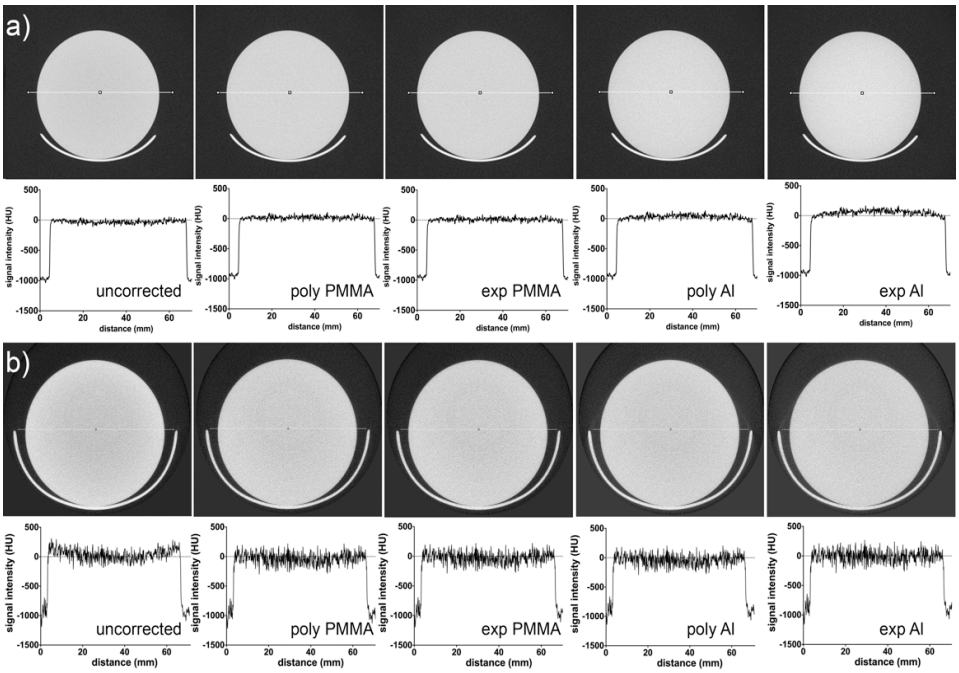

Fig. 3. *Cross-sectional images of the 63.5 mm diameter PMMA rod scanned on Ultra (a) and speCZT (b) scanners. The plots are signal intensity profiles through the line drawn in each image. The first column shows uncorrected data, followed by images corrected using the poly-PMMA, exp-PMMA, poly-Al, and exp-Al methods, as indicated in the figure. Note, the differences in noise characteristics between the two scanners (evident in the line profiles) are due to the differences in acquisition protocol and voxel sizes.*

MD) was utilized for analyzing the absorbance images. Regions of interest (ROI) – 4 x 4 pixels – were placed on each of the flat regions of each plate (representing a different thickness) of each phantom and the mean and standard deviation of the absorbance were recorded.

The absorbance-thickness relationships were fitted using non-linear Levenberg Marvquard fitting in Prism (GraphPad Software, Inc., La Jolla, CA). As described above, both a second-order polynomial (Herman, 1979; So et al., 2009) and the one-phase exponential decay function were fitted. Calibration fits were obtained using both fitting functions for each scanner and both the aluminum and PMMA phantoms.

To incorporate the beam hardening (and scatter) correction prior to reconstruction, custom software was written to linearize each absorbance value on a pixel-by-pixel basis for each projection image acquired. Linearization was performed for the polynomial and inverse exponential decay fitted functions (Fig. 2).

Sample images from the uncorrected and corrected images of the largest the PMMA test rod (63.5 mm diameter) are shown in Fig. 2 for both scanners. As expected, the effect of beam hardening and scatter can be seen as slight cupping in the uncorrected images (Fig. 3) and increases with rod diameter. The differences between acquisition protocols cause variations in the amount of cupping seen in the individual samples. Corrections using the PMMA calibration phantom (poly-PMMA and exp-PMMA) reduce or slightly modify the cupping artifact, but perform nearly identically for both scanners. Correction using the aluminum calibration phantom (poly-Al and exp-Al) perform differently on the two scanners.

Figure 4 shows uncorrected and corrected images of aluminum test rods scanned on the Ultra (Fig. 4a) and speCZT (Fig. 4b) scanners. As expected, the cupping artifacts in the uncorrected aluminum rods are significantly greater than those observed in the PMMA rods. Quantitative values of percent cupping are plotted in Fig. 5 for the two

scanners, demonstrating the expected increase in artifact with increasing rod diameter. Following correction using both polynomial and inverse exponential functions, the percent cupping is significantly reduced for all test rods scanned on the Ultra scanner and for all but the largest (50.8 mm diameter) rod scanned on the speCZT. The polynomial fit (poly-Al) outperformed exp-Al across the range of test rod diameters, resulting in smaller percent cupping. On the Ultra scanner both correction methods had a tendency to overcorrect the samples (*i.e.* –ve percent cupping); this tendency also occurred within exp-Al corrections of the speCZT tests. On the speCZT scanner, the 50.8 mm test rod caused extreme cupping, exceeding 30%. When correction was attempted, with either method, very high noise values and over correction occurred, making correction impossible in this case.

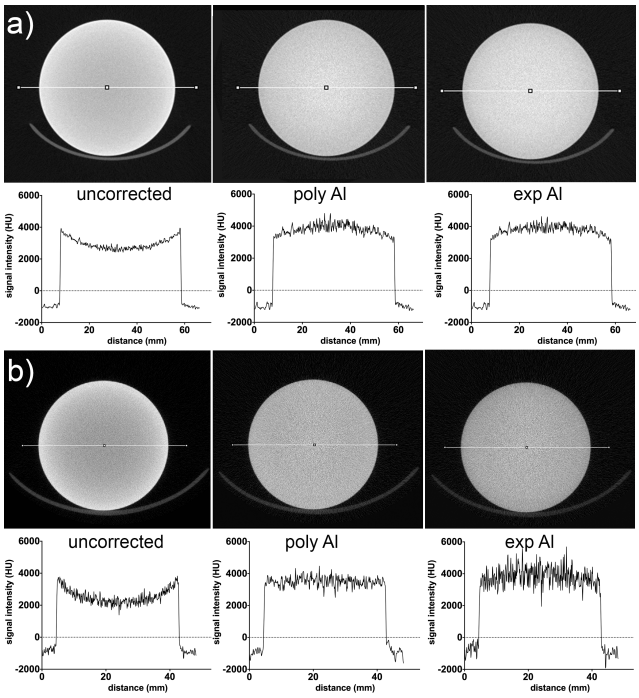

Fig. 4. *Cross-sectional images of aluminum test rods scanned on Ultra (a) and speCZT (b) scanners. The plots are signal intensity profiles through the line drawn in each image. The first column shows uncorrected data, followed by images corrected using the poly-PMMA, exp-PMMA, poly-Al, and exp-Al methods, as indicated in the figure. The rod shown for the ultra is the 50.8 mm diameter one, while the diameter of the rod in (a) (speCZT) is 38.1 mm. Note, the differences in noise characteristics between the two scanners (evident in the line profiles) are due to the differences in acquisition protocol and voxel sizes.*

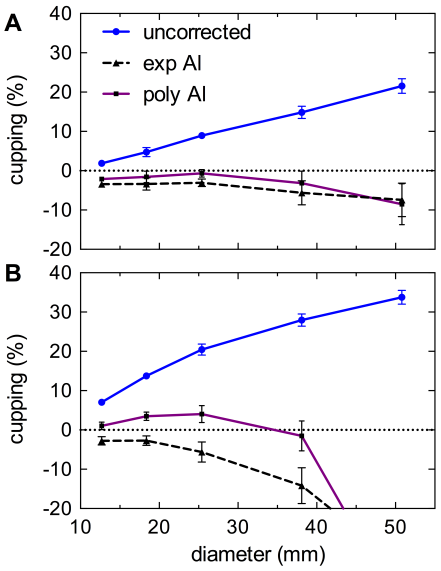

Fig. 5. *Percent cupping calculated for the aluminum test rods plotted as a function of rod diameter for the Ultra (a) and speCZT (b) scanners for the two correction methods based on the aluminum calibration phantom. The values plotted are means and standard deviation from 5 adjacent image slices.*

References

Fry, C., Melanson, D., Samson, C., McCausland, P. J. A., Herd, R. K., Ernst, R. E., Umoh, J., Holdsworth, D. W., 2013. Physical characterization of a suite of Buzzard Coulee H4 chondrite fragments. ***Meteoritics & Planetary Science****, 48(6), 1060-1073.*

Chen, C.Y., Chuang, K.S., Wu, J., Lin, H.R., Li, M.J., 2001. Beam Hardening Correction for Computed Tomography Images Using a Postreconstruction Method and Equivalent Tissue Concept. ***Journal of Digital Imaging*** *14, 54-61.*

Herman, G.T., 1979. Correction for beam hardening in computed tomography. ***Physics in medicine and biology*** *24, 81.*

Hyde, B. C., Day, J., Tait, K. T., Ash, R. D., Holdsworth, D. W., Moser, D. E., 2014. Characterization of weathering and heterogeneous mineral phase distribution in brachinite Northwest Africa 4872. ***Meteoritics & Planetary Science****, 49(7), 1141-1156*

Ketcham, R.A., Carlson, W.D., 2001. Acquisition, optimization and interpretation of X-ray computed tomographic imagery: applications to the geosciences. **Comput. Geosci.** 27, 381-400.

McCoy, T. J., Ketcham, R. A., Wilson, L., Benedix, G. K., Wadhwa, M., Davis, A. M. (2006). Formation of vesicles in asteroidal basaltic meteorites. **Earth and Planetary Science Letters**, *246*(1), 102-108.

So, A., Hsieh, J., Li, J.Y., & Lee, T.Y. (2009). Beam hardening correction in CT myocardial perfusion measurement. ***Phys Med Biol****, 54*(10), 3031-3050.

A Provenance Management System for Tomography Data Processing and Visualization

G. KNAPP*[1], J. YUAN[2], L. BUTLER[3], J. GE[4]

[1] Department of Mechanical Engineering, Louisiana State University – gknapp1@tigers.lsu.edu
[2] Department of Chemistry, Louisiana State University – jyuan4@tigers.lsu.edu
[3] Department of Chemistry, Louisiana State University – lbutler@lsu.edu
[4] Department of Chemistry, Louisiana State University – jinghuage@cct.lsu.edu
* presenting author

Keywords: Provenance, Tomography, X-Ray, Visualization, VisTrails

Abstract

In computerized tomography the algorithms used for data processing are constantly evolving and improving. Provenance management systems help to track the history of data processing. VisTrails, freeware developed at New York University, allows for the creation of modules that encompass each step of data processing and the creation of a history tree that tracks changes to the workflow as it is developed. Modules can call other programs, which can help integrate multiple pieces of software into a single workflow. We showcase a visualization workflow for neutron absorption tomography of a lithium-ion battery and another for the data processing and visualization of multi-energy X-ray grating tomography of a flame retardant polymer. The large and multiple datasets associated with the flame retardant processing required the use of high performance computing, for which job submission and file management was managed through Python scripting in VisTrails. The modules that were developed for the processing of these two datasets should lead to the development of a custom package for our research group that will then be available to the VisTrails community. Easy sharing of packages allowed by VisTrails should encourage openness of data processing techniques between research groups.

Introduction

In computerized tomography the algorithms used for data processing are constantly evolving and improving. Each research group has its own preferred platforms, be it Python, Mathematica, or MATLAB scripts, which can make it hard to integrate someone else's code into your data processing pipeline. These factors can also make it difficult to recall, years later, how any given dataset was processed. Which algorithm was used? Which version of software?

Provenance management systems help to track the history of data processing. VisTrails, freeware developed at New York University, allows for the creation of modules that encompass each step of data processing and the creation of a history tree that tracks changes to the workflow as it is developed. [Callahan 2006; Silva 2011; Freire 2012] Modules can call other programs, which can help integrate multiple pieces of software into a single workflow. The history tree allows for exploratory actions to be logged so that they can be easily returned to in the future. It is a great step towards making the development of tomography data processing more accessible and shareable.

Here we will showcase two workflows we developed that show the utility of the VisTrails software. The first is a visualization workflow of absorption tomography of a lithium-ion battery. The second is a collection of multi-energy (12 keV to 32 keV) scans

of a burnt flame retardant/polymer blend collected at LSU's CAMD synchrotron tomography beamline.

Methods

The visualization of the absorption tomography dataset was done using the VTK packages built-in to VisTrails [Fig. 1]. This workflow did not include data processing. The data was stored in an HDF5 file format and imported as a 3D point volume. Volume visualization properties (e.g. the color lookup table and thresholds) were defined in the *vtkVolumeProperty* module, which saved these values in the version tree. This allowed for the particular visualization settings to be accessed in the future.

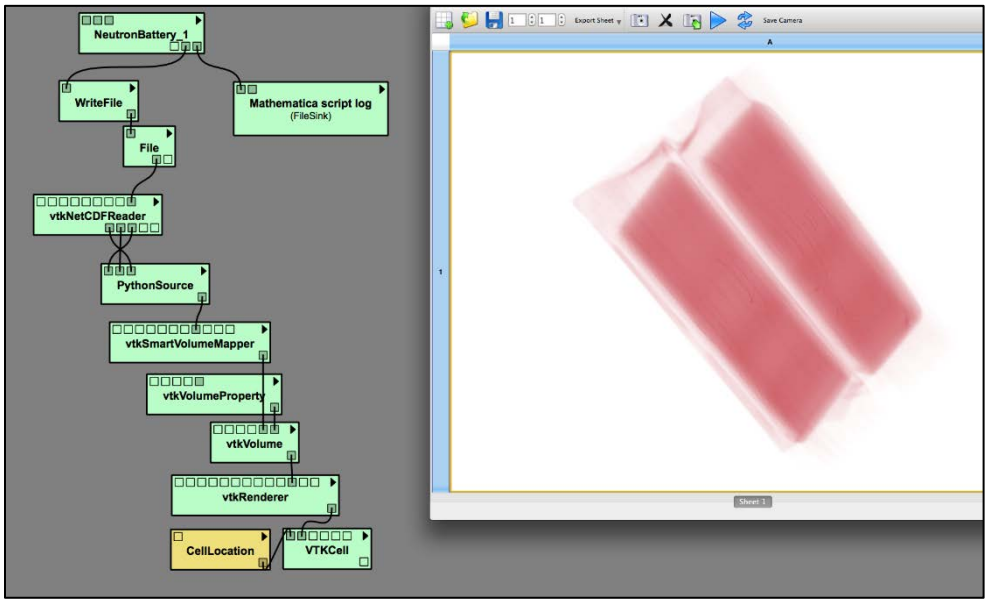

Fig. 1. *VisTrails workflow for the visualization of neutron absorption tomography of two litium-ion batteries.*

The VisTrails workflow for the multi-energy scans wrapped tomographic data processing to preserve the data provenance. The raw data was gathered at the LSU Center for Microstructures and Devices. The LSU CAMD synchrotron tomography beamline used a 7 Tesla wavelength shifter to generate X-ray flux into a double multilayer monochromator, operating over 6 to 35 keV with a 3% bandpass. The beam size at the sample was 1.3 mm high and 30 mm wide. The sample was mounted on a goniometer on a motor stack with transverse to the beam motion, two tilt stages, a vertical translation stage, and a precision rotation stage. The sample-to-scintillator distance was about 10 mm. The 0.5 mm thick Ce:YAG Marketech International scintillator was imaged with Optique Peter 45 mm working distance lens and a Princeton Instrument PIXIS 2KB CCD. The CCD pixel size was 13.5 micron; combined with the nominal 5.4X magnification, the effective pixel size was 2.5 micron. The exposure time was set to 2 seconds for a beam current of 120 mA at 12 keV. The typical field of view was 1500 x 512 pixels, corresponding to 3.75 mm x 1.28 mm.

Projections were acquired over the range of 0 to 179.5 at 0.5 degree increments. Each raw image was corrected with white and dark fields; three white fields were collected every fifteen degrees and five dark fields were collected at the beginning of the experiment. For the time-correlated image averaging, used to reduce scintillator defects, the sample was imaged, translated to one side by 20 pixels, and imaged again.

To process the time-correlated images, an ordered list of all left and right raw image filenames and reference image filenames was generated; the list was particularly

important as the reference image set was updated throughout the tomography experiment. Both left and right raw images were converted to absorption images, calculated as (L + R + |L-R|)/2 where L and R are the left and right absorption images, respectively. All absorption images were stored in both FITS and HDF5 format. MuhRec [Kaestner 2011], with FITS images, was used for test tomography reconstructions; ASTRA [Palenstijn et al. 2013] (GPU enabled), with HDF5 images, was used for for filtered back-projection reconstruction. The reconstructed volume was downsized by a factor of two to give 5 micron voxels. Custom VisTrails Python modules for wrapping the Mathematica (absorption image conversion) and ASTRA (reconstruction) code allowed the file names and input parameters of the code used to be saved with the log files and output. File paths were also transferred from Mathematica to ASTRA via a Python module in VisTrails to reduce the need for user input during processing.

Another VisTrails Python module passed the file path information back to Mathematica after reconstruction with FBP. The intensity values within the slices were compared to the values of the absorption images. The row and column sums of a slice were compared to corresponding line probes across the 0° and 90° absorption images. If needed, an averaged gain and offset correction for all slices were applied until the intensity values in the slices best matched the absorption images.

At this point, five to six volumes of tomography data were available at X-ray energies spanning 12 to 23 keV, 5 micron resolution and in absorption units. [Ham 2004; Ham 2007] Inspection of the reconstructed volumes showed related features across all X-ray energies, though with up to a several pixels position shift. Small shifts in volume registration are expected due to small change in the X-ray beam propagation based on the double-crystal monochromator settings. Simple translation was used to align all volumes. The sample formulations from Albemarle are given in weight percent, while K-edge tomography yields a volume percent. Conversion between the two units was based on an assumed 100 gram mass or 100 ml volume; densities were from literature or were calculated by a procedure developed for organic chemistry based on the empirical formula, atomic volumes, and functional units.[ref Cao] The mass attenuation coefficients, μ/ρ (cm^2/g) [ref Hubbell], for X-rays in the range of 1 to 100 keV were obtained from the NIST XCOM database (http://www.nist.gov/pml/data/xcom/); 50 values of the total attenuation with coherent scattering were downloaded and used to develop a linear interpolation function. A binary sample mask was derived from the 15 keV tomography volume; at this energy just above Br K-edge, the extent of the sample is most clearly defined.

The measured X-ray attenuation at the *i*-th voxel of side length *l* as a function of energy is given by

[1] $$A^{expt}_{xyzE} = [FR]^{expt}_{xyz}\mu^{FR}_E l + [Sb_2O_3]^{expt}_{xyz}\mu^{Sb_2O_3}_E l + [HIPS]^{expt}_{xyz}\mu^{HIPS}_E l$$

Solving for the volume fraction concentrations gives [Marathe 2014]

[2] $$\{[FR]_i, [Sb_2O_3]_i, [HIPS]_i\} = \mathbf{G}\cdot\{A^{expt}_i\}$$

where **G** is given by

[3] $$\mathbf{G} = ([\mu^{FR}_E, \mu^{Sb_2O_3}_E,\ mu^{HIPS}_E]^T \cdot [\mu^{FR}_E, \mu^{Sb_2O_3}_E,\ mu^{HIPS}_E])^{-1}\cdot [\mu^{FR}_E, \mu^{Sb_2O_3}_E,\ mu^{HIPS}_E]l$$

The measured X-ray attenuation is, after reconstruction, three-dimensional. That data is flatten into a one-dimensional vector, processed with equations [1]-[3], and then restored to three-dimensional data sets for the component concentrations. Equations [1]-[3] do not account for partially-occupied voxels as occur along the surface of the sample or at voids; the binary mask is applied to the component concentrations to set these voxels to zero. Also set to zero are voxels at the surface of the dataset that were affected by the translation operations used to align the tomography volumes. A median filter (radius = 1) is applied. Lastly, any voxels with negative component concentrations are reset to zero concentration and then the concentration volumes are saved in HDF5 format.

For each step of the data processing log files were generated and the values of the input, filepaths of volume files, any error messages, and filepaths of the Mathematica and MATLAB scripts were stored. Data provenance was also stored in the form of the VisTrails workflow. Since Mathematica and MATLAB were installed on a interactive high performance computing node, log-in and job submission was handled through a GUI integrated into the data processing workflow. Files were also transferred between the local and remote compute node via an SCP through Python. A separate VisTrails workflow was developed to visualize and export the processed volume files for mobile viewing [Fig. 2.].

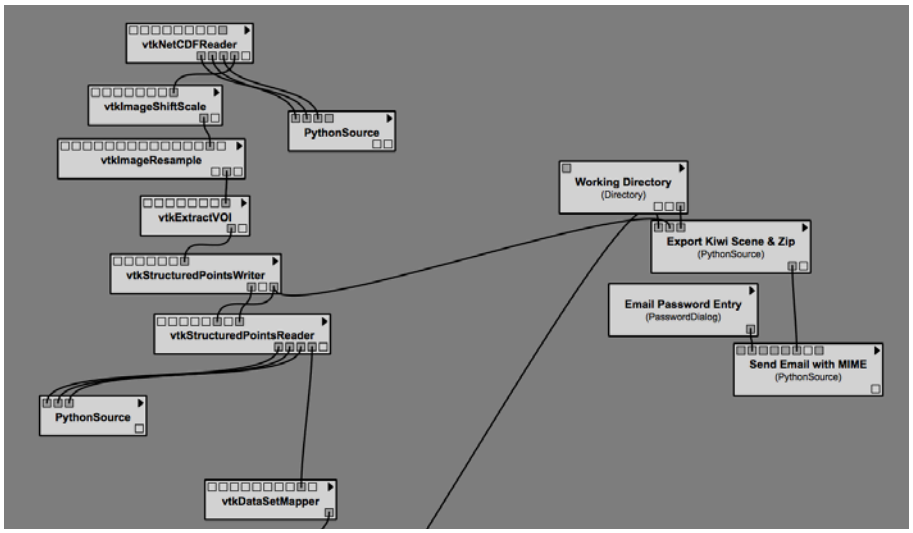

Fig. 2. *VisTrails for visualizing and exporting*

For export to mobile, VTK volume and renderer objects were stored as JSON objects via a Python script and sent via email to an iPad. The volume needed to be resampling again by a factor of 2 in order to be sent as an email attachment. The KiwiViewer open-source applicaiton (http://www.kiwiviewer.org/) was used to visualize the scene [Fig. 3]. This allows for manual control over contrast and threshold values while visualizing the volume.

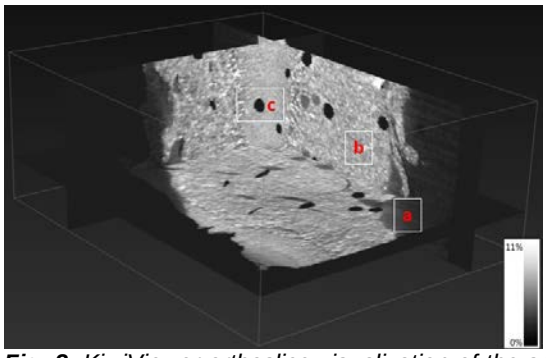

Fig. 3. *KiwiViewer orthoslice visualization of the spatial distribution of the flame retardant concentration: (a) char layer, (b) inner sample area, (c) gas bubble.*

Overall, VisTrails provided some ease in organizing and managing the provenance for visualization of the battery dataset and data processing of the flame retardant. Though thought needs to go into how the data is passed through the workflow in VisTrails, the benefits of easily rerunning the workflow with different datasets (such as the multi-energy datasets) with prompts for user input when required makes data processing go much quicker. The workflow is also more easily shared within our research group and also to others. The modules that were developed for the processing of these two datasets should lead to the development of a custom package for our research group that will then be available to the VisTrails community.

References

Kaestner, A.P., "MuhRec - a new tomography reconstructor", NIMA, **2011**, DOI: 10.1016/j.nima.2011.01.129

Callahan, S. P.; Freire, J.; Santos, E.; Scheidegger, C. E.; Silva, C. T.; Vo, H. T., "VisTrails: visualization meets data management", *Proceedings of the 2006 ACM SIGMOD international conference on Management of data* **2006**, 745-747.

Freire, J.; Silva, C. T., "Making Computations and Publications Reproducible with VisTrails", *Computing in Science & Engineering* **2012**, *14*, 18-25.

Ham, K.; Butler, L. G., "Algorithms for three-dimensional chemical analysis via multi-energy synchrotron X-ray tomography", *Nucl. Instrum. Methods B* **2007**, *262*, 117-27.

Ham, K.; Jin, H.; Al-Raoush, R. I.; Xie, X. G.; Willson, C. S.; Byerly, G. R.; Simeral, L. S.; Rivers, M. L.; Kurtz, R. L.; Butler, L. G., "Three-Dimensional Chemical Analysis with Synchrotron Tomography at Multiple X-ray Energies: Brominated Aromatic Flame Retardant and Antimony Oxide in Polystyrene", *Chemistry of Materials* **2004**, *16*, 4032-42.

Marathe, S.; Assoufid, L.; Xiao, X.; Ham, K.; Johnson, W. W.; Butler, L. G., "Improved Algorithm for Processing Grating-Based Phase Contrast Interferometry Image Sets", *Rev. Sci. Instrum.* **2014**, *85*, art. no. 013704.

Palenstijn, W.J.; Batenburg, K.J.; Sijbers, J, "The ASTRA Tomography Toolbox", 13th International Conference on Computational and Mathematical Methods in Science and Engineering, CMMSE **2013** vol. 4, pp. 1139-1145.

Silva, C. T.; Anderson, E.; Santos, E.; Freire, J., "Using VisTrails and Provenance for Teaching Scientific Visualization", *Computer Graphics Forum* **2011**, *30*, 75-84.

CT reconstruction with automated component and specimen motion corrections

B. Recur[1], *A. Kingston[1], S. Latham[1], G. Myers[1] and A. Sheppard[1]
[1]Australian National University, Dept. Applied Maths, RSPE, Canberra, Australia
* presenting author

INTRODUCTION

Relative specimen and component motion encountered during a CT-scan lead to blurry reconstructed images or multiple edge artefacts, penalizing image analysis (e.g., segmentation) and quantization. Motion errors can be divided into three classes: i) source movement, ii) stage errors, and, iii) specimen motion. i) is typically associated with the X-ray source reaching thermal equilibrium during a scan. Supposing it is stable at the end of the scan, an additional fast- or reference-scan (with a few number of projections compared to the full-scan) can be performed [1]. Projections of full and fast scans are registered [2] and each full-scan projection image is corrected by interpolating motion parameters of the two closest reference projections. ii) is due to the inaccuracies of the translation and rotation stages of the system. Despite a higher-and-higher accuracy of mechanical positioning of mobile parts of the device, some stage errors remain significant enough, leading to artefacts in reconstructed tomogram. Since these errors are often repeatable, they can often be addressed using a misalignment map (determined experimentally) [3]. Finally, iii), if specimen motion is repeatable or stable at the end of the scan, it can be corrected by projection registration or mapping as with source movement. It results that the traditional CT processing sequence (cf. Fig. 1) for all these cases performs: i) acquisition pre-processing (using reference scan and/or calibration map), and, ii) tomographic reconstruction from re-aligned projections.

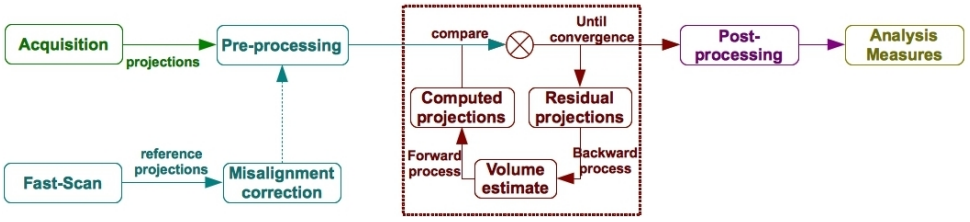

Figure 1: Traditional workflow: acquisition is pre-processed using a reference-scan and/or a calibration map in order to correct all predictable motion errors in the projections. Then, tomographic reconstruction is performed (here, iterative reconstruction scheme is provided) to recover the tomogram analysed by the end-user.

However, some source and stage errors cannot be corrected using these techniques, and specimen motion is almost always unpredictable. Since scanner calibration and reference-scan are useless in these cases, the only remaining solution consists of including a motion error correction in tomographic reconstruction. In this paper, we investigate a solution where projection mis-alignments are assessed during iterative CT reconstruction. The remainder of the paper is organised as follows: First we study the effects of motion errors into projections and propose an overall motion model. Then we develop an iterative reconstruction scheme including motion correction and suggest some optimisations. Before concluding, we discuss results from synthetic and real acquisition datasets.

MOTION ERRORS INTO PROJECTIONS

As a first order approximation, the complex specimen/component rigid body motion can be captured by translation, rotation and scaling of projection images. For instance, any source drift orthogonal to the detector leads

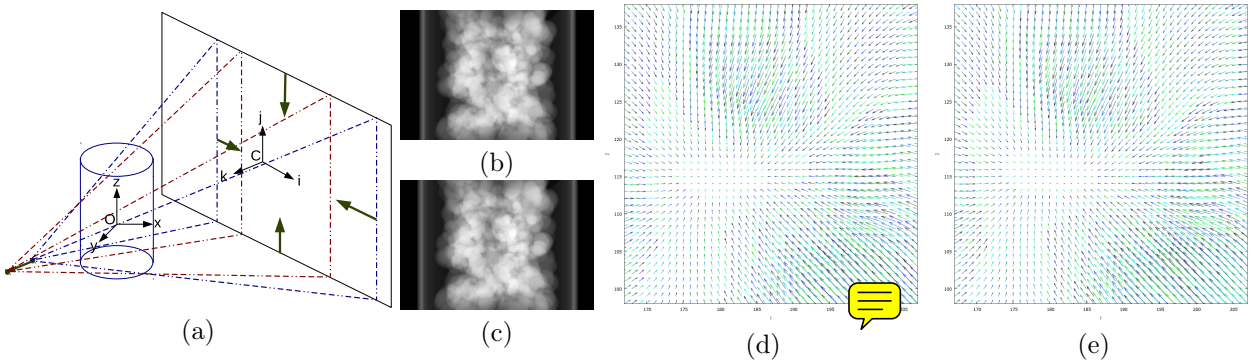

Figure 2: (a) A translation error of the source along K-Axis generates a motion error between a theoretical expected projection, (b), and the actual acquired projection, (c). Error between (b) and (c) can be represented by a vector-field, obtained by a differential optical flow (DOF) technique [4–6]. Vector footprint looks like a scale change (zoom in, in this example). (e) A motion of the object along K-Axis leads to a motion error signature similar to source drift along the same axis.

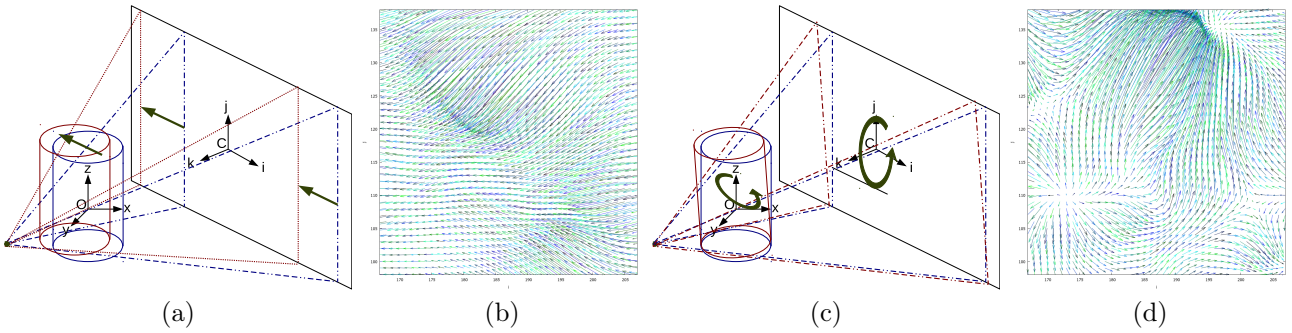

Figure 3: (a) a horizontal translation error of the specimen parallel to I-Axis generates a translational motion error between theoretical projection and acquired projections. (b) Corresponding error vector-field. (c) A rotation of the object by 1° along X, Y, and Z-Axis is partially depicted by a planar rotation. (d) Corresponding error vector-field.

to a scale change between acquired and expected projections (cf. Fig. 2). Specimen motion along the same direction leads to a similar misalignment (cf. Fig. 2(e)). Similarly, any source or specimen motion parallel to the detector leads to a translation between acquired and expected projections (cf. Fig. 3(a)). More complex object motions, as combination of several rotations along X, Y, and Z-axis, are partially depicted by a planar rotation (cf. Fig. 3(b)).

TOMOGRAPHIC RECONSTRUCTION WITH MOTION CORRECTIONS

A typical iterative CT reconstruction updates the tomogram, μ^t at iteration t, by comparing acquired θ-projection, R_θ, with corresponding projection R_θ^t, computed from the volume estimated at previous iteration. The error-projection obtained by such a comparison is back-projected into μ^t, and the overall process is performed until solution convergence (cf. red section of the workflow Fig. 1). We propose the following method to combine automated projection re-alignment with tomographic reconstruction: i) consider R_θ^t as a reference image (it is more correctly aligned irrespective with the volume estimate μ^{t-1}), and, ii) consider corresponding R_θ as sensed image to register and realign prior to the projection comparison made by CT reconstruction. In this paper, we use the Ordered Subsets Convex (OSC) algorithm [7, 8] as the iterative CT basis and the log-polar phase correlation (LPPC) technique to register projections [9, 10]. LPPC estimates translation, (t_i, t_j), planar rotation angle, ϕ, and scale rate, Λ, between two images. This registration method is based on the fact that planar rotation and scale change between two images correspond respectively to a horizontal and vertical translation when both images are expressed in log-polar coordinates. By combining iterative reconstruction

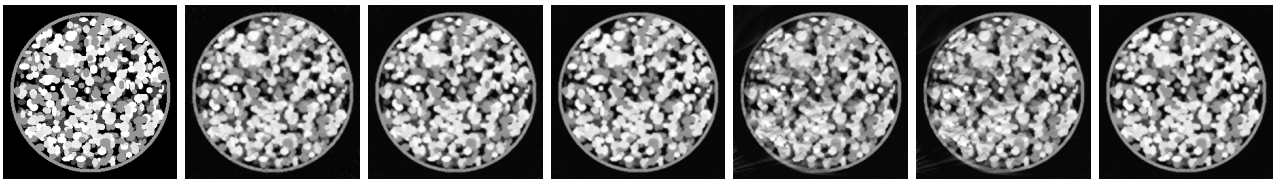

NMSE: 0	NMSE: 6.14	NMSE: 4.82	NMSE: 4.47	NMSE: 13.23	NMSE: 12.82	NMSE: 9.50
PSNR: inf	PSNR: 1.88	PSNR: 2.12	PSNR: 2.20	PSNR: 1.12	PSNR: 1.19	SSIM: 1.44
(a)	(b)	(c)	(d)	(e)	(f)	(g)

Figure 4: (a) Numerical ground-truth volume (central slice). Reconstructions from acquisition having experienced a random source drift using: (b) OSC, (c) OSC-LPPC, (d) OSC-LPPC-DE. Reconstructions from acquisition having experienced a random specimen motion using: (e) OSC, (f) OSC-LPPC, (g) OSC-LPPC-DE.

with LPPC to estimate motion, we propose the following iterative CT method including motion corrections:

1. Compute the forward-projection $\hat{R}_\theta^t$ from current volume estimate μ^t;
2. Compute LPPC between acquisition R, as sensed image, and $\hat{R}_\theta^t$, as reference image;
3. Compute corrected acquired projection R' of R, using $(t_i, t_j, \phi, \Lambda)$ provided by LPPC,
4. Update μ^t using standard iterative reconstruction step, from R' and $\hat{R}_\theta^t$;
5. As usual iterative reconstructions: repeat steps 1-4 for all projections until convergence of the solution μ^t.

The proposed reconstruction method, denoted OSC-LPPC, can be improved by modeling all motions as a unique source drift, $(\delta_{s_x}, \delta_{s_y}, \delta_{s_z})_\theta$, on each projection θ, estimated from $(t_i, t_j, \phi, \Lambda)_\theta$ (knowing CT scanner geometry) as follows:

$$\begin{cases} \delta_{s_x} = n\cos\theta + d.t_i\sin\theta \\ \delta_{s_y} = n\sin\theta - d.t_i\cos\theta \\ \delta_{s_z} = -d.t_j \end{cases}, \quad (1) \qquad \text{where} \qquad \begin{cases} n = \dfrac{d_{SO}(\Lambda-1)}{1-\frac{d_{SO}}{d_{SP}}\Lambda} \\ d = \Delta P\dfrac{d_{SO}+n}{d_{SP}+n} \end{cases} \quad (2)$$

where d_{SO} and d_{SP} are the source-object and source-detector distances, respectively, and ΔP is the detector resolution (in mm). By updating $(\delta_{s_x}, \delta_{s_y}, \delta_{s_z})_\theta$ at each iteration, we obtain a correction feedback since each motion corrected at iteration t is assessed at sub-sequent iterations throughout the new source position (used as anchor point to compute R_θ^{t+1}). This method, denoted OSC-LPPC-DE (*Drift Estimation*) in the following, performs steps 1-4 similarly than OSC-LPPC. Prior to the next iteration processing, it also updates: i) source position: $(s_x, s_y, s_z)^t = (s_x, s_y, s_z)^t + (\delta_{s_x}, \delta_{s_y}, \delta_{s_z})^t$, where $(\delta_{s_x}, \delta_{s_y}, \delta_{s_z})^t$ is given by Eq. 1; and, ii) magnification: $\frac{{d_{SO}}^t}{{d_{SP}}^t} = \frac{{d_{SO}}^t + n^t}{{d_{SP}}^t + n^t}$, where n^t is given by Eq. 2.

RESULTS AND DISCUSSION

Both proposed methods are experimented from synthetic data. A synthetic volume simulating a rock sample is computed and used as ground truth. This sample is composed of a container, 6mm diameter, filled randomly with different mineral grains, modeled as ellipsoids with radius chosen uniformly between 100μm and 250μm (cf. Fig. 4(a)). The mineral distribution of grains is 60% of quartz, 20% kaolinite and 20% calcite. The phantom (or synthetic object) is acquired at higher resolution using a detector with twice the number of pixels in each dimension to prevent the inverse crime [11], then acquisition is down-sampled to perform reconstruction at standard scale. Acquisition geometry used in this paper is high-angle cone beam, as it is the case for the μ-CT scanners manufactured at the ANU.

We investigate two kinds of random motion errors: i) random source motion leading to a maximal projection misalignment ($\propto$ 1 pixel), and, ii) specimen motion: the sample is acquired on the 3/4 without source motion; then it is translated by few voxels, and the last quarter of projections is acquired. Practically, i) leads to blurry reconstructed tomograms, whereas ii) often leads to double-edge effects in reconstructed data. Tomograms are reconstructed from these acquisitions using standard OSC, OSC-LPPC and OSC-LPPC-DE methods.

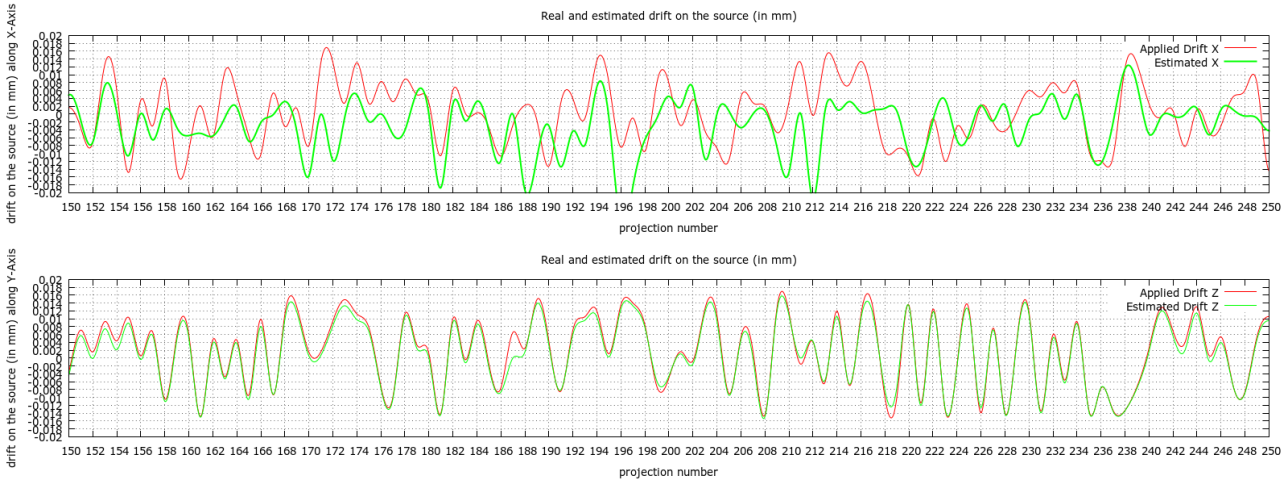

Figure 5: Comparison between random source drift applied on simulated experiment (red curves) and drift estimated by OSC-LPPC-DE (green curves), along X and Z-Axis, respectively.

Fig. 4 shows reconstruction results from simulated acquisitions having experienced a random source or specimen motions. In the case of random drift source, OSC-LPPC (c) and OSC-LPPC-DE (d) provide better results compared to standard OSC reconstruction (b). Similarly in the case of random specimen motion, we achieve better results (f-g) compared to OSC (e), especially with the OSC-LPPC-DE method (g) which offers an assessment of correction made at each iteration during the sub-sequent ones. Fig. 5 shows comparisons between random source drift applied on simulated experiment (red curves) and drift estimated by OSC-LPPC-DE (green curves). It demonstrates that random motion of the mobile parts of the scan are accurately recovered, especially on the Z-axis. As a consequence, the convergence of estimated drift could become a new parameter to automatically detect the convergence of the iterative CT reconstruction.

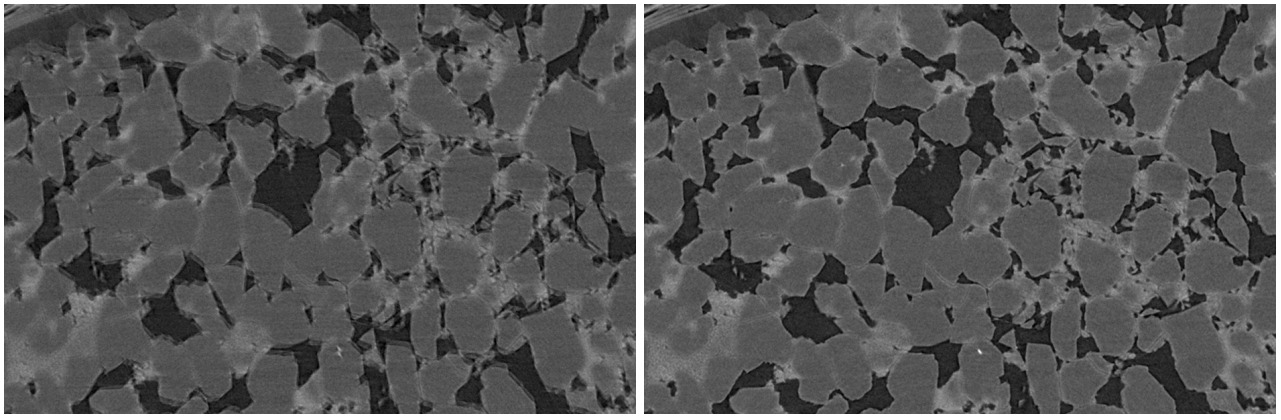

(a) (b)

Figure 6: Rock in a pressure cell (circular scan having experienced object motion): (a) Z-slice reconstructed with FDK (double edges appear as a consequence of the motion). (b) Double edge effects are corrected by the dual reconstruction / motion registration technique.

The $\mu-$CT scanner acquisitions provided by the ANU are composed of thousands of projections sized 3072^2 pixels; and reconstructed tomograms are often sized $2600^2 \times M$, where $M > 2600$. An iterative CT reconstruction is then unrealistic except with a supercomputer. To overcome this limitation, we have experimented the following pseudo-iterative workflow: we reconstruct (using analytic FDK reconstruction), reproject obtained tomogram and align projections. Then we reconstruct from scratch again and so on. Tomograms obtained with such a reconstruction are compared to standard FDK reconstructions from acquisitions having experienced: i) a

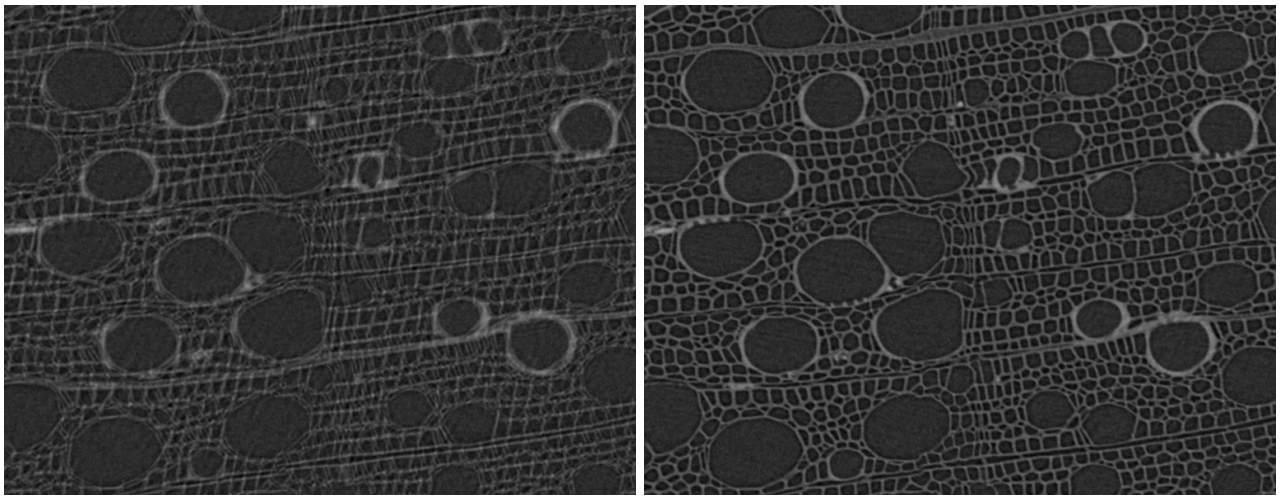

(a) (b)

Figure 7: Wood (willow) at 800nm voxel size (helical scan having experienced a random stage motion): (a) Z-slice reconstructed with FDK (blurred slices due to stage motion). (b) Blur is corrected by the dual reconstruction / motion registration technique.

motion of the object (cf. Fig. 6), ii) a random stage motion (cf. Fig. 7). Results highlight that double-edge effects due to the object motion, as well as motion blur due to unpredictable stage motion, can be corrected. It also demonstrates the flexibility of motion registration into projections whatever the adopted tomographic reconstruction workflow (especially, iterative CT reconstruction can be avoided when acquired data are too large to provide the tomogram in a reasonable computation time).

CONCLUSION

In this paper, a method consisting of a dual CT reconstruction and motion registration into projections is proposed to correct unpredictable sample motion and stage errors encountered during a scan. Thus reconstructed tomograms are no longer blurred and do not contain double-edges. However motion registration is based on rigid transformation estimation only; which could be a limiting factor to accurately correct some complex motions. Future works will focus on improving motion estimation by including nonrigid transformation models to the mis-alignement correction part of the algorithm. We will also further investigate practical implementation to make this iterative reconstruction achievable on very large datasets.

References

[1] X. Liu A. Sasov and P. Salmon. *Proc. SPIE*, 7078:70781C, 2008.

[2] Barbara Zitova and Jan Flusser. *Image and vision computing*, 21(11):977–1000, 2003.

[3] D. Gao S. Mayo, P. Miller and J. Sheffield-Parker. *J. Microsc.*, 228:257–263, 2007.

[4] Berthold K Horn and Brian G Schunck. In *Technical Symposium East*, pages 319–331, 1981.

[5] Jean-Yves Bouguet. *Intel Corporation*, 5, 2001.

[6] Andrés Bruhn, Joachim Weickert, and Christoph Schnörr. *International Journal of Computer Vision*, 61(3):211–231, 2005.

[7] Hakan Erdogan and Jeffrey A Fessler. *Physics in medicine and biology*, 44(11):2835, 1999.

[8] Chris Kamphuis and Freek J Beekman. *Medical Imaging, IEEE Transactions on*, 17(6):1101–1105, 1998.

[9] Hassan Foroosh, Josiane B Zerubia, and Marc Berthod. *Image Processing, IEEE Transactions on*, 11(3):188–200, 2002.

[10] Kenji Takita, Yoshifumi Sasaki, Tatsuo Higuchi, and Koji KOBAYASHI. *IEICE transactions on fundamentals of electronics, communications and computer sciences*, 86(8):1925–1934, 2003.

[11] Johan Nuyts, Bruno De Man, Jeffrey A Fessler, Wojciech Zbijewski, and Freek J Beekman. *Physics in medicine and biology*, 58(12):R63, 2013.

Session 202

Influence of Particle Morphology on Strain Localization of Sheared Sand

M. JARRAR[1], A. M. DRUCKERY[2] , K. A. ALSHIBLI*[3], R. AL-RAOUSH[4]

[1] Graduate student, Dept. of Civil & Env. Engineering, University of Tennessee, Knoxville, TN 37996, USA – mjarrar@vols.utk.edu
[2] Graduate student, Dept. of Civil & Env. Engineering, University of Tennessee, Knoxville, TN 37996, USA– Adruckre@vols.utk.edu
[3] Professor, Dept. of Civil & Env. Engineering, 324 John Tickle Building, University of Tennessee, Knoxville, TN 37996, USA– Alshibli@utk.edu
[4] Associate Professor, Dept. of Civil & Arch. Engineering, Qatar University, Qatar– Riyadh@qu.edu.qa
* presenting author

Keywords: in situ x-ray computed tomography, Particle kinematics

Abstract

The failure mode of laboratory specimens when sheared under axisymmetric triaxial compression is commonly described as diffuse bifurcation (bulging) or via a single or multiple shear bands. Desrues et al. (1996) and Alshibli et al. (2003) used computed tomography technique to visualize a rather complex failure mode involving multiple shear bands that developed within the specimens and reported that the bulging seen on specimen surface is just an external manifestation of a complex failure mode. This paper discusses the influence of particle morphology on the failure mode of sheared triaxial specimens by comparing the behavior of a specimen composed of spherical glass beads with one of angular sand. 3D synchrotron micro-tomography (SMT) technique was used to acquire multi in situ scans of the specimens at increasing axial strain levels. The paper compares the onset and evolution of failure modes of the two specimens and discusses them in relation to particle morphology.

Introduction

Recent research in geomechanics agrees on the significant influence of particle morphology on the constitutive behavior of granular materials (e.g. Oda et al., 1997; Hall et al., 2010; Hasan and Alshibli, 2012). Researchers have utilized the high resolution 3D x-ray computed tomography images to detect and track particle kinematic behavior in 3D. Hall et al. (2010) developed a discrete and continuum approach to track and determine particle translation and rotation within triaxial sand specimens. Ando et al. (2012) furthered that development by introducing the ID-Track technique that uses a single particle properties (i.e., particle volume) to identify grains and track them for triaxial specimens of two sheared sands with different morphologies.

In this paper, a similar approach is used on SMT images of angular dry glass sand and spherical glass beads that utilizes multiple particle properties to track particles during triaxial compression. Particles' rotation and translation are calculated and the failure modes of both specimens are discussed in relation to their morphology.

Testing and Imaging

Axisymmetric triaxial compression experiments (similar to Hasan and Alshibli, 2012) were performed on uniform dry spherical glass beads and angular sand known as dry glass sand with the size portion between U.S. sieves #40 (0.420 mm) and #50 (0.297 mm), which renders a mean particle size d_{50} of 0.36 mm. The triaxial cell was especially fabricated and has similar capabilities as a conventional triaxial cell. Specimens are cylindrical in shape with a diameter of 10.6 mm and a height of 19.3 mm. The void ratio

(e), minimum (e_{min}) and maximum (e_{max}) void ratios and specific gravities (G_s) for the specimens are listed in Table 1. Both specimens were compressed at 0.2 mm constant displacement rate and sheared while maintaining a constant confining pressure of 400 kPa.

Table 1. *Properties of tested specimens*

Material	G_s	e	e_{min}	e_{max}
Glass Beads	2.55	0.670	0.686	0.800
Dry Glass sand	2.65	0.710	0.715	0.947

SMT scans were collected at GeoSoilEnviroCARS (GSECARs), Sector 13 of the Advanced Photon Source (APS), Argonne National Laboratory (ANL), Illinois, USA. The specimens were scanned using a monochromatic energy of 33 keV with image spatial resolution of 11.18 μm/pixel. Loading was paused at nine strain stages during the experiment to collect SMT scans. Figure 1 shows the principal stress ratio (PSR) versus the nominal axial strain (ε_1) for the specimens, along with the scanning points. The dry glass sand specimen reached a peak PSR at ~6.4% axial strain followed by a small degree of softening, while the glass beads reached the peak PSR at ~3.5% axial strain followed by a small degree of softening. The glass beads exhibited oscillation in PSR due to slip stick between particles since they are spherical with smooth surfaces. It appears that the angular sand particles caused more interlocking between them which required higher strains to reach the peak state when compared to relatively smooth glass beads.

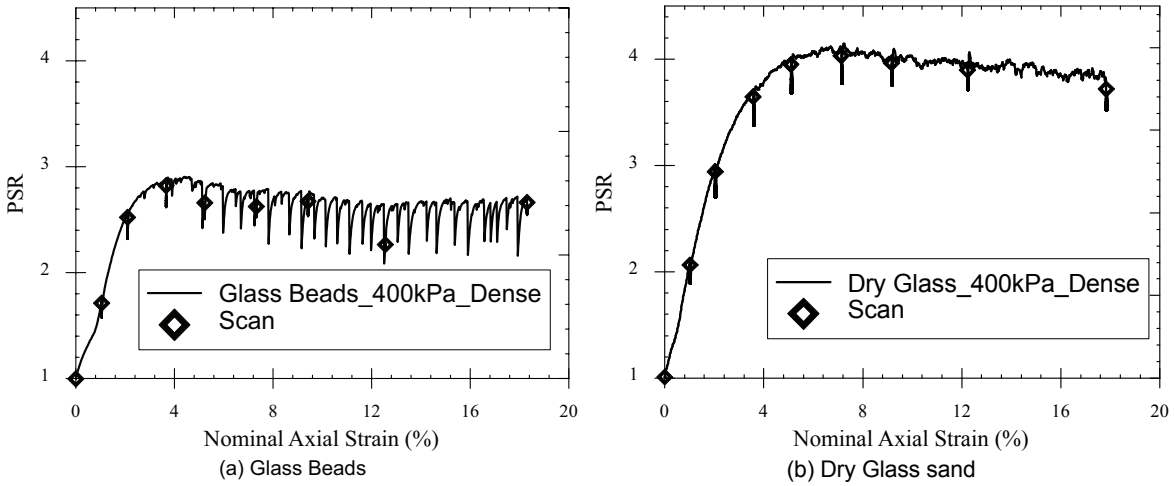

(a) Glass Beads (b) Dry Glass sand

Fig. 1. *PSR versus nominal axial strain for the specimens*

Image Processing and Particle Tracking

Processing of the SMT images was performed using Avizo Fire 8.0 software, which uses Visilog algorithms for image processing and quantification. Raw SMT images were first segmented using a consistent threshold value to separate the solid particles from the surrounding air resulting in a binarized image of solid particles (value of 1) and air (value of 0). Particles in contact were separated using the Avizo *Separate Objects* algorithm to remove small areas of contact between them. After separation, particles were individually labeled with an identification number during image analysis. Particle

labels were then expanded and masked within the binary image to restore the contact area. A full description of the image processing procedure can be found in Druckrey and Alshibli (2014).

Further analysis was conducted on the labeled images using a modified version of the code that was developed by Al-Raoush (2007). It provides a variety of physical properties of the sheared granular material particles including the coordinates of the center of mass, volume, surface area, longest, intermediate and shortest axes of particles. Although Avizo labels particles, it does not necessarily give the same label to a specific particle throughout all scans. Therefore, an algorithm was developed by the authors to track particles between two consecutive scans. It isolates a sub-volume around the centroid of each particle in the first image and uses the sub-volume in the second image to search for a matching particle in the second image. Individual particle properties within 3% to 4% are compared to the properties obtained from the particle in the first image. If the algorithm does not find a matching particle, it will be eliminated from the analysis. If more than one matching particle are found, the particle with the closest morphological properties is selected. Overall, the percentage of tracked particles was 90% for the glass beads and 80% for the dry glass sand specimens.

Particle Kinematic Properties

Particle displacement vectors were calculated by finding the difference in the particle centroid in the x, y, and z directions between two consecutive scans. The longest axis of each particle was used to calculate its rotation angle with respect to the direction of the major principal stress (z-axis). The absolute value of the angle of rotation was calculated between two consecutive scans, therefore the direction of the rotation is not specified. Particle kinematics are calculated for all 8 scan intervals, but due to space limitations, the displacements and rotations of the initial, peak and post peak loading stages are displayed in Figures 2 & 3 for dry glass sand and glass beads, respectively.

For the dry glass sand (Figure 2e), particle rotation shows an evidence of intensive shearing within the middle part of the specimen at axial strain of 7.3% which became more noticeable as shearing continued (Figure 2f). however, there is no evidence of a development of a well-defined single shear band from SMT images or the surface of the specimen. Particle translation field (Figure 2b) shows that particles translate mostly in the vertical direction at the top portion of the specimen then they change direction into down and outward direction. One expects a dense specimen of angular sand to fail via a well-defined single or multiple shear band when tested under high confining pressure (400 kPa in this case). However, it appears that interlocking between angular particles forces the development of multiple smaller shear bands and not a single shear band.

The glass beads specimen (Figure 3) do not show an evidence of strain localization into a single shear band before the peak stage followed by a preferred particle translation in the post-peak regime which points for a development of a single shear band. Particle rotation did not show a concentration of high rotation gradients along the shear band due to the fact of uniform spherical particles with similar surface roughness that resulted in a much higher particle rotation (as high as 40^{o} compared to 20^{o} for the dry glass sand). Glass beads showed a tendency of forming a single shear band whereas dry glass exhibited multiple shear bands. It is not enough to just use particle translation or rotation to identify the shear band onset and development but rather the combined effect of both. Very angular particles tend to rotate less than smooth particles due to interlocking. These findings are based on testing dense specimens under high confining pressure. More experiments that include other sands and different densities

are needed to investigate the influence of density and confining pressure on strain localization phenomena.

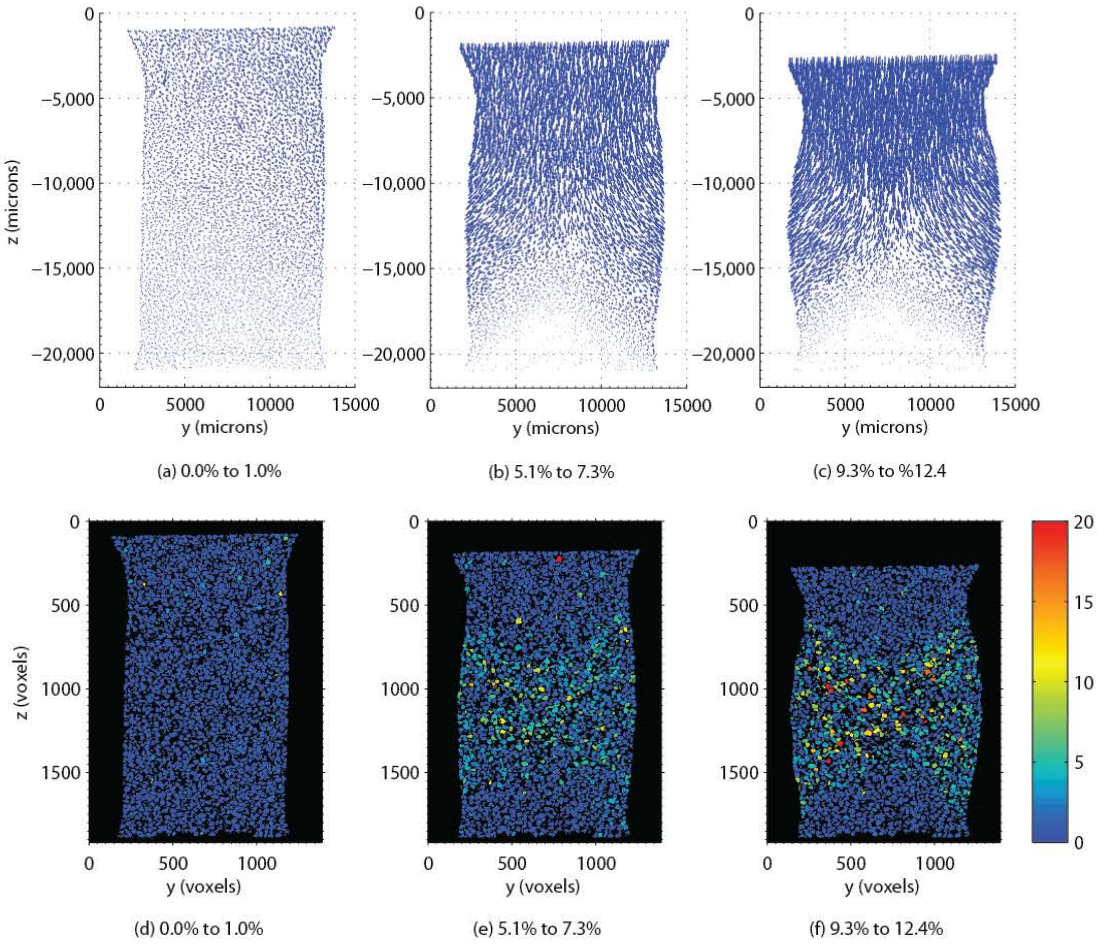

Fig. 2. *Dry Glass sand particle displacements (a), (b) and (c) and rotations (d), (e) and (f) in the initial, peak and post peak loading stages*

Conlcusion

Axisymmetric triaxial compression experiments were conducted on angular dry glass sand and spherical glass beads specimens. 3D SMT scans of multiple strain stages were acquired and particle tracking between successive scans was implemented. Significant particle rotations within a zone of intensive shearing was observed in the middle part of the dry glass sand specimen at the peak stage and became more prominent in the post-peak regime. This can also be inferred from following the particle displacement vectors and particle rotation. The glass beads specimen failed along a well defined shear band that can be seen from particle translation vectors. The uniform spherical glass beads with similar surface roughness and morphology resulted in a much higher particle rotation than angular sand. However, many particles outside the shear band still exhibited high rotation. It is not enough to just rely on particle translation or rotation to investigate strain localization and one needs both measurements since particles with different morphology will have different degrees of rotation and translation.

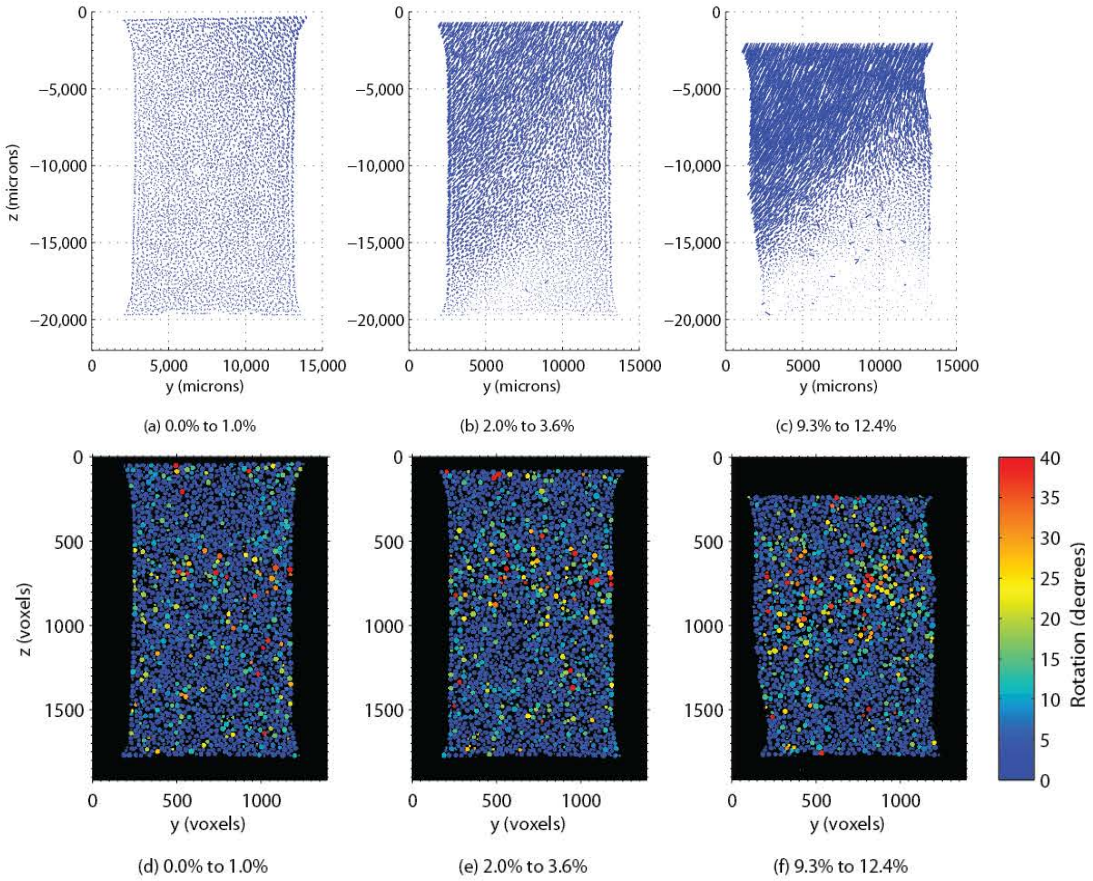

Fig. 3. *Glass beads particle displacements (a), (b) and (c) and rotations (d), (e) and (f) in the initial, peak and post peak loading stages*

References

Al-Raoush, R. (2007). Microstructure characterization of granular materials. Physica A: Statistical Mechanics and its Applications 377: 545-558.

Alshibli, K. A., Batiste, S. N., and Sture, S. (2003). Strain Localization in Sand: Plane Strain Versus Triaxial Compression. ASCE, Journal of Geotechnical & Geoenvironmental Engineering 129, 6: 483-499.

Andò, E., Hall, S., Viggiani, G., Desrues, J., and Bésuelle, P. 2012. Grain-scale experimental investigation of localised deformation in sand: a discrete particle tracking approach."*Acta Geotech.*, 7, 1: 1–13.

Desrues J, Chambon R, Mokni M, Mazerolle F. 1996. Void ratio evolution inside shear bands in triaxial sand specimens studied by computed tomography. Geotechnique 46(3): 529–549

Druckrey, A. and Alshibli, K. (2014). 3D Behavior of Sand Particles Using X-Ray Synchrotron Micro-Tomography. Proceedings of 2014 Geo-Congress - Geo-Characterization and Modeling for Sustainability, GSP 234, 2814-2821

Hall, S. A., Bornert, M., Desrues, J., Pannier, Y., Lenoir, N., Viggiani, G., and BéSuelle, P. (2010). Discrete and continuum analysis of localised deformation in sand using X-ray CT and volumetric digital image correlation. *Geotechnique* 60,5: 315–322.

Hasan, A., and Alshibli, K. (2012). Three dimensional fabric evolution of sheared sand. *Granular Matter*, 14(4): 469–482.

Oda, M., Iwashita, K., and Kakiuchi, T. (1997). Importance of particle rotation in the mechanics of granular materials. *Proc., Powder and Grains*, A A Balkema Publishers, Rotterdam, Netherlands, 207–210.

Wormhole Development in Carbonate Rocks during CO2 Acidized Water Flow

A.P.S. Selvadurai and C. Couture
Department of Civil Engineering and Applied Mechanics
McGill University
817 Sherbrooke Street West
Montréal, QC, Canada H3A 0C3

ABSTRACT

The deep geologic sequestration of greenhouse gases in fluidized forms is regarded as the most favourable option for mitigating climate change. The target reservoirs identified for such sequestration activities are primarily sandstone formations that have natural geologic barriers in the form of caprock that can enhance hydrodynamic trapping. While pure sandstone formations are considered to be the ideal sequestration horizon, these are not universally available and on occasions, the sequestration strategy could include carbonate geological formations. The amount of carbonate content will therefore be a critical factor that will ensure the integrity of the storage formation during long term injection activities. Even with sandstone formations, it is likely that seams of carbonate rocks can be encountered. The behaviour of such carbonate rocks is also important to the sequestration strategy. To this end, an experimental research program was initiated to examine the behaviour of Indiana Limestone during acidized CO2 migration. Indiana Limestone has a carbonate content of 98% and this is intended to provide a worst case scenario in terms of the impact of acidized CO2 migration. Experiments were conducted on 50 mm diameter and 100 mm long samples of Indiana Limestone. The development of “Wormholes” is a characteristic feature of the breakdown of the fabric of the Indiana Limestone. The dissolution pathways can enhance the CO2 migration in such rock and the dissolved carbonates could be trapped in locations impeding the efficiency of injection and the potential for hydraulic fracture with continued injection. CT scanning techniques provided a clear picture of the final stages of wormhole development when complete breakthrough occurs compromising the storage capacity of the formation. The work is also being extended to identical experiments conducted on grey sandstone and dolomite. These experiments complemented by CT scanning techniques provide benchmarks for determining the efficiency of geologic sequestration of greenhouse gases.

Characterisation of force chains in granular media through combined 3DXRD and x-ray tomography

*S.A. HALL[1,2], R.C HURLEY[3], J. WRIGHT[4]

[1] Division of Solid Mechanics, Lund University, Lund Sweden
[2] European Spallation Source AB, Lund, Sweden
[3] Mechanical and Civil Engineering, California Institute of Technology, Pasadena, CA, USA
[4] European Synchrotron Radiation Facility, Grenoble, France

* presenting author

The development of “force chains” in granular media, i.e., spatially continuous lines of force between contacting grains by which boundary loads are transmitted, and their importance in controlling mechanics at larger scales has received much attention in recent years. To this end, many experiments using photoelastic materials, in 2D, and “numerical experiments” using 2D/3D discrete element method (DEM) simulations have been used to investigate the development of force distributions through granular assemblies. However, measuring 3D force distributions real granular materials remains a challenge.

New results from a novel experimental method for characterising structural evolution, deformation and 3D force distribution in real granular materials will be presented. The method involves in-situ mechanical testing with “three-dimensional x-ray diffraction” (3DXRD combined with x-ray tomography). These measurements provide data on individual tensor grain strains, from 3DXRD, at different applied-load levels through a loading test in addition to the grain shapes, positions and contacts, from the tomography. From these data the transmission of forces through the granular network can be inferred to allow force chains to be identified and characterised. Results for samples of nearly spherical quartz single crystals undergoing 1D compression will be presented.

Number of words: 190

Characterization of Rock Discontinuity Morphology during Shearing using X-ray micro-CT

B.S.A. TATONE[1], N. TISATO*[2], G. GRASSELLI[3]

[1] Geomechanica Inc.,Toronto, 90 Adelaide St. West, Suite 300, Toronto, ON, Canada, M5H 3V9 – bryan.tatone@geomechanica.com
[2] Department of Civil Engineering, University of Toronto, 35 St. George street, Toronto, ON, Canada, M5S 1A4 – nicola.tisato@utoronto.ca
[3] Department of Civil Engineering, University of Toronto, 35 St. George street, Toronto, ON, Canada, M5S 1A4 – giovanni.grasselli@utoronto.ca
* presenting author

Keywords: Rock Discontinuity, Aperture, Direct Shear

Abstract

While the shear behaviour of rock mass discontinuities has been extensively studied in the past, uncertainties regarding the mechanisms by which surface asperities deform and degrade under shear and how this degradation influences the aperture distribution remain. Although studies have attempted to investigate asperity failure mechanisms, they have been hampered by the lack of appropriate visualization tools or techniques. With micro X-ray Computed Tomography (µCT) systems now more widely available, it has become possible to observe asperity damage without physically separating the joint specimen following shearing. This paper outlines a recent laboratory study which investigated asperity degradation and joint space morphology through µCT imaging.

Introduction

Rock mass discontinuities represent planes of relative weakness and enhanced hydraulic conductivity and, thus, have a substantial influence on the hydro-mechanical behaviour of rock masses. Given the key role of these features, the development of improved characterization techniques has been a subject of ongoing research for many years. The objective of the current paper is to outline a recently developed methodology to non-destructively study asperity degradation mechanisms and discontinuity morphology during direct shear tests using micro X-ray Computed Tomography (µCT) (Tatone 2014). Specifically, measurements of the statistical and spatial aperture distributions, fracture surface areas, and preferential void space orientation as a function of shear displacement and different normal loading conditions were obtained.

Methods

Specimen design and shear testing

To study the evolution of asperity damage and discontinuity void space with shear displacement via µCT imaging, a series of fracture replicas with identical discontinuity geometries were created. Both idealized ‘saw tooth’ and natural discontinuity geometries were considered. To minimize geometry-related artifacts in subsequent µCT images, cylindrical specimen geometry was adopted in lieu of the conventional prismatic specimens used in direct shear tests (Fig. 1). These specimens had an overall diameter of 54 mm and length of 84 mm.

Specimens were cast from a high strength sulphate cement mortar using urethane rubber molds of the original discontinuity geometries. A careful effort was made to mix the mortar and fill molds in a consistent manner to ensure the intact strength and shear behaviour were consistent. The filling of the molds on a vibrating table proved to be essential in minimizing the presence of entrapped air bubbles within the specimens.

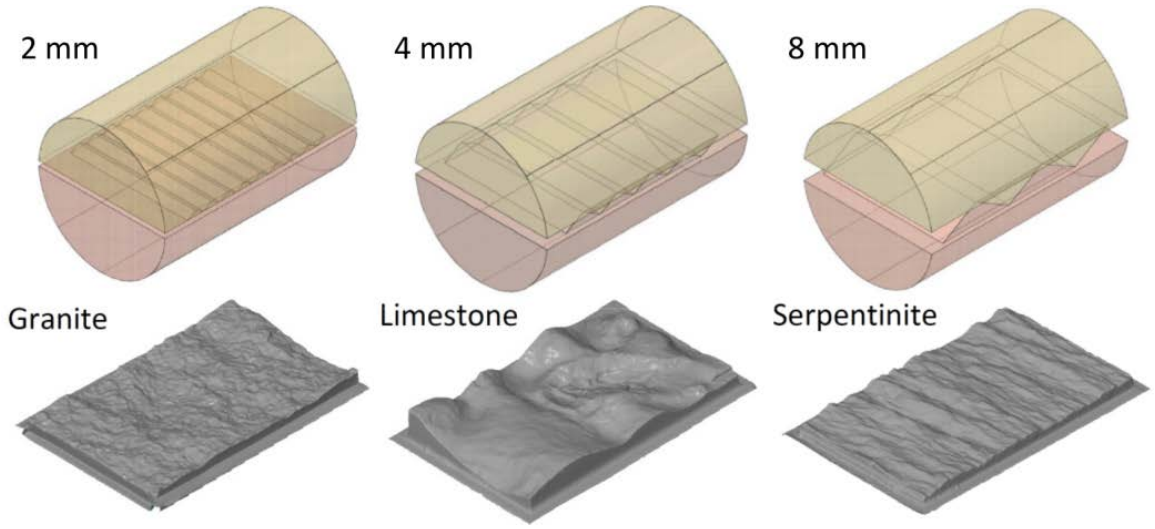

Fig. 1. Discontinuity specimen geometries (54 mm diameter x 84 mm long).

The evolution of damage with increasing shear displacement for a given discontinuity geometry was observed by testing multiple specimens up to varying final shear displacements. Testing was completed under constant normal loading conditions using a gear driven direct shear apparatus typical of soil mechanics laboratories (Fig. 2b). Instead of the conventional square shear box, a new specimen holder to test the unique cylindrical specimens was manufactured (Fig. 2a). Once the desired shear displacement in a particular test was achieved, loading was halted and the two halves of the specimen were bonded together such that their relative position could be maintained. Bonding was completed by filling a small recess around the perimeter of the discontinuity surface with an epoxy adhesive. Once the epoxy cured, the normal and static shear loads were removed and test specimens were relocated to an industrial µCT system for imaging.

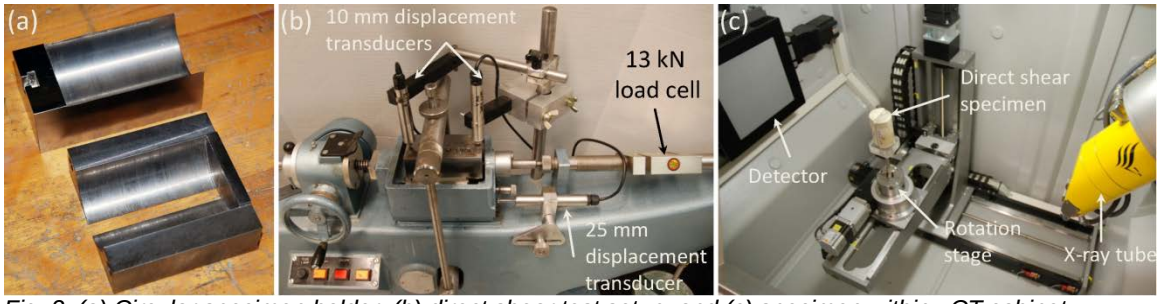

Fig. 2. (a) Circular specimen holder; (b) direct shear test setup; and (c) specimen within µCT cabinet.

µCT Imaging

CT imagery of the direct shear specimens was acquired using a Phoenix X-ray V|tome|x 240 kV µCT system manufactured by General Electric Sensing and Inspection Technologies and located within the Department of Civil Engineering at the University of Toronto (Fig. 2c). The employed scanning parameters are listed in Table 1. Image reconstruction via filtered back projection was completed using the Phoenix X-ray Datos|x-reconstruction software (v.1.5.0.22) with a beam hardening correction of 3/10, automatic ring artifact reduction applied, and a “scan optimization” performed to automatically locate the centre of reconstruction and compensate for small translations of specimens during scanning.

Tab. 1. µCT scanning parameters.

Parameter	Value
Number of rotation increments	1080
Voltage (kV)	140
Current (µA)	160
Detector timing (ms)	600
Image averaging (no. of images)	10
Voxel resolution (µm)	75
Pre-filtering	0.5 mm Cu
Nominal scanning time (hr)	2

CT Image Processing

The post-testing asperity damage and aperture of the specimens were investigated via image processing using the open-source software FIJI3. As described in detail in Tatone (2014), several existing tools and plug-ins within FIJI, along with several newly created plug-ins and macros, were utilized. In particular, image processing and analysis involved the following steps (Tatone 2014; Tatone and Grasselli 2015):

1. *Image preprocessing* - The reconstructed 16-bit images of the shear specimens were aligned such that the discontinuity plane was perpendicular to the slices of the volume. Each volume was then cropped down to a region encompassing the discontinuities with the same dimensions.
2. *Segmentation* - The approach involved coupling dual-level grey value thresholds with a spatial second derivative threshold. The dual-level global thresholds were used to obtain an approximate segmentation, referred to as the “primary” segmentation. The second derivative threshold, a method typically used for edge detection (Pera et al. 2003; Pratt 2007), was employed to refine the primary segmentation (referred to as the “secondary” segmentation).
3. *Morphological operations* - To improve the binary images for the purpose of performing image-based measurements, noise treatment, hole-filling, and a watershed algorithm were applied.
4. *Image-based measurements* - Lastly, binary image-based measurements, including: mean fracture aperture, fracture surface area, median effective aperture, spatial distribution of effective aperture, and the preferred orientation of the discontinuity void space were obtained.

Results

Considering an example of a series of replicas subjected to different shear displacements (Fig. 3), the central 10 mm thickness of the reconstructed volumes clearly illustrate the evolution of discontinuity damage and void space geometry. Yet, through the additional *µ*CT image processing steps described in the preceding section, quantitative measurement results were also obtained (e.g., Fig. 4).

The spatial distribution of effective fracture aperture (Fig. 4a) was defined by calculating the sum of void voxels in a direction normal to the shear plane. The statistical distribution (Fig. 4b) was obtained by simply considering all effective aperture measurements across the discontinuity. As shown in the figure, only select areas of the discontinuity experience an increase in aperture with shear displacement. Due to the anisotropic roughness of the surface, ‘channels’ perpendicular to the shear direction can be clearly observed (Fig. 4a).

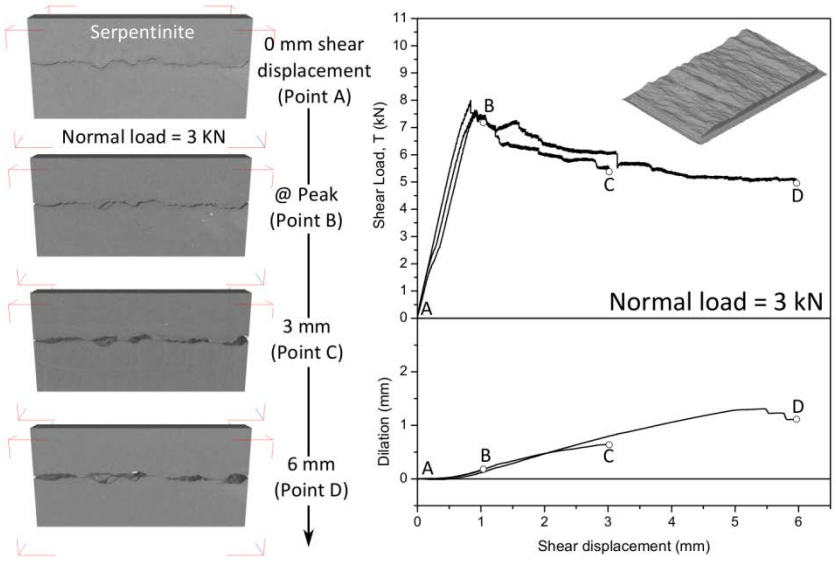

Fig. 3. Central part of reconstructed µCT volumes at increasing shear increments and corresponding load-displacement response as measured from direct shear testing.

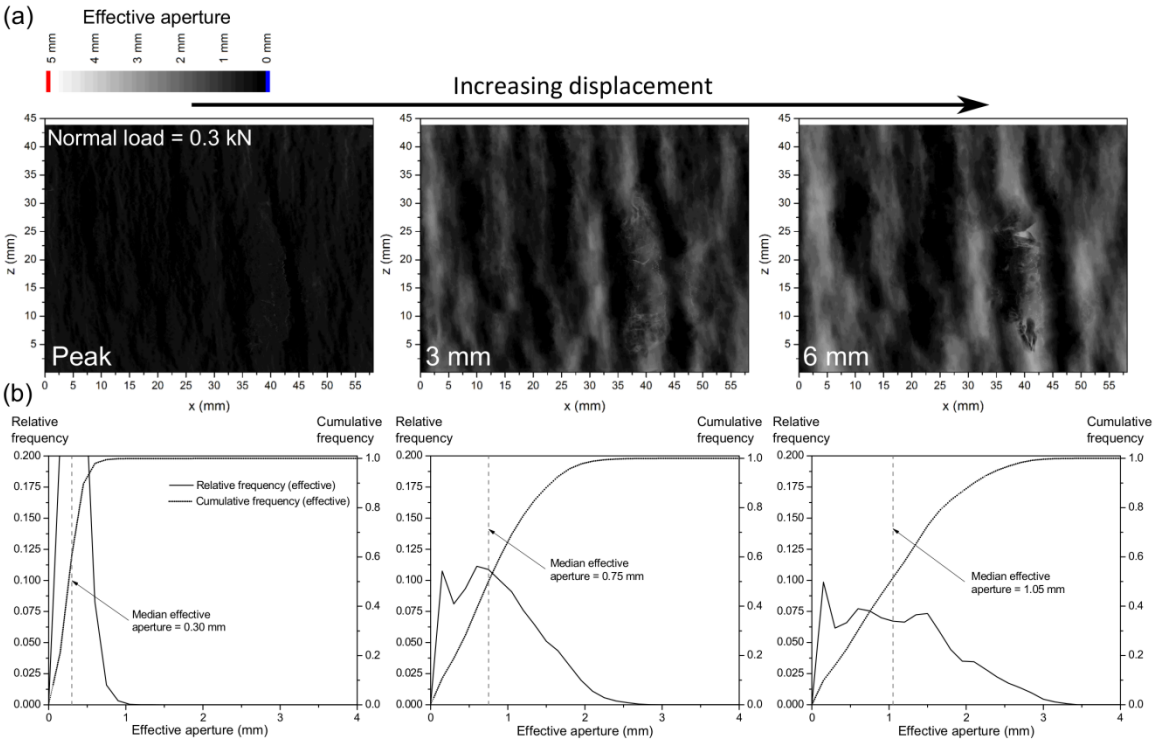

Fig. 4. (a) Evolution of the spatial effective aperture distribution for a surpentinite discontinuity surface as a function of shear displacement; (b) corresponding statistical distributions of effective aperture.

The increase in aperture is reflected by the median effective, which increased by nearly 300 % from the peak shear displacement to a final displacement of 6 mm (Fig. 5a). Over the same displacement range, the mean fracture aperture, estimated by dividing the total volume of void space by the cross-sectional area of the discontinuity specimens, increased by a similar magnitude (Fig. 5a). The total fracture surface area, defined by the interfacial area between intact materials and void space, showed little change as a function of displacement for this particular specimen due to the minor areal extent of asperity damage. (Fig. 5a)

The anisotropy in the preferential orientation of fracture void space was characterized in terms of a Mean Intercept Length (MIL). By overlaying a series of parallel lines over the discontinuity-parallel binary images, the mean length of the segments that intercept the void space was calculated. A large value for the MIL, indicates that the void space is more continuous, while a small value indicates that the void space is more discontinuous. Through consideration of parallel lines in many directions, the continuity of the void space as a function of direction was characterized. Such data can be presented in a polar plot, as shown in Fig. 5b. The MIL values for the serpentinite fracture indicate that the void space is preferentially oriented perpendicular to the shearing direction and becomes more continuous with increases in shear displacement (in agreement with Fig. 4).

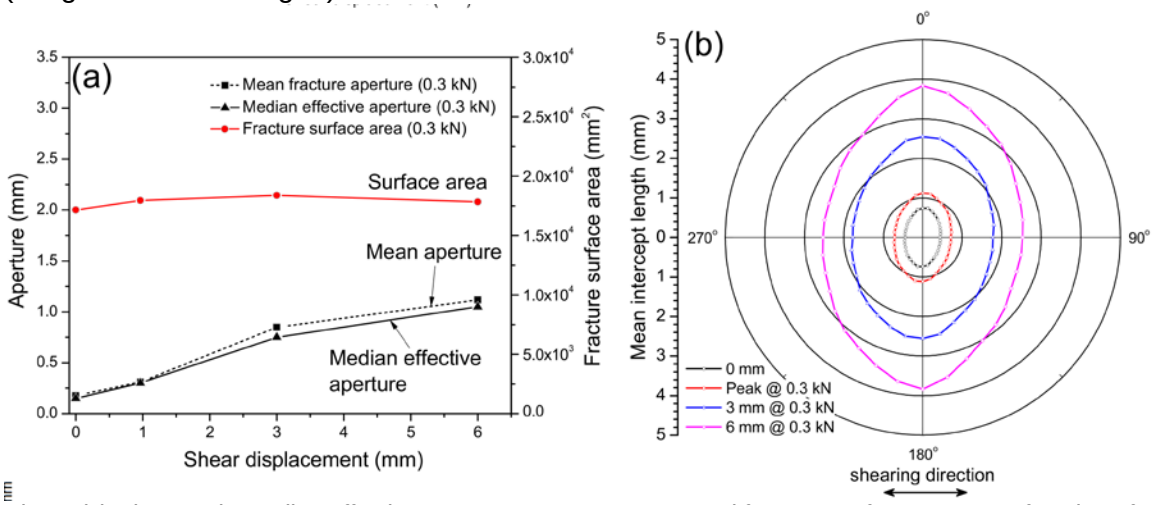

Fig. 5. (a) Changes in median effective aperture, mean aperture, and fracture surface area as a function of shear displacement for a serpentinite discontinuity surface; (b) Mean intercept length measured parallel to the serpentinite discontinuity surface at varying shear displacements.

Conclusions

In the presented methodology, replicated discontinuity specimens were designed such that specimens could be shear tested to different incremental displacements and subsequently relocated to an industrial μCT system to obtain 3D imagery of the internal structure. Via image processing and analysis using a series of newly written plug-ins and macros for FIJI, the damage and void space in test specimens were quantitatively characterized. At the time of completion, this work was the first known attempt at characterizing such features via μCT imaging. The results provide unprecedented insight into the morphology of rock discontinuities during shearing process, which is of key interest to several rock engineering and hydrogeology practitioners; including those concerned with preventing shear displacement (e.g., excavation, slope, and dam engineering) and those concerned with changes in hydraulic transmissivity resulting from shear displacement (e.g., for long-term radioactive waste disposal and reservoir stimulation via hydraulic fracturing).

References

Pera, V. E., E. L. Heffer, et al. (2003). "Spatial second-derivative image processing: an application to optical mammography to enhance the detection of breast tumors." **Journal of Biomedical Optics** 8(3): 517-524.

Pratt, W. K. (2007). Digital Image Processing: PIKS Scientific Inside. Wiley, 812 p.

Tatone, B. S. A. (2014). *Investigating the evolution of rock discontinuity asperity degradation and void space morphology under direct shear*. PhD, University of Toronto, Toronto, Canada.

Tatone, B. S. A. and G. Grasselli (2015). "Characterization of the effect of normal load on the discontinuity morphology in direct shear specimens using X-ray micro-CT." **Acta Geotechnica** 10(1): 31-54.

Insight into 3D Fracture Behavior of Silica Sand

M. CIL[1], K. ALSHIBLI*[2], P. KENESEI[3]

[1] Postdoctoral Research Fellow, Northwestern Univ., Evanston, IL, USA – mehmet.cil@northwestern.edu
[2] Professor, Univ. of Tennessee, Knoxville, TN, USA – Alshibli@utk.edu
[3] Research Scientist, Argonne National Laboratory, Argonne, Illinois, USA, – Email: kenesei@aps.anl.gov
* presenting author

Keywords: Computed tomography, contact number, fracture

Abstract

Synchrotron micro computed tomography (SMT) techniques was used to monitor the fracture behavior of natural Ottawa sand particles within a specimen that was loaded under 1D compression condition. 3D image analysis at the particle-scale showed that cracks in fractured sand particles generally initiate at contact points and propagate along the plane that connects the two contact points. The particles initially split into two or three major fragments followed by fracture into multiple small fragments. Micro-scale fracture analysis revealed that the position of contact forces and particle shape play a major role in the occurrence of particle fracture in a sand assembly.

Introduction

Fracture of particles play an important role in describing engineering properties of granular materials. Few studies employed experimental techniques to investigate fracture behavior of sand using high stress triaxial experiments (e.g., Lade and Yamamuro 1996, Nakata et al. 1999), one dimensional (1D) compression experiments (e.g., Terzaghi and Peck 1948, Roberts and de Souza 1958, Yamamuro et al. 1996), and displacement-controlled single-particle compression experiments (e.g., Nakata et al. 1999, McDowell 2002, Cavarretta et al. 2010, Cil and Alshibli 2012). Laboratory experiments generally draw conclusions based on the macro-scale measurements and are often useful in examining the effects of mineralogy, particle size, particle morphology, initial specimen density, and particle size distribution on the compression behavior of the particulate system (e.g., Hagerty et al. 1993, Nakata et al. 2001, Altuhafi and Coop 2011). However, such experimental results can not yield non-destructive fracture analysis since they only provide the stress-strain behavior of granular materials acquired at the external boundary of specimen during the test. Moreover, particle fracture information in laboratory experiments is obtained in post-test analyses by checking the change in grain-size distribution using sieve analysis or by visually inspecting the damage in individual particle morphology. This paper presents the evolution of fracture of sand particles within a specimen with emphasis on visualizing the fracture mode of particles in 3D using synchrotron micro-computed tomography (SMT) technique.

Experiment

The experiment was conducted on natural uniform silica sand known as F-75 Ottawa sand with particles size portion between US sieve #40 (0.420 mm) and Sieve #50 (0.297 mm). 1D compression experiment was conducted using a specially designed test cell that includes a specimen mold, computerized stepper motor to apply axial loading, two load cells, and a data acquisition system. The specimen mold is an acrylic cylinder with an outer diameter of 15 mm and has a 1 mm diameter hole at the center to house sand particles. Particles were carefully poured into the 1 mm hole and the specimen was

subjected to vibration to densify it. The initial height of the specimen is ~1.97 mm. Other test cell components were then assembled, and the test cell was mounted on the stage of the beamline in preparation for scanning.

In situ SMT scans were acquired at beamline 1-ID of the Advance Photon Source (APS), Argonne National Laboratory (ANL), Illinois, USA. The scans were collected using 70.5 KeV x-ray energy which yielded a spatial resolution of 1 μm/pixel. In contrast to conventional absorption-based x-ray SMT, scans at high x-ray energies provide phase-contrast which highlights particle edges and boundaries. In each SMT scan, 900 frames were collected by rotating the specimen at 0.2° angular increments over 180° and acquiring images at 0.65 second exposure time. Figure 1 shows axial SMT sections before loading with all particles identified and labelled.

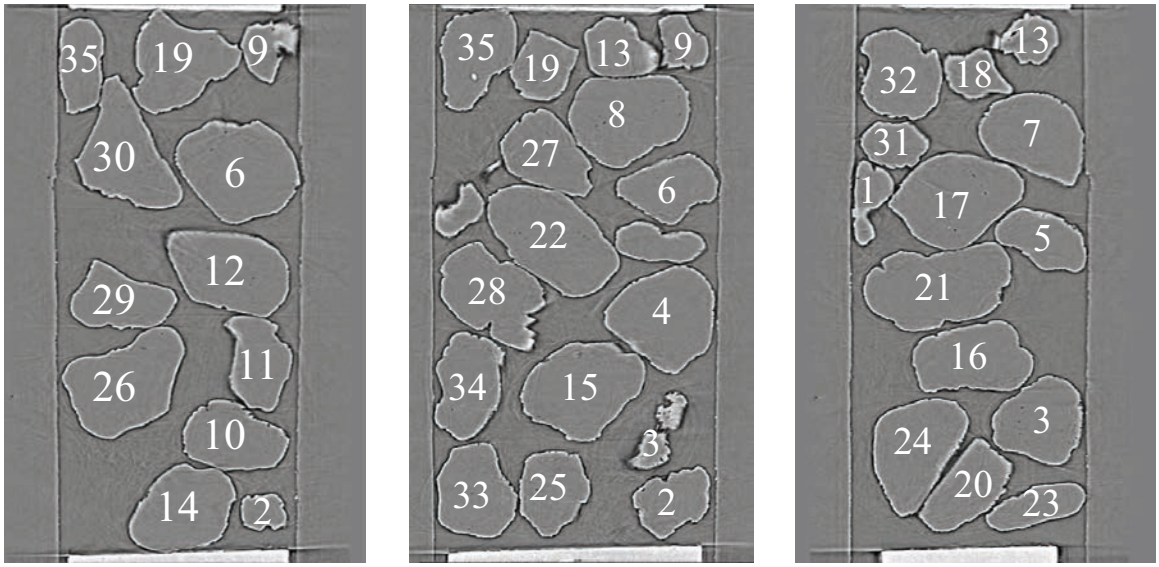

Fig. 1. *Assigned identification numbers of sand particles in SMT image analysis. Total number of particle in specimen is 35. The Figure shows axial slices at different axial sections to expose all particles*

Results

One observation made during examination of the 3D SMT images show that some of the particles aligned almost vertically during 1D compression. Since the specimen is composed of 35 particles, there is a high chance that these sand particles are part of force chains in the sand assembly. The characteristics of particle fracture and evolution of these nearly vertically aligned sand columns were investigated by visually tracking individual sand particles in SMT images. The orientation and arrangement of particles were examined using 3D renderings of sand particles generated from SMT images. Avizo Fire commercial image visualization software was used to identify particles. Only one column of sand is presented in this paper due to page limitation. The nearly vertically aligned sand particles within the column and their evolution between load steps 0 and 5 are displayed in Figure 2. In addition, the contact numbers (CN) of particles for load steps 0 through 5 is presented in Table 1.The relative position of the selected particles within the specimen are highlighted in Figure 2a. Three of the particles within the column fractured at Load 4, which demonstrates that some portion of the axially transmitted load was carried by these particles. Column 1 continued to carry some of the axial load in load step 5 despite the fracture of a few particles, Particle 5 continued to disintegrate further and Particle 6 fractured during Load 5 (see Figure 3).

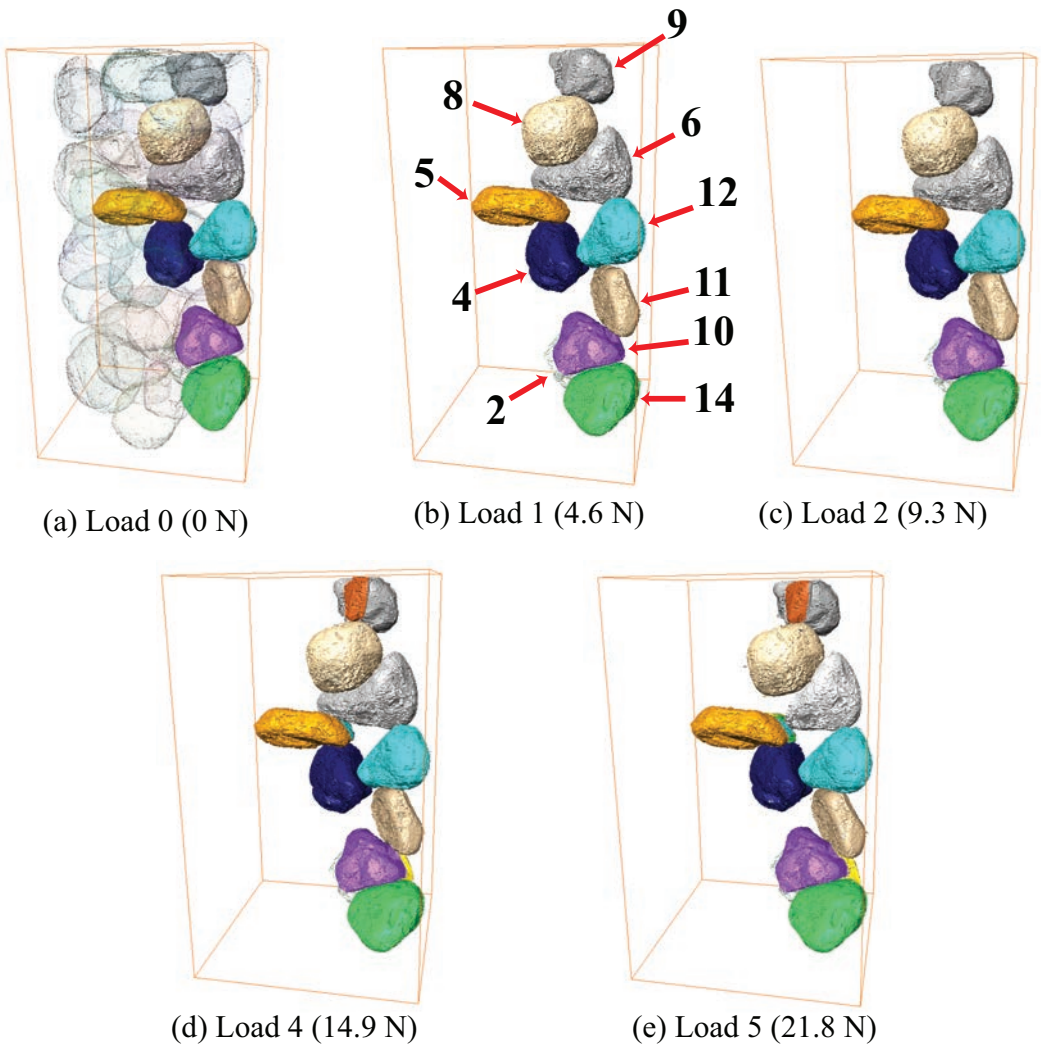

Fig. 2. *Evolution of particles of column 1 with load increment*

The fracture mode of a sand particle is influenced by several factors including mineralogy, CN, the direction and position of contact forces, particle size, particle orientation, particle morphology, and the number and distribution of flaws. In this paper, each particle within column 1 was carefully examined in order to understand the causes of fracture by considering the effect of CN, particle shape, and contact points of individual sand particles. The 3D renderings of fractured sand particles in column 1 before and after fracture are displayed in Figure 3. Particle 9 is located at the top corner of the specimen and has three contact points (CN = 3, the top plate, the mold wall in the lateral direction, and Particle 8 at its bottom). The CN did not change from Load 0 until fracture. The shape of Particle 9 can be defined as sub-rounded. The fracture likely resulted from the contact forces applied by the top loading platen and Particle 8 below it. Particle 5 is an elongated particle with CN = 5. Although there are multiple contacts, the crack propagated along a slightly slanted vertical plane that connects particle contacts above and below it. Since the particle is elongated in the horizontal direction, it is vulnerable to axially applied forces. Therefore, the orientation and shape of Particle 5 might be important factors in the occurrence of fracture. Similar fracture modes were observed in Particles 6 and 10. These 3D images demonstrate that all the particles

fractured via splitting into two fragments, and the cracks formed along the plane that connected the contact points. Although other particles in column 1 had similar CN (see Table 1) they did not experience fracture, which indicates that the coordination number is not the only determinant parameter of initial particle fractures in this sand assembly. The influence of a heterogeneous contact network needs be taken into account to characterize the onset of particle fracture.

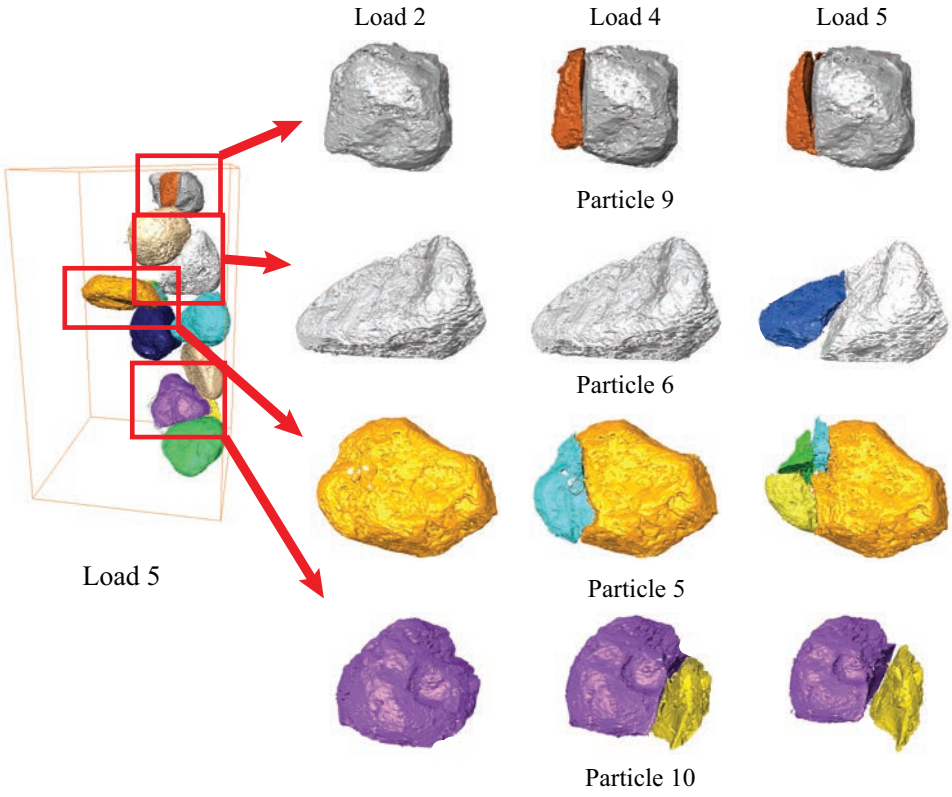

Fig. 3. *Progress of fracture mode of fractured particles in sand column 1. Orentation of particles is changed to expose fragments.*

3D renderings of sand particles before and after fracture (Figure 3) demonstrated that a small fragment generally splits from the main sand particle in all cases. Due to the irregular shape of sand particles, a portion of the particle become vulnerable to fracture if contact forces act along these parts. The fracture of three particles at a relatively small load level (Load 4 = 14.9 N) also points to the considerable role of stress localization at these weak regions on the formation of fracture. As a result, only Particles 5, 9 and 10 in the sand column fractured at Load 4 even though some other particles in the column have smaller CN. It can be concluded that CN is not a main predictive parameter for the initial particle fractures in this data set. On the other hand, the position of contact forces and particle shape play a significant role in the occurrence of particle fracture in a sand assembly as well as the magnitude of contact forces. All particle edge breakages in Figure 3; and particle fractures observed in relatively small strain values in some particles confirm this hypothesis. This analysis revealed that 3D high-resolution SMT images acquired during the deformation of sand assembly provides a unique opportunity to gain insight into the fracture behavior of individual sand particles at the particle-level non-destructively.

Table 1. Summary of coordination number (CN) for particles within column 1

Sand Particle	CN				
	Load 0	Load 1	Load 2	Load 4	Load 5
Particle 2	3	3	3	4	4
Particle 4	2	4	4	5	6
Particle 5	5	5	5	Fractured	
Particle 6	5	4	4	5	Fractured
Particle 8	6	6	6	7	8
Particle 9	3	3	3	Fractured	
Particle 10	4	5	5	Fractured	
Particle 11	3	3	3	4	4
Particle 12	4	5	5	5	5
Particle 14	2	2	2	3	4
Specimen average	4.49	4.69	4.69	4.89	5.14

Conclusions

The evolution of particle fracture was investigated using 3D SMT images, which showed that some sand particles aligned in a column structure with a nearly vertical orientation in the specimen during loading. It was observed that particles which were part of these sand columns mostly experienced fracture. After particle fracture, these columns continued to carry a portion of the axial load. The cracks in fractured sand particles generally extend along the plane that connects the two contact points of the particle with the neighbor particles and this plane is more or less parallel to the axial load direction. In most cases, particles initially split into two or three fragments. Then, fragments experience further breakage as they continue to carry load. Micro-scale fracture analysis revealed that the position of contact forces and particle shape play a major role in the occurrence of particle fracture in a sand assembly, and CN is not the main predictive parameter for the initial particle fractures.

Acknowledgments

This material is based on work supported by the National Science Foundation under Grant No. CMMI- 1362510. The SMT images were collected using the x-ray Operations and Research Beamline Station 1-ID at Argonne Photon Source (APS), Argonne National Laboratory. Use of the Advanced Photon Source, an Office of Science User Facility operated for the U.S. Department of Energy (DOE) Office of Science by Argonne National Laboratory, was supported by the U.S. DOE under Contract No. DE-AC02-06CH11357

References

Altuhafi, F. N., and Coop, M. R. (2011). Changes to particle characteristics associated with the compression of sands. *Geotechnique*, 61, 6: 459-471.

Lade, P., and Yamamuro, J. (1996). Undrained Sand Behavior in Axisymmetric Tests at High Pressures. *Journal of Geotechnical Engineering*, 122, 2: 120-129.

Cavarretta, I., and O'Sullivan, C. (2012). The mechanics of rigid irregular particles subject to uniaxial compression. *Geotechnique*, 62, 8: 681-692.

Cil, M. B., and Alshibli, K. A. (2012). 3D assessment of fracture of sand particles using discrete element method. *Géotechnique Letters*, 2, July-September: 161-166.

Hagerty, M., Hite, D., Ullrich, C., and Hagerty, D. (1993). One-Dimensional High-Pressure Compression of Granular Media. *Journal of Geotechnical Engineering*, 119, 1: 1-18.

McDowell, G. R. (2002). On the yielding and plastic compression of sand. *Soils Found*, 42, 1: 139-145.

Nakata, Y., Hyde, A. F. L., Hyodo, M., and Murata, H. (1999). A probabilistic approach to sand particle crushing in the triaxial test. *Geotechnique*, 49, 5: 567-583.

Nakata, Y., Hyodo, M., Hyde, A. F. L., Kato, Y., and Murata, H. (2001). Microscopic Particle Crushing of Sand Subjected to High Pressure One-Dimensional Compression. *Journal of the Japanese Geotechnical Society : soils and foundation*, 41, 1: 69-82.

Roberts, J. E., and de Souza, J. M. The compressibility of sand. *Proc., Proc. A. Soc. for Testing Mat.*, ASTM, 1269-1277.

Terzaghi, K., and Peck, R. B. (1948). Soil mechanics in engineering practice. Jon Wiley and Sons, Inc., New York, NY, 65-67.

Yamamuro, J., Bopp, P., and Lade, P. (1996). One-Dimensional Compression of Sands at High Pressures. *Journal of Geotechnical Engineering*, 122, 2: 147-154.

Session 203

Solid-Phase Structural Characterization in polymeric foams: Synchrotron µ-CT in the limits of resolution

S. PEREZ-TAMARIT[1,*], E. SOLÓRZANO[1], A. HILGER[2], I. MANKE[2], M.A. RODRIGUEZ-PEREZ[1]

[1]CellMat Laboratory, University of Valladolid, Paseo de Belén 7 47011, Valladolid, Spain.
[2]Helmholtz-Zentrum Berlin für Materialien und Energie, Lise-Meitner-Campus, Hahn-Meitner-Platz 1 (formerly Glienicker Str. 100) 14109, Berlin, Germany.

* saul.perez@fmc.uva.es

Keywords: X-ray tomography; synchrotron x-rays; polymeric foams; 3D analysis.

Abstract

This work presents the results for a collection of closed-cell polymeric foams studied by synchrotron µ-CT combined with innovative image analysis techniques. Measurements were performed using 0.438 microns pixel size and in absorption mode (a minimal phase contrast). Samples under study consisted on a collection of closed-cell polymeric foams with a broad range of solid fractions (from 0.018 to 0.095) and mean pore sizes between 230 and 540 micrometers.

The structural characterization has been focussed on the extraction of different parameters of the solid-phase: local thickness distribution, strut thickness, cell wall thickness, material repartition in cell walls and struts by using different methodologies. Conventional parameters of the gas-phase (pore size, anisotropy, etc) were complementarily calculated.

Introduction

Foams are two-phase structures in which a gas is dispersed throughout a solid continuous phase [1]. In our case study, solid phase consists on polymeric materials such as polyethylene (PE) or polyurethane (PU).

From the structural point of view, the solid phase can be divided into struts, or intersection of three or more pores, and cell walls which separates two consecutive pores. Furthermore, the solid constituents of polymeric foams can be classified into thermoplastic and thermosets. Thermoplastic polymers melt and solidify without changing their molecular structure and can be remelted while thermoset polymers are polymerized by temperature of chemical reaction and cannot be remelted. In this sense PE and PU are, respectively, one of the most representative polymers of each of these two classes. Likewise, these two types of polymers, require different foaming processes, resulting into foams with different architectures, and in consequence, distinct mechanical and thermal properties [2,3]. On the other hand, the gaseous-phase -pores- in foams is frequently the only phase studied while the solid one is conventionally less considered.

µ-CT is one of the most useful tools to characterize cellular structures [4]. It presents certain limits both in the spatial and contrast resolution which difficult carrying out these studies in low-density materials (density bellow 25 kg/m^3) or those with wall thicknesses bellow 2 microns. In these situations a complete/exact binarization of the solid-phase is generally not possible thus loosing valuable information. Watershed wall reconstruction

becomes an invalid process giving as a result an inexact reconstruction of those missed cell walls during the binarization and the only alternative implies a higher resolution, at a minimum 2 times better than the minimum cell wall thickness of the material. With the objective to solve the resolution limitations µ-CT measurements were done at a synchrotron facility. Thus, a complete structural of the biphasic (gas+solid) structure of the foams under study may be carried out by using synchrotron X-ray tomography.

The aim of this work is to evaluate, for a first time in three dimensions and with a high image resolution, the main descriptors of the solid phase of the foams, such as the repartition of mass between cell walls and struts and the mean cell wall thickness. Other "classical" descriptors of gaseous phase of the foams have been complementarily analysed. Two groups of samples with structural differences were selected for this work (see materials section) to exemplify the utility of this investigation.

Methods

Aspects of foams

Prior to go in depth with the methods used. it is necessary to define the main parameters of the foams, which are intimately related with the final properties of the foams such as thermal or mechanical properties [5]. These characteristics are the foam density (ρ) or more commonly the relative density or solid fraction (ρ^*) which is defined as the ratio between the foam density and the solid material density and the pore size (ϕ). Additionally, there are different parameters related to the solid phase of the cellular structure. We have selected the mean cell wall thickness (δ) and the fraction of mass in the struts (f_s) which is defined as the ratio of material fraction in the struts to the total solid phase. In addition, we can define the average material thickness (t) which is correlated with the relative density of the foams (for identical pore sizes). An exemplary comparison concerning the thickness distribution of walls and struts for an ideal and a real foam specimens, both with f_s=0.4, is shown in Fig. 1 where we can observe the differences in between theoretical and real cell models.

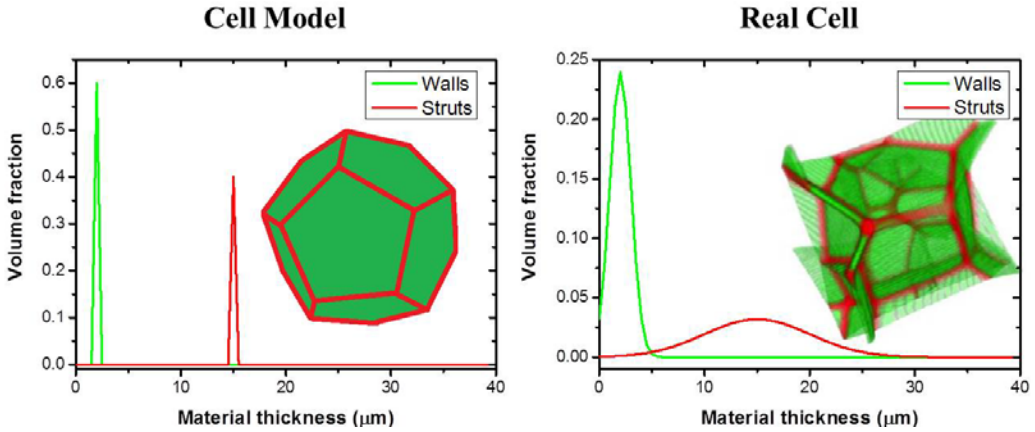

***Fig 1**. Differences between the ideal cell model of a pentagonal dodecahedron geometry and a real foam (f_s=0.4) cell with this geometry concerning the distribution of thicknesses.*

Materials

Two different types of foams are studied in this work. PU foams with densities and cell sizes in the range of 30-100 kg/m^3 and 350-550 microns, respectively, have been selected. It can be observed in figure 2 that pore size and density are correlated for

these materials and the microstructural solid distribution shows a high concentration of polymer in the struts (edges). Moreover, according to Fig. 2, PE foams owe a different structure since the material is distributed throughout the solid foam structure, and is not concentrated in the struts. In the analyzed range of densities (15-45 kg/m^3) cell size is nearly independent (250-350 microns) for these materials.

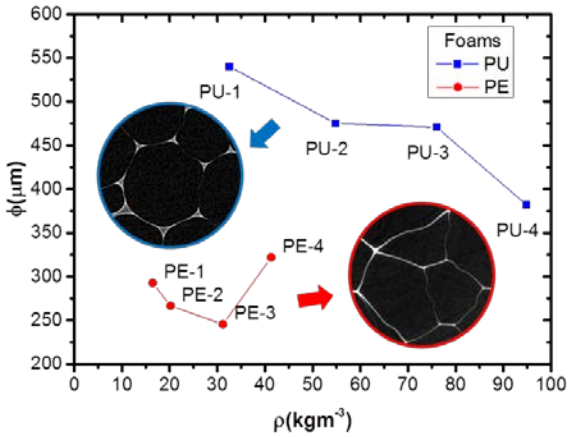

***Fig. 2**.Main characteristics of foams under study and tomography slices of their structure.*

Experimental set-up. Synchrotron facility

Measurements were done at BAM-Line, a synchrotron beamline located at Bessy II facility in Berlin (Germany). The experimental set-up achieved a pixel size of 0.438 microns, resulting in a limited field of view (1.8x1.2 mm^2) using monochromatic beam (9.8 keV) and a low sample-detector distance (nearly pure absorption, no phase contrast). The selected exposure time of the detector was 3000 ms.

Methods of Analysis

Prior to the strictly 3D analysis images were filtered using a 3D median filter and binarized. It is important to remark that the binarization level was carefully selected thus obtaining tomographic solid fractions perfectly correlated to the real ones. The 3D local thickness analysis (Fig. 3) was carried out with an Euclidean Distance Transform method to finally obtain the thickness distribution throughout the solid phase [6]. Nevertheless, strut and cell wall thickness values are mixed up. A possible separation for these two structures can be achieved by peak-fitting to bimodal distributions and analyzing the corresponding area. Then the fraction of mass in the struts can be accurately calculated (Method-1). Alternatively a simple thickness threshold could be applied to classify struts and well calls obtaining reasonably good results as observed in Fig. 3 (d) (Method-2).

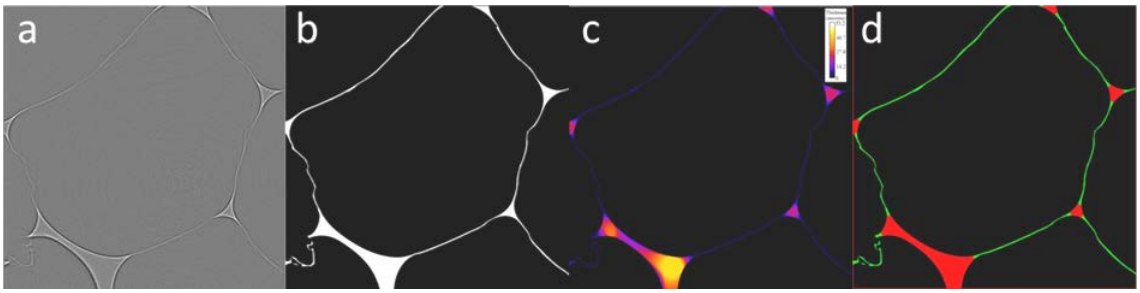

***Fig 3**.Scheme of the methodology. (a) tomo slice (b) binarization (c) 3D local thickness implementation and (d) final separation between cell walls –green- and struts –red-.*

Preliminary results

As a first result the material thickness histogram (Fig. 4) reveals remarkable differences between the two types of foams with similar densities around 30 kg/m^3 (PE-3 and PU-1) with cell size of 245.5 microns and 540.1 microns respectively. After applying the already explained methodology the mean cell wall thickness is 2.97 and 3.15 microns while f_s is 0.35 and 0.69 respectively PE-3 and PU-1.

The thickness histogram reveals that the selection of a "simple" thickness threshold seems to be a valid method for PU (distributions are separated) but, may be, not strictly correct for PE (overlapped distributions).

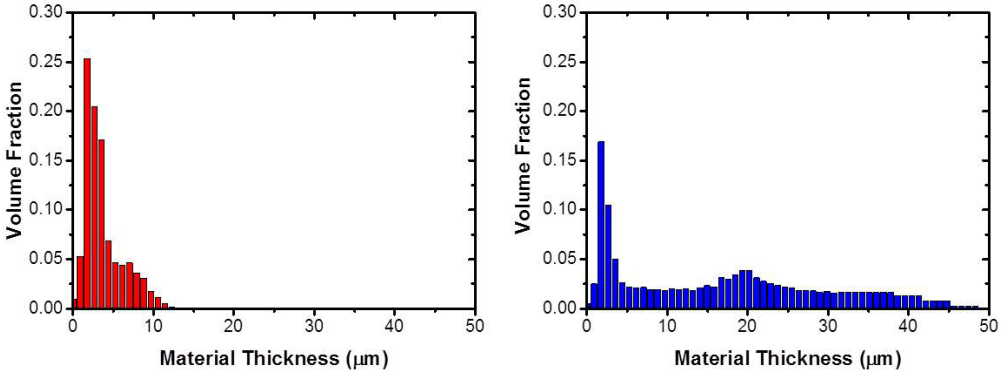

***Fig 4**. Material thickness distribution of PE-3 foam (left) and PU-1 foam (right).*

On the other hand, it is possible to elucidate the influence of the foam density in both the mean cell wall thickness and the average material thickness (Fig. 5). In the case of PU foams the cell wall thickness remains constant and therefore, the changes in density only increase the struts dimensions, leading to modifications in f_s (Fig. 6). In contrast, the results for PE foams are different and density, material thickness and mean cell wall thickness and correlated due to the homogenous material distribution.

Finally, f_s values are shown in Fig.6 (a) calculated under the two-mentioned methodologies. In the case of PE foams f_s is very influenced by the changes in density while in the case of PU foams f_s values are near the maximum allowable. A comparison between f_s (methods 1 and 2) is complementary showed in Fig.6 (b) showing a good correlation. It is clear that the first methodology for calculating f_s is more accurate particularly in the case of PE foams in which method-2 is expected to be less accurate.

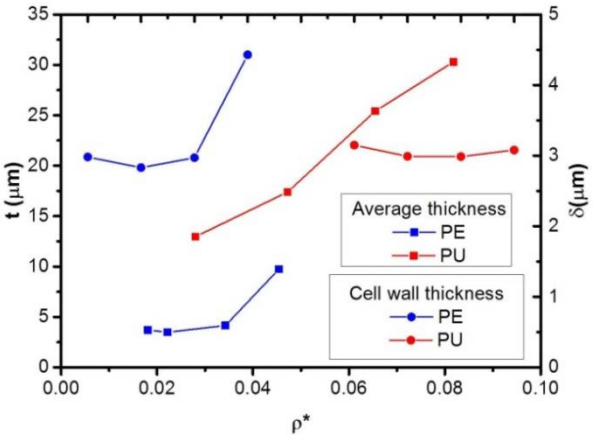

***Fig 5**. Average material thickness (t) and mean cell wall thickness (δ) as function of relative density (ρ^*) of foams under study.*

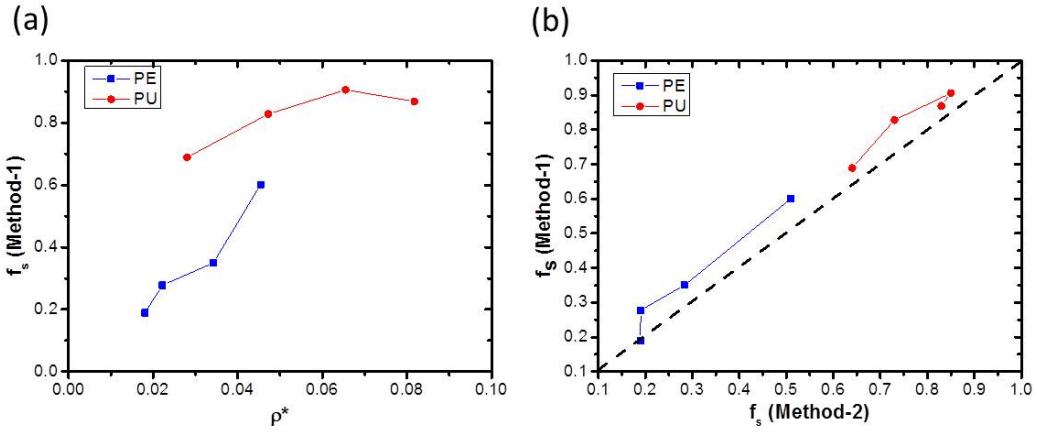

***Fig 6**.Representation of f_s versus foam relative density (left) and comparison concerning f_s of two different methodologies (right).*

Conclusions and future work

Ultra-high resolution synchrotron X-ray microtomography allowed us obtaining accurate values for certain parameters of solid phase of the foams, less studied until nowadays, particularly mean cell wall thickness and fraction of mass in the struts,. Clear differences between the materials studied and correlations with density have been found. As future work it will be interesting to study the wall curvature, tortuosity and other parameters of the solid structure.

References

[1] L. J. Gibson, M. F. Ashby, Cellular Solids – Structure and Properties, Second Edition, Cambridge University Press, Cambridge (1997).
[2] Glicksman LR. In low density cellular plastics: physical basis of behaviour. In: Hilyard NC, Cunningham A, editors. London:Chapman& Hall, (1994).
[3] M.A. Rodríguez-Pérez, The Effect of Chemical Composition, Density and Cellular Structure on the Dynamic Mechanical Response of Foams, Cellular Polymers, 21:165 (2002).
[4] S. Pardo-Alonso, E. Solórzano, I. Brabant, P. Vanderniepen, M. Dierick, L. Van Hoorebeke, M.A. Rodriguez-Perez, 3D Analysis of the progressive modification of the celular architecture in polyurethane nanocomposite foams via X-ray microtomography, European Polymer Journal, 49 (2013).
[5]A. E. Simone, L. J. Gibson, Effects of solid distribution on the stiffness and strength of metalic foams, ActaMaterialia, 46 (1998)
[6]T. Hildebrand, P. Rüesegger, A new method for the model-independent assessment of thickness in three-dimensional images, Journal of Microscopy, 185 (1997).

Metal artifact reduction using confidence maps and patch-based method

⋆ L. Frédérique[1,3], B. Recur[2], S. Genot[3], J.P. Domenger[1] and P. Desbarats[1]

[1] LaBRI, Université de Bordeaux / CNRS, 351 Cours de la Libération, 33405 Talence Cedex, France

[2] Australian National University, Dept. Applied Maths, RSPE, Canberra, Australia

[3] Tomo Adour, Zone Europa, 5 Rue Johannes Kepler, 64000 Pau, France

⋆ presenting author

INTRODUCTION

In the field of non-destructive testing of materials, computed tomography became a good way to check defects in industrial piece production [1]. However, tomographic analysis is difficult to achieve due to the presence of high density objects (such as metal) in most produced pieces, leading to the well-known metal artifacts in reconstructed data. In X-Ray tomography, metal artifact is characterized by a local and straight hyper-signal [2]. This observed phenomenon is due to high attenuations of the rays in the high density materials.

Many different approaches have been proposed for metal artifact reduction (MAR) during the last decade. In the most popular case, developed methods consider the artifact reduction as a missing data problem. Currently, two kind of methods can be distinguished. The first one is based on projection completion method [3, 11]. Missing data, represented by the metal traces in the sinogram, are replaced by synthetic data computed by interpolation or in-painting methods. The second one considers metal artifact reduction as a penalizing term in an iterative reconstruction method [4, 10]. Such a method is based on local filtering assessing the coherence of a pixel with its neighborhood.

However, these methods start their process from the original projection data. In our context, only the reconstructed image is available due to clinical scanner usage. Thus, we focus our investigations on a solution based on the reconstructed image only. We propose an algorithm that reduces the artifact by directly applying a patch-based image processing. Patches preserve geometry in the image and avoid over-smoothing [6]. However, patch-based method amends all pixels whereas only few of them have to be corrected in our case. Thus, in order to only restore corrupted pixels, we compute confidence maps from a simulated sinogram and apply them as weighting functions determining the amount of correction to perform using the patch-based method.

These maps represent hyper-signal and hypo-signal repartition generated by metal artifact in the reconstructed image. In other words, each map is a representation of the amount of hyper or hypo-signal phenomenon that occurs during the initial acquisition / reconstruction process. They are obtained using an iterative reconstruction from a simulated acquisition of metal traces. The overall output function is a combination of these two maps, where negative and positive values represent the hypo-signal and the hyper-signal, respectively.

The following of the paper is organized as follows. We first present methods selected in the literature for comparison. Then, we detail and illustrate the proposed method. Finally, we compare and discuss reconstruction results obtained by our method and methods selected in the literature.

OVERVIEW ON PREVIOUS STUDIES

Methods proposed by Yang Chen et Al. [3] and Hengyong Yu et Al. [11] have the same scheme. They first suppress metal traces from the sinogram by making a difference between the original sinogram and the metal traces. Both methods obtain metal traces by segmentation of reconstructed image and forward-projection of this segmentation. The last stage consists of completing data by in-painting (for Yang Chen et Al.) or by interpolation (for Hengyong Yu et Al.). Figure 1 illustrates these methods bringing out the common steps.

We have design a custom phantom named *Kimagure*. It is a synthetic phantom made with a 3D-printer able to receive several metal rods (of different types) like a cylinder of revolver.

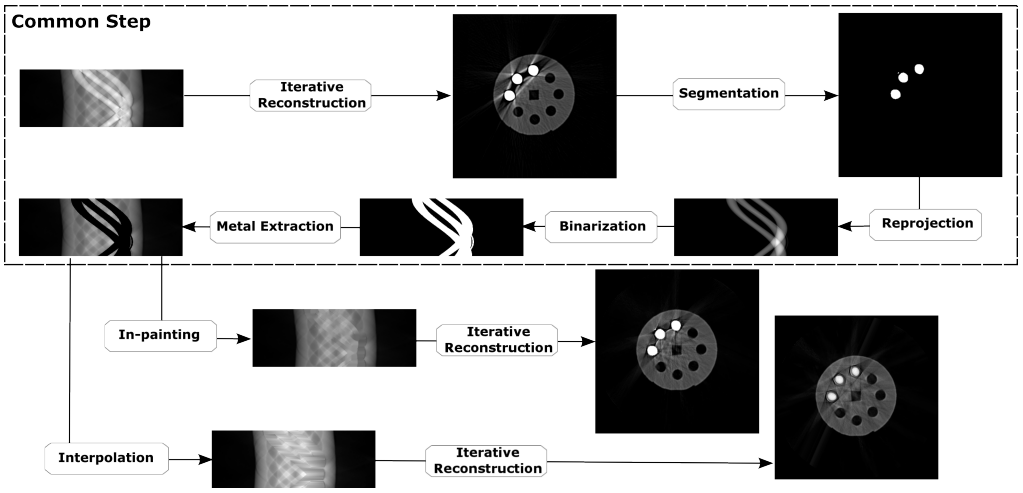

Figure 1: Steps of method selected from the state of the art [3, 11] bringing out the common steps, in our case iterative reconstruction is performed with SART.

PATCH-BASED MAR SUPERVISED BY CONFIDENCE MAPS

The proposed algorithm is based on a similar work-flow than in [3, 11], except that the interpolation or in-painting part is replaced by a patch-based image correction. Moreover, pixels that have to be corrected are selected according to two confidence maps computed from the sinogram of metal objects. These maps represent hyper-signal and hypo-signal generated by metal artifact. The values of each map correspond to the confidence of each reconstructed pixel.

Figure 2 and following sections illustrate the three algorithm steps, which are: i) metal segmentation, ii) confidence maps generation, and, iii) artifact reduction using confidence maps.

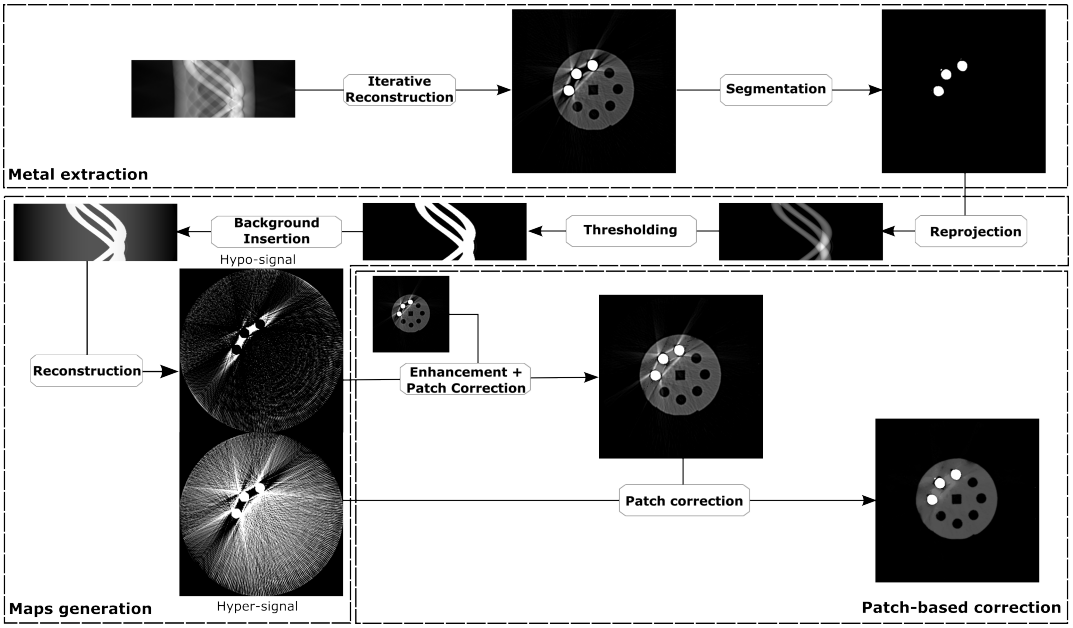

Figure 2: Proposed method algorithm: each step is delimited on the image with a block

METAL EXTRACTION

The goal of the first step is to extract metal from the image (cf. Figure 2 step "Metal extraction"). To do this, a segmentation is performed to only keep metallic objects. Segmentation is done by applying a threshold T selected using method proposed by J. Prewitt et Al. [9]. This threshold correspond to the minimum between two local maxima in a smoothed histogram. Then, all values higher than T are considered as metal.

CONFIDENCE MAPS GENERATION

The second step consists of reconstructing two images from a sinogram representing metal traces (cf. Figure 2 step "Maps generation"). Image computed in the previous step is projected to provide a normalized sinogram of these metal traces. Prior to computing the two confidence maps, we simulate a detector saturation at metal forward-projection positions by setting to 1 each pixel higher than a given threshold. Next, a bell function is added as background to avoid artifacts adding such as beam hardening and only permit to retrieve metal artifacts [8].

A first image is then obtained with an iterative process solving the linear system $S = AI_M$, where S represents the sinogram, I_M is the map we want to obtain and A corresponds the projection matrix. This process is defined by:

$$I_M^{k+1} = I_M^k + \lambda A^t(S - AI_M^k) \tag{1}$$

where A^t represents the retroprojection matrix and $\lambda \in \mathbb{R}_+^*$ is a coefficient optimizing convergence of the process.

We then obtain a representation of the confidence maps where hyper-signal represents values higher than 0 and hypo-signal represents absolute values of negative values. These maps indicate then the non-confidence of a reconstructed pixel. Thus, for each map, the higher the map intensity value, the lower the confidence.

PATCH-BASED CORRECTION

The last step (cf. Figure 2 "Patch-based correction") applies a patch-based image process supervised by the confidence maps. The idea of this method is to amend pixels using the non-corrupted ones by computing a weighted average of patches according to their similarity. A patch represents a set of pixels corresponding to a pixel and his neighborhood. In their study, Zhong et Al. [13] proposed a patch-based method where similarity between patches is computed according to both structure similarity and homogeneity. Due to a huge set of patches, a window search is defined around the considered pixel to reduce computation time. Nevertheless, in our case, because of its local application, window search could be composed of patches with very low confidence only. To improve patch research, a search patch dictionary then replaces the search domain window. This dictionary is initialized by selecting patches in the image according to confidence maps with K-Means algorithm [7]. Thus, we obtain a set of patches with the largest confidence in the whole image. By replacing the search domain window by the dictionary of patches and including confidence maps, patch process is defined by:

$$I_i = \frac{\sum_{j \in Dict} w(P_i, P_j) I_j conf(i,j)}{\sum_{j \in Dict} w(P_i, P_j) conf(i,j)} \tag{2}$$

where i and j are pixel indexes, P_i and P_j respectively represent the patches of pixels i and j, I_i is intensity of pixel i, $w(P_i, P_j)$ is a weighted function according to similarity between patches P_i and P_j, I_j is the intensity value for the pixel j, $conf(i,j) = 1$ if $I_{M_j} > I_{M_i}$ and 0 otherwise, I_{M_i} and I_{M_j} are the confidence values for pixels i and j, respectively and $Dict$ the dictionary of patches. In order to have better results, this algorithm is iteratively applied. During the iterations, both image pixels and confidence map values are updated for the sub-sequent iterations. Furthermore, to avoid hypo-signal strengthening, a contrast enhancement algorithm is applied before patch process [5].

RESULTS AND DISCUSSION

In this section, we discuss the quality of our MAR algorithm compared to several methods proposed in the literature [3, 11]. CT scanning of *Kimagure* was performed on a Siemens Somatom Open clinical scanner using helical geometry with the following parameters: voltage on X-ray source at 100 kV, tube current at 150 mA, pixel size at 0.1953 mm^2, slice thickness at 0.6 mm and the size of reconstructed CT image is 512x512 pixels.

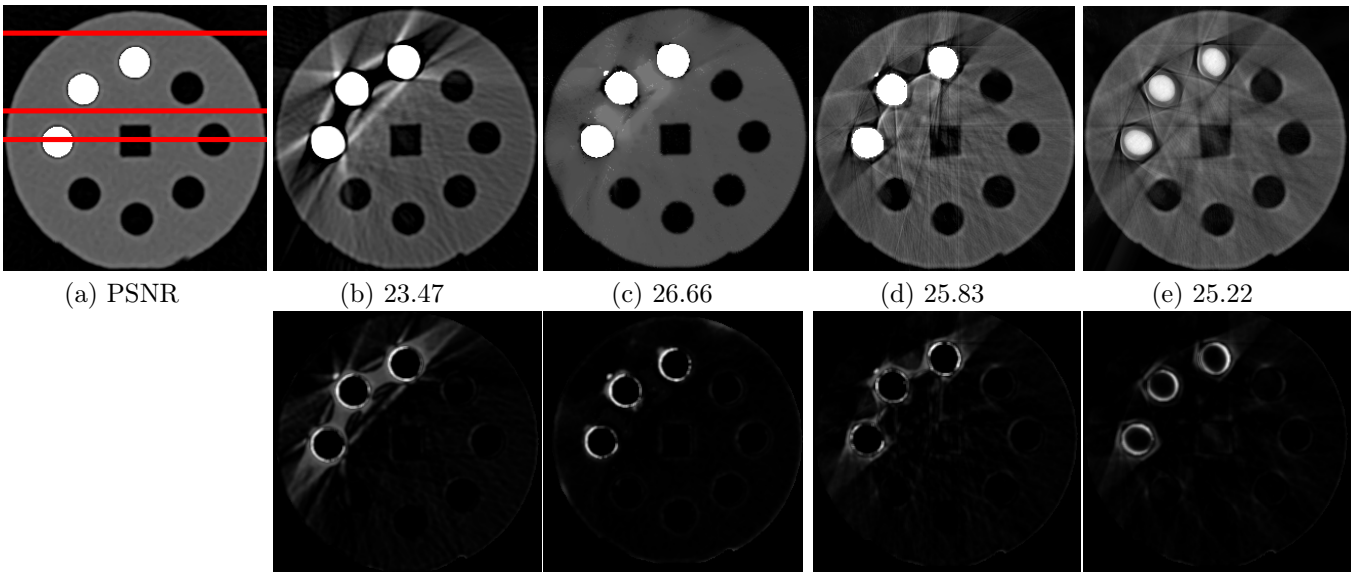

(a) PSNR (b) 23.47 (c) 26.66 (d) 25.83 (e) 25.22

(f) 292.42 (g) 140.11 (h) 169.83 (i) 195.29

Figure 3: (a) Reference image without metal artifact and line profile indexes 150, 226, 254. (b) Artifacted image, (c) Our method, (d) Sinogram in-painting, (e) Sinogram interpolation. (f-i) Local MSE values for each image.

IMAGE COMPARISON

The comparison is based on the usage of PSNR and MSE metrics. Ground truth image is obtained by acquiring *Kimagure* without metal rods and numerically adding them on the reconstructed image (cf. Figure3(a)).

Figure 3 illustrates the results from the presented method and methods selected in the literature. Image Figure 3(b) shows the reconstruction given by the clinical scanner. Image Figure 3(c) is the image resulting from our proposed algorithm with the following parameters: number of patches for the dictionary 500, sigma 30 (used in the weight function), patch size 3x3 and number of iterations 4. Image Figure 3(d) is the result from the method proposed in [3] (called in-painting). Finally, image Figure 3(e) is the result by applying the method in [11] (called interpolation). PSNR values are presented under each images Figure 3(b-e). Figure 3(f-i) are error images with corresponding MSE.

If we compare the resulting values of the image 3(b), we can notice that the coefficient values are better. If we look at the error images, MSE and PSNR values, we can see that each method globally reduces the artifacts and that our method outperforms state of the art methods.

By looking at the reconstructions, we can notice that in-painting and interpolation methods reduce hyper and hypo signal but geometric distortions still remain. One of the limitations of the image based approach we propose is the non-correction of some pixels around metal rods, due to a lack of information. However, contrary to state of the art techniques, our method well preserves original geometry and reduces a larger amount of artifacts.

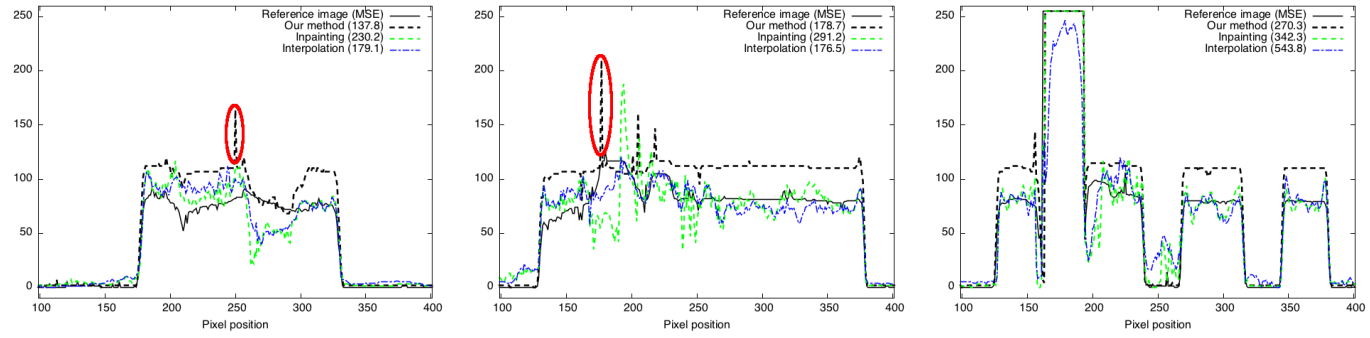

Figure 4: Intensity profiles (and respective MSE value) along lines 150, 226, 254 according to horizontal pixel indexes, for the resulting images with the non metal artifacted image as reference profile.

PROFILE COMPARISON

In order to complete the image characteristic comparison, we develop now a profile analysis of the results. Horizontal profiles are extracted from reconstructed images along the lines shown in Figure 3(a). Figure 4 shows intensity profiles at horizontal indexes 150, 226 and 254 (from left to right).

We can see that the methods from the literature have a low capacity of metal artifact reduction. Although the PSNR and MSE values indicate good result for the in-painting and interpolation method, the analysis of the different profiles shows that region homogeneities are not restored very well and artifacts are still present. On the contrary, if we look at the profiles given by our method we can see that homogeneity in most regions have been well restored. Meanwhile, few peaks appear in the profiles (pointed by red circles) due to contrast enhancement which introduces new hyper-signal and ignored by hyper-signal map.

CONCLUSION

In this paper we propose an algorithm to reduce metal artifacts from reconstructed images, without needing original projection data. Thanks to the confidence maps, we focus the patch-based correction to the pixels which have been corrupted by metal artifacts. Considering the results, our proposed method reduces significantly such degradations. However, the process introduces some hyper-signals very locally. This phenomenon is due to the enhancement process, which is too high in some area. Despite of this limitation, we achieve a competitive artifact correction compared to state of the art techniques, which are based on original sinograms.

Standard metrics usage shows that our method have a good capacity of metal artifact reduction. Meanwhile, by looking at the results from the state of the art, we can notice that these metrics do not take into account remaining artifacts due to their global computation.

Our future goals are first to create or adapt an existing metric [12] able to determine locally image quality according to the detectability of a specific signal and next to improve contrast enhancement process to avoid new hyper-signal appearance.

References

[1] J. Baruchel, J. Buffiere, and E. Maire. *X-ray Tomography in Material Science*. Hermes Science, 2000. ISBN: 9782746201156.

[2] F. E. Boas and D. Fleischmann. Ct artifacts: causes and reduction techniques. *Imaging in Medicine*, 4(2):229–240, April 2012.

[3] Y. Chen, Y. Li, H. Guo, Y. Hu, L. Luo, X. Yin, J. Gu, and C. Toumoulin. Ct metal artifact reduction method based on improved image segmentation and sinogram in-painting. *Mathematical Problems in Engineering*, 2012, 2012.

[4] B. De Man, J. Nuyts, P. Dupont, G. Marchal, and P. Suetens. Reduction of metal streak artifacts in x-ray computed tomography using a transmission maximum a posteriori algorithm. In *Nuclear Science Symposium, 1999. Conference Record. 1999 IEEE*, volume 2, pages 850–854. IEEE, 1999.

[5] V. Digalakis, D. Manolakis, V. K. Ingle, and A. Kok. Automatic adaptive contrast enhancement for radiological imaging. In *Circuits and Systems, 1993., ISCAS'93, 1993 IEEE International Symposium on*, pages 810–813. IEEE, 1993.

[6] C. Kervrann and J. Boulanger. Optimal spatial adaptation for patch-based image denoising. *Image Processing, IEEE Transactions on*, 15(10):2866–2878, 2006.

[7] J. MacQueen et al. Some methods for classification and analysis of multivariate observations. In *Proceedings of the fifth Berkeley symposium on mathematical statistics and probability*, volume 1, pages 281–297. Oakland, CA, USA., 1967.

[8] M. Paziresh, A. Kingston, G. Myers, S. Latham, and A. Sheppard. Software x-ray beam hardening correction of cylindrical specimens. *International Conference on Tomography of Materials and Structures*, pages 187–9190, 2013.

[9] J. Prewitt and M. L. Mendelsohn. The analysis of cell images*. *Annals of the New York Academy of Sciences*, 128(3):1035–1053, 1966.

[10] G. Wang, D. L. Snyder, J. O'Sullivan, and M. Vannier. Iterative deblurring for ct metal artifact reduction. *Medical Imaging, IEEE Transactions on*, 15(5):657–664, 1996.

[11] H. Yu, K. Zeng, D. K. Bharkhada, G. Wang, M. T. Madsen, O. Saba, B. Policeni, M. A. Howard, and W. R. Smoker. A segmentation-based method for metal artifact reduction. *Academic radiology*, 14(4):495–504, 2007.

[12] L. Zhang, C. Cavaro-Ménard, P. Le Callet, and J.-Y. Tanguy. A perceptually relevant channelized joint observer (pcjo) for the detection-localization of parametric signals. *Medical Imaging, IEEE Transactions on*, 31(10):1875–1888, 2012.

[13] H. Zhong, P. Han, X. Zhang, and Y. Yu. Hybrid patch similarity for image denoising. *Electronics letters*, 48(4):212–213, 2012.

3D-imaging by synchrotron X-ray micro tomography of ferroelectric composite materials and numerical modelling of their physical properties

J. LESSEUR[1,2]*, C. ELISSALDE[1,2], C. ESTOURNES[3], R. EPHERRE[3], P. VEBER[1,2], M. GAYOT[4,5], M. MAGLIONE[1,2], D. BERNARD[1,2]

[1]*CNRS, ICMCB, UPR9048, F-33600 Pessac, France - dominique.bernard@icmcb-bordeaux.cnrs.fr*
[2]*Univ. Bordeaux, ICMCB, UPR 9048, F33600, Pessac, France*
[3]*CIRIMAT et Plateforme Nationale CNRS de Frittage flash, PNF2 MHT, Univ. Paul Sabatier, F-31062 Toulouse, France*
[4]*Univ. Bordeaux, PLACAMAT, UMS3626, F33600, Pessac, France*
[5]*CNRS, UMS3626, F33600, Pessac, France*
*Presenting author

Keywords: X-ray computed micro tomography; 3D-imaging; Composite materials; Ceramic; Ferroelectric

Abstract

Ceramic materials are widely used as passive components in microelectronic apparatus. With the miniaturization of electronic components, the current trend is to develop devices able to achieve several functions, such as tunable materials: the electrical properties can be tuned according to the applied electric field. Ferroelectric oxides exhibit the intrinsic property of tunability, but are not suitable with the specific applications required. Composites made of 3D mixtures of ferroelectric ($Ba_{1-x}Sr_xTiO_3$) and dielectric (MgO) oxides are processed by Spark Plasma Sintering (SPS), and investigated by Synchrotron X-ray Computed Micro Tomography (XCMT). Tomography is a necessary step providing images of the real 3D microstructure, insuring a full control and modelling of the designed materials.

Introduction

Current applications in the field of microelectronic devices require well-controlled modulations of physical parameters (permittivity, tunability, dielectric losses…), mostly antagonistic. In mobile electronics, increasingly functionalities are requested, whereas available space is more and more limited [1]. Ferroelectric oxides are well-known candidates due to their ability to provide high permittivity, allowing size reductions of components. In this case, the component is assigned to one role. Thus, nanoscale materials were designed to achieve the required performances [2]. The reduction of the number of components can also be reached by developing multi-functional materials. Increasing the range of applications needs to lower the permittivity while preserving its tunability (i.e. the variation of the permittivity with the applied electric field). Permittivity values can be easily modified using judicious ionic substitutions and controlled grain-size. The latter aspect is a key parameter to precisely adjust both Curie temperature and permittivity values [3,4]. Nevertheless in pure ferroelectric materials, reducing permittivity leads to dramatic tunability decrease. It is also important to achieve a full control of dielectric losses in a wild range of frequencies, in order to fit with the specific requirements of frequency broadening.

To reconcile moderate permittivity ($\varepsilon \approx 2000$), high tunability (> 40 %) and low dielectric losses (< 1 %), the route of composite materials is increasingly explored resulting in

more and more complex microstructures at various scales. In this study, new designed ferroelectric / dielectric composites are presented. Dielectric particles of MgO with spheroidal geometry are dispersed in a ferroelectric matrix ($Ba_{1-x}Sr_xTiO_3$ - BST) and processed by SPS. Processing parameters of SPS (pressure, electric current, heating and cooling rates) offer a high versatility, providing a full control of the microstructure in terms of chemical inter-diffusion, interface qualities, grain size and charged defects in ceramics [5,6]. In a first series of experiment, MgO granules are deformed during the sintering process, leading to inclusions with specific flattened shapes (ellipsoids) [7,8]. In a second one, MgO granules previously sintered at high temperature (1600°C), preserve their spheroidal morphology after sintering by SPS and under the same sintering conditions as the first experiment. The possibilities offered by 3D-imaging techniques such as XCMT to investigate and quantify the three-dimensional microstructure of the composites are fully operated. A procedure, based on, first, 3D-imaging obtained by synchrotron XCMT of both initial mixed powder and sintered material and, second, numerical modelling of the effective permittivity computed from the 3D images, is used to establish the link between the inclusion morphologies and the physical properties. Comparisons between numerical and experimental results are performed and exposed in this text.

Methods

- *BST and MgO powder mixing*

$Ba_{0.60}Sr_{0.40}TiO_3$ nano-powders (200 nm) were synthetized by solid-state route at ICMCB. MgO (97%) are commercial powders purchased from Merck (Darmstadt, Germany), and made of spheroidal spray-dried soft granules (Fig.1a). Each granule is composed of nanometric elementary crystallites. A size sorting was operated with a diameter range around 40 µm and the particles were dispersed in the BST matrix (Fig.1c). MgO size-sorted particles were also annealed individually in an inductive furnace at 1600°C in order to be pre-sintered (Fig.1b), leading to a decrease of the mean diameter (around 20 µm). Mixing step is realized by hand in an agate mortar. This initial microstructure is consolidated by PMMA and investigated by XCMT.

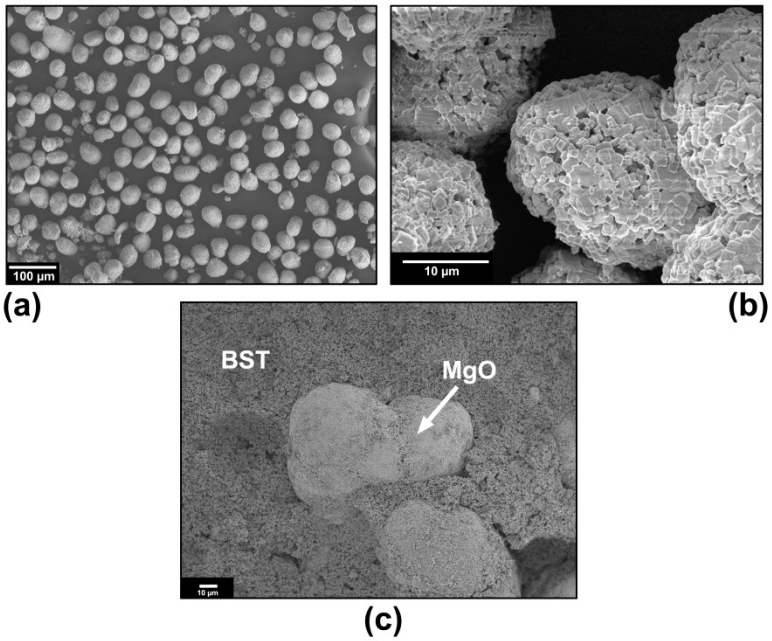

Fig. 1. *a) MgO granules sorted at 40 µm diameter. b) MgO particles annealed at 1600°C. c) MgO granules dispersed in the BST ferroelectric matrix.*

- *Sintering*

All the ceramics presented in this study were produced with the same SPS sintering conditions. A Dr Sinter 2080 SPS Syntec INC Japan from the *Plateforme Nationale de Frittage Flash* (PNF2/CNRS - Toulouse) was used. Powders were loaded onto a cylindrical graphite die (8 mm inner diameter) between two graphite punches. The temperature was raised at 100°C.min^{-1} until 1200°C. A uniaxial pressure of 50 MPa was applied during under vacuum sintering. After sintering the samples were re-oxidized at 800°C during 12 h in air.

- *3D imaging*

We have investigated both initial and final microstructures using European Synchrotron Radiation Facility XCMT (ID19 beamline). Barium is highly absorbing (Z=56) commanding the use of the very high flux “Pink Beam” set-up. Retracting the monochromator provides a higher photons flux allowing a short scanning time compared to the monochromatic set-up [9]. The mean beam energy was 37 keV and 2000 radiographs of 2048 × 2048 were recorded. The pixel size was set to 0.28 µm (F.O.V.=573 µm). Final 3D volumes comprise 2048 × 2048 × 2048 pixels coded in 32-bit floats.

Results

The initial microstructure presents a good distribution of MgO within the volume. Mixing process is soft enough to preserve the granules. MgO exhibits a very complex structure, with a variation of the local densities. Porosities are mainly located at the rim of the particle, and their volume fraction can range from 7 to 15 % (Fig.2a). MgO particles densified at 1600°C were not image within the BST matrix, but simply loaded onto glass capillary tubes (Fig.2b). The porosity of the densified MgO particles is higher than the porosity of the non-densified ones (>20 %).

3D rendering of the final microstructure with non-annealed magnesium oxides obtained by XCMT reveals an homogenous distribution inside the volume. Due to the uniaxial pressure applied during sintering, the MgO granules are deformed providing disk-shaped inclusions. The interfaces between matrix and inclusions are well preserved and a geometric anisotropy of the inclusions is clearly observed (Fig.2c). Concerning annealed magnesium oxydes, the final microstructure is different (Fig.2d). High-temperature treatment allows to preserve the MgO spheroidal shape after sintering by SPS, despite the pressure of 50 MPa. This leads to remove the anisotropy. The interfaces are also well preserved.

Dielectric measurements (permittivity versus temperature) were performed on non-annealed MgO final microstructures, in parallel (along the long axis of the inclusions) and in perpendicular (through the long axis of the inclusions) [8]. The same protocol is applied for the annealed MgO microstructures. The aim is to characterize the response of the electric field according to the different inclusion geometries obtained. Experimental results provided by these measurements are compared to numerical results produced by a code developed at ICMCB by D. Bernard to compute the effective permittivity from samples XCMT 3D images. Starting from a 3D sub-volume (500 × 500 × 500 pixels) assumed as representative of the sample, the equations to be solved using a finite volume scheme are described in [8]. A good accordance between experimental and numerical results was obtained (Fig.3a) and compared to effective medium theories [10], aiming that the numerical model is correctly taking into account the effects of the electrical field distortions induced by the inclusions. Concerning the results calculated

from the second microstructure, the model correctly considers the lower anisotropy, and permittivity values are also correctly estimated (Fig.3b).

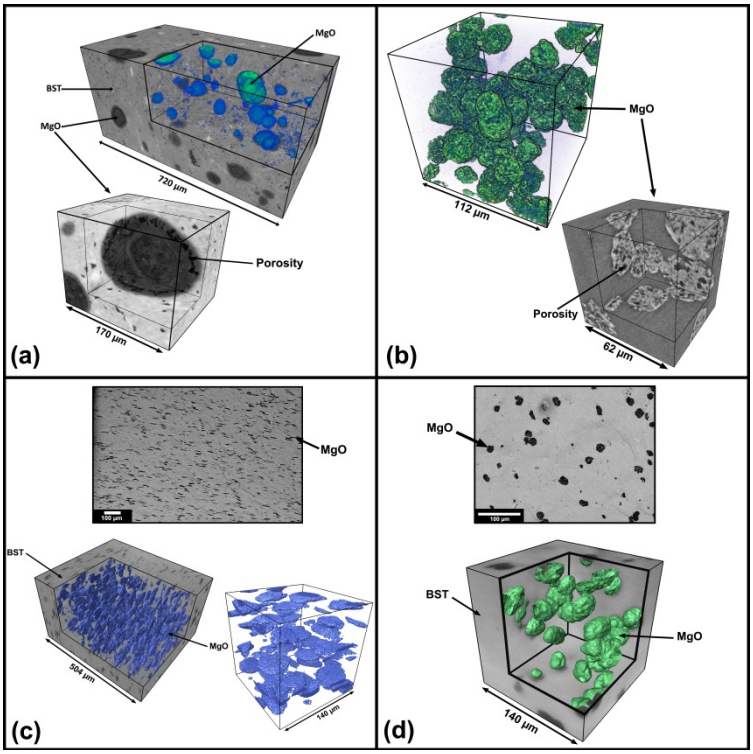

Fig. 2. *3D rendering of BST-MgO composites. a) Initial microstructure consolidated using PMMA. b) Annealed MgO particles. c) SEM fracture (back-scattered electrons mode) of the final microstructure (upper part) and 3D rendering by XCMT (lower part). d) SEM fracture (back-scattered electrons mode) of the final microstructure with MgO annealed at 1600°C, and 3D rendering obtained by XCMT (lower part).*

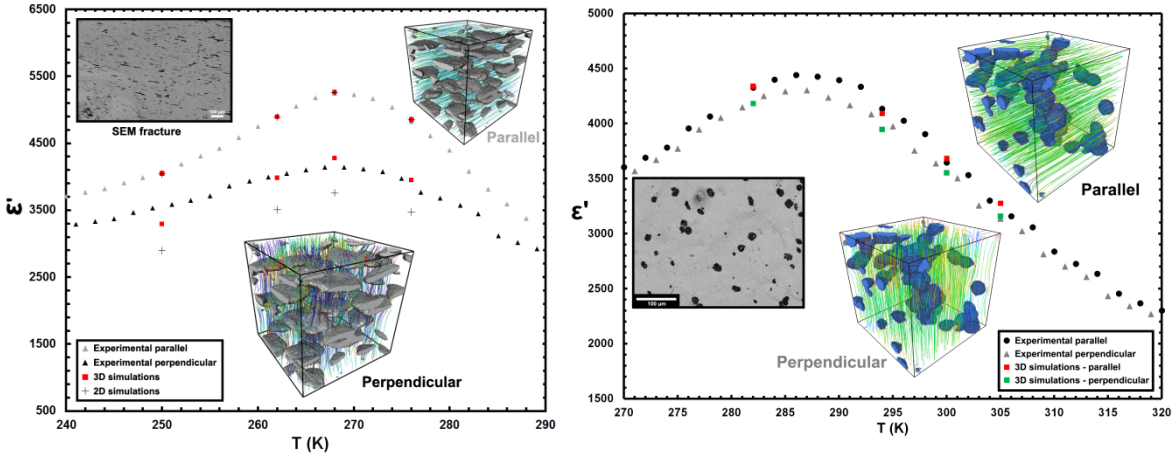

(a) (b)

Fig. 3. *Dielectric measurements and modelling of the effective permittivity versus temperature for BST-MgO composites. The electric field is applied both in parallel and perpendicular direction. a) BST with non-annealed MgO granules* [8]. *b) BST with annealed MgO granules.*

Conclusion

Combining specific sintering process, XCMT and 3D modelling, we can understand the role of inclusion morphologies in the redistribution of the electric field, and we are able to control the morphology, depending on the application requirements. Thus, thanks to the specific properties of SPS, we produce composites made of dielectric inclusions with a flattened or spheroidal shape. 3D computing micro tomography provides the necessary information both for initial microstructures and final microstructures. 3D-images are used to compute effective properties directly from the real microstructures with success, but comparisons with experimental tunability data have to be tested. This work is currently in progress.

References

[1] Ho J, Jow TR, Boggs S. (2010). Historical introduction to capacitor technology. IEEE Electrical Insulation Magazine 2010, 26:20–25.

[2] Philippot G, Elissalde C, Maglione M, Aymonier C. (2014). Supercritical fluid technology: A reliable process for high quality BaTiO3 based nanomaterials. Advanced Powder Technology.

[3] Hoshina T. (2013). Size effect of barium titanate : fine particles and ceramics. Journal Of The Ceramic Society Of Japan, 121:156–161.

[4] Buscaglia V, Buscaglia MT, Viviani M, Mitoseriu L, Nanni P, Trefiletti V, et al. (2006). Grain size and grain boundary-related effects on the properties of nanocrystalline barium titanate ceramics. Journal of the European Ceramic Society, 26:2889–2898.

[5] Chung UC, Elissalde C, Mornet S, Maglione M, Estournès C. (2009). Controlling internal barrier in low loss BaTiO3 supercapacitors. Applied Physics Letters, 94:1–4.

[6] Chung UC, Elissalde C, Mompiou F, Majimel J, Gomez S, Estournès C, et al. (2010). Interface investigation in nanostructured BaTiO3/silica composite ceramics. Journal of the American Ceramic Society, 93:865–874.

[7] Chung U-C, Elissalde C, Maglione M, Estournès C, Paté M, Ganne JP. (2008). Low-losses, highly tunable Ba0.6Sr0.4TiO3/MgO composite. Applied Physics Letters, 92:042902.

[8] Lesseur J, Bernard D, Chung U-C, Estournès C, Maglione M, Elissalde C. (2015). 3D mapping of anisotropic ferroelectric/dielectric composites. Journal of the European Ceramic Society 2015, 35:337–345.

[9] Boller E, Tafforeau P, Ludwig W, Helfen L, Salvo L, Cloetens P, et al. (2010). Techniques d'imagerie pour la caractérisation 3D des matériaux à l'ESRF. Matériaux 2010, Oct 2010, Nantes, France.

[10] Myroshnychenko V, Brosseau C. (2005). Finite-element method for calculation of the effective permittivity of random inhomogeneous media. Physical Review E - Statistical, Nonlinear, and Soft Matter Physics, 71:1–16.

Novel contrast agents for contrast-enhanced CT to visualize in 3D the blood vessel network and fat cell distribution in bone marrow

*G. KERCKHOFS[1,2], A. SAP[3], E. PLOUGONVEN[4], N. VAN GASTEL[1,5], M. DURAND[1,2], R. VANGOITSENHOVEN[5], B. VAN DER SCHUEREN[5], A. LÉONARD[4], K. VANDAMME[1,6], G. CARMELIET[1,5], T.N. PARAC-VOGT [3], F.P. LUYTEN[1,2], L. GERIS[1,7,8]

[1]Prometheus, Division of Skeletal Tissue Engineering, KU Leuven, O&N 1, Herestraat 49 - PB813, B-3000 Leuven, Belgium;
[2]Dept. Development and Regeneration - Skeletal Biology and Engineering Research Center, KU Leuven, O&N 1, Herestraat 49 - PB813, B-3000 Leuven, Belgium;
[3]Dept. Chemistry - Molecular Design and Synthesis, KU Leuven, Celestijnenlaan 200f – PB2404, B-3001 Leuven, Belgium;
[4]Dept. Applied Chemistry, Université de Liège, Institut de Chimie-Bâtiment B6, Sart Tilman, B-4000 Liège, Belgium;
[5]Dept. Clinical and Experimental Medicine - Clinical and Experimental Endocrinology, KU Leuven, O&N 1, Herestraat 49 – PB902, B-3000 Leuven, Belgium;
[6]Dept. Oral Health Sciences - BIOMAT, KU Leuven, Kapucijnenvoer 7 blok a - PB7001, B-3000 Leuven, Belgium;
[7]Biomechanics Research Unit, Université de Liege, Chemin des Chevreuils 1 - BAT 52/3, B-4000 Liège, Belgium;
[8]Dept. Mechanical Engineering - Biomechanics Section, KU Leuven, Celestijnenlaan 300C - PB 2419, B-3001 Heverlee, Belgium.
* presenting author

Intro: Long bones consist of a bone and bone marrow compartment. Both contain a complex 3D blood vessel network, which is critical for supply of oxygen, nutrients and minerals to support the process of tissue remodelling and regeneration. A detailed and 3D visualization and quantification of this network might be necessary to be able to link dysfunction or alteration in the blood vessel network with impaired bone remodelling, healing and regeneration. We propose contrast-enhanced nanofocus computed tomography (CE-nanoCT) for 3D multi-tissue imaging to visualize in a single image set the bone and bone marrow compartment including blood vessels and adipose tissue. In this study, we have compared phosphotungstic acid (PTA), a well-known contrast agent, with two novel contrast agents for their non-invasive character and their potential to visualize blood vessels and adipose tissue in the bone marrow compartment.

Methods & results: Both novel contrast agents are metal-substituted polyoxotungstates, and are further referred to as Hf-POT (Hf-substituted) and Zr-POT (Zr-substituted). To investigate whether the staining provoked tissue shrinkage, we used tissue engineering constructs (i.e. calcium phosphate-collagen scaffold with human periosteal derived cells and a growth factor) that were implanted ectopically for 6 weeks. After explantation and fixation in paraformaldehyde, the samples were scanned, stained and rescanned. Using image registration, tissue shrinkage (with focus on bone) was assessed, showing that PTA does induce shrinkage of bone after 24 hours of staining in a 2.5% PTA/PBS (phosphate buffered saline) solution. Both novel contrast agents however did not provoke shrinkage using the same concentration and staining time.

To further assess the non-invasiveness of the contrast agents, we investigated the potential to perform immunological staining after CE-nanoCT imaging. Therefore, we first stained tibias of 4 weeks old mice, scanned these using CE-nanoCT, and processed subsequently for CD31 immunostaining for blood vessel visualisation. We included control samples that were not stained using the contrast agents, and performed blind scoring. PTA staining did not allow CD31staining, while both novel contrast agents showed excellent CD31 tracing. Hf-POT performed better than Zr-POT, not showing any difference with control samples that have not been scanned nor stained with the contrast agents prior to CD31 immunostaining.

Finally, we scanned tibias of old (30 weeks - OLD), young (7 weeks - YNG) and diabetic (30 weeks - diet-induced obese model, DIO) mice to evaluate the potential of the novel contrast agents to visualize the blood vessel network and the fat cell distribution. Both contrast agents were able to pick up differences between the three groups. For the DIO mice, the bone marrow compartment contained more adipose tissue close to the growth plate compared to the YNG and OLD mice. YNG mice showed a higher content of blood vessels compared to the other groups. Full 3D analysis is ongoing to determine the interconnection and thickness

distribution of the blood vessels, and to show the added value of CE-nanoCT compared to standard histomorphometry.

Conclusion: CE-nanoCT is a multi-tissue 3D imaging technique that can reveal the 3D structure of different skeletal tissues (i.e. bone, bone marrow, fat cells and blood vessels). Since it is promising for providing additional information to standard histomorphometry, with a spatial dimension, CE-nanoCT might bring novel insights in the biological processes during tissue remodelling and regeneration.

Quantitative three-dimensional tissue imaging of lipid, protein, and water contents via X-ray phase-contrast tomography

*M. WILLNER[1], M. VIERMETZ[1], M. MARSCHNER[1], J. HERZEN[1], C. BRAUN[2], A. FINGERLE[3], P. NOEL[3], E. RUMMENY[3], F. PFEIFFER[1]

[1] Department of Physics and Institute of Medical Engineering, Technische Universität München, James Franck-Strasse 1, 85748 Garching, Germany
[2] Institute of Forensic Medicine, Ludwig-Maximilians-Universität München, Nußbaumstrasse 26, 80336 München, Germany
[3] Department of Diagnostic and Interventional Radiology, Technische Universität München, Ismaningerstrasse 22, 81675 München, Germany

* presenting author

Keywords: phase contrast, quantitative imaging, tissue characterization

Abstract

Phase-contrast imaging techniques emerged as essential tool in biomedical research and a broad spectrum of tissue analysis is currently performed by micro computed tomography at synchrotrons and laboratory X-ray sources. Besides the high contrast that can be achieved by phase-contrast imaging for small and low absorbing samples, the access to the refractive index decrement in addition to the linear attenuation coefficient enables enhanced evaluation of tissue properties.
In our study, we examined the possibilities to quantitatively assess the content of lipid, protein and water at a subpixel length scale by exploiting the complementary information obtained in absorption and phase contrast. Experimental results of dairy products, porcine fat and rind, and different human soft tissue types are presented. The three-dimensional representations of protein, lipid, and water contents open up new opportunities in the fields of biology, medicine, and food science.

Introduction

X-ray phase-contrast computed tomography (CT) is an emerging three-dimensional (3D) imaging modality based on a fundamentally different image formation process from that of conventional absorption-based CT [Momose 2005]. The method is especially beneficial for biomedical research by enhancing soft-tissue contrast and providing additional information [Bravin 2013]. A promising approach to X-ray phase-contrast imaging is grating interferometry [Weitkamp 2005]. Being operable at standard laboratory X-ray sources, grating interferometry may broaden the application of X-ray phase-contrast CT [Pfeiffer 2006], enabling quantitative assessment of material properties within investigated samples [Herzen 2009, Qi 2010]. Our investigations focus on new possibilities for enhanced tissue characterization by combining conventional CT and phase-contrast CT, in this case, the quantification of a tissue's lipid, protein, and water contents.

Methods

The typical Talbot–Lau interferometer installed at laboratory X-ray tubes consists of three gratings with micron-order periodicity (Fig. 1). A phase grating (G1) creates periodic intensity modulations at certain distances in the beam direction. A sample (S) placed in the beam path induces local shifts of this periodic intensity pattern.

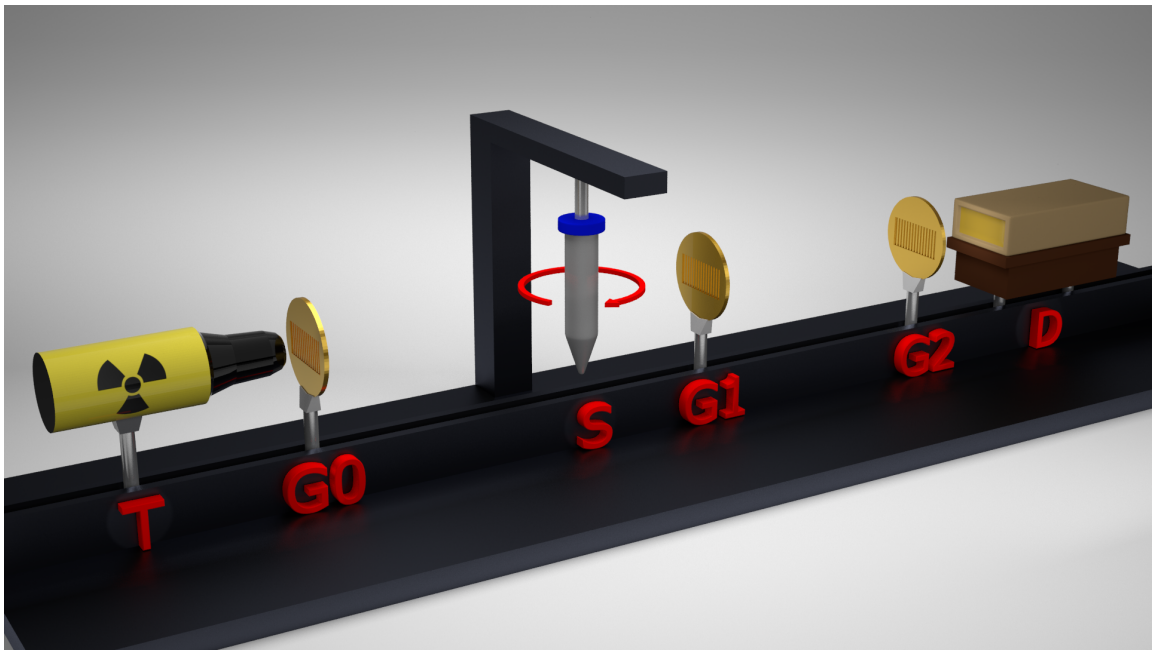

Fig. 1. *Illustration of an experimental phase-contrast computed tomography system as used for the study. A Talbot-Lau interferometer consisting of three gratings (G0, G1, G2) with micrometer-sized structures is installed between the X-ray tube (T) and the detector (D).*

Since the pixel size of a standard detector usually exceeds the period of the pattern, an analyzer grating (G2) of the same period constructed from a highly absorbing material (in our case, gold) is mounted in front of the detector (D). This analyzer grating is translated perpendicularly to the beam over one grating period while several images are acquired. During this stepping process, the intensity of each detector pixel oscillates sinusoidally. The position of this curve can be evaluated by Fourier analysis and is directly associated with the refraction, i.e. the phase-shift, caused by the examined sample. Another highly absorbing gold grating (G0) is installed behind the X-ray tube (T) and generates an array of many small, individually coherent sources. This grating ensures sufficient coherence, an important beam property for proper functioning of the interferometer. The principle of X-ray grating interferometry is detailed in Weitkamp (2005) and Pfeiffer (2006).

The phase-contrast projections obtained by X-ray grating interferometry are differential and an imaginary Hilbert filter is applied as filter function during reconstruction [Pfeiffer 2007]. Correcting for setup-dependent factors such as grating spacings and periods, the 3D distribution of the refractive index decrement δ throughout the sample can be recovered [Herzen 2009].

Hounsfield units (HU) are numerical quantities that assist the differentiation of certain tissue types from medical X-ray CT data. A similar Hounsfield scale (HUp) has been defined for phase-contrast imaging [Donath 2010]. The HU- and HUp-value of a tissue depend on its linear attenuation coefficient and its refractive index decrement, respectively. Due to the fundamentally different image formation process of both contrast modalities, the numbers yield complementary information content. Calculated HU- and HUp-values (28 keV) of muscle tissue, adipose tissue and skin are listed in Table 1 along with the tissues' water, lipid and protein contents [Woodard 1986, ICRU 1989].

Table 1. *Calculated absorption-contrast and phase-contrast Hounsfield units (HU and HUp) of three tissue types and 100% water, 100% lipid, and 100% protein. In addition, the tissues' water, lipid, and protein contents are listed. Values are based on Woodard (1986).*

	Absorption contrast	Phase contrast	Water %	Lipid %	Protein %
Muscle tissue	55.8 HU	40.3 HUp	79.4	4.9	15.7
Adipose tissue	-246.6 HU	-49.1 HUp	20.2	76.7	3.1
Skin	46.4 HU	78.0 HUp	68.2	1.2	30.4
Water	0 HU	0 HUp	100.0	0	0
Lipid	-338.6 HU	-76.1 HUp	0	100.0	0
Protein	115.1 HU	296.8 HUp	0	0	100.0

The large amount of lipid in adipose tissue has a comparably larger effect on the signal in absorption contrast than in phase contrast. Comparing the HU- and HUp-values of muscle tissue and skin, only the phase-contrast signal seems to be affected by the higher content of protein (collagen) in the skin. This implies that an advanced tissue characterization with respect to protein or lipid content might be possible when combining both contrast modes.
Table 1 additionally contains HU- and HUp-values (28 keV) calculated for 100% water, 100% lipid, and 100% protein. These points span a triangle in the corresponding HU-HUp-plot as illustrated in Fig. 2. Pure water has by definition 0 HU and 0 HUp. Assuming a linear increase and decrease of HU- and HUp-values with rising protein and lipid concentrations, every possible triplet of water, protein, and lipid can be associated to exactly one HU-HUp-pair and a vector decomposition can be applied to retrieve the respective information.

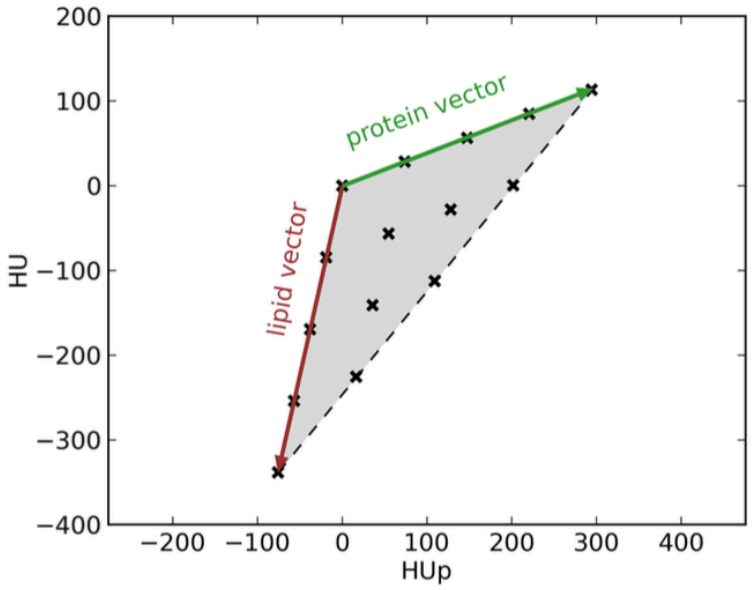

Fig. 2. *Calculated HU- and HUp-values of 100% water, 100% lipid, and 100% protein span a triangle. Measured HU- and HUp-values of a tissue can be used to draw conclusions on its water, protein, and lipid contents by performing a vector decompostion.*

Experimental results obtained for porcine rind and fat are presented in Fig. 3. The first row shows an exemplary absorption-contrast image, a phase-contrast image and the corresponding HU-HUp-plot including all voxels of the dataset. The decomposed images representing the lipid, protein, and water contents are displayed beneath. To allow for the compensation of distorting effects on the analysis results (e.g. caused by the presence of heavier elements), the protein and lipid vectors were defined to have their starting points at the experimental HU- and HUp-value of the surrounding physiological phosphate buffered solution (PBS) instead of pure water. The end points of the vectors were chosen to match the calculated values for 100% protein and 100% lipid.

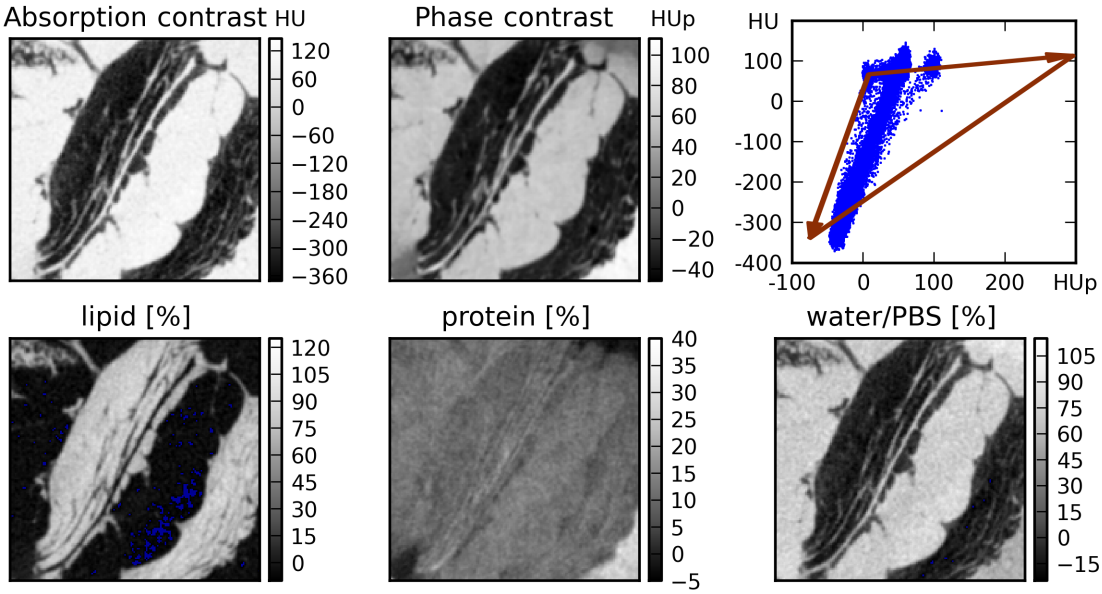

Fig. 3. *Experimental results of porcine rind and fat. The quantitative absorption-contrast (HU) and phase-contrast (HUp) images (top row) are decomposed into three images (bottom row) respresenting the respective concentration of lipid, protein, and water (PBS) within each pixel (voxel).*

References

Momose A (2005). Recent advances in x-ray phase imaging. Jpn. J. Appl. Phys. 44, 6355–67.

Bravin A, Coan P and Suortti P (2013). X-ray phase-contrast imaging: from pre-clinical applications towards clinics. Phys. Med. Biol. 58, R1–R35.

Weitkamp T, Diaz A, David C, Pfeiffer F, Stampanoni M, Cloetens P and Ziegler E (2005) X-ray phase imaging with a grating interferometer. Opt. Express 13, 6296–304.

Pfeiffer F, Weitkamp T, Bunk O and David C (2006). Phase retrieval and differential phase-contrast imaging with low-brilliance x-ray sources. Nature Phys. 2, 258–61.

Herzen J, Donath T, Pfeiffer F, Bunk O, Padeste C, Beckmann F, Schreyer A and David C (2009). Quantitative phase-contrast tomography of a liquid phantom using a conventional x-ray tube source. Opt. Express 17, 10010–18.

Qi Z, Zambelli J, Bevins N and Chen G-H (2010). Quantitative imaging of electron density and effective atomic number using phase contrast CT. Phys. Med. Biol. 55, 2669–77.

Pfeiffer F, Kottler C, Bunk O and David C (2007). Hard x-ray phase tomography with low-brilliance sources. Phys. Rev. Lett. 98, 108105.

Donath T, Pfeiffer F, Bunk O, Grünzweig C, Hempel E, Popescu S, Vock P and David C (2010). Toward clinical x-ray phase-contrast CT: demonstration of enhanced soft-tissue contrast in human specimen. Invest. Radiol. 45, 445–52.

Woodard H Q and White D R (1986). The composition of body tissues. Br. J. Radiol. 59, 1209–18.

ICRU 1989 Tissue substitutes in radiation dosimetry and measurement. International Commission on Radiation Units and Measurements Report 44 (Bethesda, MD: ICRU)

Session 204

Edge illumination x-ray phase contrast computed tomography: implementations at synchrotrons and in standard laboratories

*C.K. HAGEN[1], A. ZAMIR[1], F.A. VITTORIA[1], P.C. DIEMOZ[1], M. ENDRIZZI[1], A. OLIVO[1]

[1] Department of Medical Physics and Biomedical Engineering, University College London, Malet Place, Gower Street, London WC1E 6BT, United Kingdom – charlotte.hagen.10@ucl.ac.uk
* presenting author

Keywords: X-Ray Imaging, Phase Contrast, Computed Tomography, Phase Retrieval

Abstract

We discuss different implementations of edge illumination x-ray phase contrast computed tomography, including those used both at synchrotron facilities and in standard laboratories with commercial x-ray tubes. Tomographic reconstruction procedures are explained. Finally, we present experimental images of a carbon foam sample obtained in a laboratory environment with a Rigaku MicroMax 007 HF x-ray tube.

Introduction

X-ray phase contrast computed tomography (PC-CT) has the potential to overcome the main problem associated with conventional x-ray tomography: limited contrast for samples with weak attenuation properties. This is because contrast is generated from the phase shift that x-rays suffer while they travel through matter, rather than from x-ray absorption. Since phase effects can be much stronger than attenuation ones, this can lead to improved image contrast. Alongside the high spatial resolution and short scan times achievable with x-rays and the 3D nature of tomographic images, this has made PC-CT an attractive modality for a broad spectrum of applications, both from medical and non-medical disciplines (Bravin et al. 2013, Mayo et al. 2012). Amongst the latter are, for example, materials science and non-destructive testing of light materials such as plastics and composites.

To date, several approaches to PC-CT have been developed. These can be classified as propagation-based (Snigirev et al. 1995, Wilkins et al. 1996), crystal-based (Ingal and Beliaevskaya 1995, Davis et al. 1995), grating-based interferometric (Momose et al. 2003) and grating-based non-interferometric methods (Olivo et al. 2001). Measures to compare these approaches include coherence requirements, phase sensitivity, quantitative accuracy, stability and robustness. Edge illumination (EI) PC-CT, a grating-based non-interferometric method, was demonstrated to provide high phase sensitivity and quantitative phase reconstructions (Diemoz et al. 2013, Hagen et al. 2014a, Hagen et al. 2014b). Other advantages include a simple experimental setup, incoherence (Olivo and Speller 2007) and relatively weak requirements on stability (Millard et al. 2013). The last two aspects ensure that the method can be implemented outside synchrotrons in standard laboratory environments.

In the following, we present the working principle of EI PC-CT. In particular, we highlight how the method can be implemented in different experimental environments, including synchrotron facilities and standard laboratories. Finally, experimental images acquired with a commercially available, lab-based rotating anode x-ray tube will be presented.

Materials and Methods

For wave lengths in the x-ray range, the optical properties of a sample are given by the complex refractive index: $n(\lambda) = 1-\delta(\lambda)+i\beta(\lambda)$, where β and δ denote the attenuation and phase shifting properties, respectively, i is the imaginary unit and λ is the x-ray wavelength. After having passed through the sample, the transmission (T) and phase shift (Φ) experienced by an x-ray beam travelling along the z-axis are described by:

$$T(x,y;\lambda) = e^{-\frac{4\pi}{\lambda}\int \beta(x,y,z;\lambda)dz}$$
$$\Phi(x,y;\lambda) = \frac{2\pi}{\lambda}\int \delta(x,y,z;\lambda)dz.$$

The integration is carried out over the extent of the sample. A local phase change corresponds to a small deviation of x-rays from their original path, an effect known as refraction. The angle of refraction is related to the phase shift via:

$$\alpha(x,y;\lambda) = \frac{\lambda}{2\pi}\left|\nabla_{xy}\Phi(x,y;\lambda)\right|$$

The symbol ∇_{xy} denotes the gradient operator in the plane orthogonal to the propagation direction. On the plane of the detector, refraction translates into a displacement of x-rays by:

$$D(x,y;\lambda) = z_2\alpha(x,y;\lambda),$$

where z_2 is the object-to-detector distance. Generally speaking, imaging systems capable of measuring the refraction-induced displacement belong to the class of differential phase contrast (DPC) techniques, as D is proportional to the differential of the phase shift.

The working principle of the EI method is shown in Fig. 1(a): a beam is collimated by a slit, typically down to 10-20 µm, and a second slit positioned in front of a detector stops half of the beam, while the remaining half is allowed through. This “edge illumination” configuration is effectively the sensing mechanism for the refraction-induced beam displacement: the intensity integrated over the uncovered detector area is a function of the beam position (Diemoz et al. 2013). Consequently, a displacement causes either an increased or decreased measured intensity, depending on the refraction direction. This effect is reversed when the slit in front of the detector is repositioned such that its other edge is illuminated [Fig. 1(b)]. An image can be obtained by scanning a sample through the setup. This implementation is typically used at synchrotrons.

It should be noted that the setup described here extends uniformly into one direction; this restricts the phase sensivity to one direction only. Depending on the orientation of the slits, this can be either the x- or y-direction; the respective measurable beam displacements are given by:

$$D_y(x,y;\lambda) = z_2\alpha_y(x,y;\lambda) = z_2\frac{\lambda}{2\pi}\frac{\partial}{\partial y}\Phi(x,y;\lambda),$$
$$D_x(x,y;\lambda) = z_2\alpha_x(x,y;\lambda) = z_2\frac{\lambda}{2\pi}\frac{\partial}{\partial x}\Phi(x,y;\lambda),$$

The feasibility of achieving phase sensitivity in two directions simultaneously has been demonstrated previously (Olivo et al. 2009), and is currently under further investigation.

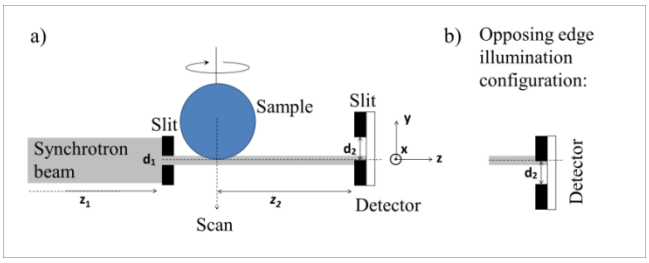

Figure 1. Edge illumination setup as it is typically implemented at synchrotrons. The sample needs to be scanned through the setup in order to obtain a mixed phase and attenuation projection image. a) and b) show the system in opposing edge illumination configurations.

The requirement to scan the sample through the setup can be eliminated if both slits are replaced by two sets of gratings [Fig. 2], which in the following will be referred to as "masks" in order to avoid confusion with gratings used by other DPC methods (Momose et al. 2003); their aspect ratio is typically much larger and the sensing mechanism substantially different. The first mask ("sample mask") splits the incoming beam into an array of "beamlets", while the second one ("detector mask") creates insensitive regions between pixels of an area detector. This arrangement replicates the EI configuration over a large field of view (Olivo and Speller 2007). The design of the sample mask must ensure that the beamlets remain physically separated; which makes the slit and mask setups formally equivalent. As the mask implementation of EI allows a faster image acquisition, this is typically used in standard laboratories with conventional x-ray tubes.

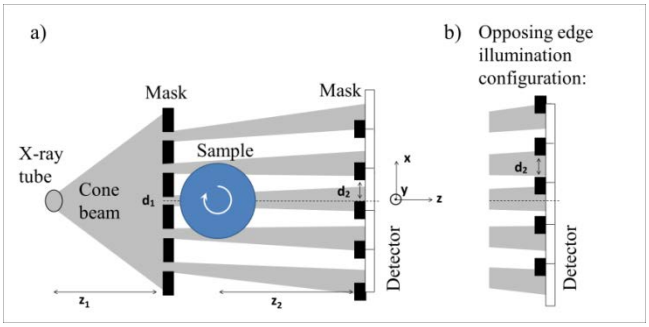

Figure 2. Edge illumination setup as it is typically implemented with lab-based x-ray tubes. Due to the use of masks, a mixed phase and attenuation projection image can be obtained in a single shot; no sample scanning is required. a) and b) show the system in opposing edge illumination configurations.

For non-scattering samples, a single image acquired with EI shows a combination of attenuation and (differential) phase contrast. It is however possible to obtain separate images of the transmission and refraction angle if two images are acquired under opposing EI conditions and processed together according to a dedicated procedure (Munro et al. 2013, Diemoz et al. 2013). With the acquisition of a ~~thrid~~third image, the sample scattering, if present, can also be detected (Endrizzi et al. 2014).

Recent experiments have demonstrated that the refraction-induced beam displacement can be sensed also without a detector slit (in the scanning implementation) or mask (in the full field implementation), provided the pixels are sufficiently small (Vittoria et al. 2014). This can be realized by resolving the beam profile on the detector plane, and integrating its intensity across the areas that were previously covered and uncovered by the detector slit or mask, generating "virtual" EI signals. A second realization involves tracking the movement of the beam profile, followed by the extraction of the refraction-induced displacements through numerical procedures. While virtual EI

and beam tracking approaches have initially been developed at synchrotrons, their translation into standard laboratories is currently underway.

The acquisition of images in CT mode (using any of the EI implementations introduced above) can yield attenuation and refraction sinograms corresponding to transverse slices through the sample (*y* = *const*.):

$$S_{att}(x,\theta;\lambda) = -\frac{4\pi}{\lambda}\int \beta(x',y,z';\lambda)dz$$
$$S_{ref}^{x,y}(x,\theta;\lambda) = \frac{2\pi}{\lambda}\frac{\partial}{\partial x,y}\int \delta(x',y,z';\lambda)dz.$$

Here, the sample was assumed to rotate around the y-axis, θ is the rotation angle and $x' = x\cos(\theta)+z\sin(\theta)$ and $z' = z\cos(\theta)-x\sin(\theta)$ are the corresponding rotating coordinates. The derivative operator in the refraction sinogram can refer either to the x- or y-direction, depending on the direction of phase sensitivity. CT images can be obtained via standard reconstruction procedures, e.g. filtered back projection (FBP). Note that the reconstruction of δ-maps requires the derivative operator in the refraction sinogram to be inverted before or after back projection ("phase retrieval"). This can be achieved through a one-dimensional integration or through other, possibly more stable approaches (Thuering et al. 2011). In cases where the derivative refers to the x-direction, a specialized filter function can be used to invert the integral implicitly as part of the FBP (Huang et al. 2006). It should be noted that when a lab-based x-ray tube with a broad energy spectrum is used, the values in the reconstructed CT slices refer to effective energies (Munro and Olivo 2013, Hagen et al. 2014b).

Results

Figure 3 shows example CT images acquired with a lab-based EI PC-CT setup. The system includes a Rigaku MicroMax 007 HF x-ray tube (Rigaku Corporation, Japan) with a rotating molybdenum target and a focal spot with a horizontal full width at half maximum dimension of approximately 70 µm. The tube was operated at 35 kV and 25 mA. The detector was the Hamamatsu C9732DK flat panel, featuring a pixel size of 50 x 50 μm^2. A full field implementation was used, and masks were manufactured to the authors' design by electroplating gold strips onto graphite substrates (Creatv Microtech, Potomac, USA). The system dimensions were approximately 1.6 m (z_1) and 0.4 m (z_2). The masks' periods were 79 µm (sample mask) and 98 µm (detector mask), with apertures of 10 µm (d_1) and 17 µm (d_2), respectively. With these dimensions, every second pixel column was covered ("line-skipping" configuration), reducing the effect of pixel cross-talk (Ignatyev et al. 2011). The CT scan was acquired over 360 degrees with an angular step of 0.5 degrees. At each angle, two projections were taken under opposing EI conditions. In addition, the sample was displaced 8 times by one eighth of the sample mask period. This procedure, known as "dithering", can increase the spatial resolution in the final CT images (Hagen et al. 2014c). Following the extraction of attenuation and refraction sinograms (Munro et al. 2013, Diemoz et al. 2013), CT reconstruction was performed via FBP with a specialized filter function (Huang et al. 2006).

The images show reconstructed attenuation and phase maps within a carbon foam sample in form of transverse slices [Fig. 3(a), 3(b)] and a volume rendering [Fig. 3(c)]. The intricate structure, which is barely visible in the attenuation slice, is clearly visualized in the phase images. The images were chosen as a typical example where PC-CT enables the visualization of structures that would be invisible to conventional, attenuation-based CT.

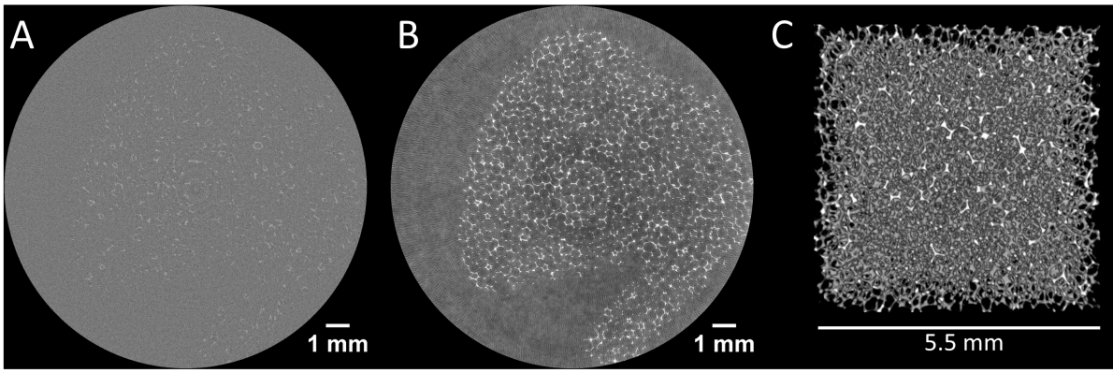

Figure 3. CT images of a carbon foam sample: A) attenuation slice, B) phase slice, C) 3D rendering of a subsection of the reconstructed phase volume.

Acknowledgments

This work was supported by the UK Engineering and Physical Sciences Research Council (Grant Nos. EP/L001381/1 and EP/I021884/1). PCD and ME are supported by Marie Curie Career Integration Grant Nos. PCIG12-GA-2012-333990 and PCIG12-GA-2012-334056 within the Seventh Framework Programme of the European Union.

References

Bravin A., Coan P. & Suortti P. (2013). X-ray phase-contrast imaging: from pre-clinical applications towards clinics. ***Phys. Med. Biol.*** 58, 1: R1-R35.

Davis T.J., Gao D., Gureyev T.E., Stevenson A.W. & Wilkinsi S.W. (1995). Phase-contrast imaging of weakly absorbing materials using hard x-rays. ***Nature.*** 373: 595-8.

Diemoz P.C., Endrizzi M., Zapata C.E., Pesic Z.D., Rau C., Bravin A., Robinson I.K. & Olivo A. (2013). X-ray phase-contrast imaging with nanoradian angular resolution. ***Phys. Rev. Lett.*** **110**: 138105.

Endrizzi M., Diemoz P.C., Millard T.P., Jones L.J., Speller R.D., Robinson I.K. & Olivo A. (2014). Hard x-ray dark-field imaging with incoherent sample illumination. ***Appl. Phys. Lett.*** **104**,2: 024106.

Hagen C.K., Diemoz P.C., Endrizzi M., Rigon L., Dreossi D., Arfelli F., Lopez F.C.M., Longo R. & Olivo A. (2014). Theory and preliminary experimental verification of quantitative edge illumination x-ray phase contrast tomography. ***Opt. Express*** **22**, 7: 7989-8000.

Hagen C.K., Munro P.R.T., Endrizzi M., Diemoz P.C. & Olivo A. (2014). Low-dose phase contrast tomography with conventional x-ray sources. ***Med. Phys.*** **41**, 7: 070701.

Hagen C.K., Diemoz, P.C., Endrizzi M. & Olivo A. (2014). The effect of the spatial sampling rate on quantitative phase information extracted from planar and tomographic edge illumination x-ray phase contrast images. ***J. Phys. D: Appl. Phys.*** **47**, 45: 455401.

Huang Z., Kang K., Li Z., Zhu P., Yuan Q., Huang W., Wang J., Zhang D. & Yu A. (2006). Direct computed tomographic reconstruction for directional-derivative projections of computed tomography of diffraction enhanced imaging. ***Appl. Phys. Lett..*** **89**, 4: 041124.

Ignatyev K., Munro P.R.T., Speller R. & Olivo A. (2011). Effects of signal diffusion on x-ray phase contrast images. ***Rev. Sci. Instrum.*** **82**, 7: 073702.

Ingal V.N. & Beliaevskaya E.A. (1995). X-ray plane-wave topography observation of the phase contrast from a non-crystalline object. ***J. Phys. D: Appl. Phys.*** **28**, 11: 2314-17.

Mayo S.C., Stevenson A.W. & Wilkins S.W. (2012). In-line phase-contrast x-ray imaging and tomography for materials science. ***Materials*** 5: 937-65.

Millard T.P., Endrizzi M., Ignatyev K., Hagen C.K., Munro P.R.T., Speller R.D. & Olivo A. (2013). Method for the automatization of the alignment of a laboratory based x-ray phase contrast edge illumination system. ***Rev. Sci. Instrum.*** **84**, 8: 083702.

Momose A., Kawamoto S., Koyama I., Hamaishi Y., Takai K. & Suzuki Y. (2003). Demonstration of x-ray Talbot interferometry. ***Jpn. J. Appl. Phys.*****42**, Part 2, No 7B: L 866-L868.

Munro P.R.T., Hagen C.K., Szafraniec M.B. & Olivo A. (2013). A simplified approach to quantitative coded aperture x-ray phase imaging. ***Opt. Express*** **21**, 9: 11187-201.

Olivo A., Arfelli F., Cantatore G., Longo R., Menk R.H., Pani S., Prest M., Proporat P., Rigon L., Tromba G., Vallazza E. & Castelli E. (2001). An innovative digital imaging set-up allowing a low-dose approach to phase contrast applications in the medical field. ***Med. Phys.*** 28, 8: 1610-19.

Olivo A. & Speller R. (2007). A coded-aperture technique allowing x-ray phase contrast imaging with conventional sources. ***Appl. Phys. Lett.*** **91**, 7: 074106.

Olivo A., Bohndiek S.E., Griffiths J.A., Konstantinidis A. & Speller R.D. (2009). A non-free-space propagation x-ray phase contrast imaging method sensitive to phase effects in two directions simultaneously. ***Appl. Phys. Lett..*** **94**, 4: 044108.

Snigirev A., Snigireva I., Kohn V., Kuznetsov S. & Schelokov I. (1995). On the possibilities of x-ray phase contrast microimaging by coherent high-energy synchrotron radiation. ***Rev. Sci. Instrum.*** **66**, 12: 5486-92.

Thuering T., Modregger P., Pinzer, B.R., Wang Z. & Stampanoni M. (2011). Non-linear regularized phase retrieval for unidirectional x-ray differential phase contrast radiography. ***Opt. Express*** **19**, 25: 25545-58.

Vittoria F.A., Endrizzi M., Diemoz P.C., Wagner U.H., Rau C., Robinson I.K. & Olivo A. (2014). Virtual edge illumination and one dimensional beam tracking for absorption, refraction, and scattering retrieval. ***Appl. Phys. Lett.*** **104**, 13: 134102.

Wilkins S.W., Gureyev T.E., Gao D., Pogany A. & Stevenson A.W. (1996). Phase-contrast imaging using polychromatic hard x-rays. ***Nature*** **384**: 335-8.

Projection-based Digital Volume Correlation: Application to crack propagation

T. TAILLANDIER-THOMAS,[1] H. LECLERC,[1] S. ROUX[1]* AND F. HILD[1]

[1] LMT, ENS-Cachan / CNRS / Univ. Paris-Saclay
61 Av. Président Wilson, 94235 Cachan Cedex, France
{thibault.taillandier-thomas, hugo.leclerc, stephane.roux, francois.hild}@lmt.ens-cachan.fr
* presenting author

Keywords: Crack, Digital Volume Correlation, Motion, Projection

Abstract

In order to follow the time evolution of a solid, which has been scanned in its reference state, it is proposed to determine the kinematic field it is subjected to from a few projections. A nodular graphite cast iron specimen containing a fatigue crack is chosen to challenge the proposed method, as the specimen geometry is complex and the kinematic field is highly heterogeneous and displays a discontinuity. Yet, it is shown that with no more than two projections, it is possible to determine the motion quite accurately.

Introduction

Tomography is not only useful for its ability to reveal the intimate 3D microstructure of materials (Baruchel, 2000) but also to track its changes with time (Salvo, 2010; Buffière, 2010), say, during a mechanical test. One useful tool in this context is Digital Volume Correlation (DVC) whose finality is to provide a 3D displacement field that allows for the registration of two 3D images of the same solid at different loading steps (Bay, 1999). However, one limiting feature is the long acquisition time that confines such studies to (quasi) time-independent behaviors. Another limitation of DVC is the presence of artifacts in the tomographic reconstruction that originates from the imperfection and noise of the X-ray detector. Although the latter noise can be considered as white (i.e., spatially uncorrelated) the reconstruction algorithm induces long-range correlations. Such correlated noise unfortunately impacts the DVC analysis.

It has been suggested to use a first 3D reconstruction of the reference configuration, and estimate the displacement field from only a few radiographs of the deformed state (Leclerc, 2015). Such a procedure was shown on one experimental case study to provide faithful displacement measurements based on a very small number of projections (as small as 2). This procedure, which is referred to as “Projection-based DVC” (or P-DVC), offers a large gain in the needed number of projections (i.e. more than two orders of magnitude). Moreover, as only raw projections are dealt with, the white noise assumption remains valid and hence the detrimental effect of noise can be much reduced.

The example that was used previously (Leclerc, 2015) consisted of a simple kinematics that could be captured with a rather coarse description. Moving to finer and finer meshes to describe the displacement field, the algorithm showed signs of poorer convergence resulting from ill-conditioning, as a fore sign of ill-posedness. Hence, it is natural to raise the question as to what extent such an approach could deal with more complex displacement fields.

The present study deals with such a complex example where a cracked solid is subjected to a tensile test. Not only does the strain field present a singular behavior at the crack tip, but additionally, the crack geometry presents some corrugations that could be evaluated from a full 3D reconstruction performed before the test. The displacement field is decomposed over a 3D finite element mesh that is refined in the vicinity of the crack. Two novel tools are implemented to reach convergence. First, a hierarchical coarsening procedure is used to allow for large displacement corrections. Second, a mechanical regularization is implemented to guide the displacement determination using the solution to a homogeneous elastic problem as a guess. These two procedures have been successfully implemented and the resulting projection residuals show a good convergence to a trustworthy solution based on no more than two projections, in spite of the numerous kinematic degrees of freedom used to describe the displacement field.

Methods: P-DVC, multiscale approach, regularization

Tomography consists of the reconstruction of a 3D image, $f(\boldsymbol{x})$, of a sample from the knowledge of its projections π_θ^f for a number of angles θ. The projection conditions are written

$$\Pi_\theta(f(\boldsymbol{x})) = \pi_\theta^f$$

where the projection is understood to be the cologarithm of the intensity attenuation on the detector. Classically, for an image width of N voxels, the number of needed projections allowing for an inversion of the previous equation, is $N\pi/2$.

Digital Volume Correlation (DVC) refers to the analysis of the displacement field $\boldsymbol{U}(\boldsymbol{x})$ that relates a reference $f(\boldsymbol{x})$ to a deformed $g(\boldsymbol{x})$ image such that

$$g(\boldsymbol{x}) = f(\boldsymbol{x} - \boldsymbol{U}(\boldsymbol{x}))$$

where the displacement field is the Eulerian variant as this choice is the most convenient for the following (Bay, 1999). This operation thus needs the deformed volume to be fully imaged and reconstructed. This is sometimes a difficult constraint to be met, as the specimen may move during an entire tomographic scan.

The spirit of P-DVC is to read the displacement field from a very few projections

$$\Pi_\theta(f(\boldsymbol{x} - \boldsymbol{U}(\boldsymbol{x}))) = \pi_\theta^g$$

after the reference image, $f(\boldsymbol{x})$, has been reconstructed with classical means (i.e. with a complete set of projections). The feasibility of this approach can be understood by noting that the number of parameters needed to characterize the displacement field is generally much less than those required to image the details of the microstructure.

In order to design a robust methodology, it is important to be able to capture large scale displacements. Following a strategy that revealed very powerful in 2D Digital Image Correlation, a multiscale approach can be envisioned. Exploiting the linearity of the tomographic reconstruction, it is worth noting that a coarse 3D volume may be computed from coarsened projections. Coarsening here refers to the convolution with a (2D) Gaussian $G_w(\boldsymbol{x})$ of width w

$$\widetilde{\pi}_\theta^f = G_w * \pi_\theta^f$$

The reconstructed image is simply the original volume convoluted with a 3D Gaussian function of the same width. This operation can be seen as a low pass filter and thus the resulting image can be down sampled to 1 voxel out of w in each spatial direction. The 3D image size is then reduced by a factor of $(1/w)^3$. All ingredients are thus present to perform P-DVC on the filtered and subsampled projections provided the same filter is used on the reconstruction of the reference volume. This operation allows large displacement amplitudes to be captured since they are effectively scaled by a factor of $(1/w)$. Moreover, the computation cost is very low because of the vast reduction in the

number of voxels. P-DVC performed on such coarse images cannot be expected to be as accurate as the original one, but it is to be considered as a way to obtain an excellent initial displacement field for the P-DVC algorithm performed at the initial scale, which is iterative. Finally, it is to be noted that the Gaussian filter can be organized in a pyramidal way with a recursive structure where level n corresponds to $w = 2^n$.

A further reduction in the number of degrees of freedom can be achieved through mechanical regularization. In the following, this idea is used in order to drastically reduce the number of parameters needed to describe the displacement field. From the reference image, a very accurate description of the geometry can be achieved and a fine mesh can be fitted to the volume. If it is assumed that the mechanical behavior of the sample obeys a known constitutive law, the entire displacement field is parameterized by the boundary conditions. Each unknown for the boundary conditions corresponds to a full 3D displacement field that can be computed, and P-DVC will finally be restricted to the generated space of displacement fields. In this way, it is observed that the mesh size is no longer a limiting factor for P-DVC, and hence, a very fine description of the geometry is possible.

Case study

The previous strategy is here illustrated with a sample of nodular graphite cast iron in which a fatigue crack is propagating. The sample has been scanned at ESRF (beam line ID19) under various load levels. These images allow a classical DVC analysis to be performed and they will provide a reference solution. The microstructure of the material is shown in figure 1a, with a voxel size of 5.4 µm. The effect of the Gaussian filtering with $w = 4$ is seen in figure 1b. Although fine scale details have disappeared, some features of the microstructure remain visible and allow a first determination of the displacement field to be computed with a number of voxels that is much reduced (by a factor of 64).

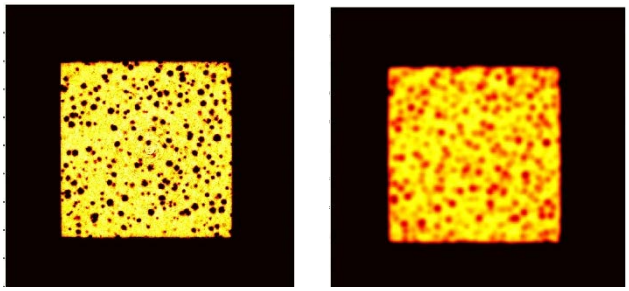

(a) *(b)*

Fig. 1. *(a) Section view of the cast iron sample used herein. The dark dots are graphite nodules. The voxel size is 5.4 µm (b) Coarsened image obtained from a convolution with a Gaussian of 4-voxel width*

A mesh is adjusted to the microstructure, including the crack that can be detected and segmented in the reference image. As previously explained, the P-DVC algorithm will not be dependent on the fineness of the mesh and hence it was chosen here to have a very accurate description of the geometry. It is an unstructured mesh composed of 8487 T4 tetrathedra elements and 2119 nodes (hence 6357 dof). It is drawn on top of the x component of the displacement field that is shown in Figure 2.

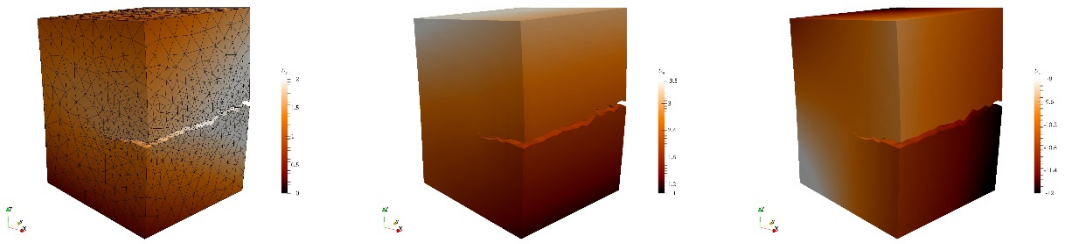

Fig. 2. *Displacement field along the three directions, x, y and z. The mesh is superimposed on top of the x component of the displacement field. Although the mechanical test aimed to open the crack in mode I, a significant mode mixity (with mode III) is observed*

The displacement fields are parameterized by the displacements at both ends of the region of interest considered to be an arbitrary rigid body motion. Hence, six degrees of freedom (i.e. three translations and three rotations) are introduced at both ends, resulting in twelve boundary condition unknowns. P-DVC is run with these 12 degrees of freedom and exploits only two projections (along the x and the y directions). In order to validate the algorithm, the differences (thereafter called "residuals") between the acquired projections and the computed ones from the reference volume advected by the current determination of the displacement field is computed. At convergence, the residuals are shown in Figure 3. For comparison, the initial residuals that are computed after a global translation determined over the whole volume by a mere intercorrelation are shown in Figure 4. Most of the features that were apparent in the projections have now disappeared, but some phase contrast artifacts, which are observed on the edge of the projection and along the crack surface, and which were not modeled in the projection.

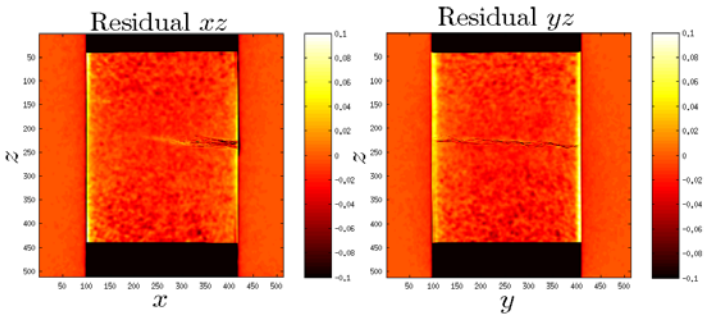

Fig. 3. *Residual on the two projection images at convergence. The yellow line in the middle of the sample is the trace of the crack. The lighter residual close to the lateral edges corresponds to phase contrast phenomena that are not described in the projection model*

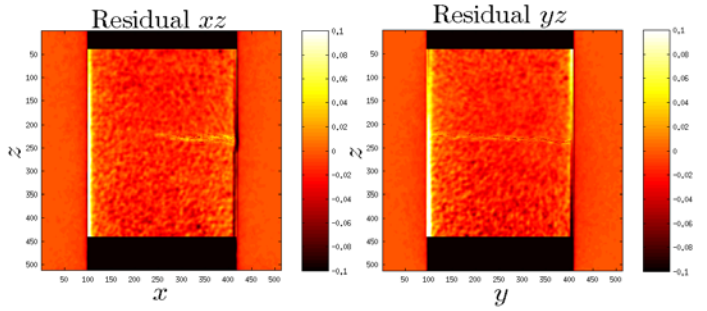

Fig. 4. *Initial residual on the two projection images after a correction of the mean sample translation*

In order to better appreciate the quality of the obtained solution, which is based on the residuals, it is instructive to compute the same residuals but for the reference image. Although the reference 3D image was computed from the full set of 600 projections, one can select the x and y projection of the reference state as a test of P-DVC for which the displacement is exactly known to be 0. They suffer from the same bias of not accounting for phase contrast effects, and their order of magnitude is quite comparable with that of the P-DVC case.

Last, the displacement field that is shown in Figure 2 can be compared to other P-DVC determinations obtained from another pair of projection angles, and although phase contrast effects are less apparent, the displacement data can hardly be distinguished. The comparison with standard DVC results, which are using the reconstructed deformed volume, and hence requiring 600 projections, is also of interest as it may appear as the gold standard. However, due to the fact that the mesh is really fine, standard global DVC based on the very same mesh does not converge. In the same spirit as the present P-DVC algorithm, mechanical regularization is to be used in order to achieve a good image registration. Although a very favorable comparison has already been obtained based on a coarser mesh, the one to one correspondance based on the very same mesh is currently being processed.

Conclusions

Projection-based Digital Volume Correlation has been shown to be amenable to a multiscale and a mechanical regularization strategy to address a complex kinematics that could be captured based on no more than two projections. From these results, one may envision as an appealing perspective to extract features such as more accurate crack surface geometry, stress intensity factors along the crack front, or precise position of crack front. On a more general ground, these extremely large savings (here a 300 fold decrease) with virtually no loss on the determination of the displacement field opens new avenues in terms of temporal resolution for fast phenomena.

Acknowledgements

The authors acknowledge beam time from ESRF (MA-501 on beam line ID19), the CETIM Foundation for project "PROPAVANFIS", and the ANR for "RUPXCUBE" (ANR-09-BLAN-0009-01) "EDDAM" (ANR-11-BS09-027-05) projects, and "MATMECA" (ANR-10-EQPX-37) "Investissements d'Avenir" program.

References

Baruchel J, Buffière J-Y, Maire E, Merle P & Peix G (2000) *X-Ray Tomography in Material Sciences*. Hermès Science, Paris, (France)

Salvo L, Suéry M, Marmottant A, Limodin N, Bernard D (2010) *3D imaging in material science: Application of X-ray tomography.* **C. R. Physique** 11:641-649

Buffière J-Y, Maire E, Adrien J, Masse J-P & Boller E (2010) *In Situ Experiments with X ray Tomography: an Attractive Tool for Experimental Mechanics*. **Exp. Mech.** 50:289-305

Bay B.K., Smith TS, Fyhrie DP & Saad M (1999) *Digital volume correlation: three-dimensional strain mapping using X-ray tomography*. **Exp. Mech.** 39:217-226

Leclerc H., Roux S. & Hild F., (2015) *Projection savings in CT-based Digital Volume Correlation,* **Exp. Mech.** 55, (1), 275-287

4D quantification and tracking of time dependent features

*L. COURTOIS[1,2], P.D. LEE[1,2], K.J. DOBSON[3], Q.LIN[4], S.J. NEETHLING[4]

[1] Manchester X-ray Imaging Facility, School of Materials, Oxford Road, University of Manchester, M13 9PL, UK
[2] Research Complex at Harwell, Rutherford Appleton Laboratory, Didcot, Oxfordshire, OX11 OFA, UK
[3] Earth & Environmental Sciences, LMU Munich, Theresienstrasse 41, 80333 Munich, Germany
[4] Department of Earth Science and Engineering, Imperial College London, SW7 2AZ, UK
* presenting author

Keywords: In-situ, Xray tomography, Tracking, Quantification, Automatic

Abstract

High flux laboratory and synchrotron tomographic imaging systems, combined with bespoke *in situ* sample environmental rigs are revolutionising our ability to perform time-resolved 3D imaging, termed 4D imaging. Experiments ranging from tracking the deformation of high temperature semi-solids (Kareh et al, 2014) through to the fracture of frozen solids (Ní Bhreasail, 2012) can be studied both dynamically and over long time periods, resulting in the acquisition of large 4D datasets (tens of terabytes). These datasets offers many advantages over traditional destructive techniques (microscopy), specifically multi-phase flow and the kinetics of phase changes can be observed. However, due to the huge quantities of data quantifification is often difficult and time consuming. This study presents automated techniques for quantifying these large experimental 4D data sets to gain a better understanding of the process and to inform and validate models of the phenomena. Although we will use data acquired using X-ray micro-computed tomography, the technique it is applicable to any 3D imaging technique used for acquiring time dependent images (e.g. Neutron, confocal, or EM tomography…).

Introduction

In recent years, time-resolved imaging experiments, both dynamic (Landron et al., 2011) and long-term (Lin,2014), have become more common following the design of bespoke in-situ sample environmental rigs (Buffiere,2010; Iglauer,2013; Puncreobutr, 2012), resulting in large amounts of 4D data. In addition to the microstructural information that can be obtain from any 3D imaging technique (X-ray or neutron tomography, FIB, Serial block-face scanning electron microscopy, confocal microscopy), these 4D datasets provide information on the temporal evolution of different types of features. However, there remains a need for a standardised and automated methodology for the quantitative analysis of 4D datasets for application to large volumes of data (Terabytes) and to a wide range of materials and structures (void growth in metals, crack propagation, thermal maturation).

Experimental methods

In this study, we present a fully automated method to track and quantify motion and morphological changes of particles across a range of scales demonstrated using the evolution of particle sizes during the processing of rocks over the period of months (Fig. 1.a, see Lin et al, 2014 for experimental details). The key steps include i) denoising, ii) phase segmentation, iii) macro-scale fragment identification, iv) individual macro-scale registration, and v) micro-scale track of particles. The analysis is aimed at limiting user-input when processing data to objectively quantify microstructural parameters.

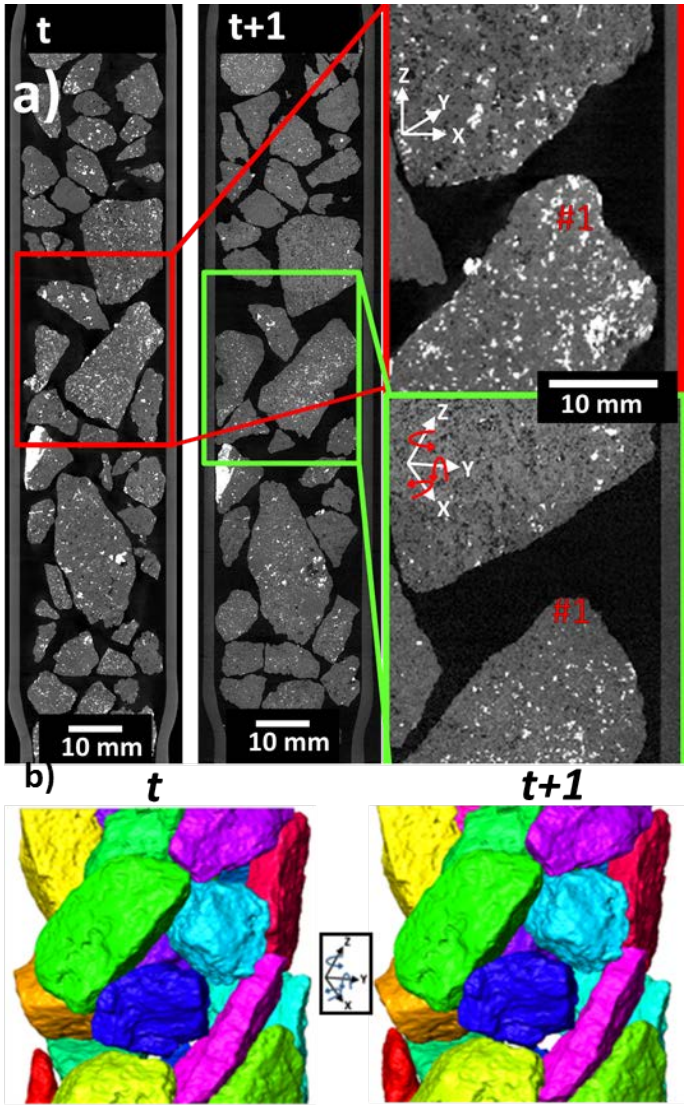

Figure 1: a) Cross section of XMT data of an ore fragment alongside two section at consecutive times (t and t+1). b) segmented and tracked macro-scale fragments

Histogram-based segmentation methods were used (Tsai, 1985; Kapur, Sahoo & Wong, 1985) to segment both macro-scale fragments and micro-scale particles (bright white spots in Fig. 1.a). A combination of morphological operations and watershed separations were used in order to individually label and identify (via their volume, shape, diameter,…) fragments before tracking. In such a case where two different scales are easily distinguishable, information from one scale can be used to help the analysis of the second one. Here, macro-scale fragments can be identified through time (Figure 1.b) via the tracking approach described below and a transformation matrix can thus be obtained for all timeframes (Figure 2.a), resulting in physically aligned 3D volumes. However, in order to avoid any further interpolation, volumes are left untransformed and the matrix alone is saved for use in subsequent tracking and analysis.

The tracking strategy used here is easily tailored to a specific experiment, using *a priori* knowledge of the behaviour of the system, *e.g.*: known displacement field, no volume change, constant shape factor or distance to nearest surface… As a result, features can be matched through time by using both experiment specific information and all identifiers previously defined for each individual feature, thus reducing the number of possible matches for a given particle considerably. A cost function based on weighted distance between matches and specific penalties (e.g. change in volume) is then minimized in order to identify particle matches through time. Figure 2.c shows the result of tracking and subsequent relabelling of particles.

Results

The ability to track particles through time first allows for the measurement error to be quantified. For this, two subsequent scans of a non-deformed sample are acquired (referred to as repeat scans) in which particles should not be submitted no any volume change. However, because of systematic (due to the definition of a threshold value, but that can be

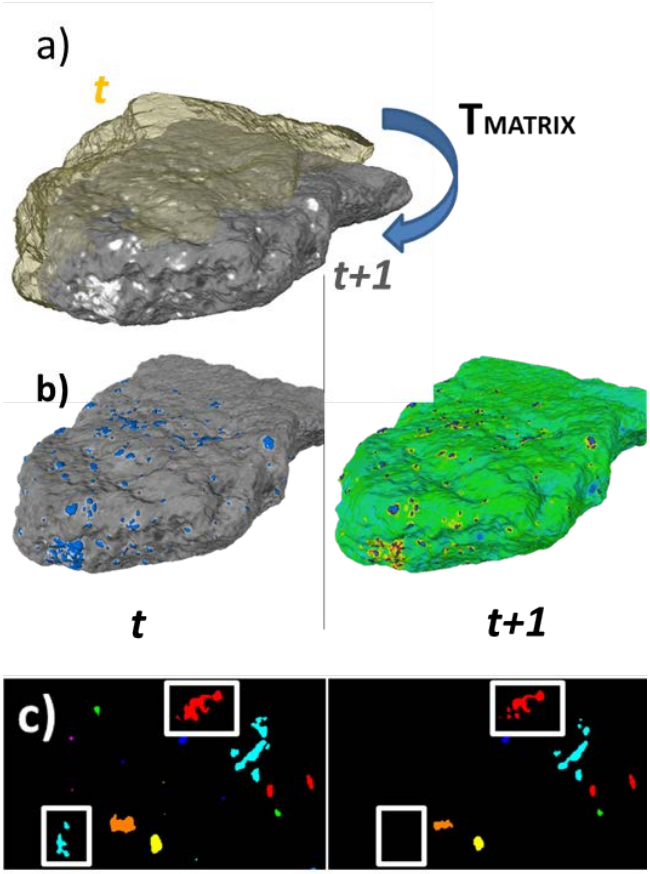

Figure 2: Isolated fragment at two different time-points before (a) and after (b) alignement (shown side-by-side using different colormaps and micros-scale particles as blue). c) Segmented and tracked micro-scale particles

corrected with using appropriate standards and calibration) and random (partial volume effect) errors (Lin et al., 2014). The expected volume change for two repeat scans being 0,

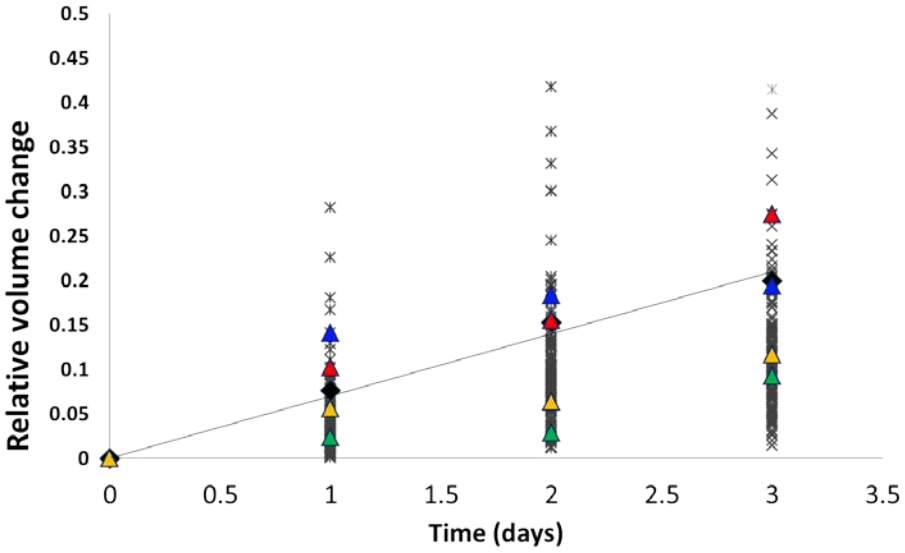

Figure 3 : Distribution of the relative volume change of micro-scale particles plotted as a function of time (x). Colored triangles show the evolution of 4 tracked micro-scale particles (figure 2.c) through time and black diamonds show the overall volume change of particles in this macro-scale fragment (figure 2.b).

the distribution of measured changes provides a quantification of the relative error on a measurement. The standard deviation of this distribution is used here as an estimate of the global error.

In this experiment, a statistical approach can then be used and the distribution of volume changes in individual fragments could then be observed. Overall, a few million particles were analysed, thus highlighting the need for advanced, multi-dimensional, and automated scientific visualisation techniques. Figure 3 shows a plot resulting in the successful track of a selection of 200 particles (for clarity, 2000 overall) in a single fragment. Such experimental data can then be used to validate models.

Conclusion

We defined a methodology for the automated quantification of 4D datasets using thresholding methods that do not require user input. We then apply a tracking algorithm based on a list of specific identifiers and cost functions to track large numbers of particles through time, thus enabling us to characterize 4D structural evolution. Although we applied this method to the spatially and temporally non-uniform reduction of particles, our method is applicable for tracking flow, porosity, cracks or bubbles, and highlights the attention needed when performing quantification based on 4D datasets

References:

Kareh, K.M., Lee, P.D., Atwood, RC, Connolley, T., and Gourlay, C.M., «Semi-solid metal deformation: illuminating new micro-mechanisms with time-resolved synchrotron tomography», Nature Commun., 5:4464, http://dx.doi.org/10.1038/ncomms5464, July 2014.

Ní Bhreasail, Á; Lee, P. D.; O'Sullivan, C; Fenton, C.H.; Hamilton, R.; Rockett, P.; Connolley, T, «In situ observation of cracks in frozen soil using synchrotron tomography», Permafrost and Periglacial Processes, Volume 23, Issue 2, pages 170–176, April 2012. DOI: 10.1002/ppp.1737

Landron, C.; Maire, E.; Bouaziz, O.; Adrien, J. ; Lecarme, L. ; Bareggi, A. ; « Validation of void growth models using X-ray microtomography characterization of damage in dual phase steels », Acta Materialia, Volume 59, pages 7564-7573, 2011

Lin, Q., Neethling, S.J., Dobson, K.J., Courtois, L., Lee, P.D., «Quantifying and minimising systematic and random errors in X-ray micro tomography based volume measurements, Computers & Geosciences, CAGEO-D-14-00434R1, 2014.

Buffiere, J.Y.; Maire, E.; Adrien, J. ; Masse, J.P. ; Boller, E. ; « In situ experiments with Xray tomography : an attractive tool for experimental mechanics », *Experimental Mechanics*, Volume 50, pages 289-305, 2010

Iglauer, S.; Paluszny, A.; Blunt, M.J.; «Simultaneous oil recovery and residual gas storage: A pore-level analysis using in situ X-ray micro-tomography», Fuel, Volume 103, pages 905-914, 2013

Puncreobutr, C.;Lee, P.D; Hamilton, R.W.; Phillion, A.B; «Quantitative 3D Characterization of Solidification Structure and Defect Evolution in Al Alloys», Jom, volume 64, Issue 1, pages 89–95, 2012

Tsai, W-H, «Moment-preserving thresholding: A New Approach», Computer Vision, Graphics, and Image Processing, 29: 377–393, 1985

Kapur, JN; Sahoo, PK; Wong, AKC, «A New Method for Gray- Level Picture Thresholding Using the Entropy of the Histogram», Computer Vision, Graphics and Image Processing, 29: 273–285,1985

‘Fast shear’ phenomena in ductile fracture assessed by Digital Volume Correlation on Laminography synchrotron volumes

T. TAILLANDIER-THOMAS[1,2*], T.F. MORGENEYER[2], L. HELFEN[3-4], F. HILD[1], S. ROUX[1]

[1] LMT, ENS-Cachan, CNRS, Univ. Paris-Saclay, 61 Av. Président Wilson, 94235 Cachan Cx., France
{email: thibault.taillandier-thomas, stephane.roux, francois.hild}@lmt.ens-cachan.fr}
[2] MINES ParisTech, PSL Research University, MAT - Centre des matériaux, CNRS UMR 7633, BP 87, F- 91003 Evry, France
{email: thilo.morgeneyer@mines-paristech.fr}

[3] ANKA/Institute for Photon Science and Synchrotron Radiation, Karlsruhe Institute of Technology (KIT), D-76131 Karlsruhe, Germany
[4] European Synchrotron Radiation Facility (ESRF), BP 220, F-38043 Grenoble Cedex, France

* presenting author

Keywords: Artifacts, Ductile failure, Digital Volume Correlation, Laminography, Strain localization

Abstract

Complex phenomena such as the ‘fast shear’ in ductile failure (*i.e.* the crack initiates in a plane normal to the loading direction and then tilts to a slanted position) require in situ measurements and observations to get a better understanding. Therefore 3D images of plates made of aluminum alloy are acquired by X-Ray synchrotron computed laminography. To measure displacement and strain fields at each step of the test on an aluminum alloy digital volume correlation (DVC) is used. Despite the lack of information intrinsic of laminography and the poor texture of the material, strain levels up to 16% were measured. Moreover strain localization occurs far before any damage or void growth can be observed.

1. Introduction

Despite the fact that the three stages of ductile fracture, namely, void nucleation, growth and coalescence, are established, the flat to slant phenomenon as shown in figure 1 is not well understood. Thanks to 3D imaging and full field measurements, the material microstructure and motion can be measured within the bulk. Synchrotron laminography gives access to volume of sheet-like samples at the microscale.

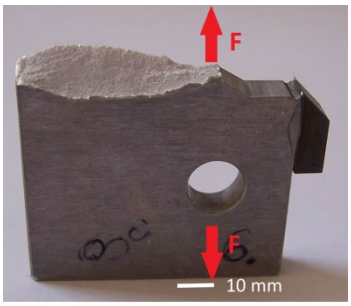

Figure 1: Flat to slant transition of an aluminum alloy sheet loaded under mode I (Taillandier-Thomas *et al.* 2014)

The natural contrast of the reconstructed volume is used to perform Digital Volume Correlation or DVC (Roux *et al.* 2008) to measure displacement (and strain) fields from the registration of 3D images at different stages of a mechanical test. Although a previous feasibility analysis of the technique has been conducted (Morgeneyer *et al.* 2013), it was not obvious that complex kinematics could be registered due to the high level of noise relative to

the poor texture of the imaged material. The present paper aims at determining the measurement resolution under such challenging conditions, and then reports on the kinematic measurements to determine whether the flant-to-slant transition is driven by plasticity or damage.

2. Experiment

2.1. Laminography

Sheet-like samples can be imaged in 3D with synchrotron radiation computed laminography. A region of interest is scanned thanks to the introduction of an angle θ < 90° between the sample and the beam direction (figure 2). The reconstruction is then performed with a filtered-backprojection algorithm.

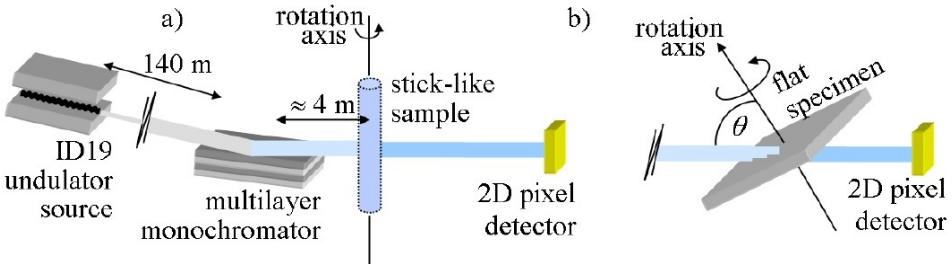

Figure 2: Schematic view of the CT (a) and CL (b) setup with the ESRF parallel beam line (Morgeneyer *et al.* 2013)

The imaging was performed at beamline ID19 at the European Synchrotron Radiation Facility with a monochromatic beam with an energy of 25 keV, a 65° angle and 1500 radiographs. The reconstructed volumes have a size of 2040 x 2040 x 2040 voxels with a voxel size of 0.7µm.

2.2. Material and experimental setup

The studied material is a 2139 aluminum alloy in T3 condition. The flat and notched specimen shown in figure 3.a. has a dimension of 60mm x 70mm x 1mm and a notch radius of 0.17mm. The presence of artifacts such as rings or phase contrast can be noticed in figure 3.a. The texture is poor with a volume fraction of porosity of 0.3% and of 0.45% for intermetallic and the contrast appears as very light. As shown is figure 3.b., the material displays some hardening in a tensile test.

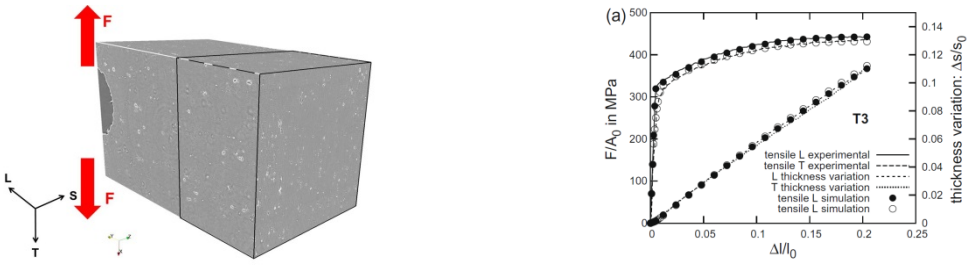

Figure 3: (a) Extracted volume of the reference volume with the Region Of Interest (ROI) used for DVC measurements in black. (b) Stress/strain curve of the studied 2139 T3 aluminum alloy (Morgeneyer *et al.* 2009)

2.3. Digital volume correlation

A global approach based on a regular 8-noded cubes (C8) mesh is used (with trilinear interpolation functions of the displacement field). The uncertainty measurements are performed on two different scans in the undeformed configuration when a rigid body motion

is applied between the two acquisitions. This allows the presence of artifacts (e.g., rings) to be accounted for since they do not move along with the microstructure. Figure 4 show the change of the standard displacement and equivalent strain resolutions of the element size.

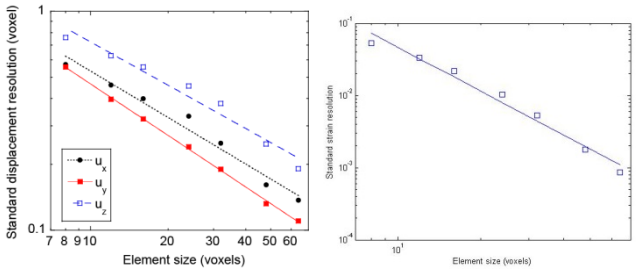

Figure 4: a) displacement and b) equivalent strain uncertainty for different elements size (Morgeneyer *et al.* 2013)

In the sequel, 32-voxel elements will be used in C8-DVC, which corresponds to a standard resolution level of 0.5% for the equivalent strain.

3. Results

A total of 26 scans was acquired to follow the test and are denoted from A to Z. Two were devoted to the uncertainty assessment and 22 are analyzed to measure the kinematic fields for the chosen ROI. The change of the crack length with the notch opening displacement during the test is shown in figure 5 by analyzing the reconstructed volumes.

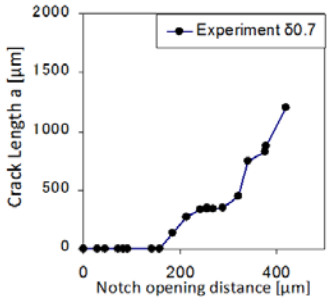

Figure 5: Crack length along with the notch opening distance.

The size of the studied region of interest is 864 x 608 x 992 voxels, which leads to the determination of about 54,000 degrees of freedom for each DVC analysis. Because of the complexity of the kinematic fields and the poor texture, direct registrations were difficult to perform. Therefore every volume has been registered with the next one, and then the cumulative displacement field has been used to initialize direct measurements. Due to the presence of damage at step V (Fig. 6), a smaller ROI had to be used (i.e., 832 x 608 x 832 voxels) for the V-W analysis. A shift in the ROI position had to be applied because of crack propagation. This shift is equal to 271 voxels in the crack propagation direction for scans R-S and S-T, and 471 voxels for scans T-U, U-V and V-W. Figure 6 shows the microstructure along the main steps, and the shifted ROIs are shown clipped in order to see the same face at every step. The same visualization is used in figure 7.

As observed in figure 6, damage nucleates only for the very late stages (*i.e.* scan W). Scan X shows the final crack pattern. Figure 7 shows the equivalent strain fields measured for the ROIs shown in figure 6. Several localized bands are present at the very early stages of loading and only one will finally lead to failure. These strain levels are at least one order of

magnitude higher than the standard strain resolution. Consequently, the present results are deemed trustworthy, and it can be stated that strain localization occurs well before any nucleation of damage.

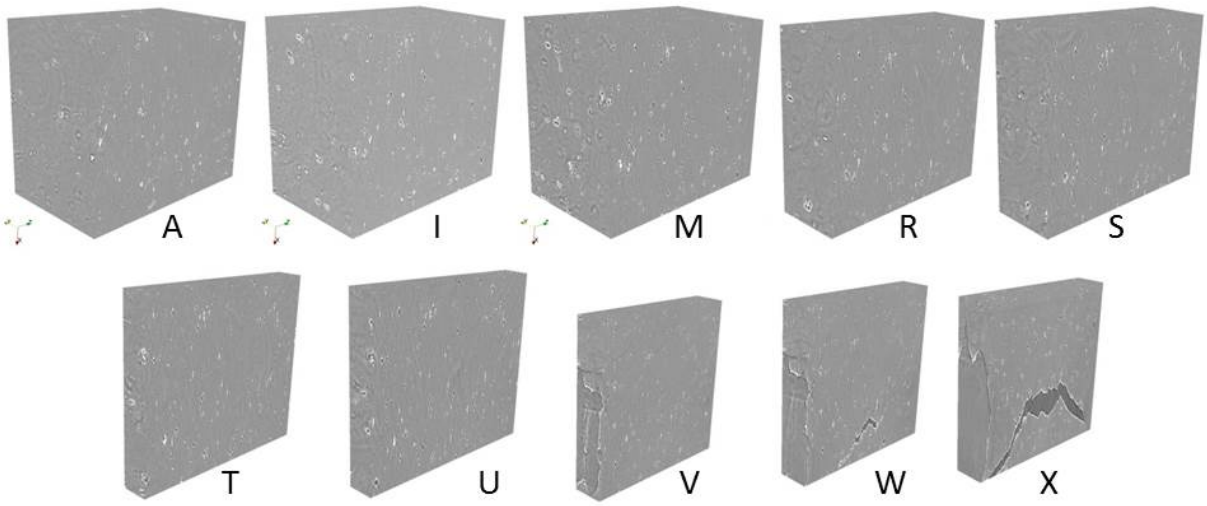

Figure 6 : Full ROIs of scans A, I, M, R shifted by 271 voxels and extracted, S, T shifted by 471 voxels and extracted, U, V, W, and X

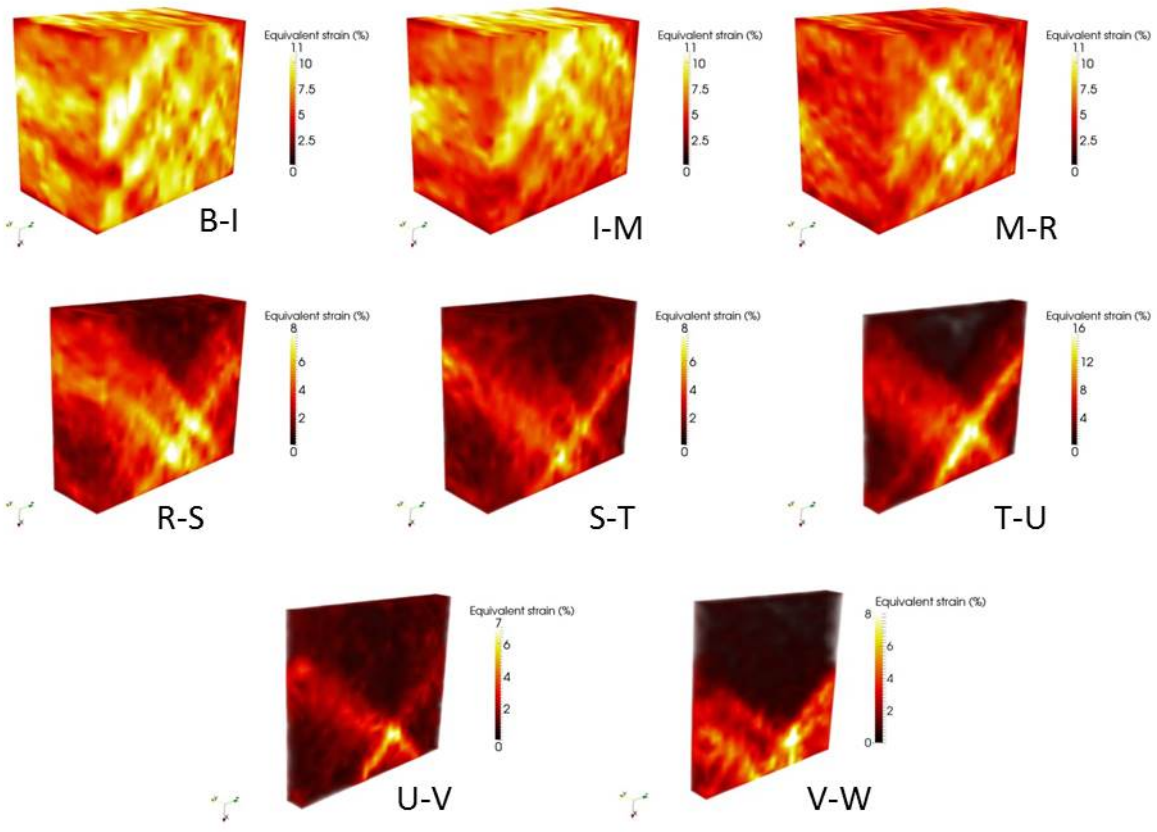

Figure 7: Equivalent strain fields measured between scans B-I, I-M, M-R, R-S, S-T, T-U, U-V, and V-W

Conclusions

The combination of laminography and digital volume correlation has enabled for kinematic measurements of complex phenomena (i.e., ductile fracture of thin aluminum sheets). Despite the artifacts and the poor texture localized strain bands were captured. It is shown that strain localization occurs well before any damage in the flat to slant failure process of 2139-T3 alloy.

Acknowledgements

The financial support of Fédération Francilienne de Mécanique and Agence Nationale de la Recherche (ANR-14-CE07-0034-02 grant for COMINSIDE project) is gratefully acknowledged. Constellium CRV supplied the material. We acknowledge the European Synchrotron Radiation Facility for provision of beamtime at beamline ID19 (experiment MA1006).

References

Morgeneyer, T. F., Helfen, L., Mubarak, H., Hild, F. (2013) 3D Digital Volume Correlation of Synchrotron Radiation Laminography images of ductile crack initiation: An initial feasibility study. **Exp. Mech**, 53(4):543–556

Taillandier-Thomas T., Roux S., Morgeneyer T.F., Hild F. (2014) Localized strain field measurement on laminography data with mechanical regularization. **Nucl. Inst. Meth. Phys. Res B** 324:70–79

Roux, S., Hild, F., Viot, P. & Bernard, D. (2008) Three dimensional image correlation from X-Ray computed tomography of solid foam. ***Comp. Part A*** 39:1253-1265.

Morgeneyer T.F., Besson J., Proudhon H., Starink M.J., Sinclair I. (2009) Experimental and numerical analysis of toughness anisotropy in AA2139 Al-alloy sheet, **Acta. Mat.** 57: 3902-3915

3D-THz imaging vs X-Ray tomography: Applications to material inspection

H. Balacey[1], *B. Recur[2], J. Bou Sleiman[3], J.-B. Perraud[3] and P. Mounaix[3]

[1] Noctylio SAS, 59 cours de l'Intendance, 33000 Bordeaux, France

[2] Australian National University, Dept Applied Maths, RSPE, Canberra, Australia

[3] IMS, Bordeaux University, UMR CNRS 5218, 351 cours de la Libération, 33405 Talence, France

* presenting author

INTRODUCTION

TeraHertz (THz) time-domain spectroscopy (THz-TDS) [1, 2] and THz tomography (THz-CT) [3, 4] are two recent imaging techniques allowing contact-free and non-destructive inspection of soft materials, such as paper, wood, plastics or ceramic. In one hand, THz-TDS imaging is performed using a pulsed laser coupled with a time delay line, providing reflection or transmission images in a range of $0.1 - 4$ THz, with a frequential resolution of about few GHz. Thanks to a good penetration depth in light or insulating materials, low scattering, free-space propagation, low photon energy and broad spectral bandwidth, a single THz-TDS projection allows one to visualise object interfaces in depth, but also to map its chemical composition using chemometric methods [5]. for instance, THz-TDS has been applied in the fields of sigillography science and drug detection [5,6]. However, despite it is sometime referred as 3D imaging, such a system only provides a 2.5D images in the sense that the depth-scale is not uniform along the overall acquisition and depends, at each point, on the traversed materials and interfaces. On the other hand, THz-CT is based on monochromatic waves (usually 0.1 or 0.3THz, provided by a Gunn diode or other sources). A raster-scanning is performed to acquire a set of 2D projections, corresponding to the transmitted signal amplitude at different viewing angles around the object. Then a dedicated tomographic reconstruction algorithm is processed to obtain a tomogram of the acquired specimen, allowing 3D visualisation and internal analysis [3, 7], similarly than the very well known X-ray tomography.

In this paper, we first introduce continuous wave (CW) THz tomography system and methods for achieving 3D inner inspection of samples. Then we detail THz-TDS systems and methods, which are quite different from the previous one. Then, by combining both system capabilities, we discuss current investigation and expectation on further works in order to achieve 3D hyper-spectral imaging using THz waves.

3D THZ CW IMAGING

Continuous wave 3D tomographic THz acquisition system is composed of two Gunn diodes coupled with a horn antenna each. The first one delivers $\nu_1 = 0.084$ THz. The second one, coupled with a frequency tripler, delivers an output power of $12mW$ at $\nu_2 = 0.287$ THz (cf. Fig. 1(a)). Each THz beam is collimated and focused by a pair of PTFE lenses ($f = 50$ mm focal length and $D = 50.8$ mm). Detection is performed by a Schottky diode and the beam is modulated at 1 kHz by a mechanical chopper. The transmitted THz signal amplitude is acquired with a lock-in amplifier. Sample is positioned on a three-axes motorized stage comprising the X,Y and θ movements, respectively. A 2D transmission radiograph is obtained by moving the object along the X and Y axis (with an usual scan step between 0.5 and 1mm in both directions, the acquisition time is about 15 minutes for a 200^2 pixel projection). Thus this setup measures ν_1 and ν_2 projections at once (cf. Fig. 1(b-c)). Then the sample is rotated to provide different radiographs distributed between 0° and 180°.

In order to reconstruct tomograms from projections, we use the iterative reconstruction denoted THz ordered-subsets convex (THz-OSC) algorithm [8,3]. It consists of iterating in t and subsets $s+1$ in order to update each voxel j of the volume f imaging the acquired object until convergence of the solution. The volume obtained at sub-iteration s is used as estimated volume for the subsequent sub-iteration $s+1$. The algorithm updates each voxel as follows:

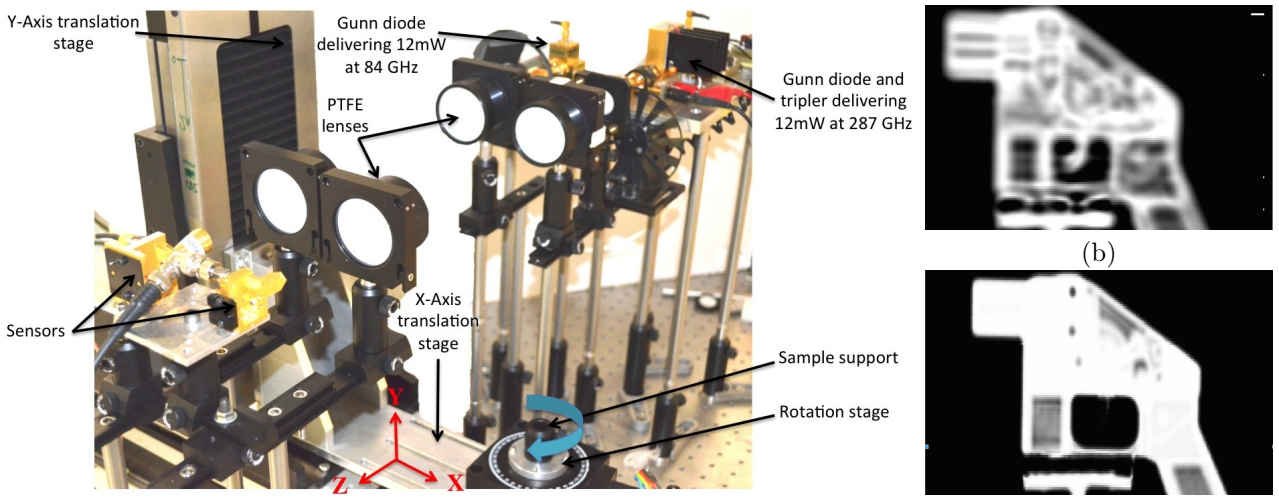

Figure 1: (a) Experimental setup: a pair of PTFE lenses collimates and focuses each THz beam delivered by a Gunn diode and a tripler (power 12 mW at 0.084 THz and 0.287 THz). Acquired sample is positioned on a three-axes motorized stage comprising the X,Y and θ movements. (b) One projection of acquired sample (plastic gun) at 84GHz, and (c), at 287GHz.

$$\mu_{s+1}^t(j) = \mu_s^t(j) + \Delta\mu_s^t(j) \quad \text{where:} \quad \Delta\mu_s^t = \frac{\sum_{i\in S(s)} w_{ij}\left(\hat{R}_s^t(i) - R(i)\right) - \beta \sum_{k\in\mathcal{N}(j)} y_{jk}\Phi'(\mu_s^t(j) - \mu_s^t(k))}{\sum_{i\in S(s)} w_{ij}\left[\sum_k w_{ik}\right]\hat{R}_s^t(i) + \beta \sum_{k\in\mathcal{N}(j)} y_{jk}\Phi''(\mu_s^t(j) - \mu_s^t(k))} \tag{1}$$

where $\hat{R}_s^t(i)$ is the expected intensity computed from μ_s^t, $S(s)$ are the radiographs in the subset s, β is a sensitivity parameter for the penalization part, $\Phi'(\cdot)$ and $\Phi''(\cdot)$ are respectively the first and second derivative of the penalization potential function $\Phi(\cdot)$, $\mathcal{N}(j)$ denotes the neighbourhood of pixel j and y_{jk} is a weight factor (usually inverse proportional to the distance between voxels j and k). $\hat{R}_s^t$ is modelled by:

$$\hat{R}_s^t(i) = I_0(i)\mathrm{e}^{-\sum_j w_{ij}\mu_s^t(j)\star G(j)} + bg(i) \tag{2}$$

where I_0 (blank calibration scan: intensity measured by detector when it is lightened by the source without sample) and bg (background noise: intensity measured by the detector without source) are determined experimentally, w_{ij} is a weight coefficient defining the voxel j contribution on the detector i and $G(\cdot)$ is the THz Gaussian beam propagation model as defined in [7] (where $\star$ denotes the convolution operator). A main iteration t is completed when all subsets have been processed. Reconstruction provides a volume of the local attenuation $\mu_\nu(x)$ which depends on the beam frequency ν. As illustration, Fig. 2 shows the reconstructed volumes of the plastin gun at 0.084 THz and 0.287 THz (voxel size: 1mm^3).

2.5D THZ TIME DOMAIN SPECTROSCOPY

THz-TDS system (cf. Fig. 3) enables the determination of the complex permitticity of a sample over a frequency range usually between 0.1 and 4 THz. A sapphire laser generates a femto-second pulse splitted into a pump pulse and a gating pulse. Pump pulse goes to an emitter producing THz waves by: i) photoconductivity in an ultrafast semiconductor, or, ii) optical rectification in crystals presenting high electro-optic coefficients. Then the emitted wave is oriented to the sample by parabolic mirror. Signal transmitted through the sample is collimated to a detector. At the same time, the gating pulse goes through an optical delay so that the amount of signal measured on the detector at a given time depends on the length of the optical delay. Thus by moving the latter, one can sample the electric field according to the THz time of transmission into the sample.

Acquired intensity signal (cf. Fig. 4(a)) can be transformed in frequency domain (cf. Fig. 4(b)) to get the absorbance according to frequency, revealing specific absorption spectra. Thus THz-TDS can be used to

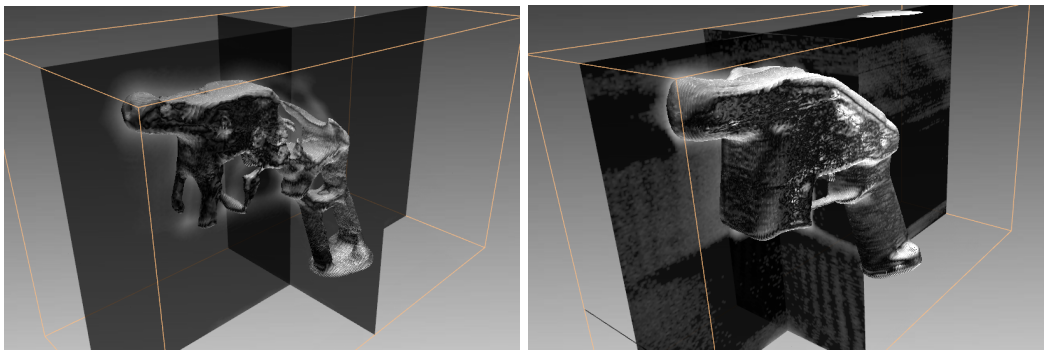

(a) (b)

Figure 2: 3D visualisation the volumes obtained from acquisitions at 84GHz (a) and 287GHz (b).

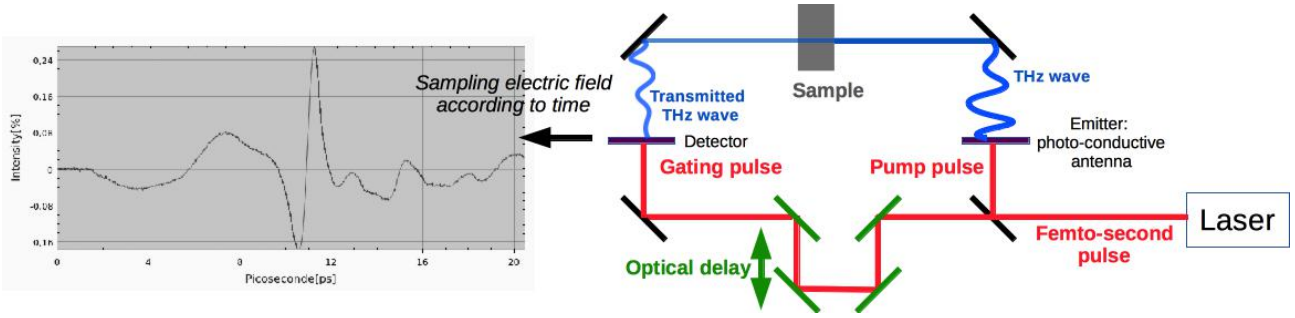

Figure 3: Typical THz-TDS acquisition setup.

detect or identify different substances (drugs, explosives, powder, gas...) since they have specific footprints in their absorption spectrum, making each of them distinguishable from the others (cf. Fig. 4(c)). As illustration, qualitative and quantitative analysis of explosives using THz-TDS combined with different chemometric methods has been studied in [5].

As for CW-THz tomography, THz-TDS can also be used as a spectro-imager using motor stages to move the object in the THz beam. The main difference is that for each XY position of the raster scan, we no longer obtain one value of the transmitted signal power, but all the intensities according to the time of flight (or, equivalently, all the absorption spectrum between 0.1 - 4 THz). Due to the raster scanning such a 2D+t acquisition time is about several hours for a 200^2 spectra projection. Conversely, it results that extraction of relevant images is almost unlimited and addresses a large field of applications. As an illustration, Fig. 5(a-c) represent 3 time-signal images of a micro-circuit at time 11.27, 15.26 and 17.84 ps,. Thus it is possible to reconstruct a 2.5D image from time-signal since it contains details about interfaces in depth. This processing has the advantage to not need a THz-TDS tomographic acquisition (which is unrealistic in term of acquisition time). However, this volumic data can not be exactly considered as a 3D data since the spatial resolution in the third dimension is not uniform. Similarly, Fig. 5(d-f) represent several absorption images according to THz frequencies, revealing different absorbance materials into the object.

TOWARDS 3D HYPER-SPECTRAL THZ IMAGING

The 3D reconstruction from CW-THz acquisition provides the 3D local attenuation $\mu_\nu(x)$ according to beam frequency ν. In the THz range this attenuation is mainly proportional to the extinction coefficient $\mathcal{K}$ (neglecting optical effects): $\mathcal{K}_\nu(x) = \frac{c}{4\pi\nu}\mu_\nu(x)$. $\mathcal{K}_m(\nu)$ for all $\nu \in [0.1 \cdots 4$ THz$]$ of an elementary chemical m can be measured using THz-TDS system. TDS measurements allow one to create a dictionary of material absorption spectra. Such a dictionary can be used to estimate chemical composition of each voxel of a 3D volume obtained by dual CW-THz acquisitions, leading to a 3D material labelling, in a similar fashion than well-known dual-energy X-ray acquisitions for material characterization [9–11]. For instance, average values of $\mathcal{K}$ plastic-gun ROIs (corresponding to the object only) have been computed at each frequency (cf. Table in Fig. 6). One can

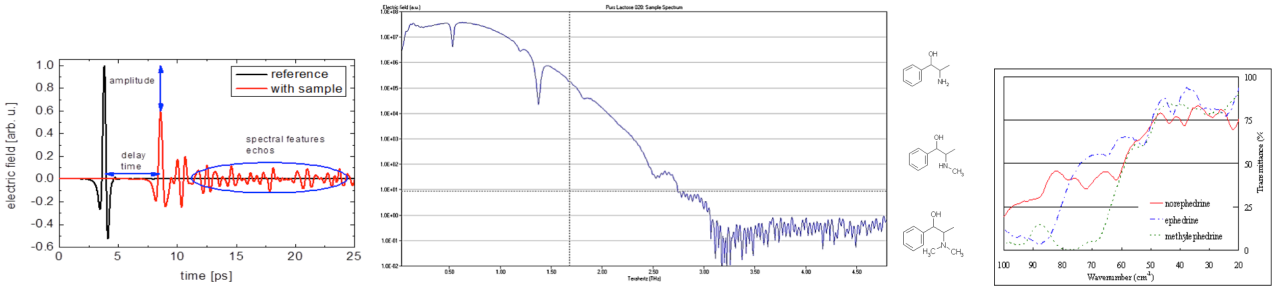

(a) (b) (c)

Figure 4: (a) Typical time-signal acquired by THz-TDS (electric-field according to time of flight of the waves in the environment/sample) and comparison between reference and transmitted signal. (b) Time-signal is transformed into frequency in order to get the absorption spectra in a range typically between 0.1 a 4 THz. (c) Absorption spectrum of methamphetamine elements (represented by transmittance according to wavenumber).

remark that $\mathcal{K}_{287\text{GHz}} = 24.23$ is very close to the value provided by THz-TDS acquisition of a piece of resin ($\mathcal{K}_{TDS} = 24.06$). $\mathcal{K}_{84\text{GHz}} = 16.57$ is less accurate since $\mathcal{K}_{TDS} = 18.42$. However this latter value corresponds to the extinction coefficient at 100 GHz since our TDS setup does not provide values below this frequency.

Even if the reconstructed average values seem close to the TDS measurements, we notice limitations mainly due to optical effects neglected in the forward processing of THz-OSC reconstruction. Another approach could be investigated to overcome this problem by considering all frequency images given by THz-TDS (such as images on Fig. 5(d-f)) as tomographic projections. Reconstruction of an hyper-volume (i.e. a volume where each voxel contains the complete spectrum in the THz range) could lead to 3D THz hyper-spectral imaging, with relevant applications in non-destructive testing, material characterisation, 3D chemical analysis, ... However, as already mentioned in the previous section, this processing is unrealistic at the moment, at least because of the acquisition time (several hours for only one THz-TDS projection).

CONCLUSION

In this paper we introduced: i) 3D CW-THz tomographic system enabling 3D acquisitions/reconstructions at two different energies and, ii) concept of THz-TDS, providing 2D+t data. The latter provides large amount of data, such as: i) different time of flights leading to a relative depth information (2.5D imaging), or, ii) all the absorption spectra between 0.1 and 4 THz. THz-TDS acquisitions can be combined to 3D CW-THz system, helping material labelling in the field of material characterization, for instance. Despite a lack of hardware at the moment, the interactions of both systems and their respective acquired data are paving the route towards 3D hyper-spectral THz tomography.

References

[1] Josette El Haddad, Bruno Bousquet, Lionel Canioni, and Patrick Mounaix. Review in terahertz spectral analysis. *TrAC Trends in Analytical Chemistry*, 44:98–105, 2013.

[2] S Wang and XC Zhang. Pulsed terahertz tomography. *Journal of Physics D: Applied Physics*, 37(4):R1, 2004.

[3] Benoît Recur, Hugo Balacey, J Bou Sleiman, Jean-Baptiste Perraud, J-P Guillet, Andrew Kingston, and Patrick Mounaix. Ordered subsets convex algorithm for 3d terahertz transmission tomography. *Optics express*, 22(19):23299–23309, 2014.

[4] S Wang, B Ferguson, Derek Abbott, and X-C Zhang. T-ray imaging and tomography. *Journal of Biological Physics*, 29(2-3):247–256, 2003.

[5] J Bou Sleiman, J El Haddad, JB Perraud, L Bassel, B Bousquet, N Palka, and P Mounaix. Qualitative and quantitative analysis of explosives by terahertz time-domain spectroscopy: application to imaging. In *Infrared, Millimeter, and Terahertz waves (IRMMW-THz), 2014 39th International Conference on*, pages 1–2. IEEE, 2014.

[6] Kodo Kawase, Yuichi Ogawa, Yuuki Watanabe, and Hiroyuki Inoue. Non-destructive terahertz imaging of illicit drugs using spectral fingerprints. *Optics express*, 11(20):2549–2554, 2003.

[7] Benoît Recur, Jean-Paul Guillet, Inka Manek-Hönninger, Jean-Christophe Delagnes, William Benharbone, Pascal Desbarats, Jean-Philippe Domenger, Lionel Canioni, Patrick Mounaix, et al. Propagation beam consideration for 3D THz computed tomography. *Optics Express*, 20(5):5817–5829, 2012.

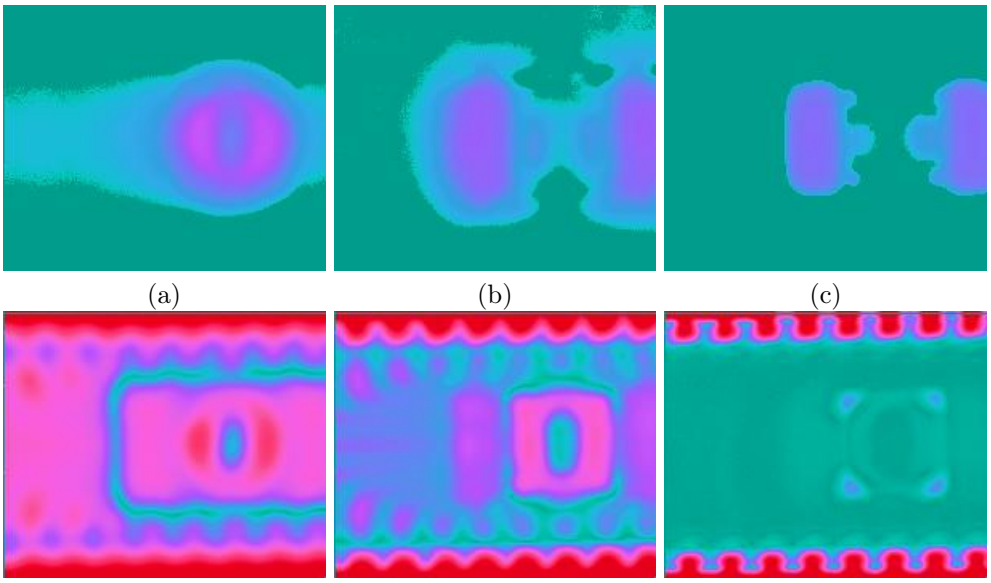

(a) (b) (c)

(d) (e) (f)

Figure 5: Time-signal images of a circuit (extracted from THz-TDS acquisition) at time (a) 11.27, (b) 15.26, and (c), 17.84 ps. Frequency module images of a circuit (corresponding to the absorption according to the wave energies) at frequency (d) 0.30, (e) 0.48, and (f), 1 THz.

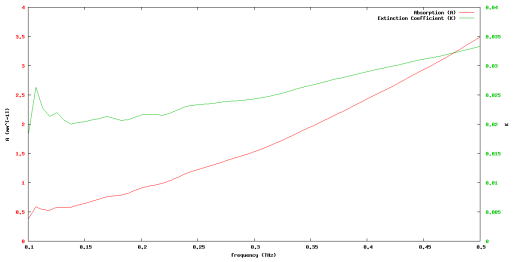

(a)

Values ($\times 10^{-3}$)	84 GHz	287 GHz
$\mathcal{K}_{TDS}$	18.42	24.06
$\mathcal{K}_{\nu_i}$	16.57	24.23
$\sigma\left(\mathcal{K}_{\nu_i}\right)$	5.16	5.93
MSE (single energy)	30.07	35.17
MSE (cumulated)	32.63	

(b)

Figure 6: (a) Absorption and extinction coefficient of the chemical (resin) composing the plastic-gun sample, according to the THz frequency (between 0.1 and 0.5 THz). (b) Theoretical extinction coefficients obtained by TDS measurements compared to the coefficients computed from reconstructed volumes of the plastic-gun.

[8] Hakan Erdogan and Jeffrey A Fessler. Ordered subsets algorithms for transmission tomography. *Physics in medicine and biology*, 44(11):2835, 1999.

[9] BJ Heismann, J Leppert, and K Stierstorfer. Density and atomic number measurements with spectral x-ray attenuation method. *Journal of applied physics*, 94(3):2073–2079, 2003.

[10] B Recur, M Paziresh, G Myers, A Kingston, S Latham, and A Sheppard. Dual-energy iterative reconstruction for material characterisation. In *SPIE Optical Engineering+ Applications*, pages 921213–921213. International Society for Optics and Photonics, 2014.

[11] Shameem Siddiqui and Aon A Khamees. Dual-energy ct-scanning applications in rock characterization. In *SPE Annual Technical Conference and Exhibition (Society of Petroleum Engineers, 2004), paper*, 2004.

Scanning-SAXS Tensor Tomography: Accessing the Orientation of Nanostructures in 3D

*M. LIEBI[1], M. GEORGIADIS[2], A. MENZEL[1], O. BUNK[1], M. GUIZAR-SICAIROS[1]

[1] Swiss Light Source, Paul Scherrer Institut, 5232 Villigen, Switzerland
[2] Insitute for Biomechanics, ETH Zurich, Wolfgang-Pauli-Str. 14 8093 Zurich, Switzerland
* presenting author

We have developed a new method combining scanning small-angle X-ray scattering (SAXS) with computed tomography (CT) to access with 3D spatial resolution the three-dimensional ultrastructural orientation.

For 2D scanning SAXS the sample is moved continuously through a focused X-ray beam while a pixel X-ray detector measures the scattering signal. Analysis of these patterns provides information about structures in the size range of nanometers to a few hundreds of nanometers along with their 2D scattering orientation [1]. Using a micrometer-sized beam allows us to gather nanoscale information over areas extending many square millimetres.

While scanning SAXS can be combined with CT using filtered backprojection [2], this method provides 3D resolved information describing either the sample's isotropic ultrastructure or its preferential orientation along the axis of rotation only [3]. However, essentially all biological tissues and most specimens investigated in materials science violate this stringent condition. Accessing the three-dimensional orientation of nanostructure is necessary for adequate interpretation of ultrastructure anisotropy, such as the degree of orientation, but is possible thus far only in 2D sectioned samples [4,5].

Compared to, e.g., absorption-based tomography, for which a single rotation axis is sufficient, scanning-SAXS projections are acquired at multiple tilt angles of the tomographic rotation axis with respect to the X-ray beam in order to reconstruct several parameters modeling the ultrastructure in each voxel and the scattering response as function of the sample orientation with respect to the X-ray beam. The reconstruction is carried out through an optimization algorithm, where for each voxel, and for an integrated q-range, the 3D X-ray scattering is modeled using spherical harmonics, which provide a continuous model in q-space where symmetries, such as uniaxial symmetry of, e.g., fibrils, can be explicitly enforced. These modeled intensities are then projected onto the plane of the detector and used to calculate the error metric with respect to the measured projections at different angular positions of the detector. The parameters of the model for each voxel are the spherical angles θ and ϕ, representing the main orientation direction of the ultrastructure and the coefficients a_0, a_1, and a_2 of the spherical harmonics, from which the degree of orientation can be obtained.

We demonstrate the technique using scattering from a model consisting of small carbon fibres, and we show results from bio-mineralized material from snail shells and characterization of collagen fibril orientation on human trabecular bone, where the anisotropic scattering of mineral crystals associated to collagen fibrils was analyzed. The information gained with this method is of interest in a broad range of applications in material science and bio-imaging as the arrangement and orientation of ultrastructure plays an important role for the mechanical properties of inhomogeneous and anisotropic materials.

References:

[1] Bunk, O., M. Bech, T. H. Jensen, R. Feidenhans'l, T. Binderup, A. Menzel and F. Pfeiffer (2009). "Multimodal x-ray scatter imaging." *New Journal of Physics* **11**.

[2] Jensen, T. H., M. Bech, O. Bunk, M. Thomsen, A. Menzel, A. Bouchet, G. Le Duc, R. Feidenhans'l and F. Pfeiffer (2011). "Brain tumor imaging using small-angle x-ray scattering tomography." *Physics in Medicine and Biology* **56**(6): 1717-1726.

[3] Schroer CG, Kuhlmann M, Roth SV, Gehrke R, Stribeck N, Almendarez-Camarillo A, Lengeler B (2006). "Mapping the local nanostructure inside a specimen by tomographic small-angle x-ray scattering. " *Appl Phys Lett* **88**.

[4] Seidel, R., A. Gourrier, M. Kerschnitzki, M. Burghammer, P. Fratzl, H. S. Gupta and W. Wagermaier (2012). "Synchrotron 3D SAXS analysis of bone nanostructure." *Bioinspired, Biomimetic and Nanobiomaterials,* **1**(2)

[5] Georgiadis, M., M. Guizar-Sicairos, A. Zwahlen, A.J. Trüssel, O. Bunk, R. Müller and P. Schneider (2015). "3D scanning SAXS: A novel method for the assessment of bone ultrastructure Orientation." *Bone* **71**

3D in situ characterisation of the impregnation of model fibre networks using real-time synchrotron X-ray microtomography

S. ROLLAND DU ROSCOAT[1,2,3*], P.J.J. DUMONT[4,5,6], P. CARION[1,2,4,5,6], L. ORGEAS[1,2], J.-F. BLOCH[4,5,6], C. GEINDREAU[1,2], M. TERRIEN[4,5,6], P. CHARRIER[1,2], P.J. LIOTIER[7], S. DRAPIER[7], M. PUCCI[7]

[1]Univ. Grenoble Alpes, 3SR, F-38000 Grenoble, France
[2]CNRS, 3SR, F-38000 Grenoble, France
[3]ESRF, ID 19 Topography and Microtomography Group, F-38043 Grenoble cedex, France
[4]Univ. Grenoble Alpes, LGP2, F-38000 Grenoble, France
[5]CNRS, LGP2, F-38000 Grenoble, France
[6]Agefpi, LGP2, F-38000 Grenoble, France
[7]Ecole des Mines de Saint-Etienne, F-42000 Saint-Etienne, France
* presenting author
sabine.rolland@3sr-grenoble.fr
pierre.dumont@pagora.grenoble-inp.fr
laurent.orgeas@3sr-grenoble.fr
jean-francis.bloch@pagora.grenoble-inp.fr
christian.geindreau@3sr-grenoble.fr

Keywords: real-time and in-situ fast-tomography, composite, impregnation

Abstract

The evolution of the microstructure of fibrous materials during impregnation is characterized quantitatively in 3D at the fiber scale. We imaged the propagation of the fluid front inside the materials using X-Ray synchrotron microtomography. The materials were made of parallel glass fibers, with different arrangements. Different fluids were used to study the influence of both the viscosity and the surface tension. The total force applied on the fibrous media induced by the capillary forces at the pore scale was simultaneously measured. The analysis of the obtained 3D images enables to compare the dynamic evolution of the fluid-air interface with theoretical values. Furthermore, phenomena such as the hysteresis of the advancing/receding contact may be studied.

Introduction

Impregnation is a crucial phase in several manufacturing processes such as polymeric composites that are reinforced by fibre bundles. Impregnation in heterogeneous materials may lead to the presence of residual pores within the polymer matrix or to non-impregnated dry zones within the fibre bundles. These phenomena are detrimental for the end-use properties of composites.

Most of the theoretical and experimental studies of the impregnation of composite materials are conducted at a mesoscopic scale, i.e., at the scale of an assembly of several fibre bundles or at a macroscopic scale, i.e., at the scale of a composite part (Park 2011). Therefore, these models do not enable a proper prediction of the impregnation of fibrous materials at the fibre scale, i.e., within the fibre bundles for example. Hence, these approaches are not sufficient to understand the presence of residual pores or inhomogeneous infiltration phenomena.

Numerical simulations are also carried out, mainly on 2D periodic materials (Bréard 2003). Thus, the objective of this study was to provide an enhanced description of the impregnation phenomena of porous media at the fibre scale. For that purpose, real time synchrotron X-ray microtomography was used. This technique was used for studying damage of magnesium alloy during high-temperature deformation in situ experiments (Lhuissier2013) or the forming of composite (Laurencin2015)

Methods

Model of fibrous materials

The study was conducted using model fibrous networks. Glass fibers were assembled to obtain different arrangements. The number and spatial organisations of fibres were varied. For example, 2D-ordered assemblies of parallel fibres or staggered rows of fibres were used (figure 1). The spacing between fibres was also varied.

Fibres had a 1.55 mm diameter. The fibre surface was also chemically treated (either raw, or corona effect treated and or silanized) to modify their surface properties, such as their wettability.

Two fluids were used: silicone oil and demineralised water. Their densities were 0.97 $g.cm^{-3}$ and 1.00 $g.cm^{-3}$, their dynamic viscosities were, 970 mPa.s and 1 mPa.s, and their surface tension 21.1 $mN.m^{-1}$ and 72.8 $mN.m^{-1}$, respectively.

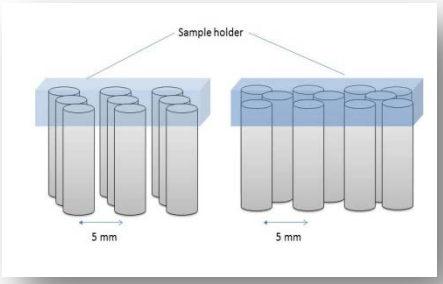

Figure 1 : scheme of the geometry of the studied samples

Experimental device

The designed device for impregnation experiments is presented schematically in Figure2. This device was equipped with a reservoir made up of PMMA, partially filled with the impregnating fluid. The fibre network was fixed above the reservoir. A 2-N force sensor enabled the measurement of the total force applied on the fibrous network developed by capillary forces at the fiber scale. The experiments consisted in immersing and removing at constant velocity model fibrous networks in the fluid.

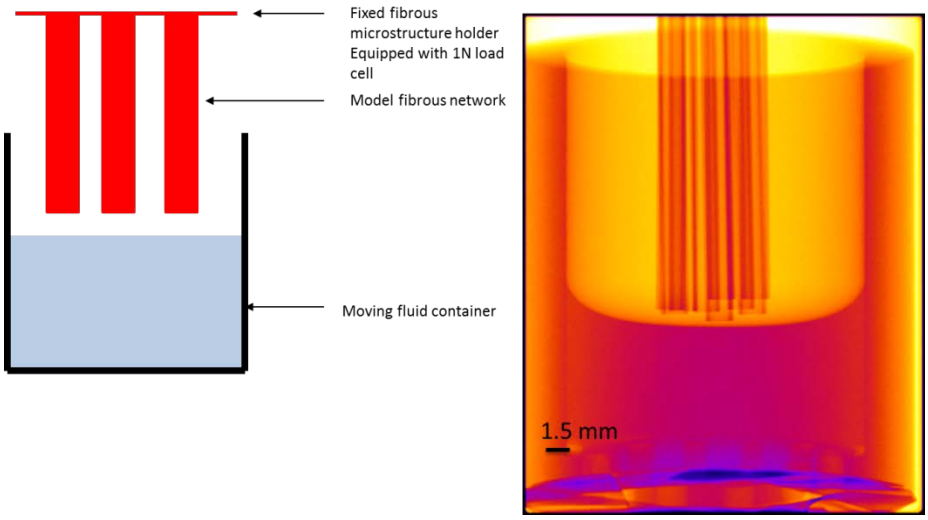

Figure 2. Scheme of the experimental device for in situ and real time impregnation experiments. (b) Radiograph of the reservoir of the device filled (with oil) and a network of parallel fibres.

Imaging conditions and image processing

The experiments were conducted using the ID19 beamline of the European Synchrotron Radiation Facility (ESRF). The beam was generated by an U17.6 undulator (Sanchez 2013) with a 15 mm gap. The intensity spectrum of the as-generated X-ray beam exhibited a maximum at energy of 18.7 keV. Once filtered with two aluminium filters with a 2.8-mm thickness, the intensity spectrum of the beam exhibited a narrow peak at 30 keV with a flux of approximately 10^{12} photons mm^{-2} s^{-1}. Its dimensions (8 mm×8 mm) were large enough to perform in situ and real time microtomography experiments. These experiments were performed using a PCO Dymax camera that enabled short exposure time (2 ms) for each projection (1584×1584 pixels). To obtain a correct description of the geometry of fibres and fluid-air interface, a pixel size of 5.1 µm was chosen. 800 projections were recorded for each scan to obtain a sufficient quality for image reconstruction. We recorded 10 scans consecutively. Each scan last approximately 1 s. The detector was set at a distance of 980 mm from the rotation axis. As absorption images could not be recorded, phase images were reconstructed using the Paganin approach (Paganin2002). The ratio of the phase decrement (δ**)** over the absorption coefficient (β) that was used to reconstruct the images was 400. The contrast obtained between the fibres, the fluid, the air, and the glass fibres using this ratio for silicone oil as shown in Figure 3.

The segmentation of the images was easily performed thanks to the good contrast of images. Microstructural descriptors, such as the volume fractions of the various images phases, were quantitatively obtained. For example, the evolution of the amount of entrapped air within the fibrous network was quantified. The geometry of the surface of the fluid-air interface was also extracted and its Gaussian curvature was estimated using specific image processing tools (Flin et al., 2001).

Concluding remarks

An experimental protocol is proposed to visualize and quantify the infiltration of a newtonian fluid by capillarity effects into a model fibrous structure using real-time and in-situ synchrotron X-ray microtomography. The obtained images will be used to validate numerical based on level set methods and to improve analytical models (Pacquaut2011).

References:

[Bréard *et al.* 2003] J. Bréard, A. Saouab, and G. Bouquet. Numerical simulation of void formation in LMC. *Composites/Part A: Applied Sci. and Manufacturing*, 34:517–523, 2003.

[Brzoska 2001] Brzoska, J.-B., F. Flin, B. Lesaffre, C. Coléou, P. Lamboley, J. F. Delesse, B. Le Saëc and G. Vignoles, 2001. Computation of the surface area of natural snow 3D images from X-ray tomography : two approaches, Image Anal. Stereol., 20, 306-312,

[Laurencin2015] Tanguy Laurencin, Laurent Orgéas, Pierre Dumont, Sabine Rolland du Roscoat, Steven Le Corre, Patrice Laure, Luisa Silva, Real time micro tomography dedicated to the *in situ* rheology of fibre-reinforced polymer composites during their forming process, Journées Nationales des Composites, Lyon, France, 2015

[Lhuissier2013] P. Lhuissier, M. Scheelb, , L. Salvoa, , M. Di Michielb, J.J. Blandina, Continuous characterization by X-ray microtomography of damage during high-temperature deformation of magnesium alloy, Scripta Materialia, Volume 69, Issue 1, July 2013, Pages 85–88

[Michaud & Mortensen, 2001] V. Michaud and A. Mortensen. Infiltration processing of fiber reinforced composites: governing phenomena. *Composites/Part A: Applied Sci. and Manufacturing*, 32:981–996, 2001.

[Pacquaut] G. Pacquaut, J. Bruchon, N. Moulin, et S. Drapier “Combining a level set method and a mixed stabilized P1/P1 formulation for coupling Stokes-Darcy flows”, International Journal for Numerical Methods in Fluids,

[Paganin2002] D Paganin, SC Mayo, TE Gureyev, PR Miller, SW Wilkins, Simultaneous phase and amplitude extraction from a single defocused image of a homogeneous object, Journal of microscopy 206 (1), 33-40

[Park 2011] CH Park, A Lebel, A Saouab, J Bréard, WI Lee, Modeling and simulation of voids and saturation in liquid composite molding processes, Composites Part A: Applied science and manufacturing 42 (6), 658-668

[Sanchez 2012] S Sanchez, PE Ahlberg, KM Trinajstic, A Mirone, P Tafforeau, Three-dimensional synchrotron virtual paleohistology: a new insight into the world of fossil bone microstructures, Microscopy and Microanalysis 18 (05), 1095-1105, 2012

[Washburn 1921] E.W. Washburn. "The Dynamics of Capillary Flow" *Physical Review*, 17(3):273–283, 1921.

Combining Nano X-ray Tomography and Nano X-ray Fluorescence to Create Time-dependent Three Dimensional Constitutive Maps

M. T. Ley*[1], Q. Hu[1], M. Aboustait[1],T. Kim[1], M. Moradian[1], J. C. Hanan[1], B. Stripe[2], V. Rose[2], R. Winarski[3], and J. Gelb[4]

[1] Oklahoma State University, 207 Engineering South, Stillwater, Oklahoma, USA – tyler.ley@okstate.edu, qinang@okstate.edu, mohammed.aboustait@okstate.edu, taehwan.kim@okstate.edu, masoud.moradian@okstate.edu, Jay.Hanan@okstate.edu

[2] Advanced Photon Source and Center for Nanoscale Materials, Argonne National Laboratory, 9700 South Cass Ave., Bldg. 437/A006, Argonne, IL 60439, USA - vrose@aps.anl.gov, bstripe@sigray.com

[3] Center for Nanoscale Materials, Argonne National Laboratory, 9700 South Cass Ave., Bldg. 440/138A, Argonne, IL 60439, USA - winarski@anl.gov

[4] Carl Zeiss X-ray Microscopy, 4385 Hopyard Rd., Ste. 100, Pleasonton, CA 94588, USA - jeff.gelb@zeiss.com

Keywords: nCT, nXRF, TACCo, data fusion, cement

Abstract

This work combines three dimensional (3D) structure and chemical mapping at the nano scale to elucidate important mechanisms of the reaction of tricalcium silicate particles in lime solution. Investigations are done before and after the reaction with a novel *in situ* reaction cell with both synchrotron and lab scale nano X-ray computed tomography (nCT) and nano X-ray fluorescence (nXRF). A novel data fusion technique is presented named nano Tomography Assisted Chemical Correlation or **nTACCo**. This technique uses the 3D structure information in combination with the nXRF data to build 3D constitutive models. These results create a powerful five dimensional data set that shows how the spatial resolution and chemistry evolve with time. The results provide useful insight into the mechanisms of cement hydration but the methods are applicable to a number of other materials.

Introduction

Progress has been halted in a number of research fields because direct investigation of three dimensional (3D) nanostructure and chemistry are very difficult to achieve. Knowledge of the mechanisms at these length scales has the potential to make game changing improvements in the sustainability, economy, and performance of these materials. This work uses a novel data fusion technique to combine nano X-ray computed tomography (nCT) and nano X-ray Fluorescence (nXRF). Although both techniques are powerful and able to make nano scale observations, each have their limitations. These challenges have been overcome by using a novel data fusion technique called nano Tomography Assisted Chemical Correlation or **nTACCo**. This work is the latest evolution of data fusion between 3D imaging and microanalysis measurements (Hu et al., 2014a and Hu et al. 2014b) and is the first application of this technique to make time resolved measurements using an *in situ* reaction cell. These results can be used for both data visualization and quantitative analysis that provides data not readily available with any other technique.

Concrete is the second most used commodity in the world. Despite being widely used for over 100 years, little is known about the fundamental mechanisms of the reaction between cement with water. This reaction creates the glue that holds aggregates together to make concrete. This process is called hydration. When water and cement are first mixed there is a sudden and violent dissolution of cement grains

over the first few seconds. Next, this reaction slows to a low rate and then suddenly increases again after about three to four hours (Mehta and Monteiro, 2014). Little is known about the details of these reactions and their mechanisms. This work focuses on how the particles change after 2.5 hours of hydration.

While this work is directly applicable to those that study cementitious systems, details are given to help guide others to use these methods to study their materials and make the same measurements. This work could be repeated for any material where combined 3D structure and chemical mapping is important. The work also highlights the power of X-ray imaging to make time resolved and quantitative measurements of volume and material changes in complex systems.

Methods

Materials

The materials investigated are a triclinic, tricalcium silicate or C_3S as it is written in cement chemistry short hand. This material is the primary component of portland cement and was produced in a laboratory kiln and then subsequently ground for these experiments.

Nano Computed Tomography

The Zeiss Xradia Ultra 810, from Carl Zeiss X-ray Microscopy, was used to collect the nCT data. The instrument uses an X-ray energy level of 5.4 Kev with the resolution of 50 nm/pixel with the wide field lens. The tomographic datasets consist of 901 radiographs taken every 0.2^o rotation through 180^o with an exposure time of 20 s per step. Total acquisition time was about 6 hours. The gray value in these scans correlates to the material's X-ray absorption, which is a combination of the chemical composition and the density. An overview of the results from a C_3S particle before and after 2.5 hours of reaction in 15 mmol/L lime solution is shown in Fig. 1.

The data sets have been aligned by using the boundary and volume of the needle. This alignment allows the exact same locations to be compared before and after the reaction. When differences in gray values are observed in the slices then, this means that the material could have a different density, chemistry, or both. These changes were used to separate or segment the data. The segmentation was done by subtracting the aligned data. Pixels where there was a significant change in gray value were identified as a "modified region". Although this technique is capable of providing detailed data sets about the structure of the sample, only limited insights can be provided about the chemistry. For example, we know that these modified regions are different than the original; however, we don't know if the chemistry, the density, or perhaps both have changed. nXRF is a good tool to gather this additional information.

Nano X-ray Fluorescence

A single sample was investigated with nXRF after completing nCT. Emitted characteristic X-ray fluorescence radiation is detected with a four-element silicon drift energy dispersive detector (Vortex ME4). All measurements were taken at the Center for Nanomaterials and Advanced Photon Source, a shared facility at Argonne National Laboratory. Additional details can be found in Hu et al. (2014b). Fitting and quantification of the fluorescence data was carried out with thin film standards (National Buereau of Standards, Standard Reference Material 1832 and 1833) as well as a piece of unreacted C_3S with a known geometry.

The nXRF technique uses an X-ray beam that penetrates through the material and causes X-ray fluorescence along its path. This means that the detected intensity is the integrated signal from all material along this path. The results are typically reported in

$\mu g/cm^2$ at each location for each element. This is the total element mass over the length of the investigated volume. This unit is used because there is no direct information about the depth from which the x-ray fluorescence is emitted. When investigating complex materials it is not possible to directly render depth-dependent information from a single nXRF analysis. Also, the fluorescence X-rays may be self-absorbed in the sample before they reach the detector. This can be overcome as the absorption artifacts are minimized if the signal travel length is minimized. For the ~ 3 micron diameter sample investigated the X-ray absorption is calculated to be less than 10% for both calcium and silicon and so a correction was not necessary.

Experimental Steps

The samples were first fixed on the top of a tungsten needle with epoxy. A polyethylene cup that fit tightly to the needle was used as a solution container. The cup could move up and down along the needle. Additional C_3S powder was attached on the side of the needle to increase the solids content so that the mass of the water to solids ratio was five.

The mounted sample was first investigated with a tomography scan without being obscured by the cup. Next the sample was placed in a nitrogen environment to prevent carbonation, and the cup was filled with 15 mmol/L lime solution and raised to start the reaction. This solution was used to simulate the high calcium and pH environment during cement hydration. More complex solutions have been investigated and will be published in the future. After 2.5 hours the solution was removed and replaced with 99% isopropyl alcohol for five minutes to stop hydration through solvent exchange. The sample was then removed from the nitrogen environment, the cup was then lowered, and another tomography scan was taken. The sample was then investigated with nXRF.

Data Fusion

As stated previously, both nCT and nXRF techniques have limitations. nCT cannot directly determine chemistry; however, it can determine the spatial distribution of the constituents based on their X-ray absorption. Subsequently, nXRF obtains average chemical information, but cannot determine the number, variation, and contribution or depth of each constituent at the sampling location. However, these challenges can be overcome by segmenting the nCT data and then aligning it with the nXRF. This method has been named nTACCo.

An overview of the nTACCo process is shown in Fig. 2. Location A and B is shown in both the nCT and nXRF data sets. At location A the beam is only interrogating anhydrous C_3S and the length of travel can be determined (L_A). The concentration density can then be calculated at point A (D_{C3S}).

This process is then repeated at location B. This location has two constituents present. However, since we know the length of each one based on the nCT data (L_{B1}, L_{B2}), then we can again calculate the concentration density of the modified region (D_{Mod}) by using the density and length of the anhydrous C_3S at that point. All equations that are used are given in Fig. 2. This process was completed for around 300 points and the average and one standard deviation are given in Fig. 2.

Results and Discussion

Detailed tomography results are shown in Fig. 1. Based on the gray values and the segmentation, it appears that all of these particles are made up of either non reacted C_3S, modified regions, or totally dissolved regions. The results show that the modified regions are randomly oriented in the particle and is not concentrated at the boundary of the particle or high surface areas. This localized region of dissolution may be caused by

regions of strained crystalline structure of the particle or damage caused by grinding (Bazzoni et al., 2014). Results from ten different particles is shown in Table 1. As can be seen from the table, on average about 33% of the material has been modified with a standard deviation of 23%. However, eight of the ten particles investigated show between 20% and 37% change in their volume with two of the particles showing very different performance. More work is ongoing to better understand why these two particles perform so differently than the others.

The nXRF data was then used to determine the chemistry of these regions. The chemistry of the anhydrous C_3S was found to be consistent with previous publications and ion conducted plasma measurements on samples from the same batch of materials. The modified region was found to have a Ca/Si of 1.66 which is very similar to what other researchers have measured for a hydration material called “inner product”. This data suggests that the “inner product” may be forming within the voids formed during the dissolution of the particle. Modeling work is ongoing to support these claims and will be discussed in future publications.

Conclusions

A novel data fusion technique between nCT and nXRF called nTACCo has been used to follow *in situ* reactions of the hydration process of tricalcium silicate, a major component of portland cement. The results show that a region of the paricle is modified over the first 2.5 hours. This region is a reaction product with a Ca/Si of 1.66. This modified region makes up on average 33% of the volume of these particles after 2.5 hours of hydration. These regions are not isolated to the particles surface and shows that regions of the particle preferentially dissolve over others. Additional work with other solutions and time periods is ongoing.

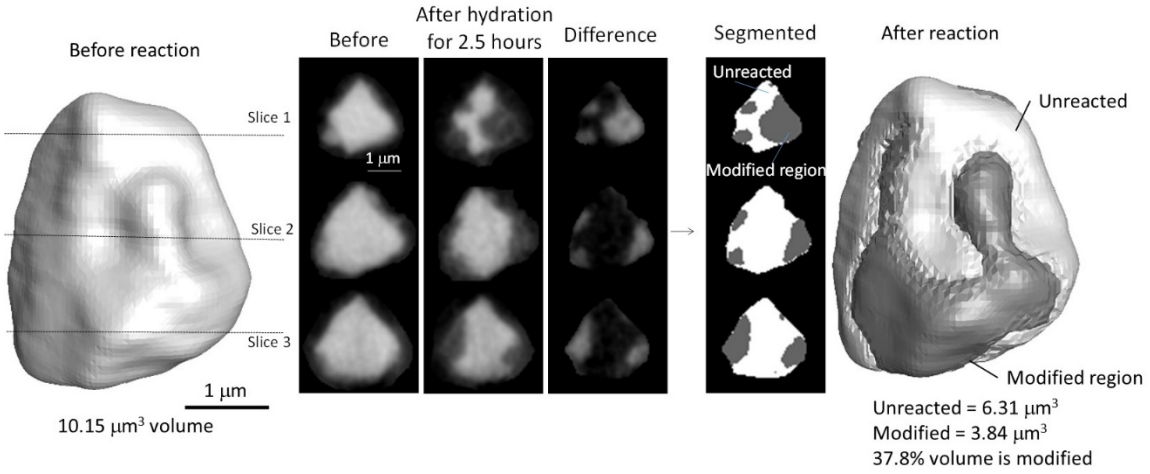

Fig. 1. *Overview of typical results from nCT. 3D data sets are shown both before and after hydration. Three different slices are also shown at these different time periods with the steps taken to complete the segmentation.*

Table 1. *Results from the nCT segmentation for ten C_3S particles.*

Original Volume (μm^3)	Unreacted (μm^3)	Changed Volume (μm^3)			Percentage of Volume That Changed
		Modified	Dissolved	Total Change	
6.27	0.75	5.51	~0	5.51	87.98%
7.83	5.68	2.16	~0	2.16	27.53%
10.16	6.31	3.84	~0	3.84	37.84%
12.63	8.65	3.98	~0	3.98	31.50%
22.95	17.37	5.58	~0	5.58	24.33%
42.01	38.23	3.33	0.44	3.77	8.98%
44.23	30.86	9.33	4.03	13.36	30.21%
50.20	39.75	10.44	~0	10.44	20.81%
				Avg=	33.65%
				Std dev	23.55%

Total Change = Modified + Dissolved

Percentage of Volume That Changed = Total Change/Original Volume

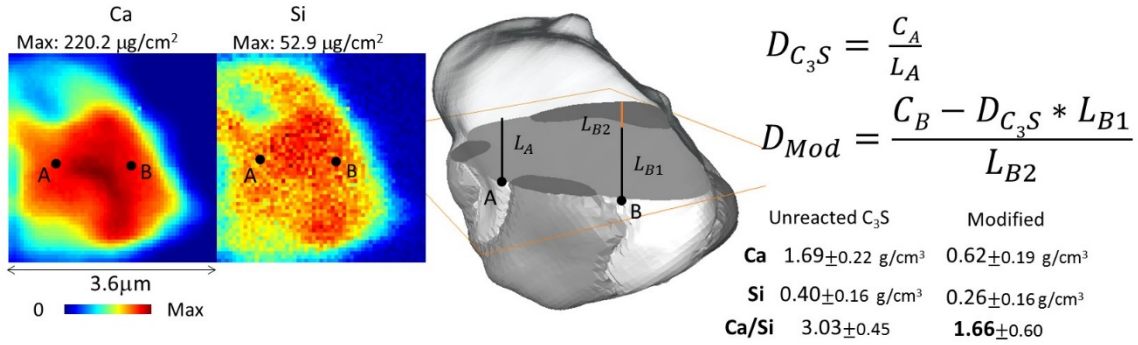

Fig. 2. *Overview of the nTACCO method. Results from the nXRF are shown on the left, next a segmented particle is shown with an exposed cross section after the reaction has occurred. Point A and B are shown in both the nXRF and the segmented nCT results showing the travel path of the X-rays. Equations used to calculate the density of each phase are shown. The travel length of the X-rays are shown by L_A, L_{B1}, and L_{B2} respectively. The concentration measurement from the nXRF analysis is shown by C_A and C_B. The chemical density of the different constituents is shown by D_{C3S} and D_{Mod}. The results from the analysis is also shown for calcium, silicon and the calcium to silicon ratio.*

References

Mehta P.K. & Monteiro P.J.M. (2014). **Concrete: Microstructure, Properties, and Materials**, McGraw-Hill, 4th ed.

Hu, Q., Ley, M.T., Davis, J., Hanan, J.C., Frazier, R., & Zhang, Y. (2014a). "3D Chemical Segmentation of Complex Particles with X-ray Computed Tomography and Electron Probe Microanalysis", **Fuel**, Vol. 116, pp. 229-236.

Hu, Q., Aboustait, M., Ley, M.T., Hanan, J.C., Rose, V., & Winarski, R. (2014b). "Combined Three-Dimensional Structure and Chemistry Imaging with Nanoscale Resolution", **Acta Materialia**, 77, pp. 173-182.

Bazzoni A., Cantoni M., & Scrivener K. (2014). Impact of annealing on the early hydration of tricalcium silicate. **J. Am. Ceram. Soc.**; 97:584.

Acknowledgements

This work was sponsored by funding from the United States Department of Transportation Exploratory Advanced Research, United States National Science Foundation CMMI 1150404 CAREER Award. The Use of the Center for Nanoscale Materials and the Advanced Photon Source were supported by the U. S. Department of Energy, Office of Science, Office of Basic Energy Sciences, under Contract No. DE-AC02-06CH11357.

A small step beyond resolution

Einat Zelinger[1], Delia Podea[2] and Vlad Brumfeld[3*]

[1] The Hebrew University of Jerusalem, Israel
[2] "Vasile Goldis" Western University of Arad, Romania
[3] The Weizmann Institute of Science, Israel
* presenting author

Keywords: X-ray tomography, skeletonization, correlative methods

From television sets to electron microscopy, all imaging devices and methods claim to surpass the resolution of previous methodologies. Micro CT is no different. We are showing in this work several tips and techniques to improve the resolution beyond accepted standards, while still using a commercial instrument (Zeiss Xradia Micro XCT-400).

1. Use of non-standard staining agents

Tannic acid was used to improve the efficacy of contrast agents (mainly barium sulfate) used in medical radiography. In vivo use of tannic acid was abandoned because of its hepatotoxicity (1). Tannic acid is a good agent for accurate visualization of the extracellular matrix in electron microscopy because it induces fixation of hyaluronic acid (2). We have used it to improve contrast in the images of Arabidopsis thaliana shoot apical meristem. Using 2% tannic acid solution together with iodine staining, we could observe details of the developing meristem with a resolution of about 1 m. We noticed that the meristem became larger and had a less round shape when different meristem development regulation genes were examined.

2. Improved images obtained by correctly setting the voltage and current of the source

Bacillus Subtilis is one of the biofilm producing bacteria (3). The formation of colonies of those bacteria is based on their ability to produce a highly organized network of wrinkles containing a tiny amount of calcium that later in time accumulates on the edges of the colony as calcite crystals. Setting the energy spectrum of the X-ray photons to be centered at about 8.6 KeV, we could image in our instrument the whole

bacterial colony at lower magnification and the individual wrinkles at higher magnification. We have used the high resolution images to design a method to estimate that a 3-days old bacterial colony produced about 0.56 mg of calcium. This value is similar with the result obtained by thermo- gravimetric analysis.

Using the same energy of X-ray photons, we were able to visualize at high resolution the eye of Cherax quadricarinatus, a fresh water crayfish. For the first time, a 3D image of this compound eye was obtained. It reveals the converging ommatidia that were not seen in X-ray before because they are made of organic crystals and do not contain minerals.

3. **Imaging nanostructures with micro resolution allows accurate mapping**

Reinforcing silica aerogels improves dramatically their mechanical properties (4). We have shown that tungsten disulfide nanotubes are a very efficient reinforcing material. In order to map the reinforcing particles, we imaged pieces of reinforced aerogels with different amounts of nanotubes. The shape of the particles could not be visualized at our resolution, but we were able to estimate the particle density in the sample and the average distance between the nanotubes.

4. **Correlative fluorescence and tomographic microscopy provide complete structural insight**

We have obtained high resolution 3D images of the mated and unmated female sperm storage organs of *Drosophila melanogaster*. For this we dissected out the female reproductive tract, fixed it with 4% PFA and mounted onto a piece of thin plastic sheet. The tissue was stained with 2% iodide and 2% tannic acid in ethanol. One can observe in the images minute structural details of the storage channels, but the 3D analysis is not complete without visualizing the sperm inside the channels. This could be made by using flies with GFP fluorescent sperm that were visualized under a confocal microscope prior to topographic analysis. By manually registering the tomographic image with the confocal one, one can visualize the position of the sperm in the storage organ.

5. Extensive post processing of images reveals unexpected information

We have shown (5) that the 3D architecture of the lamellae in the trabecular bone is similar to the spatial orientation of the trabeculae in the bone. In order to estimate the later one, we have conducted an X-Ray tomographic measurement (Figure 1). The cortical bone was segmented out and the trabecular one was skeletonized (Figure 2). The skeletonized image allowed us to estimate the orientation of the trabeculae in the bone. We have shown that the inter-trabecular angle was not random, but rather we had predominant distribution of this angle around the values of 109^0, 70^0 and 32^0, very close to an equilateral tetrahedron.

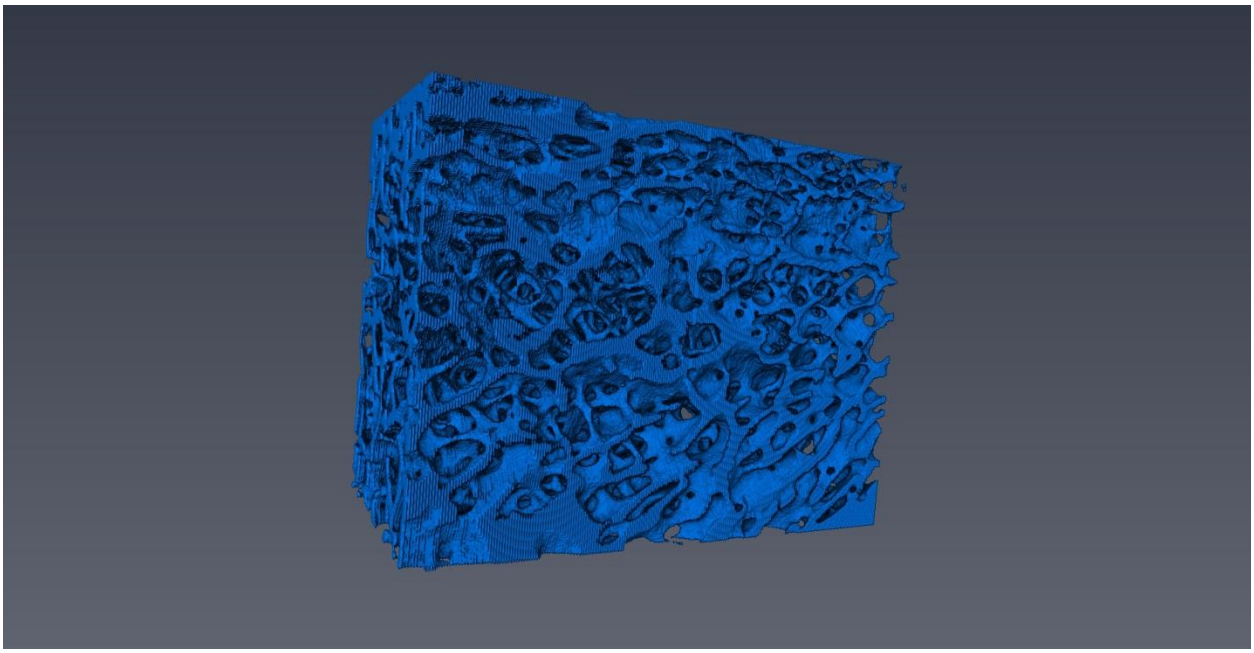

Figure 1. A selected VOI from the femur of a young female (voxel size 31 μm)

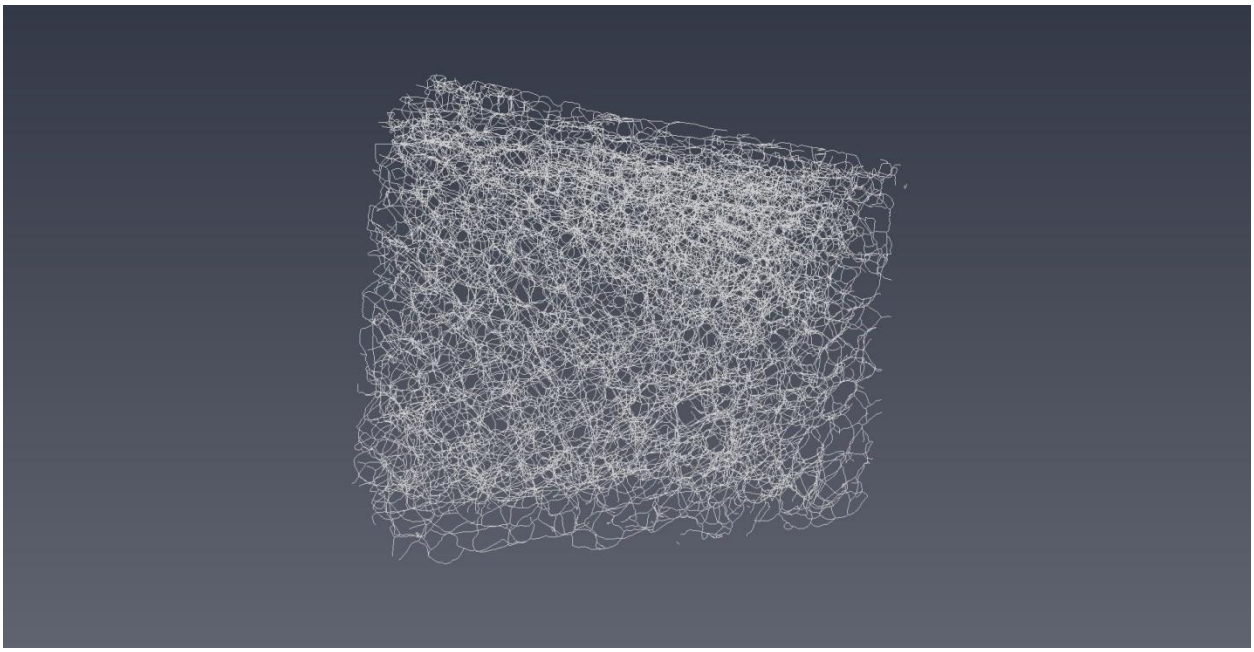

Figure 2. The same region as in Figure 1 after skeletonization

References

1. Hyman J. Zimmerman *Hepatotoxicity*, Lipincott, Williams and Wilkins, 1999, p. 734

2. **C.T.** Singley and **M.** Solursh The Use of Tannic Acid for the Ultrastructural Visualization of Hyaluronic Acid *Histochemistry 65, 93-102(1980)*

3. B.Mielich-Süss and D. Lopez Molecular mechanisms involved in *Bacillus subtilis* biofilm formation *Environmental Microbiology **17**, 555–565(2015)*

4. M.A.B. Meador, S.L. Vivod, L. Mccorkle, D. Quade, R.M. Sullivan, L.N. Ghson, N. Clark, L.A. Capaclona, Reinforcing polymer cross-linked aerogels with carbon nanofibers, *J. of Materials Chemistry* **18** 1843-1852 (2008).

5. Reznikov N, Chase H, Brumfeld V, Shahar R, Weiner S, 2015. The 3D structure of the collagen fibril network in human trabecular bone: Relation to trabecular organization

X-ray Tube Spectrum Determination for Quantitative Interpretation of Reconstructed Micro-CT Images

*O.A. KOVALEVA[1], -D.A. KOROBKOV[2], I.V. YAKIMCHUK[2]

[1] Moscow Institute of Physics and Technology, Dolgoprudny, Russian Federation
[2] Schlumberger Moscow Research, Russian Federation
* presenting author

Industrial application of X-ray CT (micro-, nano-) involves both data acquisition and the following data interpretation. Undoubtedly, the results of the latter stage strongly depend on the quality of experimental data. Nevertheless, correct interpretation of CT data is still rather independent and challenging field of research. For better understanding and subsequent analysis of the images, obtained by the means of computed tomography, it is essential to be aware of technical characteristics of the laboratory equipment, especially X-ray source properties.

One of such properties that dramatically influence on the interpretation of reconstructed images is X-ray source energy spectrum. As an example, spectrum neglecting or erroneous estimation may lead to mistakes in mineral analysis of the core plugs. This issue originates from the physics of X-ray interaction with studied sample. Experimentally observed attenuations on shadow projections are related to an ‘effective’ absorption of X-ray photons with various energies of the beam spectrum.

The direct measurement of X-ray tube spectrum is rather costly and not trivial procedure, especially for usual CT-scanner end users. Also, it should be taken into account that for the time of X-ray tube usage its spectrum may alter. For these reasons, a simple way for spectrum determination may be required. Tube spectrum reconstruction from transmission data is one of the suitable solutions for that.

The problem of X-ray spectrum reconstruction out of transmission (attenuation) values continues to be acute. We present and analyze several approaches suggested from the early days of X-rays, and propose alternative technique. Proposed idea is based on experiment with a specimen of known mineral (chemical) content and geometrical shape.

Laboratory X-ray Microscopy Using Geometric Magnification

P. STAHLHUT[1]*, A. HOELZING[2], J. ENGEL[3], R. HANKE[4]

[1] Chair of X-ray Microscopy, University Wuerzburg, Josef-Martin-Weg 63, 97074 Wuerzburg, Germany – Philipp.Stahlhut@physik.uni-wuerzburg.de
[2] Chair of X-ray Microscopy, University Wuerzburg, Josef-Martin-Weg 63, 97074 Wuerzburg, Germany – Astrid.Hoelzing@iis.fraunhofer.de
[3] Chair of X-ray Microscopy, University Wuerzburg, Josef-Martin-Weg 63, 97074 Wuerzburg, Germany – Jens.Engel@iis.fraunhofer.de
[4] Chair of X-ray Microscopy, University Wuerzburg, Josef-Martin-Weg 63, 97074 Wuerzburg, Germany – Randolf.Hanke@physik.uni-wuerzburg.de
* presenting author

Keywords: Laboratory Nano-CT, Geometric Magnification, Electrochemical Etching, Reflection Target

Abstract

We present a computed tomography (CT) setup for material characterization with significantly improved resolution as compared to state-of-the-art micro- or subµ-CT systems. The introduced system is composed of a customized JEOL-JSM7100F scanning electron microscope. By using the focused electron beam of the system with a 30 kV acceleration voltage, we create a very small X-ray source spot in a tungsten or molybdenum tip with a curvature radius of about 60 nm. We formed and optimized the shape of the metal tips by a quick and reliable electrochemical etchingprocess. Due to the ultra small X-ray sourcespot, a spatial resolution below 100 nm is approachable. The system is also capable of inline phase contrast imaging, which comes in handy especially for low contrast imaging. The system has been recently updated with the new Pixirad-2 photon counting detector with a CdTe sensorlayer and 1024x476 pixels, with the advanteous feature of increased efficiency as compared to the former Si-based Medipix detector.

Introduction

A technique to visualize small structures of a few hundred nanometers in 3D enables tayloring new materials and structures. A laboratory X-ray system resolving structures of established and new materials allows their visualization inhouse instead of performing measurements on a synchrotron source. Thus a fast and straight forward research and development process on new materials and structures is possible. Especially the visualisation of microporous technical alloys is a currently discussed issue and required feature.

The principle of geometric magnification M for a shadow microscope like the proposed system is defined by the focus-object distance z_1 and the object detector distance z_2 (Fig. 1a):

$$M = \frac{z_1 + z_2}{z_1}$$

Considering the constraints that the object-target distances (below 1 mm) are much smaller than the object-detector distances (above 40 cm) and by using a pixilated detector (55 µm pixelsize), the resolution is just defined by the X-ray sourcespot for geometric magnification.

The system is based on a modified JEOL-JSM7100F SEM (Fig. 1b) upgraded by a piezo-driven manipulator for both the X-ray reflection target and the object, which replaces the original sample stage, to provide high precision movement and stability.

The detector is placed outside of the vacuum chamber, therefore a 250 µm thick beryllium window was added to the system, to allow projections along a horizontal detector axis. The setup thus can be used for imaging magnifications up to 1000.

For detecting the X-rays, initially a Medipix2 photon counting detector with a 300 µm thick Si sensorlayer and 768x512 pixels was used but recently has been replaced by a Pixirad-2 photon counting detector with a 1 mm thick CdTe sensorlayer and 1024x476 pixels. Despite the low flux of the source, the CdTe sensorlayer is rather efficient and due to the case that no optical elements are required in the beampath, the photon saturation of the system is pretty reasonable.

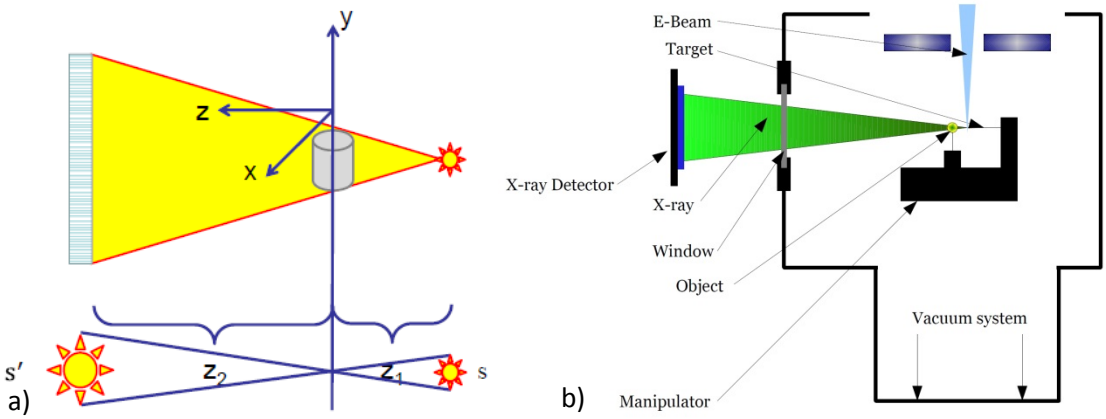

Fig. 1. *a) The principle of geometric magnification by using a pixilated detector. The resolution is influenced by the projection of the source s on the imaging plane s', as well as the effective pixel size. b) Schematic representation of the CT setup.*

Methods

The key to generate a small X-ray focal spot is – besides a highly focused electron beam – the reduction of the physical size of the electron interaction zone inside the target material, from which the X-rays are emitted. To produce anode needles with a tip diameter below 100 nm from wires made of tungsten or molybdenum, we use electrochemical etching. To etch 0,5 mm thick electrodes made of the mentioned materials we use a 2N sodium hydroxide electrolyte and apply a 10 Hz and 20 V_{pp} sinusodial AC voltage for a few hours.

With this low frequency AC voltage, the etching process is mainly controlled by the bubble growth and their movement along the electrodes, compared to the gradient of the electrochemical potential which would be far more important for etching with DC voltage. During the first half of the AC voltage cycle, the metal of the wire oxidates and dissolves and the bubble buoyancy transports the material upwards, where it gets partially reabsorbed during the second half of the cycle. This process results in a higher removal rate at the lower end of the electrode and consequently a tip is formed (Fig. 2).

The exact shape of the tip however is crucial for the overall stability of the system. These caracteristics can be tweaked over the frequency and the peak-to-peak voltage of the AC signal, as well as over the viscosity of the electrolyte which determines the size of the occuring bubbles. On this account we added a small amount of DECON®90 to the solution to tune the viscosity. The aim was to create a prefereably short but still sharp needle, to ensure electrical, mechanical and thermal stability.

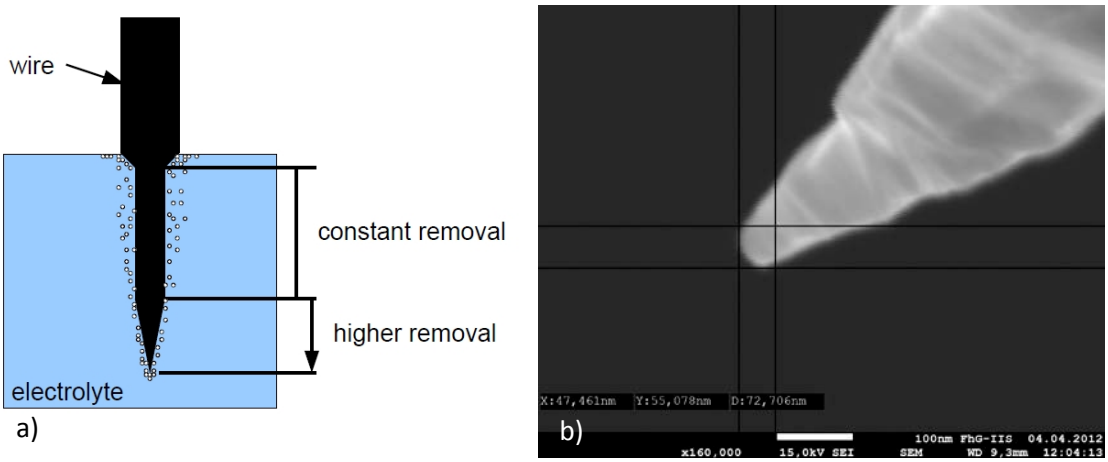

Fig. 2. *a) Preperation of a reflection target by electrochemical etching with AC voltage. The bubble stream drives the removed material upwards, where they can reconnect with the metalwire in the second half of the sinusodial AC signal, therefor a zone with higher material degradation occurs at the end of the wire. b) SEM image of a tungsten tip composed with the proposed method. The tip has a radius of 60nm.*

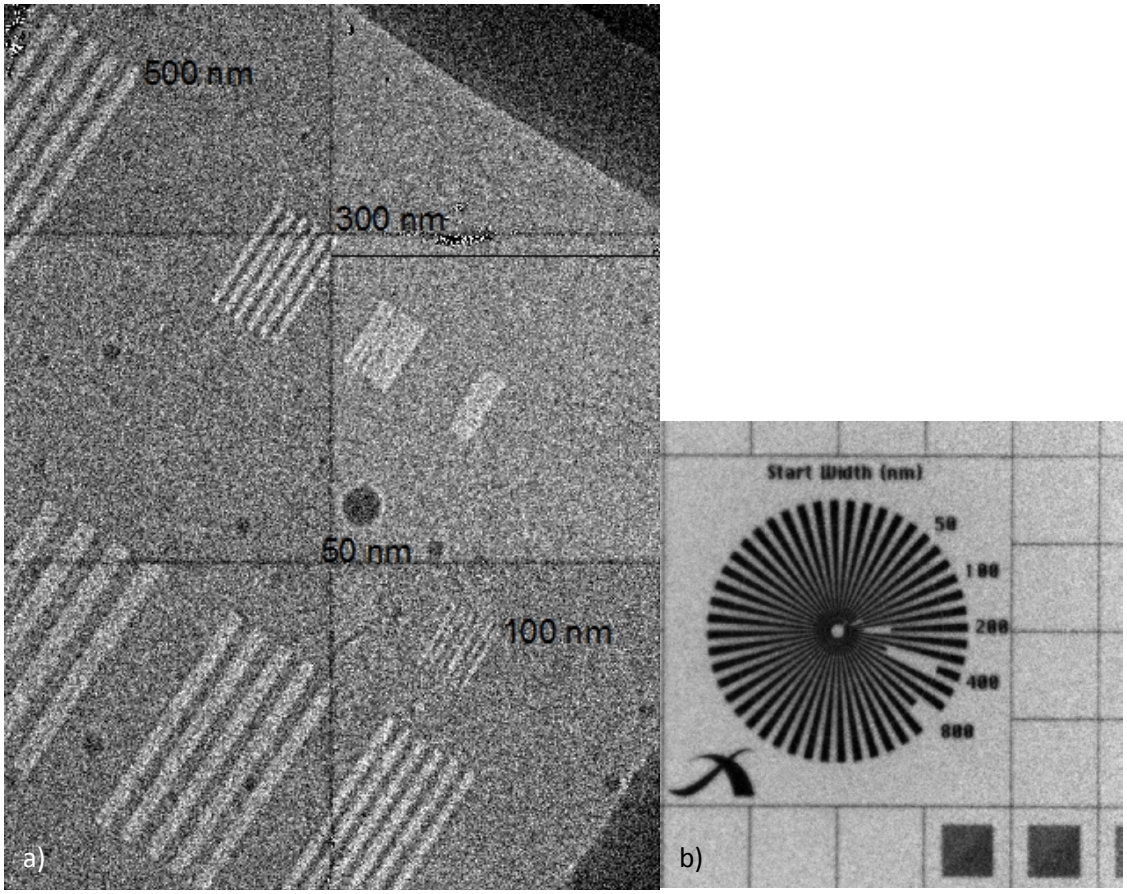

Fig. 3. *a) Radiography of an Au TEM-Grid test pattern with the proposed CT system, 5-30 kV polychromatic tungsten spectrum, MEDIPIX2 detector, 30 min exposure time. Details down to 100 nm are clearly distinguishable, whereas the 50 nm structures are not visible at all. b) A Siemens star imaged with a commercially available X-ray microscopy system based on Fresnel zone plates (Xradia UltraXRM L500), monochromatic Cu K radiation, 5 min exposure.*

Results and outlook

The spatial resolution of the proposed system was tested with an image of a TEM-Grid coated with 3 µm gold, into which line patterns were cut with a FIB gun (Fig. 3a). In terms of resolution, the proposed system is comparable to laboratory based systems using X-ray optics (Fig. 3b), whereas the required exposure times of our system are higher, especially with the MEDIPIX2. The 100 nm line pair can clearly be resolved, approving a spatial resolution below 100 nm of the presented CT system.

Fig. 4 gives an outlook of the system capabilities with the new Pixirad-2 detector for future high resolution material analysis. It shows inline phase-contrast which occurs due to the ultra small X-ray source spot which comes in handy especially for low contrast materials, as well as for discovering structural defects like holes or cracks. The phase contrast and the defect detection are required features for the investigation of technical alloys like AlSi.

The described setup works well for 2D inspection of thin low-Z materials (see fig. 4). A comparable study of both detectors as well as an upgrade to 3D visualization are in progress. The software will be adapted to the new detector and the required debugging of sample movement is done. A trade-off between reasonable signal-to-noise ratio (SNR) and minimal exposure time has to be done on dependence of contrast for each material. The most crucial issue to realize 3D-imaging is the longterm stability for source and object position, i.e. a scanning time of in sum a few days for 180 projections with illumination and read-out time per projection of 30 min. For most materials a reduction of the scanning time can only be realized by reducing the spatial resolution. This can easily be done by shifting the tip towards the sample and thus using a thicker part of the needle as X-ray source.

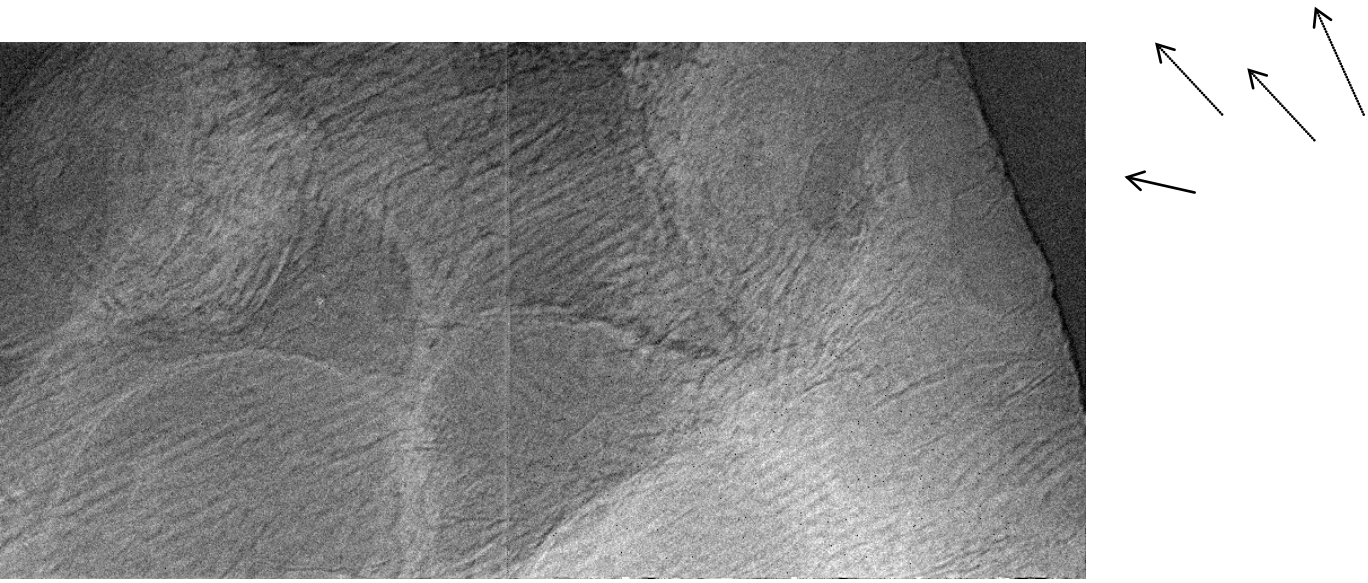

Fig. 4. *Radiography of an AlGeSi alloy demonstrating the capabilities of the system. The picture has been recorded with an Pixirad-2 photon counting detector, 5-30 kV tungsten spectrum, 120 min exposure time. The picture shows clearly the different phases of the compound, as well as periodic 500 nm stripes (arrow) which are surface details and down to 100 nm even smallest hairline cracks in the material (pointy arrows) which are mainly visible due to the inline phase-contrast characteristics of the system.*

Acknowledgements

The authors greatfully acknowledge the funding of the Bavarian State ministry of Economic Affairs, Infrastructure, Transport and Technology which supports the project group “Nano-X-ray Systems For Material Characterization” and of the German Research Council (DFG) which, within the framework of its ‘Excellence initiative’ supports the Cluster of Excellence ‘Engineering of Advanced Materials’ at the University of Erlangen-Nuremberg. Special thanks go to Dr. Peter Krüger for providing the resolution test and images from the Xradia micrsocope.

References

Stahlhut P., Ebensperger T., Zabler S. & Hanke R. (2014). *A laboratory X-ray microscopy setup using a field emission electron source and microstructured reflection targets,* **Nucl. Instr. Meth. B,** 4-10

Fotino M. (1992). *Tip sharpening by normal and reverse electrochemical etching*, **Rev. Sci. Instrum. 64,** 159-167

Ebensperger T., Stahlhut P., Nachtrab F., Zabler S., Hanke R. (2012). *Comparison of different sources for lab-based X-ray microscopy*, **JINST 7,** C1008

Schöbel M., Baumgartner G., Gerth S., Bernardi J., Hoffman M. (2014). *Microstresses and crack formation in AlSi7MgCu and AlSi17Cu4 alloys for engine components* **Acta Materiala 81**, 401-408

Salomon M., Hanke R. (2008). *Realization of computed tomography setup to achieve resolution below 1 µm,* **Nucl. Instrum. Methods Phys. Res. Sect. A *591*,** 50-53

Tkachuk A., Duewer F., Cui H., Feser M., Wang S., Yun W. (2007). X-ray computed tomography in Zernike phase contrast mode at 8keV with 50-nm resolution using Cu rotation anode X-ray source, **Z. Kristallogr. 222**, 650-655

Llopart X., Campbelli M., Dinapoli R., San Segundo D., Pernigotti E. (2002). *Medipix2: A 64-k pixel readout chip with 55-µm square elements working in single photon counting mode,* **JEEE Trans. Nucl. Sci. 49,** 2279-2283

Bellazzini R., Spandre G., Brez A., Minuti M., Pinchera M., Mozzo P. (2012). Chromatic X-ray imaging with a fine pitch CdTe sensor coupled to a large area photon counting pixel ASIC, **JINST 8,** C02028

Commerical Lithium-Ion Batteries, Neutron Tomography and Diffraction, PCA-MCR, and SNARK

A. BROOKS*, J. YUAN, L. BUTLER

Department of Chemistry, Louisiana State University, 232 Choppin Hall, Baton Rouge, LA 70806, USA – abroo38@tigers.lsu.edu
* presenting author

Keywords: Lithium-ion batteries, neutron diffraction, principal component analysis, multivariate curve resolution analysis, SNARK09

Abstract

The visualization of lithium ion batteries through neutron tomography is challenging. With high amounts of hydrogen scattering and lithium absorption, obtaining a 3D dataset in neutron imaging proves difficult. In this study, we aim at understanding inner battery workings through neutron tomography (FRM II ANTARES) and neutron diffraction (SNS VULCAN). Images utilize an iterative tomography reconstruction program (SNARK09) but are limited by low signal-to-noise ratios. Principal component analysis (PCA) and multivariate curve resolution (MCR) analysis of the neutron diffraction data provides a visual representation of the electrochemistry within a battery between fresh and worn, charged and discharged states. Combining diffraction with tomography shows the complexity of lithium ion battery systems

Introduction

Lithium ion batteries play a pivotal role in everyday use around the world, from laptops to cell phones to electric cars. With high capacity and low self-discharge, lithium ion batteries are constantly being improved upon with new materials like silicon or lithium metal. The chemistry behind a sample graphite/lithium metal oxide battery is shown in scheme 1, where lithium ions move from $LiCoO_2$ and intercalate with graphite forming LiC_6.

$$LiCoO_2 + yC \underset{\text{Discharge}}{\overset{\text{Charge}}{\rightleftharpoons}} Li_{1-x}CoO_2 + Li_xC_y \qquad \text{Equation 1}$$

$$C_y + xLi + xe^- \underset{\text{Discharge}}{\overset{\text{Charge}}{\rightleftharpoons}} Li_xC_y \qquad \text{Equation 2}$$

Scheme 1. *Chemical reactions of a graphite/lithium cobalt oxide battery*

While lithium ion batteries provide several advantages, concerns regarding cost, thermal runaway and degradation are still present. To combat these issues, there is a need to understand the inner workings of batteries through non-destructive testing.

One such way is through tomography. X-ray and neutron imaging provides a way of visualizing different battery materials based on the internal properties of a battery's materials materials. In the case of X-ray imaging, X-rays aimed at a sample interact with electrons, meaning low atomic Z elements like hydrogen, lithium, or carbon are not as

good scatterers as high atomic Z elements. Previous X-ray battery imaging observed porosity at 15% and electrode thickness of a Lishen 18650 graphite electrode (Shearing).

While X-rays show certain battery features, neutrons provide an in-depth understanding of core battery features. Neutrons penetrate a sample deeper than X-rays to interact with neuclei, allowing characterization of bulk properties of materials. As the wavelengths of neutrons are comparable with interatomic spacing, utilizing neutrons at various wavelengths provides an easy way to track structural changes in batteries. For this reason, the optimal combination for understanding batteries is thought to combine neutron diffraction with neutron imaging. Previous diffraction work of Li ion batteries along with in-depth statistical analysis (principal component analysis) has observed peak shifts and appearance/disappearance of internal battery components between fresh and worn batteries (Cai, Wang, Rodriguez). By understanding the tracking of structural components through diffraction, a new methodology for combining diffraction with tomography can lead to advanced knowledge regarding lithium ion battery chemistry.

Methods

In this study, we look at the properties of fresh and worn, charged and discharged lithium ion polymer batteries ($LiCoO_2$/graphite) through neutron diffraction and neutron tomography. Neutron diffraction was performed at Oak Ridge National Laboratory (SNS VULCAN).

3D images of a charged and discharged battery were taken at the FRM II Antares beamline. A ^{6}LiF/ZnS scintillator with thickness between 50 to 100 μm was used with an Andor CCD camera. Pixel resolution was 54 μm using a double graphite crystal monochromator. The data collected was processed using SNARK09, ASTRA-SIRT, ASTRA-SART, and Muhrec to reconstruct the battery images in 3D.

Statistical analysis (PCA/MCR) of the neutron diffraction data was performed using free matlab software (http://mcrals.info) as a function of battery discharge. Structural information used as a basis set was created via CrystalMaker and CrystalDiffract.

Discussion

Neutron tomographical reconstructions were discovered to be challenging for battery samples. Attempts using SNARK09 to explore iterative tomography reconstruction options were limited due to centering issues (Figure 1).

Fig. 1. *Reconstructions of a charged (a) and discharged (b) fresh battery at 3.6Å using SNARK09*

Despite the restricted information obtained from SNARK09, ASTRA-SART showed valuable features of the batteries. Several of the electrode layers and edges of the cells can be seen in Figure 2.

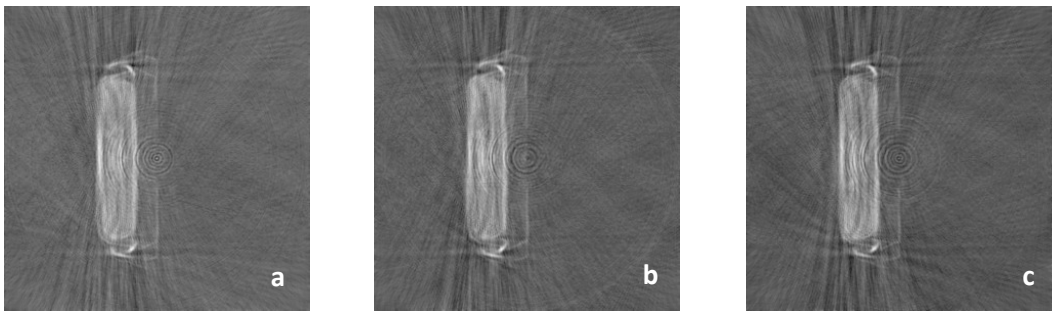

***Fig. 2**. ASTRA-SART reconstructions of slice No. 450 at 3.6Å of a battery that is: **a**, fresh charged, **b**, fresh discharged, and **c**, worn discharged.*

The curved nature of the vertical lines in the cell represents the folding of cathode and anode layers. It was expected that edges of the batteries would display the circular folds well, however this was limited by the low signal-to noise ratios in the reconstructed slices. Also of interest is the comparison of the fresh (b) and worn (c) batteries, where the fresh battery is seen to have more homogeneity across the cell than the worn battery. One explanation is that lithium may be getting trapped in certain locations in the cell, meaning the overall capacity of the battery decreases. As a result, the loss of lithium movement can be seen as a darkening of the electrodes.

To complement neutron tomography and track the chemical changes within the cell, neutron diffraction showed large structural changes between the fresh and worn, charged and discharged batteries. A decrease in the peak at 1.84 Å (Figure 3) corresponds to the depletion of LiC_6 (002) and LiC_{12} (112) as the fresh battery goes about discharging. Separation of the LiC_6 peak from LiC_{12} presented many challenges as the peaks were overlapping.

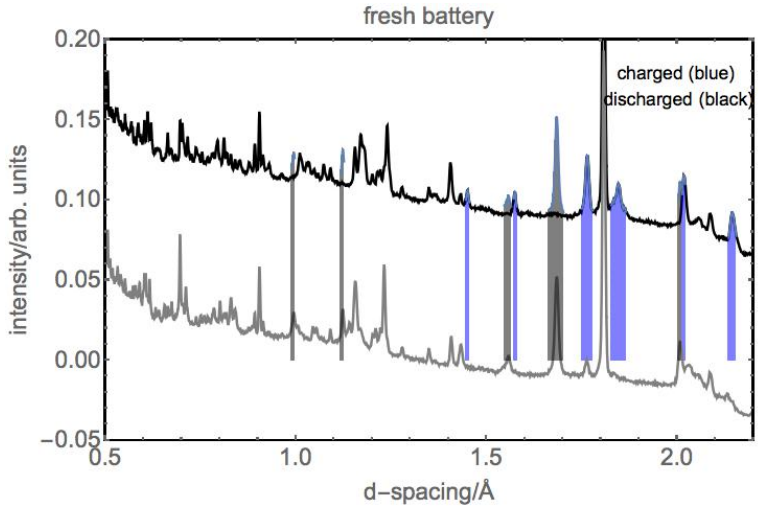

***Fig. 3.** Neutron diffraction of a fresh battery. Peak areas appearing in the charged battery are shown in blue while peaks appearing for the discharged battery are shown in black.*

While the fresh battery showed several regions of interest, the worn battery in Figure 4 has a smaller number of peak changes. The region at 1.84 Å with LiC_6 (002) and LiC_{12} (112) no longer shows peak intensity, implying that those structures may no longer be present in the battery. This could indicate that the battery is worn enough to the point that lithium intercalation with graphite is extremely limited.

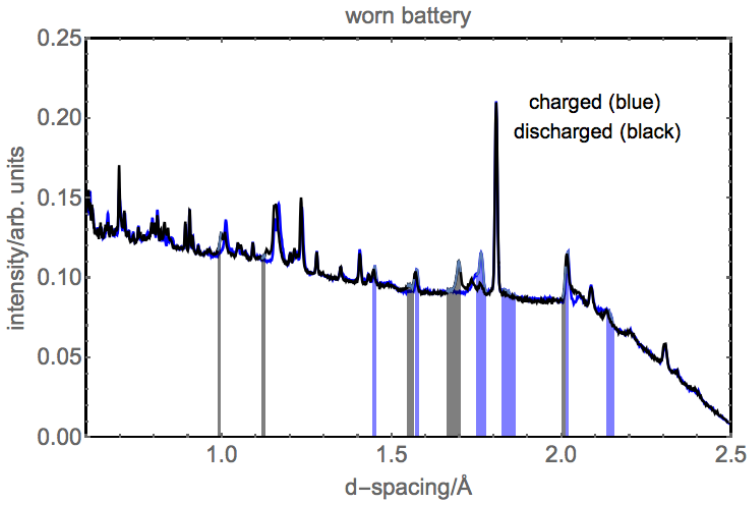

Fig. 4. *Neutron diffraction of a worn battery. Peak areas appearing in the charged battery are shown in blue while peaks appearing for the discharged battery are shown in black.*

As a way to understand the relationship between battery components better in the diffraction data, principal component analysis and multivariate curve resolution analysis were performed. Determining the number of components to use as a starting guess proved difficult, especially between the fresh and worn batteries. For fresh battery systems like in Figures 5 and 6, chemical formulas and structural information are well known (LiC_6, $LiCoO_2$, C_6). For worn battery systems, intermediate structures such as LiC_{12}, LiC_{18}, and $Li_{0.75}CoO_2$ have limited known information, meaning diffraction peaks that appear and disappearing during the middle of the discharge process are difficult to assign to one specific component. In this study, both a three (Figure 5) and six (Figure 6) component system were studied for the fresh battery system below.

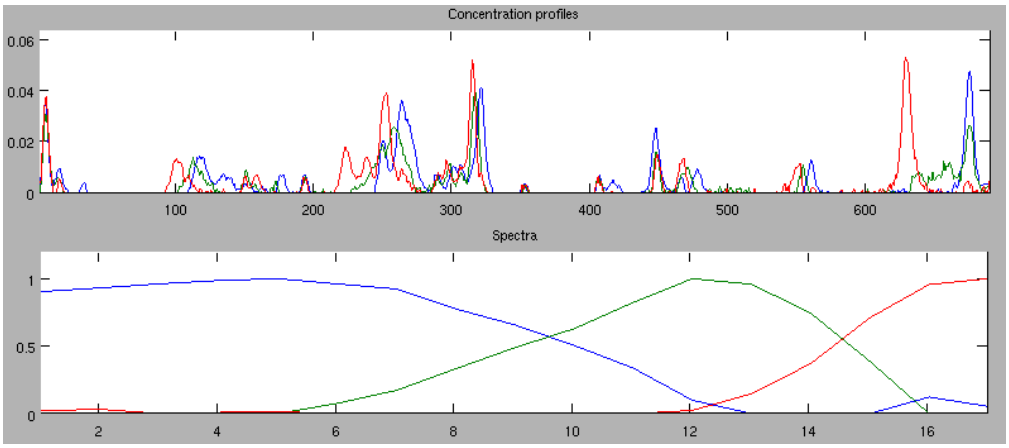

Fig. 5. *PCA/MCR analysis of a 3 component fresh battery system from 0.9 Å (left) - 1.79 Å (right). LiC_6 (dark blue), LiC_{12} (green), C_6 (red)*

In the three component system, PCA/MCR analysis works well for the graphite electrode in the d-space range of 0.9-1.79 Å. The MATLAB program accurately tracks the chemical changes of a fresh battery discharging, where structurally the battery changes from a fully charged formula of LiC_6 to an intermediate LiC_{12} to a fully discharged C_6. The small increase of LiC_6 at state of charge 16 indicates a misassigned peak from the program.

In comparison to the three component system, a six component system was also possible for the fresh battery. Shown in the six component system below is the graphite electrode species along with the cobalt oxide species, implying that PCA/MCR analysis is possible for an entire battery. Of interest in Figure 6 is the appearance and disappearance of one component at a time in sequential order. Lithium ions are seen moving through the cell with the depletion of LiC_6 first, followed by the appearance and disappearance in order of $Li_{0.5}CoO_2$, LiC_{12}, $Li_{0.75}CoO_2$, C_6 and $LiCoO_2$. The rise and fall of the individual components helps explain how lithium transfers from graphite species to cobalt species during the discharge process.

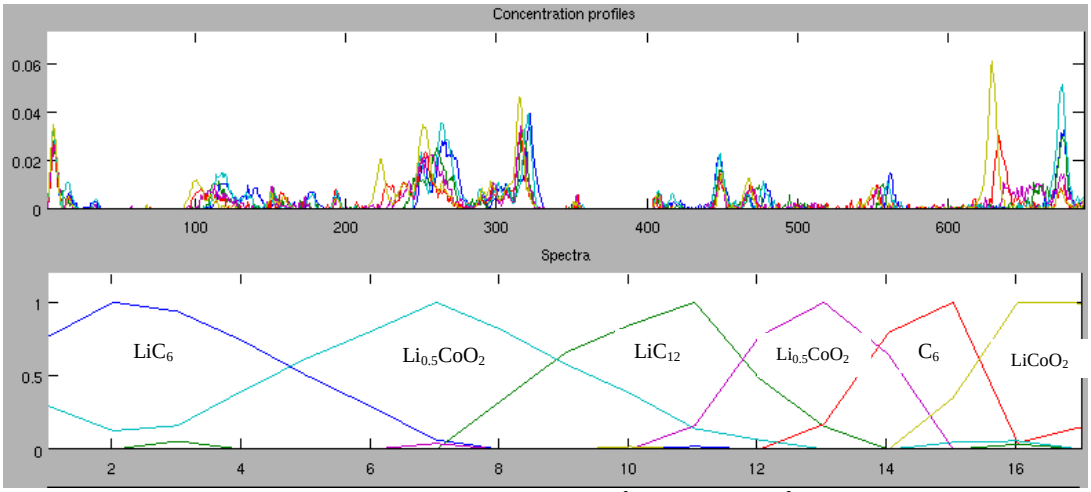

Fig. 6. *PCA/MCR analysis of a fresh battery from 0.9 Å (left) - 1.79 Å (right). $Li_{0.5}CoO_2$ (light blue), $Li_{0.75}CoO2$ (purple), $LiCoO_2$ (yellow), LiC_6 (dark blue), LiC_{12} (green), C_6 (red)*

While the fresh battery follows anticipated cycling patterns, the worn battery exhibits unique behavior. Despite using the same six components as the fresh battery, PCA/MCR analysis was unable to find LiC_6 and $Li_{0.75}CoO_2$ peaks in the worn battery. Several explanations are possible for this issue. If the basis set used as a starting guess for the analysis is incorrect due to peaks shifting during cycling, then what is useful for the fresh battery is no longer applicable for the worn battery.

Conclusion

Battery imaging is a challenging task. Through neutron imaging, we observed the difficulties in obtaining quality images of battery electrodes within the cell due to high lithium scattering. Neutron diffraction complements imaging by providing structural information unseen through images. Worn batteries exhibit a depletion of starting components as seen by PCA/MCR analysis. PCA/MCR is difficult to perform on batteries where chemical formulas are constantly changing during the charge/discharge process. Only by combining chemical intuition with imaging are we able to piece together the tomography of lithium ion batteries.

References

Cai, L., An, K., Feng, Z., Liang, C., Harris, S. J. (2013) ***J. Power Sources***. *236*, 163-168.

Rodriguez, M., Van Benthem, M. H., Ingersoll, D. (2010) ***Powder Diffr***. *25*, 143-148.

Shearing, P. R., Howard, L. E., Jørgensen, P. S., Brandon, N. P., Harris, S. J. (2010) ***Electrochem. Commun.*** 12:374

Wang, X-L, An, K., Cai, L., Feng, Z., Nagler, S. E., Daniel, C., Rhodes, K. J., Stoica, A. D., Skorpenske, H. D., Liang, C., Zhang, W., Kim, J., Qi, Y., Harris, S. J. (2012) ***Sci. Rep***. *2: 747*, 1-7.

New Capabilities in X-ray Microscopy for Understanding Microstructural Evolution Over Time and Length Scales

W. HARRIS[1], A. MERKLE*[1], J. GELB[1], L. LAVERY[1], C. HOLZNER[1]

[1] Carl Zeiss X-ray Microscopy, Inc., Pleasanton, CA, USA – arno.merkle@zeiss.com
* presenting author

Keywords: X-ray, microscopy, evolution, 4D, in situ

Introduction to X-ray Microscopy

X-ray computed tomography (CT) systems exist in a number of variations, with differing X-ray sources and detectors leading to a variety of permissible object sizes and measurable spatial resolution. However, a strong feature of X-ray tomography regardless of the instrument operating space is the non-destructive nature of the technique. This non-destructive nature yields a number of advantages of X-ray CT for materials characterization, including

- Locating and characterizing buried, subsurface features without physically cutting the sample, thus avoiding the chance of inadvertently modifying the very feature you are interested in observing in its native state
- Enabling 4D (3D + time) studies by repeated imaging of the same sample under a variety of conditions or stimuli
- Connecting X-ray tomography data with data collected on the same sample from complementary microscopy tools, such as electron microscopes, which can often require destructive sample manipulation (FIB-SEM serial section tomography, for example).

The most simple and common design for X-ray CT systems is based on a geometric magnification principle. Such an arrangement consists of an X-ray source with a small spot size, a sample, and a 2D flat panel detector downstream. High magnification (and resolution) is achieved by placing a small sample very close to the source and maximizing the geometric projection effect, producing a large image on the detector. Many such systems provide high throughput, and sufficient resolution for small samples, which can be placed very close to the source. However, such systems rapidly lose resolution as sample sizes or working distances are increased and the sample must be placed further from the source.

The latest developments of X-ray microscopy (XRM) systems have alleviated some of these classical restrictions of projection-based CT by introducing optical components originally developed at synchrotron facilities in order to provide additional magnification and lessen the coupling of working distance and resolution. In the ZEISS Xradia Versa system (Fig. 1a), the flat panel detector has been replaced by a selection of scintillator-coupled optical lenses, which serve the dual purpose of converting X-ray photons to visible light photons, and then using an optical lens to magnify the generated image onto a CCD detector. In this arrangement, the optical magnification step at the detector is able to provide the majority of the magnification needed by the system to obtain high resolution imaging, thereby reducing the need for high geometric magnification normally achieved via very small samples/working distances. In addition to permitting larger samples to be imaged without drastic loss of resolution, such an architecture also permits the incorporation of space-consuming *in situ* rigs into the beam path, again enabling high resolution imaging at a relatively large source-sample working distance.

In a second instrument, the ZEISS Xradia Ultra (Fig. 1b), X-ray focusing optics in the form of a capillary condenser lens and Fresnel zone plate objective act directly on the X-ray photons, creating a focusing arrangement similar in architecture to an optical or transmission electron microscope. The system operates with a quasi-monochromatic X-ray beam of either 8.0 or 5.4 keV, and the optics are implemented with the purpose of achieving higher spatial resolution down to 50 nm with this architecture, on samples of tens to hundreds of microns in size. This system is well-positioned to fill a non-destructive 3D imaging gap, between very high resolution TEM tomography, and micro-scale XRM and CT systems which can typically resolve features a little smaller than a micron. Like the Versa XRM, geometric magnification no longer dictates spatial resolution, since in the Ultra XRM the sample size, and working distance surrounding the sample, is now largely dictated by the beam energy and X-ray optics. The working distance around the sample again permits the incorporation of *in situ* rigs.

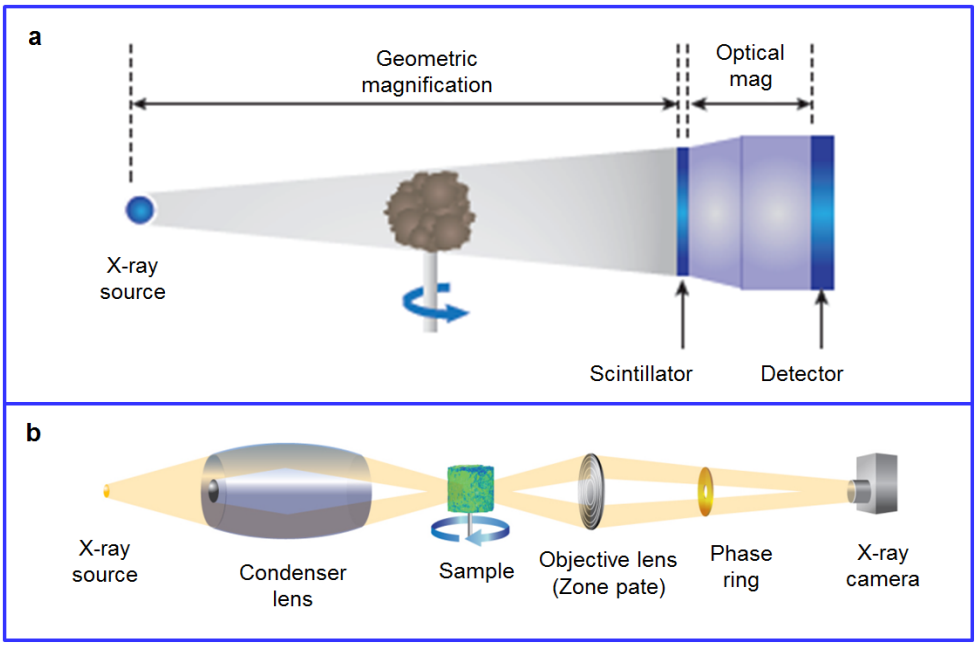

Fig. 1. *XRM architecture of the a) ZEISS Xradia Versa system, offering spatial resolution down to 700 nm, and b) ZEISS Xradia Ultra, providing spatial resolution down to 50 nm.*

Non-destructive 4D Imaging

As previously mentioned, non-destructive imaging lends itself well to 4D studies to characterize the change of a structure over time. Such a capability is important to a variety of materials research fields in which there exist complex microstructure-property relationships, which can often be a function of the specific material environment. In addition, degradation as a result of such stimuli as gas environment, mechanical loading, or simply time can cause structural evolution under extended operation, raising questions relating to the durability or lifetime of a particular material system.

Studying such phenomena using X-ray tomography can be done in either an *ex situ* or *in situ* arrangement. *Ex situ* studies provide the distinct advantage of simplicity, as the design of an experimental system does not have to consider the physical constraints of the imaging instrument. *Ex situ* studies can also be valuable for long-term processes, in which the structural change of a material is expected to take days, weeks, or longer.

This approach has been demonstrated, for example, to look at cell growth on bio-scaffold materials.

However, in many cases *in situ* testing is necessary to gain an accurate representation of the dynamic process. This is especially true for:

- Locating the same region (or volume) of interest within a sample for multiple imaging trials. This is particularly true when the volume is located within the interior of a larger sample, and repeated handling of the sample in and out of the microscope might make it difficult or time-consuming to locate the same region.
- Physical handling of the sample in and out of the system during an *ex situ* study could inadvertently alter the sample if it is sensitive to mechanical vibration, changes in environment, etc.
- In some instances the stimulus must be maintained to produce the desired results. Such is the case, for example, when performing a tension or compression test to create elastic deformation of a material, or the maintenance of a certain gas environment to keep a sample in a given chemical/structural state.

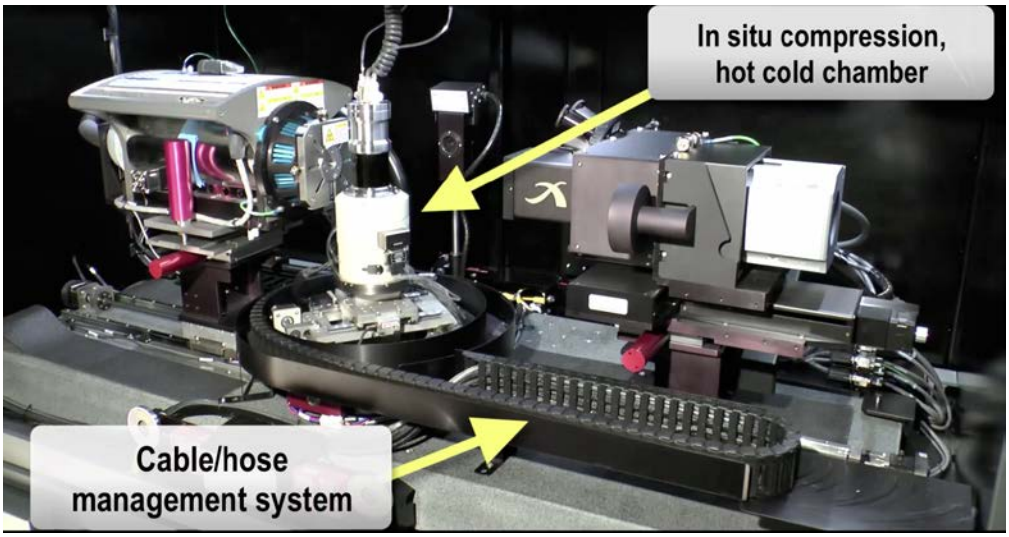

Fig. 2. *In situ experiments within X-ray tomography systems require careful routing of external connections so that the sample can still undergo rotation without producing stress on the experimental apparatus. A cable/hose management system, such as that shown above, can help alleviate some of these challenges.*

Although additional care must often be exercised in the design of *in situ* experiments (see Fig. 2), recent publications have demonstrated a number of applications providing unique insight into their respective structural systems. Figure 3 depicts the X-ray microscopy reconstructions of a steel laser weld in 3 states of tension, imaged with the Xradia Versa microscope with 1.5 micron voxel size (This work was performed in collaboration with Sandia National Laboratory). The results were achieved using a commercially available mechanical load stage (Deben UK Limited) mounted directly on the microscope's rotational stage. A dogbone-shaped sample was mounted in the stage and subjected to increasing amounts of tensile force. The force was held constant in three different states to collect the 3D data shown in the image. The renderings reveal two distinct phenomena: in the top row, a rough surface imperfection served as a crack initiation site; and in the bottom row a transparent rendering of the internal features

shows the elongation of voids in the tensile direction, with the potential to serve as failure locations at increasing levels of load.

Fig. 3. *In situ tensile testing of a steel laser weld system, at three levels of tension. Cracking initialized from a rough surface feature, as well as elongation of interior voids, are visible as the load is increased. (In collaboration with Sandia National Laboratory)*

Separate studies have been performed by numerous groups, including Khajeh-Hosseini-Dalasm et al. and Gonzalez et al., also using the Xradia Versa, to examine microstructural effects in energy materials, namely polymer electrolyte fuel cells and lithium ion batteries, respectively. In the work by Khajeh-Hosseini-Dalasm et al., a custom compression cell was utilized to perform mechanical compression of a fibrous gas diffusion layer used in PEFC electrodes. Under fuel cell operating conditions, the compressive force is applied to promote adhesion of the various cell components, as well as to ensure adequate contact, and therefore electrical conductivity, between the carbon fibres of the GDL. Therefore, observing the associated microstructural changes under varying compressive load can help to explain the effectiveness of transport processes in the porous fibre network as well as suggest optimal compressive parameters.

In another form of *in situ* manipulation, a custom electrochemical cell was produced by Gonzalez et al. to perform controlled electrochemical cycling of battery electrodes within the XRM. Using this set-up, the lithiation and de-lithiation of Si anode particles could be controlled and interrupted at set stages in order to perform a 4D imaging study of the structural evolution of the particles as they undergo the corresponding chemical

change. Drastic expansion and cracking of the particles was observed during the lithiation, indicative of a serious degradation mechanism present in Si anodes being considered as alternative host materials (to graphite) for lithium ion battery anodes. By performing the study in an *in sit*u rather than *ex situ* arrangement, the researchers were able to easily track the same particles through a large number of data sets acquired during the lithiation process without the need for frequent transfer of the sample in and out of the microscope and connection/disconnection of electrical leads.

Recent developments have also opened the door for 4D *in situ* experiments within the Ultra X-ray microscope. With the smaller sample sizes (tens to hundreds of microns scale) typical of this nanoscale system, mechanical loading presents its own unique set of challenges, as samples are inherently more fragile and the system stability more sensitive. However, a new *in situ* nanomechanical load stage developed by the ZEISS X-ray microscopy group has been designed specifically to address these challenges within the Ultra microscope. The load stage, capable of compression, tension, and indentation loading modes, has already produced some early results, including examining the plastic deformation of a porous elastomer material under compressive load, as shown in Fig. 4. Non-destructive nanomechanical testing at this length scale fills an existing void in mechanical characterization techniques, offering high spatial resolution approaching the electron microscopy regime, but offering imaging of the deformation of fine internal structures (as opposed to surfaces only in SEM) on samples large enough to begin to reflect bulk material behaviour (as opposed to very thin samples in TEM).

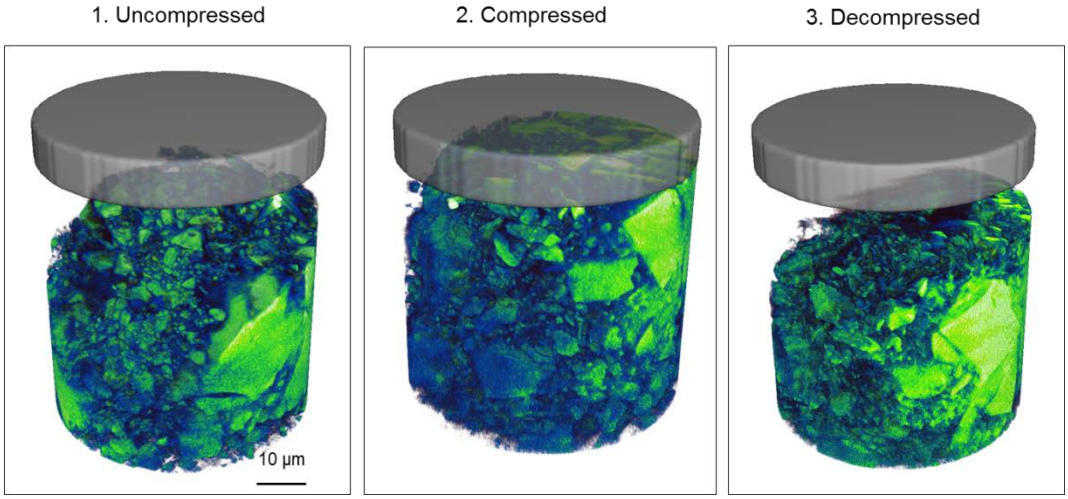

Fig. 4. *4D imaging of the compression of a porous elastomer material. The first frame shows the original structure, which is mounted on a moveable stage, and the stationary top anvil (gray shading). In the second frame, the sample has been moved vertically upwards into the stationary anvil, compressing the sample. In the third frame, the sample has been moved back down, relieving the force but also revealing plastic deformation of the submicron-scale porous structure.*

References

Merkle P. & Gelb J. (2013). ***Microscopy Today*** 21, 2: 10-15.
Bosworth L. et al. (2014). ***J. Mech. Behav. Biomed. Mater.*** 39: 175-183.
Gonzalez J. et al. (2014). ***J. Power Sources*** 269: 334-343.
Khajeh-Hosseini-Dalasm N. et al. (2014). ***J. Power Sources*** 266: 213-221.

Diffraction Contrast Tomography as an Additional Characterization Modality on a 3D Laboratory X-ray Microscope

*C. HOLZNER[1], A. MERKLE[1], P. REISCHIG[2], E.M. LAURIDSEN[2], M. FESER[2]

[1] Carl Zeiss X-ray Microscopy Inc., 4385 Hopyard Road, Suite 100, Pleasanton, CA 94588, USA
[2] Xnovo Technology ApS, Galoche Alle 15, 4600 Køge, Denmark
* presenting author

Keywords: diffraction contrast tomography, x-ray microscopy, grain mapping

Abstract

X-ray tomography has operated under two primary contrast mechanisms for some time: X-ray absorption contrast, providing density information, and phase propagation contrast, providing enhanced interfacial information. These primary mechanisms are powerful and advanced laboratory-scale X-ray microscopy (XRM) platforms have demonstrated great improvements to this in recent years. However, single-phase polycrystalline materials (e.g. steel, Al- alloys, Ti-alloys, etc.) have never exhibited any significant contrast using absorption or phase. Now, advancing one step further, XRM is enabling an additional modality known as diffraction contrast tomography (DCT) that provides crystallographic/diffraction information from polycrystalline samples, facilitating the ability to directly characterize a samples crystalline microstructure, non-destructively. Here we describe the capabilities of lab DCT on the ZEISS Xradia 520 Versa platform, and new research and characterization capabilities it enables.

Introduction

In the continued spirit of transferring synchrotron capabilities to laboratory XRM systems, ZEISS in partnership with Xnovo Technology have demonstrated the ability to obtain crystallographic (diffraction) contrast information on the Xradia 520 Versa platform.

Crystallographic imaging is commonly known from several metallographic techniques, including light and electron microscopy (EM) methods. In recent years, the introduction of 2D and 3D electron back-scattering diffraction (EBSD) techniques have made EM a routine tool for research and/or development related to metallurgy, functional ceramics, semiconductors, geology, etc. The ability to image the grain structure and quantify the crystallographic orientation relationships in such materials is instrumental for understanding and optimizing material properties (mechanical, electrical, etc.) and *in situ* processing conditions.

However, the destructive nature of 3D EBSD prevents one from directly evaluating the microstructure and grain-orientation evolution when subject to either mechanical, thermal or other environmental conditions. Understanding this evolution process on the same sample volume is key to unlocking a more robust understanding of materials performance along with improved modeling capabilities, and is a key driver of future materials research efforts.

In response to this constraint, synchrotron-based crystallographic imaging, known as Diffraction Contrast Tomography (DCT) has emerged over the past decade [Poulsen 2004, Ludwig 2009]. Utilizing non-destructive X-rays, synchrotron users could quantify grain orientation information in the native 3D environment without physical sectioning. This has led to the logical desire to study the evolution of grain crystallography *in situ* or during interrupted '4D' evolution experiments. However, limited regular access to such

synchrotron techniques has constrained the ability to perform thorough, longitudinal studies on materials evolution.

ZEISS has taken this established synchrotron modality and successfully transferred it to the Xradia Versa family of laboratory-based sub-micron XRM systems. Laboratory-based DCT may be efficiently coupled to in situ sample environments within the microscope or subject to an extended time evolution "4D" experiment (across days, weeks, months) – a unique practical strength of laboratory-based XRM/DCT experiments. Following an evolution experiment the sample may be sent to the electron microscope or focused ion beam (FIB-SEM) for post-mortem complementary investigation of identified volumes of interest. This natural correlative workflow combining multiple lab-based methods on the same sample volume remains an attractive future direction of microscopy to many researchers and is firmly enabled by ZEISS's foundation of characterization modalities.

In the following we will describe laboratory DCT, including basic principles through validation examples and comparisons to related technologies.

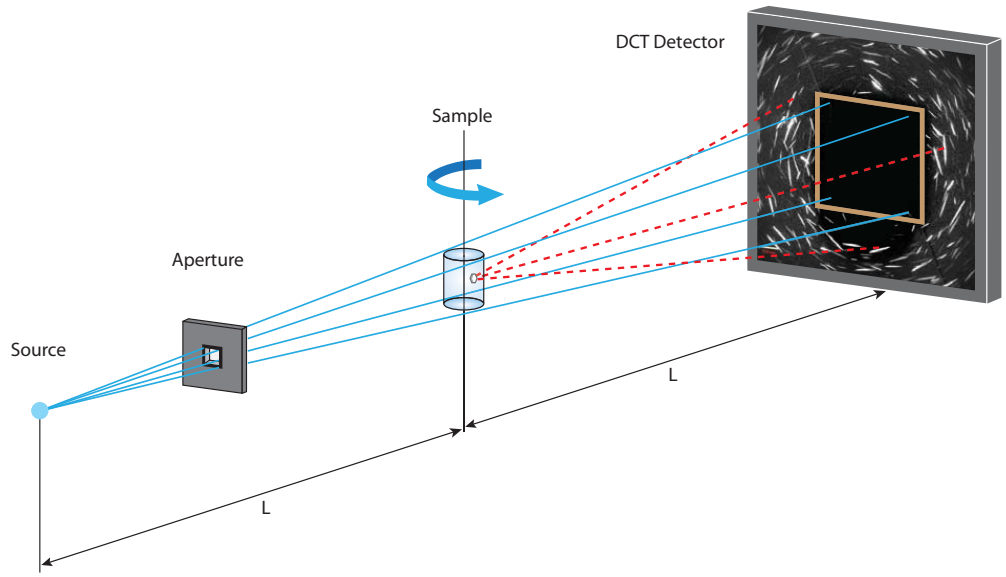

Fig. 1. *Schematic of the laboratory DCT setup. The sample is illuminated through an aperture in front of the X-ray source. Both the sample absorption and diffraction information is recorded with a high resolution detection system. Optionally, a beamstop maybe be added to the set-up in order to increase the dynamic range of the diffraction detection.*

Methods

Here, we present a method to acquire, reconstruct and analyze grain orientation and related information from polycrystalline samples on a commercial laboratory X-ray microscope (ZEISS Xradia 520 Versa) that utilizes a synchrotron-style detection system.

A schematic representation of the laboratory DCT implementation is shown in Figure 1. The X-ray beam is constrained through a specialized aperture to illuminate the sample of interest. Diffraction information is collected with a tailor-made high resolution detector that in addition allows simultaneous acquisition of the sample's absorption information. In order to increase the sensitivity to the diffraction signal a beamstop may be added. The data acquisition is performed in a symmetric geometry, which enables improved

diffraction signal strength and allows handling of many and closely located diffraction spots.

For laboratory DCT a series of projections is taken from which information on the individual grains/crystallites within the sample is derived. Figure 2 illustrates a single such 2D diffraction pattern as acquired with the ZEISS Xradia 520 Versa DCT detector. Just a few hundred projections are enough for a complete laboratory DCT data set.

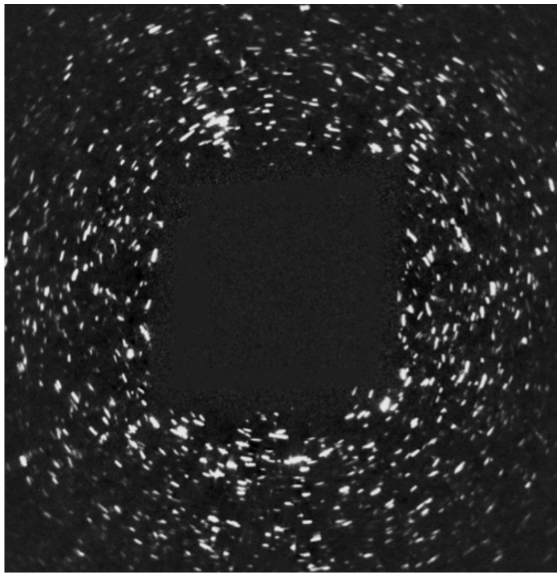

Fig. 2. *Example 2D diffraction pattern from a Ti-alloy. The central area in the projection is obscured by a beamstop; this missing data does not impact the diffraction analysis and reconstruction.*

Results

Polycrystalline Ti-alloy samples (Timet 21S) have been explored and are used here to demonstrate the output of laboratory DCT acquisitions and reconstructions. After successful 3D reconstruction of the diffraction information through Xnovo Technology GrainMapper3D^{TM} software, a number of outputs may be generated. The principle information recovered from a successful reconstruction consists of grain center-of-mass positions and crystallographic orientation values. Such values may be plotted in a 'cube plot' representation as seen in Figure 3. In such 'cube plots' the individual grains are represented by a cube indicating the orientation of the crystallographic unit cell, and scaled according to its respective grain size. The color mode chosen in Figure 3 reflects the crystallographic directions parallel with respect to the vertical sample axis. Various methods may be applied to extract grain shape and morphology of a sample. An example of this is shown in Figure 4, where a Laguerre tesselation map [Lyckegaard 2011] was constructed based on volume and centroid information. Again, color may be used to illustrate properties of the individual grains/crystallites, such as crystallographic information, or number of grain neighbors. To help validate the accuracy of this technique, comparisons to the closest related technologies, EBSD and Synchrotron DCT, were carried out. In doing so independent measurements of grain centroids, grain size, and grain orientations were obtained. Figure 4 shows the comparison of a 3D grain structure derived from Laguerre tessellation of lab DCT data, with the 3D grain structures derived from synchrotron DCT. Although there are minor differences the approximated 3D grain structure derived using the Laguerre tessellation matches the synchrotron grain map remarkably well.

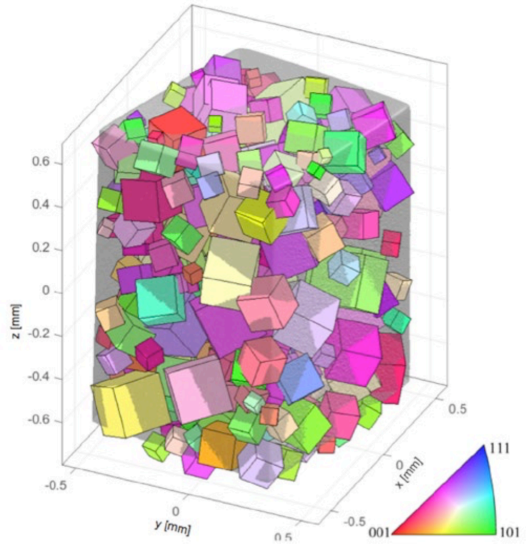

Fig. 3. *Visualization of the titanium alloy (Timet 21S) grains determined by GrainMapper3D software. The cubes illustrate crystal orientation and are scaled by the grain size. Inverse pole figure color coding highlights the crystallographic information.*

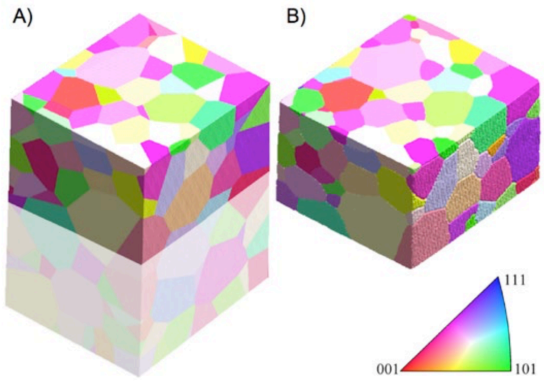

Fig. 4. *A) Tessellated representation of a Ti-alloy sample obtained via laboratory DCT and B) same grain structure obtained from synchrotron DCT. Only the overlapping region between the two data sets are highlighted.*

Also the angular accuracy of the crystallographic orientations were compared to those obtained using synchrotron DCT and EBSD. Some of the measurements are shown in Figure 5a along with the corresponding misorientations determined from the laboratory DCT measurement. It is seen that the absolute values of the misorientation obtained by the two techniques matches well within approximately 1 degree. Figure 5b shows a histogram of the difference in misorientation measured with EBSD vs laboratory DCT as well as the difference in misorientations as measured by laboratory DCT vs Synchrotron DCT. The DCT techniques – both being X-ray based – differ in crystallographic orientation by less than 0.3 degrees, whereas the differences between laboratory DCT and EBSD approach 1 degree consistent with the lower angular resolution of the EBSD technique [Stojakovic 2012].

A) B)

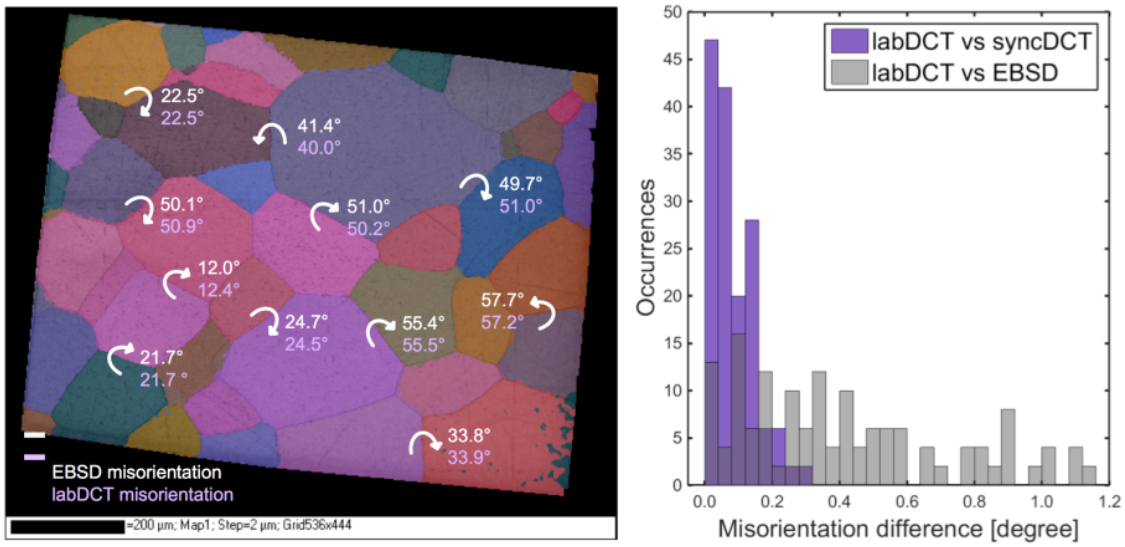

Fig. 5. *A) EBSD data from Ti-alloy sample with indications of mis-orientation angles as determined by EBSD and laboratory DCT. B) Histogram of the differences in mis-orientation as determined by laboratory DCT vs EBSD, and by laboratory DCT vs synchrotron DCT.*

Summary

We have demonstrated the ability to derive 3D crystallographic information via DCT within an XRM. It is yet another example of the continued progress of laboratory XRM to increase its diversity of imaging modalities, which are inspired from synchrotron origins, to solve problems in materials research and related fields. The unique ZEISS Xradia Versa XRM hardware architecture enables the acquisition in powerful combination with advanced reconstruction and analysis capabilities powered by Xnovo Technology and their experience in the field of DCT. The continued use and applications development of this technique will accelerate the way 3D and 4D science is pursued for studying polycrystalline materials.

References

H.F. Poulsen: Three-Dimensional X-ray Diffraction Microscopy (Springer, 2004).

W. Ludwig, P. Reischig, A. King, M. Herbig, E.M. Lauridsen, G. Johnson, T.J. Marrow and J-Y. Buffiere, Rev. Sci. Inst., 80, 033905, (2009)

A. Lyckegaard, E.M. Lauridsen, W. Ludwig, R.W. Fonda, H.F. Poulsen, Advanced Engineering Materials, 13(3), 165-170, (2011)

D. Stojakovic. Processing and Applications of Ceramics, 6(1), 1-13, (2012)

Use of distance transforms and correlation maps for advanced 3D analysis of impact damage in composite panels

F. LÉONARD*[1], J. STEIN[2]

[1] BAM – Federal Institute for Materials Research and Testing, Division 8.5 - Micro-NDE, Unter den Eichen 87, 12205 Berlin,GERMANY – fabien.leonard@bam.de
[2] TWI Ltd., Granta Park, Great Abington, Cambridge, CB21 6AL, UK – jasmin.stein@twi.co.uk
* presenting author

Keywords: low velocity impact, damage characterisation, composite panel, distance transform, correlation map

Abstract

The present study introducess an innovative CT data processing methodology based on distance transforms and correlation maps to improve the ply-by-ply segmentation of impact damage in composite laminates. Composite panels have been impacted with force ranging from 5 J up to 20 J and the impact damage subsequently characterised by X-ray computed tomography. The *damage correlation map* approach was developped here to improve the automatic through-thickness damage segmentation by combining two distance transforms with different reference points. The resulting correlation map proposes an easy to interpret 2D representation of an otherwise complex 3D damage structure. In addition to giving visual qualitative information, the *damage correlation map* can be used to perform a ply-by-ply segmentation of the impact damage and thus extract, for each ply, relevant quantitative information such as damage volume, maximum delamination legth and width, projected damage area *etc*.

Introduction

One of the major issues when using composite materials in an industry such has aerospace is their impact behaviour, particularly when subjected to low-velocity impacts. Low-velocity impacts are complex to assess as although significant damage can be generated internally, there can be little indication externally, leading to the term barely visible impact damage (BVID). The internal damage appears primarily as matrix cracking and delamination between plies of dissimilar orientation [Richardson1996] and can lead to loss in strength and stiffness. Ultimately, the load-bearing capabilities can be significantly reduced in both tension and compression, and catastrophic failure can occur under relatively low applied loads. As a result there is a concerted research effort to improve the damage resistance and tolerance of these materials. When facing such a damage tolerance problem, the geometric structure of the damage is key in understanding the basic damage mechanisms. It is only when such mechanisms are understood that the critical composites properties in regards to damage can be defined and the damage tolerance improvements implemented. X-ray computed tomography is therefore a technique of choice to deliver a full-field 3D representation of the impact damage non-destructively. However, advanced data processing methodologies are required as the sole segmentation of the damage volume does not provide sufficient information.

Previous work [Léonard2013;Léonard2014] has demonstrated that it was possible to segment the damage produced by a low velocity impact event on a composite laminate; and obtain a through-thickness damage histogram. This histogram was employed to semi-automatically separate the full damage so that the individual ply-by-ply damage

could be visualised and assessed independently. The data processing methodology developped was based on a *distance transform* operation to take into account the permanent out-of-plane deformation of the composite panel. However, the main limitation of this approach is the degradation of the damage separation for high impact energies, as the out-of-plane deformation becomes greater in the centre than at the edges of the panel. To obtain a better ply-by-ply separation of the damage, we have employed a combination of *distance transform* operations and a *correlation map* using Avizo Fire software. This new methodology will be presented based on an investigation of carbon fibre reinforced panels (CFRP) impacted with energies ranging from 5 J up to 20 J.

Materials and methods

The composite material under investigation was aimed at primary structures for aerospace applications. It was a unidirectional carbon fibre fabric with 22 Tex glass filaments yarn woven at 6 mm intervals into the fabric to hold together the 12 k carbon tows. The fabric areal density was 445 g/m^2 and the average density of carbon fibre 1.76 g/cm^3. The matrix comprised a high glass transition temperature epoxy resin system, specially formulated for aerospace applications [Stein2012, Stein2013]. All test specimens used in this study were manufactured using vacuum assisted resin film infusion (VARFI) due the high viscosity of the resin [Stein2013]. Each panel was made up of 8 plies stacked in a $[(0°/90°)_2]_s$ stacking sequence as presented in Figure 1.

Ply No.	Angle (°)	Interface
1	0	
2	90	1
3	0	2
4	90	3
5	90	4
6	0	5
7	90	6
8	0	7

a) detailled stacking sequence of composite panels

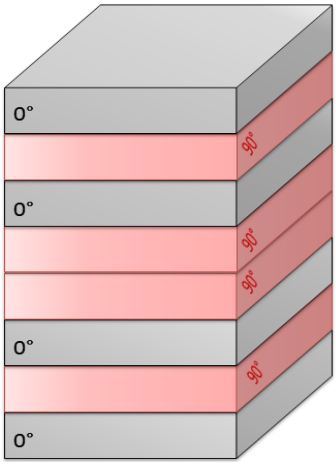

b) panel lay-up sequence

Fig. 1. *Overview of composite panel stacking sequence.*

The panels were cured under vacuum only (no applied pressure) throughout a 6 hour cure cycle comprising 2 hours at temperatures of 130 ºC, 165 ºC, and 200 ºC in turn. The resulting mean laminate thickness was 3.079 mm ± 0.028 mm. Once the laminates were cured, impact test coupons measuring 89 mm x 55 mm were cut from the cured panels using a diamond saw. Although there is no official standard for the miniaturised impact samples used in this work, the samples were cut so that edge parallelism was within the tolerance of British Standard 18352 [BS2009] (0.02 mm) and of an appropriate length in order to prevent Euler buckling during compression after impact testing (CAI).

In order to generate damage in the composite panel, a drop weight impact testing machine was used to deliver a low velocity impact. Impact testing was performed using an Instron CEAST 9350 drop weight impact testing machine controlled by CeastVIEW 5.94 3C software. The tests were carried out according to the methodology of Prichard and Hogg [Prichard1990] with a specimen size of 89 mm x 55 mm, an impactor mass of

5.048 kg and a hemispherical tup 20 mm in diameter. The sample was clamped at the bottom of the tower by a rigid holding device which consists of steel plates, clamps, and a 40 mm circular aperture (Figure 2a). In these tests, the maximum velocity of the impactor was approximately 3.15 m/s for an impact energy of 20 J. Specimens were tested at four different energies (5, 10, 15 and 20 J), to simulate the range of impact energies thin laminates experience during service, such as those resulting from tool drops. An example of the panel tested at 20 J in Figure 2b shows visible damage on the back face.

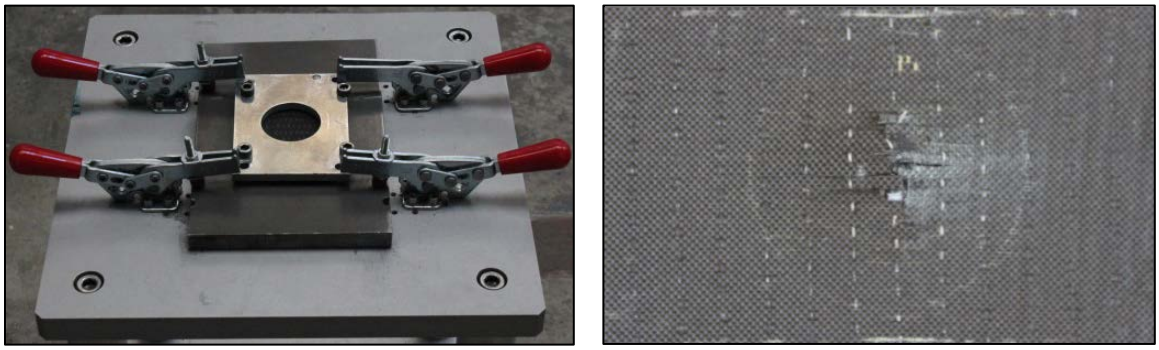

a) specimen holder for drop weight impact tests *b) visible external damage on panel tested at 20 J (back face)*

Fig. 2. *Specimen holder and visible external damage on impacted specimen.*

The impact specimens were scanned on a *Nikon Metrology 225/320 kV Custom Bay* [Manchester2012]. The system was equipped with a 225 kV static multi-metal anode source (Cu, Mo, Ag, and W) with a minimum focal spot size of 3 µm [Nikon] and a PerkinElmer 2048 x 2048 pixels 16-bit amorphous silicon flat panel detector. The X-rays were generated by the copper target using a voltage of 60 kV and a current of 175 µA. The data acquisition was carried out with an exposure time of 1415 ms and no filtration. The number of projections was set to 3142 and the number of frames per projection was 1, resulting in an acquisition time of 75 minutes. The 3D volumes were reconstructed at full resolution with a voxel size of 35.7 µm along the *X*, *Y*, and *Z* directions, using *CT Pro* software [Nikon2013]. *Avizo Fire 8.0* [VSG2012] was employed for the data visualisation, processing, and quantification.

CT data processing methodology

Previous work from *Léonard et al.* [Léonard2013;Léonard2014] has demonstrated that it was possible to segment the damage produced by a low velocity impact event on a composite laminate; and obtain a through-thickness damage histogram. However, the main limitation of this approach is the degradation of the damage separation for high impact energies, as the out-of-plane deformation becomes greater in the centre than at the edges of the panel. To circumvent such limitation and thus improve the accuracy of the ply-by-ply damage segmentation and subsequent analysis, the present work proposes the combination of two distance transforms taken from different reference points into a single map, called *damage correlation map*. An overview of the data processing methodology is given in Figure 3 The first distance transform is taken with the impact face as reference whereas the second distance transform is taken with the centre line of the damage as reference. Combining the two damage distance transform volumes gives a map of the impact damage within the composite panel.

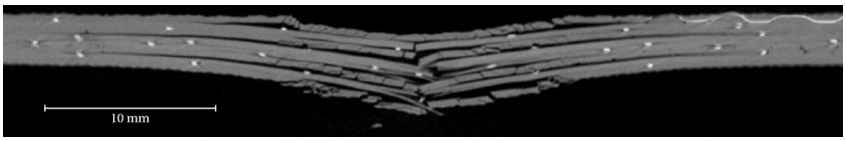

a) raw 2D CT slice

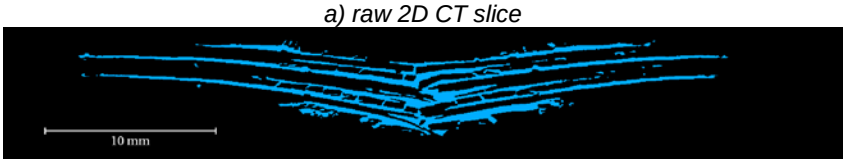

b) corresponding segmented damage

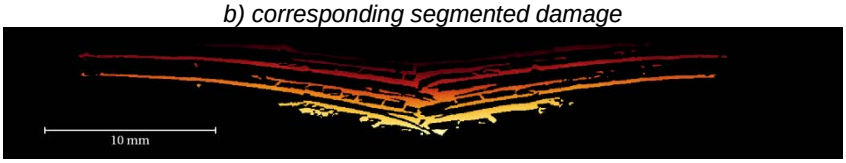

c) damage distance transform from impact face

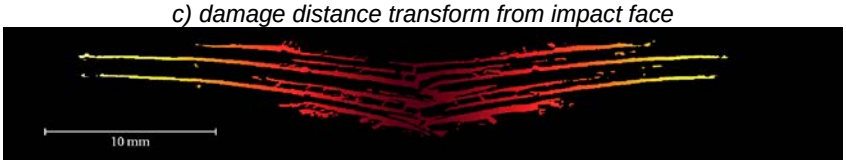

d) damage distance transfom from impact centre

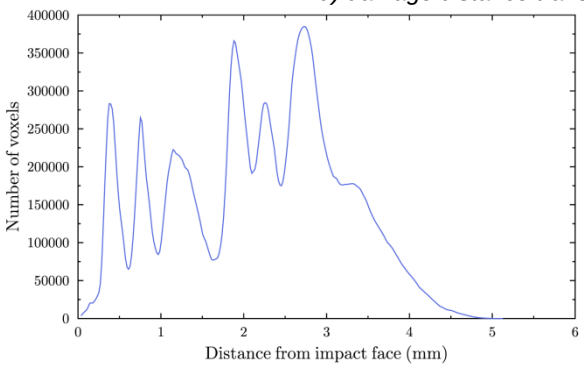

e) damage histogram from c) (impact face)

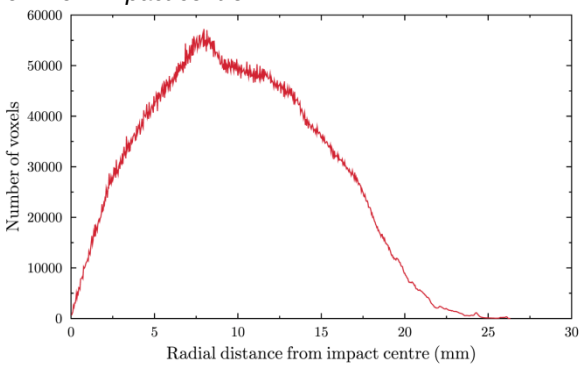

f) damage histogram from d) (impact centre)

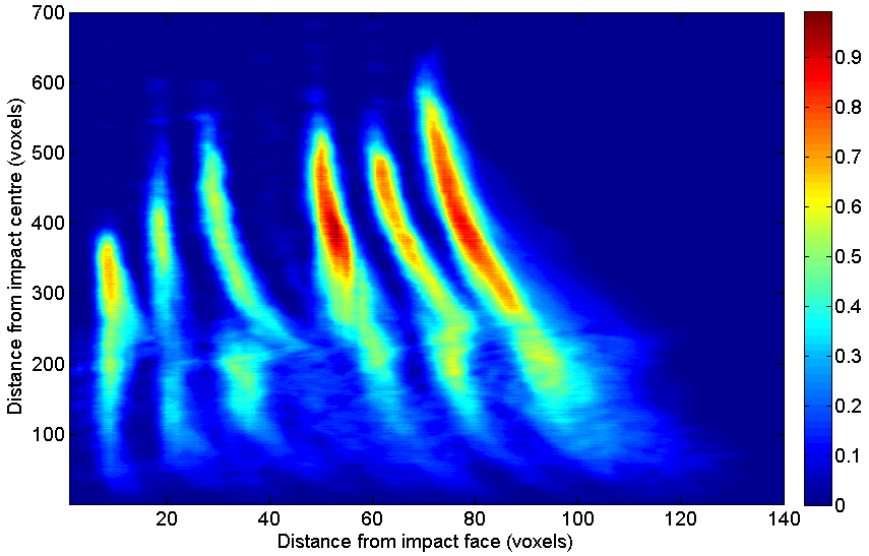

g) damage correlation map

Fig. 3. *Overview of CT data processing methodology for specimen tested at 15 J.*

Results

The *damage correlation map* approach proposed here, gives an improved representation of the impact damage occuring within the composite panel (comparison between Figure 3e and Figure 3g). Based on this map, the impact damage can also be segmented with better accuracy compared to the segmentation coming from the damage histogram approach (Figure 3e) as the panel distorsion is better accounted for. The resulting segmentation is given in Figure 4.

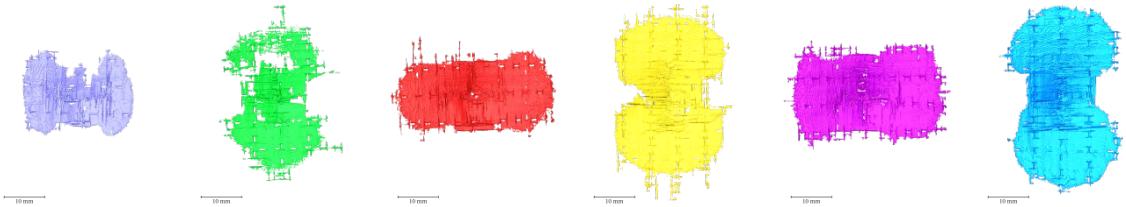

a) interface 1 *b) interface 2* *c) interface 3* *d) interface 5* *e) interface 6* *f) interface 7*

Fig. 4. *Ply-by-ply segmentatuion of impact damage for panel impacted at 15 J (interface numbers corresponding to those of Figure 1a).*

After ply-by-ply segmentation of the impact damage, quantitative data can be extracted for each individual ply, such as damage volume, maximum delamination legth and width, projected damage area *etc*.

Conclusions

Although CT is becoming an important tool for the characterisation of impact damage in fibre reinforced composite laminates, it is generally used only to obtain a qualitative visual measure. Advanced data processing methodologies, such as the one epresented here, are required to improve our ability to characterise impact damage and extract meaningful measurements from X-ray CT datasets. The separation of the impact damage ply-by-ply is needed to improve our understanding of the type (failure mode) and extent of the impact damage. This information is essential both in terms of understanding the capacity of the composite to absorb energy under impact and to predict the residual strength/capability of multi-directional composite laminates.

References

BS ISO 18352:2009 (2009). Carbon-fibre-reinforced plastics. Determination of compression-after-impact properties at a specified impact-energy level.

Léonard F., Stein J., Withers P.J., and Wilkinson A. (2013). 3D damage characterisation in composite impacted panels by laboratory X-ray computed tomography. **1st International Conference on Tomography of Materials and Structures.** Gent, Belgium.

Léonard F., Shi Y., Soutis C., Withers P.J., and Pinna C. (2014). Impact damage characterisation of fibre metal laminates by X-ray computed tomography. **Conference on Industrial Computed Tomography,** Wels, Austria.

Manchester X-ray Imaging Facility website (2012). Nikon Metris Custom Bay system specifications. http://www.mxif.manchester.ac.uk/index.php/nikon-custom-bay. Visited on the 21st November 2012.

Nikon Metrology website (2013). XT software suite specifications. http://www.nikonmetrology.com/en_EU/Products/Software/X-Ray-CT-Software/XT-Software-Suite. Visited on the 15th January 2013.

Prichard J.C. and Hogg P.J. (1990). The role of impact damage in post-impact compression testing. **Composites,** 21(6):503–511.

Richardson M.O.W., Wisheart, M.J.(1996). Review of low-velocity impact properties of composite materials**. Composites Part A: Applied Science and Manufacturing**, 27, 1123-1131.

Stein, J. and Wilkinson, A. (2012). The Influence of PES and Triblock Copolymer on the Processing and Properties of Highly Crosslinked Epoxy Matrices. **15th European Conference on Composite Materials (ECCM15)**.

Stein, J.(2013) Toughening of Highly Crosslinked Epoxy Resin Systems. PhD thesis, School of Materials, University of Manchester.

Visualization Sciences Group website (2012). Avizo Standard specifications. http://www.vsg3d.com/avizo/ standard. Visited on the 1st November 2012.

Session 205

A Computational Toolbox for the Data Processing Pipeline of Four-Dimensional Data from Phase Contrast X-ray Tomography

A. J. SHAHANI*[1], E. B. GULSOY[1], J. W. GIBBS[2], J. L. FIFE[3], X. XIAO[4], P. W. VOORHEES[1]

[1] Northwestern University, Evanston, IL 60208, USA – shahani@u.northwestern.edu, e-gulsoy@northwestern.edu, p-voorhees@northwestern.edu
[2] Los Alamos National Laboratory, Los Alamos, NM 87545, USA – jwgibbs@lanl.gov
[3] Swiss Light Source, Paul Scherrer Institut, 5232 Villigen, Switzerland – julie.fife@psi.ch
[4] Argonne National Laboratory, Lemont, IL 60439 USA – xhxiao@aps.anl.gov
* presenting author

Keywords: phase contrast, segmentation, computer vision, 4D materials science

Abstract

The growing size of data collected during X-ray computed tomography (XCT), typically on the order of terabytes, renders manual segmentation impractical. Furthermore, processing datasets acquired through phase contrast XCT is nontrivial due to the inherently low-pass characteristics of single image phase retrieval, which results in diffuse interfaces. To circumvent the problems in processing phase contrast images, we have developed a computational toolbox involving non-linear diffusion filtering and bias-corrected fuzzy c-means algorithm (BCFCM), thereby enabling the automated segmentation of such images. The computational toolbox also enables quantitative microstructural analysis of the segmented data, including the calculation of (i) interfacial normal distributions (INDs), the probability of finding an interfacial normal in a certain direction, (ii) interfacial shape distributions (ISDs), the probability of finding a patch of interface with a given pair of principal curvatures, and (iii) interfacial velocity. Using our integrated and fully automated approach, the three-dimensional coarsening morphologies of Al-Si and Al-Si-Cu alloys will be presented and discussed.

Introduction

Phase contrast X-ray tomography (PCT) enables the study of weakly absorbing samples, as well as systems consisting of elements with similar atomic numbers, e.g., Al-Si alloy. This is because the real part of the refractive index δ dominates over the imaginary part β in PCT experiments [1]. Robust segmentation and meshing of the PCT reconstructions is crucial for quantitative analysis of 3D structures, e.g., interfacial curvature and velocity measurements, as described in subsequent sections.

We propose an integrated and fully automated data processing pipeline following the collection of large datasets acquired through PCT, see Fig. 1: data are reconstructed using conventional filtered backprojection or time interlaced model based iterative reconstruction (TIMBIR) method; the latter innovation enables high spatial resolution (1μm) and high temporal resolution (1s) reconstruction, see Ref. [2] for details. While these methods apply principally to attenuation contrast datasets, Refs. [3-4] suggest that the attenuation and phase contrast images, collected at a single sample-to-detector distance in a PCT experiment, could be combined linearly in real space to achieve high contrast-to-noise ratio and high spatial resolution reconstruction. The "hybrid" images can then be robustly segmented using our suite of image processing procedures, which include diffusional filters and illumination corrections. These segmentation methods can be tailored for other tomography datasets with minimal sample-specific tuning. For subsequent analyses, the segmented structures are meshed, i.e., represented as a sequence of triangular patches and corresponding vertices along its surface. Then, in order to measure microstructural details, we determine the evolution of the orientation, curvature, and velocity of a patch of interface with time [5-6]. Such 4D analyses should provide unprecedented insights into microstructural evolution at the mesoscale.

Methods

Multimodal Reconstruction Technique

In propagation-based PCT, a phase map is commonly obtained by applying phase-retrieval algorithms to the X-ray projections. Then, filtered back projection is applied to these phase maps in order to recover the refractive index decrement δ during reconstruction. This two-step approach of phase-retrieval followed by backprojection will hereafter be referred to as PAG [7-8]. Automated segmentation of PAG images is nontrivial because the single image phase retrieval algorithms show inherently low-pass characteristics, which, in our study leads to diffuse interfaces. On the other hand, the one-step approach of using the filtered back projection algorithm (or the higher level TIMBIR method) to reconstruct the images directly from the traditional absorption-based projection images, collected at the same sample-to-detector distance, will be referred to as FBP. While FBP images offer sharp Fresnel interfaces compared to PAG images, the grayscale intensity levels of the components are very similar [3].

In our approach, we combine linearly in real space the PAG and FBP images, denoted μ_{PAG} and μ_{FBP}, respectively, to produce a hybrid PCT reconstruction μ_+ such that

$$\mu_+ = c_1 \mu_{PAG} + (1 - c_1)\mu_{FBP} \tag{1}$$

where $0 \le c_1 \le 1$. The hybrid reconstruction combines the strong contrast within the PAG image and the sharp interfaces observed in the FBP image; in other words, the FBP image is a natural source of image sharpening. In practice, we determine c_1 for our datasets by optimizing c_1 with respect to three image quality metrics: contrast-to-noise ratio, image sharpness, and power spectral density, see Ref. [3] for further details.

Segmentation of Hybrid Images

Our work aims to characterize the evolution of primary Si laths in an Al-Si system: this involves the removal of the smaller fluctuations in the matrix, which appear with the same intensity level as the primary Si laths and are a physical artifact resulting from the quenching process. In other cases, fluctuations arise due to Nyquist undersampling and ring artifacts during reconstruction. Blurring these fluctuations and enhancing the interfaces of the primary Si laths can be accomplished by using a nonlinear diffusion filter, such as the Perona-Malik (PM) filter [9], which can be applied on all 2D slices of a 3D dataset. The PM filtered image is obtained as the solution of the 2D diffusion equation, where the nonlinear diffusion coefficient D is defined as

$$D\left(\left|\nabla \mu_+\right|^2\right) = Exp\left(-\frac{\left|\nabla \mu_+\right|^2}{\kappa^2}\right) \tag{2}$$

and where μ_+ is the input hybrid image, ∇ is the spatial differential operator, and κ is the gradient threshold parameter. The PM model resembles forward diffusion for gradients whose absolute value is larger than κ, and backward diffusion for gradients smaller than κ, thereby effectively removing gradients due to small fluctuations [10].

Furthermore, we can use prior knowledge of materials structure to enhance semantically important interfaces. For instance, reconstructed Si platelets may appear rough on the mesoscale, due to the presence of speckle noise, when in fact they are crystallographically smooth along {111} [5]. For this reason, we can introduce anisotropy in the PM model by smoothing, in 3D, along the two directions of lowest grayscale fluctuations. The effect of this operation is to enhance coherent plate-like objects [10-11]. Once filtered, the images can be robustly segmented using conventional histogram-based segmentation methods, e.g., local thresholding.

Quantitative Microstructural Analyses

For the subsequent analyses, the digitized structures are meshed. The mesh consists of patches, where a "patch" is defined as a triangular surface with three vertices. Meshing binary data commonly introduces “wedding cake” artifacts to the structure; therefore, the meshed structure is smoothed by mean-curvature flow prior to processing [12]. Figs. 2(a-b) show a smooth mesh generated from binary data of a sphere, where patches are colored gray and patch edges are black.

To measure the localized evolution of the microstructure, we can measure patch curvature as a function of time using the following procedure. The minimum and maximum principal curvatures of the interface are denoted κ_1 and κ_2 such that $\kappa_2 \geq \kappa_1$. Principal curvatures κ_1 and κ_2 are determined by fitting to each patch and its first through third order nearest neighbor vertices a conic section f(x,y) of the form

$$f(x,y) = ax^2 + by^2 + cxy + dx + ey + f \tag{3}$$

with respect to the local coordinate system (x,y) of the patch. The eigenvalues of the two-by-two second derivative matrix of f(x,y) are then equal to κ_1 and κ_2 [13]. An example of this fitting procedure is shown in Figs. 2(c-d) for a spherical particle. This process is repeated for all patches in the ROI. Once principal curvatures are determined, the curvature space can be visualized by constructing an ISD, which is a bivariate histogram of κ_1 versus κ_2 [14]. However, we display the polar representation of κ_1 versus κ_2, hereafter referred to as S versus C space, where S represents the angular coordinate and C is the radial coordinate [5,15]. The major advantage of this representation is that characteristic shape and length are decoupled: S specifies shape independently of length scale, whereas C specifies the characteristic length. Patches have a concave shape with respect to the matrix phase when $S < 0$, a saddle shape when $S = 0$, and a convex shape when $S > 0$. For a planar patch, S is indeterminate while $C = 0$.

Similarly, interfacial velocity V can be determined using patch vertex positions. For each mesh vertex at time n, the corresponding nearest neighbor vertex in the mesh at time n+1 can be found via k-NN algorithm, described elsewhere [16]. The distance between a vertex at time n and its nearest neighbor at time n+1 can then be used to calculate interfacial velocity. This method assumes that the meshes have sufficiently high vertex density such that velocity vectors are in the direction of the interface normal.

Results and Discussion

The discussed data processing pipeline was applied to recent data collected at the Advanced Photon Source beamline 2-BM at Argonne National Laboratory. Figs. 3(a-c) show three reconstructions, at the indicated timesteps, during the isothermal coarsening evolution of Si particles in an Al-32wt%Si-15wt%Cu alloy at 750°C. The Si particles are orange and the liquid is transparent. Qualitatively, the increase in size scale of the structure is consistent with a coarsening process [3,5-6].

The ISDs corresponding to these three timesteps are given in Figs. 3(d-f). To compare the three timesteps, we scale the C axis by the surface area per unit volume, S_v, which is a time-dependent length scale. These results indicate quantitatively that the initially faceted structure with $C \approx 0$ in 3(d) becomes increasingly rounded in time with $S > 0$ and $C > 0$ in 3(f). Furthermore, we calculate the 3D probability space P(S,C,V) for these three timesteps, in order to determine the relationship between curvature and velocity, see Fig. 3(g-i). At early times, planar patches with near-zero velocity are highly probable, whereas curved patches with high velocity dominate the microstructure at later times. These quantitative snapshots of the realtime interfacial dynamics in the Al-Si-Cu system are made possible due to algorithmic advances in reconstruction, segmentation, and microstructural analysis. The developed toolbox has the potential to further the previously not possible quantification of 4D phase contrast based tomographic datasets.

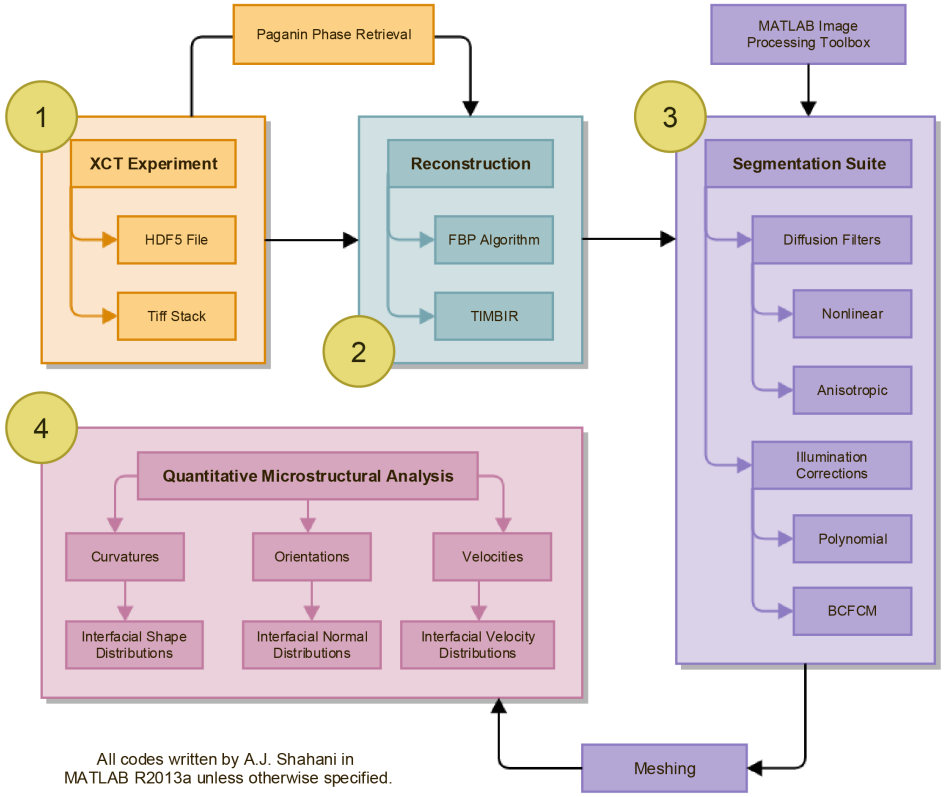

Fig. 1. *Flow chart depicting the data processing pipeline following (1) XCT experiment: (2) data are reconstructed using conventional FBP or higher level TIMBIR algorithm [2]; then, (3) reconstructions are segmented to determine accurately the location of interfaces; these interfaces are meshed, or represented as a sequence of triangle faces and vertices for (4) quantitative microstructural analyses, which include the determination of interfacial curvatures, orientations, and velocities.*

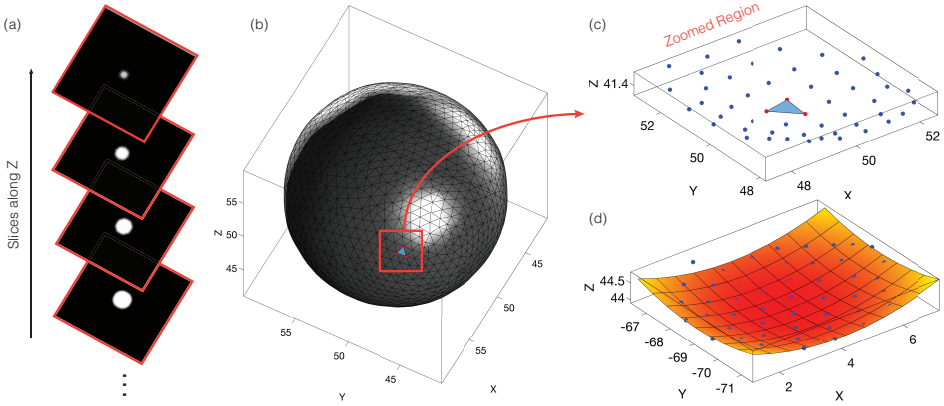

Fig. 2. *Example of curvature calculation on a spherical particle, showing (a) segmented 2D slices of 3D dataset along one dimension (e.g., axis of rotation in XCT); (b) smooth mesh generated from segmented slices, where blue patch represents the patch of interest and red datapoints are its vertices; (c) zoomed region of the patch where dark blue data points are first- through third-order mesh vertex neighbors; (d) fitting of these datapoints to a conic section allows for the determination of principle curvatures.*

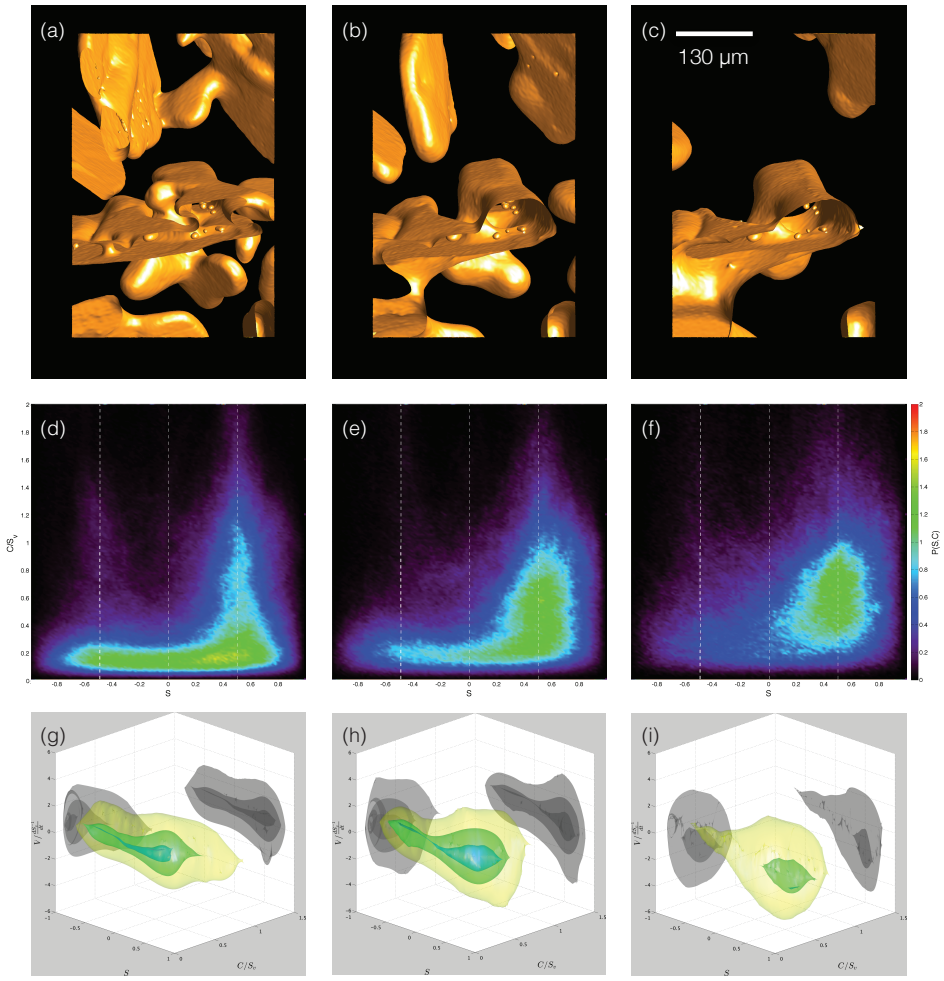

Fig. 3. *Application of microstructural analyses to the coarsening evolution of Si laths in an Al-Si-Cu liquid at 750°C. Structure is reconstructed after coarsening for (a) 1495s, (b) 5889s, and (c) 12566s. (d-f) ISDs of the reconstructions in (a-c), respectively. (g-i) Isosurfaces of the 3D probability space P(S,C,V) where the dark green surface represents P=60%, yellow-green is P=40%, yellow is P=20%, and gray is the projection of the 3D surfaces onto the 2D planes C-V and S-V. C and V axes scaled by S_v^{-1} and dS_v^{-1}/dt, respectively.*

References

[1] Cloetens P., Barrett R., Baruchel J., Guigay J.P. & Schlenker M. (1996). Phase objects in synchrotron radiation hard x-ray imaging. ***J. Phys. D Appl. Phys.*** 29, 133-146.

[2] Gibbs J.W., Mohan A.K., Gulsoy E.B., Shahani A.J., Xiao X., DeGraef M., Bouman C., & Voorhees P.W. (2015). The three-dimensional morphology of growing dendrites. ***Sci. Rep.,*** submitted.

[3] Shahani A.J., Gulsoy E.B., Gibbs J.W., Fife J.L., & Voorhees P.W. (2014). Integrated approach to the data processing of four-dimensional datasets from phase contrast X-ray tomography. ***Opt. Express*** 22, 20: 24606-24621.

[4] Lovric G., Barré S.F., Schittny J.C., Roth-Kleiner M., Stampanoni M., & Mokso R. (2013). Dose optimization approach to fast X-ray microtomography of the lung alveoli. ***J. Appl. Cryst.*** 46, 4:856-860.

[5] Shahani A.J., Gulsoy E.B., Roussochatzakis V.J., Gibbs J.W., Fife J.L. & Voorhees P.W. (2015). The dynamics of coarsening in highly anisotropic systems: Si particles in Al-Si liquids. ***Acta Mater.,*** submitted.

[6] Shahani A.J., Xiao X., & Voorhees P.W. (2015). In-situ synchrotron tomographic investigation of the coarsening evolution of Al-Si-Cu Alloy. ***J. Mater. Sci. A,*** in preparation.

[7] Paganin D., Mayo S.C., Gureyev T.E., Miller P.R., & Wilkins S.W. (2002). Simultaneous phase and amplitude extraction from a single defocused image of a homogeneous object. ***J. Microsc.*** 206, 1: 33-40.

[8] Burvall A. (2011). Phase retrieval in X-ray phase-contrast imaging suitable for tomography. ***Opt. Express*** 19, 11: 10359-10376.

[9] Perona P. & Malik J. (1990). Scale space and edge detection using anisotropic diffusion. ***IEEE Trans. Pattern Anal.*** 12, 629-639.

[10] Jähne B. & Haussecker H. (2000). Computer vision and applications. Academic Press.

[11] Weickert J. (1994). Anisotropic diffusion in image processing. Teubner-Verlag.

[12] Desbrun M., Meyer M., Schröder P., Barr A.H. (1999). Implicit fairing of irregular meshes using diffusion and curvature flow. ***SIGGRAPH '99*** 26, 317-324.

[13] Kühnel W. (2003). Curves, surfaces, and manifolds. Am. Math. Soc.

[14] Kammer D. & Voorhees P.W. (2006). The morphological evolution of dendritic microstructures during coarsening. ***Acta Mater*** 54, 6: 1549-1558.

[15] Koenderink J. & van Doorn A. (1992). Surface shape and curvature scales. ***Image Vision Comput.*** 10, 8: 557-564.

[16] Altman N.S. (1992). An introduction to kernel and nearest-neighbor nonparameteric regression. ***Am. Stat.*** 46, 3:175-185.

Advanced Noise-Reduction and Segmentation Methods in X-ray Computed Micro-Tomography

J. C. E. Mertens[1], S. S. Singh[1], J. J. Williams[1], P. Hruby[1], *A. Kirubanandham[1], X. Xiao[2], F. De Carlo[2], N. Chawla[1]

[1] Materials Science and Engineering, Arizona State University, Tempe, AZ 85287-6106, USA
[2] Advanced Photon Source, Argonne National Laboratory, Argonne, IL, USA

The study of the structure of materials has been traditionally limited to two dimensional (2D) analyses. This approach is often inaccurate or inadequate for solving many problems. Therefore, there has been an increasing demand for three dimensional (3D) analyses [1, 2]. Moreover, experiments can be performed to resolve time-dependent (4D) evolution of a variety of important phenomena such as fatigue, and stress corrosion cracking (SCC) [3]. Among these volumetric techniques, X-ray tomography and serial sectioning have been used to characterize microstructure in 3D/4D with high spatial resolution.

We have performed X-ray tomography (using the synchrotron source at the Advanced Photon Source at Argonne National Laboratory and a lab-scale x-ray source at Arizona State University) and serial sectioning to characterize the microstructure evolution of several metallic materials under a mechanical stimulus. A key aspect of microstructural data extraction and quantification from metallic tomograms involves the accurate segmentation of the resolved phases. Prior to applying segmentation methods in a raw or grayscale volume, the application of filtering for noise reduction is often critical, either due to the low signal typically achieved in microfocus x-ray imaging or very rapid synchrotron x-ray imaging, particularly in metallic systems. Noise reduction algorithms which have proven particularly effective in noisy metallic tomograms include the anisotropic diffusion, edge-preserving smoothing, and non-local means filters. These may be applied either volumetrically or slice-by-slice. The most effective segmentation method has been observed to vary depending on the contrast mode of the tomography (ex. x-ray phase vs. attenuation contrast modes), the nature of the sample, and the nature of the material phases of interest in multi-phase systems. Segmentation approaches that have been successful include semi-automatic techniques which leverage both the intensity and intensity gradients within volume.

An exemple of where raw data processing and rigorous segmentation methods are critical is in lab-scale x-ray computed tomography. A eutectic lead-tin solder volume of approximately 500 μm in diameter has been studied with a custom lab-scale x-ray computed tomography imaging system, with the goal of volumetrically quantifying lead-rich dendrites which form as a result of non-equilibrium solder solidification during reflow [4]. In the implemented CT system, a microfocus x-ray source is used for obtaining volumetric datasets with spatial resolution near 1 micrometer. In general, to obtain the highest resolution in a MicroCT system, the necessity of a minimized focal spot size at the x-ray producing target has been demonstrated [5]. In order to reduce the focal spot size in microfocus x-ray sources, very low target power is required, that is, for a given accelerating voltage the electron beam current must be very low. The result of this compromise is observed in high resolution lab-scale reconstructions which possess a very low signal-to-noise ratio, especially when compared with reconstruction volumes from imaging with a high intensity x-ray beam generated at synchrotron facility, such as the 2BM beamline at the Advanced Photon Source at Argonne National Laboratory. Apart from the relatively low signal generally observed in lab-scale x-ray CT, imaging artifacts in the reconstruction volume may also occur as a result of imaging with a polychromatic x-ray beam, such as beam hardening induced intensity cupping in the reconstruction planes [4]. As a result, before any analysis was performed on

the solder lab-scale CT reconstruction volume, it was necessary to treat the imaging data for artifact reduction and for noise filtering. Several processing steps have beneficial.

The first step in processing the reconstruction volume for feature segmentation was noise reduction. In other lab-scale CT reconstruction data, the SNN filter and the Non-Local Means filter have been preferred for fine feature preservation while reducing noise. In processing the 500μm lead-tin sample's volume reconstruction, a three-dimensional Gaussian filter was implemented due to the relatively 'large' dendrite features being targeted in terms of the number of voxels that were sampling any given dendrite. Yet, beam-hardening induced intensity cupping across the sample cross sections was still present after noise filtering. A beam-hardening artifact reduction algorithm was constructed which was used to de-convolute the signal of the targeted features from the cupping artifact and has proven effective in a multi-component system. The algorithm is applied with no knowledge of sample composition or geometry. The beam-hardening cupping effect is treated in each reconstruction plane. The algorithm requires an input of the raw data along with a mask of the material where cupping is observed. The mask is used to calculate a Euclidean Distance Map (EDM) of the material. The mean intensity value for all voxels with a similar value in the EDM in the cross section is used to scale down the raw data intensity for these voxels according the mean intensity value at the center as shown in Figure 1. The result is a cross section with greatly reduced intensity cupping, enabling segmentation.

Even after noise and artifact reduction, automatic segmentation methods may fail, particularly in the case of low contrast features, as was the case for the lead-rich dendrites within a lead containing solder phase. To capture the lead-rich dendrites, a semi-automatic approach, 3D region grow, was implemented. For 3D region grow segmentation of the dendrites, the center of each dendrite was manually selected, in other words, the 3D coordinates of part of the feature were input. The selection was then allowed to grow into surrounding voxels under an intensity range criterion: If surrounding voxels had an intensity value within the input range, then the voxels were included in the selection. A visual representation of the segmentation result is shown in both 2D and 3D in Figure 2, where by relaxing the intensity range criterion, more and more voxels were included in the dendrite segmentation. It can be seen in Figure 2(d) that nearly all of the dendrite was included in the selection at the corresponding intensity range input, but by relaxing the range too much, as shown in Figure 2(e), the selection can impinge into the surrounding material. Thus, for this example, the intensity range used for segmentation corresponded to the result shown in Figure 2(d). The final result for the entire volume is shown in Figure 3(a).

For other samples and imaging modes different image processing and segmentation routines have been used. X-ray synchrotron tomography was performed to understand the microstructure (Figure 3(b)) and the SCC and fatigue behavior of 7075 aluminum alloys (Figure 3(e)) [6-8] and Al-SiC composites (Figure 3(d)) [9]. Also, serial sectioning has been performed with Electron Back Scattered Diffraction (EBSD) to study the 3D crystallography of grains in lead-free solders using Orientation Image Mapping (OIM) (Figure 3(c)). The use of noise filtering and segmentation techniques (primarily from within the Avizo® Fire package) that have proven critical in the volumetric study of metallic systems.

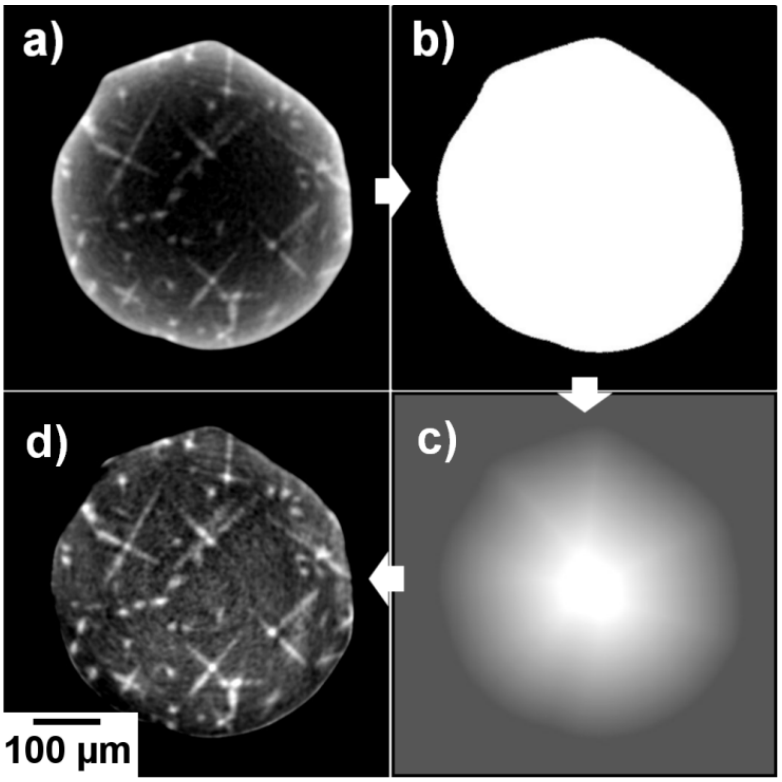

Fig. 1 A µXCT reconstruction plane through the center of a reconstructed near-eutectic composition lead-tin solder (a) Exhibiting a beam-hardening intensity cupping artifact (b) A segmented image of the beam-affected phase (c) An EDM from the mask, and (d) The beam-hardening cupping corrected plane.

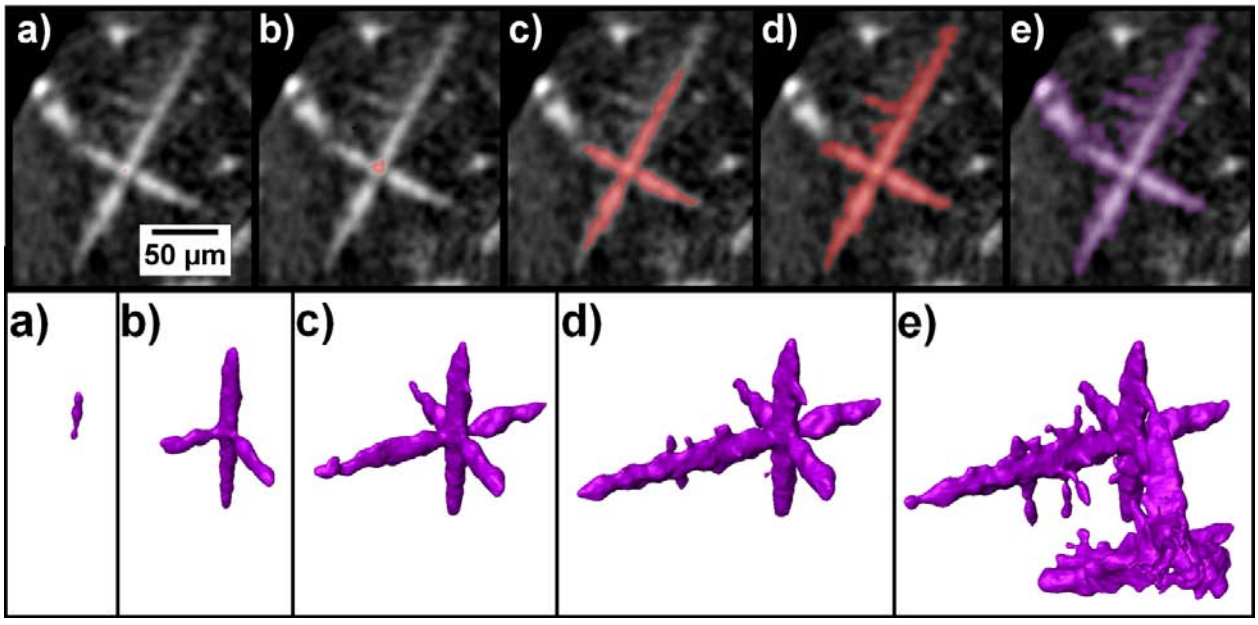

Fig. 2 Demonstration of the 3D region growth segmentation of a single lead-rich dendrite from a lab-scale µXCT dataset in 2D representation (*upper*) and 3D representation (*lower*) where the selection was seeded at the user-perceived dendrite center, and the selection's intensity range was increased (a-e).

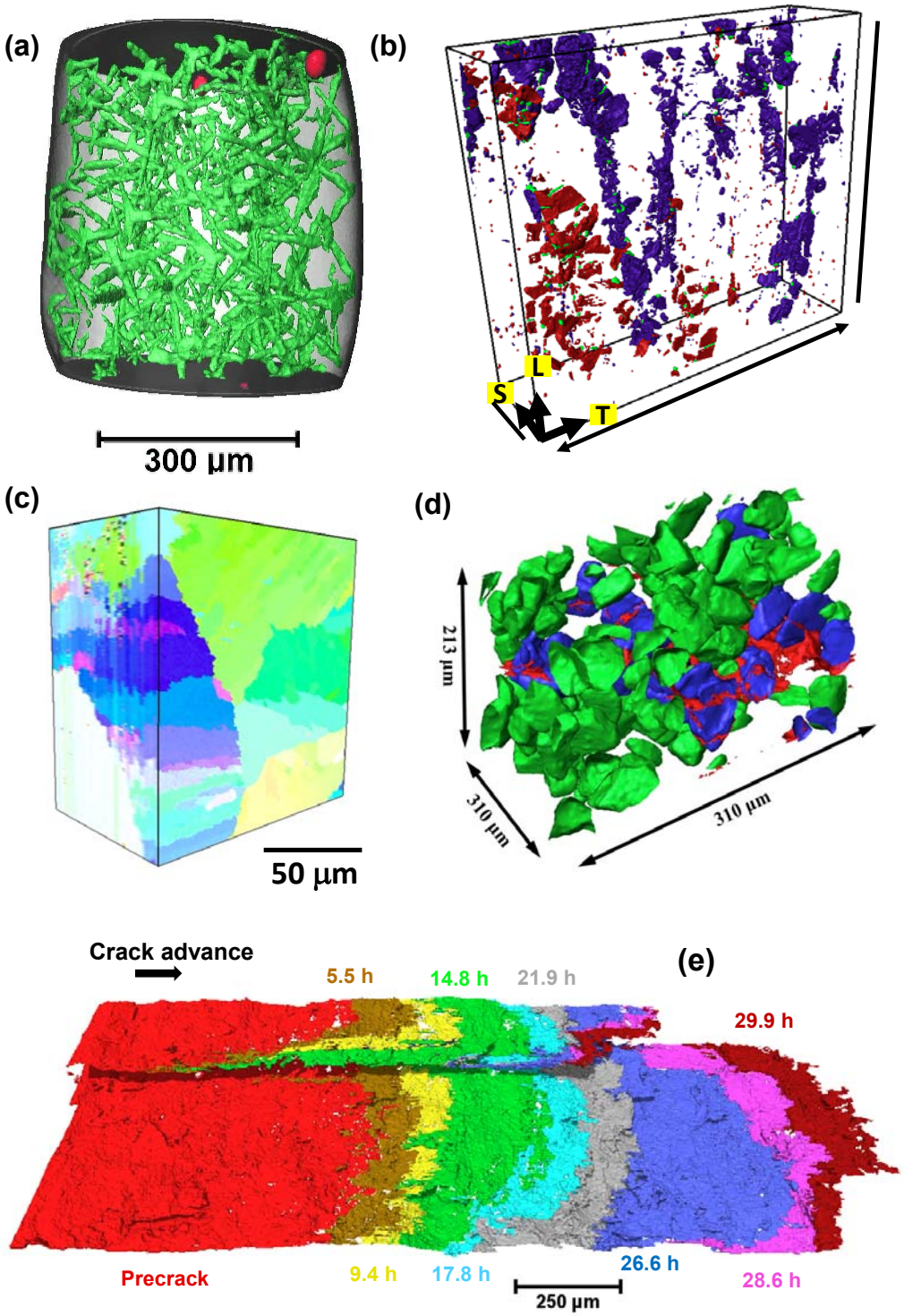

Fig. 3: (a) Lead-rich dendrites in a eutectic Pb-Sn solder alloy, (b) Inclusions and pores in AA7075, (c) A 3D EBSD OIM of grain structure in a pure tin solder, (d) A fatigue crack interaction with SiC particles in an Al-SiC composite, and (e) SCC crack in AA7075 in moisture.

References

1. S.S. Singh, C. Schwartzstein, J.J. Williams, X. Xiao, F. De Carlo, N. Chawla. J. Alloys Compounds, 602 (2014) 163-174.

2. J. C. E. Mertens, J. J. Williams, N. Chawla. Mater. Charact., 92 (2014) 36-48.

3. S.S. Singh, J.J. Williams, P. Hruby, X. Xiao, F. De Carlo, N. Chawla. Integr. Mater. Manufac. Innov., 3 (2014) 9.

4. J.C.E. Mertens, J.J. Williams and N. Chawla. Journal of Electronic Materials 43, 12 (2014) 4442-4456.

5. M.J. Flynn, S.M. Hames, D.A. Reimann, S.J. Wilderman. Nuclear Instruments and Methods in Physics Research Section A. 353, 1(1994) 312–315.

6. S.S. Singh, J.J. Williams, M. Lin, X. Xiao, F. De Carlo, N. Chawla. Mater. Res. Let. 2 (2014) 217-220

7. S. S. Singh, J. J. Williams, X. Xiao, F. De Carlo, N. Chawla. Fatigue of Materials II: Advances and Emergences in Understanding, Mater. Sci. Tech. (2012) 17-25.

8. J. J. Williams, K. E. Yazzie, E. Padilla, N. Chawla, X. Xiao, F. De Carlo. Int. J. Fatigue, 57 (2013) 79-85.

9. P. Hruby, S.S. Singh, J.J. Williams, X. Xiao, F. De Carlo, N. Chawla. Int. J. Fatigue, 68 (2014) 136-143.

Upgraded ID01 @ ESRF: nanodiffraction, full field diffraction microscopy and coherent diffraction imaging

P. BOESECKE[1], G. BUSSONE[1], G. A. CHAHINE[1], H. DJAZOULI[1], M. ELZO[1], S. FERNANDEZ[1], R. GRIFONE[1], J. HILHORST[1], R. A. HOMS-REGOGO[1], *S. J. LEAKE[1], M-I. RICHARD[1], AND T. U.SCHÜLLI[1]

[1] ESRF – The European Synchrotron, 71 Avenue des Martyrs, Grenoble, 38000, France – E-mail
* presenting author

Keywords: nanodiffraction, coherent imaging, diffraction microscopy

Abstract

With the completion of the first phase of upgrade of the European Synchrotron Radiation Facility (ESRF), the ID01 beamline has returned successfully to user operation. We offer; scanning diffraction microscopy at 100Hz with 100nm focused x-ray beams [1], full field x-ray diffraction microscopy using compound refractive lenses [2] and coherent beams for coherent diffractive imaging applications [3].

The implementation of the future upgrade of the storage ring [4] and beamline will amplify data rates by a factor of 100 or more. The need for a generic set of tools (ideally inter-synchrotron compatible) is clear given such a data deluge and to make such techniques routinely available to non-expert users. The emphasis from ID01 is to collaborate to generate a framework of such tools to avoid continuously reinventing the wheel.

A detailed breakdown from the data analysis perspective of the existing bottlenecks for all techniques will be provided from both the current and the future decade perspective. In addition the existing data flow from experiment to publication will be discussed.

Introduction

The ESRF upgrade programme, in the first phase (Phase I), has realised a new generation of beamlines for the exploitation of intense, reliable and stable x-ray nano-beams. The second phase (Phase II) will see the upgrade of the source in parallel with normal user operation until mid-2018. The implementation of a new 7-Bend Achromat lattice will decrease the horizontal emmittance by a factor of 30 leading to gains in both brilliance and coherence of the photon beam particularly at harder x-ray energies.

The ID01 beamline upgrade is part of the new generation of beamlines. Its goal being to combine x-ray diffraction with both coherent and/or nano-focused beams, and established scanning probe microscopy methods. The long beamline (118m source to sample) delivers x-ray beams in the energy range (4-45keV) in small focal spots (100nmx100nm) and encompasses two end-stations. The first employs Fresnel zone plate optics to achieve a tight focus on a sample position located on a 3+2S diffractometer, the detection system being a Maxipix (2x2). The second uses a sample position suited to in-situ studies, around which a 6.5m evacuated flight tube, enclosing a scintillator based fiber coupled scmos, capable of in plane rotation up to 93°. Here a series of compound refractive lens can be used to tailor the focal spot size from a typical 5x1mm at the sample position down to imaging the source, of the order 150x25 microns (horizontal and vertical respectively).

In the near future the detection system will be upgraded to a 1M pixel detector with sub millisecond time resolution and additional KB mirror optics introduced for achromatic focusing with higher efficiency.

Methods

The experimental methods available at ID01 include:

Nanodiffraction mapping (K-map) employs a nano-focused x-ray beam, the sample is scanned continuously using piezo motors and the 2D detector triggered at regular intervals. A typical 100micronx100micron map with 500nm intervals and 10ms exposure takes 7 minutes and generates data rates of up to 10Tb/day. To distinguish tilt (10^{-3}) and strain (10^{-5}) through the determination of peak position and shape, respectively, typically a 3D reciprocal space map is taken via the rocking curve approach. The XSOCS software package [2] was developed to handle the 5D data generated and produces two-dimensional real space maps of both strain and tilt distributions. An example is shown in Fig.1, a focused ion beam was used to pattern the ESRF logo in a SiGe layer, here the underlying remnant Si strain (a) and tilt (b) distribution are mapped.

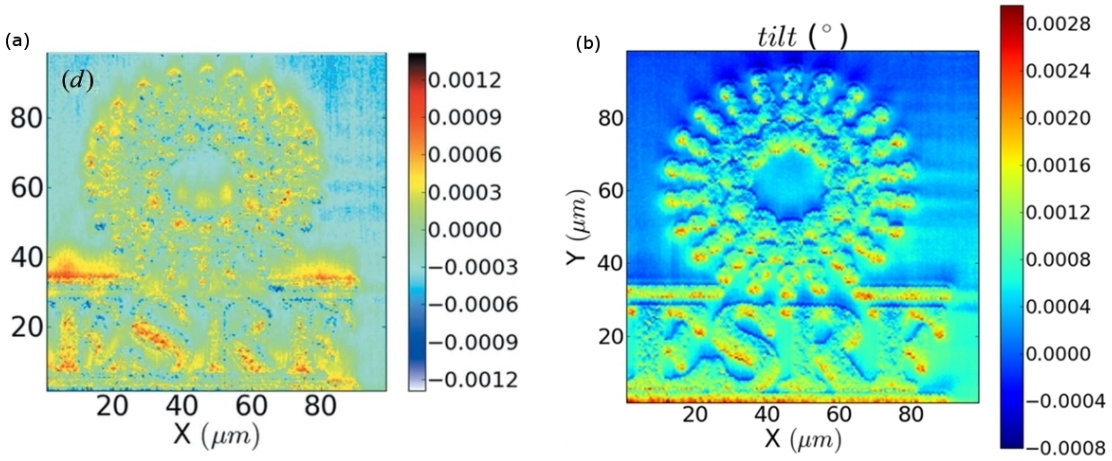

Fig. 1. *Nanodiffraction strain and tilt maps from an ESRF logo FIB etched into a SiGe layer on Silicon.*

Full field diffraction microscopy directly images the sample using compound refractive lenses between the sample and detector. The advantage being a large area (~100x100um) is imaged in a single exposure paving the way for in-situ studies, but has the caveat of limited resolution (~100nm). An example is shown in Fig.2, here 5 images from different positions on the rocking curve imaged directly. Similar information obtained in the k-map described previously in Fig.1 are obtained, the only caveat being the strain and tilt cannot be separated. The distinct advantage being one can measure a full rocking curve in minutes allowing the study of surface or interface dynamics for processes such as catalysis or growth.

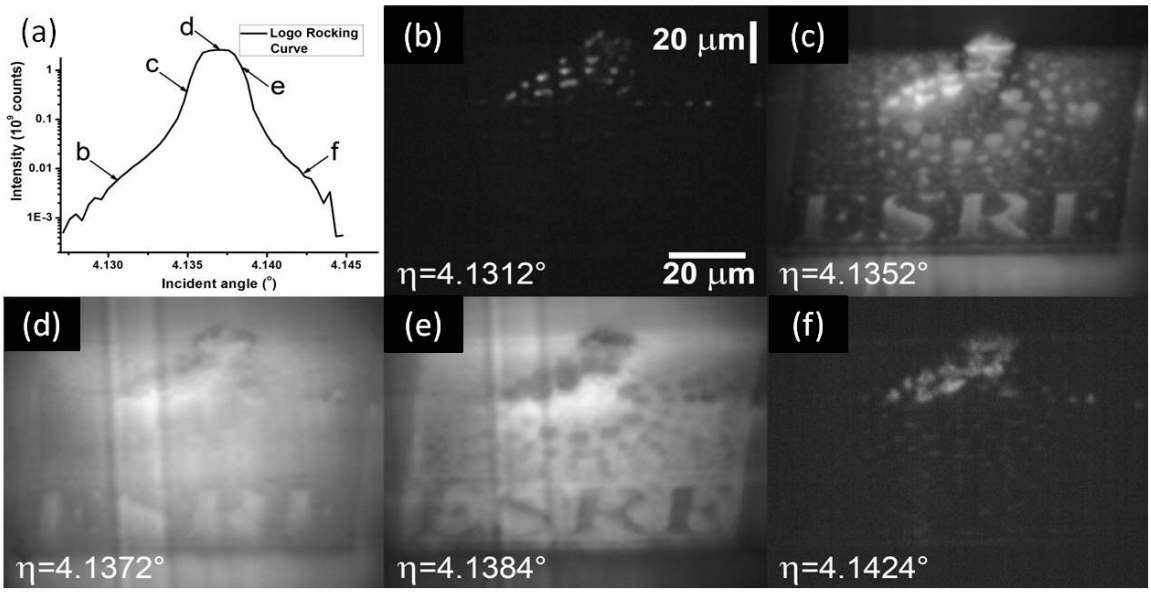

Fig. 2. *Full field diffraction microscopy*

Coherent diffraction can be employed using two methods in the bragg geometry, firstly, where the beam is larger than sample and secondly, where the sample is larger than beam, normally referred to as ptychography. Here, a 3D reciprocal space map is collected but the incident beam is coherent, thus inversion of the diffracted intensity leads recovers the shape of the object and its internal displacement field. The method is flux limited, as only the coherent part of the beam is used (typically <0.1% at synchrotrons) and thus generates relatively low data rates. The major bottleneck is encountered in the analysis stage where the lenless imaging method replaces the lens with a computer. The methods employed suffer several shortfalls and often need to be tailored to each individual dataset, the reprecussions are delays to publication measured in years rather than months, the stagnation of data and the availability of the techniques only to expert user groups. The end goal is to bring such analysis live to an inexperienced user on the beamline in time for the expected data increases courtesy of the ESRF Phase II upgrade. An example is shown in Fig.3, a typical coherent diffraction pattern (a) obtained from a GaN microrod (b), the phase retrieved displacement field demonstrates the expected domain structures separated by inversion domain boundaries.

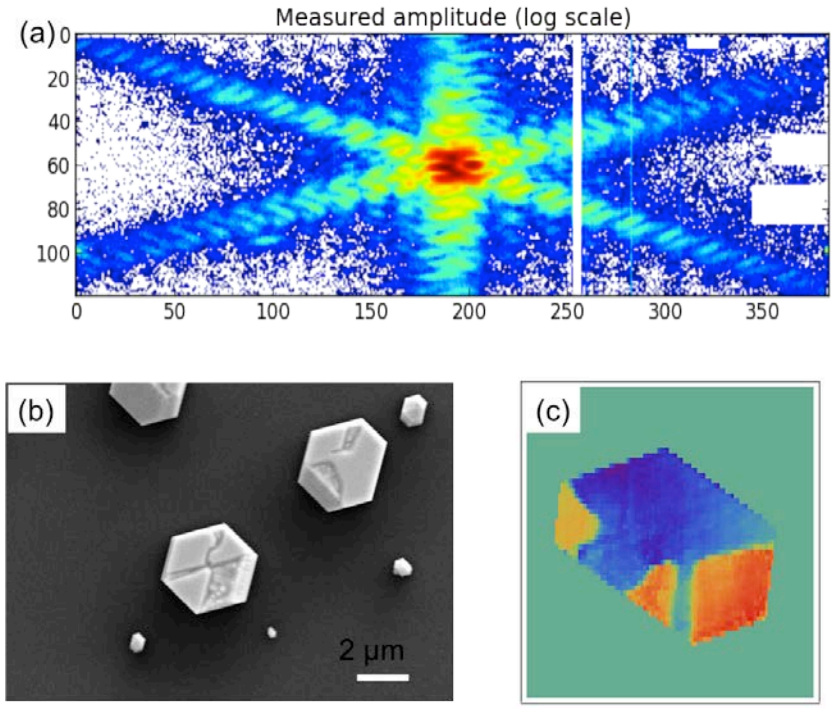

Fig. 3. *(a) Coherent diffraction pattern obtained from a GaN microrod, (b) topview SEM image of the domain structure present in microrods, due to differing polarity, (c) the phase retrieved displacement field obtained from (a) demonstrating dimain structures in the cross section of the microrod*

A summary of the state of the analysis tools for principal modes of operation at ID01 is shown in Table.4.

	Nanodiffraction	***Full Field Microscopy***	***Coherent Diffractive Imaging***
Live Analysis	***NO***	***YES***	***NO***
User input	***minimal***	***minimal***	***significant***
Automation	***feasible***	***YES***	***difficult***
Existing public frameworks	***YES***	***YES***	***few - poorly maintained***
Post processing tools	***YES***	***YES***	***few - poorly maintained***
Lead time to publication	***weeks***	***days***	***Years +***
Availability to non-expert users	***YES***	***Commissioning NOW***	***NO***

Fig. 4. *Summary of data analysis framework present for all technqiues at ID01.*

References

[1] G. A. Chahine, M.H. Zoellner, M-I. Richard, S. Guha, C. Reich, P. Zaumseil, G. Capellini, T. Schroeder and T. U. Schülli, ***Applied Physics Letters***, 106, 071902 (2015)

[2] XSOCS software package, http://sourceforge.net/projects/xsocs/

[3] J. Hilhorst, F. Marschall, T.N. Tran Thi, A. Last and T. U. Schulli***, J. Appl. Cryst.*** 47, 1882-1888. (2014).

[4] S. T. Haag, M-I. Richard, U. Welzel, V. Favre-Nicolin, O. Balmes, G. Richter, E. Mittemeijer and O. Thomas, ***Nano Lett.,*** 13 (5), 1883–1889 (2013)

[5] ESRF: Phase II - white paper (http://www.esrf.eu/files/live/sites/www/files/about/upgrade/documentation/whitepaper-upgrade-phaseII.pdf)

Tomography activities at Advanced Photon Source

XIANGHUI XIAO[1, *]

[1] Advanced Photon Source, Argonne National Laboratory – xhxiao@aps.anl.gov
* presenting author

Keywords: dynamic tomography, image analysis

Abstract

The non-destructive nature of X-ray tomography makes it a suitable tool in *in situ* dynamic phenomena studies. At APS, X-ray tomography has seen rapid growth in the past few years and it is spreading to multiple beamlines. In tomography applications image analysis is a key component in extracting quantitative structure information and further structure based modeling. Along with data complexity increase the image analysis tasks also increases and specific image analysis routines need to be designed according to the given data sets. This presentation will review all the aspects of tomography/imaging works. A general discussion on tomography/imaging workflow is given on the end.

Introduction

The non-destructive of X-ray tomography makes it a suitable tool *in situ* dynamic phenomena studies. On one hand, X-ray penetration power enables capability to look deeply into a sample, even which is enclosed in certain environment control devices. On another hand, the weak interaction between X-ray and matters provides minimum interruption to a sample system, which is critical to *in situ* type experiments. In the recent years, along with improved CMOS imaging camera technique developments, dynamic tomography has seen rapid growing in applications in biology [Moosmann 2013, Walker 2014], material science and engineering [Lemodin 2009, Terzi 2010, Gibbs 2015, Cordes 2015], geosciences [Fusseis 2012, Chaouachi 2015].

Methods

In *in situ* experiments, it is usually necessary to trade off between spatial resolution and temporal resolution. This is because of the limiting factors, e.g. radiation control to a sample system, available X-ray flux, or software/hardware constrains. For instance, in the living embryo imaging by Moosmann et al [Moosmann 2013], both radiation control and available flux played roles in determining the experimental conditions. On one hand, total dose and dose rate had to be controlled below certain level to have a living embryo develop naturally in a time duration. On another hand, the spatial and temporal resolutions had to be high enough to catch each individual cell motion without visible artifacts due to the structure evolution during a scan. The experimental solution accounting these two requirements was to use relative high energy X-ray and phase contrast in the tomography measurements. High-energy X-rays have weaker interaction with matters so the disturbance to the embryos is less fatal. Phase contrast facilities resolving cell level structure details even with high-energy X-rays. The detail discussion on the experimental condition determination can be found in the ref [Moosmann 2014].

It is noticed that the signal-to-noise ratio (SNR) in the measurements of above experiments is relatively lower than that in typical static type measurements. This is a general feature in dynamic tomography applications in which it is either photon starving or photon sicking. This imposes hardship in tomographic reconstructions. One solution is to maintain relative good SNR in each individual projection images but reduce the total

number of projection images. Aiming to the embryo imaging applications, Hofmann and his collaborators adapted iterative reconstruction technique with total variation (TV) regulation and developed a technique for finding optimal relaxation parameter to the TV term [Yang 2015]. In the TV regulated iterative tomographic reconstructions, it however does not count the signal statistics models. By accounting the signal statistics models it is possible to further reduce SNR requirements in the each individual projection images. Mohan et al developed a novel time-interlaced model-based iterative reconstruction technique (TIMBIR) [Mohan 2015]. In this approach the signal statistics models in both time and space domain are utilized in the iterative reconstructions. Therefore it can take data with significant lower SNR than that with typical static measurements and very few projection images. With this novel reconstruction technique and the corresponding scan scheme, Gibbs et al studied Al/Cu three-dimensional morphology evolution of growing dendrites with dynamic tomography [Gibbs 2015].. To catch the fast dendrite growth, the exposure time was traded off to ensure relatively fast camera operation rate. They demonstrated that it is possible to reconstruct time series of 3D structure with only 125 projection images at one time point. Compared to conventional algebraic tomography reconstruction techniques, e.g. filtered-back-projection algorithm, TIMBIR enables dynamic tomography measurements of much higher temporal resolution.

As in all other imaging applications, image analysis is a critical and challenging component in quantitative imaging applications. Although there are commercial and free image analysis software programs available, it is not uncommon that tools from few different packages are needed for a specific task. It is also often that some customized tools and routines need to be developed in many cases. In the living embryo imaging work by Moosmann et al [Moosmann 2013, Moosmann 2014], few software programs, XFlow[software under development at KIT], ImageJ/Fiji[http://rsbweb.nih.gov/ij/, http://fiji.sc/], Amira [http://www.vsg3d.com/], and Paraview [http://www.paraview.org/], were used in analyzing cells' motion based on the time series tomography of embryos. In the bundle of the programs, XFlow is customized toolbox for optical flow field computation and motion analyses, developed by Hofmann group. In the dendrite morphology studies by Gibbs et al, the group developed a specific iterative segmentation procedure based on signed distance map approach that is suitable to identify liquid/dendrite interface from time series of noisy 3D tomography data sets [Gibbs 2014]. In both cases, the key analysis tools are not available from either commercial or freeware programs.

As shown with above examples, dynamic tomography measurements are usually poorer in statistics and have less number of projection images, compared to conventional static tomography measurements. Since the data is more ill-posed, most solutions to these problems rely on optimization operations. The aforementioned two reconstruction techniques and two segmentation tools (iterative reconstruction technique based on TV regulation and optical flow-field computation in embryo imaging case, and TIMBIR reconstruction technique and liquid/solid interface segmentation in dendrite growth case) are all based on some optimization operations. Given the large data size, such operations require powerful large scale computation resources. For instance, Mohan et al [Mohan 2015] tested computation cost with TIMBIR reconstruction techniques. With a single node of 16 cores on the Conte supercomputing cluster at Purdue University, it took about 6 hours to reconstruct 100 slices of size 1536x1536 voxels. This is rather slow. Fortunately, as shown in [Mohan 2015, Bicer 2015], the performance of such algorithms have good speed-up scaling to the number of cores. With the rapid computer technology development, we can expect the complex and advanced tomographic data processing and image analysis tools based on optimization approach will become into popular routine tools in future daily practices.

Figure 1 illustrate the ideal workflow for task oriented tomography/imaging applications. With defined science questions as the core, each step, from sample preparation to image based analysis, are related to each other. To approach to this ideal scenario, it is necessary to develop and improve the data preprocessing and tomographic reconstruction algorithms in terms of accuracy and efficiency, expand the image-based analysis tool collections and integrate them into a infrastructure that is compatible to optimization framework, and access to powerful computation resources. With rapid growth of computer technology, it is likely that the necessary computation power will be routinely available to general users in near future. To achieve the first two goals, it still needs to form coalition to organize the efforts from multidisciplines, from theoretical mathematics to diverse science disciplines.

Fig. 1. *Tomography experiment workflow. From each of three steps around scientific applications, the information of the system in study is obtained at certain level. Evaluations of such information at each step can help to revise or improve the experiment design and data analysis, and verify the hypotheses on the system.*

Acknowledgment: This research used resources of the Advanced Photon Source, a U.S. Department of Energy (DOE) Office of Science User Facility operated for the DOE Office of Science by Argonne National Laboratory under Contract No. DE-AC02-06CH11357.

References

Bicer T., Gursoy D., Kettimuthu R., De Carlo F., Agrawal G. & Foster I. T. (2015). *Rapid Tomographic Image Reconstruction via Large-Scale Parallelization*. To be published in Euro-par 2015 proceeding.

Chaouachi M., Falenty A., Sell K., Enzmann F., Kersten M., Haberthur D., Kuhs W. F. (2015). *Microstructural evolution of gas hydrates in sedimentary matrices observed with synchrotron X-ray computed tomographic microscopy. Geochemistry Geophysics Geosystems*, DOI: 10.1002/2015GC005811.

Cordes N. L., Henderson K., Stannard T., Williams J. J., Xiao X., Robinson M. W. C., Schaedler T. A., Chawla N. & Patterson B. M. (2015). *Synchrotron-based X-ray computed tomography during compression loading of cellular materials. Microscopy Today* 23, 3: 12-19.

Fusseis F., Schrank C., Liu J., Karrech A., Llana-funez S., Xiao X. & Regenauer-Lieb K. (2012). *Pore formation during dehydration of a polycrystalline gypsum sample observed and quantified in a time-series synchrotron X-ray micro-tomography experiment. Sollid Earth* 3, 71-86.

Gibbs J. W., Voorhees P. W. (2014). *Segmentation of four-dimensional, X-ray computed tomography data. Integr. Mater. Manuf. Innov*. 3, 6 doi: 10.1186/2193-9772-3-6.

Gibbs J. W., Mohan K. A., Gulsoy E. B., Shahani A. J., Xiao X., Bouman C. A., De Graef M. & Voorhees P. W. (2015), *The three-dimensional morphology of growing dendrites. Sci. Rep*, accepted.

Limodin N., Salvo L., Boller E., Suéry M., Felberbaum M., Gailliégue S. & Madi K. (2009). *In situ and real-time 3-D microtomography investigation of dendritic solidification in an Al-10wt.% Cu alloy. Acta Materialia* 57, 2300–2310.

Mohan A. K., Venkatakrishnan S. V., Gibbs J. W., Gulsoy E. B., Xiao X., De Graef M., Voorhees P. W. & Bouman C. A. (2015). *TIMBIR: A method for time-space reconstruction from interlaced views. IEEE Trans. Computational Imaging* PP, 99: 1-16.

Moosmann J., Ershov A., Altapova V., Baumbach T., Prasad M. S., LaBonne C., Xiao X., Kashef J. & Hofmann R. (2013). *X-ray phase-contrast in vivo microtomography probes new aspects of Xenopus gastrulation. Nat.* 497, 374-378.

Moosmann J., Ershov A., Weinhardt V., Baumbach T., Prasad M. S., LaBonne C., Xiao X., Kashef J. & Hofmann R. (2014). *Time-lapse X-ray phase-contrast microtomography for in vivo imaging and analysis of morphogenesis. Nat. Protocol* 9, 2: 294-304.

Terzi S., Salvo L., Suéry M., Dahle A. K. & Boller E. (2010). *Coarsening mechanisms in a dendritic Al-10% Cu alloy. Acta Materialia* **58**, 20-30.

Walker S., Schwyn D. A., Mokso R., Wicklein M., Muller T., Doube M., Stampanoni M., Krapp H. G. & Taylor G. K. (2014). *In Vivo Time-Resolved Microtomography Reveals the Mechanics of the Blowfly Flight Motor. PLOS Biology 12,* e1001823.

Yang X., Hofmann R., Dapp R., van de Kamp T., Rolo T., Xiao, X., Moosmann J., Kashef J., Stotzka R. (2015). *TV-based conjugate gradient method and discrete L-curve for few-view CT reconstruction of X-ray in vivo data. Opt. Express* 23, 5: 5368-5387.

Bilateral Denoising and Region Merging Segmentation for Micro-CT Images

S.J. LATHAM*[1], A.M.KINGSTON[1], A.P. SHEPPARD[1]

[1] Department of Applied Mathematics, The Australian National University
(shane.latham@anu.edu.au, andrew.kingston@anu.edu.au, adrian.sheppard@anu.edu.au)
* presenting author

Keywords: Image Segmentation, Region Merging, Iterated Bilateral Denoising

Abstract

The multi-class segmentation (classification) of voxels in X-ray micro-tomography images of porous materials is difficult due to image artifacts such as: noise, point-spread and cupping/beam-hardening. While there are a plethora of algorithms and software for de-noising and segmenting images, few of them have the capability to adequately handle tomographic artifacts and/or large (10's of Gigabytes) image sizes. Typically, high-quality multi-class segmentations are only achieved with significant user input in each of multiple image-processing stages. This has the undesirable effect of introducing user-bias into the image analysis results, further complicating the task of comparing sample-tomograms acquired under diverse imaging conditions or analysed by different users. This paper presents a method for denoising 3D tomograms and a method for subsequent segmentation, both of which require minimal user input.

Our denoising method uses iterated bilateral-filtering [1,2], where iterations proceed by estimating the standard deviation of the noise from the image and using this estimate in the Gaussian range weighting. Iterations terminate when the relative change in estimated noise is below a specified threshold. The iterated bilateral filtering denoises more effectively in constant attenuation image regions, so further smoothing of phase boundaries is performed using anisotropic diffusion. Segmentation on the denoised image is performed using a watershed transform followed by Region Merging of the (over-segmented) watershed regions. The Region Merging uses a simple contrast predicate to determine whether regions are merged. The advantage of this image processing pipeline is that user-intervention is delayed until the final classification of region-merged *super-voxels* (*super-pixels*). No user-selected seeds or gradient-thresholding are required to generate large salient segments. We illustrate the effectiveness of our denoising and merging pipeline on a micro-CT tomogram of a multi-mineralic sandstone.

Introduction

Segmentation is the process of converting a tomographic image, in which the different phases are represented by ranges of grey-scale values, to an image where each voxel is classified (labeled) as belonging to a particular class (phase) of interest. In tomographic images of geomaterials, phases of interest include: pore-space, minerals, brine and oil.

Micro-CT tomogram multi-class segmentation remains a non-trivial task and is hindered due to shortcomings in the image acquisition and reconstruction process. Artifacts include: noise, cupping/beam-hardening, point spread blur, rings, and streaks. Quality segmentations are usually only generated for pre-processed images, where these artifacts have been minimized (or removed). Current popular micro-CT tomogram denoising, artifact-removal and segmentation methods are detailed in [4]. To generate a segmentation, a user typically chooses grey-scale (attenuation) thresholds associated with the material classes of interest, and segmentation software uses the thresholds as seeds to grow or flood any remaining image voxels complete the segmentation. This is

often a trial-and-error process where the user adjusts the thresholds in an attempt to generate a segmentation which accurately reflects the data of the tomogram. The pre-processing and segmentation steps are a time consuming process in which the user selects a set of parameters which best mitigate the tomogram artefacts. Having a large set of selectable parameters has the undesirable effect of introducing user-bias to the segmentation generation and subsequent segmentation analysis.

This paper details a segmentation pipeline which eliminates parameter selection in the denoising stage and avoids user seed selection in the segmentation step. The pipeline involves iterative bilateral filtering followed by anisotropic diffusion filtering to generate an image with very low noise. The watershed transform is used to generate an over-segmented image and subsequent region merging forms large regions (*super-voxels*) at the object (grain/pore) scale. User input is delayed until the final segmentation generation step where the watershed-merged-regions (super-voxels*)* are classified into their mineralogical groups.

Iterated Bilateral Denoising

The bilateral filter [1] is a non-linear edge-preserving smoothing filter which replaces voxel intensities by a weighted sum of intensities from a nearby neighbourhood of voxels:

$$I^{BL}(\boldsymbol{x}) = \frac{1}{W_p} \sum_{\boldsymbol{x}_i \in \Omega(\boldsymbol{x})} I(\boldsymbol{x}) f_r(\|I(\boldsymbol{x}_i) - I(\boldsymbol{x})\|) g_s(\|\boldsymbol{x}_i - \boldsymbol{x}\|),$$

where W_p is the weight normalisation, I is the input image, $\boldsymbol{x}$ the voxel index, $\Omega(\boldsymbol{x})$ the voxel neighbourhood around $\boldsymbol{x}$, f_r is the range kernel and g_s is the spatial kernel. We use a spherical neighbourhood $\Omega(\boldsymbol{x})$ of radius 3.4, a constant spatial kernel $g_s(\delta) = 1$ and a Gaussian range kernel:

$$f_r(\beta) = \omega(\beta, \sigma) = e^{-\beta^2/(2\sigma^2)}.$$

Our iterated bilateral filtering is defined as:

$$I^{(n+1)} = \frac{1}{W_p^{(n)}} \sum_{\boldsymbol{x}_i \in \Omega(\boldsymbol{x})} I^{(n)}(\boldsymbol{x}) \omega\left(\left\|I^{(n)}(\boldsymbol{x}_i) - I^{(n)}(\boldsymbol{x})\right\|, \hat{\sigma}^{(n)}\right), n = 0, \dots, N-1,$$

Where $I^{(n)}$ is the original unfiltered image, $I^{(n)}$ is the n-th bilateral filtered image and $\hat{\sigma}^{(n)}$ is the standard deviation estimate of the noise for image $I^{(n)}$. The iteration is terminated when the relative reduction in estimated noise is less than 10%, i.e. $|\hat{\sigma}^{(n+1)} - \hat{\sigma}^{(n)}| / \hat{\sigma}^{(n)} < 0.1$. The noise standard deviation estimate is calculated by generating a 2D histogram of $\mu_{\widetilde{\Omega}}$ (neighbourhood mean) versus $\sigma_{\widetilde{\Omega}}$ (neighbourhood standard-deviation) and determining the $\sigma_{\widetilde{\Omega}}$ at which peaks occur. Using the 2D histogram for estimating the noise standard deviation is effective at eliminating bias in the presence of large volumes of highly textured regions in the image, as the 2D histogram exhibits well-defined peaks for the constant-attenuation regions (even when these regions constitute only a few percent of the total image volume). Fig 1 gives an example of the iterated bilateral denoising applied to a multi-mineral sandstone sample tomogram (5mm diameter cylindrical plug, 1580x1580x2800 voxels) in which the dominant greyscales are contributed by the open pore space (mean grey-scale value ~4350), quartz (mean grey-scale value ~5560) and higher-attenuating grains (mean grey-scale value ~5900). The estimated noise standard deviation in the original image is calculated to be 85.0 and the estimated noise standard deviation in the 8th iteration denoised image is estimated to be 6.6. The constant attenuation regions have been well-smoothed and the fine features, such as the cracks, strands and edges remain preserved. The bilateral iteration de-noises more aggressively in the constant attenuation regions, and less aggressively in high gradient regions (i.e. textured and/or high standard deviation regions). To achieve

boundary de-noising (for subsequent watershed transform) further smoothing is performed using anisotropic diffusion [5,6]. The diffusion parameters are selected based on the estimated noise standard deviation of the bilateral filtered image.

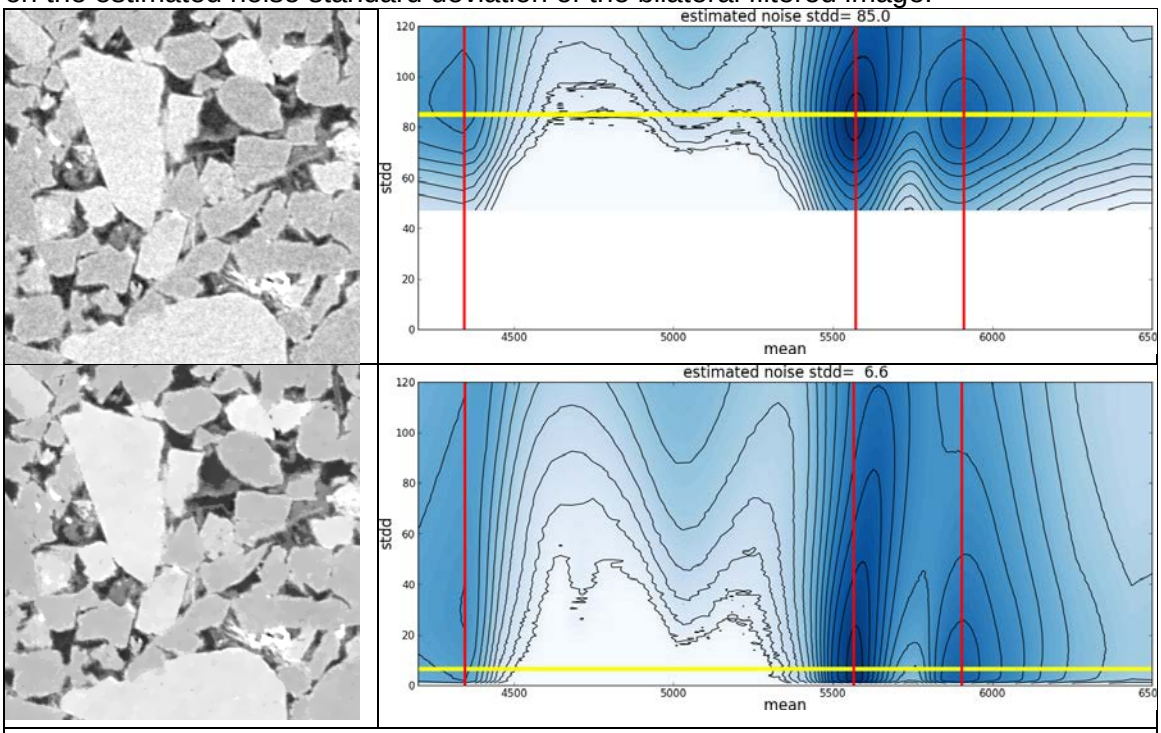

Fig. 1. *Left column: Original image (top) and 8 iteration bilateral filtered image (bottom). Right column: 2D log-density vs histogram with noise estimate indicated by yellow line. Intersection of yellow and red lines indicate the dominant 2D histogram peaks*.

Watershed Region Merging Segmentation

The watershed algorithm [6,7] uses surfaces of highest gradient to form class boundaries. The method is seeded with either: (a) Local minima of the gradient magnitude image (auto-seeding), or (b) user-selected pre-classification markers (or thresholds). In the multi-class case, (b) must additionally ensure that high-gradient regions/voxels are excluded from the set of seeds. Watershed auto-seeding results in an over-segmented image and further processing is required to aggregate/assign the watershed regions into material classes. In this paper we adopt the auto-seeding approach and perform region merging on the over-segmented watershed image to produce image regions/segments which correspond to physical objects in sample image (e.g. pores, grains, clays, etc). While the merging of watershed regions is not new, our method for performing the merging is novel. We use an approach most similar to that in [5] and the Statistical Region Merging (SRM) in [3], where adjacent region pairs are sorted by their grey-scale contrast (difference of region mean grey-scale). Our merge predicate is a simple threshold on the contrast. The region pairs are tested in sorted order, and merged if the contrast satisfies the threshold. With this approach, there is no priority queue (where the lowest contrast region pair is maintained at the head of the test-and-merge queue). To describe the region-merging algorithm more formally, let r be a region (group of voxels) of image I such that $I(r)$ is the grey-scale attenuation associated with region r (we use gradient magnitude weighted mean grey-scale, low gradients have higher weight), let $r' \in \Omega^{(r)}$ be the adjacent (neighbour) regions of r and let S^I be the set of all neighbour region pairs $\{(r,r'): r \in I, r' \in \Omega^{(r)}\}$ for image I. Also let

$R(r)$ be the region to which r belongs (initially, before any merging $R(r) = r$) and let $P\big(R(r), R(r')\big)$ be the predicate which gives *true* if regions $R(r)$ and $R(r')$ are to be merged. We use a simple contrast predicate $P\big(R(r), R(r')\big) \equiv \big|I\big(R(r)\big) - I\big(R(r')\big)\big| < \tau$. The region merging method is:

1. Bin-sort all neighbour pa.irs S^I according to $|I(r) - I(r')|$, let $B(c) = \{(r, r'): \delta_c \leq |I(r) - I(r')| < \delta_{c+1}, (r, r') \in S^I\}$ be the bin sorted set of pairs.
2. For c in $\{0, 1, 2, \dots\}$:
    a. Predicate test all pairs in $B(c)$ to generate merge pairs $M(c) = \{\big(R(r), R(r')\big): P\big(R(r), R(r')\big) = true, (r, r') \in B(c)\}$.
    b. Merge all region pairs in $M(c)$.

This algorithm differs to SRM [3] in step 2. In [3], a region pair is merged immediately if the predicate indicates true and this immediate pair-merge results in an ordering constraint which makes parallelisation difficult. In step 2 above, the predicate test and the pair merges are separated into two steps, where the pair-merges are delayed until all region pairs of $B(c)$ have been predicate-tested. Removing the order dependence facilitates parallelization of step 2. In addition, instead of choosing a single contrast threshold, we use a sequence of increasing thresholds, performing a full re-merge using the merged regions formed by the previous threshold. The advantage of these iterations is that some pair reordering is performed (i.e. Step 1) without the need for a priority queue. The success of relaxing the ordering constraint hinges on whether the resulting merged-region grey-scale is similar to the two individual pre-merged mean grey-scales. The initial bin-sort ordering and an increasing sequence of thresholds ($\tau_j = j\tau_\Delta, j = 1,2,3, \dots$, where τ_Δ is proportional to the image noise standard deviation estimate) ensures merged region grey-scale values do not vary significantly from the pre-merge region grey-scale values. Fig. 2 shows result of applying denoising, watershed transform and region merging method to a tomogram of a multi-mineralic sandstone. Petrology related analysis for this type of sample typically requires the identification of pores, clays, quartz and other minerals. The Fig. 2 pseudo-color version of the denoised image highlights the issues associated with point-spread (and phase-contrast fringing), with the boundaries of grains having grey-scale values similar to the greyscales of the clays. The watershed transform eliminates the point-spread blur and most of the phase-contrast fringing. Region merging then aggregates the watershed regions into regions which correspond to the pore, grain, clay, etc regions. The region merged image in Fig. 2 was the result of the third merging with contrast thresholds $\tau_1 = 20$, $\tau_2 = 40$ and $\tau_3 = 80$. After region merging, there typically remains a large number of regions and further classification is necessary to generate the final segmentation. Here, a final segmented image (not shown) is generated from the region-merged grey-scale image by user-selected thresholds. Future work will aim to merge non-neighbouring regions (i.e. merge regions which are which are not voxel-neighbourhood-connected) in order to ease the task of threshold selection. The choice of the terminating τ_j threshold is also an open question, but it may be able to be expressed using a region-size stability measure.

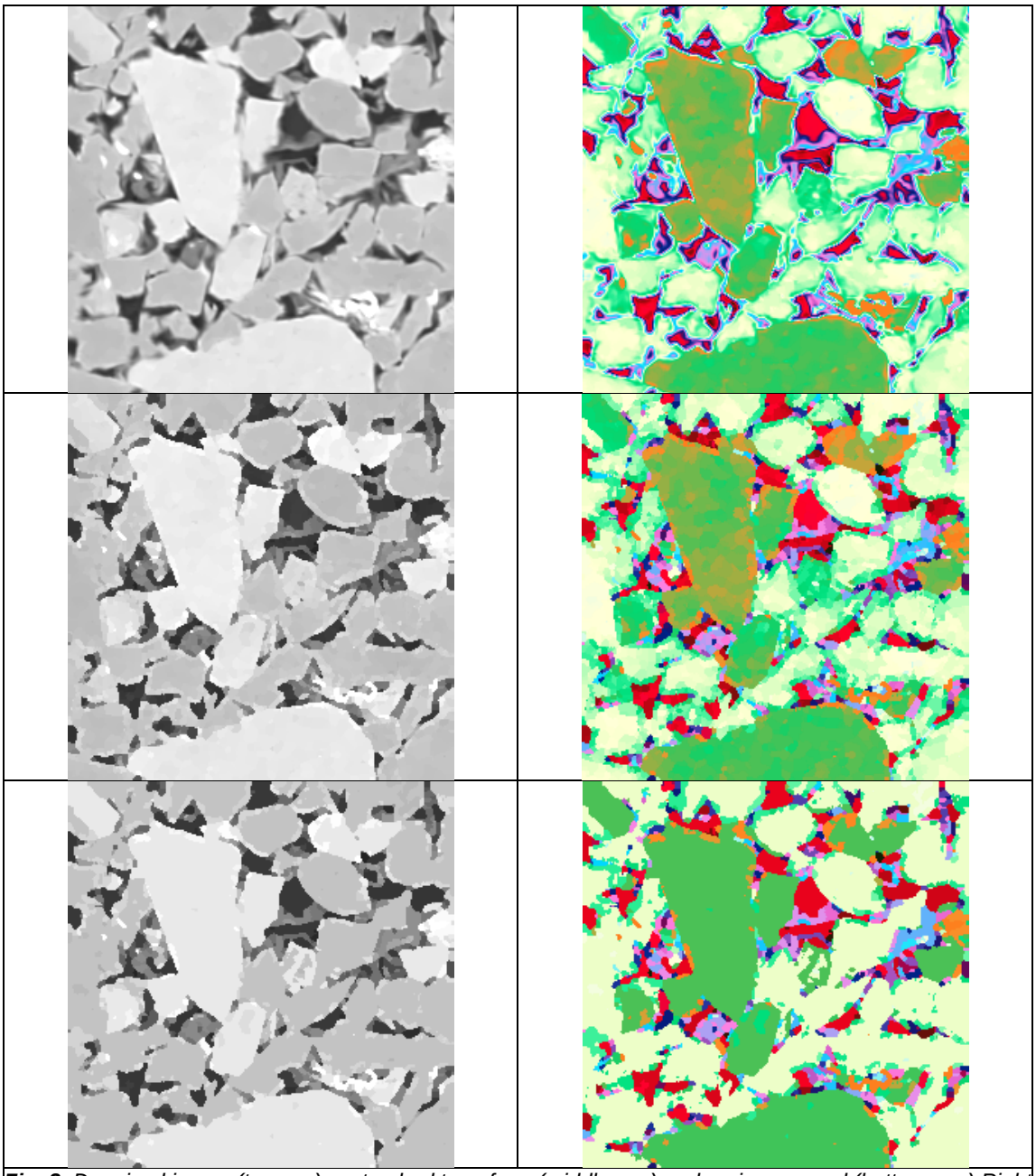

Fig. 2. *Denoised image (top row), watershed transform (middle row) and region-merged (bottom row) Right column is pseudo-colour version of the voxel/region grey-scales in left column.*

References

[1] Tomasi, C., & Manduchi, R. (1998). Bilateral filtering for gray and color images. In Computer Vision, 1998. Sixth International Conference on (pp. 839-846). IEEE.

[2] Milanfar, P. (2013). A Tour of Modern Image Filtering: New Insights and Methods, Both Practical and Theoretical. IEEE Signal Processing Magazine,30(1), 106-128.

[3] Nock, R., & Nielsen, F. (2004). Statistical region merging. Pattern Analysis and Machine Intelligence, IEEE Transactions on, 26(11), 1452-1458.

[4] Schlüter, S., Sheppard, A., Brown, K., & Wildenschild, D. (2014). Image processing of multiphase images obtained via X-ray microtomography: A review.Water Resources Research, 50(4), 3615-3639.

[5] Felzenszwalb, Pedro F., and Daniel P. Huttenlocher. (2004). "Efficient graph-based image segmentation." International Journal of Computer Vision 59, no. 2: 167-181.

[6] Beucher, S., & Lantuéjoul, C. (1979). Use of watersheds in contour detection. In International workshop on image processing, real-time edge and motion detection.

[7] Vincent, L., & Soille, P. (1991). Watersheds in digital spaces: an efficient algorithm based on immersion simulations. IEEE transactions on pattern analysis and machine intelligence, 13(6), 583-598.

Feasibility of iterative phase contrast tomography

N. T. VO*, R. C. ATWOOD, M. DRAKOPOULOS

Diamond Light Source, Harwell Science and Innovation Campus, Didcot, Oxfordshire, OX11 0DE, UK
nghia.vo@diamond.ac.uk
robert.atwood@diamond.ac.uk
michael.drakopoulos@diamond.ac.uk

Keywords: Tomography, X-ray phase contrast imaging

Abstract

Iterative phase retrieval in the Fresnel region based on the random signed feedback (RSF) technique has shown a promising performance on tomographic data as demonstrated in [Vo]. This report presents the performance of the RSF technique at various conditions to improve the convergence speed. The results are useful for evaluating the feasibility of this technique in quantitative phase contrast tomography.

Introduction

The applications of phase contrast tomography based on direct methods of phase retrieval have been limited so far by the fact that they are sensitive to noise or applicable only to limited types of samples. There are no such of limitations for iterative phase retrieval methods based on the Gerchberg-Saxton algorithm, but they are not often used in Fresnel region due to the problems of slow convergence and stagnation. The RSF accelerator proposed Vo et. al. [Vo] significantly improves the convergence speed. Here, we present more detail its performance under different conditions for optimization.

Methods

The pseudo-code of the procedure of the RSF technique is as follows; where temporary intermediate values are designated M:

input λ, *N, D1, D2,* I_{D1}, I_{D2}, *dr,* θ*;*
T=initial_ estimated_transmission_funtion;
For n=1 to Iterative_number
Step1: $T_1=GS(T,D1,I_{D1});$
Step2: $T_2= GS(T_1,D2,I_{D2});$
Step3: $T_3=(T_1+ T_2)/2;$
Step4: $M_1=Sgn(Sqrt(I_{D2}) – Abs(Fr_{D2}\ (T_3)));$
Step5: $M_2=\theta \times Random([0,1],\{N,N\});$
Step6: $T=SmoothFilter(Re(T_3))+i\times(Im(T_3)+M_1\times M_2);$
End

where λ is the wavelength, N is the size of all 2D digitized functions, $D1$ and $D2$ are the distances of the measured intensities I_{D1} and I_{D2} respectively. dr is the resolution of the recorded image which is used to compute values of spatial frequencies for numerical Fresnel transform, $Fr_D()$. θ is used for controlling the strength of the accelerator. *GS()* function returns the next estimation of the transmission function after one cycle of applying Fresnel transform (or Fresnel propagator), combining with observed intensity, and applying inverse Fresnel transform. *Re*, *Im*, and *Abs* functions return the real part, imaginary part, and the absolute value of the complex value, respectively. In order to investigate the convergence speed of the RSF technique at different settings, we change the combination of the *GS* function at different distances and adjust parameters in step 4, 5, and 6.

In the estimation stage which consists of step 1, 2 and 3, the next estimation of the transmission function can be calculated from the different combinations of the *GS* function and distances as shown in Table 1.

Table 1: Different combination of step 1, 2, and 3

	Case 1	Case 2	Case 3	Case 4
Step 1	$T_1=GS(T,D1,I_{D1})$	$T_1=GS(T,D2,I_{D2})$	$T_1=GS(T,D1,I_{D1})$	$T_1=GS(T,D1,I_{D1})$
Step 2	$T_2=GS(T_1,D2,I_{D2})$	$T_2=GS(T_1,D1,I_{D1})$	$T_2=GS(T,D2,I_{D2})$	$T_2=GS(T_1,D2,I_{D2})$
Step 3	$T_3=(T_1+T_2)/2;$	$T_3=(T_1+T_2)/2;$	$T_3=(T_1+T_2)/2;$	$T_3=T_2$

In the stage of acceleration, step 4, which applys a *Sgn* function (returning value -1, 0, or 1 depending on whether its input is negative, zero, or positive) on the difference between the measured intensity and the calculated intensity at the distance D2, can be changed by using the intensity at distance D1 instead. We use θ as the percentage of the mean of the intensity subtracted from the background to adjust the strength of the accelerator in step 5. The matrix of random values in the range of [0;1] is used to overcome the stagnation problem. The side-effect of adding a perturbation on the imaginary part is cancelled by applying a smooth filter such as Gaussian filter on the real part as described in step 6.

For testing the convergence speed at different cases, a numerical phantom made of simple shapes (Fig. 1) is used, where the ratio between the absorption function and phase shift differs between shapes. Values of absorption and phase shift used in simulation, respectively, are: triangle (0.0125; - 0.3), circle (0.04; - 0.7), inside square (0.005; - 0.9), and outside square (0.01, - 0.5). These values are chosen quite arbitrarily keeping in mind that the phase shift should be higher than the absorption in order to get a clear phase enhancement image. The image size is N×N=600×600 pixels with a pixel size of 1 μm. Intensities with a photon energy of 12 keV at 50 cm and 80 cm are used for simulation as shown in Fig.2.

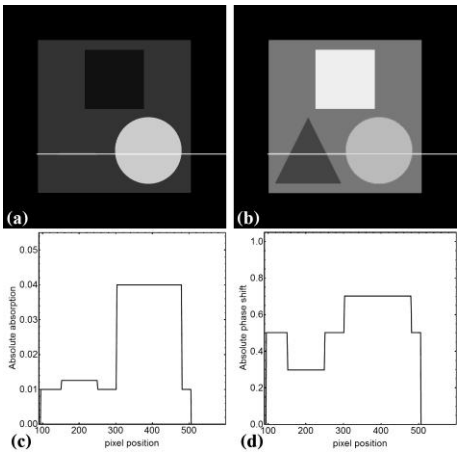

Fig. 1: Phantoms and the line profiles (white lines): (a,c) Absorption function, (b,d) phase shift

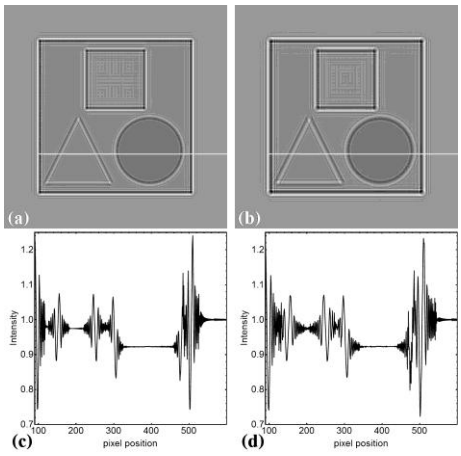

Fig. 2: Intensities and the line profiles: (a,c) at 50cm; (b,d) at 80cm

Results

Fig. 3 shows the plots of the normalized root mean square (NRMS) error, which is the root mean square of the difference between the reconstructed and original phase shift normalized by dividing the mean value of the original phantom, versus the number of

iterations of four cases in Tab. 1. As can be seen, case 1 results in the fastest convergence speed compared with the others.

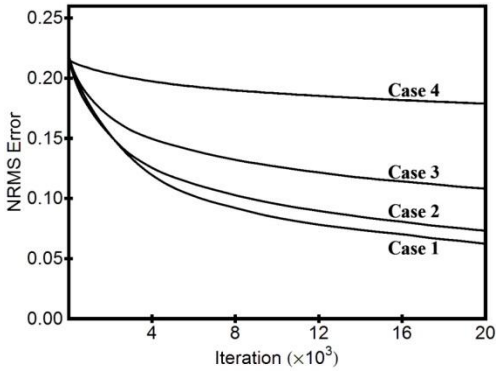

Fig. 3. NRMS error between the reconstructed and original phase shift versus the number of iterations for four cases.

The choice of distance D1 instead of D2 can enhance the convergence speed as shown in Fig. 4.

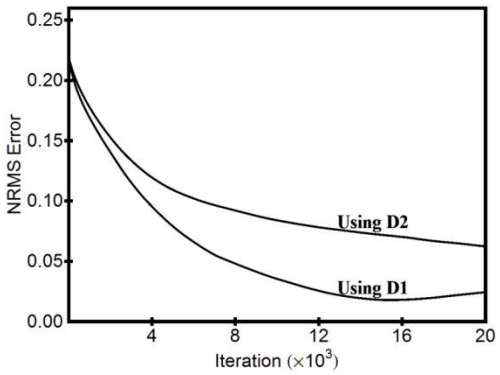

Fig. 4. NRMS error between the reconstructed and original phase shift versus the number of iterations of two choices of distances.

The strength of the accelerator apparently impacts on the convergence speed as can be seen in Fig.5, so a good choice is to use a strong accelerator for the initial stage, then subsequently reduce its strength.

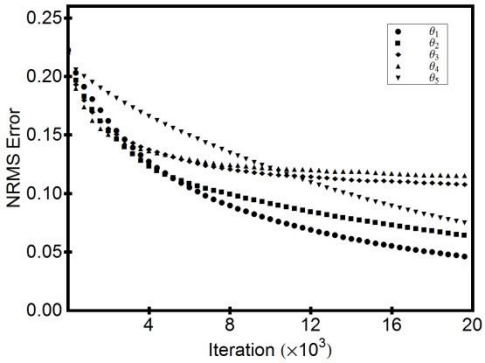

Fig. 5. NRMS error versus iteration of different values of : θ_1 = 0.5%, θ_2 = 1%, θ_3 = 2%, θ_4 = 3% and θ_5 = 0.1% of the mean of (I_{D2} -1)

A side-effect of adding a perturbation appears in the absorption function as shown in Fig. 6. This is corrected by using a Gaussian filter with sigma=2 that results the fast reconstruction of the real part after few hundreds of iterations (Fig. 7). The comparision of different values of sigma in Fig. 8 illustrates the advantage of using a stronger filter. However the computation cost needs to be considered for real applications.

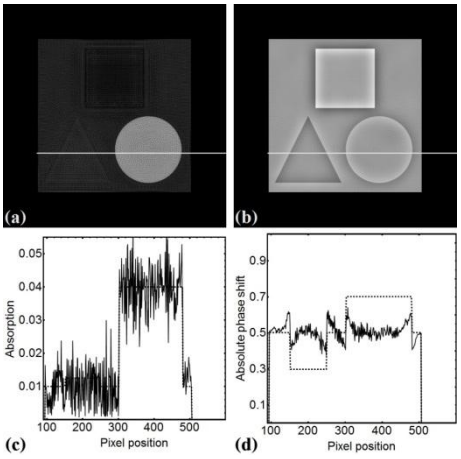

Fig. 6. Absorption function (a,c) and phase shift (b,d) after 500 iterations in the case of not using the smoothing fitter.

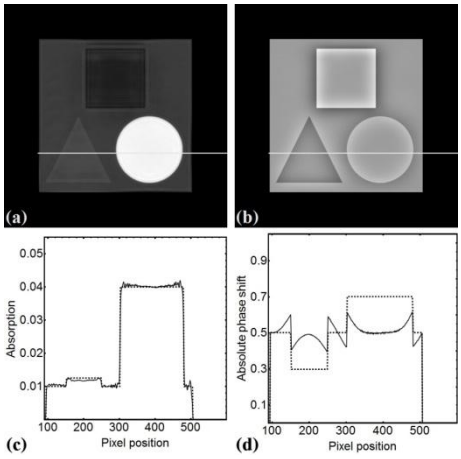

Fig. 7. Absorption function (a,c) and phase shift (b,d) after 500 iterations in the case of using the smoothing fitter.

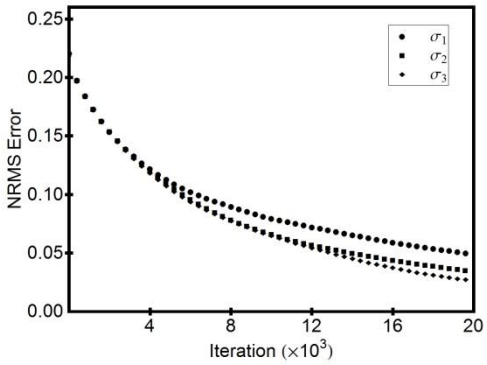

Fig.8. NRMS error versus iteration of different σ: (σ_1 = 2; σ_2 = 4; σ_3 = 6) of the Gaussian filter which shows the better performance of the larger σ.

The optimized RSF technique is applied on the tomographic dataset obtained at ESRF (European Synchrotron Radiation Facility) where the sample is the duplex steel [EXTREMA]. Intensities at 0.158 m and 0.308 m are recorded with the pixel size of 1.4 micron and the photon energy of 55 keV (Fig. 9). The retrieval of the phase shift and absorption funtion are shown in Fig. 10. A reconstructed slice (Fig. 11) from retrieved tomographic dataset is a very promising result.

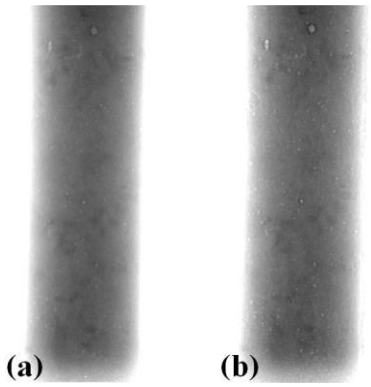

Fig. 9. Projections of the sample at the distances of 0.158 m (a) and 0.308 m (b).

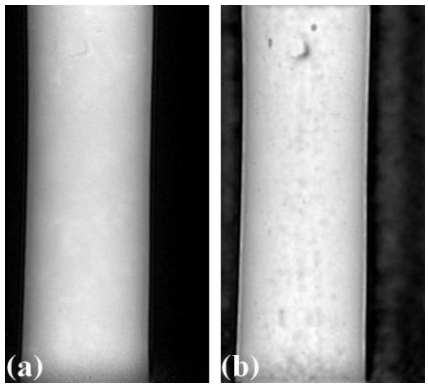

Fig. 10. Retrieved absorption function (a) and phase shift (b) after 400 iterations.

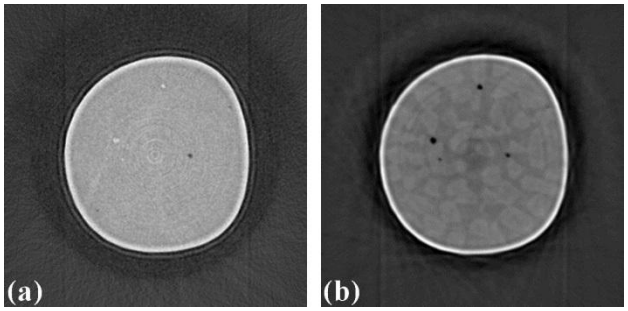

Fig. 11. Slice reconstructed from the retrieved tomographic dataset of the absorption funciton (a) and the phase shift (b).

References

Vo T. N., Atwood R. C., Moser H. O., Lee P. D., Breese M. B. H., and Drakopoulos M. (2012). "*A fast-converging iterative method for X-ray in-line phase contrast tomography,*" ***Applied Physics Letters***, 101, 224108.

EXTREMA 2015 workshop, http://www.esrf.eu/home/events/conferences/2015/extrema-2015---challenges-in-x-ray-tomography.html

Transformative synchrotron microtomography data capture metamorphic reactions in real time - and require a dedicated computational environment to process very large 4D datasets

F. FUSSEIS*[1], W. ZHU[2], T. XING[1], H. LISABETH[2], J. BEDFORD[3], H. LECLÈRE[3], X. XIAO[4]

[1] School of Geosciences, The University of Edinburgh, Edinburgh, UK – florian.fusseis@ed.ac.uk, s1266236@sms.ed.ac.uk
[2] Department of Geology, University of Maryland, College Park, USA – wzhu@umd.edu, hlisabeth@gmail.com
[3] School of Environmental Sciences, University of Liverpool, UK – John.Bedford@liverpool.ac.uk, Henri.Leclere@liverpool.ac.uk
[4] Advanced Photon Source, Argonne National Laboratory, USA – xhxiao@aps.anl.gov
* presenting author

Keywords: 4D tomography, experimental geosciences, fluid-rock interaction, x-ray transparent cell

Abstract

Fluid-rock interaction controls many geological processes of societal relevance and is thus the focus of a great number of experimental studies. Since the recent advent of time-resolved microtomographic data acquisition, these experimental studies have begun adopting the new possibilities by developing x-ray transparent experimental environments. Studies that were once restricted to reproducing crustal diagenesis and metamorphism in concealed vessels with very limited possibilities of direct monitoring can now image these processes on the micron scale in 4D (3 spatial dimensions and time). In particular synchrotron-based x-ray microtomography using pink and white beams allows documenting fluid-rock interaction as it happens, resolving metamorphic reactions in unprecedented detail. We employ our novel x-ray transparent fluid-rock interaction cell to investigate fundamental metamorphic processes. In this presentation we use the data from two recent experiments on olivine carbonation and gypsum dehydration to show the enormous potential of conducting fluid-rock interaction studies in 4D. Both processes have been investigated extensively, yet our experiments, which were conducted at beamline 2BM at the Advanced Photon Source (APS) provide completely new insights. In this presentation we will, however, also outline the difficulties that come with the analysis of 4D datasets comprising often hundreds of time steps and several tens of TB of data.

Methods

Our x-ray transparent fluid-rock interaction cell is slightly modified from the Hassler core holder type design published by Fusseis et al. (2014). The cell is portable and modular and was built for use at synchrotron imaging beamlines. It is transparent to a filtered polychromatic beam with an energy peak at 65 keV, which is provided, e.g. in the A-hutch of beamline 2BM at the APS, 25 m from the source (see Fusseis et al., 2014 for details).

In the current design (Figure 1), a confined 3 mm diameter sample can be heated to 230 °C and pressurized to 25 MPa. Current maximum limits of these parameters are defined by the seals and the materials used. With respect to the original design published by Fusseis et al. (2014), the cell was modified so that after the experiment the sample can be retrieved for further study. The optimised cell design proved robust to reliably conduct experiments over seven or more days. At the beamline, the cell remains on the rotation stage for the duration of the experiment.

In the cell, confining pressure can be applied to the sample through either a manual piston screw pump or a high-pressure syringe pump. Fluid can be pressurised and

infiltrated into the sample from both sides by two high-pressure syringe pumps. The two fluid pressure pumps allow for bulk permeability measurements by a pore pressure oscillation method during experiments. All pumps communicate with each other and can be run either flow- or pressure controlled. The pumps are fully programmable, allowing for the implementation of customized loading histories. All pump parameters are continuously logged, as is the temperature at the sample.

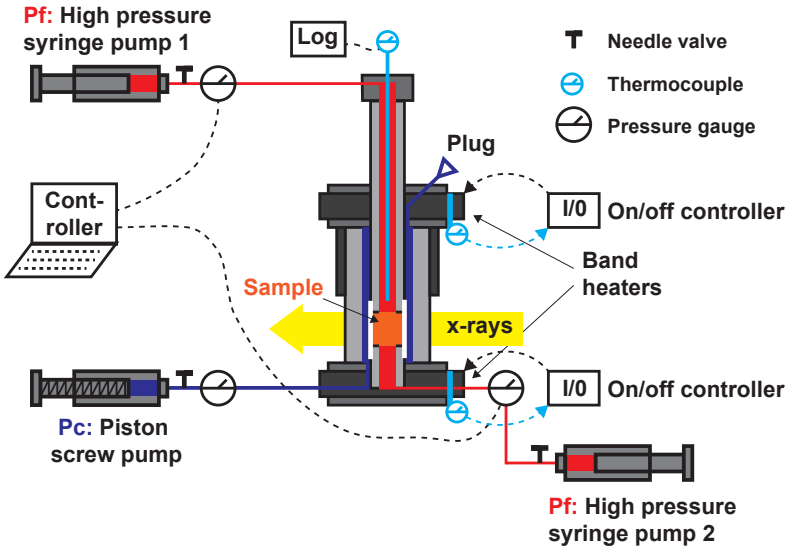

***Fig. 1**. Schematic drawing of the fluid-rock interaction cell and its periphery as used in the experiments reported here. See Fusseis et al., (2014) for details.*

Experiments

In the last two years, the cell was used in a number of experiments investigating fluid-rock interaction and low-grade metamorphic reactions, usually involving a dynamic porosity evolution. Here we report on two of these experiments:

1) In a number of natural outcrops, forsterite, which is a major component of mafic rocks that form our planet's oceanic crust, demonstrates the potential to react with CO_2 to form magnesite and quartz. The reaction consumes significant quantities of CO_2. The storage of CO_2 in solid minerals is considered the safest long-term sequestration technique, albeit also the most technically involved. While the reaction $Mg_2SiO_4 + 2\ CO_2 = 2MgCO_3 + SiO_2$ is self-sustaining at elevated temperatures, it is potentially self-limiting due to the volume increase that comes with the formation of magnesite. To investigate the effect of this volume change, we documented the reaction of forsterite with a $NaHCO_3$-saturated brine to form magnesite and quartz at 200°C and 15 MPa Pc/10 MPa Pf in 379 3-dimensional datasets. This experiment produced about 19 TB of reconstructed data.

2) In contrast to olivine carbonation, gypsum dehydration has been investigated for an entire century (Fusseis et al., 2012). Despite the reaction is as relevant for minerals processing as it is for tectonics, many aspects of the apparently simple process that transforms $Ca_2SO_4.2H_2O$ into $CaSO_4.0.5H_2O$ are still poorly understood. Amongst them is how the reaction develops in polycrystalline gypsum (alabaster). In a second series of experiments, we dehydrated alabaster to produce hemihydrate (plaster of Paris) at 115°C, 10 MPa Pc and 7 Mpa Pf. These experiments extend a previous study of Fusseis et al. (2012), who dehydrated alabaster in an x-ray transparent furnace. The recent

study using our x-ray transparent cell yielded about 120 3-dimensional datasets in four experimental runs.

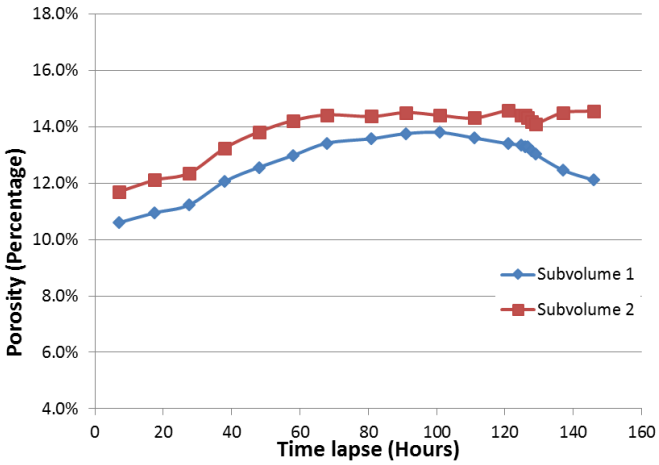

***Fig. 2**. Porosity evolution during the carbonation reaction of forsterite in a rock analogue in two representative subvolumes. The increasing difference in porosity in the two subvolumes from 100 hours onward is due to a crack forming in subvolume 2 at the time.*

Data analysis

We analyse our 4D datasets using the high-performing computing and data storage facilities provided by the Edinburgh Compute and Data Facilities (ECDF), and workstations at the School of Geosciences, both at the University of Edinburgh. All projections acquired during the two experimental series were transferred from APS via the gridFTP interface *Globus Online* (Foster, 2011). The complete 4D dataset is stored on a backed-up ECDF storage site. Data are reconstructed individually using the code *TomoPy* (Gursoy et al., 2014) with reconstruction parameters for each 4D dataset provided by the beamline on one of two high performance computing facilities. An initial screening of the data on a local workstation identifies the relevant time steps in each 4D dataset. These are then individually interrogated, further processed and visualized using *Fiji*, *Avizo Fire* and *Drishti* on the same computer.[1] Once the project has advanced to the publication stage, all data are transferred to a tape library for long-term storage.

While the analysis of the forsterite carbonation experiment is essentially completed, the analysis of the gypsum dehydration experiment is still ongoing. The former included the determination of the representative volume with respect to the porosity distribution, an analysis of the time-dependent evolution of the grey value histograms, which reflects compositional changes, the segmentation of porosity and quantification of the porosity evolution (both bulk and individual pores) and a determination of magnesite growth rates.

Results

Our two experiments yielded unprecedented insights into fluid-rock interaction processes and set a new standard in experimental geosciences.

The data acquired during the carbonation experiment indicate that throughout carbonation, new fluid pathways are created and unreacted forsterite is exposed to the CO_2-bearing fluid. We observe an overall increase in porosity (Figure 2). A relative

[1] We do currently also run a 3D image correlation code by Hall et al. (2012) and a particle tracking code called IDtrack (Andó et al., 2012). These were not used in the current study.

increase in the proportion of larger pores indicates that pores connect. We can trace and quantify the growth of idiomorphic crystals of magnesite on free forsterite surfaces: magnesite growth continues throughout the experiment. Although the carbonation reaction of olivine is volume increasing, the process shows no evidence of self-limitation in our experiment. Our study supports previous observations that emphasize the potential of forsterite as the stock for in-situ carbonation.

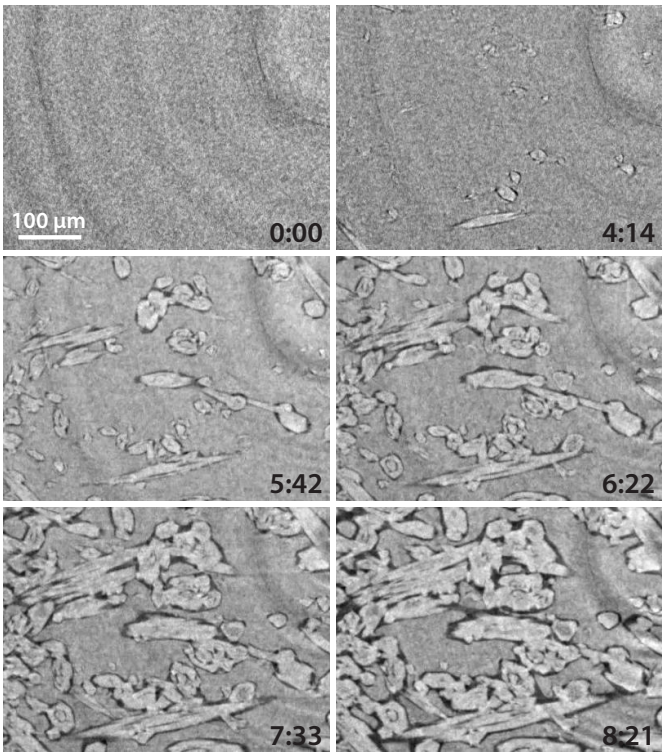

Fig. 3*. Images showing the growth of hemihydrate needles in a dehydrating polycrystalline gypsum sample in horizontal slices through the sample. Our data allow tracking individual grains from their nucleation. Time is given in hours:minutes.*

Our gypsum dehydration experiments allow us to observe the nucleation of hemihydrate grains in real time over the course of the experiments (Figure 3). The tomographic data sets permit direct monitoring and quantifying of the reaction progress and tracking the growth of individual grains, which provides an excellent opportunity to test kinetic models of mineral reactions. The observation that hemihydrate needles grow in a porous shell points towards a dissolution-precipitation type reaction mechanism.

Combined, the two experiments define the first time that metamorphic reactions have been visually captured in 4D datasets.

Outlook

While we can now conduct transformative fluid-rock interaction experiments at relevant geological conditions, our capacity to analyse these novel data is limited by the available computational software infrastructure. In particular, we lack:

- An efficient data management system that directs data from the initial transfer from the synchrotron beamline through all processing steps onto final permanent storage in our tape library.

- The possibility to prescreen 4D data already before they are reconstructed to flag the time steps that document change and confine further analysis to those. Ideally, we could discard the irrelevant time steps at this stage to reduce storage space requirements.
- Bulk process entire 4D datasets efficiently. This includes segmentation algorithms that adapt to time-dependent shifts in recorded intensities or noise levels.
- The possibility to conduct 3D volume correlation and and track particles across more than two datasets efficiently.

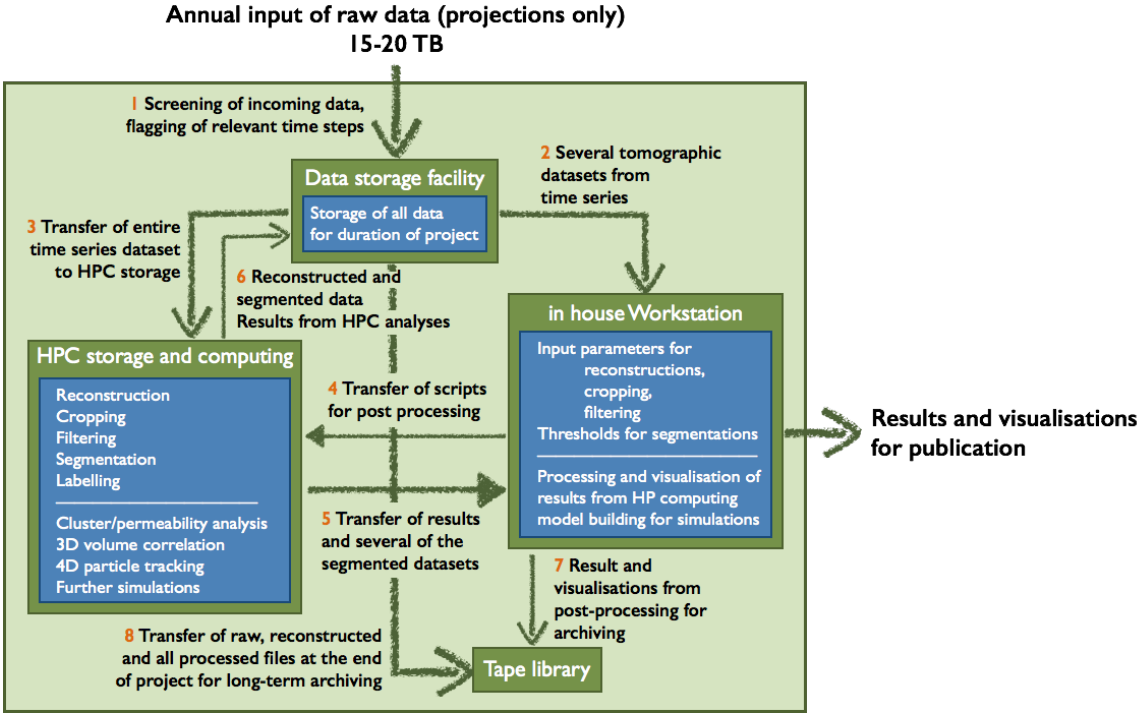

***Fig. 4**. Sketch of the computational environment we aim to establish to analyse 4D datasets efficiently.*

A potential computational infrastructure for these requirements (that excludes reconstruction in this case) is outlined in Figure 4. Realisation of an open source environment that addresses the points above requires an interdisciplinary effort of computer scientists, experimentalists and beam line staff, which we are currently coordinating in a major project proposal to a European funding body.

References

Andó E, Hall SA, Viggiani G, Desrues J, Bésuelle P (2012). **Acta Geotecnica** 7: 1-13.
Foster I. (2011). ***Internet Computing, IEEE*** 15, 3: 70-73.
Fusseis et al. (2012). **Solid Earth** 3: 71-86.
Fusseis F, Steeb H, Xiao X, Zhu W, Butler IB, Elphick S, Mäder U (2014). **Journal of Synchroton Radiation** 21: 251-253
Hall et al. (2010). **Géotechnique** 60, 5: 315-322

scikit-image and the Python ecosystem for 3-D image processing

S. VAN DER WALT[1], *E. GOUILLART[2], J. NUNEZ-IGLESIAS [3]

[1] Division of Applied Mathematics, Stellenbosch University, Stellenbosch 7600, South Africa
[2] Surface du Verre et Interfaces, UMR125 CNRS/Saint-Gobain, 93303 Aubervilliers cedex
[3] Victorian Life Sciences Computation Initiative, Carlton, VIC, Australia

Keywords: image processing, Python, denoising, segmentation, labeling

Abstract

scikit-image is an open-source image processing library for Python. Most functions of the library accept 2-D images as well as 3-D images with the same syntax. Such 3-D compatibility, and the simple API of the package, make scikit-image an interesting solution for processing 3-D tomography images. I describe here several functionalities of the package, using as a central theme the segmentation of regions of interest in an image. Different examples illustrate that both common and basic algorithms, but also some algorithms closer to the state of the art, are found in scikit-image for 3-D image processing.

Introduction

scikit-image [VanDerWalt2014] is a general-purpose image processing library for Python, a popular programming language. It is designed to interact efficiently with other popular scientific Python libraries, such as NumPy and SciPy. In particular, scikit-image leverages the powerful **data array** container of NumPy, that can store images of various dimensions (2-D, 2D RGB, 3D, 4D...). Since NumPy's arrays are natively n-dimensional, most functions of scikit-image work for 2-D (grayscale of RGB) images as well as 3-D images.

Here we shall describe how scikit-image can be used for processing 3-D images, and illustrate different image processing tasks on 3-D X-ray tomography images. Rather than giving a thorough description of the package, we will strive to explain the specificities of scikit-image. The range of possible image processing tasks is very broad; here we shall concentrate on the segmentation and labeling of objects inside a 3-D image, a common task in materials science or life science.

First steps with scikit-image

scikit-image is a free and open-source library, released under the permissive BSD license (as a large majority of the core scientific Python packages [Oliphant2007]). As such, it is available free of charge for all major operating systems, and included in several software suites shipping together a bundle of scientific Python packages, such as Enthought's Canopy or Continuum's Anaconda. Python being an interpreted language, interactive work with scikit-image can be done within the Ipython shell or the Ipython notebook [Perez2007, Rossant2013] (see Fig.1).

Figure 1 shows short examples of Python code using scikit-image in order to binarize images with an intensity threshold (using a method known as Otsu's thresholding), both for a 2-D image included with scikit-image and for a synthetic 3-D image. Note that the syntax is similar no matter the dimension of the image (here, for the function `skimage.filters.threshold_otsu`). A distinctive characteristic of scikit-image is its functional approach, meaning that typical image processing operations are always implemented as “image_output = function(image_input, optional_parameters)”. This approach contrasts with other libraries and softwares, that prefer an object-oriented or

pipeline approach. The choice made by scikit-image is to provide an API (Application Programming Interface) as simple as possible, in agreement with core Scientific Python modules. Also note that image objects are numerical arrays from the numpy module (`numpy.ndarray`), so that utilities functions of numpy can be called with images as arguments.

Unless specified, all functions and algorithms presented in this extended abstract accept 3-D images as arguments.

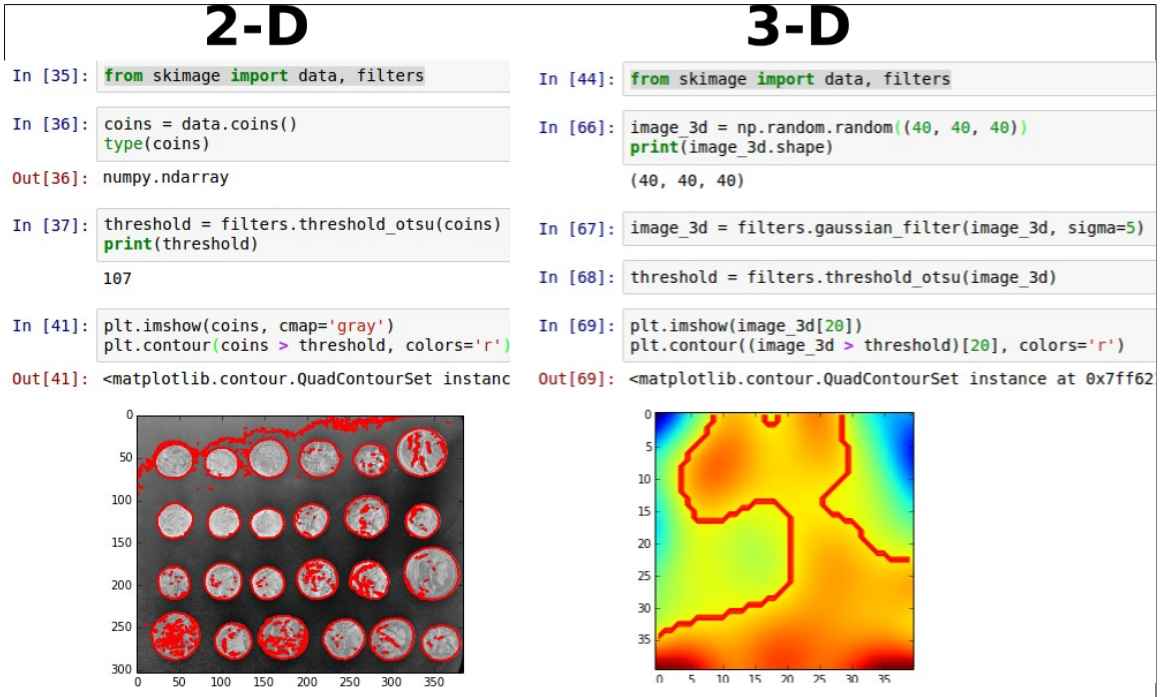

Fig. 1: *examples of scikit-image code on 2-D (left) and 3-D (right) images.*

Although we have used a synthetic image here for simplicity, input/output is easily handled for a variety of 3-D file formats, such as raw binary (using numpy) or hdf5 (using the pytables module).

Image denoising and restoration

X-ray tomography images often suffer from noise and artifacts, due to reconstruction artifacts or poor signal-to-noise-ratio, for example in in-situ experiments. The attribution of voxels to labeled regions is often easier if a first denoising step is performed.

Scikit-image offers different denoising functions, found in the submodules `filters` and `restoration`. The different algorithms correspond do different kinds of prior information on the image to be denoised, as well as different trade-offs between denoising performance and computational cost. Fig. 2 represents the denoising of a tomography image using several algorithm. The original image is the reconstruction of a phase-separated silicate glass [Bouttes2014] acquired on ID19 at the ESRF synchrotron. The two separated phases are well distinguished by human eye on Fig. 2, but important high-frequency noise (due an insufficient number of projections) corrupts the image. The histogram of pixel values consists of a single peak (see Fig. 2), and it is difficult to binarize the image as it is. A median filter (taking the median values of voxels in a neighbourhood) improves the signal-to-noise-ratio, with two peaks being present in the histogram. An interesting variant consists in using a bilateral filter, that averages

voxels with a weight corresponding to the spatial proximity with the pixel of interest, both in voxel space and in greyscale space. Finally, the total variation filter (TV) [Chambolle2004] is well suited for denoising images with a small number of phases, since it produces images that tend to be stepwise-constant. In the example of Fig. 2, the total variation filter results in the histogram with the sharpest peaks, while preserving well sharp boundaries between phases. Functions corresponding to the different algorithms have optional parameters as arguments to fix the size of the filter of the amount of denoising (for TV) that can be tuned to improve the result. However, default values are provided (using the optional keyword arguments of Python), so that functions can be tried first without the need to think about parameters' values.

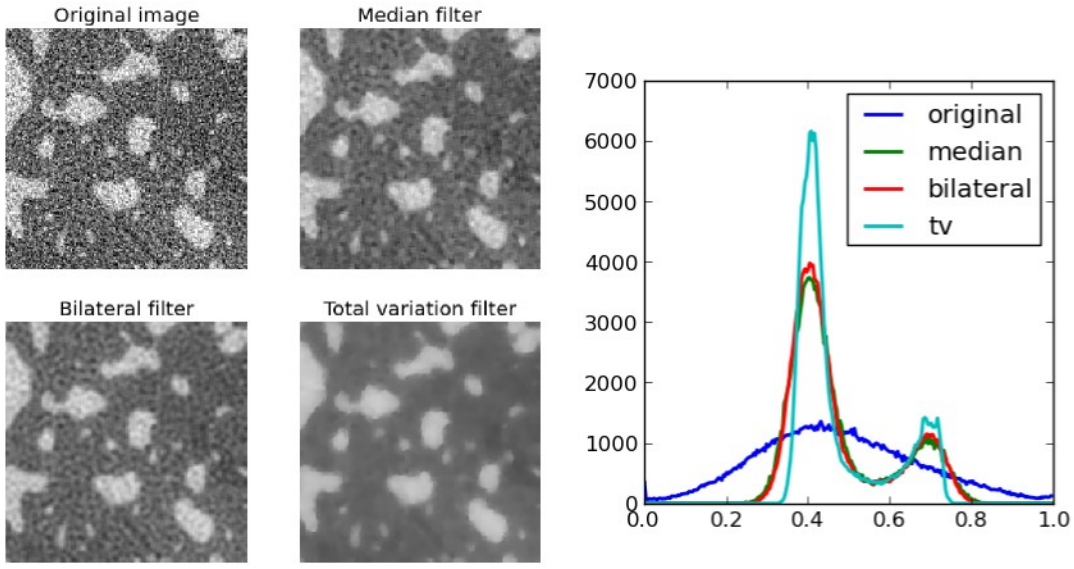

***Fig. 2**: denoising of tomography image with two phases. **Left**: original image and output of different denoising filters. **Right**: histograms of pixel values corresponding to images on the left.*

Fig. 3 shows another example of denoising, for a 3-D tomography image of the solid state reactions between quartz sand and sodium carbonate [Gouillart2012]. The reacted layer shows a strong high-frequency texturation, that would be blurred by most denoising filters. Here we have used a non-local means filter [Buades2005], that averages a voxel with other voxels if their neighbourhoods (called “patches”) are similar. As a result, only patches with similar textures are averaged together, and the algorithm improves the signal-to-noise ratio while preserving textures well. However, the execution of the non-local means algorithm is significantly longer than a median or bilateral filter.

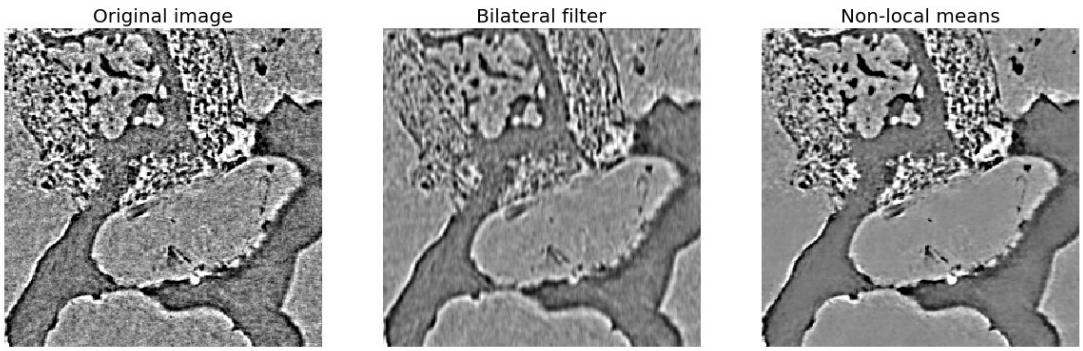

Fig. 3: denoising of an image with various textures. Note that the non-local means filter preserves well regions with a high-frequency texturation, while smoothing flat regions.

Image segmentation

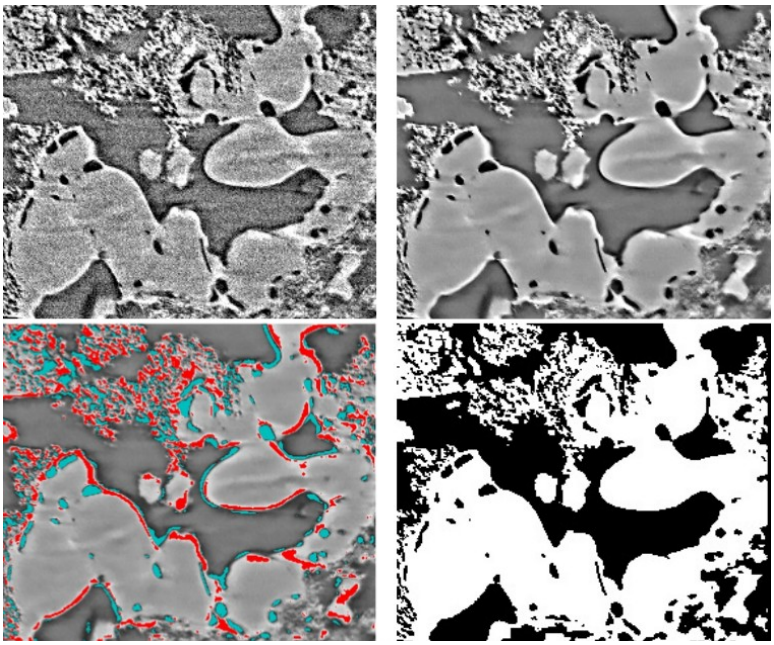

Fig. 4: denoising and segmentation. From left to right and top to bottom: original image, non-local means denoising, extraction of markers using histogram of denoised image, segmentation using random walker.

After an optional denoising step, images can be segmented into labeled regions using functions that are mostly found in the submodule `segmentation`. Basic histogram-based segmentations are available, such as different thresholding methods (like in Fig. 1 with Otsu thresholding), and a more advanced adaptive thresholding where the threshold value varies in space (for images with inhomogeneous exposure, for example). However, a more satisfying segmentation can be obtained if spatial information is used as well: neighboring pixels are more likely to belong to the same region. The random walker algorithm [Grady2006] uses markers (than can be determined from the histogram, for example) as starting points of a diffusion process, with diffusion being faster where the image gradient is small. An example of segmentation using the random walker algorithm is shown in Fig. 4: this diffusion algorithm produces here better results than a classical marker-based algorithm, the watershed algorithm (also available in

scikit-image). Other segmentation algorithms include superpixels algorithm, that automatically segment an image into a number of patches.

Development of scikit-image and documentation

scikit-image is developing fast, with an average of two new releases every year. It has more than 100 contributors, with an international core team of 10-15 people. All the development process can be watched on the github portal https://github.com/scikit-image/scikit-image, where users and developers can discuss about possible issues and propose additions to the code.

Documentation can be found on scikit-image's website http://scikit-image.org/. A noteworthy feature of the website is the graphical gallery of examples http://scikit-image.org/docs/dev/auto_examples/, that displays thumbnails of image processing figures. Clicking on a thumbnail opens a page with the page that generated the figure, so that it is possible to learn about image processing while browsing through the gallery.

Conclusion

scikit-image is a versatile image processing library for Python. Its key advantages are its simplicity of use, and the excellent compatibility with core scientific Python modules (numpy for numerical array manipulation, scipy for signal processing, matplotlib for plotting, mayavi for 3-D visualization [Ramachandran2011], scikit-learn for machine learning [Pedregosa2011]). Other more specialized libraries and softwares may offer better computational performances, for example by relying on GPU programming, or offer a selection of algorithms closer to the state of the art, but the rich scientific Python environment is a strong asset for the growing number of scikit-image users. During the conference, I will be happy to talk and demo about scikit-image.

References

[Bouttes2014] Bouttes, David, et al. "Fragmentation and Limits to Dynamical Scaling in Viscous Coarsening: An Interrupted in situ X-Ray Tomographic Study." *Physical review letters* 112.24 (2014): 245701.

[Buades2005] Buades, A., Coll, B., & Morel, J. M. (2005, June). A non-local algorithm for image denoising. In Computer Vision and Pattern Recognition, 2005. CVPR 2005. IEEE Computer Society Conference on (Vol. 2, pp. 60-65). IEEE.

[Chambolle2004] Chambolle, Antonin. "An algorithm for total variation minimization and applications." *Journal of Mathematical imaging and vision* 20.1-2 (2004): 89-97.

[Gouillart2012] Gouillart, Emmanuelle, et al. "In Situ Synchrotron Microtomography Reveals Multiple Reaction Pathways During Soda-Lime Glass Synthesis." Journal of the American Ceramic Society 95.5 (2012): 1504-1507.

[Grady2006] Grady, Leo. "Random walks for image segmentation." Pattern Analysis and Machine Intelligence, IEEE Transactions on 28.11 (2006): 1768-1783.

[Oliphant2007] Oliphant, Travis E. "Python for scientific computing." *Computing in Science & Engineering* 9.3 (2007): 10-20.

[Pedregosa2011] PEDREGOSA, Fabian, VAROQUAUX, Gaël, GRAMFORT, Alexandre, et al. Scikit-learn: Machine learning in Python. The Journal of Machine Learning Research, 2011, vol. 12, p. 2825-2830.

[Perez2007] Perez, F., & Granger, B. E. (2007). IPython: a system for interactive scientific computing. Computing in Science & Engineering, 9(3), 21-29.

[Ramachandran2011] RAMACHANDRAN, Prabhu et VAROQUAUX, Gaël. Mayavi: 3D visualization of scientific data. *Computing in Science & Engineering*, 2011, vol. 13, no 2, p. 40-51.

[Rossant2013] Rossant, C. (2013). Learning IPython for interactive computing and data visualization. Packt Publishing Ltd.

[VanDerWalt2014] VAN DER WALT, Stefan, SCHÖNBERGER, Johannes L., NUNEZ-IGLESIAS, Juan, et al. scikit-image: image processing in Python. PeerJ, 2014, vol. 2, p. E453.

Multi-resolution characterisation of grain-based measurements from x-ray tomography

E. Andò*[1,2], A. Tengattini[1,2,3], M. Wiebicke[1,2,4], G. Viggiani[1,2] , S. Salager[1,2] , J. Desrues[1,2]

[1] Univ. Grenoble Alpes, 3SR, F-38000 Grenoble, France – edward.ando@3sr-grenoble.fr
[2] CNRS, 3SR, F-38000 Grenoble, France
[3] School of Civil Engineering, The University of Sydney, Sydney, NSW 2006, Australia
[4] Technische Universität Dresden, Institute of Geotechnical Engineering, Germany
* presenting author

Keywords: x-ray tomography, inter-particle contacts, subpixel resolution

Abstract

The response of a granular medium (such as sand) to mechanical loading depends crucially on the mechanisms at the grain scale. X-ray tomography is a powerful tool allowing to obtain 3D images at this scale. However, extracting quantitative measurement of the properties of the grains and of their contacts remains challenging. This paper proposes both tools to improve the quality of the images themselves (to correct mechanical drift during x-ray scanning) and image-based measurements from x-ray tomography (using the knowledge of the material geometry *a-priori* for high-resolution template matching, as well as a fine study of interparticle contacts).

Introduction

In the mechanics of granular media, the ability to perform experiments *in-situ* inside an x-ray scanner is allowing a three-dimensional revolution in the data that can be obtained from experiments. From the 1970s, visionaries such as Oda (Oda 1972, and Oda and Iwashita 1999) have started to describe the state of a granular medium at the *grain scale*, defining quantities that describe a granular "fabric", *i.e.*, the **orientation of the grains**, the orientation of their **contacts** as well as the **pore space** around them, which drive the macroscopic (engineering) scale behaviour. This information is readily available from simple numerical simulations (*e.g.* DEM), but is much more difficult to obtain experimentally. Enter x-ray tomography: allowing not only the measurement of these quantities in 3D on real materials, but also their evolution. This in turn finally opens up the possibility for constitutive models describing the soil behaviour to be created including elements of fabric measured on real 3D granular materials (Fu and Dafalias, 2011), which can be used to greatly improve civil engineering simulations of soil structures.

Previous work on the measurement of granular kinematics (Hasan and Alshibli, 2012 and Andò *et al.,* 2012) shows that grain displacements and rotations can be measured individually and accurately (far below the pixel size of the image) in large deformation events such as shear bands, whose grain-scale behaviour can then be related back to macroscopic quantities such as stress and strain. Granular fabric is expected (by the micro-mechanics community in general) to provide a grain scale explanation for more elusive phenomena, such as the enormous change in stiffness upon load reversal, which is manifested at small levels of strain. Such problems, where grains have *minuscule displacements*, require *extremely precise tools*. Furthermore, this measurement challenge is exacerbated by the fact that a *mechanically relevant* number of grains must

be analyzed – which means (with a fixed image size) that a limited amount of information is available for each grain.

To face this challenge and to enable quantitative measurements, a number of tools have been developed – the paper will be split into three sections: 1) precision improvements for x-ray tomography, 2) improvements for image-based measurements on particles and 3) a study of inter-particle contacts. The interest of this work is to study the *behaviour of a significant number of particles* which in turn dictates a *reduced resolution for each particle*, therefore points 2) and 3) necessarily suffer from a lack of resolution – for this reason, some extremely high resolution images of a representative particle are used to calibrate measurements. The intersection of all these tools is a big step towards making measurements of the very small changes occurring at the specimen level.

1) Improving x-ray tomography images acquired in a lab scanner

Laboratory x-ray scanners are rapidly becoming a widespread tool to obtain 3D images. Compared to synchrotrons, scanning times are much longer, however access – especially for long experimental campaigns – is easier. For quantitative studies the highest quality images are essential: this typically means scanning at low power, with numerous projections and long exposures leading to long scanning times, which are vulnerable to changes – be the changes within the specimen, or of the imaging system – during scanning. Studying the RX-Solutions system in Laboratoire 3SR it was found that the mechanical stability of the system is highly dependent on temperature, which is regulated ±2°C in the room. In order to characterise the relative displacements between specimen and imaging system, a special piece of hardware called TomoFrame® (French Patent 14/53091, see Fig. 1) was developed to put four fixed reference points into the partially-used top and bottom corners of the images in cone beam geometry. The thermal dilation coefficient of materials have been chosen such that within a range of temperature, the displacement of the frame and the arms on which the reference spheres are attached compensate each other, meaning that the spheres always have the same relative positions. Furthermore the choice of materials has been made to facilitate scanning of the reference spheres.

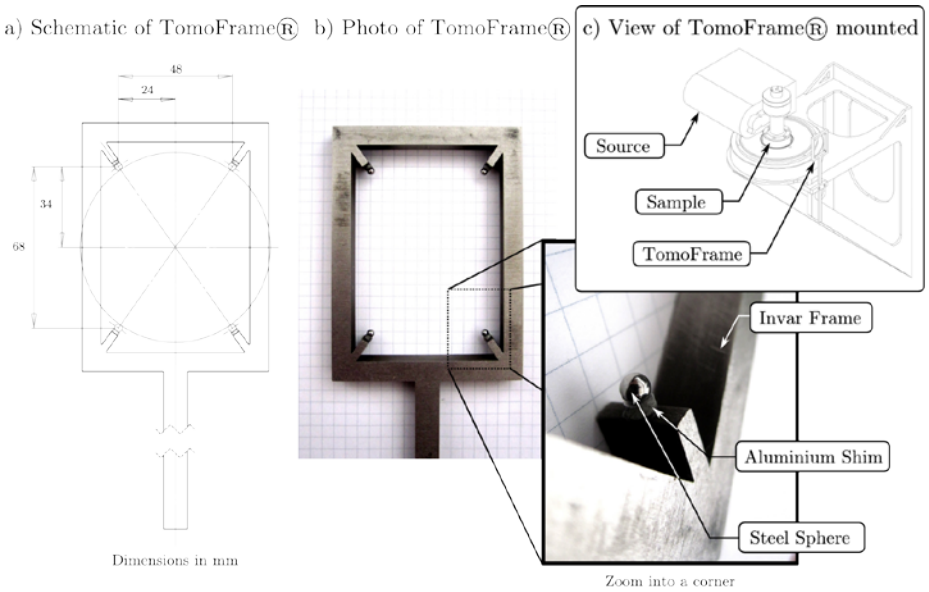

Fig. 1. *TomoFrame®, a) Schematic, b) Photo, c) Mounting on conventional x-ray scanner, with specimen close to the source, inset: zoom into a corner.*

Images acquired with this device, therefore, have four reference points which are *immobile with temperature*: this means that any displacement measured of these points in the acquired images mean that there are relative displacements of the scanned object with respect to the imaging system. The projection of four points in each x-ray radiograph allows a full 3D displacement to be calculated between any two images. Taking into account these displacements allows a very significant improvement in the reconstructed image of a partially-wet sand scanned for a long time (See Fig 2).

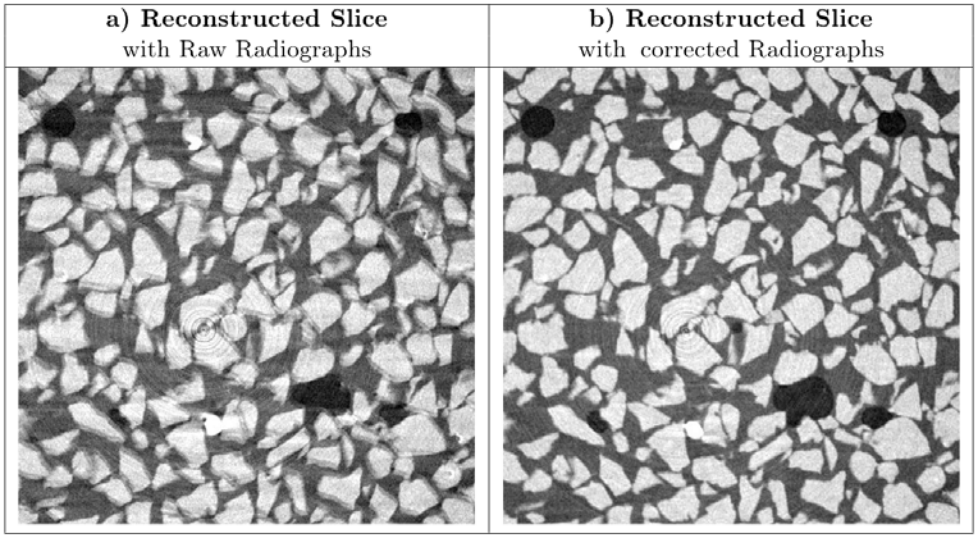

Fig. 2. *Improvement in the reconstructed image when taking into account relative displacements of the imaging system occurring while scanning.*

2) Improvements for image-based measurements on particles

In this section, a study of image-based measurements of particles is given, with some examples from work currently associated with Grenoble.

2.1) First the “Kalisphera” tool will be described: this piece of software (Tengattini and Andò 2015) is able to analytically (and therefore rapidly) create 3D images of spheres, with correct “Partial Volume” values at the border of the shape. Improvements have been made to the tool to allow it to correctly simulate the point-spread function of a real imaging system (which can be therefore measured). Its implementation within a template matching algorithm, allows it to robustly match spheres in real images. The upshot of this is that measurements of model granular materials can be made extremely precise, and the contribution of a sphere’s mass on the image can be taken into account, allowing a much more precise quantification of the remaining phases.

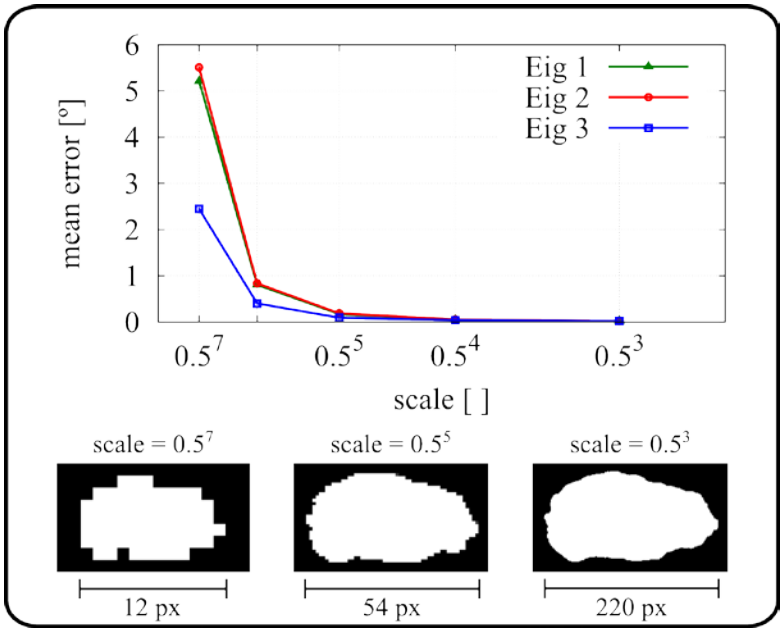

Fig. 3. *Change in the error relative to an imposed change in orientation, of the three eigen-vectors of the moment-of-interia tensor as a high resolution 3D image of a grain is degraded (see bottom row).*

2.2) Study of particle orientations: previous work has shown that calculating the eigen-vectors of the moment-of-inertia of a grain (imaged at a resolution allowing tens of thousands of grains to be imaged) is a rather unstable measurement, with a highly-varying rate of error (See Andò *et al.* 2012). In order to study this more closely, an extremely high-resolution image was acquired of a single, angular, Hostun Sand grain (at a pixel size of 0.35µm/px), and 4000 different, random, rotations were applied to this object, and the resulting effect on the moment-of-inertia eigen-vectors measured. The image was then scaled down progressively to study the metrological properties of this measurement of orientation. Figure 3 clearly shows that as the 3D image is scaled down the *mean* error increases - this can be considered a guide for the size (in pixels) that a grain should measure in order to have a given level of precision for its orientation. This study will be improved by considering different grain shapes, as well as the statistics of the individual errors.

3) A study of inter-particle contacts

The last study in this paper will show some recent results on the analysis of the detection of contacts between grains. Two “Kalisphera” spheres are generated in random orientations, at different inter-particle distances. A physically-correct threshold (*i.e.,* one giving the correct final volume of spheres) is then applied to the resulting image, and the number of objects are counted. Ideally unless the inter-particle distance is exactly 0 pixels two objects would always be detected, but unfortunately due to the interaction of their partial volume effects, even when the particles are separated (see on x-axis in Figure 4) by as much as half a pixel, they are still detected as a single object.

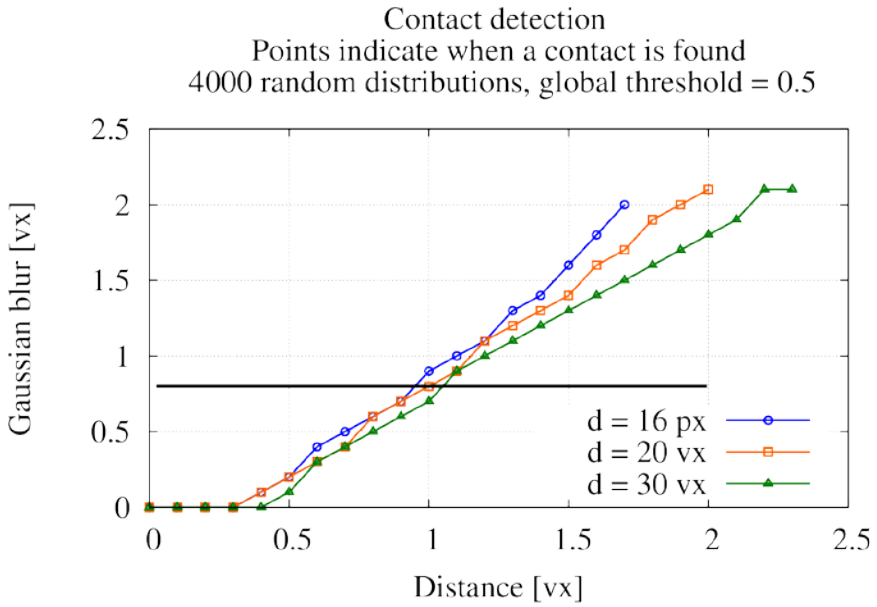

Fig. 4. *Plot showing the detection threshold for two close particles as being separate objects as a function of the distance between their surfaces, and the gaussian blur of the image, representing the cumulative point-spread-function of the imaging system.*

This effect is exacerbated by the simulation of the point-spread-function of the images (marked horizontally on Figure 4 is the value of 0.81 pixels, which represents the radius of the point-spread-function measured for these conditions in the Laboratoire 3SR system). As the blur increases, particles can be further apart than one pixel before being detected as separate objects. Of great importance is the fact that there are practically no differences between the three lines in Figure 4, which represent the two-sphere detection threshold for spheres of different diameters. This means that this *systematic over-detection* of particle-to-particle contacts is *not improved by increasing the imaging resolution!* In order to overcome this obstacle a number of remedial measured are planned in the future. With the luxury of having very high-resolution single-particle scans of irregular natural grains (such as the one used in Section 2.2) the detection and measurement of orientation of real inter-particle contacts can be studied: high-resolution grains (an almost ground-truth whose surface normal is well known in each point) can be numerically put into contact, the resulting image segmented and contact orientation measured in the usual way and compared to the ground truth. Following the philosophy of Section 3, the quality of this measurement can be studied at different resolutions.

Conclusions

This paper has shown a number of different tools developed in Grenoble and partners as part of a general imaging toolkit for the high-quality measurement of 3D granular fabric. A physical device for the improvement of scan quality has been presented, followed by a number of tools and studies on 3D images coming from such scans. The analytical tool Kalisphera has been presented, and subsequently used to study the fine metrological properties of contacting particles - making the important finding that contacts are systematically overestimated (and in no case underestimated) regardless of the imaging resolution. The multi-resolution study of grain orientations, however, shows that increased resolution does help significantly with reducing error in the measurement of grain orientations, for one given grain.

References

Ando, E., Hall, S. A., Viggiani, G., Desrues, J., & Bésuelle, P. (2012). Grain-scale experimental investigation of localised deformation in sand: a discrete particle tracking approach. Acta Geotechnica, 7(1), 1-13

Andrade, J. E., Vlahinić, I., Lim, K. W., & Jerves, A. (2012). Multiscale 'tomography-to-simulation' framework for granular matter: the road ahead. Géotechnique Letters, 2(July-September), 13

French Patent 14/53091 (2014). Dispositif de mesure de déplacements parasites dans un tomographe à rayons X

Fu, P., & Dafalias, Y. F. (2011). Fabric evolution within shear bands of granular materials and its relation to critical state theory. International Journal for numerical and analytical methods in geomechanics, 35(18), 1918-1948.

Hasan, A. and Alshibli, K. A. (2012) "Three Dimensional Fabric Evolution of Sheared Sand", Granular Matter, Vol. 14, No. 4, pp. 469-482.

Jaquet, C., Andó, E., Viggiani, G., & Talbot, H. (2013). Estimation of Separating Planes between Touching 3D Objects Using Power Watershed. In Mathematical Morphology and Its Applications to Signal and Image Processing (pp. 452-463). Springer Berlin Heidelberg

Oda, M. (1972). Initial fabrics and their relations to mechanical properties of granular material. *Soils and foundations,* 12:17–36

Oda, M. and Iwashita, K. (1999). Mechanics of Granular Materials, An Introduction. *Balkema*, Rotterdam, Netherlands, 1st edition

Tengattini, A & Andò, E. (2015) Kalisphera: an analytical tool to reproduce the partial volume effect of spheres imaged in 3D. Submitted to IOP Measurement Science and Technology, accepted

Wiebicke, M. Andò, E., Viggiani, G, Herle, I. (2015) Towards the measurement of fabric in granular materials with x-ray tomography. Submitted to IS-Buenos Aires, 2015.

Feasibility of iterative phase contrast tomography

N. T. VO*, R. C. ATWOOD, M. DRAKOPOULOS

Diamond Light Source, Harwell Science and Innovation Campus, Didcot, Oxfordshire, OX11 0DE, UK
nghia.vo@diamond.ac.uk
robert.atwood@diamond.ac.uk
michael.drakopoulos@diamond.ac.uk

Keywords: Tomography, X-ray phase contrast imaging

Abstract

Iterative phase retrieval in the Fresnel region based on the random signed feedback (RSF) technique has shown a promising performance on tomographic data as demonstrated in [Vo]. This report presents the performance of the RSF technique at various conditions to improve the convergence speed. The results are useful for evaluating the feasibility of this technique in quantitative phase contrast tomography.

Introduction

The applications of phase contrast tomography based on direct methods of phase retrieval have been limited so far by the fact that they are sensitive to noise or applicable only to limited types of samples. There are no such of limitations for iterative phase retrieval methods based on the Gerchberg-Saxton algorithm, but they are not often used in Fresnel region due to the problems of slow convergence and stagnation. The RSF accelerator proposed Vo et. al. [Vo] significantly improves the convergence speed. Here, we present more detail its performance under different conditions for optimization.

Methods

The pseudo-code of the procedure of the RSF technique is as follows; where temporary intermediate values are designated M:

input λ, *N, D1, D2,* I_{D1}, I_{D2}, *dr,* θ;
T=initial_ estimated_transmission_funtion;
For n=1 to Iterative_number
Step1: $T_1 = GS(T, D1, I_{D1})$;
Step2: $T_2 = GS(T_1, D2, I_{D2})$;
Step3: $T_3 = (T_1 + T_2)/2$;
Step4: $M_1 = Sgn(Sqrt(I_{D2}) - Abs(Fr_{D2}(T_3)))$;
Step5: $M_2 = \theta \times Random([0,1],\{N,N\})$;
Step6: $T = SmoothFilter(Re(T_3)) + i \times (Im(T_3) + M_1 \times M_2)$;
End

where λ is the wavelength, N is the size of all 2D digitized functions, *D1* and *D2* are the distances of the measured intensities I_{D1} and I_{D2} respectively. *dr* is the resolution of the recorded image which is used to compute values of spatial frequencies for numerical Fresnel transform, $Fr_D()$. θ is used for controlling the strength of the accelerator. *GS()* function returns the next estimation of the transmission function after one cycle of applying Fresnel transform (or Fresnel propagator), combining with observed intensity, and applying inverse Fresnel transform. *Re*, *Im*, and *Abs* functions return the real part, imaginary part, and the absolute value of the complex value, respectively. In order to investigate the convergence speed of the RSF technique at different settings, we change the combination of the *GS* function at different distances and adjust parameters in step 4, 5, and 6.

In the estimation stage which consists of step 1, 2 and 3, the next estimation of the transmission function can be calculated from the different combinations of the *GS* function and distances as shown in Table 1.

Table 1: Different combination of step 1, 2, and 3

	Case 1	Case 2	Case 3	Case 4
Step 1	$T_1=GS(T,D1,I_{D1})$	$T_1=GS(T,D2,I_{D2})$	$T_1=GS(T,D1,I_{D1})$	$T_1=GS(T,D1,I_{D1})$
Step 2	$T_2=GS(T_1,D2,I_{D2})$	$T_2=GS(T_1,D1,I_{D1})$	$T_2=GS(T,D2,I_{D2})$	$T_2=GS(T_1,D2,I_{D2})$
Step 3	$T_3=(T_1+T_2)/2;$	$T_3=(T_1+T_2)/2;$	$T_3=(T_1+T_2)/2;$	$T_3=T_2$

In the stage of acceleration, step 4, which applys a *Sgn* function (returning value -1, 0, or 1 depending on whether its input is negative, zero, or positive) on the difference between the measured intensity and the calculated intensity at the distance D2, can be changed by using the intensity at distance D1 instead. We use θ as the percentage of the mean of the intensity subtracted from the background to adjust the strength of the accelerator in step 5. The matrix of random values in the range of [0;1] is used to overcome the stagnation problem. The side-effect of adding a perturbation on the imaginary part is cancelled by applying a smooth filter such as Gaussian filter on the real part as described in step 6.

For testing the convergence speed at different cases, a numerical phantom made of simple shapes (Fig. 1) is used, where the ratio between the absorption function and phase shift differs between shapes. Values of absorption and phase shift used in simulation, respectively, are: triangle (0.0125; - 0.3), circle (0.04; - 0.7), inside square (0.005; - 0.9), and outside square (0.01, - 0.5). These values are chosen quite arbitrarily keeping in mind that the phase shift should be higher than the absorption in order to get a clear phase enhancement image. The image size is N×N=600×600 pixels with a pixel size of 1 µm. Intensities with a photon energy of 12 keV at 50 cm and 80 cm are used for simulation as shown in Fig.2.

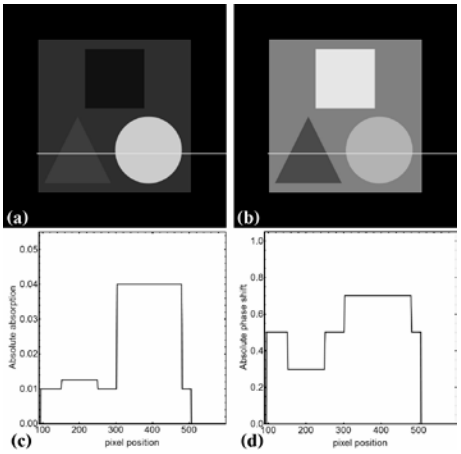

Fig. 1: Phantoms and the line profiles (white lines): (a,c) Absorption function, (b,d) phase shift

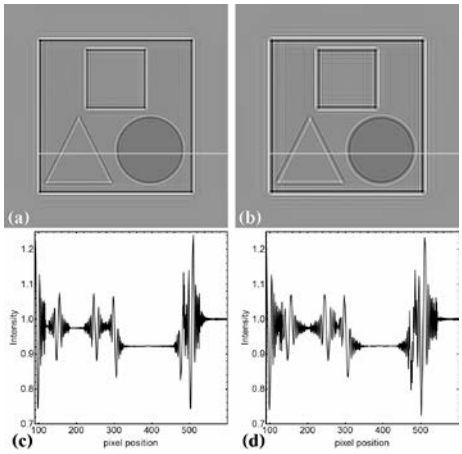

Fig. 2: Intensities and the line profiles: (a,c) at 50cm; (b,d) at 80cm

Results

Fig. 3 shows the plots of the normalized root mean square (NRMS) error, which is the root mean square of the difference between the reconstructed and original phase shift normalized by dividing the mean value of the original phantom, versus the number of

iterations of four cases in Tab. 1. As can be seen, case 1 results in the fastest convergence speed compared with the others.

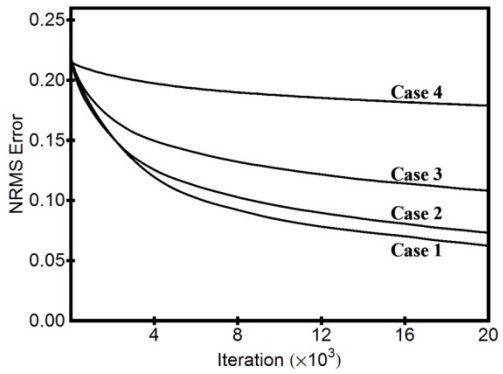

Fig. 3. NRMS error between the reconstructed and original phase shift versus the number of iterations for four cases.

The choice of distance D1 instead of D2 can enhance the convergence speed as shown in Fig. 4.

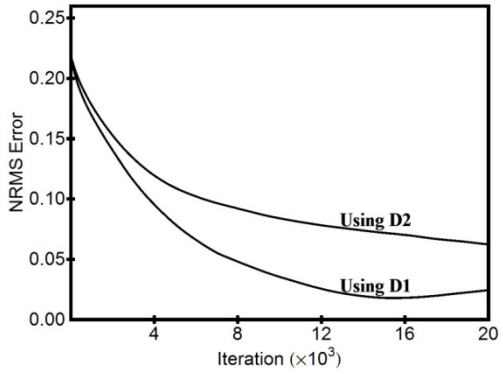

Fig. 4. NRMS error between the reconstructed and original phase shift versus the number of iterations of two choices of distances.

The strength of the accelerator apparently impacts on the convergence speed as can be seen in Fig.5, so a good choice is to use a strong accelerator for the initial stage, then subsequently reduce its strength.

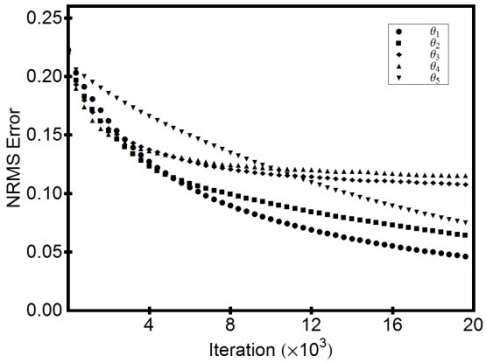

Fig. 5. NRMS error versus iteration of different values of : θ_1 = 0.5%, θ_2 = 1%, θ_3 = 2%, θ_4 = 3% and θ_5 = 0.1% of the mean of (I_{D2} -1)

A side-effect of adding a perturbation appears in the absorption function as shown in Fig. 6. This is corrected by using a Gaussian filter with sigma=2 that results the fast reconstruction of the real part after few hundreds of iterations (Fig. 7). The comparision of different values of sigma in Fig. 8 illustrates the advantage of using a stronger filter. However the computation cost needs to be considered for real applications.

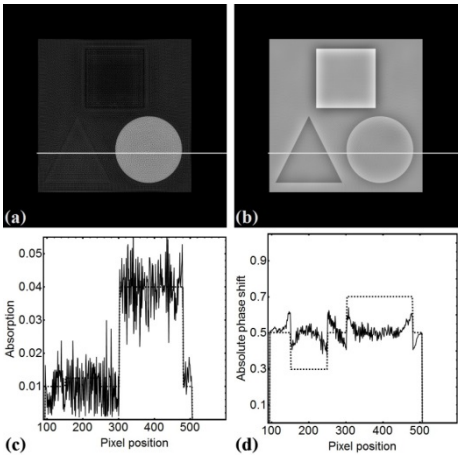

Fig. 6. Absorption function (a,c) and phase shift (b,d) after 500 iterations in the case of not using the smoothing fitter.

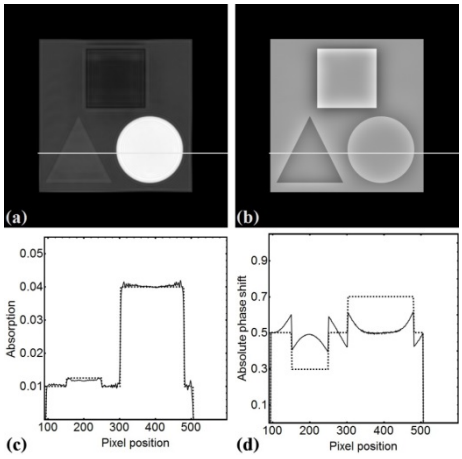

Fig. 7. Absorption function (a,c) and phase shift (b,d) after 500 iterations in the case of using the smoothing fitter.

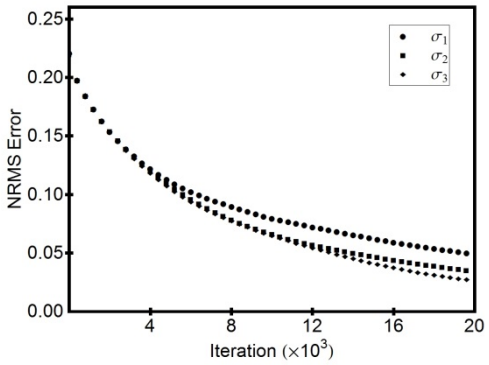

Fig.8. NRMS error versus iteration of different σ: (σ_1 = 2; σ_2 = 4; σ_3 = 6) of the Gaussian filter which shows the better performance of the larger σ.

The optimized RSF technique is applied on the tomographic dataset obtained at ESRF (European Synchrotron Radiation Facility) where the sample is the duplex steel [EXTREMA]. Intensities at 0.158 m and 0.308 m are recorded with the pixel size of 1.4 micron and the photon energy of 55 keV (Fig. 9). The retrieval of the phase shift and absorption funtion are shown in Fig. 10. A reconstructed slice (Fig. 11) from retrieved tomographic dataset is a very promising result.

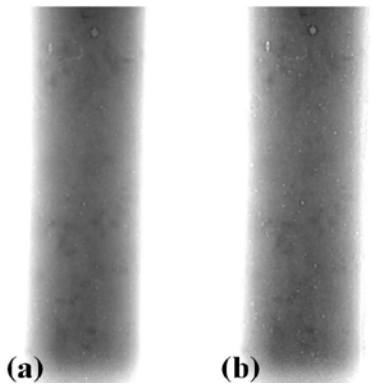

Fig. 9. Projections of the sample at the distances of 0.158 m (a) and 0.308 m (b).

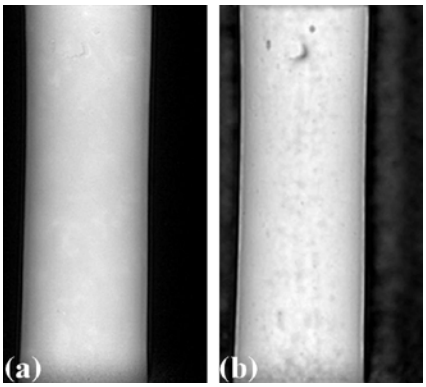

Fig. 10. Retrieved absorption function (a) and phase shift (b) after 400 iterations.

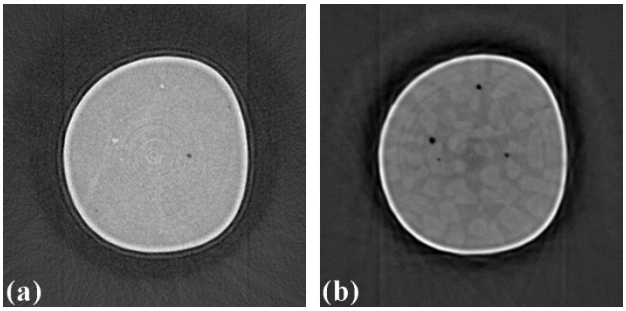

Fig. 11. Slice reconstructed from the retrieved tomographic dataset of the absorption funciton (a) and the phase shift (b).

References

Vo T. N., Atwood R. C., Moser H. O., Lee P. D., Breese M. B. H., and Drakopoulos M. (2012). "*A fast-converging iterative method for X-ray in-line phase contrast tomography,*" ***Applied Physics Letters***, 101, 224108.

EXTREMA 2015 workshop, http://www.esrf.eu/home/events/conferences/2015/extrema-2015---challenges-in-x-ray-tomography.html

Towards the reconstruction of the mouse brain vascular networks with high- resolution synchrotron radiation X-ray tomographic microscopy

A. PATERA*[1,2], A. ASTOLFO[1], K. S. MADER[1,3],
M. SCHNEIDER[4,5], B. WEBER[5], M. STAMPANONI[1,3]

[1]Swiss Light Source, Paul Scherrer Institute, Villigen, Switzerland – alessandra.patera@psi.ch
marco.stampanoni@psi.ch
alberto.asto@gmail.com
[2]Centre d'Imagerie BioMedicale, Ecole Polytechnique Federale de Lausanne, 1015 Lausanne, Switzerland
[3]Institute of Biomedical Engineering, University and ETH Zürich, Switzerland
- stampanoni@biomed.ee.ethz.ch
[4]Computer Vision Laboratory, ETH Zurich, Sternwartstrasse 7, 8092 Zurich, Switzerland
[5]Institute of Pharmacology and Toxicology, University of Zurich, Winterthurerstrasse 190, 8057 Zurich, Switzerland
*presenting author

Keywords: brain vasculature, synchrotron-radiation, tomography, reconstruction

Abstract

High-resolution synchrotron radiation X-ray tomography at the Swiss Light Source of the Paul Scherrer Institute, in Switzerland, is used as a key technology for reconstructing, in a non-descructive way, the entire vascular system of the mouse brain at 1 μm resolution. In this work, an axial area of 5.1×7.5 mm^2 of the 1 cm^3 mouse brain is covered by 60 local tomographic scans, resulting in a large amount of datasets. We address the challenge of stitching together terabytes of reconstructed data.

Introduction

The cerebrovascular system continously transports nutrients and oxygen to the brain. Inadequate energy supplies lead to fatal consequences, from impairment of the brain function to brain death. Neurovascular disease brings to long-term adult disability. Brain vessels play an important role in the development and in the process of maintaining normal brain function. As a matter of facts, an in-depth knowledge of the vascular structure and topology is essential for better understanding the pathophysiological cerebral processes. Magnetic resonance imaging has ben longer used in the study of macro-vessels (Klohs et al., 2012; Pathak et al., 2011) while two-photon laser scanning microscopy for investigating the complex micro-vessels (Tsai et al., 2009). Currently, the architecture of the cerebral vasculature is documented at 100 μm (Lauwers et al., 2008) resolution for human brain and about 10 μm for mouse brain. More recently, Micro-Optical Sectioning Tomography has shown potential in imaging the vessel network of an entire mouse brain with a voxel resolution of 0.35×0.4×2.0 $μm^3$ (Xue et al., 2014). However, the destructive nature of the technique avoids the potential options of *in-vivo* imaging. Within the context of the Human Brain Project (HBP), we aim at using synchrotron radiation X-ray tomographic microscopy at the Swiss Light Source of the Paul Scherrer Institute (Switzerland) for studying the entire vasculare system of the mouse brain with 1 μm resolution. Reconstructing the entire cerebrovascular structure will produce terabytes of datasets to analyse. We introduce a parallel and iteractive method to address this challenging problem.

Experimental method

Third generation synchrotron radiation X-ray Tomographic Microscopy at the Swiss Light Source of the Paul Scherrer Institute has shown its potentials for non-destructive high-resolution investigation of the vascular system in the mouse brain. The beamline get photons from a 2.9 T superbend with a critical energy of 11.1 keV. This makes studies at energy of 25 keV, typically used for biological samples, easily accessible. During the experimental work, we used the standard tomographic microscopy setup (Marone et al., 2009) equipped with the PCO.Edge detector and a 10x objective. This yields a pixel size of 0.65 microns and an effective resolution of about 1 micron. Each local CTs cover a portion of the sample that is a cylinder with 1.7 mm in diameter and 1.4 mm in height. We acquired local CTs with a pitch of 1.2 mm (distance between the centers of the FOV). It guarantees that the whole sample is acquired with some superposition (see Figure 1). We performed 60 local tomographies on a sub-volume of the brain samples (e.g., 5×6x2 scans along the *x y* and *z* sample directions respectively, with *z* corresponding to the beam direction), thus covering a final axial area of 5.1×7.5 mm^2 during 9 hours of scanning time.

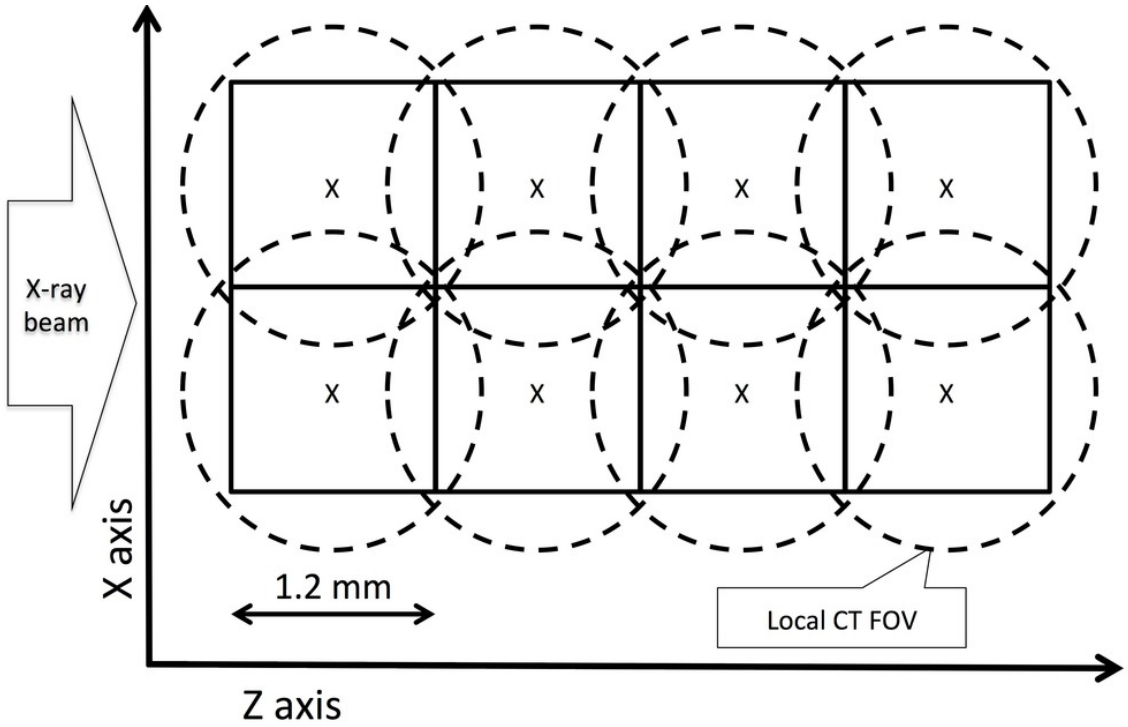

Figure 1: Scanning protocol in local tomography along the *x*-*z* plane, covering an area of 1.7×1.4 mm^2

One of the most important aspects of this project is the optimization of the sample preparation. For this work, the sample was prepared by intravascular filling with consecutive embedding of the tissue. More specifically, we adopted the approach proposed by Xue et al. 2014 and based on the Indian-ink perfusion for sample preparation in order to study the macro and micro vascular anatomical structure network. Finally, a mouse brain with a size approximately of 1 cm^3 has been infused with 50% Indian-ink and kept in glue to ensure the stability of the sample.

Results and discussion

Each dataset is reconstructed with the conventional algorithm based on the retrieval of the 3D distribution of the attenuation coefficient μ from its linear projections. We observe that the Indian-ink acts well as contrast agent. After reconstruction, the Fourier transform-based phase correlation method (Preibish et al., 2010) is successfully applied to compute translational offsets between the sub-volumes, thus providing a perfect stitching of the whole volume. A main challenge of the experiment is related to the amount of data to be handled and analysed. Each reconstructed datasets (with dimensions of 1.7×1.7×1.4 mm^3) consist of 14 GB and the volume of 5.1×7.5×2.8 mm^3 after stitching consists of 188 GB. As example, the maximum intensity of a region of interest with a size of 1.2×0.5 mm^2 is shown in Figure 2.a. In this work, we have extended the method of Preibisch et al. 2010 in order to work on several scans by enabling the use of many machines in parallel, thus reducing drastically the speed and allowing the stitching and analysis of such large datasets. The implementation is here described. After correlation, the maximum value is taken to produce an offset vector. Each positions is then iteratively updated with a smoothing function applied to these vectors. A three-dimensional visualization of the sub-ROI after stitching is shown in Figure 2.b. Additionally, we analysed a region of the brain occupying a FOV in order to estimate the thickness of the vessel. This analysis is performed by using the software VG Studio MAX and the result is reported in Figure 3. The diameters of the reconstructed vessels range between 1.5 and 4.5 μm, accordingly to literature (Blinder et al., 2013).

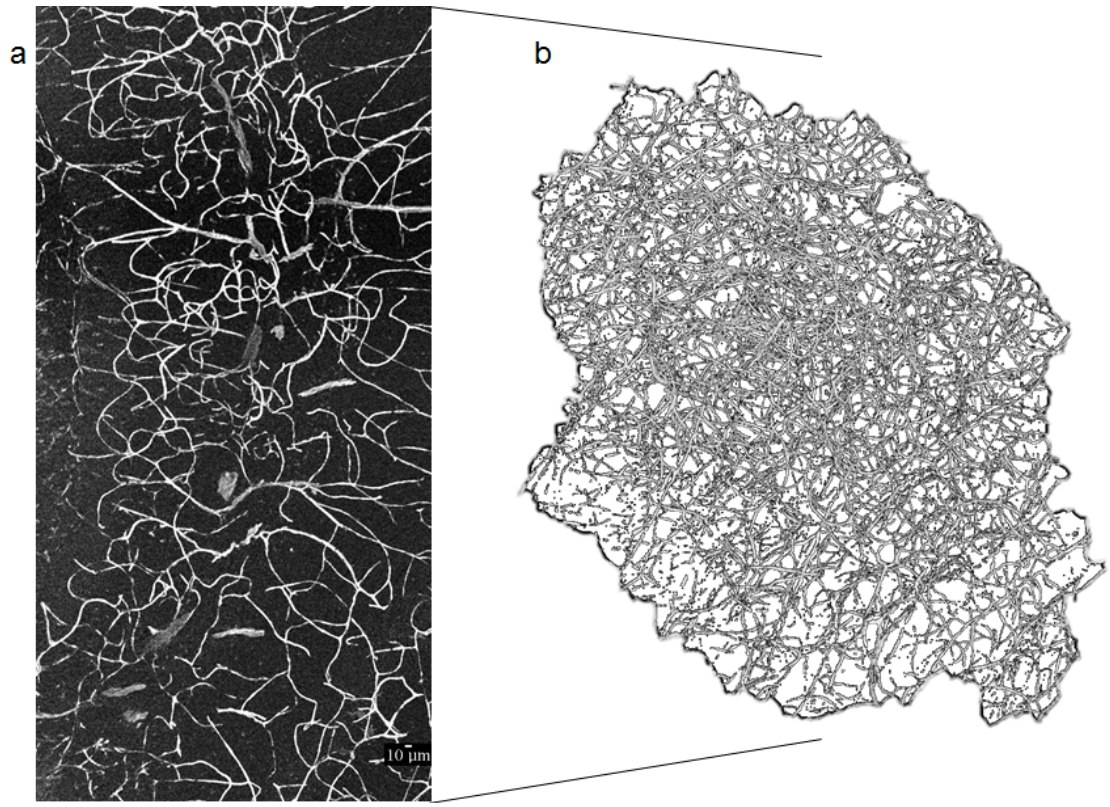

Figure 2: (a) Max. intensity of a sub-ROI in the 5.1×7.5×2.8 mm^3 stitched brain with (b) the corresponding three-dimensional rendering.

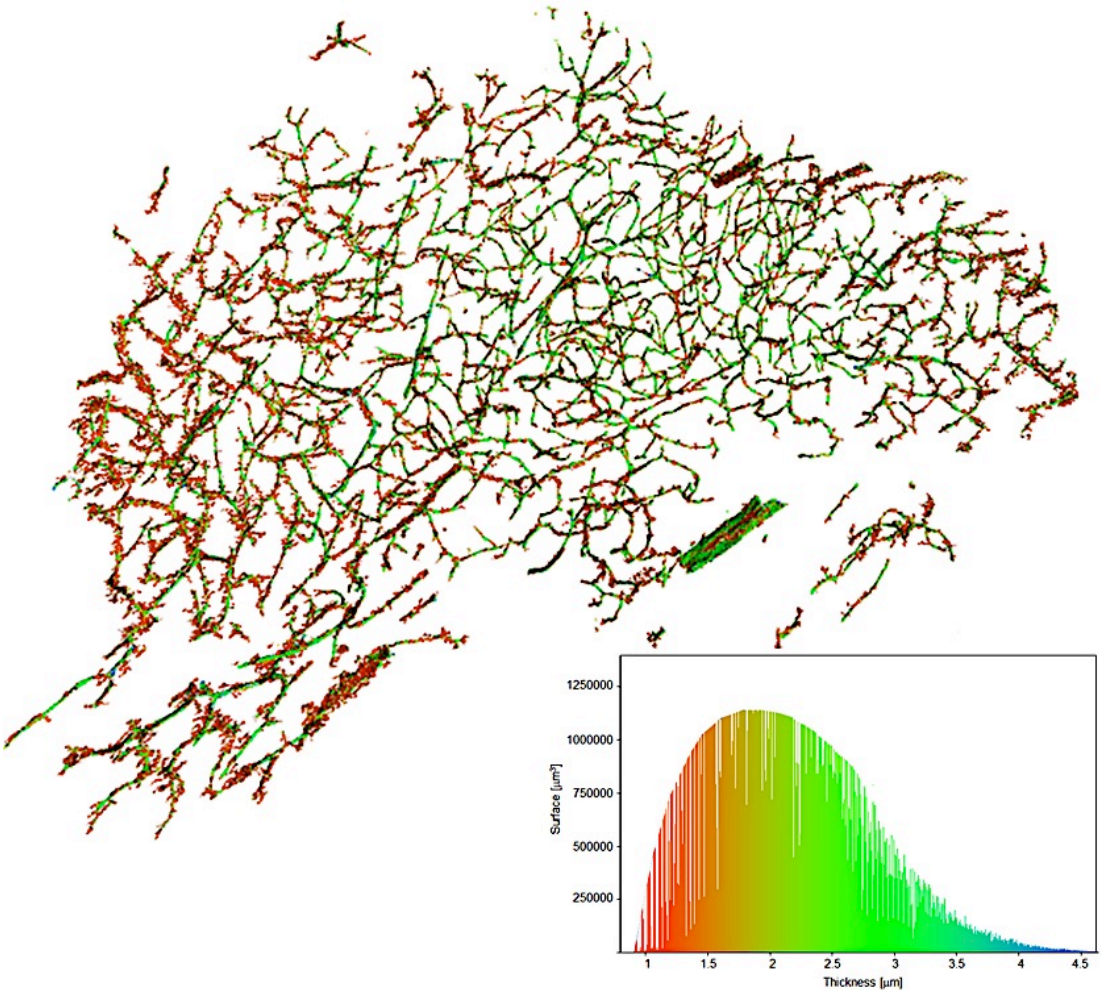

Figure 3: 3D distribution map of the vessel diameter in a sub-ROI of the mouse brain sample.

Conclusion

This study established a non-invasive method to investigate, with high-resolution, the entire vascular structure in a mouse brain. An important challenge is here addressed in terms of image processing. Sixty reconstructed datasets of 14 GB of memory each are stitched together to map the entire region of the brain considered for the analysis. We extend an existing correlation method for reconstructing 188 GB of volume. This preliminary result will be extended into the full reconstruction of the complete cerebrovascular network of the mouse brain, with a final total reconstructed volume of approximatively 7 TB. At this point, these pioneering efforts are pointing towards new horizons in the investigation of large biological samples with 3D high spatial resolution.

Acknoledgment

We thank Gordan Mikuljan for his great support in setting up the experiment at the beamline and the TOMCAT team for the fruitful discussion on the project. This study is supported by the Centre de Imagerie Biomedicale of EPFL Lausanne, Switzerland.

References

Blinder P, Tsai PS, Kaufhold JP, Knutsen PM, Suhl H, et al. (2013) The cortical angiome: an interconnected vascular network with noncolumnar patterns of blood flow. **Nat Neurosci** 16: 889–897

Klohs J, Baltes C, Princz-Kranz F, Ratering D, Nitsch RM, et al. (2012) Contrast-Enhanced Magnetic Resonance Microangiography Reveals Remodeling of the Cerebral Microvasculature in Transgenic ArcA beta Mice. ***J Neurosci*** 32: 1705–1713. doi: 10.1523/jneurosci.5626-11.2012

Lauwers F, Cassot F, Lauwers-Cances V, Puwanarajah P, Duvernoy H. (2008) Morphometry of the human cerebral cortex microcirculation: general characteristics and space-related profiles. ***Neuroimage***. 2008 Feb 1; 39 (3):936-48.

Marone F, Hintermuller C, McDonald S, Abela R, Mikuljan G, Isenegger A, Stampanoni M (2009). X-ray Tomographic Microscopy at TOMCAT. *9TH INTERNATIONAL CONFERENCE ON X-RAY MICROSCOPY 186*, *012042*. doi: 10.1088/1742-6596/186/1/012042

Pathak AP, Kim E, Zhang JY, Jones MV (2011) Three-Dimensional Imaging of the Mouse Neurovasculature with Magnetic Resonance Microscopy. ***PLoS One*** *6: e22643*. doi: 10.1371/journal.pone.0022643

Preibisch, Stephan, Stephan Saalfeld, and Pavel Tomancak. (2009) Globally optimal stitching of tiled 3D microscopic image acquisitions. ***Bioinformatics (Oxford, England)*** 25 (11): 1463–5. doi:10.1093/bioinformatics/btp184.

Tsai PS, Kaufhold JP, Blinder P, Friedman B, Drew PJ, et al. (2009) Correlations of neuronal and microvascular densities in murine cortex revealed by direct counting and colocalization of nuclei and vessels. ***J Neurosci*** 29: 14553–14570. doi: 10.1523/jneurosci.3287-09.2009

Xue S, Gong H, Jiang T, Luo W, Meng Y, et al. (2014) Indian-Ink Perfusion Based Method for Reconstructing Continuous Vascular Networks in Whole Mouse Brain. ***PLoS ONE*** 9(1): e88067. doi: 10.1371/journal.pone.0088067

Taming the flood: Distributed image processing made easy on large tomographic datasets

*K. MADER[1,2,3], R. MOKSO[1], A. PATERA[1], M. STAMPANONI[1,2]

[1] Swiss Light Source, Paul Scherrer Institut, Villigen, Switzerland
[2] Institute of Biomedical Engineering, Swiss Federal Institute of Technology and University of Zurich, Zurich, Switzerland
[3] 4Quant, Zurich, Switzerland
* presenting author

The combination of improving detector technologies, more efficient measurements, and parallel acquisition have increased both the amount and the rate of data being produced in tomographic measurements. By contrast, the tools available for analyzing these ever growing datasets have remained relatively static. Additionally, with the latest acquisitions having sustained rates of 8GB/s [Mokso, 2009], the memory of even most powerful workstations is fully saturated after 1 minute of collection. Furthermore, while transistor count has continued to grow at an exponential rate, the speed of processors has been relatively stagnant since the early 2000s. The accumulation of these effects demand a radical change in the approach to handling large datasets.

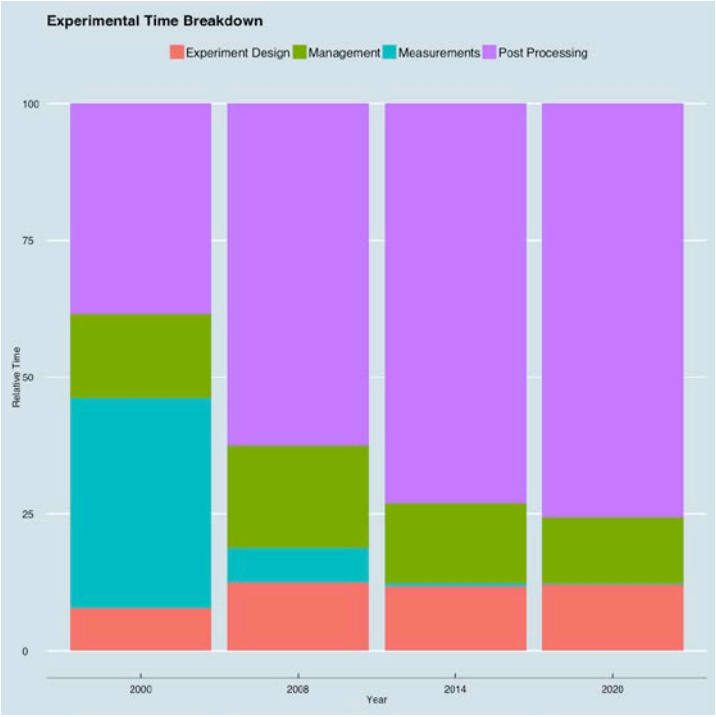

Figure 1. The graph illustrates the rapid change in the distribution of experiment time, particularly when examining the proportion used up by post-processing.

While the growth in tomography has been unique in the sheer magnitude of data produced, the fields of bioinformatics [Altintas, 2013], and web analytics [Dean, 2008] have experienced similar growth spurts and made significant progress on developing flexible, scalable frameworks for processing massive datasets in a distributed, fault-tolerant manner. Using the Apache Spark framework developed in [Zaharia, 2012], we have implemented a series of image processing tools for common image processing tasks like segmentation.

The framework we developed, Spark Image Layer, is built on top of the Apache Spark framework which provides the cloud-support, distribution, and fault-tolerance. The layer currently includes a range of basic image processing operations including filtering / noise reduction, segmentation, contouring, distance / thickness map generation, shape, distribution, and texture analysis as described in [Mader, 2012]. The various components can then be pipelined into a workflow using scripts written in Java, Python, or Scala. Alternatively the tools can be run from a web-based interface. The status of the analysis and the results can be queried interactively from the web interface which provides both image, rendered,

and plotted visualizations based on the type of analysis being performed. Given access to enough computational resources, the analysis can even be run in a streaming mode to process the images in real-time rather than single static analyses after the data are measured and saved.

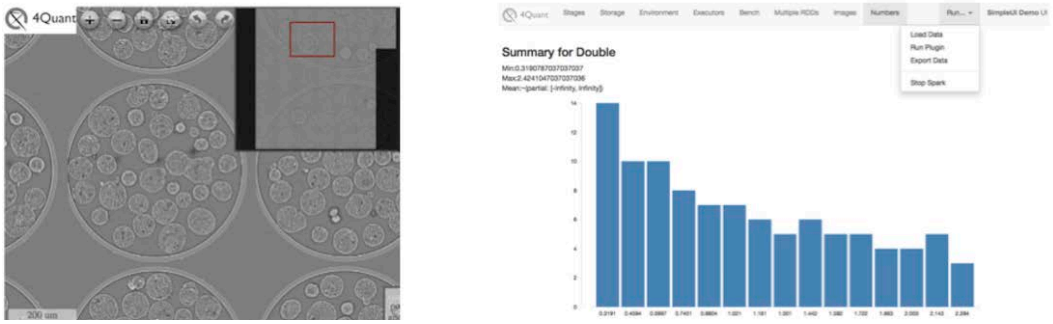

Figure 2. The GUI interface for the Spark Image Layer tools. The left panel shows the DeepZoom-based tool to explore a multi-gigabyte dataset using a web-browser. The right panel shows the D3.js-based visualizations showing histograms.

The framework can be applied to a wide variety of datasets with successful results, but where the tools really excel is the area where no existing approach provides a viable solution. Specifically we have focused on two major projects. The first is imaging of full adult Zebra fish at cellular resolution having a final volume of 11500 x 2800 x 628 → 20-40GVx / sample. The second is a full measurement of the mouses brain vasculature with capillary resolution ≈ 10,000 x 10,000 x 10,000 → 1000 GVx / sample. While the information content of the images is very different, the same sorts of analyses will need to be performed on both. In order to convert an overwhelming mass of image data into a deeper understanding, many different segmentation and analysis techniques will need to be tested and validated quickly. We demonstrate how these data can be segmented and how machine learning algorithms can be leveraged to further improve the reliability and automation of such analyses.

References:
1.Mokso, R., Marone, F. & Stampanoni, M. Real-Time Tomography at the Swiss Light Source. in AIP conf. proc. (SRI2009, 2009).
2.Altintas, I. Workflow-driven programming paradigms for distributed analysis of biological big data. in 2013 iEEE 3rd international conference on computational advances in bio and medical sciences (iCCABS) 1–1 (IEEE, 2013). doi:10.1109/ICCABS.2013.6629243
3.Dean, J. & Ghemawat, S. MapReduce: simplified data processing on large clusters. Communications of the ACM 51, 107 (2008).
4.Matei Zaharia, M. J. F., Mosharaf Chowdhury. Spark: Cluster computing with working sets. at http://citeseerx.ist.psu.edu/viewdoc/summary?doi=10.1.1.180.9662 (2012)
5.Mader, K., Mokso, R. & Raufaste, C. Quantitative 3D Characterization of Cellular Materials: Segmentation and Morphology of Foam. Colloids and Surfaces A: … 415, 230–238 (2012).

Analysis of Flame Retardancy in Polymer Blends Synchrotron X-ray K-edge Tomography and Interferometric Phase Contrast Movies

M. B. OLATINWO*[1], K. HAM[2], J. MCCARNEY[3], S. MARATHE[4], L. G. BUTLER[1]

[1] Department of Chemistry, Louisiana State University, Baton Rouge, LA 70803 – molati1@lsu.edu; lbutler@lsu.edu
[2] Center for Advanced Microstructures & Devices, Lousiana State University, 6980 Jefferson Hwy., Baton Rouge, LA 70806 - kham1@lsu.edu
[3] Albemarle Corp., PO Box 341, Baton Rouge, LA 70821 - Jonathan.McCarney@albemarle.com
[4] Advanced Photon Source, Argonne National Laboratory, Building 401, 9700 S. Cass Avenue, Argonne, IL 60439 - marathe@aps.anl.gov

* Mutairu Bolaji Olatinwo

Keywords: single-shot interferometry, stepped-grating interferometry, brominated flame fetardants, burning, K-edge concentration analysis.

Abstract

High impact polystyrene UL-94 test bars have been imaged with K-edge tomography to assess the spatial distribution of bromine and antimony across char layers of partially burnt samples. Also, single-shot grating interferometry was used to record X-ray movies of test samples during heating (IR and flame) intended to mimic the UL-94 test. One polymer test sample was formulated with sufficient brominated flame retardant, Saytex-8010® and antimony oxide, a synergist, to pass the UL-94 test; other samples were deficient in one or the other component and did not pass the UL-94 test. The range of sample formulations aided the interpretation of the tomography volumes and X-ray phase contrast movies.

Introduction

As a result of continuous advances in polymer science over the years, polymeric materials emerge to have many indispensable applications in numerous products in our daily life activity. Some of the products are computer cases and monitors, carpets, copy machines, televisions, furniture foams, mattresses, appliances, electronics, vehicles, textiles and many more [1-5]. Unfortunately, polymeric materials are often intrinsically flammable despite their huge benefits, since many are hydrocarbon-based materials [1-5]. To make these materials safe for human, and properties and environmental protection, there is need for flame-retardants incorporated into these flammable polymeric materials [6]. The flame-retardants contribute immensely for reducing the dangers associated with fires in home, public and industrial sectors [1,4]. There are various types of flame-retardants, which include inorganic (antimony trioxide, aluminum trihydroxide); nitrogen based (melamine); organophosphorous (phosphate esters) and halogenated organic compounds [3]. Examples of brominated flame-retardants are given in Fig. 1.

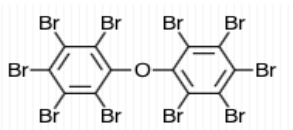

1-(2,3,4,5,6-pentabromophenoxy)-2,3,4,5,6-pentabromobenzene (Saytex 102)

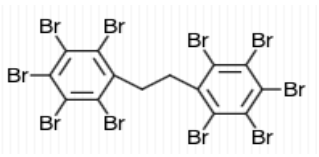

1,2-Bis(pentabromophenyl) ethane (Saytex 8010)

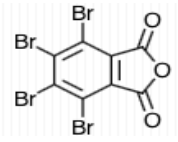

3,4,5,6-tetrabromophthalic anhydride (Saytex RB-49)

Fig. 1. Few examples of brominated flame-retardants.

Our research is currently focused on the study of brominated flame-retardants (BFRs), their synergist (Sb_2O_3) in High impact polystyrene, HIPS with the aid of X-ray synchrotron tomography and phase contrast interferometry.

Methods

Sample Preparation

The sample densities are calculated on assumption that density is equal specific gravity for Saytex 8010 [BFR] (3.25 g/cm^3), Sb_2O_3 (5.67 g/cm^3) and HIPS (1.04 g/cm^3). The formulation for each sample is shown in table 1 in both wt. and vol. % of respective components. The Underwriters Laboratories "Tests for Flammability of Plastic Materials for Parts in Devices and Appliances" (UL 94) vertical burn test is a standard test method used in the flammability classification of plastic materials. Procedures and various classifications of the test are available from Underwriters Laboratory Inc. [6]. This was performed on all samples prior to tomography studies.

Table 1. Chemical Formulation of Flame Retardant/Polymer Samples.

Composition wt. %, [vol.%]	Sample A	Sample B	Sample C	Sample D
HIPS	96, [99.241]	88, [95.819]	87, [95.579]	84, [94.836]
BFR	0, [0]	12, [4.180]	12, [4.219]	12, [4.335]
Sb_2O_3	4, [0.759]	0, [0]	1, [0.202]	4, [0.828]

CAMD: K-Edge Tomography for Concentration Volumes

Millimeter-sized samples were studied with synchrotron X-ray tomography using standard methods: white and dark field image correction, time-correlated sampling. The Br and Sb K-edge absorption tomography used 5 to 7 data sets acquired over the range of 12 to 32 keV, reconstructed with filtered back-projection, and normalized to the absorption projection images [1]. Fiducial points were used to align the volumes. Linear attenuation coefficients were taken from the NIST XCOM database. Densities of flame retardants are calculated from molecular formulas using the Cao procedure [7]. The volume fraction composition of each voxel was calculated by a vectorized least squares method [8]; a binary sample mask defined the calculated sample volume. Calculations used a 1024 GPU node for the ASTRA toolbox [9] and a 12-core, 196 GB RAM node for the Mathematica codes.

APS: Single-Shot Interferometry for Phase Contrast Movies

The interferometry 2D-movies imaging for extracting absorption, phase contrast and dark-field imaging used a 4.8 micron period checkboard phase grating and a high resolution detector. The movie frame rate was 3 Hz. The single-shot interferometry data was processed by 2D FFT and analysis of the image harmonics. Samples were heated with either a 300 W IR lamp or a small flame; soot was collected with a portable smoke extractor[8]. A definite need was noted for an active sample position control system to account for the sample consumption and motion out of the field of view. Imaging of samples while burning is very difficult especially for samples of incomplete flame retardant composition such as sample B, which burned rapidly and moved quickly out of the field-of-view.

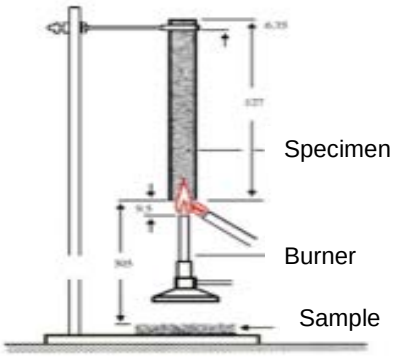

Fig. 2 (a). UL – 94 test

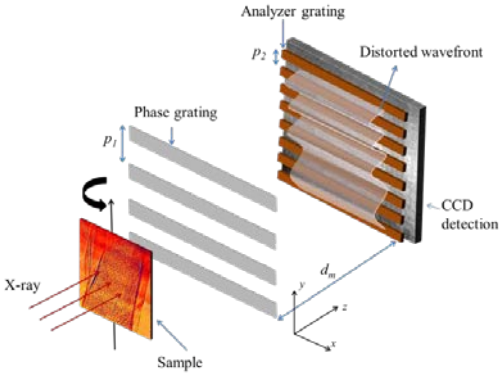

Fig. 2(b) Schematic representation of Tomography.

Results and Discussion

Optical photos of burnt polymer composites cut from UL 94 test bars are displayed in Fig. 3. Samples about 2.5 mm in diameter were used for tomography experiment. This size extends over the exterior char layer into the interior gas-bubbles formation regions. The appearance of sample D is different as compared to both sample B and C due to thick char layer and brownish-yellow coloration around the char layer.

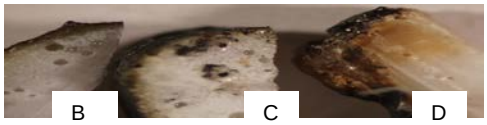

Fig. 3. Optical pictures of cuts of burned samples.

Data from more than 20 tomography experiments, each consisting of 2 to 8 GB of raw data, have been analyzed. A useful navigational strategy comes from the years of UL 94 testing by the Albemarle technicians. Samples that pass the UL 94 test have unique visual and physical characteristics. Will tomography of burning and burnt samples show features suggesting a range of internal sample temperatures and a variation of char layer formation and stability? One of the initial features noted in the tomography images are 10 to 20 micron particles (lumps). It has been suggested that neither the aromatic brominated flame retardant, Saytex 8010 nor the synergist, Sb_2O_3, completely dissolved in high impact polystyrene (HIPS) at the pixel size of the tomography experiment, 2.5 µm. However, the lumps can be visually misleading because previous tomography experiments reported by Ham et al. [1] show that the lumps result from a small fraction, <5%, of undissolved BFR and Sb_2O_3. Actually, the lumps are a strong visual guide for detecting the polymer-char interface; lumps disappear in regions that are heated, and yet protected from combustion by a char layer. Fig. 4 shows lump distributions in the four samples; the images are maximum intensities of a 512-slice stack. The irregularity of sample C's shape is due to melted polymer flowing off the sample.

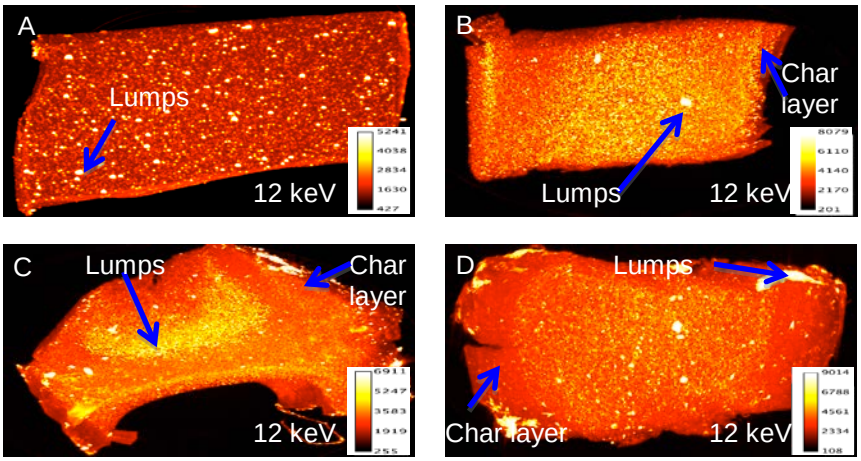

Fig. 4. Stacked slice (maximum intensity) of samples A to D.

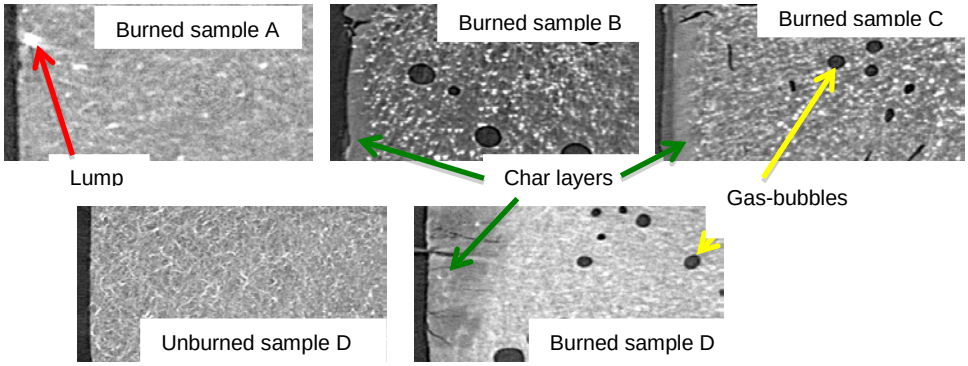

Fig. 5. Orthoslice images showing gas-bubble formation and char layers in burnt and unburned samples.

K-edge tomography: As observed in sample A (mixture of Sb_2O_3 & HIPS), there is no formation of either gas-bubbles or a char layer; this indicate the importance of BFR. The similarity of unburned D with burnt A indicates gas bubble formation is not intrinsic with polymer heating, i.e., polystyrene thermal decomposition or entrapped air during polymer extrusion. The gas-bubbles are associated with BFR decomposition into HBr and, with Sb_2O_3, $SbBr_3$.. Samples B to D share similar features such as gas bubbles, char layers, and lumps in the interior. Interesting, gas-bubbles are found in the interior but not near burnt surfaces. The main difference in samples B to D is the thickness of char layer and concentration of Br and Sb across the sample. To investigate concentrations, K-edge tomography element line probes show a concentration gradient of Br in sample C & D across the char layer (Fig. 6). The char layer has low concentration gradient than the interior. The char layer is noticeably homogeneous with respect to particles of BFR (Br) or Sb_2O_3 (Sb). The absence of gas bubbles in the char layer suggests a deflation mechanism is operative near the burn surface. Atop the char layer, surface deposits rich in Br and or Sb are occasionally detected in the burnt samples. This is mainly observed in samples C and D.

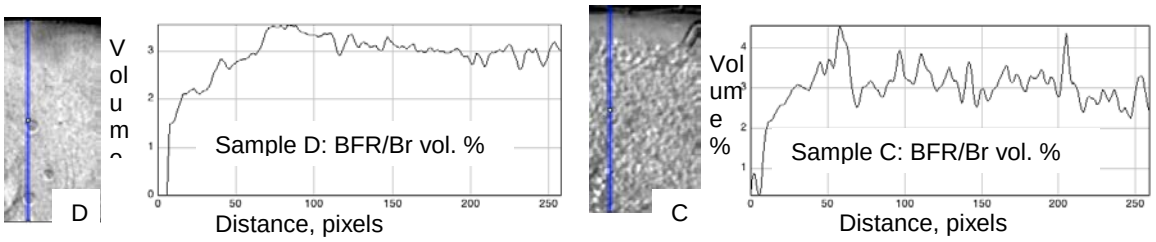

Fig. 6. Specific slice with line probe for bromine concentration gradient across sample D and C.

Single-Shot Interferometry Movies: Phase contrast interferometry movies were acquired while heating the samples with either an IR-heater or a small candle so as to simulate the UL 94 test at the beamline. The movies are complementary to tomography, displaying gas-bubble development, lump dissolution, and melt flow. The gas bubble formation is nicely observed with absorption and differential phase contrast; as for the burnt sample described above, gas bubbles deflate before reaching the burning surface. The dark-field images have poor contrast for bubbles; this indicates samples homogeneity at the 100-200 nm scale.

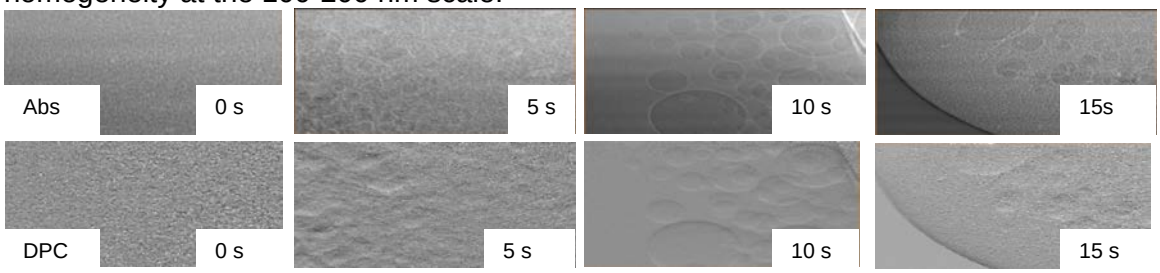

Fig. 7. Selected slices of differential phase contrast and absorption movies acquired through interferometry.

Conclusions

K-edge tomography enabled observation of differences with the sample that pass or fail the UL 94 test. Key features such as char layer, gas bubble formation, microcracks, and dissolution of the flame retardant in the char layer regions are used in understanding the efficiency of the flame retardants and its synergist. The samples that pass the UL 94 test have a thick, highly visible char layer as well as an interior rich in gas bubbles. Growth of bubbles in flame retardant thermal decomposition is noted in the X-ray phase contrast movies and an absence of bubbles at the burning surface of the polymer; dark-field images after burning suggest a crack structure between interior bubbles and the surface.

References

Ham, K.; Jin, H.; Al-Raoush, R.; Xie, X.; Willson, C. S.; Byerly, G. R.; Simeral, L. S.; Rivers, M. L.; Kurtz, R. L.; Butler, L. G. (2004). Three-Dimensional Chemical Analysis with Synchrotron Tomography at Multiple X-ray Energies: Brominated Aromatic Flame Retardant and Antimony Oxide in Polystyrene. ***Chemistry of Materials*** 16, 21: 4032-4042.

Alaee, M.; Arias, P.; Sjödin, A.; Bergman, Å. (2003). An overview of commercially used brominated flame-retardants, their applications, their use patterns in different countries/regions and possible modes of release. ***Environment International*** 29, 6: 683-689.

Bourbigot, S.; Duquesne, S. (2007). Fire retardant polymers: recent developments and opportunities. ***Journal of Materials Chemistry*** 17, 22: 2283-2300.

Ham, K.; Butler, L. G. (2007). Algorithms for three-dimensional chemical analysis via multi-energy synchrotron X-ray tomography. ***Nuclear Instruments and Methods in Physics Research Section B: Beam Interactions with Materials and Atoms*** 262, 1: 117-127.

Holbrook, R. D.; Davis, J. M.; Scott, K. C. K.; Szakal, C. (2012). Detection and speciation of brominated flame retardants in high-impact polystyrene (HIPS) polymers. ***Journal of Microscopy*** 246, 2: 143-152.

Underwriters Laboratory Inc. UL-94 Standard for "Tests for Flammability of Plastic Materials for Parts in Devices and Appliances" 5th Ed.,**1996**, Northbrook IL.

Cao, X., N. Leyva, S. R. Anderson and B. C. Hancock (2008). Use of prediction methods to estimate true density of active pharmaceutical ingredients. ***International Journal of Pharmaceutics*** 355, (1-2): 231-237.

Marathe, S., L. Assoufid, X. Xiao, K. Ham, W. W. Johnson and L. G. Butler (2014). Improved Algorithm for Processing Grating-Based Phase Contrast Interferometry Image Sets. ***Rev. Sci. Instrum.*** **85**: art. no. 013704.

ASTRA toolbox, iMinds - Vision Lab, University of Antwerp, http://visielab.uantwerpen.be/research/tomography.

Coherent X-ray Diffraction Imaging of Strain on the Nanoscale

R. HARDER[1*]

[1] Argonne National Laboratory, 9700 S Cass Ave, Argonne, IL, U.S.A.
* presenting author

In nanoscience, the bulk concepts of lattices and crystal defects must be reconsidered in order to explain why nanomaterials have new and exciting properties. To study these properties, we have developed the method of Coherent X-ray Diffraction (CXD) Imaging to obtain quantitative three-dimensional maps of the deformation of a crystal from its equilibrium lattice spacing. By measuring the coherently scattered photons in the vicinity of Bragg peaks of the samples, and computationally inverting the intensities to an image, we gain this powerful capability.

Very recently we have developed instrumentation and methods that allow us to image, in three dimensions, the total lattice deformation field of micro and sub-micro meter size crystals with high spatial resolution. Using this data, the entire strain tensor of the sample can be determined in three dimensions.

The images being produced by this method have lead to a tremendous need for image analysis in three and even four dimensions. With the advance of ultra high brightness synchrotron sources, like those being planned in an upgrade the Advanced Photon Source of Argonne National Laboratory, coherent imaging is poised to produce sub-nanometer resolution images of vector lattice distortions and strain tensor fields that describe material properties as a function of time during in-situ and operando experiments.

This talk will introduce describe the methods used to acquire such data and include some of the first images of nanoscale strain mapping.

Number of words: 198

References:
If you want to add references, please use an author/date style.

Use of distance transforms and correlation maps for advanced 3D analysis of impact damage in composite panels

F. LÉONARD*[1], J. STEIN[2]

[1] BAM – Federal Institute for Materials Research and Testing, Division 8.5 - Micro-NDE, Unter den Eichen 87, 12205 Berlin,GERMANY – fabien.leonard@bam.de
[2] TWI Ltd., Granta Park, Great Abington, Cambridge, CB21 6AL, UK – jasmin.stein@twi.co.uk
* presenting author

Keywords: low velocity impact, damage characterisation, composite panel, distance transform, correlation map

Abstract

The present study introducess an innovative CT data processing methodology based on distance transforms and correlation maps to improve the ply-by-ply segmentation of impact damage in composite laminates. Composite panels have been impacted with force ranging from 5 J up to 20 J and the impact damage subsequently characterised by X-ray computed tomography. The *damage correlation map* approach was developped here to improve the automatic through-thickness damage segmentation by combining two distance transforms with different reference points. The resulting correlation map proposes an easy to interpret 2D representation of an otherwise complex 3D damage structure. In addition to giving visual qualitative information, the *damage correlation map* can be used to perform a ply-by-ply segmentation of the impact damage and thus extract, for each ply, relevant quantitative information such as damage volume, maximum delamination legth and width, projected damage area *etc*.

Introduction

One of the major issues when using composite materials in an industry such has aerospace is their impact behaviour, particularly when subjected to low-velocity impacts. Low-velocity impacts are complex to assess as although significant damage can be generated internally, there can be little indication externally, leading to the term barely visible impact damage (BVID). The internal damage appears primarily as matrix cracking and delamination between plies of dissimilar orientation [Richardson1996] and can lead to loss in strength and stiffness. Ultimately, the load-bearing capabilities can be significantly reduced in both tension and compression, and catastrophic failure can occur under relatively low applied loads. As a result there is a concerted research effort to improve the damage resistance and tolerance of these materials. When facing such a damage tolerance problem, the geometric structure of the damage is key in understanding the basic damage mechanisms. It is only when such mechanisms are understood that the critical composites properties in regards to damage can be defined and the damage tolerance improvements implemented. X-ray computed tomography is therefore a technique of choice to deliver a full-field 3D representation of the impact damage non-destructively. However, advanced data processing methodologies are required as the sole segmentation of the damage volume does not provide sufficient information.

Previous work [Léonard2013;Léonard2014] has demonstrated that it was possible to segment the damage produced by a low velocity impact event on a composite laminate; and obtain a through-thickness damage histogram. This histogram was employed to semi-automatically separate the full damage so that the individual ply-by-ply damage

could be visualised and assessed independently. The data processing methodology developped was based on a *distance transform* operation to take into account the permanent out-of-plane deformation of the composite panel. However, the main limitation of this approach is the degradation of the damage separation for high impact energies, as the out-of-plane deformation becomes greater in the centre than at the edges of the panel. To obtain a better ply-by-ply separation of the damage, we have employed a combination of *distance transform* operations and a *correlation map* using Avizo Fire software. This new methodology will be presented based on an investigation of carbon fibre reinforced panels (CFRP) impacted with energies ranging from 5 J up to 20 J.

Materials and methods

The composite material under investigation was aimed at primary structures for aerospace applications. It was a unidirectional carbon fibre fabric with 22 Tex glass filaments yarn woven at 6 mm intervals into the fabric to hold together the 12 k carbon tows. The fabric areal density was 445 g/m^2 and the average density of carbon fibre 1.76 g/cm^3. The matrix comprised a high glass transition temperature epoxy resin system, specially formulated for aerospace applications [Stein2012, Stein2013]. All test specimens used in this study were manufactured using vacuum assisted resin film infusion (VARFI) due the high viscosity of the resin [Stein2013]. Each panel was made up of 8 plies stacked in a $[(0°/90°)_2]_s$ stacking sequence as presented in Figure 1.

Ply No.	Angle (°)	Interface
1	0	
2	90	1
3	0	2
4	90	3
5	90	4
6	0	5
7	90	6
8	0	7

a) detailled stacking sequence of composite panels

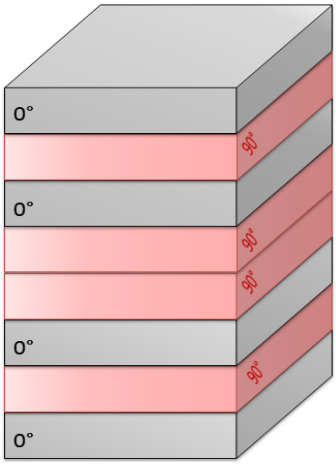

b) panel lay-up sequence

Fig. 1. *Overview of composite panel stacking sequence.*

The panels were cured under vacuum only (no applied pressure) throughout a 6 hour cure cycle comprising 2 hours at temperatures of 130 ºC, 165 ºC, and 200 ºC in turn. The resulting mean laminate thickness was 3.079 mm ± 0.028 mm. Once the laminates were cured, impact test coupons measuring 89 mm x 55 mm were cut from the cured panels using a diamond saw. Although there is no official standard for the miniaturised impact samples used in this work, the samples were cut so that edge parallelism was within the tolerance of British Standard 18352 [BS2009] (0.02 mm) and of an appropriate length in order to prevent Euler buckling during compression after impact testing (CAI).

In order to generate damage in the composite panel, a drop weight impact testing machine was used to deliver a low velocity impact. Impact testing was performed using an Instron CEAST 9350 drop weight impact testing machine controlled by CeastVIEW 5.94 3C software. The tests were carried out according to the methodology of Prichard and Hogg [Prichard1990] with a specimen size of 89 mm x 55 mm, an impactor mass of

5.048 kg and a hemispherical tup 20 mm in diameter. The sample was clamped at the bottom of the tower by a rigid holding device which consists of steel plates, clamps, and a 40 mm circular aperture (Figure 2a). In these tests, the maximum velocity of the impactor was approximately 3.15 m/s for an impact energy of 20 J. Specimens were tested at four different energies (5, 10, 15 and 20 J), to simulate the range of impact energies thin laminates experience during service, such as those resulting from tool drops. An example of the panel tested at 20 J in Figure 2b shows visible damage on the back face.

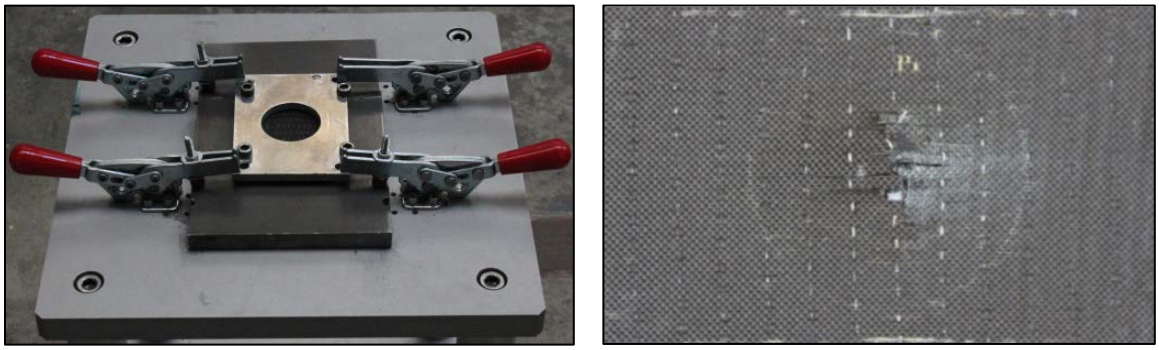

a) specimen holder for drop weight impact tests *b) visible external damage on panel tested at 20 J (back face)*

Fig. 2. *Specimen holder and visible external damage on impacted specimen.*

The impact specimens were scanned on a *Nikon Metrology 225/320 kV Custom Bay* [Manchester2012]. The system was equipped with a 225 kV static multi-metal anode source (Cu, Mo, Ag, and W) with a minimum focal spot size of 3 µm [Nikon] and a PerkinElmer 2048 x 2048 pixels 16-bit amorphous silicon flat panel detector. The X-rays were generated by the copper target using a voltage of 60 kV and a current of 175 µA. The data acquisition was carried out with an exposure time of 1415 ms and no filtration. The number of projections was set to 3142 and the number of frames per projection was 1, resulting in an acquisition time of 75 minutes. The 3D volumes were reconstructed at full resolution with a voxel size of 35.7 µm along the *X*, *Y*, and *Z* directions, using *CT Pro* software [Nikon2013]. *Avizo Fire 8.0* [VSG2012] was employed for the data visualisation, processing, and quantification.

CT data processing methodology

Previous work from *Léonard et al.* [Léonard2013;Léonard2014] has demonstrated that it was possible to segment the damage produced by a low velocity impact event on a composite laminate; and obtain a through-thickness damage histogram. However, the main limitation of this approach is the degradation of the damage separation for high impact energies, as the out-of-plane deformation becomes greater in the centre than at the edges of the panel. To circumvent such limitation and thus improve the accuracy of the ply-by-ply damage segmentation and subsequent analysis, the present work proposes the combination of two distance transforms taken from different reference points into a single map, called *damage correlation map*. An overview of the data processing methodology is given in Figure 3 The first distance transform is taken with the impact face as reference whereas the second distance transform is taken with the centre line of the damage as reference. Combining the two damage distance transform volumes gives a map of the impact damage within the composite panel.

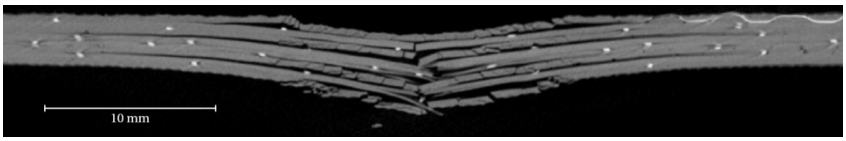

a) raw 2D CT slice

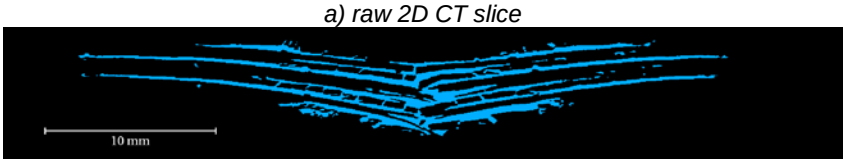

b) corresponding segmented damage

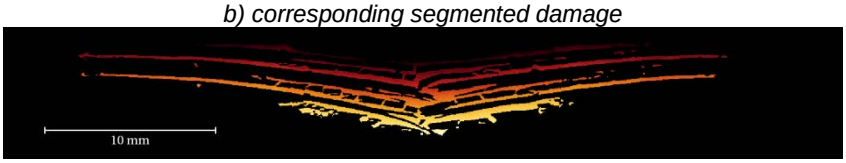

c) damage distance transform from impact face

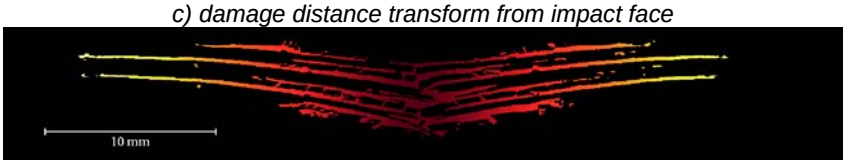

d) damage distance transfom from impact centre

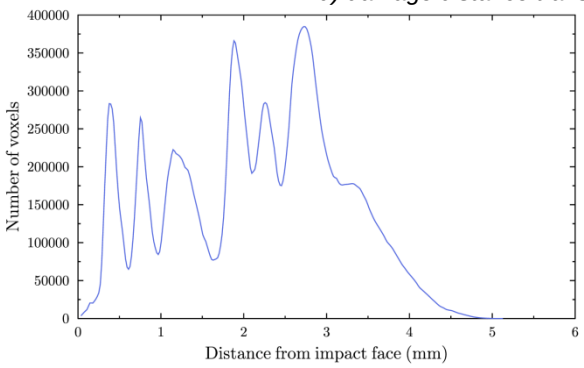

e) damage histogram from c) (impact face)

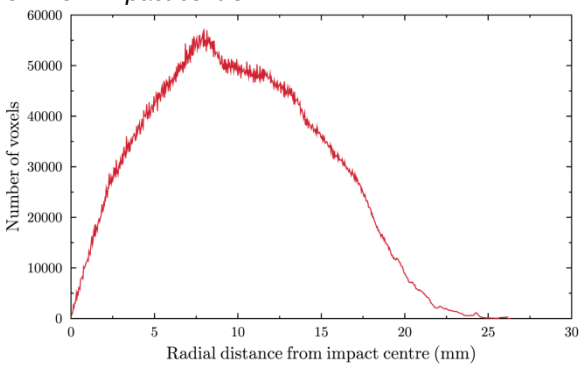

f) damage histogram from d) (impact centre)

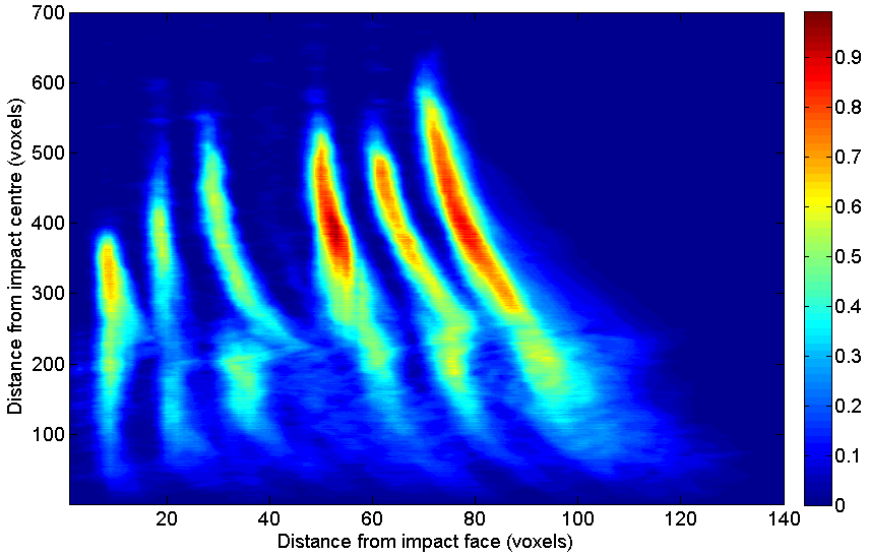

g) damage correlation map

Fig. 3. *Overview of CT data processing methodology for specimen tested at 15 J.*

Results

The *damage correlation map* approach proposed here, gives an improved representation of the impact damage occuring within the composite panel (comparison between Figure 3e and Figure 3g). Based on this map, the impact damage can also be segmented with better accuracy compared to the segmentation coming from the damage histogram approach (Figure 3e) as the panel distorsion is better accounted for. The resulting segmentation is given in Figure 4.

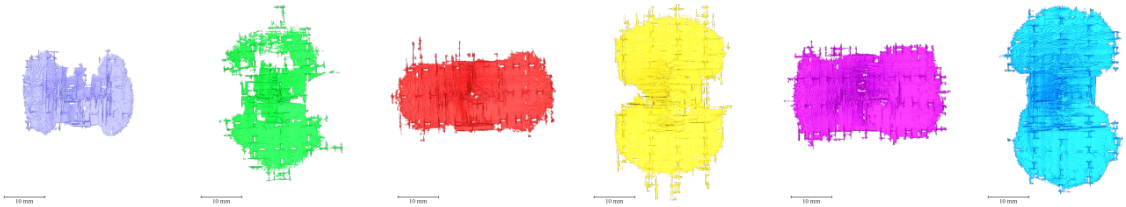

a) interface 1 *b) interface 2* *c) interface 3* *d) interface 5* *e) interface 6* *f) interface 7*

Fig. 4. *Ply-by-ply segmentatuion of impact damage for panel impacted at 15 J (interface numbers corresponding to those of Figure 1a).*

After ply-by-ply segmentation of the impact damage, quantitative data can be extracted for each individual ply, such as damage volume, maximum delamination legth and width, projected damage area *etc*.

Conclusions

Although CT is becoming an important tool for the characterisation of impact damage in fibre reinforced composite laminates, it is generally used only to obtain a qualitative visual measure. Advanced data processing methodologies, such as the one epresented here, are required to improve our ability to characterise impact damage and extract meaningful measurements from X-ray CT datasets. The separation of the impact damage ply-by-ply is needed to improve our understanding of the type (failure mode) and extent of the impact damage. This information is essential both in terms of understanding the capacity of the composite to absorb energy under impact and to predict the residual strength/capability of multi-directional composite laminates.

References

BS ISO 18352:2009 (2009). Carbon-fibre-reinforced plastics. Determination of compression-after-impact properties at a specified impact-energy level.

Léonard F., Stein J., Withers P.J., and Wilkinson A. (2013). 3D damage characterisation in composite impacted panels by laboratory X-ray computed tomography. **1st International Conference on Tomography of Materials and Structures.** Gent, Belgium.

Léonard F., Shi Y., Soutis C., Withers P.J., and Pinna C. (2014). Impact damage characterisation of fibre metal laminates by X-ray computed tomography. **Conference on Industrial Computed Tomography,** Wels, Austria.

Manchester X-ray Imaging Facility website (2012). Nikon Metris Custom Bay system specifications. http://www.mxif.manchester.ac.uk/index.php/nikon-custom-bay. Visited on the 21st November 2012.

Nikon Metrology website (2013). XT software suite specifications. http://www.nikonmetrology.com/en_EU/Products/Software/X-Ray-CT-Software/XT-Software-Suite. Visited on the 15th January 2013.

Prichard J.C. and Hogg P.J. (1990). The role of impact damage in post-impact compression testing. **Composites,** 21(6):503–511.

Richardson M.O.W., Wisheart, M.J.(1996). Review of low-velocity impact properties of composite materials**. Composites Part A: Applied Science and Manufacturing**, 27, 1123-1131.

Stein, J. and Wilkinson, A. (2012). The Influence of PES and Triblock Copolymer on the Processing and Properties of Highly Crosslinked Epoxy Matrices. **15th European Conference on Composite Materials (ECCM15)**.

Stein, J.(2013) Toughening of Highly Crosslinked Epoxy Resin Systems. PhD thesis, School of Materials, University of Manchester.

Visualization Sciences Group website (2012). Avizo Standard specifications. http://www.vsg3d.com/avizo/ standard. Visited on the 1st November 2012.

Proposal of a data evaluation chain for the inspection of thermoplast clips

U. HASSLER[1], M. REHAK[2], W. HOLUB[3], E. PENNE[4], T. GRULICH[5]

[1] ulf.hassler@iis.fraunhofer.de
[2] wolfgang.holub@iis.fraunhofer.de
[3] markus.rehak@iis.fraunhofer.de
[4] eva.penne@iis.fraunhofer.de
[5] tobias.grulich@iis.fraunhofer.de

Keywords: Data analysis, computed tomography, segmentation, porosity detection, surface roughness

Abstract

The Europeen project QUICOM is dealing with the application of X-ray computed tomography methods (CT) to carbon fiber reinforced plastic (CFRP) components from aerospace industry. Here, CT is mainly intended to be an escalation method in certain nondestructive testing situations (NDT), where conventional tests do not produce clear indications. Further, CT is investigated related to a production-integrated quality control. This type of application makes sense for relatively small parts, produced in a large volume. This is the case for so called 'clips', manufactured using CFR thermoplastic material. They are mainly used as connecting elements within larger aeronautic structures. Within QUICOM, the capabilities and limits of such an application case are evaluated. In this contribution, we present a specific data evaluation chain, which could be used for an automatic interpretation of such data. Main interest herein is the determination of the local porosity within the parts.

Introduction

Main challenge using CT for those thermoplastic clips is the relation of object dimension (approx. 200*100*300 mm³) and complex geometry to the minimum size of relevant defects (approx. 10 to 100 µm), which results in very large reconstructed volume data. In this contribution, we rather focus on efficient handling and the principle of the evaluation procedure than on reliable analysis itself. The goals of the usage of the evaluation chain is twofold: to provide a tool for quality assessment of the CT reconstruction itself, in order to be able to optimize scanning and reconstruction parameters, and to show the principle transition of the established ultrasonic inspection procedure to an automated interpretation of CT data in the near future.

The evaluation chain consists of the following steps:

a) multi-clip separation
b) clip dissection
c) analysis.

The efficiency of the CT inspection raises with the possibility of scanning several parts at the same time. The separation step is then used to create individual volume representations of the clips. The segmentation step is used to reduce the data volume and to subdivide the volume to similar geometrical primitives, which are in the case of clips on one hand the flat and planar main faces and on the other hand the connecting radii. These simple geometric objects are then fed into the analysis step, which consists of the following steps:

a) detection of surface anomalies
b) detection of internal inhomogeneities (porosity)
c) determination of geometric properties.

Within the contribution, we will focus mainly on the clip dissection and the determination of the internal inhomogeneities by means of a resampling of the volume data relative to the clip surface. The result of the approach is an estimation of the local porosity as a function of depth (distance to the surface). From that, an overall or volume porosity can be deduced and visualised. Results achieved with the presented approach will be shown using both simulated and real data.

Separation

Multi-clip separation is an optional step, if several clips are measured simultaneously. The algorithm detects each single clip by means of an user defined attenuation coefficient corresponding to the clip material. For this purpose mountings have to consist of a low attenuating material like polystyrene to be nearly invisible in the reconstructed 3d-volume.

Dissection

Once the clips are separated the dissection step divides the 3d-volume of the clip into several partial volumes. In this case the volume is divided into its planar parts and its radii. This step will reduce the data volume for further analysis and allows the possibility to use different analysis approaches depending on the geometry of the individual partial volume. To achieve this dissection the planes and radii are distinguished by a local eigenvalue analysis and labeled by a connected component analysis. Once the individual planes and radii are identified the partial volumes are aligned using the principal component analysis.

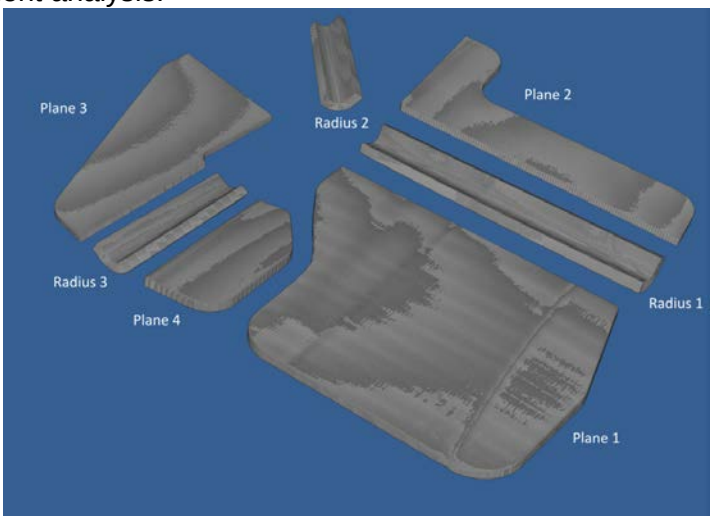

Fig. 3. *Dissection of a separated clip measurement, 3D view*

Fig. 3 shows a clip that is dissected in its planes and radii. In this case the method detected 4 different planes and the three connecting radii.

Analysis

Since CFRP components are composed of layers, a layer-by-layer inspection method is a reasonable approach. After dissection the planar faces are already oriented such that the internal layers of the object are almost parallel to the XY-plane of the 3D-volume. Additionally a planarization step may correct slight curvatures prospectively. Hence we can realize a layer-by-layer inspection by processing the 3d-volume slice-by-slice.

The main step of the analysis is the determination of the reconstruction quality. For this purpose we segmented the reconstructed data into background and object voxels to calculate the mean attenuation coefficient, the standard deviation and the signal-to-noise

ratio (SNR). While the CFRP components consist of a homogeneous material the standard deviation is expected to have a low value and therefore the SNR a high value. For all clips the SNR of the planes is much higher than the SNR of the Radii. This can be explained by the beam hardening artefacts which typically occur in the curved regions of the clip (see Fig. 4.).

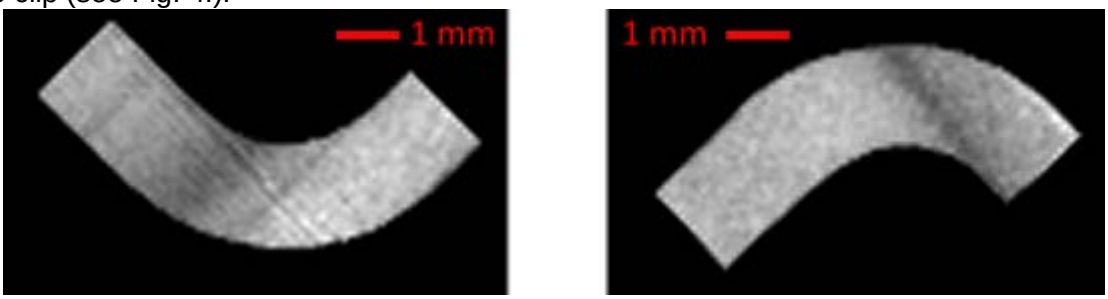

Fig. 4. *Beam hardening artefacts inside the radii of a clip*

Secondly the presented method is able to detect internal inhomogeneities without using an already measured zero-defect object as reference. The required reference data are generated from the measured data instead. In this step of the evaluation chain the user has to define a rectangular region of interest (ROI) to be analyzed. Everything else outside this region is excluded from data processing. Then we calculate the median of all voxel values and use this as reference value for the entire slice. From this we can calculate linear porosity values for each voxel that depends on the quotient of the voxel's intensity value and the porosity threshold.

Fig. 5 shows a plane that contains a lot of porosities between the single fiber layers.

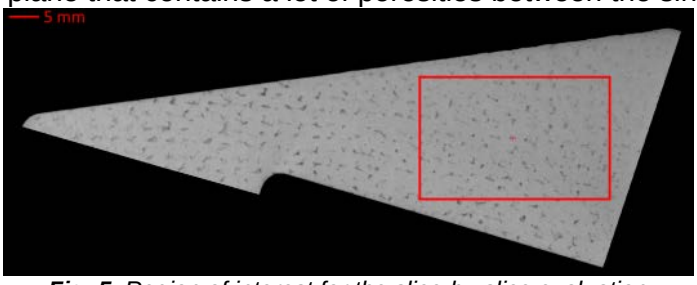

Fig. 5. *Region of interest for the slice-by-slice evaluation*

Using the linear porosity curve (Fig. 6.) the single porous layers can be identified very well, the maximum porosity is about 0.35%.

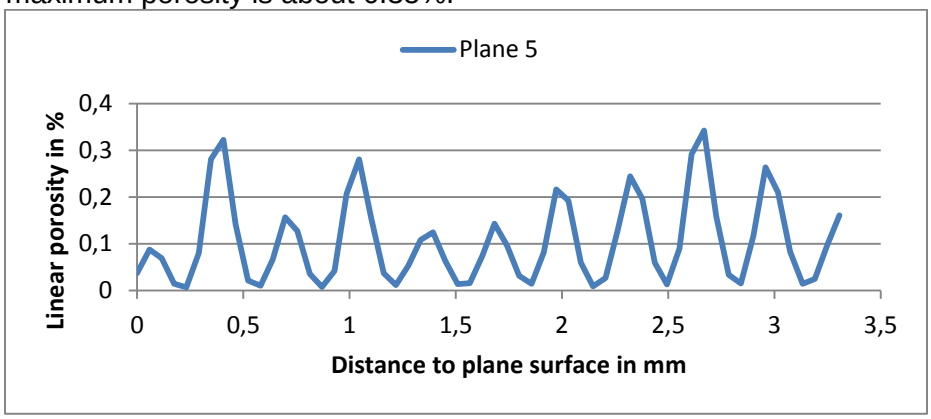

Fig. 6. *Linear porosity over the distance for the slice-by-slice evaluation*

The estimated linear porosity seems to have too low values compared to the visual appearance. Unfortunately the true porosity is currently unknown; hence the correctness of the results cannot be guaranteed in this case. A possible explanation for the too low values is the shape of the porosities. The simulated clips contain spherical porosities, while the porosities inside the measured clip are flat shaped (Fig. 7). The reconstructed voxel size of 57.5 µm either could be insufficient to fully resolve such porosities or inherent unsharpness of the applied scan was too high, both resulting in a blurred representation and an underestimation of the porosity.

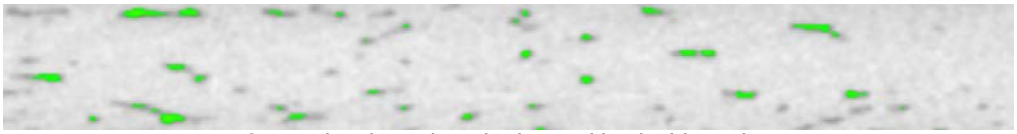

Fig. 7. *Flat shaped marked porosities inside a plane*

To detect anomalies of the given top and bottom surface of the analyzed plane the presented slice-by-slice analysis will fail in most cases. Most of the time these surfaces will not completely coincide with the given plane of the coordinate system because they are not entirely planar but slightly curved. That is why a different approach is used to classify these anomalies.

For this purpose a subpixel precise heightmap $z(x,y)$ is determined using the known absorption coefficient of the material. Given this information a qualitative measure of the root mean squared roughness can be computed for a defined neighborhood $N = \{(x_m, y_n) \mid m = 1,\dots,M, n = 1 \dots N\}$ at pixel position (x,y) of the surfaces given the following formula:

$$R(x,y) = \sqrt{\frac{1}{MN}\sum_{m=1}^{M}\sum_{n=1}^{N}\left(z(x_m,y_n) - \overline{z(x,y)}\right)^2}$$

$$\overline{z(x,y)} = \frac{1}{MN}\sum_{m=1}^{M}\sum_{n=1}^{N} z(x_m,y_n)$$

Fig. 8 shows this local roughness measure applied to the top surface of a dissected plane of an exemplary measured clip. The bright spots on this map indicate the presence of a surface anomaly. In this case a 3×3 neighborhood was chosen that includes only adjacent pixels.

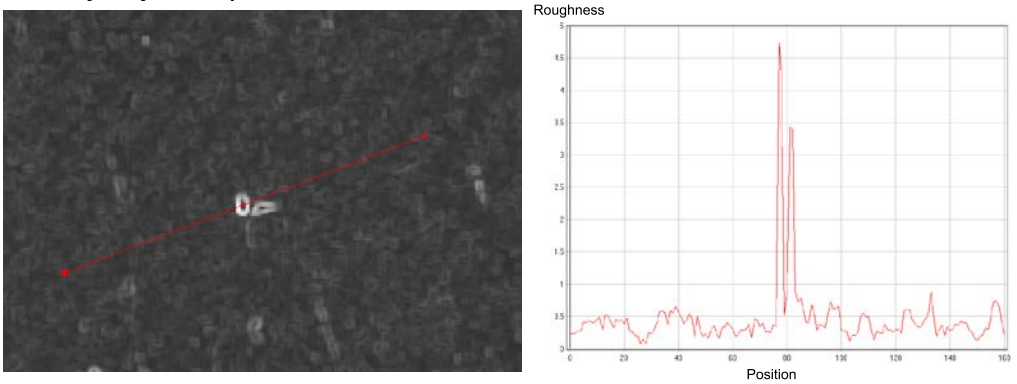

Fig. 8. *The roughness map of a given ROI of the top surface of a dissected plane*

A concrete instance of such an anomaly on the surface of a plane is shown in Fig. 9 and indicated by a blue circle.

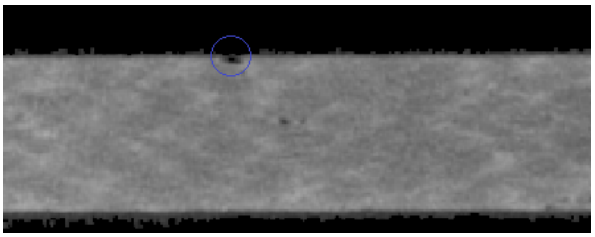

Fig. 9. *An exemplary surface anomaly that is detected by the roughness measure*

Conclusion / Outlook

In this study we presented a method to estimate the reconstruction quality by means of the homogeneity of the measured object. This is done by calculating the SNR inside the dissected planes and radii. Firstly the measured clips were separated into single partial volumes for each clip. This step is necessary only, if the measurement contains more than only one clip. In a second step each clip was dissected into its planes and radii. To prepare a layer-by-layer analysis the dissection realigned each clip component such, that the principal axes were oriented along axes of the coordinate system. After that the SNR and porosity statistics was calculated for each plane. To improve the detection of surface anomalies a roughness measure was computed from the heightmap and used to detect flaws on the surface.

The complete evaluation process including the clip separation took around 24 minutes to compute when applied to an input volume of 2473×1272×5676 voxels (33.2GB).

For the future several tasks have to be accomplished. A planarization procedure has to be applied to the radii to allow a slice-by-slice analysis similar to the planes. This kind of analysis should then be extended such that not only a small region of interest but the entire clip can be analyzed. For this the size of the region is reduced as well as it is moved over the entire clip to adapt the approach to the state of the art ultra sound methods. Furthermore the slice-by-slice analysis needs a consistent parametrization for estimating the porosity regardless of the resolution of the reconstructed volume as well as the shape and size of the porosities.

Acknowledgements

This study has been funded by the European Commission through the project QUICOM (Quantitative Inspection of Complex Composite Aeronautic Parts Using Advanced X-ray Techniques, 7th Framework Programme). Thanks to Airbus for providing the parts.

References

Gadelmawla, E. S., et al. (2002). *Roughness parameters.* **Journal of Materials Processing Technology**, 123. Jg., Nr. 1, S. 133-145.

S.Mohr, U. Hassler, S. Oeckl (2012). *Process Integrated Inspection of Fiber Composite Parts Using Computed Tomography.* 4th International Symposium on NDT in Aerospace, (Augsburg, Germany). **Production Integrated NDT II**.

In-situ 3D nano-imaging at the Advanced Photon Source

V. De Andrade, M. Wojcik, D. Gursoy, A. Deriy, F. De Carlo

Advanced Photon Source, Argonne National Laboratory, Lemont, Il-60439, USA

Abstract

The new in-house Transmission X-ray Microscope (TXM) at Sector 32-ID-C of the Advanced Photon Source (APS) at Argonne National Laboratory has just accomplished a first year of operation. The highest resolution full-field imaging system of Argonne is taking up challenges of nanomaterial science in the field of energy storage, microelectronics, nanoporous materials and environmental science. The TXM is equipped with a fixed exit double crystal monochromator (Si111). It operates from 6 to 14 keV. The available set of optics (in-house 60 and 20 nm Δr_n Fresnel zone plates) offers fields of view ranging from 70 to 20 µm for spatial resolution of 60 and 20 nm. Techniques available include absorption, Zernike type phase contrast and XANES tomography. The design enables operations in a wide range of environments. 3D nano-tomography can be performed under controlled atmosphere, for temperature ranging from -160^{o}C to 1500^{o}C, with ability to supply electric current to the sample. An overview of the first experiments performed at 32-ID will be given.

Session 301

X-ray measurement of sand ripples bedload transport

*S. MONTREUIL[1], B. LONG[2]
[1] Institut National de la Recherche Scientifique, 490 rue de la Couronne, Québec (Québec) G1K 9A9 Canada – blong@ete.inrs.ca
[2] Institut National de la Recherche Scientifique, 490 rue de la Couronne, Québec (Québec) G1K 9A9 Canada – stephane.montreuil@cll.qc.ca
* presenting author

Keywords: Sediment bedload transport, CT-Scan, Sand ripple

Abstract

Innovative CT-Scanner results bring discussion about suspended and bedload transport during erosion and deposition processes. X-ray is leading to a new way of looking inside active sediment transport. Protocols and processes developed in this study provide new definition of sand ripple surface opening many opportunities in sediment transport research.

Introduction

Sediment transport CT-Scanner-flume experiments (Montreuil & Long, 2007) provide information about internal bedform structures offering the best setup ever for fundamental and applied research. This innovating technique generates, without any intrusion and perturbation, a view inside sediment ripples. It reveals the dynamic phenomena acting on bedform internal architecture and bedload transport parameters. Analysis results have already provided a set of sedimentary parameters (Montreuil, 2014) defining internal migrating ripple architecture. The aim of this study is focused on the upper bedload transport layer definition providing a new definition of datum (Reineck & Singh, 1975) used as ripple surface, influencing sediment transport estimation.

Methods

The 30 x 30 x 700 cm flume used in this research (Fig. 1) was specially built to fit into a CT-Scanner room and technically designed to avoid X-ray artefacts (Ketcham & Carlson, 2001). The flume is filled with a 5 cm-thick pure silica sand layer and a 20 cm-high water column at 20 °C to create a sand ripple field (Raudkivi, 1963, Baas, 2003 and Bagnold, 1977). The flow (0 – 80 $cm \bullet s^{-1}$) is measured and controlled by an electro-pneumatic valve inside a recirculating circuit build between two tanks, used for damping, in combinasion with diffuser.

Two CT-Scanner measurement techniques have been developed for migrating sediments: a global measurement technique uses a 3D matrix of 512 x 512 x 1500 voxels of 0.6 x 0.6 x 0.6 mm, resulting in a volumetric view, at a precise moment in time (Lagrangian); the second (Eulerian) one is the periodic event technique generating a matrix set of 512 x 512 x 30 voxels. Each 512 x 512 x 30 voxels slices are separated by a Δt from 30 s to hours.

Fig. 1. *Laboratoire multidisciplinaire de tomodensitométrie pour les ressources naturelles et le génie civil de l'INRS-ETE (Montreuil, 2014).*

This technique provides an observation window (Fig. 2) showing sand ripple migrating. From both techniques, matrixes are considered as vertical density profiles, imaging the density from the water column to the bottom bed, and passing through the boundary suspension-bedload, until bedload transport and this without intrusive disturbance effect.

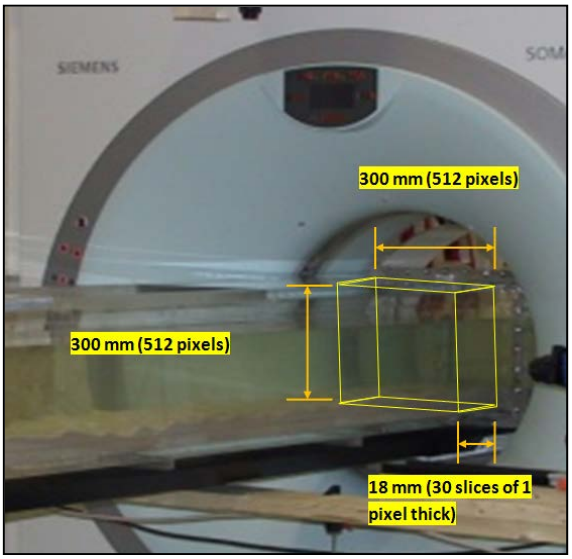

Fig. 2. *Measurment windows used in the periodic event technique with the matrix set of 512 x 512 x 30 voxels (Montreuil, 2014).*

Interpretation of raw data images from CT-Scanner-flume experiments requires processing through medical reconstruction software. Best results were obtained with the SpineSpi B20s (Siemens) reconstruction filter. Results in HU (Hounsfield, 1973) based on relative density (Moore, 2004), are converted in SI units of density following a linear equation. Afterward, SI values are calibrated taking into account flume composition, sand properties and fluid density.

Results

Vertical density profiles (Fig. 3) for a 3D matrix provide values from the suspension-bedload transition towards the sediment bed's interior (For this case: d_{50} = 0.470 mm

and U = 28 cm•s^{-1}). This reveals the impact of water, penetrating up to 10 mm deep into the sediment (Fig. 4 and Fig. 5). This penetrating process demonstrates the existence of an unknown internal phenomenon present during sediment transport (Fig. 4). The thickness of the upper bedload transport layer varies from 5.5 mm to 1.9 mm respectively for the ripple trough and summit with an observed extremum from 0.6 mm until 10 mm. Density at the upper suspension-bedload boundary varies, respectively for trough and summit, between 1.318 and 1.026 g•cm^{-3} and at its lower end between 1.903 and 1.645 g•cm^{-3}. Novelty in this study is the fluctuation of stoss-side thickness, including a breach at fluid reattachment point and avalanching zone (Fig. 4). Results show an augmentation of available sediment for bedload transport.

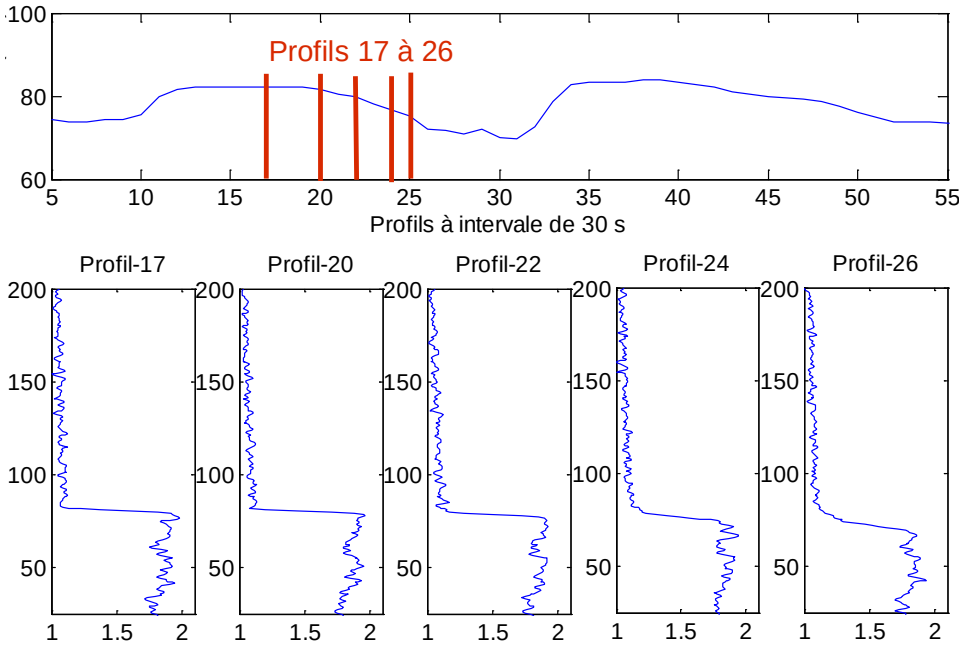

Fig. 3. *Density profiles along the ripple stoss-side(Montreuil, 2014)..*

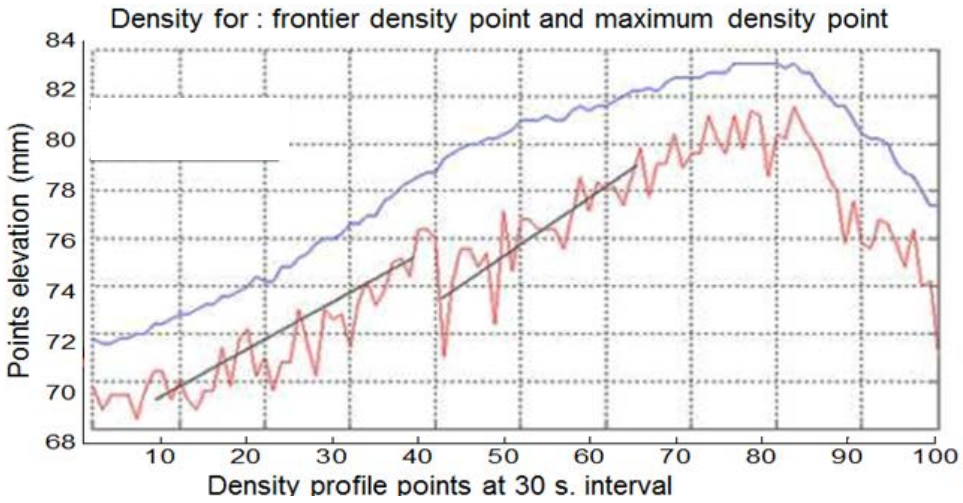

Fig. 4. *Density of upper bedload transport zone limits, upper curve: ripple visible surface (topography) and lower curve: density maximum (ripple surface stricto sensu).*

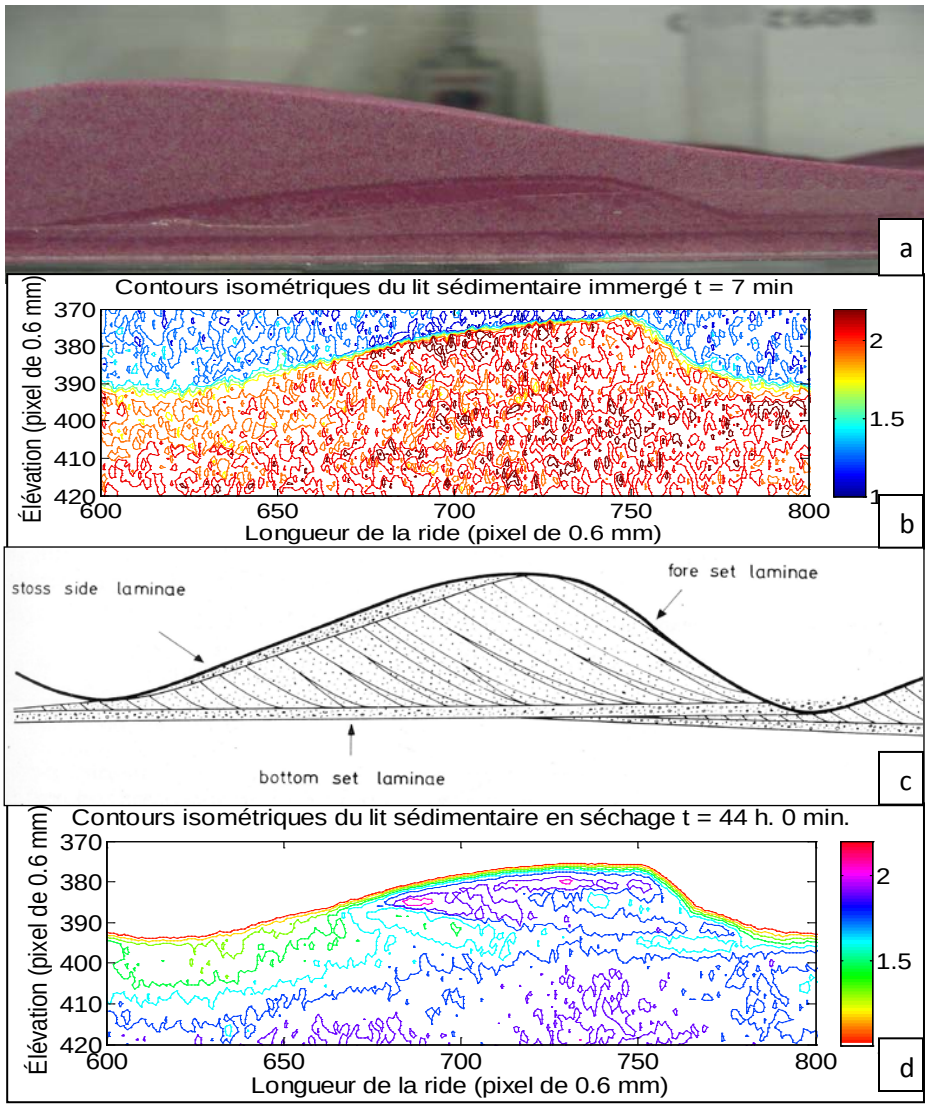

Fig. 5. *a: Picture of buried sand ripple formation after removal of water. b: X-ray isometric imaging of submerged sand ripple. c: Drawing of observed sand ripple lamination (Reineck & Singh, 1975). d: X-ray isometric imaging of sand ripple after removal of water. Color bar represents density in SI units.*

Discussion

When observing density profiles along a migrating sand ripple (Fig. 3), it appears that the bed surface used as a datum is located deeper into the sediment, at maximum density point. Density values and profiles form at the water column base as a conduct to the definition of a frontier density point (former datum) limiting the top of an upper bedload transport zone. Underneath this bedload transport zone, the maximum density is reached leading to the definition of a *stricto sensu* ripple surface (Fig. 3). This new ripple surface location can be 10 mm deeper than the one used in literature (Fig. 6) (Yalin, 1977) and depends on d_{50}, flow current and position along the ripple. Dynamic and static averaged bed levels are therefore different. (Fig. 6). Variation in surface position modifies deeply the stoss-side/lee-side frontier along sand ripple.

The augmentation of available sediment for bedload transport is explained by the discovery of a new datum, located at maximum density (Fig. 3). Former datum, used in literature (Baas, 2003 and Middleton & Southard, 1977), is mark by a frontier density

point providing the bedform topography. Those two point delimits the upper bedload transport zone, where, at its base, is located the ripple surface *stricto sensu*.

Ripple geometry, as present by Yalin (1977) is modified to include the active ripple surface and the bedload transport (Fig. 6).

Observability of sand ripple lamination is nearly impossible during active process (Fig. 5) but when removing a part of water, the lamination, the injected and trapped water inside sediment matrix can be seen (Montreuil & Long, 2011).

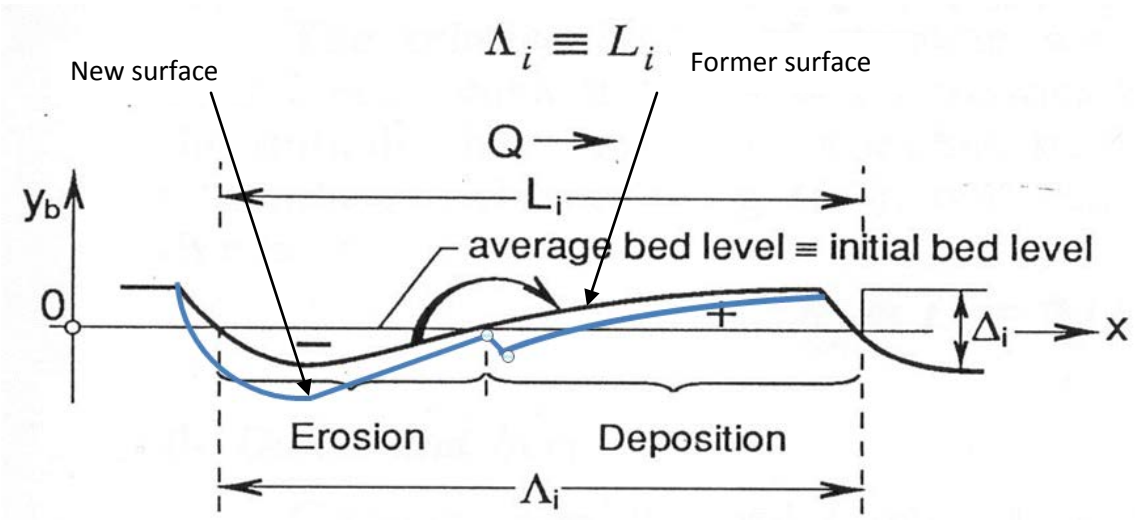

Fig. 6. *Ripple geometrical parameters (modifiy from Yalin, 1977).*

Conclusion

Innovative CT-Scanner results re-open the discussion about suspended and bedload transport during erosion and deposition processes, leading to a new way of looking inside active sediment transport. Protocols and processes developed in this study open new research opportunities in the field of sediment transport.

References

Baas JH (2003) Ripple, ripple mark, ripple structure. In: Encyclopedia of Sediments and Sedimentary Rocks (Ed. by G.V. Middleton), Kluwer Academic Publishers, Dordrecht, Netherlands, 565-568.

Bagnold RA (1977) Bed load transport by natural rivers. Water Resources Research 13: 303-312.

Hounsfield GN (1973) Computerised transverse axial scanning (tomography) Part 1: Description of system, British Journal of Radiology, 46:

Ketcham RA & Carlson WD (2001) Acquisition, optimization and interpretation of X-ray computed tomographic imagery: applications to the geosciences, Computers & Geosciences 27: 381-400. 1016-1022,

Middleton GV & Southard JB (1977) Mechanics of sediment movement, S.E.P.M. Short Course Number 3, Binghamton.

Montreuil S & Long B (2007) Flume experiments under CAT-Scan to measure internal sedimentological parameters during sediment transport, Proceedings Coastal Sediments '07 Conference, ASCE, New Orleans, LA, 1: 124-136. Québec, (unpub.).

Montreuil S & Long B (2011) Relationship between vortex activity and pseudo liquefaction at a lower stoss-side ripple surface, Proceedings Coastal Sediments '11 Conference, ASCE.

Montreuil S (2014) Définition des paramètres sédimentologiques mesurés au scanographe densitométrique et estimation de la contrainte de cisaillement sur une ride sableuse. Thèse de Doctorat, 339 p. Inst. Nat. de la Rech. Sci., Centre Eau, Terre, Environ, Québec, (unpub.).

Moore F (2004) Application de la scanographie à l'étude de la déposition consolidation : Modélisation physique et théorique, Mémoire de maîtrise, 131 p., Inst. Nat. de la Rech. Sci., Centre Eau, Terre, Environ., Québec, (unpub.).

Raudkivi AJ (1963) Study of sediment ripple formation. ASCE J. Hydraul. Div., 89: 15-33.

Reineck H-E & Singh IB (1975) Depositional sedimentary environments, Springer study edition, New York, 439 p.

Yalin MS (1977) Mechanics of sediment transport 2ed. Pergamon Press. 298 p.

The Internal Density Structure of Sediment-Propelled Turbidity Currents as Revealed by CT Imagery

[1]Arnott, R.W.C., [1]Tilston, M., [2]Rennie, C., [3]Long, B.
[1]Department of Earth Sciences, University of Ottawa, Ottawa ON
[2]Department of Civil Engineering, University of Ottawa, Ottawa ON
[3] Centre Eau Terre Environnement, INRS, Québec City QC

Gravity currents exist due to a density difference between two fluids, and when the denser of the two flows moves, principally horizontally and under the influence of gravity, it does so by displacing the lighter fluid. In turbidity currents the density difference driving their movement results from spatial differences in suspended sediment concentration, namely between the current and the ambient fluid, which generally is seawater. In nature these suspended-particle-driven currents are common, and in the deep marine are the principal sediment transporting agents that build up the largest sediment accumulations on Earth – the Bengal submarine fan, for example, is 3000 km long, 1000 km wide and 16.5 km thick (Curray et al. 2002). However natural turbidity currents are highly episodic and notoriously destructive, which has made *in situ* measurements difficult, and virtually impossible in the high-energy, sand-rich, near-bed region of the flow. As a result, scaled physical (laboratory) models are used to investigate turbidity current processes, which then are validated against the sedimentary structures and granular textures observed in the ancient geologic record. Many researchers have investigated the mean flow field of density currents in straight (e.g. Garcia, 1994) and curved channels (e.g. Corney *et al.*, 2006), and the way that mean flow characteristics change between the head, body and tail of density currents (e.g. McCaffery *et al.*, 2003). Yet due to a combination of scaling issues and instrument limitations, obtaining high-resolution multi-dimensional velocity and concentration datasets has proven difficult. As consequence, fluvial systems and concepts of open channel flow have been applied as close analogues for the processes governing turbidity currents (Leeder, 1999). In part this is an intuitive consequence of the similarity in a number of geomorphic attributes, including straight, meandering and braided planforms, bend cut-offs (Kolla et al., 2007), point bars (Arnott, 2007) and depositional styles of stratification formed by migrating bedforms (Leeder, 1999). However it also has been noted that there are number of fundamental differences between these two systems, and therefore the notion of dynamic similarity is at best equivocal (Wynn *et al.* 2007). Most fundamentally is the effect(s) related to suspended sediment. In open channel flows (i.e. rivers) suspended sediment concentration is negligible and therefore ignored in physical and mathematical formulations. In turbidity currents, on the other hand, the suspended sediment **IS** the flow, and characteristics of its spatial and volumetric composition represents an obvious first order control.

Generating particle-propelled turbidity currents in the lab is easy. However these currents, unlike those in nature, are immediately depositional and as a consequence unsteady and short-lived. Moreover, their high sediment concentrations makes collecting velocity data with most velocimeters, which typically operate at 10 MHz, impossible, and measuring density, using even novel acoustic and imagery techniques, highly suspect. Accordingly, researchers have turned to studying density currents using variably concentrated saline currents with the implicit assumption, or explicit statement, that they faithfully mimic the dynamics of sediment-propelled (turbidity) currents. In these currents density can be easily manipulated by varying the amount of dissolved solute (i.e. salt). In addition the elimination of acoustic-wave-scattering sediment particles makes the acquisition of velocity data simpler and more accurate, even at high concentrations, and high-quality density data can be collected with high resolution resistivity instruments. In this regard the work of Sequerios and others is noteworthy (Sequeiros et al. 2010; Sequeiros 2012). These authors showed that depending on concentration, which in turn controlled flow speed, flows exhibited two end-member vertical concentration and related velocity profiles: an exponentially decreasing concentration profile with a velocity profile with its velocity maximum (Umax) near the bed; and a more "plug- and step-like" concentration profile in which the velocity maximum was situated well above the bed and coincided with the rapid change in concentration (Fig. 1). Moreover, these authors point out that based on the densiometric Froude number, flows with an exponential concentration profile were supercritical whereas plug-like profiles were representative of subcritical flows. Attendant also with these differences were significant changes in the degree of mixing along the upper surface of the flows, namely supercritical flows showed extensive mixing with the ambient fluid via well-developed Kelvin-Helmholtz instabilities, whereas poorly-developed Kelvin-Helmholtz instabilities resulted in negligible mixing in subcritical flows (hence plug-like concentration profile).

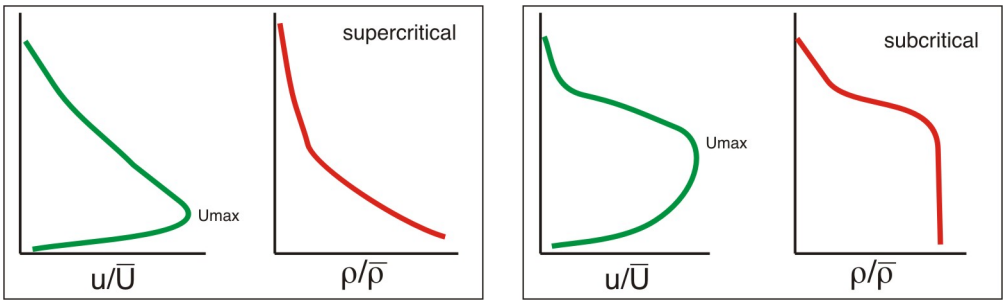

Fig 1. Normalized velocity (green) and density (red) profiles for supercritical and subcritical experimental saline density currents (modified from Sequeiros et al. 2010)

These differences, for example, have been used to explain the long-runout distance of turbidity currents, which in the case of the Bengal Fan can be as much a few

thousand kilometers over an otherwise horizontal seafloor. To achieve such distances over a no-slope surface requires these momentum-driven flows to maintain their density contrast with the ambient fluid, which in turn necessitates limited mixing with the ambient fluid. Based on Sequeiros' work such flows would be subcritical, which then begs the question as to how low energy (subcritical) flows can maintain sediment particles in suspension, and therein, are saline currents meaningful surrogates for particle-driven turbidity currents?

In this study, we created a variety of particle-driven turbidity currents of varying grain size (d_{50}: 70, 150, 230, 330 μm), concentration (up to ~18% by mass) and flow velocities (up to ~0.7 m/s). Velocity data was captured with a 2MHz 3D acoustic velocity profiler with 1 mm vertical resolution through the full thickness of the flow. More importantly, full-depth sediment concentration (truly density) was continuously measured by passing flows through the gantry of a medical grade CT scanner. Merged together, the velocity and density data show, for the first time, the detailed internal composition of particle-driven turbidity currents. Results, like those in the saline flows of Sequeiros et al., show two end-member concentration and velocity profile types, but instead of being related to concentration and flow velocity, the differences here are related to grain size, since all flows were supercritical (Fig. 2). Specifically, the velocity, density and mixing characteristics of fine-grained runs were similar to subcritical saline flows whereas coarse-grained runs were similar to supercritical saline flows. The reasons for these observations are twofold. First, increased particle mass (in the coarser flows) necessitates higher impulse to change particle trajectory and thus are less sensitive to weak or brief fluctuations in fluid stress. Second, the higher settling velocity of coarser particles promote flows that are highly stratified between the base and top of the current, which in turn promotes the development of large rather than small Kelvin-Helmholtz instabilities, and accordingly result in extensive mixing. Collectively these differences have important implication for the conservation of flow energy, and therefore runout distance of turbidity currents in the deep sea.

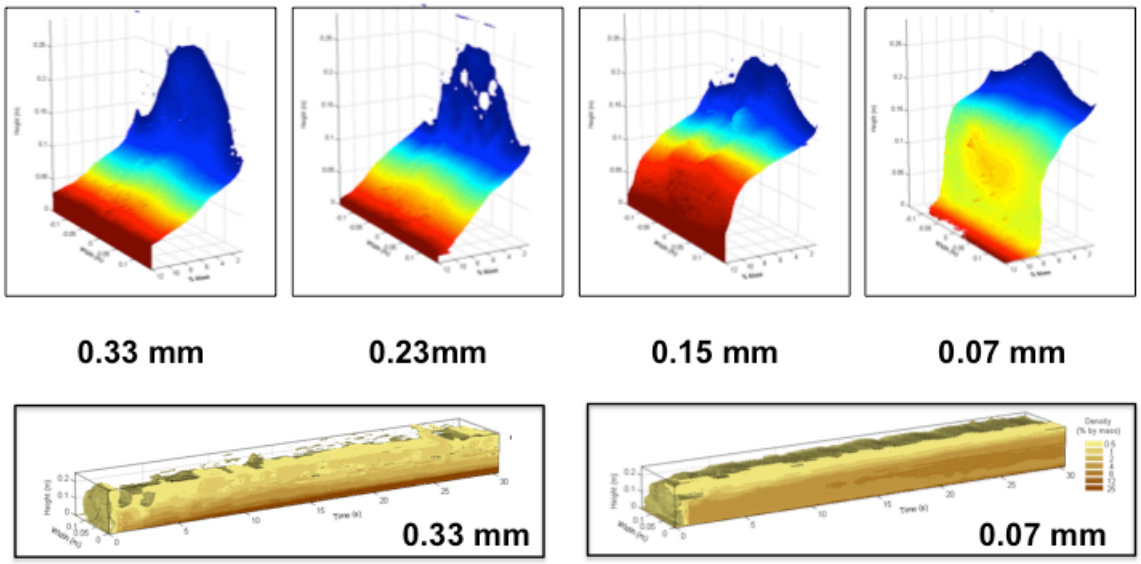

Fig. 2. Density profiles measured with the CT scanner of 9.5 mass% turbidity currents composed of differing grain size – red to blue colours indicate high to low sediment concentration. Lower panel shows density volumes that illustrate the temporal and spatial characteristics of density.

References

Arnott, R.W.C. (2007). Stratal architecture and origin of lateral accretion deposits (LADs) and conterminuous inner-bank levee deposits in a base-of-slope sinuous channel, lower Isaac Formation (Neoproterozoic), East-Central British Columbia, Canada. Marine and Petroleum Geology, v. 24, p.515–528.

Curray, JR, Emmel FJ, Moore DG. 2002. The Bengal Fan: morphology, geometry, stratigraphy, history and processes. Marine and Petroleum Geology. V. 19, p.1191-1223.

Corney, R.K.T., Peakall, J., Parsons, D.R., Elliott, L., Amos, K.J., Best, J.L., Keevil, G.M., and Ingham, D.B. (2006). The orientation of helical flow in curved channels. Sedimentology, v. 53, p. 249-257.

Garcia, (1993). Hydraulic Jumps in Sediment-Driven Bottom Currents. Journal of Hydraulic Engineering, ASCE v. 119, p. 1094-1117.

Garcia, M.H. (1994). Depositional turbidity currents laden with poorly sorted sediment. Journal of Hydraulic Engineering ASCE, v. 120, p. 1240-1263.

Kolla, V., Posamentier, H.W., and Wood, L.J. (2007). Deep-water and fluvial sinuous channels—Characteristics, similarities and dissimilarities, and modes of formation. Marine and Petroleum Geology, v. 24, p. 388-405.

Leeder, M.R. (1999) Sedimentology and sedimentary basins; from turbulence to techtonics. Blackwell, Oxford. 592 p.

McCaffrey, W.D., Choux, C.M., Baas, J.H. and Haughton, P. D.W. (2003). Spatio-temporal evolution of velocity structure, concentration and grainsize stratification within experimental particulate gravity currents. Marine and Petroleum Geology, v. 20, p. 851-860.

Sequerios, O. et al. 2010. Characteristics of velocity and excess density profiles of saline underflows and turbidity currents flowing over a mobile bed. J. Hydraulic Engineering, v. 136, p. 412-433.

Sequerios, O. 2012. Estimating turbidity current conditions from channel morphology: a Froude number approach. J. Geophysical Res. v. 117 C04003

Wynn, R.B., Cronin, B.T. and Peakall, J. (2007). Sinuous deep-water channels: Genesis, geometry and architecture. Marine and Petroleum Geology, v. 24, p. 341-387.

The influence of grain size on the velocity and sediment concentration profiles and depositional record of turbidity currents

M. Tilston[1], R.W.C. Arnott[1], C.D. Rennie[2] and B. Long[3]
[1]Department of Earth Sciences, University of Ottawa, Ottawa ON
[2]Department of Civil Engineering, University of Ottawa, Ottawa ON
[3] Centre Eau Terre Environnement, INRS, Québec City QC

Turbidity currents, like open channel flows, are unidirectional. But unlike open channel flows, where gravity acts on the fluid and causes it to move, turbidity currents are propelled by gravity acting directly on the suspended sediment and the interstitial fluid is simply entrained by the particles to form the current. However, since the suspended sediment particles are constantly settling, and eventually become lost from the flow and added to the bed, turbidity currents will at some point in their flow history decelerate and eventually come to rest. While deposition, or at the very least net deposition, should occur mostly during the waning phase of these currents, their deposits (turbidites) should then exhibit a suite of sedimentological features that, stratigraphically upward, suggest progressively lower energy conditions. Such patterns were first popularized by Bouma (1962) who described distinctively upward-fining beds with a consistent vertical assemblage of depositional characteristics. Notably absent in this idealized succession, however, is dune cross-stratification, which based on an extensive literature of open channel flow, and in bed sediment between about 0.2-0.7 mm, should, under waning conditions, occur above upper plane bed and below ripples. The absence of dune cross-stratification in the Bouma turbidite model, but also its paucity in the ancient or modern deep-marine sedimentary records as a whole, has been noted by a number of authors and remains the subject of a long-standing debate (see Arnott, 2012). Previous explanations focused on the requisite bed configuration and hydraulic conditions needed for their development, including insufficient time for growth (Walker, 1965), (negative) influence of suspended sediment-fallout on the development of incipient bed features (Lowe, 1988) (negative) impact of turbulence suppression associated with higher suspended sediment concentrations (Allen and Leeder, 1980), and the (negative) effect of increasing clay content on flow structure and bed rheology (Baas and Best, 2002). Additionally, the lack of dunes may relate to the fact that most natural turbidity currents are supercritical, and the fact that ripples and dunes, at least in open channel flow, form under subcritical conditions; thus the absence of dunes in turbidites is an inherent byproduct of their unique velocity and concentration profiles (Parker et al. 2013). And lastly, the most recent argument is based on (particle) advection length, which here would be argued to exceed the scale of the near-bed processes and transport patterns that are involved in the development of ripples or dunes (Ganti et al. 2013). In large part these questions and many more remain unresolved because of our inability to monitor natural sediment-transporting turbidity currents, which are high-energy, notoriously destructive events. In particular the lack of knowledge concerning the distribution of sediment within these currents remains a major impediment to an improved understanding. The use of CT imagery, however, provides, for the first time, the opportunity to resolved the internal density structure within these currents, and therein important insight into these and many other questions.

Experimental set-up

Experimental currents were created in a 7 m long acrylic closed-topped flume with inner cross-sectional dimensions of 0.3 × 0.3 m. Initial sediment slurries were homogenized in a 0.8 m^3 cylindrical mixing tank suspended 1.87 m above the flume with an orifice valve at the base of the mixing tank to control outflow rates. Velocity measurements were recorded using a three-dimensional ultrasonic Doppler velocity profiler (UDVP-3D), and instantaneous cross-sectional density images (normal to flow direction) were obtained by passing the flume through the gantry of a medical grade computed tomography (CT)-scanner. This combination of equipment offers the advantages of being non-obtrusive, minimal offset in sampling position of the two flow properties, and yields datasets with very high spatial and temporal resolution. A total of 12 experimental currents were run using four different, well-sorted grain size distributions of Ottawa sand (d_{50}: 70μm, 150μm, 230μm and 330μm) and three concentrations (C_{slurry}: 5%, 9.5% and 17.5% by mass).

Results

At sediment concentrations of 9.5% or more, a smooth, planar surfaced bed aggraded rapidly beneath all flows, and remained so to the end of flow movement. Flows at 9.5% or less showed different bed morphologies as a function of grain size in the overriding sediment suspension. In the fine-grained runs (D_{50} – 0.07, 0.15 mm) a plane bed remained stable throughout the run. In the coarser runs- (D_{50} – 0.23, 0.33 mm), in contrast, small, straight-crested, asymmetrical bed forms appeared everywhere on the surface of the bed (**Figure 1**). In only a matter of several seconds, and flow speeds of several tens of cm/s these features grew rapidly, most notably in height, on the earlier deposited planar sand bed. Importantly, in addition to differences in the response of the bed, the density and velocity structure of fine- vs. coarser-grained flows were distinctly different (**Figure 2**). The obvious question, therefore, is what is the physical basis for the difference in bed response, and does it related somehow to the current velocity and/or density structure?

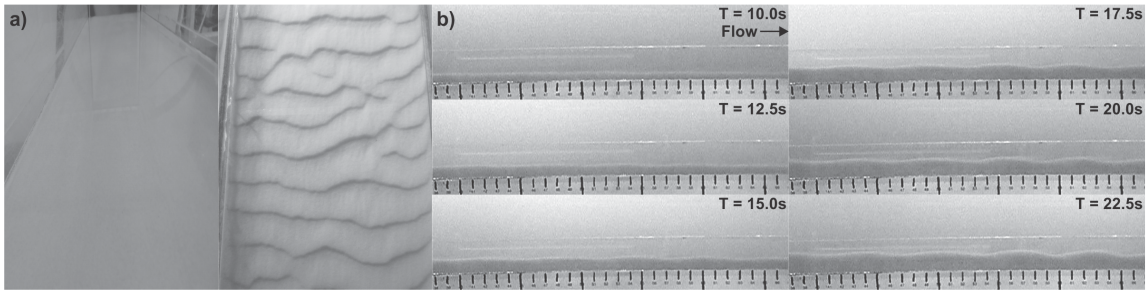

Figure 1: a) End member bed morphologies: planar bed (left), and downstream migrating angular bedforms (right). b) Temporal development of angular bedforms

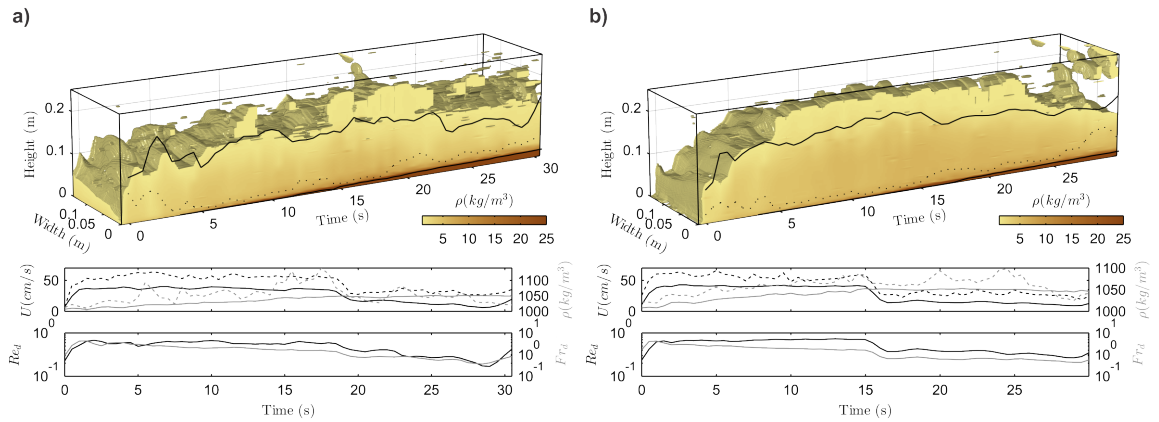

Figure 2: Temporal evolution of sediment and hydraulic properties in the 230μm (a) and 150μm (b) runs (9.5% by mass). The upper part of the figure shows the volumetric reconstructions from time-lapse CT images, positions of $\boldsymbol{u_{max}}$ (dotted line) and $\boldsymbol{\delta = u_{max}/2}$ (solid line); lateral 0m position corresponds with the centerline of the flume. The lower part of the figure shows temporal variations in the Reynolds and Froude number.

As summarized by (Best, 1992), ripple development in open channel flows is preceded by incipient features termed bed defects, although the mechanism governing their initiation remains a source of debate. Historically, envisioned as a single mound formed by fluid turbulence, defects cause spatial variations in local bed shear that eventually lead to the formation of ripples. However this model fails to explain the rapid development and spatially regularity of many defects, and especially their development in laminar flow. The more recent work of Venditti et al. (2006) suggested that open channel flow can be regarded as a two-phase fluid flow consisting of a faster-flowing, low density upper layer and a slower moving, more dense basal layer, which in their case coincided with the bedload layer. Under appropriate conditions, the interface separating the two fluids becomes hydrodynamically unstable, ultimately causing spatio-temporal variations in sediment transport and deposition on the bed, and eventually defects. We believe that this same mechanism can explain our findings in the coarser grained flows. Here, the coarse, high concentration basal layer and slower, significantly more dilute overlying fluid are, respectively, analogous to the bedload layer and overlying clear water in open channel flows. As a consequence the hydrodynamic instability is sufficiently strong and close to the bed that it becomes imprinted, leading to the initiation of defects, and ultimately downstream migrating angular bedforms. Conversely, higher concentrations, or equivalently all finer grained flows, lack the requisite strong vertical density stratification in their near-bed region, and as a result the hydrodynamic instability is either too weak, too high above the bed, or too poorly developed to become imprinted, and accordingly a plane bed remains stable.

References

Allen, J. R. L., and Leeder, M. R., 1980, Criteria for the Instability of Upper-Stage Plane Beds: Sedimentology, v. 27, no. 2, p. 209-217.

Arnott, R. W. C., 2012, Turbidites, and the Case of the Missing Dunes: Journal of Sedimentary Research, v. 82, no. 5-6, p. 379-384.

Baas, J. H., and Best, J. L., 2002, Turbulence modulation in clay-rich sediment-laden flows and some implications for sediment deposition: Journal of Sedimentary Research, v. 72, no. 3, p. 336-340.

Best, J., 1992, On the Entrainment of Sediment and Initiation of Bed Defects - Insights from Recent Developments within Turbulent Boundary-Layer Research: Sedimentology, v. 39, no. 5, p. 797-811.

Bouma, A. H., 1962, Sedimentology of some flysch deposits: a graphic approach to facies interpretation, Amsterdam, Elsevier, 168 p.:

Ganti, V., Lamb, M. P., and McElroy, B., 2014, Quantitative bounds on morphodynamics and implications for reading the sedimentary record: Nat Commun, 5:3298.

Lowe, D. R., 1988, Suspended-Load Fallout Rate as an Independent Variable in the Analysis of Current Structures: Sedimentology, v. 35, no. 5, p. 765-776.

Parker, G., Fu, X., Zhang, Y., Zinger, J., and Konsoer, K., Bedform Regime Diagram for Rivers and Turbidity Currents: Conditions for the Formation and Obliteration of Dunes, *in* Proceedings Proceedings of 2013 IAHR Congress2013: Beijing, Tsinghua University Press.

Venditti, J. G., Church, M., and Bennett, S. J., 2006, On interfacial instability as a cause of transverse subcritical bed forms: Water Resources Research, v. 42, no. 7, Doi: 10.1029/2005wr004346.

Walker, R. G., 1965, The Origin and Significance of the Internal Sedimentary Structures of Turbidites: Proceedings of the Yorkshire Geological Society, v. 35, no. 1, p. 1-32.

Wave-sediment interaction imaging with X-ray tomography: A small-scale experiment to characterize the artefacts

*C. B. BRUNELLE[1](CORINNE.BOURGAULT-BRUNELLE@ETE.INRS.CA), B. LONG[1], P. FRANCUS[1], L. F. DAIGLE[1], M. DES ROCHES[1], H. TAKAYAMA[2]

[1] Institut national de la recherche scientifique, 490, rue de la Couronne, G1K 9A9, Québec, Canada
[2] Kumamoto University, 2-40-1 Kurokami Chuo-ku, Kumamoto City, 860-8555, Japan

Complexity of currents dynamics with porous sand beds has no analytical solutions. Hence, empirical relations are needed to validate fluid-sediment interaction models. To achieve this, travelling waves were generated in a small-scale physical model (1:17) to investigate the wave-sediment processes over a sloping beach at the Multidisciplinary Laboratory of CT-Scan for Non-Medical Use (INRS). A hydraulic flume, filled with sediments and water, was inserted into the medical CT-scanner. The experiment simulates storm waves, with the equivalent real-scaled periods and heights, approaching the beach in shallow waters. The aim of this research is to improve the monitoring system of sediments dynamics in coastal regions. This experimental setup provided a complete overview of the density variations (i.e., water infiltration) into thte beach which is impossible to cover in a real-scale experiment. The two main sources of artefacts of the reconstructed X-ray images are: 1) the tube power limitation and 2) the geometry of the beach. These limitations are caused by the high density of material, inducing noise, and the square form of the beach (axial plane) creating black streaks during the image reconstruction. The X-ray tomography method showed anyhow promising results to measure key parameters such as the sediment transport and the grain size sorting as well as 4D measurements. Algorithms for image interpretation (i.e., error delimitation, edge tracking, statistical analysis, etc.) are presented.

1. Introduction

Field studies normally provide the best representation of the reality in coastal dynamics because each site is specific. However, these kinds of database are rare, collected in complex systems and only available on a limited grid. The numerical models that simulate the interaction of fluid with sediment under wave action need to be validated. The physical model, a reproduction of a system at a different scale, is interesting in this case because no simplified assumptions of the equations of movement are required, which must be done in numerical models. In the size-reduced model, the major dominant forces should be represented proportionally to the large scale effects. Such physical models have been built similarly in small flumes to characterize the sediment transport (Grasso et al., 2011; Yamada et al. 2013; Montreuil et Long 2007). In this study, a movable-bed physical model for short-term events is used to study the cross-shore transport of beach profile during high intensity events.

To visualize the temporal variation of bed profiles under currents, the X-ray computed tomography (CT) scanning technique is used. Medical CT-Scanner is a fast method to capture the overall bed deformation and the density variation in time, at a location of interest. The advantage is that no dose reduction or processing time are required. However, there are major concerns about the artefacts in reconstructed images. The objective of the experiment is to identify and quantify the errors caused by the main artefact observed (i.e., streaks). The geometry of the setup is studied and some recommendations are provided to interpret the HU values correctly. Two different types of beach sediment mixture are tested: 1) sand only and 2) sand, gravel and cobbles. The results section is divided in two parts: spatial and temporal measurements. The interpretation of the X-ray tomography images is discussed in regards of useful sedimentary parameters in coastal dynamics.

2. Materials and methods

2.1 Experimental setup

A small-scale model (1:17) was built in the Multidisciplinary Laboratory of CT-Scan for Non-Medical Use at the Institut National de la Recherche Scientifique (INRS). A rectangular flume (0.30 m x 0.30 m x 7.0 m) made with 0.025 m transparent acrylic material, partially filled with water (h=0.20 m) and sediments, and equipped with a wavemaker was inserted into the CT-scanner as conducted by Yamada et al. (2013). The experiment simulates regular plunging waves (i.e. storm waves) with the equivalent real-scaled period (T) of 1.5 seconds and heights (H) of 0.04 m until the beach reaches the equilibrium profile. The scale conversion was evaluated as described by Hughes (1993) for a movable-bed physical model coupled with short-wave hydrodynamics. The prototype-to-model length ratio (N_L) is 17, with the particular ratios $H/L \approx 0.45$ and $h/L \approx 0.12$, where L is the wavelength of waves. The similarity conditions require that the scale factor for time (N_T) equals the square root of the length scale; $N_T=(N_L)^{1/2}$. The first tested sediments mixture was composed of Ottawa Sand (SiO_2) with a median diameter (D_{50}) of 215 µm. The second type of sediments mixture was composed of sand (30%), gravel (30%) and cobble (40%) with a D_{50} of 650 µm. This mixture was composed of quartz, feldspath and mica for each grain size class. Consequently, the density is not totally homogeneous. The sediments used come from natural beaches located in the Gulf of Saint Lawrence (Quebec, Canada).

2.2 Data acquisition

A medical X-ray CT-Scanner (Siemens, Somatom Definition AS+ 128) moves automatically on rails along the flume. The tube voltage is 140 keV. The sediments atomic numbers and the tube voltage lead to both the photoelectric and Compton effects during the X-ray dense material penetration (Knoll, 1989). Consequently, the CT-scanner X-ray attenuation measurements are not exactly proportional to matter density (Boespflug et al. 1994). The measured relative density varies from -1024 to +3071 HU providing 4096 levels of grey, where air and water values are respectively -1000 and 0 HU. The field of view (FoV) used during reconstruction was different according to the experiment, the maximum being 50 cm. The pixel size is 0.1 mm for a FoV of 5 cm, 0.6 mm for a FoV of 30 cm. The air calibration was done before each series of experiments.

First, the spiral mode was used to study a core (diameter of 10 cm) of sediment mixture with a pitch factor of 0.35 using the SAFIRE reconstruction (smooth filter I30). The tube current was 300 mA and the pixel size was 0.21 mm. In this case, 668 images were taken in 29 seconds (23 images sec^{-1}). Secondly, the perfusion mode was used for temporal measurements (4D) with an acquisition sequence of 20 times (only 10 presented) 64 slices of 0.6 mm using reconstructed images of IRIS (smooth filter B30) for a tube current of 600 mA. The pixel size was 0.75 mm. The perfusion mode acquisition is faster with 64 images taken in 0.15 seconds (427 images sec^{-1}). The wave heights and current velocities were measured with capacitance type wave gauge and acoustic Doppler velocimeter.

3. Results and discussion

3.1 Spatial density variations

Different experiments were conducted to validate the HU values interpretation. First, some tests provided a quantification of the major errors observed due to the geometry of the experimental set up. The acrylic box filled of sand and water creates a square form with 4 corners in the axial plane. This creates black diagonal streaks on the images after reconstruction. A piece of quartz (5 cm^3) of known HU values was displaced into the uniform sand beach (not illustrated). The scan measurements with the quartz placed at different locations into the beach, inside and outside the black cross, showed that the HU values could vary of ±100 HU around the mean value. This error is the most important (Figure 1a) and has the equation form of the equation 1.

$$f(x,y) = \left(\sqrt{(x^2+y^2)}\cos^2(2\theta)\,(1+e^{y}) - a\right)(b+e^{-y}) \qquad \text{Eqn. 1}$$

Where *a* and *b* are two constants calibrated according to each reconstructed images. This characterization considered that the pixels in the black cross were underestimated and the others (outside the cross) were overestimated. The center of sand is at pixel -88 (Figure 1a), but the center of the cross is at pixel -70. The cross also affects pixels in the water. The correction was applied this way to the Figure 1b, for the quality of the presentation only. However, a lot of noise appears on the figure. This is caused by the tube power limitation and also by the thickness of the beach. For a thickness of 0.20 m, only 5 % of the x-ray reaches the detectors. A solution could be to replace a part of the sediments (i.e., 10 cm), not involved in the beach dynamics, with another material of lowest density increasing the x-ray penetration up to 25%. Anyhow, the sand and water surfaces were easy to delimitate using the HU value variations only (Figure 1b). Thus, it is possible to calculate the sediment transport by calculating the volume deformation before, during and after the experiment.

The Figure 1c shows a well-known sorted sediments core. The standard deviation (SD) was calculated for each slice of 10 pixels (N≈4500 points). All the values lower than 500 HU were removed of the standard deviation (SD) calculation, removing water and air bubbles of the analysis (in red at Figure 1c). Previously, the scan resolution was set to be 200 µm for this experience with a minimum of 4 pixels needed to detect properly the HU value of a grain. This means that the scan measurements provide a uniform distribution of HU values with a small SD for grain sizes less than 800 µm. This way, it was possible to have a significant relation between the SD and the grain size distribution. This is possible because the density of grains is not homogeneous and has a similar natural variability in each size class. Thus, according to the HU values, the SD is 69 for the sediments < 1000 µm, 177 for the sediments between 1000 µm and 2000 µm, 375 for the sediments between 2000 µm and 3350 µm. The regression of the mean grain size (Y) as a function of the SD (X) is Y=6.96*X+117 (R^2=0.98, N=3). The SD is 144 for the sand mix. Using the aforementioned regression, the mean grain size would be 1120 µm, which is in reality 1250 µm (error ≈ 10%). The result shows that it is possible to characterize grain size sorting using CT-Scanner values.

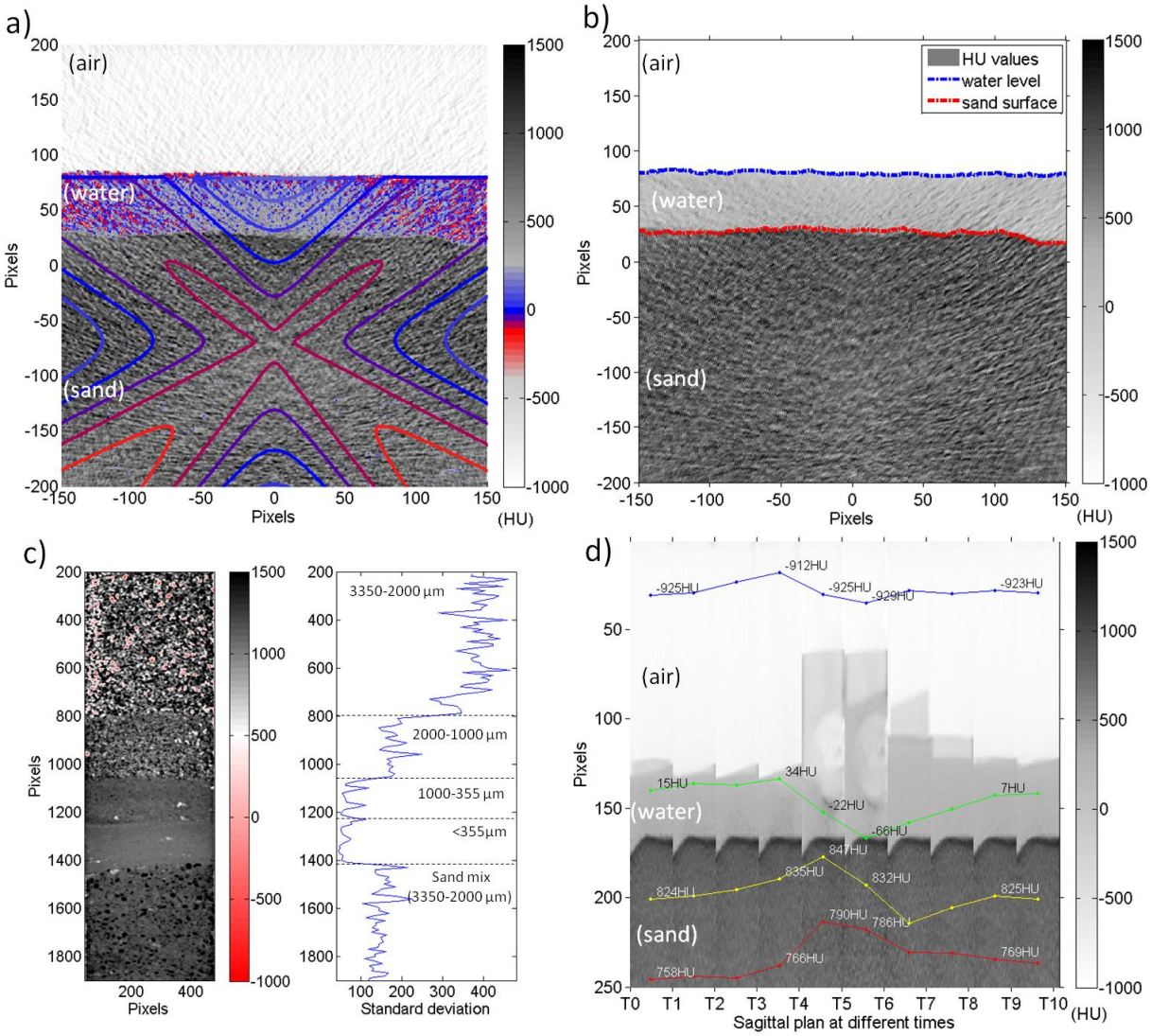

Figure 1. HU values variations. Highest densities are illustrated in black and lowest densities in white (reverse scale), a) axial plane of the sand beach with streaks errors delimitation, b) axial plane of the sand beach (streaks removed) with water and sand surface boundaries (dashed lines) c) sagittal plane of a well-known sorted sediments core (left) with the corresponding SD of HU values for each grain size class (right), d) sagittal planes (38.4 mm width) of the sand beach with temporal mean HU value variations before, during and after wave passage in air (10 to 50) water (140 to 160), beach surface (180 to 200) and beach subsurface (225to 250) pixels (see section 3.2).

3.2 Time series

In this section, measurements were done into the wave breaking zone using the perfusion mode of CT scan, during the wave passage. The measurements were covering the wave breaking zone, at the top of the sand beach, containing fine sediments, water and air bubbles (Figure 1d). This figure shows a time series of scans, taken with a 0.30 second interval, when a wave breaks on a sand bar. The HU values are anomaly higher at the interface water-sand, and it is most probably due to beam hardening. This problem occurs when part of the X-ray energy spectrum is absorbed at the different density interfaces. This complicates the calculation of density variation in non-uniform materials. It would be preferable to do not consider the pixel near the surface or directly on the edge. Series of tests characterizing the

beam hardening according to the object forms is thus recommended to conduct before analyzing these regions.

The mean HU values in the air (blue), in the water column (green), at the beach surface (yellow) and in the beach subsurface (red) were calculated. After the wave passage, the suspended matter concentrations increase in the water column from the time T_0 to T_4. This corresponds to the beach destabilization and the increase of sediment transport (Butt et al., 2001; Bakhtyar et al. 2011). This fits the increase of HU values in the air varying from -925 HU to -912 HU, which is similar to the general HU value variations into the beach at that moment. However, the HU values still increase in the beach (T_4) while it decreases in the water column and in the air. This corresponds to the water exfiltration (i.e., HU increase) process occurring in the destabilization phase, after the wave passage, named the backwash process. During this phase, the horizontal velocities are oriented offshore. Inversely, the uprush process occurs during the wave passage inducing water infiltration into the beach (i.e., HU decrease) and the diminution of sediment transport (T_5 to T_7). During this phase, the horizontal velocities are oriented onshore. At the time T_{10}, a new cycle begins.

4. Conclusion

An experimental setup to measure the dynamic of waves breaking on beaches was mounted into a CT-Scanner. The image post-treatments provided a better understanding of the artefacts effect. The tube power seems to be low and the image reconstruction algorithm included errors. Anyhow, evolution of beach morphology, sediment transport processes, air entrapment, suspended matter concentration and grain size distribution were detected and possibly quantified with further investigations. The next researches will focus on the optimization of the acquisition parameters and the possibility to use homemade models-based iterative reconstruction with beam hardening correction. The present work is a contribution to the shore dynamics experimental research using physical models for coastal protection studies.

5. Acknowledgments

The authors want to thank the Research Chair in Coastal and River Engineering of Quebec, the Canada Foundation for Innovation and the Multidisciplinary Laboratory of CT-Scan for Non-Medical Use (INRS).

Number of words: 2501

References:

Bakhtyar, Roham, Alessandro Brovelli, David Andrew Barry, et Ling Li. 2011. « Wave-induced water table fluctuations, sediment transport and beach profile change: Modeling and comparison with large-scale laboratory experiments ». *Coastal Engineering* 58 (1): 103‑18.

Boespflug, X., N. Ross, B. Long, et J. F. Dumais. 1994. « Tomodensitométrie axiale: relation entre l'intensité tomographique et la densité de la matière ». *Canadian Journal of Earth Sciences* 31 (2): 426‑34.

Butt, Tony, Paul Russell, et Ian Turner. 2001. « The influence of swash infiltration–exfiltration on beach face sediment transport: onshore or offshore? ». *Coastal Engineering* 42 (1): 35‑52.

Grasso, Florent, Hervé Michallet, et Eric Barthelemy. 2011. « Experimental simulation of shoreface nourishments under storm events: A morphological, hydrodynamic, and sediment grain size analysis ». *Coastal Engineering* 58 (2): 184‑93.

Hughes, Steven A. 1993. *Physical models and laboratory techniques in coastal engineering*. Vol. 7. World Scientific.

Knoll, Glenn F. s. d. « Radiation Detection and Measurement (1989,) ». *Edition John Wiley & Sons USA*.

Montreuil, Stéphane, et Bernard F. Long. 2007. « Flume Experiments under CAT-Scan to measure internal sedimentological parameters during sediment transport ». In *Proceedings Coastal Sediments' 07 Conference, ASCE, New Orleans, LA*, 1:124‑36.

Yamada, Fumihiko, Ryuta Tateyama, Gozo Tsujimoto, Seiya Suenaga, Bernard Long, et Constant Pilote. 2013. « Dynamic monitoring of physical models beach morphodynamics and sediment transport using X-ray CT scanning technique ». *JOURNAL OF COASTAL RESEARCH*, 1617‑22.

Session 302

Oral presentation

Through-porosity induced corrosion under a Fe-based amorphous coating revealed by in-situ X-ray tomography

S.G. WANG[1]*, S.D. ZHANG[1], J.Q. WANG[1], S.C. WANG[1], L. ZHANG[1]

[1] Shenyang National Laboratory for Materials Science, Institute of Metal Research, Chinese Academy of Sciences, Shenyang 110016, PR China
* presenting author

In-situ X-ray tomography (XRT) or 4D imaging is one important technique that allows the researchers to track and visualize the internal structure evolution of various materials with the changes of load, temperature or other environment conditions. Corrosion resistance is one of the basic properties to be evaluated for materials in service. In-situ visualization of corrosion process will be helpful for understanding the corrosion mechanism and improving the material performance.

Thermal sprayed coatings are widely used to protect surfaces of metals and alloys against corrosion and wear in industry. The coating delamination and peeling off caused by corrosion is commonly encountered failure types. It is well known that the corrosion resistance of the materials coated is strongly related to its porosity that normally categorized as through-porosity and non-through porosity. However, the correlation between the porosity and the corrosion behavior of the thermally sprayed coating still remains ambiguous.

In this work, the volume fraction, size and distribution of the porosity in Fe-based amorphous coating were measured and analyzed via 3D XRT technique. Combined with an electrochemical test and the 3D XRT technique using lab-based VersaXRM-500 system, an ingenious in-situ experiment was designed to investigate the correlation between porosity and corrosion. A number of in-situ evidences acquired during the whole corrosion process clearly gave the fact that the preferential substrate corrosion was caused by the through-porosity rather than the other type of porosity. The dissolved volume of substrate was directly observed and calculated from the 3D visualization of the coated sample after potentiostatic polarisation test, and basically matched to the result calculated by measured charge with a negative deviation of about 6%. It was also found that through-porosity is sensitive to the coating thickness. The critical coating thickness for the presence of through-porosity was determined, which could provide a guide for the design of corrosion resistant coatings.

Number of words: 304

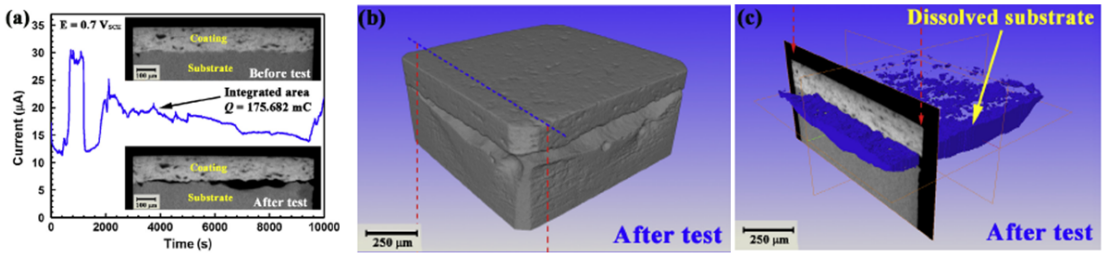

Fig. 1 (a) Current-time curve of potentiostatic polarisation at 0.7 V_{SCE} for 10,000 s, insets: the cross-sections of the coated sample before and after potentiostatic polarisation test; (b) 3D visualisation of the coated sample after potentiostatic polarisation test; (c) the cross-section indicated by the dashed lines in (b) and 3D visualisation of the volume of dissolved substrate after potentiostatic polarization test.

Characterization of three-dimensional fatigue pre-crack propagation for 316L stainless steel with lab-based X-ray tomography

S.G. Wang[1], L. Xiong[1], S.C. Wang[1], L. Zhang[1*]

[1] Shenyang National Laboratory for Materials Science, Institute of Metal Research, Chinese Academy of Sciences, Shenyang 110016, PR China– wangshaogang@imr.ac.cn
* presenting author

Keywords: X-ray, Tomography, Steel, Crack, Toughness

Abstract

For crack characterization, traditional SEM and metallography only provide limited information with 2D imaging. As the spatial resolution down to micron or even tens of nanometers using laboratory-based tomography, X-ray tomography (XRT) is regarded as a powerful tool to nondestructively reveal interior information of 3D crack. In this work, we present the vivid 3D features of the crack morphology of nanostructured 316L steel with nano-scale twin bundles embedded in micro-sized grains. The origin of the crack sharpening is proved to be the micropores. The specific feature of the plastic zone is also discussed. Both the plastic zone and crack deflection make contributions to the fracture toughness of nanostructured 316L steel.

Introduction

316L stainless steel can be widely used in many engineering fields such as petrochemical, medical, nuclear, and food industries owing to their attractive properties including the excellent oxidation and corrosion resistance and good formability [1]. However, its applications as structural materials are restricted by the low yield strength (σ_y) of 250 MPa [2]. In comparison with coarse-grained (CG) state, the σ_y of nanostructured (NS) 316L stainless steel consisting of nano-scale twin bundles embedded in micro-sized grains can be as high as 1000-2000 MPa [3]. One compromise of such a strengthening is the reduction of the fracture toughness (K_{IC}) from 230 MPa·m$^{1/2}$ to ~120 MPa·m$^{1/2}$ [4, 5]. It indicates that the toughening mechanism for CG sample and NS sample ought to be different. Revealing all the intrinsic and extrinsic toughening factors is a big challenge because they often associate with the three-dimensional (3D) complicated crack propagation happened in the interior of the sample.

Although the interior information can be obtained by the destructive metallographic method, some artifacts are often introduced by grinding and polishing of the sample. In comparison with the traditional two-dimensional (2D) techniques e.g. scanning electron microscope (SEM), X-ray tomography (XRT), as a non-destructive method, has many advantages. On one hand, the 3D distribution of pores, cracks, particles and fibers can be rendered flexibly [6, 7]. On the other hand, the volume, surface area and volume fraction of a particular phase could be calculated quantitatively [8, 9]. For crack growth alone, a wide range of information, not only the intrinsic mechanisms of crack advance ahead of the crack tip, e.g., plastic zone, micro-void coalescence and micro-cracking but also the extrinsic mechanisms of shielding behind the crack-tip, e.g., fiber bridging and crack deflection, can be provided by XRT [10-12].

The aim of this work is to investigate the 3D features of crack propagation in single-edge-notch-bend (SENB) test for NS 316L steel. First of all, the relation between voids and fatigue crack propagation is revealed by means of XRT. Several vivid 3D characteristics of crack propagation are demonstrated. Next, the 3D morphology of

tensile side, neutral axis and compression side is shown and compared. Finally, the shape of plastic zone for 316L stainless steel is given, and the corresponding fracture mode is also analyzed.

Methods

The commercial 316L stainless steel rods of 8 mm in diameter and 15 mm in length were used as starting materials. Cylindrical plates with a diameter of 28 mm and a length of 3 mm were obtained after a process of dynamic plastic deformation (DPD) [13] with a strain rate of 10^2-10^3 s^{-1}. The as-DPD samples with an average grain size of ~80 nm were annealed at 730 °C for 20 min to obtain a microstructure with an average grain size of ~200-300 nm.

Samples for SENB test were grinded and polished into a dimension at a ratio of 1:2:8 for B (thickness = 2 mm): W (width): S (span). The SENB sample process is described in Ref. [5]. The SENB tests were performed on an Instron 5848 micro mechanical tester at a constant displacement rate of 0.3 mm·min^{-1}. The morphology was examined in a FEI Quanta 600 SEM.

XRT were performed using an Xradia "Versa XRM-500" desktop system. The voltage is about 150 kV. The exposure time was about 10 s for each of 2400 projections while the sample was rotated 360°. The voxel size is 4.2 μm. The projections were reconstructed by a filtered back projection algorithm, and then, processed and visualized by Avizo Fire.

Results and discussions

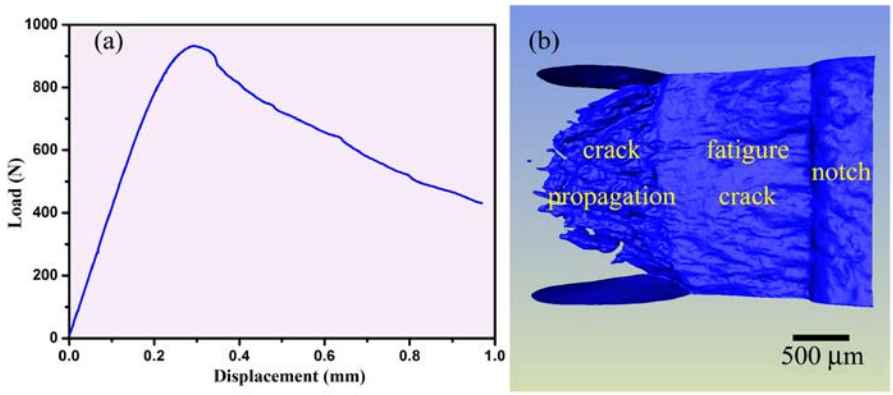

Figure 1. *(a) load-displacement curve (b) 3D volume rendering of the notch, fatigue crack and crack propagation of the SENB sample by XRT for NS 316L steel.*

Figure 1(a) shows the load-displacement curve of the SENB sample for NS 316L steel. Obviously, the non-linear curve indicates that plastic deformation may happen ahead of the crack tip. The slope of the curve changes abruptly at the displacement of 0.34 mm, and then, keeps almost the same. This transition point can be considered as the starting point of stable crack propagation which is used to calculate J_{IC}. The profiles of the notch, fatigue pre-crack and crack propagation obtained by means of XRT are displayed in fig. 1(b). To clearly show the 3D crack shape, 316L steel is processed transparently. As indicated in fig. 1(b), the region of the crack propagation presents a semi-elliptical shape. This part is rougher than the fatigue crack or notch which implies a sophisticated crack growth. Some preferred sites grow more quickly than other zones at the crack tip. An isolated pore which may have some connection with those preferred sites exists ahead of the crack tips. In addition, "plastic zones" on both sides of the thickness for the sample are also displayed in fig. 1(b). The materials in these two zones migrate to adjacent places because of the plastic deformation, leaving an empty space on each side. The thickness of the "plastic zones" (~150 μm) near the border between

fatigue crack and crack propagation is larger than that near the front of the crack propagation. This characteristic can not be revealed by traditional 2D techniques.

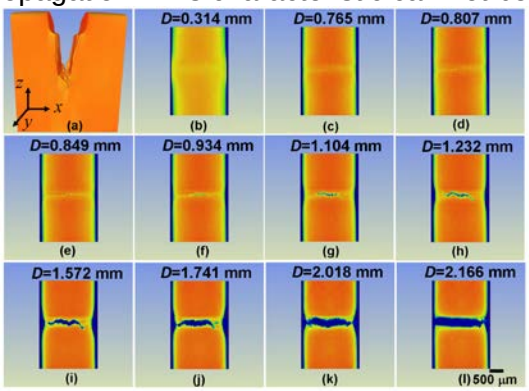

Figure 2. *XRT graphs of the SENB sample for NS 316L steel (a) 3D volume rendering (b)-(l) 2D tomographic slices on behalf of different xy planes shown in (a).*

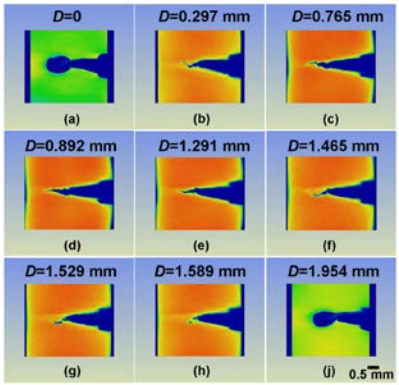

Figure 3. *2D tomographic slices corresponding to different xz planes of SENB sample for NS 316L steel.*

Figure 2(a) gives the 3D XRT volume rendering of SENB sample for NS 316L steel. To better understand the deformation and fracture mechanism, 2D tomographic slices on behalf of different *xy* planes shown in fig. 2(a) are displayed in fig. 2(b)-(l). In bending test, the typical stress states are divided as tensile stress, zero and compressive stress on different profiles perpendicular to the direction of the major crack propagation. As indicated in fig. 2(b), the drum-like shape gives the evidence of the existence of compressive stress. The parallel sides in fig. 2(c) at least mean that no compressive stress or very limited tensile stress acts on this plane. In other words, this slice is probably located in the neutral area. As for the tensile stress, the necking phenomenon in fig. 2(i) is no doubt a best illustration. Considering every region in the sample will endure the same strain under the same stress, 2D slices in fig. 2(d)-(l) with different strains can be regarded as the same plane recorded at different time, although they are the planes at different sites recorded at the same time. Under this assumption, the time-related events of crack evolution can be deduced from fig. 2. In fig. 2(d), two voids appear. One void grows bigger than that in fig. 2(d), and some new voids can be observed from fig. 2(e). Some short cracks which may result from the growth of the voids form, as shown in fig. 2(f). The coalescence of these short cracks can be seen in the slice which is only 0.297 mm away from the slice with visible voids. This macroscopic crack is about 2 mm in length and 0.1 mm in width. The long-winding crack continues to grow until it traverses the whole cross-section of the sample, as indicated in fig. 2(k). The serration-like edges of the crack in fig. 2(i)-(k) show hints of tearing or pull-out phenomenon happened in the sample. Such a fracture is very similar with the double cone fracture. In fig. 2(f), the cross-section of the sample thoroughly divides into two parts. Most of the edges are smooth with the exception of one corner. Obviously, the smooth edges come from fatigue pre-crack while the rough corner is the initiation of the crack propagation. Hence, the total length of the propagation of the crack calculated according to the slices between fig. 2(f) and fig. 2(i) is about 1.2 mm which is larger than the displacement of about 1 mm.

To reveal more features of fatigue pre-crack propagation, 2D tomographic slices corresponding to different *xz* planes of SENB sample are shown in fig. 3. The profiles of the plastic zone near the surfaces can be seen in fig. 3(a) and 3(j), respectively. The fatigue pre-crack propagates almost straightly in the center of sample while it deflects significantly near the surface. A second crack appears with an angle of ~110° from the

main crack, as indicated in fig. 3(b). Several voids are either ahead of the crack tip or adjacent to the crack tip, further giving the evidence that void coalescence plays important role in the crack propagation. Figure 3(c)-(f) show a phenomenon of tearing or pull-out which is consistent with that observed in fig. 2(i)-(k).

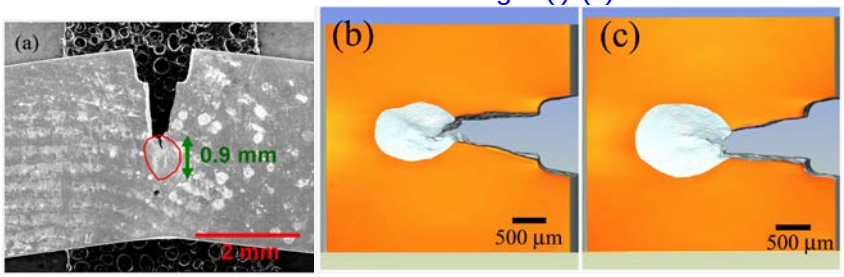

Figure 4. *(a) SEM graph, (b) and (c) 2D tomographic slices of two xz planes corresponding to the two surface of the SENB sample for NS 316L steel. The red curve in (a) as well as the white zones in both (b) and (c) roughly indicates the profile of the plastic zone.*

The size of the plastic zone is crucial for the ductile material. As shown in fig. 4(a), the red curve drawn according to the area with obvious plastic deformation roughly describes the shape of the plastic zone. The length along the direction of the crack propagation is about 0.9 mm. Similarly, 2D slices from XRT can also show the shape and the size of the plastic zone of the SENB sample for NS 316L steel. Fig. 4(b) shows the same surface as that in fig. 4(a). In accordance with the thickness variation, the white zone is marked as the plastic zone, the size of which is about 1.2 mm. The difference between SEM and XRT may explain as follows: the plastic strain in the zone of 0.9 mm of 1.2 mm is large and easily viewed from SEM graph while that of the other 0.3 mm is rather small. From this perspective, XRT can give us more precise information than SEM. Figure 4 (c) displays the plastic zone from the other side surface. Apparently, the plastic zone from either SEM or XRT shows olive-like profile.

The olive-like profile of the plastic zone implies much more information than the plastic deformation itself. Both the theoretical analysis and finite element simulations manifests that it corresponds to a mixed loading mode, involving both Mode II and Mode I [14, 15]. In addition, the mixed mode is one consequence of the crack deflection [14]. If the crack propagates straightly, the loading mode will be Mode I, and if the meandering crack appears, it should be a mixed Mode. In the typical case of Mode I, the fracture surface is very flat or shows little rough patterns [16]. In our case, as indicated in fig. 3, the direction of the crack propagation near the midpoint of the sample thickness keeps straight while that approach to the surface deflects with some angles. It means most parts of the sample are in a situation of mixed loading mode.

One contributor of the plastic zone for NS 316L steel is the microvoid coalescence. This process is always considered as the characteristic of ductile tensile fracture [17]. Although this progress is not easily measured experimentally, different evidences based on SEM observation of fracture surface and side view or on simulations are recently given to show that the voids are responsible for the ductile fracture [18,19]. However, these evidences are often 2D information, and come from a specific surface. Thus, the information about the relation between voids and cracks is limited and incomplete. 3D observation of microvoid coalescence by XRT can clearly show some pieces of the whole process of microvoid development, as indicated in fig. 2 and fig. 3. Although it is not a real in-situ observation, the XRT information is still more plentiful than that from traditional 2D techniques.

Apart from the plastic zone, other toughening mechanisms include crack deflection and meandering, zone shielding e.g. transformation toughening and microcrack toughening and contact shielding e.g. oxide wedging, grain and fiber bridging [11]. As for

NS 316L steel, the crack deflection and meandering is verified from fig. 3. Thus, fracture toughness of NS 316L steel is believed to result from the plastic zone plus the crack deflection and meandering. On one hand, the plastic zone blunts the crack-tip, and the continue loading resharpens it. On the other hand, the crack deflection and meandering act as an impeder of crack advance [20]. This result is consistent with some other tough materials [21]. However, since absorption XRT is only sensitive to the density, atomic number and the thickness, grain-related information adjacent to the crack can not be obtained. Hence, it is hard to develop the relation between the crack advance and nanocrystalline or nanotwins.

Conclusions

Lab-based X-ray tomography is used to non-destructively characterize the 3D behaviors of crack propagation in SENB test for nanostructured 316L stainless steel. The results of the 3D-XRT analysis indicated that both the intrinsic small 3D plastic zone and the extrinsic minor crack meandering contribute to the relatively low fracture toughness of NS 316L steel (120 MPa·$m^{1/2}$) in comparison with the coarse-grain state (230 MPa·$m^{1/2}$). The shapes of three special zones including tension side, neutral area and compressive side that are difficult to acquire using 2D techniques are also clearly visualized as necking, the initial shape and barrel-like, respectively.Such a 3D-XRT technique can also be applied to the complex crack analysis for other materials.

References

[1] P. Marshall.(1984). *Austenitic stainless steel: microstructure and mechanical properties*, New York, NY: Elsevier Applied Science Publishers, , 408-412.

[2] X.H. Chen, J. Lu, L. Lu, K. Lu. (2005). Tensile properties of a nanocrystalline 316L austenitic stainless steel, *Scr Mater.*, 52:1039-1044.

[3] K. Lu, F.K. Yan, H.T. Wang, N.R. Tao. (2012). "Strengthening austenitic steels by using nanotwinned austenitic grains," *Scr Mater.*, 66: 878-883.

[4] S.A. Maloy, M.R. James, G. Willcutt, W.F. Sommer, M. Sokolov, L.L. Snead, M.L. Hamilton, F. Garner.(2001). The mechanical properties of 316L/304L stainless steels, Alloy 718 and Mod 9Cr-1Mo after irradiation in a spallation environment, *Journal of Nuclear Materials*, 296: 119-128.

[5] L. Xiong, L. Lu, (2013) as prepared.

[6] S.R. Stock. (2008). Recent advances in X-ray microtomography applied to materials, *Inter. Mater. Rev.*, 53:129-181.

[7] S.R. Stock. (1999) .X-ray microtomography of materials," *Inter. Mater. Rev.*, 44:141-164.

[8] S.G. Wang, S.C Wang, l. Zhang. (2013). Application of High Resolution Transmission X-Ray Tomography in Material Sciense, *Acta Metallurgica Sinica*, 49: 897-810.

[9] S.G. Wang, M.Y. Sun, Z.Q. Song, J. Xu. (2012). Cast defects induced sample-size dependency on compressive strength and fracture toughness of Mg-Cu-Ag-Gd bulk metallic glass, *Intermetallics*, 29:123-132.

[10] P.J. Withers, M. Preuss. (2012), Fatigue and Damage in Structural Materials Studied by X-Ray Tomography, *Annual Review of Materials Research,* 42: 81-103.

[11] R.O. Ritchie. (1999). Mechanisms of fatigue-crack propagation in ductile and brittle solids, *International Journal of Fracture*, 100: 55-83.

[12] P.J. Withers. (2011).3D Crack-tip Microscopy: Illuminating Micro-Scale Effects on Crack-Tip Behavior, *Adv. Eng. Mater.*, 13: 1096-1100.

[13] N.R. Tao, K. Lu. (2007). Dynamic plastic deformation (DPD): A novel technique for synthesizing bulk nanostructured metals, *J. Mater. Sci. Tech.*, 23: 771-774.

[14] Q. He, J.K. Shang, E. Ma, J. Xu.(2012).Crack-resistance curve of a Zr-Ti-Cu-Al bulk metallic glass with extraordinary fracture toughness, *Acta Mater.*, 60: 4940-4949.

[15] P. Tandaiya, U. Ramamurty, R. Narasimhan. (2009). Mixed mode (I and II) crack tip fields in bulk metallic glasses, *J. Mech. Phys. Solids*, 57:1880-1897.

[16] S.G. Wang, L.L. Shi, J. Xu. (2011). Mg-based bulk metallic glasses: Elastic properties and their correlations with toughness and glass transition temperature, *J. Mater. Res.*, 26:923-933.

[17] T. Pardoen, J.W. Hutchinson. (2000). An extended model for void growth and coalescence, *J. Mech. Phys. Solids*, 48:2467-2512.

[18] T. Pardoen, I. Doghri, F. Delannay. (1998). Experimental and numerical comparison of void growth models and void coalescence criteria for the prediction of ductile fracture in copper bars, *Acta Mater.*, 46: 541-552.

[19] D.F. Ma, D.N. Chen, S.X. Wu, H.R. Wang, C.Y. Cai, G.T. Deng. (2012). Dynamic experimental verification of void coalescence criteria, *Mater. Sci. Eng. A*, 533:96-106.

[20] K.G. Samuel, O. Gossmann, H. Huthmann. (1990).Temperature dependence of fracture toughness (J-R-Curves) of a modified type 316L austenitic stainless steel, *Int. J. Pres. Ves. & Piping*, 41: 59-74.

[21] D.C. Hofmann, J.Y. Suh, A. Wiest, G. Duan, M.L. Lind, M.D. Demetriou, W.L. Johnson. (2008). Designing metallic glass matrix composites with high toughness and tensile ductility, Nature, 451:1085-1089.

Microstructural characterization of SiC foams used as solar absorber devices

J. MOLLICONE[1], B. DUPLOYER[1], P. LENORMAND*[1], C. TENAILLEAU[1], J. VICENTE[2], F. ANSART[1]

[1] CIRIMAT, UMR - CNRS 5085, Université de Toulouse, 118 route de Narbonne, 31062 Toulouse Cedex 9, France
[2] Laboratoire IUSTI, Technopôle de Château-Gombert, 5 rue Enrico Fermi, 13453 Marseille cedex 13, France

Keywords: Materials Characterization, Microstructure Analysis, Silicon Carbide, Solar Receiver, X-ray Computed Tomography.

Abstract

The optical properties of solar receivers used in solar energy conversion devices depend on the chemical composition, on the structure and the microstructure of the materials. Silicon carbide foams are usually used as receivers and X-ray Computed Tomography are performed in order to characterize the initial porous foams of silicon carbide (SiC). Tomography is a non-destructive technique which allows obtaining statistical information on the samples. It is of a great interest for the analysis and the comprehension of the microstructure of such systems. First microstructural information have been obtained, data necessary to model the radiative properties of these systems.

Introduction

This work was conducted in the framework of OPTISOL project funded by the French National Agency (A.N.R.). The main purpose of the project was to increase the competitiveness of solar thermal power plant by increasing the solar conversion efficiency at high temperature in particular through the implementation of combined cycles. The key component of such solar process is the solar receiver that must deliver air in the temperature range between 700°C and 1100°C. The optical properties of the porous structures used as receiver must have a selective behaviour in relation to the solar radiation in order to limit the radiative losses of the surface and increase heat transfer by convection.

Receivers usually used are silicon carbide (SiC) foams [1-3]. Increasing the efficiency of such systems is directly related to the geometrical and optical properties of the receivers (ceramic foam, porosity, grain size, additional layer…). Also, the structure and microstructure of the foam have to be controlled at each stage of the process. X-ray Computed Tomography (XCT) was firstly used to characterize the microstructure of various SiC foams. Structural modifications with temperature were then studied by XRD, DTA-TGA and dilatometry [4] since SiC foams are usually used at high temperatures, corresponding to the one required for solar receivers. An oxide has to be formed at the surface of the raw material during the thermal treatment in order to increase radiative transfers and stand such a thermal treatment.

SiC foams cells network are complex (obstructed pores, oriented cells etc…) so the coating process can be difficult. XCT is then a really well suited technique to determine precisely the different foam microstructure features due to the manufacturing process and/or thermal treatment, in a non-destructive manner.

Methods

The structural properties of the SiC foams were studied by X-ray Diffraction using a Cu-Kα radiation source (Bruker AXS D4) and operating with a $(\theta - 2\theta)$ Bragg-Brentano geometry.

The microstructural characterizations of the samples were carried out with a X-ray Tomography set-up, Phoenix/GE Nanotom 180, using the W target, Mode 0 and a 100 µm Cu filter with U = 90kV and I = 140 µA (FOD and FDD = 47 and 250 mm, respectively; 9.40µm/voxel). A timing of 1250 ms was used for the data acquisition with 7 images averaged per step while the first two

were skipped to avoid image reminiscence after each rotation and a total of 1440 images were recorded. Typically, X-ray tomography was performed on a few mm^3 of sample.
Additional microstructural information, such as specific surface area, and density was obtained by BET (Micromeritic ASAP 2010) and weight/volume measurements.
Finally, thermal gravimetric (Setaram TGA-DTA 92) and dilatometric (Setaram Setsys) measurements were carried out in order to specify the thermal behaviour of the foams.

Results

We studied two types of silicon carbide foams (α-SiC and β-SiC). The average pore size of β -SiC foams can be controlled and we received two kind of samples with 2.8 mm and 3.5 mm in diameters from the SICAT Company. These foams have been prepared by a pyrolysis process of a polyurethane template. Furthermore, SiC foam chemical contents were controlled by Inductively Coupled Plasma (ICP): the stoichiometry is not preserved, an excess of carbon has been evidenced. Indeed, the composition of α-SiC foams is about 47% of silicon and 53% of carbon (atomic percentage) and for β-SiC, the carbon content is even more important since the results of the analysis provided 44% of silicon and 56% of carbon.
X-ray diffraction patterns were performed on α-SiC and β-SiC foams at room temperature (figure 1). SiC can be found in various polytypes as cubic and hexagonal structures. The β-SiC is crystallised and the XRD pattern is indexed in the cubic structure (like a blende structure) with a F-43m space group and noted 3C in the Ramsdell notation (JCPDS n°00-029-1129).

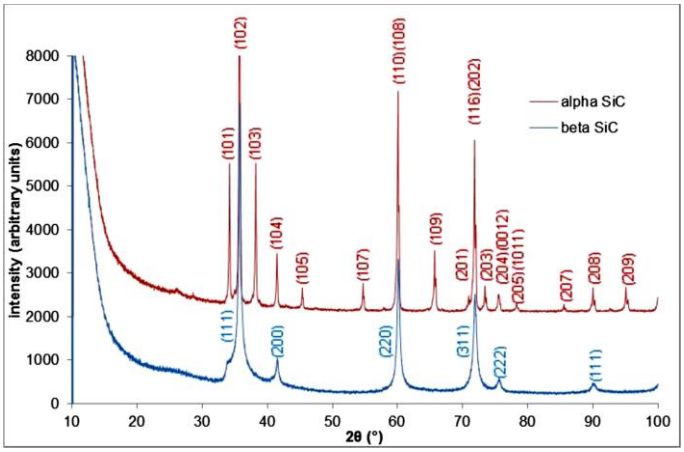

Figure 1: Room temperature XRD patterns of α-SiC and β-SiC.

The XRD pattern of α-SiC is indexed in the hexagonal structure with a $P6_3$ space group and named 5H (JCPDS n°00-042-1360).
The microstructural properties of the α-SiC and β-SiC have different features since the measured specific surfaces areas (BET measurements) are equal to 1 m²/g and 28 m²/g respectively. Similarly, the densities measured macroscopically reveal differences between the two types of SiC, 76% of porosity for α-SiC and 89% and 92% for β-SiC (ϕ=2.8 mm, ϕ=3.5 mm respectively). X-ray tomography measurements have been carried out on the two types of SiC foams. The data acquired have been used to reconstruct and visualise (using the VG Studio Max 2.1 software) the 3D microstructure of α-SiC and β-SiC ϕ=2.8 mm (figures 2a and 2b). As a first approach, we observe a denser microstructure for the α-SiC with a smaller cell size than for β-SiC. A more detailed and statistical analysis of the data is reported in the table 1. Firstly, the porosities measured are in good accordance with the values obtained from the macroscopic measures. Secondly, for the two β-SiC foams, the cell sizes are in good accordance with the specifications given by the SICAT Company. In addition, we report the average sizes of the

windows and the struts constituting cells. On the 2D cross section micrographs (figures 2c and 2d), we confirm the decrease of the size of cells and windows and the increase of the struts' size of α-SiC foams relative to β-SiC which explains the denser microstructure of α-SiC foams. In addition, internal porosity is also highlighted on β-SiC, which also justifies the difference in density between the two types of foam.

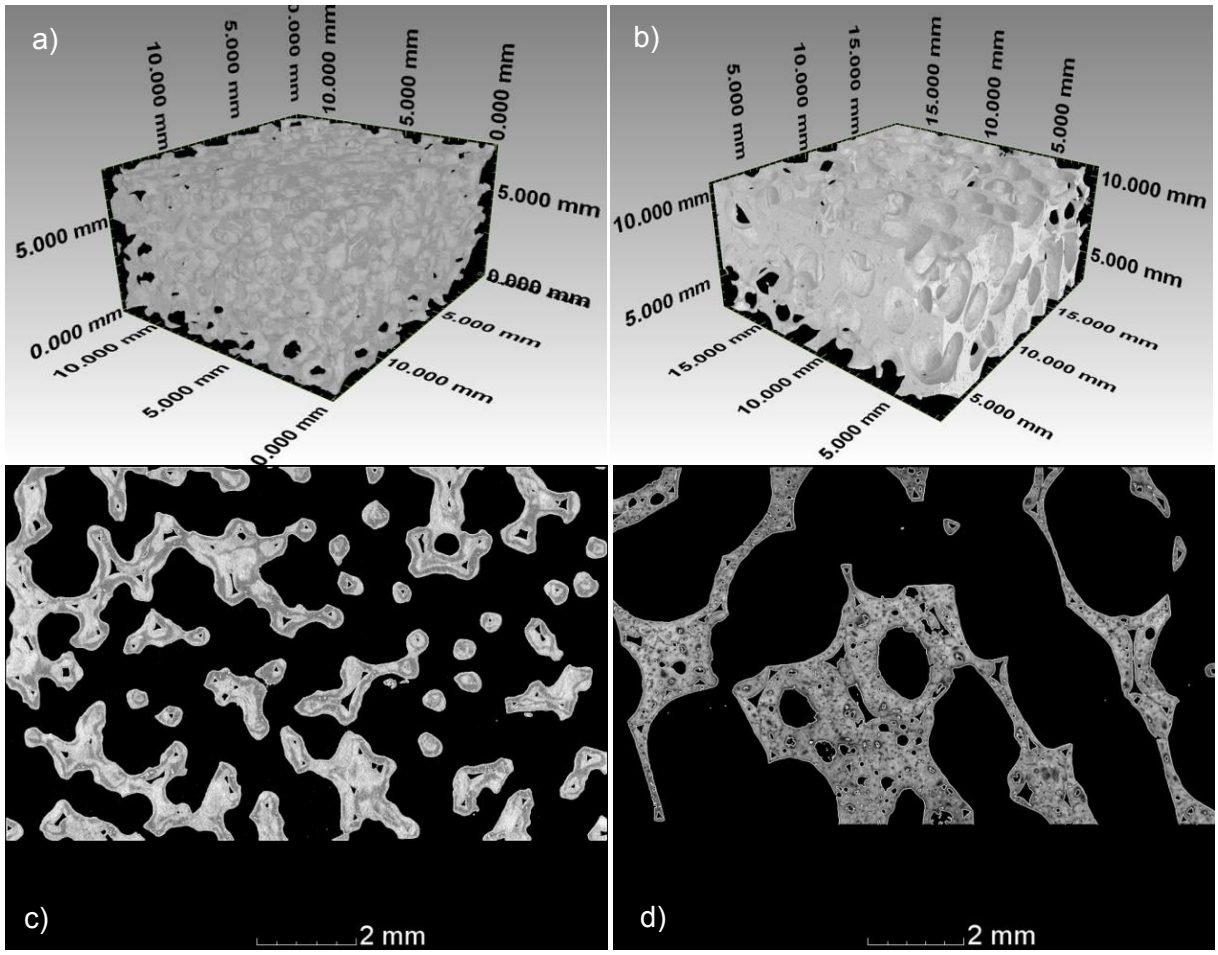

Figure 2: X-ray computed tomography 3D images of α-SiC (a) and β-SiC ϕ=2.8 mm (b), 2D cross section of α-SiC (c) and β-SiC ϕ=2.8 mm (d).

Table 1: Results of X-ray tomography analysis

Sample	Cell size [mm]	Window size [mm]	Strut size [mm]	Porosity [%]
α-SiC	1.8 ± 0.1	0.9 ± 0.1	0.4 ± 0.1	72
β-SiC ϕ=2.8 mm	2.6 ± 0.1	1.1 ± 0.1	0.2 ± 0.1	81
β-SiC ϕ=3.5 mm	3.6 ± 0.1	2.0 ± 0.1	0.3 ± 0.1	85

As previously mentioned, receivers are working at high temperature. The covering of the foam by an oxide layer is necessary in order to control the optical properties of the system. This requires a thermal treatment in air at high temperature. In this part, we study the thermal behaviour of β-SiC foams.

Two temperature range phenomena can be deduced from the DTA-TGA and dilatometric

curves (figure 3). The first one, between room temperature and 650-700°C where there is no mass loss and also a linear increase of the dilatometric curve with the temperature. The thermal expansion coefficient measured is about 4.3×10^{-6} K^{-1}, very close value from the theoretical one which is 4.7×10^{-6} K^{-1}. Up to 650°C, these results confirm the stability of β-SiC foams. After 650°C, there is a strong exothermic mass loss on the DTA-TGA curves and a break of slope is observed on the dilatometric curve. This behaviour is attributed to the elimination of the residual carbon (12% at.). At higher temperature, there is an increase of the mass. It results from the competition between the oxidation of the carbon in CO and CO_2 (confirmed by mass spectrometry measurements) which are volatile species and the oxidation of the silicon in silica [5]. At this temperature range, the non-linear increase of the dilatometric curve confirms a regular change of composition of the foam. At temperature higher than 1200°C, shrinkage of the foam appears and SiO_2 crystallises in the cristobalite structure.

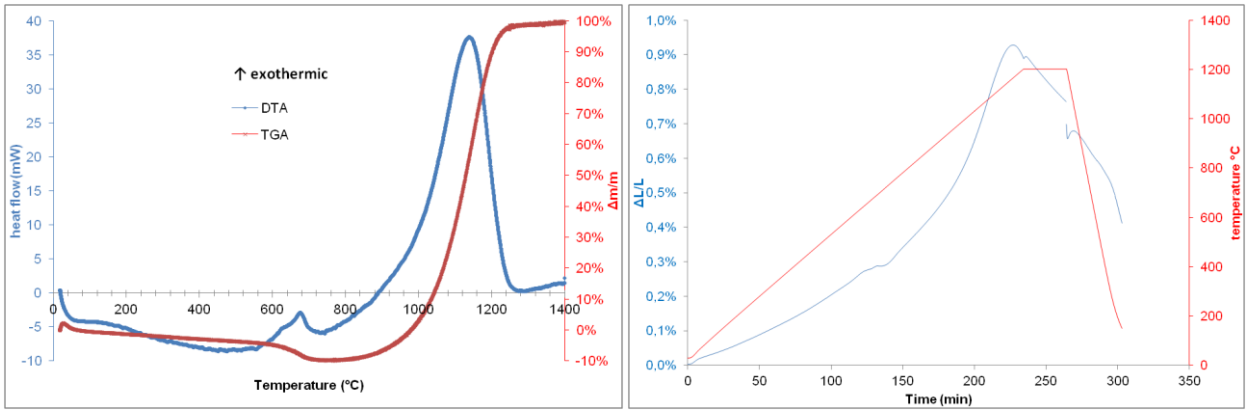

Figure 3: TGA-DTA (left) and dilatometry (right) curves obtained on β-SiC powder

Calculations based on the XCT images collected and further analyzes using the iMorph program showed that cells are not spherical but have an ellipsoidal shape, which can be described by 3 orthogonal axes *a*, *b* and *c* (*a* > *b* > *c*) in a 3D referential O,x,y,z (table 1 and figure 4). These three axes have a specific orientation characterized by the elevation angle ϕ and the azimuth angle θ. SiC foams have actually a closed porosity due to the manufacturing process (pyrolysis of a polyurethane template), which is included in the pores analyzes. Porosity is constituted of cells interconnected through throats, which are separated by struts. SiC foam throats are described by 2 parameters *a*' and *b*' corresponding to the equivalent oval included in the throat. Struts have a triangular shape and inner and outer circles can describe them. Note that a filter needs to be applied during image analysis to determine all three axes. This process is also responsible for the closed and intergranular porosities, and closed throats observed.

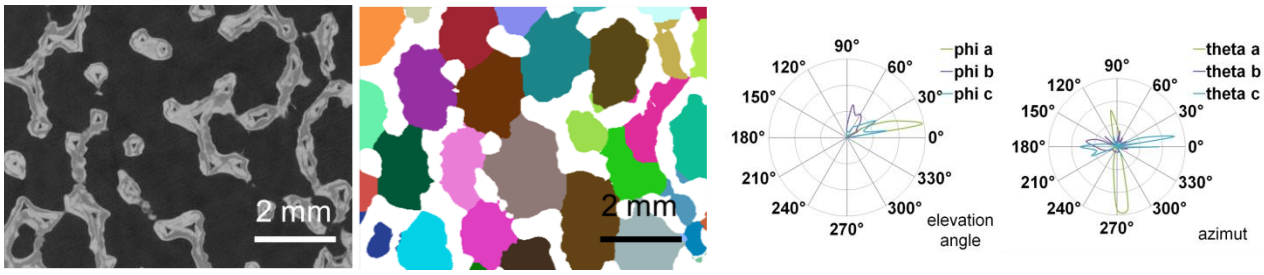

Figure 4: 2D image (a), segmentation of each cell on the corresponding 2D view (b), elevation ϕ of a, b, c vectors (c), and azimuth θ of a, b, c vectors (d) of α-SiC foam.

This typical morphology was the main difficulty to consider for the implementation of the coating process. Microstructural information here obtained was of great interest for the understanding and modelling of the radiative properties of these systems.

Conclusion

X-ray tomography measurements was carried out on α-SiC and β-SiC foams and their former microstructures have been completely described. Microstructural information obtained is of a great interest for the understanding and modelling of the radiative properties of these systems. Preliminary detailed investigations on the thermal behaviour of SiC foams by both thermogravimetric and dilatometric investigations have been presented.

Valuable information about the temperature range structure stability is collected in relationship with physical properties. These results are in good agreement with those reported in the literature and show that its chemical stability has to be improved in the range of the working temperature of a solar receiver (700-1000°C).

The future works will be dedicated to the functionalization of the SiC receiver in order to improve the optical properties and increase the foam chemical stability. This functionalization will be made by adding a thin oxide layer on all the apparent surface of the foam. Based on a soft chemistry process, a sol impregnation under vacuum will be developed. The microstructural information obtained from the X-ray tomography measurements will also be highly important to control all the process parameters allowing the deposition of a thin oxide layer on the surface of the SiC foam.

Acknowledgements

The French FERMaT Midi-Pyrénées Federation FR3089 is acknowledged for providing X-ray tomography laboratory facility. Authors would like also to thank the French National Agency (A.N.R. SEED Program) for its financial support.

References

[1] Menigault, T., Flamant, G. and Rivoire, B. (1991), Advanced High-Temperature Two-Slab Selective Volumetric Receiver, Solar Energy Materials, 24: 192-203.

[2] Pitz-Paal, R., Morhenne, J. and Fiebig, M. (1991), A new concept of a selective solar receiver for high temperature applications, Solar Energy Materials & Solar Cells, 24: 293-306.

[3] Fend, T., Hoffschmidt, B., Pitz-Paal, R., Reutter, O. and Rietbrock, P. (2004), Porous materials as open volumetric solar receivers: Experimental determination of thermophysical and heat transfer properties, Energy, 29: 823-833.

[4] Mollicone J., Ansart F., Lenormand P., Duployer B., Tenailleau C., Vincente J. (2014) Characterization and functionalization by sol–gel route of SiC foams, J. European Ceramic Society, 34: 3479–3487.

[5] Kouamé, N.A., Roberta, D., Kellerb, V. Kellerb, N., Pham, C. and Nguyen, P. (2011), Preliminary study of the use of β-SiC foam as a photocatalytic support for water treatment, Catalysis Today, 161: 3-7.

In-operando fast tomography of lithium-ion batteries during operation and failure

Donal P. Finegan[1], Mario Scheel[2], James Robinson[1], Bernhard Tjaden[1], Ian Hunt[3], Marco Di Michiel[2], Gregory Offer[3], Gareth Hinds[4], Dan J.L. Brett[1], Paul R. Shearing[1]

1. Electrochemical Innovation Lab, Department of Chemical Engineering, University College London, Torrington Place, London, WC1E 7JE, UK [email: donal.finegan.13@ucl.ac.uk; p.shearing@ucl.ac.uk]
2. ESRF, The European Synchrotron, 71 Rue des Martyrs, 38000 Grenoble, France
3. Department of Mechanical Engineering, Imperial College London, South Kensington Campus, London SW7 2AZ, UK
4. National Physical Laboratory, Hampton Road., Teddington, Middlesex, TW11 0LW, UK

Keywords: X-ray computed tomography, lithium-ion batteries, diagnostics, rapid failure mechanisms

ABSTRACT

The safety and reliability of commercial lithium-ion batteries is essential for their success as a ubiquitous energy storage device. In this study, high speed synchrotron X-ray computed tomography (CT) is used to capture in 3 dimensions the evolving internal architecture of commercial lithium-ion batteries (LG 18650 NMC cells) leading up to and during catastrophic failure. X-ray CT is also performed *post-mortem* to identify the extent of damage within the cells. Important failure mechanisms such as electrode layer delamination, internal structural collapse and the propagation of thermal runaway are elucidated, and the influence of mechanical design on the failure mechanisms of commercial cells is also assessed.

1. INTRODUCTION

Lithium-ion batteries have become the technology of choice for portable energy storage applications in particular for automotive applications due to their high specific energies and energy densities. The increasingly demanding applications require high energy density cells to safely and effectively operate under a wide range of environmental and operating conditions such as high temperatures and high charge and discharge rates. However, the combination of high energy density cells and extreme conditions can result in catastrophic failures and although the risk of failure is low, several well publicised incidents[1, 2] have resulted in numerous airlines ceasing bulk shipments of lithium-ion batteries due to safety concerns.

When lithium-ion batteries reach a critical temperature their internal active materials begin to exothermically breakdown[3, 4]. Without appropriate cooling, this process can lead to a detrimental sequence of events whereby the internal contents of the cells rapidly break down exothermically, realising of lot of heat in a process known as thermal runaway. Little is understood about the internal behaviour of commercial cells during failure. In this study non-destructive high speed tomography is used to capture the evolution of the internal architecture of commercial lithium-ion batteries during the initiation and propagation of thermal runaway. X-ray CT is also performed before and after catastrophic failure to identify the extent of material degradation and critical temperatures reached within the cell during failure. High speed tomography at up to 2.5 Hz is

performed at ID15A at The European Synchrotron (ESRF). The use of high speed tomography is shown to be an effective diagnostic tool for tracking the progression of degradation of the internal architecture of commercial cells leading up to and during catastrophic failure. Failure mechanisms such as electrode layer delamination, structural collapse are observed in 3D and the effect of cell venting on the safety of cells in modular systems is discussed.

2. EXPERIMENTAL

Two commercial 18650 batteries (2.2 Ah and 2.6 Ah 18650 LG Li($Ni_{1/3}Mn_{1/3}Co_{1/3}$)O_2 (NMC) cells) in fully charged states were imaged under a 76 keV monochromatic beam with a field of view of 10.5 mm x 7.6 mm. A custom built containment system shown in Figure 1 which allowed simultaneous X-ray CT, thermal imaging, electrical and thermal abuse of commercial 18650 cells was designed for ID15A's rotation stage (ABR1000, Aerotech, USA). The containment withstood the catastrophic battery failures while directing any generated gases via a continuous flow of inert gas (N_2) to the beamline gas extraction system. An infra-red transparent sapphire window was used for thermal imaging and two X-ray transparent Kapton windows were placed in the path of the beam as shown in Figure 1b.

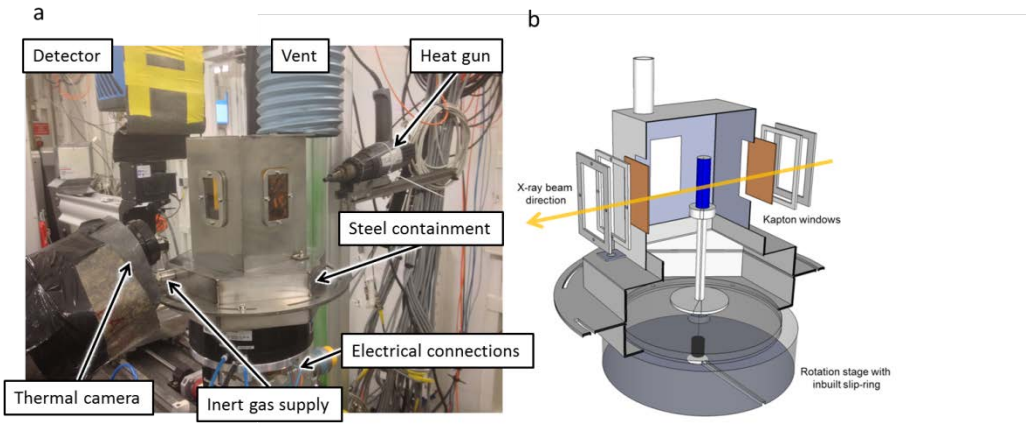

Figure 1. a) Containment systems designed to the safe abuse testing of commercial cells at ID15A in ESRF. **b)** Sectioned view of the containment system showing battery placement, rotation stage and inbuilt electrical slip ring.

Tomograms were captured at a rate of 2.5 Hz and 1.25 Hz which consisted of 500 projections and 1000 projections respectively. Higher image frequency (lower number of images for tomographic reconstruction) with reduced image quality was preferred when significant motion was expected to occur within the cell. A high speed detector (PCO dimax, PCO AG, Germany) stored 17 s of images at 1,250 fps to its on-board memory (36 GB) for fast intermediate storage. The 17 s leading up to catastrophic failure of each cell was captured by activating a post-event recording trigger. The projections were reconstructed into 7.6 mm high 3D cylindrical sections of the cell which were 18 mm in diameter, with a voxel resolution of 10.87 µm.

Both cells were imaged during external thermal abuse (*ca.* 250 °C) by application of a heat gun (Figure 1a). The external surface temperature of the cells was recorded using a thermal camera (FLIR SC5000MB FLIR Systems France, Croissy-Beaubourg, France) from the opposite side to where the heat was applied (Figure 1a). During high speed tomography the batteries were rotated continuously

by 360°. Further details about the experimental setup and data processing can be found in our recent paper[5].

3. RESULTS AND DISCUSSION

3.1. In-operando tomography

The two LG 18650 NMC cells were imaged during the moments leading up to and during thermal runaway. For simplicity, the two cells will be referred to as cell 1 and cell 2 (Figure 2). At the core of cell 2 there is an internal cylindrical support which holds the inherent safety advantage of providing mechanical support to the internal architecture of the cell. Cell 1 and cell 2 were imaged at 2.5 Hz and 1.25 Hz respectively.

In-operando high speed tomography revealed a collapse of the internal architecture of cell 1 following venting (Figure 2b). The sudden collapse stems from the rapid release and channelling of gases towards the vent. The collapse caused severe structural deformation resulting in sharp bends in the active material layers. This heightens the risk of internal short circuits due to the increased strain on the active material and separator. Additionally, the wide opening caused by the collapse exposes regions deep within the cell to the atmosphere. The increased exposure of the active materials within the cell to oxygen in the air could accelerate the propagation of thermal runaway. Sequential tomograms during 15 seconds leading up to thermal runaway showed increasing divergence of the collapse opening due to the continuous generation and flow of gas from the cell.

In contrast, cell 2 showed only slight delamination around the inner regions of the cell (Figure 2d-f) with little change in the cells internal architecture during the 15 seconds leading up to thermal runaway. The separation of the electrode layers occurs between the positive and negative electrodes where the separator and electrolyte are present. Local gas generation is likely to stem from solvent decomposition and the breakdown of the solid electrolyte interphase (SEI).

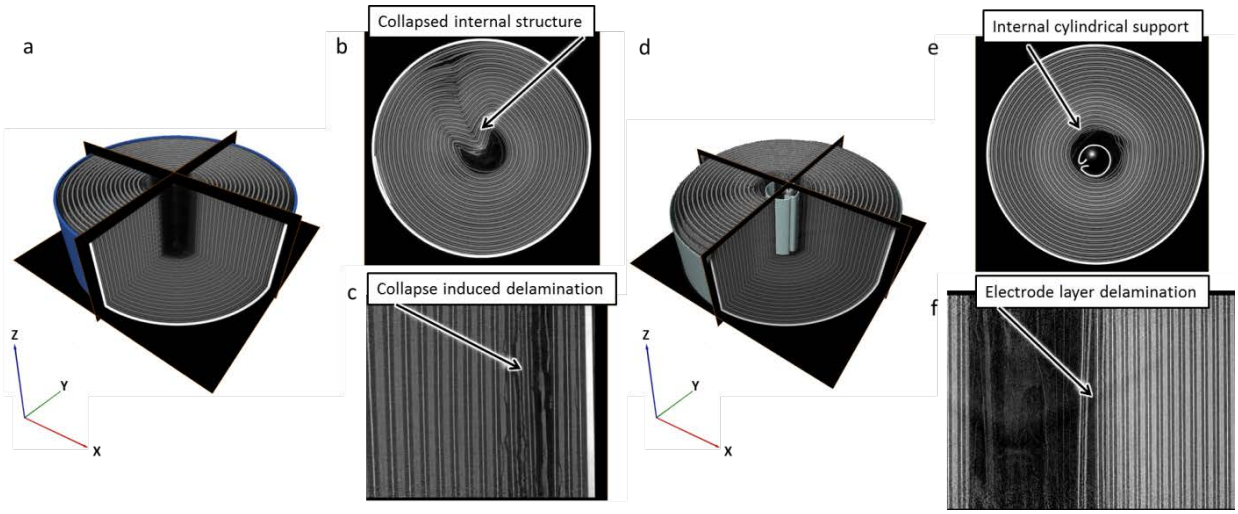

Figure 2. a) 3D reconstruction of 18650 cell (before venting) without internal support (cell 1) showing orthoslices in the *XY*, *YZ* and *XZ* planes. **b)** *XY* slice from image (a) showing collapsed internal structure after venting. **c)** *YZ* slice from image (a) showing depth of collapse and consequent electrode layer delamination. **d)** 3D reconstruction of 18650 cell with internal support (cell 2). **e)** *XY* slice from image (d) showing little structural degradation after venting. **f)** *YZ* slice from image (d) showing a small degree of electrode layer delamination after venting.

3.2. *Post-mortem* tomography

Post-mortem images were taken to assess the aftermath of thermal runaway (Figure 3). Tomograms of both cells exhibit globules of copper indicating that local temperatures reached in excess of the melting point of copper (1085 °C). However, during thermal runaway the contents of cell 1 were ejected from the battery casing via an uncontrolled detachment of the battery cap. The mostly intact remains of the copper current collecting foil in cell 1 (Figure 3a) show that most of the cell did not reach the extreme temperature required for copper to melt. The ejection of the degrading material resulted in a rapid dissipation of the heat generated from exothermic decomposition reactions.

In contrast, the casing of cell 2 maintained its mechanical integrity during thermal runaway. The thermal runaway process ran to completion within the cell, evidence of which is seen in the *post-mortem* tomogram of cell 2 (Figure 3b). The widespread melting of the copper current collector indicates that the extreme temperatures necessary for melting copper were reached throughout the cell except for around the surface of the shell due to the shell cooling effect.

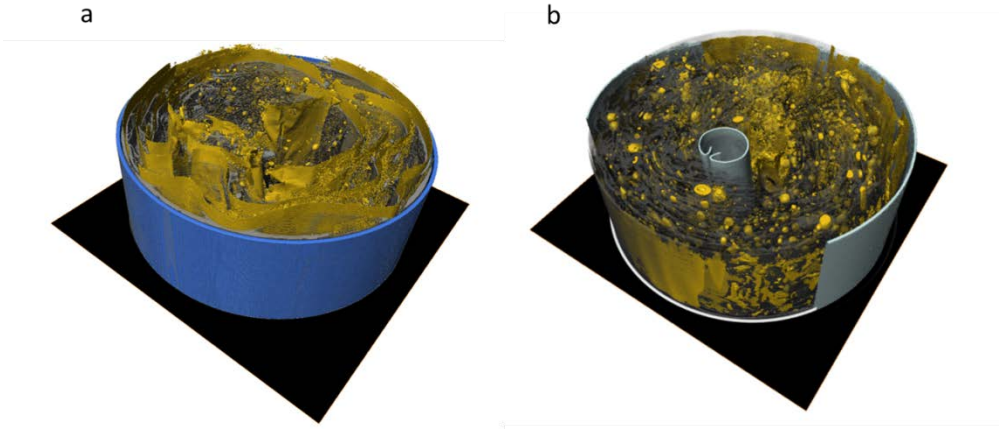

Figure 3. a) Post mortem 3D reconstruction of cell 1 and **b)** cell 2, showing presence of copper phase (yellow), other broken down material (semi-transparent grey) and casing (blue and teal).

4. CONCLUSION

In-operando high speed tomography has been demonstrated as an effective diagnostic tool for rapid failure mechanisms in commercial lithium-ion batteries. The high energy beamline ID15A at the ESRF provided the exceptional photon flux density required for the high frequency and high resolution X-ray CT performed in this study. This high speed imaging has provided a unique insight into the behaviour of the internal architecture of commercial cells during the moments leading up to, during and after failure. The progression of electrode layer delamination leading up to thermal runaway highlights the importance of effective compression of the spiral wound electrode materials. Additionally, this study has highlighted the influence of mechanical design on the safety of commercial cells by comparing the failure mechanism of similar cells with and without an internal structural support; the magnitude of the structural collapse seen in cell 1 may compromise the safety of the cell, a risk which may be avoided by including an internal support. The results of this study are expected to guide the development of safer and more reliable commercial cell designs.

5. ACKNOWLEDGEMENTS

The authors acknowledge funding from the Royal Academy of Engineering, the EPSRC and National Physical Laboratory. We are grateful to the STFC for travel funding through the Global Challenge Network in Batteries and Electrochemical Energy Devices. These experiments were performed on the ID15A beamline at the ESRF, Grenoble, France. We are grateful to Marco Di Michiel and Mario Scheel at ESRF for providing assistance in using beam-line ID15A.

6. REFERENCES

1. NTSB *Aircraft Incident Report, Auxiliary Power Unit Battery Fire, Japan Airlines Boeing 787-8, JA829J*; PB2014-108867; National Transport Safety Board: January 7, 2014, 2014.

2. JTSB *Aircraft Serious Incident Investigation Report, All Nippon Airways Co., LTD JA804A*; AI2014-4; Japan Transport Safety Board: September 25, 2014, 2014.

3. Ribiere, P.; Grugeon, S.; Morcrette, M.; Boyanov, S.; Laruelle, S.; Marlair, G., Investigation on the fire-induced hazards of Li-ion battery cells by fire calorimetry. *Energy & Environmental Science* 2012, 5, 5271-5280.

4. Golubkov, A. W.; Fuchs, D.; Wagner, J.; Wiltsche, H.; Stangl, C.; Fauler, G.; Voitic, G.; Thaler, A.; Hacker, V., Thermal-runaway experiments on consumer Li-ion batteries with metal-oxide and olivin-type cathodes. *RSC Advances* 2014, 4, 3633-3642.

5. Finegan, D. P.; Scheel, M.; Robinson, J. B.; Tjaden, B.; Hunt, I.; Mason, T. J.; Millichamp, J.; Di Michiel, M.; Offer, G. J.; Hinds, G.; Brett, D. J. L.; Shearing, P. R., In-operando high-speed tomography of lithium-ion batteries during thermal runaway. *Nat Commun* 2015, 6.

Carbon anodes investigation through computed tomography

D. PICARD*[1], H. ALAMDARI[2], D. ZIEGLER[3], L.-F. DAIGLE[4], M. FAFARD[5]

[1] Université Laval, Aluminium Research Centre, 1065 De la Médecine Avenue, Quebec (Quebec), G1V 0A6, Canada – Donald.Picard@gci.ulaval.ca
[2] Université Laval, Aluminium Research Centre, 1065 De la Médecine Avenue, Quebec (Quebec), G1V 0A6, Canada – Houshang.Alamdari@gci.ulaval.ca
[3]Alcoa Primary Metals, Alcoa Technical Center – 100 Technical Drive, Alcoa Center, PA, 15069-0001, USA – Donald.Ziegler@alcoa.com
[4] INRS-ÉTÉ, Environmental Technology Laboratories, 2605 du Parc-Technologique, Quebec (Quebec) G1P 4S5, Canada – Louis-Frederic.Daigle@inrs.ca
[5] Université Laval, Aluminium Research Centre, 1065 De la Médecine Avenue, Quebec (Quebec), G1V 0A6, Canada – Mario.Fafard@gci.ulaval.ca
* presenting author

Keywords: Computed tomography, Anode, Carbone, Aluminium, Crack detection

Abstract

The aluminium production at industrial scale is done through the electrolysis of alumina, also known as the Hall-Héroult process. This process requires carbon electrodes that can withstand a highly corrosive environment at elevated temperature. The carbon anodes, which are consumed after approximately 26 days of operation, operate in molten cryolite (Na_3AlF_6) at 960 °C. Given the limited lifespan of the anodes, they are made from low cost raw materials, having high variation of their physical properties over time due to sourcing from different suppliers. Hence, these variations have a direct impact on anode forming process, the green and baked properties and performance in the electrolysis cell. Over the past years, a large research programme has been set-up to investigate the anode properties using different approaches, including non-destructive techniques such as the computed tomography (CT). The CT technique has been used as a diagnostic tool to highlight density gradient in lab scale and industrial scale anodes, metal impurity levels and total porosity percentage. Also, an existing crack detection algorithm based on the percolation method has been adapted to low resolution CT images of large sample obtained with a Siemens Somatom Sensation 64 to detect large cracks in baked anodes.

Introduction

In the Hall-Héroult electrolysis process [1], the cell, illustrated in Figure 1, is composed of various materials including steel potshell, insulators, refractory concrete, cathodes and anodes. Actually, the electrodes (anode and cathode) required to perform the electrolysis are made of carbon. This material is one of the few, if not the only one electrical conductive material, that can sustain simultaneously, from a thermo-chemo-electromechanical point of view, a high temperature (960 °C) and a highly corrosive environment (molten cryolite Na_3AlF_6) while being economically viable [2].

Of all materials of the electrolysis cell, only carbon anodes (approximately 30 anodes/cell) could be considered as consumable items requiring regular replacement. These anodes are consumed during electrolysis and replaced after approximately 26 days of operation. Depending on the cell technology, approximately one anode per cell is replaced each day. Hence a large number of anodes and consequently a large quantity of raw materials are required to operate a plant (larger plants, like the Jebel Ali site of DUBAL, operate more than 1500 cells). Also, to stay economically competitive and considering the large amount of anodes consumed each year, aluminium producers need to reduce the cost of their anode production. A part of the solution is to reduce the

cost of the raw materials. The drawback is that producers now have to deal with continuous changing of raw materials properties, resulting in a wide variation of physical properties of the baked anodes.

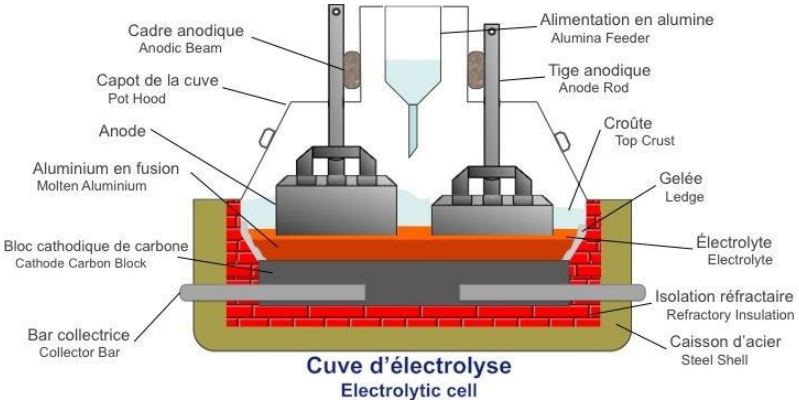

Figure 1 *Diagram of the Hall-Héroult electrolysis cell*

One solution to minimize the effect of the variation of raw materials properties is to use numerical simulation methods to model the manufacturing process. The objective is to predict the anode characteristics, to control the process parameters more efficiently, and to take corrective actions before the anode is produced. To achieve this goal, a series of experimental data must be first collected in order to validate the models. From a density point of view, the most efficient way to get all the needed 3D information is through the use of computed tomography. The non-destructive anode investigation had thus three main objectives: 1) to obtain the apparent density distribution, 2) to estimate the porosity distribution and 3) to quantify the larger cracks inside the anodes [3].

Methods

Computed tomography considerations

The CT scan used in the studies was the Siemens Somatom Sensation 64 at INRS-ETE research centre located in Quebec City. The scanning area was limited to sample of section of 0.3 x 0.3 m^2 and had a relatively low resolution (512 x 512 pixels with a maximum resolution of 0.097 x 0.0.097 x 0.4 mm^3). Anode block dimensions being approximately 0.6 x 0.7 x 1.5 m^3, it has to be cut in smaller blocks in order to fit inside the working area of the CT scan. Hence, the anodes investigated have been cut in slices of two inches thick instead of bigger blocks to meet the requirements of other NDT investigations performed in parallel to the CT. The anode cutting pattern is detailed in [4]. Also, the low resolution of the CT scan was not problematic since the studies were at a macroscopic scale. Moreover, a large amount of the anode pores are at nanoscale level thus the threshold method to estimate the porosity level could not be used except with a Nano CT. However, the main concern about Nano CT is the very limited sample size (few mm) which is non representative of the anode macroscopic properties of interest. The non-cylindrical shape of anode slices combined with a varying amount of material across the scanning axis (geometrical features such as stub holes) affect the density estimation. However, CT was mainly used for comparative studies between similar anodes. Nevertheless, slices were scanned in pack of four in order to get closer to a cylindrical shape, as shown in Figure 2. Considering all the aforementioned points, the most suitable CT parameters for those studies were: 140 KV, 300 MAS, B25s reconstruction filter, 300 mm field of view and voxel resolution of 0.7 x 0.7 x 0.6 mm^3.

Figure 2 Setup of anode slices for the CT

Anode properties evaluation

Density

Computed tomography has been used in the early 2000 on baked carbon anode material by Adams et al. [5] and they could not correctly estimate the apparent density base on a standard relation (Eq. (1)) for low atomic number material such carbon.

$$\rho = 0.001 \times \text{ CT number } [HU] + 1 \quad (1)$$

A calibration campaign [6] has then be performed to define a more suitable relation for baked carbon anode. The relation obtained for the baked apparent density (g/cm^3) is

$$\rho = 0.0011 \times \text{ CT number } [HU] + 1.1081 \quad (2)$$

Also, as already mentioned, anodes have been scanned in several pieces of smaller dimensions than the original carbon anode size. Scale effect has thus been investigated [6] and no relevant effect has been found on the apparent density evaluation at the macroscopic scale. A typical apparent density distribution inside an anode is shown in Figure 3 (density averaged on slice thickness). The mean CT number is approximately 500 HU. This figure also highlights the influence of geometrical features (slots and stub hole) on the density distribution as well as their effect on the anode cracking. Moreover, it is expected that the maximum CT number would be close to the one of carbon. Any voxel with a density higher than the carbon is thus considered as an impurity, generally a metallic one. From the CT results, it has been estimated that the investigated anodes contain less than 0.02% in volume of dense impurities. Most of them are usually less than 1 mm in diameter.

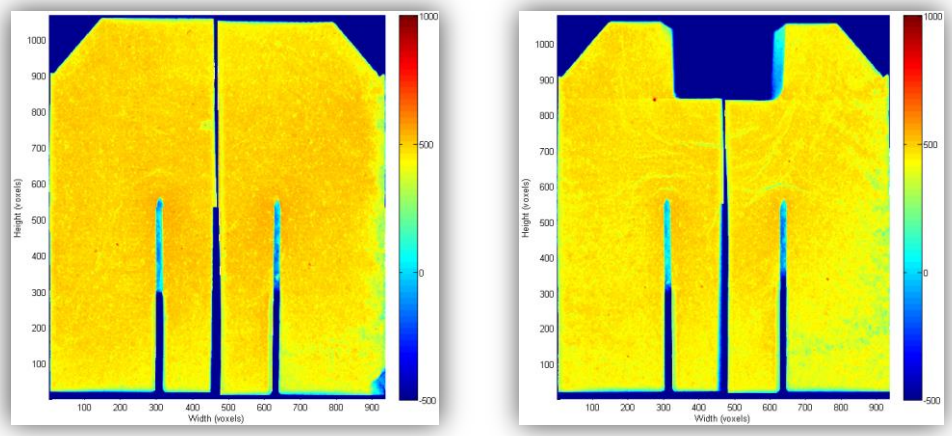

Figure 3 Typical average density distribution inside baked carbon anode. CT numbers have been saturated to 1000 HU. Left image: anode end. Right image: with a stub hole.

Porosity

Porosity evaluation of materials is always challenging. Carbon anodes are no exception. Three different approaches has been used to estimate the porosity of baked anodes [7] which can be macroscopically considered as a homogeneous material. The approach giving the best results was the one based on the ratio of apparent density (density with open and closed pores) obtained with Equation (2) and real density (density without any porosity) of the material as shown in the following equation:

$$porosity = 1 - \frac{\text{apparent density}}{\text{real density}} \tag{3}$$

This approach implies to measure the real density of the material. However, the real density doesn't vary significantly inside an anode and between anodes having a relatively constant anode paste recipe. Hence, it has to be measure only once for these studies. The first main drawback of this approach is that real density must be measured again if significant raw material properties variations occur. The other drawback is the underestimation of the porosity level in regions containing large impurities of high density. In the present case, this effect is negligible.

Cracks

During the baking process, cracks may also develop inside the anode [3] as seen on Figure 3 above the anode slots. Cracks properties (number of cracks, length, width, area, etc.) are good quality indexes of the baking process. It is thus relevant for the industry to quantify them through image analysis. Usually, crack detection algorithms require high resolution images. In the present case, crack detection must be done on low resolution images. Percolation based algorithms [8-11] have the advantage to be able to deal partially with this problematic [4]. A modified percolation algorithm has been proposed and adapted to carbon anodes [4] by including geometrical restrictions on the crack pattern. Figure 4 shows the results of the algorithm proposed by Yamaguchi et al [8-11] and the modified algorithm on a images of a baked carbon anode (with a stub hole and at the anode end). Quantification example of the cracks of the right images of Figure 4 (modified algorithm) is presented in Table 1.

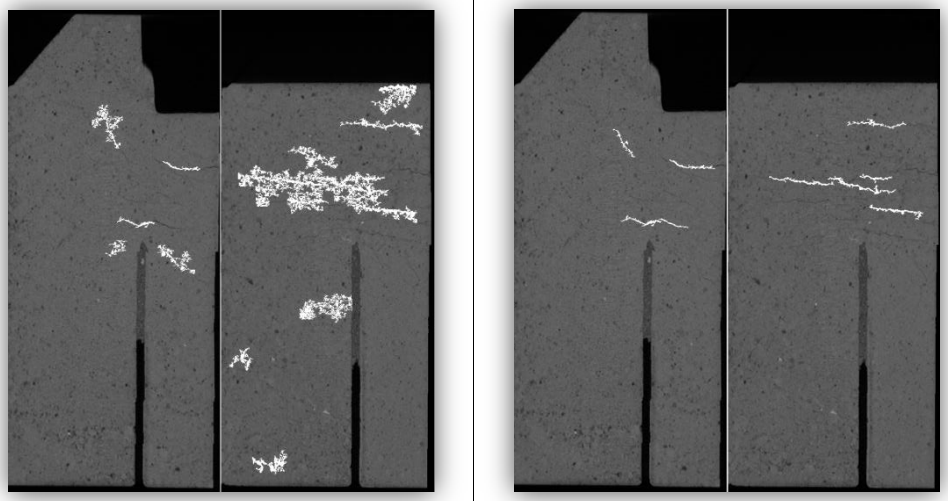

Figure 4 Results of crack detection methods. Left: Yamaguchi et al [8-11]. Right: modified algorithm

Table 1 Properties of percolated regions of Figure 4

Images	Number of cracks	Area (pixels)	Area (mm^2)	Surface ratio (%)
With a stub hole	3	1164	489	0.28
Anode end	4	2566	1078	0.67

Conclusion

Following calibration works to establish a relation between the X-Ray attenuation coefficient and baked anode apparent density, the anode baked density distribution has been mapped inside anodes block. It also highlighted the dense impurities distribution inside anodes, the cracking pattern and more importantly CT scan allowed their quantification. Because of the low spatial resolution of the images, a modified crack detection method has been used to detect and quantify the larger cracks. Finally, baked carbon anodes contain pores from nanometer to millimeter in diameter. Threshold methods were then unsuitable to estimate the porosity level. A method based on the ratio of apparent density over the real density (measured) gave the best results.

References

1. Thonstad, J., *Aluminum electrolysis : electrolyte and electrochemistry*. 1987, Amsterdam: Elsevier. S. 73-126.
2. Sørlie, M. and H.A. Øye, *Cathode in Aluminium Electrolysis*. 3rd edition ed. 2010, Düsseldorf, Germany: Aluminium-Verlag Marketing & Kommunikation GmbH.
3. Keller, F. and P.O. Sulger, *Anode Baking*. R&D Carbon Ltd.
4. Picard, D., et al. *Automated crack detection method applied to CT images of baked carbon anode*. in *Light Metals 2014 - TMS 2014 Annual Meeting and Exhibition, February 16, 2014 - February 20, 2014*. 2014. San Diego, CA, United states: Minerals, Metals and Materials Society.
5. Adams, A.N., et al., *The non-destructive 3-D characterization of pre-baked carbon anodes using X-ray computerized tomography.* Light Metals 2002, 2002: p. 535-539.
6. Picard, D., et al., *Characterization of a full-scale prebaked carbon anode using X-ray computerized tomography.* Light Metals 2011, 2011: p. 973-978.
7. Picard, D., et al. *Characterization of prebaked carbon anode samples using X-ray computed tomography and porosity estimation*. in *Light Metals 2012 - TMS 2012 Annual Meeting and Exhibition, March 11, 2012 - March 15, 2012*. 2012. Orlando, FL, United states: Minerals, Metals and Materials Society.
8. Yamaguchi, T. and S. Hashimoto. *Automated Crack Detection for Concrete Surface Image Using Percolation Model and Edge Information*. in *IEEE Industrial Electronics, IECON 2006 - 32nd Annual Conference on*. 2006.
9. Yamaguchi, T. and S. Hashimoto, *Image Processing Based on Percolation Model.* IEICE - Trans. Inf. Syst., 2006. **E89-D**(7): p. 2044-2052.
10. Yamaguchi, T. and S. Hashimoto, *Fast crack detection method for large-size concrete surface images using percolation-based image processing.* Mach. Vision Appl., 2010. **21**(5): p. 797-809.
11. Yamaguchi, T., S. Nakamura, and S. Hashimoto. *An efficient crack detection method using percolation-based image processing*. in *Industrial Electronics and Applications, 2008. ICIEA 2008. 3rd IEEE Conference on*. 2008.

Coarsening in phase-separated silicate melts observed by in-situ tomography

D. BOUTTES[1], *E. GOUILLART[2], W. WOELFFEL [2], E. BOLLER[3], L. SALVO[4], P. LHUISSIER[4], D. VANDEMBROUCQ[1]

[1] Laboratoire PMMH, UMR 7636 CNRS/ESPCI/Univ. Paris 6, UPMC/Univ. Paris 7 Diderot, 10 rue Vauquelin, 75231 Paris cedex 05, France
[2] Surface du Verre et Interfaces, UMR 125 CNRS/Saint-Gobain, 93303 Aubervilliers, France
[3] European Synchrotron Radiation Facility (ESRF), BP 220, 38043 Grenoble, France
[4] SIMAP, GPM2 group, CNRS UMR 5266, University of Grenoble 38402 Saint Martin d'Hères
* presenting author

Keywords: phase separation, glass, in-situ tomography, coarsening, fragmentation

Abstract

Using fast in-situ synchrotron microtomography, we investigate the coarsening dynamics of barium borosilicate melts during phase separation at high temperature. The 3-D geometry and connectivity of the two phases is determined thanks to quantitative image processing. We observe a linear growth of the typical size of bicontinuous phases, associated to viscous flow inside connected liquid bridges, while disconnected domains do not obey the same scaling. Topological changes of the phases are observed in-situ. An increasing fraction of isolated domains of the less viscous phase comes from the fragmentation of the percolating phase, for a volume fraction smaller than 1/2.

Introduction

Many silicate glasses compositions undergo phase separation under a critical temperature, in the stable liquid or undercooled melt state [Mazurin1984]. The resulting microstructure can be used for various applications, such as porous membranes [Kukizaki2010]. Numerous theoretical and numerical studies [Bray1994, Ahmad2012] have considered the kinetics and the morphology of the separated phases in the so-called coarsening regime, when the composition of the phases is fixed during a isothermal treatment and fixed-composition domains grow with time. However, few experimental results exist for inorganic materials about the 3-D morphology of the phases, and the formation mechanisms of the microstructure, although a few experimental results about 3-D morphology exist in the field of polymers [Aarts2005].

In this work, we investigate in-situ the coarsening stage of a barium borosilicate-glass forming melt, using in-situ synchrotron tomography in the range 1000-1300°C. Several compositions lying on the same tie-line are studied, resulting in different volume fractions of the phases. Quantitative image processing allows us to measure the growth of the typical size of domains with time. Thanks to 3-D imaging, both a percolating phase and disconnected domains can be observed. In-situ timeseries reveal the origin of disconnected domains that break-up from the percolating phase.

Methods

Glass composition and preparation - We study silicate melts in the system SiO_2 – B_2O_3 – BaO, in which a large immiscibility domain exists at temperatures far above the glass transition (see Fig. 1), resulting in liquid-liquid phase separation. Starting from a first composition of (SiO_2 59 wt%, BaO 21.5 wt%, B_2O_3 19.5 wt%), we measured the composition of the separated phases using electron microprobe analysis (see [Bouttes2015] for more details) and synthesized a total of 10 different glass

compositions lying on the same tie-line (i.e., separating into the same phases at a given temperature, see Fig. 1). As can be seen on the phase separation diagram, all compositions separate into a silica-rich phase and a barium-oxide-rich phase, with the boron oxide content being almost the same in the two phases. Because of the different silica content in the two phases, the barium-rich phase is several (3 to 5) orders of magnitude less viscous than the silica-rich phase [Bouttes2015]. In the following, glasses are labeled by the volume fraction ϕ of the barium-rich phase. For all compositions, an interconnected bi-continuous microstructure of a few microns size is observed in glasses quenched after their elaboration.

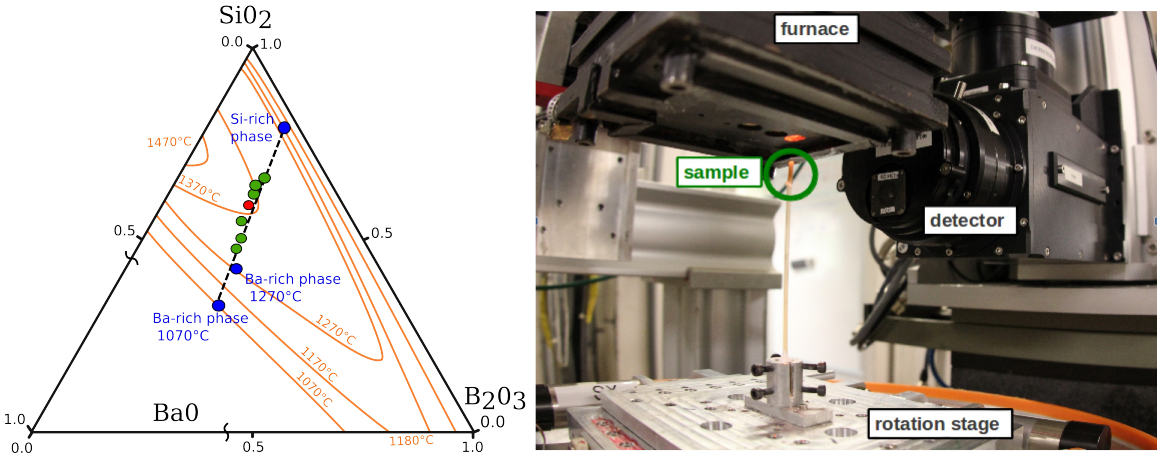

Fig. 1: Left: phase diagram of the system. The first glass composition corresponds to the red dot, blue dots are the compositions of the separated phases, and green dots are the compositions of glasses on the same tie-line, that have been studied in tomography experiments. Note that the composition of the silica-rich phase does not vary with temperature in the temperature range studied here. Right: in-situ tomography set-up on ID19 (ESRF).

In-situ tomography experiments – 2-mm-diameter cylinders where drilled in the different glasses, and placed in alumina crucibles glued on top of a long alumina rod (see Fig. 2). Tomography experiments were realized on the ID19 beamline of the ESRF. A high-speed Leuven rotation stage as well as a high-sensitivity PCO Dimax camera enabled us to take a full tomography scan (between 500 and 1000 projections) in about 5 s, at an energy of 35 keV in pink beam and with a pixel size of 1.1 micron. High energy is required because of the high absorption of the barium. We used a dedicated furnace available at ID19, that operates in the range 700 – 1500°C. Experiments consist in heat treatments at constant temperature, during which tomography scans are acquired at regular time intervals. At the beginning of experiments, a translation stage allowed us to move the hot furnace so that the sample is introduced into the furnace through a hole at the furnace bottom (see Fig. 1); this resulted in a fast heating (of the order of 10°/s) of the sample to the temperature of the heat treatment. 3-D absorption images are reconstructed from projections using a filtered backprojection algorithm available in ESRF's PyHST software [Mirone2014].

Absorption images are segmented into barium-rich and silica-rich phases using first a total-variation filter [Chambolle2004] for denoising, and then the random walker algorithm [Grady2006] for the segmentation of the phases. 3-D images were processed using Python's scikit-image [VanDerWalt2014] package, where these algorithms are available.

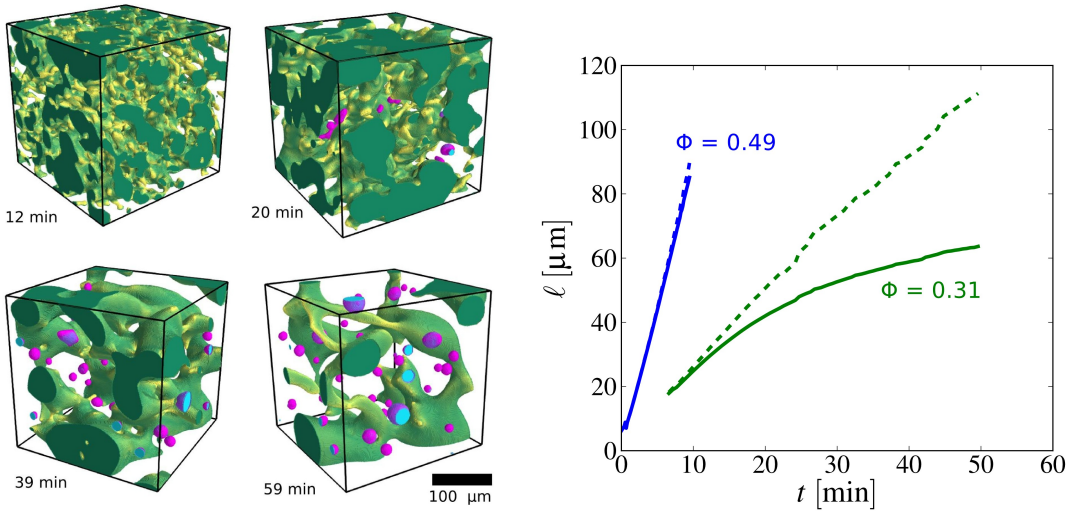

Fig. 2. Left – Visualization of the barium-rich-phase surface, for an experiment at 1130°C and a volume fraction $\phi \simeq 0.4$. The percolating phase is color-coded in green, and disconnected domains in purple. Different hues correspond to levels of mean curvature. While the typical size of the microstructure increases, a larger number of disconnected domains is observed at longer times. Right – Evolution of the typical size of the microstructure at 1280°C, for two different volume fractions. Solid line: all barium-rich phase is used for computing the typical size. Dotted line: only the percolating phase is used.

The evolution of the microstructure is shown in Fig. 2 for a typical experiment, where the surface of the barium-rich phase is represented. We observe that the typical size of the microstructure grows with time, in order to reduce the interfacial energy associated to boundaries between the phases. Although most barium-rich phase is found in a percolating phase, an increasing number of disconnected domains are also observed. Fig. 2 shows the evolution of the typical scale for two experiments realized at the same temperature, but for two different volume fractions of the barium-rich phase. The typical scale is measured as the volume over surface ratio of the phase (other measures derived from the correlation function or the chord distribution were found to correlate well with the volume over surface ratio). For both experiments, we observe a linear growth of the typical size with time, when the percolating phase is considered. Such linear growth has already been observed in phase-separating polymers [Aarts2005], but is unprecedented in inorganic materials. This regime is associated to the viscous flow of fluid from high-curvature regions to lower-curvature ones, because of Laplace pressure, whereas only coarsening due to diffusive transport had been reported in the glass literature transport so far. Theoretical analysis [Siggia1979] suggests that the growth rate should scale as the ratio of interfacial tension over viscosity. We found an excellent agreement with this prediction (see [Bouttes2015] for more details on the estimation of viscosity and interfacial tension).

Nevertheless, we see from Fig. 2 that for the smaller volume fraction, a linear growth is obtained only for the percolating phase, and not for the whole barium-rich phase, in which case a sub-linear growth is observed. The different growth law for the percolating phase and the whole barium-rich phase is a good illustration of the interest of 3-D imaging, that gives direct access to the topology of the phases. Also, one might wonder why a smaller volume fraction results in a slower growth rate for the percolating phase, as seen on Fig. 2.

Break-up and fragmentation

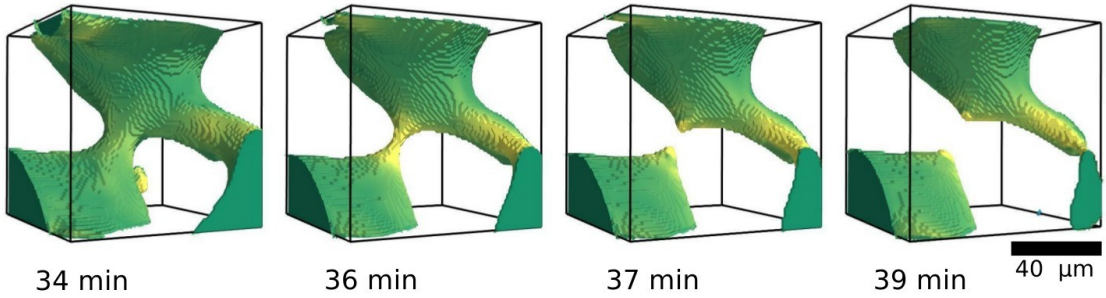

Fig. 3: Break-up event for an experiment at 1130°C. The mean curvature of the surface increases for hues from green to yellow.

In order to understand the different growth rate for different volume fractions, it is useful to observe the local evolution of the microstructure during coarsening, as shown in Fig. 3. For coarsening resulting from viscous flow (and not from diffusive transport, which is several orders of magnitude slower here [Bouttes2015]), coarsening of the typical size is only possible if the topology of interconnected phases evolve, i.e. if fluid bridges are broken or fluid loops are filled in. A break-up event is shown in Fig. 3, in which a fluid bridge thins out because of Laplace pressure until it breaks. Fluid at the two ends of the former bridge retracts towards regions of lower curvature that become locally coarser. We only observe break-ups of bridges in the barium-rich phase, that correspond to a loop-closing event for the complement silica-rich phase. This dichotomy stems from the large viscosity contrast between the two phases, since the strong shear needed to break up a bridge costs less energy within the less viscous (barium-rich) phase.

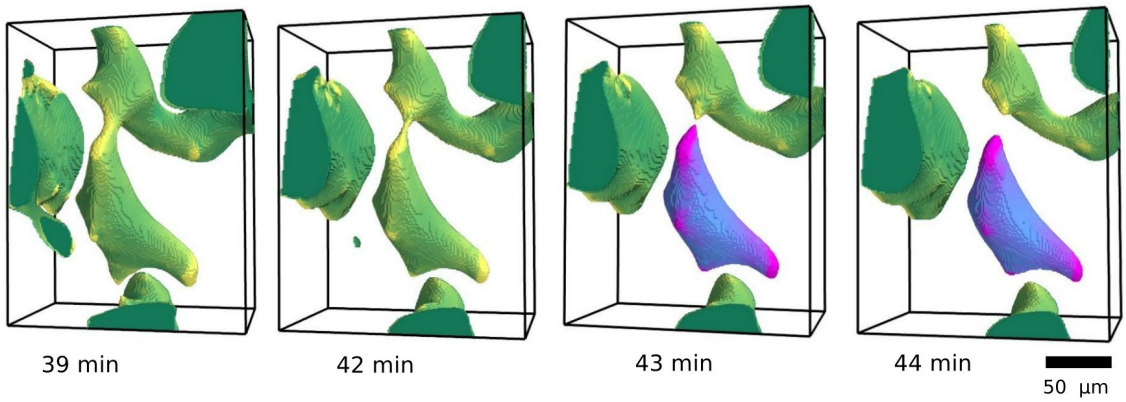

Fig. 4: fragmentation event observed in an experiment at 1180°C, for a volume fraction $\phi \simeq 0.43$ of the barium-rich phase.

The connectivity of the barium-rich percolating phase (as measured for example by the number of loops inside the phase, using Euler characteristic) depends on the volume fraction of the phase. The larger the volume fraction, the more redundant the network of fluid bridges. On the contrary, for a small volume fraction there exist critical liquid bridges that are the sole connection to the network of terminal branches. One such example is shown in Fig. 4. Such critical bridges are analogous to so-called *red links* in percolation theory: if the bridge is removed, a new domain detaches from the percolating phase. This process can be witnessed on Fig. 4. Since the fluid that detaches from the percolating phase does not feed the percolating phase, fragmentation is the reason why

the coarsening rate is smaller for smaller volume fractions of the barium-rich phase. Another possible origin of the fragmentation is the instability of a retracting thread of fluid, that has been evidenced for an extended drop of fluid by Stone and Leal [Stone1989]. However, the connectivity of the network seems to be the major reason, since the fragmentation rate increases significantly when the volume fraction of the barium-rich phase decreases. In Fig. 2 for example, the difference between solid and dotted lines correspond to fragmented domains, almost nonexistent for a volume fraction of 0.49. Since the fragmentation rate is larger for a smaller volume fraction, fragmentation can accelerate in the course of an experiment. For a few experiments, we witnessed fragmentation proceed until the barium-rich phase was completely disconnected, although it was percolating at the beginning of the experiment.

Conclusion

In-situ microtomography is a tool of choice for studying microstructure evolution associated with topology changes. During the high-temperature coarsening of phase-separated silicate melts, we witnessed how microstructure evolves because of viscous flow inside connected liquid tubes, and resulting break-ups of high-curvature liquid bridges. As a side-effect, isolated may detach from the percolating phase if the connectivity of the less viscous phase is small enough. A complex microstructure is therefore created, with a mixture of percolating phase and isolated domains. Understanding how the fragmentation rate is linked to the volume fraction is a challenge left for future work, in order to understand the different kinds of microstructure that can be created during the viscous coarsening regime, for a large contrast of viscosity between phases.

References

[Aarts2005] D. G. A. L. Aarts, R. P. A. Dullens, H. N. W. Lekkerkerker, Interfacial dynamics in demixing systems with ultralow interfacial tension, New Journal of Physics 7 (40), 2005.

[Ahmad2012] S. Ahmad, S. Das, S. Puri, Crossover in growth laws for phase-separating binary fluids: Molecular dynamics simulations, Physical Review E 85 (3) (2012) 1–9.

[Bouttes2014] D. Bouttes, E. Gouillart, E. Boller, D. Dalmas, D. Vandembroucq, Fragmentation and Limits to Dynamical Scaling in Viscous Coarsening: An Interrupted in situ X-Ray Tomographic Study, Physical Review Letters 112 (24) (2014) 245701.

[Bouttes2015] Bouttes D. et al., Hydrodynamic coarsening in phase-separated silicate melts, Acta Materialia 92 (2015), 233.

[Bray1994] A. J. Bray, Theory of phase-ordering kinetics, Advances in Physics 43 (3) (1994) 357–459.

[Chambolle2004] Chambolle, Antonin. "An algorithm for total variation minimization and applications." *Journal of Mathematical imaging and vision* 20.1-2 (2004): 89-97.

[Grady2006] Grady, Leo. "Random walks for image segmentation." Pattern Analysis and Machine Intelligence, IEEE Transactions on 28.11 (2006): 1768-1783.

[Kukizaki2010] M. Kukizaki, Large-scale production of alkali-resistant Shirasu porous glass (SPG) membranes: Influence of ZrO2 addition on crystallization and phase separation in Na2O-CaO-Al2O3-B2O3-SiO2 glasses; and alkali durability and pore morphology of the membranes, Journal of Membrane Science 360 (1-2) (2010) 426–435

[Mazurin1984] Mazurin O. V. & Porai-Koshits E. A., Phase Separation in Glass, North-Holland, Amsterdam, 1984.

[Mirone2014] A. Mirone, E. Brun, E. Gouillart, P. Tafforeau, J. Kieffer, The pyhst2 hybrid distributed code for high speed tomographic reconstruction with iterative reconstruction and a priori knowledge capabilities, Nuclear Instruments and Methods in Physics Research Section B, 324 (2014) 41–48.

[Ramachandran2011] RAMACHANDRAN, Prabhu et VAROQUAUX, Gaël. Mayavi: 3D visualization of scientific data. *Computing in Science & Engineering*, 2011, vol. 13, no 2, p. 40-51.

[Siggia1979] E. D. Siggia, Late stages of spinodal decomposition in binary mixtures, Physical Review A 20 (2) (1979) 595.

[Stone1989] Stone, H. A. and Leal, L. G. (1989). Relaxation and breakup of an initially extended drop in an otherwise quiescent fluid. Journal of Fluid Mechanics, 198 :399–427.

[VanDerWalt2014] VAN DER WALT, Stefan, SCHÖNBERGER, Johannes L., NUNEZ-IGLESIAS, Juan, et al. scikit-image: image processing in Python. PeerJ, 2014, vol. 2, p. E453.

Mineralogy Mapping on 3D Digital Rock Models Based on X-ray MicroCT and Electron Microscopy Techniques

I.V. VARFOLOMEEV[1,2], O.A. KOVALEVA*[1,2], I.V. YAKIMCHUK[2]

[1] Moscow Institute of Physics and Technology, Dolgoprudny, Russia
[2] Schlumberger, Moscow, Russia
* presenting author – okovaleva@slb.com

Keywords: digital rock (DR), microCT (X-ray micro-computed tomography), SEM-EDX (scanning electron microscopy with energy dispersive x-ray microanalysis), image registration

Abstract

One of the most efficient imaging techniques for rock core studies is X-ray absorption micro-computed tomography (microCT), which provides 3D spatial distribution of X-ray attenuation inside the core sample.The data obtained from laboratory X-ray microCT covers a wide range of scientific interests, but the method is not self-sufficient due to certain limitations. Still, microCT can provide more profound and complete data in combination with other methods of core exploration. In this work, we propose an approach that is based on a combination of X-ray microCT data and scanning electron microscopy with energy dispersive X-ray microanalysis (SEM-EDX).

Introduction

Over time, mineralogical studies have played a significant role in the development of oil and gas in a variety of ways. Understanding and predicting the behavior of hydrocarbon reservoirs strongly relies on knowledge of reservoir properties. For example, volumes of oil recovery highly depend on rock permeability and porosity, which, in turn, are defined by mineralogical structure of the rock. Among all the methods for studying reservoirs, core studies are the most reliable for obtaining information of the internal rock structure. As a rule, laboratory core analysis involves a series of multidirectional and multipurpose experiments. They are especially necessary for the application of the increasingly widespread digital rock approach.

The general procedure in the digital rock approach involves constructing a 3D model of a rock sample and performing numerical simulations of the processes of interest using the digital model. The most straightforward way for building such models is binarization of rock images into two main classes—voids and solids. In this case, only pore space geometry is taken into account. Still, porous media are always very complicated exploration objects, consisting of numerous compounds and phases, which means more detailed methods are required. Information about the spatial distribution of minerals allows making more reliable digital rock models (with different solid phases according to mineralogy) that potentially increase the accuracy of calculations.

The input for calculation of such digital models of core plugs (see the example in Fig. 1) can be obtained by the means of microCT [Koroteev, 2011]. The object under study is illuminated by an X-ray beam at different orientations, which results in the registration of a set of shadow projections. Using specially developed mathematical algorithms, taking into account beam geometry, a dataset of slice-by-slice images is obtained, in which a pixel's gray value reflects the degree of X-ray radiation attenuation of a corresponding sample point.

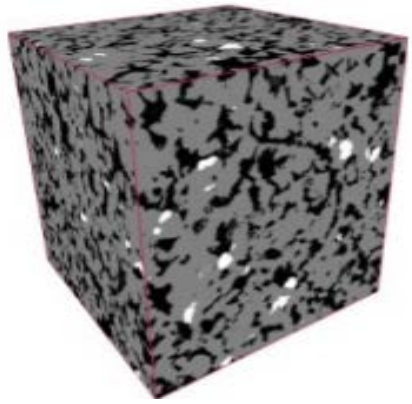

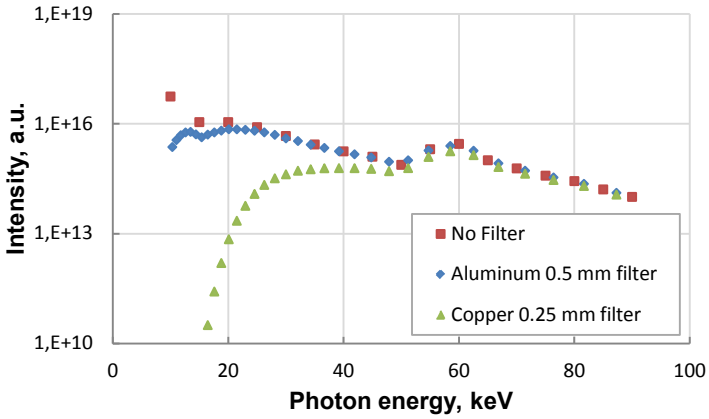

Fig. 1. *3D model of a core sample*

Fig. 2. *Tube spectrum shape depending on voltage and the addition of filters*

According to physics laws, the degree of X-ray attenuation of an object is determined by its elemental composition and overall density. Applied to the digital rock approach, this means that different minerals attenuate X-rays differently and hence can be distinguished in images. This makes microCT a suitable tool for nondestructive mineralogical analysis of a sample. However, difficulties arise while making a detailed examination of the sample. Firstly, most laboratory microCT instruments deal with a “white” (polychromatic) beam (Fig. 2), which comes from the necessity of using as many photons as possible to obtain statistically reliable images within a reasonable amount of time. Secondly, the energy of the beam should be high enough (>50 keV) to penetrate through dense rock samples. Moreover, there are several chemically and structurally different minerals that are characterized by an equal degree of X-ray attenuation and, consequently, can be confused or misinterpreted in reconstructed images (for example, albite and quartz in Table 1). It also should be taken into account that correspondence between attenuation of different elements of the sample and their gray-scale values is not known a priori and this becomes an obstacle for image analysis. The assumption that gray-scale values linearly correspond to theoretical attenuation tends to be incorrect (Fig. 3).

Mineral	μ, cm^{-1}
Albite	*15.8*
Quartz	*15.9*
Dolomite	*25.1*
Halite	*27.4*
Calcite	36.0
Apatite	50.6
Pyrite	177.1

Table 1. *Effective attenuation values of some minerals in the photon energy range 10 to 100 keV*

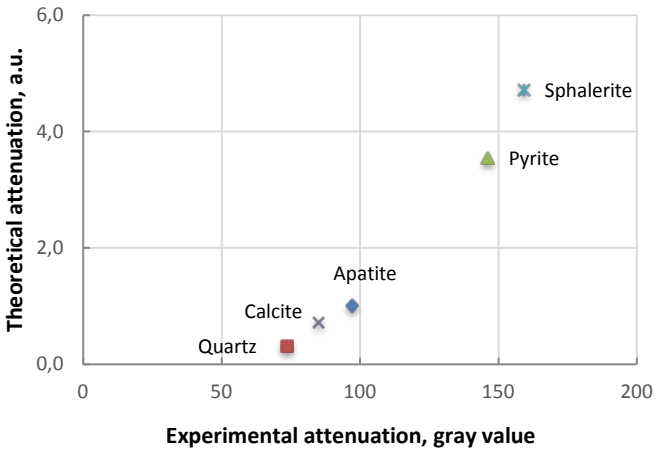

Fig. 3. *Comparison of experimental and theoretical mineral attenuation*

Currently, there are alternative methods for overcoming most of the aforementioned problems, such as synchrotron X-ray tomography, performed at several different radiation energies, or X-ray fluorescence tomography (XRF). However, both of these methods are either costly or not yet time-efficient and cannot be applied to routine scanning.

Scanning electron microscopy (SEM) is a powerful technique for material study that is based on analysis of the interaction between the matter and the accelerated electron beam. SEM-EDX is a method based on SEM that relies on analysis of characteristic X-ray emission of investigated objects arising due to the mentioned interaction. Application of SEM-EDX is widespread because it enables automatic determination of chemical composition in each pixel of large images within a reasonable amount of time. (In our work, it takes 24 hours to analyze images of 4000×4000 pixels.) An example of such classification is demonstrated in Fig. 4.

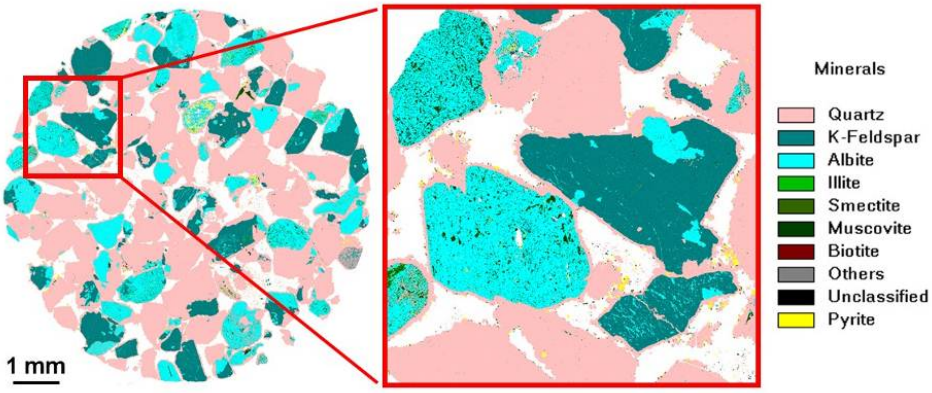

Fig. 4. *Example of mineral classification using SEM-EDX*

Nevertheless, because of physical limitations, SEM-EDX can provide only 2D images. That is why we see the development of successive application of X-ray microCT and SEM-EDX [Yakimchuk, 2014]. The essence of the proposed method consists in finding a correspondence between the various local characteristics of microCT image voxels and their mineral content, known from SEM-EDX image.

Methods

MicroCT does not require any specific sample preparation; therefore, it is conducted first. An 8-mm-diameter cylindrical core miniplug sample is fixed on a special stage inside the microtomograph chamber. The conditions of our experiment allow us to achieve a quality of ~2 μm in pixel size in reconstructed images. After carrying out X-ray scanning, the sample is cut to obtain its cross section for further SEM-EDX analysis. Several cross sections may be obtained, if needed. Unlike microCT, SEM-EDX is conducted on a flat, polished surface of the sample.

An essential part of the study is spatial registration of acquired 2D and 3D images. During the past few decades, numerous image registration methods have been developed for various types of images [Zitova, 2003]. We propose our own approach, which considers the special characteristics of the images in question. Namely, the outer surface of the cylindrical rock miniplug is never ideally smooth due to the nature of rock (grains, fractures, voids). The profile of the side surface is presumed to be a unique descriptor of the sample. Moreover, the 1D contour of the 2D SEM image explicitly corresponds to the 2D side surface of a 3D microCT image. This correspondence enables extraction of all necessary spatial transformation

parameters (x-, y-, z-shifts, Euler angles, scale) with acceptable accuracy. An example of a 1D contour is shown in Fig. 5.

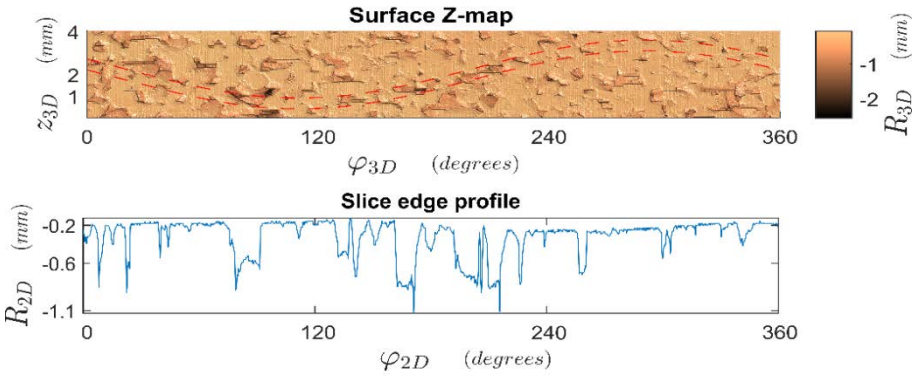

Fig. 5. *Correlation between side surface of the sample (top) and 2D slice edge profile (bottom)*

After registration of the microCT image with the 2D mineral map, it is possible to analyze directly (pixel by pixel) the correspondence between the data in both images. The key point is that simple correlation of the microCT pixel value with mineral type is inefficient. Various local structural characteristics should be calculated and analyzed instead.

Such characteristics can refer to shapes or textural specialties of mineral grains, which can be defined using special techniques, such as local binary patterns [Ojala, 2004]. For example, in Fig. 6, the distinction between grains 1 and 2 or 2 and 3 is effortless, but distinction between grains 1 and 3 is not so evident. However, grain 1 contains some microcracks whereas grain 3 looks solid. This fact underlines the importance of considering tiny details, as they can identify mineral type.

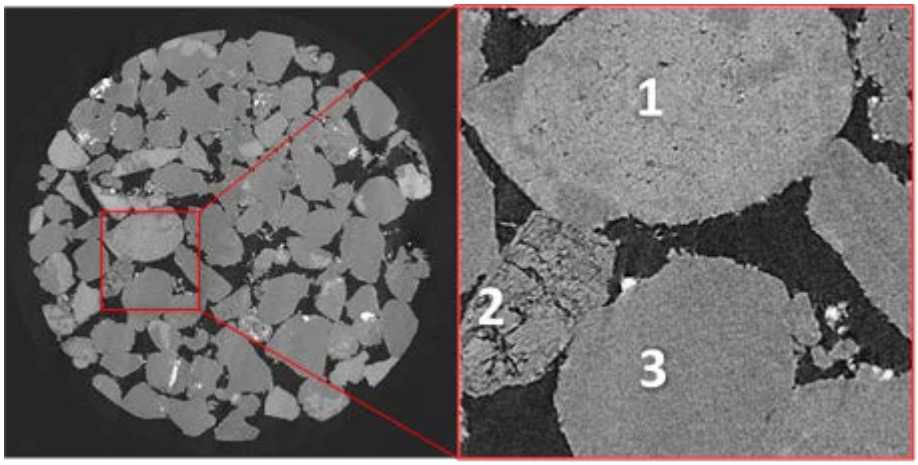

Fig. 6. *A slice of a 3D microCT image and magnified view of a portion of the slice*

Having discovered a set of local features on the microCT image that would more or less explicitly identify the mineral type, we perform a machine learning procedure to classify the whole 3D microCT image and construct a 3D mineral map.

Results and Discussions

With the workflow described above, we can register microCT images to SEM-EDX ones, thus enhancing 3D model construction possibilities (Fig. 7). In addition to geometric structure, pore distribution, and overall porosity, supplemental data characterizing intrinsic features of each mineral grain are acquired. These data are the basis for the 3D mineral map.

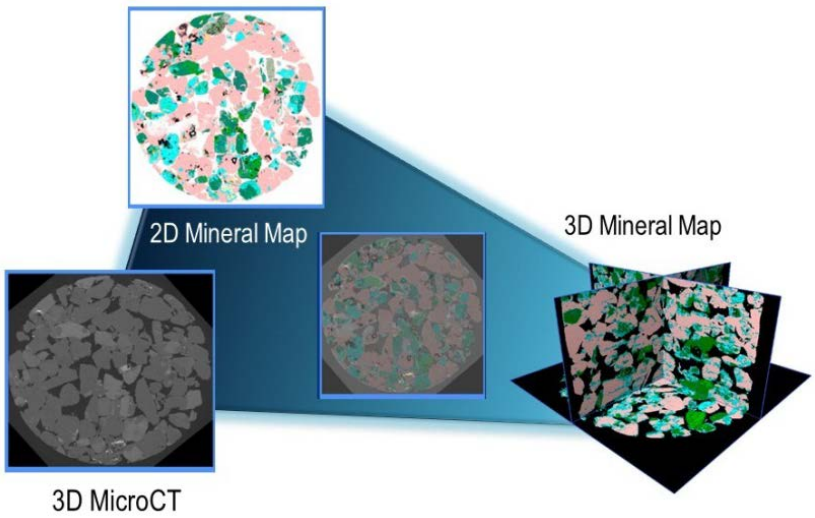

Fig. 7. *Construction of a 3D mineral map for sandstone core*

Overall, although the gray value of microCT images is not sufficient for mineral identification, a properly calibrated microCT technique enables reliably distinguishing certain groups of minerals, which helps in classification. The demonstrated ability to predict observed mineral attenuation permits extraction of mineralogical information even in the case of a polychromatic X-ray source. This serves as an effective alternative to existing costly techniques.

References

Koroteev D., Mutina A., and Sasov A. (2011). ***Book of Abstracts of MicroCT User Meeting***: 40–45.

Yakimchuk I., Varfolomeev I., and Korobkov D. (2014). 18th International Microscopy Congress, Prague, Czech Republic, 7–12 September 2014. http://www.microscopy.cz/abstracts/2759.pdf.

Zitova B. & Flusser J. (2003). ***Image Vision Computing*** *21: 977-1000.*

Ojala T. & Matti P. (2002). ***IEEE Transactions on Pattern Analysis and Machine Intelligence*** *24, 7*: 971-987.

Measuring in-situ fragment size distributions caused by melt inclusion decrepitation and other mechanisms using HRXCT

T. CLOW*[1], R.A. KETCHAM[1]

[1] University of Texas at Austin, Department of Geological Sciences, University Station C1100, Austin, Texas 78712, U.S.A. – travis.clow@utexas.edu, ketcham@jsg.utexas.edu
* presenting author

Keywords: fragmentation, melt inclusion, fragment distribution, decrepitation, in-situ

Abstract

In comparison to crystal nucleation and growth, fragmentation of crystals has received little attention in igneous and metamorphic petrology despite playing an important role in crystal size evolution and overall particle dynamics of magma chambers. Evidence of multiple mechanisms for fragmentation has been observed in previous studies – syn-eruptive fragmentation/shattering due to shockwaves, clot disaggregation, and pre- and syn-eruptive melt inclusion decrepitation – with particular importance placed on the last as the dominant fragmentation mechanism in batholith-sized magma bodies. Each process has been proposed to generate a distinctive fragment size distribution (FSD) that can be distinguished statistically; much can be discovered about fragmentation processes based on these distributions. The present study tests theoretical FSDs for different fragmentation mechanisms as described in Bindeman (2005) by using high-resolution X-ray computed tomography (HRXCT) to analyze plagioclase and hornblende fragments found *in-situ* in dacitic pumice samples from the Popocatepetl stratovolcano in central Mexico. By using HRXCT, we can analyze crystal fragments in a textural context that is lost when samples are disaggregated and sieved, as in previous studies. We interpret unusually large vesicles that have plagioclase and/or hornblende fragments plating their sidewalls as decrepitation textures, where decompression caused crystals with melt inclusions to explode into fragments lining the vesicle. Crystal fragments that have been fractured without having a large effect on vesicle size are also observed, which we interpret as fragmented due to syn-eruptive shock. HRXCT allows us to quantitatively measure fragment sizes, shapes, distributions, relative positions, and orientations in 3D by isolating individual vesicles within the pumice using *ImageJ* (NIH) and analyzing the associated crystal fragments using *Blob3D* (Ketcham 2005). In addition to long-axis measurements akin to those used in previous work that employed disaggregation, we are able to acquire volumetric measurements that were not practical in previous studies. Frequency versus volume plots show a lognormal distribution for both melt-inclusion decrepitated plagioclase and hornblende fragments as well as fragments generated by syn-eruptive shock. This may contradict Bindeman (2005), who posited a fractal size distribution for fragments generated by syn-eruptive shock fragmentation. Finally, heavily fragmented hornblende, which is previously reported to have a low susceptibility to fragmentation via melt inclusion decrepitation, is also observed plating the sidewalls of enlarged vesicles.

Introduction

Fragmentation of crystals has been observed to be an integral component of overall particle dynamics in magma chambers, serving as an important mechanism for transforming crystalline matter (Bindeman 2005). While textural evidence of fragmentation via pre-eruptive and syn-eruptive processes is well estabilished (Best and

Christiansen 1997), size distribution analysis of melt inclusion generated fragmentation (known as decrepitation) and other fragmentation mechanisms has only recently become a topic of interest. Most notably, Bindeman (2005) posited that each fragmentation process generates a unique fragment size distribution (FSD) that can provide a snapshot of its eruptive history, with decrepitation being the dominant mechanism occurring in a large magma body. Through mass disaggregation and sieving of samples and laboratory heating experiments at 1atm, he found that decrepitation generates a lognormal FSD, while shattering of parent crystals into fragments via shockwaves during an eruption generates a fractal FSD.

An important aspect in analyzing FSDs not possible in previous studies is the textural context of fragmentation; by disaggregating samples to measure the fragments, it's impossible to ascertain which crystal fragments are associated with each other. We test Bindeman's theoretical size distributions *in-situ* using three dacitic pumice samples from the Popocatepetl stratovolcano of central Mexico, each with a varying degree of fragmentation. By analyzing these samples using HRXCT, we are able to interpret each instance of resulting fragmentation and obtain volumetric and long-axis measurements of only those fragments associated with decrepitation or syn-eruptive shock, in addition to all fragments in the sample as a whole, in order to generate in-situ FSDs for both plagioclase and hornblende.

Methods

Three dacitic pumice samples from Popocatepetl, POPO-05-15, POPO-14a-61, and POPO-14a-28, were scanned in May 2005 at the University of Texas at Austin's CT facility. Each sample was scanned at an energy of 180 kV and has an inter-slice spacing of .01602 mm and an inter-pixel spacing of .0146875 mm, with drift correction and ring removal employed to remove any artifacts. Before long-axis and volumetric measurements of crystal fragments can be determined using *Blob3D* analysis, isolation of overly enlarged vesicles in POPO-05-15 and closely associated fragments in POPO-14a-61 and POPO-14a-28 was necessary to ensure that only fragments associated with a fragmentation mechanism (i.e. decrepitation or syn-eruptive shock) will be analyzed to determine the effective FSD in-situ. Isolation was carried out by using standard cropping and paintbrush tools in *ImageJ* (NIH) for each data set. We employ a set of criteria for each instance of fragmentation to texturally determine which mechanism is mainly responsible for the resulting texture seen in CT.

We interpret unusually large, expanded vesicles with fragments of plagioclase or hornblende plating their sidewalls as melt-inclusion decreptitation textures. Typically a larger, sub-to-euhedral fragment exists which upon decompression and/or overheating explodes and generates smaller, more anhedral fragments with each successive

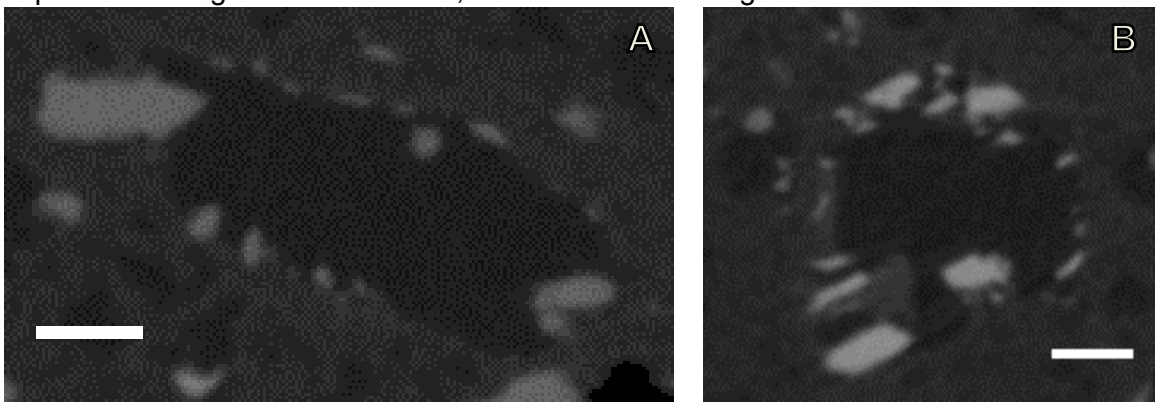

Fig. 1. *Close ups of (A) plagioclase and (B) hornblende melt inclusion decrepitation textures from POPO-05-15. Scale bar in each image is 500 microns.*

decrepitation event (Fig. 1A, 1B). It is common for both plagioclase and hornblende to have a large number of fragments with chaotic splits for the final decrepitation textures seen, with total fragments per vesicle exceeding 100 for the larger vesicles (1mm+ in diameter). Additionally, it is difficult, if not impossible, to accurately establish original crystal shape/orientation due to reorientation of fragments around their associated vesicle due to each decrepitation event.

Textures showing a small number (commonly 2-8) of associated, relatively equal sized fragments of plagioclase and hornblende with little change in vesicle size are interpreted as fragmented due to syn-eruptive shock (Fig. 2A, 2B). Fragmentation is not as energetic compared to decrepitation textures, and fragments are often trivial to reconfigure to their original orientation due to a limited amount of reorientation; in some cases, the fragments are still in their original orientation with obvious fractures (Fig. 2A).

When the fragmentation texture was not immediately evident (Fig. 2C), the main criteria used to differentiate mechanisms included the size of the fragments compared to each other (if equal; likely due to syn-eruptive shock) and the amount of displacement and shape of fragments plating an enlarged vesicle. In a case such as Fig. 2C, despite the expanded vesicle, the clear fracture path, limited displacement, and relatively equal sized fragments indicate a syn-eruptive shock texture.

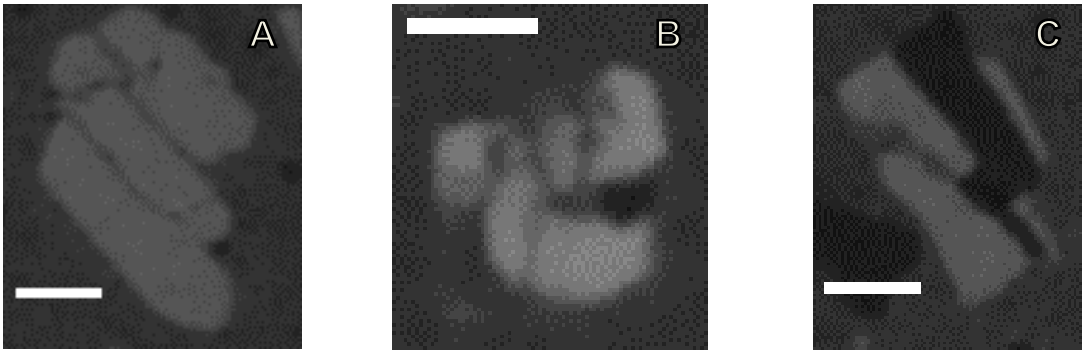

Fig. 2. *Close ups of plagioclase (A) and hornblende (B) syn-eruptive shock textures from POPO-14a-28 and POPO-14a-61, respectively. (C) shows a close up of an intermediate syn-eruptive shock textural case of plagioclase fragmentation from POPO-14a-28. Scale bar in each image is 500 microns.*

After identification of dominant mechanism and isolation in *ImageJ*, each instance of fragmentation associated with a single vesicle was brought into *Blob3D* for long-axis and volumetric measurements (Ketcham 2005). Segmentation of plagioclase and hornblende was carried out using the same parameters for all fragments within each sample, and fragments were manually separated using erosion/dilation and plane-definition tools when necessary (due to overlap in gray values between fragments, for example, as seen in Fig. 2A). Volumes were calculated using partial volume ellipsoid (PVE) corrected methods to accurately determine the proportion of component present in each voxel, which is particularly useful for accurate volumetric measurements of the smallest fragments that only comprise 6-10 voxels (Ketcham 2006).

Results and Discussion

Based on textural analysis, the dominant fragmentation mechanism for associated fragments in POPO-05-15 is melt inclusion decrepitation, while POPO-14a-61 and POPO-14a-28 are dominated by syn-eruptive shock. The number of fragments per associated vesicle is significantly higher on average for POPO-05-15, likely due to multiple decrepitation events before and during eruption in comparison to one major syn-eruptive shock event for the other two samples. Log-log frequency versus volume plots

(Fig. 3) show that both POPO-05-15 and POPO-14a-61 experience similar amounts of total fragmentation for plagioclase, while POPO-14a-28 shows a much smaller number of generated fragments. FSD's only provide a snapshot of an eruption rather than characterizing the eruption as awhole (Bindeman 2005); thus it is possible that POPO-14a-28 was ejected at a later time than POPO-14a-61, when the explosion was not as violent.

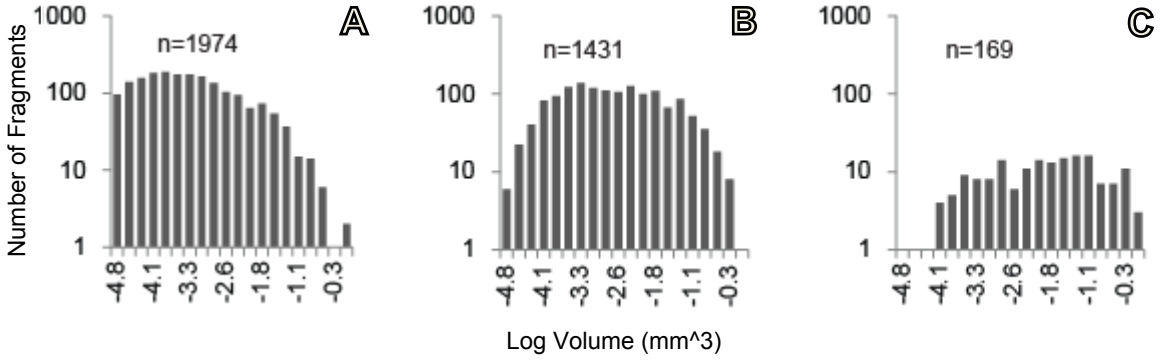

Fig. 3. *Log-log frequency versus volume histograms of only associated plagioclase fragments for A) POPO-05-15, B) POPO-14a-61, and C) POPO-14a-28; 'n' refers to total number of fragments analyzed.*

Using long-axis measurements, Bindeman (2005) posited that melt inclusion decrepitation yields a lognormal FSD and low number of fragments per breakage cycle, while syn-eruptive shock fragmentation yields a fractal FSD with large breakage probabilities and fractal dimensions of 2 to 3. Our in-situ volumetric results of only associated fragments confirm that melt inclusion decreptiation generates a lognormal FSD for both plagioclase and hornblende (Fig. 3A, 4A). Syn-eruptive shock fragmentation in POPO-14a-61 for both minerals also shows a log-normal distribution (Fig. 3B, 4B), which contradicts Bindeman's findings. In particular, an absense of smaller fragments in both POPO-14a-61 and POPO-14a-28 indicates that in these samples, syn-eruptive shock does not necessitate large breakage probabilities, nor any fractal dimension. For a more complete look at total fragmentation in the syn-eruptive shock samples (POPO-14a-28 in particular), FSD's of all plagioclase fragments within each sample (including those floating in the matrix) were generated showing a more complete lognormal FSD (Fig. 5). Long-axis measurements from all samples show a virtually indistinguishable FSD to volumetric log-log plots, however volumetric measurements are more accurate and are thus displayed in this study.

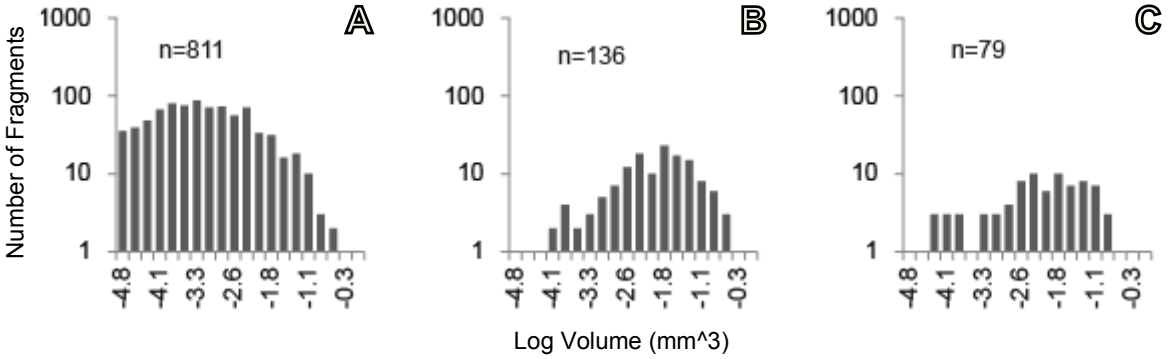

Fig. 4. *Log-log frequency versus volume histograms of only associated hornblende fragments for A) POPO-05-15, B) POPO-14a-61, and C) POPO-14a-28; 'n' refers to total number of fragments analyzed.*

Additionally, Bindeman posits that plagioclase has the highest susceptibility to decrepitation based upon bulk and shear modulus, ability to capture melt inclusions, cleavage, and shape, and suggests that amphiboles have a low potential for decrepitation. We find that the latter is not necessarily the case, as there are abundant cases of heavy decrepitation in hornblende found throughout POPO-05-15 (Figs. 1B, 4A).

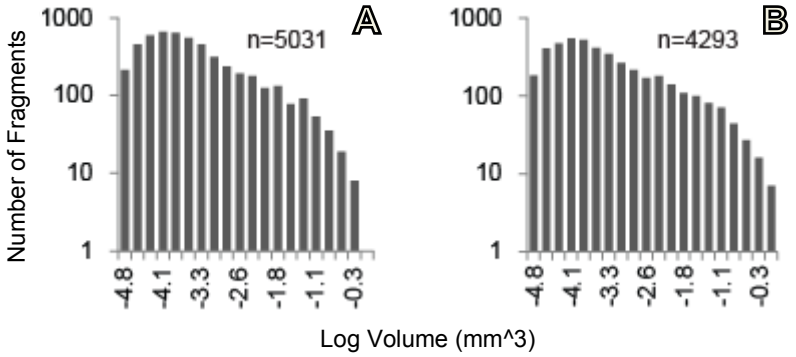

Fig. 5. *Log-log frequency versus volume histograms of all plagioclase fragments for A) POPO-14a-61 and B) POPO-14a-28; 'n' refers to total number of fragments analyzed.*

We can also use the CT data to visualize these fragmentation textures in 3D (Fig. 6), which highlights the nature of the expanded vesicles and exploded fragments. This also allows us to possibly reconstruct parent crystals prior to fragmentation in the future, although the challenge is evident.

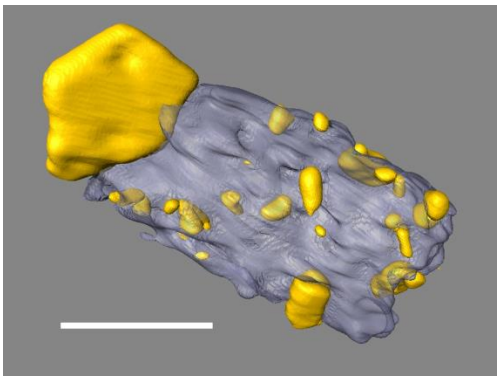

Fig. 6. *3D visualization of Fig. 1A. Gold objects are plagioclase fragments; semi-transparent object is the expanded vesicle. Scale bar is 1mm.*

Conclusions

HRXCT is a novel application in generating in-situ FSD's in volcanic rocks, allowing for more accurate measurements and textural observations unavailable in previous studies. Our findings may indicate that FSD's themselves are not as robust in determining fragmentation mechanisms from snapshots of volcanic eruptions as previously thought due to overlapping distributions between mechanisms, but nonetheless are useful for quantitatively describing melt inclusion decrepitation seen in volcanics.

References

Best, M.G. & Christiansen, E.H. (1997) Origin of broken phenocrysts in ash-flow tuffs. Geological Society of America Bulletin, 109, 63-73.

Bindeman, I.N. (2005) Fragmentation phenomena in populations of magmatic crystals. American Mineralogist, 90, 1801-1815.

Ketcham, R.A. (2005) Computational methods for quantitative analysis of three-dimensional features in geological speciments. Geosphere, 1, 32-41

Ketcham, R.A. (2006) Accurate three-dimensional measurements of features in geological materials from X-ray computed tomography data. In j. Desrues, G. Viggiani, and P. Besuelle, Eds. Advances in X-ray Tomography for Geomaterials, p. 143-148. ISTE, London.

Evaluation by Computed Tomography of the Quality of Carbon Anodes Used in Aluminum Industry

S. Amrani*[1], D. Kocaefe[1], Y. Kocaefe[1], D. Bhattacharyay[1], M. Bouazara[1], B. Morais[2]

[1] University of Québec at Chicoutimi 555 Boulevard de l'Université, Chicoutimi, Québec, Canada G7H 2B1-
salah.amrani1@uqac.ca
Duygu_Kocaefe@uqac.ca
Yasar_Kocaefe@uqac.ca
Dipankar_Bhattacharyay@uqac.ca

[2]Aluminerie Alouette Inc. 400, Chemin de la Pointe-Noire, Sept-Îles, Québec, Canada G4R 5M9-
brigitte.morais@alouette.qc.ca

Keywords: Carbon anodes, defects, baking conditions, tomography.

Abstract

Aluminum is produced by the reduction of alumina in an electrolysis cell. The carbon anode is one of the key elements in this process. The quality of these anodes has a considerable impact on the electrolysis process; thus, the evaluation of their quality is important. One problem that is of great interest is the formation of cracks, which affects the quality of anodes. Cracking results in increase in cost as well as in energy and environmental emissions including greenhouse gases. To reduce the cost, the energy consumption, and the impact on environment, aluminum smelters require high quality carbon anodes with a high density and a low electrical resistivity. Anode quality depends on the raw materials and the parameters of the green anode production and the baking processes. Each step may have an impact on the formation of cracks. The physical and chemical properties of the raw materials have a great influence on anode quality and their performance in electrolysis.

In this project, several anodes were made with different raw materials and under various operating conditions. The green anodes produced were characterized using the computed tomography (CT) technique which is a nondestructive method, and the internal defects created during their fabrication were determined. These anodes were baked under different conditions (heating rate, final baking temperature). Then, the baked anodes were again characterized using the CT technique. The principal objective of this study is to evaluate the impact of different anode production parameters on their quality based on the CT analysis. In this article, the results of the CT analysis of various anodes are presented.

Introduction

The carbon anode comprises of two essential elements (petroleum coke and coal tar pitch) in well-defined proportions. An anode with cracks increases energy consumption and greenhouse gas emissions. Also, such an anode is usually consumed more rapidly than a good-quality anode. For environmental protection, the treatment of gas which contains residual volatile compounds coming from pitch during baking has become a necessary step in the production of anodes for the aluminum industry [1].

Crack formation can be investigated using different techniques. The morphology of the cracking of a baked-anode sample (the structure of the cracks) was the objective of a study carried out using the scanning electron microscopy; and the purpose of this work was to determine the cracking mechanism [2]. This study demonstrated also the analysis of cracks using ultrasound in anode samples baked at different heating rates, which is a non-destructive technique capable of giving information on the location and the size of cracks [2]. The characteriziation of the anode quality may also be based on the determination of physical properties.

The X-ray CT is a non-destructive technique for the complete visualization of the structural features within an opaque solid. It gives information in 3D about the quality of the sample. It is used for a wide variety of materials, including rocks, bones, ceramics, and metal [3,4]. This technique also provides information on the structure (porosity and cracks) of carbon anodes, which is obtained through the analysis of high resolution 2D images of the cross-sections in the sample. It also gives the density distribution in the sample and allows the determination of the heterogeneity of materials at the macroscopic scale. Its advantage compared to other techniques is that it gives an insight into the internal structure of the anodes [5].

Methodology

Two series of green anodes were produced with the same recipe (same amount and same type of coke and pitch). One series consisted of three green anodes which were later baked to different temperatures (200°C, 400°C, and 800°C) to study the evolution of structure and cracks during baking. The other series contained also three green anodes which were then baked at different heating rates (high, medium, low) to the same final temperature (>1000°C) to investigate the impact of heating rate on anode cracking.

Green anode manufacturing

Pilot-scale green anodes were manufactured using the same recipe for the dry aggregate (solid particles of different granulometric fractions) including recycled carbon materials (butts, rejected green and baked anodes). The mass percent of butts did not exceed 30% of the total aggregate. After preheating the dry agregates, the pitch was added, and the mixture was mixed to produce the anode paste. Using a vibro-compactor, the paste was compacted producing a pilot-scale green anode of about 10 kg.

Anode baking

The green anodes were placed in a baking furnace (Pyradia) and were surrounded by packing coke. The evolution of the temperature in the furnace was programmed to provide the desired heating rate and the final baking temperature. After cooling, the anodes were collected to evalute their quality.

First, three green anodes were baked individually at different heating rates to the same final temperature. Then, the baking of three anodes was carried out also individually using the same heating rate (medium) to different final temperatures (200°C, 400°C, and 800°C).

Characterization by tomographic analysis

All manufactured anodes were characterized by converting the raw data (CT numbers) generated by the computed tomography on scanned cross-sections in an anode to 2D images, and then analysing these 2D images of numerous cross-sections of that anode. The processing of the raw data and the 2D images could be highly time consuming, which makes it difficult to determine the structural features in the total sample volume. A program was developed using Matlab to analyse the entire volume by treating all 2D images in a given sample. This allowed the visualization and the determination of defects.

The final images obtained help visualize in color the defects caused by the baking conditions. Also, the exploitation of the tomography data makes it possible to quantitatively estimate the various defects in manufactured anodes by determining the percentage of defects.

Results and discussion

The quality of the manufactured anodes can be estimated by studying the processed images obtained using the program. In the figures presented in this section, blue indicates areas representing the matrix of the anode while red shows the areas with defects.

Impact of the baking level (final anode temperature)

The results of the tomography analysis are shown in Figure 1 for anodes baked to different final temperatures: (a) 200°C, (b) 400°C, and (c) 800°C. The results indicated that the amount of cracks increased with increasing temperature. Figure 1 (a) shows that the anode baked to 200°C has fewer defects. At this stage, the pitch is in liquid state, but the devolatilization from the pitch has not started yet. At 400°C (Figure 1 (b)), the devolatilization is taking place, and more areas display defects. This is expected since the devolatilization of pitch leaves behind pores and cracks in the solid matrix. At 800°C (Figure 1 (c)), the pitch is going through the carbonization stage accompanied by fairly low levels of devolatilization. The areas affected by defects continue to increase gradually.

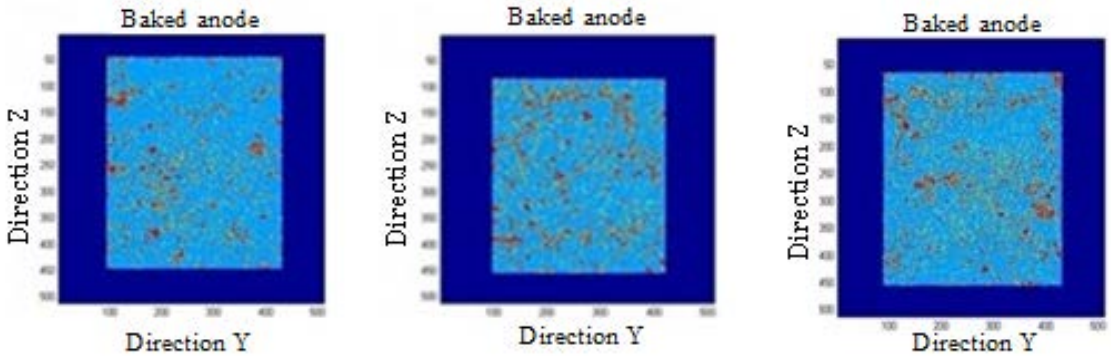

(a) (b) (c)

Figure 1. Evaluation by the tomographic analysis of the quality of anodes baked to different levels (to different final temperatures): (a) 200°C, (b) 400°C, and (c) 800°C.

Impact of the heating rate on the anode cracking

The three anodes of the second series were baked at different heating rates (high, medium, low). The results of the tomographic analysis of these anodes are given in Figure 2. It can be clearly seen from Figure 2 that more defects are present in the anode baked at the high heating rate (Figure 2 (a)) compared to others, and the anode baked at the low heating rate displays less defects (Figure 2 (c)). This can be explained by the formation of cracks and/or pores due to the devolatilization of pitch during the baking of anodes. The rapid devolatilization at the high heating rate causes more defects, which may result in the rejection of such anodes. Lower heating rates allow the volatiles that evolve from the anode to diffuse through the anode more slowly and thus creating fewer defects. These results agree with those of Fischer and Keller [6] who stated that the baking parameters have a major influence on the final quality of anodes and the desired maximum heating rate is between 10°C/h and 14°C/h depending on the raw materials and the dimensions of the anode.

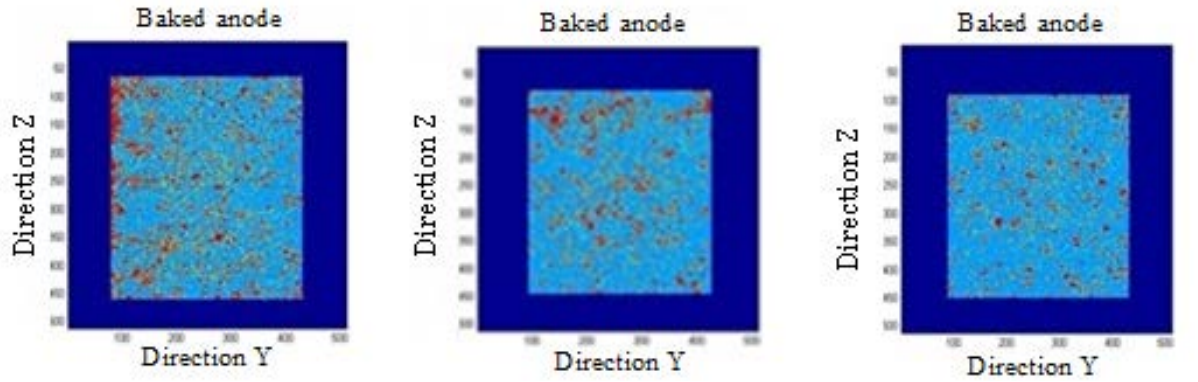

(a) (b) (c)

Figure 2. Evaluation by the tomographic analysis of the quality of anodes baked at different heating rates: (a) high, (b) medium, and (c) low.

Conclusions

This study demonstrates the use of the CT technique for the evaluation of the cracking of anodes. The results show that the use of a low heating rate results in a good quality anode compared to higher heating rates. The baking to different levels (maximum temperatures) helps identify at which stage the cracking starts and how it develops.

References

[1] S. Sendid , A. Courau , High performance of “Eolios” pitch fume treatment system, Light Metals (2014), 1157-1162.

[2] S. Amrani, D. Kocaefe, Y. Kocaefe, B. Morais, G. Blaney, Effect of heating rate on the crack formation during baking in carbon anodes used in aluminum industry, Light metals, (2014), 1175-1180.

[3] R. A. Ketcham, W. D. Carlson, Acquisition, optimization and interpretation of X-ray

computed tomographic imagery: applications to the geosciences, Computers & Geosciences, (2001) 381-400.

[4] F. Mees , R. Swennen, M. V. Geet, P. Jacobs, Applications of X-ray computed tomography in the geosciences, Geological Society, London, Special Publications, (2003), 1-6.

[5] A. N. Adams, O. Karacan, A. Grader, J. P. Mathews, P. M. Halleck, H. H. Schobert, The non-destructive 3-D characterization of pre-baked carbon anodes using x-ray computerized tomography, Light Metals, The Minerals, Metals and Materials Society, (2002), 535-539.

[6] W. K. Fischer et F. Keller, Baking parameters and the resulting anode quality, Light Metals 1993, Essential readings in Light Metals (2013), 427-433.

Pore engineering of copper foams made by space holder technique through XMCT characterization

A.M.Parvanian[1], M.Saadatfar*[2], M.H.Shahzeydi[3], M.Panjepour[4]

[1] Department of Materials Engineering, Isfahan University of Technology, 84156-83111 Isfahan, Iran – a.parvanian@ma.iut.ac.ir
[2] Research School of Physics and Engineering, The Australian National University, Canberra 0200, Australia – mos110@physics.anu.edu.au
[3] Department of Materials Engineering, Isfahan University of Technology, 84156-83111 Isfahan, Iran – mh.shahzeydi@ma.iut.ac.ir
[4] Department of Materials Engineering, Isfahan University of Technology, 84156-83111 Isfahan, Iran – panjepour@cc.iut.ac.ir
* presenting author

Keywords: metallic foams, powder metrallurgy, Lost Carbonate Sintering (LCS), tomography

Abstract

Metallic foams belong to a class of highly porous materials known for their high stiffness combined with a very low specific weight. Their unique mechanical, acoustic, thermal, electrical and transport properties renders them ideal for high performance applications. These properties are primarily affected by their structural and geometrical features such as porosity percent, pore size distribution and pore shape. In this study, utilizing X-ray micro-CT (XCT), we explore the effect of powder metallurgical (PM) method, which uses sacrificial materials as a pore forming agent on the geometrical and mechanical properties of the porous metallic materials. We used lost carbonate sintering (LCS) technique to manufacture Copper foams with different process parameters namely the volume fraction and particle size of the potassium carbonate as the sacrificial agent. XCT results combined with advanced image processing reveals excellent correlations between the shape, size and volume percentage of the foam structure with the space holding agents used in PM process. We show that physio-mechanical properties of the copper foams made through PM space holder technique can be largely controlled and engineered for a specific application.

Introduction

Porous metallic materials have found industrial applications during the past two decades due to their unique mechanical, acoustic, thermal, electrical, and chemical properties. These special materials have low density, good specific strength, high impact energy absorption, excellent sound dampening and high thermal conductivity. Based on the connectivity of cells, porosity in metallic foams is divided into two groups of closed and open pores. The closed-pore metallic foams have higher moduli and strength; therefore, they are suitable for structural applications such as energy absorption. The open-pore metallic foams are multi-functional, especially for mass and heat transfer applications. Therefore, open-pore metallic foams have wider applications in functional structures [1-5].

In spite of the availability of numerous methods for the production of porous metals, only a handful are able to manufacturing open-cell foams with desired target structural and specific geometry [3]. One of the latest and most widely used methods is powder metallurgical (PM) process, which is based on using space holder agents. Until recently metallic foams have been produced by a variety of space holder materials such as organic [4, 6], inorganic [7], ceramic [8] and metallic hollow spheres [9]. The main factors that determine the physical and mechanical properties of metallic foams are the intrinsic properties of the space holder particles. For instance, volume fraction, shape, and particle size of the space holders affect the foam's structural features such as porosity percentage and cell distribution, cell shapes and sizes of the foams.. Nemours research have been dedicated to understanding the role that to these factors play in determining the foam's physical properties [6, 7, 10-12]. Some of these researches have also led to the

development of new techniques for metallic foam production [10, 13] such as Lost Carbonate Sintering (LCS) method patented by Zhao et al. [10]. In this method, highly porous open-pore copper foams have been produced by potassium carbonate space holder. The capability of this method in controlling the size, and distribution has not yet been studied. A full understanding of foam's structural and geometrical characteristics requires a full body three-dimensional 3D investigation of the foams. High-resolution X-ray Computed Tomography (XCT) or MRI techniques have been used to study porous structures in recent years [14, 15]. Here we combine XCT imaging with accurate foam production methodology to show the ability of LCS method in controlling important structural and mechanical properties of copper foams.

Methods

Foam production method

The LCS method, patented by Zhao et al. [10], was employed to produce open-pore copper foams. As raw materials, pure copper powder (99.9% purity) with a particle size of <45 μm for matrix phase. Commercial purity potassium carbonate powder was also provided in different sizes as space holder agent. According to the ASTM standard of mesh numbers, the potassium carbonate powder was divided into three different powder sizes of -20+30 mesh, -30+40 mesh, and -40+50 mesh represented as 30, 40, and 50 respectively. In order to enhance the strength of foam products [3], Cu powder was ball milled at 350 rpm with ball per powder (BPP) ratio of 5 about 5 hours. The typical morphologies of raw materials are shown in Fig. 1.

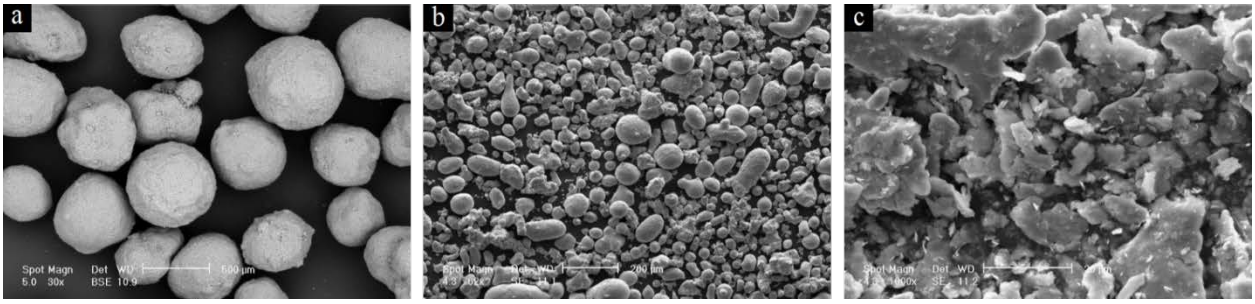

Figure 1: SEM micrographs of: a) potassium carbonate powder, b) as-received Cu powder, c) ball-milled Cu powder.

To produce the foams, first, the Copper and potassium carbonate powders were blended in proper volume fraction of K_2CO_3. Then 30×30 mm^2 green bodies were produced under 250 MPa axial loading. The green bodies were sintered at 850 °C for 4 hours and then were heated at 1000 °C for 4 hours in an electric furnace with an inert atmosphere to decompose potassium carbonate particles. Finally, the products were slowly cooled to room temperature. The experimental foam synthesis procedure is detailed elsewhere [3]. A code in the form of Mxxyy was assigned to each foam samples where xx represents the vol.% of K_2CO_3 and yy demonstrates the K_2CO_3 powder mesh number.

Characterization

Detailed 2D morphology of the powders were obtained by Scanning Electron Microscopy (SEM)[1] was used. Further, we utilized X-Ray Computed Tomography (XCT) to study the microstructural features of the foam samples in 3D with a spatial resolution (voxel size) of 8.1 μm. To study the distribution of

[1] Seron Technology model 550i

porosity in foams, tomographic images were sectioned in x, y, and z direction and were analyzed by a commercial image analysis software[2].

Result and discussion

Table 1 lists some of the microstructural and physical features of the foam samples obtained through XCT characterization. This table shows a slight difference between the total porosity of the samples (ε_t) and the volume fraction of the space holder agent ($f^*_{K_2CO_3}$). This is due to the competition between two phenomena: (i) the generation of micro-pores in the foams' structure as a result of protruding of carbonate decomposition products, which results in an increase of the porosity percentage, and (ii) the volumetric shrinkage due to densification of hollow structure while drainage of carbonate decomposition products occurs. For instance, Figure 2 shows the 3D tomograms of sample M7030. As seen in this figure, porosity of the foams can be divided into two categories of macro and micro pores. The latter is responsible for open pore cell structure and the connection between macro pores. These micro pores are located in the cell walls as shown by dotted and full arrows respectively. Consequently these micro-cracks are responsible for the increase of the foams' total porosity percentage.

Table 1: Some microstructural and physical properties of produced foams by LCS method

Sample code	vol% of potassium carbonate ($f_{K_2CO_3}$ =)	Total porosity (ε_t)	$\Delta\ (\varepsilon_t - f^*_{K_2CO_3})$	Potassium carbonate particle size (μm)	Pore size (μm)
M6030	60	62.1	2.1	585-841	669.4±15
M6040	60	63.8	3.8	420-595	505.5±175
M6050	60	62.8	2.8	297-420	426.2±162
M7030	70	70.4	0.4	585-841	674.4±216
M7040	70	73.6	3.6	420-595	540.8±244
M7050	70	67.5	-2.5	297-420	411.2±172
M8030	80	79.3	-0.7	585-841	658±26
M8040	80	77.8	-2.2	420-595	497±193
M8050	80	79.2	-0.8	297-420	408.2±122

$f_{K_2CO_3}$ = Potassium carbonate volume fraction in powder mixture.

Table 1 also indicates that the difference between measured total porosity percentage and the carbonate volume fraction is not significant implying that the LCS method is able to control the porosity percentage of the foams. Similar results can be obtained by comparing the pore size of the foams and the potassium carbonate particle size, which shows that the LCS method is also capable of controlling the pore sizes of the final foam products.

[2] Clemex Technologies Inco v. 2015

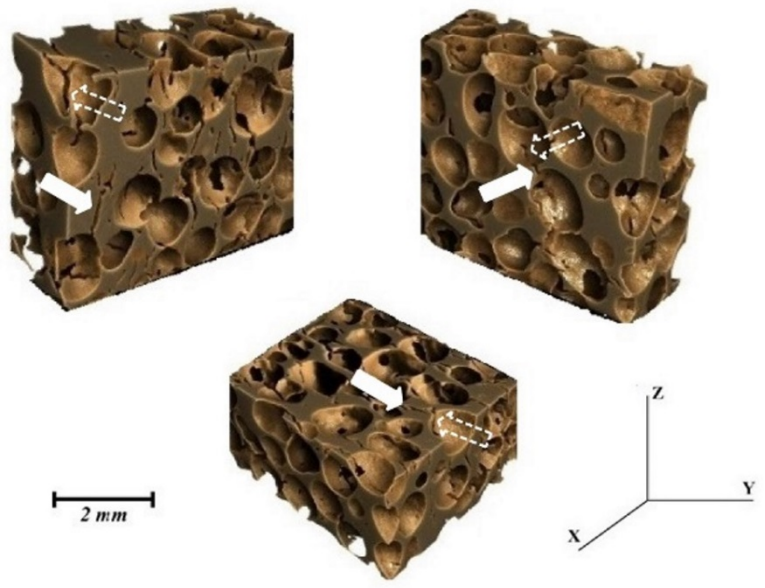

Figure 2: 3D rendering of the tomogram of sample M7030 illustrating different micro-pores shown as dotted (cell wall ones) and full (strut ones) arrows.

Figure 2 shows that macro pores have a spherical shape similar to that of potassium carbonate particles used as raw materials. Conversely the LCS method can control the shape of pores in addition to their size and percentage. Figure 3 shows the result of porosity measurement of sectioned planes of M6040 and M8030 tomograms in x, y, and z directions and the distance from the sample surface.

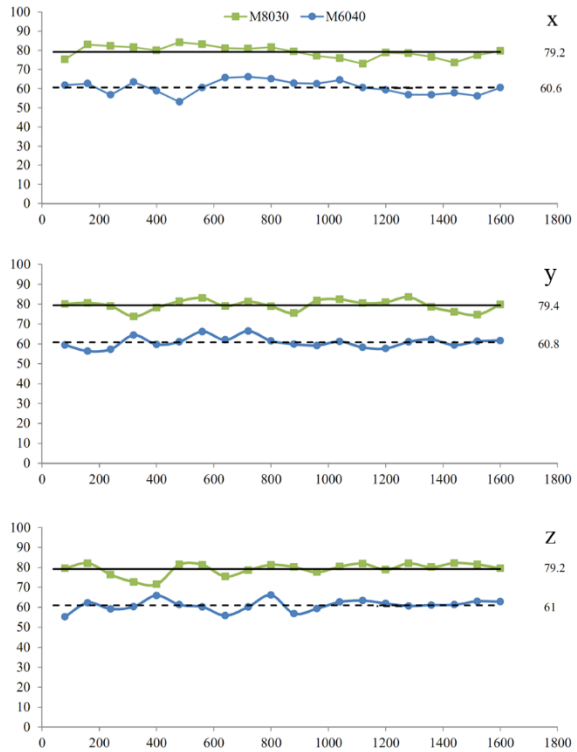

Figure 3: Porosity percentage of the sectioned planes of the M6040 and M8030 foam tomograms in x, y, and z directions.

Figure 3 implies that the average surface porosity percent in parallel planes has a good agreement with the volume fraction of potassium carbonate in the samples. Also we observe around 10% fluctuation in the porosity distribution between planes across the samples be observed. The amount of this fluctuations is strongly dependent on the homogeneity of the Cu-K_2CO_3 initial mixture.

Conclusions

In this paper, production of open-pore Copper foams by Lost Carbonate Sintering (LCS) method using potassium carbonate as space holder agent was investigated. 3D characterization of foam samples was performed using X-Ray micro-computed tomography (XCT) and advanced 3D image analysis methods to study the effect of LCS on the properties of metallic foam products. The main conclusions can be summarized as follows:

1. The LCS method has is fully capable of controlling the porosity of the produced foams including size distribution and shape of pores.

2. The porosity distribution in foam's structure produced by the LCS method is heterogeneous. The fluctuations in porosity distribution across different cross sections of the foam samples can be up to 10%.

Our results show that the LCS method is fully capable to produce porous metallic foams for specific applications.

References

1. Banhart J. (2001). Manufacture, characterization and application of cellular metals and metal foams. ***J. Progress in Materials Science*** 46, 559-632.
2. Ashby M. F. & Evans A. & Fleck N. A. & Gibson L. J. & Hutchinson J. W. & Wadley H. N. G. (2000). *Metal foams: a design guide.* Butterworth-heinemann, Woburn press, 251 p.
3. Parvanian A.M. & Panjepour M. (2013). Mechanical behavior improvement of open-pore copper foams synthesized through space holder technique. ***J. Materials and Design*** 49, 834-841.
4. Jiang B. & Zhao N.Q. & Shi C.S. & Du X.W. & Li J.J. & Man H.C. (2005). A novel method for making open cell aluminum foams by powder sintering process. ***J. Materials Letters*** 59, 3333-3336.
5. Zhao Y.Y. & Fusheng H. & Thomas F. (2004). Optimisation of compaction and liquid-state sintering in sintering and dissolution process for manufacturing Al foams. ***J. Materials Science and Engineering*** 364, 117-125.
6. Hassani A. & Habibolahzadeh A. & Bafti H. (2012). Production of graded aluminum foams via powder space holder technique. ***J. Materials and Design*** 40, 510-515.
7. Surace R. & De Filippis L.A.C. & Ludovico A.D. & Boghetich G. (2009). Influence of processing parameters on aluminium foam produced by space holder technique. ***J. Materials and Design*** 30, 1878-1885.
8. Mondal D.P. & Majumder J.D. & Jha N. & Badkul A. & Das S. & Patel A. & Gupta G. (2012). Titanium-cenosphere syntactic foam made through powder metallurgy route. ***J. Materials and Design*** 34, 82-89.
9. Neville B.P. & Rabiei A. (2008). Composite metal foams processed through powder metallurgy. ***J. Materials and Design*** 29, 388-396.
10. Zhao Y.Y. & Fung T. & Zhang L.P. & Zhang F.L. (2005). Lost carbonate sintering process for manufacturing metal foams, ***J. Scripta Materialia***, 52, 295-298.
11. Bafti H. & Habibolahzadeh A. (2010). Production of aluminum foam by spherical carbamide space holder technique-processing parameters. ***J. Materials and Design*** 31, 4122-4129.
12. Wang Q.Z. & Cui C.X. & Liu S.J. & Zhao L.C. (2010). Open-celled porous Cu prepared by replication of NaCl space-holders. ***J. Materials Science and Engineering*** 528, 1275-1278.
13. Zhao Y.Y. & Sun D.X. (2001). A novel sintering-dissolution process for manufacturing Al foams. ***J. Scripta Materialia*** 44, 105-110.
14. Saadatfar M. & Garcia-Moreno F. & Hutzler S. & Sheppard A.P. & Knackstedt M.A. & Banhart J. & Weaire D. (2009). Imaging of metallic foams using X-ray micro-CT. ***J. Colloids and Surfaces A: Physicochemical and Engineering Aspects*** 344, 107-112.
15. Saadatfar M. & Mukherjee M. & Madadi M. & Schroder-Turk G.E. & Garcia-Moreno F. & Schaller F.M. & Hutzler S. & Sheppard A.P. & Banhart J. & Ramamurty U. (2012). Structure and deformation correlation of closed-cell aluminium foam subject to uniaxial compression. ***J. Acta Materialia*** 60, 3604–3615.

Analysis of coupled electrochemical-mechanical phenomena in Li-ion batteries through 4D X-ray tomography

J.M. PAZ-GARCIA[1], O.O. TAIWO[2], *S.A. HALL[1,3], P.R. SHEARING[2], R. MOKSO[4]

[1] Division of Solid Mechanics, Lund University, Lund Sweden
[2] Electrochemical Innovation Laboratory, Dept. Chemical Engineering, University College London, UK
[3] European Spallation Source AB, Lund, Sweden
[4] Swiss Light Source, Paul Scherrer Institut, CH-5232 Villigen, Switzerland
* presenting author

Lithium-ion batteries (LIBs) have widespread application in portable electronic devices and are of significant interest in automotive and grid storage applications. There is thus significant research interest in the development of new generations of advanced LIBs with higher energy-densities. For example, alloying silicon anodes are promising electrodes with theoretical energy density up to ~ 4200 mAh/g against the ~ 375 mAh/g of graphite, which is still the most common anode material in commercial batteries. Silicon electrodes, however, have the drawback of exhibiting drastic volume changes during the lithiation/delithiation processes (~ 310 % against the ~ 10 % of graphite). Volume changes within a battery's constrained case involve mechanical strains on the fundamental components of the material, which eventually causes the battery to fail.

Electrochemical reactions in LIBs are supported by porous electrode materials, the microstructure of which affects the capacity, charging behaviour, durability and lifetime of a cell. Microstructural evolution that occurs in these electrodes affects a battery's electrochemical performance, but these relationships are poorly understood. Non-destructive 3D X-ray imaging techniques are of significant interest for the study of these coupled electrochemical and mechanical phenomena, as they allow the visualization of the evolution of the microstructure properties during cycles of charge/discharge. In this work, results from in-operandi testing (i.e., simultaneous tomographic imaging and electrochemical testing) of silicon-based LIB cells with synchrotron x-ray tomography (at the TOMCAT beamline of the Swiss Light Source, PSI) supported by additional imaging with ex-situ charge/discharge using laboratory x-ray tomography (Xradia MicroXCT-520 at the 4D-Imaging Lab, Lund University) will be presented. For these experiments, custom-made x-ray transparent, functional Si–Li cells have been assembled to enable *in situ* and *in operandi* experiments. Observed microstructural volume changes have quantified using full 3D strain/deformation measurements from digital volume correlation (DVC) analysis. The lithiation of the silicon, based on clear changes in the x-ray attenuation, is also quantified along with analysis of the changes in the granular structure due to the lithiation-induced swelling of the silicon grains. Finally these changes are related to changes in the electrochemistry of the cells.

Number of words: 334

$BaTiO_3$-based composite materials for Electronics characterized by X-ray computed tomography

C. TENAILLEAU*[1], S. DUPUIS[1], P. DUFOUR[1], B. DUPLOYER[1], S. GUILLEMET-FRITSCH[1]

[1] CIRIMAT, UMR - CNRS 5085, Université de Toulouse, 118 route de Narbonne, 31062 Toulouse Cedex 9, Fr

Keywords: Composite, Barium titanate $BaTiO_3$, Spark Plasma Sintering SPS, colossal permittivity, X-ray computed tomography XCT

Abstract

Dense $BaTiO_3$-based composite ceramics containing either nickel (metal) or alumina (insulator) inclusions were prepared by Spark Plasma Sintering. The influence of the particle quantity and distribution over the dielectric properties was studied in detail. X-ray computed tomography (XCT) showed a random distribution of the particle inclusions in the $BaTiO_3$ matrix. The preparion of $BaTiO_3$-Ni composite materials with top and bottom layers of pure $BaTiO_3$ was made possible thanks to SPS and contribute to increase considerably the permittivity while strongly reducing the losses, for a same amount of Ni inclusions. In the case of the $BaTiO_3$-Al_2O_3 composite materials, a small amount of the insulating phase drives to the best dielectric properties. XCT shows also that alumina nanopowders formed spherical microparticles which are well distributed thourghout the whole $BaTiO_3$ matrix.

Introduction

Barium titanate ($BaTiO_3$) is a well-known material for its excellent dielectric ($\varepsilon \sim 3500$) and piezoelectric properties (190 pC/N), which makes it essential for various electronic applications such as thermistors and capacitors. The high relative permittivity and low dielectric losses are the main targets for the materials to be used in microelectronics allowing device miniaturization. The relative permittivity of $BaTiO_3$ can be varied in the range of 4000–6000 depending on the grain size of the sintered ceramic, and the maximum relative permittivity can be typically achieved at the grain size of about 1 μm when sintered through conventional sintering methods.

However, we recently reported that abnormally colossal relative permittivity ($\varepsilon \sim 10^4$–10^5) can be induced in the synthesized nano-crystalline (250 nm) $BaTiO_3$ ceramic using starting nano-crystalline $BaTiO_3$ powder and spark plasma sintering (SPS) technique.[1] SPS is a fast sintering technique that allows for the densification of ceramics while maintaining small grain size due to the short sintering time and relatively low sintering temperatures used. A number of investigations have reported dielectric properties of SPS $BaTiO_3$ ceramics.[1-4] Sr-doped $BaTiO_3$ ceramics exhibit stabilized dielectric constants over a wider range of temperatures and frequencies, though the permittivity value is decreased compared to pure $BaTiO_3$ ceramics, while the dielectric losses are improved.[5] High relative permittivity has also been found in a number of ceramics and composites such as $CaCu_3Ti_4O_{12}$ (CCTO), $Ba(Zr_{0.2}Ti_{0.8})O_3$-carbon nanotube, and $BaTiO_3$-Ni particle composites…

3D mapping of anisotropic ferroelectric/dielectric composites with $Ba_{0.6}Sr_{0.4}TiO_3$ ferroelectric matrix, in which MgO inclusions were spread, was very recently performed with a synchrotron source.[6] Beyond an accumulation of properties due to the mixture of two different materials, there is a real composite effect that modifies the electronic properties. Thanks to the specific conditions of SPS, it is possible to produce inclusions with a large aspect ratio (ellipsoid) while preserving the chemical integrity of both phases.

This is the first step towards realistic mapping of a possible electric field focusing that would fit with the available empirical models. The 3D anisotropy enhanced by the increase of the SPS pressure affects the electric field redistribution between the two phases and appears to be an efficient way to reduce the dielectric permittivity while maintaining electric field tunability. We here present, for the first time to our knowledge, a systematic study of $BaTiO_3$-based composites microstructures observed by laboratory X-ray Computed Tomography (XCT) in relationships with their dielectric properties.

Methods

Powder Synthesis and Spark Plasma Sintering

$BaTiO_3$ powders were synthesized by an oxalate coprecipitation route following our optimized process.[1] Briefly, $BaCl_2.2H_2O$ (Prolabo) and $TiOCl_2$ (Cristal) were used as precursors. The precursors were weighted in appropriate proportions to control the powder stoichiometry, dissolved in water and added to an ethanolic oxalic acid solution. The solution was stirred and aged for 5 h, then centrifuged and dried overnight at 80°C. The oxide powders were obtained after calcination at 850°C for 4 h in static air. Nickel powder (Acros Organics, 99.9%) or alumina nanopowder (Tamei Chemical, 99.99%) was intimately mixed with the $BaTiO_3$ nanopowder in a mortar for 5 minutes before SPS.

To densify the $BaTiO_3$-based composites, SPS was carried out using a Dr. Sinter 2080 device from Sumitomo Coal Mining, Japan. Briefly, 0.5 g of each batch was loaded in an 8-mm-inner-diameter graphite die. A sheet of graphite paper was inserted between the punch and the powder as well as between the die and the powder for easy removal of the pellet after sintering. Powders were sintered in vacuum (residual cell pressure < 10 Pa). A pulse pattern of twelve current pulses periods followed by two periods of zero current was used. A heating rate of 25°C/min was used from 600 to 1150°C, where a 3-min dwell time at the sintering temperature was applied. An optical pyrometer focused on a small hole at the surface of the die was used to measure and monitor the temperature. An uniaxial pressure of 75 MPa was applied for 2 min before reaching the dwell temperature. After the 3-min dwell, the electric current was switched off and the pressure was released. In situ dilatometry-based shrinkage curves for the different powders were recorded during the sintering process. The as-sintered pellets presented a thin carbon layer due to graphite contamination from the graphite sheets. This layer was removed by polishing the surface. The presence of residual carbon due to SPS processing technique was determined through the spectrometric quantification of CO_2 and appeared to be very low with a concentration of 93 ppm.[1] Samples appeared dark blue, consistent with the presence of Ti^{3+} caused by the reducing atmosphere used during SPS (low vacuum and carbon environment). SPS pellets were finally annealed 15 minutes at 850 °C in oxidizing atmosphere in an attempt to partially restore the oxygen stoichiometry and reduce considerably the losses ($tg\ \delta < 0.5$).

Material Characterization

The chemical composition of the oxide powder was determined using inductively coupled plasma–atomic emission spectroscopy (ICP-AES) with a JY 2000 device (Horiba Jobin Yvon, Kyoto, Japan). The morphology of the powders was characterized with a field emission gun scanning electron microscope (FEG-SEM, JSM 6700F, JEOL, Tokyo, Japan). The crystalline structure was investigated by X-ray diffraction analysis using a D4 Endeavor X-ray diffractometer ($CuK\alpha1$ = 0.154056 nm and $CuK\alpha2$ = 0.154044 nm; Bruker AXS, Karlsruhe, Germany) from 20° to 80° (2-theta). The density of the pellets was determined by the Archimedes method using an ARJ 220-4M balance (KERN, Murnau-Westried, Germany). Prior to electrical measurements, the ceramic disks were coated with thin gold electrodes (thickness ~ 30 nm) by sputtering (108 Auto, Cressington Scientific

Instruments, Watford, U.K.). The relative permittivity and the dielectric losses were obtained from impedance measurements using a 4294A Precision Impedance Analyzer (Agilent Technologies, Palo Alto, CA) in the range of 40 Hz to 100 kHz at room temperature and an applied ac voltage of 1 V.

Multi-dimension microstructural characterizations were carried out using X-ray Computed tomography with a Phoenix/GE Nanotom 180 apparatus, using the W target, Mode 0 and a 100 µm Cu filter with U = 120kV and I = 100 µA (FOD and FDD = 6 and 250 mm, respectively; 1.2µm/voxel). A timing of 1000 ms was used for the data acquisition with 10 images averaged per step while the first two were skipped to avoid image reminiscence after each rotation and a total of 1440 images were recorded. Typically, X-ray tomography was performed on a few mm^3 of sample.

Results

$BaTiO_3$-Ni composites

XRD measurements show that dense $BaTiO_3$-Ni composites are pure after SPS treatment. Some nickel is transformed to NiO after the short pellet oxidation step which is though necessary to obtain the capacitor properties (with low losses) related to the oxygen vacancies and number of Ti^{3+} present in our $BaTiO_3$ (BTO) materials. We also sintered dense ceramics of $BaTiO_3$-Ni composites surrounded by pure $BaTiO_3$ top and bottom layers (BTO/BTO+Ni/BTO) with SPS to avoid Ni oxidation. Then, for 5wt% Ni in $BaTiO_3$, the former composite material shows a dielectric constant of 332000 and losses of 0.36 while the latter (BTO/BTO+Ni/BTO) exhibits a permittivity of 914000 and losses about 5 times less (tg δ = 0.08), while ε_r = 696000 and tg δ = 0.07 for pure $BaTiO_3$.

Figure 1. shows XCT images obtained on $BaTiO_3$-5wt%Ni composites. While Ni particles diameters can strongly vary, these are randomly distributed inside the $BaTiO_3$

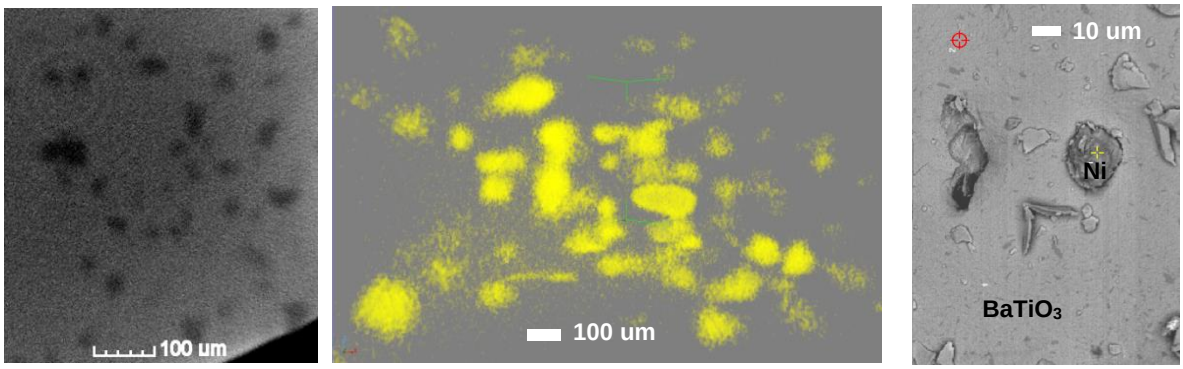

Fig. 1. *XCT 2D (left) and 3D (middle) images of $BaTiO_3$-Ni composites dense ceramics prepared by SPS. BSE (right) image of the material for comparison.*

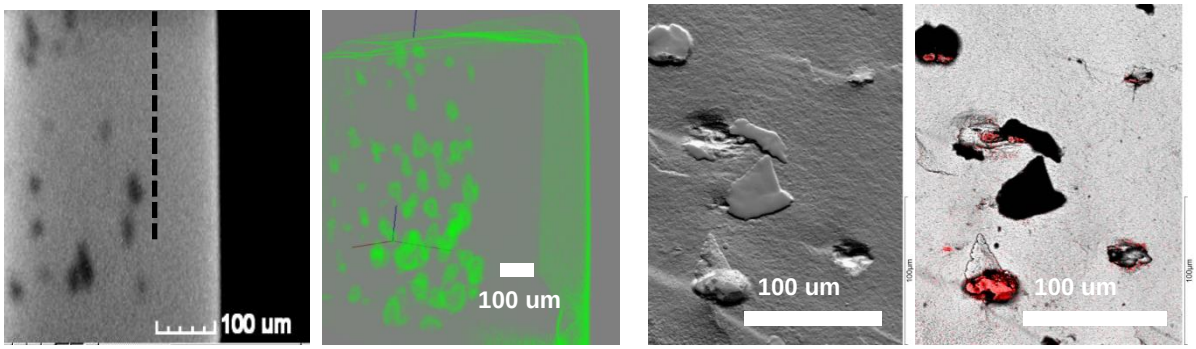

Fig. 2. *XCT 2D (left) and 3D (middle) images of (BTO/BTO+Ni/BTO) composites dense ceramics prepared by SPS. SEM and BSE (right) images of the material for comparison.*

matrix and can act as small accelerator charge conduction. Figure 2 shows similar distributions in the (BTO/BTO+5wt%Ni/BTO) composite but smaller Ni particles in average, probably due to the top and bottom layers constraints. Pure $BaTiO_3$ and the composite mixture are clearly distinguished evidencing for no phase diffusion that could have occurred during the SPS processing. No lamination is observed at the phase separation and the sample densification remains really high (D> 98%).

$BaTiO_3$-Alumina composites

Alumina is a very well known material mainly for its strong mechanical resistance and insulating properties. Dense $BaTiO_3$-Al_2O_3 composites were also prepared by SPS. Increasing the quantity of alumina particles in the $BaTiO_3$ matrix contributes to decrease the permittivity value and increase the losses. The highest permittivity value is obtained for 2wt% Al_2O_3 with ε_r = 340000 (tg δ = 0.04) in comparison with ε_r = 248000 (tg δ = 0.05) and ε = 20000 (tg δ = 0.08) for 4wt% and 20wt% Al_2O_3, respectively. Note that two other phases ($BaAl_2O_4$ and $Ba_4Al_2Ti_{10}O_{27}$) are observed by XRD for the alumina-rich sample. Figure 3 shows XCT images of the 4wt% and 20wt% Al_2O_3 mixed with $BaTiO_3$ nanopowders. While alumina nanopowders (diam. ~ 140 nm) were mixed with our barium titanate material, XCT clearly shows some microparticles that demonstrate that alumina nanopowder aggregates during the sample preparation. The particles are symmetrical with the biggest populations being ~ 50um in diameter, though much smaller particles of a few microns (in the observation limits of the microtomograph instrument). The random particle distribution insure a good efficiency in the capacitive properties of the ceramics. Meanwhile, a stron proportion of alumina in $BaTiO_3$ leads to a loss of the main physical characteristics of the dielectric material.

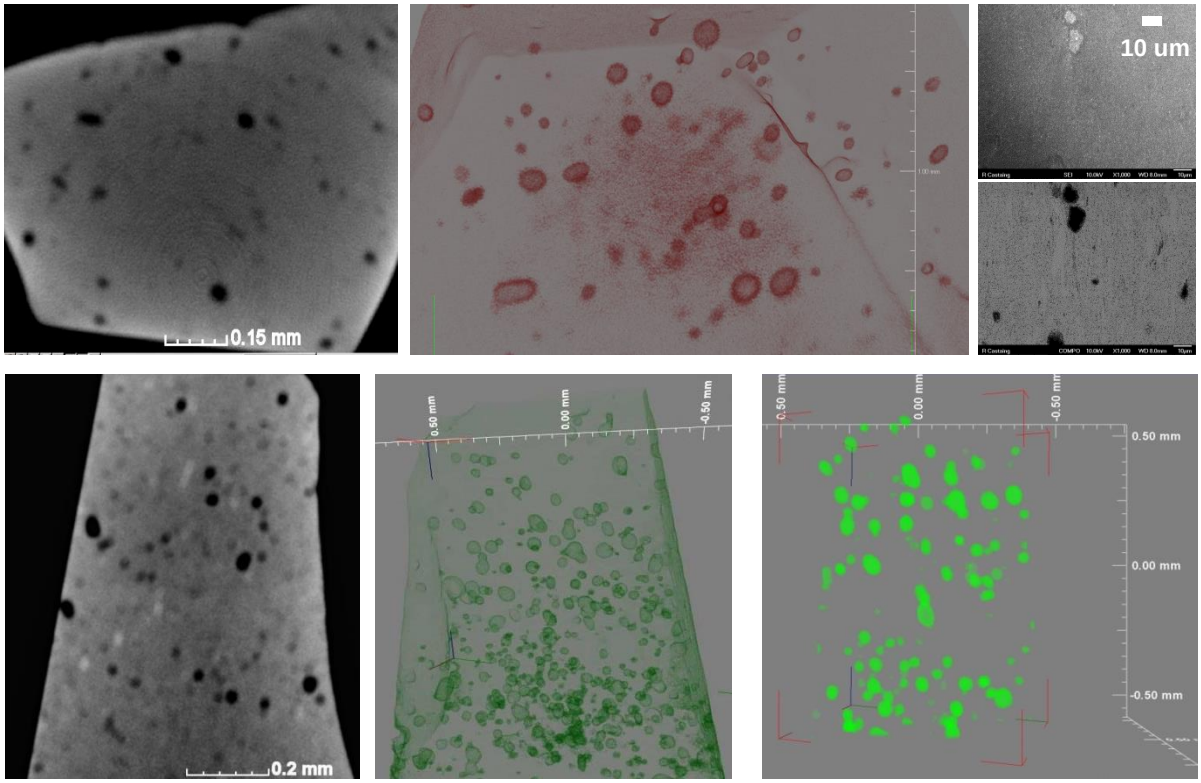

Fig. 3. *XCT 2D and 3D images of 4wt% (top) and 20wt% (bottom) Al_2O_3 mixed $BaTiO_3$ composite dense ceramics sintered by SPS. SEM and BSE (top right) images for the former material are shown for comparison.*

Conclusion

$BaTiO_3$-(Ni metal) and $BaTiO_3$-(Al_2O_3 insulator) composites were synthesized and sintered by the SPS technique. The inclusions shape, size and distribution was determined by XCT. Their influence over the materials dielectric properties were discussed. While Ni inclusions in $BaTiO_3$ shows high losses, the presence of pure $BaTiO_3$ surrounding the $BaTiO_3$-Ni composite layer tends to strongly increase the material dielectric properties. In the $BaTiO_3$-Al_2O_3 composite, spherical particles are homogeneously distributed in the $BaTiO_3$ matrix, though their size can vary from a few microns to a few dozens of microns. A small amount of alumina inclusions (less than 5wt%) is required for the composite material to exhibit interesting properties for industrial applications.

Acknowledgements

The French FERMaT Midi-Pyrénées Federation FR3089 is acknowledged for providing the X-ray tomography laboratory facility.

References

[1] S. Guillemet-Fritsch, Z. Valdez-Nava, C. Tenailleau, T. Lebey, B. Durand, J. Y. Chane-Ching, *Adv. Mater.* 20, 551 (2008).
[2] T. Takeuchi, C. Capiglia, N. Balakrishnan, Y. Takeda, H. Kageyama, *J. Mater. Res.* 17, 575 (2002).
[3] M. T. Buscaglia, V. Buscaglia, M. Viviani, J. Petzelt, M. Savinov,L. Mitoseriu, A. Testino, P. Nanni, C. Harnagea, Z. Zhao, M. Nygren, *Nanotech.* 15, 1113 (2004).
[4] B. R. Li, X. H. Wang, M. M. Cai, L. F. Hao, L. T. Li, *Mater. Chem. Phys*. 82, 173 (2003).
[5] C. Fu, C. Yang, H. Chen, Y. Wang and L. Hu, *Mater. Sci. Eng. B*, 119, 185–188 (2005).
[6] J. Lesseur, D. Bernarda, U.-C. Chunga, C. Estournès, M. Maglione, C. Elissalde, *J. Europ. Ceram. Soc*., 35, 337 (2015).

Session 303

Oral presentation

In-situ study of wood hygro-mechanical behaviour by phase contrast X-ray tomography at cellular and sub-cellular scales

*A. PATERA[1,2], D. DEROME[3], J. CARMELIET[3,4], M. STAMPANONI[1,5]

[1] Swiss Light Source, Paul Scherrer Institute, Villigen, Switzerland
[2] Centre d'Imagerie BioMedicale, Ecole Polytechnique Federale de Lausanne, 1015 Lausanne, Switzerland
[3] Laboratory for Building Science and Technology, Swiss Federal Laboratories for Materials Science and Technology, EMPA, Dübendorf, Switzerland
[4] Chair of Building Physics, ETH Zurich, Switzerland
[5] Institute of Biomedical Engineering, University and ETH Zürich, Switzerland

* presenting author

Synchrotron radiation-based phase contrast X-ray tomographic microscopy at the Swiss Light Source, PSI Villigen in Switzerland (Stampanoni et al., 2006), is a powerful technique for studying the response of cellular materials to environmental stimuli. We report on softwood but the presented approach can be applied to other cellular materials. Wood is hygromorphic, thus it responds to changes in environmental humidity by changing its geometry. At the cellular scale, new findings in the anisotropic and reversible swelling behaviour of softwood and in the origin of swelling hysteresis in porous materials are explained from a mechanical perspective (Patera et al., 2013). A main conclusion is that the swelling anisotropy depends exponentially on the porosity. Wood tissues with higher porosity present a more anisotropic swelling behaviour compared with the less porous tissues. However, the anisotropy of wood tissues is importantly modified in restrained swelling experiments due to the lowering of swelling in the restraining direction. Further investigations on the swelling coefficients highlight that the cellular structure plays an important role on the hygro-mechanical behaviour of wood (Figure 1.a). With the mechanism of swelling identified, the occurrence of hysteresis of moisture content versus relative humidity is discussed. Hysteresis appears when swelling and moisture content are considered as a function of relative humidity, while it disappears when swelling is plotted versus moisture content. This shows the main origin of hysteresis to be due to sorption, thus leading to the conclusion that the same amount of moisture entering or exiting the cell wall material leads to the same swelling deformation of the cell material. Swelling due to moisture sorption displays also a non-affine component. The results highlight that the mechanical and moisture properties of wood highly depend on sub-cellular features of the wood cell wall. Phase contrast full-field nano-tomography exploits the possibility of capturing the moisture induced deformations in sub-cellular features of wood, such as bordered pits and middle lamella, with 50 nm pixel size and a field of view of 36×36 μm^2 in the horizontal and vertical directions. For these experiments, the total scanning time is of approximately 34 min. Local tomography is performed on toothpick-like pins wood specimens of 50×50 μm^2 and the scans are performed with an energy of 16 keV and no binning factor. High resolution and contrast allow an easy detection of the non-affine swelling deformations occurring in bordered pits of earlywood and the torus movement (which presents a thickness in the order of a few hundred nm) towards the pit surfaces. The middle lamella, obtained by focused ion beam (FIB) milling of an earlywood tissue with cross-sectional dimension equal to 1.3 μm and height of 13 μm, shows an isotropic swelling behaviour (Figure 1.b). The middle lamella is found to swell less than the S2 layer in the wood cell wall. Although the middle lamella shows an isotropic affine deformation behaviour, non-affine strains may occur locally, but more experimental evidence is required to study this phenomenon. Overall, this work presents an experimental approach which aims at bridging the gap from sub-cellular to macroscale in cellular materials.

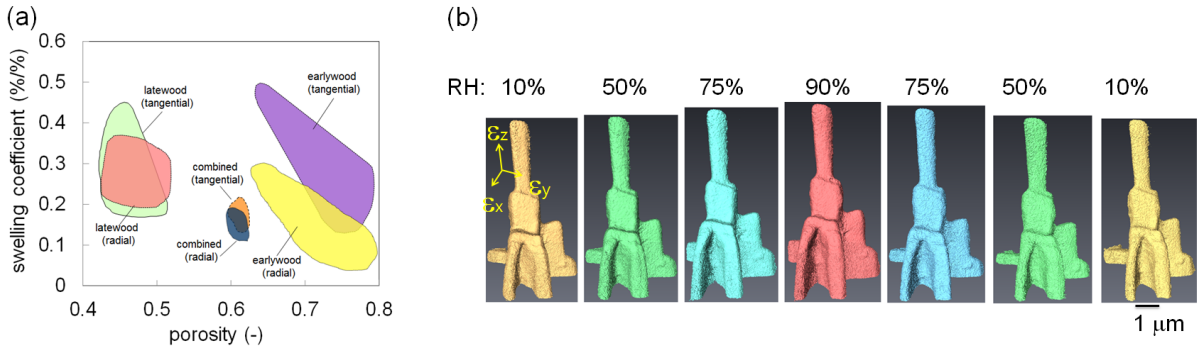

Figure 1: (a) Swelling coefficients of latewood and earlywood for different porosity. (b) Volume renderings of middle lamella in adsorption (10% - 50% - 75% - 90%) and in desorption (75% - 50% - 10%)

References:

Patera, A., Derome, D., Griffa, M., & Carmeliet, J. (2013). Hysteresis in swelling and in sorption of wood tissue. Journal of Structural Biology, 182(3), 226–234. doi:10.1016/j.jsb.2013.03.003

Stampanoni, M., Groso, A., Isenegger, A., Mikuljan, G., Chen, Q., Bertrand A., Henein S., Betemps R., Frommherz U., Böhler P., Meister D., Lange M., Abela, R. (2006). Trends in synchrotron-based tomographic imaging: the SLS experience. Proc. S PIE 6318, Developments in X-Ray Tomography V, 63180M. doi:10.1117/12.679497

Non-destructive research on wooden musical instruments: from macroscale to submicron imaging with lab-based XCT systems

*J. VAN DEN BULCKE[1], D. VAN LOO[2,3], M. DIERICK[2,3], B. MASSCHAELE[2,3], M.N. BOONE[2], L. VAN HOOREBEKE[2], J. VAN ACKER[1]

[1] UGCT - Laboratory of Wood Technology, Department of Forest and Water Management, Faculty of Bioscience Engineering, Ghent University, Coupure Links 653, 9000 Gent, Belgium – Jan.VandenBulcke@UGent.be, Joris.VanAcker@UGent.be
[2] UGCT – Dept. Physics and Astronomy, Ghent University, Proeftuinstraat 86/N12, B-9000 Gent, Belgium
[3] XRE, X-Ray Engineering bvba, De Pintelaan 111, 9000 Gent, Belgium – Denis.VanLoo@xre.be, Manuel.Dierick@UGent.be, Bert.Masschaele@xre.be, Luc.VanHoorebeke@UGent.be

* presenting author

Keywords: wooden musical instruments, multi-scale imaging, UGCT

Abstract

X-ray CT scanning is growing of age as a research tool and of essential importance in many disciplines, which is certainly true for the study of wood, given its inherent hierarchical structure. The study of wooden musical instruments is even more challenging since these objects need to be handled with care such that non-destructive imaging is vital. Moreover, the different dimensions of the musical instruments as well as the interest in assessment of the instruments at different scales necessitates flexible scanning modes and equipment. In the framework of COST Action FP1302 WoodMusick, a set of wooden musical instruments has been scanned at UGCT and part of them have been analysed to illustrate the potential of X-ray CT scanning in this field of research. By combining different lab-based systems, a wide range of instruments can be scanned, of which examples are given in this paper for violin and standard recorder. Examples of analysis of board and wall thickness for these instruments are given as well.

Introduction

The use of X-ray CT in wood research has increased considerably during the last decade. Most researchers use commercially available desktop micro-CT scanners. The Ghent University Centre for X-ray Tomography (UGCT) however develops in-house open modular scanners for more experimental freedom, both for applied research in various fields as for research on tomography itself. UGCT is a collaboration between three research groups (physicists, geologists and bio-engineers) operating as an open user facility offering researchers from different fields access to the infrastructure and expertise [Dierick et al. 2014]. The different CT systems at UGCT allow scanning from submicron resolution of very small samples up to scanning of large objects at resolutions depending on sample size. Here we present the possibilities and opportunities of X-ray CT for research on wooden musical instruments using two particular scanners of UGCT: Nanowood and HECTOR.

Methods

Nanowood (Figure 1A) is a multi-resolution X-ray CT scanner,consisting of an 8-axis motorized stage with two X-ray tubes and two X-ray detectors and is specifically designed to obtain scans with a resolution of 0.2 mm for samples of maximum 37 cm in diameter and a maximal length of approximately 20-30 cm down to a resolution of

approximately 400nm for objects that have about the size of a splinter. Nanowood is dedicated to wood research sensu lato [Van den Bulcke et al. 2009, 2014].

The other scanner that is used is HECTOR (Figure 1B), the High Energy CT scanner Optimized for Research [Masschaele et al. 2013], and this scanner is built in collaboration with the spin-off company XRE (www.xre.be).

Both systems have a generic in-house developed CT scanner control software platform [Dierick et al. 2010] that allows full control of the scanner hardware. Reconstruction of the scans is performed with Octopus Reconstruction [Vlassenbroeck et al. 2007; www.insidematters.eu].

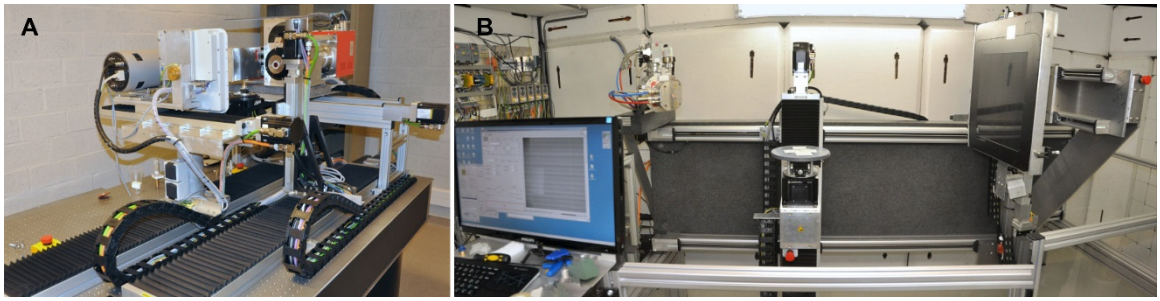

Fig. 1. *Nanowood (A) and HECTOR (B).*

Methods

Different musical instruments (standard recorder, violin, guitar, cello, etc) have been scanned with different acquisition modes (step and shoot, smooth, ROI, helical, tiled) and some of the instruments have been analysed (local thickness analysis, volume labelling, growth ring demarcation, etc). Figure 2 illustrates the 3D reconstruction of a violin and part of a standard recorder.

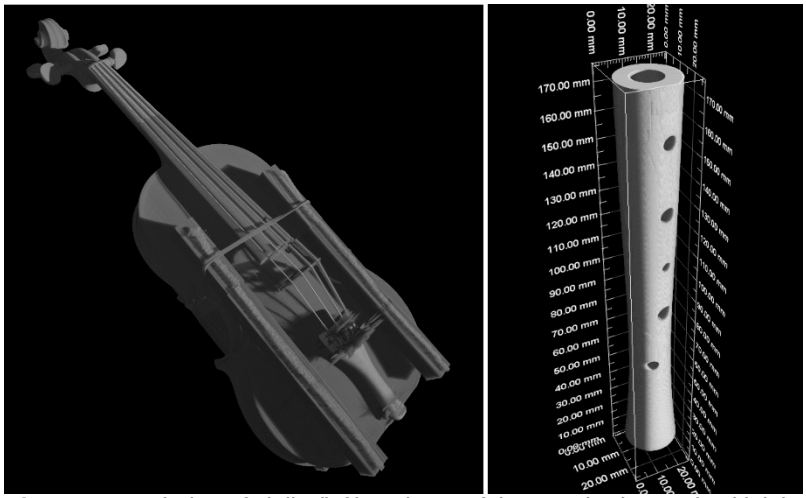

Fig. 2. *3D rendering of violin (left) and part of the standard recorder (right).*

Figure 3 illustrates thickness analysis on both violin and standard recorder.

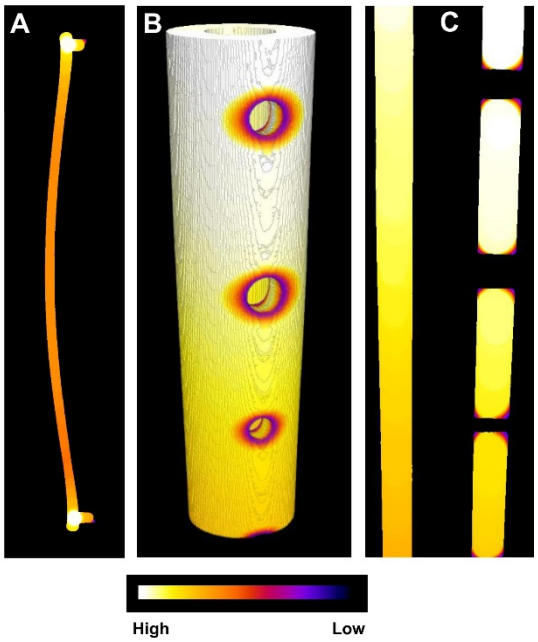

Fig. 3. *Thickness analysis on a cross-section of the violin (A) and on part of the standard recorder (B and C). Thickness colour scale at the bottom.*

Discussion

The fast evolving field of X-ray computed tomography and its broad employability make it one of the leading techniques for non-destructive visualization and quantification in many different research fields. The flexible Nanowood scanner offers a wide range of opportunities, with specific focus on helical and submicron scanning, yet large object size can be a limiting factor when studying wooden musical instruments. The HECTOR scanner [Masschaele et al. 2013] can be used to scan larger and heavier objects at high resolution and therefore complements the Nanowood scanner. By combination of both scanners a wide range of wooden musical instruments can be analysed for a large range of purposes such as general evaluation, glue line inspection, wood identification, coating inspection, growth ring analysis, etc.

Acknowledgements

The authors acknowledge the fruitful collaboration with all current and former team members of the UGCT, as well as the project SimForTree of IWT Flanders (Strategic Basic Research – SBO 060032) for financial support for obtaining the Nanowood equipment. The authors also acknowledge the financial support of the Flemish community through the Strategic Initiative Materials in Flanders, the special Research Fund of Ghent University and the Research Foundation – Flanders (FWO) for obtaining the HECTOR equipment.

References

Dierick M., Van Loo D., Masschaele B., Van den Bulcke J., Van Acker J., Cnudde V. & Van Hoorebeke L. (2014). Recent micro-CT scanner developments at UGCT. *Nuclear Instruments & Methods in Physics Research Section B-Beam Interactions with Materials and Atoms* 324: 35-40.

Van den Bulcke J., Boone M., Van Acker J., Stevens M. & Van Hoorebeke L. (2009). X-ray tomography as a tool for detailed anatomical analysis. *Annals of Forest Science* 66.

Van den Bulcke J., Wernersson E.L.G., Dierick M., Van Loo D., Masschaele B., Brabant L., Boone M., Van Hoorebeke L., Haneca K., Brun A., Luengo Hendriks, C.L. & Van Acker J. ((2014). 3D tree-ring analysis using helical X-ray tomography. *Dendrochronologia* 32, 1: 39-46.

Masschaele B., Dierick M., Van Loo D., Boone M.N., Brabant L., Pauwels E., Cnudde V., Van Hoorebeke L. (2013). HECTOR: A 240kV micro-CT setup optimized for research. *11th International Conference on X-Ray Microscopy (Xrm2012)* 463.

Dierick M., Van Loo D., Masschaele M., Boone M. & Van Hoorebeke L. (2010). A LabVIEW (R) based generic CT scanner control software platform. *Journal of X-Ray Science and Technology* 18: 451-461.

Vlassenbroeck J., Dierick M., Masschaele B., Cnudde V., Van Hoorebeke L. & Jacobs P. (2007). Software tools for quantification of X-ray microtomography. *Nuclear Instruments & Methods in Physics Research Section a-Accelerators Spectrometers Detectors and Associated Equipment* 580: 442-445.

Using X-ray microtomography to assess the vulnerability to drought-induced embolism in plants

N. LENOIR[1*], S. DELZON[2], E. BADEL[3], R. BURLETT[2], B. CHOAT[4], H. COCHARD[3], S. JANSEN[5], J.M. TORRES-RUIZE[2]

[1] PLACAMAT, UMS3626 CNRS-Univ. of Bordeaux, 87 av. Dr A. Schweitzer, 33600 Pessac (FRANCE)
[2] INRA, UMR BIOGECO, Talence, France
[3] INRA, UMR PIAF, Clermont-Ferrand, France
[4] University of Western Sydney, Sydney, Australia
[5] University of ULM, ULM, Germany
* presenting author

Keywords: Synchrotron, tomography, cavitation, plant xylem

Abstract

Introduction

Embolism resistance is a critically important trait for evaluating the ability of plants to survive and recover from drought periods and predicting future drought-induced forest decline. As current methods for measuring xylem embolism in trees are indirect and prone to artifacts, there is ongoing controversy over the capacity of plants to resist or recover from embolism. Indeed, the majority of techniques used to estimate cavitation resistance are indirect and/or invasive. Therefore, artifacts relating to invasive techniques are particularly relevant since xylem sap under tension is in a metastable state and may easily vaporizes as a result of disturbance. The debate will not end until we get direct visualization of vessel content. Recently, two distinct technologies have been employed to visualize xylem embolism in intact samples: Magnetic Resonance Imaging (MRI) and X-ray microtomography (micro-CT). MRI systems suffer from poor spatial resolution (20 µm at best) and limited access to the technology. Micro-CT, in contrast, offers a spatial resolution typically around 1 µm, which is more than enough to visualize the lumen content of xylem tracheids or vessels. Thus far, non-invasive imaging on intact plants has only been used to measure cavitation resistance in few species (*Vitis vinifera*, *Quercus* and *Populus*). Further measurement of cavitation resistance using non-invasive imaging on intact plants across a range of species is therefore a high priority.

Embolised and water filled conduits

Successful observations of water transport were made in a number of plant species by HRCT at different synchrotron in Europe (ESRF, DLS, SLS and SOLEIL). Experiments were directed towards establishing the degree to which the formation of gas emboli in xylem conduits impairs plant water transport with progressive drought. We evaluated vulnerability to embolism of several plant species. Synchrotron based microCT produced excellent visualization of xylem tissue in living, intact plants. The high quality of signal and contrast produced by synchrotron based microCT allowed the location and dimensions of both embolised and water filled conduits to be measured to a resolution of 1.62 µm (see Figure 1).

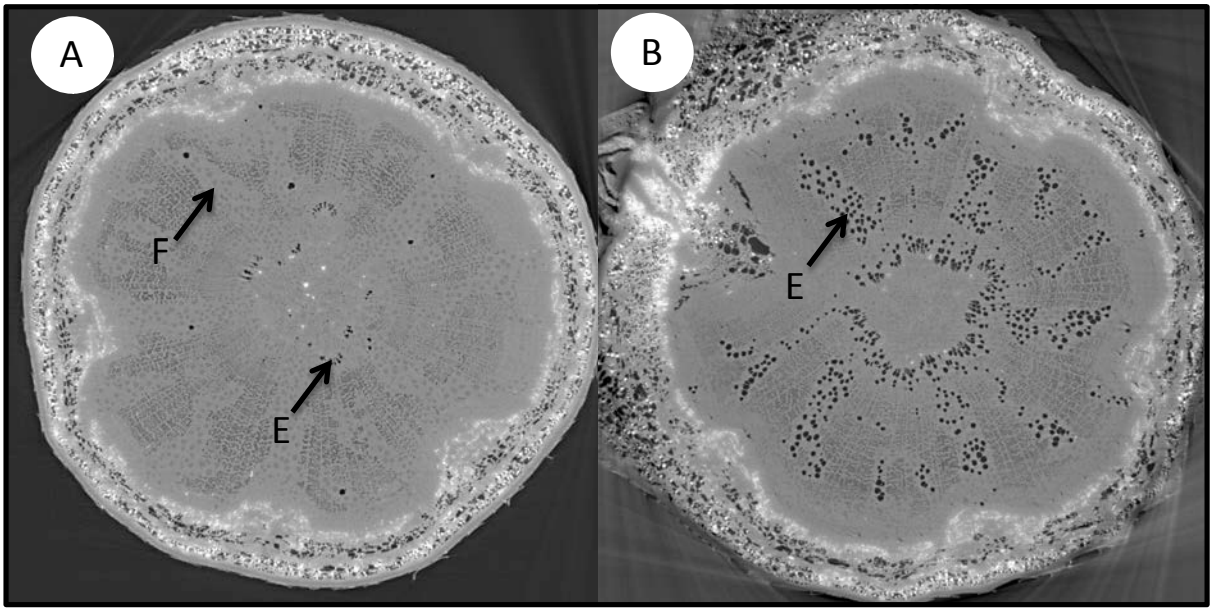

Figure 1. *Cross sectional slice from scan of stems in well-watered (A) and water-stressed Oak seedlings. Embolised (E) and full (F) xylem conduits are easily distinguished.*

Issues concerning highly vulnerable species

Cochard et al. (2013) conducted an extensive literature survey on the methods used to estimate cavitation resistance and concluded that the long-vessel species reported to be highly vulnerable to cavitation had actually been evaluated with biased techniques. New methods have been introduced based on air injection (Cochard et al., 1992) or centrifugation (Alder et al., 1997; Cochard, 2002) for the assessment of cavitation resistance, and these attractive methodologies are now widely used. Recent studies have shown that all centrifuge techniques are prone to the open vessel artifact and could therefore overestimate vulnerability to cavitation in species with very long vessels (Torres-Ruiz et al., 2014; Cochard et al., 2010; Martin-St Paul et al., 2014). Our recent direct observations of vessel function using microCT have confirmed the remarkable ability of long vessels to resist cavitation. Our direct observations made at the the Swiss Light Source (SLS, Villigen, Switzerland) and the SOLEIL synchrotron (Paris, France) demonstrate that the four studied species are highly resistant to embolism and not vulnerable to drought-induced embolism in a normal range of xylem tensions (Choat et al. 2015). In addition, three dimensional analysis of scan volumes illuminated the fine spatial patterns of embolism spread within each xylem type. We therefore recommend that embolism studies in long-vessel species should be validated by direct methods such as micro-CT to clear up any misunderstandings on their physiology.

Methods

Daily cavitation is not routine in trees

We used two different Synchrotron-based micro-CT facilities (the Swiss Light Source [SLS] in Villigen, Switzerland, and the Advanced Light Source [ALS] in Berkeley, CA) to test the excision artifact described by Wheeler et al. (2013). Specifically, we examined the impact of cutting xylem under tension and under water in three woody and one herbaceous species: Acer campestre, Eucalyptus pauciflora, Juglans microcarpa, and Helianthus annuus. By direct visualizations, we tested whether (1) the degree of embolism of the samples varied before and after cutting them (underwater) for all four species and (2) how much xylem tension affected the degree of embolism observed in E. pauciflora, A. campestre, and J. microcarpa after cutting under water.

Discussion

For all the species studied, images showed an increase in the degree of embolism after cutting while the xylem was under tension, whether the measurements were done on intact

plants (Fig. 2A) or cut branches (A. Campestre). Although more access to micro-CT facilities is required for confirmation, the variability in our results suggests that the intensity of the cutting artifact is not constant within or between species even at similar xylem tensions, probably being affected by other factors.

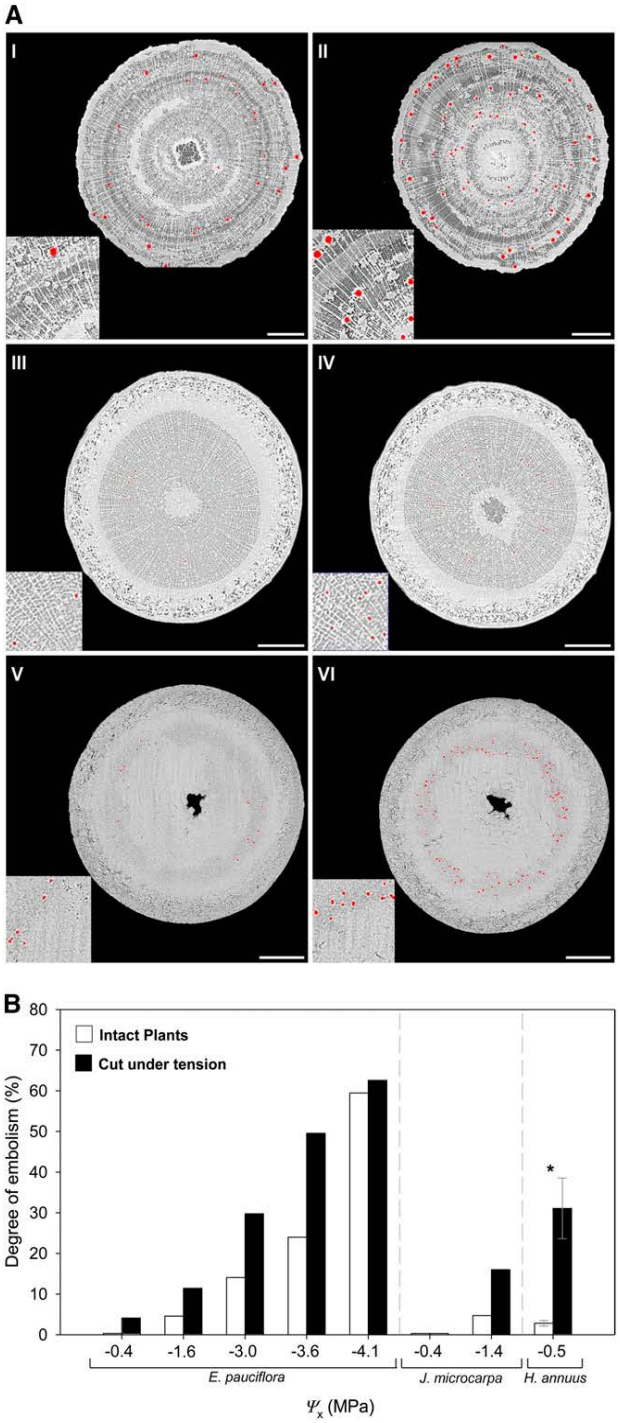

***Figure 2**. A, Transverse sections based on consecutive micro-CT scans for E. pauciflora (I and II), J. microcarpa (III and IV), and H. annuus (V and VI) at C x of 23.6, 21.4, and 20.4 MPa, respectively. Images show the amount of cavitated or air-filled conduits before (intact seedling; left) and after (right) cutting the sample under water without releasing the xylem tension. Both images were scanned at the same height to allow before and after comparison. Cavitated or air-filled vessels are observed as red. Insets show the same magnified areas (23) of each section. Bars = 500 mm. B, Degree of embolism in E. Pauciflora, J. microcarpa, and H. annuus at different C x in intact plants (white columns) and after cutting them under tension and under water (black columns). Due to limited access to Synchrotron micro-CT facilities, only one replication per C x was carried out except for H.*

annuus (n = 3). Columns indicate averaged values, error bars represent SE , and the asterisk indicates a significant difference (P , 0.05).

References:

Cochard, H., Cruiziat, P., & Tyree, M. T. (1992). Use of positive pressures to establish vulnerability curves further support for the air-seeding hypothesis and implications for pressure-volume analysis. **Plant Physiology**, 100(1), 205-209.

Alder, N. N., Pockman, W. T., Sperry, J. S., & Nuismer, S. (1997). Use of centrifugal force in the study of xylem cavitation. **Journal of Experimental Botany**, 48(3), 665-674.

Cochard, H. (2002). A technique for measuring xylem hydraulic conductance under high negative pressures. **Plant, Cell & Environment**, 25(6), 815-819.

Torres-Ruiz, J. M., Cochard, H., Mayr, S., Beikircher, B., Diaz-Espejo, A., Rodriguez-Dominguez, C. M.. & Fernández, J. E. (2014). Vulnerability to cavitation in Olea europaea current-year shoots: further evidence of an open-vessel artifact associated with centrifuge and air-injection techniques. **Physiologia plantarum**, 152(3), 465-474.

Martin-StPaul, N. K., Longepierre, D., Huc, R., Delzon, S., Burlett, R., Joffre, R., ... & Cochard, H. (2014). How reliable are methods to assess xylem vulnerability to cavitation? The issue of 'open vessel'artifact in oaks. **Tree physiology**, tpu059.

Cochard, H., Herbette, S., Barigah, T., Badel, E., Ennajeh, M., & Vilagrosa, A. (2010). Does sample length influence the shape of xylem embolism vulnerability curves? A test with the Cavitron spinning technique. **Plant, Cell & Environment**, 33(9), 1543-1552.

Choat et al. 2015 - Non-invasive measurement of vulnerability to embolism. **Plant Physiology** (accepted)

Wheeler, J. K., Huggett, B. A., Tofte, A. N., Rockwell, F. E., & Holbrook, N. M. (2013). Cutting xylem under tension or supersaturated with gas can generate PLC and the appearance of rapid recovery from embolism. **Plant, Cell & Environment**, 36(11), 1938-1949.

Coarse-Resolution High-Speed CT Scanning for Sawmill Log Sorting and Grading

Y. AN*[1], G. SCHAJER [2], B. LEHMANN[3], D. WONG [4], Z. PIROUZ [5]

[1,3,4,5] FPInnovations, 2665 East Mall, Vancouver, BC, V6T 1Z4 – yuntao.an@fpinnovations.ca
[2] UBC, 6250 Applied Science Lane, Vancouver, BC, V6T 1Z4 – schajer@mech.ubc.ca
* presenting author – yuntao.an@fpinnovations.ca

Keywords: Log Scanning, Low-cost CT, Coarse-Resolution CT, Feature Identification

Abstract

Significant economic gain can be achieved by grading logs at the inlet of a sawmill so that they can be optimally processed to manufacture the highest possible value products from the available raw material. Computed Tomography (CT) has been extensively used as a medical diagnostic tool, and increasingly for scientific and industrial research. For log scanning, CT is of particular interest because it can identify the locations, orientations and sizes of internal quality-controlling features such as knots, heartwood/sapwood extent, cracks, rot and holes. Conventional CT technology is based on medical-style equipment, which needs to have very high spatial and density resolution. Therefore, it requires high standards from scanner hardware and software, and thus substantially increases equipment complexity and cost. These features make such equipment unsuited for typical sawmill applications. However high spatial and measurement accuracy are not needed for log scanning because most targeted internal features are fairly large and have specific geometrical shapes. Based on these thoughts, this paper proposes a greatly simplified low-cost CT scanning system with novel geometry-based CT density reconstruction models and algorithms. A generation 1 lab prototype was designed and built at the University of British Columbia (UBC). Log scanning results compare well with those from an industrial CT scanner using conventional reconstruction technique. FPInnovations is currently designing and developing a generation 2 industrial prototype for practical log sorting and breakdown in sawmills.

Introduction

Wood is a highly variable natural material that requires an individual decision to be made for each piece to identify the most advantageous processing method. At present, log inspection is based on visual observation of surface defects and optical measurement of external features (Oja et al. 2004). The logs are then cut according to their observed characteristics. However, many quality-controlling features are not visible on the surface, causing the subsequent cutting to be far from optimal. Studies indicate that only half of inspected logs are classified correctly by a human inspector (Pietkäininen et al. 1996). Consequently, many logs are placed at the wrong breakdown position, dramatically reducing the amount of high-value products obtained (Rinnhofer et al. 2003).

Computed Tomography (CT) is powerful technique to create cross-sectional views of an object from X-ray measurements called “projections”. Traditionally, CT has mainly been used as a medical diagnostic tool, but now is increasingly applied in industry and brings new opportunity for log scanning. FPInnovations studies have shown that 8-10% value could be added to each log by simply being able to detect knots for North American lumber grades. If higher value products and other characteristics were considered, the potential added value would increase many times. Although detailed CT provides abundant information, how to implement CT scanning in sawmills is still a challenging task. The main difficulty is that commercial system is beyond the affordability for most sawmills. Despite the cost issue, the scanning and associated reconstruction process is also very time consuming. In contrast, log CT scanning in a sawmill is a more tolerant and less exacting process. In logs, the main features to be identified are knots, sapwood/heartwood region, cracks and rots, most of which have dimensions measured in centimeters; thus a coarse resolution is sufficient. Logs also have a very specific geometry; they are circular in shape and all

features of interest have their own specific shapes, therefore making available much a-priori information (An and Schajer 2014).

Based on the actual need from the sawmill, the coarse resolution requirement and the log geometry information, the authors propose a new approach: customize a coarse-resolution high-speed CT scanner specifically for logs, which utilizes cost-effective setup and more efficient CT models and algorithms. Detailed research work is explained in the following sections.

Methods

The research work was composed in two major parts: 1. Designing and prototyping a novel CT log scanner. 2. Developing efficient coarse-resolution geometry-based CT log models and reconstruction algorithms.

Log Spiral Motion CT Setup

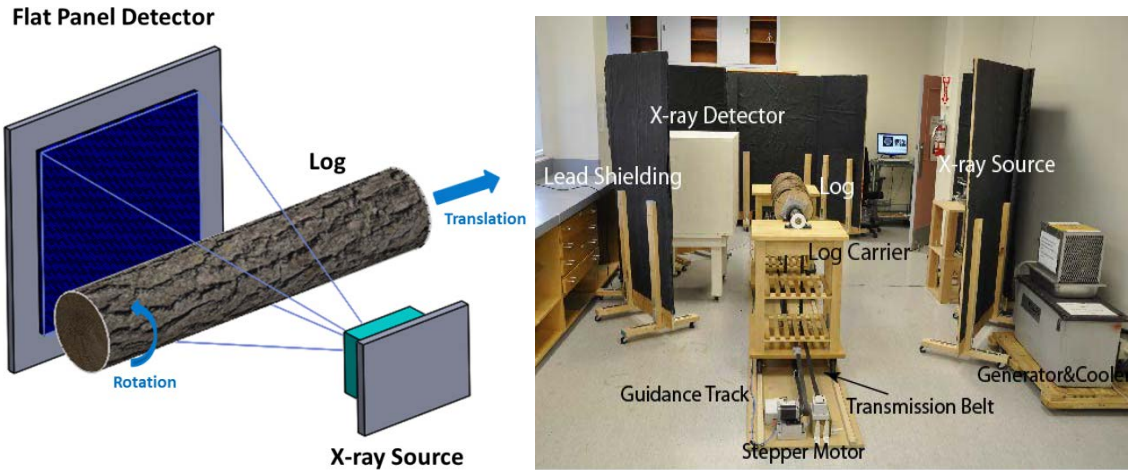

(a) *(b)*

Fig 1. *Proposed CT log scanner: (a) Schematic design, (b) UBC log CT prototype.*

Fig. 1 (a) shows the schematic of the proposed CT log scanner. The scanner uses a cone-beam collimated X-ray source, a large area X-ray detector and a log spiral-motion mechanism. The log to be inspected is rotated and translated within the X-ray beam between the source and detector. During log rotation, X-ray images are taken at a series of incremental angles, from which the log cross-sections of interest are reconstructed. The proposed setup has two important features: firstly, a log spiral motion mechanism and a large-area detector. The log motion mechanism allows the source and detector to remain stationary, which greatly simplifies the required scanner hardware and makes the design practical and convenient for sawmill log transmission line integration. Secondly, the large-area detector dramatically increases the scanned volume and makes efficient use of the available X-rays.

Prototype I log scanner following the proposed design has been constructed at Renewable Resources Lab at the University of British Columbia. Fig. 1(b) shows the physical setup. In this photo, the sample log appears at the center, the X-ray source is at the right and the customized detector is at the left. The sample log used in the pilot scanning is an amabilis fir (*abies amabilis*) from the Port Alberni region of British Columbia, Canada. The rotation of the log is driven by a stepper motor system whose angular position is monitored by an encoder attached to the log rotation shaft. The detector is designed and assembled by using an Electron-Multiplying-CCD (EMCCD) camera with a large X-ray phosphor (Gd2O2S:Tb) screen (An 2013). The CT scanner has been fully commissioned with a capability of scanning at 0.5m/s scanning speed for up to 40cm diameter log samples.

Coarse-resolution CT approach

A very important challenge for successful real time log scanning is the CT computation efficiency and reliable feature identification. Fig. 2(a) schematically shows a medical-style 3rd generation CT scanner, where the scanner operates by making X-ray measurements from

multiple directions and mathematically combining them to generate a 3-dimensional model of the scanned object (Kak and Slaney 1995). The conventional CT approach uses fixed square-grid pattern reconstruction geometry as shown in the upper right corner in Fig 2(a). Then, the X-ray attenuation coefficient at each square, called a "voxel", is determined ("reconstructed") from the X-ray measurements. This generalized geometry is chosen because it can accommodate internal structures of any geometry and it enables fine features to be identified for medical diagnosis purpose.

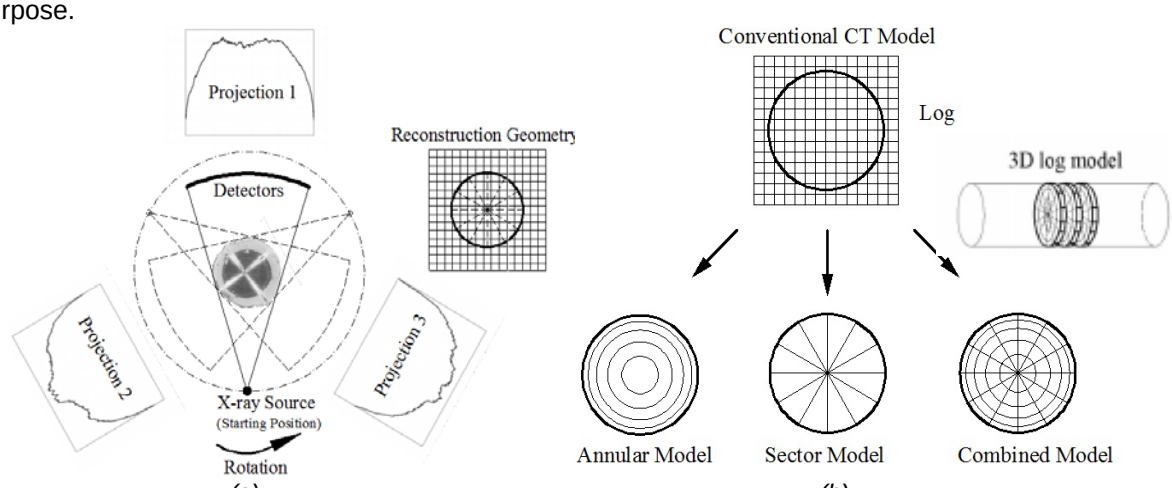

Fig 2. *Coarse-resolution CT approaches: (1) Conventional CT approach (2) Geometry based log models*

The a-priori information available with saw-logs makes possible the use of some simpler feature-specific log cross-section models instead of the commonly used fine-meshed square pattern. Specifically in clear wood areas, logs are generally circular and have axi-symmetric features. In knotty wood areas, the knots start from the center and grow approximately in a sector shape through the perimeter. Based on these observations, three coarse-resolution, geometry-based CT log models are proposed in Fig.2 (b). These three geometric models target different internal features. The annual model comprises annular regions, which is suited for identifying the clear wood regions between knots, where heartwood/sapwood, rings and rot tend to be axi-symmetric. The sector model comprises sector-shaped regions, which is suited for identifying the knot regions where the features are sector-shaped. The combined model comprises finer subdivided voxels (by both annulus and sectors), which is suitable when multiple features are present simultaneously. All three log models divide the cross-section into feature-specific regions and guide the resulting cross-sectional reconstructions towards physically realistic solutions.

Results

A series of log scanning tests were done to demonstrate the effectiveness of the proposed approach. Voxel models corresponding to Fig. 2 (b) with 18 annuli, (b) 72 sectors, and 72 sectors with 18 annuli were used. 72 X-ray projection measurements, each with 1s exposure time, were made. This lengthy exposure time was chosen here to give a base case for best quality of X-ray measurement. In practice, much shorter exposure times (minimum 10ms) can be implemented for high-speed scanning.

Detector Sample Image and Sinogram Data

Fig. 3(a) shows a typical CT raw data image from the prototype scanner. In this image, the white areas indicate high material density (high X-ray absorption) and the dark areas indicate low material density (low X-ray absorption). The vertical white regions near the center indicate the knots within the log section and the horizontal bright gap shows a radial crack. Another good way to visualize the CT data is to form a sinogram, which comprises a sequence of the X-ray projections taken within a full measurement rotation. Fig. 3(b) shows the sinogram of a total 72 projections (5° apart) of the cross-section along the central column of pixels in each projection. The sinogram is essentially the raw data for subsequent CT reconstruction, where light spiral

paths represent the knots within the cross-section and the dark spiral represents a large radial crack.

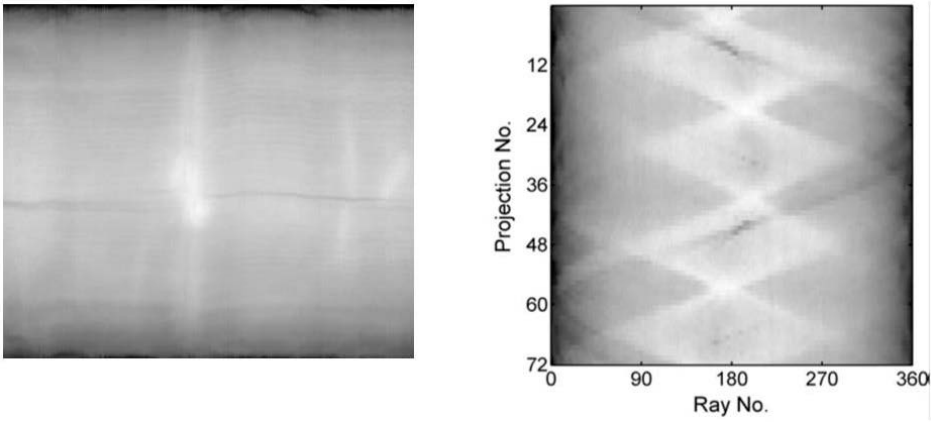

(a) *(b)*

Fig 3. *CT raw data: (1) CT raw data from the detector (2) Processed sinogram*

Coarse-resolution feature specific CT scanning

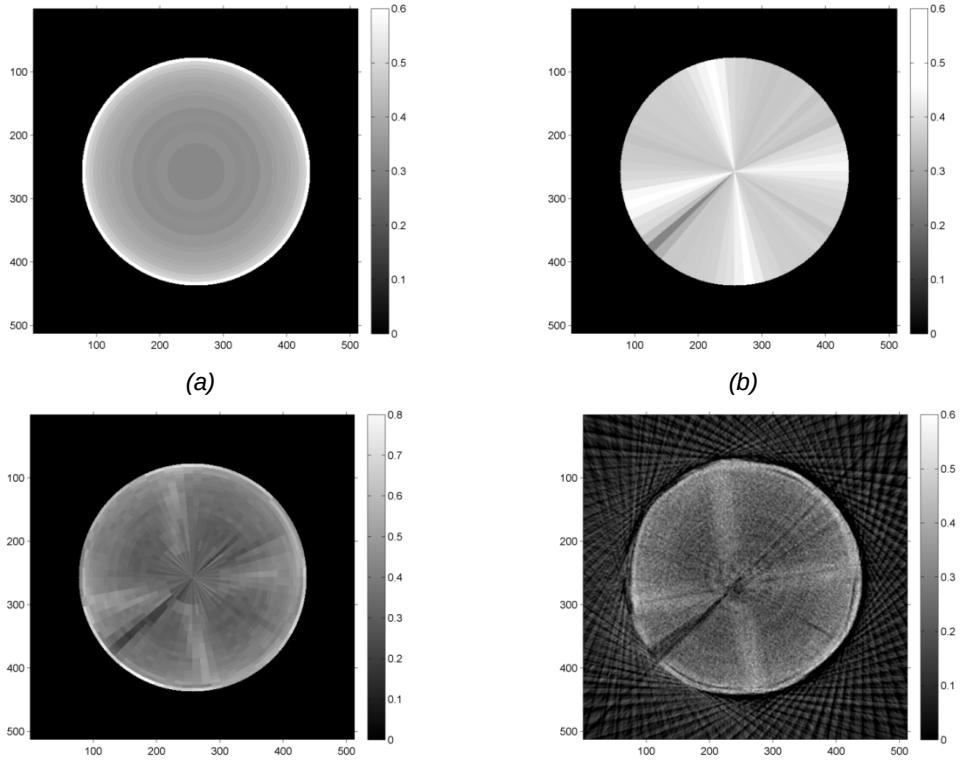

(a) *(b)*

(c) *(d)*

Fig 4. *Log CT reconstruction results: (a) Annular reconstruction, (b) Sector reconstruction, (c) Combined reconstruction, (d) Reference from filtered back projection.*

Fig. 4 shows log cross-section density reconstruction results calculated using the proposed coarse-resolution model and algorithms with X-ray data from the prototype 1 scanner. Fig. 4(a) shows the reconstruction result from the annular model (18 annuli). It clearly indicates the high-density bark near the perimeter (Plomion et al., 2001). Fig. 4(b) demonstrates the sector reconstruction from the sector model (72 sectors). It accurately detects the four knots and the crack. Fig. 4(c) shows the reconstruction results from the combined model (72 sectors x 18 annuli). This provides finer density details: the bark, knots and crack features are all clearly identified. For comparison, Fig. 4(d) is the cross-section reference computed using the

conventional filtered back-projection (FBP) method using the same CT data set. In Figure 4(d), the bark, knot and crack features are also visible in the reconstruction, but with greatly increased noise, causing the contrast to become low. In addition, substantial artifacts are created in the area around the outside of the log where no material density exists.

The good reconstruction result proves that geometry-based course-resolution log models and the corresponding reconstruction algorithm is an effective approach for practical saw-log CT scanning. Of particular significance is the way in which the feature-specific models in Fig. 2 (b) focus the action of the CT reconstruction. Features such as cylindrical geometry can be ‘‘assumed’’ rather than painstakingly computed. The models also specify in advance either that the log features are axisymmetric or that any knots start at the center and radiate towards the perimeter as a sector shape. These advanced specifications have the effect of guiding the CT reconstruction towards physically realistic results. As location and scale information of internal feature is inherent with the model representation, therefore no post analysis such as segmentation and registration is needed any more.

Conclusion

This paper proposes a novel, mechanically convenient and computationally efficient CT system for log scanning. This proposed approach has several advantages over conventional CT scanning:

1. It reduces scanner mechanical complexity by using a stationary source and detector while moving the log. It allows to use relatively straightforward equipment whose robustness and cost are appropriate for sawmill use.

2. It uses feature-specific coarse-resolution voxel geometries that guide and stabilize the CT reconstruction and reduce the work needed for feature identification.

3. It provides direct density measurement, more stable than conventional CT approach and requires fewer X-ray projections, thus reducing the scale of data acquisition.

In the pilot tests, the proposed geometry-based coarse-resolution CT scanner prototype produced good scanning result. The availability of the location and size of internal features provide rich information to determine the grade of input logs and to optimize the subsequent processing to improve the yield of high-quality products in sawmills. The good scanning results so far give confidence in the usefulness and applicability of the proposed approach to practical log scanning in sawmills. FPInnovations is currently researching and developing the generation 2 industrial CT prototype for practical log sorting and breakdown in sawmills.

References

An, Y. & Schajer, G. S. (2014). Geometry-based CT scanner for measuring logs in sawmills. Computers and Electronics in Agriculture, 105, 66-73.

An, Y. & Schajer, G. S. (2014). Cone-Beam Feature-Specific CT Log Scanning. Experimental Mechanics, 1-10.

An, Y. (2013). Coarse-resolution CT scanning for sawmill logs sorting and grading. The University of British Columbia. PhD Thesis

Herman, G.T. (Ed.) (1979). Image Reconstruction from Projections: Implementation and Applications. Springer, New York

Kak, A.C. & Slaney, M (1987) Principles of computerized tomography. IEEE press.

Oja, J., Grundberg, S., Fredriksson, J., Berg, P. (2004). Automatic grading of sawlogs: A comparison between Xray scanning, optical three dimensional scanning and combinations of both methods. Scandinavian Journal of Forest Research, v.19, pp.89-95.

Pietkäininen, M. (1996). Detection of Knots in logs using X-ray Imaging. Dissertation, Technical Research Centre of Finland, Espoo. VTT Publications 266.

Plomion, B., Leprovost, G., Stokes, A., Andreu, J.P. (2001). Wood formation in trees. Plant Physiol 127 (4), 1513-1523.

Rinnhofer, A., Petutschnig, A. and Andreu, J.P. (2003). Internal log scanning for optimizing breakdown. Computers and Electronics in Agriculture, v.41, pp.7–21.

Usenius, A. (2003). Optimization of Sawing Operation Based on Internal Characterization of the Logs. Proc. ScanTech 2003, Wood Machining Institute, Seattle, WA, USA. pp.11-18.

Temperature effect and tree species on the damage progression of whitespotted sawyer, Monochamus scutellatus scutellatus (Say), larvae in recently burned logs, by X Ray CT measurement.

Sébastien Bélanger[*1], Éric Bauce[2], Richard Berthiaume[2], Bernard Long[3], Jacques Labrie[3], Louis Frédéric-Daigle[3] & Christian Hébert[4]

[1] Ministère de la Forêt, de la Faune et des Parcs, 2700 rue Einstein, local D.2.370a, Québec, Canada G1P 3W8. sebastien.belanger@mffp.gouv.qc.ca
*Presenting author

[2] Laboratoire Entomologie forestière (Consortium iFor), Département des Sciences du Bois et de la Forêt, Faculté de Foresterie, de Géographie et de Géomatique, Pavillon Abitibi-Price, Université Laval, Québec, Canada G1V 0A9. Eric.Bauce@vrex.ulaval.ca, Richard.Berthiaume@sbf.ulaval.ca

[3] Institut national de la recherche scientifique, Centre Eau, Terre & Environnement, 490 de la Couronne, Québec Canada G1K 9A9. Bernard.Long@ete.inrs.ca

[4] Ressources naturelles Canada, Centre de foresterie des Laurentides, 1055 du P.E.P.S., P. O. Box 10380, Stn. Sainte-Foy, Québec, Canada G1V 4C7. Christian.Hebert@RNCan-NRCan.gc.ca

Keywords : whitespotted sawyer, fire-killed trees, salvage logging, damage progression, CT scan.

Abstract

The whitespotted sawyer, Monochamus scutellatus scutellatus (Say), is one of the most damaging wood-boring insect in recently burned boreal forest. In Canada, salvage logging can contribute to maintain timber volumes required by the industry but larvae of this insect cause important damage by burrowing galleries into the wood thus reducing the economic value of lumber products. This study aimed to estimate damage progression as a function of temperature in recently burned black spruce and jack pine trees. Using the new axial tomograph technology (CT-Scan), successive pictures of each log were reconstructed in three dimension and galleries depth were determinated with a program developed using Matlab (Natick, MA). These gallery measurements obtained at different time made it possible to model subcortical development, defined as the time elapsed between oviposition and larval entrance into sapwood, as well as gallery depth progression rates as function of temperature for both tree species.

Gallery depth progression was modeled using the Chapman-Richards function. Generally, these rates were slightly higher in black spruce than in jack pine logs. Eggs laid on logs placed at 12°C did not hatched or larvae were unable to establish under bark as no larval development was observed. At 16°C, larvae stayed under the bark for>200 d before penetrating into the sapwood. At 20°C, half of the larvae entered the sapwood after 30-50 d, but gallery depth progression stopped for ≈70 d, suggesting that larvae went into diapause. The other half of the larvae entered the sapwood only after 100-200 d. At 24 and 28°C, larvae entered the sapwood after 26-27 and 21 d,

respectively. At 28°C, gallery depth progressed at a rate of 1.44 mm/d. Temperature threshold for subcortical development was slightly lower in black spruce (12.9°C) than in jack pine (14.6°C) and it was 1°C warmer for gallery depth progression for both tree species.

These results indicate that significant damage may occur within a few months after fire during warm summers, particularly in black spruce, which highlights the importance of beginning postfire salvage logging as soon as possible to reduce economic losses.

Introduction

Salvage logging is considered as an efficient way to minimize the economic impact of large-scale wildfires in all forested regions of the world (Lowell et al., 1992; Saint-Germain and Greene, 2009). In USA, this is an important issue because of the reductions in land base available for timber harvesting (Lowell et al., 1992). In Canada, it is viewed as a measure that can contribute to maintain timber volumes required by the industry, particularly within the context of recent reductions in the annual allowable cuts (Lowell et al. 1992; Saint-Germain and Greene, 2009).

Insects are major agents of deterioration of fire-damaged and fire-killed trees (Lowell et al., 1992). They rapidly attack trees, loosen the bark by feeding on phloem and some species, such as the whitespotted sawyer, *Monochamus scutellatus scutellatus* (Say) (Coleoptera: Cerambycidae), excavate deep galleries into the wood (Raske, 1972). This insect is considered as the most damaging xylophagous species in recently burned boreal forest of Canada (Gardiner, 1957).

The preparation of salvage logging plans requires time and often the construction of new roads to reach inaccessible burned forests, particularly in the boreal region. Meanwhile, woodborer deposit eggs and larval development start and progresses rapidly because temperature in burned forest is much warmer than in unburned forest (Hossack et al., 2009). Therefore, it is a race against time to salvage burned trees before woodborer's galleries reduce wood value to such an extent that it would become worthless to salvage. If several studies have estimated economic losses caused by woodborer damage on fire-killed trees (Richmond and Lejeune, 1945; Prebble and Gardiner, 1958), none has addressed the issue of predicting damage progression over time. This crucial information for improving management of burned forests is the aim of our study. It requires studying damage progression into the wood as a function of temperature in order to acquire basic information that might be incorporated later into a predictive model.

Considering the small size of tunnels and the speed at which damage progresses within the trees, one should rely on a non-destructive and highly precise technology to characterize the process. Axial tomography (CT-Scan) is a non-destructive technology that has been originally designed for medical applications but it is now used for other purposes. For instance, sedimentologists use this technology to identify and quantify the space occupied by benthic organisms in marine sediments (Gagnoud et al., 2009). More recently, Jennings and Austin (2011) also used a micro-CT scanner to characterize the shape and position of tunnels formed by larval xiphydriid woodwasps into the wood. In our study, we used 3-D high resolution images processed by CT-scan in order to follow whitespotted sawyer larval galleries inside logs over time. Specifically, the objectives of our study were to determine 1) the time of larval entrance into the sapwood of burned

black spruce (*Picea mariana* Mill.) and jack pine (*Pinus banksiana* Lamb.) logs to determine subcortical development rates and 2) the progression of gallery depth to estimate ongoing damage, both a as a function of temperature and tree species.

Methods

To achieve these objectives, black spruce (Picea mariana (Mill.) and jack pine (Pinus banksiana (Lamb.) log sections were harvested after the passage of a fire located in north of Lac St-Jean, Québec, Canada. In laboratory, logs were individually exposed to whitespotted egg laying females in the bark to monitoring development and progression of larvae. Logs were reared at fives temperatures (12, 16, 20, 24 and 28 ° C) in growth chambers and were scanned periodically with an axial tomograph technology (CT-Scan). Pictures of each log were reconstructed in 3D with a program developed using Matlab©, a software developed for treating medical images. Using successive pictures of the same logs (Fig. 1) made it possible to identify each gallery and measure its depth (from inner bark toward center in mm), which was considered as the best estimate of woodborer damage. It also allowed estimating the time of entrance of each larva into the wood as well as their progression toward tree center at different rearing temperatures and tree species.

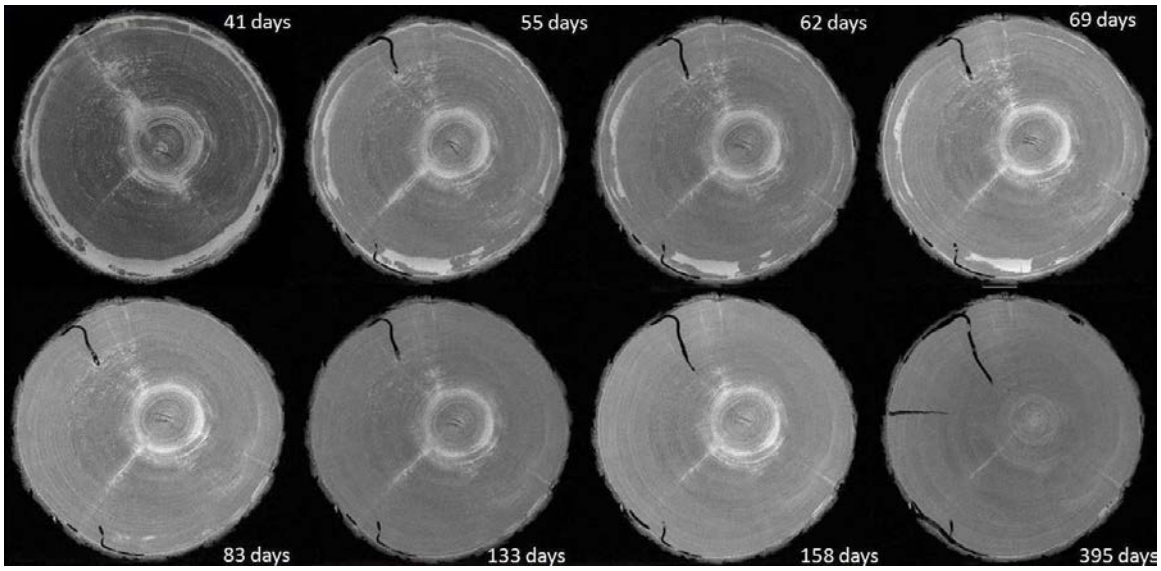

Fig. 1: *Gallery progression of a Monochamus scutellatus scutellatus larva in the same log as a function of time at 20°C.*

Results

We modeled subcortical development and gallery depth progression rates as function of temperature for both tree species. Gallery depth progression was modeled using the Chapman-Richards function. Generally, these rates were slightly higher in black spruce than in jack pine logs. Eggs laid on logs placed at 12°C did not hatched or larvae were unable to establish under bark as no larval development was observed. At

16°C, larvae stayed under the bark for >200 days before penetrating into the sapwood (Fig. 2 D). At 20°C, half of the larvae entered the sapwood after 30-50 d, but gallery depth progression stopped for ≈70 d, suggesting that larvae went into diapause. The other half of the larvae entered the sapwood only after 100-200 days (Fig. 2 C). At 24 and 28°C, larvae entered the sapwood after 26-27 and 21 days, respectively (Fig. 2 A-B). At 28°C, gallery depth progressed at a rate of 1.44 mm/d. Temperature threshold for subcortical development was slightly lower in black spruce (12.9°C) than in jack pine (14.6°C) and it was 1°C warmer for gallery depth progression for both tree species. These results indicate that significant damage may occur within a few months after fire during warm summers, particularly in black spruce, which highlights the importance of beginning postfire salvage logging as soon as possible to reduce economic losses.

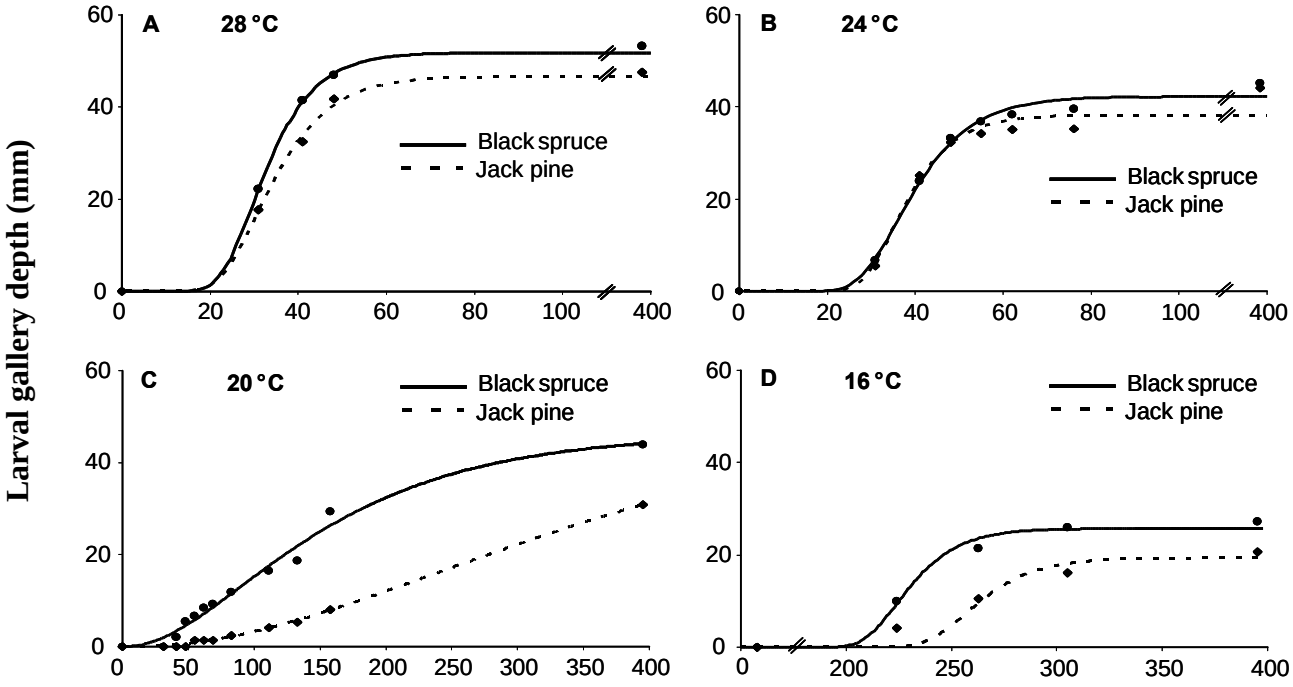

Fig. 2*: Larval gallery depth of Monochamus scutellatus scutellatus as a function of time at different temperatures. Solid lines fitted for black spruce (BSP) and dotted lines for jack pine (JPI).*

It has been shown that fire frequency and area burned had increased over the past 4 decades (Flannigan et al., 2005) and this upward trend is anticipated to continue (Gillett et al., 2004). Faced with the decreasing availability of timber resources, we also anticipate that salvage logging in burned areas will continue to help maintaining wood volumes allocated to the forest industry. The use of CT scan, provides the opportunity to characterize damage and improve knowledge on the biology of the whitespotted sawyer and could also be used for other woodborers. The subcortical development and gallery depth progression rates determined in this study will allow developing a model for predicting whitespotted sawyer larval damage as a function of temperature to help forest managers to improve salvage logging plans.

References

Flannigan, M., Logan, K., Amiro, B., Skinner, W. & Stocks, B. 2005. Future area burned in Canada. ***Climatic change*** 72: 1-16.

Gagnoud, M., Lajeunesse, P., Desrosiers, G., Long, B., Dufour, S., Labrie, J., Mermillod-Blondin, F. & Stora, G. 2009. Litho-and biofacies analysis of postglacial marine mud using CT-Scanning. ***Engineering Geology*** 103: 106-111.

Gardiner, L. M. 1957. Deterioration of fire-killed pine in Ontario and the causal wood-boring beetles. ***Canadian Entomologist*** 89: 241-263.

Gillett, N., Weaver, A., Zwiers, F. & Flannigan, M. 2004. Detecting the effect of climate change on Canadian forest fires. ***Geophysical Research Letters*** 31: L18211, doi:18210.11029/12004GL020876.

Hossack, B. R., Eby, L. A., Guscio, C. G. & Corn, P. S. 2009. Thermal characteristics of amphibian microhabitats in a fire-disturbed landscape. ***Forest Ecology and*** Management 258: 1414-1421.

Jennings, J. T. & Austin, A. D. 2011. Novel use of a micro-computed tomography scanner to trace larvae of wood boring insects. ***Australian* Journal *of Entomology*** 50: 160-163.

Lowell, E. C., Willits, S. A. & Krahmer. R. L. 1992. Deterioration of fire-killed and fire-damaged timber in the Western United States. Department of Agriculture, Forest Service, Pacific Northwest Research Station Gen. Tech. Rep. PNW-GTR-292. Portland.

Prebble, M. L. & L. M. Gardiner, 1958. Degrade and value loss in fire-killed pine in the Mississagi area of Ontario. In. Forest Chron. 34(2):139-158 1958.

Raske, A. G. 1972. Biology and control of *Monochamus* and *Tetropium*, the economic wood borers of Alberta (Coleoptera: Cerambycidae). Canadian Forest Service, Northern forest Research Center, Edmonton Intern Report NOR-9: 1-48.

Richmond, H. A. & Lejeune, R. R. 1945. The deterioration of fire-killed white spruce by wood-boring insects in northern Saskatchewan. ***Forestry Chronicle*** 21 168-192.

Saint-Germain, M. & Greene, D. F. 2009. Salvage logging in the boreal and cordilleran forests of Canada: Integrating industrial and ecological concerns in management plans. ***Forestry Chronicle*** 85: 120-134.

Oral presentation

Cricket bat characterization based on X-Ray Computed Tomography and image processing

*J. TAO[1], P. EVANS[2], M. SAADATFAR[1]

[1] Department of Applied Mathematics, The Australian National University, Australia
[2] Faculty of Forestry, The University of British Columbia, Canada
* presenting author

This research employed the tomographic technology and related analyzing tools to investigate the unique properties of cricket bat willow/Engilish willow (salix alba var.caerulea), which premium cricket bats are predominantly made from. The cricket bat willow is preferred due to its being lightweight, very tough and shock-resistant, and not being significantly dented nor splintering on the impact of a cricket ball at high speed. Wood, as a major material for construction and sports tools, has not been studied widely by the tomography in terms of relationship between cellular structure and mechanical performance. Micro Computed Tomography (Micro-CT) opens a door for wood scientists to investigate the multi-scale structures of different species in three dimensions.

Wood is a natural composite and porous material, which could inspire various designs of engineered advanced materials in regarding to the layout and binding schemes. It mainly consists of lignin, cellulose and hemi-cellulose, where lignin serves as the adhesive matrix in composite materials while cellulose being the continuous fibre and hemi-cellulose being the non-continuous fibre.

By taking the 3D images of the wood, the interior structure of wood is available as the basis of analysis, e.g. pore inter-connectivity, mass distribution statistics and cell wall orientational anisotropy trend. The image can also be segmented based on binarization of solid and void, and serves as the input for finite element analysis (FEA) method(Saadatfar, Mukherjee, et al., 2012),, where the modulii of the sample as a whole are able to be calculated by simulations.

Samples used in this research derive from two cricket bats, one used premium bat and the other brand new first-class bat. Samples are taken from the bats in all three directions of the wood, longitudinal-radial section(LRS), longitudinal-tangential section(LTS) and transverse section (TS). Specimens are conditioned at 65% relative humidity and 20 °C for at least 48 hours prior to mechanical testing.

Specimens are imaged using a Micro-CT facility at 120kV throughout all steps of the in-situ compression with strain interval of 0.005. The series of images obtained are then compared by digital volume correlation (DVC), where we calculate the displacement to the sub-voxel level by locating displaced pixels based on the correlation coefficients of the surrounding pixels (Bay, 1999). Strain tensors of every pixel are also available to generate a strain field map to study the local deformation. The DVC results of displacement and strain are partially displayed in Fig. 1 of a sample before and after in-situ compression from the used bat oriented in LRS. The results from three orthogonal directions will be compared to discover the difference. Then the variance between the new and used bats can be analyzed to distinguish them quantitatively. The ultimate objective of the research is to solve the empirical rule of thumb, that why first-class cricket bat shall be made from English Willow with LRS as the batting surface.

References:

Saadatfar M, Mukherjee M, Madadi M, Schröder-Turk GE, Garcia-Moreno F, Schaller FM, Hutzler S, Sheppard AP, Banhart J, Ramamurty U. (2012) Structure and deformation correlation of closed-cell aluminium foam subject to uniaxial compression. Acta Materialia, 60.8 p. 3604-3615.

Bay BK, Smith TS, Fyhrie DP, SaadM. (1999) Digital volume correlation: three-dimensional strainmapping using X-ray tomography. Exp Mech 39 p. 217–226

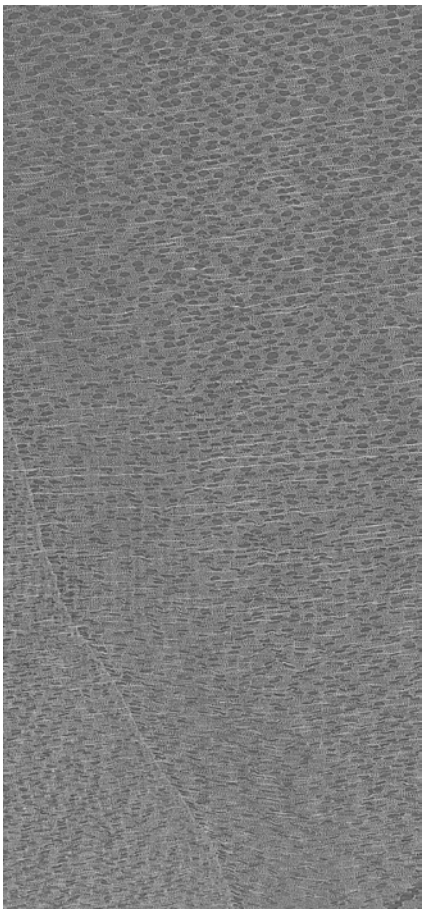

a

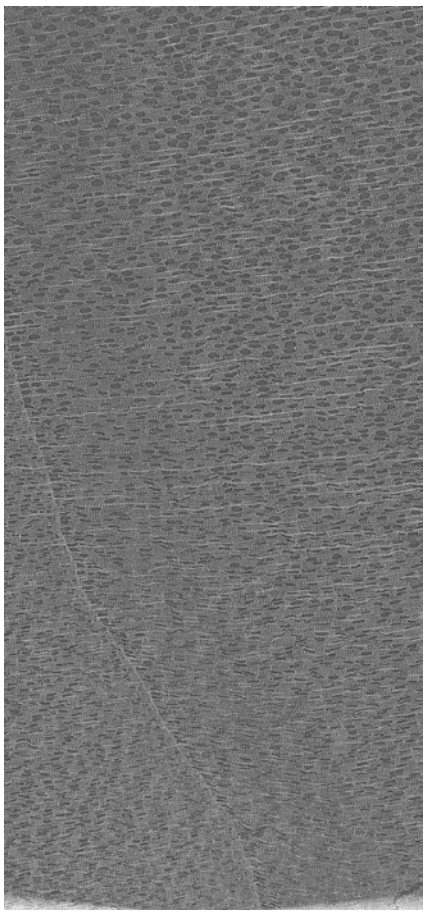

b

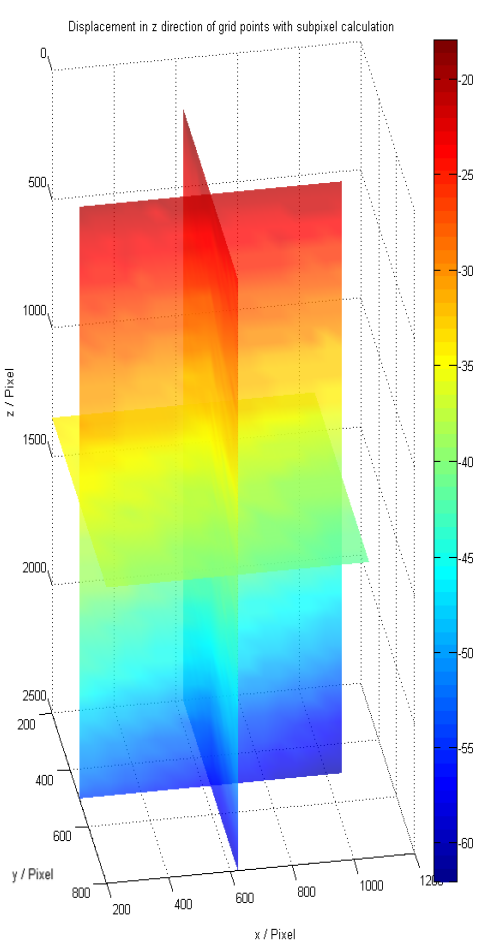

c

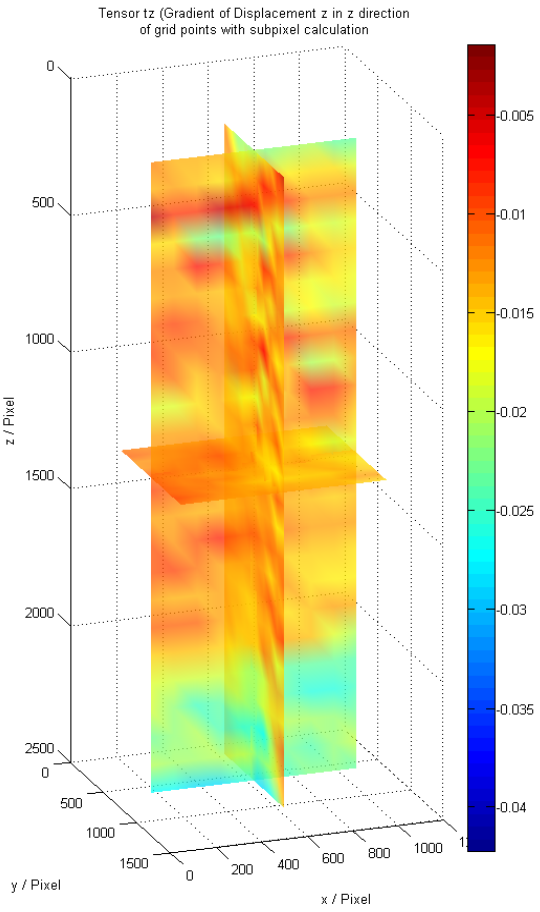

d

Figure 1. The cross section of the specimen at the same position taken from the tomography at (a)initial step (step 0) and (b)the third step (step 3). The displacement field map in z (compression) direction is shown in (c) and the strain ε_{zz} is calculated and presented in (d).

Session 304

DYNAMIC MICRO-CT ANALYSIS OF FRACTURE FORMATION IN ROCK SPECIMENS SUBJECTED TO MULTI-PHASE FLUID FLOW.

*J. VAN STAPPEN[1], T. BULTREYS[1], M.A. BOONE[1,2], T. DE KOCK[1], V.CNUDDE[1]

[1] UCGT/PProGRess – Dept. Geology and Soil Science, Ghent University, Krijgslaan 281/S8, B-9000 Gent, Belgium – www.pprogress.ugent.be – jeroen.vanstappen@ugent.be
[2] X-ray Engineering BVBA (XRE), De Pintelaan 111, B-9000 Gent, Belgium – www.xre.be –

* presenting author

Keywords: Fracture formation, multi-phase flow, micro-CT

Abstract

In this study, fracture formation in rocks is ~~being~~ studied at the pore-scale through the combination of high-resolution X-ray CT scanning with custom-made add-on modules. The Deben CT5000 system, an in-situ load cell, was used at the scanners at the Centre for X-ray Tomography at Ghent University (UGCT), providing information on mechanical properties of the tested rocks. Micro-CT scans made at the High Energy CT system Optimised for Research (HECTOR) allowed the visualisation of the fractures~~k~~ and their formation as well as the analysis of porosity changes in the material, related to the changes in stress.

Introduction

In geological formations throughout the world, fractures are widspread and contribute significantly to fluid flow and transport (Berkowitz, 2002). Particularly in low-permeable fractured rocks, often referred to as dual-porosity systems, the fractures are considered to be principal pathways for fluid flow and pollutant transport (Berkowitz, 2002; Noiriel, Gouze, & Madé, 2013). More and more often, such low-permeable rock formations in the underground are targeted for exploitation (storage of CO_2, tight oil reservoirs, geothermal energy production). Therefore, the study of ~~the~~ fluid flow behavior in tightly fractured rock formations is of great importance in many fields of geology. However, in numerous investigations, whether ~~it is~~ related to CO_2 sequestration, oil production, or some other applications, direct information from the subsurface reservoir is only available in the form of drill core samples, which are limited in size. Remaining questions in these studies are often related to the pore scale processes in the systems, thus phenomena at the microscopic scale (submicron to approximately 100 µm) are the first which need to be understood in order to determine up-scaled parameters for the reservoir. In this study, the focus lies on the process of fracture formation and its effect on the fluid distribution within rock specimens.

Methods

In order to investigate fracture initiation and propagation in rock samples, as well as the influence on fluid flow through them, different add-on modules are combined with the high-resolution X-ray Computed Tomography (µCT) systems available at the Centre for X-ray Tomography at Ghent University (UGCT, www.ugct.ugent.be).

Primarily, fracture formation in rocks was investigated. An in-situ load cell, the CT5000 system developed by Deben, United Kingdom, was combined with the High Energy CT system Optimised for Research (HECTOR) at UGCT (Masschaele et al., 2013). The load cell allows for both compressive and tensile tests with forces up to 5kN. Although compressive tests are usually performed on cilindrical rock samples with a

length/diameter ratio higher than 1 (Siegesmund & Dürrast, 2014), rock samples with a diameter of 20 mm and a height of approximately 15 mm were used in this study. These dimensions were chosen due to limitations of the current set-up. The CT5000 system consist of a moving bottom jaw, to which a water bath can be connected for compressive tests of saturated samples, and a stationary top jaw. The water bath and outher wall of the load cell is made with glassy carbon (figure 1).

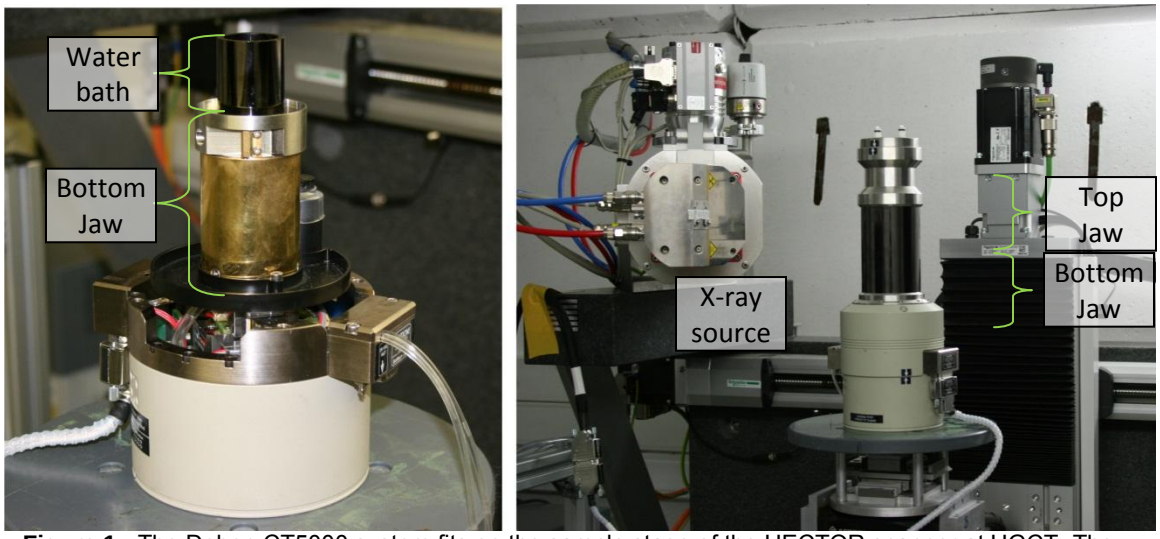

Figure 1 : The Deben CT5000 system fits on the sample stage of the HECTOR scanner at UGCT. The load cell consists of a moving bottom jaw, to which a water bath is connected, and a stationary top jaw.

Using the CT5000 system, both unsaturated and fully water-saturated Savonnières limestone samples were subjected to compressive tests. In order to analyze fracture initiation and propagation, scans were made at different stresses, equal to certain percentages of the compressive strength of the samples. These scans were analyzed for the change in porosity and fracture presence with increasing load.

Results and discussion

Two different types of samples were tested: macroscopically homogeneous (16 samples) and macroscopically heterogeneous (10 samples) Savonnières limestone samples . Their porosity was calculated using the Archimedes method with water saturation at vacuum conditions and linked to their compression strength as tested with the Deben CT5000 system (figure 2). Part of the samples were tested unsaturated, while others were fully saturated and surrounded by water in the water bath. Three macroscopic homogeneous samples were partly saturated (70% to 76% of the pores filled with water) when tested, while two macroscopic heterogeneous samples were fully saturated with water, but not surrounded by water during scanning. As figure 2 shows, there is no clear trend visible in the distribution of compressive strength to the samples' porosity. This is probably due to microscopic heterogeneities within the sample, causing the unpredictable behavior of the samples.

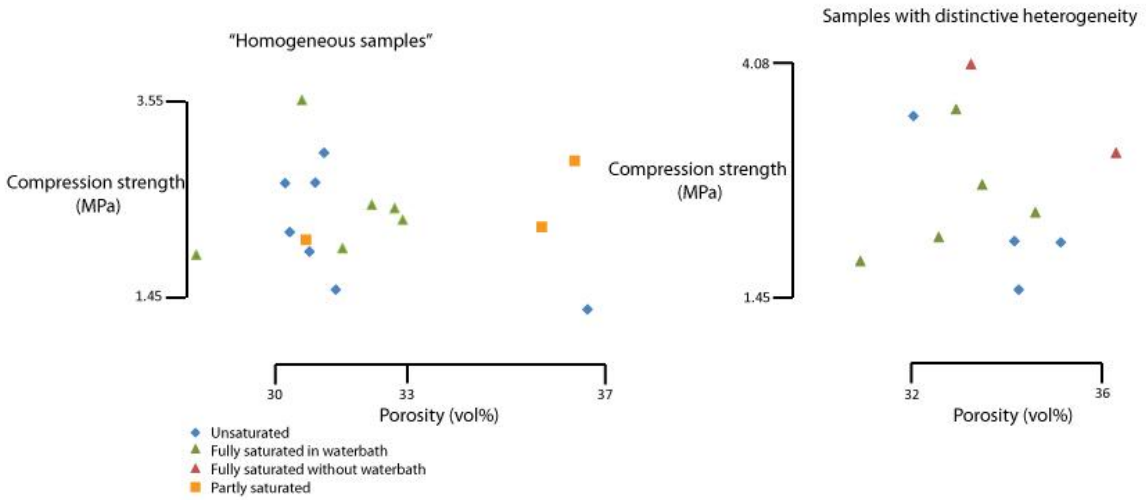

Figure 2: Compressive strength was calculated for different samples, ranging in porosity values. Also, a subdivision was made based on the macroscopic heterogeneity. Because of the microscopical heterogeneity in the samples, there is no clear trend in the distribution of the samples' compressive strength to their porosity.

To elaborate on the experiments, results of sample SL10 are described below. Figure 3a and 3b gives the stress-strain curves obtained during the compressive test of this sample. The vertical strain is constantly measured by the CT5000 system, whereas the horizontal strain can only be measured when a CT scan is made at a certain stress.

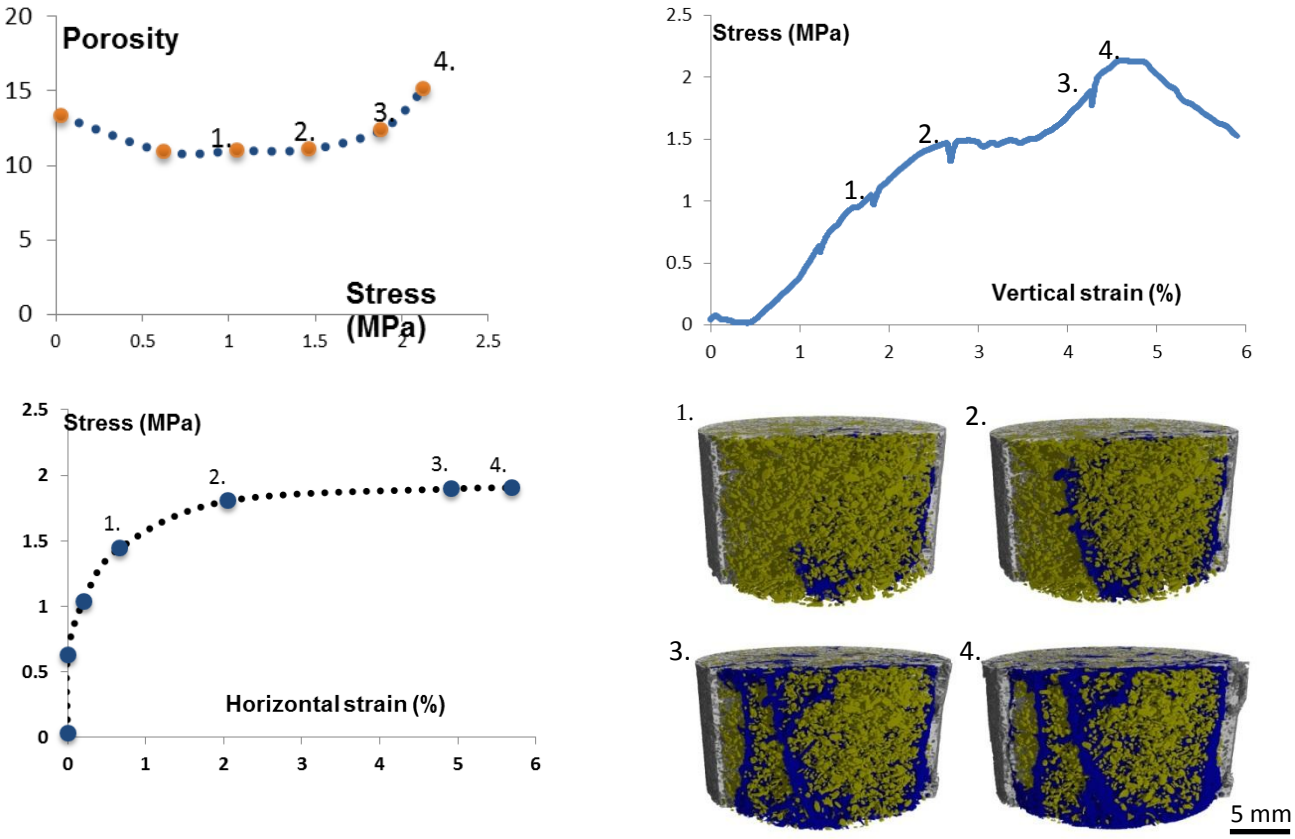

Figure 3: Stress (MPa) – strain (%) curves for both vertical as horizontal strain. Vertical strain is constantly measured in the CT5000 system, while the horizontal strain is measured in the CT scans. Also the porosity changes with stress are indicated and the 3D visualisation of the 4 last scans of this sample (blue = porosity affected by fractures, yellow = porosity unaffected by the fractures).

The stress-strain curve in figure 3 is explained by the 3D images, taken from the last four scans in this test series. These show that the fractures become more and more important as stress increases. They open up more, providing more horizontal strain. The porosity change illustrated in figure 3 tells a similar story: as macro-fractures are formed, porosity increases due to the opening of the fractures. The change in porosity is most distinct just before and at the point of failure (step 3 and 4) in figure 3. This graph also shows an initial decrease in porosity. This is probably related to an early stage of fracturing in the lowermost regions of the sample. Higherup these first fractures cause closing of initial pores, thereby lowering the porosity in the uppermost regions of the sample. The lowermost parts were not taken into account because of metal artefacts due to ~~the closeby~~ lower jaw of the CT5000 system. This could explain the initial decrease in porosity as seen in this sample.

Future outlook

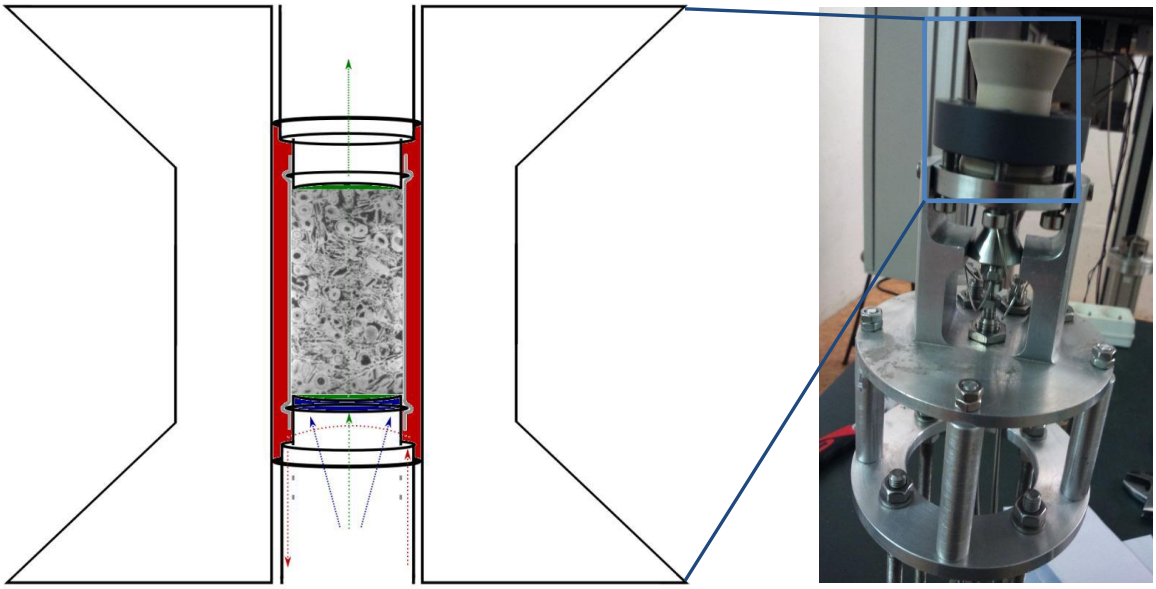

Figure 4: Schematic representation of the experimental set-up in which a Savonnières limestone sample is subjected to a radial pressure (red), multi-phase fluid flow through the sample (green) and an axial pressure is transfered to a mobile piston below the sample (blue). The rock sample is contained in a sleeve and the entire set-up is surrounded by PEEK material.

To incorporate the effect of the fractures on fluid distributions within samples subjected to multi-phase fluid flow, experiments are currently being carried out using an in-situ triaxial flow cell as shown in figure 4. Because of the time-rate related to the propagation of the fractures, scans are performed at the Environmental X-ray CT (EMCT) at the UGCT. This gantry-based system allows CT scans to be made at a time resolution of 12 seconds (Dierick et al., 2014).

Acknowledgments

Work by these authors was partially supported by FWO, project G.0041.15N and FCWO-UGent. The authors are also grateful to Ba. student Laura Segers for the assistance during the experiments in this study.

References

Berkowitz, B. (2002). Characterizing flow and transport in fractured geological media: A review. *Advances in Water Resources*, *25*(8-12), 861–884. doi:10.1016/S0309-1708(02)00042-8

Dierick, M., Van Loo, D., Masschaele, B., Van den Bulcke, J., Van Acker, J., Cnudde, V., & Van Hoorebeke, L. (2014). Recent micro-CT scanner developments at UGCT. *Nuclear Instruments and Methods in Physics Research Section B: Beam Interactions with Materials and Atoms*, *324*, 35–40. doi:10.1016/j.nimb.2013.10.051

Masschaele, B., Dierick, M., Loo, D. Van, Boone, M. N., Brabant, L., Pauwels, E., … Hoorebeke, L. Van. (2013). HECTOR: A 240kV micro-CT setup optimized for research. *Journal of Physics: Conference Series*, *463*, 012012. doi:10.1088/1742-6596/463/1/012012

Noiriel, C., Gouze, P., & Madé, B. (2013). 3D analysis of geometry and flow changes in a limestone fracture during dissolution. *Journal of Hydrology*, *486*, 211–223. doi:10.1016/j.jhydrol.2013.01.035

Siegesmund, S., & Dürrast, H. (2014). Physical and Mechanical properties of Rocks: Strength properties. In *Stone in Architecture: Properties, durability.* (pp. 168–199).

CT-Scan analysis of bioturbation structures: from intertidal mudflat to young mangrove forest in French Guiana (South America)

A.Aschenbroich[1], E. Michaud[1], F. Fromard[2], A. Gardel[3], E. Desoche[1], LF. Daigle[4], B. Long[4], G Thouzeau[1]

[1] Laboratoire des Sciences de l'Environnement Marin (LEMAR, UMR 6539, CNRS-IRD-UBO), IUEM, Rue Dumont d'Urville, 29280 PLOUZANE, France,

[2] Laboratoire d'écologie fonctionnelle et Environnement (EcoLab, UMR 5245, CNRS-UPS-INPT), Université Paul Sabatier, 118 Route de Narbonne – Bat 4R1, 31062 Toulouse Cedex 9, France.

[3] CNRS Guyane, équipe Mer et Littoral de Guyane, Résidence Le Relais, 2, avenue Gustave Charlery, 97300 CAYENNE Guyane française

[4] Institut national de la recherche scientifique, Centre – Eau Terre Environnement 2605, boulevard du Parc-technologique, Québec (Québec) G1P 4S5, Canada

1. Introduction

Bioturbation activity has considerable impact on ecosystem functioning. By digging and maintaining burrows, transforming and burying organic matter, fauna and roots affect biogeochemical cycles and sedimentary structures at the benthic interface. In French Guiana (South America), the role of bioturbation on mangrove functioning is, however, still unknown. These mangroves are adapted to recurrent sediment disturbances because of huge mud inputs from the Amazon River (Fromard et al., 2004; Gardel et al., 2006; Anthony et al., 2010; figure 1).

The trees colonize new substrata rapidly, which makes possible the study of distinct stages of mangrove development over small spatial scales (i.e., from mudflat to young mangrove). First data on benthic community in the Guyanese littoral highlighted its ecological adaptation to recurrent erosion/accretion phases, and mainly dominated by pioneer species with low species richness (Clavier et al., 1999). The Pearson and Rosenberg model (1978) simulates generally increasing of species richness and biomass from unstable to stable environments. We then expected that benthic communities of Guyanese littoral are constituted of pioneer species within the mudflat, whereas species richness and biomass increase in the more developed stages of mangroves leading to more intense bioturbation activity. From Rhoad and Germano (1982) (Figure 2), it is also expected that types of structures diversify and that volume as well as depth of burrows increase along a mangrove ecosystem establishment and stabilization gradient. In this study, we thus hypothesize that biogenic structures (fauna burrows and roots) depend on the structure and composition of the benthic fauna and the vegetation, and may vary with mangrove growth.

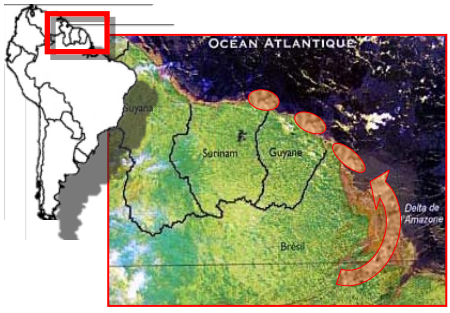

Figure 1 : Schematic illustration of mud bank migration along the Guianese coast (at the North West of the Latin American continent) resulting from sediment input from the Amazon River mouth (from Anthony et al., 2010).

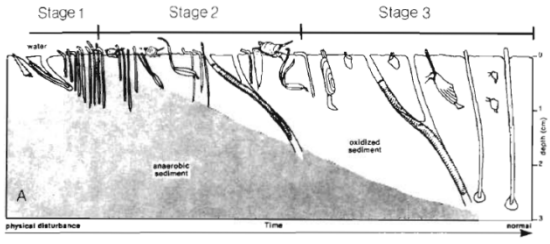

Figure 2: Development of organism-sediment relationships over time following a physical disturbance. In Rhoads and Germano (1982) modified from Pearson and Rosenberg (1978).

2. Material and methods

This study was conducted at the East part of the French Guiana, at the mouth of the Sinnamary estuary (figure 3a, b). Mudflat, pioneer and young mangrove forest habitats were investigated respectively in stations A, E and I (figure 3c). Vegetation structure was assessed through tree species identification, density measurements as well as biomass calculations according to Fromard et al (1998). Each station was represented by 3 points parallel to the tidal level.

Each point was sampled during the day by manual coring (10 cm Ø, 20cm length). At each point, two series of cores were sampled for fauna species composition and sediment characteristics, and one series was sampled for biogenic structure quantification. Cores for fauna were sliced and sieved on 250 µm mesh to recover macrofauna. Abundance, and biovolume were characterized for each encountered species. Also, cores for sediment characteristics were sliced and distinct subsamples were frozen for subsequent analysis of photosynthetic pigments (fluorometer), organic carbon and nitrogen (CHN analyser), water content and porosity as well as grain size.

Sediment cores intended for biogenic structures analysis were swiftly sent to the Institut National de la Recherche Scientifique (INRS, Quebec, Canada) for subsequent tomography analysis. During the analysis, cores were horizontally placed on a table. Sediment slices were scanned every 0.6 mm with the power settings of 140 kV, 250 mA and a pitch of 0.35. We used a matrix of 512 × 512 and the field of view was 120, which gave a voxel resolution of 0.23 mm × 0.23 × 0.6 mm. Each picture from 2D transverse section was obtained in dicom format to be later analyzed by Mathworks software. We analyzed the sedimentary structure of each core by using a tomogram representing tomographic intensities (TI) expressed in Hounsfield units (HU) along a longitudinal plane for the entire length of the core (Gagnoud et al. 2009; Michaud et al. 2003). The calibration gave specific values for tomographic intensities according to analyzed materials (i.e., TIair = -1000; TIwater = 0; TIcalcite = 2500). Biogenic structures were visualized and quantified with depth in terms of burrow and root volumes.

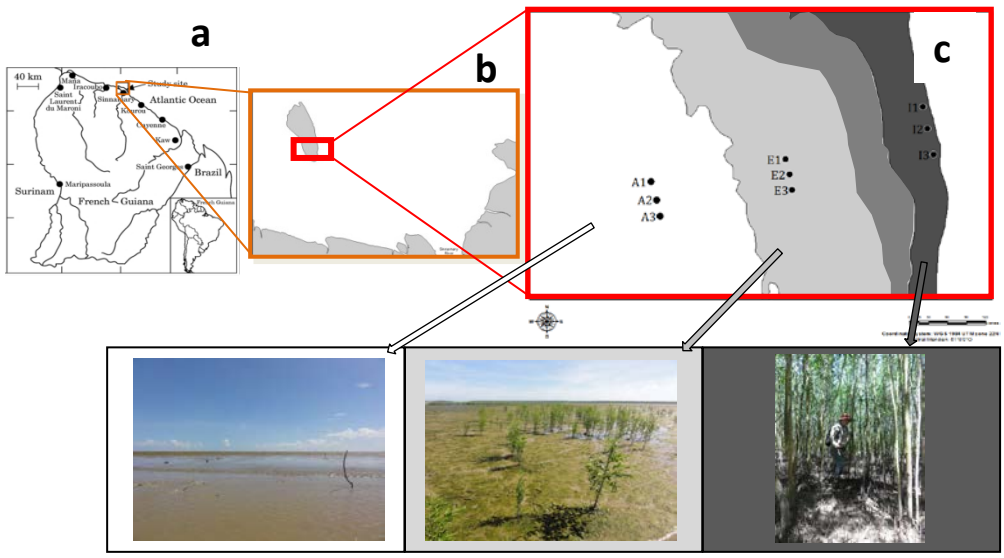

Figure 3: The study site was located in French Guiana (a) at the Sinnamary River Mouth (b). Three stages of mangroves development were considered and each was represented by three stations (c). Stations A, E and I represent the mud flat, the pioneer mangrove and the mangrove forest respectively.
Photos: @EMichaud and FFromard/cnrs

3. Results and discussions

Mangrove establishment and development were characterized by changes in environmental conditions in term of vegetation structure and of physico-chemical properties of sediment.

In response, structure and composition of macrobenthic community varied between sites in term of total species richness, density, and biovolume. Lowest individual density with lowest total biovolume and burrow volume characterize the pioneer mangrove, whereas mudflat and young mangrove forest are inhabited by higher individual density and biovolume. Bioturbation structures are more voluminous and complex within those sediments despite of the different species richness between the mudflat and the young mangrove forest. We attributed such differences to different sediment compaction and desiccation between each stage of mangrove development. Effects of roots on vertical distribution of burrow and animals, in comparison with mudflat stations will be discussed.

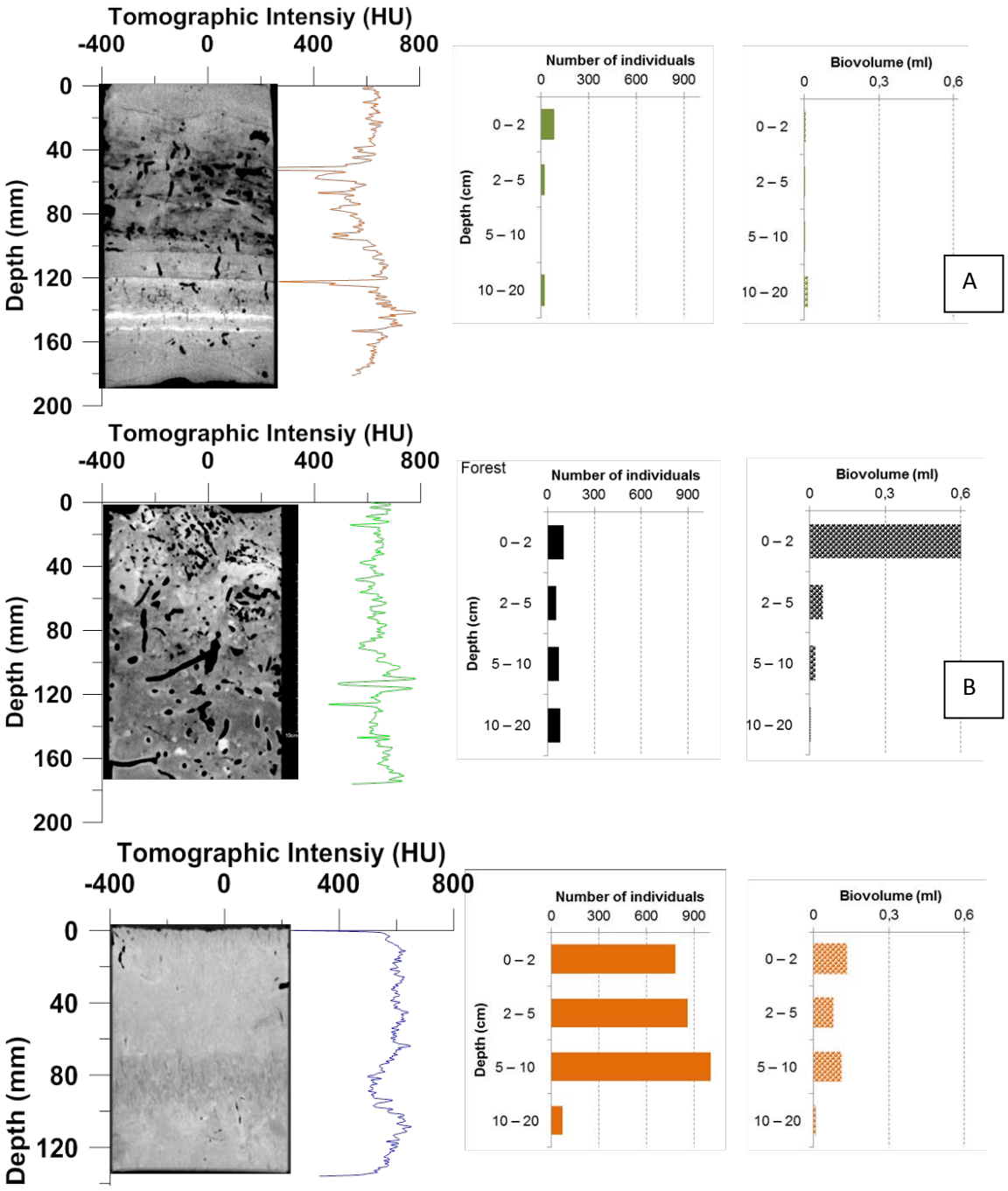

Figure 4: *tomographic vertical profiles of tomographic intensity (TI, HU) and bi-dimensional CT scan pictures from the three stages of mangrove development (A: mudflat; B: pioneer mangrove; C: young mangrove forest) in October 2013. Total species abundance (ind.m^{-2}) and biovolume (mL) per sediment slice.*

References:

Anthony, E. J., Gardel, A., Gratiot, N., Proisy, C., Allison, M. a., Dolique, F., & Fromard, F., 2010. The Amazon-influenced muddy coast of South America: A review of mud-bank–shoreline interactions. *Earth-Science Reviews*, *103*(3-4), 99–121.

Clavier, J., 1999. Macrobenthos de petite taille dans les vasières et la mangrove de Kaw. *Document de travail. Plouzané : IRD*, 11 p.

Fromard, F., Puig, H., Mougin, E., Marty, G., Betoulle, J.L., Cadamuro, L., 1998. Structure, above-ground biomass and dynamics of mangrove ecosystems: new data from French Guiana. *Oecologia, 115*, 39–53.

Fromard, F., Vega, C., & Proisy, C., 2004. Half a century of dynamic coastal change affecting mangrove shorelines of French Guiana. A case study based on remote sensing data analyses and field surveys. *Marine Geology*, *208*(2-4), 265–280.

Gagnoud, M., Lajeunesse, P., Desrosiers, G., Long, B., Dufour, S., Labrie, J., Mermillod-Blondin, F., Stora, G., 2009. Litho- and biofacies analysis of postglacial marine mud using CT-Scanning. *Engineering Geology*, *103*(3-4), 106–111.

Gardel, A. and Gratiot, N., 2006 Monitoring of coastal dynamics in French Guiana from 16 years of SPOT images. *Journal of Coastal Research*, SI39, 1503-1506.

Michaud, E., Desrosiers, G., Long, B., Locat, J., Gilbert, F., & Stora, G. (2003). Use of axial tomography to follow temporal changes of benthic communities in an unstable sedimentary environment (Baie des Ha ! Ha !, Saguenay Fjord), *Journal of Experimental Marine Biology and Ecology, 286*, 265–282.

Pearson TH, Rosenberg R (1978) Macrobenthic succession in relation to organic enrichment and pollution of the marine environment. *Oceanography and Marine Biology - An Annual Review, 16*, 229-311.

Rhoads DC, Germano JD (1982) Characterization of organism-sediment relations using sediment profile imaging: an efficient method of remote ecological monitoring of the seafloor. *Marine Ecology Progress Series, 8,*115-128

Computerized Coaxial Tomography (CT-Scanning) in paleoclimatic studies

P. FRANCUS[1,2], F. LAPOINTE[1,2], C. MASSA[3], D. FORTIN[4], K. KANAMARU[5], G. ST-ONGE[6,2]

[1] Institut National de la Recherche Scientifique, Centre ETE, Québec, Canada
[2] GEOTOP Research Centrer, Québec, Canada
[3] Earth and Environmental Science, Lehigh University, Bethlehem, PA, USA
[4] Earth Sciences and Environmental Sustainability, Northern Arizona University, AZ, USA
[5] Department of Geosciences, University of Massachusetts, Amherst, MA, USA
[6] ISMER, UQAR, Rimouski, Québec, Canada

Medical CT-Scanners allow the rapid 3D visualisation of sediment cores. CT-Scans images correspond to 3-D linear X-ray attenuation pixel or voxel matrix, where higher density and higher atomic numbers result in higher attenuation of X-rays.

This paper illustrates that CT-scanning sediment cores is a powerful tool to identify and visualize, amongst others, physical sedimentary structures (e.g. turbidites), biogenic structures (e.g. bioturbation), coring artefacts, sediment disturbances, hiatus and other erosional features, and therefore is a powerful tool to establish a high-resolution stratigraphy. Moreover, it can be used to establish physical properties of sediments, such as density. This paper presents a comparison of density measurements obtained from CT-Scans images with conventional measurements (Gamma-Ray attenuation, bulk density) over a 100m-long sediment profile and evaluate the quality, sources of error and the comparative advantages of the different methods in terms of accuracy of the signal, and time necessary to perform analyses.

Finally, we applied this technique to the varved sediments of Strathcona Lake sediment, northern Ellesmere Island, in order to obtain annually resolved sedimentary fluxes. Over the last 65 years, annual sediment accumulation rates in Strathcona Lake documented an increase in high-energy hydrologic discharge events from 1990 to 2009. This timing is in agreement with evidence for an increase in the amount of melt on the adjacent Agassiz Ice Cap, as recorded in ice cores.

Number of words: 221

References:
If you want to add references, please use an author/date style.

Assesment of a new method to estimate the thermal conductivity of undisturbed permafrost samples using CT scan analyses

M-A. DUCHARME*[1,2], M. ALLARD[1,2], J. CÔTÉ[3] AND E. L'HÉRAULT[2]

1 Université Laval, Départment de géographie, Faculté de foresterie, géographie et de géomatique, [email: marc-andre.ducharme.1@ulaval.ca; michel.allard@cen.ulaval.ca]
2 Centre d'études nordiques,[email: emmanuel.lherrault@cen.ulaval.ca]
3 Université Laval, Département de génie civil et de génie des eaux, Faculté des sciences et de génie,[email: jean.cote@gci.ulaval.ca]
* presenting author

Keywords: permafrost, thermal conductivity, CT scan,

1 Introduction

Defined as soil or rock that remains at or below 0 °C for a long period of time, permafrost (i.e. perennially frozen ground) covers extensive areas in Arctic regions. It occurs in all types of geological surface material such as solid, fractured and weathered bedrock, gravel, sand, silt, clay or peat and contains ice in various forms and amounts. Precise knowledge of the thermal and geotechnical properties of the permafrost often is needed as input parameters in numerical modelling to asses the dynamic behevior of physical system in both fundamental science and engineering. Although permafrost properties are rather well known, essays of a new approach to measure them can yield insights of the factors that define concepts such as thermal conductivity. Involved factors include ice content, soil grain-size and the structural organisation of ice within the soil. The aims of this study are (1) to developed an innovative and nondestructive approach using CT scan to compute the thermal conductivity of undisturbed permafrost samples and (2) to validate the computed results with derived proven thermal conductivity data obtained on undisturbed permafrost samples.

2 Methods

Nineteen undisturbed permafrost samples with different textures and cryostructures (ice and soil structural arrangement) extracted from various sedimentary environments (glacial, alluvial, marine, organic, etc.) were selected. Ranging from homogeneous fine grained soils with stratified ice lenses to coarse-grained diamictons well-bonded with pore ice (Fig. 1), the samples choosen cover a large variety of Arctic soils.

Fig. 1. *A) Silty ice-rich permafrost sample with a suspended cryostrucure, B) coarse sand permafrost sample with a lenticular cryostructure base on the north-american cryostructure classification proposed by Murton and French (1994).*

All samples were cored using a portable earth drill quipped with a 100 mm diameter core barrel. This equipment allows a 100 mm diameter core to be retrieved almost unaltered. Cores were precisely cut using a concrete saw to obtain samples with length ranging from 8 to 8,5 cm. Permafrost samples were scanned using a Siemens Somatom 64TM scanner at the Institut National de la Recherche Scientifique (INRS) (Fig. 2) in Québec city. According to the core diameter (100 mm) and scanner specification, a voxel resolution of 0.2 x 0.2 x 0.6 mm was obtained.

Fig. 2. *A) Permafrost cores are cut with a concrete saw at a temperature of -18°C B) Final dimension of a sample.C) .The Siemens Somatom 64TM scanner allowed a fast data acquisition, thus keeping the frozen state of the samples.*

Analysis of the cryostructure was done using ORS Visual ™ software. This initial treatment aims to quickly visualize the permafrost internal cryostructure (Fig. 3) and summarily isolate tomographic intensity of permafrost components values.

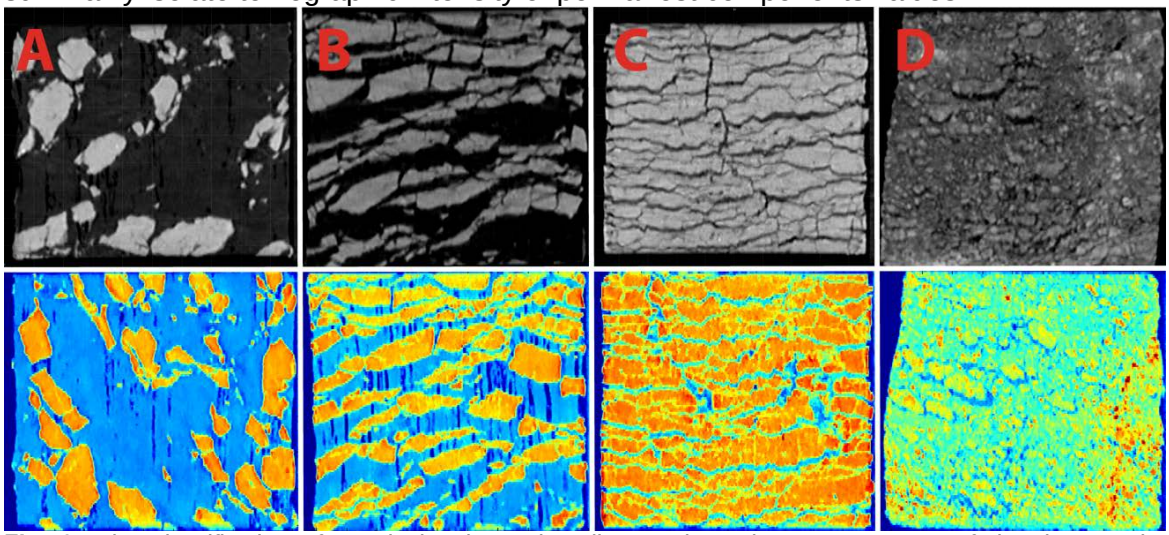

Fig. 3. *The classification of voxels by the script allows volumetric measurements of the three main components of permafrost: ice (blue), sediments (yellow to orange), ice and sediment (yellowish green) and gas (black). Examples from the wide range of cryostructure A) suspended B) irregulate reticulate C) from lenticular to irregular reticulate D) crustal.*

Previous studies from Jiang *et al.,* (2007) and Calmels *et al.,* (2010) measured the different extents of tomographic intensity that can occur in a permafrost sample. These values were used in a MatLab ™ script described in the work of Clavano *et al.,* (2011). The script was refined by the research team at the Center for northern studies with the

agreements and cooperation of the authors. It is designed to automatically discretize permafrost components and perform highly accurate volumetric measurements. For each samples, the volumetric content of the frozen sediment and bubbly ice (x_{soil}, x_{bi}) was measured.

The volumetric CT scan results were the central parameters used in the thermal conductivity model. The proposed model uses three general conditions: 1) the soil type (gravel and coarse sand, silt and clay, peat); 2) the porosity of the ice; 3) the cryostructure. The model also assumes that the permafrost consists of two separate main components:

1) frozen soil (x_{soil}, k_{soil})
2) bubbly ice (x_{bi}, k_{bi})

where x_{soil} and x_{bi} are the volumes of frozen soil and bubbly ice, and k_{soil} and k_{bi} are the thermal conductivities of the frozen soil and the bubbly ice, respectively. Therefore, the effective conductivity of a specimen is function of:

$$k_{eff} = fct(x_{soil}, k_{soil}, x_{bi}, k_{bi}) \qquad [2.1]$$

where thermal conductivity values (k_{soil}) are derived from known values from Côté and Konrad (2005b) and volumes data (x_{soil}, x_{bi}) are measured with CT scan analysis.

The combined effects of the volumetric ratio and the cryostructure of a sample are computed by selecting a theoretical heat flow model depending of structural organization of the sample determined by visual analysis. The k_{eff} components have been use in three simple heat exchange models proposed by Farouki (1981):

$$k_{eff} = x_{soil} k_{soil} + x_{bi} k_{bi} \qquad [2.2]$$

$$\frac{1}{k_{eff}} = \frac{x_{soil}}{k_{soil}} + \frac{x_{bi}}{k_{bi}} \qquad [2.3]$$

$$k_{eff} = {k_{soil}}^{x_{soil}} * {k_{bi}}^{x_{bi}} \qquad [2.4]$$

where the parallel flow model (vertical cryostructure) follows equation [2.2], the series flow model (lenticular and reticulate cryostructure) equation [2.3] and the geometric flow model (porous and suspended cryostructure) equation [2.4].

The thermal conductivity of the bubbly ice (k_{bi}) was found using an equation derived from Maxwell (1892), proposed by Shwerdfeger (1963) used to compute the thermal conductivity of sea ice:

$$k_{bi} = \frac{2k_i + k_a - 2v(k_i - k_a)}{2k_i + k_a + v(k_i - k_a)} * k_i \qquad [2.5]$$

considering the volumetric ratio of thermal conductivity of the air (k_a) and the thermal conductivity of the ice (k_i). The porosity of the ice (v) was estimated using HU values (during the CT scan analysis) of the ice contained in the sample with a statistical approach developed by Long *et al.,* (2012):

$$v_{CT} = 1 - \frac{HU_{mean} + 1024}{HU_{max} + 1024} \qquad [2.6]$$

where HU_{mean} and HU_{max} are the mean and maximum values for permafrost ice.

3 Results and discussion

The numerous assets and breakthroughs offered by the CT scan find all their significance when calculating volumes of permafrost components. To validate these calculations, the masses of melted water samples were transformed into ice volume to compare the results obtained with the CT images analysis. A strong correlation (Fig. 4) has been established between actual ice volumes (laboratory) and volumetric measurements from CT scan data.

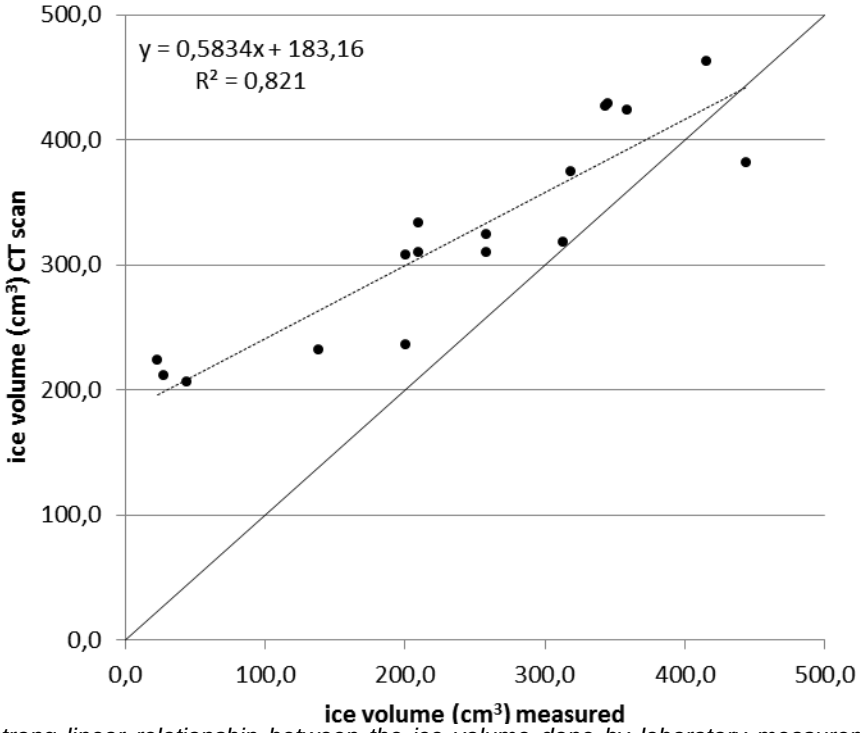

Fig. 4. *The strong linear relationship between the ice volume done by laboratory measurements and CT scan volumetric measurements*

The average error relative to the actual volume of ice is -18,6 %. The results demonstrate that the CT scan usually tends to underestimate the volume of ice with a negative error, since the volume of ice measured in the laboratory is considered the actual value. This negative error can be attributed to the rather low resolution of the CT scan that is lower than the sample porosity. Thus, we can assume that there is a direct correlation between a porous and interstitial cryostructure and the increase of error.

Our results obtained from CT scan compare well with results obtained on similar permafrost soils by Slusarchuk and Watson (1975) on undisturbed ice-rich permafrost (Fig 5.). Indeed, the particles size characteristics of the samples used in their study are very similar to those obtained during our geotechnical analysis *i.e.* 9% sand, 55% silt and 36% clay. These authors' results and our (Fig 5) show that the thermal conductivity of permafrost is strongly controlled by the volumetric ice content of the permafrost. Samples with ice content between 25% and 80% have an effective thermal conductivity from 1.81 to 2.12 W/m°C. Whereas samples having ice contents ranging from 95% to

231% are showing thermal conductivities between 1.57 to 1.75 W/m°C. In general, the data show a decrease of the thermal conductivity as the ice content increases.

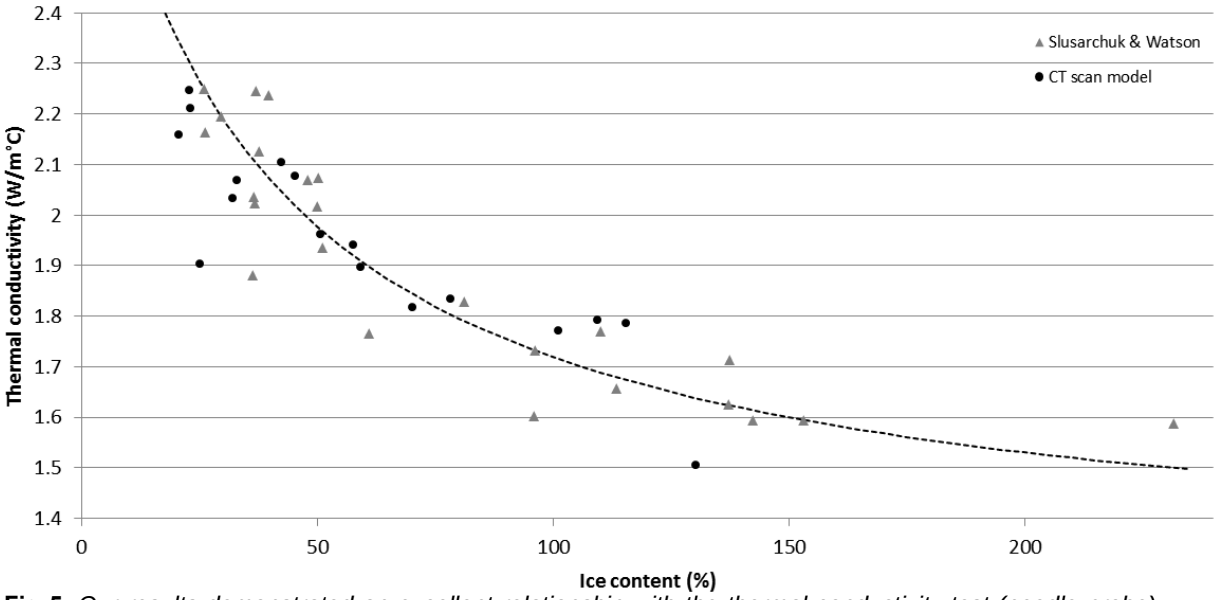

Fig 5. *Our results demonstrated an excellent relationship with the thermal conductivity test (needle probe) data done on undisturbed ice-rich permafrost samples. When compared with a best fit curve derived from the data of Slusarchuk and Watson, the average margin of error is 0.6%.*

4 Conclusion

The accurate and rapid measurement of volumetric CT scan is a leap forward for permafrost science. The new method (CT scan / model) is an ideal tool for geotechnical analysis; especially upon preparation and when designing engineering works established on permafrost (roads, airstrips and buildings). It is also a nondestructive approach and leaves the specimens intact for other geotechnical analyses. The method could be improved in several ways. A higher image resolution would better target voxels causing less underestimation of ice and gas inclusion. By establishing a better understanding of voxels composed of ice/air and ice/ sediment, the error would be significantly reduced. Therefore the use of micro CT scan would improve the conductivity determinations. For cons, the acquisition time of micro CT scan can take several hours and must therefore be done in a cold room under the freezing point, thus making the application more time consuming. Along these same lines of thinking, the script could be reviewed and enhanced with a new voxel classification to better discern the permafrost phases.

References

Calmels, F., Clavano, W.R. et Froese, D.G. 2010. Progress on X-ray computed tomography (CT) scanning in permafrost studies. GEO2010: 63rd Canadian Geotechnical Conference & 6th Canadian Permafrost Conference. Canadian Geotechnical Society: Richmond, B.C. 1363 – 1368.

Clavano, W.R., Calmels, F. et Froese, D.G. 2011. Quantitative processing of X-ray CT images of permafrost cores for cryostratigraphy : limitations and prospects. Submitted to Permafrost and Periglacial Procesesses (in review). 35 p.

Côté,J. et Konrad, J.M. 2005b. A generalized thermal conductivity model for soils and construction materials. Can. Geotech. J. 42: 443-458

Farouki, O.T., 1981. Thermal Properties of Soils. CRREL Monograph 81-1, Hanover, 151 pp.

Jiang, H., Seco, J. et Paganetti, H. 2007. Effects of Hounsfield number conversion on CT based proton Monte Carlo dose calculations. Medical Physics 34: 1439–1449. DOI: 10.1118/1.2715481.

Long, B., DesRoches, M., Mechti, N., Cnuddle, V et Jacobs, P., 2012. Porosity variations in function of deposit architecture. CT Scan Workshop, Development on non-medical environment, march 2012, 7-9.

Maxwell, J.C. et Thompson, J.J. 1892. A treatise on electricity ans magnetism. Vol.1 Clarendon

Murton, JB. et French, H.M. 1994. Cryostructures in permafrost, Tuktoyaktuk coastlands, western arctic Canada. Canadian Journal of Earth Sciences 31: 737–747. DOI: 10.1139/e94-067.

Schwerdtfeger, P. 1963. The thermal properties of sea ice. Journal of Glaciology. Vol. 4. No. 36. p. 789- 807.

Slusarchuk, W.A. et Watson, G.H. 1975. Thermal conductivity of some ice-rich permafrost soils. Canadian Geotechnical Journal, 12: 413-423.

Application of X-ray Interferometry to a Highly Structured Calcium Carbonate Shell (Foraminifera)

G. KNAPP*[1], J. YUAN[2], L. BUTLER[2], M.B. OLATINWO[2], J. GE[3]

[1] Department of Mechanical Engineering, Louisiana State University – gknapp1@tigers.lsu.edu
[2] Department of Chemistry, Louisiana State University – jyuan4@tigers.lsu.edu, lbutler@lsu.edu, molati1@tigers.lsu.edu
[3]Center for Computation and Technology, Louisiana State University – jinghuage@cct.lsu.edu
* presenting author

Keywords: X-ray interferometry, reconstructors, foraminifera, VisTrails and KiwiViewer.

Abstract

A convenient test sample for X-ray interferometry are the millimeter-sized foraminifera. A tomography dataset was acquired at the Advanced Photon Source with stepped, two-grating interferometry at 25 keV, then processed with a vectorized least squares algorithm into projections. Several reconstructors, MuhRec, SNARK09, and ASTRA, were tested. The ASTRA reconstructor has been integrated into a VisTrails provenance-supporting workflow. The workflow exports the volume data (cropped) in a format appropriate the KiwiViewer app on mobile devices.

Introduction

Grating-based interferometry has been implemented at X-ray and neutron imaging beamlines worldwide to perform phase contrast imaging and tomography with applications in materials science, biomedical science, and beam wavefont and optics characterization. Herein, we describe stepped-grating interferometry of a favorite test sample, a foraminifera, a single-cell protist with a highly detailed calcium carbonate structure. The results shown here were obtained on test interferometry systems at the Advanced Photon Source Beamline 1-BM. Foraminifera will continue to be used to assess data quality at two X-ray tomography/interferometry systems under construction at LSU, CAMD (Center for Advanced Microstructures and Devices, http://www.camd.lsu.edu/).

The foraminifera data has been used to develop software and procedures. The software tools range from Mathematica notebooks for interferogram analysis, VisTrails for workflow, and SNARK14, ASTRA, and MuhRec for reconstruction. Kiwiviewer is a convenient, portable visualization app.

Experimental

The APS data was acquired at 25 keV with a stepped, two-grating interferometer, shown in Fig. 1 (Marathe et al., 2012); absorption grating before the sample (G0) was omitted due to high phase coherence of the bending magnet source; the sample stage was 23 meters downstream of a double multilayer monochromator. The phase grating (G1) was optimized for a pi-phase shift at 25 keV with a period of 4.8 micron. The analyzer grating (G2) had a period of 2.4 micron; a piezoelectric stage moved the grating in 16 steps over 1.5 periods. The 100 micron thick LuAG:Ce scintillator was imaged with an optical lens system giving an effective pixel size of 0.645 microns. For the tomography data set, 601 projections (interferograms) were acquired over [0,180] degrees, totalling 9616 sample images.

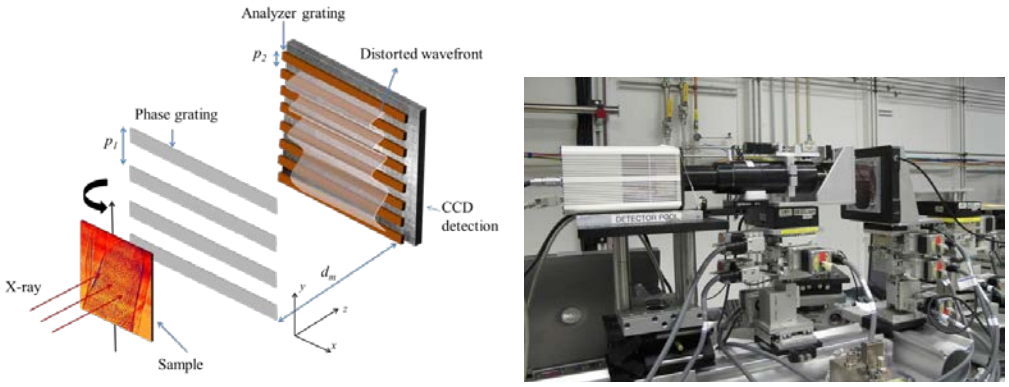

Fig. 1. (left) Schematic drawing of the X-ray Talbot interferometer set-up. The X-ray illuminates the sample, and the transmitted beam passes through the phase grating and creates a distorted self-image at distance d_m that is imaged by the CCD. (right) One of the experimental setups used at the APS for two-grating stepped interferometry(Marathe et al., 2012).;

Methods

The interferometry data are a set of X-ray counts c_{gp}, where g = 1, ..., M is the index that identifies the exposure, with one exposure at each grating displacement x_g; and p = 1, …, N is the index that identifies the pth pixel. Typically M is in the range of 7-16 and N is on the order of 10^6. We have adapted a fitting algorithm from mathematical physics that transforms the fitting operation into a simple matrix problem (Marathe et al., 2014).

We fit each set of exposures pixel by pixel, c_{gp}, to each pixel's expected dependence on grating position x_g:

$$\hat{c}_{gp} = a_{1p} + a_p \sin\left(\frac{2\pi}{p_{grat}} x_g + \phi_p\right) \qquad (1)$$

$$\equiv [1]\, a_{1p} + \left[\sin\left(\frac{2\pi}{p_{grat}} x_g\right)\right] a_p \cos(\phi_p) + \left[\cos\left(\frac{2\pi}{p_{grat}} x_g\right)\right] a_p \sin(\phi_p) \qquad (2)$$

$$\equiv \sum_{\mu=1}^{3} B_{g\mu} a_{\mu p} \qquad (3)$$

$$a_{2p} \equiv a_p \cos(\phi_p),\ a_{3p} \equiv a_p \sin(\phi_p), \qquad (4)$$

where a_p and φ_p are the amplitude and phase of the interference term for the p-th pixel, and p_{grat} is the period of the translated grating. The interference term is expressed in both polar form (Eq. (1)) and Cartesian form (Eq. (4)). The latter is used to define the M × 3 matrix B (Eq. (3)) that represents the three fitting functions shown in brackets in Eq. (2): constant, sine, and cosine. The $a_{\mu p}$ is one element in the coefficient matrix a, which is a 3 × N matrix of amplitudes, or weights, of the three fitting functions for the N pixels. Later, we will reshape a into a 3D matrix with dimensionality [rows, columns, 3].

The best fit can be chosen to be the set of coefficients $a_\mu p$ that minimize the deviation-squared, D_p, for each pixel, defined by

$$D_p \equiv \sum_{g=1}^{M} (c_{gp} - \hat{c}_{gp})^2. \qquad (5)$$

To minimize D_p, we need only calculate the derivatives of each deviation-squared with respect to each component of a, set all deviations to zero, and solve the resulting matrix equations. The closed form expression for the coefficient matrix a is found to be

$$\mathbf{a} = \mathbf{G} \cdot \mathbf{c}, \qquad (6)$$

where

$$\mathbf{G} = (\mathbf{B}^T \cdot \mathbf{B})^{-1} \cdot \mathbf{B}^T, \qquad (7)$$

and where the superscript T indicates the matrix transpose. So the optimization problem is reduced to multiplying a 3×M fixed matrix G into the M×N data matrix c, to find the 3×N coefficient matrix a. With an efficient matrix manipulation program like MATLAB, the multiplication is extremely fast, of the order of 1 s for 1k×1k images times 16 grating steps.

In Fig. 2, we show a flow diagram of X-ray data processing for the case of K-edge imaging; a similar workflow is also used for interferometry data processing. We use a number of programs to convert raw images into interferograms, then into projections; to convert projections into sinograms of different modalities---up to five sinograms when two-directional interferometry is employed; and then reconstruction into volume data.

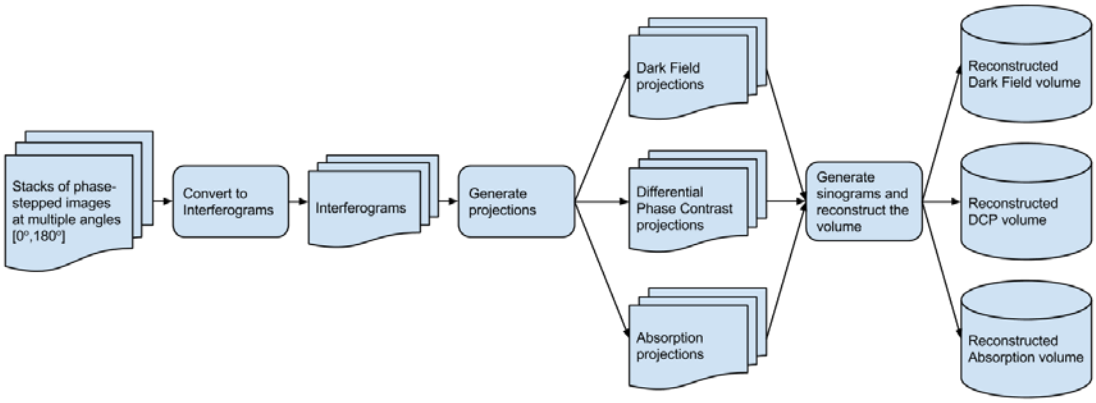

Fig. 2. *Diagram of a the foraminifera interferometry VisTrails data processing workflow.*

The interferogram data is transformed into absorption, differential phase-contrast (vertical) and dark-field (vertical) projections. Shown in Fig. 3 are the projections at 0° degree. The vertical sensitivity is due to the grating orientation shown in Fig. 1.

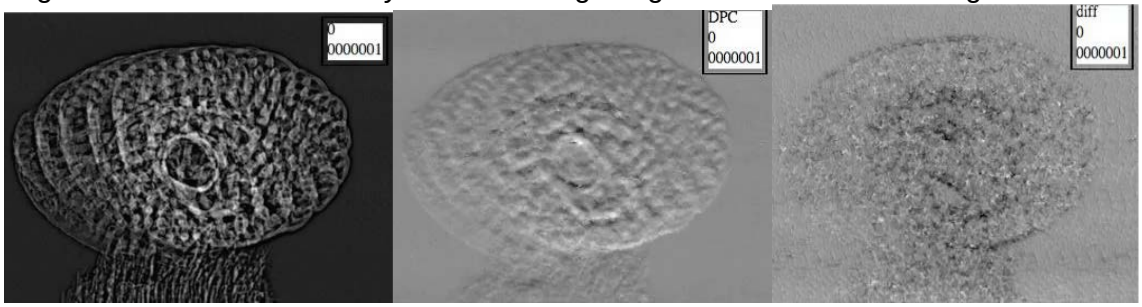

Fig. 3. *Projections: absorption, differential phase-contrast (vertical) and dark-field (vertical).*

Each imaging modality---absorption, differential phase contrast, and dark-field---is converted into a distinct sinogram. In this work, several reconstructors are used: MuhRec [Kaestner, 2011] is a fast reconstructor and has recently been ported to Macintosh. SNARK09 [Klukowska, 2013] offers a wide range of options for exploring reconstructions. ASTRA is compatible with CPU and GPU clusters (Palenstijn et al., 2013).

The analysis tools within SNARK09, especially the simulation options, have been used to explore reconstruction options for the interferometry data. We note the differential phase contrast data requires a unique kernel if reconstructed with filtered back-projection (Pfeiffer, 2007).

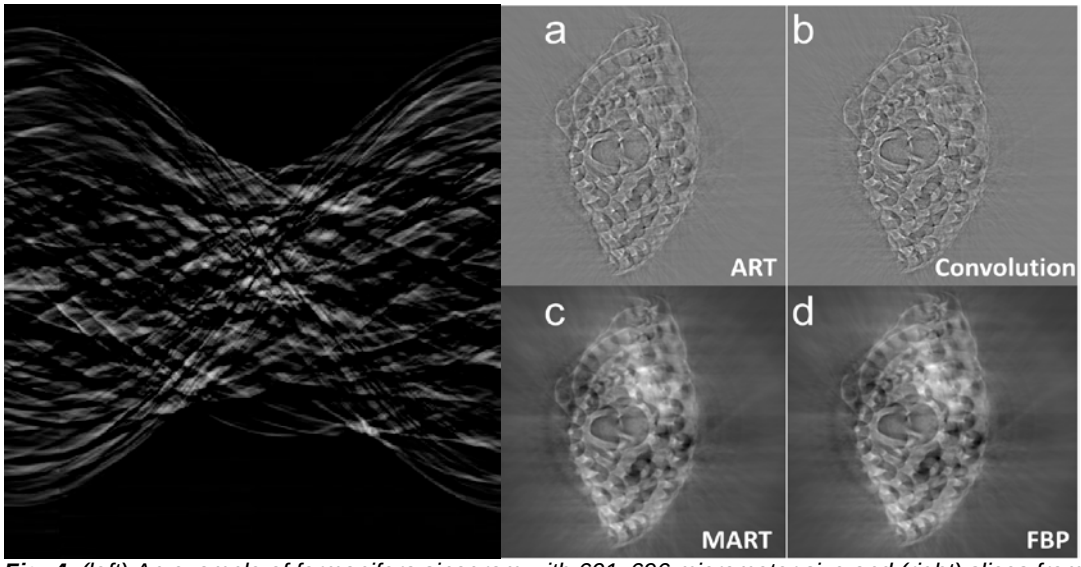

Fig. 4. *(left) An example of formanifera sinogram with 601x696 micrometer size and (right) slices from a tomographic volume with SNARK09 (created by CUNY). (a) An ART reconstruction of the asborption images. (b) Convolustion reconstruction. (c) extensive multiplicative algebraic reconstruction (EMART) and (d) traditional filtered back-projection reconstruction.*

In summary, the data workflow consists of Mathematica and Matlab codes within Python wrappers to create modules for a VisTrails workflow(Freire et al., 2012). VisTrails was chosen to serve a wide user base and create a data provenance. The VisTrails workflow uses both local computational resources and an interactive HPC system. One feature of our VisTrails workflow is the ability to export a cropped and downsampled version of the reconstructed volume to be viewed on a tablet with KiwiViewer (Kitware). KiwiViewer is a free, open-source visualization app for exploring scientific and medical datasets that runs on Android and iOS mobile.[http://www.kiwiviewer.org] By using VisTrails and KiwiViewer, we gained the ability to track data provenance and view 3D images on an iPad. The VisTrails workflow for KiwiViewer file generation and a screen shot from KiwiViewer are shown in Fig. 5.

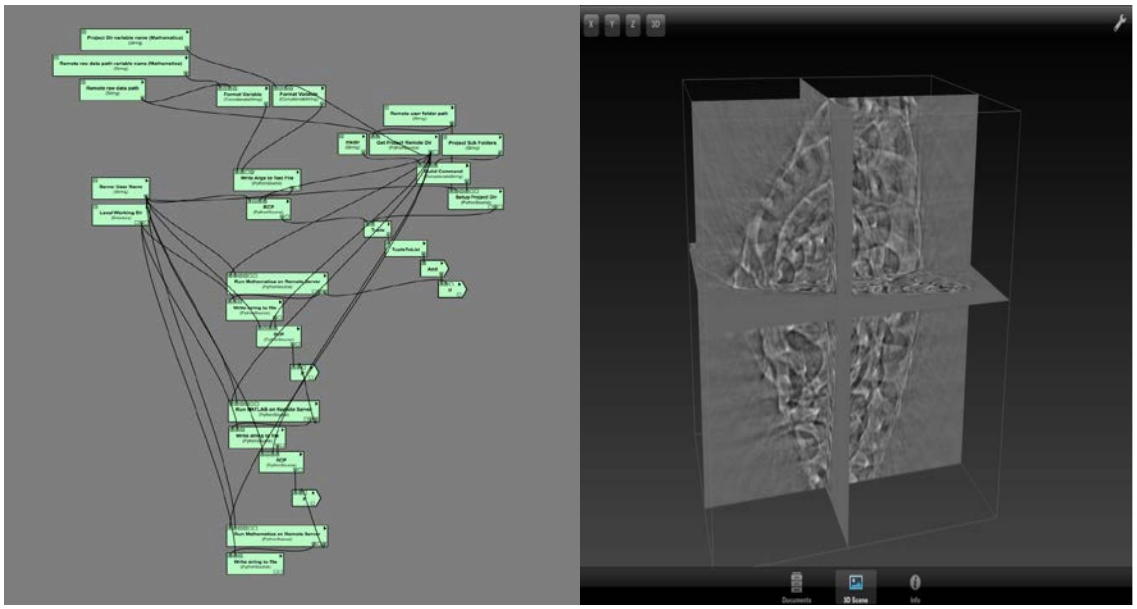

Fig. 5. *(left) VsTrails workflow for visualization for data processing and (right) KiwiViewer orthoslice visualization of the foraminifera absorption volume.*

Conclusions

To conclude, we introduced a case study of foraminifera reconstruction with Mathematica, SNARK09, ASTRA, MuhRec, and VisTrails. With VisTrails, the workflow is more easily shared within our research group and with others. In SNARK09, more than 30 reconstruction methods are available. With Kiwiviewer, 3D visualization becomes convenient and portable.

References

Freire, J.; Silva, C. T. Making Computations and Publications Reproducible with VisTrails. *Computing in Science & Engineering* **2012**, *14*, 18-25.

Kaestner, A. P. MuhRec--A new tomography reconstructor. *Nucl. Instrum. Methods A* **2011**, *651*, 156-160.

Klukowska, J.; Davidi, R.; Herman, G. T. SNARK09 - A software package for reconstruction of 2D images from 1D projections. *Comput. Methods Programs Biomed.* **2013**, *110*, 424-440.

Marathe, S.; Assoufid, L.; Xiao, X.; Ham, K.; Johnson, W. W.; Butler, L. G. Improved Algorithm for Processing Grating-Based Phase Contrast Interferometry Image Sets. *Rev. Sci. Instrum.* **2014**, *85*, art. no. 013704.

Marathe, S.; Xiao, X.; Wojcik, M. J.; Divan, R.; Butler, L. G.; Ham, K.; Fezzaa, K.; Erdmann, M.; Wen, H. H.; Lee, W.-K.; Macrander, A. T.; De Carlo, F.; Mancini, D. C.; Assoufid, L. Development of grating-based x-ray Talbot interferometry at the advanced photon source. *AIP Conference Proceedings* **2012**, *1466*, 249-254.

Palenstijn, W. J.; Batenburg, K. J.; Sijbers, J.: The ASTRA Tomography Toolbox. In *13th International Conference on Computational and Mathematical Methods in Science and Engineering*; CMMSE 2013, 2013; Vol. 4; pp 1139-1145.

Pfeiffer, F.; Kottler, C.; Bunk, O.; David, C. Hard X-ray phase tomography with low-brilliance sources. *Physical Review Letters* **2007**, *98*, 108105.

The potential of CT-scan as a high-resolution tool for facies analysis of laminated sediments from deep fjord-like lakes from the Québec North Shore

O. NZEKWE*[1, 4], P. FRANCUS[1, 4], G. ST-ONGE[2, 4], P. LAJEUNESSE[3, 4]

[1]Institut national de la recherche scientifique, Centre Eau Terre et Environnement, Québec, Canada
[2]Institut des sciences de la mer de Rimouski (ISMER), Université du Québec à Rimouski, Canada
[3]Centre d'études nordiques, Département de géographie, Université Laval, Québec, Canada
[4]GEOTOP Research Centre, Montreal, Canada
*Presenting author, Email: obinna_peter.nzekwe@ete.inrs.ca

Keywords: CT-scan, limnogeology, laminations, sedimentary structures, Québec North Shore

Abstract

This research aims at reconstructing Late Holocene paleoclimate based on annually laminated sediments (varves) from three deep lakes on the Québec North Shore: Lakes Walker, Pentecôte and Pasteur. In this region, climate data are available from instrumental records covering a 50 years period, and from tree-rings covering 200 years to a millennium. However, the possible identification of annually laminated sediments in deep lakes offers the possibility to explore this unique paleoenvironmental archive in order to reconstruct continuous and annually resolved Holocene sediment records of past climatic conditions. During a two-week fieldwork in June 2014, we obtained 43 short sediment cores ranging from 25 to 75 cm. We examined whole core sections with a "SIEMENS SOMATOM Definition AS+ 128" CT-scan at the INRS-ETE *Laboratoire Multidisciplinaire de Scanographie*. CT-scan allowed for the acquisition of longitudinal and transversal images revealing the internal structure of the sediment cores. In addition, digital photographs were taken immediately after splitting prior to oxidation of the sediment core surface. The digital photographs capture slight variations in colour and texture, but were generally characterized by low contrast. The presence or absence of laminations was better appreciated when digital photographs were analyzed alongside CT-scan images. These analyses allowed for identification of five main sedimentary facies characterized by: parallel laminations, oblique laminations, convolute laminations, homogenous mud, and hemipelagic mud. At least 10 out of the 16 cores from Lake Walker are characterized by parallel to inclined laminations, while less than 5 cores from Lakes Pasteur and Pentecôte show distinct laminations. The annual character of the laminations will be verified by image analysis of thin-sections, and an age-depth model, which will be established by varve counting, supported by radiometric dating (^{210}Pb, ^{137}Cs and ^{14}C) and paleomagnetic measurements.

Introduction

Within the North Shore region of Québec, three lakes are under study for the possible occurrence of annually laminated sediments (varves). These lakes were selected based on preliminary studies of the ARCHIVES (*Analyse Rétrospective des Conditions Hydroclimatiques à l'aide des Indicateur de leur Variabilité à l'Échelle Séculaire*) project, a university research initiative in collaboration with industry, which suggested that the glacial history and paleolimnological charateristics of these lakes could favour the formation of varves (Fortin *et al.*, 2013). To date, mainly instrumental data and paleoclimatic reconstructions from tree rings and stable isotopes from tree stems, covering 200-years to a millennium are available in northern Québec (Arseneault *et al.*, 2013, Naulier *et al.*, 2014, Nicault *et al.*, 2014), while annually laminated lake sediments have not yet been fully exploited. Annually laminated sediments serve as excellent archives of past environmental conditions due to their potential of providing an

annual to seasonal-scale resolution (Francus *et al.*, 2013, Ojala *et al.*, 2012, Ojala *et al.*, 2013). Through the counting of laminae succession deposited over the course of at least 1-year, precise varve-based chronologies can be established (Francus *et al.*, 2013, O'Sullivan, 1983, Ojala *et al.*, 2012, Schnurrenberger *et al.*, 2003, Zolitschka *et al.*, 2015). In this paper, we use CT-scan to analyze sediments from three deep fjord-like lakes in the Québec North Shore region in order to identify the sedimentary facies, and locations in the lakes with high potentials for the occurrence of annually laminated sediments.

Study area

The three lakes under study: Lakes Walker, Pentecôte and Pasteur are located within the North Shore region of Québec, which is north of the Gulf of St. Lawrence in Eastern Canada. Notable characteristics that distinguish these lakes among others in the region include their location, glacial history and morphological characteristics, specifically: they are located downstream of glacial valleys, thus receive seasonal input of detrital materials into the lake basins, respectively; they are relatively deep, and may have formed sub-glacial lakes during the last glaciation episode with prevailing conditions that favoured the preservation of deposited sediments. More so, these lakes are located in the *Reserve faunique de Port-Cartier–Sept-Îles*, so have been be fairly undisturbed by human activities such as dredging or modification for hydropower generation except for controlled fishing and boating. Some characteristics of the lakes are shown in Table 1. The North Shore region lies within the Greenville geologic province. Bedrock geology consists of Precambrian rocks that are Archean or Proterozoic in age. Archean rocks comprise migmatite and gneiss, which contain plagioclase, biotite and/or hornblende and/or amphibolite. Proterozoic rocks comprise mafic to ultramafic rocks, as well as sedimentary rocks, which contain paragneiss and quartzite (Ministère des ressources naturelles Québec, 2002). The climate of the region is subarctic (Köppen climate classification *Dfb/Dfc*; Environment Canada).

Table 1. *Some characteristics of the studied lakes (Ouellet, 1997)*

Lake	Basin area (km^2)	Latitude (˚)	Longitude (˚)	Lake area (km^2)	Maximum depth (m)	Altitude (m) asl
Pentecôte	1748	49.867	-67.333	18.9	130	88
Pasteur	777	50.217	-66.067	19.3	70	88
Walker	2187	50.267	67.150	41	280	119

Methods

The cores were examined with a “SIEMENS SOMATOM Definition AS+ 128” CT-scan at the INRS-ETE *Laboratoire Multidisciplinaire de Scanographie* in July 2014. The studied cores consisted of 43 short gravity cores (16 cores from Lake Walker, 10 from Lake Pentecôte and 17 from Lake Pasteur) ranging from 30 to 73 cm in length. The CT-scans allowed for the non-destructive acquisition of longitudinal and tranversal images showing the internal structure of the cores (e.g., St-Onge *et al.*, 2009, St-Onge *et al.*, 2007, Van Daele *et al.*, 2014b). The acquisition was done at a voltage of 140 kVp, current of 410 mAS and a rotation time of 1000 ms/rot. Longitudinal images were acquired in three forms: (1) a sagittal image, which runs in the mid left to right plane (x-axis), (2) a coronal image, which runs from the mean anterior to posterior direction of the core in place (y-axis), and (3) an unwrapped image, which represents a section along

the circumference of the core. Comparatively, the unwrapped image was best suited for visualisation of the sedimentary facies (Fig. 1). Resolution of the axial planes (x/y axes) is 0.17 mm while the slice thickness (z-axis) is 0.6 mm. The resulting images were shown in gray scale, with lighter and darker areas indicating higher and lower X-ray attenuation, respectively. Gray scale values are expressed as Hounsfield units.

In addition, digital photographs of split short sediment cores were taken with the aid of a GEOTEK Geoscan III line-scan camera that was mounted on a Multi-Sensor Core Logger (MSCL), at UQAR-ISMER. This was followed by detailed visual descriptions of colour, grain size, sedimentary structures such as presence of laminations, and any degree of disturbance of sediments caused by the coring process. Colour of sediments was expressed based on the Munsell Soil Colour Chart (Munsell Color Xrite).

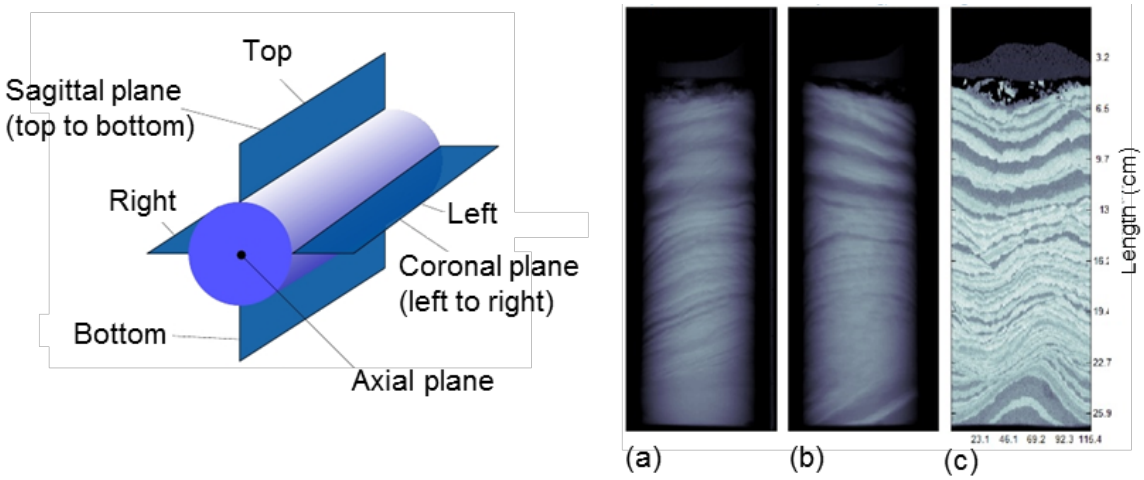

Fig. 1. *The different projection planes of the CT-scan images (left) and sedimentary structures seen in images produced along (a) sagittal plane, (b) coronal plane, and (c) axial plane (unwrapped image). (The core is from Lake Pentecôte.*

Results

Digital photographs capture slight variations in colour and texture, but are generally characterized by a low contrast. On the other hand, CT-scan images supported by visual description enabled us to distinguish sedimentary facies based on the presence or absence of sediment laminations and their continuous or discontinuous nature. Identified facies are: parallel laminations, inclined laminations, convolute laminations, hemipelagic mud, and homogenous mud (Table 2). Sediment cores from Lake Walker were characterized by the parallel- to inclined - to convolute laminated facies, with intervals of the hemipelagic mud facies. Laminated sections are marked by alternating thin or thick (sometimes banded) layers of silty clay and clay. The silty clay layers appear to be yellowish brown to light olive brown or grayish to very dark gray in colour (Munsell colour: 10YR 5/6 to 2.5Y 4/3, 10YR 6/1 to 10YR 3/1, respectively). Clay layers seem to be grayish brown/dark brown to very dark brown in colour (Munsell colour: 10YR 5/2 to 10YR 2/1, respectively). Lake Pentecôte is characterized by facies that are parallel- to convolutely laminated, with relatively thick intervals of hemipelagic mud, and homogenous mud facies. Lake Pasteur comprises less distinct parallel laminated facies, but with thicker sections of hemipelagic mud facies, and homogenous mud facies. There is also evidence of sediment deformation due to gas expansion. This is observed in facies that are laminated, but more pronounced in the intervals of hemipelagic- and homogenous mud.

Table 2: *Digital photo, CT-scan frontal view, and characteristics of the main sedimentary facies observed in sediments from Lakes Walker, Pentecôte and Pasteur*

Facies	Characteristics	Photo	CT-scan	Lake
Parallel laminated	- Grain size: silty clay to clayey silt - Colour: alternation of yellowish to olive brown and grayish to dark gray laminae - Structure: parallel laminae, more visible on the CT-scan images, may be visible to the naked eye or on digital photos		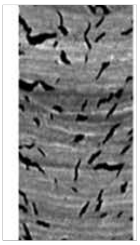	Walker
Inclined laminated	- Grain size: silty clay to clayey silt - Colour: alternation of yellowish to olive brown and grayish to dark gray laminae - Structure: inclined laminae, more visible on the CT-scan images, less visible to the naked eye or on digital photos		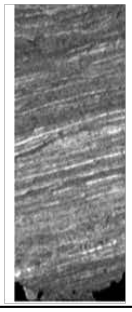	Walker
Convolutely laminated	- Grain size: silty clay to clayey silt - Colour: alternation of yellowish to olive brown and grayish to dark gray laminae - Structure: folding and crumpling of laminae, more visible on the CT-scan images, less visible to the naked eye or on digital photos		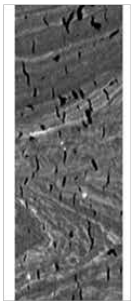	Walker
Hemipelagic mud	- Grain size: predominantly mud, poorly sorted, with small amounts of clayey silt and silty clay - Colour: presence of yellowish to olive brown to grayish to dark gray sediments - Structure: mottled, bioturbated and unclear laminations that are more visible on the CT-scan images		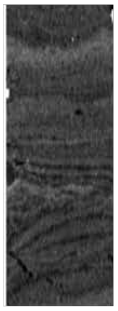	Walker
Homogenous mud	- Grain size: predominantly clay, with small amounts of clayey silt - Colour: grayish brown to dark brown - Structure: clay with high plasticity, or massive, or with unclear laminations that may be visible on the CT-scan images		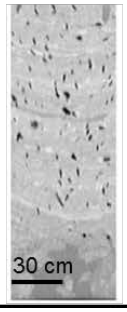	Pasteur

Summary

The use of CT-scan images enabled the idenfication of distinct sedimentary facies based on the type of laminations. CT-scan images also showed sedimentary structures that were less visible on digital photographs and unclear to the naked eyes. Such structures like laminations, folds, slumps or convolutions can provide useful information in interpreting paleoenvironmental conditions (Van Daele *et al.*, 2014a). With respect to occurrence of varves, the parallel laminated sections have the most potential. It is noteworthy that CT-scan images of short sediment cores (supported by seismic and bathymetric profiles) provided the basis for the selection of the most suitable locations from which we recently obtained longer sediment cores from Lakes Walker and Pentecôte. CT-scan images from these cores are expected to provide a longer sequence of laminated intervals, which could be varved. The annual character of the laminations will be verified by thin-section study and an age-depth model, which will be established by laminae counting, supported by radiometric dating (^{210}Pb, ^{137}Cs and ^{14}C) and paleomagnetic measurements.

References

Arseneault D, Dy B, Gennaretti F, Autin J & Begin Y (2013) Developing millennial tree ring chronologies in the fire-prone North American boreal forest. *J Quaternary Sci* 28(3):283-292.

Fortin D, Francus P, Gebhardt AC, Hahn A, Kliem P, Lise-Pronovost A, Roychowdhury R, Labrie J, St-Onge G & Team PS (2013) Destructive and non-destructive density determination: method comparison and evaluation from the Laguna Potrok Aike sedimentary record. *Quaternary Sci Rev* 71:147-153.

Francus P, Ridge JC & Johnson MD (2013) The rise of varves. *Gff* 135(3-4):229-230.

Ministère des ressources naturelles Québec (2002) *Carte géologique du Québec.* Ministère des ressources naturelles Québec, (échelle 1:2 000 000)

Naulier M, Savard MM, Begin C, Marion J, Arseneault D & Begin Y (2014) Carbon and oxygen isotopes of lakeshore black spruce trees in northeastern Canada as proxies for climatic reconstruction. *Chem Geol* 374:37-43.

Nicault A, Boucher E, Begin C, Guiot J, Marion J, Perreault L, Roy R, Savard MM & Begin Y (2014) Hydrological reconstruction from tree-ring multi-proxies over the last two centuries at the Caniapiscau Reservoir, northern Quebec, Canada. *J Hydrol* 513:435-445.

O'Sullivan PE (1983) Annually-laminated lake sediments and the study of Quaternary environmental changes — a review. *Quaternary Sci Rev* 1(4):245-313.

Ojala AEK, Francus P, Zolitschka B, Besonen M & Lamoureux SF (2012) Characteristics of sedimentary varve chronologies - A review. *Quaternary Sci Rev* 43:45-60.

Ojala AEK, Kosonen E, Weckstrom J, Korkonen S & Korhola A (2013) Seasonal formation of clastic-biogenic varves: the potential for palaeoenvironmental interpretations. *Gff* 135(3-4):237-U212.

Ouellet M (1997) Lake sediments and Holocene seismic hazard assessment within the St. Lawrence Valley, Quebec. *Geol Soc Am Bull* 109(6):631-642.

Schnurrenberger D, Russell J & Kelts K (2003) Classification of lacustrine sediments based on sedimentary components. *Journal of Paleolimnology* 29(2):141-154.

St-Onge G & Long BF (2009) CAT-scan analysis of sedimentary sequences: An ultrahigh-resolution paleoclimatic tool. *Eng Geol* 103(3-4):127-133.

St-Onge G, Mulder T, Francus P & Long B (2007) Continuous physical properties of cored marine sediments. *Proxies in Late Cenozoic Paleoceanography. Elsevier*:63-98.

Van Daele M, Cnudde V, Duyck P, Pino M, Urrutia R & De Batist M (2014a) Multidirectional, synchronously-triggered seismo-turbidites and debrites revealed by X-ray computed tomography (CT). *Sedimentology* 61(4):861-880.

Van Daele M, Cnudde V, Duyck P, Pino M, Urrutia R & De Batist M (2014b) Multidirectional, synchronously-triggered seismo-turbidites and debrites revealed by X-ray computed tomography (CT). *Sedimentology* 61(4):861-880.

Zolitschka B, Francus P, Ojala AEK & Schimmelmann A (2015) Varves in lake sediments – a review. *Quaternary Sci Rev* 117(0):1-41.

Acquisition of the Natural Remanent Magnetization in Varved Sediments: Laboratory Sedimentation Experiments, CAT-Scan imaging and Modeling

*E.G.H. PHILIPPE[1], G. ST-ONGE[2], J.-P. VALET[3], P. FRANCUS[4]

[1]Institut des sciences de la mer de Rimouski (ISMER), Université du Québec à Rimouski, Rimouski, QC, Canada et GEOTOP and [2]Institut de Physique de Globe de Paris, Paris, France – edouard.philippe01@gmail.com
[2]Institut des sciences de la mer de Rimouski (ISMER), Université du Québec à Rimouski, Rimouski, QC, Canada et GEOTOP - guillaume_st-onge@uqar.ca
[2]Institut de Physique de Globe de Paris, Paris, France - mailto:valet@ipgp.fr
[3]Institut national de la recherche scientifique, Centre Eau Terre Environnement (INRS-ETE), QC, Canada et GEOTOP - mailto:Pierre.Francus@ete.inrs.ca
* presenting author

Keywords : Paleomagnetism, Natural remanent magnetization, Varved sediments, CAT-Scan

Abstract

The natural remanent magnetization (NRM) of sediments can be used to reconstruct variations of Earth's magnetic field in the past. Reconstructing variations in Earth's magnetic field is essential for understanding the dynamics of the geodynamo, in addition to serving as a powerful stratigraphic tool. However, the NRM is not only related to the magnetic field behavior and strength, but also depends, to a lesser extent, on the depositional environment and lithology. To accurately determine the paleomagnetic signal from sediments, it is necessary to define the parameters involved in the acquisition of the magnetization. Such parameters include the mineralogy and size of the magnetic particles, as well as other processes which tend to inhibit the alignment of the magnetic grains with the magnetic field such as the deposition of turbidites or debris flows, and bioturbation. To succeed in faithfully tracking the geomagnetic variations, it is necessary to determine the processes involved during the acquisition of magnetization. This problematic is tackled in three steps: 1) measurement of the NRM of sediments using sediment cores, 2) laboratory sedimentation experiments, and 3) numerical modelling. We selected annually laminated sediments (varves) from three deep lakes of the North Shore of the Gulf of St. Lawrence, Quebec (Lakes Walker, Pasteur, and Pentecôte) to perform high-resolution sedimentological, physical, geochemical (^{10}Be) and magnetic measurements. Each core will be measured with a CAT-Scan to verify the presence of laminations in the sediment. CAT-Scan imaging also allows determining density variations in all the studied cores at a high-resolution. The different properties will be compared in order to identify the factors responsible for the variations of the magnetic signal. Experiments of sediment deposition and compaction will be made in parallel in the laboratory under a controlled magnetic field in order to assess the influence of compaction on the recording of the magnetic signal. CAT-Scan imaging will also be used during the experiments to assess the creation and evolution of sedimentary structures and, thanks to the measurement speed, to monitor in real time changes in compaction associated with a varying pressure applied to the sediments. Finally, all the data will be integrated to develop a model of the acquisition of the NRM in laminated sediments.

Introduction

The natural remanent magnetization (NRM) of sediments can be used to reconstruct variations of Earth's magnetic field in the past. Reconstructing variations in Earth's magnetic field is essential for understanding the dynamics of the geodynamo, in addition to serving as a powerful stratigraphic tool. However, the NRM is not only related to the magnetic field behavior and strength, but also depends, to a lesser extent, on the depositional environment and lithology. To accurately determine the paleomagnetic signal from sediments, it is necessary to define the parameters involved in the acquisition of the magnetization. Such parameters include the mineralogy and the size of the magnetic particles. Other processes can also inhibit the alignment of the magnetic grains with the magnetic field such as the deposition of turbidities or debris flows, bioturbations and seisms.

Simulating the depositional processes in the laboratory allows characterizing the response of the magnetization for different types of sediments or environments by varying parameters such as salinity, porosity, the presence of rapidly deposited layers or the water content. Despite early studies on the mechanisms responsible for the acquisition of the magnetization in the 60's (Nagata, 1961), relatively little progress was made in recent decades to quantify and/or model the acquisition of the magnetization by sediments (Tauxe, 1993 ; Tauxe et al., 2006 ; Spassov and Valet, 2012).

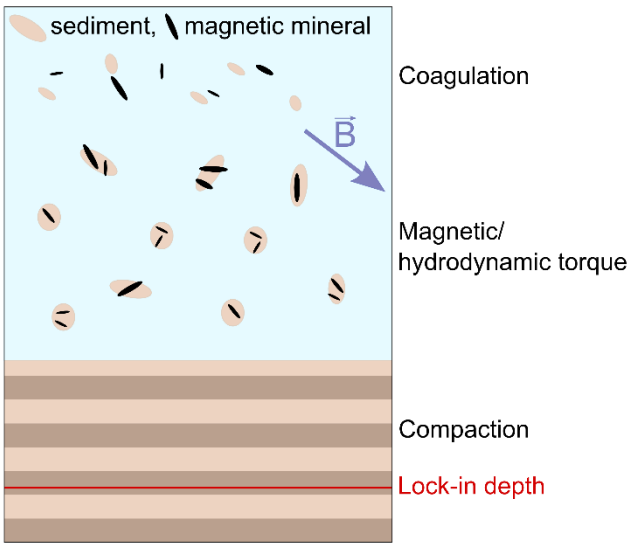

***Fig. 1**. Schematic illustration of the journey of magnetic particles (black ellipsoids) from the water column to burial with the processes that are likely to contribute to the eventual recording of the paleomagnetic field by the particles (modified from Roberts et al., 2013).*

Several parameters intervene during the recording of the Earth's magnetic field by the sediment : floculation, alignment and compaction of the magnetic grains (Fig. 1). The experiments we are planning to conduct aim at improving the knowledge of these parameters playing an undeniable role during the acquisition of the magnetization by the sediment, more particularly those laminated.

The first objective of these experiments is to recreate, in controlled conditions, the sedimentation of laminated sediments. These sediments will be collected from the Lake Walker, where the sediments are finely laminated. These experiments will allow us to create a physical model of the acquisition of the magnetic field by the sediment. The various parameters controlled during these experiments will be, in particular, the grain size, the magnetic field and the pressure exercised during the compaction. The below sections describe the planned experimental setup and its finality.

Experimental setup and samples

Control of the magnetic field during the deposition of the sediment will be provided by Helmholtz coils to generate the magnetic field, and by a Faraday cage to attenuate any external magnetic disturbances. During several series of depositions, the magnetic field will vary in order to compare the difference between the magnetization measured in the sediments and the ambiant magnetic field during the deposition (Table 1).

Table 1. *Magnetic field for 6 series.*

	Serie 1	*Serie 2*	*Serie 3*	*Serie 4*	*Serie 5*	*Serie 6*
Declinaison	0	0	0	0	0	0
Inclinaison	90	60	30	0	60	0
Intensity	50 µT	50 µT	50 µT	50 µT	10 µT	0

The sediments will be seived in order to create laminations typical of the lake Walker sediments and not of turbidites during successive depositions. After this preparation, core samples will be created in tubes (50 cm long; 63 mm of diameter), allowing the setup of 86 tubes for each deposition series (Fig. 2). Every day, a layer of 1 cm in thickness will be deposited by allowing the sediment to settle. The time between the deposition of each layer is calculated so that the deposition of the new layer does not perturb the underlying layer. Based on the mean grain size of the laminations from the sediments of Lake Walker (to be determined), it will be possible to create a 40-cm thick series of centimetric laminations. Out of these 86 samples, 43 will be sedimenting in water added with a chemical deflocculating chemical component and 43 without.

After this deposition, compaction will be recreated using weights (Fig. 3). Weights will be used to test the hypothesis that the lock-in depth is affected by the sedimentation rate (Roberts et al., 2013). The lock-in-depth correspond to the depth where the acquisition of the NRM is completed. During each series, 42 different weights will be used corresponding to the weight of 2 to 84 cm of sediment. The weights will be in Teflon and therefore will not disturb the magnetization of the sediments during the deposition experiments.

Furthermore, the same series will be deposited in parallel without a controled magnetic field.

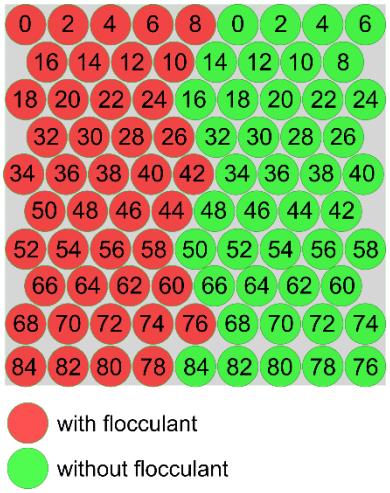

Fig. 2. *Shematic plan of the composition of all series. The number indicates the sediment weight applied.*

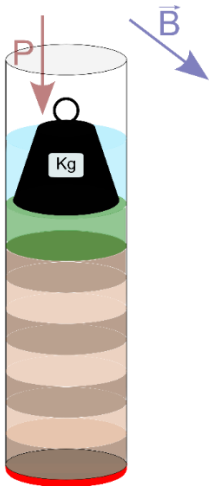

Fig. 3. *Schematic plan of the experimental setup to characterize sediment compaction. P = sediment pressure and B = 50 µT.*

Measurements

Each compacted sample will be measured by CAT-Scan (Fig. 4). Furthermore, the duplicate of each sample, which has not been subjected to the influence of the Helmholtz coils, will also be measured by CAT-Scan before and after the sediment deposition to obtain data on the influence of the compaction. The tubes will then be opened for u-channel sampling. The u-channel will be measured by CAT-Scan to verify that its sampling did not cause any sediment perturbations. The archive half will also be measured with a MSCL (Multi Sensor Core Loger) to determine the magnetic susceptibility, density, chemical composition and color. In addition, a high-definition picture of each sample will be taken. Magnetic measurements will be performed with a u-channel cryogenic magnetometer. Conventional magnetic measurements (NRM, ARM, IRM and SIRM) will then be conducted for deriving directional (inclination and declination) data and

constructing a relative paleointensity proxy (e.g., Tauxe, 1993 ; Valet and Meynadier, 1998 ; Stoner and St-Onge, 2007).

Fig. 2. *CAT-scan imaging of tube after compaction. This Siemens SOMATOM Definition AS CAT-scan at INRS-ETE will be employed for the proposed experiments.*

Conclusion

This experimental study will allow, thanks to the large number of studied parameters, to better understand the mechanisms of acquisition of the magnetic field by the sediments. The impact of flocculation can be measured through the creation of identical sample with and without deflocculation. One could likely understand and estimate the variation of the inclination derived from the NRM compared with the magnetic field which created this NRM. Finally, all these data will be used for the creation of a numerical model of the acquisition of the NRM in laminated sediments.

References

Nagata, T., 1961. Rock Magnetism, 350 pp. Maruzen Tokyo.

Roberts, A.P., Tauxe, L., Heslop, D., 2013. Magnetic paleointensity stratigraphy and high-resolution Quaternary geochronology: successes and future challenges. Quat. Sci. Rev. 61, 1–16. doi:10.1016/j.quascirev.2012.10.036

Spassov, S., Valet, J.-P., 2012. Detrital magnetizations from redeposition experiments of different natural sediments. Earth Planet. Sci. Lett. 351, 147–157.

Stoner, J.S., St-Onge, G., 2007. Magnetic stratigraphy in paleoceanography: reversals, excursions, paleointensity and secular variation. Proxies Late Cenozoic Paleoceanogr. Elsevier 99–137.

Tauxe, L., 1993. Sedimentary records of relative paleointensity of the geomagnetic field: theory and practice. Rev. Geophys. 31, 319–354.

Tauxe, L., Steindorf, J.L., Harris, A., 2006. Depositional remanent magnetization: Toward an improved theoretical and experimental foundation. Earth Planet. Sci. Lett. 244, 515–529. doi:10.1016/j.epsl.2006.02.003

Valet, J.-P., Meynadier, L., 1998. A comparison of different techniques for relative paleointensity. Geophys. Res. Lett. 25, 89–92. doi:10.1029/97GL03489

Ferrous iron in bioturbated sedimentary deposits: a three-dimensional exploratory analysis using planar optodes coupled to tomographic reconstructions.

J. SOTO NEIRA[1], E. MICHAUD[2], B. LONG[3], *R. ALLER[1]

[1] Stony Brook university, Stony Brook, NY, 11790,USA.
[2] Université de Bretagne Occidentale, Institut Universitaire Européen de la Mer, 29238, Brest, France.
[3] Institut National de la Recherche Scientifique, G1K 9A9, Québec, Canada.
* presenting author

Both iron and manganese are essential for all living organisms, and are widely distributed in both terrestrial and marine environments. These elements participate in a wide spectrum of biological, physical and chemical processes in marine environments, including a diverse set of organic and inorganic reactions, from being used by phytoplankton as micronutrients in the photic zone, to being electron acceptors during organic matter remineralization by microbes in sedimentary deposits under suboxic conditions. Thus both elements are directly linked to carbon, nitrogen and sulfur cycles through the formation, preservation and remineralization of organic matter (Froelich et al., 1979; Boyd et al, 2000; Pollard et al. 2009).

The key roles of iron and manganese in the global biogeochemical cycling have been widely discussed in the literature. Iron in particular can be one of the main controls on phytoplankton growth rates and planktonic community structures (de Baar et al., 2005). Benthic fluxes of dissolved Fe and Mn are important sources of these metals to phytoplankton in shallow water (Severmann, et al., 2010). During organic matter decomposition in marine sedimentary deposits, when oxygen and nitrate become depleted, both iron and manganese play important respiratory functions as electron acceptors, and the solid species of these elements are reduced to dissolved forms. Dissolved Fe and Mn concentration gradients in sediments sustain benthic fluxes to overlying water. The spatial distributions of pore water solute concentrations in marine deposits are influenced by physically and biologically mediated sediment reworking and can be extremely complex. Pore water distributions are altered by macrobenthic animal activities such as feeding and burrowing, which increase the bidirectional sediment/water exchange of solutes between surface and deeper sediments, with the eventual input of oxygen and nutrients into the deposit and release of reduced species to overlying waters. Thus, worm tubes can act as a "piping" system for both gas and liquid exchange.

Traditional one-dimensional methods of quantification for both Fe(II) and Mn(II) fail to resolve the natural complexity of chemical distribution patterns in biotubated sediments. Planar optodes, allow us to quantify two- and three-dimensional distributions of specific analytes in marine pore waters. These sensors permit measurements with minimal impact on the natural sedimentary structures of samples, with a dynamic range appropriate for typical environmental applications. We coupled the use of planar optodes for Fe(II) and Mn(II) with CT-scan measurements during sediment incubation experiments, to study the role of *Nereis* sp. (polychaetes) and *Macoma* sp. (bivalve) as modifiers of geochemical environments in marine sedimentary deposits.

In our experiments at INRS, Quebec, Canada, planar optodes based on using Ferrozine and Cd- 4,4‘,4“,4“‘-(Porphirine-5,10,15, 20-tetrayl) Tetrakis (benzenesulfonic acid) for Fe(II) and Mn(II) respectively , were deployed into pre-sieved sediment incubations containing a specific number of organisms for each species, allowing 2- and 3-dimensional measurements to elucidate Fe and Mn cycling and associated biogeochemical processes in these heterogeneous sediments.

During planar optode deployments, consecutive CT-scanning of each incubation were performed for tracking animal activities, visualizing burrowing structures, as well as the interaction between the organisms and their associated sedimentary structures with our sensing schemes (Figure 1). Quantitative analysis for the planar optode signals where performed by using color space transformations scripts, as well as solving partial differential equations to translate the electronic signal from the detector device into chemical units of concentration in Matlab ®, while CT-Scan data analysis was carried using the proprietary software of the instrument and Matlab image processing toolbox for visualization purposes (Figure 2)

Very low manganese concentrations were measured during our experiments, so, in this work we present the results of multidimensional measurements of Fe(II) and model flux calculations

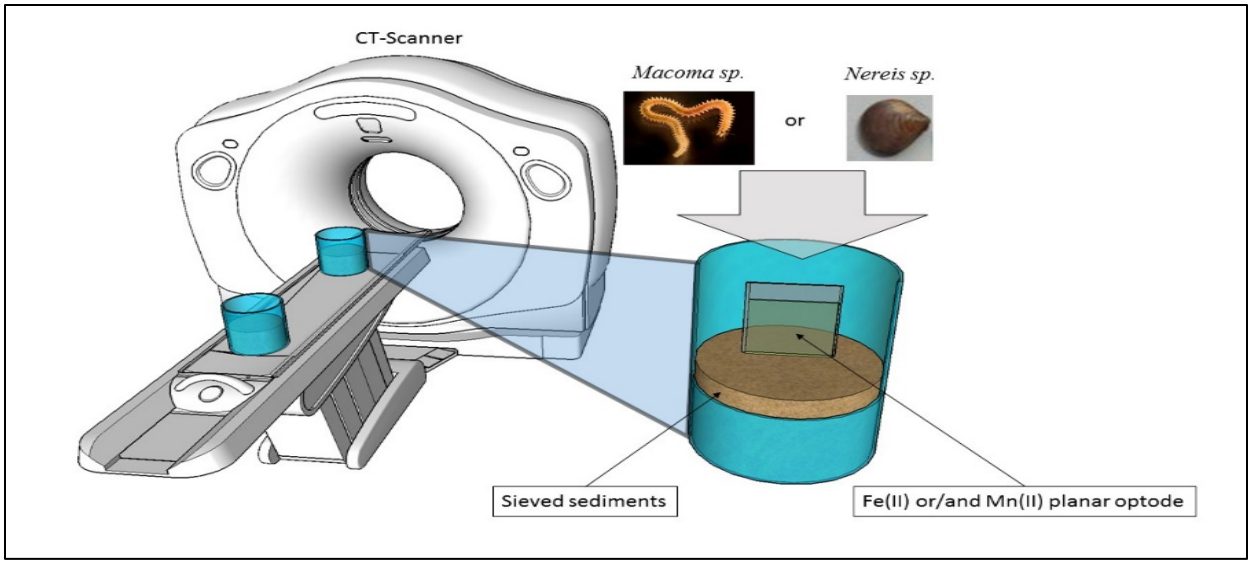

Figure 1: schematic representation for the experimental design followed during the specie-specific incubation experiments carried at INRS, Quebec, Canada.

across the sediment-water interface using a novel planar optical sensor and simultaneous tomographic reconstructions from CT-Scan during laboratory microcosm experiments designed to characterize the impact of the polychaete *Nereis* sp. and the bivalve *Macoma* sp. on Fe cycling and redox reactions in the bioturbated zone.

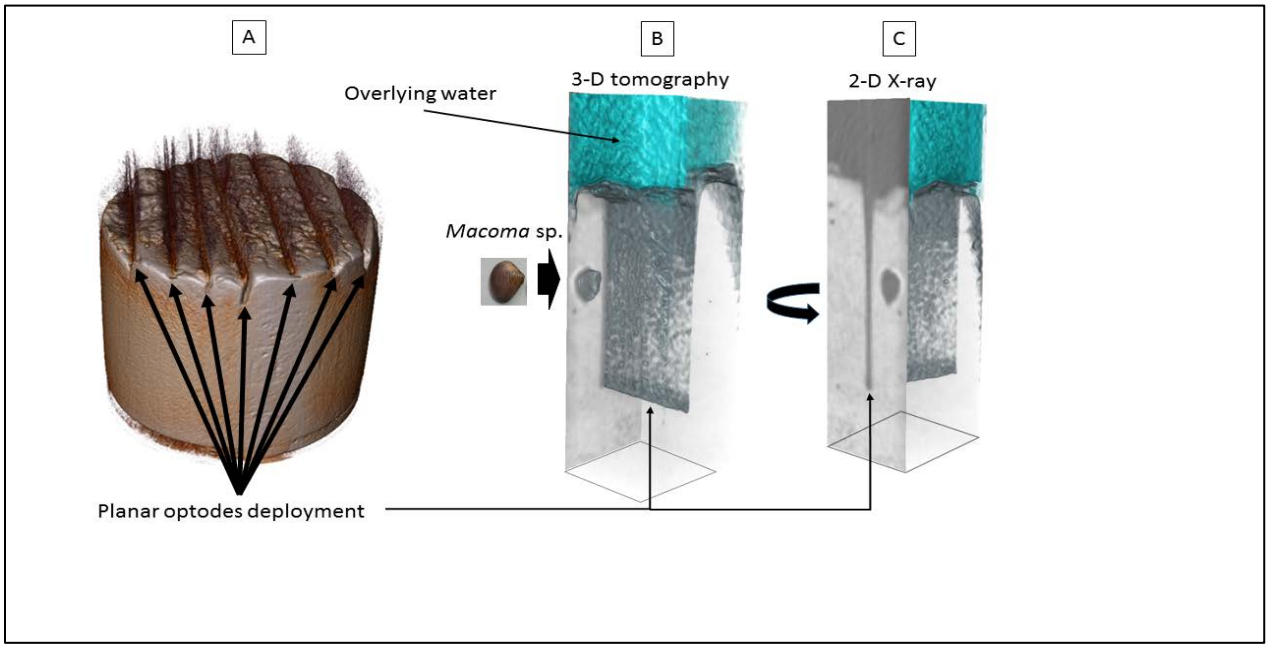

Figure 2: surface reconstruction of a sediment core bioturbated by Macoma sp. (A). 3-D reconstruction depicting interactions between Macoma sp. and a planar optode (B). Rotated figure depicting a 2-D x-ray view in parallel to 3-D reconstruction showing Macoma sp interacting with deployed planar optode.

4. Reference

• Boyd, P. W., et al. (2000), A mesoscale phytoplankton bloom in the polar Southern Ocean stimulated by iron fertilization, Nature, 407(6805), 695-702.

• de Baar, H. J. W., et al. (2005), Synthesis of iron fertilization experiments: From the Iron Age in the Age of Enlightenment, Journal of Geophysical Research: Oceans, 110(C9), C09S16, doi:10.1029/2004JC002601.

• Froelich, P. N., G. P. Klinkhammer, M. L. Bender, N. A. Luedtke, G. R. Heath, D. Cullen, P. Dauphin, D. Hammond, B. Hartman, and V. Maynard (1979), Early oxidation of organic matter in pelagic sediments of the eastern equatorial Atlantic: suboxic diagenesis, Geochimica et Cosmochimica Acta, 43(7), 1075-1090, doi:10.1016/0016-7037(79)90095-4.

• Pollard, R. T., et al. (2009), Southern Ocean deep-water carbon export enhanced by natural iron fertilization, Nature, 457(7229), 577-580.

- Severmann, S., J. McManus, W. M. Berelson, and D. E. Hammond (2010), The continental shelf benthic iron flux and its isotope composition, *Geochimica et Cosmochimica Acta*, *74*(14), 3984-4004, doi:http://dx.doi.org/10.1016/j.gca.2010.04.022.

EVALUATION OF EXPERIMENTAL DISSOLUTION OF DOLOMITE USING X-RAY COMPUTED TOMOGRAPHY

B. BAGLEY*[1], B.M. TUTOLO[1], A.J. LUHMANN[1], M.O. SAAR[1,2], AND W.E. SEYFRIED, JR.[1]

[1] University of Minnesota, Department of Earth Sciences, Minneapolis, MN 55455 – bagley@umn.edu ,tutol001@umn.edu, luhm0031@umn.edu, wes@umn.edu
[2] ETH-Zurich, Department of Earth Sciences, Zurich, Switzerland – saarm@ethz.ch
* presenting author

Keywords: Dolomite dissolution, Fluid–rock reaction, Reactive surface area, X-ray computed tomography

Abstract

Flow-through experiments were conducted on nine dolomite cores to simulate CO_2 injection into dolomite reservoirs during geologic carbon sequestration. The cores were scanned at the University of Minnesota X-ray Computed Tomography (XRCT) facility before and after each experiment to capture mineral volume changes resulting from experimental dissolution. We characterized each dissolution structure using center of gravity, a centerline tree, and volume.

Introduction

Flow-through experiments were conducted on nine dolomite cores to simulate CO_2 injection into dolomite reservoirs during geologic carbon sequestration. We will focus on experiments 1-8 since no pre-experimental scan exists for experiment 9. Experiments at 100°C and 150 bar pore-fluid pressure were conducted in single-pass mode using CO_2-charged brine and flow rates that spanned two orders of magnitude. The cores (1.3 cm diameter and 2.6 cm long) were scanned at the University of Minnesota X-ray Computed Tomography facility before and after each experiment to capture mineral volume changes resulting from experimental dissolution. Experimentally-produced dissolution features (i.e., porosity development) were visualized by carefully aligning the pre- and post-experiment cores in three dimensions. Dissolution produced a range of dissolution patterns, including highly permeable flow channels or wormholes.

Previous work provided insight for a porosity-surface area model using the general shapes of the dissolution channels that developed from fluid-rock reaction (Luhmann et al., 2014). Here, we produce a more complete quantification and characterization of the experimentally produced dissolution structures. We examine the colocation of post-experimental dissolution features and preexisting pore structures in order to guide future work into predicting the development of these dissolution structures.

Methods

All cores were scanned at similar energy and current conditions and reconstructed at a resolution of 8 μm, which is a result of the relatively large size of the experimental cores. However, the full resolution volumes have a file size ~10 GB, making it difficult to work with multiple volumes. For this reason, we rescaled the core volumes to 15 μm prior to analyzing them using Avizo Fire 9.0. Pre- and post-experimental volumes were registered using a rigid transformation which is restricted to translation and rotation in three directions. Once aligned, the cores were segmented to select macro-scale pore space using interactive thresholding which produced a binary volume; we then subtracted the pre-experimental volume from the post-experimental volume. The resulting binary volume contains the new pore space that developed during the experiment, and in all nine experiments the result was a dissolution structure of varying size and complexity.

For each dissolution structure, we calculated center of gravity (COG), a centerline tree, and volume (Fig. 1). Avizo's centerline module (Sato et al., 2000) was used to calculate the centerline tree, and we allowed it to find all available branches. The total length of all the branches was divided by the length of the bounding box to obtain a normalized path length of

the dissolution structure. For cores that developed multiple dissolution features, we calculated centerline trees and center of gravity for all of them. However, for calculations using COG we used the COG Z coordinate of the largest feature.

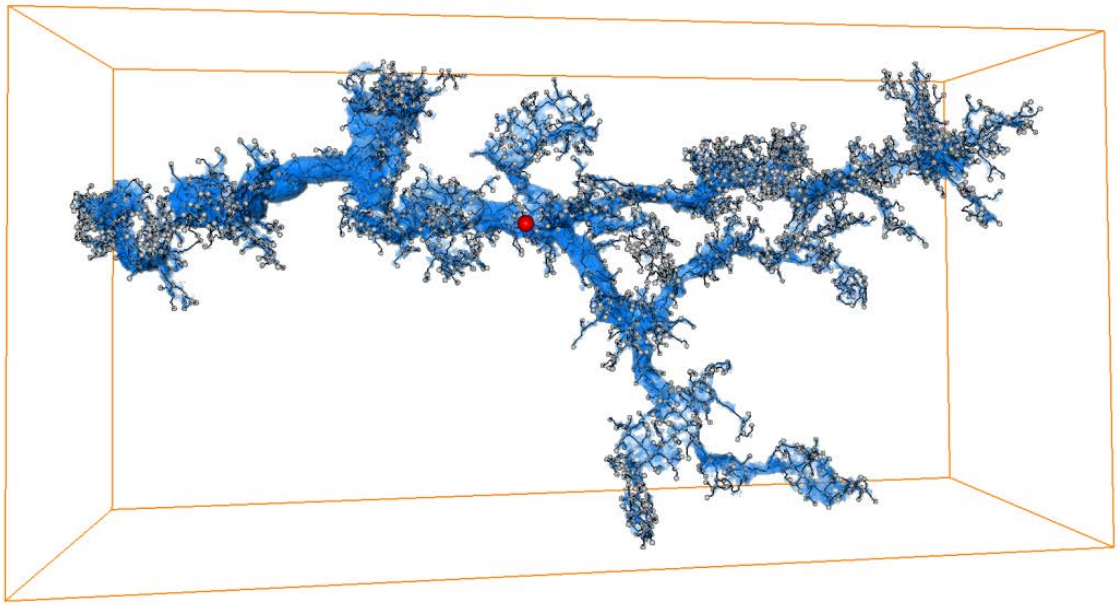

Fig. 1. This is the dissolution structure (blue) that developed in Experiment 3 at a flow rate of 0.1 ml/min. The total length of the dissolution structure is 18.2 mm and the sphere (COG) is located at 8.4 mm. The black lines and gray spheres are the branches and nodes of the centerline tree, respectively.

Results and Discussion

Flow rates of 0.1 and 0.316 ml/min were the most efficient at producing relatively long dissolution structures, requiring the least injected fluid volume for a given dissolution structure length (Fig. 2). Because the 0.01 ml/min flow rate produced extensive dissolution at the upstream end of the core, dissolution structures penetrated relatively little for a given volume of fluid that flowed through the core. With dissolution occurring across a broader cross section at the highest flow rate of 1 ml/min, the length of the dissolution structure from Experiment 1 was shorter than the structures in Experiments 2-6 per volume of fluid injection. Since our experiments were terminated before dissolution breakthrough (i.e., before the initial pressure gradient decreased by a factor of 100 (Fredd and Fogler, 1998; Panga et al., 2005; Kalia and Balakotaiah, 2007)), the y-axis in Figure 2 includes division by the dissolution structure length to facilitate comparison of our experiments to previous research. Trends in Figure 2 show good agreement to plots of pore volumes to breakthrough versus flow rate or Damköhler number (e.g., Fredd and Fogler, 1998).

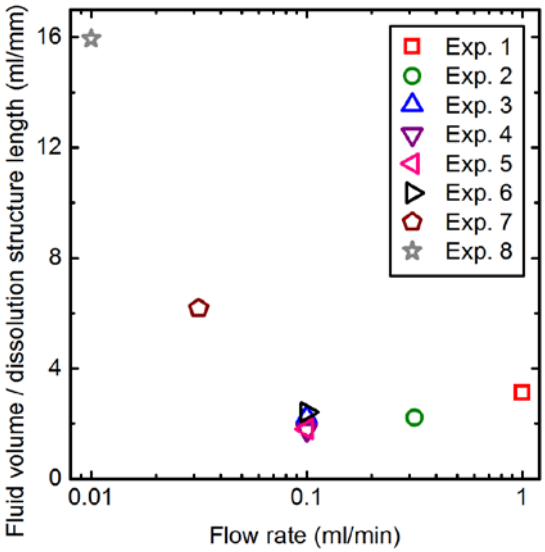

Fig. 2. Total injected fluid volume divided by the dissolution structure length as a function of flow rate. Experiments 2-6 using flow rates of 0.1-0.316 ml/min yielded the longest dissolution structures per amount of fluid volume that flowed through the cores.

Dissolution structures from Experiments 2-6 using flow rates of 0.1-0.316 ml/min were also more symmetrical lengthwise than the dissolution structures from the other experiments (Fig. 3). With the z-coordinate of the COG calculation divided by the dissolution structure length, COG normalized values approaching a value of 0.5 for Experiments 2-6 indicate dissolution across a relatively uniform cross section along the entire length of the dissolution structure. COG normalized values of 0.2 to 0.4 for the other experiments indicate more asymmetry, requiring cross sectional areas of dissolution to decrease as a function of core length.

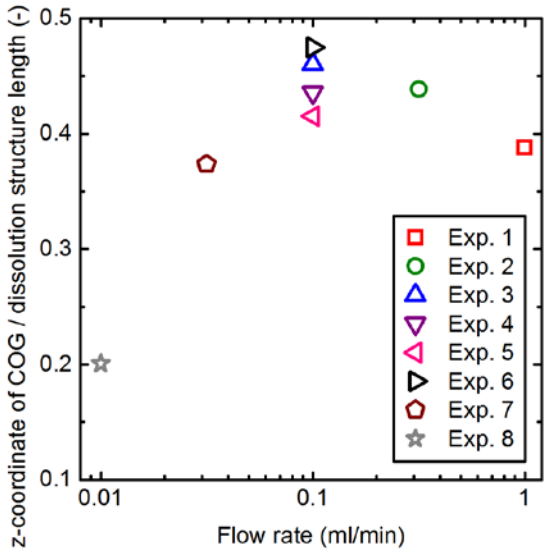

Fig. 3. Z-coordinate of the Center of Gravity (COG) of the dissolution structure divided by the dissolution structure length as a function of flow rate. Experiments 2-6 with flow rates of 0.1-0.316 ml/min yielded dissolution structures with relatively constant cross sections of dissolution as a function of core length, whereas other experiments produced dissolution structures that were more asymmetric along the lengths of the cores.

Luhmann et al. (2014) regressed pore volume-normalized reactive surface area changes $\bar{\sigma}(t)$ during these experiments according to:

$$\bar{\sigma}(t) = \bar{\sigma}^* \left(\frac{\bar{\phi}(t)}{\bar{\phi}^*}\right)^{-w}, \quad (1)$$

where $\bar{\sigma}^*$ is the initial pore volume-normalized reactive surface area, $\bar{\phi}(t)$ is the sample-averaged porosity at time t, $\bar{\phi}^*$ is the initial sample-averaged porosity, and w is an exponent that depends on geometry (Lichtner, 1988; Luquot and Gouze 2009). Luhmann et al. (2014) suggested that the exponent w in the porosity-surface area model is inversely related to flow path tortuosity. Using the center line tree method, Figure 4 shows that the exponent w is generally inversely related to the normalized path length (i.e., the total length of all braches divided by the bounding box length). However, the normalized path length calculation for the core from Experiment 2 appears to be an outlier. It's possible that the registration of the pre- and post-experimental volumes did not work well for this particular core, which could have resulted in a rough surface that creates excessive branching in the centerline tree. Outside of this outlier, the general trend indicates that shorter normalized path lengths with larger values of w are able to reduce reactive surface area more for a given change in porosity than longer normalized path lengths with smaller values of w.

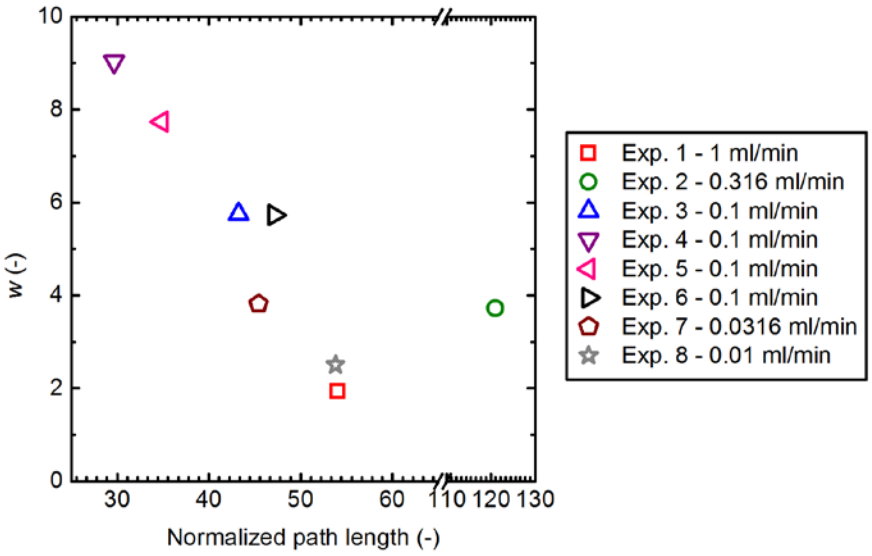

Fig. 4. Fitting parameter, w, as a function of the normalized path length. Except for the outlier from Experiment 2, w is inversely related to the normalized path length.

Comparison of the 3D distribution of large pores within the pre-experimental reconstructed core with the post-experimental dissolution structure clearly demonstrates that the dissolution structures preferentially connect regions of preexisting pore space (Fig. 5). This result is intuitive, based on the consideration that these regions have a higher initial permeability than the surrounding matrix and likely result in local focusing of the reacting fluid. Nonetheless, many of the large, preexisting pores are not connected by the dissolution structure, and the post-experiment spatial location of the dissolution structure is clearly dependent upon the location in the upstream face of the core where the dissolution structure initiates and the proximity of high permeability pores in the downstream direction. Future work will seek to quantify and predict the colocation of dissolution structure development with large pore spatial distribution as a function of flow rate and fluid reactivity. The development and parameterization of such a predictive capacity will yield new opportunities to examine coupled reactive transport processes in geologic systems.

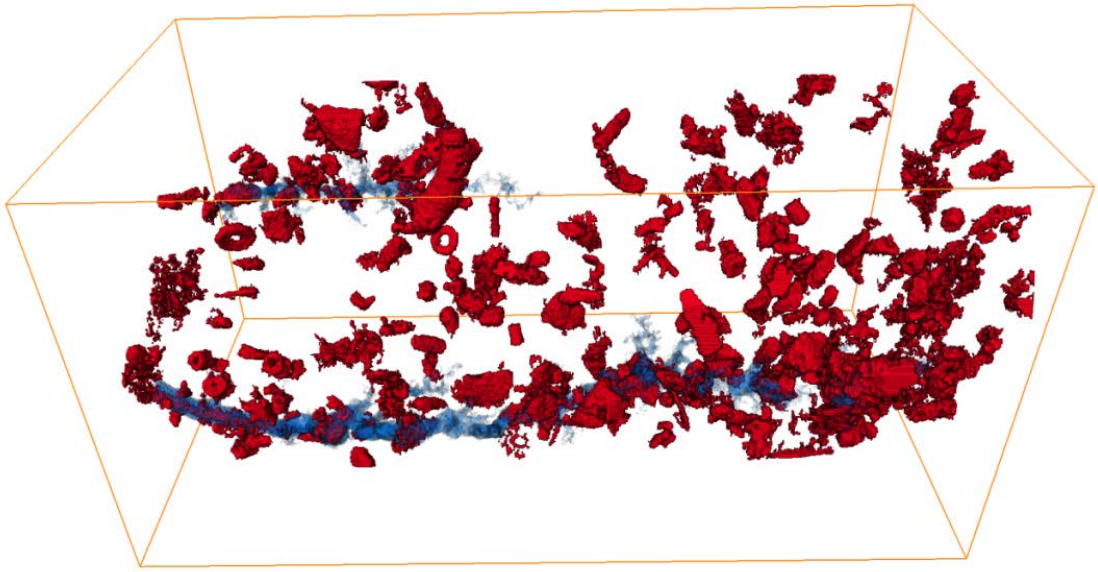

Fig. 5. Red objects are pores that existed in the core prior to Experiment 5. The blue object is the dissolution structure that developed during the experiment. Notice that the dissolution structure appears to nucleate in pre-existing pores.

To capture porosity and mineral reactivity at scales below the XRCT resolutions reported here, we have additionally conducted combined Small and Ultra Small Angle Neutron Scattering ((U)SANS) analyses. These techniques permit investigation of features in the range of ~10 nm to ~10 μm. Simultaneous consideration of calculations based on the invariants of the (U)SANS curves, the XRCT data sets, and full-core porosity measurements demonstrates that ~50% of the porosity within the experimental samples are within this lower (<10 μm) pore size range. This combined result suggests that the characteristic length scales for dissolution phenomena in dolomites may be below the resolution of the XRCT measurements, and that a combined approach of this type may be warranted to develop appropriate scaling functions.

Attempts to measure porosity of the dolomite cores using traditional image processing techniques have not yielded robust, repeatable results. Accurate segmentation of pore space from the surrounding dolomite matrix has proven particularly difficult for these experimental cores, because even small deviations in the threshold value produce large variations in the calculated porosity. Instead of pore segmentation, future work will attempt to characterize macro-scale porosity using grayscale statistics.

References

Fredd, C.N., Fogler, H.S., 1998. Influence of transport and reaction on wormhole formation in porous media. AIChE J. 44 (9), 1933–1949.

Kalia, N., Balakotaiah, V., 2007. Modeling and analysis of wormhole formation in reactive dissolution of carbonate rocks. Chem. Eng. Sci. 62, 919-928.

Lichtner, P.C., 1988. The quasi-stationary state approximation to coupled mass transport and fluid-rock interaction in a porous medium. Geochim. Cosmochim. Acta 52 (1), 143-165.

Luhmann, A.J, X.Z. Kong, B.M. Tutolo, N. Garapati, B.C. Bagley, M.O. Saar, W.E. Seyfried Jr., (2014) Experimental dissolution of dolomite by CO2-charged brine at 100 °C and 150 bar: Evolution of porosity, permeability, and reactive surface area, Chemical Geology, 380, 145-160, doi:10.1016/j.chemgeo.2014.05.001.

Luquot, L., Gouze, P., 2009. Experimental determination of porosity and permeability changes induced by injection of CO_2 into carbonate rocks. Chem. Geol. 265 (1-2), 148–159.

Panga, M.K.R., Ziauddin, M., Balakotaiah, V., 2005. Two-scale continuum model for simulation of wormholes in carbonate acidization. AIChE J. 51 (12), 3231-3248.

Sato, M., Bitter, I., Bender, M.A., Kaufman, A.E., Nakajima, M., 2000. Teasar: tree-structure extraction algorithm for accurate and robust skeletons. Computer Graphics and Applications, Proceedings. The eighth Pacific Conference on Volume, 281-449., doi: 10.1109/PCCGA.2000.883951.

Determination of the REDOX paleoconditions: A High Resolution X-ray Tomography study of micro pyrite occurrence

*V. CARDENES[1], V. CNUDDE[1], R. MERINERO[2], J. DEWANCKELE[1], W. DE BOEVER[1], J.P. CNUDDE[1]

[1] UGCT/PProGRess - Dept. Geology and Soil Science, Ghent University, Krijgslaan 281/S8, B-9000 Gent, Belgium

[2] Crystallography and Mineralogy Department, Complutense University of Madrid, Avda. Complutense s/n, 28040 Spain

* presenting author

Abstract

Microscopic pyrite (MPy) is a very common mineral usually found under the form of framboids or euhedral crystals, with an average size between 5 and 60 microns. In sedimentary basins, the occurrence of MPy in sediments reflects the primitive REDOX conditions.

For euxinic and anoxic conditions, MPy are small and abundant, while with higher contents of oxygen, under dysoxic conditions, MPy are bigger and relatively scarce. The characterization of MPy population distribution is then a reliable proxy of the environmental paleoconditions. However, formation of MPy is not restricted to sedimentary environments. In low degree metamorphic and hydrothermal conditions, MPy may also form (be formed???). Again, the size and shape of MPy depends on the environment.

In previous works related to this subject, measurement of the MPy populations were done using traditional microscopy techniques (SEM, ore microscopy), which means counting the objects one by one and measuring between 80 and 400 objects per sample. In recent times, the development of High Resolution X-ray tomography (micro-CT) techniques has opened a new horizon for measuring MPy. Pyrite usually has a higher X-ray attenuation coefficient than the rest of minerals composing these type of sediments (quartz and mica). In this way, segmentation of MPy is possible. In addition, the use of micro-CT for characterizing MPy populations is much faster and accurate than the traditional microscopy techniques, since MPy can be classified according to several parameters (maximum diameter, volume, abundance, etc.). Up to several thousands of objects can be measured for each sample, giving much more reliable statistical information than the manual examination with microscopic techniques.

This work presents the results of the MPy determination in a sample of anchimetamorphic green slate from Brazil, just on the boundary between diagenesis and metamorphism. This slate shows no traces of further metamorphism and keeps the original population of MPy deposited during the sedimentation. Resulting micro-CT scans were analyzed using Octopus Analysis, which is able to perform an accurate estimation of the MPy present in the slate matrix, and hence deduce the paleoconditions of the original basin.

Introduction

The occurrence of microscopic crystals of pyrite (MPy) is a reflection? of the sedimentary paleoconditions of a basin. These MPy may present different morphologies, varying from framboids to euhedral shapes. Framboids [1] consists in a micrometric spherical cluster of idiomorphic nanometric crystals. Size and spatial arrangement are two important parameters that define a framboid itself. Size of framboids depends on the genetic conditions, but most of the authors agree with the range of 5 – 20 µm [2]. Euhedral crystals frequently occur together with the framboids, usually having higher sizes, from 5 to 20 µm, and rarely up to 250 µm [3]. The optimal conditions for MPy formation are in the water column of a euxinic basin with a continuous supply of dissolved H_2S [4]. Under these conditions, the MPy are formed in the water column until they fall by effect of gravity to the sediment bottom, stopping their growth when buried to adepth of about 15 cm. On the other hand, under oxic conditions the MPy can continue their growth inside the sediment until they are buried at a depth between) 15 and 30 cm ~~deep~~ [2]. The distribution and sizes of MPy populations are different for each situation (Table 1), allowing to deduce the paleoenvironmental conditions. Then, framboids formed in ~~a~~ euxinic environment have small sizes and a narrow size population distribution, since their growing time was very limited, while framboids formed under oxic conditions had more time to grow and therefore have bigger sizes and a more spread size population distribution. In other

environments affected by later processes of MPy formation, such as low-degree metamorphism, several populations of MPy can be found.

Conditions	MPy parameters
Euxinic (persistently sulphidic lower water column)	Small (mean 3-5 µm), abundant, with narrow size range. Framboids dominate pyrite fraction
Anoxic (no oxygen in bottom waters for long periods)	Small (mean 4-6 µm), abundant, with a few, larger framboids. Framboids dominate pyrite fraction
Lower dysoxic (weakly oxygenated bottom waters)	Mean 6-10 µm, moderately common, with a few, larger framboids and some euhedral crystals
Upper dysoxic (partial oxygen restriction in bottom waters)	Moderately common to rare, broad range of sizes, only a small proportion over 5 µm. Majority of euhedral crystals.
Oxic (no oxygen restriction)	No framboids, rare euhedral crystals.

Table 1. Morphology and population distribution of pyrite framboids in different environments. From Bond and Wignall 2010 [2].

This work uses the potential of High Resolution X-ray Tomography (micro-CT) to quantify the occurrence of MPy in a anchi-metamorphic slate from the Serra de Santa Helena Formation Minas Gerais (Brazil), together with a SEM study of the morphologies of the MPy. The differences in the attenuation coefficients between the MPy and the bulk sample, composed by quartz, mica and chlorites, are significant (Figure 1), allowing to accurately distinguish them if their size is large enough compared to the resolution of the X-ray CT scans. Resulting population histograms were statistically analysed with the Mclust package v 4.4 for R [5]. This statistical package is focused on the analysis of normal mixture of log-normal distributions populations. The results give a new approach to the depositional conditions for this slate.

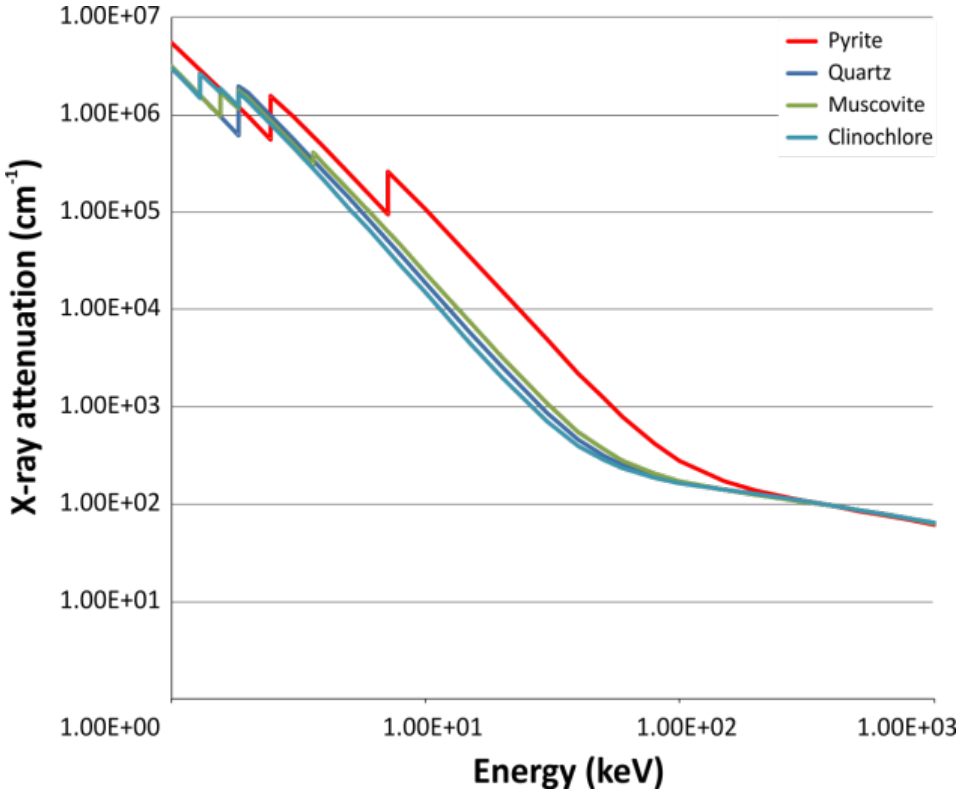

Figure 1. Attenuation coefficient of the main components of the slates studied. Data from NIST database (http://physics.nist.gov/PhysRefData/Xcom/html/xcom1.html)

Sampling and Geological settings

Four samples (BRA01 to BRA04) were obtained from the quarry Felixlândia 1, belonging to the company MICAPEL. This quarry is located to the N of the municipality of Felixlândia, Minas Gerais. The slate samples belong to the Serra de Santa Helena Formation (Fm.), which is a characteristic pelitic formation from the region of Minas Gerais, enclosed in the Bambui Group [6], of Neoproterozoic age. From a regional point of view, the Bambui group covers the São Francisco Craton, and it is interpreted as a Rift-type basin, resulting from offshore sedimentation over a crystalline substrate. From a stratigraphic point of view, the Bambui Group represents an succession of siliciclastic shore facies deposited in a marine environment [7]. The Serra de Santa Helena Fm. is composed by a sequence of argillites and slates, with occasional sandy and carbonate intercalations. The depositional paleoenvironment is interpreted as a progressive deepening of the shore, with sedimentation of fine materials below the base level of the waves, in a moderately deep environment. The result is a fine grained rock that can be placed at the boundary between diagenesis and metamorphism, in the anchimetamorphic zone [8]. These conditions changed for the following formation, the Lagoa do Jacare Fm., consisting on siltstone and limestone deposited in a littoral environment. Slates from the Serra de Santa Helena Fm. can be distinguished by their characteristic colour, existing different varieties that are commercially exploited. The variety used in this work was the green one, where the colour reflects the reducing conditions of the original basin. There are no published data about the paleoconditions of the basin, but the geological context points out to a poorly oxygenated (dysoxic) environment.

Methodology

From each sample, a cylinder of 4 mm was drilled using a diamond core drill. Each cylinder had an approximate length of 10 mm. The resulting four cylinders were scanned with the HECTOR setup [9], located at the facilities of the Centre for X-ray Tomography at Ghent University (UGCT; www.ugct.ugent.be). A high voltage of 130 kV and a tube power of 10W were used for the measurements, with a 1 mm aluminium filter. About 1800 projections of each sample were obtained during a complete rotation along a vertical axis, achieving a voxel size of 3 µm. At an exposure time of 1 second per projection image, the total scanning time amounts to approximately 40 minutes. The resulting images were reconstructed using the software Octopus Reconstruction v.8.8.2 [10] and analyzed with Octopus Analysis v.1.1.0.5 [11]. The images were rescaled from 16-bit to 8-bit and filtered with the function *Bilateral filter.* In order to characterize the petrography and mineralogical composition, thin section examination together with SEM determination were carried out. A thin section was elaborated from sample BRA01, in a perpendicular direction to the sedimentary beds (S_0), and examined with an optical microscope Zeiss Axioscope.A.1. The SEM examination was carried out with a JEOL JSM-5310-LV with an EDAX System 2000 X-ray analysis incorporated. SEM images were taken in BSE mode, obtaining the maximum contrast between the MPy and the bulk sample.

The statistical analysis was performed with the program R v.3.1.2, using the function Mclust. This function is designed to analyze mixture of normal populations. In this particular case, it was found that the MPy distribution fitted to a log-normal distribution and therefore no mixture of log-normal distributions was found.

Results and discussion

Petrological and SEM analysis highlighted the occurrence of the MPy under the shape of euhedral crystals, finding scarce framboids (Figure 2). From a petrographical point of view, the slate is composed of mica, chlorite and quartz, showing a strong alignment parallel to the sedimentation planes. Regarding the micro-CT analysis, the segmentation of the images of the MPy (Figure 3) showed a clear distinction between them and the rest of the sample, making it possible to obtain data for the statistical analysis. In order to filter the noise, results were adjusted, in the lower size ranges, to a theoretical log-normal distribution (Table 2).

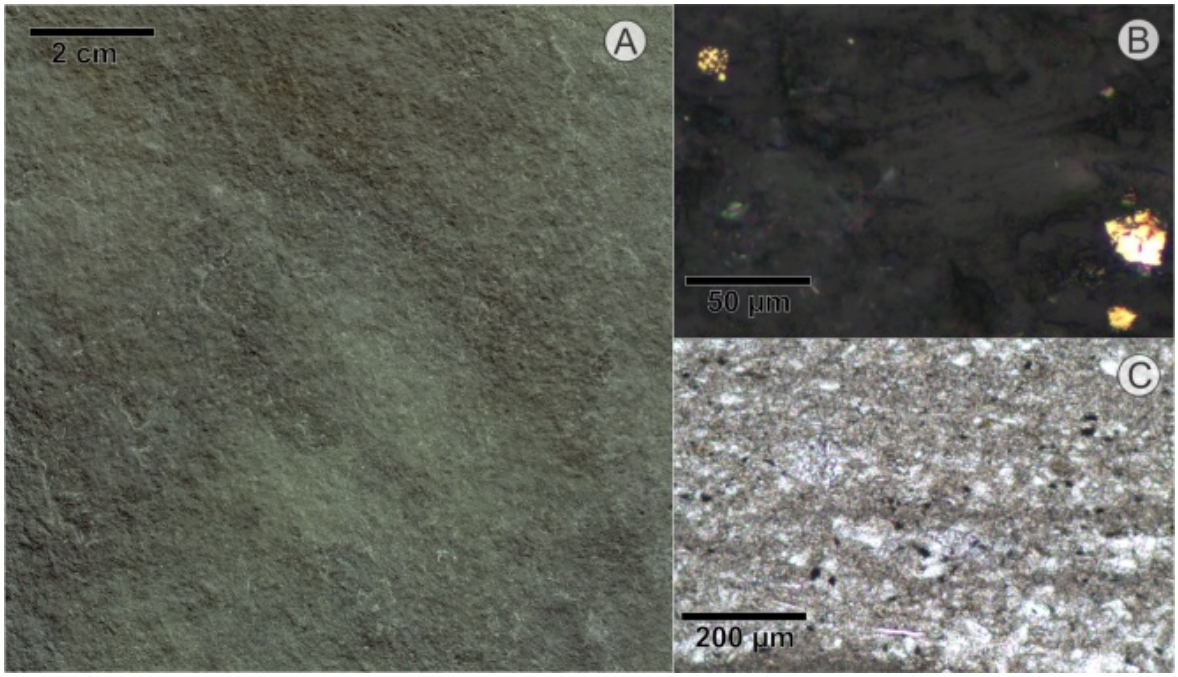

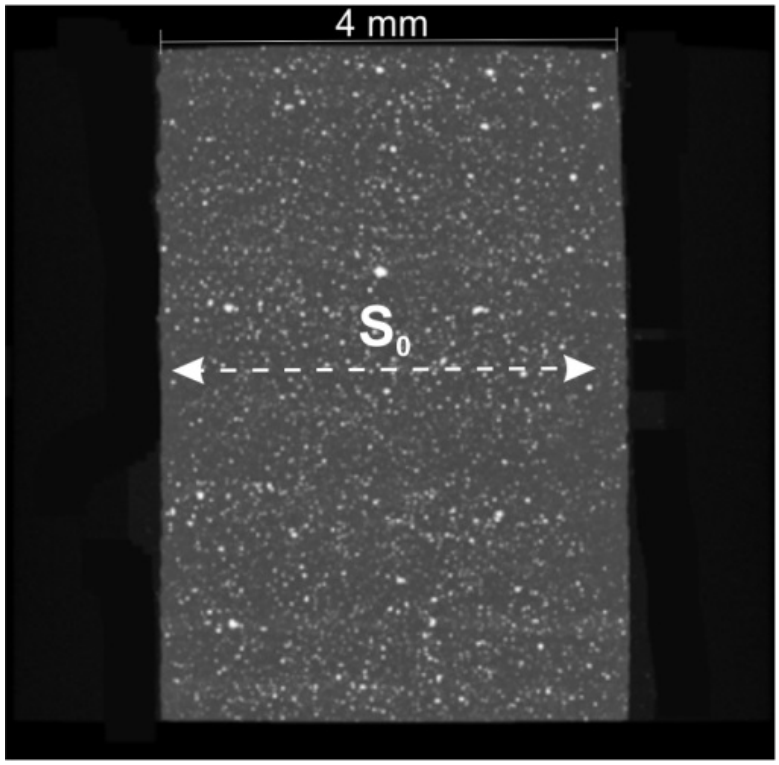

Figure 2. A: Aspect of the slate samples. B: microphotograph of a framboid (upper left corner) and euhedral crystals of pyrite (lower right corner). Reflected light. C: Microphotograph of the slate, showing the sedimentary beds. Opaque minerals correspond to MPy.

Figure 3. Distribution of the MPy along the sedimentary beds (S_0) in the slate bulk. Image obtained with Octopus Visualization v.2.0.0.07 (insidematters.eu) in mode *Maximum projection*.

	Sample	N	Mean	Lower 95%	Upper 95%	Median	Standard deviation
Original	BRA01	5754	11.79	11.63	11.95	12	6.32
	BRA02	5897	11.95	11.79	12.12	12	6.43
	BRA03	5309	11.85	11.68	12.02	12	6.39
	BRA04	8522	12.32	12.17	12.46	12	6.74
Noise filtered	BRA01	5601	11.97	11.8	12.13	12	6.31
	BRA02	5731	12.15	11.98	12.31	12	6.41
	BRA03	5139	12.07	11.9	12.24	12	6.38
	BRA04	8283	12.52	12.38	12.67	12	6.72

Table 2. Statistical parameters of the study of the population distributions.

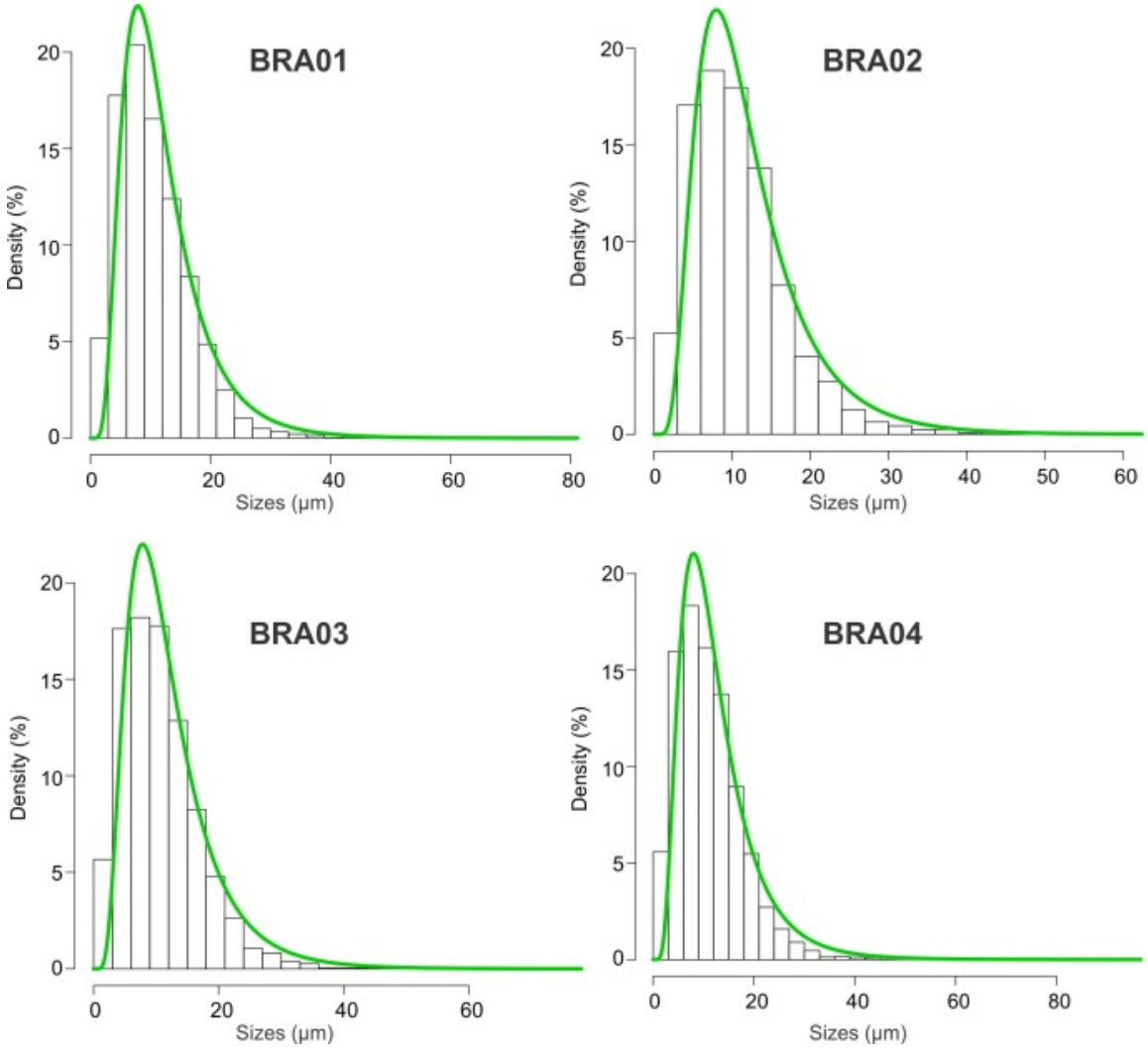

Figure 4. Size distribution histograms of the MPy populations analyzed.

Between 2.7 and 3.2% of the MPy obtained could be attributed to noise. Statistical analysis of the data showed the existence of one log-normal population of MPy for each sample, with means between 12.0 and 12.5 μm, and standard deviations between 6.3 and 6.7 μm. According to Bond and Wignall, 2010 [2], these size intervals would correspond to an upper dysoxic environment, as pointed before on table 1.

Conclusions

From a sedimentological point of view, the statistical analysis of MPy gives accurate information about the paleoenvironmental conditions on the basin. The use of micro-CT to perform this task is much powerful than the techniques previously used (SEM), since micro-CT is able to measure a huge number of objects compared to SEM. In this case, the paleoenvironment deduced from the statistical analysis showed a partial restriction of oxygen, which is consistent with works from previous authors. The methodology expressed in this paper constitutes a new, fast and efficient way to elucidate the paleoconditions of rock formations with occurrence of MPy.

Acknowledgements

Victor Cárdenes is grateful to his IEF Marie Curie Grant 623082 TOMOSLATE.

References

[1] Rust GW. Colloidal primary copper ores at Cornwall mines, south-eastern Missouri. Journal of Geology 1935; 43: 398-426.

[2] Bond DPG, Wignall PB. Pyrite framboid study of marine Permian-Triassic boundary sections: A complex anoxic event and its relationship to contemporaneous mass extinction. Geological Society of America Bulletin 2010; 122(7-8): 1265-79.

[3] Scott RJ, Meffre S, Woodhead J, Gilbert SE, Berry RF, Emsbo P. Development of framboidal pyrite during diagenesis, low-grade regional metamorphism, and hydrothermal alteration. Economic Geology 2009; 104(8): 1143-68.

[4] Wilkin RT, Barnes HL, Brantley SL. The size distribution of framboidal pyrite in modern sediments: An indicator of redox conditions. Geochim Cosmochim Acta 1996; 60(20): 3897-912.

[5] Fraley C, Raftery AE, Murphy TB, Scrucca L. mclust Version 4 for R: Normal Mixture Modeling for Model-Based Clustering, Classification, and Density Estimation: Department of Statistics, University of Washington; 2012.

[6] Costa MT, Branco JJR. Roteiro para a excursão Belo Horizonte-Brasília. In: SBG, Congresso Brasileiro de Geologia 14. Belo Horizonte, 1961: 1-25.

[7] Iglesias M, Uhlein A. Stratigraphy of the Bambuí Group and phanerozoic covers at the São Francisco river valley, northern Minas Gerais, Brazil. Revista Brasileira de Geociências 2009; 39(2): 256-66.

[8] Valeriano CM, Machado N, Simonetti A, Valladares CS, Seer HJ, Simões LSA. U–Pb geochronology of the southern Brasília belt (SE-Brazil): sedimentary provenance, Neoproterozoic orogeny and assembly of West Gondwana. Precambrian Research 2004; 130(1–4): 27-55.

[9] Masschaele B, Dierick M, Van Loo D, et al. HECTOR: A 240kV micro-CT setup optimized for research. 11th International Conference on X-Ray Microscopy (Xrm2012) 2013; 463.

[10] Vlassenbroeck J, Dierick M, Masschaele B, Cnudde V, Van Hoorebeke L, Jacobs P. Software tools for quantification of X-ray microtomography. Nuclear Instruments & Methods in Physics Research Section a-Accelerators Spectrometers Detectors and Associated Equipment 2007; 580(1): 442-5.

[11] Brabant L, Vlassenbroeck J, De Witte Y, et al. Three-Dimensional Analysis of High-Resolution X-Ray Computed Tomography Data with Morpho+. Microsc Microanal 2011; 17(2): 252-63.

Session 306

X-ray Computed Tomography Investigation of Structures in Claystone at Large Scale and High Speed

G. ZACHER*[1], A. KAUFHOLD[2], M. HALISCH[3], J. URBANSKI[4]

[1] GE Sensing & Inspection Technologies GmbH, phoenix|x-ray, Niels-Bohr-Str. 7, 31515 Wunstorf, Germany – gerhard.zacher@ge.com
[2] Federal Institute for Geosciences and Natural Resources, Stilleweg 2, D-30655 Hannover, Germany – Annette.Kaufhold@bgr.de
[3] Leibniz Institute for Applied Geophysics, Stilleweg 2, D-30655 Hannover, Germany – Matthias.Halisch@liag-hannover.de
[4] GE Inspection Technologies, 50 Industrial Park Road, Lewistown, PA 17044, U.S.A. – jeffrey.urbanski@ge.com
* presenting author

Keywords: X-ray micro CT, microstructure, mechanical testing, claystone

Summary

In the past years X-ray Computed Tomography (CT) became more and more common in geo-scientific applications and is used from the µ-scale (microfossils) up to the dm-scale (cores or soil columns). Hence a variety of different systems was adapted to these applications.

In the present paper we investigate CT results from an Opalinus Clay core (diameter ~100 mm) considering the 3D distribution of cracks. Two CT systems are compared both, with specific ad- and disadvantages:

the large and flexible phoenix v|tome|x L300 high energy CT scanner and the high throughput speed|scan CT 64 helix CT system (both GE Measurement & Control).

The results are compared regarding the contrast resolution, spatial resolution, and scanning speed. The fast medical scanners provided a quick overview whereas the microfocus tube provided a more detailed view on cracks.

Introduction

During the last years, the non-destructive investigations using X-ray Computed Tomography (CT) of geomaterial became more and more important. Especially in the field of geomechanical investigations, it is essential to get information about the mineral composition, spatial distribution of minerals, pores, and fractures – before and after mechanical tests. All these parameters have to be characterized to be able to increase the understanding of deformation processes.

The Opalinus Clay sample was first scanned with the speed|scan CT 64 located at the GE facility in Ahrensburg (Germany). The scan was recorded with 140 KV and 140 mA within 13 seconds at a spatial resolution of approx. 0.3 mm. The reconstruction was performed automatically. The 3D data, therefore, could be evaluated after 30 seconds.

Secondly, a CT scan of the same sample was recorded with the v|tome|x L300 system at the GE facility in Wunstorf (Germany). The scan parameters were 270 KV and 0.3 mA and the scan duration was 145 min. With this system a spatial resolution of approx. 60 µm could be achieved.

Material and Methods

The specimen “file 13001” (drilling BLT-A6) was derived from the Underground Rock Laboratory (URL) Mont Terri (St. Ursanne, Switzerland) and belonged to the sandy facies of the Opalinus Clay (Kaufhold et al., 2013). The investigated core sample had a diameter of 100 mm and a length of 180 mm. The drilling was orientated perpendicular to the bedding. The material of the sandy facies in the URL Mont Terri consists of 20-40 wt.% carbonates, 30-50 wt.% quartz, and 15-25 wt.% clay minerals (< 5 wt.% swellable clay minerals). The natural water content of the specimen was preserved as good as possible.

Mechanical Testing

The claystone was investigated by triaxial strength tests until a failure was developed. The test was executed in deformation controlled mode with a deformation rate of $d\varepsilon/dt=10\text{-}5\ s\text{-}1$ and carried out under undrained condition. After the mechanical testing the core was embedded in resin to stabilize the specimen.

Fast Computed Tomography

Based on a medical CT gantry adopted for high throughput and harsh production environments, the new speed|scan CT scanner allows to record CT scans several hundred times faster than with a conventional fan beam CT. The system consists of a radiation protection cabinet with an integrated, rotating ring-shaped scanning device (gantry) and sample transport system. Samples of up to 900 mm in length and 500 mm in diameter can be examined.

CT scanning, volume reconstruction and evaluation, documentation, archiving, network transfer, and result display happen simultaneously allowing an overall cycle time of typically 1 minute per inspected sample (Ambos et al., 2014).

Results

Large Scale and High Speed X-ray CT results

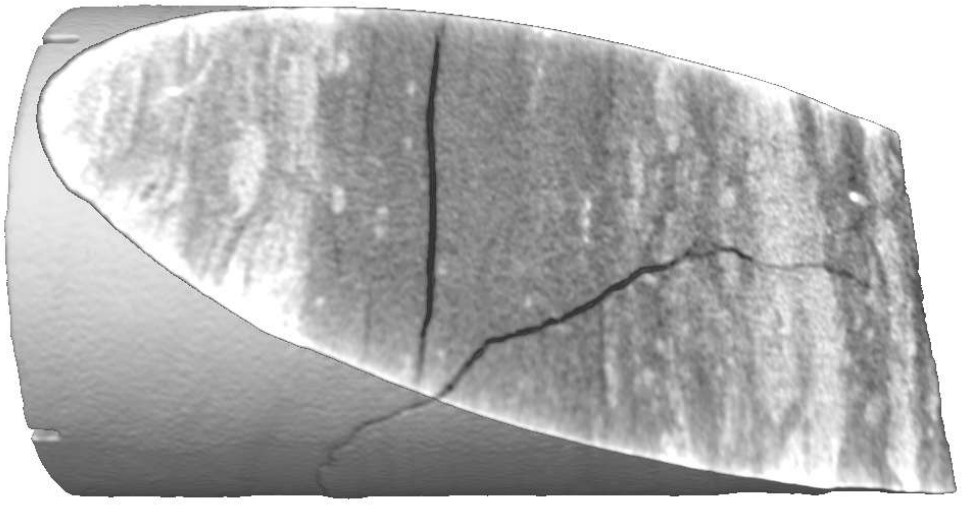

Fig. 1. *3D view of the speed|scan CT result. The virtual slice shows the inner structure (layering, cracks).*

The CT results of the speed|scan CT 64 show good contrast resolution due to its high power (up to 72 kW). Layering within the core can be easily detected based on slightly

changing density (see figure 1). Cracks and pores can be spatially resolved down to 0.5 mm. The 3D data set can be virtually sliced in any direction to emphasize the specific layering or location of the crack system.

Large Scale and High Resolution X-ray CT results

Compared to the faster device explained in the preceeding paragraph, the CT results of the v|tome|x L300 show much better spatial resolution (down to ~60 µm for 10 cm sample width). As the highest power of this system is 0.5 kW, the contrast is not as high but still sufficient to detect different densities. On the other hand the fractures are much better resolved (5 times better resolution) and the delicate network can be nicely visualized (see figure 2). The segmentation was performed in the central part of the sample, where one large horizontal crack is intersected by a diagonal oriented crack system. Additionally, many cracks which are located close to the core surface could be observed.

Fig. 2. *Transparent 3D view of the L300 CT data. Cracks are segmented (red colour).*

Conclusions and Outlook

The fast analysis with X-ray CT based on medical scanners (here speed|scan CT 64 in the first example) is suitable to give an overview of large core samples and the high throughput enables a 3D documentation of large core archives.

On the other hand, the use of microfocus tubes (as in the second example on the v|tome|x L300) can provide much more detailed images necessary for special high resolution core analysis.

For the understanding of deformation processes during mechanical testings detailed information before and after the mechanical testing are required. Thus, it is necessary to get micro fabric information of the undisturbed specimen and after the mechanical test an overview of the deformed specimen. Using the overview scan it is possible to select

regions of interest (ROI) which then can be analysed in more detail using high resolution CT devices. An example is given in Figure 3. The fast scan 3D data set was analysed and a suitable position for further micro plugging could be identified.

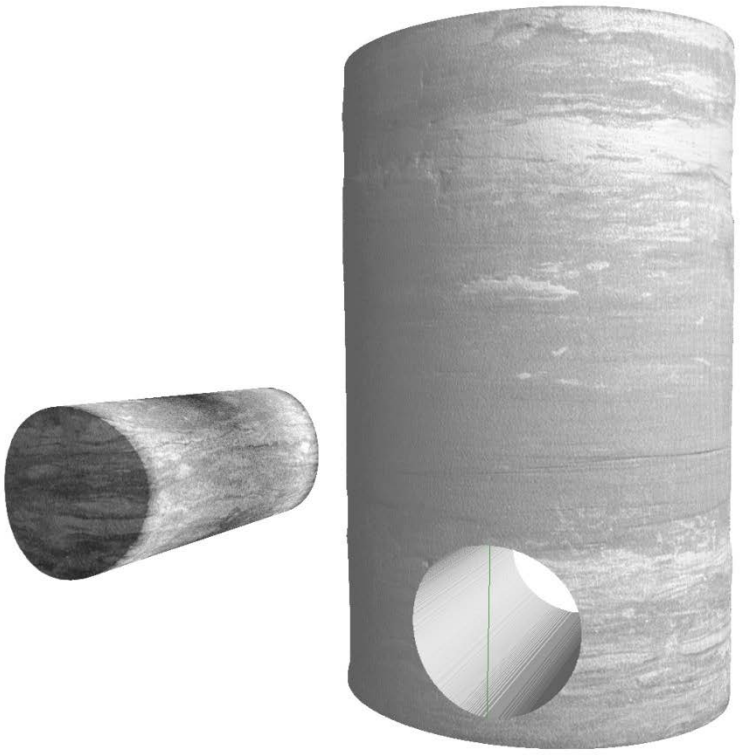

Fig. 3. *3D view of the L300 CT result. The virtual plug has a typical diameter (~4 cm) used for additional experiments.*

The selected area will be analysed using high-resolution CT techniques, as well as mineralogical and geochemical methods. The overall aim of the investigation of the Opalinus Clay (LT-A Project, Mont Terri) is to understand the rock deformation processes upon mechanical stresses. This behaviour is largely governed by microstructure. CT investigations, therefore, are the key methods.

Additionally, chemical and mineralogical methods are used not only to characterize the stiffness of the matrix but also to identify homogeneous areas which can be considered representative of the entire rock. Hence, the CT information gathered from a small volume can be used to understand the mechanical processes of the entire rock.

Acknowledgments

The authors are grateful to Holger Lux, Björn Stockfisch and the GE-Ahrensburg team for the support at the speed|scan CT 64 helix CT system. We are also grateful to the Mont Terri project and the LT-A project partner for their cooperation.

References

Ambos, E., Brunke, O., Neuber, D., Lux, H., Besser, W., and Ziesemann, M., 2014, Porosity and Dimensional 3D Process Control – Fast Computed Tomography in High Pressure Die Casting, Materials Evaluation, 978-984.

Kaufhold A., Gräsle W., Plischke I., Dohrmann R., Siegesmund S. (2013). Influence of carbonate content and microfabrics on the failure strength of the sandy facies of the Opalinus Clay from Mont Terri (Underground Rock Laboratory). Eng Geology 156:111–118.

Crack localization in Digital Volume Correlation: Regularization with a damage law

A. BOUTERF[1], B. SMANIOTTO[1], S. ROUX[1,*], F. HILD[1]

[1] LMT, ENS-Cachan / CNRS / Univ. Paris-Saclay
61 Av. Président Wilson, 94235 Cachan, France
{amine.bouterf; benjamin.smaniotto;stephane.roux; françois.hild}@lmt-cachan.fr
* presenting author

Keywords: Digital Volume Correlation,damage,plasterboard, regularization

Abstract

To make progress in the understanding of the failure mechanisms of lightweight plasterboard subjected to flexural tests, three-point flexural testshave been performed *in situ* within a tomograph.In this work, two approaches of regularized digital volume correlation have been used to analyse the tomographic observations. For a betterdescription of the kinematics of the test (*i.e.* to have a better mechanical admissibility of the measured displacement field as well as to enhance the spatial resolution of localized damage/cracks) a specific form of damage law used for regularization is introduced and adjusted to the studied case. The two procedures are presentedand applied to a three-pointflexuraltest of a lightweight gypsum sample conductedup to failure. The global digital volume correlation procedure regularized with the damage law allows for a significant increase in registration quality as measured by the residuals, and in the spatial resolution of the localized damage and strain.

Introduction

Lightweight plasterboard is a product composed of a foamed plaster core whose porosity can reach 75% lined with two sheets of paper. To optimize the compromise between thermal resistance and mechanical strength, it is important to understand and characterize the mechanical behavior of plasterboard. One of the most important properties is its high resistance to flexure(as definedin the ASTM C11 standard). The analysis of aflexural test showed that the failure mode of the sample is quite complex, namely, it combines multiple core cracking and paper facing debonding. It was also shown that the behavior of the plate is controlled essentially by the mechanical properties of the paper and the quality of the paper-plaster interface [Bouterf 2015]. The present study aims to better understand the failure mechanismsin the bulk of the lightweight plasterboard sample subjected to in-situ (*i.e.* in a tomograph) flexure using regularized digital volume correlation.

Three-point flexural test

To better understand the failure mechanisms, an in-situ three-point flexural test is conducted. The 90 x 13 x 15 mm^3 specimen is prepared from an industrial plasterboard.Load is applied onto the sample throughcylindrically shaped contacting elements (16 mm in diameter). The support span is 80 mm. The loading device is made out of PMMA(Fig. 1), which is virtually transparent to X-rays. The specimen is scanned first in an unloaded state and then at four different loading steps until failure. After each loading step, a dwell time of 20 minutes is chosen during which the load is held constant

before CT imaging to avoid displacement of the sample caused by relaxation processes. The experiment is conducted in-housein an NSI-X50 lab tomograph (90 KV-voltage, 200 µA intensity, voxel size of 25 µm, 1944 × 1536 pixel flat panel).

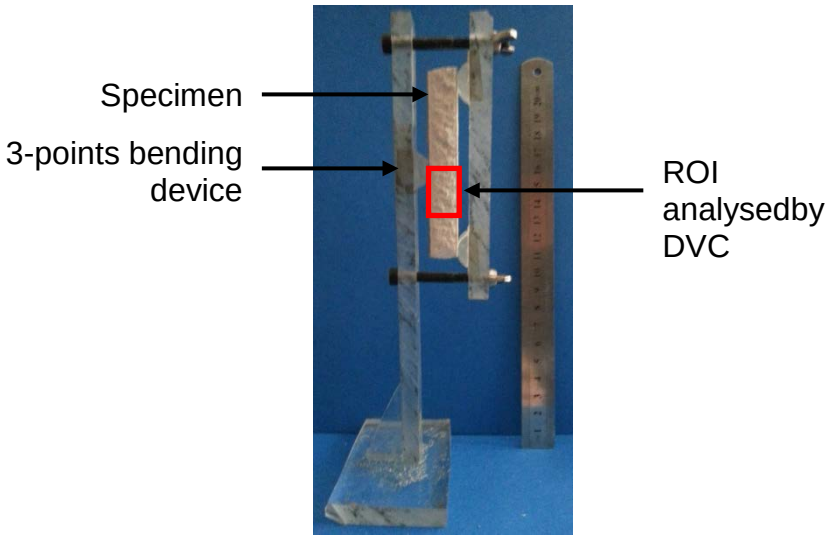

Fig. 1. *Specimen within the loading device*

Figure 2 shows two 3D renderings of half of the reconstructedvolume in its reference configuration and atthe last loading step.The material presents a very heterogeneous texture of foamed plaster. A crackis clearly visible on the lateral face of the sample (Fig. 2. (b)).On the deformed configuration two types of cracks are distinguished, namely, the first corresponds to an opening crack at roughly 45° (multiple core cracking) and the second corresponds to a delamination crack at the interface between the paper and the foamed plaster (paper facing debonding).

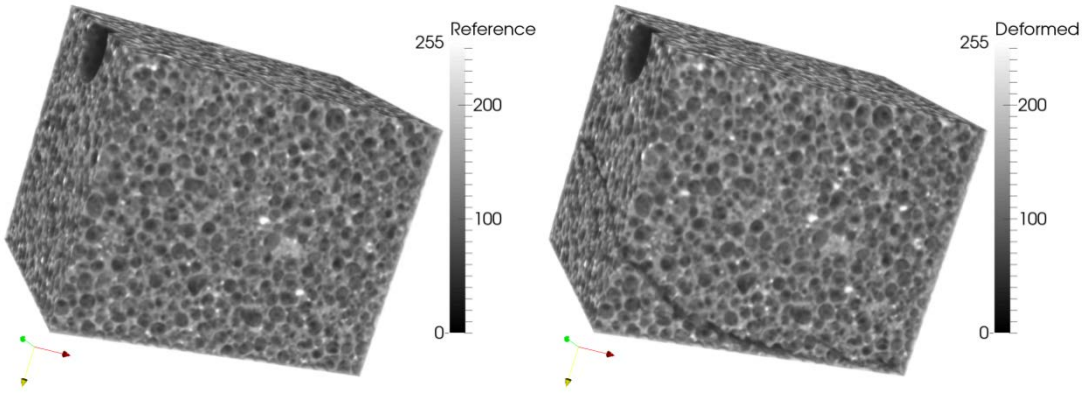

(a) ***(b)***

Fig.2.*(a) 3D rendering of the microstructure of foamed gypsum sample to be subjected to 3-point flexure. (b) The crack is visible on the lateral face of the sample at the last loading step*

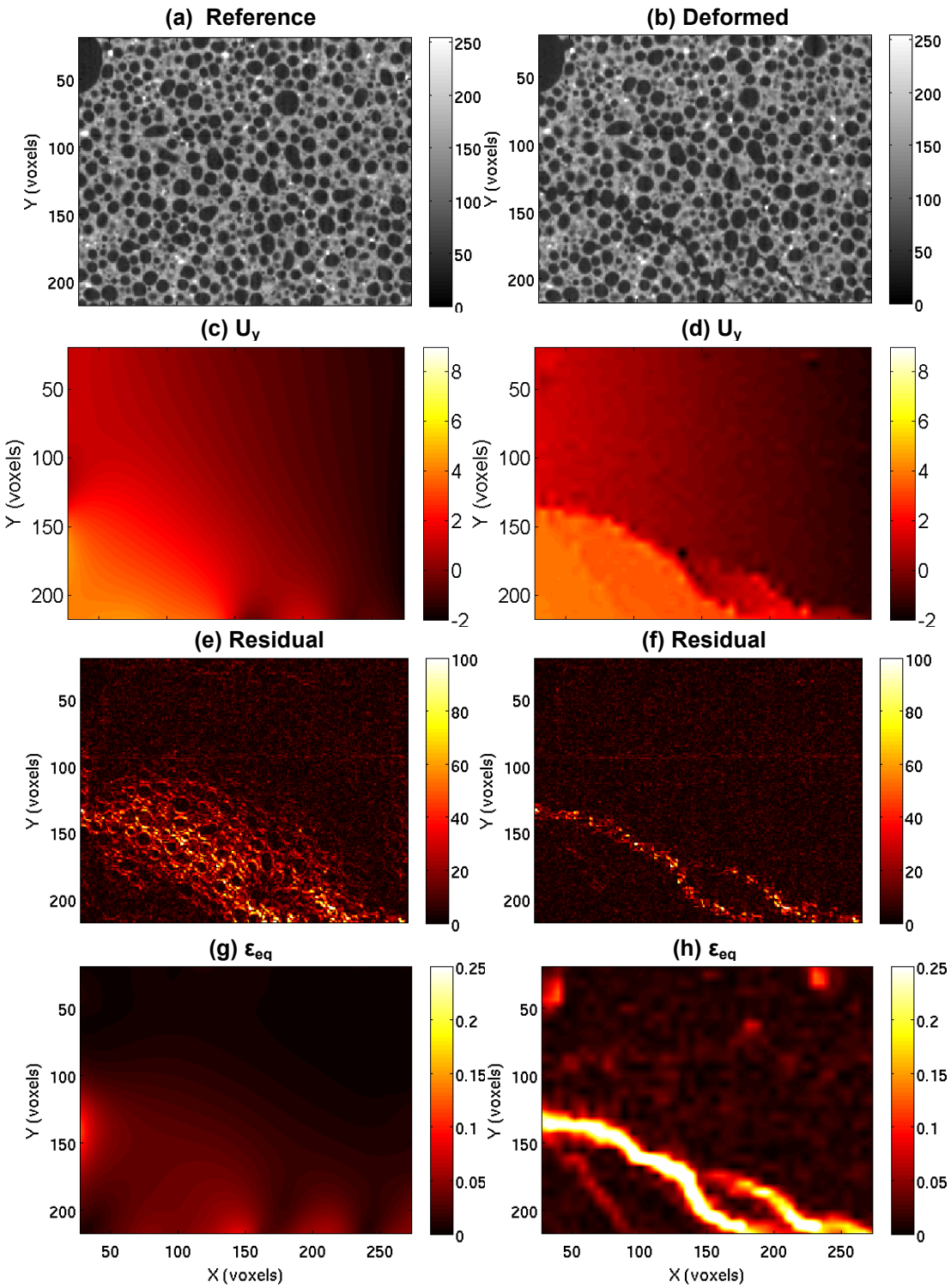

Fig.3.*DVC results: all sectional maps are presented in the x-y plane at z = 96 voxels. Illustration of the gray level reference (a) and deformed (b) images. Displacement field U_y(expressed in voxels, 1 voxel ↔ 25 µm) without (c) and with (d) damage. Correlation residuals (expressed in gray levels) without(e) and with (f) damage.Major principal strain ε_{eq}maps without (g) and with (h) damage. All the results havebeen obtained via DVC regularized with a large regularization length (l_m = 160 voxels)*

Full-field measurements

The reconstructed volumes are exploited using Regularized Digital Volume Correlation (RDVC) [Taillandier-Thomas 2014] to measure the displacement fields in the bulk of the sample thanks to the very heterogeneous texture of plaster. The sub-volume size used in the correlation analysis is 246 x 198 x 180 voxels^3, corresponding to a physical region of size 6.15 x 4.95 x 4.5 mm^3. Displacements are decomposed over a regular mesh composed of C8 elements whose size is chosen to be 6 voxels. An elastic regularization is used with a regularization length$l_m = 160$ voxels.

The measured correlation results are shown in Fig.3 (c, e and g).Due to the choice of a large regularization length used in the correlation procedure, the kinematic fields are smoothened over a large area. The discontinuities in the measured displacement field are barely marked (Fig. 3 (c)) and the correlation residual (Fig. 3 (e)) is spread far out of the cracked area.The level of mean correlation residuals at convergence is equal to 3.17 % of the dynamic range of the volume in the reference configuration. The map of the major principal strain ε_{eq} does not even showstrain localization in the crack vicinity.

In order to better localize the crack pattern, a refined calculation is proposed. It consists of implementing a damage law in the regularization instead of an elastic one [Hild 2015].The damage law was chosen to beisotropic$D = D_\infty \left(1 - \exp\left(-\left(\varepsilon_{eq}/\varepsilon_c\right)^m\right)\right)$, with ε_c the threshold major principal strain ($\varepsilon_c = 0.03$) and $m$an exponent controlling the abruptness of damage evolution ($m = 2$, the higher the m exponent, the more brittle the behavior). The ultimate damage level D_∞ is chosen to amount to 0.9.The idea is to first be more faithful to the actual mechanical behavior and second to reduce the smoothing effect of the elastic regularization in regions where strains are already high. Comparing thedisplacement fields obtained by the two approaches (Fig.3 (c) and (d)), it is noted that the same range is measured.However the discontinuity is better markedin the RDVC results with damage.Considering the low threshold chosen for the major principal strain the displacement field measured (outside the crack surfaces) with the latter version presents small fluctuations(Fig.3 (d)). The localization property of a softening damage law tends to concentrate damage and hence strains (Fig.3 (h)) onto the crack surfaces (at the element scale).The introduction of damagealsoledto a fairly sharp decrease in the mean correlation residuals. Convergence is observed to beexcellent, and the level of mean correlation residuals(2 %) is significantly lower than that measured with the initial version (3.17 %).This result confirms that the kinematics of the test is better capturedby the last version in which the crack pattern is clearly apparent in the RDVC results.

Conclusion

Samples of lightweight gypsum are tested via*in-situ* three-point flexural tests. The tomographic observations and the analysis of the data by regularized DVC show that the failure mechanisms of the sample are quite complex, namely, it is a combination ofmultiple core cracking and paper facing debonding.

If a too large regularization length is selected, the kinematic fields are no longer faithfully evaluated. Conversely, when too small regularization lengths are chosen, measurement uncertainties are no longer dampened. Consequently a trade-off is needed to account for these two opposite effects. The mechanical regularization used

herein is based on an elastic assumption for the underlying behavior of the analyzed material coupled with an isotropic damage law. This stategy allows both the real kinematics of the test to be described near the cracked zone andsmooth displacement fields to be obtained elsewhere despite the very small size of the elements used in the global correlation procedure.

The strategy developed herein reveals well-suited to the study of complex strain patterns and opens new pathways for the identification of mechanical properties.Additionally it provides a quantitative estimate of the crack opening.

Achnowledgements

A.B. acknowledges the support of Saint-Gobain Recherche. The tomograph equipment has been partly supported by the French “Agence Nationale de la Recherche” through the “Inverstissements d’avenir” program (ANR-10-EQPX-37 MATMECA grant).

References

Bouterf, A., Roux, S,. Hild, F., Vivier, G., Brajer, X., Maire, E. Damage law identification from full field displacement measurement: Application to four-point bending test for plasterboard. European Journal of Mechanics - A/Solids,49,60-66, 2015.

Taillandier-Thomas, T., Roux, S., Morgeneyer, T.F., Hild, F. Localised strain field measurement on laminography data with mechanical regularization. Nuclear Instruments and Methods in Physics Research Section B, 324, 70-79, 2014.

Hild, F., Bouterf, A., Roux. S. Damage measurements via DIC. International Journal of Fracture,191 (1-2),77-105, 2015.

A microstructural finite element analysis of cement damage on Fontainebleau Sandstone

S. NADIMI[1], J. FONSECA*[1], P. BESUELLE[2], G. VIGGIANI[2]

[1] City University London, UK
[2] Laboratoire 3SR, Grenoble, France
* presenting author

Keywords: Microstructure of soil, tomography, sandstone, image, μFE

Abstract

This paper presents a numerical simulation that uses tomographic data to reproduce the grain-scale mechanisms taking place during deformation of Fontainebleau sandstone. Previous investigation using x-ray tomographic images acquired during triaxial compression has highlighted the role of bonding rupture mechanisms in the failure mode of the material (Fonseca et al., 2013). The model the deformation of the sandstone, images of the internal topology were used to generate an image-based finite element mesh and the grain-scale phenomena such as, the opening and propagation of the cracks associated with the debonding of the cemented grains, were reproduced using a simple constitutive model.

Introduction

Fontainebleau sandstone from the Paris basin in France is a quartzitic sandstone with a median grain size of 260μm and a degree of cementation that can vary considerably (Thiry and Maréchal, 2001). These differences in the amount of cement in the specimen lead to notable distinct microstructures and consequently significantly different failure mechanims. Fonseca et al. (2013) has investigated the grain-scale deformation mechanims associated with a soft Fontainebleau specimen with 21% porosity and a very hard, tightly cemented sandstone with 6% porosity. This study highlighted the role of bonding rupture mechanisms to explain the differences in behaviour between the soft and the hard sandstone. Using tomographic data of the full specimen under triaxial compression, axial splitting was observed to occur in the sample shortly after 2% axial deformation, as a consequence of tensile failure at the grain-to-grain cemented interface. The grain-scale phenomena was observed to involve progressive contact damaging or 'cracking' leading to the debonding of the cemented contacts. This processe eventually coalesced into larger geometrical discontinuities or 'vertical ridges', which resulted in the formation of vertical columns of horizontally unbonded grains able to transfer stresses along the direction of the major principal stress.

In the past decades, the reconstruction of microstructure of natural porous rock has become of increasinly interest for the petroleum industry and a number of numerical approaches have been proposed (Tacher et al. 1997; Yeong and Torquato, 1998; Pilotti, 1998; Jin et al. 2003; Holtzman, 2012). Stochastic reconstruction is an example of a commonly used approach. It consists of matching the statistical properties of a model to those of the microstructure to simulate the relevant physical processes of a rock formation, such as, sedimentation, compaction and diagenesis (Yeong and Torquato, 1998; Jin et al. 2004). The computational effort for microstructure reconstruction, which is the first stage to investigate the mechanical behaviour of geomaterials, raises with the complexity of the depositional method adopted and represents, generally, the lengthier part of the simulation.

In the present paper, a microstructural finite element (μFE) model which combines x-ray micro-computed tomography data with finite element analysis is developed. It follows on Nadimi et al. (2015) work to simulate the grain-to-grain interaction in an uncemented sand. The present study enables numerical simulation of the tightly cemented Fontainebleau specimen that accounts for the microstructural features, such as, the geometrical arrangement of the grains and pores, grain shape and contact topology including degree and spatial distribution of the cement.

Methodology

The μFE model proposed in this paper uses a finite element mesh produced from a two-dimensional (2D) image containing all the geometrical microstructural information. The input data for the μFE model was obtained in three key stages: image acquisition and image segmentation, image-based meshing and constitutive modelling, as decribed in this Section.

Image acquisition and segmentation

Non-invasive images of the initial microstructure of Fontainebleau sandstone were acquired using high resolution x-ray computed tomography (μCT). The images have a spatial resolution of 8.5μm, i.e. $0.033 \times d_{50}$, which allows the identifications of the constituinte microstructural features, such as, the grains, pore space and cement. As shown in Figure 1a, the pixels representing the grains, or solid phase, have brighter color (denser material) while the pore space is assocated with darker pixels. The cement is essentially formed of quartz overgrows, which difficults the dissociation between cement and quartz grains, however, it was observed that in general the cement is usually darker tha the grains. An intensity-based threshold technique was used to classify (or segment) the three phases, i.e. solid grains, void space and cemented contacts.The obtained segmented image was the starting point to develop the image-based mesh.

Image-based meshing

An open source software package OOF2 (Object Oriented Finite Elements v2, NIST) was used to create the mesh directly from the image (Reid et al. 2008). A simple and straightforward way to generate the mesh is using a direct pixel-to-element approach. However, the computational costs of running the model can be very high for large images. A more efficient approach is proposed here, which assumes that the grains are homogenous and therefore each grain can be represented by larger elements containing more than one pixel. These elements can be defined by various polygonal shapes, for which the size and shape depend on the size and shape of the respective grain. Using this approach, the initial mesh was defined according to the geometrical characteristics of each grain. The correction of the elements containing more than one phase can be carried out by either subdividing the elements, which increases the number of elements, or running a routine that changes the topology of element without increasing the number of elements. In this routine, nodes can be added, removed or reconnected to increase the homogeneity of the mesh. The assessment of the quality and efficiency of the mesh was taken into account by quantifying i) the ability of the mesh to represent the features in the images, using the *homogeneity index,* and ii) the mesh convergence behaviour, using the *shape index*. In the case of all the pixels in the image being associated to a mesh element, the *homogeneity index* equals 1. The *shape index* of regular shaped elements, such as triangles and squares equals 0, while the *shape index* of thin and

elongated elements takes higher values. Following the necessary corrections and improvements of the mesh, it was subsequently imported to the finite element code.

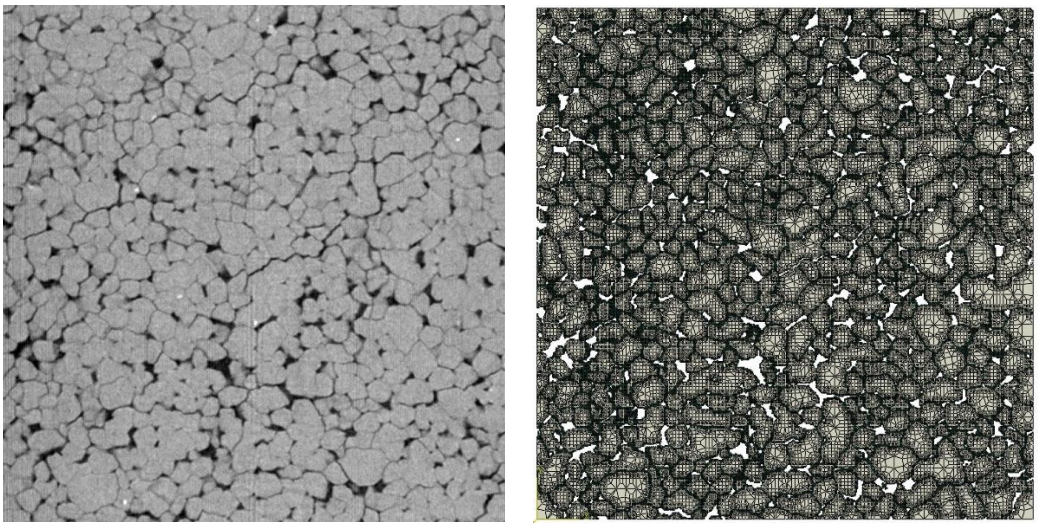

(a) *(b)*

Fig. 1. *a) µCT raw image; b) Image-based Finite Element mesh, elements representing the bonding between grains contain smaller elements and are shown in darker colour.*

Constitutive model

Following observations from Fonseca et al. (2013), it is assumed that the deformation of the material is governed by bond rupture, thus, representation of this cracking and post cracking response are the key aspects in the modelling. The simulation of bonding damage and crack formation was carried out by using a constitutive model which takes the cracking response into finite element calculations.

Cracking was modelled by assigning a smeared cracking constitutive model to the cement (Belytschko et al. 1988; Borst et al. 2004). By using this constitutive model, cracks remain for the full finite element calculation and may open or close. The presence of cracks enters into this calculation by the way in which the crack affects the current strength and stiffness associated with the integration point. It is considered that a crack is initiated when the stress at an integration point satisfies a specified condition, e.g. the major principal stress reaching the tensile strength. The initial small cracks tend to connect to form one, or more than one, dominant crack, as deformation progresses.

Numerical Model

This µFE model consists of a 2D array of approximately 560 grains subjected to triaxial compression. A segmented image with a size of 680 × 700 pixel was used to generate the mesh. Mesh enhancement and refinement, resulted in a *homogeneity index* of 0.94 and a *shape index* of 0. In total, it comprised 126,923 nodes and 121,389 elements as shown in Figure 1b. The image-based mesh was imported into a commercial finite element package, Abaqus v6.13 (Dassault Systèms). In order to simulate triaxial compression conditions, the bottom and left boundaries were fixed in the normal direction and 2MPa isotropic compression was applied to the top and to the right boundaries, in the first step, in order to reproduce the experimental conditions (Figure 2a). Axial loading was subsequently applied by defining a prescribed displacement at the top of the model, up to about 4% axial strain (Figure 2b), this was the point at which the deviatoric stress was seen to reach a plateau in the stress:strain experimental curve

from Fonseca et al. (2013). The grain-to-grain contact interaction was simulated by assuming hard contact in the normal direction and Coulomb friction in the tangential direction. Values of 100 GPa for Young's modulus and 0.15 for Poisson's ratio, corresponding to bulk modulus of K=47.6GPa and shear modulus of G=43.5GPa, were assigned to the grains. It was assumed that the cement has an Young's modulus of 30% of the grain's value and that the strain softening reduces the stress linearly to zero at a 0.5% strain after failure.

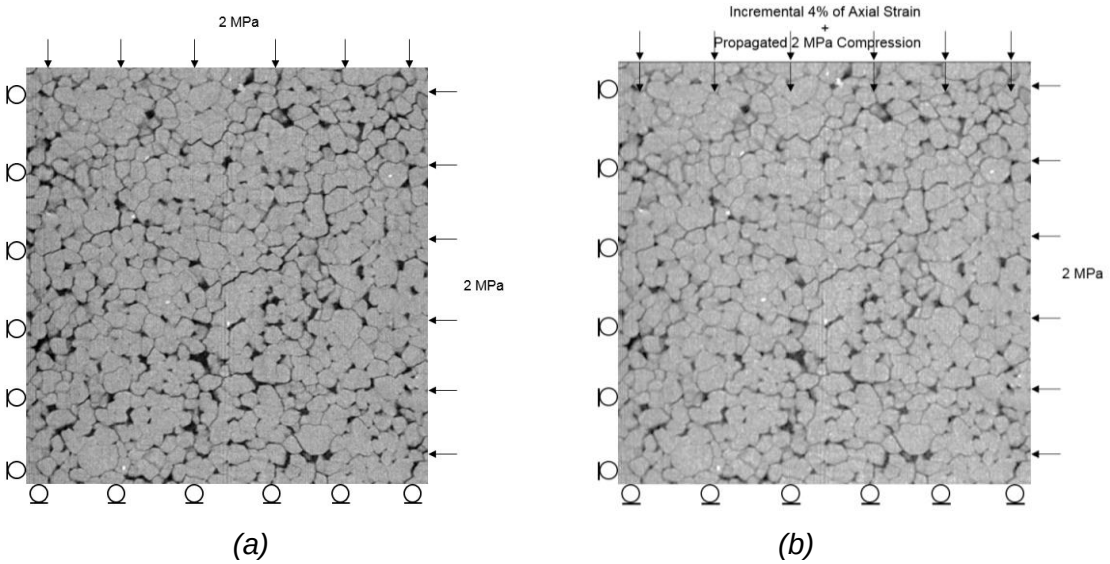

(a) *(b)*

Fig. 2. *Boundary conditions a) Stage 1: isotropic compression; b) Stage 2: incremental axial displacement during shearing.*

Results and discussion

The results were investigated in terms of maps of the stress and strain distribution. Figure 3a shows the formation of vertical columns of highly stressed grains, i.e. represented by brighter colours, which is in line with the experimental observations reported in Fonseca et al. (2013). The experimental data has shown that these columns are formed by horizontally unbonded grains following cement rupture along vertical ridges. In the present study, in order to investigate the cracking pattern, it was assumed that the direction of the minimum principal strain is parallel to the direction of cracking. The direction of the minimum principal strain is presented in Figure 3b by short arrows, which as expected, tend to exhibit a near vertical orientation. The strain distribution also presented in Figure 3b shows the higher strain concentration at the contacts between grains.

Conclusion

The present paper contributes the first step towards the development of microstructure-informed numerical modelling of bonded geomaterials. The numerical approach proposed here uses a 2D image, of the internal microstructure of a tighly cemented sandstone, to reproduce the grain-scale phenomena observed to take place on real specimens investigated using tomographic data acquired at different stages of deformation. The results presented, although preliminary, clearly show the potential of this analysis to overcome some of the challenges associated with modelling the mechanical behaviour of cemented geomaterials to failure. Future work includes the 3D extension of this μFE model.

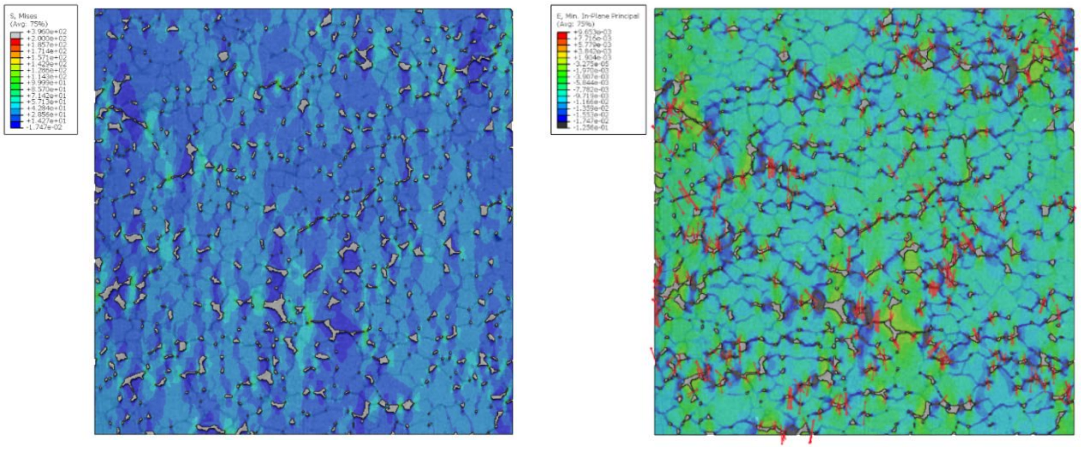

(a) *(b)*

Fig. 3. *a) Stress distribution map; b) Strain distribution map with arrows indicating the direction of the cracks in the cement given by the direction of the minimum principal strain.*

Acknowledgments

The authors would like to acknowledge the National Institute of Standards and Technology (NIST) for the code OOF2 used in this study.

References

Belytschko, T., Fish, J., Engelman, B.E. (1988) A finite element with embedded localization zones. ***Computer Methods in Applied Mechanics and Engineering***, 70, 59-89.

Borst, R., Remmers J.C., Needleman, A., Abellan M.A. (2004) Discrete vs smeared crack models for concrete fracture. ***International Journal for Numerical and Analytical Method in Geomechanics***, 28,583-607.

Fonseca, J., Besuelle, P. and Viggiani, G. (2013) Micromechanisms of inelastic deformation in sandstones: an insight using x-ray micro-tomography, ***Geotechnique Letters*** 3, No. 2, 78–83.

Hillerborg, A., Modéer, M., Petersson, P.E. (1976) Analysis of crack formation and crack growth in concrete by means of fracture mechanics and finite elements, ***Cement and Concrete Research***, 6, No. 6, 773-781.

Holtzman, R. (2012) Micromechanical model of weakly-cemented sediments, ***International Journal for Numerical and Analytical Method in Geomechanics*** 36, 944-958.

Jin, G., Patzek, T.W., Silin, D.B. (2004) *Dynamic reconstruction of sedimentary rock and simulation of its mechanical properties*, U.S. Department of Energy, LBNL-55038.

Jin, G., Patzek, T.W., Silin, D.B. (2003). *Physics-based reconstruction of sedimentary rocks (SPE83587).* SPE Western Regional/AAPG Pacific Section Joint Meeting, Long Beach, CA.

Mourzenko, V.V., Thovert, J. F., Adler, P.M. (2001). Percolation in two-scale porous media, ***The European Physical Journal B***, 19, No. 1, 75-85.

Nadimi, S., Fonseca, J., Taylor, N. (2015). A microstructure-based finite element analysis of the response of sand, *6th Int. Sym. On Deformation Characteristics of Geomaterials*, Buenos Aires, Argentina.

Pilotti, M. (1998) Generation of realistic porous media by grains sedimentation. ***Transport in Porous Media***, 33, 257-278.

Potyondy D.O., Cundall P.A. (2004). A bonded-particle model for rock. ***International Journal of Rock Mechanics and Mining Sciences*** 41, No. 8,1329–1364.

Reid, A.C.E., Langer, S.A., Lua, R.C., Coffman, V.R., Haan, S., García, R.E. (2008). Image-based finite element mesh construction for material microstructures, ***Computational Materials Science*** 43, 989-999.

Tacher, L., Perrochet, P., Parriaux, A. (1997) Generation of granular media. ***Transport in Porous Media***, 26, 99-107.

Thiry, M. and Marechal, B., (2001) Development of Tightly Cemented Sandstone Lenses in Uncemented Sand: Example of the Fontainebleau Sand (Oligocene) in the Paris Basin, ***Journal of Sedimentary Research*** 71, No. 3, 473-483.

Yeong, C.L.Y., Torquato, S. (1998) Reconstructing random media. II. Three-dimensional media from two-dimensional cuts. ***Physical Review B***, 58, No. 1, 224–233.

Method of X Ray CT Evaluation For Filling Porous Asphalt Mixture wtih Permeable Repair Material

T. FUMOTO*[1], S. MOTOMATSU[2], M. OHARA[3], K. UESAKA[4] , A. ADACHI[5]

[1] 3-4-1 Kowakae, Higashiosaka, Osaka 577-8502, JAPAN – fumoto@civileng.kindai.ac.jp
[2] Dojima Avanza 18F 1-6-20 Dojima Kita-ku Osaka, 530-0003, Japan – s.motomatsu.aa@w-nexco.co.jp
[3] Dojima Avanza 18F 1-6-20 Dojima Kita-ku Osaka, 530-0003, Japan – m.ohara.ab@w-nexco.co.jp
[4] 30-1 Hara Taishi Ibo-gun Hyogo, 671-1502, Japan – k.uesaka@shoreki.co.jp
[5] 30-1 Hara Taishi Ibo-gun Hyogo, 671-1502, Japan – a.adachi@shoreki.co.jp
* presenting author

Keywords: Porous asphalt mixture, Repairing material, CT value distribution, method of least squares.

Abstract

A porous asphalt mixture can be treated with an industrial method of spraying a repairing material (asphalt emulsion) from the pavement surface. However, the filling state has yet to be confirmed up until now. Therefore, we intend to numerically express the internal filling state with X-ray computed tomography for specimens filled with the repairing material. As a result, we propose a method for estimating the volume rates of an asphalt based material, aggregates, and voids. Also, the change of the filling rate in each depth of the specimens was successfully clarified by the proposed method.

Introduction

A porous asphalt mixture having continuous pores is a road material with water permeability and sound absorption. The porous asphalt mixture consists of a high viscosity modified asphalt coating thinly crushed stone surfaces, and the crushed stones bonded to each other. The high viscosity modified asphalt has high durability. However, the asphalt deteriorates due to dynamic fatigue and weather. When the deterioration of the bond strength is small and the performance of a bese layer is low, the porous asphalt mixture should be repaired.

One method of repairing the porous asphalt mixture is to spray the repairing material (asphalt emulsion shown in Fig. 1) from the pavement surface. The repairing material coats the inner surface, and collects at the bottom of the porous asphalt mixture. The resultant formation of a water interception layer and the improvement of the adhesive strength between coarse aggregates may be the effects of the repair. However, such effects are not understood well, because the visualization in the porous asphalt mixture has been difficult.

The X-ray computed tomography (CT) can visualize the inside of the porous asphalt specimen. At the same time, the X-ray CT method would allow estimation of the mixture

Fig. 1. *The Repairing Material (Asphalt Emulsion).*

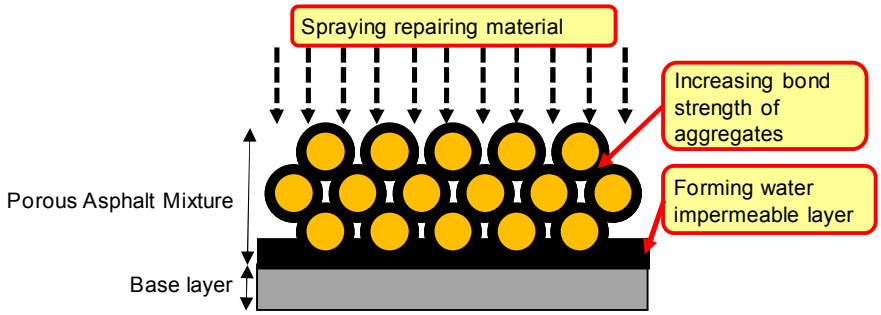

Fig. 2. *Image of the Repairing Material Spray Method.*

ratio of materials in the porous asphalt specimen where the repairing material has been sprayed. This is because the CT value distribution obtained by the X-ray CT is composed of overlapping CT value distributions of different materials. If the CT value distribution of each material has the same shape as the normal distribution, the mixture ratio of the materials is calculated by the method of least squares. Then, the filling distribution in the height direction in the porous asphalt mixture can be estimated based on the change in the mixture ratio of materials. This study shows that the X-ray CT enables determination of the filling distribution in the height direction in the porous asphalt test specimen.

Experiment 1

Outline

First, the CT value distribution of specimens was measured before and after the voids of each specimen was saturated with the repairing material.

Materials for the porous asphalt mixture were the polymer modified asphalt (its density is 1.04 g/cm^3), a stone powder (its density is 2.70 g/cm^3), a blast furnace granulated slag fine aggregate (its density is 2.79 g/cm^3) and a crushed stone (its density is 2.75 g/cm^3). The mixing rates of the stone powder, the blast furnace granulated slag fine aggregate, and the crushed stone were 5%, 9.5%, and 89.5% respectively, and the amount of the polymer modified asphalt was 4.9% in unit weight of the porous asphalt mixture. Four test specimens of 100 mm in diameter and 40 mm in height were made so that the voids became 20%. After that, the outside and the bottom of each test specimen was covered with a packing tape. For each specimen, the repairing material was poured from the upper surface and the air left inside it was sucked by a vacuum pump.

X-ray CT images of the specimens were generated by the X-ray CT apparatus before and after the filling with the repairing material. The X-ray tube was operated under 200 kV and 60 μA. The spatial resolution is 0.1226 x 0.1226 x 0.1226 mm. From the X-ray CT image, the CT value distribution was calculated.

Results and Discussion

Fig. 3 shows a sectional image of each X ray CT image. Before the filling with the repairing material, the aggregates and the asphalt were white and the voids were dark gray. When the repairing material was poured to the specimen, the voids change from dark gray to light gray.

Fig. 4 shows the CT value distribution before and after the filling with the repairing material. Because the voids of the specimen were filled with the repairing material, the CT value distribution changed from the CT value distribution of the unrepaired specimen. Of such changes, the decrease would relate to the CT value range of the voids and the increase would relate to the CT value range of the asphalt in the repairing material. On the other hand, the unchanged range would relate to the aggregate.

Here, the CT value distribution of each material can be assumed to have the same shape as the normal distribution. In addition, the CT values of fine and coarse aggregates have no difference because those densities were almost the same. Similarly, the CT values of the asphalt and the repairing material were also almost equal. The stone powder would be contained in the volume of asphalt by a partial volume effect. Based on such information, the mixture ratios of the three materials in the porous asphalt mixture were represented by formula (1) and calculated by the method of least squares.

$$F(x) = \alpha exp\left(-\frac{(x-\mu_{AgG})^2}{2\sigma_{AgG}{}^2}\right) + \beta exp\left(-\frac{(x-\mu_{AsG})^2}{2\sigma_{AsG}{}^2}\right) + \gamma exp\left(-\frac{(x-\mu_{VoG})^2}{2\sigma_{VoG}{}^2}\right) \quad (1)$$

where *AgG* is the fine aggregate and the coarse aggregate, *AsG* is the asphalt, the repairing material and the stone powder, *VoG* is the voids, α is the largest frequency of the CT value distribution for the fine and coarse aggregates, μ_{AgG} is the average of the CT value distribution for the fine and coarse aggregates, σ_{AgG} is the standard deviation of the CT value distribution for the fine and coarse aggregates, β is the largest frequency of the CT value distribution for the asphalt, the repairing material and the stone powder, μ_{AsG} is the average of the CT value distribution for the asphalt, the repairing material and the stone powder, σ_{AsG} is the standard deviation of the CT value distribution for the asphalt, the repairing material and the stone powder, γ is the largest frequency of the CT value distribution for the voids, μ_{VoG} is the average of the CT value distribution for the voids, σ_{VoG} is the standard deviation of the CT value distribution for the voids, and x is the CT value.

Then, the formula (1) and the method of least squares were used to estimate the volume rates of materials in the porous asphalt mixture. Fig. 5 shows examples of the results estimated by the formula (1) and the method of least squares. For the four specimens, the estimated results had a measuring error of 5% for the volume rates of the porous asphalt mixture.

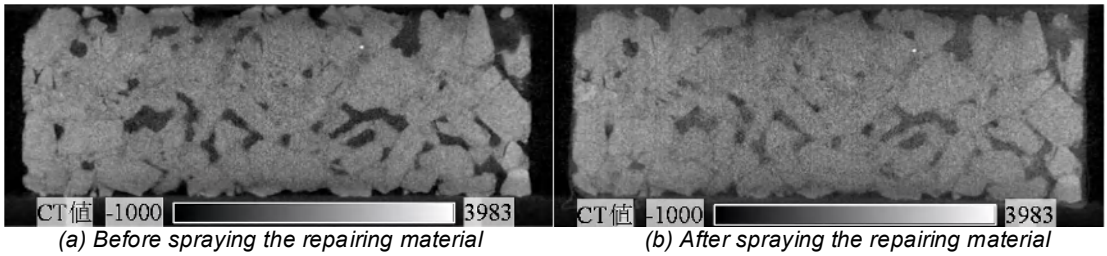

(a) Before spraying the repairing material *(b) After spraying the repairing material*

Fig. 3. *A sectional image in the X ray CT image.*

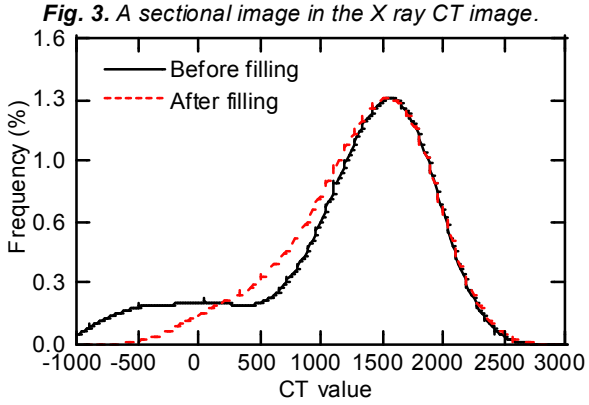

Fig. 4. *Example CT value distribution of the specmen before and after filling with the repairing material.*

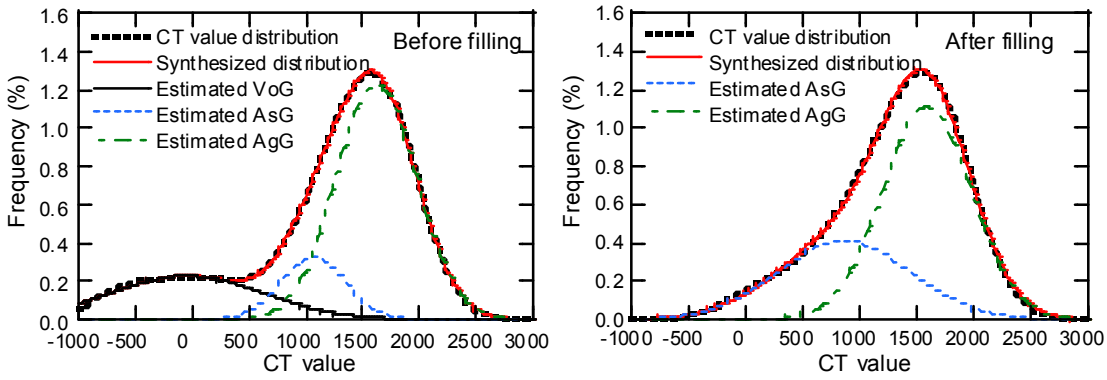

(a) Before spraying the repairing material *(b) After spraying the repairing material*

Fig. 5. *Results estimated by the formula (1) and the method of least squares.*

Experiment 2

Outline

The porous asphalt specimen was made from the polymer modified asphalt (its density is 1.04 g/cm^3), a stone powder (its density is 2.72 g/cm^3) and a crushed stone (its density is 2.75 g/cm^3). The mixing volume rates of the asphalt, the stone powder, and the crushed stone were 64.1%, 3.4%, 7.1%, and 25.4%., respectively. The shape of each specimen is 100 mm in diameter and 76.4 mm in height.

In the four cases, X-ray CT images of the specimens were generated by the X-ray CT apparatus. In Case 1, the porous asphalt specimen was not repaired. The porous asphalt specimen was soaked to the height of 15 mm in the repairing material poured into a cup in Case 2. The repairing material was then poured to the height of 30 mm from around the specimen in Case 3. Finally, the repairing material was sprayed over the specimen in Case 4. The X ray tube was operated under 200 kV and 60 μA. For each case, the X ray CT image was divided by every 5 mm in height. The formula (1) and the method of least squares for the CT value distribution obtained from the X-ray CT image were used to estimate the volume rates of materials in every layer of 5 mm in height.

Results and Discussion

Fig. 7 shows the results of volume rates of AgG, AsG and VoG. In Case 1, the volume rates of AsG, AgG, and VoG were almost constant in all depths. In Case 2, the volume

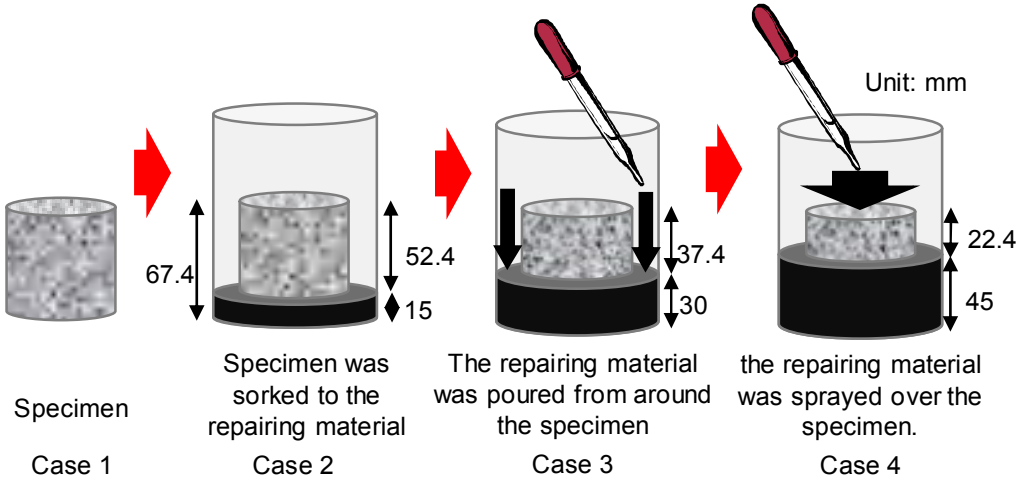

Fig. 6. *Image of each case in experiment 2.*

rate of VoG became 0% and the volume of AsG increased to 50 mm or more in depth. For the layer of 50 mm or more in depth, the voids would be filled with the repairing material.

The voids were filled with the repairing material at a depth of 40 mm or more in Case 3, and at a depth of 20 mm or more in Case 4. In addition, in Case 4, the volume rate of voids also decreased at depths from 5 to 20 mm. This decrease should show that the repairing material could adhere to the inner surface of the specimen at an upper layer because of the spraying from the upper surface.

The above indicates that the difference in the mixture ratio of materials before and after the filling with the repairing material can be used to calculate the filling rate of the repair material.

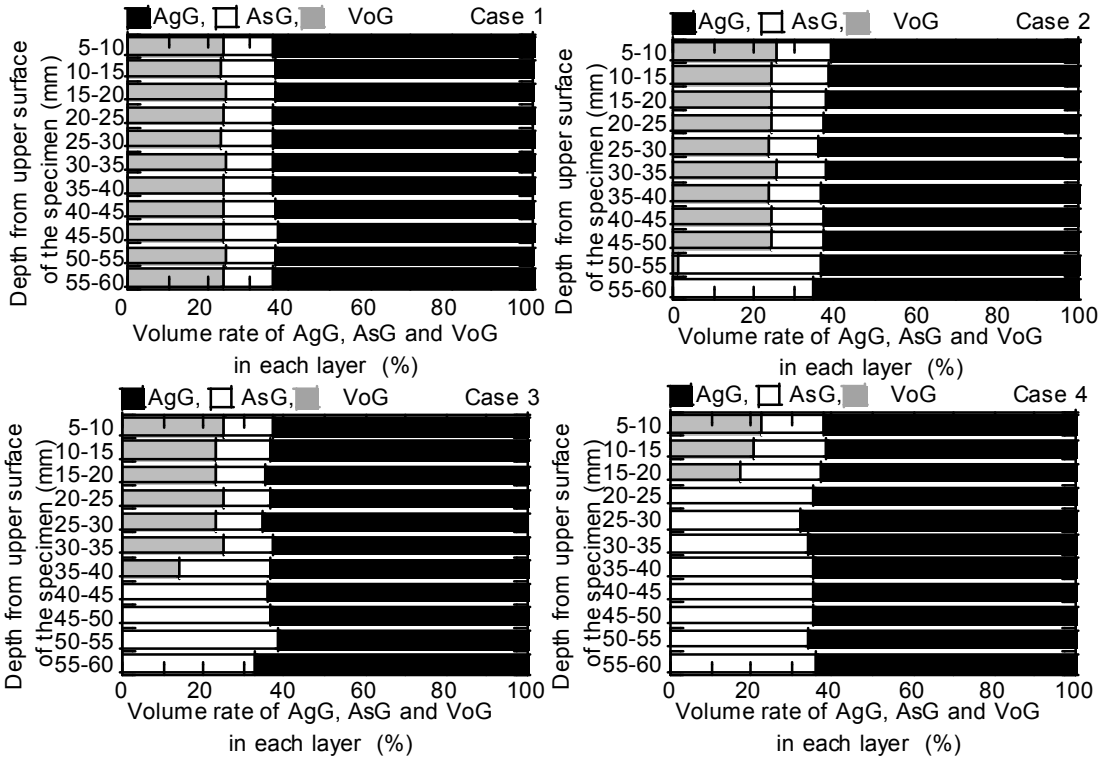

Fig. 7. *The estimated volume rates of AgG, AsG and VoG.*

Results

We proposed the method of estimating the volume rate of materials in the porous asphalt mixture by using the CT value distribution and formula (1). When the porous asphalt mixture with the sprayed repairing material was measured by the proposed method, the filling state of the repairing material in the specimen became clear. The volume rate of the repairing material adhering to the inner surface near the specimen surface became clear. In the future, the repairing material will have the best qualities by clarifying the relationships between the repairing effects and the qualities of the repairing material.

References

Ohara M., Motomatsu S. & Uesaka K. (2014). Development of method of preventive maintenance and repair for the high-performance pavement type I - Penetration type repair materials dispersion and infusion method -, ***Proceedings of Annual Conference of the Japan Society of Civil Engineers*** 69, v-558. (in Japanese)

Takano D. & Otani J. (2013). Visualization of the Structure of Geomaterials Using X-ray CT I: Overview of X-ray CT and Application of Image Analysis Technique, ***Journal of the Society of Materials Science*** 62, 10, 654-659. (in Japanese)

Fumoto, T.(2013): Development of a new industrial X-ray CT system and its application to compression test of polymer concrete, ***Journal of Japan Society of Civil Engineers, Ser. E2 (Materials and Concrete Structures)*** , 69, 2:182-191.(in Japanese)

A topological description of granular systems using persistent homology

Mohammad Saadatfar[1*],Hiroshi Takeuchi,[2] Yasuak Hiraoka[2],
Nicolas Francois[1], Vanessa Robins[1]

[1]Department of Applied Mathematics, Research School of Physics and Engineering,
Australian National University, Canberra, Australia
[2]AMIR, Tohoku University, Sendai, Japan

[*] E-mail: mohammad.saadatfar@anu.edu.au

Abstract

A complete structural description of amorphous systems is an open problem that has challenged mathematicians for centuries. The existing conventional methods used to characterise such systems are insufficient to reveal their hidden topology and intrinsic structures. In this presentation, we discuss an algorithmic framework based on algebraic-topological computational tools, known as Persistent Homology, which can successfully characterise the topology of massive amorphous structures.

Keyword: topology, granular materials, persistant homology, tomography

Introduction

Advances in three dimensional (3D) imaging technology, as well as rapid progress in computing power has given rise to the production and accumulation of high-resolution and multi-dimensional large data sets. The challenge of dimension reduction and extracting useful information from these large data sets has been taken on by mathematicians and topologists [4, 10] along with many others. Quantitative analysis of large 3D images often requires computing the 3D space based on the alpha shapes and combinatorial complex. This Recently, computational homology [4] has provided us with tools for systematically characterising complex, high dimensional and geometric objects in physical and biological systems. A particularly important tool in computational homology is based on the novel proposition of using persistence diagrams (PD), a relatively new concept in applied algebraic topology, as the fundamental modelling tool.

Granular materials are an example of high-dimensional, multi-scale, extremely complex and nonlinear systems, where a simple ingredient of hard-sphere interaction gives rise to a highly complex collective behaviours that render such systems the most significant modelling challenges of our time [1, 11]. These materials appear in a broad spectrum of practical settings from heavy industry to pharmaceuticals. As such, they are of intense interest to the engineering and scientific world. Our goal in this study is to demonstrate that new ideas associated with computational topology provide an efficient, robust and faithful approach to providing tractable models to decipher the complexity of the spatial structures in granular systems. The abstract nature of these topological methods imply that these will be applicable to a wide range of systems demonstrating complex spatio-temporal structures. More specifically, here we present

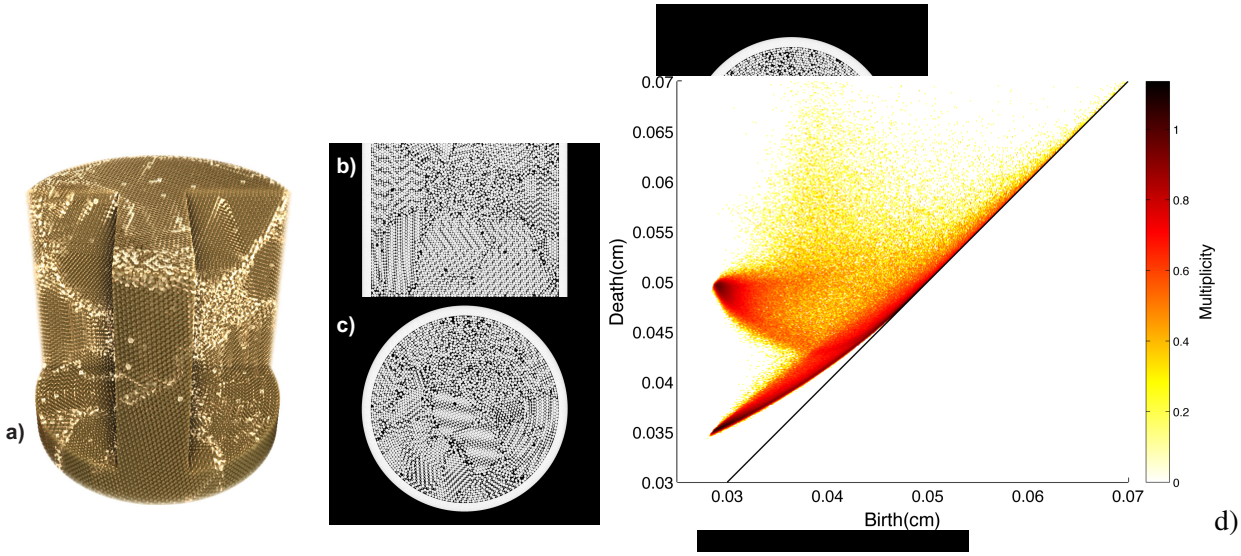

Figure 1 a) 3D visualisation of a partially crystallised packing . b-c) 2D vertical and horizontal slices through the tomogram shown in a). d) Birth-De d) diagram partially crystallised packing made of $\approx 200,000$ beads.

a novel topological characterisation tool, Persistent Homol to study dense nular systems. We first detail the experimental system and the imaging procedure owed by the ematical description of the persistent homology, and in particular its application fo

1 Experimental data

Our experimental system is a dense packing of hard spheres made of monosized acrylic beads (diameter d = 1 mm, polydispersity = 0.025 mm), which are packed into a large cylindrical container (diameter = 66 mm). A batch of approximately 200,000 beads is initially poured into a container forming a random packing with a volume fraction ϕ (fraction of volume occupied by the grains) ranging from 60% to 63%. The container is then placed on a shaker allowing for both vertical and horizontal vibrations. The resulting packing shows substantial crystallisation, with a global volume fraction ranging from 68.5% well beyond Bernal's limit ($\phi \approx 0.64$) [6, 7].

Helical x-ray micro-CT [12] is utilised to image the internal 3D structure of the packing with a voxel size of 30 microns [1]. Fig. 1 shows a 3D rendering of such a partially crystallised structure. The bright regions correspond to locally disordered aggregates of beads; a disordered core and boundaries between different crystal domains are thus highlighted. Both random and crystalline phases coexist in the packing (see Fig.1(b-c)).

2 Persistent Homology

Persistent homology is a technique for quantifying the topological structure in data [9, 5]. In the past ten years it has become a popular tool for studying shape in areas of application from dynamical systems [8] to high-dimensional data-mining [2] to digital images [3].

The starting point for computing homology is a cell complex, $\mathscr{C}$; this is essentially a collection of building blocks whose union is the shape of interest. In a *simplicial complex* the building blocks are points, edges, triangles, tetrahedra, and higher dimensional simplices. A *k-chain* is a formal sum of *k*-dimensional simplices and the *boundary operator* is a linear map from *k*-chains to $(k-1)$-chains, which

is defined by adding up the $(k-1)$-dimensional faces of the k-simplices in the k-chain. The filtration parameter α, which allows us to explore the configuration space, can be length scale or time or another scalar ordering parameter. When a k-simplex is added to a cell complex, all of its faces must already be present and so the new cell must either create a new k-cycle, or fill in a "hole" and make the existing $(k-1)$-cycle formed by its faces into a boundary. By tracking homologous cycles as cells are added to the filtration, persistent homology is able to pair the k-simplex that creates a k-cycle with the $(k+1)$-simplex that fills it in and destroys it.

Each homology class has two values of the filtration parameter associated with it: a birth value and a death value. Some cycles may be present in the terminal cell complex; these are called *essential cycles* and are assigned a death value of infinity. It is common practice to represent this information in a *persistence diagram* for each dimension of homology. *PDk* contains all pairs (b,d), $b \leq d$, associated with a persistent homology class in dimension k. Fig.1.b shows the persistent diagram of our experimental packing. It reveals distinct features, which are unique to the granular systems. Below we will explain the process and the underlying mechanisms which result in producing some of these features.

The bead packing data is specified by coordinates for the centre of each bead (and its radius), extracted from the micro-CT images. For simplicity, assume the beads are mono-disperse, with radius $r = 0.5mm$, and consider the union of balls with a radius of α growing around each bead centre, $X(\alpha) = \bigcup B(x,\alpha)$. The topology of $X(\alpha)$ is conveniently captured by the *alpha shape*, a subset of the Delaunay tessellation.

First note that each tetrahedron in our data set has four data points at its vertices and a circumsphere that contains no other data point. The triangular faces and edges also have circumspheres (with radius less than any adjacent tetrahedra) but the circumspheres of these lower-dimensional faces may contain other data points in their interior. This is the case, for example, with the edge opposite an obtuse angle of a triangle. A circumsphere that does not contain any other data points is called *empty*. The alpha shape is then simply defined as the union of all Delaunay simplices (and their faces) with an empty circumsphere and circumradius $\leq \alpha$. Each simplex data set has a critical value $\rho(\sigma)$ so that for $\alpha < \rho(\sigma)$, $\sigma \notin X(\alpha)$ and for $\alpha > \rho(\sigma)$, $\sigma \in X(\alpha)$. This provides the filtration ordering for the simplices in our data set. Note that the critical value $\rho(\sigma)$ is simply the circumradius of σ, only when the circumsphere is empty.

For a perfectly mono-disperse bead pack with no "rattlers", each point in *PD*2 represents a kind of "pore" in the interstices between the beads. The simplest and smallest pore is that formed inside four beads close packed as a regular tetrahedron. This pore is born when α reaches the circumradius of an equilateral triangle and dies when α is the circumradius of the regular tetrahedron, i.e. $(b,d) = (2r\sqrt{\frac{1}{3}}, 2r\sqrt{\frac{3}{8}})$ (see Fig. 2.b). Another simple pore is that which is formed by six beads close packed as a regular octahedron, with $(b,d) = (2r\sqrt{\frac{1}{3}}, r\sqrt{2})$. Spheres in a close packing arrangement with the maximal volume fraction of 0.74, have tetrahedral and octahedral pores only. These pores are also seen in our data as the "hot spots" in PD2 shown in Fig.2.b.

2.1 Tetrahedral and octahedral deformations

There are numerous forms of deformation that a tetrahedron or an octahedron can undergo. Here we consider only three that are able to reproduce the boundaries of the PD diagram of our bead pack as seen in Fig.1.b. These boundary regions have a large density implying that a considerable number of points in the PD2 diagram are concentrated on or around these bounds.

We consider two types of tetrahedral deformations permitted in close-packed beads:
1. Suppose the beads have radius r, then four beads can close pack with centres at the vertices of a regular tetrahedron with edge length $2r$ (see Fig.2.a). This configuration has $(b,d) = (2r/\sqrt{3}, r\sqrt{3/2})$. Now let the top bead roll across the other three (through the saddle point), which stay fixed. The deformation of

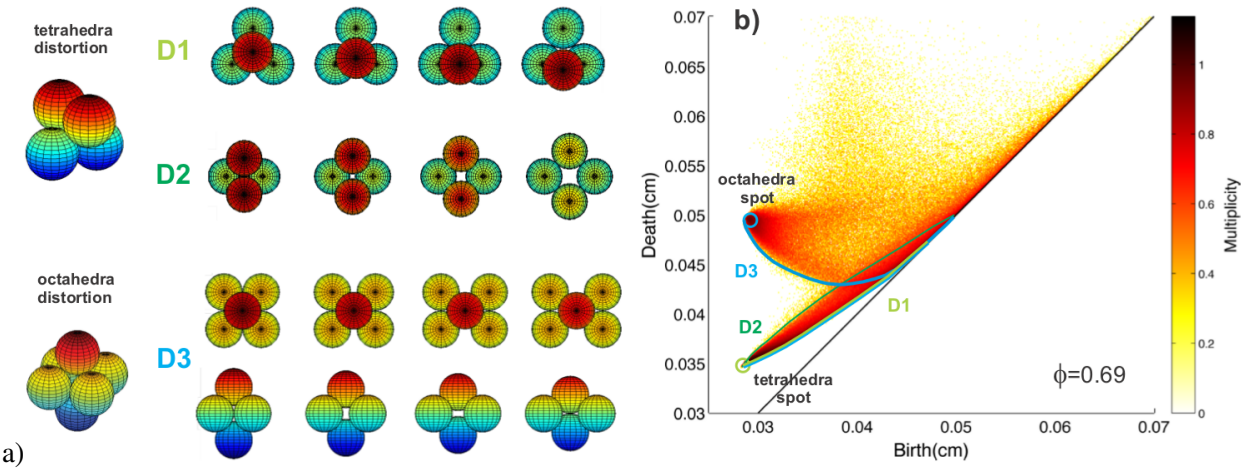

Figure 2 a) Two tetrahedra and one octahedral deformation scenarios as described in the text. b) D1, D2 and D3 are the curves associated with the deformation mechanisms in (a). These curves describe the majority of points in the PD plot.

the tetrahedron can be modelled by two faces remaining as equilateral triangles, and one edge opening up.

2. The second deformation scenario is a symmetrical lengthening of two opposite edges in the tetrahedron while the other four edges maintain the fixed length $= 2r$ (see Fig.2.a).

For the octahedral deformation we consider a simple scenario, where two opposite edges of the octahedron symmetrically lengthen while keeping all other edges equal to $2r$ (see Fig.2.a). This deformation closely matches the observed "lower curve" in PD2 as shown in Fig.2.b by D1.

D1 and D2 curves clearly delineate the highly populated strip in PD2, which we identified as a region made of weakly distorted tetrahedral cavities. The extent of this domain confirms the variety and ubiquity of weakly distorted tetrahedra in the packing, with a density $\phi < 0.7$. It has recently been shown that the formation of polytetrahedral aggregates is a geometrical principle of densification for amorphous frictional packings and a resilient feature in partially crystallised structures up to $\phi = 0.72$ [6]. The curve D3 provides a lower boundary to the octahedral "horn". Moreover numerous cavities are located along this curve. This suggests that edge-adjacent tetrahedra have a propensity to merge/coalesce and form octahedral cavities.

3 Conclusions

We have introduced a new tool, persistent homology, to describe and fully characterise the structure and topology of granular systems. PH is capable of unravelling hidden topologies within similar complex structures as well as revealing prominent features that are unique to point-cloud systems such as granular materials. In particular we have identified two main "'hot-spots" in the persistent diagram, which belong to tetrahedral and octahedral cavities. By introducing three deformation mechanisms, we were able to recover some of the densely populated boundaries of the persistent diagram. These deformation scenarios give in-depth insight into the shape of the persistent diagram and highlight the fundamental grain scale rearrangement process that underpins granular crystallisation.

References

[1] T. Aste, M. Saadatfar, and T. Senden. Geometrical structure of disordered sphere packings. *Physical Review E*, 71(6):061302, 2005.

[2] G. Carlsson. Topology and data. *Bulletin of the American Mathematical Society*, 46(2):255–308, 2009.

[3] O. Delgado-Friedrichs, V. Robins, and A. Sheppard. Skeletonization and partitioning of digital images using discrete morse theory. 2014.

[4] H. Edelsbrunner and J. Harer. *Computational topology: an introduction*. American Mathematical Soc., 2010.

[5] H. Edelsbrunner, D. Letscher, and A. Zomorodian. Topological persistence and simplification. *Discrete and Computational Geometry*, 28(4):511–533, 2002.

[6] N. Francois, M. Saadatfar, R. Cruikshank, and A. Sheppard. Geometrical frustration in amorphous and partially crystallized packings of spheres. *Physical review letters*, 111(14):148001, 2013.

[7] M. Hanifpour, N. Francois, S. V. Allaei, T. Senden, and M. Saadatfar. Mechanical characterization of partially crystallized sphere packings. *Physical review letters*, 113(14):148001, 2014.

[8] K. Mischaikow. Topological techniques for efficient rigorous computation in dynamics. *Acta Numerica*, 11:435–477, 2002.

[9] V. Robins. Towards computing homology from finite approximations. In *Topology Proceedings*, volume 24, pages 503–532, 1999.

[10] V. Robins, P. J. Wood, and A. P. Sheppard. Theory and algorithms for constructing discrete morse complexes from grayscale digital images. *Pattern Analysis and Machine Intelligence, IEEE Transactions on*, 33(8):1646–1658, 2011.

[11] M. Saadatfar, A. P. Sheppard, T. J. Senden, and A. J. Kabla. Mapping forces in a 3d elastic assembly of grains. *Journal of the Mechanics and Physics of Solids*, 60(1):55–66, 2012.

[12] T. Varslot, A. Kingston, G. Myers, and A. Sheppard. High-resolution helical cone-beam micro-ct with theoretically-exact reconstruction from experimental data. *Medical physics*, 38(10):5459–5476, 2011.

Observation of ground displacement field around the driven open-section piles

T. SATO*[1], K. ONDA[2], J. OTANI[1]

[1] X-earth Center, Kumamoto University, 2-39-1, Kurokami, Chuo-ku, Kumamoto, 860-8555, Japan – sato@tech.eng.kuymamoto-u.ac.jp
junotani@kumamoto-u.ac.jp

[2] JFE Steel Corporation, 1-1, Minamiwatarida-cho, Kawasaki-ku,Kawasaki, 210-0855, Japan – ku-onda@jfe-steel.co.jp

Keywords: open-section pile, model tests, pile penetration, digital image correlation

Introduction

In the field of civil engineering, the sheet-pile is indispensable structural form for the public works on land development, flood-control, structural foundations and basements. The interlocked sheet-piles form a wall for temporary construction as earth retaining structures with reducing groundwater inflow. Sheet piling has the advantages of requiring a little on-site construction, which simplifies on-site work control and shortens work periods. Sheet-piles are also a sustainable option since recycled steel is used in their construction, and the piles can often be reused. Further, new sheet-pile foundations have been proposed, such as the jacking methods, which can reduce both the noise and vibration during installation. The new sheet piling method can reduce the environmental loads than so far.

Recently, the usability of sheet-piles have been re-evaluated and many sheet-pile constructions have been proposed for permanent structure as revetments of road or bridge pier foundation. Furthermore, the bulkhead method as continuous impermeable walls have been used as a countermeasure for liquefaction on loose sandy ground and retarding settlement on soft ground in Japan. It is expected that the sheet-pile construction will be able to cover wider fields for public work in the future. Therefore, the demand of the development about advanced construction method using sheet-piles are highly expected. The sheet-piles have been applied to any kinds of soil conditions such as soft clay and dense sand. Also, there are various methods of its construction such as hammering, vibrating and jacking. As a problem of this sheet-pile constructions, the deterioration of work efficiency and defective construction are expected. However, those problems are not clear yet because it is difficult to check the behavior in the ground at sites. Fig.1 shows the conventional cross-sectional shapes of the steel-piles. The sheet-pile form is not closed as for pipe piles but is open-shaped. Further, the form is not symmetry as for H-type steel pile. It seems that the asymmetric shape of the sheet-pile causes the occurrence of the stress imbalance in the ground. Presumably, the stress imbalance leads to the inclined installation of sheet-piles.

The main purpose of this study is to investigate the cause of the deterioration of work efficiency and defective construction of sheet-pile wall. A series of laboratory model tests were conducted in order to determine the behavior of model pile and surrounding ground in the ground. These penetration tests were examined to discuss the effects of pile shape on the bearing capacity, pile deformation, and ground displacement. A micro focused X-ray CT scanner and the digital image correlation (DIC) method was used to observe the pile deformation and ground displacement.

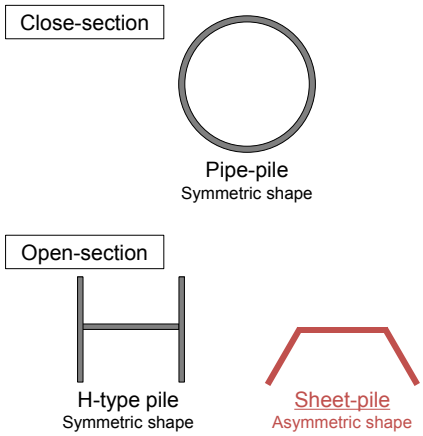

Fig. 1. *Cross-sectional shape of the steel-pile.*

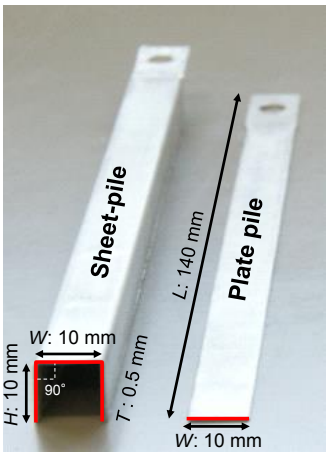

Fig. 2. *Model piles.*

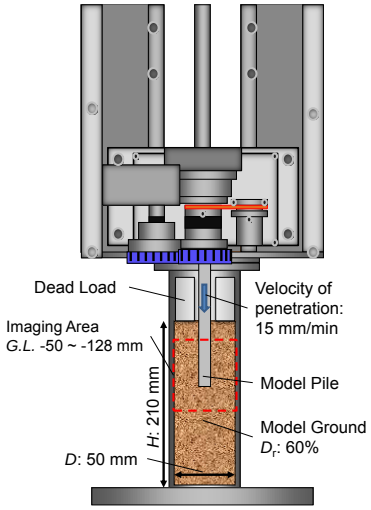

Fig. 3. *Summary of penetration test.*

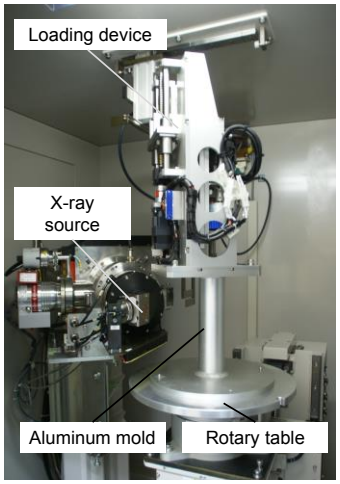

Fig. 4. *Set of apparatus on the X-ray CT scanner.*

Methods

Fig. 2 shows the model piles. To compare the effects of cross-sectional shape of the model pile for its bearing capacity and ground behavior, sheet-pile and plate pile were prepared. The both piles made from aluminum sheet with 0.5 mm thickness. The web length of the sheet-pile and plate pile was 10 mm. The sheet-pile has flange of 10mm length. Therefore, the sheet-pile has the perimeter that is three times longer than that of plate pile. Fig. 3 shows the summary of penetration test. The tests were carried out in the cylindrical aluminum mold with 50 mm diameter. Soil used in the tests was dry *Toyoura* sand(D_{50} = 0.175 mm, U_c : 1.29). The sand was packed in the mold by the free-fall method, where the drop height of the sand was controlled to satisfy the relative density condition of D_r = 60% which was 210 mm in height. Through the whole penetration process, the load and vertically penetration displacement at the pile head was measured. The velocity of penetration was 15 mm/min. The test apparatus was fixed on the rotary table in the CT scanner room, and the penetration tests were conducted on the rotary table. Fig. 4 shows the set of test apparatus on the X-ray CT scanner. The mold was scanned at initial condition and at the positions of pile penetration depth of 60, 80 and 81 mm. The displacement field of the model ground were obtained from the digital image correlation (DIC) using the *TomoWarp* code developed at Laboratoire 3SR at Université Joseph Fourier, France (Hall 2006).

Results

The relationship between the pile head load and the penetration depth is shown in Fig. 5. These results were obtained from preliminary experiment. The sheet-pile has much resistance of penetration than plate pile. At the position of pile penetration depth of 80 mm, the resistance of sheet-pile is ten times as large as that of plate pile, although that of the surface area is just three times of plate pile. Needless to say, these results included the effect of the size of the mold. Therefore it is necessary to make additional experiments for checking these uncertainties. Although it seems that the effect of the pile shape is shown qualitatively.

Arbitrary horizontal cross-sectional CT images, X-Y plane, are shown in Fig. 6 at the position of pile penetration depth of 80 mm. The sheet-pile was observed to have deformed close to the pile tip. This trend has been observed at the other penetration experiments of sheet-piles, Taenaka et al. (2008).

Figs. 7(a), (b), (c) and (e), (f), (g) show vertical cross-sectional images of the displacement as X, Y, Z direction and Fig. 7(d) and (h) shows the vector map of spatial displacement. These figures show the X-Z plane, which through the model piles center as A-A' and a-a' line as shown in Fig.6. The DIC method applied to the CT images that at the position of 80 and 81 mm. It was shown from the DIC results that the sand around the plate pile deformed at just surface and under the real part of pile tip. In contrast, the sand which exist inside of cross sectional area, concave zone, of sheet-pile was moved with pile. Further, the deformation area at the sheet-pile tip was wider and deeper than plate piles one. It was revealed that the difference of deformation area at the cross-sectional inside and outside of sheet-pile. Fig. 8 shows the vector map of horizontal displacement at the pile tip. The displacement of sand was symmetric for the axis of web at the tip of plate pile. In contrast, the displacement of sand was asymmetric for the axis of web at the tip of sheet-pile. At the long driving of sheet-pile, the pile tip may well be installed with incline.

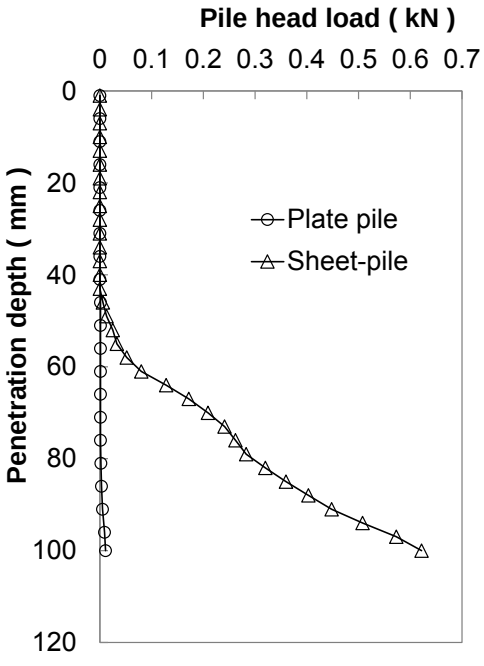

Fig. 5. *Relationship between pile head load and penetration depth.*

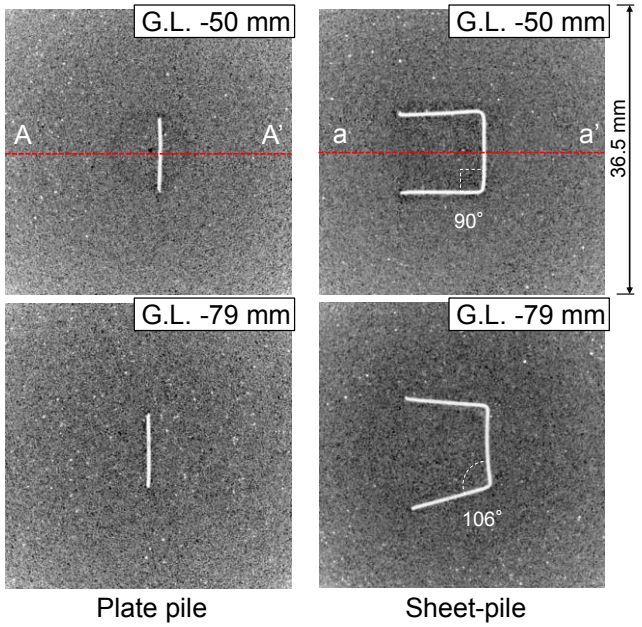

Fig. 6. *CT images of horizontal cross-section : After 80 mm installed.*

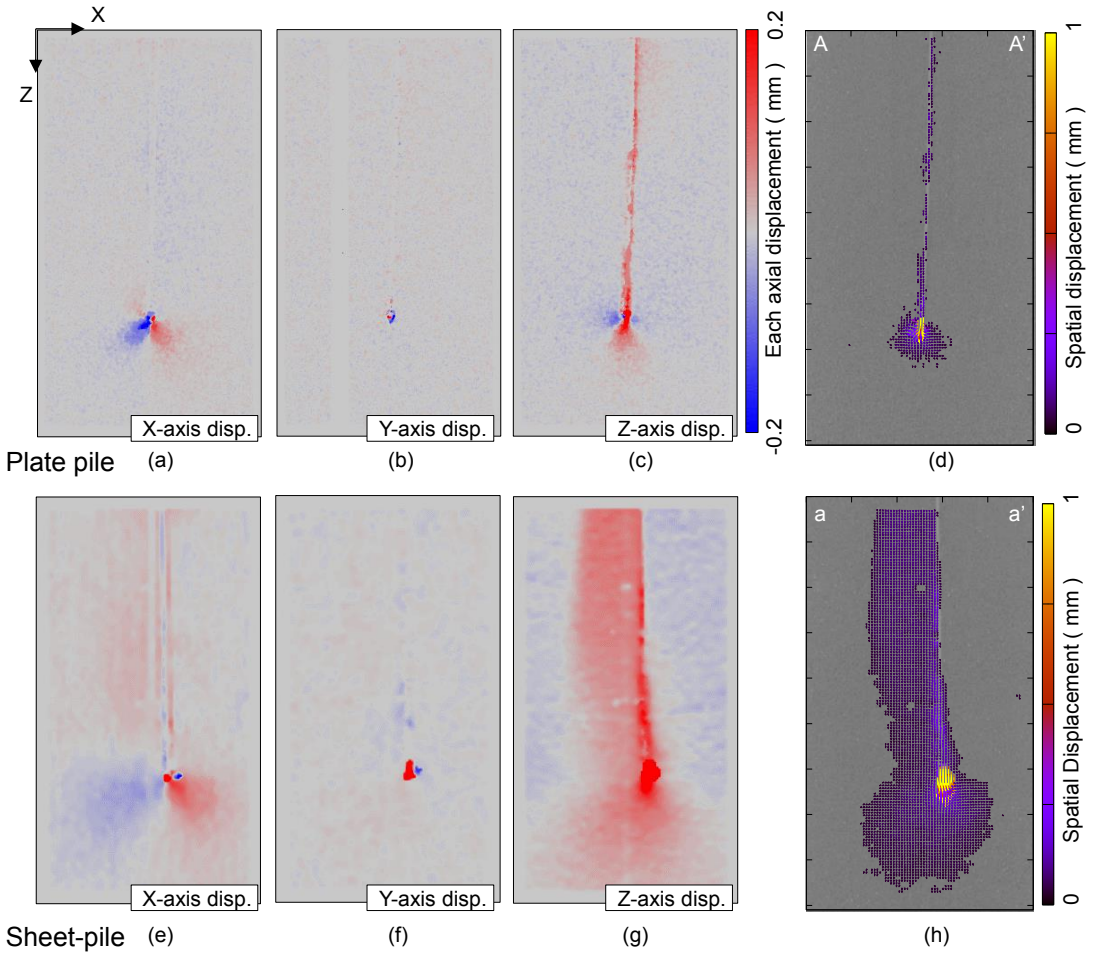

Fig. 7. *Vertical cross-sectional displacement and vector map*
: The DIC analysis applied to the CT images that at the pile penetrated depth of 80 and 81 mm.

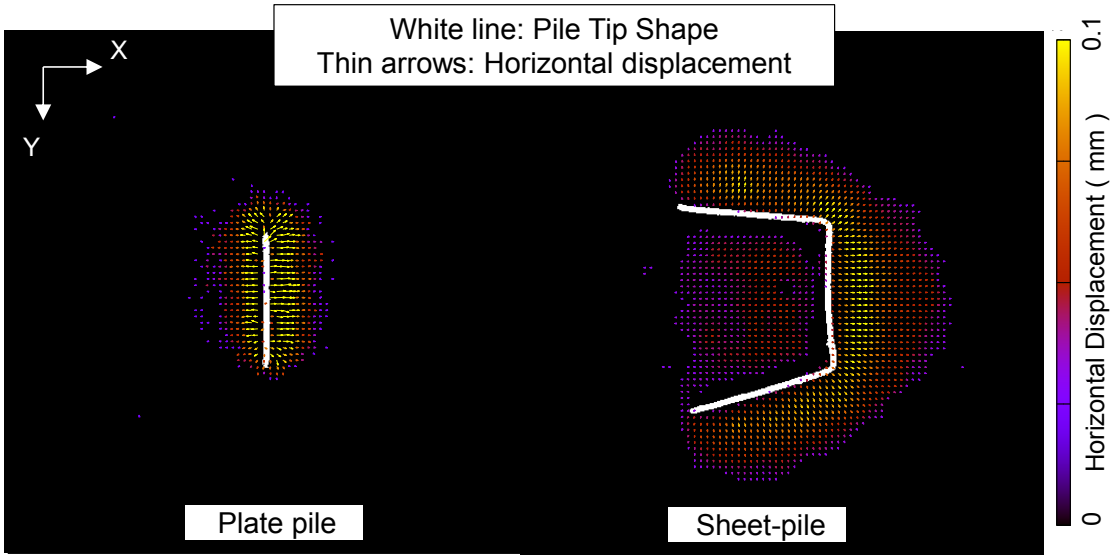

Fig. 8. *Horizontal cross-sectional vector map of horizontal displacement at the pile tip.*

Conclusion

There are many researches of open-ended pipe piles about plugging with arching effects, e.g. Kishida et al. (1977), White et al. (2000), Lüking et al. (2013). It has been recognized that pipe piles generate soil plugging during penetration. In contrast, the research of open-section piles such as sheet-pile and H-type pile are not enough. Taenaka et al. (2008) explained the partial plugging of sheet-pile based on arching theory, and that the deformation of sheet-pile tip may occur with a high stress concentration close to the tip, induced by partial plugging. Although, there are many uncertainties associated with estimating the deformation of open-section piles during driving. With the sheet-pile has asymmetric open-sectional shape as the cause, the pile tip may well be unevenly deformed. Also, the shape induce the imbalance of stress state with partial plugging wedge at the concave zone. It is thought that those imbalance causes the inclined installation of the sheet-pile.

In order to investigate the shape effects for deformation of sheet-pile tip and inclined installation, the authors focused on observing the displacement of the model ground during the penetration of sheet-pile using micro-focused X-ray CT scanner.

The X-ray CT scanner have been applied to the research about plugging on pile tip, e.g. Taenaka et al. (2007), Kikuchi et al. (2008). It is a powerful and effective apparatus to observe the internal ground alteration during penetration tests.

To conduct pile penetration experiments, the rigidity of the model piles are an important parameter and a ratio of a pile size and a mold size affects the results of the experiment. Because of the limitation of the capacity of scanner, the authors could not pay enough attention to these parameters. Extended research on these points are required. The topics of continuing research are tip shape, surface friction, ground conditions and size effects.

References

Hall S.A. (2006). A methodology for 7D warping and deformation monitoring using time-lapse seismic data, **GEOPHYSICS**, 71(4), O21-O31.

Taenaka S., White D.J., Randolph M.F., Nakayama H. & Nishiumi K. (2008). The effect of cross-sectional shape on the performance of sheet piles, **Foundations: Proceedings of the Second BGA ICOF2008**, New Orleans, Vol.1, pp.319-330.

Kishida H., Isemoto N. (1977). Behaviour of sand plugs in open-ended pipe piles, **Proceedings of 9th Int. Conf. Soil Mechanics**, Tokyo, Vol.1, pp. 601-604.

White D.J., Sidhu H.K., Finlay T.C.R., Bolton M.D., Nagayama T. (2000). Press-in piling: The influence of plugging on driveability, **Proceedings of the 8th ICDFI**, New York, pp.299-310.

Lüking J., Kempfert H.-G. (2013). Plugging effect of open-ended displacement piles, **Proceedings of the 18th ICSMGE**, Paris, pp.2363-2366.

Taenaka S., Otani J., Sato T. (2007). Characterization of vertical bearing capacity of sheet-piles, **JSCE Journal of Geotechnical and Geoenvironmental Engineering**, Vol.63, No.1, pp.285-298. (in Japanese)

Kikuchi Y., Morikawa Y., Sato T. (2008). Plugging mechanism in a vertically loaded open-ended pile, **Foundations: Proceedings of the Second BGA ICOF2008**, New Orleans, Vol.1, pp.169-180.

Study on displacement and strain field analysis in wheel-tracking test of asphalt mixture using X-ray CT and digital image correlation

S. TANIGUCHI*[1], J. OTANI[2], T. SATO[3], T. KIMURA[4]

[1] Road Technology Research Group, Public Works Research Institute
1-6, Minamihara, Tsukuba, Ibaraki, 305-8516, Japan – taniwork1535@gmail.com
[2] X-earth Center, Graduate School of Science and Technology, Kumamoto University
2-39-1, Kurokami, Chuo-ku, Kumamoto, 860-8555, Japan – junotani@kumamoto-u.ac.jp
[3] X-earth Center, Faculty of Engineering, Kumamoto University
2-39-1, Kurokami, Chuo-ku, Kumamoto, 860-8555, Japan – sato@tech.eng.kumamoto-u.ac.jp
[4] Cold-Region Maintenance Engineering Research Group, Civil Research Institute for Cold Region
1-3-1-34, Hiragishi, Toyohira-ku, Sapporo, 062-8602, Japan – kimura-t22ae@ceri.go.jp

Keywords: Asphalt mixture, Digital image correlation, Rutting, Longitudinal cracking, Top-down cracking

Abstract

The objective of this study is to clarify the internal displacement and strain field of asphalt concrete pavement. For this purpose, wheel-tracking test, X-ray computed tomography (CT) scanning, and digital image correlation (DIC) has been conducted. In consequence of DIC, the damage characteristics has been clarified such as propagation of large displacement in the dense-graded asphalt mixture using straight asphalt, and large horizontal strain on the surface of the dense-graded using polymer modified asphalt and within the porous asphalt mixture.

Introduction

Asphalt concrete pavement has been subjected to various distresses under various load, temperature conditions and so on. Wheel-tracking test is a dynamic test performed to assess the flow deformation of asphalt pavements. However, wheel-tracking test can only evaluate the deformation on surface of specimens. Since wheel-tracking test does not evaluate within the specimens, internal deformation and strain has hardly been discussed. This paper presents the analysis result of displacement and strain fields in the wheel-tracking test using the industrial X-ray CT scanner and DIC. In addition, this paper mentions the causes of damage in the asphalt concrete pavement such as rutting and cracking from these analysis results.

Methods

Mixture and binder types of specimens used in this study are shown in Table 1, and properties of specimens are shown in Table 2. Shape of specimens was rectangular parallelepiped and size was 150mm width, 300mm length and 50mm height to avoid the artifact effect (Taniguchi et al. 2013). In addtion, electric arc fumace oxidizing slags were installed as the targets in order to compare the CT images effectively. Each mixture took wheel-tracking test under the conditions of 0.63MPa contact stress and 60°C temperature.

X-ray CT scanner used in this study was the industrial one operated by the X-Earth Center of Kumamoto University. Scan type is Transverse/Rotation, and X-ray beam type is fan beam. The voltage of the X-ray source was set to 300kV to avoid artifact, the beam thickness was set to 1.0mm, and the spacial resolution was set to 0.073 x 0.073 x 1.0 mm^3. X-ray CT scanning was conducted before and after 600, 2400 and 6000 (only No.1) times loadings of the solid tire for each specimen. Irradiation position is shown in Fig. 1.

The deformation field for specimens were determined from the DIC using the TomoWarp code developed at Laboratoire 3SR at Université Joseph Fourier, France (Hall et al. 2009). The key parameters in the DIC such as the distance between calculation node, size of the correlation and serch window was set as shown in Fig. 2. Size of the correlation window was set from the logarithmic mean value of 13 to 5mm crushed stones, and the serch window was set from the result of wheel-tracking test and comparison of CT images before and after loading. After computation of the deformation field, the strain field was calculated at the center of four calculation node.

Table 1. *Type of specimens.*

	Mixture type	**Binder type**	**Main Function**
No.1	Dense-graded	Straight asphalt	-
No.2	Dense-graded	Polymer modified asphalt	Rutting resistance
No.3	Porous	High viscosity polymer modified asphalt	Rain permeability and noise reduction

Table 2. *Properties of specimens.*

	Percent mass of aggregate [%]			**Asphalt content [%]**	**Void Ratio [%]**	**Density [g/cm³]**
	Coarse agg.	**Fine agg.**	**Filler**			
No.1	60.0	34.5	5.5	5.8	2.9	2.395
No.2	60.0	34.5	5.5	5.7	3.8	2.375
No.3	85.0	10.0	5.0	4.9	20.9	1.982

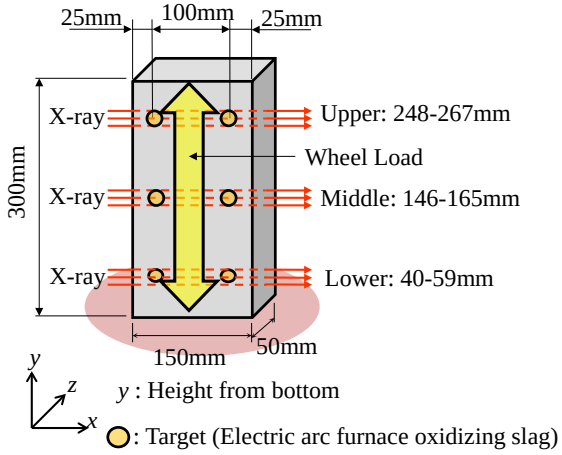

Fig. 1. *Irradiation position.*

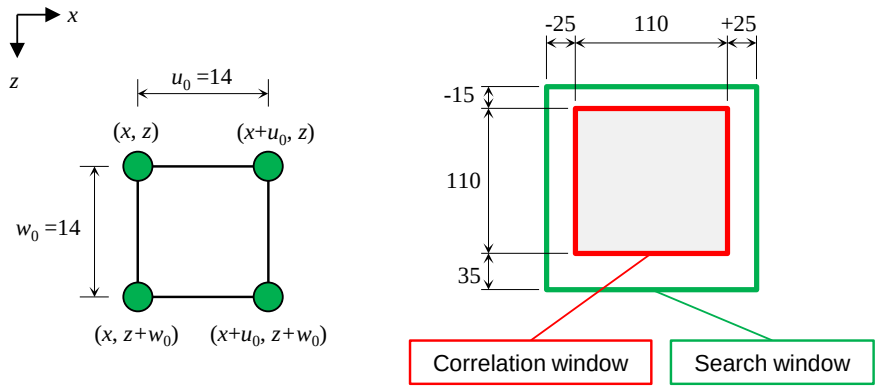

(a) Distance between calculation node (b) Correlation and search window

(Unit: Voxel)

Fig. 2. *Key parameters in the DIC.*

Result and Discussion

Fig. 3 shows the CT images at the center of the specimens after 2400 times loading in the wheel-tracking test. The displacement of three specimens was 4.18mm in No.1, 1.55mm in No.2 and 1.92mm in No.3.

Fig. 4 shows the vector map of the displacement field at the rear part of the specimens.

In the specimen No.1 (Dense-graded asphalt mixture using straight asphalt), 2mm or more downward vectors were confirmed under the loading position after 600 times loading. This is considered to be the deformation due to consolidation. After 2400 times loading, the displacement was smaller than 600 times, and upward and outward vectors were confirmed. This is considered to be reduction of the void and engagement of the aggregate. After 6000 times loading, 1.2mm or more downward and outward vectors were confirmed not only upper part but also lower part of the specimen. This indicate the progress of rutting.

In the specimen No.2 (Dense-graded asphalt mixture using polymer modified asphalt), most of vectors was directed vertically downward under the loading position after 600 times loading. This is because the plastic deformation resistance and flexibility of the polymer modified asphalt worked to reduce the rutting. However, some vectors horizontally moved in the opposite side on the surface. After 2400 times loading, displacement was very small.

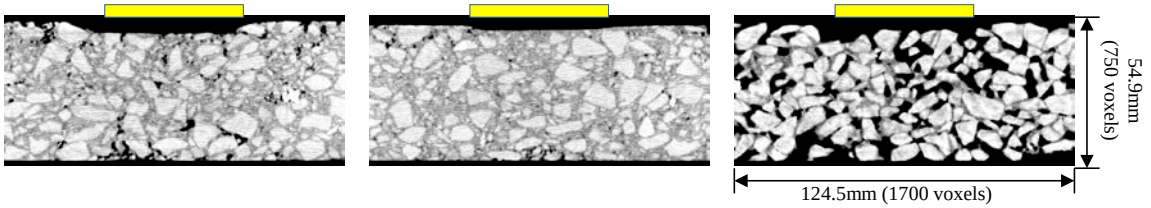

Fig. 3. *CT images at the rear part of the specimens.*

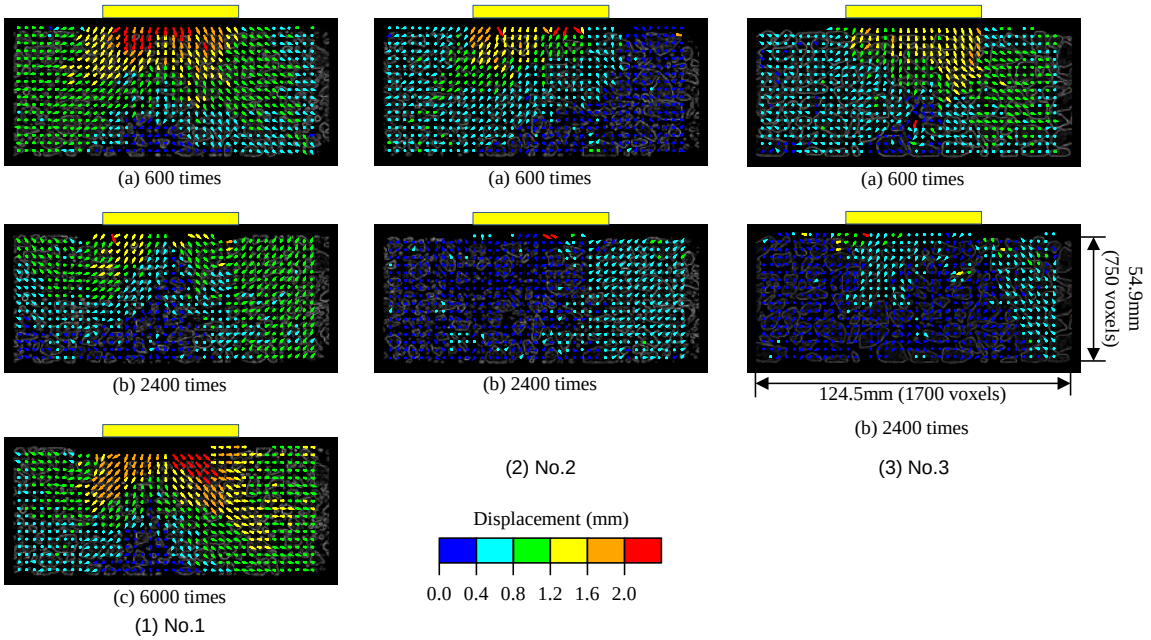

Fig. 4. *Vector map of displacement field.*

In the specimen No.3 (Porous asphalt mixture), almost the same behavior was shown to No.2 after 600 times loading. However, horizontal movement was larger than No.2. After 2400 times loading, displacement was very small, similar to No.2.

Fig. 5 shows the horisontal strain field at the rear part of the specimens.

In the specimen No.1, large tensile strain was locally generated and spread to the lower part of the specimen with the increase of loading times. However, strain is smaller than No.2 and No.3.

In the specimen No.2, large tensile strain was generated on the specimen surface after 600 times loading. This indicate the possibility for occurrence of longitudinal cracking called 'top-down cracking'. After 2400 times loading, strain was smaller than after 600 timed loading. Matsuno et al. (1984) says that there are many examples of longitudinal surface cracking which appeared within a few years after paving. This DIC result substantiate this remark.

In the specimen No.3, large tensile strain was generated in the center or lower partior of the specimen after 600 times loading. After 2400 times loading, strain was smaller than after 600 timed loading. Taniguchi et al. (2009) says that the longitudinal cracking develops not only from the surface but also within the asphalt concrete. This DIC result substantiate this remark.

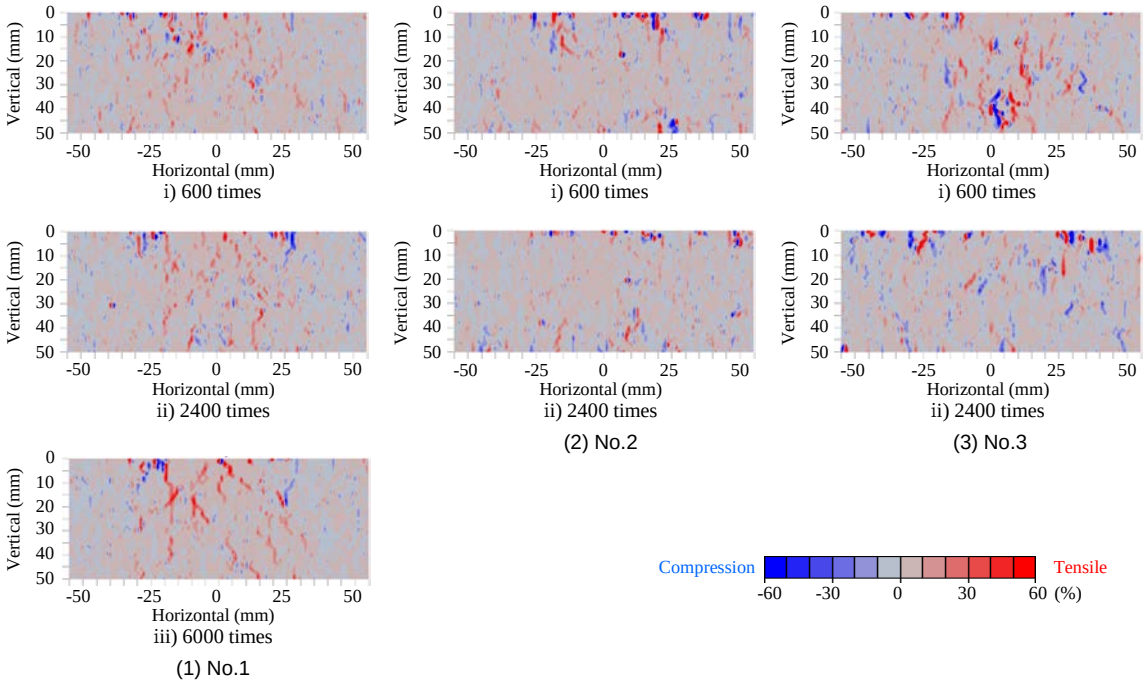

Fig. 5. *Horisontal strain field.*

Conclusion

Displacement of asphalt mixture using straight asphalt is larger than polymer modified asphalt. However, tensile strain of asphalt mixture using polymer modified asphalt is conversely larger than straight asphalt. Thus, X-ray CT and DIC in order to grasp the inside of the asphalt mixture are very effective in the assessment of asphalt concrete pavement damages. Besides, to evaluate not only the surface but also the internal of the asphalt mixture is preferable in order to evaluate the long-term durability of the asphalt pavement.

References

Hall S.A., Lenoir N., Viggiani G., Desures J. & Besulle P. (2009). Strain Localization in Sand under Triaxial Loading: Characterization by X-ray Micro Tomography and 3D Digital Image Correlation, ***Proceedings of International Symposium on Computational Geomechanics (COMGeo09)*** , IC²E, 239-247

Matsuno S. & Nishizawa T. (1984) Longitudinal Surface Cracking of Flexible Pavement, ***Proceedings of Paving in Cold Areas Mini-Workshop***, Technical Memorandum of Public Works Research Institute No.2136, Tsukuba, Japan,779-796

Taniguchi S., Nishizaki I. & Moriyoshi A. (2009). A study of Longitudinal Cracking in Asphalt Pavement using CT scanner, ***Road Materials and Pavement Design***, Vol. 9, Issue 3, Lovoisier, 549-558

Taniguchi S., Ogawa K., Otani J. Nishizaki I. & Himeno K. (2013). Visualization of Aggregate Movement in the Wheel-tracking Test of Asphalt Mixture using X-ray Computed tomography, ***Tomography of Materials and Structures –Book of abstracts, Posters-,*** *1st International conference on Tomography of Materials and Structures*, Ghent, Belgium, 269-272

Poster presentation

Nanoscale mechanical properties of chalk from X-ray tomography

D. MÜTER[1,*], H. O. SØRENSEN[1], K. N. DALBY[1], S. L. S. STIPP[1]

[1] Nano-Science Center, Dept. of Chemistry, University of Copenhagen, Denmark
* presenting author

Chalk is a biogenic limestone found prominently along the coastline of countries bordering the North Sea, e.g. White Cliffs of Dover (UK) and Stevns Klint (DK) and other locations world wide. It can serve as groundwater aquifers and hydrocarbon reservoirs. Chalk is composed of microscopic shields (coccoliths) that remain from ancient algae. Even after millions of years, many of the original coccoliths (<10 µm diameter) and other fossils remain intact. Both particles and pores in chalk are on the nanometre scale and their geometry is complex, which makes the material properties of chalk, e.g. mechanics, difficult to predict. On the macroscale, chalk is known to be "very weak", i.e. its Young's modulus drops rapidly with increasing porosity.

To understand how the macroscale properties of chalk are controlled by the micro- and nanoscale structure, we recorded high resolution X-ray tomography data, from chalk samples from a cliff at Stevns Klint (Rødvig Formation, Denmark), at the European Syncrotron Research Facility (ESRF). Figure 1 shows a slice of the reconstructed tomography data (50 nm voxel size) together with a 3D subvolume. Intact fossils can be seen throughout the sample; a large one is located at the top left side of the slice. Given that the fossil has retained much of its original morphology, we can assume that its mechanical properties deviate from the random arrangement of calcite crystals seen in the rest of tomography slice.

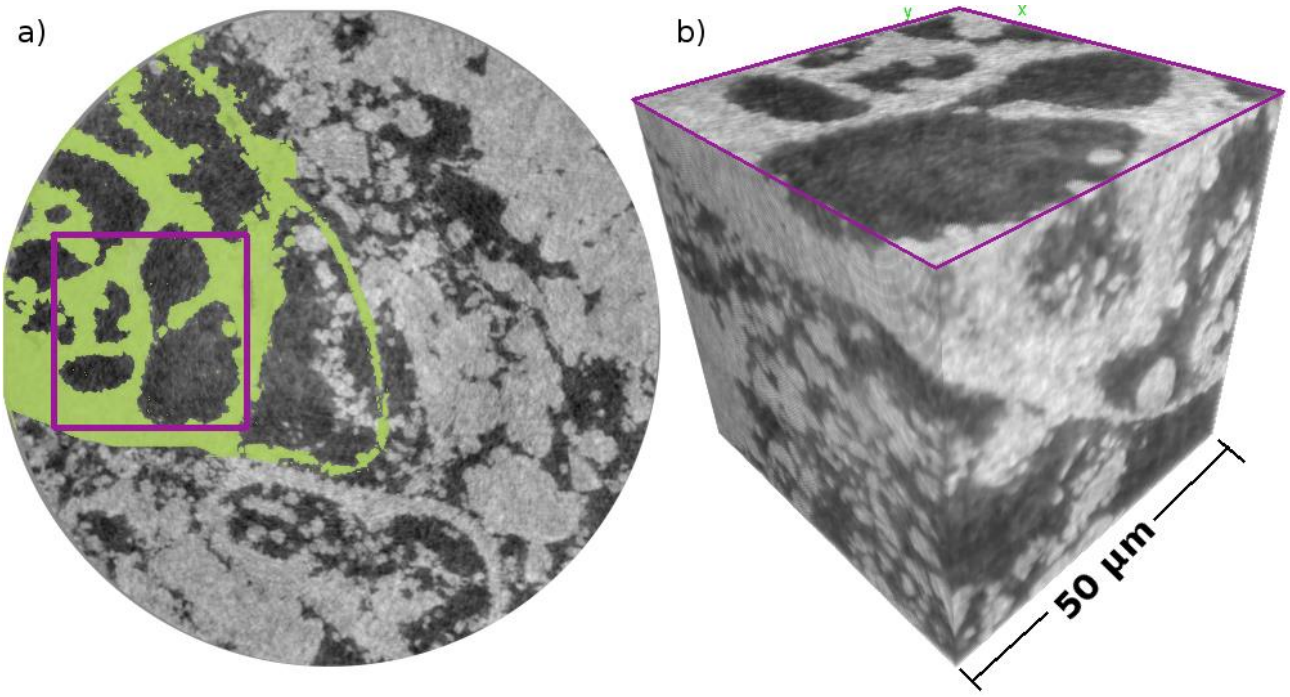

Figure 1: Slice of tomography data for a coccolith limestone (chalk) from a cliff at Rødvig, Denmark (a) and 3D subvolume of the data set (b). The purple square indicates the position of the top side of the 3D subvolume in the slice. A large intact fossil can be seen (shaded in green).

To compare mechanical properties between regions containing mainly crystals and intact fossils, we computationally cut out cubic subregions of the data set with an edge length of 300 voxels (15 µm). Subsequently, these subregions were rescaled to a volume of 150^3 and treated with the contrast enhance technique outlined in Müter et al. (2012), i.e. using Unsharp Mask and median filters. Segmentation into void and material phases was performed using Otsu

thresholding. From the segmented data, a surface mesh (isosurface) was produced, which was imported into finite element (FE) software. We set up a tensile testing arrangement using the material properties of calcite by holding one of the sides of the cube fixed and applying a load of 0.05-1% of the bulk Young's modulus to the opposite side. This small load ensures that even at high porosity, the resulting strain is small, i.e. within the linear elastic regime.

Calculating the ratio of applied load and strain integrated over the sample leads to the Young's modulus of the subvolume. Averaging the Young's modulus for the three spatial directions finally delivers the effective Young's modulus, E_{eff}. Plotting E_{eff} over porosity for all subvolumes (Figure 2) shows how the pore morphology or distribution of porosity, influences the mechanical properties. For both regions, E_{eff} drops rapidly with increasing porosity but for the regions lacking intact fossils this decrease is consistently stronger than for the fossil regions. We fitted both data sets individually with an empirical function commonly used in material science to describe the influence of porosity on the Young's modulus (Kováčik, 1999):

$$E_{eff} = \frac{E^*}{E_0}\left(1 - \frac{\varphi}{\varphi_0}\right)^n,$$

where n and φ_0 are fitting parameters, E^* is the Young's modulus of the bulk material and φ_0 describes the porosity at which E_{eff} becomes zero.

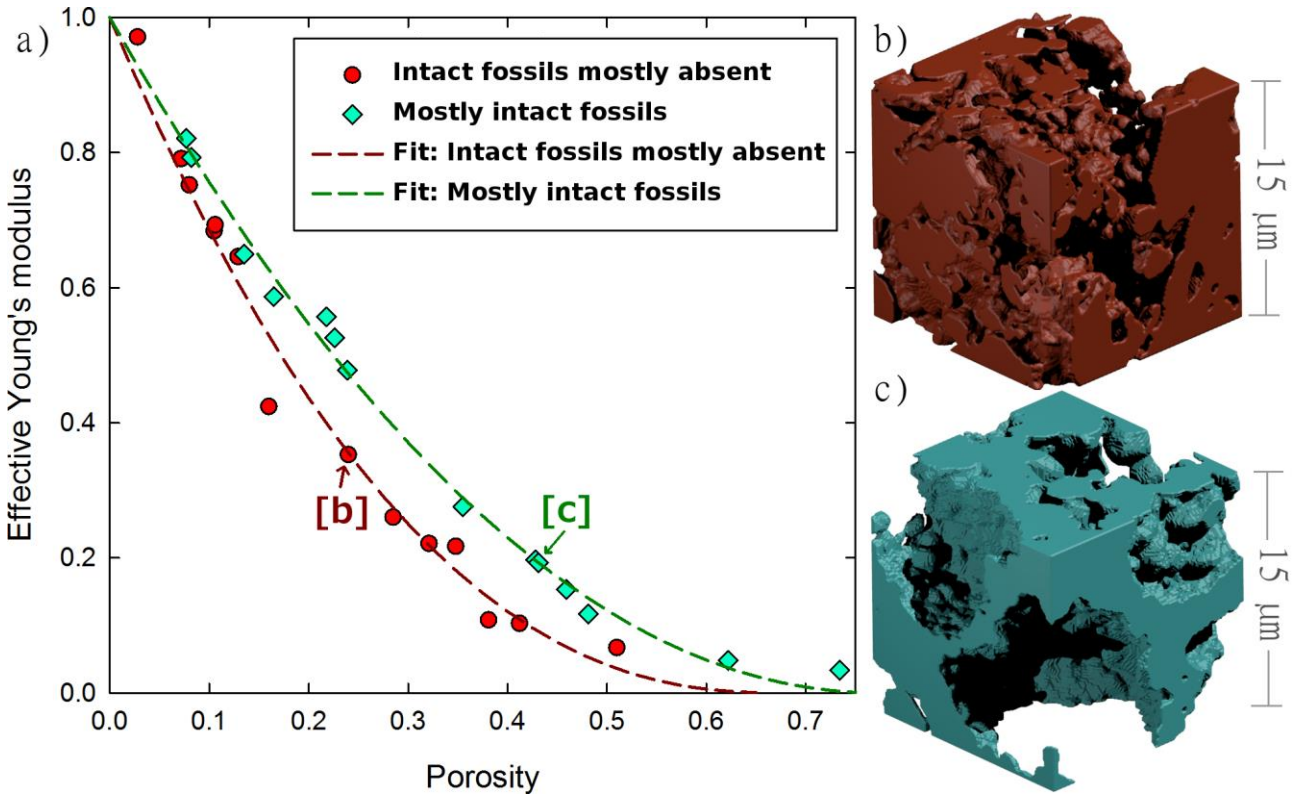

Figure 2: Effective Young's modulus for subregions with and without intact fossils, from the tomography data and its dependence on porosity (a); 3D renderings of subvolumes without (b) intact fossils and (c) with mostly intact fossils, that arerepresentative for the data used in the finite element simulations.

For the intact fossil region, we find the fitting parameters, n = 2.02 and φ_0 = 0.77, whereas for the regions lacking intact fossils, best fit is achieved with n = 2.35 and φ_0 = 0.67. An analytical solution for the above equation exists for an ideal material, i.e. for an open foam with cubic struts,

where n = 2 and φ_0 = 1 (Gibson and Ashby, 1997). Comparing the results for our tomography data to the open foam clearly shows that chalk is much weaker, which we can attribute to the small contact area between the individual calcite crystals in the regions lacking intact fossils. The intact fossil parts are in general stronger and reach higher porosity because, even after millions of years of rock forming processes, they have retained much of their original microstructure. The fossil microstructure is by no means random but is carefully adapted by nature to reach high mechanical properties with a minimum of ressources (high porosity). This has been shown using the same approach, i.e. X-ray tomography and finite element simulations, for recent marine species that produce exoskeletons, i.e. sea urchins (Müter et al., 2015).

Thus, we conclude that the amount of intact fossils in a biogenic rock can significantly affect the mechanical performance of the rock. At porosities above 40%, the presence of fossils leads to a factor of 2 difference in the effective Young's modulus. Therefore, for predicting the macroscopic mechanical properties from tomography data, primary petrophysical parameters alone, e.g. porosity (Müter et al., 2014) may not be sufficient. Instead, it is the pore morphology and the fundamental difference in porosity distribution between regions of intact fossils and regions of random arrangements of calcite crystals that ultimately determines the mechanical properties of the rock.

References:
Müter, D., Pedersen, S., Sørensen, H.O., Feidenhans'l, R., Stipp, S.L.S.: Improved segmentation of X-ray tomography data from porous rocks using a dual filtering approach. Computers & Geosciences 49 (2012), 131
Kováčik, J.: Correlation between Young's modulus and porosity in porous materials. J. Mater. Sci. Lett. 18 (1999), 1007-1010
Gibson, L.J., Ashby, M.F.: Cellular Solids Structure and Properties, 2nd Edition, Cambridge University Press (1997)
Müter, D., Sørensen, H.O., Oddershede, J., Dalby, K.N., Stipp, S.L.S.: Microstructure and Micromechanics of the Heart Urchin Test from X-ray tomography. Acta Biomaterialia, in press (2015)
Müter, D., Sørensen, H.O., Jha, D., Harti, R., Dalby, K.N., Suhonen, H., Feidenhans'l, R., Engstrøm, F. & Stipp, S.L.S.: Resolution Dependence of Petrophysical Parameters derived from X-ray Tomography of Chalk. Appl. Phys. Lett. 105 (2014), 043108

FE-analysis of granular materials based on X-ray CT data

D. TAKANO*[1], Y. MIYATA[2]

[1] Port and Airport Research Institute, 3-1-1 Nagase Yokosuka Japan – takano-d@pari.go.jp
[2] National Defence Academy of Japan, 1-10-20 Hashirimizu Yokosuka Japan – miyamiya@nda.ac.jp
* presenting author

Keywords: Microfocus X-ray tomography, granular material, FE-analysis

Abstract

The authors discuss a finite element (FE) modelling of sand with micro-characterization. The proposed FE method is implemented with particle discretization whose mesh size and geometry is determined from X-ray CT data. In this research, a series of analysis result for triaxial compression test on sand is discussed. Laboratory test results and simulation results are compared, and validation of the comparisons is discussed. Utilization of micro-data gives excellent results.

Introduction

In geotechnical engineering, understanding the mechanisms of deformation and failure of granular materials is essential. For detailed analysis, not only macro but also micro-scale condition should be considered. However geotechnical analysis methods which can consider the micro-scale condition is not well developed.

The authors discussed new geotechnical analysis method which can consider the micro-scale condition of granular material from X-ray CT data. In this paper, the authors proposed a FE-analysis method based on X-ray CT data for granular materials. The FE-analysis is implemented with particle discretization, both mesh size and geometry is determined from X-ray CT data. The numerical simulation method of failure behavior, namely Particle Discretization Scheme (PDS) FEM, is used. PDS-FEM can solve a boundary value problem by applying particle discretization to a displacement field; domain is decomposed into a set of Voronoi blocks and the non-overlapping characteristic functions for the Voronoi blocks are used to discretize the displacement function. In this research, a series of analysis result for the triaxial compression test on sand is discussed. Laboratory test results and simulation results are compared, and validation of the proposed is discussed.

Triaxial compression test on sand

(a) Test setup

In-situ triaxial compression tests (scanning and loading at the same time) under drained condition were performed on a series of sand specimens. Soma Silica Sand #2 with mean grain size of 1.89 mm was used as a test material. Two specimens with different relative density were prepared by air-pluviation with a dry density of 1630 kg/m^3 (Dr = 90 %) and 1430 kg/m^3 (Dr =50%). The porosity of the sample was evaluated as 0.206 for dense specimen and 0.587 for loose one by the binarization processing of X-ray CT data. Confining pressures of 150 kPa was applied to two test specimens. The specimens were scanned during the tests to obtain full 3D volumes during the process of compression at different axial strain levels. The size of the CT image voxels, was 0.051×0.051×0.051 mm^3.

3D images of the specimens were then analyzed by Digital Image Correlation (DIC). The DIC analysis presented in this paper was based on the method proposed by Hall et al. (2006). In the method, 3D volume of displacement vectors between in-situ acquired CT images at different loading stages can be provided.

(b) Test Results

Figure 1 shows the deviator stress-axial strain responses from both triaxial compression tests on the sand specimens with 50 and 90 % of relative density. Comparing the test results in dense and loose specimens, the dense specimen presents a stiffer behavior with higher values of deviator stress at the same strain condition. In the dense specimen, there is a roughly linear increase that is followed by a curvature to the peak stress at around 5% of axial strain. On the other hand, clear peak does not appear in the case of loose specimen.

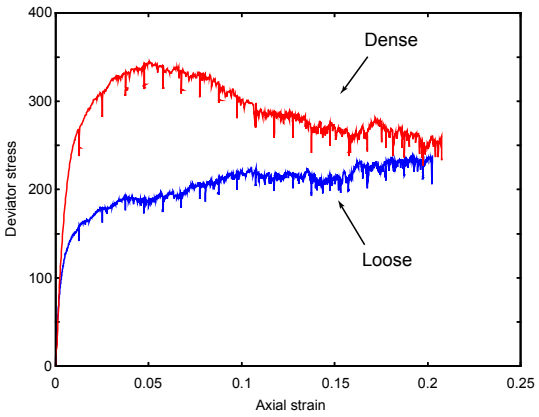

Figure 1. The results of triaxial tests

Figure 2 (a) shows vertical cuts the CT images of the middle part of the specimen at different scanning stages in the test. Both series of vertical sections along the tests show the shortening of the specimen due to the axial loading from the top and the well-known barreling effect caused by the friction at the top and bottom boundaries. The CT images were analyzed using 3D-volumetric DIC in order to obtain the full incremental displacement and strain field for each loading step. Figure 2 (b) shows the distribution of the incremental maximum shear strain at a vertical cross-section. In dense specimen, localized band is clearly formed and the specimen is divided in some rigid bodies. In loose specimen, localization can be

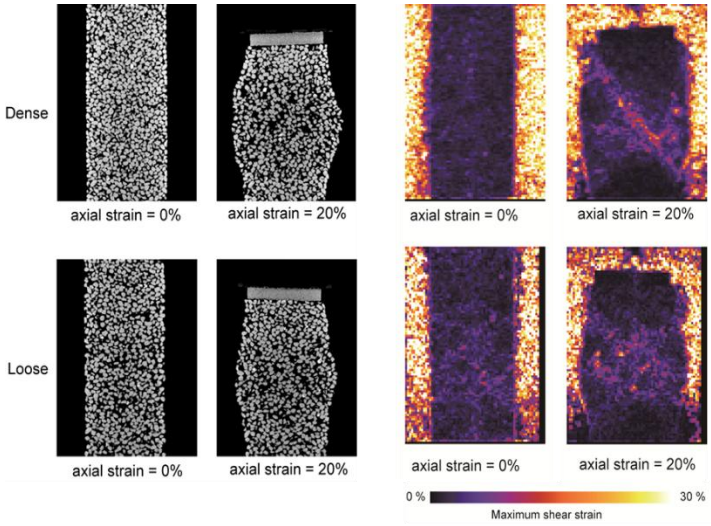

Figure 2. 2D CT slices and DIC results of the middle part of the specimen at different scanning stages.

observed at middle of the specimen as well. However, the localization is not remarkable comparing with the dense specimen until the end of the test.

Numerical simulation

(a) Analytical method

The failure behavior of granular material, as shown in the preceding section, can be simulated by some numerical methods, as shown in the preceding section. PDS-FEM proposed by Hori et al. (2005) is one such analysis method that can deal with such behavior. The biggest difference between PDS-FEM and ordinary FEM lies in the manner in which the displacement field is discretized. As shown in Figure 3, in an ordinary FEM, the displacement field is discretized by the shape functions that overlap each other. In PDS-FEM, the displacement field is discretized by the characteristic functions that do not overlap each other. More specifically, the displacement field is discretized by Voronoi tessellation and the stress (or strain) field is discretized by Delaunay tessellation. The failure is judged with the traction size calculated on Voronoi block boundaries. If the traction exceeds the failure threshold, it will be considered that the concerned Voronoi block boundary failed.

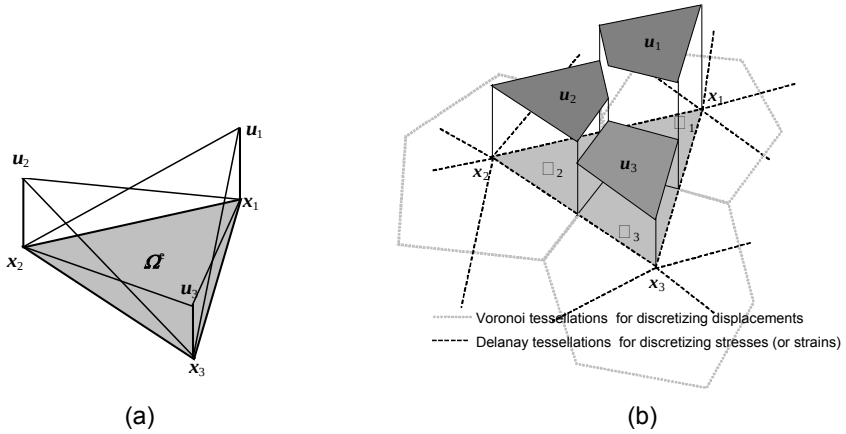

Figure 3. Comparison of discretization for (a) FEM and (b) PDS-FEM

In this research, the authors applied new procedure of judgment of failure at the boundary the Voronoi block. As shown in Figure 4, the compression failure is judged by the direction of traction calculated on the Voronoi block boundaries, and the failure is judged by the strass ratio $|t_N/t_S|$ of traction t. Further, failure is expressed by setting the stiffness matrix component k_L to zero, corresponding to the Voronoi block boundary that is judged to be broken. Moreover, the elastic modulus E was determined based on the laboratory test result. Poisson's ratio v=0.33 was used.

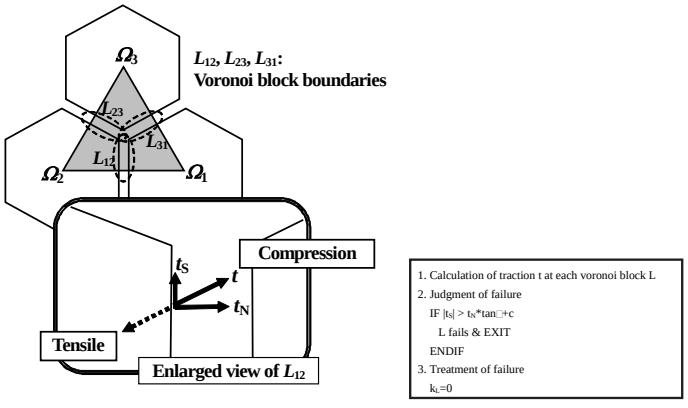

Figure 4. Procedure of judgment of failure at the boundary of Voronoi blocks

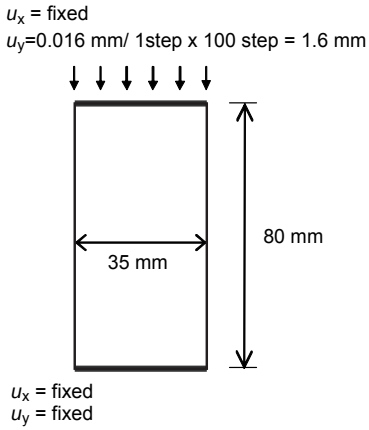

Figure 5. Boundary conditions of the analysis

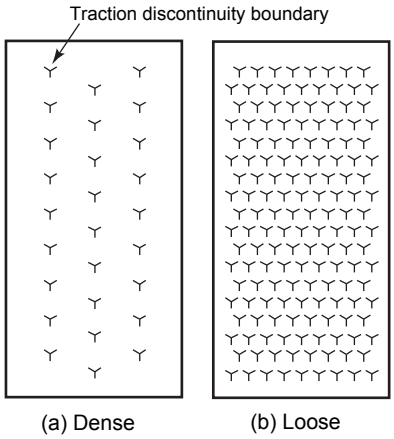

Figure 6. Traction discontinuity at initial condition

Table 1. Input parameters

	Dense	Loose
Young's modulus, E	10 MPa	
Poisson's ratio, ν	0.33	
interparticle friction, ϕ	10 degrees	
interparticle cohesion, c	30 kPa	
Ratio of traction discontinuity boundary to all boundaries at initial condition	0.2	0.5
Confining pressure	150 kPa	

The shear strength between the Voronoi blocks was determined based on the laboratory test. Moreover, in order to express the void ratio dependency of shear strength, part of the boundaries of Voronoi blocks was set as failure boundary from the beginning of the calculation. Thus, there were no stress transmission on the failure boundary and these can be considered as void area.

The boundary value problem, as shown in Figure 5, was solved based on the laboratory test conditions shown in the preceding section. In this research, to simulate the compression behavior of sand depending on the density, new analytical method was examined. This method can consider the density effects by setting the traction discontinuity boundary at the initial condition using the X-ray CT data. The initial conditions set for two cases: dense and loose conditions are shown in Figure 6. The traction discontinuity boundary was uniformly-distributed over the model for both conditions. To consider that the number of boundary to transfer the traction in the dense condition is greater than that in loose condition, the number of the traction discontinuity boundary was determined using the X-ray CT data. Then, the ratio of traction discontinuity boundary to all boundaries was determined from void ratio evaluated from results shown in Fig. 2 (a).

The input parameters are summarized in Table 1. After performing parametric analysis, these values were selected. Especially, in order to discuss the discontinuity

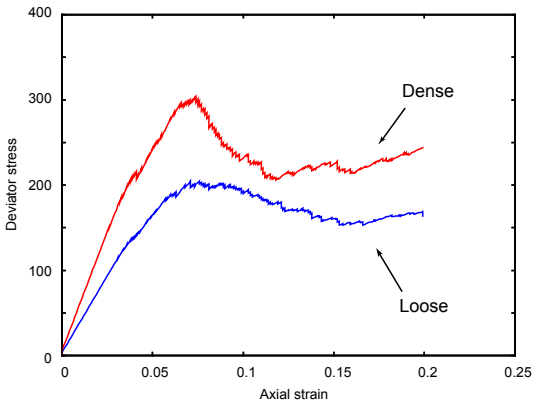

Figure 7. Calculated stress-strain relations

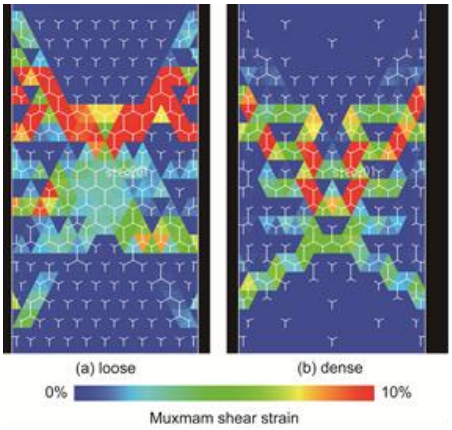

Figure 8. Calculated results for shear strain distributionstress-strain relations

boundary treatment, same numbers were used for modulus and interparticle friction and cohesion in the dense and loose conditions.

(b) Simulation Results

The calculation stress-strain relations for dense and loose conditions are shown in Figure 7. In dense case, the calculated deviator stress shows clear peak after linear increasing at small strain then it reaches to residual state. On the other hand, in loose case, the calculated deviator stress peak is not sharp. The analysis reproduces the behavior of the soil observed in the laboratory test result by only the discontinuity boundary treatment.

Distributions of shear strain calculated are shown in Figure 8. Strain localization due to axial compression is described by this analysis to some extent. Especially in loose case, evolution of localization can be observed.

Conclusions

The proposed FE method is implemented with particle discretization whose mesh size and geometry is determined from X-ray CT data. In this study, laboratory testing data and analysis results were compared. The proposed method can simulate the observed behavior by only the discontinuity boundary treatment.

Aknowledgements

The author is grateful for the funding awarded by the Japan Ministry of Education, Culture, Sports, Science and Technology (Grant-in-Aid for Scientific Research (B) No. 24360195 and Grant-in-Aid for Scientific Research (C) No. 15K06222)

References

Alshibli, K.A., Sture, S., Costes, N.C, Frtanck, M.L., Lankton, M.R., Bastiste, S.N., Swanson, R.A. (2000) Assessment of localises deformation in sand using X-ray computed tomography: **Geotechnical Testing Journal**, 23 (3): 274-299.

Bay, K.B. (2008) Methods and application of digital volume correlation. Journal of strain analysis, 42: 745-760.

Desrues, J., Chambon, R., Mokuni, M., Mazerolle, F. (1996) Void ratio evolution inside shear bands in triaxial sand specimens studied by computed tomography. **Géotechnique** 46 (3): 529-546.

Hall, S.A. (2006) A methodology for 7D warping and deformation monitoring using time-lapse seismic data. **Geophysics**, 71 (4): O21-O31.

Hall, S.A., Bornert, M., Desrues, J., Pannier, Y., Lenoir, N., Viggiani, G., Bésuelle, P. (2010) Discrete and Continuum analysis of localised deformation in sand using X-ray μCT and Volumetric Digital Image Correlation. **Géotechnique**, 60 (5): 315-322.

Hori,M., Oguni,K., Sakaguchi,H. (2005) Proposal of FEM implemented with particle discretization for analysis of failure phenomena, **J. Mech. Phys. Solids**, 53: 681–703.

Measurement of three-dimensional deformation inside construction material using X-ray CT and Particle Tracking Velocimetry

K. TAKEHARA[1], T. FUMOTO*[2]

[1] 3-4-1 Kowakae, Higashi-Osaka, Osaka, 577-8502 Japan –takehara@civileng.kindai.ac.jp
[2] 3-4-1 Kowakae, Higashi-Osaka, Osaka, 577-8502 Japan – fumoto@civileng.kindai.ac.jp
* presenting author

Keywords: X-ray CT scan, Particle Tracking Velocimetry, movement of aggregates

Abstract

The X-ray computed tomography (CT) scan can measure the interior structure of construction materials without any damage. Especially, the movements of aggregates in the construction material under some stress conditions are important factor for strength and strain of the materials. Fumoto have developed a new X-ray CT scan system which can measure the interior structure of a construction material under relatively large compression stresses. In this research, the movements of aggregates inside a construction material are measured by Super-Resolution KC method which was developed as a Patricle Tracking Velocimetry (PTV) for fluid flows. The results show that the three dimensional movements inside the materials were measured with very high resolution by the PTV.

Introduction

The X-ray computed tomography (CT) is one of the most powerful tools which can measure structures inside materials without any intrution of sensors. The standard industrial X-ray CT usually has a fixed X-ray tube and detector, and the specimen has to be rotated for the scannning of X-ray. In this case, the size of the specimen becomes relatively small and the load to act on the specimen becomes relatively low. For the measurements of construcion material specimens, it is important to measure deformations under the load which is acting on the actual construction material.

Fumoto (2013) have developed a new X-ray CT system which can measure the interior structure of a specimen of construction material under relatively large load acting on the specimen. In this X-ray CT system, the specimen is fixed on a stage and the X-ray tube and detector turn around the specimen. Large load, which acts on the actual construction, can be loaded on the specimen because the rotatiing X-ray tube and detector system is mechanically separated from the specimen stage. The developed X-ray CT system can measure the three dimensional movements of the aggregates inside the construction materials. However, it is very difficult to measure the movements of many aggregate inside the construction material by human eyes.

In the flow measurement techniques, the Particle Image Velocimetry, called PIV, is a very powerful tool to measure temporal and spatial movements of many particles automatically. The advantage of the PIV can measure the instantaneous two dimensional or three-dimensional movement distributions. When video cameras are used for image capturing devices, the two-dimenaional or three-dimensional movement distribution data are acquired as time series data.

Particle Tracking Velocimetry, called PTV, is one of the PIV, which evaluate velocity by measruing a movement of each tracer particle. Takehara et.al. (2000) developed the super resolution Particle Tracking Velocimetry, which consists of Kalman filtering theorem and Chi-square test. The developed super resolution PTV is called the super resolution KC

method and is one of the highest resolution PIVs. In the super resolution KC method, three dimensional particle movement can be tracked automatically, if the three dimensional particle location can be measured.

In this research, the movements of aggregates inside a construction material are measured by the super resolution KC method, which was develped for the measurement of velocimty distribution of fluid flow. The position of each aggregate is measured by the developed X-ray CT system. The movements of aggregates inside a construction material is caused by large load which is acting on the acutual construction. As the construction materials, a porous polymer concrete solidifying aggregates with some polymer are used in this research. The results of measurements of the aggregate movements in the construction material gave good agreement with those in the elastic body by the compression load.

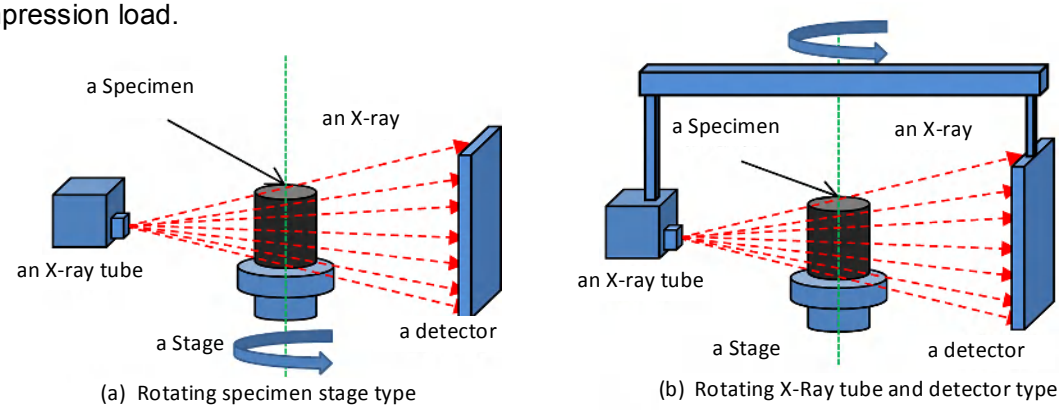

(a) Rotating specimen stage type (b) Rotating X-Ray tube and detector type

Fig. 1 Schematic diagram of X-ray CT scan

Outline of the X-ray CT used in this experiment

The standard X-ray CT is consist of the speriment table, X-ray tube, and the detector of the X-ray. The generated X-ray is passing through the specimen and the X-ray is absorbed by the specimen. The X-ray transmitted through the specimen reaches the two demensional detector of the X-ray. The X-rays is irradiated from various angles and the transmitted X-rays are recorded in the control computer. Based on the recorded transmitted X-rays, the three dimensional distribution of the X-ray absorption coefficients of the specimen is calculated by the inverse analysis.

General industrial X-ray CT employs the rotating specimen stage type in which the X-ray tube and the detector are fixed and the specimen stage is rotated between them, as shown in Fig.1 (a). It is a great advantage for the rotating specimen stage type to manufacture the smaller X-ray CT system. On the other hand, the disadvantage of the rotating stage type is to measure the specimen with a small load, because of the structure of the system. For the construction material testing, a large load is necessary to measure deformation of the specimens.

For medical X-ray CT, the specimen is fixed between the X-ray tube and detector which are rotating around the specimen as shown in Fig.1 (b). This system can set larger space between the tube and detector than that of the rotating stage type. Therefore, the rotating X-ray tube and detector type is able to set larger loading system in that large space between the X-ray tube and the detector.

Fumoto (2013) has developed the rotating X-ray tube and detector type X-ray CT which can measure the internal structure of construction materials with large load condition of which maximum load is 300 kN as shown in Fig. 2 and Photo. 1.

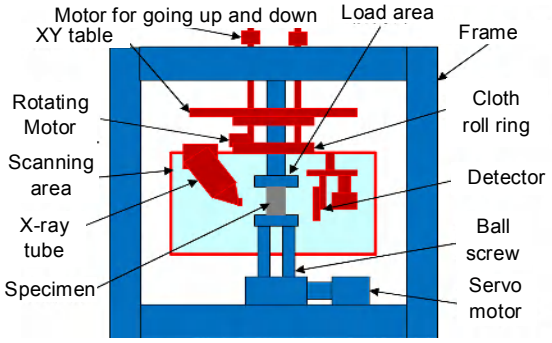

Fig. 2 X-ray CT scan system developed by Fumoto

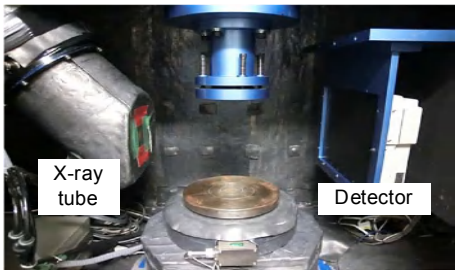

Photo.1 Interior of the measurement section

Outline of PTV used in this research

The Particle Tracking Velocimetry, called PTV, is one of the Particle Image Velocimetry, called PIV which has been developed for flow fields measurements. The PTV used in this study was originally developed by Etoh and Takehara (1990, 1995), consists mainly of a Kalman filter theorem and the Chi-square test, so-called KC method. In the KC method, the particle information, such as position, size and brightness of a particle, is predicted by the Kalman filter theorem and the same particle is identified between successive two images by using the Chi-square test. The KC method was modified by incorporating of the idea of Super-resolution PIV proposed by Keane and Adrian (1992). The modified KC method is referred to as the Super-resolution KC method (2002). The Super-resolution KC method is one of the highest resolution PTV.

Results of PTV measurements inside movement of the material

The materials used in this study are polymer concretes which are solidified with resin derived from a cedar. The sawdust of a cedar is liquefied by adding certain chemicals and heat. The liquefied sawdust of a cedar is reacted with a curing agent as a main agent, and aggregates bond with a reacted resin. The softness of materials changes by the ratio of the main agent and the curing agent. In this study, the ratio is fixed at 1:0.6, under this condition the porous polymer concrete becomes relatively softer compared with the standard construction concrete.

The shape of the specimen is the clynder of which diameter and height are 75 mm and 150 mm, respectively. The load acting on the specimen is controlled by the displacement of the loading plate which is acting upwards from the underface. In this study, the movements of the aggregates inside the porous polymer concrete is measured when the loading plate moves from 10 mm to 15 mm.

The sample images of the measured X-ray CT are shown in Photo.2. Each aggregate can be recognized on the obtained X-ray CT image. The X-ray CT images are recorded

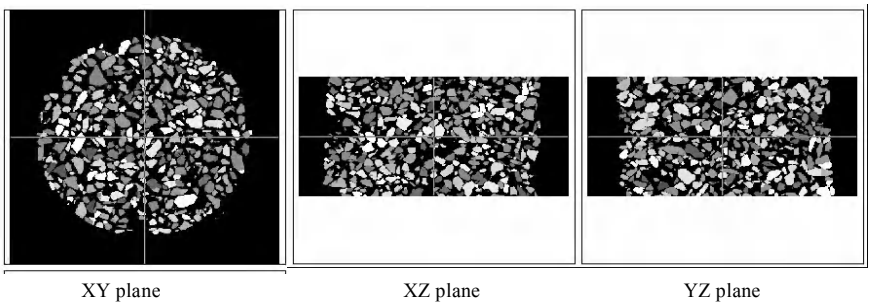

Photo.2 Example images taken by the X-ray CT scan

as three dimensional voxel data. Each aggregate image inside the concrete is picked up from the recorded voxel images by using the image processing software (TRI-3D-BON-PRT). The centroid position, size, volum, aspect ratio, and so on of each aggregate are measured by the image processing software. The conditions of the image processing software to pick-up the aggregates are shown in Table 1.

Table 1 Conditions of image processing

Compression of X-ray CT image	none
Height of the measuring subject (mm)	86.3
Target subject	aggregate
Repetation number of erosion (times)	3
Neighborhood deletion size (times of aggregate diameter)	1.0
Neighborhood identification size (times of aggregate diameter)	1.4
Repetation number of dilation (times)	3
Microparticle unification diameter (mm)	2.0

The movement of each aggregate inside the porous polymer concrete is automatically tracked by the super-resolution KC method. The movement vectors distribution of aggregates are shown in Fig. 3. The bird's-eye view of the movement vector shown in Fig.3(a). The load is acting on the specimen from the undersurface, and aggregates of lower part of the specimen move towards the upper part. In addition, aggregates inside the upper part of the specimen move horizontally because the movement of the aggregates is limited by the upper plate of the loading system.

To understand clearly, XY plane-view and XZ plane-view of the movement vector are shown in Fig.3 (b) and (c). From the XY plane-view of the Fig3.(b), the aggregates move radially from the point of X=85 mm and Y=60 mm. From the XZ plane-view of Fig.3(c), the aggregates move upwards in lower part of the specimen than z = 15 mm and move horizontally upper part of the specimen than z = 15 mm.

For the further study, the deformation ratio, such as divergent ratio, shear ratio, compression ratio, and so on, can be estimated precisely from the obtained movements of aggregates.

Conclusion

A newly developed X-ray CT system can measure the interior structure of a specimen of construction material under relatively large load acting on the specimen. And the super resolution KC method is one of the highest resolution PIVs. The combination of a newly developed X-ray CT and the super resolution KC method is applied to the measurement of movements of aggregates inside the porous polymer concrete. The three dimensional information of aggregates inside the porous polymer concrete is measured by the newly developed X-ray CT system and the movement of the aggregates with large load is measured by the super-resolution KC method.

The results show that the obtained vectors inside the specimen are measured with very high-spatial resolution and the movements of the aggregates inside the specimen under compression force are reasonable for elastic materials.

For the further study, it is necessary for the precise measurements of the deformation ratio to develop the new method to esitame deformation ratio with the randomly located movement vectors obtained by the PTV.

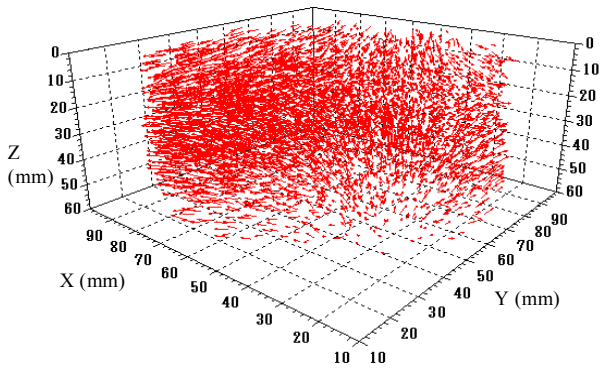

(a) Bird's-eye view

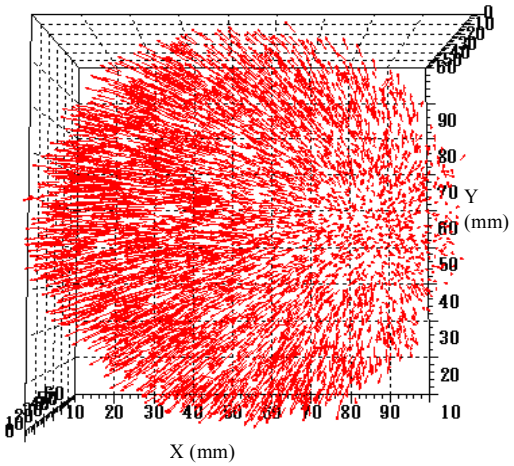

(b) XY plane

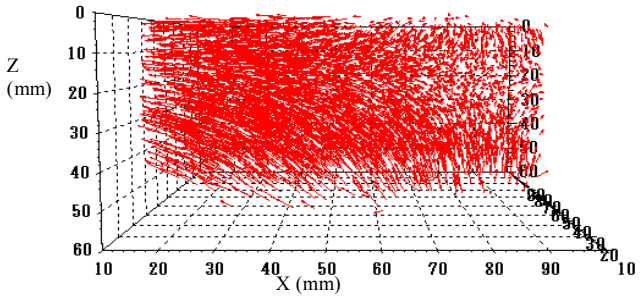

(c) XZ plane

Fig. 3 An example of PTV measurements of the arrogates in the construction material

References

Etoh, G. T. & Takehara, K. (1990): A new algorithm for automatic tracking of particles, ***Ann. J. Hydraulic Engr.,*** JSCE, 34:689-694 (in Japanese).

Etoh, G. T. & Takehara, K. (1995): Development of a new algorithm and supporting technologies for PTV, ***Proc. of the International Workshop on PIV***, Fukui, Japan, 91-106.

Fumoto, T.(2013): Development of a new industrial X-ray CT system and its application to compression test of polymer concrete, ***Journal of Japan Society of Civil Engineers, Ser. E2 (Materials and Concrete Structures)*** , 69, 2:182-191(in Japanese).

Keane, R.D. & Adrian, R.J.(1992): Super-resolution particle imaging velocity, ***Meas. Sci Technol.***, 6: 754-768.

Takehara, K., Adrian, R. J., Etoh, G. T. & Christensen, K. T. (2000): A Kalman tracker for super-resolution PIV, ***Experiments in Fluids***, 29: S34-S41.

Session 308

Non-destructive Integrated CT-XRD Method Developed for Hardened Cementitious Material

T. SUGIYAMA*[1], T. HITOMI[2], K. KAJIWARA[3]

[1] Faculty of Engineering, Hokkaido University, Sapporo, Japan – takaf@eng.hokudai.ac.jp
[2] Technical Research Institute, Obayashi Corporation, Tokyo – Hitomi.takashi@obayashi.co.jp
[3] Japan Synchrotron Radiation Research Inst, SPring 8, Hyogo, Japan – kajiwara@spring8.or.jp

Keywords: Integrated CT and XRD, Concrete, Crack, Portlandite, Calcite

Abstract

Non-destructive Integrated CT-XRD Method (hereinafter, CT-XRD) has been developed to study the characterization of hydrated cement systems. This newly proposed CT-XRD allows to determine simultaneously both microstructure and crystals present in the cement system. Three dimensional (3D) image is obtained from X-ray computed tomography (CT). Then, X-ray diffraction analysis (XRD) is conducted in the specific region of specimen to study the chemical change over time and space. To demonstrate the CT-XRD, a leaching test using pure water was conducted for cracked cement paste. The alteration of microstructure characteristics in the specimen after the action of flowing water was studied. As a result, a map with resolution at the micrometer scale is obtained for the distribution of Portlandite and Calcite in the specimen.

Introduction

Conventional instruments such as Electron Probe X-ray Micro-Analyzer (EPMA) and powder XRD that have been employed for the analysis of hydrated cement system exhibit a given limitation and disadvantage over each other. Primarily, these techniques are destructive so that sequential samples over time and space need to be prepared if one intends to study the process of an alteration due to the action of deterioration. In addition, although EPMA permits measurement on the order of 0.1 mm in resolution, chemical compounds cannot be identified – only the profile of atoms. On the other hand, XRD is a powerful tool to determine minerals and some hydration products. However, concrete needs to be ground to powder and hence the space resolution of the chemical analysis is limited. Even CT is used only for the study of physical characteristic in concrete such as pore structure characteristics, air voids distribution and crack geometry (Promentilla el al. 2009, Sugiyama et al. 2010, Darma et al. 2013).

In order to overcome the problem of conventional techniques, a Non-destructive Integrated CT-XRD Method (hereinafter, CT-XRD) has been developed at the Synchrotron Radiation Facility in Japan (SPring 8). In this study, cracked cement paste of ordinary Portland cement was prepared and leaching test using pure water was conducted. In this way, the leaching behavior of the cracked cement paste was studied by means of CT-XRD, where the alteration of the hydrated cement system was clarified.

Non-destructive Integrated CT-XRD method

CT-XRD was conducted at BL28B2, SPring-8, Japan. White X-ray was used as the incident X-ray which covers a wide range of wavelength. First, synchrotron white X-ray was applied to the specimen. X-ray that transits the sample was passed through a silicon monocrystal located in the downstream position and captured by CCD camera (Fig.1). Silicon monocrystal was used to convert from the polychromatic X-ray to monochromatic X-ray with the employed energy of X-ray for CT measurement being 25 keV. Monochromatic X-ray was used to enhance the image quality in CT measurement.

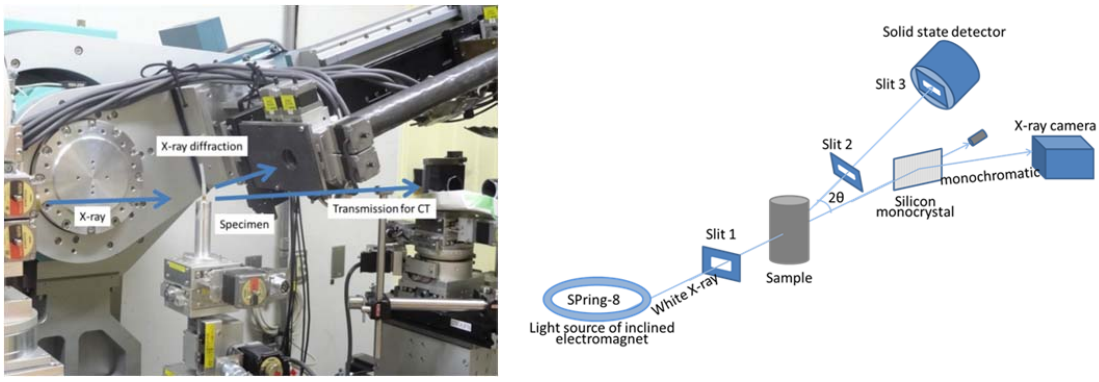

Fig. 1. *Non-destructive Integrated CT-XRD Method system around the specimen in BL28B2 (Kajiwara et al. 2013, Sugiyama et al. 2014)*

As the extraction of the monochromatic X-ray was conducted in the downstream position, there was no need to change the relative position of the incident X-ray to the sample. In this way, the coordinate system for CT measurement and XRD measurement was unified. During the CT measurement, the specimen was placed on the rotating stage and X-ray was applied to the rotating sample. The step angle was 0.2 degrees. Transmission images of X-ray with different angles were obtained, followed by image reconstruction with back projection procedure. The numbers of projections was 912, with an exposure time of 0.15 s. The number of pixels was 694 and the pixel size was 7.19 μm in the horizontal and 584 and 5.10 μm in the vertical. The overall field of view was about 5 mm.

By observing the reconstructed image in three dimensions, the regions of interests (ROI) were determined for the XRD measurement. In order to extract the signal of the X-ray diffraction only at the specific position of interest (POI) in a given ROI, various slits were used. The size of the slit in the upstream position was 0.05 mm in width and 0.15 mm in height. Two slits were in the downstream position (Fig. 1) to obtain the signals of X-ray diffraction from a given space, called the gauge volume. The sizes of the slits were controlled so that the gauge volume could cover the region of a parallelogram with a maximum of 200 μm in length. In addition, the specimen was rotated during the XRD measurement to obtain adequate signals of the XRD in the corresponding volume. To capture the signals, a solid-state detector was used. Downstream slits and detector were all in position on the arm of the detector tube. During measurement, the angle of the arm (2θ) was fixed corresponding to twice the diffraction angle (θ=10°). The preset time was 600 s. The diffracted X-ray energy and the intensity was obtained from XRD.

Specimen Preparation

Ordinary Portland cement (OPC) was used in this study. Hardened OPC paste was made with a water to cement ratio of 0.3. After curing in water, a cylindrical specimen of about 5 mm diameter and 5 mm height was cut from the hardened paste, and a crack was induced on the specimen. Aluminum tape was used to cover the cracked specimen and to connect plastic tubes of 2 mm inner diameter at both ends of the specimen. Next, demineralized water was passed through the tube to carry out the leaching test.

Leaching Test

The leaching test was conducted using a tubing pump to pass water through the specimen. Demineralized water was kept in a tank from which water was passed through the cracked specimen via the tube pump. For the first week, discharged water was collected to monitor pH and calcium ion concentration, and from the second week water was circulated. The water flow rate was 50 cc/h and continued for a period of nine

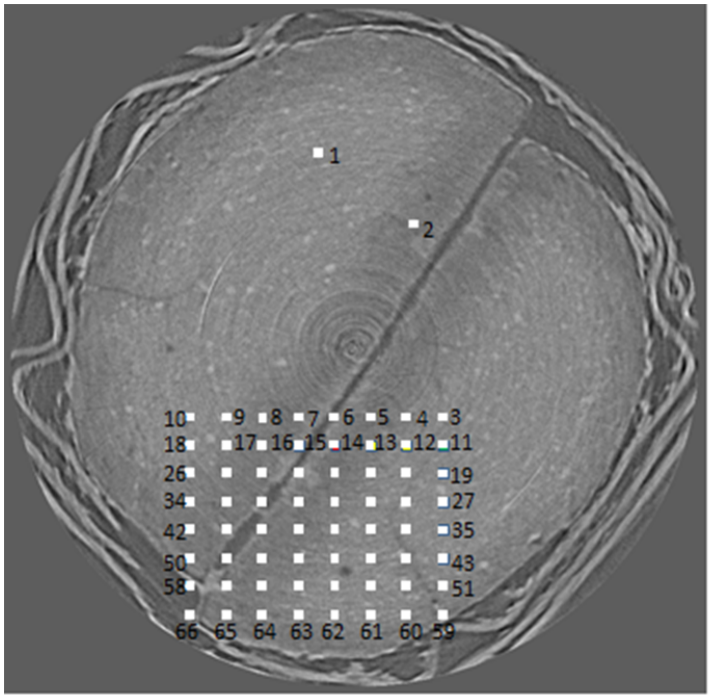

Fig. 2. *CT image of cracked cement paste after leaching test and positions of interest for XRD*

months. After a certain leaching period, the specimen was moved to SPring-8 for conducting CT-XRD.

Results and Discussion

Fig. 2 shows the cross sectional CT image of the cracked cement paste after leaching test. This layer was located around the central portion of the specimen with respect to the specimen's top surface. Gray scale values (GSV) CT images, which were converted from the linear absorption coefficients (LAC), provide the physical information, such as location of crack, air voids, and low or high density substances. Higher density substances appear whiter in color, while air is black. After segmentation, the pore structure and crack network can be extracted in three dimensions. In addition, the distribution of chemical substances may be estimated using the LAC, since it corresponds to the density and the type and number of elements. In this study, the distibution of portlandite and calcite can be determined by CT-XRD.

In Fig. 2, specific positions of interest (POI) where XRD measurements were conducetd are also shown. A total of 68 POIs were selected, followed by sequential measurement of XRD at each POI in this specimen. The POI one can be selected in an arbitary manner.

Fig. 3 shows typical examples of the results of XRD measurements. The observed diffraction peak energy was compared with the calculated diffraction peak energy of either Portlandite or Calcite. The calculated diffraction peak energy was obtained using Bragg's law, specific wavelength, different combination of possible miller indices (hkl) and lattice parameters of these crystals (Pecharsky and Zavalij, 2005). From Fig. 3(a) some peaks of the observed diffraction energies match well with those of the calculation for Portlandite. This means that Portlandite is present at the position of 35. It is well-known that Portlandite in a hydrated cement system is susceptible to dissolution due to contact with water. However, because position 35 was relatively far from the crack

boundary, the effect of water flow through the crack was minimized so as not to dissolve the Portlandite.

Fig. 3(b) shows the results of XRD at position 14, which was in the vicinity of the crack. Contrary to the case of position 35, significant peaks of the diffraction energy match with these for Calcite at position 14. For the handling of the specimen, the flow of water was intermittenly halted so that air could partially fill in the crack space. In addition the flowing water might be carbonated during the leaching test. In this way, Calcite was produced near the crack boundary. Furthermore, the action of flowing water may weaken the boundary of Portlandite. This altered the Portlandite to Calcite.

Fig. 4(a) and (b) show the mapping of the position in which Portlandite and Calcite were dominantly present in the cracked cement paste after the leaching test. From Fig. 4(a), it is acknowledged that the positions of Portlandite are distributed in the regions that are relatively far from the crack boundary. On the other hand, Calcite was formed near cracks in the cement paste. Therefore, CT-XRD enables to obtain the distribution of major chemical compounds in hydrated cement system.

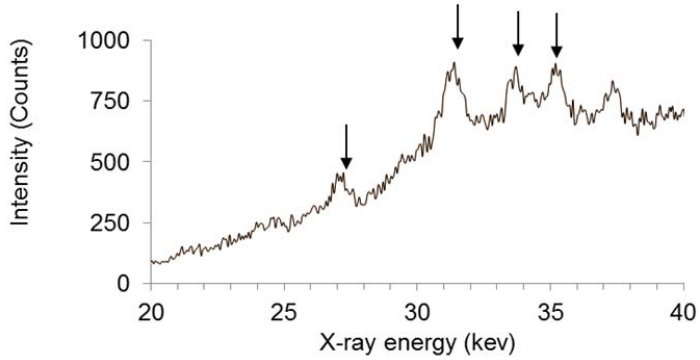

(a) At position of 35 : Arrows indicate the calculated diffraction peak for Portlandite

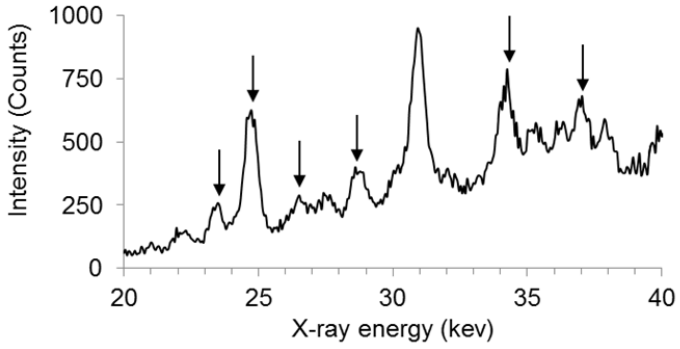

(b) At position of 14 : Arrows indicate the calculated diffraction peak for Calcite

Fig. 3. *Result of XRD measurements*

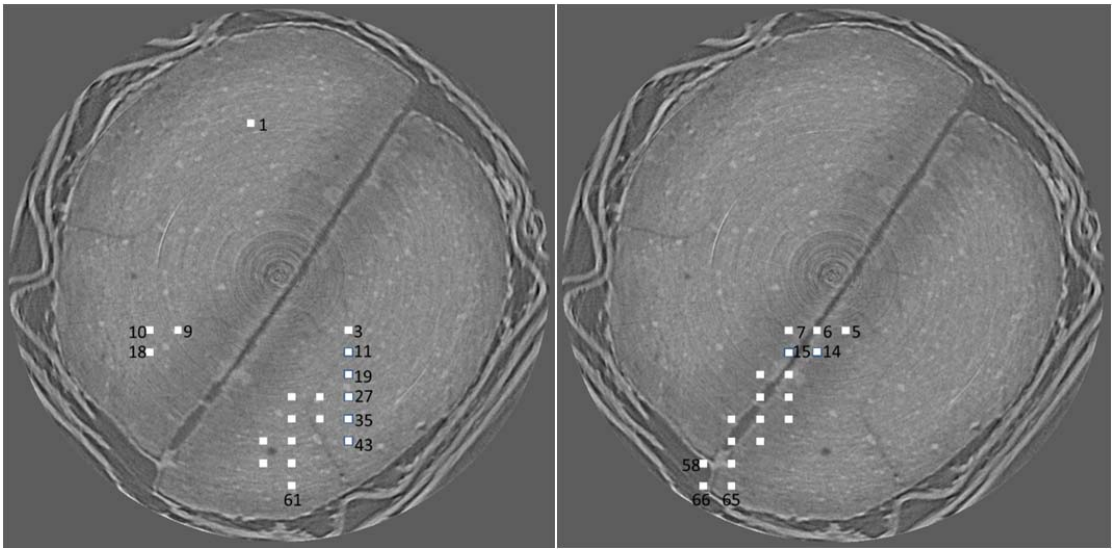

(a) Portlandite ***(b)*** Calcite

Fig. 4. *Map of Portlandite and Calcite distributions*

Conclusions

Non-destructive Integrated CT-XRD Method demonstrates its originality for the study of the alteration of hydrated cement system. After leaching test, cracked cement paste showed that Portlandite remained in the region far from the crack boundary, whereas Calcite was produced in the vicinity of the crack. The resolution was on the order of micrometers.

Acknowledgements

Part of this research was funded by the Japan Society for the Promotion of Science (Research No.: 2628913384, 2663020004). The synchrotron radiation experiments were performed at the BL28B2 in SPring-8 with the approval of the Japan Synchrotron Radiation Research Institute (JASRI) (Proposal No. 2013B1511, 2014A1559, 2014A1512 and 2014B1010). Authors would like to thank graduate students Mr. J.C. Kuri and Mr. S. Ikeda for their efforts to carry out this research.

References

Promentilla, M.A.B., Sugiyama, T., Hitomi, T. & Takeda, N., (2009). Quantification of tortuosity in hardened cement paste using synchrotron-based X-ray computed microtomography. **Cement and Concrete Research**, 39(6), 548-557.

Darma I.S., Sugiyama T. & Promentilla M.A.B. (2013). Application of X-ray CT to study diffusivity in cracked concrete through the observation of tracer transport. **J. Advanced Concrete Technology**, 11, 266-281. .

Kajiwara, K., Hitomi, T., & Sugiyama, T. (2013). "Development of non-destructive integrated CT-XRD method for the evaluation of mineral distribution in cementitious materials." 67th Annual Conference, **Japan Cement Association**, 82–83. [In Japanese].

Pecharsky, V.K., & Zavalij, P.Y. (2005). Fundamentals of Powder Diffraction and Structural Characterization of Materials, Springer, USA, 405-415.

Sugiyama, T., Promentilla, M.A.B., Hitomi, T. & Takeda, N., (2010). Application of synchrotron microtomography for pore structure characterization of deteriorated cementitious materials due to leaching." **Cement and Concrete Research**, 40(8), 1265-1270.

Sugiyama, T., Hitomi, T., & Kajiwara, K. (2014). Nondestructive Integrated CT-XRD Method for Research on Hydrated Cement System, 4th International Conference on the Durability of Concrete Structures, Purdue University, West Lafayette, IN, USA, pp. 298-303.

Salt crystallization dynamics in building rocks: a 4D study using laboratory X-ray micro-CT

H. DERLUYN*[1], M.A. BOONE[1,2], M.N. BOONE[3], T. DE KOCK[1], J. DESARNAUD[5], S. PEETERMANS[4], L. MOLARI[6], S. DE MIRANDA[6], N. SHAHIDZADEH[5], V. CNUDDE[1]

[1] UGCT – PProGRess, Dept. Geology and Soil Science, Ghent University, Krijgslaan 281/S8, B-9000 Gent, Belgium – hannelore.derluyn@ugent.be, marijn.boone@ugent.be, tim.dekock@ugent.be, veerle.cnudde@ugent.be
[2] XRE – X-ray Engineering bvba, De Pintelaan 111, B-9000 Gent, Belgium
[3] UGCT, Dept. Physics and Astronomy, Ghent University, Proeftuinstraat 86/N12, B-9000 Gent, Belgium – matthieu.boone@ugent.be
[4] NIAG, Spallation Neutron Source Division, Paul Scherrer Insitute, CH-5232 Villigen PSI, Switzerland – stevenpeetermans@gmail.com
[5] Van der Waals-Zeeman Institute, Institute of Physics, University of Amsterdam, Science Park 904, NL-1098 XH Amsterdam, The Netherlands – j.e.desarnaud@uva.nl, n.shahidzadeh@uva.nl
[6] DICAM, University of Bologna, V. le Risorgimento 2, IT-40136 Bologna, Italy – luisa.molari@unibo.it, stefano.demiranda@unibo.it
* presenting author

Keywords: building stones, 4D X-ray micro-CT, salt weathering, crystallization dynamics, drying kinetics

Abstract

We employ laboratory X-ray micro-computed tomography (µCT) during climate-controlled salt weathering experiments to acquire data on the kinetics of drying and salt precipitation and the distribution of crystals within the pore space of Mšené sandstone. For that purpose, a custom-designed setup was built at the UGCT's scanners of the Ghent University Centre for X-ray Tomography (UGCT) that allows to acquire 4D scans while drying. Samples were initially capillary saturated with a saturated NaCl-solution and subsequently dried at 20% RH and at 50% RH, at room temperature. These RH-values are representative for winter and summer conditions for the salt NaCl, which is not temperature sensitive. Different salt precipitation dynamics result in different drying kinetics at the two RH's. These crystallization and transport dynamics can be directly linked as revealed by the 4D X-ray µCT datasets.

Introduction

Salt crystallization is a major cause of weathering of building stones and cementitious materials. When saline solutions are present in these materials, the surrounding climatic conditions, i.e. temperature and humidity variations, may induce the precipitation of salts at the surface (efflorescence) or in the pore space beneath (subflorescence). During drying-induced crystallization, the distribution of salt crystals in the pore space and on the material's surface strongly influences the drying rate. Desarnaud et al. (2015) describe the effect of the crystal growth on the drying behaviour of sandstone initially saturated with NaCl solution, by comparing drying at 20% RH and 50% RH. Drying at 20% RH is found to take longer than at 50% RH, which is addressed to the formation of a salt skin on the surface at 20% RH. The drying was monitored by measuring the weight change of the sample, while the salt precipitation was characterized by SEM images and X-ray µCT after the samples had dried out. Thus, the dynamics of salt growth during evaporation was not measured up to now. Experimental data of drying and salt growth measured simultaneously would aid the advancement of the understanding of coupled drying-crystallization dynamics. This kind of data is also essential for numerical models that predict salt damage risks in building materials, as model parameters for drying as well as crystallization kinetics need to be defined.

Methods

Two cylindrical samples of 8 mm in diameter and 10 mm in height were cored from a Mšené sandstone plate. This sandstone has a unimodal pore system with an average pore size of 30 µm (Shahidzadeh-Bonn et al. 2010). The samples were initially scanned in their dry state at the X-ray µCT scanner HECTOR (Masschaele et al. 2013) of the UGCT. Next, the samples were capillary saturated by immersing them in a saturated NaCl solution for 30 minutes. The samples were then scanned in their wet state, and subsequently during their drying, by scanning them every 30 minutes during the first 3 hours, and every hour during the succeeding 12 hours. Drying was controlled by placing the sample in a custom-built climatic chamber, compatible with the µCT setup, depicted in Fig. 1. Conditioned air is produced by the GenRH-T generator (Surface Measurment Systems Ltd., UK) and blown in the plexi-glass test chamber at a slow rate (3.3 ml/s). The inner volume of the test chamber is 4x4x3 cm^3. The outlet of the chamber is connected to a separate RH-T sensor. Polyimide windows of 2x2 cm^2, which are quasi transparent to X-rays, are present at the front and the backside of the chamber. The chamber is clamped at its upper rod and has a hole in the bottom of 2 cm diameter that allows for the sample's rotation while scanning. The sample is attached to a 1 cm diameter plastic rod fixed on the rotation stage, and the flow loss was found to be minimal. This setup ensured that the samples were dried at a constant temperature of 19.2°C and a RH of 20% and 50% for the first and the second sample, respectively.

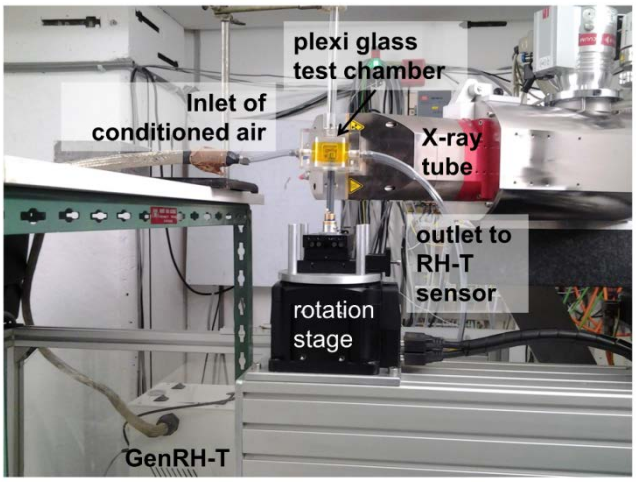

Fig. 1. *Experimental setup at the X-ray µCT scanner HECTOR of the UGCT for performing dynamic scans of salt weathering cycles.*

For each scan, a total of 1351 projections was acquired over an angle of 360°, with an exposure time of 400 ms per projection. A thin aluminum filter (1 mm) was used to block low-energetic X-rays at the source to reduce beam hardening. In order to correct for inhomogeneities of the detector and beam, 32 dark-field and 200 flat-field images were acquired before the initial scan. The X-ray tube provided a voltage of 100 kV with a target power of 10 W. The source-detector distance was 1530.7 mm and the source-object distance 38.3 mm. The projections were binned by a factor 2x2 in order to increase the signal-to-noise ratio, resulting in a reconstructed voxel size of 10^3 μm^3. The raw data were reconstructed using the software Octopus Reconstruction (Inside Matters bvba, Belgium; Vlassenbroeck et al. 2007). The same set of parameters for ring and spot removal, tilt and skew of the detector and beam hardening were adopted for all scans. Small shifts in the reconstructed volumes with respect to the reference volume were corrected by aligning all volumes to the reference scan using the software

DataViewer (SkyScan, Belgium). This ensured the same positioning in 3D space for all datasets.

The datasets were further analyzed with the software Avizo (FEI). As it was not possible to directly threshold the salt crystals and the salt solution from the image histogram, due to an overlap of the grey values of crystals and solution, the following procedure was applied: the wet scan was subtracted from the series of scans taken while drying, resulting in differential images (Boone et al. 2014), where all negative values correspond to the solution that has dried-out, and all positive values correspond to salt crystals that precipitated. Two volumes-of-interest (VOI's) were defined, one including only the sample's volume and one including the sample's volume and the salt efflorescence at the end of drying. The evolution of the volume fractions of the salt solution, the total amount of precipitated salt, the salt efflorescence and salt subflorescence were then calculated with respect to the volume of the second VOI.

Results and discussion

The drying of the two samples is given in Fig. 2a. We can observe that drying at 20% RH is initially faster than at 50% RH, due to the higher difference in RH between the sample's surface and the environment. This first drying stage is characterized by a constant rate, due to the capillary action which induces a hydraulic connection between the surface and the inner pore space. Subsequently, the evaporation at the surface mainly results in salt efflorescence. At 50% RH, this constant rate period lasts until the sample is almost completely dried out. At 20% RH, the drying changes to a slower, exponential regime after about 1 hour, i.e. after approximately half of the initial salt solution has dried out.

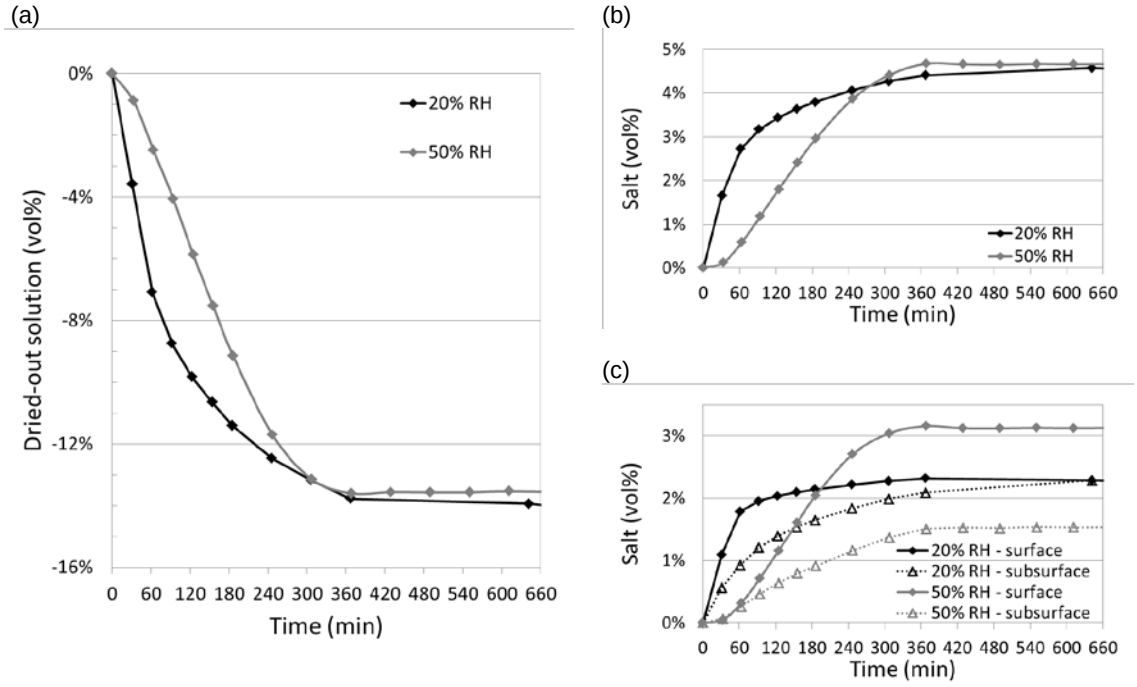

Fig. 2. *The drying (a) and crystallization dynamics (b-c) of Mšené sandstone at 20% RH and 50% RH. Fig 2c disseminates between the salt crystals forming on the outer surface (efflorescence) and the salt crystals precipitating just below, in the pores of the subsurface.*

The differences in drying kinetics are caused by the differences in salt precipitation dynamics, which are presented in Figs. 2b-c. As the initial amount of salt is equal for

both samples, the resulting total amount of salt precipitation is the same (Fig. 2b). The crystal precipitation develops however slower at 50% RH, where the salt crystals forming on the surface (efflorescence) and the salt crystals precipitating in the pores close to the surface, develop at the same relative rate during the whole duration of drying (with respect to their respective total amounts, Fig. 2c). No salt crystals were found deeper inside the volume. While drying at 20% RH, the crystal growth at the surface develops first, and much faster than at 50% RH, mainly during the first hour of the experiment and then reaches a plateau. The salt crystals precipitating just below the surface at this lower RH develop more gradually, during the whole duration of the drying. The period of the formation of efflorescence at 20% RH is congruent with the period of the constant drying rate in the drying curve. The second exponential drying stage at 20% RH must thus be resulting from this salt efflorescence, corroborating the statement that a salt skin is forming on the surface during the first stage of drying (Desarnaud et al. 2015), partially closing the pores and causing a slower drying during the continuation of the process. The salt skin still grows slightly during this second period, but most of the salt crystals precipitate just below this layer. Typical snapshots of the sample drying at 20% RH are given in Fig. 3.

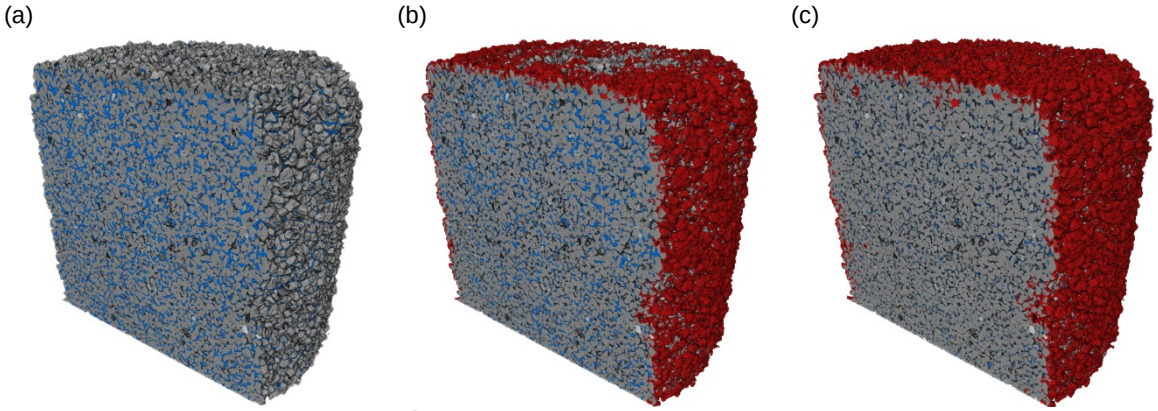

Fig. 3. *Typical snapshots of the Mšené sandstone sample while drying at 20% RH at the wet state (a), after 1 hour (b) and after 6 hours (c). Blue: salt solution – red: salt crystals.*

Acknowledgements

H. Derluyn holds a postdoctoral fellowship from the Research Foundation – Flanders (FWO) and acknowledges its support. The work reported in this paper has been supported by the KISADAMA project, funded by JPI Cultural Heritage within the Joint Heritage European Programme JHEP and by BOF research fund 01B00512 entitled 'Systems for controlling temperature and relative humidity' and by FWO research grant 1521815N. The Special Research Fund (BOF) of the Ghent University is acknowledged for the post-doctoral grant of M.N. Boone.

References

Boone, M.A., De Kock T., Bultreys T., De Schutter G., Vontobel P., Van Hoorebeke L. & Cnudde V. (2014). 3D mapping of water in oolithic limestone at atmospheric and vacuum saturation using X-ray micro-CT differential imaging. ***Materials Characterization*** 97: 150-160.

Desarnaud J., Derluyn H., Molari L., de Miranda S., Cnudde V. & Shahidzadeh N. (2015). Drying of salt contaminated porous media: effect of primary and secondary nucleation. ***Journal of Applied Physics***: under review.

Masschaele B., Dierick M., Van Loo D., Boone M.N., Brabant L., Pauwels E., Cnudde V. & Van Hoorebeke L. (2013). HECTOR: A 240kV micro-CT setup optimized for research. ***Journal of Physics: Conference Series*** 463: 012012.

Shahidzadeh-Bonn N., Desarnaud J., Bertrand F., Chateau X. & Bonn D. (2010). Damage in porous media due to salt crystallization. ***Physical Review E*** 81: 066110.

Vlassenbroeck J., Dierick M., Masschaele B., Cnudde V., Van Hoorebeke L. & Jacobs P. (2007). Software tools for quantification of X-ray microtomography. ***Nuclear Instruments & Methods In Physics Research Section A-Accelerators Spectrometers Detectors And Associated Equipment*** 580: 442-445.

Use of X-ray scan to assess the extent of defects in concrete elements

J. MARCHAND[1], R. CANTIN[1]*, E. SAMSON[1]

[1]SIMCO Technologies, Québec (QC) CANADA – jmarchand@simcotechnologies.com
[2]SIMCO Technologies, Québec (QC) CANADA – rcantin@simcotechnologies.com
[3]SIMCO Technologies, Québec (QC) CANADA – esamson@simcotechnologies.com
* presenting author

Key words: field concrete, defects, detection, scan, durability

Abstract

Stringent durability requirements are now commonly included in tender documents to ensure long-term service-life of concrete structures. Requirements are often expressed as a target duration before major repairs are needed. For instance, the construction protocol for new concrete structures of the US Defense Department asks for a service-life of 75 years before repairs are needed and 60 years before steel reinforcement corrosion starts in waterfront structures. The expected performance of concrete mixtures can be significantly impeded by alterations to the original design occurring during construction. When that occurs, it is important to quantify the extent of defects to see how they affect the targeted durability and eventually propose remediation solutions. The presentation focuses on a case study where X-ray scan was used to investigate concrete cores from a secant pile wall where defects were observed during construction. The defects translated into reduced concrete cover over the steel reinforcement and potentially compromised the ability of the material to resist steel corrosion before the intended 125-year service-life target. X-ray scan was used to quantify the spatial extent of defects. The information gathered from the observations was then incorporated into a modeling protocol to see if the long-term durability of the concrete structural elements was compromised.

Background

Secant piles are typically constructed so that there is an intersection of one pile with another. The usual practice is to construct alternative piles along the line of the wall leaving a clear space of less than the diameter of the required intermediate piles. Concrete is added and, then, intermediate holes are drilled in such a way to cut into the first piles. The intermediate piles are placed through a heavy casing whose cutting edge is toothed, which enables the casing to cut into the concrete of the primary piles on either side. Subsequent concreting results in a continuous retaining wall that forms the perimeter of the structure to be built. Approximately a few months after casting, water level is lowered and the inner face of the wall is excavated to allow construction of the underground portion of the structure.

Methodology

In order to characterize the properties of in-place concrete, 50 horizontal cores were extracted at different elevations from randomly selected secant piles. Most cores were extracted in sound areas to determine the properties of the in-place concrete.

CT scans were performed on all 50 cores to complete the visual observations with a Siemens Somatom Definition as+ 128. All samples were scanned using the following parameters:

- 140 kV
- 425 mAs
- 1 rotation / second
- 0.6 mm of slice thickness

- Field of view FOV 105 mm
- Pitch 0.4
- Resolution X, Y, Z : 0.205 x 0.205 x 0.600 mm
- Spiral mode : 128 slices per rotation

For each sample, four reconstructions were made:

- Axial scan, Normal HU scale (– 1024/3070 HU), filter I70h /safir5
- Axial scan, extended HU scale (-10240 / 30710 HU), filter B70 s
- Coronal scan, extended HU scale (-10240 / 30710 HU), filter B70 s
- Sagittal scan, extended HU scale (-10240 / 30710 HU), filter B70 s

Visual observations

Defects such as segregation could be visually observed on cores, as shown on Figure 1a. Segregation was characterized by the presence of tightly packed aggregates, low paste content and the presence of numerous voids between the aggregates. Segregation was observed over the entire length of 3 cores out of the 4 that showed signs of this specific problem, to a depth of up to 170 mm. Soil inclusions were also present on some investigated cores. On the cores, inclusions appeared as swirling patterns in which soil and concrete layers alternated on a depth of 45 to 60 mm from the surface (Figure 1b).

a) Typical example of segregation

b) Typical example of soil inclusion (note swirling pattern)

Fig. 1. *Defects observed on cores*

Following these observations, X-Ray CT Scans were performed on the cores with defects to assess their extent and see if the latter correspond to density variations.

X-Ray CT Scan results

Typical examples of scan spectra are provided in Figure 2. For cores extracted from apparently sound areas, observations did not reveal the presence of any serious defect “hidden” within the concrete, thus confirming the preliminary conclusions drawn from the visual examination. Concrete appeared to be generally dense, homogeneous and well consolidated.

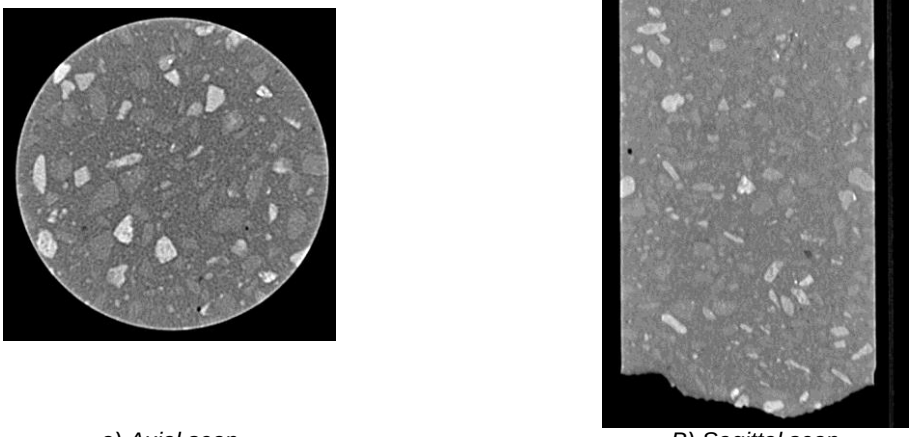

a) Axial scan *B) Sagittal scan*

Fig. 2. *Examples of axial and sagittal scans*

Scans performed on cores showing segregation (Figure 3) clearly confirmed that concrete in these areas was mainly made of aggregates bound by a limited paste content. The scans also indicated that voids present in the segregated areas formed an interconnected network that offers no resistance to the penetration of contaminants. This observation indicated potential problem for long-term durability of concrete. Based on the only core for which sound concrete was present beneath the segregated area, there appeared to be a clear and sudden change in concrete composition where segregation stops.

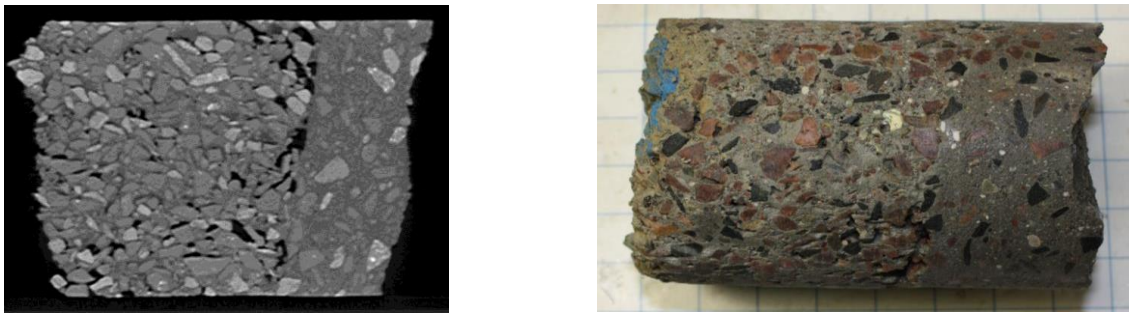

a) Scan view *b) Core picture*

Fig. 3. *Scan of segregation*

Scans were also performed on cores where soil inclusions (see Figure 1b) were observed. Scan observations (see Figure 4) did not indicate a clear trend regarding the depth and geometry of inclusions. Most inclusions appeared darker, thus less dense. However, inclusions were not found to be systematically more porous and they did not appear to have a lower aggregate content than the underlying concrete. The same conclusion was reached regarding the lighter-colored concrete at the surface or embedded in sound concrete. The paste content and large pore content was found to be variable.

Scan observations were helpful in this case to validate that soil inclusions did not systematically lead to significant increase in porosity and thus could offer resistance to contaminant ingress in concrete. This was later confirmed by other test series that yielded, in some cases, similar diffusive properties for the altered concrete, compared to the sound one.

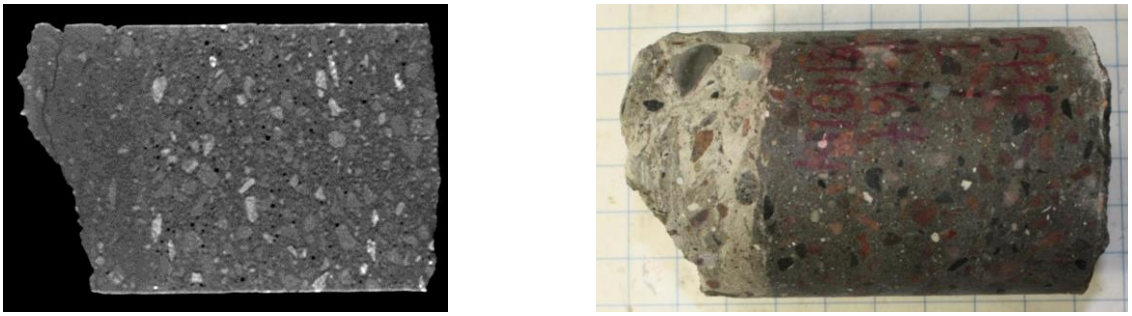

a) Scan view *b) Core picture*

Fig. 4. *Scan of soil inclusion*

Conclusions

More than 50 cores were extracted from the construction site of concrete secant walls. Cores were analyzed using a wide range of different experimental techniques in order to generate reliable information on properties and variability of in-place concrete. CT scan observations were used to detect the presence of local defects in the concrete, their extent and their degree of interconnection.

The use of X-Ray CT scan in the context of field concrete analysis is not a common practice at this point. The present case study showed that it could become a useful tool in the future to provide additional information to other common investigation methods.

Freeze-thaw decay in sedimentary rocks: a laboratory study with CT under controlled ambient conditions

T. DE KOCK*[1], M.A. BOONE[1,2], T. DE SCHRYVER[3], H. DERLUYN[1]., J. VAN STAPPEN[1], D. VAN LOO[2], B. MASSCHAELE[2,3], V. CNUDDE[1]

[1] UGCT – PProGRess, Dept. of Geology & Soil Science, Ghent University, Krijgslaan 281/S8, 9000 Ghent, Belgium. – tim.dekock@ugent.be marijn.boone@ugent.be hannelore.derluyn@ugent.be jeroen.vanstappen@ugent.be veerle.cnudde@ugent.be
[2] X-ray Engineering BVBA (XRE), De Pintelaan 111, 9000 Ghent, Belgium. – marijn.boone@XRE.be denis.vanloo@XRE.be bert.masschaele@XRE.be
[3] UGCT, Dept. of Physics and Astronomy, Ghent University, Proeftuinstraat 86/N12, 9000 Ghent, Belgium. – thomas.deschryver@ugent.be
* presenting author

Keywords: building stones, 4D X-ray µCT, freeze-thaw decay, experimental study

Abstract

This study presents an experimental X-ray micro-CT study of the freeze-thaw processes in limestone under controlled ambient conditions. The processes weres studied with time-lapse micro-CT and dynamic micro-CT, using the Environmental X-ray CT (EMCT) at the Centre for X-ray Tomography of the Ghent University (www.ugct.ugent.be). The EMCT is a gantry-based system on which full µCT scans were aquired in approximately 80 s. A custom made freezing cell was used for freezing experiments to -15 °C with 9 mm diameter samples.

The experimental data show that the observed decay is strongly related to the local water saturation and to the rock texture, i.e. pore size distribution. The decay is expressed by the fracture development in limestone due to ice crystallization. These fractures show a dynamic response to the imposed freeze-thaw cycles. Ice wedging occurs upon the moment of ice crystallization, which is indicated by the release of latent heat. During subsequent thawing, the fractures close. The timing indicates that ice crystallization alone is sufficient to instigate fracturing. Assumptions based on the ice crystallization theory allow to calculate the theoretical pore sizes where ice crystallization occurred. This shows that in these experiments, water crystallizes in the nanometric pores, thus under transient conditions. The existence of such pores were validated with other techniques such as SEM and were linked to the rock features observed with CT.

Introduction

Freeze-thaw processes play an important role in the physical weathering of porous rocks in cold and humid environments (e.g. Ruedrich and Siegesmund, 2007; Matsuoka and Murton, 2008). In the built environment, freeze-thaw deterioration threatens the aesthetic properties of monuments and artwork in our cultural heritage and it can cause actual danger by affecting the structural integrety of building materials. Therefore, it is important to assess the susceptibility of building stones to prolonged freezing and freeze-thaw cycling. This is typically done by normalised freeze-thaw testing. Nevertheless, the extrapolation from laboratory tests to natural conditions is not always easy (Ingham, 2005), and therefore the historical performance is an important criterium as well as are field measurements of freeze-thaw processes (Hall, 2006; Thomachot *et al.*, 2005; McAllister *et al.*, 2013).

To improve the interpretation of macro-scale laboratory experiments, it is important to study the processes involved on the micro-scale (Hall and André, 2003). X-ray CT lends

itself as good tool to study the micro-scale effects of freeze-thaw processes. Hence, since the development of laboratory micro-CT, different studies of freeze-thaw processes have been done using micro-CT (Ruiz de Argandona *et al*, 1999; Dewanckele *et al.*, 2013). As these studies focus on the resulting micro-structural effect of freeze-thaw decay on rocks, we focus on the real-time processes of freezing and thawing in porous, sedimentary rocks. Therefore, we perform dynamic imaging of samples under ambient freeze-thaw cycling, with a gantry-based X-ray CT system capable of acquiring full micro-CT scans in the time order of a minute.

The cause for freeze-thaw decay is the stress induced by the crystallization of ice within the pore network (Scherer, 1999; Steiger, 2005), where the freezing point is depressed for capillary water according to the Kelvin equation (e.g. Ruedrich *et al.*, 2011). The main precondition for freeze-thaw decay is that the macroscopic stress induced by ice crystallization pressure exceeds rock strength, fixed by a strength-controlling flaw. Hence whether or not building stones will experience freeze-thaw decay depends on their intrinsic properties and the environmental conditions to which they are subjected. In these experiments, we focus on the spatial pore size distribution of the samples, local water saturation and freezing temperature.

Methods

X-ray micro-CT was performed at the Centre for X-ray Tomography of the Ghent University (UGCT; www.ugct.ugent.be; Masschaele *et al.*, 2007) using two custom-built laboratory micro-CT scanners: HECTOR (Masschaele *et al*., 2013) and EMCT (Dierick *et al.*, 2014). HECTOR was used to obtain high resolution (< 10 µm) images of reference samples or subsamples from laboratory freeze-thaw experiments.

Dynamic X-ray micro-CT experiments were performed with EMCT, using cylindrical samples of 9 mm diameter. The samples were water-saturated by atmospheric imbibition for 24h. Subsequently, they were subjected to ambient freeze-thaw cyling from 20°C -15 °C using a custom made freezing stage (De Schryver *et al.*, 2015). The sampled were scanned in the middle of each freezing and thawing phase. Moreover, continuous scanning was performed for 24 minutes during the cooling phase, resulting in 14400 projections of 100 ms exposure time over 18 full-360° rotations. The X-ray tube was operated at a tube voltage of 65 kV and a power of 14.3W. The reconstructed voxel resolution was around 20 µm.

Laboratory freeze-thaw cycling was performed according to the European Standard EN 12371 (2010) on 40 mm edge cubic samples with 6h of freezing at -12°C, followed by 6h of thawing while immersed in water of 20 °C.

A Zeiss Axioscope with camera was used for petrographical description of uncovered 30 µm thin sections stained with Alizarine Red-S. Scanning electron microscopy (SEM) was done with a FEIT Quanta 200F on gold-coated samples. Petrophysical properties were determined according to the appropriate European Standards.

The experiments were performed on different sedimentary rocks, used as building materials in Belgium. Here we focus on some results of a porous miliolid limestone from the Paris basin, which are more thoroughly discussed in De Kock *et al.*, 2015 and some preliminary results of a sandy limestone, Lede stone, and an oolitic limestone Massangis, whos properties were discussed in De Kock *et al.*, 2013.

Results and discussion

Micro-CT allows to visualize the micro-scale freeze-thaw decay of the porous samples. The freeze-thaw cycling results in the development of fractures within the sample (Figure 1). This is the result of ice wedging, a process where the ice crystals push the fracture surfaces apart. The development of the fractures is strongly related to the rocks' fabric. More specifically, they develop within the planes of discoidal forams, which are microfossils. It was already shown by Dewanckele *et al.* (2013) that these act as flaws. Capillary rise experiments show that these forams acts as preferential water uptake paths. Therefore it is assumed that the water saturation is relatively high in the volume fraction of the rock around these forams during freezing, increasing the volume that can be affected by freezing. Hence, there seems to be a clear link between local saturation and freeze-thaw decay.

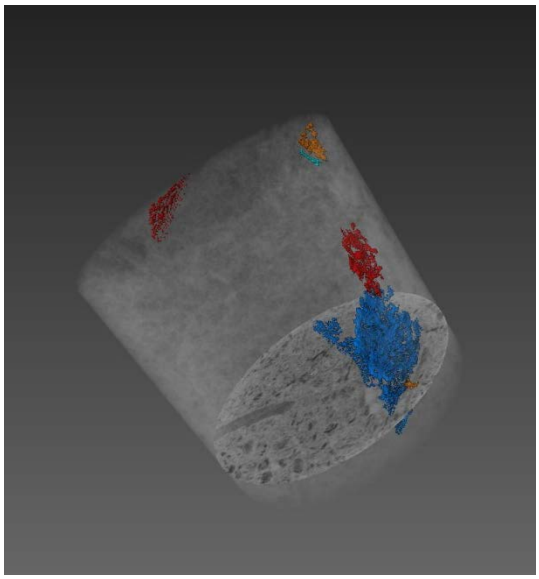

Fig. 1. *Fractures segmented (in colour) within the bulk volume (transparent) and one reference slice (opaque). Sample diameter is 9 mm.*

Figure 2 shows the development and growth of the fracture in size in function of the freeze-thaw cycles. During the second cycle, it can be seen that a fracture develops, which cannot be segmented due to the partial volume effect. From the 3rd freeze-thaw cycle, however, the fracture is large enough to be segmented and this enables that its volume can be analysed. First of all, it can be seen that the fracture opens during freezing en closes during subsequent thawing. This is in favour of the ice crystallisation theory as discussed in the introduction. After successive freeze-thaw cycling, there is a progressive opening of the fracture, allowing to observe fracture propagation. After the 4th cycle, the fracture does not close entirely and there is residual strain. Finally, the crack size also stagnates in the last cycles, illustrating that the facture volume accommodates the ice crystallization.

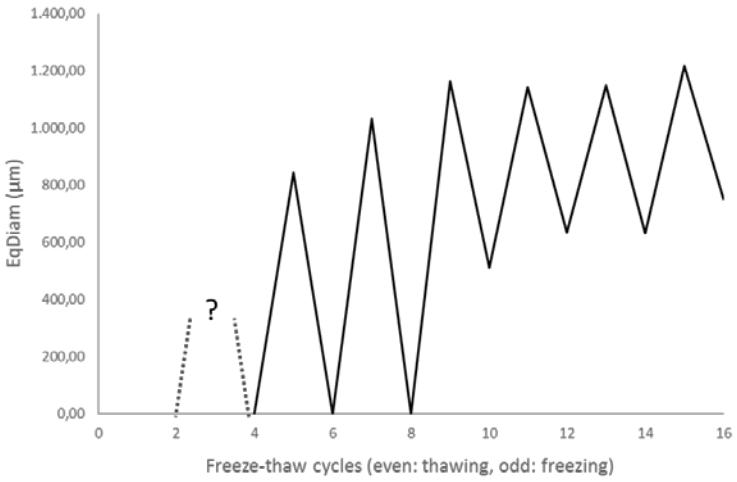

Fig. 2. *Size of a fracture expressed as equivalent diameter in function of successive freeze-thaw cycles.*

During cooling a temperature exotherm, considered as a proxy for ice crystallization, was recorded at a temperature of -9.7°C. According to the Kelvin equation for freezing point depression, this corresponds to crystallisation in pores smaller than 20 nm. As it is thermodynamical more favorable to crystallize within larger pores (Everett, 1961), crystallization in these experiments occurs under transient conditions. Most likely, this is related to the probability of having a nucleation site within such a small sample (Sun and Scherer, 2010). Figure 3 consists of a SEM image showing the presence of such small pores within the tests of these forams. The susceptibility of this sample to freeze-thaw decay is thus related to a combination of larger pores as the foram's test chambers which have a higher capillary suction velocity resulting in higher local water saturation, with nanometric pores from the test itself that provide a higher probability of nucleation sites.

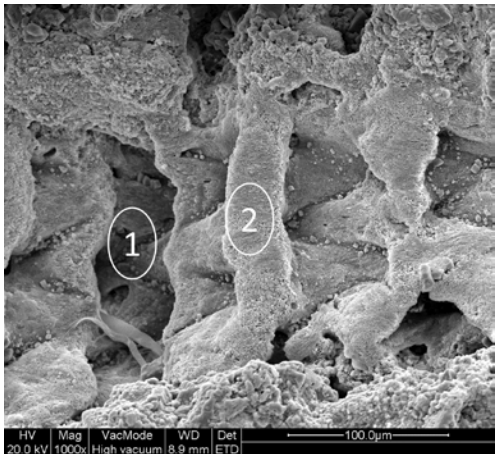

Fig. 3. *SEM image of part of the foram's test, with larger interparticular micrometer pores (1) and nanometric pores in the test (2).*

In addition, continuous scanning allows to visualise the dynamics in the sample during freezing. It can be seen that the fracturing is abrupt and coincides perfectly in

time with the occurrence of the exotherm. This validates the ice crystallization theory as mechanism for freeze-thaw decay in these experiments.

Preliminary results of experiments with other stones also illustrate the relation of freeze-thaw fractures with the rock's fabric, more specifically with the fabrics that promote a high local saturation degree.

Acknowledgements

This work was partially supported by the Research Foundation Flanders (FWO) project G.0041.15N. H. Derluyn is supported by the FWO and Thomas De Schryver is supported by the Agency for Innovation by Science and Technology in Flanders (IWT, SBO project 120033 "TomFood"). Tim De Kock is grateful to the FWO for travel grant K178415N.

References

De Kock T., Dewanckele J., Boone M.A., De Schutter G., Jacobs, P., Cnudde V. (2013). Replacement stones for Lede Stone in Belgian historical monuments. J. Cassar, M. G. Winter, B. R. Marker et al. (eds) ***Stone in Historic Buildings: Characterization and Performance***. London, Geological Society Special Publications, 391: 31-46.

De Kock T., Boone M.A., De Schryver T., Van Stappen J., Derluyn H., Masschaele B., De Schutter G., Cnudde V. (2015). A Pore-Scale Study of Fracture Dynamics in Rock Using X-ray Micro-CT Under Ambient Freeze-Thaw Cycling. ***Environ. Sci. Techn***. 49, 5: 2867-2874.

De Schryver T., Boone M. A., De Kock T., Masschaele B., Dierick M., Van Hoorebeke L. (2014). A compact, low cost cooling stage for X-ray micro-CT setups. ***12th International conference on X-ray Microscopy: conference program handbook***, p. 155-155.

Dewanckele J., Boone M. A., De Kock T., De Boever W., Brabant L., Boone M. N., Fronteau G., Dils, J., Van Hoorebeke L., Jacobs P., Cnudde V. (2013). Holistic approach of pre-existing flaws on the decay of two limestones. ***Sci. Total Environ.***, 447: 403-414.

Dierick M., Van Loo, D., Masschaele B., Van den Bulcke J., Van Acker J., Cnudde V., Van Hoorebeke L. (2014) Recent micro-CT scanner developments at UGCT. ***Nucl. Instrum. Methods Phys. Res., Sect. B*** 324, 35-40.

Everett D.H. (1961) The thermodynamics of frost damage to porous solids. ***Trans. Faraday Soc.*** 57, 9: 1541-1551.

Hall K. (2006) Monitoring of thermal conditions in building stone with particular reference to freeze-thaw events. S. K. Kourkoulis (Ed***) Fracture and Failure of Natural Building Stones – Applications in the Restoration of Ancient Monuments,*** Springer: Dordrecht, The Netherlands: 373-394.

Hall K., André M.-F. (2003) Rock thermal data at the grain scale: applicability to granular disintegration in cold environments. ***Earth Surf. Proc. Land.*** 28, 8: 823-836.

Ingham J. P. (2005). Predicting the frost resistance of building stone. Quarterly Journal of Engineering Geology and Hydrogeology 38: 387-399.

Masschaele B. C., Cnudde V., Dierick M., Jacobs P., Van Hoorebeke L., Vlassenbroeck J. (2007) UGCT: New x-ray radiography and tomography facility. ***Nucl. Instrum. Methods Phys. Res., Sect. A*** 580, 1: 266-269.

Masschaele B. C., Dierick M., Van Loo D., Boone M. N., Brabant L., Pauwels E., Cnudde V., Van Hoorebeke, L. (2013) HECTOR: A 240kV micro-CT setup optimized for research. ***J. Phys. Conf. Ser.*** 463: 4p.

Matsuoka N., Murton J. (2008) Frost Weathering: Recent advances and future directions. ***Permafrost Perigl.*** 19, 2: 195-210.

McAllister D., McCabe S., Smith B. J., Srinivasan S., Warke P.A. (2013) Low temperature conditions in building sandstone: the role of extreme events in temperate environments. ***Eur. J. Environ. Civ. En*** 17, 2: 99-112.

Ruedrich J., Siegesmund S. (2007) Salt and ice crystallization in porous sandstones. ***Environ. Geol.*** 52, 2: 343-367.

Ruedrich J., Kirchner D., Siegesmund S. (2011). Physical weathering of building stones induced by freeze-thaw action: a laboratory long-term study. ***Environ. Earth Sci.*** 63, 7-8: 1573-1586.

Ruiz de Argandona V. G., Rodriguez-Rey A., Celorio C., Calleja L., Llavona J. (1999) Characterization by computed X-ray tomography of the evolution of the pore structure of a dolomite rock during freeze-thaw cyclic tests. ***Phys. Chem. Earth (A).*** 24, 7: 633-637.

Scherer, G. (1999) Crystallization in pores. ***Cem. Concr. Res.*** 29, 8: 1347-1358.

Steiger, M. (2005) Crystal growth in porous materials - I: The crystallization pressure of large crystals. ***J. Cryst. Growth*** 282, 3-4: 455-469.

Thomachot C., Matsuoka N., Kuchitsu N.; Morii M. (2005) Frost damage of bricks composing a railway tunnel monument in Central Japan: field monitoring and laboratory simulation. ***Nat. Hazards Earth Syst. Sci.*** 5, 4: 465-476.

A 3D Investigation of Interface Porosity and Fracture Characteristics of Cement-Based Composites

C. GANGSA, L. FLANDERS, E. LANDIS*

University of Maine, Dept. of Civil & Environmental Engineering, Orono, Maine USA – landis@maine.edu
* presenting author

Keywords: concrete, fracture, interfacial transition zone

Abstract

In this work, we analyzed x-ray microtomographic images to quantify the porosity of small mortar specimens, with a particular focus on the porosity of the in- terfacial transition zone (ITZ). Specimens were nominally 5 mm diameter, 4 mm long cylinders with 0.5 mm diameter glass bead aggregates. Specimens were scanned via synchrotron-based x-ray microtomography while they were positioned in an in situ loading frame in a split cylinder configuration. Scans of undamaged specimens were evaluated for porosity both in the bulk paste and in the ITZ. Specifically, voids in the paste and porosity in the ITZ were superimposed onto a map of the tensile stress in the specimen in an attempt to identify critical flaws, and to measure their role in split cylinder strength. Preliminary results indicate that the ITZ porosity has a lower effect on split cylinder strength than the large flaws that occur either in the ITZ or the bulk cement paste.

Introduction

Properties of the interfacial transition zone (ITZ) in concrete have long been recognized as critical to both transport properties and mechanical properties (e.g. Buyukozturk and Wecharatana 1995). The high porosity characteristic of the ITZ can provide a critical flaw that can dictate fracture toughness, as well as provide a path of least resistance for fluid transport. Despite its importance, high quality 3D quantitative measurements of ITZ porosity have been limited.

In this work, we have employed x-ray microtomography to make 3D measurements of porosity around artificial aggregates in a cement matrix. Within the resolution of the imaging technique, we are able to quantify porosity with respect to distance from the aggregate and spatial variation relative to casting direction and load axis. We are also able to look at the spatial variation of interface porosity in the zone of maximum split cylinder tension to partially examine variability of split cylinder strength. Finally, we are able to identify preferential pathways for mass transport via interfaces and shortest matrix distances.

The focus of the work described here is an analysis of voids in both the bulk cement past and the ITZ, and to assess the relative importance of the voids with respect to average tensile stress at the location of the void. This analysis gives us the potential to identify critical flaws that dictate fracture behavior, and as such, the question we wish to answer is: is the ITZ porosity a better predictor of strength than the size of bulk voids in the matrix? Previous experiments and simulations (Asahina et al 2011) showed that an increasing fraction of coarse aggregates lowered the split cylinder strength. Presumably the strength is dictated by critical flaws, so these begs the question of whether a higher fraction of aggregates increases the probability of a critical flaw by having a greater overall ITZ region, or does a greater overall ITZ region by itself reduce the strength without necessarily introducing a larger flaw.

Materials & Methods

The specimens used for this work were prepared using a high early strength (ASTM Type III) portland cement, very fine silica (passing #80 sieve), small glass bead aggregates (nominally 0.5 mm), and water. The glass beads were used for their well-defined geometry, and because the surface can be easily modified to change interface properties. In this work, two different surfaces were considered: smooth (untreated) and etched using an ammonium bifluoride solution. The mix proportion of the mortar matrix was 1:2:0.5, by weight cement:fine sand:water. Glass beads were added as ``coarse'' aggregates at a dosages of roughly 10% and 50% by volume. Additionally, a set of specimens without glass beads was prepared to investigate properties of the cement matrix. The material was mixed with a benchtop rotary mixer and cured in wet conditions for seven days. The nominally 5 mm cylindrical test specimens were extracted from the bulk material using a 5.5 mm inside diameter diamond coring bit and then cut to size.

Three dimensional imaging of the specimens were made using synchrotron-based x-ray microtomography (XMT). For these experiments, the x-ray source was a 30 keV monochromatic, collimated beam from a synchrotron at the Advanced Photon Source (APS). The high flux source led to high contrast images with a voxel size of 6 µm. In the experiments, specimens were scanned in the x-ray beamline while positioned in an *in situ* loading frame that could monitor load and platen-to-platen displacement. Scans were made at nominally zero load and again after fracture.

Digital image processing techniques were applied to the acquired 3D images. First, the images were segmented such that both individual aggregate particles could be isolated, as well as the porosity surrounding the aggregates. In order to isolate pores, beads, and other constituents, the specimen had to be isolated from the background. To achieve this, a shrinkwrapping function was employed. Then, the isolated volume could be used in conjunction with informed selection of a threshold and binary operators to isolate constituents such as pores, aggregates, and unhydrated cement particles. A similar but slightly more complicated process, which used a standard deviation filter to identify edges, was used to isolate the beads.

For the ITZ analysis, varying interfacial zone widths were applied as shells around the beads, and pores within those shells were isolated, resulting in information about ITZ width and porosity. A rough illustration of this process is presented in Fig. 1. In this work, we only considered ITZ zones in which the aggregate surface was nominally normal to the plane of maximum principal tensile stress. As detailed below, this was determined by superimposing the ITZ zone onto a map of the tensile stress in the specimen, and defining a shell defined by a 45º arc centered on the normal vector. Of interest here is the porosity of the ITZ, which could simply be calculated by dividing the number of void voxels by the total number of voxels in the defined ITZ zone.

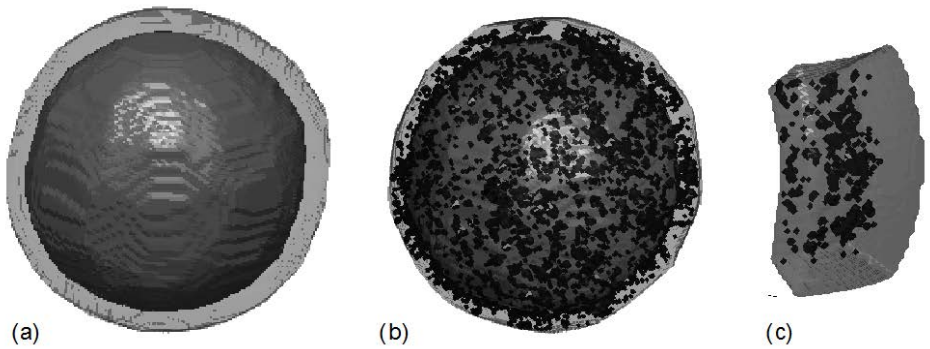

Fig. 1. *Illustration of (a) isolated bead and ITZ, (b) ITZ porosity, and (c) section of ITZ in tension zone.*

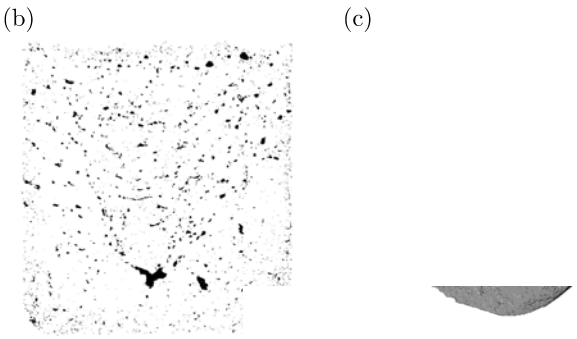

Fig. 2. *(a) Cross sectional slice, (b) slice segmented for pores, and (c) 3D rendering of largest pore in specimen.*

Regarding the analysis of void space in the cement matrix, we simply conduct a connected component analysis of the void space (obtained through image segmentation) inside the specimen. The individual pore spaces are then analyzed for size and location. An example of the analysis is illustrated in Fig.2.

Analysis

The isolated ITZ regions and the bulk void spaces, while useful in predicting fracture strength, is incomplete information. de Wolski et al (2014) showed a correlation between bulk porosity and split cylinder strength, however, it was not a strong correlation. The split cylinder configuration is a popular measure for tensile strength because the test is easy to run, and the tensile stress is fairly uniform along the axis of the load. Thus, for a void to truly have an impact on the tensile strength it must be located on or near that central axis. The effect of a large void decreases if it is away from that axis.

Using the well documented stress field for a split cylinder configuration (e.g. Petroski and Ojdrovic 1987), a 3D image could be constructed such that the voxel intensity is proportional to the principal tensile stress. The relative influence of the void space is assumed to be a function of its size and the tensile field where it lies. This can be visualized in Fig. 3, where a void object isolated in the specimen is superimposed on the tension field. The tension field is set based on a unit compressive force.

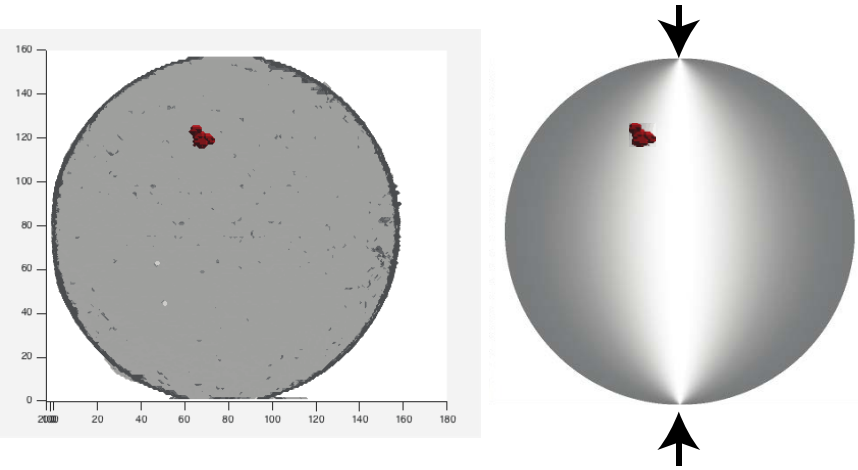

Fig. 3. *Void object isolated in specimen (left) superimposed on principal stress field (right).*

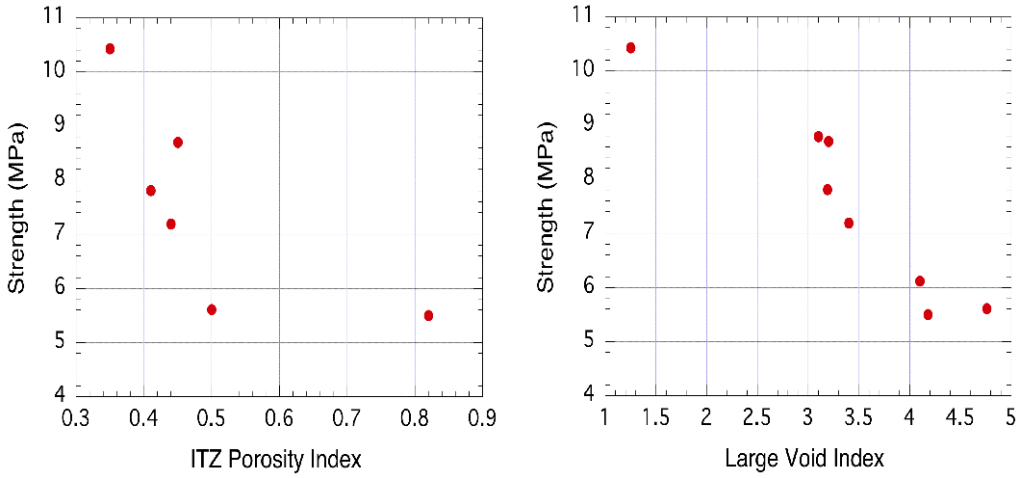

Fig. 4. *Plots illustrating the effect of ITZ porosity index and large void index on split cylinder strength.*

This superposition was applied two different ways in order to address the question of whether bulk pores have a greater affect on split cylinder strength than the ITZ porosity. First, the porosity of all tensile zone ITZ regions was evaluated as described above. Each tensile zone porosity value was then multiplied by the principal tensile stress acting at the centroid of the the ITZ region. We refer to this product as the ITZ porosity index, and of particular interest is the largest ITZ porosity index in each specimen.

A similar procedure was then applied to the isolated void objects. The volume of each object is multiplied by the maximum principal stress at the centroid of the object. We refer to this product as the Largest Void Index. The presumption, again, is that the combination will have the greatest impact on specimen strength.

The results of both of these analysis are plotted in Fig. 4, which show split cylinder strength plotted against ITZ porosity index and largest void index. Qualitatively, the results show that both indices correlate inversely with strength, as expected. While sample sizes are admittedly small, it would seem that the large void index shows less scatter, indicating perhaps a stronger relationship. It should be noted that the sample size is slightly larger for the large void index data due to the inclusion of specimens that did not include any bead aggregates (and thus no ITZ can be defined).

Conclusions

While not conclusive, the preliminary answer to the original question of the role of the ITZ in fracture strength, the results suggest that the largest void, relative to principal tensile stress, produces a stronger correlation, and is therefore a more important factor in dictating split cylinder strength than the high porosity regions in the ITZ. However, as previous results have shown that higher aggregate fractions reduce the split cylinder strength, this would imply that either the ITZ produces large voids, or the addition of more aggregates somehow promotes larger void spaces, perhaps due to mixing or entrapped air issues.

Among the implications of the work are that the results can be incorporated into discrete models such that the models can properly incorporate spatial variability. Specifically, it shows the interacting role of ITZ variability and void distribution relative to stress fields as the likely source of fracture initiation.

Acknowledgements

Portions of this work were per- formed at the DuPont-Northwestern-Dow Collaborative Access Team (DND-CAT) located at Sector 5 of the Advanced Photon Source (APS). DND-CAT is supported by E.I. DuPont de Nemours & Co., The Dow Chemical Company and the State of Illinois. Use of the APS was supported by the U. S. Department of Energy, Office of Science, Office of Basic Energy Sciences, under Contract No. DE- AC02-06CH11357. An additional acknowledgement goes to Dr. Denis Keane, DND-CAT director, for his assistance at the beamline.

References

Asahina, D., Landis, E. N., and Bolander, J. E. (2011) Modeling of Phase Interfaces During Pre-Critical Crack Growth in Concrete**. *Cement and Concrete Composites***, 33(9): 966-977.

Buyukozturk, O., and Wecharatana, M. (1995) ***Interface Fracture and Bond*** SP-156, American Concrete Institute, Detroit.

de Wolski, S. C., Bolander, J. E., and Landis, E. N. (2014) An In-Situ X-ray Mi- crotomographic Study of Split Cylinder Fracture in Cement-Based Materials. ***Experimental Mechanics***, 54(7): 1227-1235.

Petroski, H. J., and Ojdrovic, R. P. (1987) The Concrete Cylinder: Stress Analysis and Failure Modes. ***International Journal of Fracture***, 34: 263-279.

Application of X-ray CT to the Observation of Cracking in a Corroded RC Bridge Slab

J.C. KURI[1], I. ZAFAR[1], T. SUGIYAMA*[2]

[1] Graduate School of Engineering, Hokkaido University, Sapporo 060-8628, Japan - jhutankuri@yahoo.com, izsatti@hotmail.com
[2] Faculty of Engineering, Hokkaido University, Sapporo 060-8628, Japan - takaf@eng.hokudai.ac.jp
*Presenting author

Keywords: Crack geometry, Chloride ions penetration, Corrosion, Real structure

Abstract

The effect of cracks on the penetration of chloride ions in a corroded RC bridge slab was studied by means of X-ray CT (Computed Tomography). X-ray CT analysis of cores taken at or near the crack was done to evaluate the crack depth and the crack width distribution. In addition, the chloride ion concentration was also measured along the depth of the core. It was found that the core with the maximum crack depth had the highest chloride ion concentration at the level of reinforcement, demonstrating to a good analogy between the results of X-ray CT and chloride ion measurement analysis.

Introduction

X-ray CT is a powerful tool to examine the internal structure of an object in three dimensions. Recently, X-ray CT has been applied to a variety of research areas in concrete engineering, such as pore structure characteristics, air bubble distribution, freeze–thaw and fire damage, and diffusivity in the crack. This technology is quite appropriate to specifically analyse crack characteristics, as the X-ray absorption properties of air voids in concrete, both isolated and connected (in the form of cracks), differ highly from the cement paste and aggregates. However, to date most of these experiments were conducted on the laboratory-made specimens, and X-ray CT has not been applied to real concrete structures in service. Potentially, X-ray CT technique is useful as a tool for the diagnosis of existing concrete structures.

In a snowy, cold region like Hokkaido, Japan, during the winters de-icing salt is applied on the bridge to keep the right-of-way accessible to traffic. De-icing salts can penetrate through the bridge deck causing the top rebars to corrode. However, in spite of the thick concrete present between the top and bottom rebars, the bottom rebars in RC slab had shown corrosion after a certain period of service life. It's still not clear whether the chloride ions are penetrating from the top surface or travelling through cracks formed on the tension fibres of the slab are responsible for the corrosion of bottom rebars. In this study, with the aid of X-ray CT, an effort was made to estimate the chloride penetration in the cracked RC slab in a highway road bridge which had been in service for 38 years.

Materials and Methods

Electrochemical Measurement and Sample Preparation

The deteriorated RC slab was removed and brought to another location, where electrochemical measurement of the top (UP) and bottom (DO) rebars was done. An alternating current impedance spectroscope (corrosion meter) was employed to measure the half-cell potential (Ecorr) and corrosion current (Icorr) of the rebars. The working principle and current line distribution of corrosion meter is referred to Zafar et al. (2014).

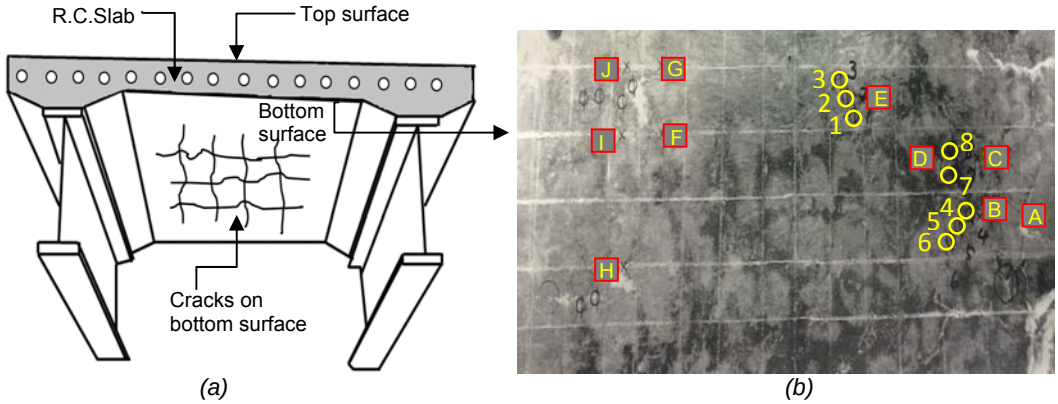

Fig. 1. *(a) Schematic diagram of RC slab, (b) Location of electrochemical measurements (A to J) and Cores (1 to 8) at the bottom surface of the RC slab*

The electrochemical measurements were done to evaluate the corrosion state of the rebars in the slab. Fig. 1 shows the location of electrochemical measurement points (A to J) and cores (1 to 8) being taken from the bottom side of the bridge slab. The cores were drilled for X-ray CT analysis and chloride ion measurement. Cylindrical core specimens had a diameter and height of 25 mm and 100 mm respectively. Five (CT02, CT04, CT05, CT07 and CT08) core specimens were selected based on the appearance of cracks on the bottom surface of the slab for X-ray CT and chloride ion measurement.

X-ray CT

In this study, a micro-focus X-ray CT system (TOSCANER-30000μhd, Toshiba IT & Control Systems Corporation) was used to obtain the 3D image of the internal structure of core specimen. The microfocus X-ray CT scanner (Fig. 2) consists of a microfocus X-ray emitter, a specimen manipulator, an image intensifier (II) detector coupled to a CCD camera and an image processing unit (Promentilla et al. 2010). A power setting of 130 kV (tube voltage) and 124 μA (tube current) was used for full (360°) cone-beam scans with 1500 projection views. The specimen was set in the holder mounted on a precision rotation table, and then the table position was adjusted to fit the image within the field-of-view. The position of FCD (focus chamber distance), FID (focus image distance) was adjusted to get the high resolution images as well as to reduce the noise and artifacts in

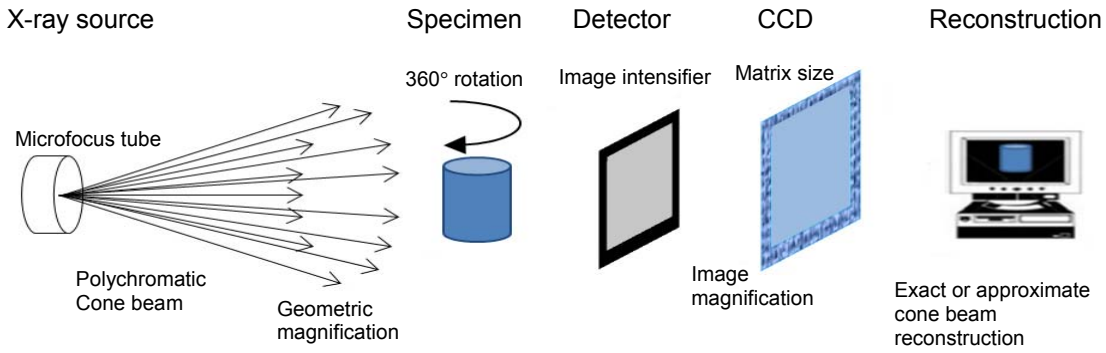

Fig. 2. *Schematic illustration of X-ray CT system (Promentilla et al. 2010)*

the images during acquisition. The data set obtained from cone beam scanning of the core specimen consists of contiguous slices of reconstructed CT images with a thickness of about 40 micron each. Stacking up these slices creates a 3D image of the scanned section of the specimen. Each slice was 1024 by 1024 pixels in size, with each pixel about 27 micrometres by 27 micrometres.

Chloride ion concentration

The chloride ion concentration of the cores was measured after the completion of X-ray CT measurement. The cores were sliced in approximately 15 mm thick layers and then ground to get about 10 grams of powder for the chloride analysis. Japanese Industrial Standard (JIS A1154 2003) was used to determine the total chloride ion concentration in each sample of the concrete.

Results and Discussions

Fig. 3 shows the result of Ecorr and Icorr of UP and DO rebars of the RC slab. According to ASTM C 876, the corrosion had occurred for all the measurement points and the values of Icorr are also supplementing the corrosion initiation of UP and DO rebars.

Fig. 4 shows the results of X-ray CT measurements and the profiles of chloride ions concentration for cores obtained from RC slab. For image analysis, a volume of interest (VOI) was extracted from the original data set of each specimen. For void space segmentation, global thresholding was used to separate the void from the solid matrix by defining the range of gray scale value (GSV) associated with void voxels (Promentilla et al. 2010). SLICE program (Nakano et al. 2006) was used to obtain the largest percolating void through cluster multiple labeling techniques. Fig. 4(b) shows the crack network derived from microtomographic images of different core specimens after void segmentation and clusters multiple labeling. From visual and CT observation, it was seen that there was no crack on CT02 specimen. From Fig. 4(b) it is seen that the crack depths of CT04, CT07 and CT08 specimens are 36.60 mm, 22.70 mm and 36.00 mm respectively. CT05 specimen has a maximum (81.38 mm) crack depth among all specimens. This crack depth has reached the level of bottom rebar (50 mm) from the bottom surface while other cracks diminished within the concrete cover. As another index of the crack characteristics, the crack width distribution was calculated using the *Thickness* plugin on the basis of the segmented X-ray CT data (Darma et al. 2013). Fig. 4(c) shows the crack width distribution of crack network of all core specimens.

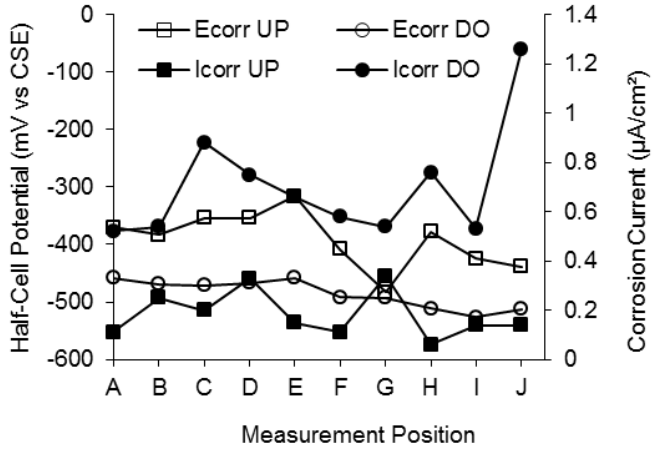

Fig. 3. *Half-cell Potential (Ecorr) and Corrosion Current (Icorr) of UP and DO rebars*

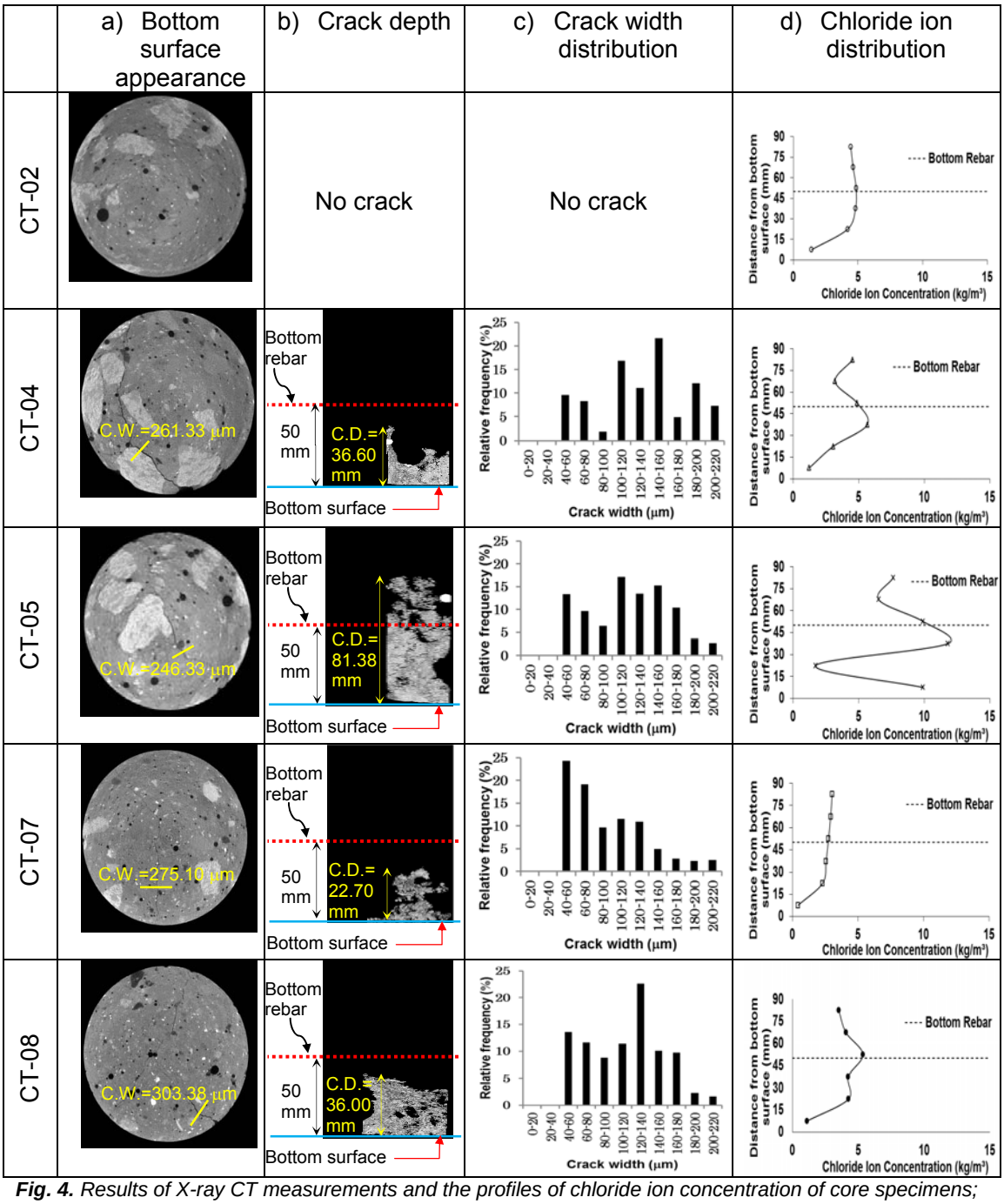

Fig. 4. *Results of X-ray CT measurements and the profiles of chloride ion concentration of core specimens; a) Near bottom surface appearance, b) Crack depth (C.D.), c) Crack width (C.W.) distribution and d) Profile of Chloride ion*

From Fig. 4(c) it can be seen that, for CT04, CT05 and CT08 specimens, about 55% to 60% of the crack widths fall between 100 μm and 180 μm. On the other hand, for CT07, about 55% of the crack widths are less than 100 μm. Fig. 4(d) shows the profiles of the chloride ion concentration along the depth of the core specimens. It was observed that the chloride ion concentration for CT05, which had the maximum crack depth, also

had the highest chloride ion concentration value at the bottom rebar with a cover depth of 50 mm. On the other hand, the CT02, CT04, CT07 and CT08, with either no crack or crack diminishing in the concrete cover, had lower values of chloride ion concentration as compared to that of CT05. The average value of chloride ion concentration at the level of bottom rebar for CT02, CT04, CT07 and CT08 was observed to be 3.9 kg/m³. Although CT02 showed no crack, from the result of chloride ion it is expected that the majority of the chloride ions penetrated from the top surface of the slab through the application of de-icing salts.

It was observed that the CT07 specimen had a small crack depth (22.70 mm), small crack width distribution (55% less than 100μm), and correspondingly less chloride ion concentration as compared to other specimens. Although CT04, CT05 and CT08 specimens have almost the same crack width distribution within the range of 100 μm and 180 μm, the values of chloride ion concentration are quite different. In this way, it appeared that the crack width distribution was less influential on the penetration of chloride ions.

Conclusions

A good correlation was found to exist between the crack depth as compared to crack width obtained by X-ray CT and the chloride ion concentration. The highest chloride ion concentration at the depth of the bottom rebar was observed in the core having the maximum crack depth.

Acknowledgements

The authors would like to thank Mr. Tetsuji Ohta of NEXCO Engineering Hokkaido Company Limited for his help in carrying out the on-site measurements and drilling of cores. Part of this research was funded by the Japan Society for the Promotion of Science (Research No. 2628913384). The first and second authors would like to acknowledge MEXT for providing their scholarships.

References

Darma I.S., Sugiyama T. & Promentilla M.A.B. (2013). Application of X-ray CT to study diffusivity in cracked concrete through the observation of tracer transport. ***Journal of Advanced Concrete Technology***, 11, 266-281.

Japanese Industrial Standards JIS A 1154: 472-482, (2003). *Methods of test for chloride ion content in hardened concrete*. (In Japanese).

Nakano T., Tsuchiyama A., Uesugi K., Uesugi M. & Shinohara K. (2006). *SLICE – Software for basic 3-D image analysis* [online]. Japan Synchrotron Radiation Research Institute (JASRI). <http://www-bl20.spring8.or.jp/slice/ >

Promentilla M.A.B. & Sugiyama T. (2010). X-ray microtomography of mortars exposed to freezing-thawing action. ***Journal of Advanced Concrete Technology***, 8(2), 97-111.

Zafar I. & Sugiyama T. (2014). Laboratory investigation to study the corrosion initiation of rebars in fly ash concrete. ***Magazine of Concrete Research***, 66(20), 1051–1064.

Evaluation of Fiber Characteristics and Crack Structures in Conventional and High-Performance Concretes Using X-Ray Computed Tomography

*T. OESCH[1], E. LANDIS[2], D. KUCHMA[3]

[1] U.S. Army Engineer Research and Development Center (ERDC), Vicksburg, MS 39180
[2] Department of Civil and Environmental Engineering, University of Maine, Orono, ME 04469
[3] Department of Civil and Environmental Engineering, Tufts University, Medford, MA 02155
* presenting author

Keywords: anisotropic fiber orientation, computed tomography, UHPC

Abstract

To make significant advances in concrete engineering, it will be necessary to understand the behavior of cementitious materials at the micro-scale. To reach this goal, the location and orientation of constituent materials within concrete members as well as the nature of damage initiation and growth need to be understood at very small scales. This research program sought to increase that understanding through the use of x-ray computed tomography (CT). The phenomena investigated included the tension, compression, and reinforcing bar pull-out behavior of both high-strength fiber reinforced concrete (HSFRC) and conventional concrete. These testing efforts yielded a number of important results. First, relationships were identified between mechanical performance and cracking parameters that could be quantified mathematically and implemented into future finite element analysis models. Second, these test results demonstrated that the cracking structures of HSFRC specimens subjected to the double-punch test (DPT) are heavily influenced by fiber anisotropy. This can lead to actual crack structures that are significantly at variance with the theoretical crack structure, which may decrease DPT accuracy in predicting tensile strength. Third, fiber orientations within both small and large specimens of HSFRC were demonstrated to be highly anisotropic. Thus, the assumption of randomly oriented fibers within HSFRC could lead to significant over-predictions of strength in some structural members. The results of this research program have the potential to both improve the accuracy and resiliency of numerical models as well as provide insight to the materials engineering and structural design communities about the optimal use of HSFRC.

Introduction

The use of fiber reinforced concretes (FRCs) in structural members, such as in beams and columns, has shown that great ductility can be achieved with cracks that are barely visible to the naked eye (Li et al. 1995). However, ACI 318-11 (2011) does not contain provisions for the use of FRC in structural design as tests show too wide a variability in the strength of members cast with FRC and there is no fundamental model on which to base design code standards. Previous research has demonstrated that the strength of HSFRC members is very dependent on fiber orientations within the members (Smith et al. 2014). Thus, it has become clear that for safe and efficient use of HSFRC in design and construction, anisotropy of fiber orientation will need to be taken into account when characterizing mechanical performance (di Prisco et al. 2013; Pujadas et al. 2014a).

Given the uncertainties involved in their use, HSFRCs would benefit greatly from the creation of high quality finite element analysis (FEA) models for assessing optimal mix designs and the effects of anisotropy on mechanical performance. However, for these models to be accurate for a heterogeneous material such as HSFRC, it will be necessary to develop a framework for relating crack parameters to bulk material properties (Landis et al. 2007). Key to making these improvements will be the definition of a quantifiable, realistic description of damage, which at the present time is often very loosely defined. The ultimate goal of this definition would be to link any new damage variable that is implemented into FEA codes directly to measured concrete cracking (Landis 2006).

X-ray CT has been used to examine and characterize the internal structure of concrete for over 30 years (e.g., Morgan et al. 1980; Martz et al. 1993). The technique has been

applied to a number of concrete materials problems, including concrete pore structure (Bentz et al. 2000; Landis et al. 2000), sulfate attack (Stock et al. 2002), and fracture (Landis et al. 1999; Poinard et al. 2012; Trainor et al. 2013). The technique is particularly well suited for quantifying and elucidating internal cracking patterns in plain concretes and FRCs exhibiting varying degrees of heterogeneity and anisotropy. Fibers can also be identified, measured, and characterized according to directional orientation using CT (Trainor et al. 2013).

Experiments

A material called Cor-Tuf was selected as the HSFRC mix for this investigation. Cor-Tuf is the name that was given to a family of ultra-high performance concretes (UHPCs) developed at the ERDC. Cor-Tuf is a reactive powder concrete distinguished by a high compressive strength that generally ranges from 190 MPa to 244 MPa (Williams et al. 2009; Roth et al. 2010). The volumetric content of fibers in Cor-Tuf is 3.6%. The steel fibers used in making Cor-Tuf are the Dramix® 3D-55/30 BG product of N.V. Bekaert S.A. These fibers are approximately 30-mm long and are hooked at each end. The conventional concrete used in these experiments is called SAM-35. Its target compressive strength is approximately 24.1 MPa (Williams et al. 2006).

The unconfined compression (UC) test was used throughout these experiments to quantify compressive material behavior (ASTM 2012). The test method selected for quantifying tensile performance was the DPT (Fig. 1). The DPT has found increased acceptance within the engineering community during recent years, especially in relation to the testing of FRCs. Both the UC and DPT specimens were loaded using a large hydraulic loader. These specimens had to be removed from the loader in order to scan them. Reinforcing bar pull-out experiments were conducted using a specially designed load frame that allowed specimens to be scanned under load.

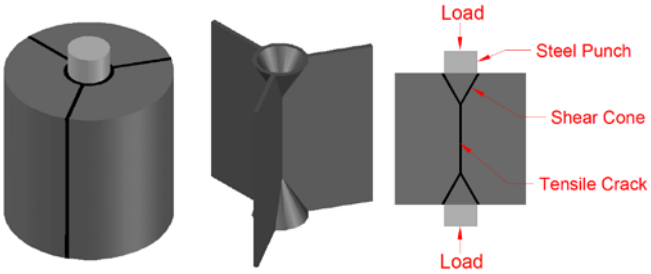

Fig. 1. *DPT layout and ideal failure mechanism. Isometric view of failed specimen (left), isometric view of failure surface (center), and center cross section of failed specimen (right).*

Relatively large specimen sizes, compared with other x-ray CT investigations, were necessitated by the inclusion of aggregate and fibers within the concrete compounds tested. Nominal specimen diameters of 72 mm were found to be optimal for these experiments. Cylindrical specimens for the UC and DPT experiments were cut from cores drilled out of the middle of thick concrete slabs rather than cast in cylindrical molds. This was done so that the structure of the material within the cylinders would most closely represent concrete properties in structural members. The specimens for the reinforcing bar pull-out experiments were cast individually by hand since their geometry did not accommodate coring.

All x-ray CT scanning was completed at the University of Florida using a 225-kV x-ray tube and an active image sensor with an area of 285 mm x 406 mm containing an array of 2240 x 3200 pixels with a pixel size of 127 µm (Thales Electron Devices 2003). During the experiments, specimens were scanned using x-ray CT at small deformation increments. This was done both to observe crack propagation and to record quantitative measurements of changes in crack volume and surface area relative to stiffness and work of load.

Image Analysis

A fiber orientation analysis was completed using a method similar to that of Trainor (2011). By calculating the Hessian matrix, partial second derivatives of intensity can be computed for all fiber voxel points (Trainor 2011). At a point within a fiber, the second derivative of intensity in the direction of the longitudinal axis of the fiber will be much less than those in the transverse directions (Lorenz et al. 1997). The orientation of fibers can,

thus, be calculated by computing the eigenvalues and eigenvectors of the Hessian matrix (Fig. 2). The primary fiber orientation recorded at a single point is, therefore, the eigenvector corresponding to the smallest eigenvalue (Trainor 2011).

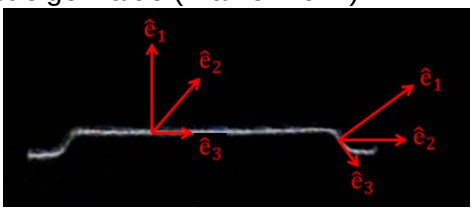

Fig. 2. *Eigenvectors of the Hessian matrix at two points within a Dramix® 3D-55/30 BG fiber (after Trainor 2011).*

The images were then processed in order to obtain quantitative damage measurements. This image processing method involved the selection of intensity thresholds appropriate for isolating solid and void material within the images, the identification of specimen boundaries through a "shrink-wrap" type procedure, and the isolation of internal voids using logical image comparison operations (de Wolski 2011; Oesch 2015). Once the images of the internal voids had been created, the volume of voids for each image could be calculated by adding up all white voxels (denoting internal voids) within the images. The total surface area of all internal void objects could also be calculated by determining the total area of all external faces of the white voxel objects in the images (de Wolski 2010).

The assumption was made that all void volume and surface area within the initial, undamaged scan of a specimen was related to entrained and entrapped air. Thus, any additional void volume or surface area seen in later scans of damaged specimens could be assumed to be due to cracking and, thus, represented crack volume or surface area. This allowed conclusions to be drawn about the relationship between measured crack volume or surface area and mechanical performance without the intensive, qualitative crack tracing process used in other research efforts.

Results and Conclusions

Through a qualitative assessment of the CT images, it was possible to evaluate the internal structure of DPT specimen cracking. These images demonstrated that the DPT crack structure for the Cor-Tuf specimens was significantly different from the theoretical structure typically assumed to occur (Fig. 3). This indicated that DPT failure for the Cor-Tuf specimens probably included a large contribution from shear-type mechanisms. Further, a strong correlation was identified between fiber orientation and cracking structure, which provided a compelling example of the dependence of the DPT on the orientation of fibers within a specific specimen. Although similar relationships between cracking patterns and fiber orientations were also seen in the UC experiments, the impact of fiber orientation on measured strength was expected to be less severe than for the DPT. This is because fibers are generally considered to contribute proportionately less to compressive strength than to tensile strength.

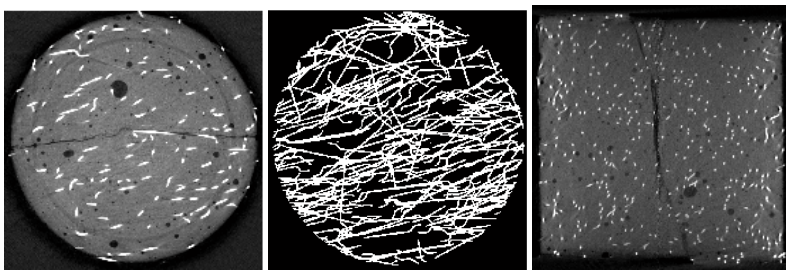

Fig. 3. *Mid-height plan views of a typical Cor-Tuf DPT specimen (left) and fiber distribution (center) as well as a typical specimen elevation view at mid depth (right).*

The observation of fiber orientation dependency in tension test results provided confirmation for similar results shown by other researchers and validated many of their assumptions (Barnett et al. 2010; Ferrara and Meda 2006; Pujadas et al. 2014a). These results also provided evidence that for safe and efficient use of FRC in design and construction, anisotropy of fiber orientation will need to be taken into account when

characterizing the mechanical performance of the material (di Prisco et al. 2013; Pujadas et al. 2014b).

Analysis of CT images from the reinforcing bar pull-out experiments was also responsible for identifying unique failure mechanisms around the bars that were particular to each material. These experiments demonstrated that the brittleness of concrete mixes has a major impact on their ability to accommodate variable levels of expansion along the length of the reinforcing bars. In extremely brittle compounds, such as Cor-Tuf without fibers, this can lead to a flexure-related failure at the embedded end of the reinforcing bar, contributing to lower pull-out strength.

Fiber orientation measurements extracted from the x-ray CT images of cored specimens showed that the fibers were significantly anisotropically oriented (Fig. 4). As these specimens were extracted from a larger slab cast directly from a concrete mixing truck, these results have implications for the use of FRC at the structural level. Specifically, they show that the orientation of fibers within a specific portion of a structure is likely to be highly dependent on the casting method and the flow pattern of the material. A detailed understanding of these phenomena is critical for both numerical modeling and for structural design since fibers oriented parallel to cracks create zones of weakness rather than strengthening the material.

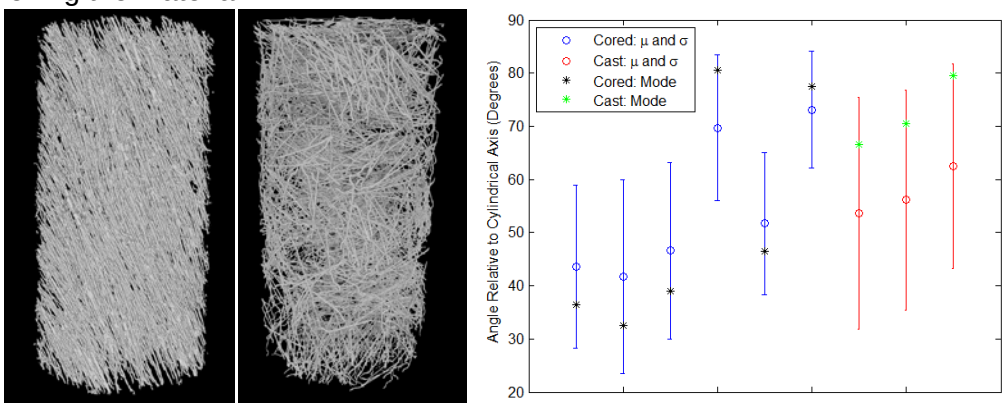

Fig. 4. *Typical fiber distributions for cored (left) and individually cast (center) specimen as well as the plotted mean (μ), standard deviation (σ), and mode for all sample fiber orientations (right).*

When compared with the cored specimen data, the fiber orientations measured in the individually cast specimens showed characteristics closer to those expected of the uniform distribution of fiber orientations, such as wider standard deviations. This decrease in the severity of anisotropic fiber orientation was probably a result of the casting process used to fabricate individually cast specimens, in which molds were filled by hand with concrete scoops. This prevented the thorough alignment of fibers during flow into the molds.

Crack volume and surface area measurements collected from x-ray CT images showed clear relationships with mechanical performance characteristics, such as work of load and stiffness (Fig. 5). These trends exhibited a negative gradient in the relationship between stiffness and both crack volume and surface area. A clear positive gradient was also identified in the relationship between work of load and both crack volume and surface area. Quantitative relationships could be developed from these measurements and implemented directly into FEA codes.

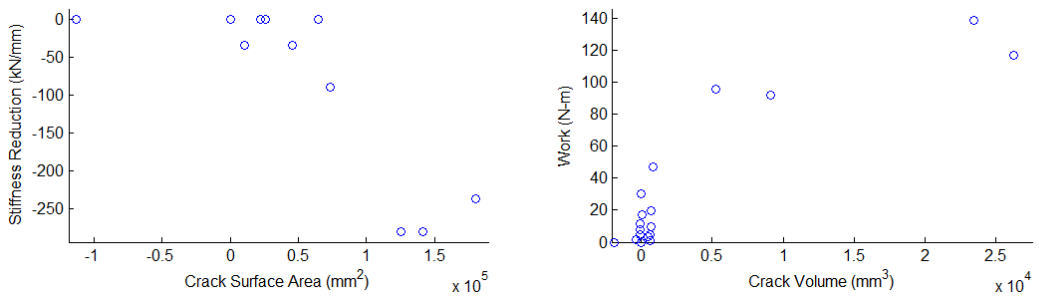

Fig. 5. *Typical performance-damage relationships between specimen stiffness reduction and crack surface area for Cor-Tuf (left) and between work of load and crack volume for SAM-35 (right).*

Either crack volume or surface area could be used as the basis for predicting updated values of a mechanical damage variable, which could be based on either stiffness degradation or fracture energy. From a fracture mechanics perspective, the use of crack surface area as a basis for these predictions would be ideal because of the strong ties between crack surface area and fracture energy in the linear elastic fracture mechanics (LEFM) theory (Bažant and Planas 1998).

All background and results presented in this abstract are covered in much more detail by Oesch (2015). The further study of the phenomena documented in this research program, such as fiber orientation effects, material characterization test deficiencies, and mechanical performance-damage relationships, can be used to facilitate the continued progress of HSFRC research through improving existing FEA models and informing the creation of future building code provisions.

Acknowledgements

This research was funded by the U.S. Army Military Engineering Basic Research (6.1) program under the Material Modeling for Force Protection work package. Permission to publish this research was granted by the Director of the Geotechnical and Structures Laboratory, U.S. Army Engineer Research and Development Center.

References

ACI (American Concrete Institute). (2011). "Building Code Requirements of for Structural Concrete," *ACI 318-11*, Farmington Hill, MI, pp. 503.

ASTM (American Society of Testing and Materials International). (2012). "Standard Test Method for Compressive Strength of Cylindrical Concrete Specimens," *ASTM C39/C39M*. West Conshohocken, PA.

Barnett, S.J., Lataste, J.F., Parry, T., Millard, S.G., and Soutsos, M.N. (2010). "Assessment of fibre orientation in ultra high performance fibre reinforced concrete and its effect on flexural strength," *Materials and Structures*, Vol. 43, pp. 1009-1023.

Bažant, Z.P. and Planas, J. (1998). *Fracture and Size Effect in Concrete and Other Quasibrittle Materials*. CRC Press LLC.

Bentz, D.P., Quenard, D.A., Kunzel, H.M., Baruchel, J., Peyrin, F., Martys, N.S., and Garboczi, E.J. (2000). "Microstructure and transport properties of porous building materials. II: Three- dimensional X-ray tomographic studies," *Materials and Structures*, Vol. 33, Issue 3, pp. 147-153.

de Wolski, S.C. (2010). *perim3D*, MATLAB Program.

de Wolski, S.C. (2011). *shrinkWrap*, MATLAB Program. <http://www.mathworks.com/matlabcentral/fileexchange/29175-shrinkwrap>

di Prisco, M., Ferrara, L., and Lamperti, M.G.L. (2013). "Double edge wedge splitting (DEWS): an indirect tension test to identify post-cracking behaviour of fibre reinforced cementitious composites," *Materials and Structures*, Vol. 46, pp. 1893-1918.

Ferrara, L. and Meda, A. (2006). "Relationships between fibre distribution, workability and mechanical properties of SFRC applied to precast roof elements," *Materials and Structures*, Vol. 39, pp. 411-420.

Landis, E.N. (2006). "Toward a Physical Damage Variable for Concrete," *Journal of Engineering Mechanics*, Vol. 132, No. 7, pp. 771-774.

Landis, E.N., Nagy, E.N., Keane, D.T., and Nagy, G. (1999). "A Technique to Measure Three-Dimensional Work-of-Fracture of Concrete in Compression," *Journal of Engineering Mechanics*, Vol. 125, No. 6, pp. 599-605.

Landis, E.N., Petrell A.L., Lu, S., and Nagy, E.N. (2000). "Examination of pore structure using three dimensional image analysis of microtomographic data," Concrete Science and Engineering, Vol. 2, Issue 8, pp. 162-169.

Landis, E.N., Zhang, T., Nagy, E.N., Nagy, G., and Franklin, W.R. (2007). "Cracking, Damage, and Fracture in Four Dimensions," *Materials and Structures*, Vol. 40, pp. 357-364.

Li, V.C., Mishra, D.K., and Wu, H.-C. (1995). "Matrix design for pseudo-strain-hardening fibre reinforced cementitious composites," *Journal of Materials and Structures*, Vol. 28, No. 10, pp. 586-595.

Lorenz, C., Carlsen, I.-C., Buzug, T.M., Fassnact, C., and Weese, J. (1997). "Multi-scale line segmentation with automatic estimation of width, contrast and tangential direction in 2D and 3D medical images," *Lecture Notes in Computer Science*, Volume 1205, pp. 233-242.

Martz, H.E., Schneberk, D.J., Robertson, P.G., and Monteiro, P.J.M. (1993). "Computerized tomography analysis of reinforced concrete," *ACI Materials Journal*, Vol. 90, Issue 3, pp. 259-264.

Morgan, I.L., Ellinger, H., Klinksiek, R., and Thompson, J.N. (1980). "Examination of concrete by computerized tomography," *ACI Materials Journal*, Vol. 77, pp. 23-27.

Oesch, T. (2015). "Investigation of Fiber and Cracking Behavior for Conventional and Ultra-High Performance Concretes using X-Ray Computed Tomography," Dissertation. University of Illinois at Urbana-Champaign, Urbana, IL.

Poinard, C., Piotrowska, E., Malécot, Y., Daudeville, L., and Landis, E.N. (2012). "Compression triaxial behavior of concrete: The role of mesostructure by analysis of X-ray tomographic images," *European Journal of Environmental and Civil Engineering*, Vol. 16, pp. S115-S136.

Pujadas, P., Blanco, A., Cavalaro, S.H.P., de la Fuente, A., and Aguado, A. (2014a). "Multidirectional double punch test to assess the post-cracking behavior and fibre orientation of FRC," *Construction and Building Materials*, Vol. 58, pp. 214-224.

Pujadas, P., Blanco, A., Cavalaro, S., and Aguado, A. (2014b). "Plastic fibres as the only reinforcement for flat suspended slabs: Experimental investigation and numerical simulation," *Construction and Building Materials*, Vol. 57, pp. 92-104.

Roth, J.M., Rushing, T.S., Flores, O.G., Sham, D.K., and Stevens, J.W. (2010). "Laboratory Investigation of the Characterization of Cor-Tuf Flexural and Splitting Tensile Properties," Technical Report, *ERDC/GSL TR-10-46*. U.S. Army Engineer Research and Development Center, Vicksburg, MS.

Smith, J., Cusatis, G., Pelessone, D., Landis, E., O'Daniel, J., and Baylot, J. (2014). "Discrete Modeling of Ultra High Performance Concrete with Application to Projectile Penetration," *International Journal of Impact Engineering*, Vol. 65, pp. 13-32.

Stock, S.R., Naik, N.K., Wilkinson, A.P., and Kurtis, K.E. (2002). "X-ray microtomography (microCT) of the progression of sulfate attack of cement paste," *Cement and Concrete Research*, Vol. 32, No. 10, pp. 1673-1675.

Thales Electron Devices. (2003). *FlashScan 35 Flat Panel Imaging System*, User Manual, Version 5.0.3.

Trainor, K.J. (2011). "3-D Analysis of Energy Dissipation Mechanisms in Steel Fiber Reinforced Reactive Powder Concrete," Thesis, University of Maine, Orono, ME.

Trainor, K.J., Foust, B.W., and Landis, E.N. (2013). "Measurement of Energy Dissipation Mechanisms in the Fracture of Fiber-Reinforced Ultrahigh-Strength Cement-Based Composites," *Journal of Engineering Mechanics*, Vol. 139, No. 7, pp. 771-779.

Williams, E.M., Akers, S.A., and Reed, P.A. (2006). "Laboratory Characterization of SAM-35 Concrete," Technical Report, *ERDC/GSL TR-06-15*. U.S. Army Engineer Research and Development Center, Vicksburg, MS.

Williams, E.M., Graham, S.S., Reed, P.A., and Rushing, T.S. (2009). "Laboratory Characterization of Cor-Tuf Concrete With and Without Steel Fibers," Technical Report, *ERDC/GSL TR-09-22*. U.S. Army Engineer Research and Development Center, Vicksburg, MS.

Session 309

From 3D X-ray micro tomography images of porous materials to pore network: Image processing and fluid flow modelling

D. BERNARD*[1,2], N. COMBARET[3], J. LESSEUR[1,2], A.K. DIOUF[1,2], E. PLOUGONVEN[4]

[1] CNRS, ICMCB, UPR9048, F-33608 Pessac, France – bernard@icmcb-bordeaux.cnrs.fr
[2] Univ. Bordeaux, ICMCB, UPR9048, F-33608 Pessac, France – lesseur@icmcb-bordeaux.cnrs.fr
[3] FEI, Visualization Science Group, F-33708, Mérignac, France – Nicolas.Combaret@fei.com
[4] Univ. Liège, Lab. Chemical Engineering, B-4000, Liège 1, Belgium – eplougonven@ulg.ac.be
* presenting author

Keywords: X-ray micro tomography, pore space partitioning, flow in porous media, pore network model.

Abstract

A robust pore space partitioning approach is presented for 3D images of porous media in relation with pore network modelling of pore scale fluid flow. The porels (i.e. pore elements) are precisely delimited and a solution for the cases where a separating surface is shared by more than two porels is proposed. The existence of a linear relation between local pressure drop and local fluid flow is demonstrated, but the uniqueness of the linear coefficients is not proved. Numerical tests are exposed to enlighten this fundamental problem.

Introduction

Pore network models (PNM) are widely used to study transports in porous media at the pore scale. The basic idea is that the intrinsic complexity of porous media can be addressed considering a large number of simple elements (the pores) connected through simple rules. Most of the PNM are based on building blocks having predetermined geometries positioned on regular grids. Now that 3D imaging techniques like X-ray computed macro tomography allow very precise representations of pore space geometry, it is logical to try building PNM directly from 3D images. But, even if 3D images are now easy to obtain, this appears to be still difficult.

Skeletonization

The starting point of the methodology presented in this text is a 3D binary image of a porous sample. To decompose the pore space in pores, a definition of what is a pore is necessary. Stating a strict definition effective for any 3D voxelized image is very difficult and here we only postulated that at any intersection of possible flow paths there is a porel (pore space element). Skeletonization appears as the natural tool to detect these intersections. Existing algorithms are generally based on homotopic thinning that produces a skeleton defined as a homotopic subset, of lesser dimensionality, of the pore space. Recent works in the field of discrete geometry clarified the mathematical framework and skeletonization can be considered as a reliable process. The main drawback of skeletonization is its sensitivity to noise. The noise affecting binary 3D images obtained by segmentation of noisy grey level images can produce different topological artefacts (surfaces, multiple branches, etc.) that are generally attenuated using classical morphological filters. A different approach has been selected here: all the cases where a single voxel generates a 0D, 1D or 2D artefact have been identified and filtering a 3D image consists in deleting the corresponding voxels present in the image. This approach is more efficient than classical filtering as only voxels producing skeleton artefacts are removed [E. Plougonven & D. Bernard, 2011].

Graphs construction

From the clean skeleton it is easy to detect the junction points and localize the porels. Discrete nature of the images can induce multiple junctions in the same compact volume, giving an over-partitioning. This is solved defining merging rules between identified porels. Once the number and location of porels are determined, the porel volumes are constructed using a watershed algorithm. The resulting pore space partition covers entirely the pore space and the intersections of its elements (porels) are surfaces. The skeleton can be directly used to build the graph corresponding to the future pore network. Unfortunately this graph is not correct in cases where more than two porels share a limiting surface (Fig. 1). In order to handle these cases as well as the porels at the boundaries of the domains, a new graph is built directly from the partition to construct the PNM [E. Plougonven et al., 2015].

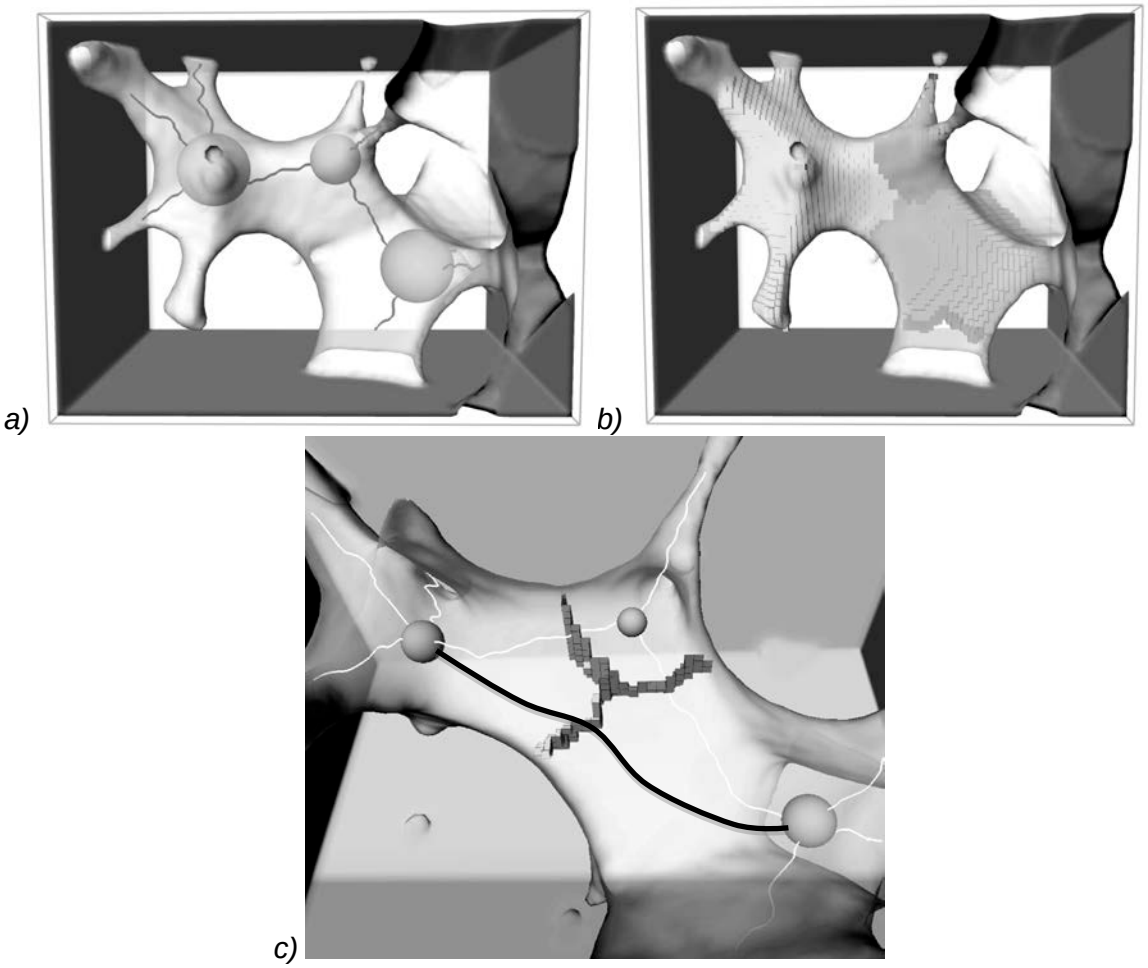

Fig. 1. *Example of the pairwise connection problem: a) Portion of the pore space extracted from an image obtained by synchrotron micro-tomography of a glass beads packing during sintering. The skeleton is represented by the continuous line and the centre of the different porels by solid balls. b) Representation of the three reconstructed porels. c) Superposition of the surface separating the three porels represented in b, of the skeleton (white line) and of the porels centres (solid balls). It is obvious that one connexion is lacking between the two lower porels. To solve this problem, a new branch is added to the graph (black line) modifying the topology of the network, but insuring that all the identified porels having connections are effectively connected.*

Flow modelling

The graph built as presented above is composed of nodes (the porels centres) and branches connecting porels. To compute the permeability of the porous sample, the Stokes equations are integrated, over porel volumes for mass conservation, and along the connecting branches for momentum conservation. It is easy from these integrations to prove the existence, but not the uniqueness, of the coefficients linking the local pressure drop and the local flow rates, and from that obtain the linear system to be solved for permeability evaluation.

Assuming the uniqueness of these coefficients, a procedure allowing computing them solving a local flow problem has been developed. To explore the crucial problem of uniqueness, we compared, for different pore scale geometry, the results provided by the PNM and by direct numerical modelling of the flow at the global scale, i.e. through the entire domain. A first series (Fig. 2) has been produced in order to be easily represented by a PNM, at least at the beginning.

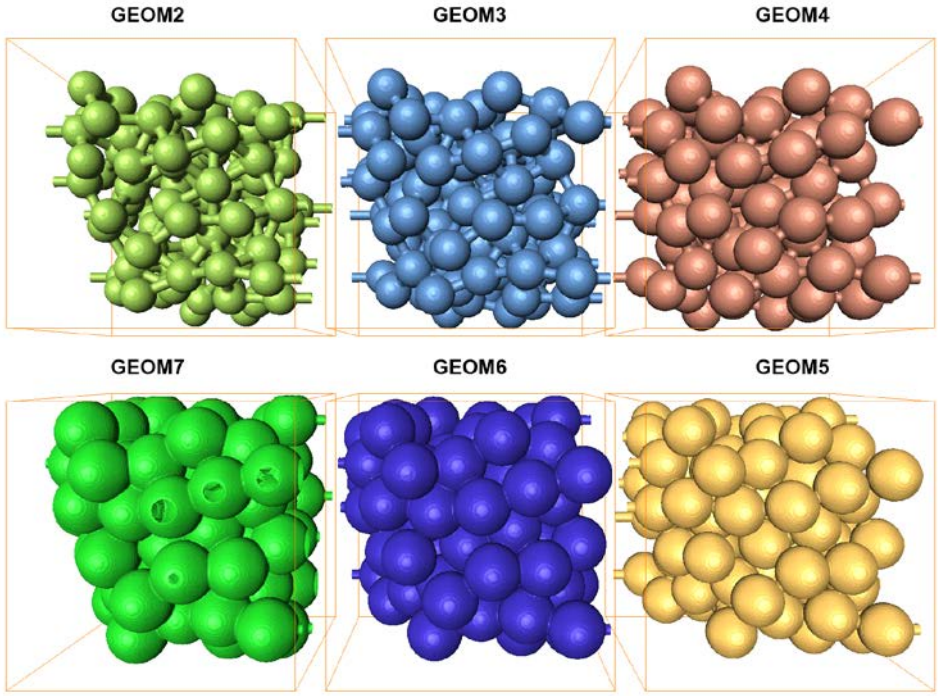

Fig. 2. *First series of geometry used to compare direct numerical modelling and PNM results. The basic geometry is the same for all (i.e. GEOM2) and the size of the spherical porels is slowly increased step by step.*

The agreement between both numerical approaches is very good (Fig. 3) even when the spherical pores have an important overlap (GEOM6). The interpretation of this agreement is linked to one decisive characteristics of the local flow; induced local pressure drop is mainly localized at the throats between large volumes at an almost constant pressure. This is not always verified in real porous media and another series of tests began on a different kind of geometry (Fig. 4).

The expected results will enlighten the theoretical unsolved problem of uniqueness introduced above. It seems that even if the uniqueness of the linear coefficients between local pressure drops and fluid flows is not proved, it can be assumed for some kinds of porous media. In these cases, the numerical method we proposed to compute those coefficients can be considered as a reference method to evaluate other approximate models.

For all the different geometry we tested, the partitioning methodology we developed gave very good results proving its robustness even for complex cases.

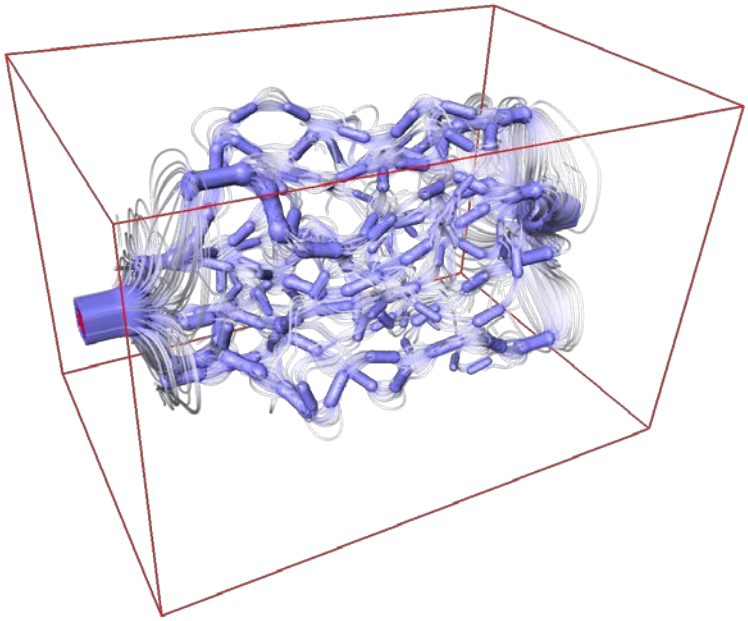

Fig. 3. *Visualization of the flow field obtained by direct numerical modelling for GEOM2.*

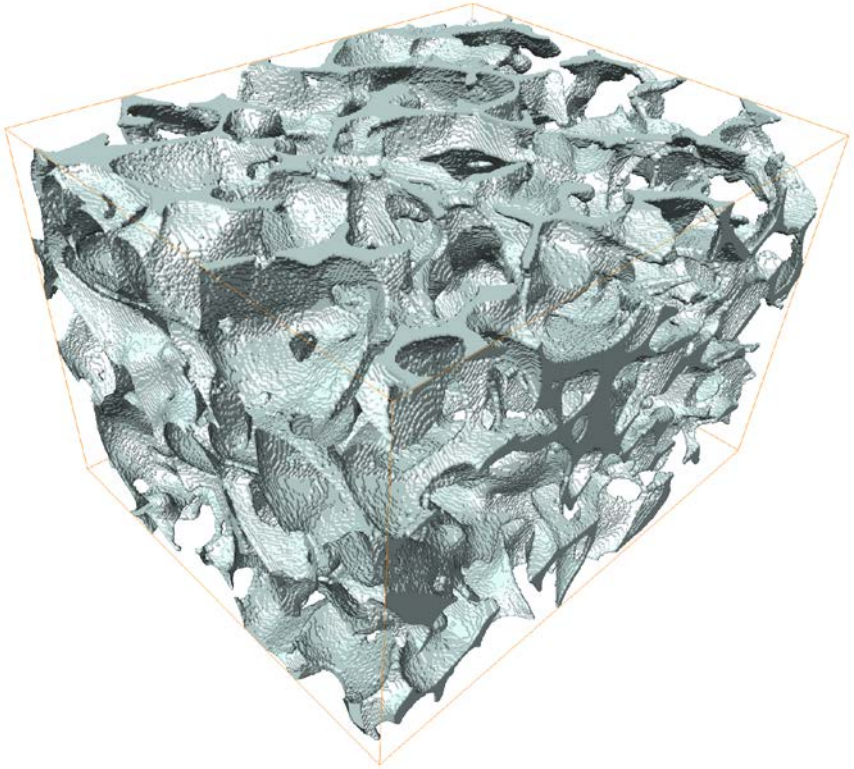

Fig. 4. *More complex pore scale geometry under test.*

References

Plougonven E. & Bernard D. (2011). Optimal removal of topological artefacts in micro tomographic images of porous materials. ***Adv. water Res.*** 34, 731-736.

Plougonven E., Combaret N. & Bernard D. (2015). An overview of pore space partitioning methods for network model generation from micro tomographic data. ***Submitted***

Phase-contrast synchrotron X-ray fast tomography of wicking in yarns

*M. PARADA[1,2], D. DEROME[2], R. M. ROSSI[3], J. CARMELIET[1,2]

[1] Chair of Building Physics. ETHZ, Swiss Federal Institute of Technology in Zurich. Stefano-Franscini-Platz 5, 8093 Zürich, Switzerland.
[2] Laboratory for Multiscale Studies for the Built Environment. Empa, Swiss Federal Laboratories for Materials Science and Technology. Überlandstrasse 129, 8600 Dübendorf, Switzerland.
[3] Laboratory for Protection and Physiology. Empa, Swiss Federal Laboratories for Materials Science and Technology. Lerchenfeldstrasse 5, 9014 St. Gallen, Switzerland.

* presenting author

Keywords: textiles, yarns

Abstract

Wicking is the flow of liquids in textiles due to capillary forces. At the smallest scales wicking occurs inside single yarns, i.e. bundles of fibers twisted together. We used synchrotron X-ray micro tomography with short exposure time to document the phenomenon at the yarn scale in a time-resolved manner. Moisture quantification is possible as exemplified here by analysis of polyester yarn.

Introduction

Understanding wicking in textiles is fundamental to prevent injuries related to inappropriate moisture management in specialized garments, such as firefighter protection (e.g. steam burns, (Keiser 2007)), hospital bed sheets (e.g. decubitus (Derler et al. 2012)) and soldier's apparel (e.g. blisters (Baussan et al. 2012)). The transport of liquids in textile materials is a multi-scale phenomenon ranging from the yarn to the multi-layer clothing assembly. To properly investigate wicking it is necessary to study the phenomenon in all of its scales. In this study we present the results of an experiment where the imaging of wicking at the smallest scale (i.e. yarns) was achieved.

There are three challenges for the imaging of the wicking phenomenon in yarns:

a) The yarn complex geometry consists of a bundle of individual fibers twisted together. These fibers are usually made of a flexible synthetic or natural polymer and the interaction with the wicking liquid may result in a changing geometry depending on saturation level or short intertwined natural fibers, e.g. cotton, that can adsorb moisture and swell, further changing the geometry.
b) The wicking process starts with the wetting of the fibers, followed by a film formation and, if the fibers are close together, the formation of a meniscus that advances between the fibers within the yarn. This is a relatively fast process that happens in a relatively small length scale.
c) The fiber materials investigated are hydro-carbon-based polymers and the liquid tested is water, all of these are 'light' materials (i.e. low atomic number) with low X-ray absorption, resulting in poor contrast.

The technique applied in this study, namely synchrotron based phase contrast fast X-ray tomography, is able to overcome these challenges.

Materials

Yarns of four fiber types—cotton, polyester (polyethylene terephtalate, PET), polyamid (PA) and polypropylene (PP)—were investigated. We chose synthetic yarns with circular cross section, similar number of fibers (between 32 and 34 for circular cross section) and twisting levels between 100 and 300 tpm (turns per meter). For PP yarns

we also used different cross sections. Both cotton types used have twisting levels of 800 and 1000 tpm. A summary of the investigated samples can be found in **Table 1**.

Each sample was manually washed with a neutral detergent and rinsed with deionized water to remove any lubricant remaining from the manufacturing process. After drying for at least 24 hours at 25°C and 35% relative humidity, the samples were assembled in the holder depicted in **Fig. 1** and kept at the same conditions until the experiment.

The sample holder consists of a Kapton tube and a reservoir, with the sample yarn held in place by two screws (bottom and top of sample holder). Four holes in the base of the tube allow contact between the liquid and the sample.

Methods

The experimental setup is a vertical uptake of deionized water. The liquid is brought to the reservoir with a syringe in a syringe pump operated remotely. Ambient temperature and relative humidity are monitored during the experiment.

The experiment was performed at TOMCAT (Tomographic Microscopy and Coherent rAdiology experimenTs) beamline at the synchrotron light source (SLS) at the Paul Scherrer Institute (PSI) in Villigen, Switzerland. More details about the facility can be found in (Stampanoni et al. 2006).

First, a dry tomograph of the sample is captured. Then, the sample starts rotating and acquisition starts in stand-by mode, i.e. projections are monitored and recording is not yet started. Next, the liquid is poured in the reservoir by a remotely controlled syringe pump. The projection images are monitored in real time to identify the coming of the water front. As soon as the water is identified in the field of view the experimenter starts recording. Circular buffer was enabled allowing the recording of time steps before the trigger.

The beam energy is set at 14 keV. Exposure time is 1 ms for each projection, with 300 projections for a full tomography, resulting in a time resolution of 0.3 s. Total acquisition for each sample is 130 full tomographs, resulting in 39 s. The pixel size of the setup is 3.16 µm and the field of view covered 5 mm of the sample (with a 1.2 mm width).

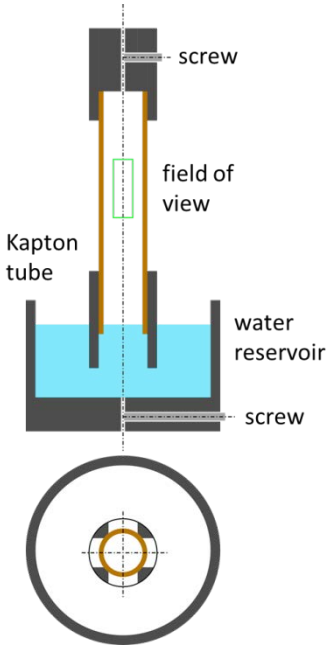

Fig. 1: *Schematic representation of sample holder (not to scale). Top: Side cross section. Bottom: Reservoir horizontal cross section. Yarn suspended in the middle (along central axis) and held by two screws. Four holes at the base allow contact with water. Field of view marked in green. Water brought to reservoir during experiment with a syringe.*

The propagation-based phase contrast images were reconstructed using Paganin algorithm.

Analysis

The samples were segmented using a threshold value that identified both the fibers and the water. The first (dry) image was used as a reference. Since the fiber size did not change during the experiment, by subtraction of the reference image, it was possible to identify the volume of liquid at each height and time step.

All the analysis was done using MATLAB software as well as ImageJ.

As an example, cross sections of PET yarn with 300 tpm at different heights and different time steps can be seen in **Fig. 2**.

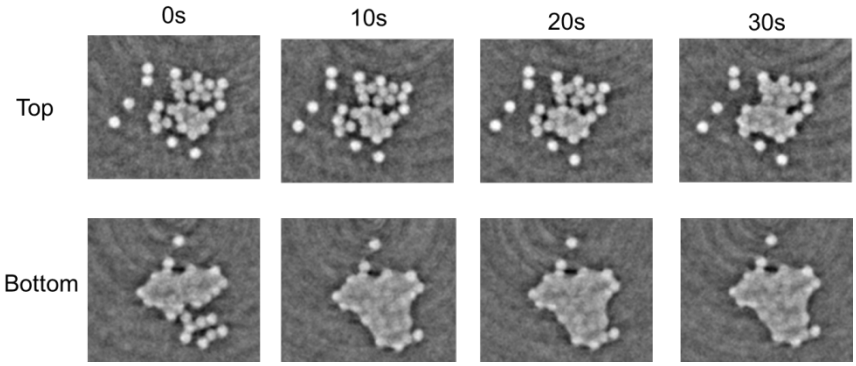

Fig. 2: *PET yarn cross sections during wicking. Top and bottom slices at different time steps.*

With the volume of water and density, moisture content can be calculated. A plot of moisture content versus time for the PET yarn is shown in **Fig. 3**.We see an evolution of the moisture content that happens in small jumps. One possible explanation could be a film formation preceding the meniscus formation.

The images in **Fig. 2** show that a thin column of liquid is present in the middle of the sample even at the beginning of imaging but the bulk of the transport comes later enveloping almost all fibers. This thin column can also be indirectly seen in **Fig. 3** because the initial moisture content is not zero. Wicking imaging techniques that detect the surface liquid only (e.g. visible light technique with colorants) The presence of an initial, almost instantaneous, thin liquid column at the core of the yarn followed by a larger column that wets almost all fibers puts into question whether other imaging techniques that only detect the liquid at the surface (e.g. using a colorant and visible light illumination) would be capable of detecting this initial, close to the center, liquid rise.

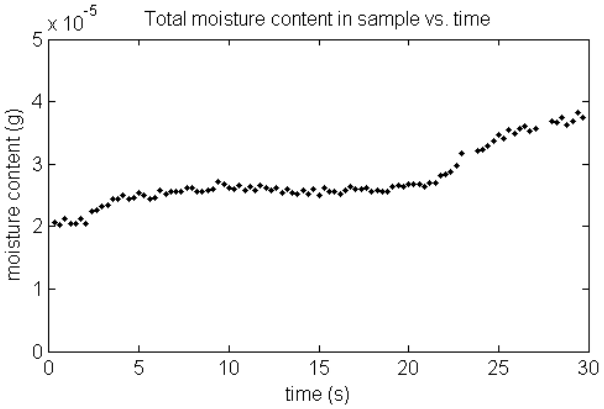

Fig. 3*: Moisture content versus time for full FOV of PET yarn.*

Table 1: Yarn characteristics

Material	Cross section	Number of fibers	Twisting level (tpm)
Cotton (natural brown)	Natural	-	800, 1000
Cotton (natural white)	Natural	-	800, 1000
PET	Circular	32	100, 200, 300
PA	Circular	34	100, 200, 300
PP	Circular	33	110, 230
	Hollow circular	43	110, 230
	Triangular	33	110, 230
	Tetra channel	43	110, 230

References

Baussan, E. et al. (2012). *Analysis of current running sock structures with regard to blister prevention*. **Textile Research Journal**, 83(8), 836–848.

Derler, S. et al. (2012). *Medical textiles with low friction for decubitus prevention*. **Tribology International**, 46(1), 208–214.

Keiser, C. (2007). *Steam burns moisture management in firefighter protective clothing*. PhD Thesis, ETH Zurich.

Stampanoni, M. et al. (2006). *Trends in synchrotron-based tomographic imaging: the SLS experience*. Proc. SPIE 6318, Developments in X-Ray Tomography V.

Neutron imaging of coupled deformation and fluid flow in sandstones

E. TUDISCO[1], *S.A.HALL[1,2], J. HOVIND[3], N. KHARDJILOV[4], E-M. CHARALAMPIDOU[5], H. SONE[6]

[1] Division of Solid Mechanics, Lund University, Lund Sweden
[2] European Spallation Source AB, Lund, Sweden
[3] Paul Scherrer Institute, Villigen, Switzerland
[4] Helmholtz Zentrum Berlin, Germany
[5] Institute of Petroleum Engineering, Heriot Watt University, Edinburgh, UK
[6] GFZ-Potsdam, Germany

* presenting author

X-ray tomography, in combination with Digital Volume Correlation (DVC), has been used in a number of recent geomechanics investigations to map the 3D heterogeneity of strain fields inside test samples, either during loading ("in-situ" tests performed with the loading device mounted within the imaging set-up) or with imaging before and after loading (pre-/post-mortem tests). In such studies, in-situ measurements have mostly been performed on sand and clays at low confining pressures. However, the poor penetration of x-rays through triaxial pressure cells capable of sustaining elevated fluid pressures limit the use of x-ray imaging for in-situ rock testing. This restriction is reduced by using neutron instead of x-ray imaging, as neutrons are more able to penetrate the metal confining vessels. Furthermore, the high sensitivity of neutrons to hydrogen makes them very useful to study water (or other hydrogen-rich fluid) related phenomena, which paves the way towards coupled deofrmation and fluid-flow studies.

In this work, the use of neutron imaging to measure deformation in sandstone samples and the resultant effect on fluid flow are explored using both pre-/post-mortem and in-situ testing. New results will be presented demonstrating the use of time-lapse neutron tomography in combination with DVC to provide 3D strain field mapping in deformed (pre-post-mortem imaging) and deforming (in-situ tests) sandstone specimens. Furthermore, analysis of fluid flow evolution through the same specimens will be presented. The coupling of the full-field deformation and flow mapping provide previously-inaccesible insight into how fluid-flow properties are changed in the regions where the most significant deformation is actually occuring, as opposed to measuring just bulk changes.

Number of words: 260

Microcomputed tomography as a tool during the development of pharmaceutical tablets

JERRY KLINZING[1*]

[1] Merck Research Laboratories, West Point, PA, USA – gerard.klinzing@merck.com
* presenting author

Keywords: microCT, density distributions, wall thickness, bilayer tablets

Abstract

Porosity in the size range of nanometers to micrometers can be found in the starting and intermediate materials as well as in the final marketed products for most pharmaceutical tablets. Understanding the processing-porosity-property relationships is of the upmost importance to insure robust processing and a quality final product. Microcomputed tomography (microCT) has been used in pharmaceutical development to assess pore density and pore sizes of materials in order to develop this relationship. Moreover, microCT has proven to be invaluable in optimizing process parameters for various unit operations. Several key case studies are discussed where the use of microCT aided in i) validating porosity distributions from numerical models, ii) measuring pore size and pore density of foam extruded materials, iii) and identifying the root cause of bilayer tablet defects.

Introduction and Methods

Based on a review of literature over the past decade, the use of microCT in the characterization of pharmaceutical materials has become increasingly prevalent. MicroCT has been used to study the porosity of tablets and granules at varying levels of detail from macropores to micropores [1], [2]. The study of swelling kinetics of pharmaceutical tablets has been characterized with the use of tracking beads [3]. In addition, microCT has helped establish that swelling stresses cause cracking in bilayer tablets when exposed to elevated humidity [4]. MicroCT has been used extensively to validate porosity distributions of finite element models of powder compaction [5]. The work presented here shows several examples where microCT has been used in novel ways to characterize pharmaceutical materials and diagnose production issues which have not been widely discussed in the literature.

Imaging was performed on the Zeiss XRadia Versa XRM500 microcomputed tomography machine. The source voltage and power settings were varied between 80-100kV and 7-9W depending on the x-ray absorption. A 0.4x and 4x objective lens was used throughout scanning without the use of a source filter. Images were acquired using a 2048x2048 pixel CCD detector at bin 2 (1024x1024 pixels). Dynamic ring removal (DDR) was utilized throughout all scans. Image analysis and post processing was performed with the commercial software Avizo Fire 8.

Results

i. Using microCT to validate finite element modeling of powder compaction with tablet embossing

Finite element modeling (FEM) of powder compaction allows for relative density (RD) predictions within tablets of different shapes and sizes (RD is equal to 1-porosity of the tablet). This current work shows the use of FEM to quantitatively predict the 3D relative density distributions within an embossed tablet. A model material, microcrystalline cellulose, was numerically compressed to 55MPa and analyzed for RD distributions.

Figure 1a shows RD distributions through a cross section of one half of the tablet. The color scale represents RD distributions predicted from the numerical model where regions of blue represent low RD and red present high RD. Compaction was performed in a uniaxial manner in which only the upper punch moves resulting in the asymmetric RD gradient through the band/thickness of the tablet as seen by high RD regions towards the upper edge of the tablet. In addition, regions of low RD are found surrounding the embossing to a depth equal to the embossing. The regions at the surface of the tablet, indicated by arrows, are low RD regions which could pose a potential risk for sticking or picking, which are common compression related process failure modes. Validation of the numerical RD prediction was performed by scanning a tablet along with several calibration tablets compressed to known densities under ideal frictionless conditions. Figure 1b shows a color rendition of the RD distributions within the tablet which is in excellent agreement with the FEM model (note that the color scale bar is descriptive for both the FEM results and microCT results). Based on the microCT validation, FEM has been used to aid in the design of compression tooling.

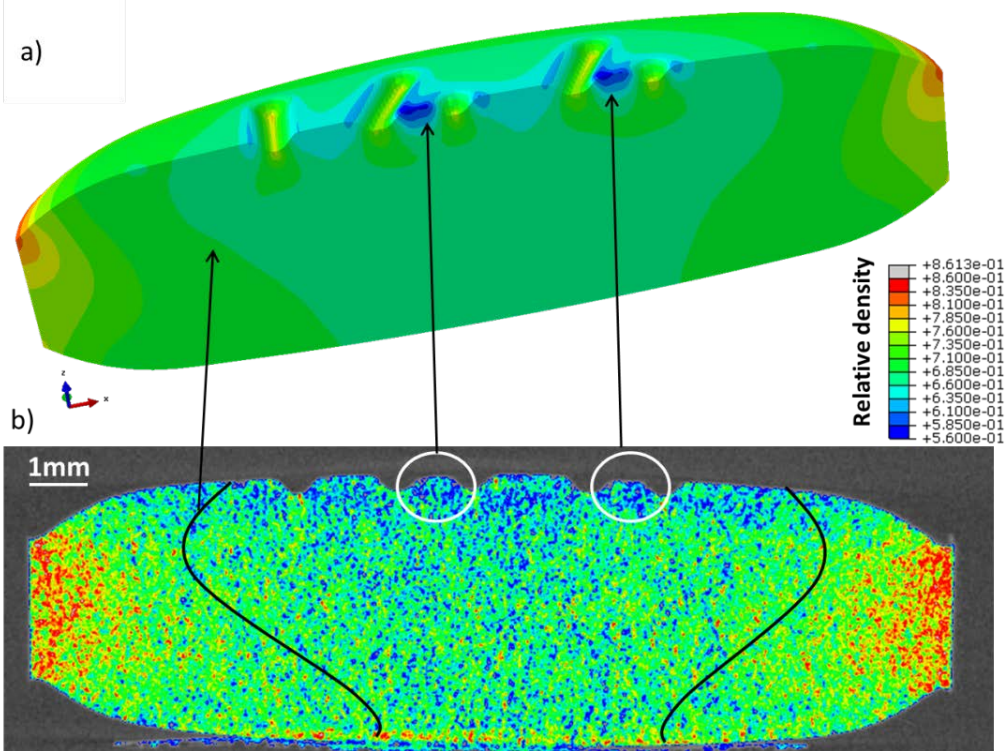

Figure 1. a) FEM model showing the RD distribution through a cross section of the center of the tablet and b) the microCT results showing the measured RD distributions.

ii. Characterizing foam materials with the use of microCT

In an effort to better understand the processing-property-porosity relationship of extruded cylindrical foam rods, microCT was utilized to measure quantitatively the pore density and pore size. Figure 2a/b show cross sections through the diameter of foam 1 and foam 2, respectively. These two foams have identical composition but were extruded under different processing conditions. Figure 2c/d show cross sections along the direction of extrusion for foam 1 and foam 2, respectively.

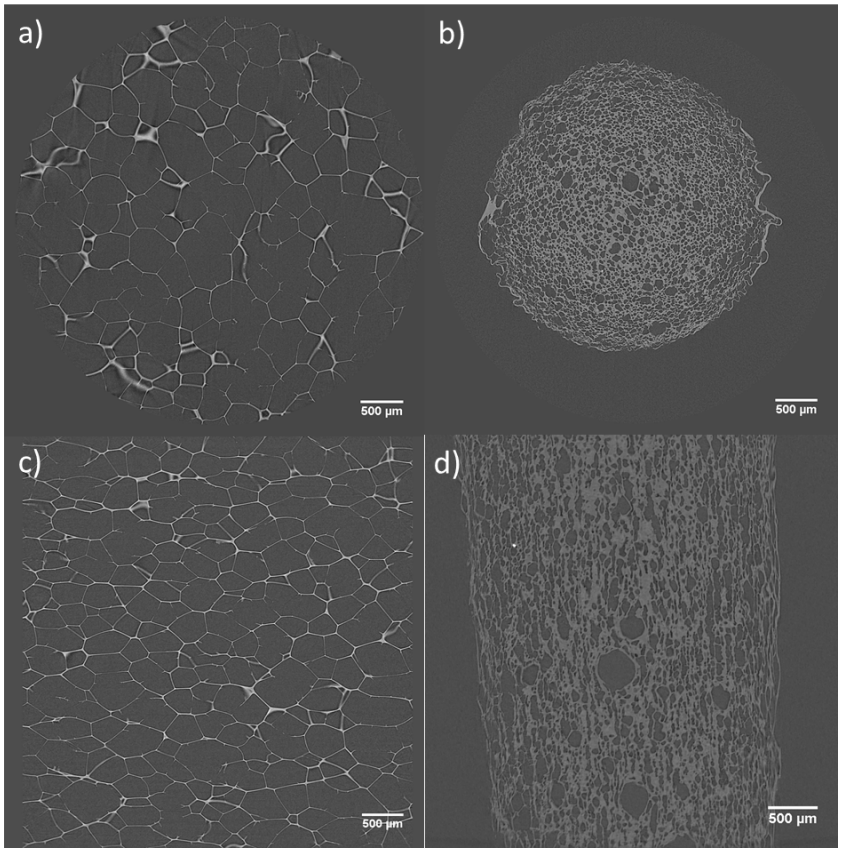

Figure 2. Cross sections of extruded foam rods, a)-b) are cross sections through the diameter of Foam 1 and Foam 2, respectively, and c)-d) are cross sections through the extrusion direction of Foams 1 and Foam 2, respectively. Scale bar is 500µm.

The change in processing conditions shows a dramatic reduction in pore size (average equivalent pore radius) and an increase in pore density as shown in Table 1. In addition, along the direction of extrusion foam 1 shows relatively isotropic pores, whereas for foam 2 the pores are narrower and align with the direction of extrusion.

Table 1. Foam properties measured with Avizo and ImageJ->BoneJ (+/- indicates standard deviation).

Sample	**Foam 1**	**Foam 2**
Pore density (pores/mm^3)	~50	~1450
Average equivalent pore radius (µm)	135.4 (+/- 72.8)	31.8(+/- 20.1)

Image analysis was performed in Avizo Fire 8. The equivalent pore radius was calculated by assuming a spherical pore geometry and using the pore volume measured by Avizo Fire 8 to back calculate pore radius. The measurement technique was sensitive to the thresholding applied during the binarization process and results of pore density and average equivalent pore radius could change dramatically based upon this process. To understand the relationship between structure and property, the foam rods were milled into primary particles, compressed into tablets at 200MPa compressive stress,

and measured for tensile strength by diametrical compression. Results of the strength test are shown in Table 2. The strength of the resulting tablet made from the foam with larger pores and less pore density resulted in the higher strength. An increase in pore density drastically reduced the resulting tablet strength. Additional studies on foams produced at varying processing conditions will be performed to better understand the relationship between tablet strength and pore size/pore density.

Table 2. Tablet tensile strength of milled foams compressed to 200MPa compressive stress and tested in diametrical compression.

Sample	**Foam 1**	**Foam 2**
Tablet tensile strength (MPa)	4.6	1.8

iii. Identifying root cause of bilayer tablet defects with microCT

Bilayer defects such as interfacial cracking and delamination are well known problems within the pharmaceutical industry [4], [6]. Processing conditions and material properties influence the likelihood of defect formation during compression and post compression storage or handling. However, defect formation due to press vacuum conditions has not been studied previously. Bilayer tablets produced on a rotary tablet press with normal press vacuum conditions showed signs of interfacial cracking upon visual inspection. The size and extent of cracking was deemed acceptable for further development and scale-up; however, issues relating to improper quantity of drug in each layer were observed.

MicroCT was utilized to visualize the integrity of the interface throughout the tablet. It was discovered that the bilayer interface became compromised with the use of normal press vacuum (Figure 4 a/ b). In this situation, the lower layer (darker phase) had part of the first layer tablet apex removed via vacuum during production. The dashed line in Figure 4a/b illustrates the region where the cup of that first layer should exist. Tablets produced with the non-optimal press vacuum resulted in a lower than desired quantity of drug in layer one and a greater than desired quantity of drug in layer 2 (top layer). Titration of the vacuum level was achieved and the cup remained intact during compression and bilayer tablets were made successfully and within release specifications as shown in Figure 4c/d.

Furthermore, cracking that was observed along the interface of the bilayer (Figure 4b) was reduced with the optimization of press vacuum level (Figure 4d). It was also observed that the crack no longer penetrated along the interface but deflected into layer 1. This observation provided justification for further study of the material properties and process parameters of layer 1 to help reduce this type of cracking. Ultimately, the problem described above could not have been identified without the use of microCT because tablets shown in Figure 4a/b and c/d look identical upon visual inspection and are indistinguishable with the use of in-process weight measurements.

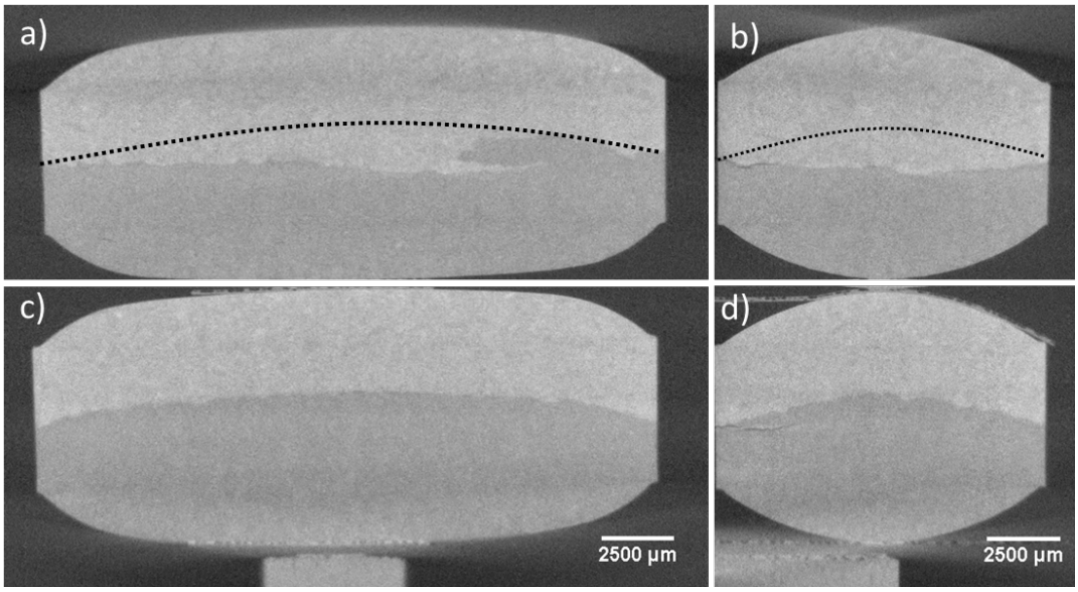

Figure 3. Cross sections of bilayer tablets. Images a) and c) show a cross section along the long axis of a bilayer tablet and b) and d) show a cross section along the short axis of the tablet. Images a/b are the same tablet with the use of press vacuum and c/d are the same tablet with the optimized press vacuum.

Conclusions

MicroCT, in combination with the use of quantitative image analysis software, has proven to be an invaluable technique for quantifying porosity distributions in tablets, understanding how process-property relationships of foams correlates to tablet strength, and identifying root causes of cracking during bilayer processing. The use of microCT provided a non-destructive and efficient method of material characterization in which other techniques would have compromised the integrity of the sample and possibly altered the results.

References

[1] L. Farber, G. Tardos, and J. N. Michaels, “Use of X-ray tomography to study the porosity and morphology of granules,” *Powder Technol.*, vol. 132, no. 1, pp. 57–63, 2003.

[2] I. C. Sinka, S. F. Burch, J. H. Tweed, and J. C. Cunningham, “Measurement of density variations in tablets using X-ray computed tomography,” *Int. J. Pharm.*, vol. 271, no. 1–2, pp. 215–224, Mar. 2004.

[3] P. R. Laity, M. D. Mantle, L. F. Gladden, and R. E. Cameron, “Magnetic resonance imaging and X-ray microtomography studies of a gel-forming tablet formulation.,” *Eur. J. Pharm. Biopharm.*, vol. 74, no. 1, pp. 109–19, Jan. 2010.

[4] G. Klinzing and A. Zavaliangos, “Understanding the effect of environmental history on bilayer tablet interfacial shear strength.,” *Pharm. Res.*, vol. 30, no. 5, pp. 1300–10, May 2013.

[5] I. C. Sinka, J. C. Cunningham, and a Zavaliangos, “Analysis of tablet compaction. II. Finite element analysis of density distributions in convex tablets.,” *J. Pharm. Sci.*, vol. 93, no. 8, pp. 2040–53, Aug. 2004.

[6] F. Podczeck, “Theoretical and experimental investigations into the delamination tendencies of bilayer tablets.,” *Int. J. Pharm.*, vol. 408, no. 1–2, pp. 102–12, Apr. 2011.

Study on the effects of porous structure on carbon composites manufacture based on synchrotron X-ray CT imaging and 3D visualization analysis

Nicholas Vito[1], Ming Lei[1], Jeremy Olson[2]

[1] FEI, Houston, USA

[2] Canadian Light Source Inc., Saskatoon, SK, Canada

Abstract

Studying porosity in composite materials will aid in understanding the manufacturing process and lead to more efficiently produced, longer lasting materials. In this experiment, the microstructure of an uncured and cured composite was characterized using the combination of high energy synchrotron-based CT experiments with powerful image analysis software, Avizo, to generate detailed 3D images along with quantitative data. The methodology discussed here is also applicable to other materials when measuring phase fraction or porosity.

1. Introduction

Carbon fiber composites are being developed for use in a wide variety of applications ranging from sports equipment to aerospace structures. Studying how the porous structure changes during the manufacturing process plays an important role in making better materials with enhanced properties, such as better interlaminar shear strength and elastic modulus. Using the synchrotron CT capabilities at the Canadian Light Source (CLS), we were able to non-destructively inspect the carbon composites.

The Biomedical Imaging and Therapy Facility (BMIT) at the Canadian Light Source is a multi-technique facility that has been designed to address unsolved problems in medicine, agriculture and other biomedical sciences [1]. Taking advantage of the beamline tunability, the high brilliance and the variety of imaging modalities, the Industrial Science team at the CLS has found strong applications of the beamline for CT imaging of materials ranging from geological core samples, sand packed columns for modelling oil recovery, and composite materials among many others.

The composite materials analysed for this paper were prepared by the Composites Research Network (CRN) at UBC. The goal of the study is to quantify the differences in pore space between a cured and uncured sample. Using the Avizo software package, bulk and fibrous void space were observed and quantified.

2. Experimental

2.1 Composite Manufacturing

Two samples were studied for this paper. The first sample has undergone no curing process and the data was collected at time = 0. The second sample was cured using an out-of-autoclave process in a vacuum bag at a temperature of 80 °C for 2.23 hours.

2.2 XCT Measurement

Images were acquired at the BMIT-BM beamline of the CLS, which is a third generation, 2.9 GeV storage ring operating at a ring current of 250 mA. The bending magnet beamline in this facility can produce monochromatic or filtered white beam with an energy range of 8 - 40 keV, and a vertical beam size of 200 mm. The brightness of the bending magnet source is 1.5 x 10^{11} ph/s/mr^2/0.1% at 10 keV (1). The composites were prepared by the Composites Research Network at UBC and were cut to approximately 30 mm x 30 mm x 4mm, as shown in figure 1. The samples were mounted onto a 360 degree rotation stage, where 3750 projections were taken every 0.048 degrees for 180° and captured with a Hamamatsu camera with 8.89 µm pixel size.

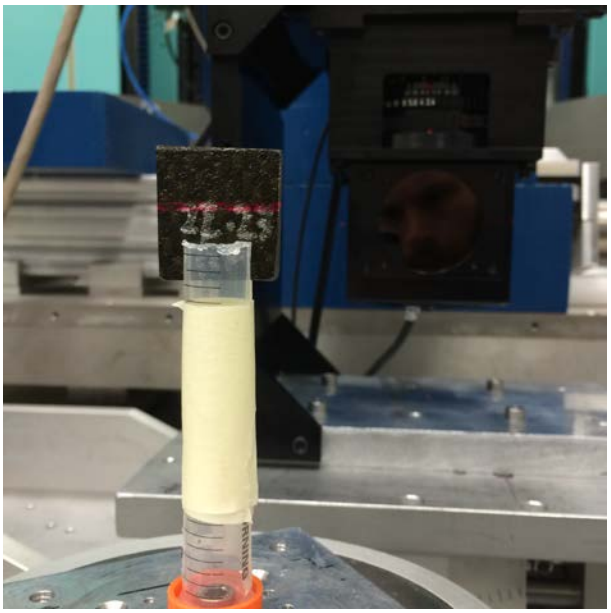

Figure 1. Shows the composite material mounted on a 360° rotational stage on the BMIT-BM beamline at the Canadian Light Source. The red laser line indicates the beam position. The Hamamatsu camera is seen in the background.

2.3 Image Analysis

Avizo 9 was used for image processing and quantification. The voxel data was segmented into four regions: carbon fibers, resin, fibrous pore space, and bulk pore space. To help with segmenting the larger regions, a box filter was applied to reduce the impact of artifacts and intensity variations. The workflow for this segmentation is shown in figure 2. The boundary of the composite sample was determined by a closing operation on a threshold including the fiber and resin regions. The bulk pore

space was then extracted by a lower threshold within the working volume, while the resin and fiber combination by the higher side of the threshold. The carbon fibers were tracked and labeled using interpolation, while the resin was defined by volume excluded from the fibers. Finally, the fibrous pore space was segmented by using a top-hat function [2] which highlights local minima in the voxel data. The segmented data was quantified to determine the volume fraction of the pore spaces.

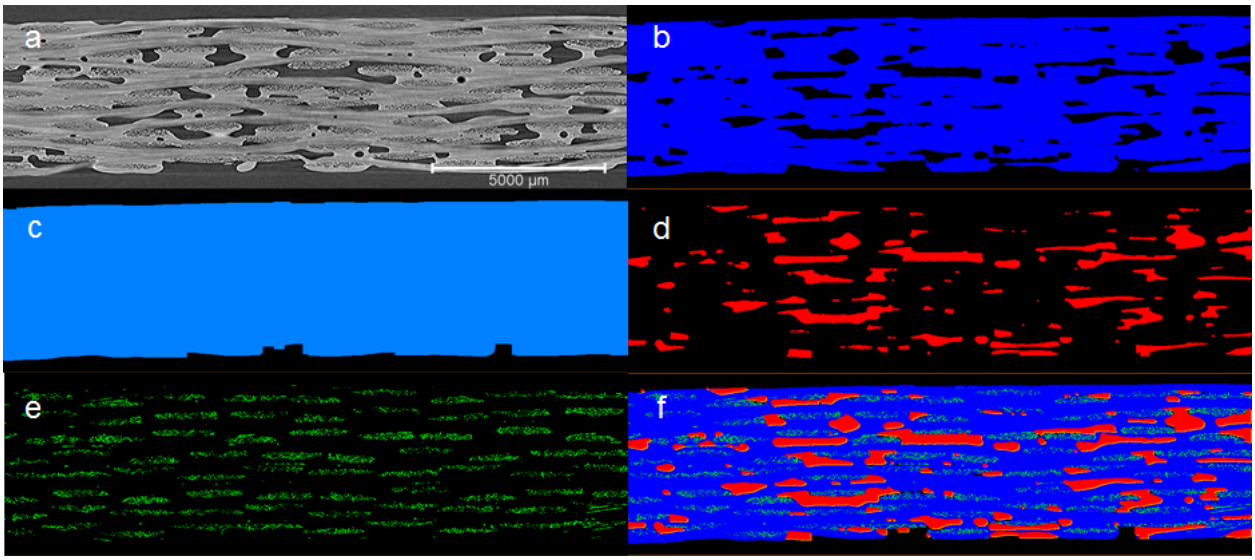

Figure 2. Segmentation workflow in Avizo: (a) grayscale image from synchrotron CT, (b) fiber and resin region by threshold, (c) composite volume mask by closing (b), (d) bulk pore space by threshold, (e) fibrous pore space by top-hat segmentation, and (f) a combination of all segmented regions.

3. Results

The synchrotron CT images from the uncured and cured composites are shown side by side in figure 3, along with a volume rendering. Both composites have 8 layers of fibers; however, the distance separation between the top and bottom layers of the uncured sample is approximately 4.4 mm while the same separation is only 3.1 mm in the cured sample.

The interwoven fiber structure and pore distribution within the volume can be seen in figure 4. The bulk pore space in the uncured sample totaled 16.4% with large, connected pore networks consisting of 91.1% of the total bulk pore volume. After curing, the bulk porosity is reduced to 0.7% with all the porosity being isolated. The average isolated pore size is on the order of 0.02 mm^3 (2 x 10^7 um^3). The fibrous porosity is also reduced during curing from 8.5% in the uncured sample to 1.1% in the cured sample. The ratio of the total porosity to the solid composite in the uncured sample is 33.1% in the uncured sample and 1.8% in the cured sample, relating to a 94.5% reduction in total porosity after the curing step.

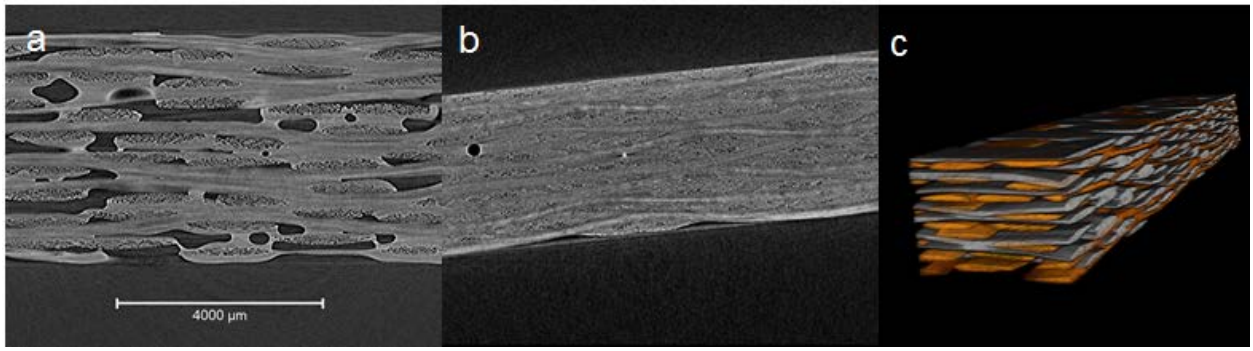

Figure 3. Synchrotron CT image of the (a) uncured and (b) cured composite. (c) Volume rendering of the fiber layers of the cured composite.

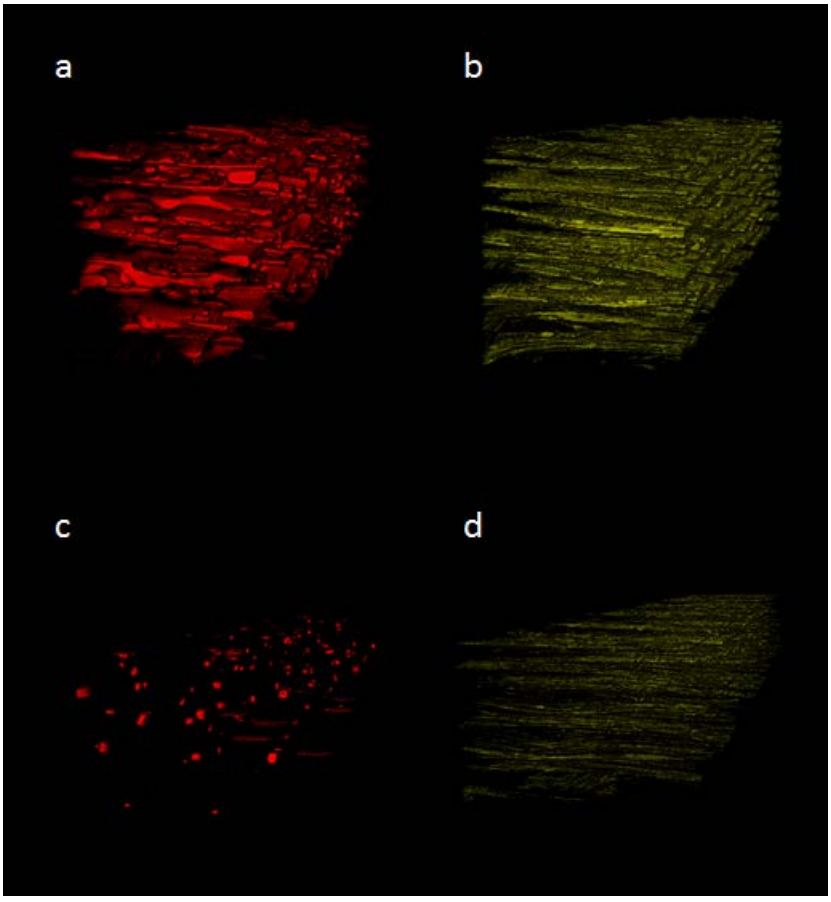

Figure 4. Volume rendering of the (a) bulk and (b) fibrous porosity for the uncured composite and the (c) bulk and (d) fibrous porosity of the cured composite.

4. Conclusion

The proposed workflow allows the study of porosity in composite structures from 3D CT data sets. The composite shows a decrease in both bulk and fibrous porosities after curing. The combination of synchrotron CT and Avizo can determine the size, spatial distribution, connectivity, and volume fraction of the pore space, allowing a better description between material microstructure and physical properties.

Acknowledgement

Research described in this paper was performed at the Canadian Light Source, which is supported by the Canada Foundation for Innovation, Natural Sciences and Engineering Research Council of Canada, the University of Saskatchewan, the Government of Saskatchewan, Western Economic Diversification Canada, the National Research Council Canada, and the Canadian Institutes of Health Research.

Composite preparation was done by Dr. Leyla Farhang at the Composites Research Network at the University of British Columbia.

References

[1] Wysokinski, T.W.; et al. Beamlines of the biomedical imaging and therapy facility at the Canadian Light Source – Part 1. *Nucl. Instrum. Meth. Phys. Res. A.* 2007, 582, 73-76.

[2] Serra J., Image Analysis and Mathematical Morphology, Academic Press, 1983. ISBN 0-12-637240-3

3D detection of damage evolution in porous brittle cement or plaster based materials

T.T. NGUYEN[1,2], C. CHATEAU*[1], M. BORNERT[1], J. YVONNET[2], Q.-Z. ZHU[2]

[1] Université Paris-Est, Laboratoire Navier, CNRS UMR8205, ENPC, IFSTTAR, 6 et 8 avenue Blaise Pascal, 77455 Marne-la-Vallée Cedex, France – camille.chateau@enpc.fr
[2] Université Paris-Est, Laboratoire Modélisation et Simulation Multi Echelle, 5 Bd Descartes 77454 Marne-la-Vallée Cedex 2, France
* presenting author

Keywords: Damage detection, Digital Volume Correlation, In-situ testing, Laboratory tomography

Abstract

This paper presents an approach to detect and extract cracks from computed tomography (CT) images of quasi-brittle heterogeneous materials under in-situ mechanical loading. Using Digital Volume Correlation and associated image subtraction, the crack network and its evolution through the heterogeneous microstructure can be characterised in two different porous materials under compressive loading.

Introduction

The behaviour of many civil engineering materials is governed by damage caused by microcracking phenomena. Their mechanical description is still an open issue, in terms of initiation, propagation or localisation leading to macroscopic ruin. A detailed experimental characterisation of damage and its evolution under mechanical loading is necessary to validate 3D models of crack nucleation and propagation in heterogeneous materials (Nguyen et al., 2015). Such characterisation is made available through X-Ray Computed Tomography (XRCT) combined with Digital Volume Correlation (DVC).

This work presents the in-situ observation of microcracking processes in porous concrete and plaster based materials under compressive loading. Damage location and propagation can be characterised after cracks detection and extraction from the heterogeneous microstructure based on DVC-assisted image subtraction.

Materials

This study focuses on two porous quasi-brittle materials where an evolving damage by microcracking develops under compressive loading. The first sample is an expanded polystyrene (EPS) lightweight concrete (Miled et al., 2007), made from quartz sand (about 1mm average grain size) and EPS beads (2 mm diameter in average) embedded in a cement matrix (see Fig.1a). The high porosity (~20%) of this concrete is suitable for crack initiation at relatively low compressive loads and stable propagation. This material is appropriate to develop specific experimental and modelling tools devoted to heterogeneous microstructures. Nevertheless, a simpler microstructure is also needed for detailed comparisons between these new numerical tools and experimental results. Thus, specific samples composed of a limited and controlled number of EPS beads embedded in an almost homogeneous plaster matrix have been manufactured.

The presented experiments were performed on cylindrical specimens (11.6 mm in diameter and 18.2 mm long for EPS concrete, 8.96 mm in diameter and 18.4 mm long for EPS plaster). While several tests were conducted over EPS plaster specimens with

various porosities, we focus here on a sample that contains 2 EPS beads (~4.5% porosity, see Fig.1b).

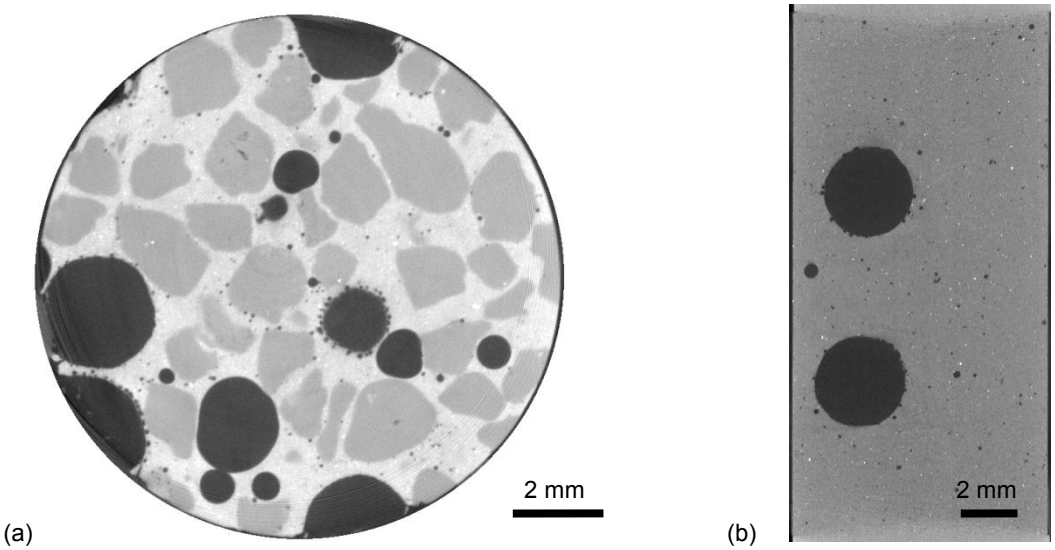

Fig. 1. *(a)Transverse slice of the EPS concrete specimen and (b) longitudinal slice of the EPS plaster specimen.*

In-situ X-ray computed tomography testing

A dedicated experimental set-up (Fig.2) was used to perform in-situ compressive tests on an XRCT laboratory scanner available at Laboratoire Navier (Ultratom from RX-Solutions). Several load levels were successively applied to each specimen. Acoustic emissions were also monitored to detect the beginning of the damage accumulation. CT images of the whole EPS concrete (resp. EPS plaster) sample, with a 15 µm (resp. 8 µm) voxel size and about 800x800x1200 (resp. 1150x1150x2150) voxels in size, were recorded under constant load in about 1.5 hours (resp. 3 hours). While one scan was sufficient for the whole EPS concrete sample, two scans were necessary to cover the whole EPS plaster height using a helical image acquisition.

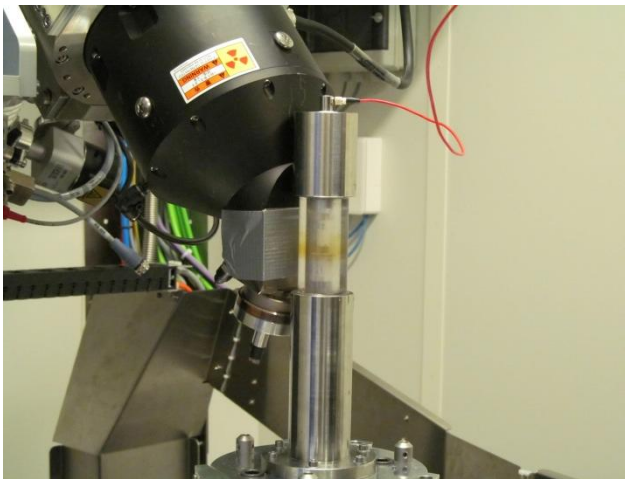

Fig. 2. *Experimental device for compression test with XRCT imaging.*

Detection of damage from DVC-assisted image subtraction

CT images of the last loading steps show cracks that progressively develop in both samples. However, a qualitative observation is not enough to quantify their precise location and propagation. Because their grey level is very similar to that of the porosity and close to that of the various constituents, the extraction of cracks from CT images with conventional segmentation tools is not straightforward (see Fig.3a). Moreover, they may be hard to detect in their early stage. Therefore, a method to detect and extract cracks more accurately was developed based on DVC techniques.

DVC is a straightforward 3D extension of Digital Image Correlation (Bornert et al., 2004, Bornert et al, 2012) and gives access to an evaluation of the mechanical transformation Φ inside a sample, at a scale at which some image contrast is available. In the case of EPS plaster, the latter is provided by the plaster matrix (inclusion, microporosity). In the case of EPS concrete, because grey levels in EPS beads and sand grains are rather uniform, local DVC routines have been run on positions in cement matrix only, especially near interfaces.

The sparse evaluation of the transformation map Φ can be continuously extended throughout the whole sample, by means of an interpolation procedure: the transformation at any voxel in the reference image is obtained by a first order fit of the displacement of at least 4 non-coplanar near neighbour positions successfully investigated by DVC. The grey level $g\big(\Phi(x)\big)$ in the deformed image, at the final position $\Phi(x)$ of any voxel x with grey level $f(x)$ in the reference image, is obtained by a tricubic interpolation of the deformed image. Thus, the deformed image is back convected in the same frame as the reference image according to the estimated transformation. Finally, the difference of both reference and deformed images defines the "residuals image" $r(x) = f(x) - \big[a\,.\,g\big(\Phi(x)\big) + b\big]$, corrected if necessary from an overall contrast a or brightness evolution b. It reflects the local evolutions of the material, not described by the fit of the coarse evaluation of the transformation. For a brittle material, it essentially gives access to the cracks. Note that on areas with sufficient local contrast, where DVC routines are run successfully, the residuals image would coincide with standard so-called "correlation residuals" (Bornert et al, 2012), if a=1 and b=0. The presented procedure extends this approach to the current situation of non uniformly distributed contrast and non perfect grey level convection.

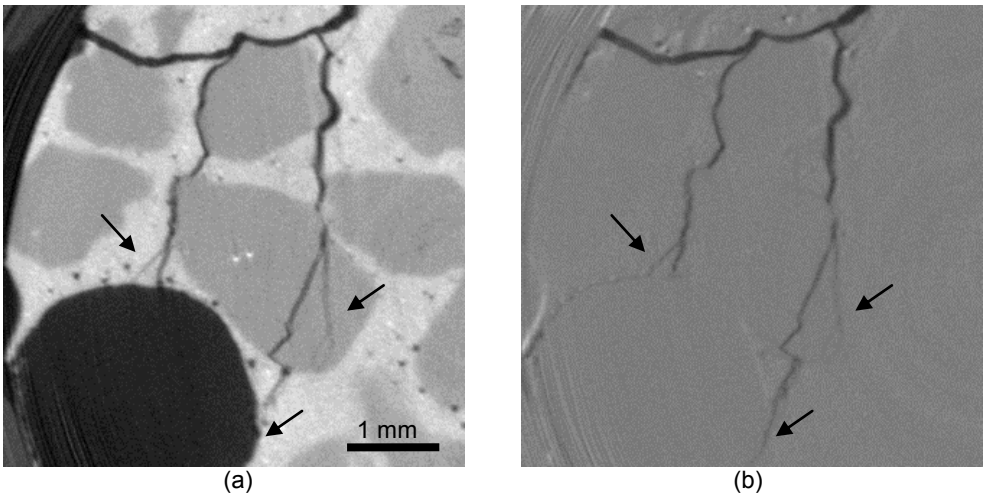

Fig. 3. *(a) Observed cracks in the EPS concrete specimen under 1.26 kN compressive load and (b) corresponding residuals image. Arrows show microcracks and EPS/cement matrix decohesion.*

An example of a residuals image for the EPS concrete sample is depicted in Fig.3b. The grey level is almost uniform, except in areas with ring artefacts and at some interfaces. In fact, the transformation map may be less precisely evaluated in highly cracked zones. But these features are less pronounced than the signature of cracks, the path of which is clearly visible. A direct segmentation by thresholding of cracked areas is possible in the residuals image, while it would have been very hard to separate cracks from porosity in the deformed XRCT images. Moreover, very tiny cracks can also be detected. The crack network and its evolution through the cement matrix and sand grains can thus be characterised, as in Fig.4, showing crack propagation and opening.

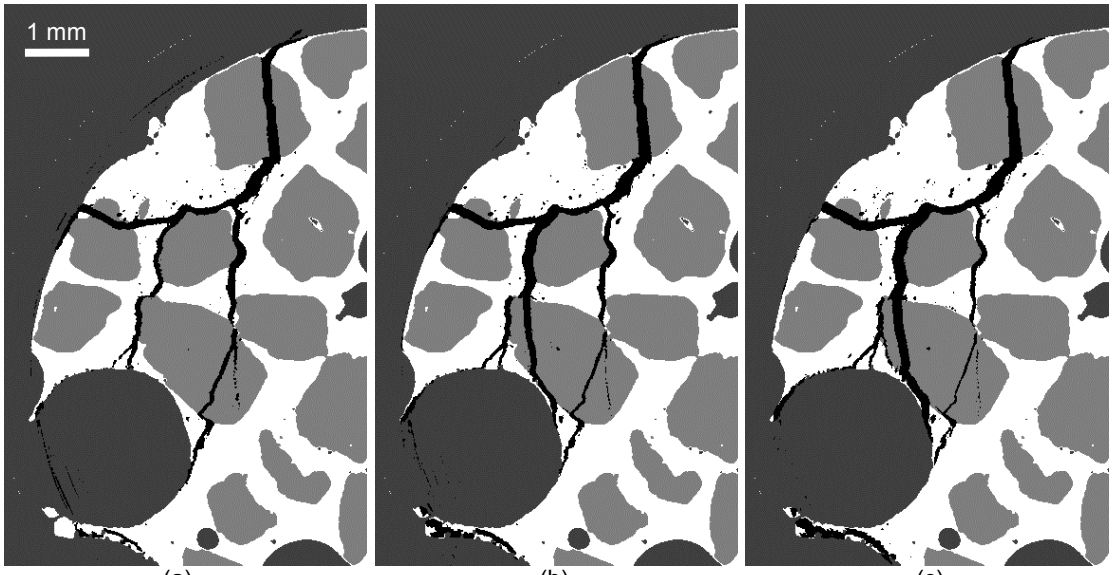

Fig. 4. *Segmentation of residuals images of the EPS concrete specimen under 1.26kN (a), 1.28kN (b) and 1.36kN (c).The detected crack network is superimposed on the segmented microstructure of the reference image.*

For the EPS plaster specimen, the accuracy of DVC and the image resolution are low compared to the size of cracks, leading to a poor contrast-to-noise ratio in the residuals image. An additional analysis of the residuals images was necessary to extract the cracks. A filter based on the analysis of the largest eigenvalue (in amplitude) of the 3D Hessian matrix was used as a first approach (see e.g. Sato et al., 2000). An example is presented in Fig.5.

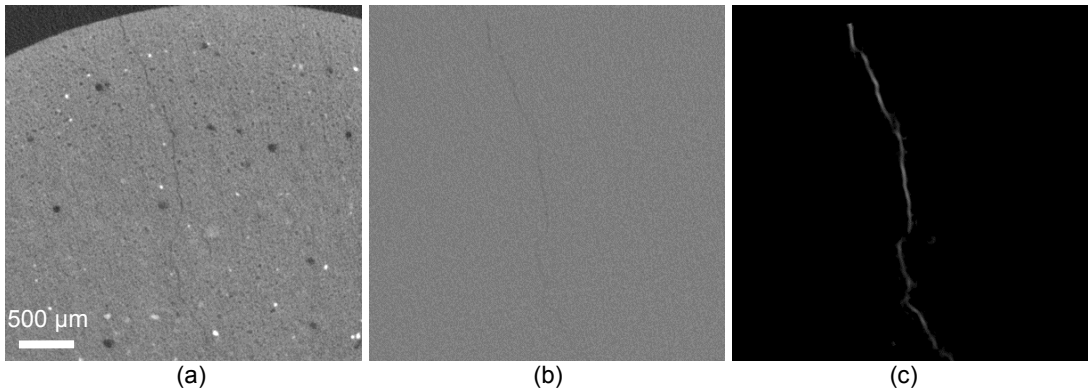

Fig. 5. *(a) CT image of the EPS plaster under compression (transverse slice), corresponding residuals image before (b) and after filtering (c).*

Thus, the propagation of the crack that developed in the top half part of the sample can be tracked with a threshold of the filtered residuals image (see Fig. 6).

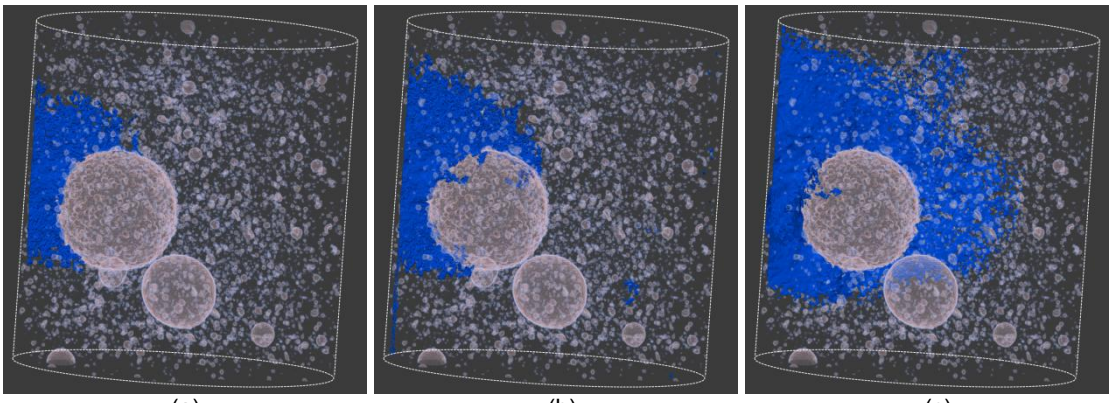

(a) (b) (c)

Fig. 6. *3D view of the crack propagation in the EPS plaster specimen (top half part) under 1.64kN (a), 1.93kN (b) and 2.64kN (c) compressive loading.*

Conclusion

DVC residuals, associated to a Hessian eigenvalues filter if needed, allow the detection and extraction of cracks in the porous microstructure of cement and plaster matrix based materials. Such approach is necessary to characterise the crack network and its propagation, giving results that will directly be compared to numerical simulations.

Further developments of this technique will aim at improving the description of the local transformation, especially in highly cracked areas, for a better separation of cracks from other features in the residuals images. A quantification of the damage will also be attempted, in view of comparisons with numerical simulations.

Acknowledgement

The authors are grateful to Dr. K. Miled for providing the EPS concrete material. The XRCT device used in this work has been funded with the help of the Region Ile de France (SESAME Program). This work has been funded by LABEX MMCD (Multi-Scale Modelling & Experimentation of Materials for Sustainable Construction).

References

Bornert M., Chaix J.M., Doumalin P., Dupré J.C., Fournel T., Jeulin D., Maire E., Moreaud M., Moulinec H. (2004) Mesure tridimensionnelle de champs cinématiques par imagerie volumique pour l'analyse des matériaux et des structures. ***Instrumentation, Mesure, Métrologie*** 4, 43-88

Bornert, M., Hild, F., Orteu, J.J., and Roux, S. (2012), Digital image correlation, Chapter 6, Full-Field Measurements and Identification in Solid Mechanics , Grédiac, M. and Hild, F. Eds., ISTE Wiley

Miled, K., Sab, K., Le Roy, R. (2007). Particle size effect on EPS lightweight concrete compressive strength: Experimental investigation and modelling. ***Mech. Mater.*** 39, 222–240.

Nguyen T.T., Yvonnet, J., Zhu, Q.-Z., Bornert, M., Chateau, C (2015) A phase field method to simulate crack nucleation and propagation in strongly heterogeneous materials from direct imaging of their microstructure. ***Eng. Fract. Mech.*** 139, 18-39.

Sato Y., Westin C.-F., Bhalerao A., Nakajima S., Shiraga N., Tamura S., Kikinis R. (2000) Tissue Classification Based on 3D Local Intensity Structures for Volume Rendering. ***IEEE Transactions on Visualization and Computer Graphics*** 6(2), 160-180.

Session 310

Evolution of Soil Hydraulic Properties Under Drainage Conditions

Y. PÉRIARD[1]*, S. JOSÉ GUMIERE [1], B. LONG[2], A. N. ROUSSEAU[2], J. CARON[1]

[1] Department of Soils and Agri-Food Engineering, Laval University, 2480 Hochelaga Blvd, Quebec, QC, Canada, G1V 0A6 – yann.periard-larrivee.1@ulaval.ca
[1] Department of Soils and Agri-Food Engineering, Laval University, 2480 Hochelaga Blvd, Quebec, QC, Canada, G1V 0A6 – silvio-jose.gumiere@fsaa.ulaval.ca
[2] Institut national de la recherche scientifique : Centre Eau, Terre et Environnement, Quebec, QC, Canada – Bernard.Long@ete.inrs.ca
[2] Institut national de la recherche scientifique : Centre Eau, Terre et Environnement, Quebec, QC, Canada – Alain.Rousseau@ete.inrs.ca
[1] Department of Soils and Agri-Food Engineering, Laval University, 2480 Hochelaga Blvd, Quebec, QC, Canada, G1V 0A6 – Jean.Caron@fsaa.ulaval.ca
* presenting author

Keywords: Soil Hydraulic Properties, tomodensitometry, consolidation, soil compaction

Abstract

Caracterization of soil hydraulic properties is essential for modelling water flow and solute transport in the vadose zone. These properties are often assessed assuming that the soil is a non-deformable (rigid) porous media both in time and space. However, under real conditions such as those found in agricultural systems, the soil is constantly exposed to external stresses induced by farm machinery as well as wetting and drying cycles constantly modifying the soil hydraulic properties. The main objective of this work was to develop a methodological framework to predict the evolution of the hydraulic properties of a soil sample under drainage conditions. In this study, tomodensitometry was used to characterize the evolution of these properties. The results are very promising. The proposed methodological framework provides a realistic description of water flow through the soil system during drainage which induces hydroconsolidation, a physical process experienced by artificially drained and irrigated soils in cranberry production.

Introduction

Human activities, such as agriculture, have an important influence on soil formation and evolution (Montagne et al., 2008). Several studies have shown that farming practices and crop management can significantly affect soil hydraulic properties (Hu et al., 2009). Indeed, when compared to natural conditions, some water management operation such as flooding, irrigation and subirrigation, can increase the frequency of water table oscillations, leading to significant changes in physicochemical properties (Montagne et al., 2009). More recently, it has been shown that implementation of a drainage system can promote an increase in horizontal flow inducing changes in soil structure and water retention properties (Frison et al., 2009; Montagne et al, 2009; Montagne et al, 2008). Zhang et al. (2013) observed for rice paddies that repeating flooding cycles and drainage can have a significant impact on percolation properties as well as on soil shrinkage and density. Périard et al. (2014) determined that anthropic soil genesis can induce the formation of a soil horizon with restrictive hydraulic properties, reducing significantly the drainage capacity. The evolution of soil properties may also have a strong impact on crop yields. For tile-drained sandy soils under cranberry production, Gumiere et al. (2014) found a direct relationship between areas of low yields and soil horizons with a low saturated hydraulic conductivity.

Rapid structural changes in sandy soils are not expected under natural conditions. But flow-induced migration of fine particles and reorganization of the porous media may change the soil drainage capacity and adversely affect crop yield. That being said, these

processes, which can occur in intensive cranberry production, are poorly documented in the literature. Therefore, the main objective of this paper was to investigate using a CT-scanner the evolution of the hydrodynamic properties of a heterogeneous sandy soil during the drainage process.

Methods

Soil column preparation

The experiment was performed with a repacked cylindrical soil column (56-cm long and 15 cm in diameter) made of two different sand layers. The first layer (sand 705) was 14-cm thick (Fig. 1) and had a d_{50} of 150 µm, while the second layer (Flint) was 42-cm thick (Fig. 1) and had a d_{50} of 500 µm. To ensure uniform flow conditions and an evenly distributed pressure, each end of the column was covered with Nitex (20-µm mesh); providing good contact between the water film and the diffusion plate. A first saturation-drainage cycle was performed to firmly pack the sand inside the column.

Scanography

The experiment was performed at the «*Laboratoire Multidisplinaire de Scanographie du Québec*» using a Somatum Volume Access CT scanner (Siemens, Oakville, ON, CA) (Fig. 1). The energy level used was 140 keV and the resolution obtained for a voxel was 0.45x0.45x0.60 mm. The CT images were recorded in DICOM format, and analyzed using the R software (R Development Core Team, 2008) and the oro.dicom library (Whitcher et al., 2011). The column was set up under the tomograph to monitor the evolution of CT throughout the experiment and the images were taken at several time intervals (0, 13 sec, 26 sec, 39 sec, 52 sec, 5 min, 10 min, 20 min, 30 min, 1 h, 3 h, 5 h, 22 h, 24 h, 26 h, 28 h, 30 h, 47 h, 73 h, 95h).

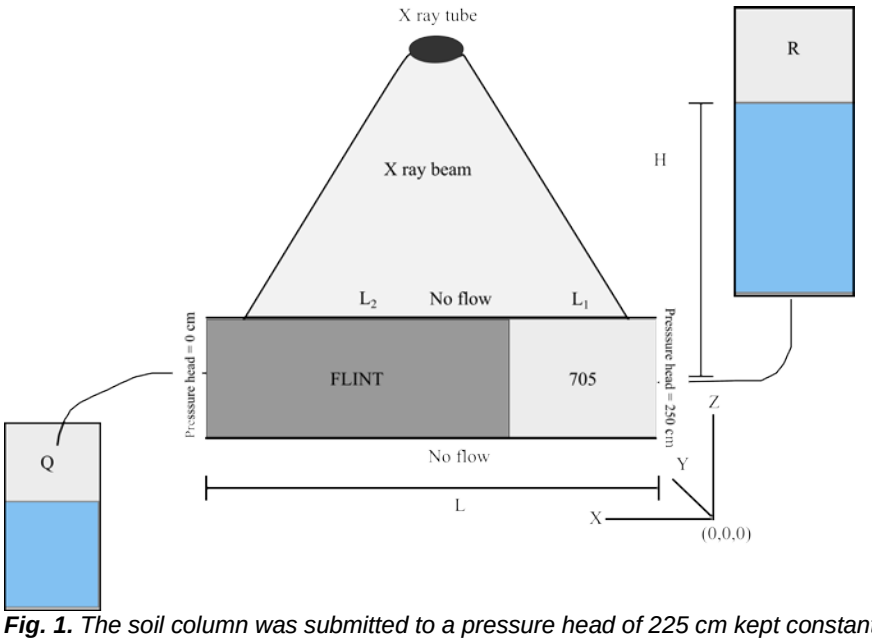

Fig. 1. *The soil column was submitted to a pressure head of 225 cm kept constant throughout the experiment on the side of sand 705 and a pressure of 0 cm at the other end of the cylinder. The pressure heads inside the reservoir (R) and in the drainage tank (Q) were measured using an absolute pressure sensor (Hobo U20 Water Level Logger, ONSET, Bourne, MA, USA) at time intervals of one minute throughout the duration of the experiment. The pressures were converted into water height by subtracting the atmospheric pressure monitored at intervals of one minute.*

Spatial and temporal variability of saturated hydraulic conductivity

The saturated hydraulic conductivity, K_s (cm h^{-1}), can be linked to the fractal dimension of longitudinal slices of soil (*x*-direction). Here, it was calculated using the approach proposed by Guarracino (2007):

$$K_s(x,y,z) = 3600\left(\frac{2-D(x)}{4-D(x)}\frac{\sigma^2\cos(\beta)}{2\rho g\mu}\phi(x,y,z)\alpha(x,y,z)^2\right) \quad (1)$$

Where *D* is the fractal dimension calculated with the semivariance approach. The parameter β is the angle of contact between water and soil matrix (0); σ, the surface tension (72.75 g/s^2); μ, the dynamic viscosity (10^{-2} g/cm s) of water; ρ the density of water (0.998 g/cm^3); *g*, the gravitational acceleration (980 cm/s^2); ϕ, the pixel porosity α, the reciprocal of the matric potential at the air entry point on the retention curve. The spatial variability of the voxel porosity was assessed using a semivariance analysis. The fractal dimension of the distribution of voxel porosity obtained from image slices was assumed to be the same as the fractal dimension of the distribution of pore size of the soil. For each longitudinal slice (*z*), a semivariogram was calculated on a matrix of 10.6 cm by 10.6 cm inside the cylinder 237, therefore given by 237 data. A random sample of 10,000 values was calculated in this matrix to limit the computational time. The spatial variability of a pixel porosity of a transverse cut, *z*(*x*), was studied with the aid of semivariograms:

$$\gamma(h) = \frac{1}{2N(h)}\sum_{i=1}^{N(h)}\left[\phi(x_i)-\phi(x_i+h)\right]^2 \quad (2)$$

Where $\gamma(h)$ is the semivariance of a separation distance *h* between pairs of points. *N*(*h*) is the number of pairs of equidistant points. $\phi(x_i)$ is the porosity value at point x_i and $\phi(x_i + h)$ is the value of the porosity at the point $x_i + h$. In this study, the fractal dimension (*D*) was estimated from the slope (M) of the relationship between the log of the semivariance and the log of the distance. According to the method proposed by Burroughs (1983) and Perfect et al. (1990), the fractal dimension is:

$$D = 2 - \frac{H}{2} \quad (3)$$

Where *H* is the Hurst exponent which is determined by regression for a distance (*x*), varying from 0 to 1.5 cm. This distance was selected to determine the fractal dimension of a smaller scale that is nearly that of a macropore network.

The air entry point was calculated using the relationship between the radius of a particle (*R*) and the matric potential presented by Mohammadi and Vanclooster (2011):

$$\alpha(x,y,z) = 18867.92453 R_i \xi(x,y,z) \quad (4)$$

ξ is a dimensionless coefficient that depends on the state of the soil column and particle organization in the porous medium and is theoretically less than 1.9099:

$$\xi(x,y,z) = \frac{1.9099}{1+e(x,y,z)} \quad (5)$$

Where the void ratio (*e*) is calculated from the porosity:

$$e(x,y,z) = \frac{\phi(x,y,z)}{1-\phi(x,y,z)} \quad (6)$$

For each type of sand, it was assumed that the air entry point corresponded to the matric potential which is related to the maximum radius of the particle size.

Results

Hydraulic conductivity

For the fine sand (705) and the coarse sand (Flint), reductions in the harmonic mean of the saturated hydraulic conductivity from 4.37 to 4.32 cm h^{-1} and 68.2 to 49.5 cm h^{-1} were observed (Fig. 2) after 94 h, respectively. For the whole soil column, reductions of22 to 14 cm h^{-1} were obtained using the proposed method compared to observed reductions of 31.35 to 3.54 cm h^{-1}. A significant space- and time-dependent increase in the fractal dimension indicates (Fig. 3A) that the environment became more homogeneous and dense and that there was reorganization of coarser particles in the soil matrix, causing a significant space- and time-dependent decrease in the saturated hydraulic conductivity (Fig. 2; Fig. 3B).

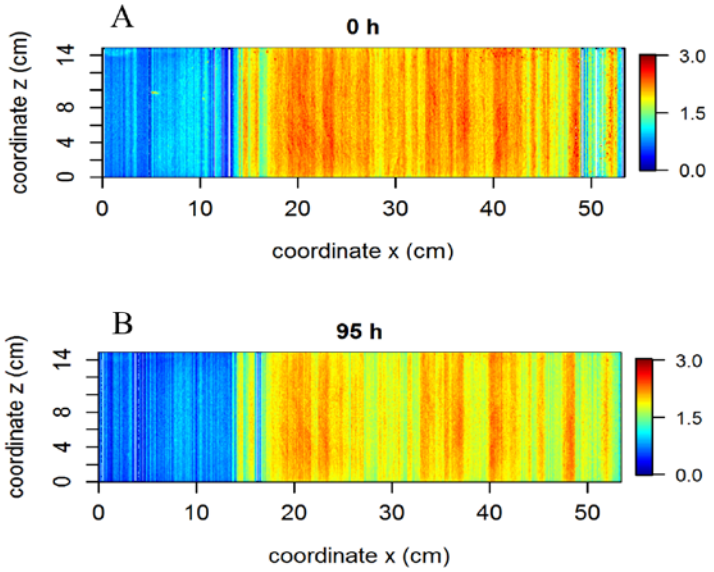

Fig. 2. *Temporal (at the onset of the experiment and after 95h) and spatial variation of the logarithm of the saturated hydraulic conductivity (cm h^{-1}) (0 h,95 h)* (N.B. the origin is located at the left-end side of these graphs which corresponds to beginning of the fine sand (705) located at the right-end side of the column introduced in Fig. 1).

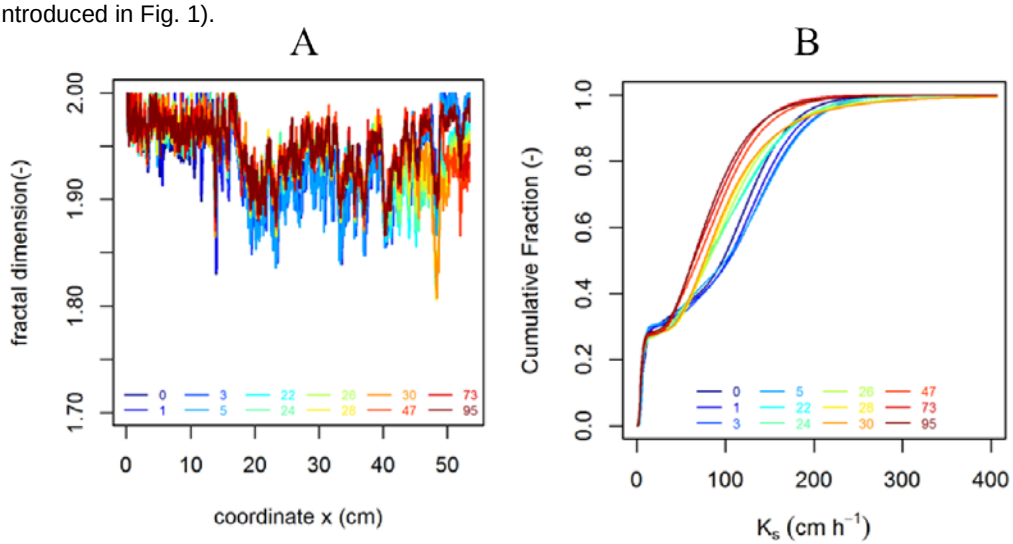

Fig. 3. *Fractal dimension of each longitudinal image as a function of coordinate x (A) and Cumulative fraction of the saturated hydraulic conductivity in the cylinder (B*). The colour legend represents the elapsed

time since the onset of the experiment. (N.B. the origin is located at the left-end side of these graphs which corresponds to beginning of the fine sand (705) located at the right-end side of the column introduced in Fig. 1)

Conclusion

This study has shown that CT-Scan data linked to a fractal-variogram analyses can be used to detect changes in soil porosity and saturated hydraulic conductivity of a sandy soil under drainage conditions. The method proposed here could be generalised to other studies. Results revealed the existence of mechanisms of hydroconsolidation during the drainage cycle in saturated soil. They indicated that hydraulic properties were significantly altered by consolidation consequently affecting the drainage capacity.

The development of the proposed method to predict saturated soil hydraulic properties using CT scan has provided a poweful framework to quantify at a very detailed resolution the consolidation process and to advance our understanding of what is in al likelihood happening in cranberry fields during flooding.

That being acknowledged, it has also became necessary to study the various anthropogenic genesis mechanisms of the soil under unsaturated conditions during the repeated cycles of drainage and recharge taking place over the course of one growing season. Therefore, there is a need to develop a method to achieve this using CT scans.

References

Frison, A., Cousin, I., Montagne, D., & Cornu, S. (2009). Soil hydraulic properties in relation to local rapid soil changes induced by field drainage: a case study. ***European Journal of Soil Science*** 60(4), 662-670.

Guarracino, L. (2007). Estimation of saturated hydraulic conductivity Ks from the van Genuchten shape parameter α. ***Water Resources Research*** 43(11), W11502.

Gumiere, S.J., Lafond, J.A., Hallema, D.W., Périard, Y., Caron, J., & Gallichand, J. (2014). Mapping soil hydraulic conductivity and matric potential for water management of cranberry: Characterisation and spatial interpolation methods. ***Biosystems Engineering*** 128(0), 29-40.

Hu, W., Shao, M., Wang, Q., Fan, J., & Horton, R., (2009). Temporal changes of soil hydraulic properties under different land uses. ***Geoderma*** 149(3–4), 355-366.

McDaniel, P.A., R.W. Gabehart, A.L. Falen, J.E. Hammel & R.J. Reuter. (2001). Perched Water Tables on Argixeroll and Fragixeralf Hillslopes. ***Soil Science Society of America Journal*** 65: 805-810. doi:10.2136/sssaj2001.653805x.

Mohammadi, M.H. & M. Vanclooster. (2011). Predicting the Soil Moisture Characteristic Curve from Particle Size Distribution with a Simple Conceptual Model. ***Vadose Zone Journal*** 10: 594-602. doi:10.2136/vzj2010.0080.

Montagne, D., Cornu, S., Le Forestier, L., & Cousin, I. (2009). Soil Drainage as an Active Agent of Recent Soil Evolution: A Review. ***Pedosphere*** 19(1), 1-13.

Montagne, D., S. Cornu, L. Le Forestier, M. Hardy, O. Josière, & L. Caner. (2008). Impact of drainage on soil-forming mechanisms in a French Albeluvisol: Input of mineralogical data in mass-balance modelling. ***Geoderma*** 145: 426-438. doi:http://dx.doi.org/10.1016/j.geoderma.2008.02.005.

Périard, Y., Gumiere, S.J., Rousseau, A.N., Caron, J., & Hallema D.W. (2014). Characterization of the temporal evolution of soil hydraulic properties under anthropomorphic conditions by X-ray tomography, ASA, CSSA, & SSSA International Annual Meeting, Long Beach, CA.

R Development Core Team. (2008). R: A language and environment for statistical computing. Vienna, Austria: R Foundation for Statistical Computing, 1-1731.

Whitcher, B., Schmid, V.J., & Thornton, A. (2011). Working with the DICOM and NIfTI Data Standards in R. ***Journal of Statistical Software*** 44(6), 1-28.

Zhang, Z.B., Peng, X., Wang, L.L., Zhao, Q.G., & Lin, H., (2013). Temporal changes in shrinkage behavior of two paddy soils under alternative flooding and drying cycles and its consequence on percolation. ***Geoderma*** 192(0), 12-20.

Micro-CT scanning of soil aggregate: the importance of image thresholding

A. AKBARI*[1], S. GHOSHAL[2]

[1] Department of Civil Engineering, McGill University, Montreal, Canada – ali.akbari@mail.mcgill.ca
[2] Department of Civil Engineering, McGill University, Montreal, Canada – subhasis.ghoshal@mcgill.ca
* presenting author

Keywords: Micro-CT, X-ray scanning, Image analysis, soil, aggregate, biodegradation

Abstract

Characterization of soil bacterial habitat advances our knowledge about soil biogeochemistry that could be useful in diverse fields such as greenhouse gas emissions from soil due to decomposition of soil organic matter and, fate and transport of pathogens, remediation of contaminated sites and enhanced oil recovery in petroleum reservoirs. Soils have complex intra- and inter- particle pore network characteristics which influence the accessibility of carbon sources, nutrients, oxygen and moisture to soil microorganisms. For example, a major microbial uptake mechanism of poorly soluble hydrocarbon compounds in soil is through direct contact between hydrocarbon and hydrocarbon degrading bacteria. It is expected that biodegradation of poorly soluble hydrocarbons to be severely limited when hydrocarbon compounds are trapped in small pores that are not accessible to soil microbial community.

We characterized the soil pore network of representative aggregates from two soils with distinct textures from two sites contaminated with petroleum hydrocarbons by micro-CT scanning and N_2 adsorption analysis. An image analysis procedure was developed in order to extract intra-aggregate pore network information. Given the complexity of image thresholding in case of heterogeneous porous materials such as soils with constituents with different densities as well particle sizes smaller than scanning resolution, applying simple global thresholding methods which doesn't consider spatial and intensity values of each pixel would not adequately represent the real aggregate micro-structure. Among different thresholding methods investigated (alternating mean thresholding and median filtering, two sigma smoothing and low pass filter and finally indicator kriging (IK)), the IK method provided the most representative images when compared to original gray-scale images. Moreover, the alpha-shape of each single scanned aggregate was determined in order to extract the pore information from whole aggregate body rather than just considering a sub-sample of total aggregate volume as done in most previous studies. Because soil aggregates are usually denser at the center compared to the loose structure near the boundary, considering just the core of aggregate would result in biased porosity calculations.

Introduction

X-ray computed tomography (CT) has been used for more than two decades in the environmental field for purposes such as characterization of porous medium (Lindquist, Lee et al. 1996) or studying the transport of NAPL phase in subsurface environment (Goldstein, Prasher et al. 2007). Recent advanced scanning instruments such as micro-CT with resolutions as low as 1 µm have provided new opportunities for more in depth characterization of micro-structure and pore network of porous medium (Werth, Zhang et al. 2010).

To obtain the desired information from acquired images by CT scanner, a series of steps are usually employed, among which the image thresholding is believed to be the critical step. By thresholding each pixel in the image is assigned as either background

(void) or object (soil). This is a complicated process in case of natural porous media for several reasons such as limited attainable resolution by scanners which is still larger than some soil constituents, noise in scanning and reconstruction processes and finally the heterogeneous nature of environmental porous media which is composed of constituents with a range of densities.

The thresholding methods could be classified as global and local methods. For global methods, a single threshold value is applied to whole image, while in local methods different values are considered as threshold values for different regions of the image. Another classification is based on if the spatial information of the image is incorporated in the threshholding process. The Otsu method is an example of global methods without considering the spatial information, which is based on minimization of standard deviation of the range of grey scale values of object and background (Otsu 1979). The method introduced by O'Gorman which is based on maximizing the connectivity in image regions is an example of global methods which considers the spatial information of the image (O'Gorman 1994).

The Two-Sigma method with low pass filter is a local thresholding method involving the smoothing of image by averaging pixels surrounding each pixel. Only pixel with intensities in two-sigma range are considered for averaging. The technique assumes a Gaussian nature of image noises (Nunan, Ritz et al. 2006). The indicator kriging (IK) is another method introduced by Oh and Lindquist, which is essentially a local method. The Method includes the spatial information in terms of covariance function for the image (Wonho and Lindquist 1999). Based on comparisons with ground truth image, Wang et al. found that IK method produced the most similar results to ground truth image (Wang, Kravchenko et al. 2011). Overall, CT scanning followed by proper image analysis procedure can provide information on distribution, length, connectivity, neck diameter of pores inside the porous media, as well as dynamic of change in pore network properties as a results of physic-chemical processes such as dissolution and/or precipitation of salts in groundwater.

Methods

1. Micro-CT Scanning of Soil

Soil aggregates were scanned using an X-ray micro CT scanner (SkyScan 1172). Air dried aggregates were fixed in pipette tips and placed on the rotating base of scanner. By adjusting the energy, exposure time and resolution, the average X-ray transmission was kept at about 50%. To avoid beam hardening, a 0.5 mm aluminium filter was used. The object was rotated over 360˚ at 0.28˚ step intervals, and three or four projections were acquired at each angular positions. The obtained images were later reconstructed using NRECON software (SkyScan). An example of reconstructed image is presented in Fig. 1.

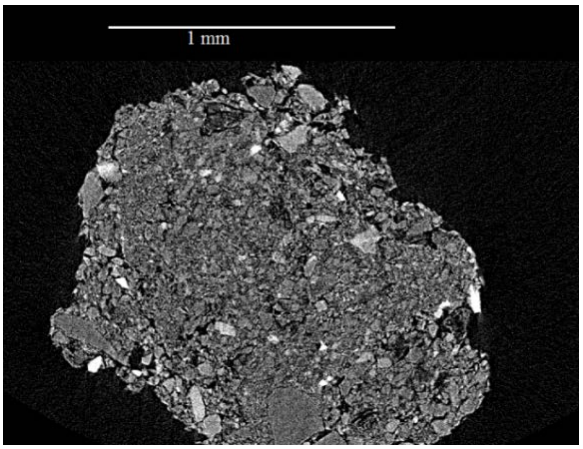

Fig 1. A reconstructed cross section from micro-CT scanning of soil aggregate.

1. Image Analysis

A variety of techniques has been proposed for thresholding as critical step in image analysis. We investigated several thresholding methods. A brief description of these methods are presented below.

Two-Sigma method with low pass filter: This filter is a local thresholding method based on the sigma probability of the Gaussian distribution and involves smoothing the image by averaging only those neighbouring pixels which lie within fixed intensity ranges of the central pixel. The technique is based on the fact that most image noises are Gaussian in nature. The two sigma probability is defined as the probability of a random variable being within two standard deviations of its mean. The Two-sigma probability of Gaussian distribution is 0.955 meaning that it covers 95.5% of random samples lying within the range of two standard deviations. It is assumed that any pixel outside this range comes from a different population and should be excluded from the average.

The resulting smoothed image, was then subtracted by a low pass filter. The low pass filter is created by replacing the intensity value of each pixel by the average of a larger window (255×255) centred at the pixel. The process was iterated to smooth out the filter. Finally, the filter is subtracted from the previously smoothed image. The resulting image is then globally thresholded at zero to binarize the image.

Alternating Mean Thresholding and median filtering: The alternating mean thresholding and median filtering consist of two sub cycles of local mean thresholding and median filtering. The local mean thresholding separates the pixels into two populations based on the mean of the greyscale values of all pixels. The means are then calculated for these two populations separately. The spatial threshold is then calculated using the following formula:

$$t^*_{1,2} = 0.5*(\overline{z_1} + \overline{z_2}) + (\sigma^2 / (\overline{z_1} - \overline{z_2}))*\log(n_2 / n_1) \qquad (1)$$

where $\overline{z_1}, \overline{z_2}$ are the means of the populations, n_2, n_1 are the number of pixels in each population and σ is the standard deviation of all the pixels in the image. The windows of 3×3 pixel×pixel are centred on each pixel and the mean is calculated for each window. If the mean is less than the spatial threshold, the pixel is assigned as air, otherwise it will be considered as soil. The thresholded image is then smoothed by assigning each pixel the median of the values of a 3×3 window centred on the pixel.

Indicator Kriging method: Indicator kriging (IK) is a thresholding method which is based on minimizing the spatial variance of the indicator kriging to segment the image (Oh and Brent Lindquist 1999). The algorithm involves four major steps as initial

thresholding, kriging and two filtering steps. First step is partial assignment of each pixel as soil or air based on two low and high threshold values (T0, T1 in Fig. 2). The IK method is very sensitive to the initial threshold values. Entropy method and bi-normal mixture method methods have been originally proposed to determine the low and high threshold values (Wonho and Lindquist 1999). In the latter one, both populations are assumed to be univariate normal. The expectation maximization algorithm is used to get these values (Equations 2-5). The r_b value is a positive constant decided on the basis of misclassified pixel population. However we achieved better results when we manually adjusted the thresholding values.

After first step of thresholding, the previously unassigned pixels were segmented as air or soil based on kriging. According to Equation 6 the probability of the pixel belonging to air or soil in a 3 pixels diameter window was determined. $P(T_i; x_0 \mid n)$ in the equation represents the probability of the pixel blonging to air or soil, i denotes the indicator variable, λ_α is the assigned weight to each pixel in the kriging window, x_o is the location of an unassigned pixel and x_α represent the neighbouring pixels. By solving a set of equations of ordinary kriging system based on semi-variogram model, the weights were determined. Majority filtering was performed before and after kriging to remove noises.

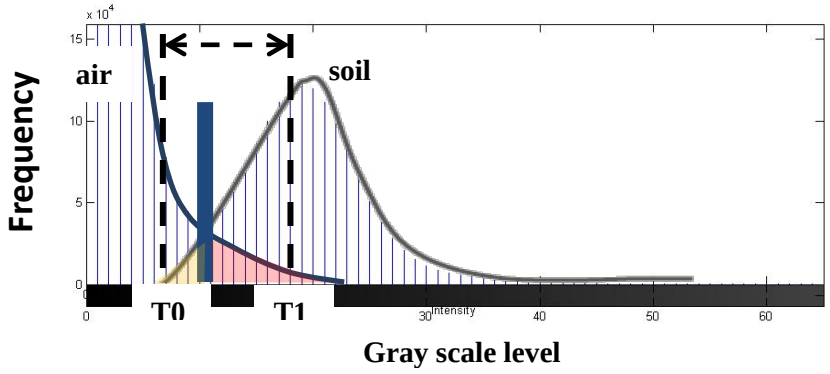

Fig 2. Typical histogram with initial thresholding values for IK method

$$z_0 = \min(\mu_0 + r_b * \sigma_0, \mu_1) \quad (2)$$

$$z_1 = \max(\mu_1 - r_b * \sigma_1, \mu_0) \quad (3)$$

$$T_0 = \min(z_0, z_1) \quad (4)$$

$$T_1 = \max(z_0, z_1) \quad (5)$$

$$P(T_i; x_0 \mid n) = \sum_{\alpha=1}^{n} \lambda_\alpha (T_i; x_0) i(T_i; x_0) \qquad i = 0,1 \quad (6)$$

Results

Comparing the thresholded images with different methods indicated that global thresholding is not a preferable method because it blurs edges and conceals subtle details. The threshold value is particularly difficult to determine because the statistical models for both the populations as well as noise are generally unknown. The alternating mean thresholding method (AMT) produces fewer pores even in comparison to an image

that has been globally thresholded at the same value as the spatial threshold. This is because in the AMT the average values of 3×3 windows are compared to the spatial threshold which increases the number of soil particles at the interface with air. The two sigma method with low pass filter produces too many pores in the thresholded image. This is because of the high values of the elements of the low pass filter. The low pass filter averages the values across the entire window. The smoothed image has the values averaged from the two sigma range thus giving it lower values in areas of the image where soil interfaces with pores. Upon subtraction and thresholding at zero, these values appear as pores. The Indicator Kriging Method is quite sensitive to the two threshold values T0 and T1. Two automated methods have been suggested for determining the thresholding values. However, these lead to inferior results when compared to that of an experienced user manually determining these values.

References

Goldstein, L., S. O. Prasher and S. Ghoshal (2007). "Three-dimensional visualization and quantification of non-aqueous phase liquid volumes in natural porous media using a medical X-ray Computed Tomography scanner." Journal of Contaminant Hydrology 93(1–4): 96-110.

Lindquist, W. B., S.-M. Lee, D. A. Coker, K. W. Jones and P. Spanne (1996). "Medial axis analysis of void structure in three-dimensional tomographic images of porous media." Journal of Geophysical Research: Solid Earth 101(B4): 8297-8310.

Nunan, N., K. Ritz, M. Rivers, D. S. Feeney and I. M. Young (2006). "Investigating microbial micro-habitat structure using X-ray computed tomography." Geoderma 133(3-4): 398-407.

O'Gorman, L. (1994). "Binarization and Multithresholding of Document Images Using Connectivity." CVGIP: Graphical Models and Image Processing 56(6): 494-506.

Oh, W. and W. Brent Lindquist (1999). "Image thresholding by indicator kriging." IEEE Transactions on Pattern Analysis and Machine Intelligence 21(7): 590-602.

Otsu, N. (1979). "A Threshold Selection Method from Gray-Level Histograms." Systems, Man and Cybernetics, IEEE Transactions on 9(1): 62-66.

Wang, W., A. N. Kravchenko, A. J. M. Smucker and M. L. Rivers (2011). "Comparison of image segmentation methods in simulated 2D and 3D microtomographic images of soil aggregates." Geoderma 162(3–4): 231-241.

Werth, C. J., C. Zhang, M. L. Brusseau, M. Oostrom and T. Baumann (2010). "A review of non-invasive imaging methods and applications in contaminant hydrogeology research." Journal of Contaminant Hydrology 113(1–4): 1-24.

Wonho, O. and W. B. Lindquist (1999). "Image thresholding by indicator kriging." Pattern Analysis and Machine Intelligence, IEEE Transactions on 21(7): 590-602.

Frequency mapping of local degree of saturation in partially saturated sand subjected to drying and wetting process

*Y. HIGO[1], R. KIDO[2], G. KHADDOUR[3], S. SALAGER[4], R. MORISHITA[5]

[1] Department of Urban Management, Kyoto University, C1-211 Kyotodaigaku-Katsura, Nishikyo-ku, Kyoto 615-8540 Japan – higo.yohsuke.5z@kyoto-u.ac.jp
[2] Department of Civil and Earth Resources Engineering, Kyoto University, C1-587 Kyotodaigaku-Katsura, Nishikyo-ku, Kyoto 615-8540 Japan – kido.ryuunosuke.87n@st.kyoto-u.ac.jp
[3] Grenoble-INP, UJF, CNRS UMR5521, Laboratoire 3SR, 1301 rue de la piscine, Domaine Universitaire, Saint Martin d'Hères, BP53 38041 Grenoble, Cedex 9, France – ghonwa.khaddour@3sr-grenoble.fr
[4] Grenoble-INP, UJF, CNRS UMR5521, Laboratoire 3SR, 1301 rue de la piscine, Domaine Universitaire, Saint Martin d'Hères, BP53 38041 Grenoble, Cedex 9, France – simon.salager@3sr-grenoble.fr
[5] Department of Civil and Earth Resources Engineering, Kyoto University, C1-587 Kyotodaigaku-Katsura, Nishikyo-ku, Kyoto 615-8540 Japan (Currently in Oil, Gas and Metals National Corporation (JOGMEC), Japan) – morishita-ryoichi@jogmec.go.jp
* presenting author

Keywords: soil, partial saturation, micro x-ray CT, water-retention curve, hysteresis

Abstract

Pore water in unsaturated soils is macroscopically homogeneous but spatially distributed depending upon microscopic natures including particulate structures and history of suction loading. The distribution of degree of saturation is a key to understanding macroscopic hydraulic and mechanical behaviors such as hysteresis during drying and wetting processes. In the present study, in order to clarify the link between distribution of degree of saturation and overall water retention behavior of unsaturated sand, local degree of saturation in unsaturated sand during water retention test was evaluated using micro x-ray tomography and segmentation technique for trinarization into the soil particle phase, the pore water phase and the pore air phase. Two experiments and their image analyses have been done in two laboratories under different but almost the same conditions using different sand samples, Toyoura sand with smaller diameter and Hostun sand with larger diameter. Frequency mapping of the relation between the local porosity and the local degree of saturation for prismatic representative subsets was presented in the two-dimensional histograms through which the effect of the drying and wetting processes and the hysteresis on the distribution of degree of saturation were discussed.

Introduction

Water-retention characteristic is one of the key issues for modeling mechanical and hydraulic behaviour of partially saturated sand because suction level and degree of saturation have a great influence on the strength and permeability of soils. It is well known that the main drying curve and the main wetting curve are not identical, which is referred as hysteresis. The mechanism of the hysteresis has been interpreted by a conceptual manner such as ink-bottle effect. It is however still necessary to study the causes of the hysteresis at grain scale.

In the present study, water-retention behaviour of sand during drying and wetting process has been observed microscopically using micro x-ray computed tomography (CT). Micro x-ray CT provides high resolution three-dimensional images which allow the visualization of pore water volume changes at different suction levels, for drying and wetting curves at the grain scale. Furthermore, the x-ray CT images are trinarised into the soil phase, pore water phase and pore air phase. Trinarisation technique of CT images for partially saturated sand is required to take into account the partial volume

effect: in particular, voxels shared by the soil phase and the air phase are wrongly identified as the water phase since the mixture of the soil and the air often gives CT value similar to the water (Hashemi et al. 2014, Higo et al. 2014).

Local porosity and degree of saturation for the given size of subset centered at reference points were calculated using the trinarised images. Then frequency maps of local porosity and local degree of saturation were drawn to investigate the relation between these two local values. In addition, the difference between the frequency maps of the drying process and the wetting process is discussed.

Methods

The sand sample used in the present study is Toyoura sand. The physical properties include a particle density of 2.64 g/cm3, a maximum void ratio of 0.975, a minimum void ratio of 0.614, a D50 of 185μm and a uniformity coefficient of 1.6.

The specimen was prepared by the water pluviation technique with a void ratio of 0.822 (porosity: 45.1%). The size of the specimen was 18.0 mm in diameter and 17.7 mm in height. The specimen was initially almost water-saturated, and then suction was applied to obtain a main drying curve by the water head difference between the top of the specimen and the burette connected to the bottom of the specimen. Similarly, a main wetting curve was obtained by reducing suction.

During this water-retention test, x-ray CT scanning was performed at several different water-retention states. The x-ray CT facility used in this study is KYOTO-GEOμXCT (Higo et al. 2011) extended by installing a flat panel detector. A small part of the specimen located in the middle of the specimen was partially scanned. Voxel size of the obtained images was 5.5×5.5×7.0μm3 by which D50 of Toyoura sand particle is drawn by 33 voxels. This spatial resolution is high enough to distinguish individual sand particles from each other.

The soil, water and air phases are segmented from the original image using the region growing method (Higo et al., 2013, 2014). Since x-ray CT images are an assembly of discrete gray values, they inherently have an artifact referred as the partial volume effect: voxels shared by two phases (mixel) with a gray value equal to the average between grain and air gray values. In particular, mixel of the soil and the air often gives the gray value closely similar to the gray value of the water. In order to reduce the wrong identification caused by the partial volume effect, in particular, between the soil phase and the air phase, mixels were taken into account by the maximum likelihood estimation method (e.g., Kitamoto and Takagi 1999) when determining the tolerance of the region growing method. For the soil-water, soil-air and water-air mixels, uniform distributions of gray value histograms are assumed, while normal distributions are assumed for pure soil, water and air voxels. When the superposition of the weighted distributions is determined by the maximum likelihood estimation method, the gray value at the intersection of the pure soil distribution and the pure water distribution was chosen as the tolerance of region growing of soil phase. Tolerance of the air phase was given by the intersection of the distributions of the pure air and the pure water similarly.

Fig. 1 shows a procedure for frequency mapping of local degree of saturation and correcponding porosity. Reference points were placed in the images evenly at a certain interval in vertical and horizontal directions. Local porosity and degree of saturation were calculated for the cubic subsets centered at the reference points. For the size of the cubic subsets, in the present study, 60 voxels were employed to investigate the distribution of the local values. The interval of the reference point was 30 which provides overlapping of 50% between the subsets in each direction.

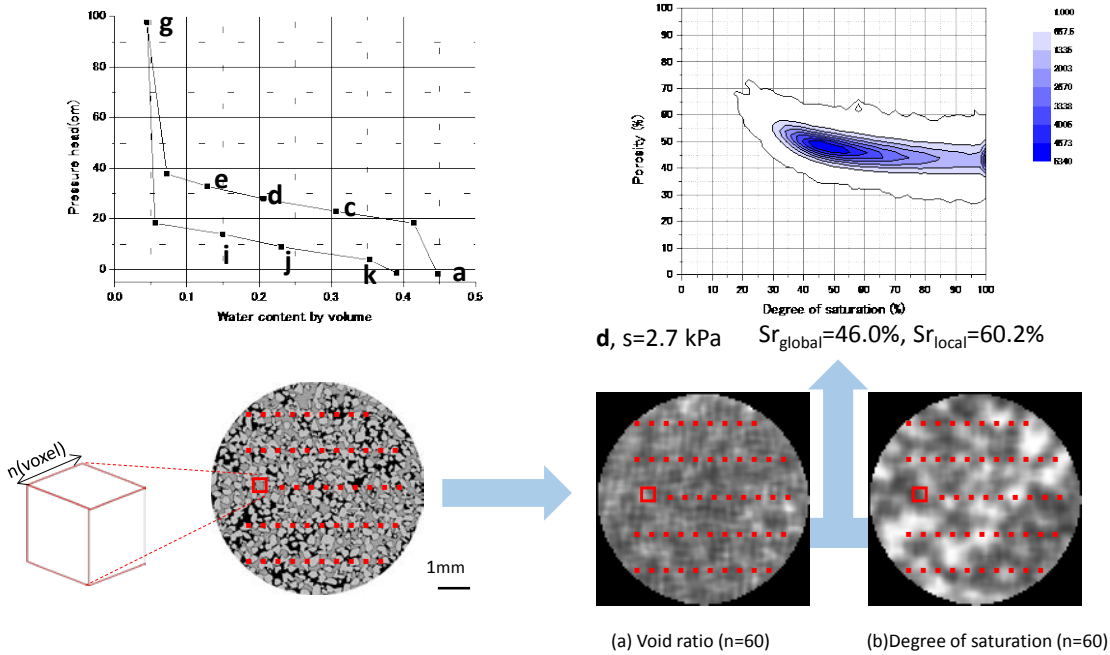

Fig. 1. *Procedure for frequency mapping of local degree of saturation in partially saturated sand*

Results and Discussion

As can been seen in the water-retention curve of Fig. 1, the drying path is located above the wetting path, i.e, the hysteresis can be clearly observed. During the drying process, the sand specimen starts to be desaturated when the suction level reaches 1.9 kPa. At higher suction of 10 kPa, the sample is in the pendular state. The degree of saturation starts to increase at suction level of 1.9 kPa during the wetting process and finally slight partial saturation was observed with zero suction, i.e., the specimen reaches insular-air saturation.

Letters “a” to “k” indicate the points at which x-ray CT scanning was performed. Horizontal slices of the CT images and the trinarised images at the center of the specimen during drying and wetting process are demonstrated in Fig. 2(a) and Fig. 2(b), respectively. Yellow, blue and gray portions indicate the soil particles, the pore water and the pore air, respectively. Porosity and degree of saturation of the scanned area were calculated using the trinarised images. The calculated porosities are comparable to the measured global porosity but the degree of saturation values are larger than the global one probably because the portion of the scanned area contains larger amount of water than the other portions of the specimen, i.e., the heterogeneity of the degree of saturation.

Frequency maps of the local porosity and degree of saturation from point ‘c’ to ‘e’ during drying process and from point ‘i’ to ‘k’ during wetting process are shown in Fig. 3. The solid line drawn along the edge of the whitest portion indicates the boundary of the frequency map, i.e., zero frequency outside the line, and the darkest blue portion denotes the peak of the frequency map. The degrees of saturation of these two water-retention states are almost the same. In this two-dimensional histogram, 50 bins are considered for both axes, and the total number of measurement is 18696.

It is clear for both the wetting and drying process that the degree of saturation of the subsets with high porosities tend to be smaller, while those with the lower porosities are

larger. This is compatible with the fact that the larger voids have lower water-retention ability, and vice versa.

Through comparison between ‘c’ and ‘k’, it is found that the degree of saturation of ‘k’ is lower than that of point ‘c’ because of trapped pore air as shown in the trinarized image in Fig. 2. In addition, it can be seen in Fig. 3(b) that the larger voids have less degree of saturation. This means that the pore air is likely trapped into relatively larger voids.

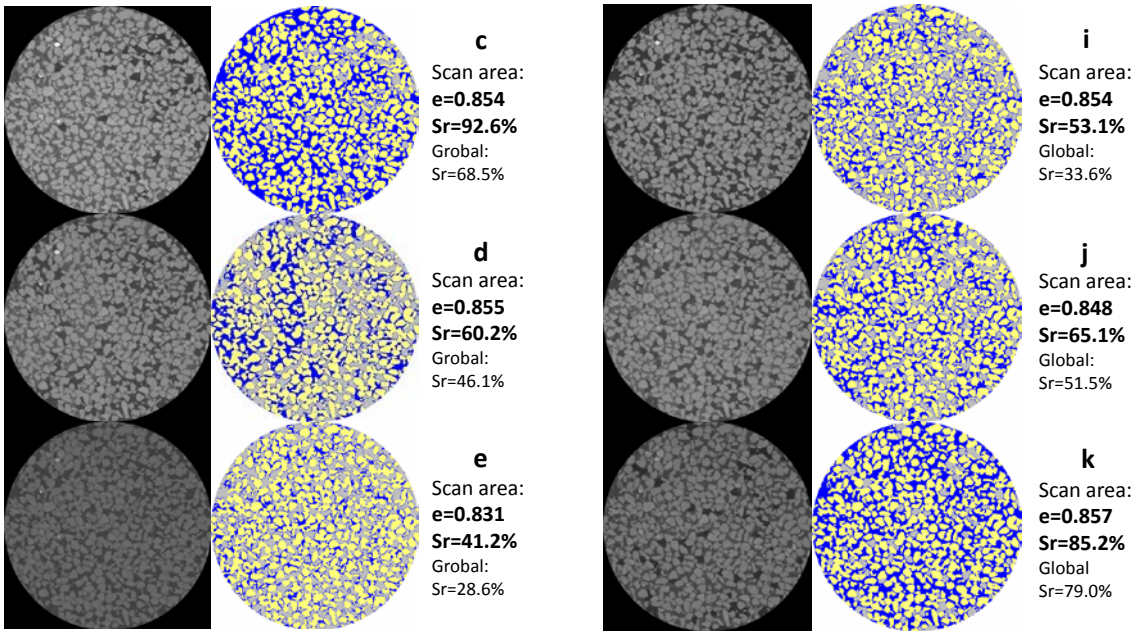

Fig. 2. *CT images and the trinarised images obtained with the void ratio and the degree of saturation of the scanned zone: (a) during drying process and (b) during wetting process.*

The histograms with the similar degree of saturation during drying and wetting process are almost the same, e.g., histograms at ‘e’ and ‘i’, ‘d’ and ‘j’, ‘c’ and ‘k’, although it is clear that the spatial distribution of pore water of ‘d’ and that of ‘j’ are obviously different from each other. Namely, the distributions of local degree of saturation during drying and wetting process are similar to each other in the case where the global degree of saturation is the same but the suction levels are different. This means that the distribution of pore water with respect to the porosity does not contribute to the hysteresis. Hence, it is possible that the difference of the curvatures of menisci, which provide different suction even when the degrees of saturation are similar, could contribute to hysteresis.

Conclusions

Micro x-ray tomography with trinarization technique has provided two-dimensional histogram of the porosity and the degree of saturation which makes it possible to discuss the distribution of pore water in partially saturated soil. It is found that larger voids are desatureted faster and re-saturated again slower than small voids. The distribution of the degree of saturation with respect to the porosity, for drying and wetting process of similar degree of saturation, are almost the same. The effect of the difference of curvature on the hysteresis is desired to be investigated in the future. It would also be necessary to

use different variables instead of porosity (void ratio), e.g., shape and size of the voids, to discuss more on the mechanism of hysteresis.

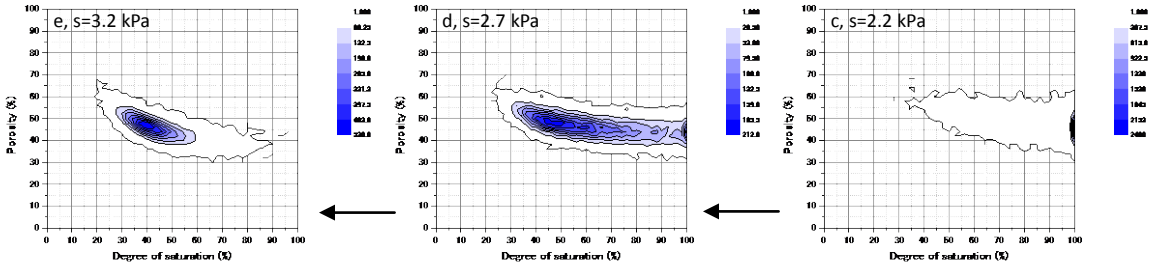

(a) Drying process (point: c, d, e)

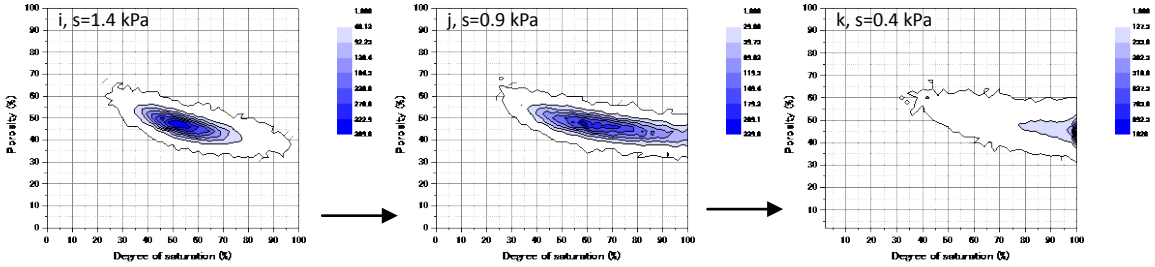

(b) Wetting process (point: i, j, k)

Fig. 3. *Frequency maps for local porosity and local degree of saturation during drying and wetting process.*

Ackowledgements

This research was partly supported by the grants given by Tec 21, the Obayashi foundation and SPIRITS project of Kyoto University.

References

Hashemi, M.A., Khaddour, G., François, B., Massart, T.J. and Salager, S. (2014). A tomographic imagery segmentation methodology for threephase geomaterials based on simultaneous region growing, ***Acta Geotechnica***, 9, 5, 831-846.

Higo, Y., Oka, F., Kimoto, S., Sanagawa, T. and Matsushima, Y., (2011). Study of strain localization and microstructural changes in partially saturated sand during triaxial tests using microfocus X-ray CT, ***Soils and Foundations***, 51, 1, 95-111.

Higo, Y., Oka, F., Sato, T., Matsushima, Y. and Kimoto, S. (2013). Investigation of localized deformation in partially saturated sand under triaxial compression by microfocus X-ray CT with digital image correlation, ***Soils & Foundations***, 53, 2, 181-198.

Higo, Y., Oka, F., Morishita, R., Matsushima, Y. and Yoshida, T. (2014): Trinarization of μX-ray CT images of partially saturated sand at different water-retention states using a region growing method, ***Nuclear Instruments and Methods in Physics Research Section B***: Beam Interactions with Materials and Atoms, 324, 1, 63-69.

Kitamoto, A. and Takagi, M. (1999): Image classification using probabilistic models that reflect the internal structure of mixels, ***Pattern Analysis and Applications***, 2, 1, 31-43.

Predicting soil hydraulic properties from tomodensitometric analysis and particle size distribution

Y. PÉRIARD[1]*, S. JOSÉ GUMIERE[1], A. N. ROUSSEAU[2], D. W. HALLEMA[1,3] ,J. CARON[1]

[1] Department of Soils and Agri-Food Engineering, Laval University, 2480 Hochelaga Blvd, Quebec, QC, Canada, G1V 0A6 – yann.periard-larrivee.1@ulaval.ca
[1] Department of Soils and Agri-Food Engineering, Laval University, 2480 Hochelaga Blvd, Quebec, QC, Canada, G1V 0A6 – silvio-jose.gumiere@fsaa.ulaval.ca
[2] Institut national de la recherche scientifique : Centre Eau, Terre et Environnement, Quebec, QC, Canada – Alain.Rousseau@ete.inrs.ca
[1] Department of Soils and Agri-Food Engineering, Laval University, 2480 Hochelaga Blvd, Quebec, QC, Canada, G1V 0A6
[3] Eastern Forest Environmental Threat Assessment Center, USDA Forest Service, 920 Main 9 Campus Dr., Raleigh, NC 27606, United States of America – hallema@gmx.com
[1] Department of Soils and Agri-Food Engineering, Laval University, 2480 Hochelaga Blvd, Quebec, QC, Canada, G1V 0A6 – Jean.Caron@fsaa.ulaval.ca
* presenting author

Keywords: Tomodensitometric analysis, soil hydraulic porperties, particle size distribution

Abstract

Knowledge of soil hydraulic properties such as water retention and hydraulic conductivity are essential for modelling water flow and contaminant transport in soils. However, characterization of these properties requires many technical manipulations that are very costly and time consuming. Tomographic imagery provides a cost-effective and rapid methodological approach to characterize a number of soil hydraulic properties. Indeed, micro scanning can be used to describe porous media at high spatial resolution and to obtain pore size distribution and pore network. However, the use of micro scanning has limits on sample size making inappropriate the study of a representative volume of a specific process described by a macroscopic model. The main objective of this work was to develop a framework to determine soil hydraulic properties using a combination of X-ray tomographic imaging and particle size analysis. A sandy soil sample was characterized with a medical CT scan at a resolution of 100 µm for a voxel. Water retention and hydraulic conductivity curves were derived using the instantaneous profile method for sorption and desorption curves. Results showed good prediction of soil hydraulic properties. The development of this novel framework has provided an opportunity to study the spatiotemporal variability of soil hydraulic properties of a porous media at the soil profile scale (1 m of length) under experimental conditions inducing hydroconsolidation and particle transport.

Introduction

Understanding the mechanisms governing water movement through, and storage within, porous media is of fundamental importance for conservation of this ressource and the protection of the environment.Knowledge of soil hydraulic properties such as water retention and hydraulic conductivity are essential for comprehending the dynamic of soil water. However, to truly understand how water moves through the soil during drainage and capillary rise, a nondestructive and fast method of characterisation of soil hydraulic properties is needed. The use of X-ray Computed Tomography (CT) to study the 3-D soil pore structure represents a conventional framework in soil science and has been used to predict numerous characteristics, and elucidate mechanisms of soil water dynamics (Wildenschild and Sheppard, 2013). Different technics are used to derive the soil hydraulic properties but at this moment most of them use the segmentation approach. This method is limited by the resolution of the CT-scan, by the efficiency of the algorithm to detect and discremimate different phases, and by the computational cost. The

macroscopic-scale flow in saturated and unsaturated porous media is generaly described by Darcy's law and Richards equation both requiring knowledge of the unsaturated hydraulic conductivity and soil water retention curves. The most recent advances in CT imaging technology now allow 3-D nondestructive imaging of soils at high resolutions (<3 µm) but there are limits on sample size making inappropriate the study of a representative volume of a specific process described by a macroscopic model. From a mathematical perspective, Darcy's law can be derived from the underlying Stokes equations using the method of homogenization and Lattice Boltzmann simulations and in return be used to predict hydraulic conductivity (Tracy et al., 2015). But this method is very time consuming and requires the perfect description of the pore network by the algorithm, but can neglect important pore-scale phenomena. Therefore, the main objective of this work was to develop a framework to determine soil hydraulic properties using a combination of X-ray tomographic imaging and particle size analysis.

Methods

Sample preparation and characterisation

The experiment was performed on a cylindrical soil column (length: 15 cm; diameter: 13 cm) repacked with unconsolidated Ottawa sand. Water retention and hydraulic conductivity curves were derived using the instantaneous profile method for sorption and desorption curves.

Tomodensitometric analysis

The CT study was performed at the "*Laboratoire Multidisplinaire de Scanographie du Québec*" using a Somatum Volume Access CT scanner (Siemens, Oakville, ON, CA). The energy level used was 140 keV and resolution obtained for a voxel was 0.1x0.1x0.6 mm. The CT images were recorded in DICOM format and analyzed using the R software (R Development Core Team, 2008) and the oro.dicom library (Whitcher et al., 2011). The images of each of the longitudinal sections was carried out in the center of the sample over an area of 5 cm by 5 cm.

Voxel Porosity

The porosity of a voxel, ϕ, using tomodensitometric analysis was obtained using the following equation which is similar to that used by Luo et al. (2008):

$$\phi(x,y,z)=\frac{CT_{Quartz}-CT_{Sol\_air}(x,y,z)}{CT_{Quartz}-CT_{air}(x,y,z)} \quad (1)$$

Where CT_{Quartz} is the absorption coefficient of the quartz at 140 keV which is 1798 HU, $CT_{sol\_air}(z)$ is the average absorption coefficient of dry soil (HU) at depth z and CT_{air} is the absorption coefficient of the air which is −1024 (HU). We defined a dimensionless reduced density as:

$$\eta(x,y,z)=1-\phi(x,y,z) \quad (2)$$

Particle distribution

The cumulative mass fraction ($M(R)$) of particle radius (R (cm)) was fitted with a bimodal lognormal distribution obtained with a LA950v2 Laser Particle Size Analyzer (Horiba):

$$M(R)=W\left(1-\frac{1}{2}erfc\left(\frac{\ln R-\left(\mu_y+3\sigma_y^{\,2}\right)}{\sqrt{2}\sigma_y}\right)\right)+(1-W)\left(1-\frac{1}{2}erfc\left(\frac{\ln R-\left(\mu_{2y}+3\sigma_{2y}^{\,2}\right)}{\sqrt{2}\sigma_{2y}}\right)\right) \quad (3)$$

where μ_y is the mean and σ_y is the standard deviation of *ln(R)*, subscript 2 indicates subdomain 2 of the distribution and W is a weighting factor for the subcurves, subject to $0 < W < 1$.

The nth moment, m_{ni}, of each sub lognormal distribution is given by:

$$m_{ni} = \exp\left(n\mu_{yi} + \frac{n^2 \sigma_i^{\,2}}{2} \right) \tag{4}$$

S_i is the surface area ratio given by:

$$S_i = \frac{m_{1i} m_{2i}}{m_{3i}} \tag{5}$$

Void nearest-surface complementary cummulative density function

We used the Carnahan–Starling approximation of void nearest-surface complementary cumulative density function (Chan and Govindaraju, 2004):

$$e_{vi}(\delta, x, y, z) = \left(1 - \eta(x, y, z)\right) \exp\left\{ -\eta(x, y, z) S_i \left[a_{0i}(x, y, z) \left(\frac{\delta}{m_{1i}} \right)^3 + a_{1i}(x, y, z) \left(\frac{\delta}{m_{1i}} \right)^2 + a_{2i}(x, y, z) \left(\frac{\delta}{m_{1i}} \right) \right] \right\} \tag{6}$$

δ is the particle radius and defined as follows:

$$\delta = ae^{br},\ r = \frac{2\sigma \cos\beta}{\rho_w g \psi} \tag{7}$$

Where *a* and *b* are empirical parameters accounting for the complex geometric relationship between the radius of a particle and the radius of a pore (*r (cm)*). σ is the surface tension (72.75 g/s^2) and β is the contact angle between water and the solid matrix (0), ρ_w is the water density (0.998 g/cm^3), g is the gravitational acceleration (980 cm/s^2) and ψ is the matric potential (cm) ranging between 0 to 120 cm. For a sandy soil, the hydraulic properties are most sensitive and dynamic within this latter range of potential. Beyond this range the hydraulic properties do not change so much and have little impact on the prediction of water movement. Subscript *i* indicates the subcurves *i* of the multimodal void nearest-surface complementary cumulative density function and the coefficients a_{0i}, a_{1i}, and a_2 are determined as follows:

$$a_{0i}(x, y, z) = \frac{\left(m_{1i}^{\,2} / m_{2i} \right) \left(1 - \eta(x, y, z)\right) \left(1 - \eta(x, y, z) + 3\eta(x, y, z) S_i\right) + 2\eta(x, y, z)^2 S_i^{\,2}}{\left(1 - \eta(x, y, z)\right)^3} \tag{8}$$

$$a_{1i}(x, y, z) = \frac{6\left(m_{1i}^{\,2} / m_{2i} \right) \left(1 - \eta(x, y, z)\right) + 9\eta(x, y, z) S_i}{2\left(1 - \eta(x, y, z)\right)^2},\ a_2(x, y, z) = \frac{3}{1 - \eta(x, y, z)}$$

Hydraulic properties

In a similar fashion to that for the multimodal retention function of Durner (1994), effective saturation is defined by:

$$S_e(r, x, y, z) = W\left(1 - \frac{e_{v1}(r, x, y, z)}{\phi(x, y, z)} \right) + (1 - W)\left(1 - \frac{e_{v2}(r, x, y, z)}{\phi(x, y, z)} \right) \tag{9}$$

The relative hydraulic conductivity function is computed by numerical evaluation of Mualem's (1976) predictive model using the multimodal representation of $\psi(S_{ei})$.

$$Kr(x, y, z) = S_e^{\,\tau} \left(W \left(\frac{\int_0^{S_{e1}} \frac{1}{\psi(S_{e1})} dS_{e1}}{\int_0^{w} \frac{1}{\psi(S_{e1})} dS_{e1}} \right) + (1 - W) \left(\frac{\int_0^{S_{e2}} \frac{1}{\psi(S_{e2})} dS_{e2}}{\int_0^{1-w} \frac{1}{\psi(S_{e2})} dS_{e2}} \right) \right) \tag{10}$$

$S_e^{\,\tau}$ is an empirical correction function, which accounts for the effects of pore connectivity and tortuosity and τ is given by:

$$\tau = \frac{Le}{L} \tag{11}$$

L is the straight-line water path and Le is the tortuous water path. We used the package *gdistance* (van Etten 2015) to simulate the water movement from one point to another. This procedure uses a 3 x 3 matrix and moves water from the central location of the matrix point having the lowest density (highest porosity). This is iterated until the water reaches the desired point (Fig. 1). The procedure was carried out for 32 coordinates distributed in the image, then the arithmetic mean was calculated and this was done for each image. The tortuous water path Le was calculated with the pythagorean formula:

$$Le = \sum_{i=1}^{n} \sqrt{\left(x_j - x_i\right)^2 + \left(y_j - y_i\right)^2} \tag{12}$$

Where *x* and *y* are the coordinates of each points. Subscript *i* indicates the antecedent point and *j* the next point and *n* represents the number of segments between two points along the water path.

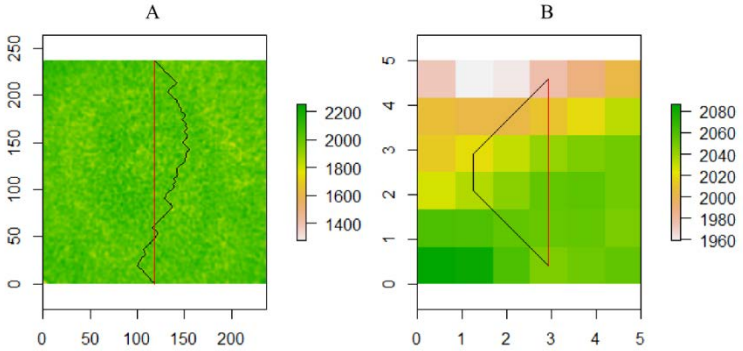

Fig. 1. *Simulation of water path from an image obtained with the CT scan. The Red line is the straight-line water path (L) and black line is is the tortuous water path (Le). A is the water path from the image slice and B is a zoom in this water path*

Saturated hydraulic conductivity (Ks (cm h^{-1}) was obtained with the model proposed by Nasta et al., (2013):

$$Ks = 3600\left(\frac{\rho_w g}{8\eta_w}\left(\frac{1}{\tau}\right)^2 \int_0^{R_{\max}} \frac{dS_e}{dr} r^2 dr\right) \tag{13}$$

η_w is the dynamic viscosity of water (0.0102 g $cm^{-1}s^{-1}$) at a temperature of 20°C. $R_{\max}$ corresponds to the pore radius of the air entry matric potential. Following the aproach proposed by Ghezzehei et al. (2007), the point of maximum curvature ($R_{\max}$) of second and third derivatives of S_e in the *r* function should satisfy the following constraints:

$$\frac{\partial^3 S_e}{\partial r^3} = 0 \quad and \quad \frac{\partial^2 S_e}{\partial r^2} < 0 \tag{14}$$

The hydraulic conductivity is given by:

$$K\left(\psi, x, y, z\right) = K_s\left(x, y, z\right) K_r\left(\psi, x, y, z\right) \tag{15}$$

The equivalent hydraulic conductivity of a three-dimensional heterogeneous porous media was calculated by the approximation proposed by Desbarats (1992):

$$K_{eq} = \mu_f + \frac{\lambda_f}{2} + \sigma_f^{\,2} \tag{16}$$

Where μ_f is the average of the log transformed of $K(\psi, x, y, z)$ and σ_f is the variance of the log transformed of $K(\psi, x, y, z)$ and since the flow was vertical $\lambda = -1$ for a harmonic average.

Results

The framework porposed in this study produced good predictions of soil hydraulic properties with a high coefficient of determination (R^2) (0.98 and 0.93) and a low root-mean-square error (RMSE) (0.03 $cm^3\ cm^{-3}$, 3.34 $cm\ h^{-1}$) (Fig 2) for a range of matric potential of 0 to 120 cm. The methodology used in this study gave good prediction of the soil hydraulic properties for a sandy soil.

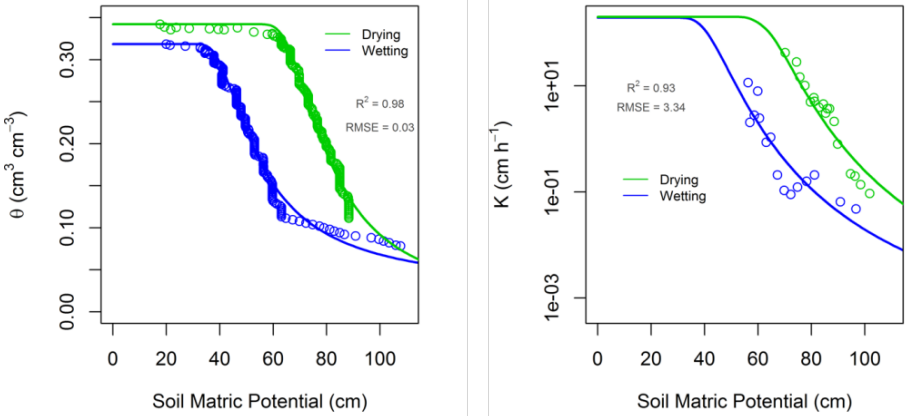

Fig. 2. *Soil hydraulic properties. The simulated data are represented by lines and the observed data are represented by hollow circles.*

Conclusion

In this paper, we demonstrated the application of a high-resolution CT scan method to determine soil hydraulic properties (hydraulic conductivity and water retention curves). The proposed methodology gave good results with high coefficients of determination and low RMSE. The development of this novel framework provided an opportunity to study at a high resolution the variability of hydraulic properties at the soil profile scale (1 m of length).

References

Byrd, R., Lu, P., Nocedal, J., Zhu, C. (1995). A Limited Memory Algorithm for Bound Constrained Optimization. ***SIAM Journal on Scientific Computing*** 16(5), 1190-1208.

Chan, T.P. and R.S. Govindaraju. (2004). Estimating Soil Water Retention Curve from Particle-Size Distribution Data Based on Polydisperse Sphere Systems. ***Vadose Zone Journal*** 3: 1443-1454. doi:10.2136/vzj2004.1443.

Desbarats, A.J. (1992). Spatial averaging of hydraulic conductivity in three-dimensional heterogeneous porous media. ***Mathematical Geology*** 24: 249-267. doi:10.1007/BF00893749.

Durner, W. (1994). Hydraulic conductivity estimation for soils with heterogeneous pore structure. ***Water Resources Research*** 30: 211-223. doi:10.1029/93WR02676.

Ghezzehei, T.A., T.J. Kneafsey & G.W. Su. (2007). Correspondence of the Gardner and van Genuchten–Mualem relative permeability function parameters. ***Water Resources Research*** 43: n/a-n/a. doi:10.1029/2006WR005339.

Luo, L., Lin, H., Halleck, P. (2008). Quantifying Soil Structure and Preferential Flow in Intact Soil Using X-ray Computed Tomography. . ***Soil Science Society of America Journal*** 72(4), 1058-1069.

Mualem, Y. (1976). A new model for predicting the hydraulic conductivity of unsaturated porous media. ***Water Resources Research***. 12: 513-522. doi:10.1029/WR012i003p00513.

Nasta, P., J.A. Vrugt & N. Romano. (2013). Prediction of the saturated hydraulic conductivity from Brooks and Corey's water retention parameters. ***Water Resources Research*** 49: 2918-2925. doi:10.1002/wrcr.20269.

R Development Core Team. (2008). R: A language and environment for statistical computing. Vienna, Austria: R Foundation for Statistical Computing, 1-1731.

Tracy, S.R., K.R. Daly, C.J. Sturrock, N.M.J. Crout, S.J. Mooney and T. Roose. (2015). Three-dimensional quantification of soil hydraulic properties using X-ray Computed Tomography and image-based modeling. ***Water Resources Research*** 51: 1006-1022. doi:10.1002/2014WR016020.

Wildenschild, D., Sheppard, A.P. (2013). X-ray imaging and analysis techniques for quantifying pore-scale structure and processes in subsurface porous medium systems. ***Advances in Water Resources*** 51(0), 217-246.

Whitcher, B., Schmid, V.J., & Thornton, A. (2011). Working with the DICOM and NIfTI Data Standards in R. ***Journal of Statistical Software*** 44(6), 1-28.

van Etten, J. (2015). gdistance: Distances and Routes on Geographical Grids. R package version 1.1-7. http://CRAN.R-project.org/package=gdistance

Oral presentation

A combination of radiography and micro-tomography X-ray techniques for studying shear-induced migration of particles in yield stress fluids

S. HORMOZI[1]*, M. GHOLAMI[1], N. LENOIR[2], G. OVARLEZ[2]

[1] Department of Mechanical Engineering, Ohio University, 251 Stocker Center, Athens, OH 45701-2979, USA. [2] PLACAMAT, UMS3626-CNRS/University of Bordeaux, Pessac, 33608, France.

Dense suspensions are materials with broad application both in industrial processes (e.g. waste disposal, concrete, drilling muds and cuttings transport, food processing, etc) and in natural phenomena (e.g. flows of slurries, debris and lava). These suspensions may consist of solid particles with a broad range of sizes. Often the fine colloidal particles interact to form a shear thinning yield stress carrier fluid, i.e., visco-plastic fluid, which itself transports the coarser solid particles. Hereafter, this system will be termed visco-plastic suspension.

From physical perspective, distribution of particles can be attributed to the hydrodynamics and multi-body interactions of the particles. In a non-homogeneous shear flow of Newtonian suspensions (i.e., systems of Newtonian carrier fluid and non-colloidal particles), it is observed that particles migrate from the high velocity gradient region to the low velocity gradient region, see Leighton & Acrivos (1987) and Phillips et al. (1992). This phenomenon is called shear-induced migration. Therefore, estimating the particle phase diffusion in visco-plastic suspensions requires understanding of this phenomenon.

We present our preliminary results of an experimental study on visco-plastic suspension flows in a circular Couette configuration. Here, the outer cylinder is rotating and the inner cylinder is stationary. We have used a system of non-Brownian spherical hard particles suspended in a concentrated emulsion with yield stress. A systematic series of experiments were carried out to capture all flow regimes in a wide range of solid volume fraction and outer cylinder rotational speed. The transient evolution of solid volume fraction under shear is measured by an X-ray radiography imaging technique. In addition, an X-ray 3D micro-tomography is performed to scan the exact particles distribution when steady state is established.

In Newtonian suspension, the linearity of the suspending fluid allows to study the shear-induced migration phenomenon at the steady state regime independent of the transient regime. Turning to visco-plastic suspension, the main problem relates to nonlinearity of the constitutive law for the suspending fluid, meaning that many of the analytical results that underlie some Newtonian suspension techniques are not directly applicable. Here, the study of shear-induced migration requires the distribution of particles at the transient regime as well as the steady state regime. To our knowledge, this is the first time that the X-ray radiography imaging technique has been exploited for investigation of such a complex system.

Computational programs are developed to post-process radiography and micro-tomography data with the purpose of calculating the average solid volume fraction during the flow and the exact particles distributions at the steady state. Moreover, we have followed the suspension balance framework of Nott and Brady (1994) to develop a continuum model for visco-plastic suspension flows. Our experimental results complete a continuum modelling closure perspective for the dispersion of solids in visco-plastic suspension.

References:

Leighton, D., and Acrivos, A. The shear-induced migration of particles in concentrated suspensions. J. Fluid Mech. 181, pp. 415–439, (1987)

Phillips, R., Armstrong, R., Brown, R.A., Graham, A. and Abbott, J.R. A constitu- tive model for concentrated suspensions that accounts for shear-induced particle migration. Phys. Fluids A 4, pp. 30–40, (1992)

Nott, P.R, and Brady, J.F, Pressure-driven flow of suspensions: simulation and theory. J Fluid Mech 275 (1994).

Session 311

Celtic drum fibula morphology, preparation technique and conservation state determined by X-ray computed tomography

C. TENAILLEAU*[1], E. DUBREUCQ[2], B. DUPLOYER[1], L. SEVERAC[1], P.Y. MILCENT[2], L. ROBBIOLA[2]

[1] CIRIMAT, UMR - CNRS 5085, Université de Toulouse, 118 route Narbonne, 31062 Toulouse Cedex 9, France
[2] TRACES, UMR - CNRS 5608, Université de Toulouse, 5 allée A. Machado, 31058 Toulouse Cedex 9, France

Keywords: Celtic, Fibula, Bronze, Corrosion, X-ray computed tomography XCT.

Abstract

A celtic bronze drum fibula dating from the middle Iron Age (5th Century BC) and recently excavated from the Corent site in France was characterized in detail for determining the morphology, composition and microstructural features that allow understanding the production method as well as the conservation state. A deeper and original characterization of the archeological object was performed thanks to X-ray Computed Tomography (XCT) at micrometric level, including detection of mineral/metallic phases. A systematic thickness mapping determination revealed an important homogeneity of the thickness in the whole structure of the fibula, though widening towards the edges. For the first time, important information on the internal corrosion state is revealed with a network of internal cracks transversally located throughout the thickness of the drum part of the fibula. By compiling these results with historical data it was concluded that this celtic drum fibula was thorougly prepared by stamping of a preform. It was also demonstrated the importance of the decay of bronze even when the external observation prejudge of a well preserved state. Complementary spectroscopic data and imaging information lead us to a clearer insight in the corrosion mechanism.

Introduction

Preservation of archaeological objects often involves restoration, but always requires the knowledge of their original context, including environment and history, as well as their state of conservation.This is a specific study regarding the usual dammaged or corroded state of an archeological object, in which the stages of state recognition and cleaning are very important to avoid misinterpretation. Such study will improve conservation and knowledge of both the degradation state and making process.

For understanding the alteration of an ancient object, radiography is usually the most frequent technique used for characterising the object and looking at the surface. XCT offers new perspectives. Indeed, XCT is a fantastic tool that provides 3D information of an archeological object in a non destructive manner and makes it possible to investigate the inside its surface by preserving the entire original aspect [1,2]. The resolution found with lab. micro-XCT (usually ~ 0.5 micron voxel size resolution) can easily give extreme information about the object typology, its raw surface and possible defects, cracks or corrosion features. The knowledge of these features are essential for avoiding the sample deterioration during restoration and allow its preservation. Also, XCT time acquisitions are usually of a few hours and can considerably shorten the work of the restoration. In some cases, the cleaning part for the archeological observation can then be skipped.

Here are presented the results of a detailed XCT analysis on a celtic drum fibula found in Corent, East of France [3]. Celtic drum fibulae are mostly located from the North West of the Mediterranean Sea and Spanish border to the current South West Germany and along the

Rhone river to the Austrian Alpes, while the known workshops of fibula are mainly found along the Rhone river all the way up to the Rhin river (see Figure 1).

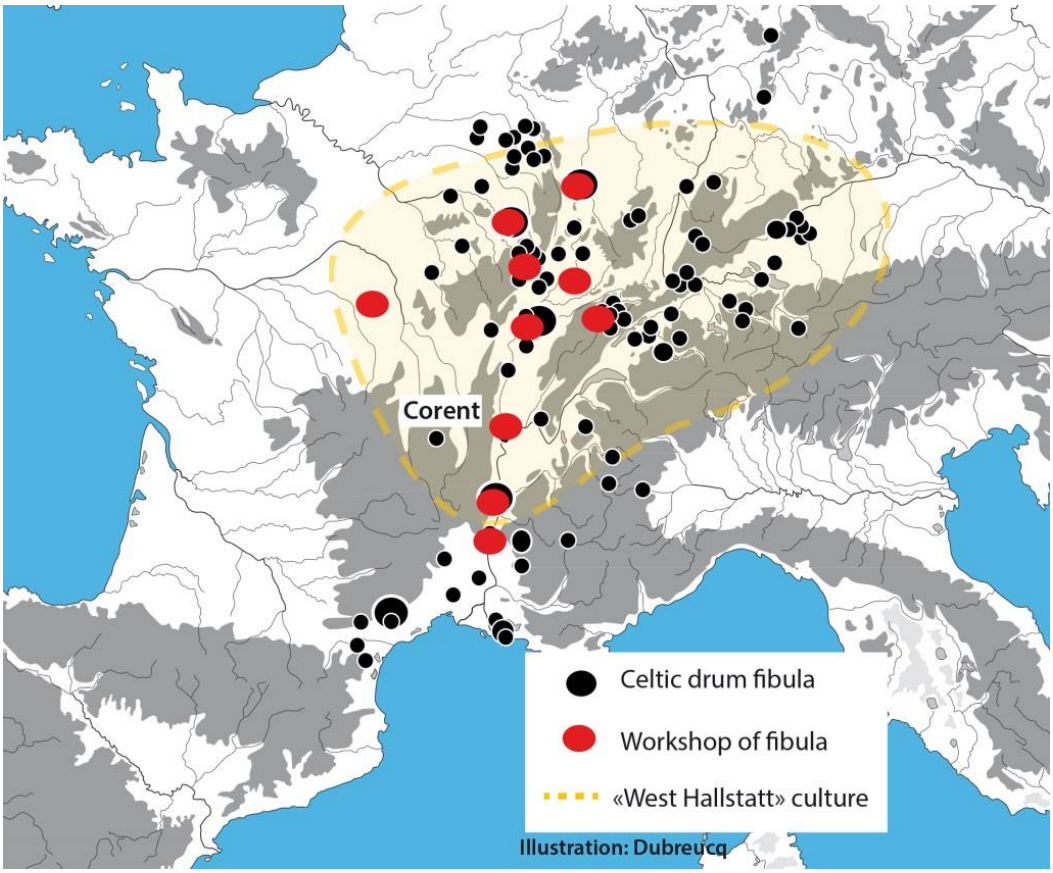

Fig. 1. *View of the European places identified for celtic drums and workshops of fibula, including the French Corent site where the celtic drum fibula under study and dating from the First Iron Age was extracted.*

The fibula is a kind of safety-pin usually aiming at fastening clothings together and would also be decorative as a brooch. They were largely produced by Greeks, Persians, Phrygians, Celts, Germans, Slavs … and Romans. Appearing at the Bronze Age, fibulae were used until the Middle Age. Fibulae were shaped and used differently from various communities. Its morphological modification can therefore be a chronological indicator.

The celtic drum fibula from the Corent site presented in this study is less than 5 cm in length. The arch central part with its round shape influenced the conventional drum name attributed to this spoon-like fibula which can also be found at the tip of the fibula. The celtic drum fibulae were essentially produced between 550 and 450 B.C. corresponding to the first development of the Celts in the geographical region (see Figure 1) going from Central France to South-Western Germany (named the «Hallstatt occidental») [4]. Although this bronze fibula is a rare and well preserved specimen, note that it is not complete since the needle part and the foot are missing.

Methods

X-ray Computed tomography was performed with a Phoenix/GE Nanotom 180 apparatus, using the W target with U = 130kV and I = 30 µA (FOD and FDD = 25 and 200 mm, respectively; 6.25µm/voxel on the zero Mode). A timing of 1000 ms was used for the data acquisition with 7 images averaged per step and the first two at each step were

skipped to avoid image reminiscence after each rotation and a total of 1440 images were recorded.

Precise and meticulous thickness determination was realized every 0.5 mm in all three perpendicular directions in the drum part of the fibula. The capillaries used for thickness determination were always taken perpendicular to the surface curvature. 4D information was then extracted after XCT data analysis with 430 points of (X, Y, Z) coordinates, each associated with a sample thickness.

Results

The bronze fibula fabrication of a simple (or double) celtic drum fibula like the one found in the Corent site is based on the use of a preform and can be described by six main steps (Figure 2). First, a preform is usually obtained by casting a stem of 64 mm average length and triangular section ended by one or two circular globules of hemispherical or cone shape. The latter, between 6 and 9 mm in diameter, constitute a metal storage area for the final shaping of the drum fibula. Hammering of a stalk of quadrangular section and a flat circularly shaped end constitute an other important stage of preparation. The hammering of the fibula pin support and bow is also essential. Then comes the hammering stage of the fibula bow, spring and pin. After stamping the circular part to form the drum, the object is finally formed by folding the drum towards the long end of the fibula.

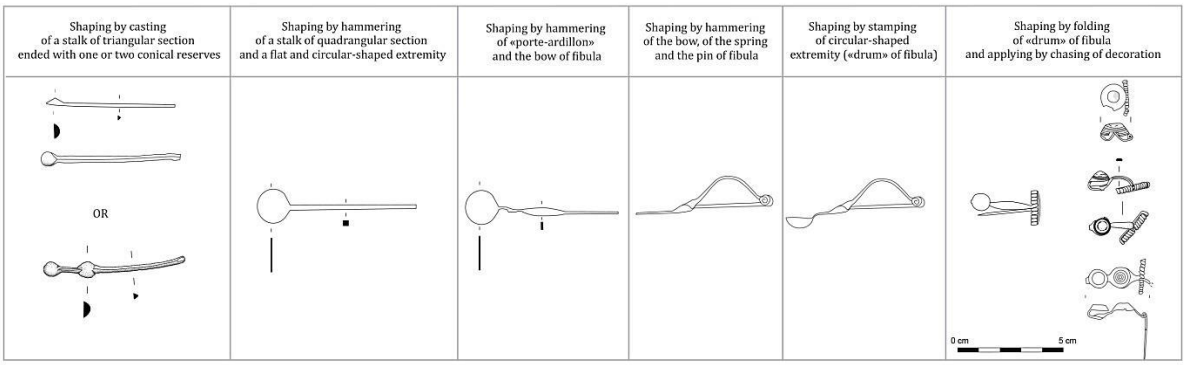

Fig. 2. *Description of the six main stages used for preparing a celtic drum fibula (after Carrara et al. 2013 [3] and modified).*

Ancient bronzes (Cu-Sn alloy) are often affected by severe corrosion during long burial periods of time, but can also be preserved when a stable patina is formed [4-7]. Noble patina can indeed well protect the original surface even after several millennia of burying. Investigation of these corroded but preserved surfaces was firstly performed applying a complementary set of non invasive techniques (including SEM, EDS and microRaman spectrometry) to determine composition and structure of natural patina and gilded part. The alloy is a pure tin-bronze with a tin content of about 8 at.% (14 wt.%), determined from X-ray microdiffraction measurements applying Vegard's law. The natural patina with a very poor copper content and preserving original surface is of type I patina [7] (also called "noble patina"). It is linked to the internal oxidation of the alloy with a selective dissolution of copper, namely decuprification which is very pronounced here. The gilded aspect is only the result of a desquamation of the outer patina layer at the interface outer/inner corrosion layer, revealing the gold colour of the bronze matrix. Element-specific mapping allowed precise detection of atomic distribution of environmental and alloying elements.

XCT was performed on the celitc drum fibula in order to determine the precise morphology of the whole object, visualize the corrosion effects on the material and get a better insights in the fabrication process (Figure 3). Patches of corrosion layers of ~30 um

thick are observed at the surface of the fibula. The corrosion phases represent about 10% of the whole object evidencing an alterated state despite a satisfying visual aspect. Small cracks (often a few dozen of a micron in length) are seen in the XCT images, mainly close to the internal surface. Longer cracks can also be observed, which cross completely through the material perpendicularly to the surface of the drum part of the fibula (see bottom left of Figure 3).

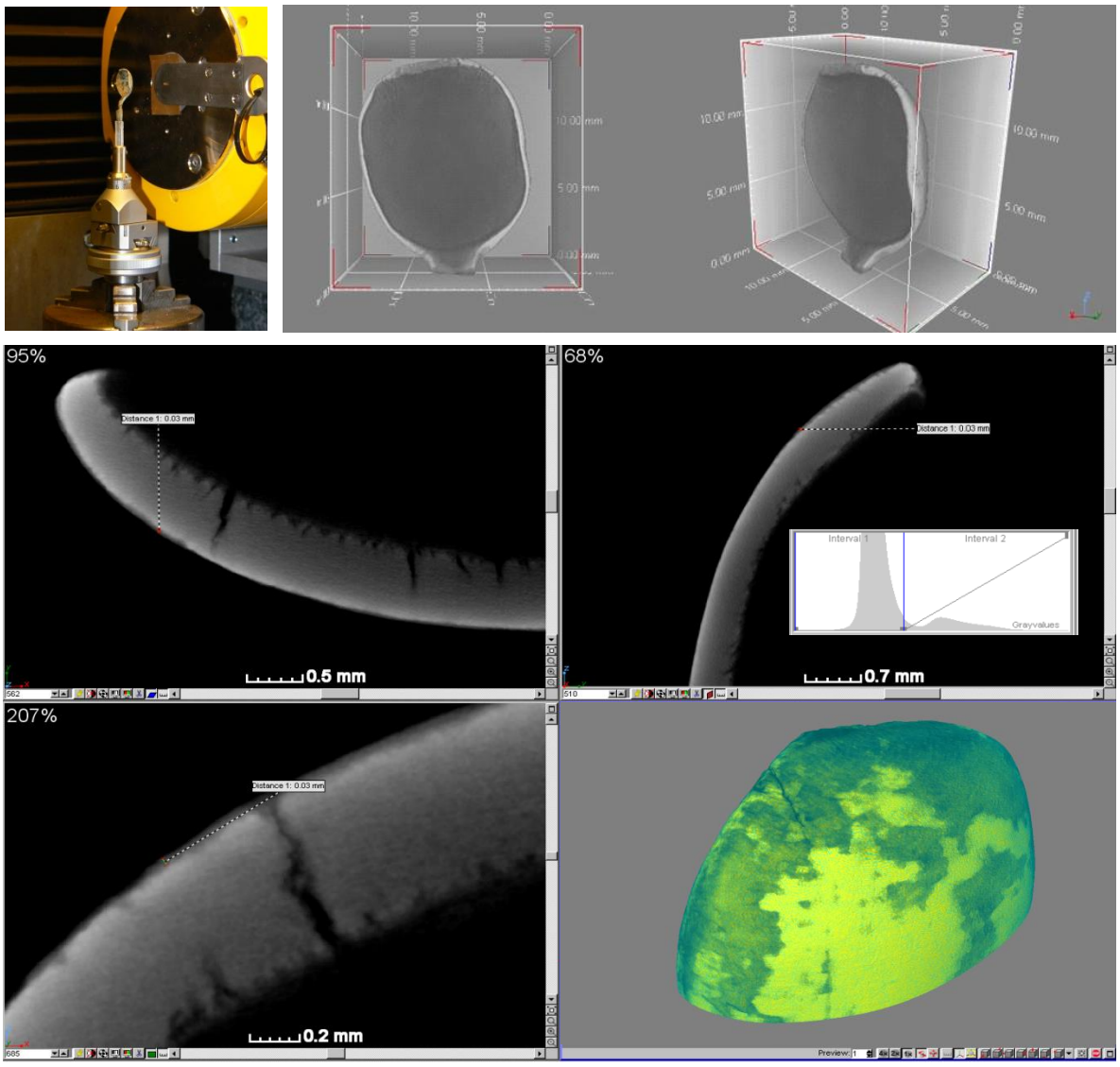

Fig. 3. *XCT images showing the thickness, cracks and corrosion layer… of the drum part of the celtic fibula.*

The sample thickness was carefully studied after XCT data analysis for the two main components (drum and handle) of the fibula. Therefore, 430 coordinates determined throughout the whole drum were associated with a sample thickness (Figure 4). The drum fibula thickness varies from 0.4 to 1.1 mm through most of the object, with increasing values up to ~ 1.5 mm towards the very edges. The drum thickness is smaller at the broken side (top part of Figure 4, where the barb would seat) and in the central part (diam. < 0.7 mm). The thicker parts are concentrated down the stem and on both extreme border sides (diam.

> 1 mm). These variations tend to confirm the fibula fabrication process by flattening a volume in the centre and towards the barb.

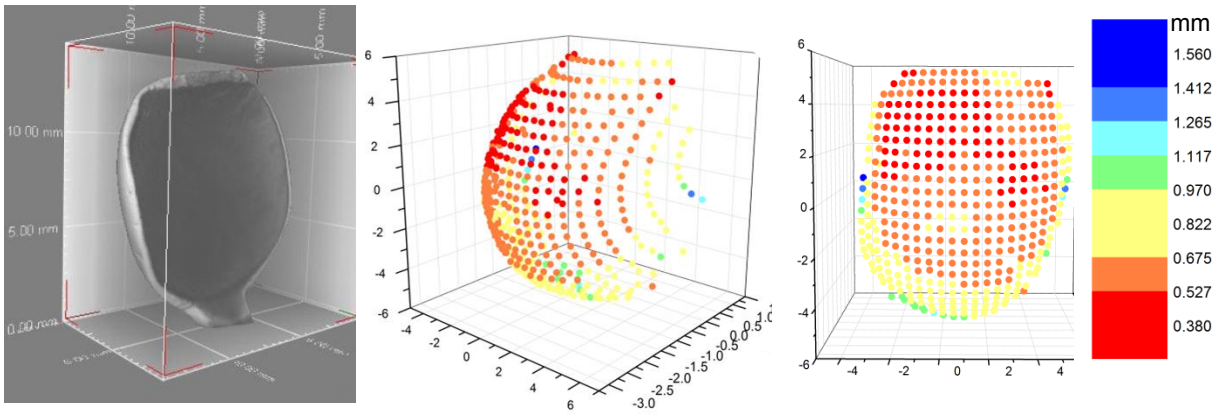

Fig. 4. *3D thickness variation in the celtic drum fibula determined after XCT data analysis.*

By using such data analysis and archeological information [4], it is concluded that the fibula drum was shaped by stamping (and not by necking) of a V shape preform. Also, the volume of the drum is 96 ± 10 mm^3.

A similar approach was used for the pin support part of the fibula and we show that the highest thickness values (~ 1.7 mm) are determined for the tip and at the opposite end, close to the drum, probably for reinforcement at the connexion. It can be deduced that after the stem was flatten, a notch was created and the metal was slighlty folded around to form the barb. The pin also presents different corrosion layers, thin and homogenous (~25 um) in most of the stem with a scarse maximum of 70 um observed at the broken end and in the internal part. A sets of cracks is also noticed thanks to XCT measurements, which are essentially developed in the folded area.

Conclusion

A celtic bronze drum fibula from the Corent site in France was characterized in detail by using XCT. The morphology study revealed some internal cracks that are mostly located in the inner part of the drum. Small corrosion layers (~ 25 um) are also observed. A homogenous thickness was determined throughout the whole drum fibula with metal reinforcement towards the edges and in between the drum and pin parts. It was concluded that a meticulous work based on the stamping method of a preform was used to prepare this archeological specimen.

Acknowledgements

The French FERMaT Federation FR3089 of Midi-Pyrénées is acknowledged for providing X-ray tomography laboratory facility.

References

[1] N Ebinger-Rist et al., Metal (2010) Charleston – South Carolina, P. Mardikian et al. Eds, USA, 342-347.
[2] J. Stelzner et al., Studies in Conservation 55 (2010) 95-106.
[3] P.-Y. Milcent, G. & Saint-Sever (2011) Avant la ville gauloise. In : Poux M. (dir.) Corent. « Voyage au cœur d'une ville gauloise. Errance », Paris, pp. 257-271.
[4] S. Cararra et al., Symposium « L'age du fer en Aquitaine et sur ses marges » (2013) Aquitania, pp. 595-608.
[5] F. Koleini et al., Journal of Cultural Heritage 13 (2012) 246–253.
[6] E. Figueiredoa et al., Metal 07, When archaeometry and conservation meet, 1 (2008) 61-66.
[7] L. Robbiola et al., Corrosion Sci. 40 (1998) 2083-2111

MICRO-CT CHARACTERIZATION OF ARCHEOLOGICAL BONES

H. COQUEUGNIOT[1,2], A. COLOMBO[2,1], C. RITTEMARD[3], O. BAKER[3],
B. DUTAILLY[1], O. DUTOUR[3,1,4],*N. LENOIR[5]

[1] UMR 5199 PACEA, Bat B8, Université de Bordeaux, Allée Geoffroy St Hilaire, 33615 Pessac cedex, FRANCE. helene.coqueugniot@u-bordeaux.fr ; bruno.dutailly@u-bordeaux.fr
[2] Department of Human Evolution, Max Planck Institute for Evolutionary Anthropology, Deutscher Platz 6, 04103 Leipzig, GERMANY. antony_colombo@eva.mpg.de
[3] Laboratoire d'Anthropologie biologique Paul Broca, Ecole Pratique des Hautes Etudes, FRANCE. charlotte.rittemard@etu.ephe.fr ; oussamareha@yahoo.com ; olivier.dutour@ephe.sorbonne.fr
[4] Department of Anthropology, University of Western Ontario, CANADA.
[5] UMS 3626 PLACAMAT, 87 avenue Docteur Albert Schweitzer, 33608 Pessac cedex FRANCE. nicolas.lenoir@placamat.cnrs.fr,
* presenting author

Keywords: micro-CT, growth processes, paleopathology, species identification, archeology

Abstract

The goal of this presentation is to illustrate, in 3 case studies, the interest of micro-CT for studying archaeological bones focusing on growth processes, paleopathological conditions and species identification.

Introduction

Archeology is developping a growing interest in the use of micro-CT for characterizing its artifacts. Among them, ancient bones studies could take a substantial benefit from micro-CT analyses using both experience from fundamental researches on porous materials and clinical survey on microarchitectural bone changes due to osteoporosis.

Using 3 case studies, we illustrate the interest of micro-CT for studying archeological bones focusing on growth processes, paleopathology and species identification. These 3 examples underline the great interest of micro-CT in the study of bone as an archeological artifact.

Methods

In the perspective of characterizing microscopically archeological artifacts, we have developed a complete 3D digital chain dedicated to archaeology, going from CT/micro-CT acquisitions to 3D printing and named VIRCOPAL®, standing for VIRtual COllection of PALeo-specimens (Coqueugniot et al., 2011).

Micro-CT acquisitions of artifacts were performed on a v|tome x|s device (General Electric) at a resolution ranging from 3 µm to 21 µm. Tridimensional reconstructions were carried out using TIVMI® (*Treatment and Increased Vision for Medical Imaging*), a specific software program developed by one of us (Dutailly et al., 2009). It implements a 3D HMH (Half Maximum Height) algorithm that ensures a high fidelity digital model from CT data of archeological items.

For trabecular and cortical canal network characterization, we used a specific algorithm of “skeletonisation” (Palagyi et al. 2001) implemented in TIVMI® software program. This step consists in the use of thinning algorithm and gradually removing pixels from the objects contour, leaving only its “skeleton”. This method provides a simplified version of the bone micro-architecture from which a number of quantitative parameters can be directly measured.

Results

We applied this methodology on archeological bones for exploring variability of microarchitectural parameters that can be observed during growth processes, paleopathological changes and among mammal species.

1. µ-CT and growth process

Microtomodensitometry is opening up new perspectives in bioarchaeology and bioanthropology. Trabecular bone micro-architecture (TBMA) has been so far mostly studied for medical purposes in osteoporosis; it has been little used in anthropology for studying growth processes (Chappard et al. 2008). However, a better understanding of skeletal growth processes is a crucial issue for ancient human populations studies. Indeed, exploring at high resolution TBMA variability linked to the growth processes could solve fundamental issues in research on past populations.

The present study (Colombo 2014) is based on 42 humerus from 3 identified skeletal collections. Selected individuals of known age (0 – 20 years old) and sex did not present any skeletal pathological changes. They represent main post-natal period of development (infancy: [0-3[years-old, n=8; childhood: [3-13[years-old, n=13; adolescence: ≥ 13 years old, n=21). Proximal humeral metaphysis has been selected because its growth plate is responsible for about 80% of adult size. Choice of humerus offers other advantages: contrarily to femur, it does not experience important changes in its global morphology during growth, despite an important increase in size and it is not submitted to biomechanical constraints linked to bipedalism. µCT-scans were acquired to a resolution lower than 20 µm and were reconstructed and analyzed with TIVMI® software program. Trabecular characterization was performed by "skeletonisation", that allows to directly measure trabecular thickness, number and length (respectively Tb.Th, Tb.N, Tb.Le), connectivity (Conn.D) and trabecular bone volume ratio (BV/TV). A semi-automatic protocol, reducing the experimenter actions, based upon scaling criterias and reliable anatomical landmarks present at any moment of the development (metaphyseal contour) was applied on 4 selected volumes of interest (VOI) strictly comparable from one humerus to another (Fig. 1a).

TBMA variability depends on growth processes: the majority of the measured variables are correlated to the individual age. For all the developmental periods, trabecular bone become less dense, because less trabeculae are produced; but trabeculae are thicker and longer. Connectivity doesn't change with age. Changes in the trabecular bone, produced by the growth cartilage, are function of the increasing distance from the cartilage, up to its disappearance at the metaphyseal distal end. Bone maturation, by remodeling, leads to a decrease of BV/TV, both thickness and number of trabeculae. Remodeling activity increases with distance from the cartilage. The farest bone tissue from plate is the oldest produced and the more influenced by environment. During infancy, we can notice the significant decrease of BV/TV, Tb.N and Conn.D whereas Tb.Th increases. From the first to the last VOI, only Tb.N and Tb.Th change significantly. Growth seems to influence the development of variables more than remodeling. During childhood, TBMA varies with age only for Tb.Th which increases again. Remodeling appears very active for this period because all variables (except Conn.D) change significantly. During adolescence, no more variables change with age, only the remodeling still seems to influence BV/TV, Tb.N and Tb.Th. This micro-architectural evolution pattern of trabecular bone could be specific of a given period (infancy, childhood, adolescence) of post-natal growth (Fig. 1b, c). This pattern may be linked to the variations of the various growth regulation factors. Indeed, growth and maturation processes leading to individual adult size and shape are regulated by various interacting factors (nutritive, hormomal, genetic) (Ulijaszek et al. 1998).

Further works in this topic will allow developing new methodologies to identify specific indicators of growth and development in immature individuals remains from archaeological context.

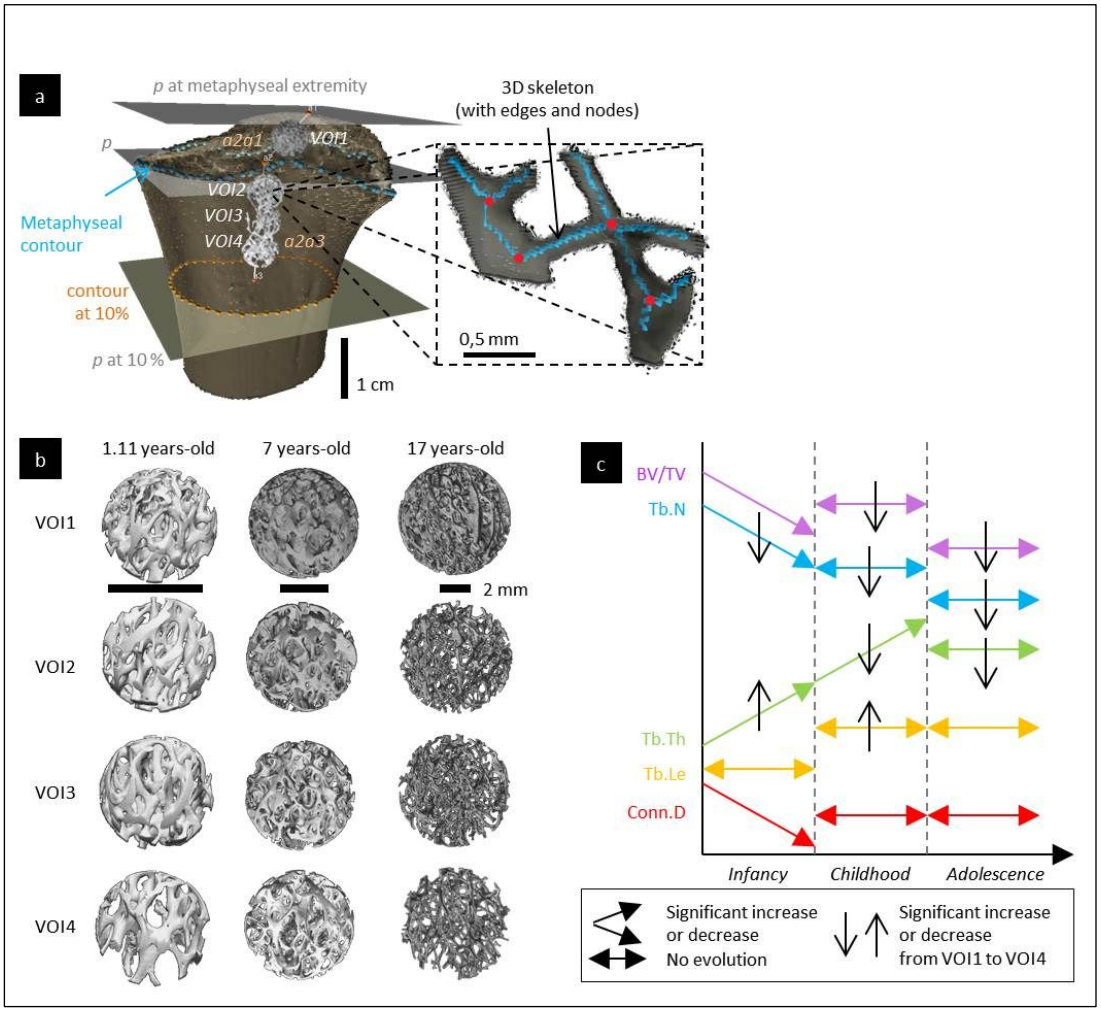

Fig.1. *Microtomodensitometry applied to growth process analyses in archeological context: (a) VOI selection protocol and illustration of the 3D skeleton, (b) examples of TBMA for each growth periods, (c) scheme showing TMBA evolution in function of post-natal growth periods.*

2. µ-CT and paleopathology

It has been previously demonstrated that computed tomography (CT and µ-CT) completed by 3D reconstructions can provide specific information for retrospective diagnosis and recognition of pathological processes in paleopathology (Coqueugniot et al., 2010). This approach has been recently applied to the issue of tuberculosis in the past (Coqueugniot et al, 2015). As an example, we focused on the early emergence of human tuberculosis in the Fertile Crescent (Baker et al, 2015). Paleopathological cases suspected for presenting tubercular lesions were identified in the Early Pre-Pottery Neolithic B (PPNB) site of Dja'de-el-Mughara in Syria (Baker, 2014).

Among the 3 individual suspected cases identified at the DJ3 phase (cal 8540-8290 BCE), a young immature individual with estimated age of 4-5 years old (indicated by dental maturation stage) shows a slight pathological pattern on the anterior part of thoracic and lumbar vertebrae. This morphological aspect is characterized by a slight periosteal reaction observed on the anterior part of 9 vertebral bodies (6 thoracic and 3 lumbar vertebrae) associated with enlargement of the vascular foramina of the anterior venous plexuses (fig 2a). The third lumbar vertebra, analysed by 3D reconstruction of micro-CT acquisition at a resolution of 3 µm, showed internal focal microarchitectural

changes on the antero-lateral part of the vertebral body (figure 2b). This focal reorganisation is characterized by diminution of trabecular connectivity defined by reduction of trabeculae number and thickening, that was quantified (table 1). This pattern corresponds to an early stage of hematogenous infection. Vascular pathways corresponds to the anatomical location of equatorial branches of the vertebral artery. TB has been further confirmed by molecular biology.

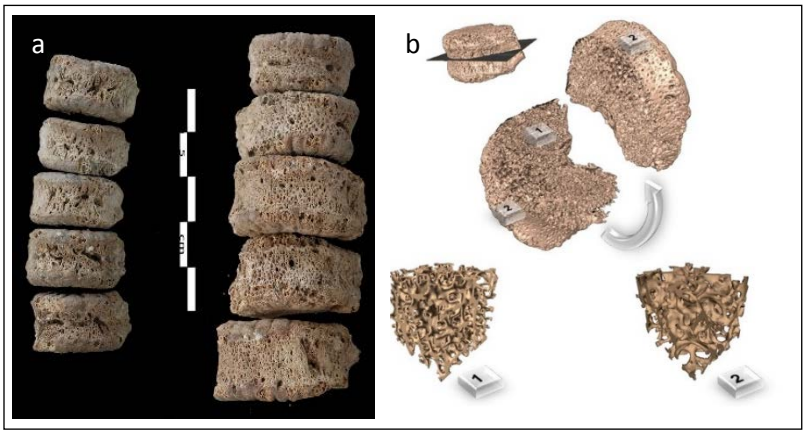

Fig. 2. *Individual B108 from Dja'de el Mughara: (a) paleopathological lesions observed on the anterior part of the vertebral bodies, (b): 3D reconstruction of micro-CT of the third lumbar vertebra showing local disorganization of trabecular architecture and 3D reconstruction of the vertebra showing the two zones of interest: 1 normal architecture; 2 remodeled area, characterized by a greater trabecular separation (decreased number of trabeculae) and an increased trabecular thickness.*

	Involved Area	Normal Area
Trabecular separation (mm)	0.86	0.44
Mean trabecular number / mm	0.66	1.21
Trabecular bone volume (%)	20%	20%
Trabecular thickness (mm)	0.23	0.14

Table 1. *Micromorphometric parameters of involved and normal zones of interest*

3. µ-CT and species identification

Identification of excavated skeletal remains is essential for understanding archaeological sites, and distiguishing human remains from non-human bones is a current task for anthropologists and zooarchaeologists, often faced with difficulties in recognizing fragmentary material. In the lack of discriminant anatomical elements, bone macro-morphological observation might not be sufficient. In this perspective, microscopic study of bone structure can be an alternative. Cortical bone canal network may help for distinguishing between human and animal bones (Cuijpers 2006; Hillier and Bell, 2007; Martiniaková et al., 2007). Histology is the main technique used so far to access bone microstructure. Weakenesses of this technique are twofold : (i) it is destructive, (ii) it is based on 2D analysis of slices. Indeed, the 3D organization of bone (Stout et al., 1999) makes observations in 2D biased, for instance concerning the spatial orientations and connections of cortical canals. Thus, 3D reconstructions of µCT acquisitions appear to be a valid alternative, providing a higher level of analysis compared to the 2D approach. This non-destructive methodology has already been successfully used to analyze for example cortical porosity (Cooper et al., 2007).

In this perspective, we performed a prospective analysis by µCT of cortical bone microstructure on various mammal's species. We compared human (*Homo sapiens*), cow (*Bos Taurus*) and sheep (*Ovis aries*) femoral diaphysis as well as horse's (*Equus Caballus*) metacarpal which can be confused if fragmented with human diaphyses. The analyzed VOIs correspond to the anterior mid-diaphysis region of the bone. Resolutions ranged between 3 to 17 µm. Main studied parameters were cortical porosity and canals organization. In addition to 3D reconstructions, we "skeletonized" these networks for

measuring canal number, diameter, orientation and connections number. Moreover, this method allows a better visualization of networks.

Our results (fig. 3) showed that the microarchitecture of cortical bone clearly differs between human and animal species. Human pattern presents a mature Harversian organization while animal bone is organized as primary laminar bone. Besides, human bone has fewer and straighter canals that are more longitudinally orientated and less interconnected. Metric data corroborate these observations, especially for the number of canals and connections, that is highly greater in the non-human specimens. Moreover, bone microstructure also differs between the animal specimens that display different types of primary bone (plexiform, radial or reticular) as well as metric variations.

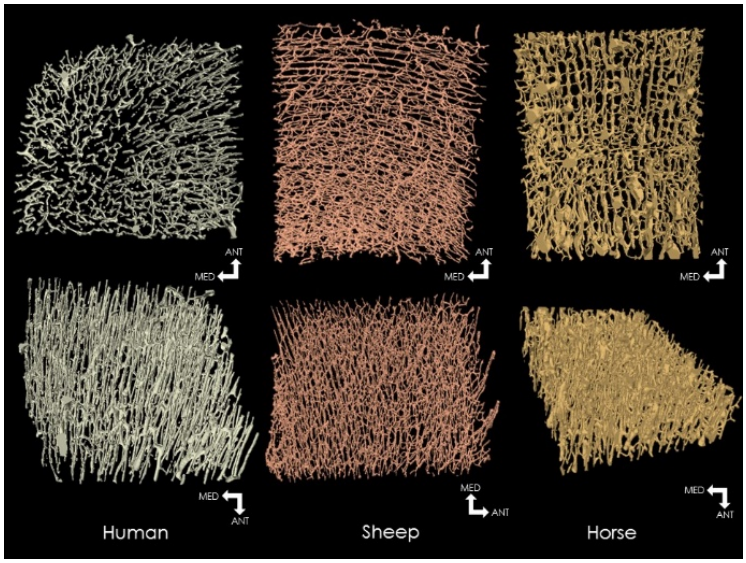

To sum up, µCT and 3D reconstructions performed in this prospective study provided new data on cortical bone microstructure variability among mammal species. Indeed, the 3D approach allows a more accurate analysis and provides an improved visualization of the intra-cortical canal networks for a better understanding and quantification. This approach appears very promising to distinguish on the basis of skeletal fragments, various mammal taxa, including *Homo sapiens*.

Fig. 3. *3D reconstructions (superior views) of the cortical canal networks of human (*Homo sapiens*) and sheep (*Ovis aries*) femurs and metacarpal bone from horse (*Equus caballus*): human bone presents a mature Harversian organization while animal bone is organized as primary laminar (plexiform and radial).*

References

Baker O. (2014). *Paleoepidemiologie de populations neolithiques datant du PPNB (Syrie). Nouvelles données sur la tuberculose avant la domestication*. PhD, Ecole Pratique des Hautes Etudes.

Baker O., Lee O.Y-C, Wu H.H-T., Besra G.S., Minnikin D.E., Llewellyn G., Williams C.M., Maixner F., O´Sullivan N., zink A., Chamel B., Khawam R., Coqueugniot E., Helmer D., Le Mort F., Gourichon L., Dutailly B., Pálfi G., Coqueugniot H., Dutour O. (2015). Human tuberculosis predates domestication in ancient Syria. **Tuberculosis**, in press.

Chappard D, Baslé MF, Legrand E, and Audran M. 2008. Trabecular bone microarchitecture: A review. **Morphologie** 92, 299:162-170.

Colombo A. (2014). *La micro-architecture trabéculaire de l'os en croissance : variabilité tridimensionnelle normale et pathologique analysée par microtomodensitométrie*. [Biological Anthropology]: Bordeaux University. 283 p.

Cooper DM, Turinsky AL, Sensen CW, Hallgrimsson B (2007) Effect of Voxel Size on 3D Micro-CT Analysis of Cortical Bone Porosity. **Calcified Tissue Int** 80,3: 211-219

Coqueugniot H., Desbarats P., Dutailly B., Panuel M., Dutour O. (2010). Les outils de l'imagerie médicale et de la 3D au service des maladies du passé. Actes du Colloque Virtual Retrospect 2009, Collection Archéovision, volume 4, Ausonius Editions : 177-180.

Coqueugniot H., Desbarats P., Dutailly B., Dutour O. (2011). *Procédé de modélisation d'une pièce formée de tissu osseux*. Brevet n°1151284, délivré en France en 2013. CNRS, Université Bordeaux 1, Université Aix-Marseille 2.

Coqueugniot H., Dutailly B., Desbarats P., Boulestin B., Pap I., Szikossy I., Baker O., Montaudon M., Panuel M., Karlinger K., Kovács B., Kristóf L.A., Pálfi G., Dutour O. (2015). Three-dimensional imaging of past skeletal TB: from lesion to process. **Tuberculosis**, in press.

Cuijpers A (2006) Histological identification of bone fragments in archaeology: telling humans apart from horses and cattle. **Int J Osteoarchaeol** 16: 465–480.

Dutailly B, Coqueugniot H, Desbarats, P, Gueorguieva S, Synave R (2009) 3D surface reconstruction using HMH algorith. Proceedings of IEEE International Conference on Image Processing, Le Caire, 7-10 november 2009, p. 2505-2508.

Hillier ML, Bell LS (2007). Differentiating human bone from animal bone: a review of histological methods. **J Forensic Sci** 52:249–263.

Martiniaková M, Grosskopf B, Omelka R, Dammers K, Vondráková M, Bauerová M (2007) Histological study of compact bone tissue in some mammals: a method for species determination. **Int J Osteoarchaeol** 17:82–90.

Palagyi K, Balogh E, Kuba A, Halmai C, Erdohelyi B, Sorantin E, and Hausegger K. (2001). *A Sequential 3D Thinning Algorithm and Its Medical Applications. Information Processing in Medical Imaging*. Springer Berlin Heidelberg. p 409-415.

Stout SD, Brunsden BS, Hildebolt CF, Commean PK, Smith KE, Tappen NC (1999) Computer-assisted 3D reconstruction of serial sections of cortical bone to determine the 3D structure of osteons. **Calcified Tissue Int**, 65,4: 280-284.

Ulijaszek SJ, Johnston FE, and Preece MA. (1998). *The Cambridge encyclopedia of human growth and developement.* Cambridge University Press. 497 p.

THE USE OF METALS AND METAL PRODUCTS ON URBAN AND RURAL ARCHAEOLOGICAL SITES: Reconstructing Technologies Employed by Native American and European Artisans in New France During the 17th and 18th Centuries.

[1] Geneviève Treyvaud*, INRS ETE, Quebec, Canada – Genevieve.Treyvaud@ete.inrs.ca

Keywords: Metal, archaeological, technological choices, tomography, chaînes opératoires

Abstract

This research aims to document the context in which metallurgy occured during the transition period and the colonisation of New France and, through the application of theoretical concepts, principally that of the chaînes opératoires of Leroi-Ghouran developed in his study, L'homme et la Matière, conducted in 1943, to provide a better understanding of an important period in the colonial history of North America. Topics specifi c to the processing of metals, the craftsmanship of objects and the infl uence of technology have only been briefl y described in studies of material culture in North America. Knowledge concerning metalworkers as well as the social and economic impact of their craft during the 17th and 18th centuries is limited. This research focuses on the study of the chaînes opératoires and the metallurgical techniques employed by Native American and European artisans, as well as the technological choices made throughout the process of metal production during a period of technological adaptation to the environment of New France. The artefacts are studied using tomography (CT scan) and by principles of materials engineering with the goals of identifying the source of the metal, the technical signature of the artisans, and the technological problems related to a lack of raw material, as well as to climate and fuel.

Introduction

Our study is of archaeometallurgy. This specialty of archeology, developed in Europe in the seventies. It uses research techniques in conservation of metals, metalwork, chemistry and materials engineering. Since then, the discipline has developed in different laboratories of archaeological research or coservation of archaeomaterials. For this research, we have developed an analytical method based on the use of CT (CT scan). This 3D reconstruction tool of X-ray material (OSIRIX), first developed for medical research, allowing us to get inside the artefact to characterize materials, construction and use without endangering its integrity.

Regarding the archaeometallurgical studies, the choice of the characterization method should be dictated by the archaeological inquiry and based on four main groups. The first brings together the problems of corrosion and conservation of metal objects. The second is the study of the alloy proportion. The third is the study of the development of metals working technology and elaboration of object. These help to rebuild the « *chaînes opératoires* » and, by extension, to highlight the social and environmental impact of metallurgical production. The fourth and final issue is the origin of minerals used for producing metals and objects. The origin of materials allows archaeologists and historians to approach the raw material circulation and to answer questions about the

technological, economic, social and political opérations. This approach to understanding the « chaines opératoires » of American Indians and European artisans of the period of contact and the French regime in New France involves the contribution of archeology, materials engineering, anthropology and history .

Methods

The Tomography can identify the material with which the artifact was designed and also to characterize its manufacturing process. Visual and density data anto identify such materials present in the object under study, or the type of alloy of an artifact, and characterize the inclusions or the other material intake at recycling. Visual analysis during the X-ray passing through the object and 3D reconstruction show the physical transformations that the object during its manufacture. The marks left by tools, repairs and ornementation are also visible. The data acquired by the scanner is received in DICOM format, then processed and analyzed on OsiriX. The results are recorded on analysis card index for each subject studied. They are presented for all studied artifacts of a summary table. Each artifact has been taking a morphological data, to complete the engineering analyzes of materials and technological analysis.

The use of Tomography to archaeological study is unusual, and we constructed a reference system with archaeological samples. This reference has been tested and verified several times. To our knowledge, there is no other archaeological materials database with which we could make useful comparisons for verification. A difficulty associated with the scanning results from the use of data processing software, which is suitable for medical applications. This results in duplication of nomenclature and an additional control when taking data. However, the study of archaeological materials with tomography methods in recent years allow to develop a computer program and a referential for archaeological research.

Results

The main objective of identifying with the tomography « chaînes opératoires » during the production of metal objects by Native Americans and European craftsmen of the transition period and the French regime, between 1500 and 1760 in New France is succesful. For this research we have remains to incomplete for « chaînes opératoires » : the finished objects, tools and some metal scrap, artifacts during manufacture and soil samples for metallurgical work. The identification of manufacturing processes started by collecting all the clues related to metal production and artisans. Each evidence have been studied individually compared and placed in an « chaîne opératoires » in which the missing process of an archaeological point of view are reconstructed. Our contribution to knowledge is twofold: the first is the production of a archaeometallurgy technological study allowing for a Native American craft production. The second results from the use of Tomography as a method of analysis of metal objects.

The study documented and characterized the metallurgical process production, technology and the materials used by Native American artisans and European transition periods and colonial New France. We have developed, using Tomography and engineering materials, new analytical data on a corpus of 197 archaeological items. These results allowed the reconstruction of metallurgical « chaînes opératoires » of colonial power sites and peripheral sites. This documentation allowed us to demonstrate

that on sites of colonial power, Quebec and Montreal, metallurgical work consisted of metallurgical testing, exercise of the metallurgy of iron and copper, repair and manufacture according to the needs of Colony (hardware, edge-tool, etc.). Metallurgical production at the peripheral site of the colonial power, the Fort Témiscamingue, trading posts Pano, Chicoutimi, Métabetchouane and the Bérubé site DDGT-9 reveals shaping processes based on metal recycling of European origin.

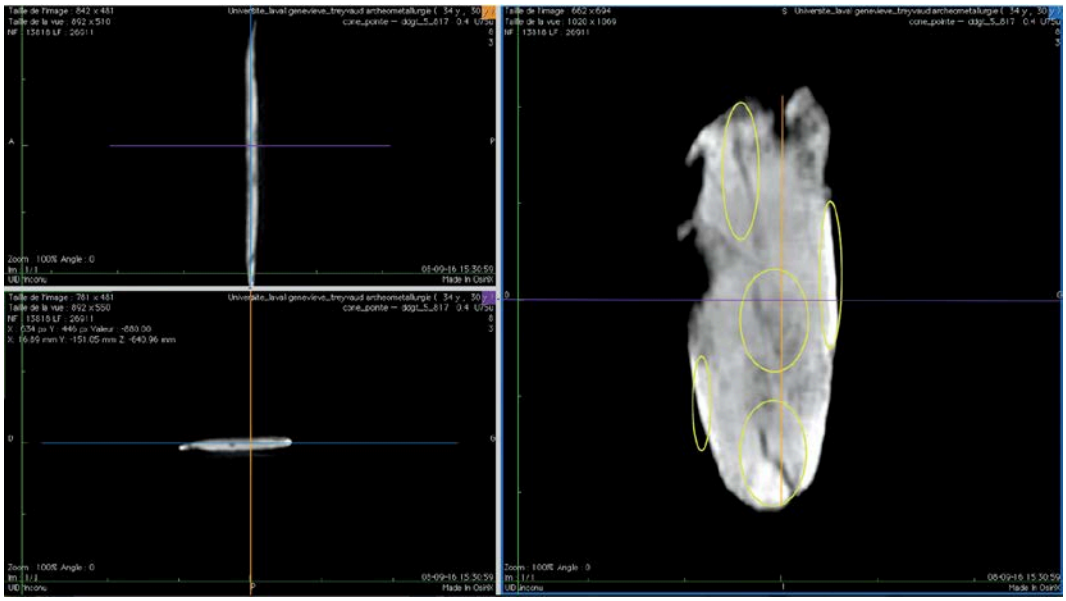

Fig. 1. *Reconstruction and specifications from Tomography to sample CT* n^{o} 817.

Fig.2. *Reconstruction and specifications from Tomography to samples* n^{o} 3830 et n^{o} 2552.

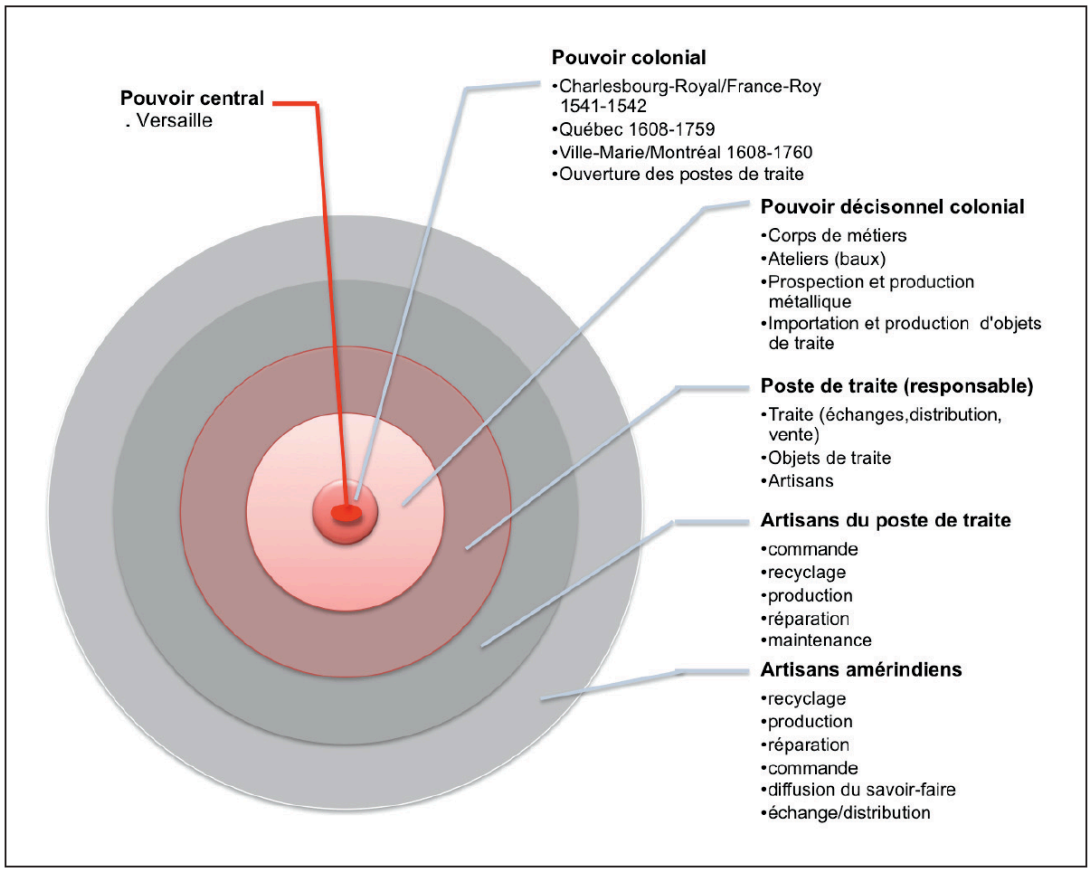

***Fig.3**. Schematic overview of technological spaces of the centers of colonial power and outlying sites.*

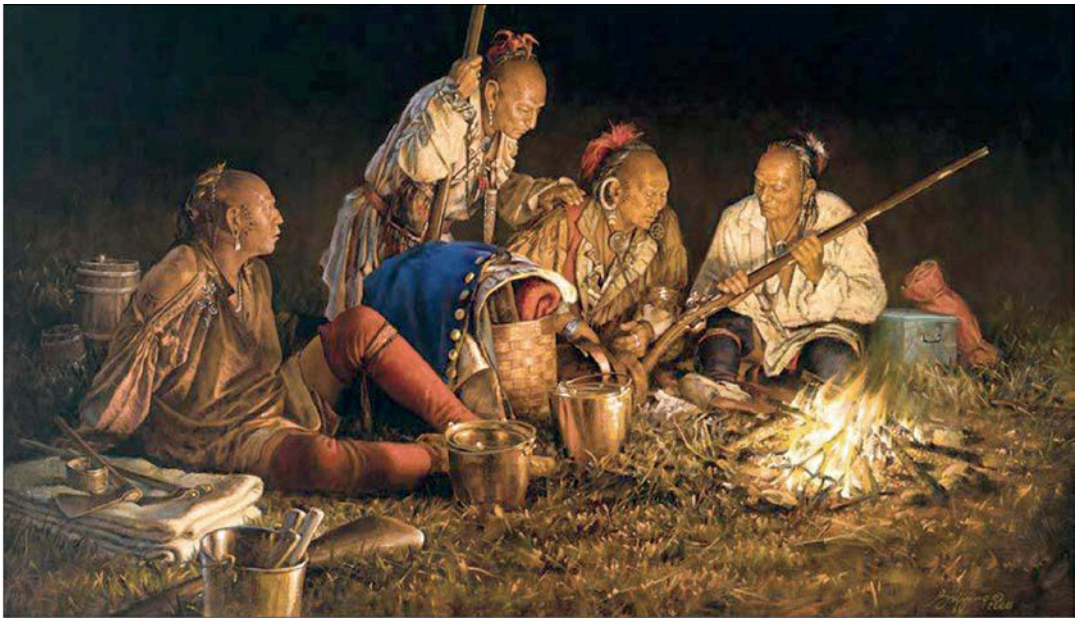

***Fig.4.** By Robert Griffi ng entitled After the Trade, illustrating discussions between Indians following the exchange of material goods (Lord Nelson's Gallery,Gettysburg, PA).*

References

Archaeology

Pérez, Liliane, et Verna, Catherine, 2009, « La circulation des savoirs techniques du Moyen Âge à l'époque Moderne. Nouvelles approches et enjeux méthodologiques », *Tracés, Revue de Sciences humaines* 16. Disponible en ligne : http://traces.revues.org/12473

Redman, Charles L. , 1999, *Human Impacts on Ancient Environments*, University of Arizona Press, Tucson, 219 p. (plus 17 p, références et index).

Redman, Charles, et FOSTER, David R., 2008, *Agrarian Landscapes in Transition : Comparisons of Long-Terms Ecological and Cultural Change*, Oxford University Press, New York.

Thomas, Nicolas, 2009, Les ateliers urbains de travail du cuivre et de ses alliages au bas Moyen Âge : archéologie et histoire d'un site parisien du XIVe siècle dans Villeneuve du temple (1325-1350), Université Paris 1-Panthéon-Sorbonne.

Tomography

Boesflug, X., Ross, N., Long, B.F., et Dumais, J.F., 1994, « Tomodensitométrie axiale: relation entre l'intensité tomographique et la densité de la matière », Canadian Journal of Earth Sciences 31 : 426–43.

Brochu, C., et Ketcham, R.A., 2002. « Computed tomographic analysis of the skull of Tyrannosaurus rex. » CD supplement to : Society of Vertebrate Paleontology Memoir 7, Journal of Vertebrate Paleontology 22 (supplement to No.4).

Callister, William, D., et Callister, Jr., William, 2001, Foundamentals of Materials Science and Engineering : An Interactive CDROM.

Carlson, W.D., Denison, C., et Ketcham, R.A., 1999, « High-resolution X-ray Computed Tomography as a Tool for Visualization and Quantitative Analysis of Igneous Textures in Three Dimensions. » Electronic Geosciences 4 : 3.

Development of a CT-scan data bank for paleopathological analyses: a case study of a protestant cemetery, St-Matthew, Quebec City (1771-1861)

ZOCHA HOULE-WIERZBICKI[1], GENEVIÈVE TREYVAUD[2], EMELINE RAGUIN[3], RÉGINALD AUGER[4] & ISABELLE RIBOT[5]

[1] Département d'anthropologie, Université de Montréal, C.P.6128 Succursale Centre-ville, Montréal, QC H3C 3J7, Canada zocha.hw@hotmail.com
[2] INRS, Institut National de recherche scientifique Centre Eau Terre Environnement 2605, rue du Parc-Technologique Québec, QC G1P 4S5 Canada genevieve.treyvaud@ete.inrs.ca
[3] Département d'anthropologie, Université de Montréal, C.P.6128 Succursale Centre-ville, Montréal, QC H3C 3J7, Canada emeline.raguin@umontreal.ca
[4] Département des Sciences historiques, Université de Laval, Pavillon Charles-De-Koninck, 1030 avenue des Sciences Humaines, Québec, QC G1V 0A6, Canada reginald.auger@celat.ulaval.ca
[5] Département d'anthropologie, Université de Montréal, C.P.6128 Succursale Centre-ville, Montréal, QC H3C 3J7, Canada i.ribot@umontreal.ca

*** presenting author : ZOCHA HOULE-WIERZBICKI**

Keywords: Human paleopathology, Euro-québécois population, Macroscopy, CT-Scan, bone changes

Abstract

As part of a paleopathological research project, human skeletons from the protestant cemetery of St-Matthew (1771-1861 A.D.), have been CT-scanned at the Institut National de Recherche Scientifique, Quebec City (Scanographie – Eau Terre Environnement Laboratory). To overcome key issues in Quebecois bioarchaeology (reburials and loss of information on past health), the main objectives were: 1) to create a repository of CT-scans from the skeletons that were the most well-preserved and the most representative (age, sex, pathology); and 2) to combine this data set with previous macroscopical observations in order to improve paleopathological interpretations. Using a Siemens CT-scanner (SOMATOM model), 56 skeletons (more than 50% of them are young adults) have been entirely CT-scanned. The images in sagittal, coronal and transversal views were then analysed with OsiriX software, searching for abnormalities according to a well-defined protocol for describing both type and distribution of lesions. Finally, they were compared with previous macroscopical observations and then discussed in the light of the possible diagnoses proposed for some cases. Three skeletons that are the most interesting are presented here, to illustrate the necessity to combine macroscopical observations with CT-scan data. The development of this data bank enables us to explore further the etiology of lesions. It provides additional data and interpretations on various diseases (e.g. rickets, scurvy, trauma) that possibly affected the urban Euro-québécois population in the early to mid 19th century.

Introduction

Our knowledge in the field of human paleopathology has grown tremendously, especially following the recent developments in medical imaging. The number of collaborations between research laboratories and academic institutions has increased, providing the opportunity to explore new avenues in bioarchaeology (e.g. isotopes, DNA, radiography, CT-scan, etc). As part of a large team project exploring health and diet of past Euro-québécois populations, this Master's thesis focused on the paleopathological analysis of a well-preserved historic population (Houle-Wierzbicki, in preparation).

The objective was purely methodological, as two approaches were compared to improve the paleopathological diagnoses. A study of this kind is unique in Quebec, and provides a large data bank of CT-scans that resulted from a close collaboration between two Quebecois institutions: Université Laval (Laboratoires d'Archéologie); and the Institut National de Recherche Scientifique (INRS) (Eau Terre Environnement, Laboratoire de Scanographie).

If paleopathologists do not have access to medical imaging, their interpretations on the lesions may remain limited, especially in terms of the possible diagnoses. As a consequence, frequency and severity of some diseases cannot be well ascertained at both individual and population levels. The preliminary results of the present project are presented here, focusing on three archaeological cases. They aim to show how macroscopical observations, when compared with CT-scans, can improve paleopathogical diagnoses.

Material and Methods

From the two hundred skeletons available from St-Matthew's cemetery (1771- 1861 A.D.), only a few (N=56) have been selected for the present analysis, as they were the most well-preserved. Out of this sub-sample, three specimens were chosen to illustrate bone changes related to metabolic disease and trauma. During phase one, all the skeletons were observed macroscopically, for age and sex estimates, as well as, for recording distribution and severity of bone lesions (according to Buikstra & Ubelaker, 1994).

Phase two of the work consisted of creating a data bank of CT-scans. All the CT-scans were done using a Siemens CT scanner, SOMATOM model (Definition AS+ 128) with settings varying slightly according to bone density (e.g. scale: 0.4-0.6mm in Z; Pitch: 0.6-1; Mas 90; reconstruction filters: U90U, B60). Each skeletal element was placed on a table in a standard anatomical position and then CT-scanned from the cranium to the feet.

All the images (CT-scans in sagittal, coronal and transversal sections) were viewed and analysed with OsiriX software. Any abnormality in the bone tissue (e.g. osteolytic or osteoblastic reaction) was identified and recorded in detail and compared to previous macroscopical observations of the bone surface.

All the osteological data (e.g. data, measurements, photos, CT-scans) were grouped and organized using FileMaker Pro. Lastly, on the basis of what was observed macroscopically and using the CT-scans, a set of hypotheses was proposed for each specimen showing lesions. The paleopathological conditions that were most probable on the basis of the observations, are discussed here for three cases.

Three unique paleopathological cases

CeEt 41-11A2.5: a child with severe vitamin deficiencies.

Despite its skeletal incompleteness, this young specimen (age: ±1 year) showed palaeopathological evidence that he or she was affected possibly by some rather severe metabolic disorder (Brickley & Ives 2009). Macroscopically, a high number of diagnostic features related to rickets (and a few for scurvy) were observed on the skull and post-cranial skeleton, such as:

i) medial angulation of the mandibular ramii;
ii) marked hypoplastic defects on various deciduous teeth and first permanent molars;
iii) alterations of ribs (e.g. angle of neck, *rachitic rosary* or enlargement of costochondral junction);
iv) alterations of long bones (e.g. flaring/swelling and cupping deformities of distal metaphyses, bowing of diaphyses especially *genu varum* for femora, *coxa vara* or femoral head/shaft angulation <120°); and,
v) alterations of growth plates (e.g. porosity, cupping deformities).

A series of more general and less diagnostic features than those above (related not only to metabolic diseases but also other conditions) were also observed:

i) *craniotabes* or bone softening behind ears and next to lambdoid suture;
ii) retarded growth of pelvis;
iii) periosteal porosity on long bones.

However, the hypothesis of a metabolic condition was further supported by CT-scans showing poor bone mineralization and therefore osteopenia. Both trabecular and cortical bone density appeared to be severely decreased especially in the lower limbs (e.g. long bones metaphyses, growth plates). It is not impossible that this child was affected by both rickets as well as scurvy (since fetal development). In fact, periods of seasonal starvations causing various vitamin deficiencies (e.g. A, C, D) were rather frequent in 19th century Quebec City, and pregnant women, mothers and infants were those at higher risk.

CeEt 41-10A1 gr.2: a mature adult with healed trauma on the right calf.

This complete male skeleton (age: ±20-39 years) presents clear signs of a healed bone injury on the right fibula. Macroscopically, the proximal third of this bone showed the formation of a large callus, probably as a consequence of the healing of a shaft fracture (Ortner, 2003). As the two broken ends of the diaphysis have not been realigned, the total length of the fibula was slightly shorter. The use of the CT-scan enabled us to confirm that it was a well healed oblique fracture and that the impact must have originated mainly from a superior angle, affecting mainly the postero-lateral side of the calf bone.

CeEt 41-10A1 gr.16B: a mature adult with healed trauma on both ankles.

Despite its skeletal incompleteness, this male skeleton (age: ±20-39 years) also shows lesions on both lower limbs. Macroscopically, a complete fusion of the two bones (fibula and tibia) on the left ankle can be observed. Distal epiphyses of both fibula and tibia are bridged by abnormal lamellar bone. A similar bony fusion on the right side is also partially visible. As the CT-scans showed no lines of fractures on both ankles, two possible diagnoses are proposed. On one side, as other degenerative bone changes were observed on the vertebral column and sacro-iliac joints, these lesions on the ankles could be caused by osteoarthritis and therefore various factors (e.g. age, joint overuse, and/or genetic predisposition) (Aufderheide & Rodriguez-Martin 1998; Adler 2000). However, on the other side, the hypothesis of post-traumatic lesions cannot be

rejected, although CT-scans showed no lines of fractures on both ankles. In fact, according to sports medicine, repeated dislocations of the ankles can lead indirectly to the fusion of the tibia and fibula *via* the ossification of various tibio-fibular ligaments. It is therefore assumed that this male specimen who lived in a pre-industrial context with a high load of manual work, could have been exposed to repeated biomechanical stress.

Conclusions and perspectives

These three examples presented above show the importance of combining different approaches in palaeoptahology, in order to avoid confusion with taphonomical processes and to improve possible diagnoses. Nevertheless, when two diseases possibly coexist as in the first case (rickets and/or scurvy), it is worth considering additional histological analyses of the bone's microstructure, as it could help to distinguish between various metabolic disorders.

References

Adler C. (2000). *Bone Diseases : Macroscopic, Histological and Radiological Diagnosis of Structural Changes in the Skeleton*. Springer-Verlag, New York, USA, 588 p.

Aufderheide A, and C. Rodriguez-Martin (1998). *The Cambridge Encyclopedia of Human Paleopathology.* Cambridge University Press, New York, USA. 478 p.

Buikstra J. and D. Ubelaker (1994). *Standards for Data Collection from Human Skeletal Remains: Proceedings of a Seminar at the Field Museum of Natural History*. Arkansas Archeological Survey Series #44, Fayetteville, USA, 272 p.

Grauer A. (2012). *A Companion to Paleopathology*. Blackwell companions to anthropology, Malden, USA, 626 p.

Houle-Wierzbicki, Z. (In preparation). *Étude paléopathologique à travers l'analyse macroscopique et scannographique: Exemple du cimetière protestant Saint-Matthew, ville de Québec (1771- 1861)*, mémoire de maîtrise, Montréal. Université de Montréal, co-dir. Université Laval.

Ortner DJ. (2003). *Identification of pathological conditions in human skeletal remains.* Smithsonian Institution Press, San Diego, USA, 645p.

Session 313

Statistical Interpretation of Heterogeneity based on the CT Scanning Data

SINAN CALISKAN[1]* AND ABDULLAH SHEBATALHAMD[2]

[1] Saudi Aramco, EXPEC Advanced Research Center, Dhahran, Saudi Arabia – sinan.caliskan@aramco.com
[2] Saudi Aramco, EXPEC Advanced Research Center, Dhahran, Saudi Arabia – abdullah.shebatalhamd@aramco.com
* presenting author

Keywords: Core analysis, Heterogeneity index, Coefficient of variation, Histogram

Abstract

Core analyses are carried out on selected rock samples with to establish a database to provide direct and quantitative measurements and interpretations about reservoir characteristics. During a careful sample selection process, besides available conventional data such as porosity and permeability, it is also important to understand the degree of heterogeneity of core samples. In this respect, Computerized Tomography (CT) scanning technique has been selected due to its non-destructive cross sectional imaging capability. CT scanning images obtained by medical type CT scanners are reconstructed on a 512x512 grid of pixels, with a typical resolution of 50 to 300μm depending on the sample size. Since the CT numbers are based on the density of rock samples, the heterogeneity analysis based on the CT numbers reflects the lithology of the samples being examined. Therefore, understanding the statistics of the CT images can significantly contribute towards an accurate classification and improved sample selection of the rock samples into different level of heterogeneities/homogeneities, which in turn significantly contributes towards the success of specialized studies, e.g. Special Core Analysis (SCAL) tests, Enhanced Oil Recovery and Acid Treatment. To examine the level of heterogeneity of rock samples on the basis of CT numbers, this study focuses on the application of statistical parameters, including *Coefficient of Variation* (*CV*) and *Heterogeneity Index* (*HI*) as well as histogram. The results indicated that only visual examination of CT images are not adequate but more thorough examination, such as statistical methods are effective and required to document the heterogeneity of rock samples.

Introduction

One of the important stages of core analysis is to select representative plugs from various depth intervals of a reservoir. Selection of samples for particular laboratory tests for homogeneous zones in clastic material can relatively be straight forward through visual inspection and does not exhibit great challenges. However, selecting representative samples for laboratory tests in heterogeneous zones could be a challenging task and require a good understanding of reservoir and detailed study will be necessary. Core analysis (e.g. petrophysical, petrographic, paleontological, sedimentological and diagenetic information) plays a major role in the understanding of a reservoir, allows to reduce uncertainties incorporated into static and dynamic reservoir models as well as the overall field production and development planning. Therefore, a good design of a core analysis programme requires representative core material is prerequisite for successful laboratory tests. Hence, well drilling programmes should be planned meticulously with respect to coring of the important parts of the reservoir, retrieval of core material from reservoir to surface, surface handling, and transport to the laboratory.

Within the laboratory core sample tests, the SCAL tests which include wettability, capillary pressure, and relative permeability are very important and time consuming. Therefore, after obtaining core plug samples, further sample selection with respect to the level of porosity, permeability or homogeneity/heterogeneity will be necessary. This process greatly increases the success rate of the lengthy laboratory experiments that will be conducted on the samples (Siddiqui et al, 2003; Ottesen and Hjelmeland, 2008). In this study, the significance of understanding of the heterogeneity with respect to sample selection through some statistical approach based on CT scanning data will be discussed. Example samples mainly of carbonate origin will be presented along with standard samples of fused quartz and macor (ceramic).

Methodology

When a rock sample is CT scanned (see Fig. 1), focused and collimated beams from an X-ray source penetrate and travel through matter and the attenuated beams are recorded by detectors. The attenuation of the energy in the X-ray beams is related to the density, the thickness and the mineralogical of the sample being scanned. Each mineral has a distinct linear attenuation coefficient and hence the total response received by the detectors is a combination of these coefficients. In the current study, energy level of 135 kV / 150 mA is used with each volume element representing a parallelepiped element with dimensions of about 0.1×0.1×1.0 mm. This means that each slice image includes approximately 250,000 pixels with unique CT numbers. Therefore, understanding the statistical interpretation of these CT images is of great value with respect to the level of heterogeneity.

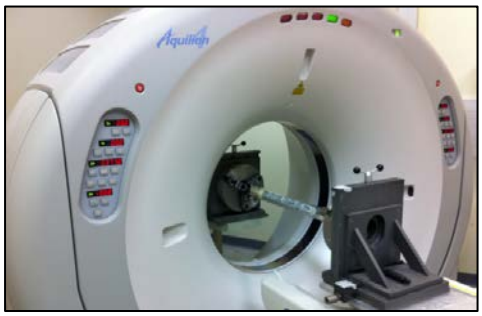

Fig. 1. *The medical CT scanner used in this study.*

Results

To demonstrate the use of CT scanning data as a statistical tool, a total of seven cylindrical rock samples (two standards, two Edwards limestone and three local limestones) have been used in this study. The basic properties of the samples are given in Table 1., On each slice images, a series of statistical comparisons have been made to examine the level of heterogeneity (Figs. 2 to 4). These comparisons included the coefficient of variation (*CV=Standard Deviation/Mean*) and histogram of the CT numbers. Furthermore, the *Heteregoneity Index* (*HI*) (Coen et al., 1996) is also used in this study and defined as the ratio between maximum and minimum values and the mean value (*HI=(Max–Min)/Mean*). Similar to the *CV*, homogeneity tends towards a *HI* value of zero whereas the heterogeneity increases when *HI* values are drifting away from 0. In addition to these, CT slice images are included alongside the histograms.

Table 1. *Basic characteristics of the samples in this study.*

Samples	Porosity (%)	Permeability (mD)	(Diameter x Height) mm
Quartz	0	0	65 x 150
Macor	0	0	65 x 150
Edwards-1*	~ 17	~ 10	38 x 75
Edwards-2*	~ 17	~ 10	38 x 75
Limestone-1	26.9	563	38 x 50
Limestone-2	27.4	1680	38 x 55
Limestone-3	2.9	0	38 x 55

* (kocurekindustries.com, 2015)

The statistical comparisons for the standard samples (quartz and macor) given in Fig. 2 show that the level of homogeneity is rather large (*HI* and *CV* are closer to zero) as expected and is exhibited by all the statistical tools used in this study. A slight increase in the level homogeneity of Macor with respect to quartz has been observed and displayed statistically. Fig. 3 shows the comparison of two different Edwards limestone samples; the first and second samples are respectively more and less heterogeneous. Whilst the CT slice images are not able to display the heterogeneity quantitatively and with full clarity, the statistical tools highlights the heterogeneity in details. Particularly, it is evident that the heterogeneity of the Edwards samples increased significantly with respect to the standard samples (Fig. 3).

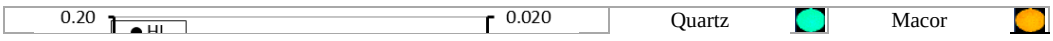

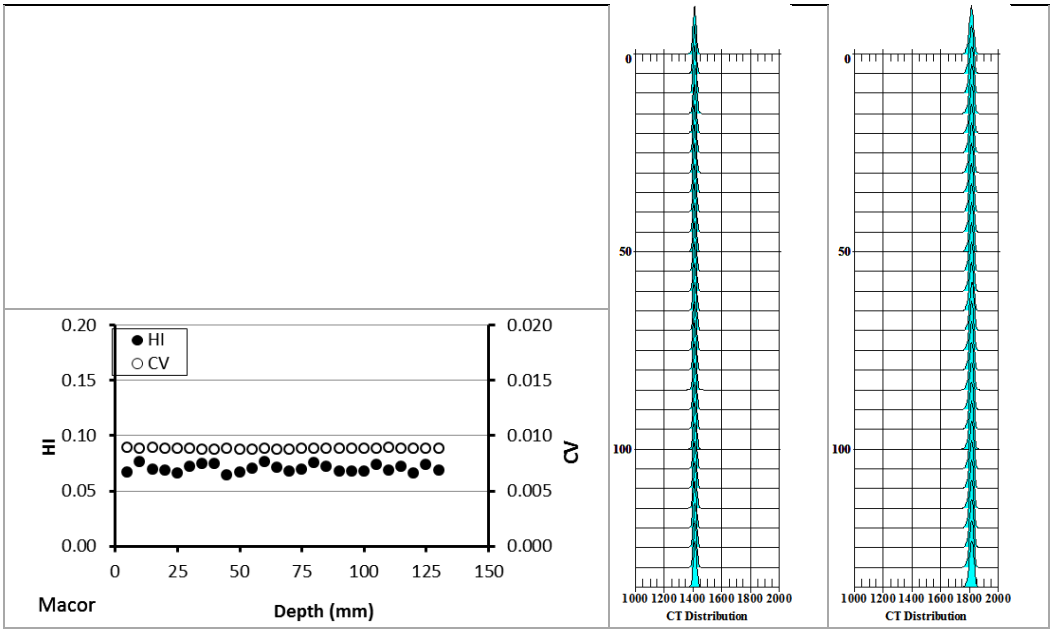

Fig. 2. *Standard samples (Quartz and Macor)*

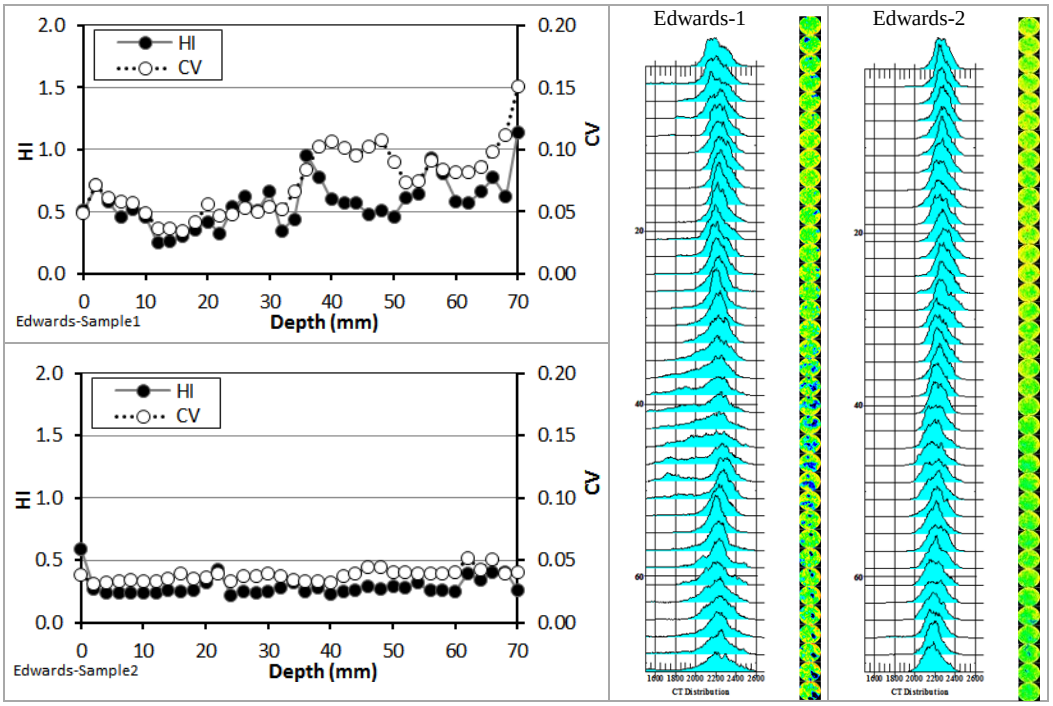

Fig. 3. *Details of Edwards limestone samples 1 and 2*

Furthermore, samples of local limestones were included in the study and their comparison is given in Fig. 4, where it is shown that there are inter-sample as well as intra-sample heterogeneities. All the statistical tools used in this study indicated high heterogeneity showing that the use of statistical tools are a necessary part of the sample selection process in addition to conventional sample selection techniques, e.g. visual examination, porosity and permeability.

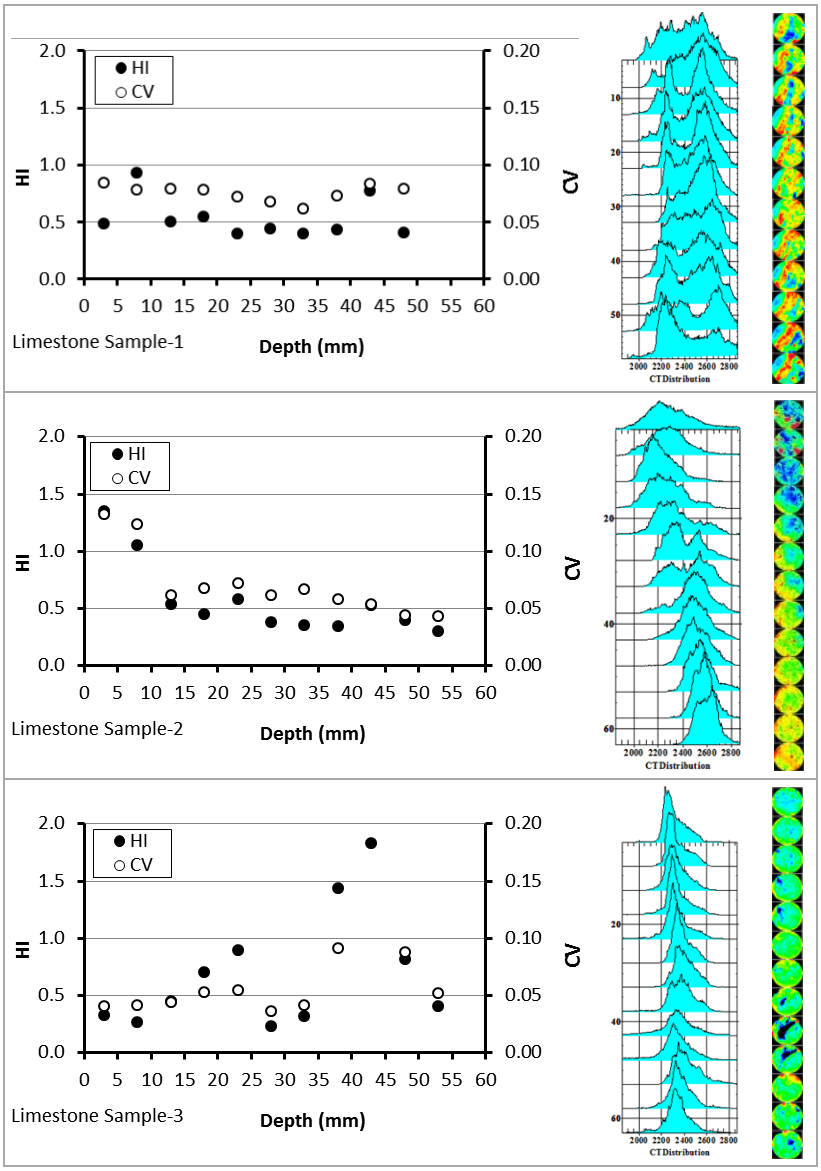

Fig. 4. *Details of Limestone samples 1, 2 and 3.*

Conclusions

From the application of statistical tools to evaluate rock samples heterogeneity from CT scan data the following conclusions can be drawn:

- Obtaining basic properties, such as porosity, permeability and density of the rock samples would not be adequate in understanding the level of heterogeneity or homogeneity and that statistical tools should be used.
- To understand and evaluate the heterogeneity or homogeneity of the rock samples, CT scanning images are not sufficient, though they provide quick and approximate inspection.
- Further statistical tools, such as *CV*, *HI* and histograms should also be used alongside the CT images.
- The CT scanning data analysis and the statistical interpretation enables the comparison of rock samples within each sample (intra-sample heterogeneity) as well as between different rock samples (inter-sample heterogeneity).

References

Ottesen B. & Hjelmeland O. (2008). *The Value Added From Proper Core Analysis*, (SCA2008-04) Int Symposium of the Society of Core Analysts, Abu Dhabi, UAE

Siddiqui S., Okasha T. M., Funk J. J. & Al-Harbi A. M. (2003). *New representative sample selection criteria for special core analysis*, (SCA2003-40) Int Symposium of the Society of Core Analysts, Pau, France

Coen V.; Lartigau E.; Haie-Meder C.; Lambin P.; Marsiglia H.; Briot E. & Gerbaulet A (1996), **J. Radiotherapy and Oncology** 39, 1: 9-9

www.kocurekindustries.com (2015). *edwards-white-cores*

3D imaging of clay minerals inside sandstone – Pushing the spatial resolution limits using ptychographic tomography

W. De Boever*[1], H. Derluyn[1], J. Van Stappen[1], J. Dewanckele[1], T. Bultreys[1], M.N. Boone[2], T. De Schryver[2], Tim De Kock[1], E. T. B. Skjønsfjell[3], A. Diaz[4], M. Holler[4], V. Cnudde[1]

[1] PproGRess – UGCT – Dept. of Geology and Soil Science – Ghent University, Ghent, Belgium – Wesley.Deboever@ugent.be
[2] Radiation Physics Group – UGCT – Dept. of Physics and Astronomy – Ghent University, Ghent, Belgium
[3] Dept. of Physics – Norwegian University of Science and Technology – Norway
[4] Swiss Light Source (SLS) - Paul Scherrer Institute – Villigen - Switzerland
* presenting author

Keywords: Ptychography – Tomography – Clays – X-ray Scattering

Abstract

Characterization of microporous, clay-sized particles in natural stone is essential for the understanding of their dynamics. These processes are importand in the fields of oil and gas, groundwater, building stone weathering and soil science. Methods such as X-ray micro-computed tomography is an excellent tool to study features larger than or just under 1 µm, but below the 400 nm limit, the technique falls short. Although destructive methods exists (e.g. FIB/SEM), non-destructive imaging at these very high resolutions has been impossible, until recent developments at synchrotron beam lines.

In this study, we use ptychographic tomography at the cSAXS beam line of the PSI in Switzerland, for imaging of clay microstructure at resolutions down to 45 nm, which is the first application of ptychographic tomography for geological samples to our knowledge. During these experiments, relative humidity of the sample's environment was controlled, in order to asses the influence of R.H. on the analyzed clay minerals. Based on these images, quantitative data on mineral content, porosity, connectivity and behavior under changing environmental conditions of clay mineral clusters was acquired.

Introduction and methodology

High resolution X-ray tomography (µ-CT) has proven to be a valuable tool in geosciences (Cnudde and Boone, 2013; Ketcham and Carlson, 2001; Wildenschild and Sheppard, 2013). The development of the method provided new insights on the internal structures of rocks and sediments, adding an extra dimension in comparison with more traditional techniques such as electron and optical microscopy. With µ-CT it is possible to image and analyse samples from the centimeter to the millimeter scale, a key feature for the study of heterogeneous geological materials.

However, the resolution of X-ray tomography is typically limited to a few hundreds of nanometers for standard laboratory setups (Dierick et al., 2014), or just under one hundred nanometer for synchrotron tomography or laboratory systems using optics (Kastner et al., 2010). This leaves an important resolution gap between scanning electron microscopy and µ-CT data. For this reason, the quantitative study of microporous or fine-grained materials is typically not done using µ-CT. We propose the novel application of ptychographic tomography at synchrotron beam lines for geological samples, to quantitatively study porosity and pore network characteristics of fine-grained clay minerals inside two varieties of sandstone (French Vosges sandstone and Indian Kandla Grey sandstone). The behavior of clay minerals is of great importance in the prediction of weathering of building materials, and direct imaging of their structure under changing conditions has been impossible up until now, a problem that has been traditionally solved

by indirect measurements on large samples (Van Den Abeele et al., 2002; Wangler et al., 2011).

Ptychography is a coherent diffraction imaging technique in which a coherent, confined X-ray illumination is used to scan the specimen in such a way that the illumination spot overlaps at consecutive scanning positions. Coherent diffraction patterns are recorded in the far field at each position, and iterative phase retrieval algorithms are then used to reconstruct the complex-valued transmissivity of the specimen (Rodenburg and Faulkner, 2004). The resolution of this technique is only limited by the scattering angles at which diffraction intensities can be reliably recorded, and can be as little as 16 nm (Holler *et al.*, 2014), much better than the size of the illumination or the scanning step size. By combining 2D phase projections acquired at different incident angles of the X-ray beam (Fig. 1), quantitative 3D distributions of electron density can be obtained (Diaz et al., 2012; Dierolf et al., 2010). Geological samples are very suited for ptychographic imaging, as they are very stable and do not tend to suffer from radiation damage. This is an important characteristic, as ptychographic tomograms take several hours up to a full day to acquire. However, as in most high-resolution imaging techniques, a drawback is that the samples have to be very small to achieve these extreme resolutions.

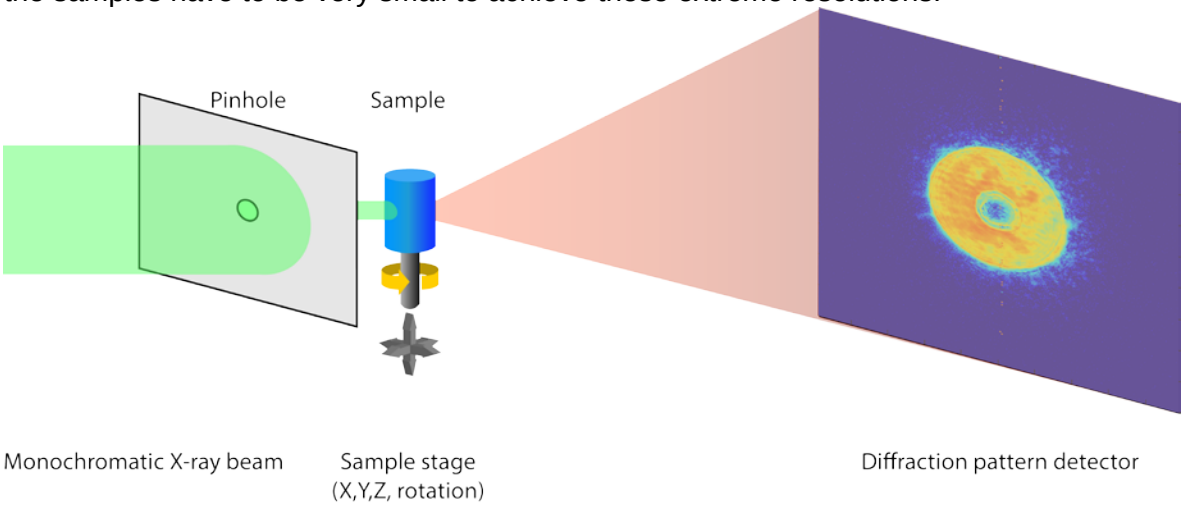

Fig. 1. *Schematic representation of the layout of the cSAXS beam line.*

Clay mineral samples were extracted from the stone, and mounted on a sample pin for analysis. The samples (< 50 µm) where imaged at the cSAXS beam line of the Paul Scherrer Institut in Villigen (www.psi.ch), obtaining a voxel size of 34 nm, and a corresponding spatial resolution of 89 to 136 nm in 3D. During these measurements, we were able to control the relative humitidy of the sample's environment, enabling us to analyze and compare the behavior of extracted clay minerals at high (95 %) and low (5 %) relative humidiy. In following experiments, a 25 µm sized sample was measured using the setup described in Holler et al. (2014), achieving a spatial resolution of 45 nm (voxel size 17 nm) in 3D.

Summary of results

The resulting images show excellent contrast between pores and grains, and different mineral phases were clearly distinguishable. This enabled us to get quantitative results on clay microporosity, connectivity and shape of the pore network, and distribution of different mineral phases in these clay clusters. The nanoporosity inside mica minerals from the Kandla Grey sandstone was visualized, and the preferantial absorption of liquids

through these paths was proven (Fig.2). Images recorded during relative humidity control showed a small volume increase from dry to wet state in a sample from the Vosges sandstone. Furthermore, different mineral phases could be identified based on their refracion index, and their distribution of could be visulaized and analyzed. This way, it was possible to see the relative amount of different clay minerals (Fig. 3). At the highest resolution, we could observe how tiny iron oxide particles coat the exterior of larger grains, causing the macroscopical red to pink color of the Vosges sandstone.

The results prove that ptychographic tomography is a novel method that provides outstanding images of geological materials. The possibility of adding peripheral equipment during these measuremen

Ptychographic tomography proves to be a novel method providing outstanding images of geological materials. The possibility of adding peripheral equipment during these measurements, whilst maintaining very high resolutions makes it a unique method, with many possibilities for the entire geoscience community.

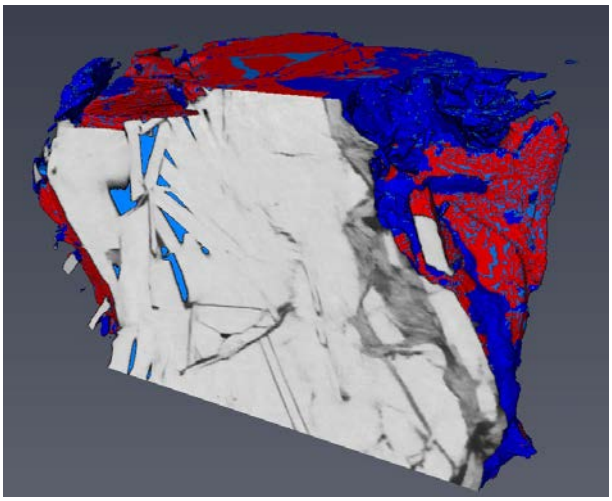

Fig. 2. *3D render of sample K1: A muscovite cluster with narrow cleavage porosity, filled with liquid. Sample size is about 40 µm.*

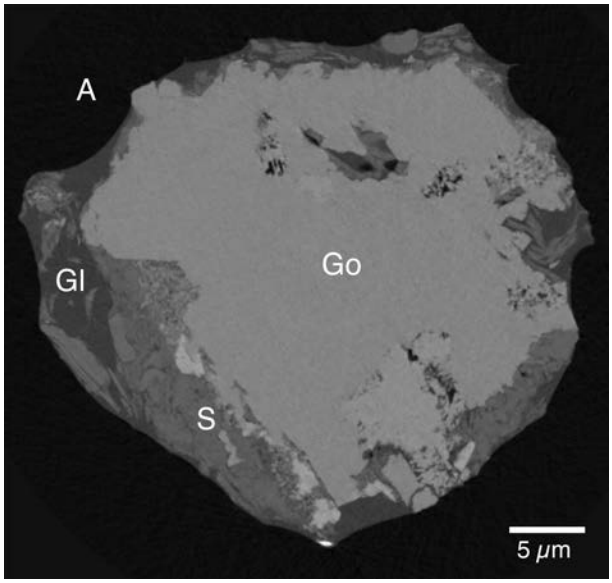

Fig. 3. *Horizontal slice through a sample imaged at a resolution of 106 nm. Different phases inside the sample can be observed: Air (A), glue holding the sample in place (Gl), smectite clay minerals (S) and goethite iron oxide (G).*

References

Cnudde, V., Boone, M.N., 2013. High-resolution X-ray computed tomography in geosciences: A review of the current technology and applications. Earth-Science Rev. 123, 1–17. doi:10.1016/j.earscirev.2013.04.003

Diaz, A., Trtik, P., Guizar-Sicairos, M., Menzel, A., Thibault, P., Bunk, O., 2012. Quantitative x-ray phase nanotomography. Phys. Rev. B 85, 020104. doi:10.1103/PhysRevB.85.020104

Dierick, M., Van Loo, D., Masschaele, B., Van den Bulcke, J., Van Acker, J., Cnudde, V., Van Hoorebeke, L., 2014. Recent micro-CT scanner developments at UGCT. Nucl. Instruments Methods Phys. Res. Sect. B Beam Interact. with Mater. Atoms 324, 35–40. doi:10.1016/j.nimb.2013.10.051

Dierolf, M., Menzel, A., Thibault, P., Schneider, P., Kewish, C.M., Wepf, R., Bunk, O., Pfeiffer, F., 2010. Ptychographic X-ray computed tomography at the nanoscale. Nature 467, 436–9. doi:10.1038/nature09419

Kastner, J., Harrer, B., Requena, G., Brunke, O., 2010. A comparative study of high resolution cone beam X-ray tomography and synchrotron tomography applied to Fe- and Al-alloys. NDT E Int. 43, 599–605. doi:10.1016/j.ndteint.2010.06.004

Ketcham, R.A., Carlson, W.D., 2001. Acquisition, optimization and interpretation of X-ray computed tomographic imagery: applications to the geosciences. Comput. Geosci. 27, 381–400.

Rodenburg, J.M., Faulkner, H.M.L., 2004. A phase retrieval algorithm for shifting illumination. Appl. Phys. Lett. 85, 4795. doi:10.1063/1.1823034

Van Den Abeele, K.E., Carmeliet, J., Johnson, P.A., Zinszner, B., 2002. Influence of water saturation on the nonlinear elastic mesoscopic response in Earth materials and the implications to the mechanism of nonlinearity. J. Geophys. Res. Surf. 107, 1–11.

Wangler, T.P., Stratulat, A., Duffus, P., Prévost, J.H., Scherer, G.W., 2011. Flaw propagation and buckling in clay-bearing sandstones. Environ. Earth Sci. 63, 1565–1572. doi:10.1007/s12665-010-0732-y

Wildenschild, D., Sheppard, A.P., 2013. X-ray imaging and analysis techniques for quantifying pore-scale structure and processes in subsurface porous medium systems. Adv. Water Resour. 51, 217–246. doi:http://dx.doi.org/10.1016/j.advwatres.2012.07.018

Construction of Complex 3D Digital Rock Models

I.V. YAKIMCHUK*[1], I.A. VARFOLOMEEV[1,2], N.V. EVSEEV[1], B.D. SHARCHILEV[1], O.A. KOVALEVA[1,2], D.A. LISICIN[1,2], D.A. KOROBKOV[1], S.S. SAFONOV[1]

[1] Schlumberger, Moscow, Russia – iyakimchuk@slb.com
[2] Moscow Institute of Physics and Technology, Dolgoprudny, Russia
* presenting author

Keywords: Digital rock, X-ray tomography (CT), scanning electron microscopy (SEM), energy dispersive X-ray spectroscopy (EDX)

Abstract

The complex method for constructing 3D digital models of rock media for numerical simulation is considered. The general concept consists of increasing the digital rock model's information content by combining independent experimental studies of the various properties of the same rock specimen. Particularly, two possibilities are evaluated: 3D mineral mapping and mapping of porosity nonresolved by imaging technique on a digital rock models originally derived from X-ray microtomography (microCT) data. The importance of such complications is demonstrated in the present study.

Introduction

The concept of creating a digital representation of a reservoir rock sample for further numerical analysis of its petrophysical properties was reported in the literature several decades ago (Kostek et al., 1992; Auzerais et al., 1996). This concept has a number of benefits and shortcomings with respect to traditional laboratory core analysis. The digital rock method is becoming more and more attractive nowadays due to the recent advances in the development of imaging methods, new areas of applications, and increasing performance and accuracy of numerical simulations.

Ordinarily, digital models are constructed using the least complex method; i.e., by binarization of gray-scale microCT images on voids and solids (Figure 1), which is sufficient to obtain qualitative results from certain flow simulation experiments. Modern sophisticated numerical simulation techniques allow taking into account a sizeable set of physicochemical properties during calculation (e.g., mineralogy, mechanical strength, thermal conductivity, wettability) with respect to their volumetric spatial distributions. This type of information can be obtained to some extent by using continuously developing experimental imaging techniques.

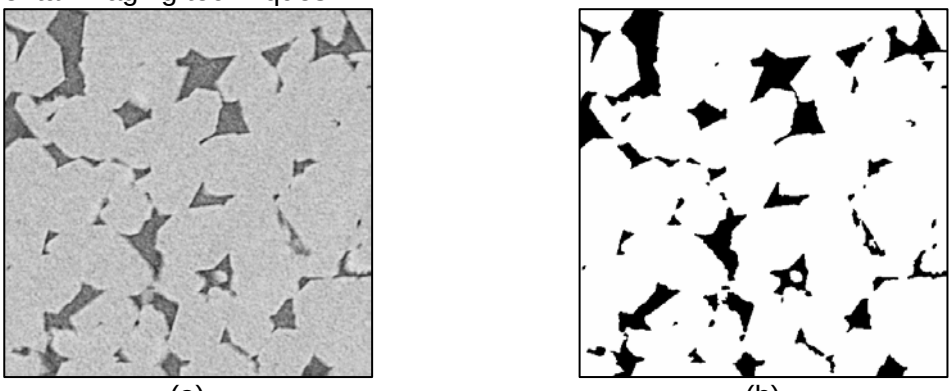

(a) (b)

Fig. 1. *The least complex and most straightforward method for constructing digital rock models:(a) microCT image of a sandstone and (b) its binarization.*

We present several approaches aimed at extending the content of the digital rock models that makes them more informative. The current results are related to evaluating a 3D mineral map and estimating the 3D distribution of nonresolved pore space. These proposed approaches are based on merging of X-ray microCT and scanning electron microscopy (SEM) data. Our first results and implementation in the simulation process justify the necessity of the suggested improvements for the digital rock model construction workflow.

Methods

One of the most efficient and traditional ways for digitizing rock specimens is 3D scanning using X-ray absorption micro computed tomography (X-ray microCT), which provides a volumetric distribution of X-ray attenuation coefficients inside the object being studied. Due to considerable absorption contrast between the pores (normally filled with air, water or oil) and mineral phase (e.g., quartz, calcite), this method is reliable for reconstructing pore space geometry with characteristic sizes greater than the spatial resolution of the CT (microCT) machine.

In the work being reported, the Bruker high-resolution SkyScan 1172 system was used. This scanner as most laboratory microCT instruments deals with a polychromatic beam using as many photons as possible to obtain statistically reliable images in a reasonable time. The energy of the beam should be sufficient to penetrate through dense rock samples. In our case, the operating parameters of the X-ray tube were 100 kV and 100 µA. In such conditions resolving the spatial distribution of chemical elements and/or the minerals contained in the sample is much complicated. This information would assist in the creation of more sophisticated digital rock models than binarized models; thus, potentially increasing the accuracy of numerical simulations.

Fig. 2. *Standard mini-plug sample for microCT and SEM studies.*

Another classical limitation of any imaging system is spatial resolution. Our scanner produces reconstructed datasets up to 4000×4000×2000 voxels in size in the standard single-section mode. The rock samples (mini-plugs) that we used in our microCT (Figure 2) study were cylindrical with a diameter of approximately 8 mm and approximately 10 mm in length. This shape allows obtaining an effective pixel size of 2.1 to 2.4 µm. For conventional reservoirs, this micron scale resolution provides decent agreement between the important properties of reservoir rocks (porosity and permeability) derived experimentally and numerically. However, such resolution is insufficient and the higher details are required for uncoventional samples (e.g., tight rocks, shales) that have become more relevant nowadays.

One of the potential solutions of these issues consists of combining various imaging techniques with their specific benefits. In this work, X-ray microCT limitations were partially overcomed with the use of scanning electron microscopy (SEM) and energy dispersive X-ray analysis (EDX).

The modern SEM provides much higher resolution (Figure 3) than does the X-ray microCT (down to ~1 nm). Besides, the SEM is a direct imaging method. Thus, the SEM images reflect the geometry of the rock's internal structures in greater details that can be used for accurate numerical simulations of physical processes in porous rock. However, bear in mind that SEM imaging is a 2D technique. Nevertheless, it will be shown below

that the spatial registration of a high-resolution 2D SEM image with a 3D micro-CT image allows mapping the subvoxel characteristics. For example, the effective subvoxel porosity can be assigned to each voxel of the 3D X-ray microCT image; i.e., some voxels are classified as neither fully solid, nor fully void, but partially void with some porosity value.

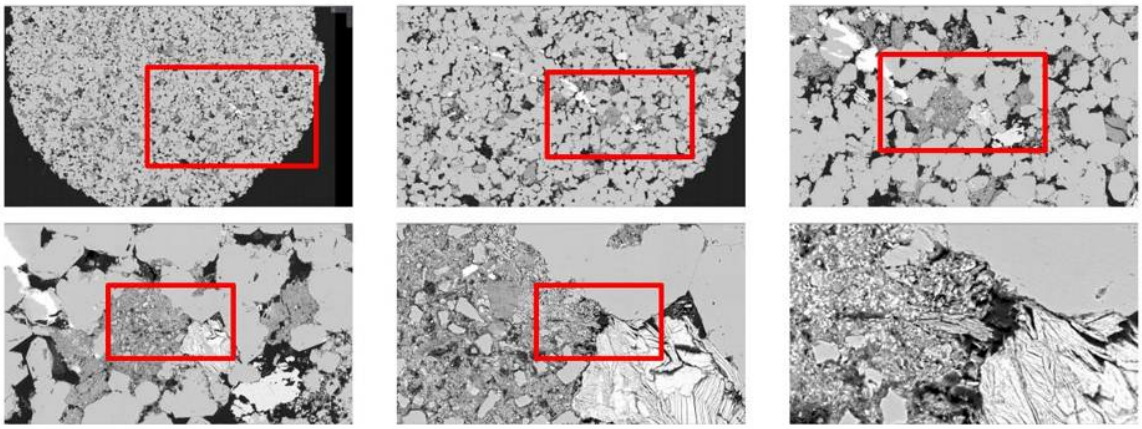

Fig. 3. *High-resolution SEM image of a sandstone Ø8 mm mini-plug, consecutive zooming in.*

In this study all SEM results were obtained by using a QEMSCAN 650F (FEI) microscope, which is a special modification of a Quanta 650F (FEI) microscope. For the aforementioned 8-mm mini-plugs, the tile-by-tile scanning of a full slice with 1-nm resolution would produce an enormous image (8 million × 8 million pixels, >50 TB). As a result, the acquisition parameters should be modified by decreasing the region of interest and/or the resolution. High-resolution maps were collected from the full slice of the mini-plug with a resolution of approximately 100 nm (image size: ~80,000 × 80,000; file size: ~8 GB).

Energy Dispersive X-Ray Analysis. The EDX analysis is one of the most popular elemental analysis techniques among various options and modes of the SEM method. The current generation of EDX detectors was developed in the late 1990s. However, even a decade ago these detectors were still too slow to map a distribution of elements along the surface of a typical rock mini-plug (Figure 2). Instead, EDX analysis was used to characterize individual points of the sample. Recent advances in EDX technology decreased the time required to analyze 4,000×4,000 points of the sample surface to about 24 h, which is similar to the X-ray microCT imaging duration. Based on EDX spectrum, existing software allows automatic determination of mineralogy in each pixel (Butcher et al., 2000). An example of such classification (i.e., a 2D mineral map) is shown in Figure 4.

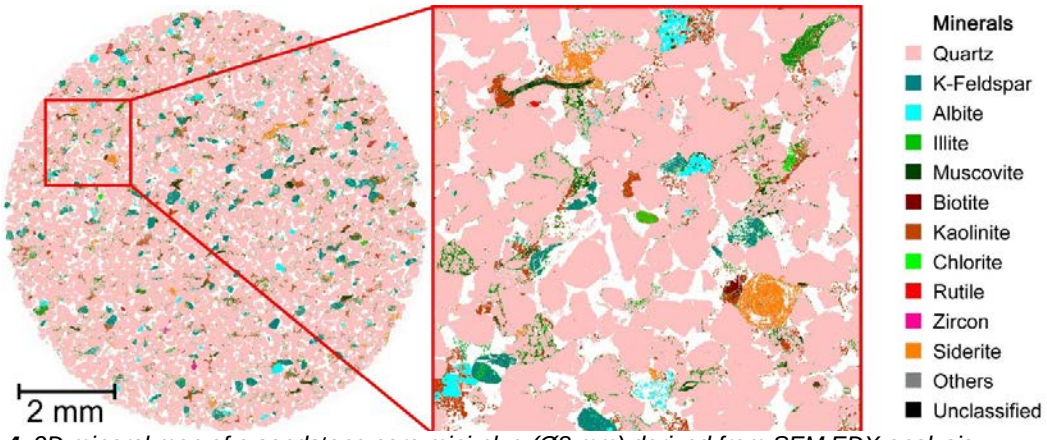

Fig. 4. *2D mineral map of a sandstone core mini-plug (Ø8 mm) derived from SEM EDX analysis.*

As in the case of high-resolution imaging, the 2D mineral map can effectively complement the 3D X-ray microCT results. Such a symbiosis significantly assists in constructing a 3D mineral map of the sample. We note at once that in some cases, it is possible to construct a 3D mineral map based only on tomographical data because of sufficient X-ray attenuation contrast between the minerals constituting the sample (Koroteev et al., 2011).

Image Registration. The aforementioned combination of 3D microCT with 2D SEM images is associated with a well known problem of image registration. The correct and efficient registration of rather large 2D and 3D images is a challenging task by itself. Generally, mechanical cutting of the sample for SEM imaging could not be performed precisely parallel to X-ray microCT slices. Thereby, some mismatching in coordinates and orientation angles occurs between both images. To solve the problem, we applied a contour registration approach, reducing the task from 2D–3D to 1D–2D. This approach is based on the assumption that porous core mini-plugs have a rather individual 2D side surface and each slice would have a 1D contour uniquely matched with the entire side surface.

Results

3D Mineralogy Mapping. The essence of the method consists of finding correspondence between the various local characteristics of the X-ray microCT image voxels and their mineral content, which is defined from the SEM-EDX image (Yakimchuk et al. 2014). This technique involves spatial registration of the 2D elemental or mineral distribution image with the 3D X-ray microCT image. A number of local features are considered to characterize each voxel of a 3D X-ray microCT image: reconstructed X-ray attenuation coefficient value, and local textural and morphological properties. Unfortunately, the gray-scale value (attenuation) itself is not sufficient for distinguishing different minerals in a general case. Finally, the full 3D microCT image is classified according to its mineral type (Figure 5).

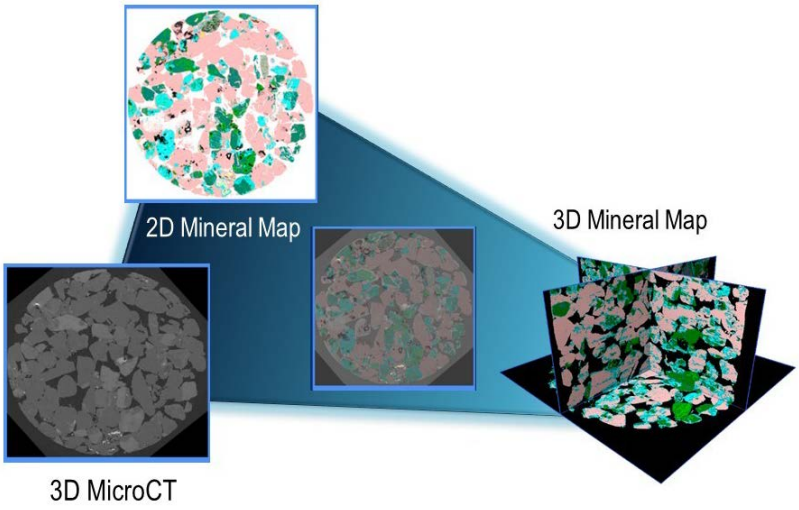

Fig. 5. *Construction of 3D Mineral Map for sandstone core (Ø8 mm) mini-plug.*

Evaluating the 3D Distribution of Nonresolved (by microCT) Pore Space. Two concepts have been implemented to make this estimation. First, the porosity of a 3D X-ray microCT image can be fitted to the laboratory-measured porosity. During this procedure, a part of voxels are classified as fully void (the darkest) and fully solid (the brightest), while the voxels in the range of ambiguous colors are considered as a mixture of solid and void phases with the ratio corresponding to the local X-ray attenuation. The proportionality coefficient should be tuned to satisfy the equality of image and laboratory-measured porosity. Second, high-resolution SEM imaging can be used in the X-ray microCT interpretation. Proper registration of the SEM 2D image with a virtual slice of the 3D X-ray microCT image allows adjusting the parameters of correspondence between the gray-scale levels and subvoxel porosity values. Besides, having registered the 2D SEM with the 3D X-ray microCT images of the same sample, it is possible to use machine learning techniques for further classification of the entire 3D image.

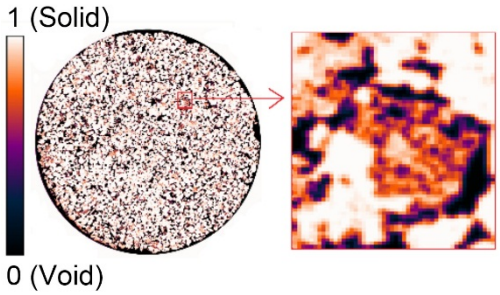

(a) (b)

	Binarization		Porosity Map	Experiment
	A	B		
Porosity, %	9.2	17.6	*17.2*	**17.2**
F	3051	1078	26	**30**

Fig. 6. *(a) 2D slice of a porosity map of a core mini-plug and (b) comparison of calculated form-factors F with experimental data. Method A – optimal image-based binarization, B – threshold calibrated by experimental porosity.*

An example of the porosity distribution obtained by combining the two methods is shown in Figure 6 (a). The importance of adding the “invisible” porosity to the digital model has been born out by simulating electrical resistivity of a sample and further comparison with laboratory measurements. One can see (Figure 6(b)) that neglecting the nonresolved pore space leads to the loss of connectivity and, thus, overestimated electrical resistivity that is proportional to formation factor F (Archie, 1942). The

proposed microporosity map model by definition coincides with the experimental porosity value, and in addition, the map provides an F value close to the experimentally registered one.

Conclusions

To perform more advanced research, additional sophisticated methods have to be applied. Modern imaging techniques coupled with progressive image processing algorithms allow creating rather complex solutions for material studies and in particular, for digital rock analysis. We have presented a few examples in our work. The results show promise for constructing digital rock models, which would contain information about the distribution of mineralogy and unresolved porosity, preserving connectivity between resolved pores. The necessity of such information strongly depends on the sample peculiarities and final goals of the investigation.

References

Archie G.E. (1942). The electrical resistivity log as an aid in determining some reservoir characteristics. ***Petroleum Transactions of AIME*** 146: 54–62.

Auzerais F.M., Dunsmuir J., Ferreol B.B. et al. (1996). Transport in sandstone: A study based on three dimensional microtomography. ***Geophysical Research Letters*** 23, 7: 705–708.

Bruker Micro-CT Skyscan 1172. Technical Specification. http://www.skyscan.be/products/1172.htm.

Butcher A.R., Helms T.A., Gottlieb P. et al. (2000). *Advances in the quantification of gold deportment by QemSCAN*. Seventh Mill Operators' Conference, Australian Institute of Mining and Metallurgy: 267–271.

Koroteev D., Mutina A., and Sasov A. (2011). *Using X-ray microCT for 3D mineral mapping.* Book of Abstracts of MicroCT User Meeting: 40–45.

Kostek S., Schwartz L.M., and Johnson D.L. (1992). Fluid permeability in porous media: Comparison of electrical estimates with hydrodynamical calculations. ***Phys. Rev. B*** 45, 1: 186–195.

Yakimchuk I.V., Varfolomeev I.A., and Korobkov D.A. (2014). *Use of X-Ray MicroCT and Scanning Electron Microscopy for Constructing 3D Mineral Maps of Rock Samples*. 18th International Microscopy Congress, Prague, Czech Republic. http://www.microscopy.cz/abstracts/2759.pdf

Sensitivity analysis for micro-tomography data segmentation in digital rock physics

H. BERTHET[1*], M. BLANCHET[1], R. RIVENQ[1]

[1] , Avenue Larribau 64018 Pau Cedex France – helene.berthet@total.com
* presenting author

Keywords: Digital Rock Physics, segmentation, uncertainty, sensitivity, petrophysics

Abstract

Digital Rock Physics is a fast-growing branch of petrophysics based on the analysis of the internal structures of rock samples observed by x-ray micro-tomography. Such data requires extensive image processing, including in particular segmentation. Though critical for the reliability of the results, segmentation is known to be extremely user-dependent due to the variety of the available algorithms and to their sensitivity to input parameters. In this work, we performed a converging-active-contour segmentation on a dry Berea sandstone 3D image available in the literature for benchmarking purposes. We show that several segmentations can be deemed acceptable according to existing criteria, if a robust workflow is followed, if parameters are carefully chosen and if the image is of sufficient quality. We propose a method to evaluate the uncertainty brought by the segmentation step in such favourable situations. The underlying principle is that this uncertainty is not an error range that should be reduced with better algorithms; it is rather the true description of the imperfect information available in the image. This method has the advantage of allowing to derive probability distributions instead of single values for the computed petrophysical properties, such as porosity, pore surface area, percolation radius and pore throat distribution.

Introduction

Precise, high-resolution investigation of the internal structures of rock samples using advances in x-ray micro-tomography opened a new area of research for the oil industry, often called “digital rock physics” (DRP). Most of DRP technology is based on the digital extraction of the rock pore network and the prediction of petrophysics properties such as porosity, permeability, formation factor through numerical simulations [1]. Processing micro-tomography data of rocks is mostly based on the grey level contrast between the minerals, highly attenuating features, and the pores, typically darker (see Figure 1). The segmentation into such phases is non-trivial in the presence of low-density minerals, fluids, features smaller than the image resolution, and noise. A large number of algorithms are now available for 3D image segmentation, but their results are criticized for their inconsistency and their user-dependency [2, 3, and 4]. Errors in the processing may result from inappropriate definitions of the algorithms input parameters, but also from the imperfection of these methods, even with optimized input parameters. However, the algorithms are increasingly precise and the images are of increasing quality and resolution. It is now a common situation to obtain several segmentations in good accordance with existing criteria and satisfactory to the expert’s eye. No rationale can say which one is the closest to reality or the fittest for petrophysics property extrapolation. This is typically the case for porosity at and below resolution [5] and for thin wetting films in multi-phase images [6].

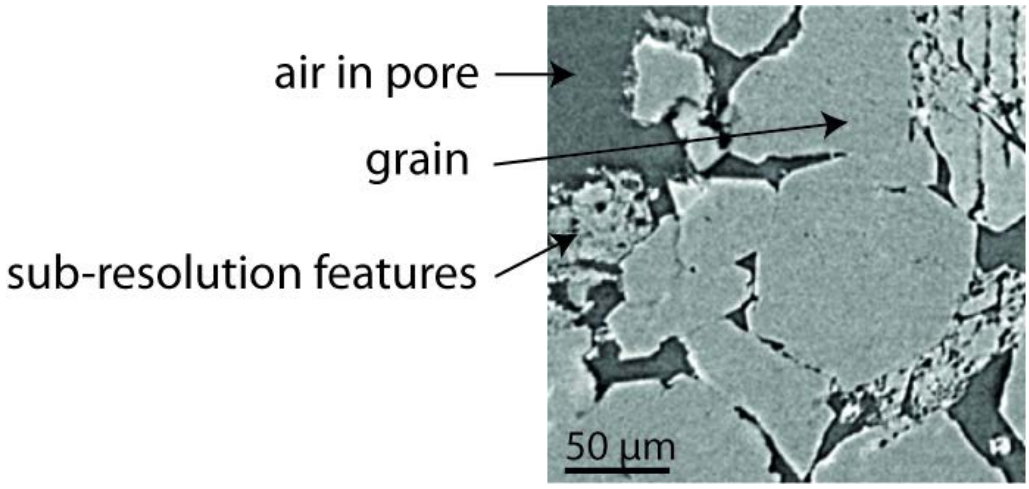

Figure 1: raw image extracted from the reconstructed volume of a Berea sandstone scan, voxel resolution 740 nm [4].

In this work, we propose a statistical approach, leading to not only one “true” segmented image but a range of possible ones, based on a sensitivity analysis around a base processing workflow. Similarly, for morphological values like porosity, we can give distribution ranges instead of single values. Binary pore-grain segmentation is treated for the sake of simplicity, but we extended the method to multi-phase problems. A micro-tomograph of a dry Berea sandstone is used for demonstration, originally made available for benchmarking purposes [4].

Methods

Our workflow is composed of four steps:

- Perform a base-case segmentation (including denoising and post-processing)
- Identify the most critical input parameters in this workflow
- Define their realistic variation intervals (avoid inter-dependent cases)
- Run the best case and all the input parameters combinations cases
- Statistically analyze the segmentation results

The base-case segmentation step is performed by an expert user. The 3D image of the Berea sample was acquired on a synchrotron at a high resolution of 740nm per voxel. We chose to perform denoising with a median filter, followed by edge-enhancing. We then ran a region-growing segmentation (Converging Active Contours, CAC, [7]). The intensity thresholds for its initialization are chosen by taking a percentile of Otsu’s objective function [6,8] and a gradient threshold is chosen by visual inspection. We corrected the segmentation results by combining it with a thresholded top-hat transform of the denoised image. In the last step, we removed all unconnected pores. Figure 2 shows the successive transformations, illustrated on a 2D extracted image. The final 3D image is our base-case for the sensitivity analysis.

We identified the most critical choices of parameters in the segmentation workflow:

- The smoothing radius ***r*** of the median filter
- The percentile ***p*** on Otsu's optimization function (related to the seed region thresholds) for the CAC segmentation
- The gradient threshold t_g for the CAC segmentation
- The segmentation threshold t_h used to segment the top-hat image

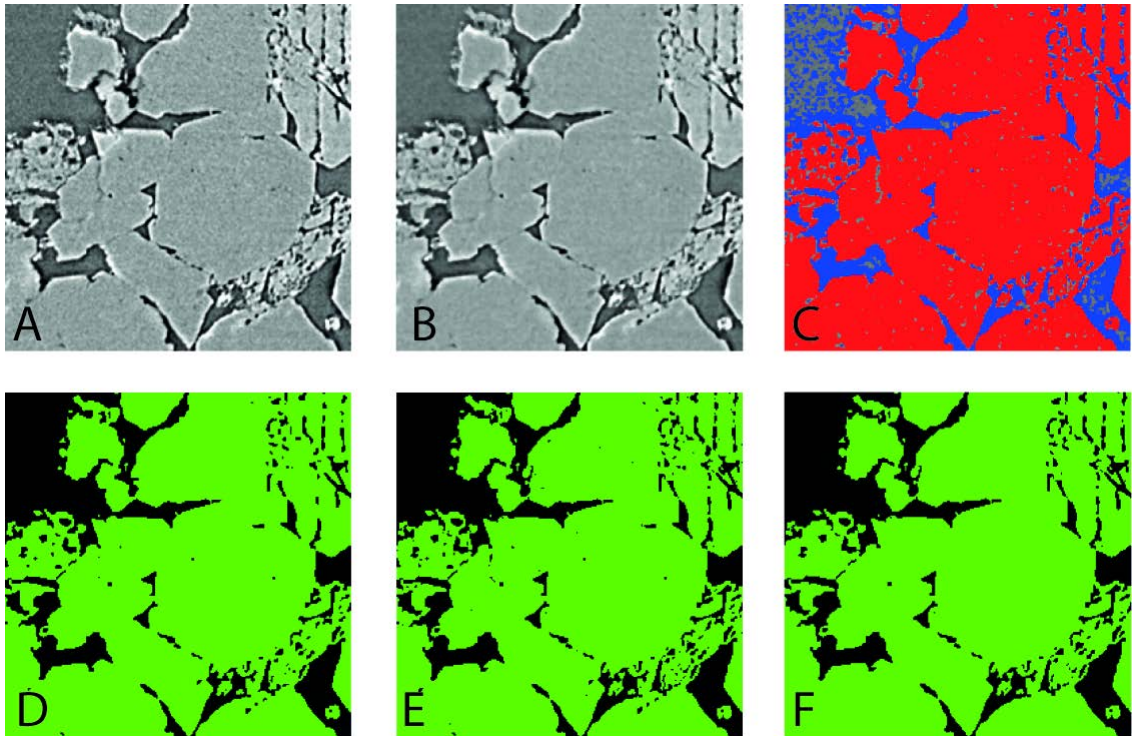

Figure 2: transformation of image by successive denoising and edge enhancing (A-B), segmentation (C-D, with blue and red the pore/grain seed regions), adding the top-hat transform (D-E) and removal of disconnected pores (E-F) applied to the full 3D volume.

The size of the structuring element in the top-hat transform was considered negligible compared to the threshold. We also chose to introduce a second degree of liberty to the initialization of the CAC method by adding a shift s to both t1 and t2, which encompasses the bias of Otsu's definition of an optimum threshold. Parameters r and p are both related to the balance between noise reduction and small features preservation in the image. With a high p, seed voxels may be misclassified unless the image was well denoised. We will therefore consider the parameter (r,p) rather than varying them independently.

The final parameters for the sensitivity study are ***(r, p), s,*** t_g and t_h.

A low case and high case are defined for each parameter around the base-case segmentation. All four parameters are considered independent and varied jointly to get a probability distribution, leading to 54 segmentation cases for the Berea sandstone image.
Practically, the base case and the 53 other cases were run through a routine, automatically launching the image processing software and extracting the key results. Running time was only 10 hours on 92 processors thanks to the parallelization of the algorithms.

Results and discussion

Base case absolute porosity is 0.190, which is consistent with the results of the three DRP laboratories commissioned by Andrä *et al.* [4] which found porosities of 0.184, 0.195 and 0.209 respectively. Effective porosity – when only the main connected pore body is conserved – is 0.185. All morphological values shown here after are effective.

Figure 3 presents the frequency distributions over the 54 cases for three morphological parameters chosen for their importance in petrophysics applications. Specific surface area will govern adsorption or wettability-induced phenomena. The percolation radius (radius of the largest sphere able to percolate the pore network from the inlet to the outlet) gives insight into the rock connectivity and has consequences on its flow properties. We found in this study a variation of specific surface area within ±20% of its base case value. This is not surprising, as surface area is extremely affected by small features and surface roughness. The percolation radius varies by around 18% around the best case, which corresponds to approx. one voxel size.

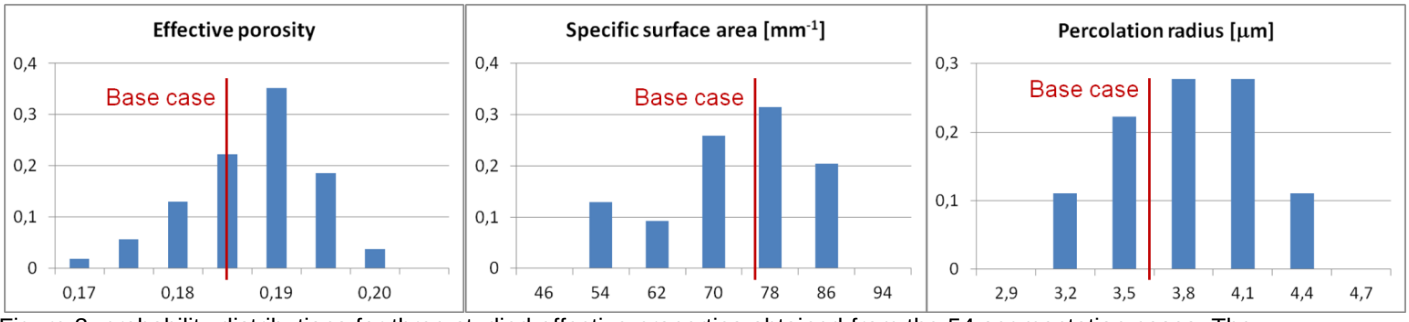

Figure 3: probability distributions for three studied effective properties obtained from the 54 segmentation cases. The base case value is indicated by a red line.

There is a difference of 1 porosity unit (p.u.) between the most probable porosity value and the macroscopic measurement [4]. We checked that the difference was not due to sample heterogeneity, in other words that the explored volume was sufficiently large. The mercury injection porosimetry [4] shows that 3 p.u. are below the image resolution. The porosity from our 54 segmentation cases ranges from 17 to 20 p.u., covering between none to all of the micro-porosity. However it is not clear which parameters are critical for the preservation of such small features.
The porosimetry study gives a specific surface area of 7.5 m^2/g for pore throat radii higher than 740 nm (image resolution). There is one order of magnitude difference with the digital values. The voxel counting method is known to over-estimate surface areas, while the limitation in image resolution leads to an underestimation of the surface areas. Mercury injection experiments interpretation make strong assumptions [5]. A direct measurement of specific surface area (BET method) would be useful to validate the digital result.

We combined the 54 result images to visualize the segmentation differences voxel by voxel, in a “probability image” as illustrated in Figure 4. Voxels of probability 0 or 1 (voxels segmented as pore in all 54 cases, respectively as grain) are white. Voxels assigned to grain in n cases out of 54 have the value n/54. The ambiguous voxels are found on the grain surface and in the regions where the porosity is under the resolution (partial volume effect). Visual inspection of the raw image (Figure 4, left) does not give any indication as to the correct assignation of the ambiguous voxels, except for a small percentage of obvious errors. This validates the sensitivity program used in this study, which aims to present only meaningful segmentation cases. This also

demonstrates that a probabilistic approach to segmentation makes sense: there is indeed a degree of uncertainty inside segmented images.

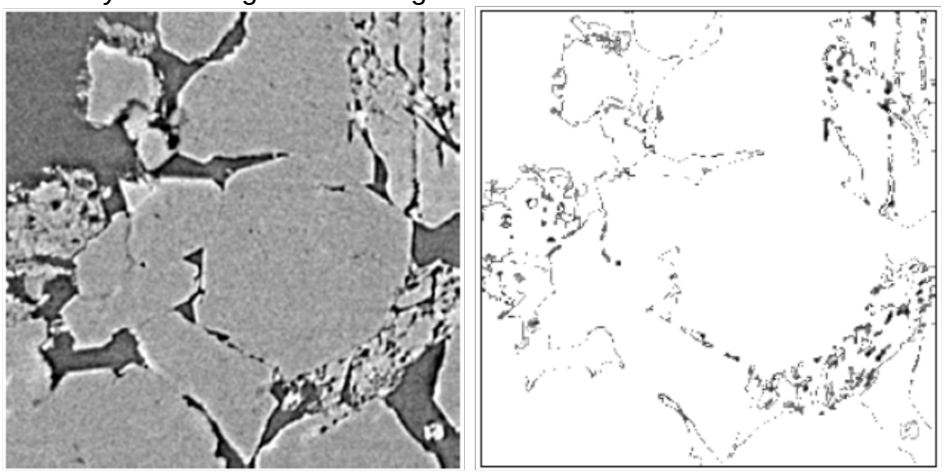

Figure 4: (left) image from raw scan. (right) Probability image: white voxels were always assigned to grain, or always to pore, in the 54 cases. Voxels assigned to grain in n cases out of 54 get a greylevel of n/54.

Conclusion

We proposed a statistical approach to investigate the uncertainty associated with the segmentation step of micro-tomography images of rock samples. Using a sensitivity analysis around a base-case segmentation, we were able to evaluate the impact of a selection of input parameters on the segmentation results as well as derive the variations of key ouput values like porosity, specific surface area, percolation radius. The sensitivity analysis generates a series of segmented images that are all satisfactory and should all be used for further processing.

This approach requires a reliable base-case segmentation since it does not quantify the error between any given segmentation and the reality but the uncertainty around the base case. Distribution ranges obtained on low-quality images or images with a lot of sub-resolution features may be completely off-range.

Our approach is a first step towards systematic uncertainty quantification in Digital Rock Physics. DRP results will be more efficiently used when error and uncertainty can be quantified and propagated at each step of image processing and upscaling.

References

1. Blunt, M.J. *et al.*, "Pore-scale imaging and modelling" *Adv Water Resour.*, 2012, doi:10.1016/j.advwatres.2012.03.003
2. Iassonov, P., T. Gebrenegus, and M. Tuller, "Segmentation of X-ray computed tomography images of porous materials: A crucial step for characterization and quantitative analysis of pore structures", *Water Resources Research*, 2009, **45**, W09415, doi:10.1029/2009WR008087
3. Wildenschild, D., and A. P. Sheppard, "X-ray imaging and analysis techniques for quantifying pore-scale structure and processes in subsurface porous medium systems", *Adv. Water Resour.*, 2013, **51**, 217–246, doi:10.1016/j.advwatres.2012.07.018
4. Andrä, H. *et al.*: "Digital Rock physics benchmarks – Part I: Imaging and segmentation", *Computers & Geosciences*, 2013, **50** 25-32.
5. Peng, S., F. Marone, S. Dultz, "Resolution effect in X-ray microcomputed tomography imaging and small pore's contribution to permeability for a Berea sandstone", *Journal of Hydrology,* 2014*,* **510**, 403–411, doi: 10.1016/j.jhydrol.2013.12.028
6. Schlüter, S., A. Sheppard, K. Brown and D. Wildenschild, "Image processing of multiphase images obtained via X-ray microtomography: A review", 2014, *Water Resour. Res.*, **50**, doi:10.1002/2014WR015256.
7. Sheppard, A., R. Sok, and H. Averdunk, "Techniques for image enhancement and segmentation of tomographic images of porous materials », *Physica A*, 2004, **339**(1), 145–151.
8. Otsu, N., "A threshold selection method from gray-level histograms", *Automatica*, 1975, **11**(285-296), 23–27

Characterization of Reservoir Quality in the Upper Devonian Wabamun Group using Micro-CT and Helical-CT Imaging Techniques

Greg M. Baniak, BP Canada Energy Group ULC, Calgary, Alberta, Canada

(20 min PPT Talk)

In the Pine Creek gas field of west-central Alberta, Canada, the primary reservoir intervals occur in the Upper Devonian Wabamun Group. A common feature of the Wabamun Group is the presence of the dolomitized burrow fabrics. Notably, the dolomitized burrows have permeabilities ranging between 1 and 350 millidarcies (mD), while the lime mudstone-wackestone matrix adjacent to the burrows has permeabilities of less than 1 mD. Because of the moderate to extreme contrasts in permeabilities between the burrows and matrix, the burrows most likely act as the primary flow pathways within the Pine Creek gas field.

To better understand the impact of bioturbation of bulk reservoir permeability in the Wabamun Group, high-resolution X-ray microtomography (micro-CT) and helical computed tomography (helical-CT) imaging techniques were used. In short, micro-CT and helical-CT images show that the burrows (comparable to examples of *Thalassinoides* and *Palaeophycus*) are spatially heterogeneous and their dimensions and orientations are highly variable at the centimeter to millimeter scale. When viewed in 2D cross-sectional slices at various levels, the overall volumes of dolomite and calcite were found to vary considerably. As a result, the Wabamun Group is composed of an interconnected network of burrows, with the burrow density and burrow interconnectivity varying considerably throughout the sample. Notably however, horizontal burrow connectivity was found to be more common than vertical burrow connectivity, except in the most pervasively bioturbated sections (i.e., 90 to 100% bioturbation). As such, fluid flow within the burrow fabrics is dominantly anisotropic with a preferred bedding parallel flow direction. It was from these high-resolution images that a more detailed and accurate depiction of the bulk reservoir permeability could be constructed using numerical modeling. In short, numerical modeling showed that bulk reservoir permeability is best estimated using the harmonic and geometric mean in scenarios where burrow-associated dolomite is minimal. Conversely, bulk reservoir permeability is best estimated using the arithmetic mean in scenarios where burrow-associated dolomite is moderate to high.

How can computed tomography improve the remote detection of hydrocarbons using seismic methods?

M.J.DUCHESNE*[1,3] AND B. GIROUX[2,3]

[1] Geological Survey of Canada, 490 rue de la Couronne, Quebec City, Qc, Canada, G1K 9A9 – mathieuj.duchesne@rncan-nrcan.gc.ca
[2] Institut National de la Recherche Scientifique –Centre Eau-Terre-Environnement – bernard.giroux@ete.inrs.ca
[3] Laboratoire d'Imagerie et d'Acquisition des Méthodes Géophysiques – http://www.liamg.ca
* presenting author

Keywords: density, photoelectric, poroviscoelastic, hydrocarbon, seismic reflection

Abstract

Seismic reflection is the preferred technique for remotely detecting hydrocarbon accumulations in geological media. Nevertheless, before a prospective seismic anomaly is drilled, forward modeling is essential to reduce investment risk. Poroviscoelastic (PVE) modeling is the only formalism that provides a forward solution where matrix-fluid interactions are considered to model the attenuation of a seismic wavefront as it propagates in geological media. However, one drawback of this approach is the large number of variables (i.e. 12 in total) required to solve the wave equation. This contribution shows how a single computed tomography (CT) dataset can help estimate 8 of the 12 variables of the PVE scheme. The impact of the photoelectric effect caused by X-ray interaction with matter on the derivation of those variables and the need to upscale the data in order to satisfy numerical modelling criteria and for the computing code to perform to an acceptable level are also briefly addressed.

Introduction

Physical and mathematical concepts fundamental to X-ray CT and reflection seismology are very similar as both electromagnetic and seismic waves propagate through matter to illuminate its internal structure (Ikelle and Amundsen, 2005; Toptygin, 2015). As they propagate into matter, X-rays and seismic waves are attenuated respectively by absorption and scattering of photons, and by dispersion and partitioning of seismic energy, density being their common attenuating property.

CT provides a nanometer to micrometer-scale resolution whereas seismic reflection generally pictures the subsurface at a meter-scale resolution. Therefore, the methods differ by approximately 9 orders of magnitude in resolution. Interestingly, this difference is also beneficial as the information derived from CT imaging reveal details on the distribution of the physical properties influencing the attenuation of seismic waves. In fact, the scale of heterogeneity that is typically relevant at seismic frequencies is the micrometer-scale or pore-scale (Müeller et al., 2010). This is particularly true for hydrocarbon-saturated porous rocks as the elastic behavior of fluids is transferred into the rigid matrix leading to increased attenuation of seismic amplitude (Batzle et al., 2006). It is this phenomenon that allows the detection of hydrocarbons using seismic reflection.

Seismic forward modeling schemes (e.g. acoustic, elastic, poroelastic or PVE) solve the wave equation using different levels of simplifications. Complex solutions involve a larger number of variables but also describe wavefront propagation and attenuation with more accuracy, providing more realistic results. The PVE solution requires 12 variables

since matrix-fluid interactions are necessary to model the propagation and attenuation of a seismic wavefront in geological media (Quintal et al., 2009). One of the challenges for computing the PVE solution is to gather the information needed to calculate those variables (Table 1).

Table 1: Poroviscoelastic variables*.

Parameter	Symbol	CT?	Equation	Reference
Solid density	ρ_s	✓	$\rho_s = \frac{\rho_b - \phi\rho_f}{1-\phi}$	Sheriff and Geldart (1995)
Fluid density	ρ_f	✓	$\rho_f = \frac{\rho_b + \phi\rho_s - \rho_s}{\phi}$	Sheriff and Geldart (1995)
Matrix porosity	ϕ	✓	$\phi = \frac{vol_b - vol_{gr}}{vol_b}$	Tiab and Donaldson (2012)
Fluid Viscosity	η		$\eta = \eta_T + 0.145PI$	Batzle and Wang (1992)
Solid bulk modulus	K_s	✓	$K_s = \rho(V_P^2 - {}^4/_3 V_s^2)$	Carcione et al. (2006)
Drained matrix bulk modulus	K_m	✓	$K_m = (1-\phi)\rho_s(V_p(m)^2 - {}^4/_3 V_s(m)^2)$	Carcione et al. (2006)
Fluid bulk modulus	K_f	✓	$K_f = \frac{\gamma P}{\left(1 - \frac{P}{Z}\frac{\partial Z}{\partial P}\right)_T}$	Batzle and Wang (1992)
Matrix shear modulus	μ	✓	$\mu = (1-\phi)\rho_s V_S(m)^2$	Carcione et al. (2006)
Permeability	κ		$k = \frac{A_x\phi^3}{(1-\phi^2)S^2}$	Mavko et al. (2009)
Tortuosity	T	✓	$T = 1 - r\left(1 - \frac{1}{\phi}\right)$	Mavko et al. (2009)
Quality factor	Q		$\frac{1}{Q} = \frac{\omega V}{\pi f}$	Sheriff and Geldart (1995)
Relaxation frequency	f		N/A –fixed value determined by user	N/A

*Symbol notation for Table 1 in order of appearance: ρ_b: bulk density, vol_b: bulk volume, vol_{gr}: grain volume, T: fluid temperature, V_p: compressional wave velocity, V_s: shear wave velocity, (m): dry rock, P: fluid pressure, Z: fluid compressibility factor, γ: adiabatic compressibility, A_X: cross-section area, S: pore surface area divided by the sample volume, ω: absorption coefficient, v: phase velocity.

After ~30 years of application in the field of geology, CT has established itself as a reliable source of quantitative information (Cnudde and Boone, 2013). CT has been traditionally used since the late 1980s by the petroleum industry to document porosity distribution in reservoirs (Wellington and Vinegar, 1987). More recently, progress has been made for imaging pore-fluids properties (e.g. saturation and phase), quantifying minerals and evaluating rock anisotropy (Cnudde and Boone, 2013; Berg et al., 2013; Yun et al., 2013). Both classical and emerging uses make CT technology very appealing to derive variables necessary to solve the wave equation in PVE media. Furthermore, this can be achieved by collecting a single CT dataset. Table 1 shows that 8 of the 12 variables of the PVE scheme can be derived from CT data, density and porosity values being the key estimations provided by CT-scanning.

Mathematical background

This section provides a mathematical background to clarify how CT-derived properties can be used into the PVE scheme.

X-ray computed tomography

Following Beer's Law, X-ray attenuation is a function of the density, the effective atomic number and the thickness of the matter

$$I = I_0 \exp(-\alpha x) \quad (1)$$

where I and I_0 are respectively the intensity of the attenuated and the transmitted X-ray, α is the attenuation coefficient and x is the sample's thickness. Three main phenomena occur through X-ray interaction with matter. Photoelectric effect and Compton scattering are the two dominant phenomena induced by medical CT-scanners which are operating at energies between ~40 and 140 keV, while pair production is produced by industrial CT systems that use energy up to 1000 keV. Here, the focus is on the study of rock samples using medical CT-scanners, thus pair production is neglected.

Contribution of the photoelectric effect and Compton scattering to X-ray attenuation can be estimated by expressing α as follows

$$\alpha = \rho\left(a + b\frac{Z^n}{E^{3.2}}\right) \tag{2}$$

where ρ is the density of the sample, a is the Klein-Nishina coefficient, b an empirical coefficient, Z is the atomic number and E is the energy in keV (White-Grodstein, 1957; Wellington and Vinegar, 1987). The term a describes Compton scattering in terms of energy of the incident photon, A, and the angle of scattered photon, θ :

$$a = \left\{\frac{1}{1+A(1-cos\theta)}\right\}^2\left\{1\frac{A^2(1-cos\theta)^2}{[1+A(1-cos\theta)](1+cos^2\theta}\right\}. \tag{3}$$

The term $b\frac{Z^n}{E^{3.2}}$ is the photoelectric effect occurring <100 keV and for Z^20.

CT-scanners provide 2-D and 3-D attenuation matrixes at different positions of an object by expressing the attenuation in Hounsfield Units (HU) given by

$$HU = \frac{\alpha_{(x,y)-}\alpha_w}{\alpha_w} \times 1000 \tag{4}$$

where $\alpha_{(x,y)}$ is the attenuation coefficient of the sample at position (x,y) and $\alpha_{(w)}$ is the attenuation coefficient of the water.

Poroviscoelastic formalism

The four elastic coefficients that describe porous elastic media are the stiffness of the drained matrix E_m defined as

$$E_m = K_m + {}^4/_3\,\mu \quad , \tag{5}$$

whereas the second, the diffusion function D corresponds to

$$D = K_s\left[1 + \phi\left(K_sK_f^{-1} - 1\right)\right] \ , \tag{6}$$

while the third, the poroelastic coefficient of effective stress σ_{pe} is given by

$$\sigma_{pe} = 1 - \frac{K_m}{K_s} \tag{7}$$

and the fourth, the coupling modulus M, is

$$M = \frac{K_s^2}{D-K_m} \tag{8}$$

captures fluid-solid interactions (Carcione, 1998). Viscoelasticity unifies mechanical properties of solids with time derivatives of a system's strain following the propagation of a seismic wavefront into a medium. The introduction of viscoelasticity into poroelasticity allows modeling attenuation mechanisms induced by the stiffness and viscodynamic propagation of the seismic energy. Viscoelasticity is introduced by generalizing M into the time-dependent relaxation function $\psi(t)$ such that

$$\psi(t) = M\left(1 + \frac{1}{L}\sum_{l=1}^{L}\varphi_l\right)^{-1} \times \left[1 + \frac{1}{L}\sum_{l=1}^{L}\varphi_l\exp\left({}^{-t}/_{\tau_l}\right)\right]H(t) \ , \tag{9}$$

where L is the number of frequency-dependent relaxation mechanisms and $H(t)$ is the Heaviside function,

$$\varphi_l = \frac{\tau_{\varepsilon l}}{\tau_{\sigma l}} - 1 \ , \tag{10}$$

in which $\tau_{\varepsilon l}$ and $\tau_{\sigma l}$ are relaxation times for given mechanisms. Those relaxation times can be formulated in terms of quality factor Q_l and fixed relaxation frequency f_l following

$$\tau_{\varepsilon l} = \frac{1}{2\pi f_l Q_l}\left(\sqrt{Q_l^2 + 1} + 1\right) \tag{11}$$

and

$$\tau_{\sigma l} = \frac{1}{2\pi f_l Q_l}\left(\sqrt{Q_l^2 + 1} - 1\right). \tag{12}$$

Therefore the compressional phase velocity υ is function of M and equal to

$$v^2 = \frac{B+\sqrt{B^2-4M_cE_m\rho_c\bar{\rho}}}{2\rho_c\bar{\rho}} \quad , \tag{13}$$

where M_c is the Fourier transform of M,

$$B = M_c\left(\rho - 2\sigma_{pe\rho_f}\right) + \bar{\rho}(E_m + \sigma_{pe}^2 M_c) \quad , \tag{14}$$

$$\rho_c = \rho_b - \frac{\rho_f^2}{\bar{\rho}} \, , \tag{15}$$

$$\bar{\rho} = \frac{T}{\varphi}\rho_f - \frac{i}{2\pi f}\frac{\eta}{\kappa} \, , \tag{16}$$

T is the tortuosity, η the viscosity of the fluid, κ the permeability of the rock, and $i = \sqrt{-1}$.

Impact of the photoelectric effect on PVE variables derived from CT data

Boesflug et al. (1994) suggested combining (2) and (4) to approximate the photoelectric contribution to HU measurements such that

$$HU_{photoelectric} = \left[\left(\frac{1+CZ_{eff}^n}{1+CZ_{eff}^{water}}\right)\rho - 1\right] \times 1000 \tag{17}$$

where C is a coefficient defined the following relationship

$$C = \frac{b}{aE^{3.2}} \tag{18}$$

Boesflug et al. (1994) and Duchesne et al. (2009) showed that λ and HU of geological samples are better correlated when HU values are corrected for the photoelectric effect. Since PVE variables derivable from CT rely on density estimation, the photoelectric effect must be removed beforehand (Table 1). For a photoelectric correction method to be effective, it is preferable that the chemical composition of the matrix is known. However, grains generally forming sedimentary rocks cover a wide range of mineral classes. Hence the likelihood to find elements with Z^20 in those compounds is very high and the idea of a grain-by-grain correction method is unrealistic. The combined use of buoyancy density measurements made on representative rock samples along with equation (17) was proposed by Duchesne et al. (2009) to approximate and subtract $HU_{photoelectric}$ from HU measurements. Additional insights on $HU_{photoelectric}$ can also be derived from gamma-ray density readings obtained by Compton scattering. Gamma-rays are generally produced from a Cesium-137 source that has a peak energy at ~662 keV and thus is completely devoid of the photoelectric effect. Such a procedure was tested by Orsi and Anderson (1999) on unconsolidated marine sediment cores. Results obtained demonstrated a good correspondence between density provided by gamma-ray attenuation and X-ray attenuation derived from CT-scanning. However the authors admitted that the relationship between both methods is complicated by the photoelectric effect. Another problem is the volume of geological material on which attenuation gamma-ray versus X-ray attenuation is measured. Indeed the diameter of the collimator (2.5 or 5mm) of the Cesium-137 source forces attenuation measurements to integrate a volume of material that is over one order of magnitude greater than measurements made by X-ray CT (Weber et al., 1997). An empirical relationship established between CT and density values from samples of known density and mineralogy representative of the studied material is another approach (Ketcham and Carlson, 2001). Such a relationship can be useful to evaluate the photoelectric contribution to HU values by simply computing the difference between CT-derived density and density measurements.

Upscaling from pore- to mesoscale

Even if pore-scale information provided by CT is relevant at the seismic scale, it needs to be upscaled so that the wave equation is solved at a reasonable computational cost. Upscaling implies at 1) replacing a heterogeneous volume by a homogeneous

volume that has comparable physical properties and 2) capturing the influence of pore-scale information that is pertinent at the mesoscale. This is generally achieved using the effective medium theory that preserves the fine-scale information of the different phases of a medium and their geometric arrangement to describe their influence at a coarser scale (Choy, 1999). This is particularly important for PVE modeling of hydrocarbon accumulations, so that the dissipation of seismic energy due to delays in solid–fluid interactions captured by M (Eq. (8)) is adequately pictured. Upscaling can also be achieved numerically using a method similar to the one of Rubino et al. (2009) where equivalent viscoelastic solids are computed stochastically using a Monte Carlo approach assuming that their behavior obeys Biot's constitutive equations for fluid-filled porous media (Biot, 1956).

Conclusion

One CT dataset allows for the derivation of 8 of the 12 PVE variables required to model the seismic response of hydrocarbon accumulations. In order to provide an accurate estimation of those variables, the photoelectric effect must be approximated before being removed from CT-data. This can be achieved by using buoyancy density, gamma-ray density or the empirical relationship between CT data collected on samples of known density and mineralogy. However for efficient PVE modeling, variables estimated using CT data must be upscaled following the effective medium theory so that the wave equation can be solved at a reasonable computational cost.

References

Batzle, M. & Wang, Z. (1992). Seismic properties of pore fluids. ***Geophysics***, 57, 11: 1396-1408.

Batzle, M. L., Han, D.-H. & Hofmann, R. (2006). Fluid mobility and frequency-dependent seismic velocity -- direct measurements, ***Geophysics****, 71*, N1-N9

Berg S., Ott, H., Klapp, S.A., Schwing, A., Neiteler, R., Brussee, N., Makurat, A., Leu, L., Enzmann, F., Schwarz, J.O., Kersten, M., Irvine, S. & Stampanoni, M. (2013). Real-time 3D imaging of Haines jumps in porous media flow. ***Proceeding of the National Academy of Sciences***, 110, 10: 3755-3759.

Biot, M. A. (1956). Theory of propagation of elastic waves in a fluid-saturated porous solid. I. Low-frequency range. ***Journal of the Acoustical Society of America***, 28, 2: 168-178.

Boespflug, X., Ross, N., Long, B. & Dumais, J.-F. (1994). Axial tomodensitometry — relation between the CT intensity and the density of the sample. ***Canadian Journal of Earth Sciences***, 31, 2: 426–434.

Carcione, J. M. (1998). Viscoelastic effective rheologies for modelling wave propagation in porous media. ***Geophysical Prospecting***, 46, 3: 249-270.

Choy, T. C. (1999). Effective Medium Theory: Principles and Applications. Oxford University Press, New York: 192p.

Cnudde, V. & Boone, M. N. (2013). High-resolution X-ray computed tomography in geosciences: A review of the current technology and applications. ***Earth-Science Reviews***, 123, August: 1-17.

Duchesne, M. J., Moore, F., Long, B. F. & Labrie, J. (2009). A rapid method for converting medical Computed Tomography scanner topogram attenuation scale to Hounsfield Unit scale and to obtain relative density values. ***Engineering Geology***, 103, 3-4: 100-105.

Ikelle, L. T. & Amundsen L. (2005). Introduction to Petroleum Seismology. Society of Exploration Geophysicists, Tulsa, Oklahoma, 679p.

Ketcham, R. & Carlson, W. D. (2001). Acquisition, optimization and interpretation of X-ray computed tomographic imagery: applications to the geosciences. ***Computers & Geosciences***, 27, 4: 381-400.

Mavko, G., Mukerji, T. & Dvorkin, J. (2009). The Rock Physics Handbook. Cambridge University Press, New York, 511p.

Müeller, T. M., Gurevich, B. & Lebedev, M. (2010). Seismic wave attenuation and dispersion resulting from wave-induced flow in porous rocks – A review. ***Geophysics***, 75, 5: 75A147-75A164.

Orsi, T. H. & Anderson, A. L. (1999). Bulk density calibration for X-ray tomographic analyses of marine sediments. ***Geo-marine Letters***, 19, 4: 270-274.

Quintal, B., Schmalholz, S. & Podladchikov, Y. Y. (2009). Low-frequency reflections from a thin layer with high attenuation caused by interlayer flow. ***Geophysics***, 74, 1: N15-N-23.

Rubino, J. G., Ravazzoli, C. L. & Santos (2009). Equivalent viscoelastic solids for heterogeneous fluid-saturated porous rocks. ***Geophysics***, 74, 1: N1-N13.

Sheriff, R. E. & Geldart, L. P. (1995). Exploration Seismology. Cambridge University Press, New York, 592p.

Tiab, D. & Donaldson, E. C. (2012). Petrophysics: Theory and Practice of Measuring Reservoir Rock and Fluid Transport Properties. Gulf Professional Publishing, Waltham, U.S.A.: 950p.

Toptygin, I. N. (2015). Electromagnetic Phenomena in Matter: Statistical and Quantum Approaches. Wiley-VCH, Singapore, 720p.

Weber, M. E., Niessen, F., Kuhn, G. & Wiedicke, M. (1997). Calibration and application of marine sedimentary physical properties using a multi-sensor core logger. ***Marine Geology***, 136, 3-4: 151-172.

Wellington, S.L. & Vinegar, H.J. (1987). X-ray computerized tomography. ***Journal of Petroleum Technology***, 39, 8: 885–898.

White Grodstein, G. (1957). X-ray Attenuation Coefficients from 10 keV to 100 meV. National Bureau of Standards, Circular 583, Washington, DC: 54p.

Yun, T. S., Jeong, Y. J., Kim, K. Y. & Min, K.-B. (2013). Evaluation of rock anisotropy using 3D X-ray computed tomography. ***Engineering Geology***, 163, August, 11-19.

Image Restoration for Oil Bearing Sandstones

S. BRUNS*[1], S.S. HAKIM[1], K.N. DALBY[1], H.O. SØRENSEN[1], S.L.S. STIPP[1]

[1] University of Copenhagen, Department of Chemistry, Universitetsparken 5, 2100 Copenhagen, Denmark – bruns@nano.ku.dk
* presenting author

Keywords: Reservoir Rock, 3D Image Denoising, Artefact Removal, Digital Rock Physics, Iterative Non-Local Means

Abstract

Quantitative hydrodynamic parameters acquired in digital rock physics are biased by artefacts characteristic of the selected imaging method. In nanotomography of reservoir rock, we are faced with images that are degraded by high frequency noise, streaking and / or ring artefacts. It is fast and easy to apply enhancing image filters to handle such disturbances but this is at the expense of signal information. Aside from the principle problem of affecting recorded signal information, image enhancement is not an option with fine grained materials, such as chalk, because the signal information is not dispensable. Therefore, it is essential to treat noise and artefact handling as an image restoration problem and preserve as much of the signal information as possible. We evaluated the noise characteristics in microtomograms of sandstone, to develop a three dimensional, iterative, denoising framework, based on nonlocal means neighbourhood filtering (NLM). Our extension of the algorithm handles typical artefacts in high resolution tomography of hard matter materials, such as line and ringing artefacts. Our approach provides a minimally invasive restoration of tomography reconstructions from crystalline materials and allows their deconvolution without the need for excessive regularization.

Introduction

Acquiring synchrotron images takes a lot of effort. If we want to be quantitative rather than qualitative in the analysis of these data, we should have the same standards in processing the data as we have in acquiring them. This is especially important for materials where nanometre scale details are important. Especially in such cases, image processing ought to be a restoration procedure rather than a mere sequence of steps where images are enhanced. As a matter of principle, this means that we need model assumptions for the formation of the image noise and impulse response in the reconstructions so that the image formation process can be treated as an inverse problem.

From an image processing point of view, sandstone is simpler than more fine grained natural materials, such as chalk. Therefore, sandstone constitutes an ideal environment for developing image restoration methods geared toward application with tomographic reconstructions of reservoir rock. Compared with chalk, the sandstone particle scale is much larger. Aside from the much larger pores that are relatively easily resolved, the characteristics that simplify tomogram reconstructions of sandstone are: (i) a crystalline structure with clearly identifiable interfaces between pores and solid and (ii) a range of minerals, each with their own X-ray attenuation coefficients. These characteristics can be used to set up efficient models that determine the noise characteristics and the impulse response function from the reconstruction to be used for signal restoration, which we have outlined in this sample study.

Materials and Image Acquisition

All data were recorded on samples chosen from drill cores of sandstone from the North Sea. The reservoir did not behave as was predicted from the well log analysis so we explored for the reason using high resolution imaging. Here we present reconstructed tomograms of four samples, one each taken from an oil zone (I-O), a transition zone (II-T), a water zone (III-W), and a carbonate cemented zone (IV-C). Microtomograms were recorded at the TOMCAT beamline at the Swiss Light Source at 21.5 keV using a detector with 2560 by 2160 pixels, with a size of 650 nm, and exposures of 250 ms. Reconstructions were based on 1501 projections using the Gridrec algorithm [1]. Smoothing during reconstruction was minimized (Shepp-Logan filter [2]). Therefore, reconstructions are very detailed but suffer from a comparable high level of noise. All processed volume images were subvolumes of the recordings, cropped to 1024 x 1024 x 1024 voxels (Figure 1).

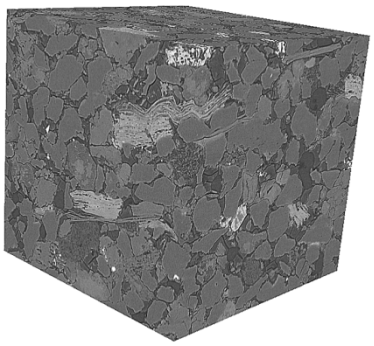

Fig. 1. *Volume rendering of the mineral phase in the processed 1024^3 voxel tomography reconstruction of Sample I-O.*

Noise Level Estimation

Notably, noise in reconstructed data is a mapping of the detector noise from Radon space to the reconstruction, i.e., it is neither Poissonian nor fully uncorrelated. Additional line artefacts are caused by the presence of highly attenuating minerals that result in abrupt changes of the attenuation coefficient. Based on the literature, we expected an exponential relationship between the signal intensity and the local noise level [3]. Its characterization is facilitated by the piecewise constant layout of the crystalline samples. A data driven approach was used, that plots local signal intensity for low gradient patches vs. signal variance and provides a lower boundary fit to the data (Figure 2).

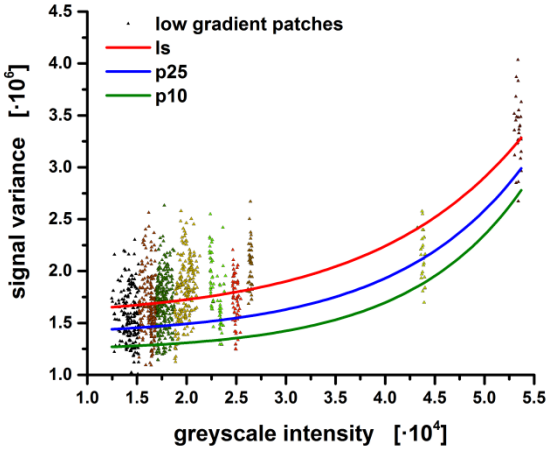

Fig. 2. *The signal dependent noise level modelled for Sample I-O. Data are low gradient patches of 15 x 15 voxels clustered for a weighted fit of the expected exponential noise model: least squares fit (ls, red line) and lower boundary fits: 1st quartile regression (p25, blue line) and 1st decile regression (p10, green line).*

Denoising Method

Nonlocal means (NLM) is a neighbourhood filter that makes use of redundant image information. This makes it an optimal choice for denoising crystalline structured data. It was developed by Buades, Coll and Morel in 2005 [4] and provides a weighted average of voxels using a distance measure between patches of voxels. The weight, w, of location, x_j, for denoising the voxel at location, x_i, is defined as:

$$w(x_i, x_j) = \frac{1}{Z_i} \exp\left(- \frac{\left\| u(N_i) - u(N_j) \right\|_{2,a}^2}{h^2} \right),$$

where Z represents a normalization constant, u, the noise corrupted signal, N, a patch, i.e. it depicts the neighbourhood of a location, $\|\cdot\|_{2,a}^2$ represents the distance measure defined as L_2 norm convolved with a Gaussian kernel of standard deviation, a, and h represents a smoothing parameter [5].

In a recent review, Schlüter et al. [6] promoted the use of nonlocal means denoising with tomography data from rocks. They evaluated the denoising quality from synthetic images with added Gaussian noise and artefacts. Denoising parameters were chosen deliberately high, illustrating that NLM would be capable of handling artefacts as well. Yet, with a carefully chosen noise level this should not be the case in a one-step approach but it would be the result of smoothing, i.e., lost signal information. It is however possible to modify the NLM algorithm to selectively remove textures to the given noise level and still preserve the detailed surfaces found in mineral structures. For that we have to investigate the parameters used in the algorithm and adjust its application to textures.

Smoothing parameter (h): To be restorative h has to be linked to the local noise standard deviation, s, that we provide as a precomputed map. It has been shown that for modest noise levels, h and s can be used interchangeably [5].

Patch layout: In a crystalline medium, the signal is piecewise constant, i.e. a voxel is either within, at a surface of or outside an object. Gradients are merely a result of limited resolution and are therefore uniformly distributed along the edges of an object. This is an important distinction from soft matter materials, where larger patches are needed to characterize complex gradients. It implies, given a modest noise level, that redundancy of information would be high and that the immediate 6 neighbours of a voxel are sufficient for its characterization. Still, 3D information cannot be neglected. Smaller patches also assure that rare surface structures are not smoothed or obliterated by the lack of redundancy. Thus, we constructed our denoising algorithm to handle three dimensional spherical patches. It is most efficient with a patch radius of 1 voxel.

Search space layout: The theory of NLM requires weighting all voxels. In practise, search spaces larger than the typical object size provide no further improvement in denoising quality. It is desirable to limit the computational burden by limiting the size of the search space. Technically, limiting the search space to two dimensions could suffice for tomography denoising because slices in a tomography reconstruction are reconstructed independently. This means, ideally there is no correlation in the noise between slices. Still, the highest redundancy can be expected in adjacent regions, making 3D information valuable. We experienced optimal performance when using ellipsoidal search spaces by incorporating neighbouring slices for denoising.

Texture removal: We assume that the noise level estimate results from flat or untextured patches. It provides a threshold for textures that can be associated to the object and textures that result from imaging artefacts. NLM is unable to remove artefacts

because of their reoccurrence and the denoising quality with experimental data is unsatisfactory (Figure 3). For uncorrelated noise, applying NLM iteratively allows refining the distance measure. The noise level has to be adjusted at every iteration step. Skipping the adjustment step would remove textures up to the initial noise level. Yet, given the lower boundary fit for the noise level estimate as information cut off, all signal information that can be discerned from the artefacts would be preserved at convergence. In most cases, with minor artefacts, two denoising iterations are sufficient, resulting in a denoising scheme as outlined in Figure 4.

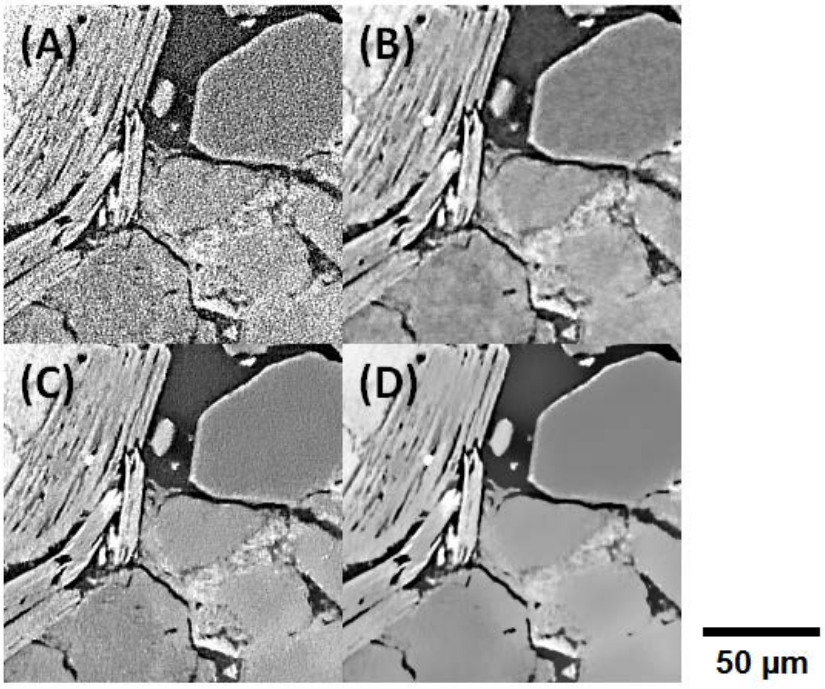

Fig. 3. *Zoom (220 x 220 pixels) from a reconstructed tomography slice from Sample II-T (A). The image is corrupted by weakly correlated noise and line artefacts. Denoising results are compared for iterative wavelet shrinkage (B), three dimensional nonlocal means (C) and our suggested algorithm (D).*

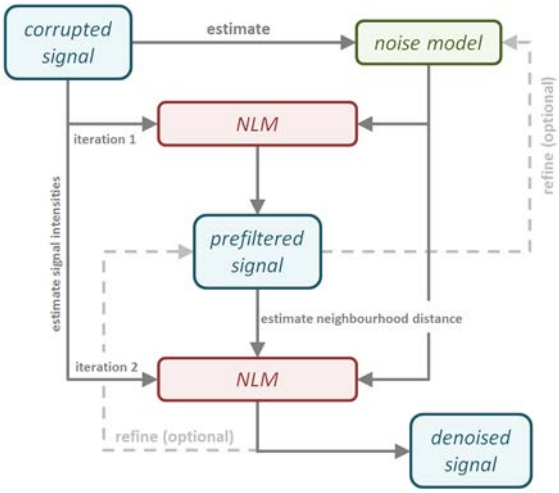

Fig. 4. *Denoising scheme for the controlled removal of reconstruction artefacts.*

Results and Analysis

Figure 3 compares our new method for controlled artefact removal with iterative wavelet shrinkage [7] and one step NLM denoising [4,5]. Because the latter methods assume random noise, the denoising results for tomography reconstructions are unsatisfactory. Note that using a conservative noise estimate for a two-step denoising approach allowed restoring a constant signal intensity level within the grains and void regions of the sample while preserving the details in the fine structured regions of the rock (e.g. the clay booklet in Figure 4D). The intensity distribution of the input signal was unimodal whereas the denoised signal shows several distinct bands (Figure 5A). This already enables basic quantitative analysis by assigning phases based on their X-ray absorption capacity. It is now a simple multithresholding task for the samples considered. It is possible to identify oil components and carbonate cementation, progressing through the imaged zones (Figure 5B). Therefore, high yield, oil rich zones in the sandstone can be distinguished from already depleted zones or zones where residual oil is located in regions of low permeability.

In nanotomographic reconstructions of chalk where resolution is considerably higher, approaching ~100 nm, addressing artefacts becomes an increasing concern because the intensity of ring artefacts increases. Fortunately, transferring our method to other finer structured reservoir rocks is straightforward. The signal preserving layout of the denoising approach even allows for soft deconvolution of such high resolution samples without the requirement for regularization. That provides us with an important advantage for the future analysis of fine grained natural porous media.

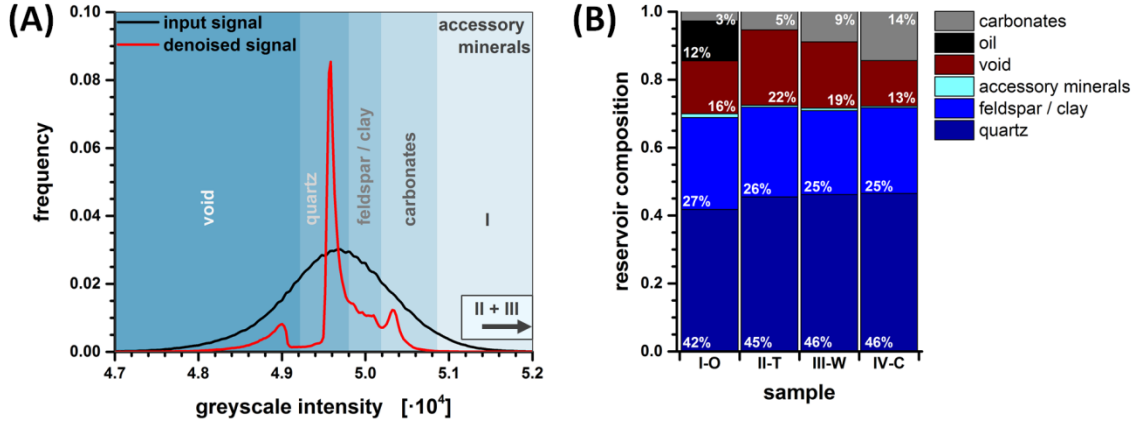

Fig. 5. *Histogram of Sample IV-C before and after application of the proposed denoising framework. Mineral phases were assigned using Multi Otsu thresholding.*

References

[1] Marone, F., Stampanoni, M. (2012). *Regridding reconstruction algorithm for real-time tomographic imaging*, ***J. Synchr. Rad.*** 19, 1029–1037.

[2] Shepp, L.A., Logan, B.F. (1974). *The Fourier reconstruction of a head section.* ***IEEE Trans. Nucl. Sci.*** Ns–21, 21-43.

[3] Faulkner, K., Moores, B.M. (1984). *Noise and contrasat detection in computed tomography images*, ***Phys. Med. Biol.*** 29, 329–339.

[4] Buades, A., Coll, B., Morel, J.M. (2005). *A review of image denoising algorithms, with a new one*, ***Multiscale Model. Simul.*** 4, 490–530.

[5] Coupé, P, Yger, P., Prima, S., Hellier, P., Kervrann, C., Barillot, C. (2008). *An optimized blockwise nonlocal means denoising filter for 3-D magnetic resonance images*, ***IEEE T. Med. Imaging*** 27, 425–441.

[6] Schlüter, S., Sheppard, A., Brown, K., Wildenschild, D. (2014). *Image processing of multiphase images obtained via X-ray microtomography: a review*, ***Adv. Water Resour.*** 50, 3615–3639.

[7] Luisier, F., Vonesch, C., Blu, T., Unser, M. (2010). *Fast interscale wavelet denoising of Poisson-corrupted images*, ***Signal Process.*** 90, 415–427.

Ackowledgements

Funding for the restoration work came from P^3, a project supported by the Innovation Fund Denmark,Maersk Oil and Gas A/S for the data collection, from Dong Energy A/S, who also provided the samples.

Porosity assessment of sandstones of the Potsdam Group, St. Lawrence Platform, Québec, Canada: utilisation of the CT scanning techniques

J.-F. Grenier*[1], M. Malo*[2], B. Long, D[3], D. Lavoie[4]

[1] INRS-ETE, 490 de la Couronne, Québec, Canada, G1K 9A9 – jeanfrancoisgrenier@hotmail.com
[2] INRS-ETE, 490 de la Couronne, Québec, Canada, G1K 9A9 – michel.malo@ete.inrs.ca
[3] INRS-ETE, 490 de la Couronne, Québec, Canada, G1K 9A9 – bernard.long@ete.inrs.ca
[4] Geological Survey of Canada, 490 de la Couronne, Québec, Canada, G1K 9A9 – Denis.Lavoie@RNCan-NRCan.gc.ca
* presenting author

Keywords: CT scan, sandstone, Potsdam, St. Lawrence platform, CCS

Abstract

Tomodensitometry was used to evaluate the porosity of sandstones of the Potsdam Group in the St. Lawrence Platform in Québec. The heterogeneous lithologic siliciclastic sub-units of the Covey Hill Formation exhibit porosity ranging from 1 to 10%, whereas arenite of the Cairnside Formation shows a more regular porosity between 3,6 to 7,1%. The porosity values from tomodensitometry are usually lower than those obtained from porosimetry, whereas there is a good correlation with those calculated from the density log.

Introduction

Carbon Capture and Storage (CCS) is considered by the Intergovernmental panel on climate change (IPCC, 2005), as well as by the International Energy Agency (IEA, 2008), as a mitigation option for reducing anthropogenic carbon dioxide (CO_2) emissions from the industrial sectors in response to climate change. Geological storage in porous and permeable rocks, such as sandstone and carbonate within sedimentary basins, is one of the best options investigated in many countries. In 2010, an assessment of sedimentary basins in Québec was conducted to identify the best geological formations for CO_2 geological storage (Malo and Bédard, 2012). The Potsdam Group, the basal lithostratigraphic unit of the St. Lawrence Platform basin, overlying the Precambrian basement, represents the best target for CO_2 geological storage in the Province of Québec (Malo and Bédard, 2012; Bédard et al., 2013). The sandstones of the Potsdam Group, already known for their deep aquifers containing brines, represent a good candidate for CO_2 geological storage. This research project lingered on the well A-203 that has been drilled in 1986, near the town of Sorel-Tracy, Québec, Canada (Figure 1) to better assess the Potsdam sandstones porosity. The well A-203 was cored from the surface to the Precambrian basement and it represents the most complete and uninterrupted succession of the platform stratigraphic sequence in Québec.

Geological background

In the Well A-203, the Potsdam is cored from the base of the overlying Beekmantown Group, 1158 m, to the top of the underlying basement at 1738 m. The group is comprised of two formations, the Covey Hill and Cairnside. The Covey Hill is composed of quartz-feldspar-pebble conglomerate, feldspathic and quartz arenites with shale and

siltstone intervals, interpreted in the study area, as deposited in a terrestrial to fluvial and estuarian environments. The Cairnside is composed of a fine- to coarse-grained, massive to laminated and well-sorted quartz arenite deposited in a littoral to marine environment.

The Covey Hill Formation in the well was divided into three sub-units. CV1, at the base (1738 to 1672 m), and CV3 (1359 to 1270 m), at the top of the Covey Hill Formation are two heterogeneous sub-units with various siliciclastic rocks, conglomerate, sandstone, siltstone and shale. The middle CV2 sub-unit consists of medium- to coarse grained quartz and feldspathic arenite with local siltstone intervals. The Cairnside Formation is a homogeneous fine- to coarse-grained quartz arenite of 142 m thick.

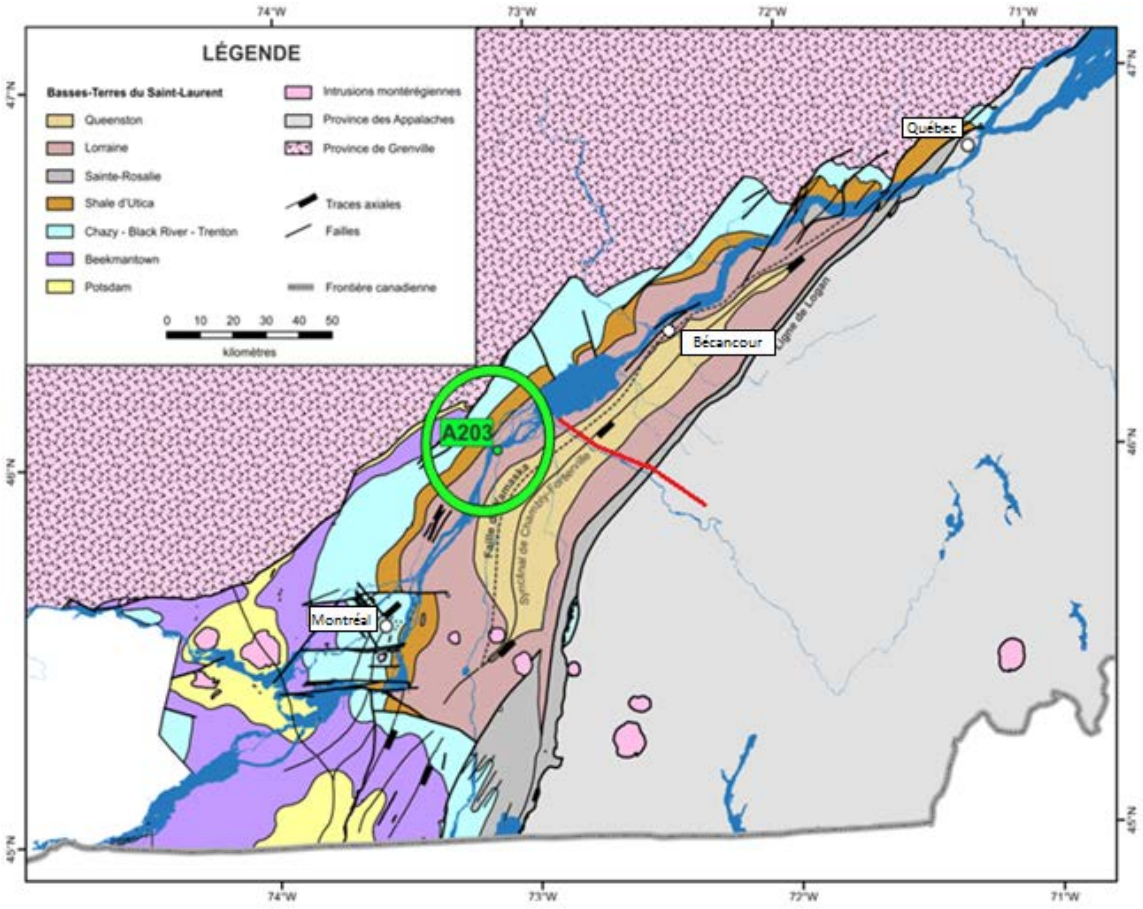

Figure 1 –Geology of southern Québec and localisation of Well A-203.

Methods

The porosity of the core was evaluated by three methods: density log diagraphy in well, porosimetry, and a medical CT scanner (Siemens SOMATOM Sensation 64). The first technique can be considered as a mean porosity measurement on small intervals of depth, whereas the latter techniques can be considered as punctual porosity measurements (Figure 2). The porosimetry is an analytical technique that evaluates porosity of a chosen rock sample using a non-wetting liquid that is intruded at high pressure into the sample (Figure 2). The value of porosity with the CT-scan in this study is also given for a specific zone on the core (Figure 2). This difference between a mean value for an interval of depth (density log diagraphy) and punctual values may prevent

comparisons of porosity values between these methods, particularly when density-log diagraphy is used in shales or alternating shale and sandstone beds where the resulting log diagraphy has not enough resolution for assessing porosity because thin beds are not necessarily measured individually. The sandstone samples used in the CT-scan were collected adjacent to samples where a porosity value from the porosimetry technique was performed (Fleury, 1988). We made a petrographical thin section of each sample for determining the mineralogical composition of the rock in the CT-scan data files. The quartzite to subarkosic arenite compostion composition determined on thin section was considered similar to the CT-scan data files. Moreover, samples from the bottom of CV1 unit contained calcite cement in different proportions. Those characteristics were taken into consideration in the calculation of porosity, using this equation:

$$\varphi = 1 - \left(\frac{Hu_{moy} + 1024}{Hu_{\max} + 1024} \right),$$

where HU_{moy} corresponds to the mean Hounsfield Unit measurement taken on an area of a scanned core slice and HU_{max}, the theoretical maximal Hounsfield measurement on the sample. In this study case, the maximal theoretical HU measurement corresponded to a quartz value of 1798 HU for all arenites, and adjusted to a calcite value of 2300 Hu for samples that contained it. Results for the Cairnside Formation are shown in figure 2.

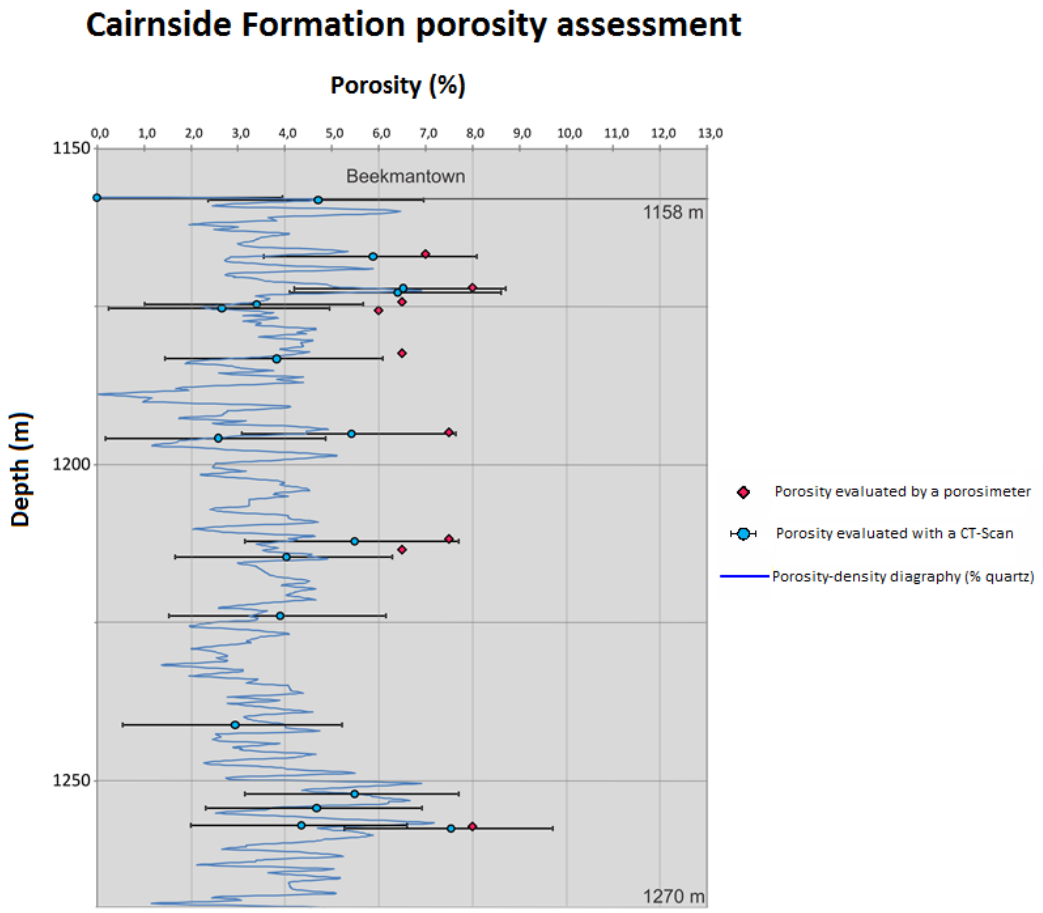

Fig. 2 : Porosity assessment in Cairnside Formation in borehole A-203

Results

Mean porosity values obtained for the four different units identified in the Potsdam Group are synthetized in the table below:

Table 1 Mean porosities (%) obtained by three methods

	Mean porosity (%)		
	Diagraphy	Porosimeter	CT-Scan
Cairnside CA	3.6	7.1	4.7 ± 2.5
Covey Hill CV1	2.0	4.0	2.0 ± 2.5
Covey Hill CV2	3.9	10.0	4.0 ± 2.3
Covey Hill CV3	1.0	5.5	4.7 ± 2.7

The two more heterogeneous lithologic CV1 and CV3 sub-units show low porosity usually below 2% on the diagraphy log and higher porosities from the porosimetry and the CT-scan techniques. The same difference is observed for the mean porosities of the CA and CV2 units where the CV2 sub-unit exhibits mean porosity of 3.9% and of 3.6% for the CA sub-unit, whereas porosimetry values are higher and those from CT-Scan are higher but comparable. The comparison must take into account that the CV1 and CV3 sub-units are composed of an alternance of shale and sandstones, which affect the diagraphy log resolution and can induce noise and variability on the density-porosity log. More homegenous arenites of the CV2 sub-unit of the Covey Hill Formation and of the Cairnside Formation (CA sub-unit) show more regular porosities (Figure 2).

Conclusion

The porosity values from tomodensitometry are usually lower than those obtained from porosimetry, whereas there is a good correlation with those calculated from the density log. An element of answer to explain this gap may be explained by the fact that the porosimetry technique is a precise measurement of the effective porosity whereas the density-porosity log and CT-scan assessments depend of the resolution of the apparels used, which can be considered as not high enough to allow a direct comparison with the porosities measured with the porosimeter.

On the carbon storage capacity perspective in the Potsdam Group, the stratigraphy observed in the A-203 well shows two main depth intervals with better porosities in the sub-units CA and CV2, However, these two potential reservoirs are separated by beds or lens of shales as observed in the CV3 sub-unit. On a global scale, this heterogeneity of the formations may reduce the regional injection capacity (volume of available pores) for CO_2 geological storage within the Potsdam Group.

References

Bédard K., Malo M. & Comeau F. (2013). CO_2 geological storage in the Province of Québec, Canada : Capacity evaluation of the St. Lawrence Lowlands basin. ***Energy Procedia*** 37: 5093-5100.

Fleury A. (1988). Évaluation pétrophysique du puits Tioxyde Tracy No.1. Ministère de l'Énergie et des Ressources du Québec, 19p.

IEA (2008). *CO_2 capture and storage: a key carbon abatement option*. OE CD/IEA, Paris.

IPCC (2005). *Intergovernmental panel on climate change special report on carbon dioxide and storage*. Cambridge University Press, Cambridge, New York.

Malo M. & Bédard K. (2012). Basin-scale assessment for CO_2 storage prospectivity in the Province of Québec, Canada. ***Energy Procedia*** 23: 487-494.

Sanford B.V. & Arnott R.W.C. (2010). Stratigraphic and structural framework of the Potsdam Group in Eastern Ontario, Western Quebec, and Northern New York State. ***Geological Survey of Canada Bulletin*** 597, 84p.

Deriving a 3D Map of Sub-Resolution Pores in Rock Samples from X-ray Micro-CT and SEM Data

I.A. VARFOLOMEEV[1,2], B.D. SHARCHILEV[1], D.A. LISICIN[1,2], *I.V. YAKIMCHUK[1]

[1] Schlumberger, Moscow, Russia
[2] Moscow Institute of Physics and Technology, Dolgoprudny, Russia
* presenting author

Imaging of rock samples always experiences the problem of multiscale structural features. Any imaging techniques can lose some peculiarities that are below the resolution or above the field of view. This is essentially true for rock samples where it is hard to conduct completely independent single scale studies. All scales from nanometers to meters may affect rock physicochemical and petrophysical properties. For example, hydrodynamical behavior of a conventional oil and gas reservoir at the pore scale level is influenced by the micron size pores in a cubical millimeter size of a structural volume. At the same time, nanometer scale clay particles, thin oil/water films on the pore space surface play a significant role in the oil and gas recovery process and affect wettability and permeability of the porous structure. Besides, in order to take into account the heterogeneity of the media and connectivity of specific regions, it is often required to consider scales from centimetres up to meters.

This work is focusing on a technique that was developed to derive spatial distribution of rock pore space that is not resolved in X-ray micro-CT experiment. It is based on a laboratory porosity measurements and a special processing of reconstructed micro-CT images. Additionally, high-resolution images from scanning electron microscopy (SEM) may be utilized in order to fine-tune the procedure. Furthermore, SEM images provide better understanding of structure and connectivity of non-resolved parts of the pore space.

The proposed approach comprises two options. (1) A pore structure model of a sample, obtained using X-ray micro-CT, and laboratory measured porosity values that are used to create a 3D digital rock model, that takes into account both resolved and unresolved pores. This is achieved by fitting image “porosity” calculated from segmented 3D micro-CT image to the laboratory measured porosity. During this procedure voxels are considered as mixture of solid and void phases with the proportion corresponding to the local X-ray attenuation. Proper registration of the high-resolution SEM 2D images of the sample with virtual slice of 3D micro-CT image allows to adjust parameters of correspondence between greyscale levels and subvoxel porosity values. (2) Having registered 2D SEM with 3D micro-CT images of the same sample, it is possible to use machine learning techniques for further classification of the whole 3D image. Both options result in the construction of 3D map (or a model) of sub-pore resolution.

The model obtained is suitable for further calculation of various physical properties of a sample (Digital Rock concept). For example, in a tight oil and gas reservoirs large pores are usually connected with each other via a network of small void channels non-resolvable by X-ray micro-CT. Due to this fact, numerical simulation of electrical conductivity on a conventional binary (voids and solids) models, which incorporate only the large pores, results in overestimation of the sample resistivity, while the method described herein provides much more adequate results.

Number of words: 474

ICTMS 2015

ictms2015.ete.inrs.ca

Lab CT Scan

Laboratoire multidisciplinaire de tomodensitométrie
pour les ressources naturelles et le génie civil

ctscan.ete.inrs.ca

INRS

UNIVERSITÉ DE RECHERCHE
A RESEARCH UNIVERSITY

inrs.ca